Springer Proceedings in Energy

Mohammad O. Hamdan
Hassan A. N. Hejase
Hassan M. Noura
Abbas A. Fardoun *Editors*

ICREGA'14 - Renewable Energy: Generation and Applications

Springer

Springer Proceedings in Energy

For further volumes:
http://www.springer.com/series/13370

Mohammad O. Hamdan
Hassan A. N. Hejase · Hassan M. Noura
Abbas A. Fardoun
Editors

ICREGA'14 - Renewable Energy: Generation and Applications

Springer

Editors
Mohammad O. Hamdan
Faculty of Engineering, Department of Mechanical Engineering
United Arab Emirates University
Al Ain
United Arab Emirates

Hassan A. N. Hejase
Hassan M. Noura
Abbas A. Fardoun
Faculty of Engineering, Department of Electrical Engineering
United Arab Emirates University
Al Ain
United Arab Emirates

ISSN 2352-2534 ISSN 2352-2542 (electronic)
ISBN 978-3-319-05707-1 ISBN 978-3-319-05708-8 (eBook)
DOI 10.1007/978-3-319-05708-8
Springer Cham Heidelberg New York Dordrecht London

Library of Congress Control Number: 2014942276

Printed on acid-free paper

Springer is part of Springer Science+Business Media (www.springer.com)

Preface

The third international Conference on Renewable Energy, Generation and Applications 2014, organized by the Faculty of Engineering, UAE University, is the third conference in a new series of important meetings and technical forums, with the first conference held in March 2010 and the second in March 2012. These conferences aim at gathering scientists and engineers from academia and industry to discuss the latest developments and innovations in the area of renewable energy. They further provide an opportunity to assess the challenges and the future of renewable energy technologies worldwide.

The interest in Renewable energy has gained a lot of attention in the last decade due to environmental reasons, such as greenhouse abatement and ozone layer protection and economic and strategic ones, such as the limited fossil fuel. United Arab Emirates has committed to produce about 20 % of its energy consumption from renewable energy by 2020. To achieve this objective many renewable energy projects are currently going on in the UAE.

ICREGA'14 features an outstanding group of keynote speakers addressing significant topics in the applications of renewable energy. In addition, the conference also includes three technical workshops.

The current conference attracted a large participation from universities and industry from 19 different countries. A total of 79 papers have been submitted, among which 70 papers are accepted for presentations. A total of 15 % of the accepted conference papers will be selected to be considered for publication in the "Renewable Energy" Journal published by Elsevier Publishers. In addition, 26 student posters will also be presented at the conference.

We are committed on organizing this conference every 2 years, and believe that it will continue to grow in importance and size.

Contents

Chapter 1
The Potential of Castor as a Biodiesel Feedstock Crop for the Arabian Peninsula

Kiran Menon, S. Irshad Ahmed, Neeru Sood and Nanduri K. Rao

Abstract There is an increasing need to turn to biofuels to meet growing world fuel requirements. Oil-rich regions such as the Arabian Peninsula should be no exception in exploring alternative, renewable and environment-friendly fuel options in order to decrease their dependency on non-renewable fossil fuels. In this study we have carried out field trials of castor (*Ricinus communis*) in order to assess its suitability as a biodiesel feedstock crop in the region. We have also studied the response of 11 hybrid accessions of castor to three saline irrigation water treatments (5, 10 and 15 dS/m) and determined that castor can tolerate up to 5 dS/m salinity in irrigation water without any negative effect on oilseed yield.

Keywords Castor · Biodiesel feedstock · Salinity tolerance

1.1 Introduction

Castor (*Ricinus communis* L.) is a member of the Euphorbiaceae family. It is a perennial plant growing to a height of 2–3 m. The fruit is a globose capsule, 2.5 cm in diameter, usually containing three seeds. Yields of up to 5,000 kg/ha have been reported under irrigated conditions, but they can be less without adequate moisture [1]. In India, castor is cultivated in marginal lands and under rainfed conditions and so productivity is limited to around 1,200 kg/ha. In the wild, castor is able to adapt to arid conditions and withstand long periods of drought [2]. Castor seeds contain up to 60 % oil which is inedible. This makes it an ideal candidate for bio-diesel

K. Menon (✉) · S. I. Ahmed · N. Sood
Department of Biotechnology, Birla Institute of Technology and Science Pilani, Dubai Campus, Dubai, United Arab Emirates
e-mail: p2011003@dubai.bits-pilani.ac.in

N. K. Rao
International Center for Biosaline Agriculture, Dubai, United Arab Emirates

M. O. Hamdan et al. (eds.), *ICREGA'14 - Renewable Energy: Generation and Applications*, Springer Proceedings in Energy, DOI: 10.1007/978-3-319-05708-8_1,

production due to the absence of competition with food crops. Bio-diesel from castor oil has properties such as very low cloud point and pour point which make it suitable for use in extreme winter temperatures. A single reaction step is required for the trans-esterification process of castor oil because of its favorable acidity level. Therefore, in a large-scale process, it would be less costly to produce bio-diesel from castor seeds than with others with a higher acidity level. The properties of the B100 (100 % biodiesel) combustible and its B10 and B20 blends (10 % and 20 % bio-diesel blends in petroleum diesel respectively) are comparable to those of petroleum diesel and acceptable within international bio-diesel standards (ASTM D 6751) with the exception of viscosity and humidity of B100 [2].

The countries in the Arabian Peninsula are at present entirely dependent on fossil fuels to meet increasing energy requirements. Oil and gas reserves will be depleted in the next 30–35 years [3]. According to the World Resources Institute, countries of this region such as Kuwait and UAE have some of the highest greenhouse gas emissions per capita as of the year 2010 [4]. Due to these reasons, the local governments have been taking serious initiatives for the reduction of carbon footprint and investing in alternative fuels.

There is also presently great interest worldwide in the use of marginal lands for the production of biodiesel feedstock crops because all arable lands need to be employed in meeting world food requirements. More than 6 % of the world's land area is affected by salinity [5]. Salts accumulate in soil over a period of time due to the weathering of parental rocks, which releases soluble salts of various types, mainly chlorides of sodium, calcium, and magnesium, and to a lesser extent, sulfates and carbonates [6]. Salinity is of increasing concern in the region due to overexploitation of groundwater, which is leading to a disturbance in the balance between sea and groundwater and deterioration of groundwater quality [7]. There have been reports on the salinity tolerance of castor, with some varieties being touted as more tolerant to salinity and sodicity than others [8, 9]. A few other studies however report that castor is sensitive to salt stress and that this may be due to a lack of efficient activity of guaiacol peroxidase and catalase enzymes, which probably leads to imperfect H_2O_2 scavenging [10]. Salinity levels above 10 dS/m have also been seen to affect the germination of castor seeds [11]. In this study we report the results of a field trial to assess the salinity tolerance and the suitability of UAE's growing environment for the large-scale production of castor oilseeds.

1.2 Materials and Methods

1.2.1 Field Trials

Eleven hybrid accessions of castor obtained from Vibha Seeds^{TM}, Hyderabad, India were used in this study, conducted at ICBA research station (25.09°N, 55.38°E) during the cropping season 2012–2013. The soils of the experimental site were sandy with very low organic matter, hence, farm yard manure was added at

the rate of 40 tons/ha to improve the fertility. A Completely Randomized Block Design (CRBD) with three replications was used to evaluate the performance of the eleven hybrids. The seeds were sown in field plots, each of 4 rows of 3 m, with a distance of 50 cm both between the rows as well as between the plants within the row. Three salinity treatments with electrical conductivities (ECw) of 5, 10, 15 dS/m were established by mixing saline ground water (22–25 dS/m) with sweet water (3–0.5 dS/m), in addition to the control treatment, irrigated with low quality municipal water having an electrical conductivity of 0.3–0.5 dS/m. The plants were irrigated twice daily by drip irrigation at the flow-rate of 4 l/h per dripper.

From each plot, five plants were selected randomly and tagged for recording observations, which included qualitative traits such as growth habit, stem color, leaf color, spike type, spike compactness, waxy coating, fruit surface and fruit dehiscence, and quantitative traits such as plant height, number of branches, stem diameter, leaf surface area, leaf dry weight, leaf specific weight and moisture content, leaf chlorophyll content, spike length, number of spikes and fruits per plant, fruit size, seed yield and 1,000 seed weight.

1.2.2 Leaf Measurements

The leaf at the node of the primary inflorescence was chosen as a standard for all leaf measurements. Leaves from five plants in each plot were harvested at maturity and images were captured against a marked scale. In all instances, the surface area was determined using the ImageJ Image processing and the analysis software provided as freeware by the National Institutes of Health (NIH), US, which is a benchmark tool for image analysis and area measurements [12–14]. Leaf dry weight was recorded after the collected leaves (five from each plot) were washed in tap water to remove dirt and dried in a ventilated oven at 80 °C for up to 96 h until all the moisture had been removed and a static weight was reached. Leaf punches of 4 cm^2 surface area were weighed for specific weight values. The punched sections were then dried at 60 °C till a static weight was attained to obtain the dry weight. These values were then used to determine standard leaf weight (SLW) and moisture content (%) [15]. Leaf chlorophyll content (a, b and total) was estimated using the Mackinney method that was described in 1941 [16], improved by Arnon in 1949 [17], which is still the most widely used method for simple chlorophyll quantification [18].

1.2.3 Soil and Water

Five soil samples each were collected from the root zone of all four treatment plots. The pH of saturated soil paste was recorded using a pH meter. The salinity readings were recorded using a Conductivity Meter. Irrigation water samples were collected from each treatment to measure the pH and EC values.

1.2.4 Seed Oil Content

Oil was extracted using n-Hexane for solvent extraction using a Soxhelet apparatus. Oil weight was measured periodically and extraction was stopped when static weight was obtained.

1.2.5 Leaf K^+/Na^+ Ratio

Castor leaves (from the node of the primary inflorescence, 5 samples per plot), were dried at 80 °C till a static weight was observed (to remove all moisture). Dried leaves were ground using mortar and pestle and weighed samples were wet digested using concentrated HNO3 for 48 h. Leaf extract was filtered using ashless filter paper and analyzed using Inductively coupled plasma/optical emission spectrometry (ICP-OES). K^+ and Na^+ concentrations in leaf extracts were determined by ICP OES and K^+/Na^+ ratios calculated.

1.2.6 Ion Concentrations in Irrigation Water

Na and K ion concentrations (average of 5 samples for each treatment) in irrigation water were determined by flame photometry.

1.2.7 Statistical Analysis

Analysis of variance (two-factor ANOVA) was used to identify the traits that differed significantly among the accessions and those significantly affected by salinity, with the limit for statistical significance set at $p = 0.05$. Seed yield is expressed in kilograms per hectare based on extrapolation of the average yield of the five plants from each plot and assuming a stand of 36,000 plants per hectare, at the same density in the current field trial.

1.3 Results and Discussion

The results show that qualitative traits such as leaf and stem color and growth habit were not affected by salinity and stayed the same for any given accession across the different saline treatments. In contrast, quantitative traits were significantly affected when irrigated with saline water as revealed by the analysis of variance.

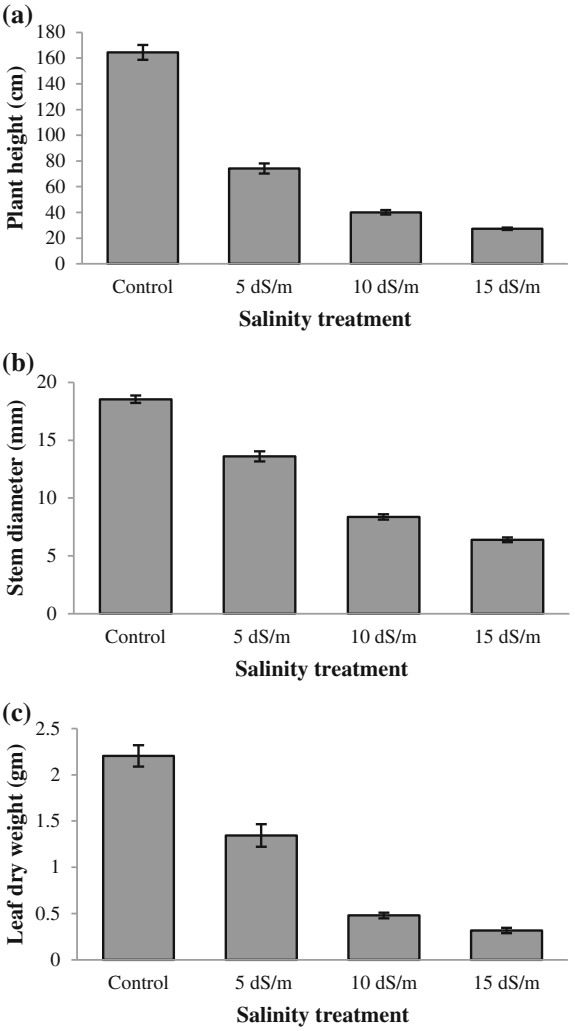

Fig. 1.1 Decrease in plant height (**a**), stem diameter (**b**) and leaf dry weight (**c**), with increase in salinity. Variance of data is denoted by standard error bars

Thus, compared with the control, plant height, stem diameter and leaf dry weight have all decreased considerably when irrigated with saline water (Fig. 1.1). As with many other abiotic stresses, plant growth is inhibited by salinity. A possible reason is stomatal closure resulting in decreased uptake of carbon dioxide and reduced photosynthesis or inhibition of cell growth and division [19]. The direct effects of salinity stress on cell expansion and division are not yet fully understood. In our study however, the rapid and extreme response of the plants in the 10 and 15 dS/m treatments suggests that the osmotic stress at such high salinity induces a stress response and stalling of growth in these plants. This is because high salinity in the root area decreases the plants capability to absorb water (osmotic stress) [20]. Within each treatment, the differences among the accessions were found to be

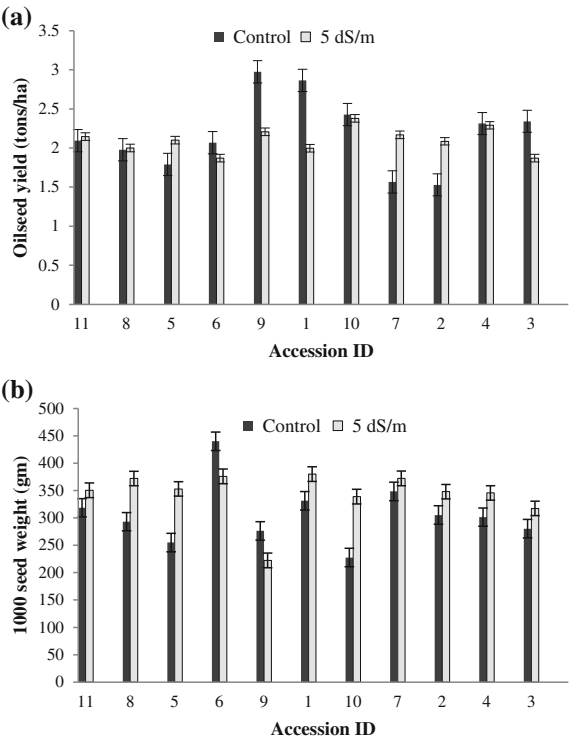

Fig. 1.2 Oilseed yield (**a**) and 1,000 seed weight (**b**) values for control and 5 dS/m treatments

insignificant. Analysis of variance also showed significant effect of salinity on leaf surface area, primary inflorescence length and leaf moisture content (data not presented). The reduction in leaf are is expected, as this reduces the amount of water used up by the plant. Compared to the control, leaf chlorophyll content increased in the 5 dS/m treatment and then decreased in the 10 and 15 dS/m treatments. The reasons for this were not clear, but further analysis needs to be carried out to confirm these findings.

With regard to seed yield and 1,000 seed weight, the results show that castor could tolerate salinity of up to 5 dS/m without a statistically significant decrease (Fig. 1.2). ANOVA results show that the difference in yield is not statistically significant between the freshwater and 5 dS/m treatments. The differences in yield of individual accessions (a decrease of yield in accession nos. 9 and 1 but increase in 7 and 2) can be attributed to genetic variation and associated differences in response to stress, but these differences are not of statistical significance. In the 5 dS/m salinity treatment, the seed yields were between 1.8 and 2.3 tons/ha for different accessions while freshwater cultivation yielded between 1.5 and 3 tons/ha of seed. In comparison with the freshwater treatment, seed yield decreased by 66 and 82 % with increase in salinity to 10 and 15 dS/m, respectively. The fact that seed yield is not significantly affected by salinity in the 5 dS/m treatment suggests that the possible ionic stress faced by the plant which results in decreased plant

Table 1.1 Salinity measurements for soil and irrigation water

Treatment	Salinity eC (dS/m)	
	Soil	Water
Control	1.714	0.339
5 dS/m	4.9542	4.68
10 dS/m	12.246	9.16
15 dS/m	18.586	16.06

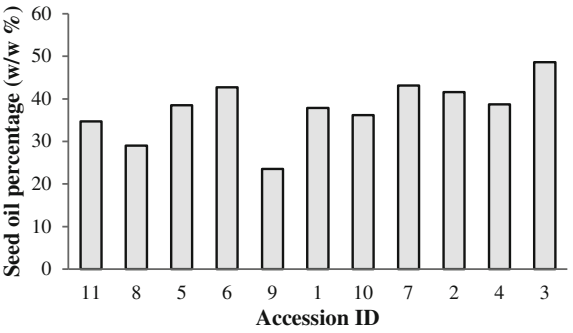

Fig. 1.3 Seed oil content in control treatment (w/w %)

height is not very damaging. Sodium ions may accumulate to an extent enough to reduce the plants' metabolic activity and growth, but not to a toxic level. This result is key because seed yield is the most important parameter in terms of commercial viability of cultivation. Within each treatment, differences between accessions for seed yield and 1,000 seed weight were found to be insignificant.

The marginal effect of salinity of up to 5 dS/m on seed yield may also be largely be due to the fact that sandy soils do not retain salts in the manner that clayey soils do. Our results support this assumption, as it was seen that the soil salinity values were on par with those of the irrigation water even after 6 months of irrigation with saline water (Table 1.1). In contrast, salts corresponding to 1 dS/m could accumulate within 3–7 days in more loamy soils [21].

In the control treatment average seed oil percentage by weight (of oil extracted) was determined to be in the range of 23–48 % (Fig. 1.3). According to literature castor seeds generally contain up to 48 % oil of which 42 % can be extracted [22]. The analysis of seed oil content in other treatments is underway, but preliminary results suggest that the oil content is not affected by salinity.

1.4 Conclusions

The results of our study suggest that castor is a suitable candidate for cultivation as a biodiesel feedstock crop in the UAE and in countries with similar climatic conditions. The yield obtained in this study upon irrigation with water of salinity

5 dS/m is on par with the global average [23]. This supports the possibility of cultivating castor using low-moderately saline groundwater and even recycled wastewater. Since castor is not a food-crop none of the associated food versus fuel conflicts apply to its potential as a biodiesel feedstock crop.

Currently, extraction and analysis of oil from the field trials is in progress. In-depth analysis of the systemic and genetic mechanism of salinity tolerance/sensitivity of castor is also underway. Plant samples are being analyzed to determine the concentrations of various salts in different plant tissues in relation to that of the water and soil in order to understand the specific mechanisms involved in castor's response to salinity. The quantity and quality of oil obtained, efficiency of conversion to biodiesel and fuel performance will also be analyzed in order to confirm that castor seed oil is an economically and qualitatively viable feedstock for biodiesel production in saline environments.

Acknowledgments I would like to thank Dr. Trupti Gokhale and Dr. S. Ramachandran at BITS Pilani - Dubai Campus for their valuable guidance. I also extend my most sincere gratitude to Dr. Mohammad Shahid and Dr. Henda Mahmoudi from the International Center for Biosaline Agriculture (ICBA) for their help and guidance during the course of this study.

References

1. J.A. Duke, *Handbook of Energy Crops*. (Center for New Crops & Plants Products, Purdue University, 1983), Unpublished
2. C. Forero, Biodiesel from castor oil: a promising fuel for cold weather, in *ICREPQ*, Zaragoza (2005)
3. S. Shafiee, E. Topal, When will fossil fuel reserves be diminished? Energy Policy **37**, 181–189 (2009)
4. W. R. Institute, WRI's climate data, WRI [Online] (2010). Available http://cait2.wri.org/wri. Accessed 2013
5. FAO, Land and plant nutrition management service [Online] (2008). Available http://www.fao.org/
6. I. Szabolcs, *Salt-Affected Soils*. (CRC Press, Boca Raton, 1989)
7. Murad, F. Mahgoub and S. Hussein, Hydrogeochemical variations of groundwater of the Northern Jabal Hafit in eastern part of Abu Dhabi Emirate, United Arab Emirates (UAE), Int. J. Geosci. **3**, 410–429 (2012)
8. C.V. Raghaviah, C. Lavanya, T.J. Jeevan, Differential response of castor (Ricinus communis) genotypes to agronomic interventions on salt-affected sodic soils in semi-arid tropical region. Indian J. Agric. Sci. **76**, 19–22 (2006)
9. C.V. Raghaviah, C. Lavanya, S. Kumaran, T.J. Jeevan, Screening castor (Ricinus communis) genotypes for salinity tolerance in terms of germination, growth and plant ion composition. Indian J. Agric. Sci. **76**, 196–199 (2006)
10. M. Janmohammadi, A. Abbasi, N. Sabaghnia, Influence of NaCl treatments on growth and biochemical parameters of castor bean (*Ricinus communis* L.). Acta Agric. Slov. **99**, 31–40 (2011)
11. R. Singh, D.K. Kundu, Soil salinity effect on germination of wheat (*Triticum aestivum* L.), castor (*Ricinus communis*), safflower (*Carthamus tinctorius*) and dill seed (*Anethum graveolens*) in Vertic Ustochrept of Bhal region of Gujarat. Indian J. Agric. Sci. **70**, 559–560 (2000)

12. D.M. Johnson, D.R. Woodruff, K.A. McCulloh, F.C. Meinzer, Leaf hydraulic conductance, measured in situ, declines and recovers daily: leaf hydraulics, water potential and stomatal conductance in four temperate and three tropical tree species. Tree Physiol. **29**, 879–887 (2009)
13. M. Bylesjö, V. Segura, R.Y. Soolanayakanahally, A.M. Rae, J. Trygg, P. Gustafsson, S. Jansson, N.R. Street, LAMINA: a tool for rapid quantification of leaf size and shape parameters. BMC Plant Biol. **8**, 82 (2008)
14. L. Sack, K. Frole, Leaf structural diversity is related to hydraulic capacity in tropical rain forest trees. Ecology **87**, 483–491 (2006)
15. M.J. Steinbauer, Specific leaf weight as an indicator of juvenile leaf toughness in Tasmanian bluegum (Eucalyptus globulus ssp. globulus): implications for insect defoliation. Aust. Forest. **64**, 32–37 (2000)
16. G. Mackinney, Absorption of light by chlorophyll solutions. J. Biol. Chem. **140**, 315–322 (1941)
17. D.I. Arnon, Copper enzymes in isolated chloroplasts. Polyphenoloxidase in Beta Vulgaris. Plant Physiol. **24**, 1 (1949)
18. A. Girma, A.K. Skidmore, C.A.J.M. Bie, F. Bongers, M. Schlerf, Photosynthetic bark: Use of chlorophyll absorption continuum index to estimate Boswellia papyrifera bark chlorophyll content. Int. J. Appl. Earth Obs. Geoinf. **23**, 71–80 (2013)
19. J.K. Zhu, Plant salt tolerance. Trends Plant Sci. **6**, 66–71 (2001)
20. R. Munns, M. Tester, Mechanisms of salinity tolerance. Annu. Rev. Plant Biol. **59**, 651–681 (2008)
21. J. Camberato, Irrigation water quality, in *Update from the 2001 Carolinas GCSA Annual Meeting*, (2001)
22. H.Y. Shrirame, N.L. Panwar, B.R. Bamniya, Bio diesel from castor oil: a green energy option. Low Carbon Econ. **2**, 1–6 (2011)
23. L.S. Severino, D.L. Auld, Seed yield and yield components of castor influenced by irrigation. Ind. Crops Prod. **49**, 52–60 (2013)

Chapter 2
The Effect of Internal Parameters on Biohydrogen Production in Batch Microbial Electrolysis Cell Reactor

M. Azwar, M. A. Hussain and A. K. Abdul-Wahab

Abstract Production of biohydrogen has the potential to be a renewable energy alternative to current technology. Microbial electrolysis cell (MEC) system is new bio-electrochemical processes that are capable of producing hydrogen gas and has higher efficiency when compared with other processes. This study describes the mathematical model of MEC for hydrogen production from wastewater batch reactor. The model is based on material balances with the integration of bio-electrochemical reactions describing the steady-state behaviour of biomass growth, consumption of substrates, hydrogen production and power current characteristics. The model predicts the concentration of anodophilic, acetoclastic methanogenic and hydrogenotrophic methanogenic microorganisms. In this study the effect of varying changes of initial concentration, effect of stoichiometric and kinetic parameters on MEC in a batch reactor to be used with open-loop identification test. In this model will also be examined effect of competition between the three microbial populations between anodophilic, hydrogenotrophic and acetoclastic.

Keywords Mathematical model · Batch microbial electrolysis cells reactor · Hydrogen gas · Internal parameter

List of Symbols

S	Substrate concentration (mg-S L^{-1})
x_a	Concentration of anodophilic microorganisms
x_m	Concentration of acetoclastic microorganism
x_h	Concentration of hydrogenotrophic microorganisms

M. Azwar
Faculty of Engineering, Department of Chemical Engineering, University of Syiah Kuala, Banda Aceh 23111, Indonesia

M. A. Hussain (✉) · A. K. Abdul-Wahab
Faculty of Engineering, Department of Chemical Engineering, University of Malaya, 50603 Kuala Lumpur, Malaysia
e-mail: mohd_azlan@um.edu.my

M. O. Hamdan et al. (eds.), *ICREGA'14 - Renewable Energy: Generation and Applications*, Springer Proceedings in Energy, DOI: 10.1007/978-3-319-05708-8_2,

Q_{H_2} Hydrogen production rate (mL/day)
$q_{max,a}$ Maximum reaction rate of the anodophilic microorganism [mg-A mg-x^{-1} d^{-1}]
$q_{max,m}$ Maximum reaction rate of the acetoclastic methanogenic microorganism [mg-A mg-x^{-1} d^{-1}]
$K_{S,a}$ Half-rate (Monod) constant of the anodophilic microorganism [mg-A l^{-1} or mg-M l^{-1}]
$K_{S,m}$ Half-rate (Monod) constant of the acetoclastic methanogenic microorganism [mg-A l^{-1} or mg-M l^{-1}]
K_M Mediator half-rate constant [mg-M l^{-1}]
$K_{d,a}$ Microbial decay rates of the anodophilic microorganism [d^{-1}]
$K_{d,m}$ Microbial decay rates of the acetoclastic methanogenic microorganism [d^{-1}]
$K_{d,h}$ Microbial decay rates of the hydrogenotrophic microorganism [d^{-1}]
K_h Half-rate constant [mg l^{-1}]
Y_M Oxidized mediator yield [mg-M mg-A^{-1}]
Y_{H_2} Dimensionless cathode efficiency [dimensionless]
Y_h Half-rate constant [mg l^{-1}]
V_r Anodic compartment volume [l]
m Number of electrons transferred per mol of H_2 [mol-e^- mol-H_2^{-1}]
F Faraday constant [A d mol-e^{-1}]
R Ideal gas constant [ml-H_2 atm K^- mol-H_2^{-1}]
T MEC temperature [K]
P Anode compartment pressure [atm]
$E_{applied}$ Electrode potentials [V]
R_{ext} External resistance [Ω]
R_{int} Internal resistance [Ω]
I_{MEC} MEC current [A]
E_{CEF} Counter-electromotive force for the MEC [V]
M_{Total} Total mediator weight percentage [mg-M mg-x^{-1}]
M_{red} *Reduced mediator fraction per each* electricigenic microorganism (mg-M mg-x^{-1})
M_{ox} Oxidized mediator fraction per *each* electricigenic microorganism (mg-M mg-x^{-1})
$A_{sur,A}$ Anode surface area [m^2]

Greek letters

$\mu_{max,a}$ Maximum growth rate of the anodophilic microorganism [d^{-1}]
$\mu_{max,h}$ Maximum growth rate of the hydrogenotrophic microorganism [d^{-1}]
β Reduction or oxidation transfer coefficient [dimensionless]
i_0 Exchange current density in reference conditions [A m^{2-1}]
γ Mediator molar mass [mg-M mol_{med}^{-1}]
α_1 Dimensionless biofilm retention constant for layers 1

α_2 Dimensionless biofilm retention constant for layers 2
μ_h Hydrogen growth rate [d^{-1}]
η_{ohm} Ohmic losses due to resistance to the flow of ion in the electrolyte and electrode [V]
η_{conc} Concentration loss due to mass transfer limitation [V]
η_{act} Activation loss due to activation energies and electrochemical reactions [V]

2.1 Introduction

Electrochemical systems represent a novel alternative for energy recovery from organic waste and biomass residue, where microorganisms can be employed to catalyze electrochemical oxidation-reduction reactions. Microbial electrochemical cells such as Microbial Fuel Cells (MFCs) and Microbial Electrolysis Cell (MEC) are among such bioelectrochemical systems. Performance of MFC and MEC largely depends on anaerobic biofilm occupied by anodophilic (electrogenic) microorganisms, which transfer electrons to the anode during their metabolism [3]. Though anodic compartments in all MFC and MEC are similar, the cathode reactions differ. MFCs operate with cathodes exposed to air resulting in oxygen reduction reaction at the cathode and electricity production [6]. In contrast, MEC require a small additional input of electrical energy provided by an external power supply to facilitate the reaction of hydrogen formation on the cathode [13].

Microbial electrolysis cells (MEC) and microbial fuel cells (MFC) are part of the microbial electrochemical cell technology which is one of the renewable energy alternatives today. Anodophilic microorganisms in anaerobic bioreactor is capable of oxidizing substrate containing organic materials in the compartment anode into electric energy [8]. Anodophilic microorganisms or microbial electricigenic is able to break the organic material and wastewater that has been diluted or low concentrations of organic compounds [3, 6]. MFC can generate spontaneous current due to the oxidation and reduction of the electron-proton from the organic material in the cathode bioreactor, whereas in MECs system, due to the addition of voltage into the cathode anaerobic- bioreactor, reaction between protons and electrons occurs leading to the formation of hydrogen gas [7, 13].

A Microbial Electrolysis Cell (MEC) is a slightly modified MFC where a small amount of electricity is applied to the anode chamber to suppress the production of methane and oxygen is kept out of the cathode chamber to assist bacterial oxidation of organic matter present in wastewater, to produce hydrogen. Although Microbial Electrolysis Cell (MEC) has tremendous potential, the development of this technique is still in its infancy. Information about the anode materials and microorganisms used in MFCs are also applicable to MEC systems due to their similar anodic process.

However the MEC present many technological challenges that goes beyond modelling studies, that need to be overcome before commercial application. For instance, the nonlinear and highly complex process in this hydrogen production process is due to the microbial interaction which also depends on the microbial activity. These difficulties and complexity makes the MEC system difficult to be operated and control under the best of condition.

These problems can be alleviated using an integrated process system engineering approach involving process modelling, optimisation, and control simultaneously in the study of the MEC system. To improve the productivity of bioreactor one alternative is to find the optimum conditions so that the rate of hydrogen production can be increased. Through the study of the experimental work for predicting the behavior of MEC in the bioreactor in a variety of operating conditions, the optimum value of the MEC can be obtained [5] or through developing the mathematical model of the MEC system.

One of the important and interesting phenomena for MFC and MEC model is the competition between anodophilic and methanogenic microorganisms to consume the substrate in the anode compartment [11]. Competition from microbial populations severely affect the performance of the MFC and MEC bioreactor. Several studies have been conducted to analyse the models, one of which is competition from anodophilic, methanogenic acetoclastic and hydrogenotrophic methanogenic microorganisms in the biofilm as conducted by Pinto et al. [10].

This study describes the mathematical models of MECs for hydrogen production modified from Pinto et al. [10] model based on the anaerobic digestion model proposed by Bernard et al. [2]. One method to improve the performance of MECs process is to design a proper mathematical model that can be used to optimize the design and develop process control strategies of the MECs system. This study has assessed the maximum hydrogen production rate by varying the anodic compartment volume, electrode potentials applied, effect of varying changes of initial concentration, effect of stoichiometric and kinetic parameters on MECs in the batch reactor. It was used for analysis and tested with open loop identification. In this model the effect of competition between the three microbial populations between anodophilic, hydrogenotrophic and acetoclastic will also be examined. The equation of this model involves unified model as well as activity of microbes in the anode chamber of a microbial fuel cells and microbial electrolysis cells in the cathodic reaction.

2.2 Modified Model of MEC in Batch Reactor

2.2.1 Mathematical Models

The main goal of any development of mathematical models for MEC is to get the maximum hydrogen production rate by calculating the effect of electric current and voltage prediction at different operating conditions. The MEC model used here

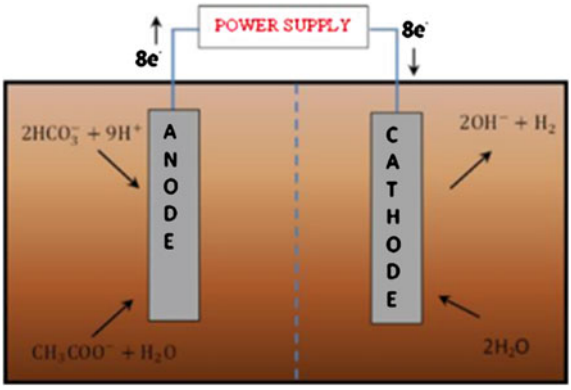

Fig. 2.1 A simplified diagram of the microbial electrolysis cells set-up showing anode and cathode in batch reactor

has been modified as the model presented by Pinto et al. [12]. The modification to Pinto model involves: batch process operation, phase of biofilm growth, metabolic activities, and the reactor size. In this model, to some assumptions such as that the acetate is to be the only carbon source, the fermentation process involving the conversion of the hydrolysis of acetate organic is ignored, and the carbon source in the anode compartment well distributed so that acetate gradient in the biofilm is neglected have been made.

This section presents a model for the MEC in batch reactor, developed from Pinto et al. [10] based on the anaerobic digestion model (ADM) proposed by Bernard et al. [2]. The mathematical models presented here aim to simulate the competition of three microbial in MECs. The model represents competition between anodophilic and methanogenic microorganisms for the substrate. Charge transfer at the anode is modeled using substrate (acetate) and intracellular mediator by three microbial populations between anodophilic, acetoclastic methanogenic and hydrogenotrophic methanogenic. The proposed MEC model system is shown in Fig. 2.1.

The reactions at the anode and cathode are described as [10]:

$$C_2H_4O_2 + H_2O + 4M_{ox} \rightarrow 4M_{red} + CO_2 \tag{2.1}$$

$$4M_{red} \rightarrow 4M_{ox} + 8e^- + 8H^+ \tag{2.2}$$

$$C_2H_4O_2 \rightarrow CH_4 + CO_2 \tag{2.3}$$

$$CO_2 + 4H_2 \rightarrow CH_4 + 2H_2O \tag{2.4}$$

where acetate represent substrate concentration; and M_{ox} and M_{red} are the reduced and oxidized forms of the intracellular mediator.

The influent and effluent of flow rate for MEC in batch reactor are the same and the dynamic mass balance equations of the model for substrate and microorganisms can be written as:

$$\frac{dS}{dt} = \frac{F_{in}}{V}(S_0 - S) - q_{max,a}\frac{S}{K_{A,a} + S}\frac{M_{ox}}{K_M + M_{ox}}x_a - q_{max,m}\frac{S}{K_{A,m} + S} \tag{2.5}$$

$$\frac{dx_a}{dt} = \mu_{max,a}\frac{S}{K_{A,a} + S}\frac{M_{ox}}{K_M + M_{ox}}x_a - K_{d,a}x_a - \alpha_1 x_a \tag{2.6}$$

$$\frac{dx_m}{dt} = \mu_{max,m}\frac{S}{K_{A,m} + S} - K_{d,m}x_m - \alpha_1 x_m \tag{2.7}$$

$$\frac{dx_h}{dt} = \mu_{max,h}\frac{H_2}{K_h + H_2} - K_{d,h}x_h - \alpha_2 x_h \tag{2.8}$$

$$\frac{dM_{ox}}{dt} = \frac{\gamma}{Vx_a}\frac{I_{MEC}}{mF} - Y_M q_{max,a}\frac{S}{K_{A,a} + S}\frac{M_{ox}}{K_M + M_{ox}} \tag{2.9}$$

$$M_{Total} = M_{red} + M_{ox} \tag{2.10}$$

$$Q_{H_2} = Y_{H_2}\left(\frac{I_{MEC}}{mF}\frac{RT}{P}\right) - Y_h\mu_h x_h V \tag{2.11}$$

The model as given by Eq. (2.5) is for filling time period (t_f) in the process. During reaction time in the batch reactor process, the volumetric flow rate (F_{in}) is nil and the V_t is constant at *Vo*. The values of the coefficients can be found in Pinto et al. [11].

2.2.2 Electrochemical Equations

The potential losses of internal resistance can give additional information about the performance of an MEC, especially when comparing different systems [4]. Since the voltage needed for hydrogen production is constant, the current density depends on the total internal resistance of the system, which in itself is a function of the current density. The total internal resistance is a sum of the partial resistances of the system [1].

Figure 2.2 gives an overview of partial internal resistances in an MEC, which can be represented by a series of resistances in an equivalent circuit. These partial resistances consist of: (i) counter-electromotive force ($\mathbf{E_{CEF}}$), (ii) activation loss ($\boldsymbol{\eta}_{\mathbf{act}}$), concentration loss ($\boldsymbol{\eta}_{\mathbf{conc}}$), ohmic loss ($\boldsymbol{\eta}_{\mathbf{ohm}}$). Each of these polarizations has a different magnitude for different current density degrees. At low current densities, activation losses are dominant due to reaction energy barriers at the electrode-electrolyte interface, which need to be overcome to start the reaction. At high current densities, reactant and product diffusion limitations lead to high concentration losses. Finally, ohmic losses increase linearly with current due to electron and ion conduction at the electrodes, electrolytes, and contact resistance across

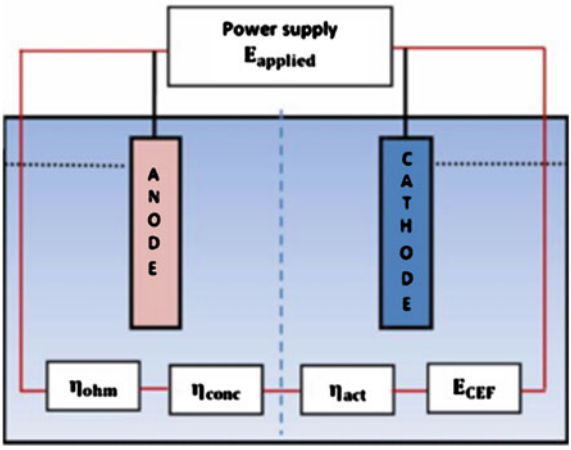

Fig. 2.2 The potential losses of microbial electrolysis cells in batch reactor

each material's interface, and interconnections to electrodes. Note that the output voltage of a fuel cell is directly proportional to the cell current, following Ohm's law:

$$E_{output} = R_{ext} I_{cell} \tag{2.12}$$

MEC voltage can be calculated using theoretical values of electrode potentials by subtracting ohmic, activation, and concentration losses. Therefore the following electrochemical balance can be written as [9]:

$$-E_{applied} = E_{CEF} - \eta_{ohm} - \eta_{conc} - \eta_{act} \tag{2.13}$$

Here, concentration losses at the cathode can be neglected due to the small size of H_2 molecules resulting in a large diffusion coefficient of H_2 in a gas diffusion electrode used as a cathode. The concentration losses at the anode are then calculated using the Nernst equation.

$$\eta_{conc,A} = \frac{RT}{mF} \ln\left(\frac{M_{Total}}{M_{red}}\right) \tag{2.14}$$

The cathodic activation losses can be calculated by the Butler-Volmer equation. Assuming that the reduction and oxidation transfer coefficients that express the activation barrier symmetry are identical, the Butler-Volmer equation can be approximated as

$$\eta_{act,C} = \frac{RT}{\beta mF} \sinh^{-1}\left(\frac{I_{MEC}}{A_{sur,A} i_0}\right) \tag{2.15}$$

Therefore, the MEC current can be calculated by combining Eqs. (2.13)–(2.15):

$$I_{MEC} = \frac{E_{CEF} + E_{applied} - \frac{RT}{mF}\ln\left(\frac{M_{Total}}{M_{red}}\right) - \eta_{act,C}(I_{MEC})}{R_{int}} \frac{M_{red}}{\varepsilon + M_{red}} \tag{2.16}$$

where ε is null [mg-M mg-x^{-1}]; $\varepsilon \approx 0$, Eq. (2.16) can be written as:

$$I_{MEC} = \frac{E_{CEF} + E_{applied} - \frac{RT}{mF}\ln\left(\frac{M_{Total}}{M_{red}}\right) - \eta_{act,C}(I_{MEC})}{R_{int}} \tag{2.17}$$

2.3 Results and Discussion

In all simulations studies, the total time was set at 20 days. Figure 2.3 shows the block diagram which consists of multi input and multi output parameters. All input and output parameter are divided in two types namely; internal and external parameters. Internal input is the parameter that we assume or are taken from literature. However, external output is the parameter that can be seen and manipulated such as volume reactor; substrate feed concentration, electrode potential applied and MEC current (external load).

The model described previously is used to study the sensitivity of effect internal parameters changes in biohydrogen production via microbial electrolysis cells in batch reactor. Figures 2.4 and 2.5 shows the dynamic behaviour of initial concentration of the anodophilic microorganisms (X_{ao}) on the I_{MEC} current and the hydrogen production rate.

Figures 2.4 and 2.5 illustrate the results for the effect of initial concentration of the anodophilic microorganisms (X_{ao}), varied with values of 0.1 mg/l, 0.5 mg/l, 1.0 mg/l and 1.5 mg/l, on the hydrogen production rate profiles and the I_{MEC} current. The investigation was carried out for the anodophilic microorganisms initial concentration (X_{ao}) range of $0.1 \leq X_{ao} \leq 1.5$ (mg-x/l), the balance (i.e. the difference from the base value X_{ao} which is 1.0) was added to X_{ao}. As the growth rate of the hydrogenotrophic and initial concentration of X_{ao} increased, the I_{MEC} current and hydrogen production rate also increases up to the period of 2 days. Hence, it is evident from Figs. 2.4 and 2.5 that performance of I_{MEC} current and the hydrogen production rate were affected by changes in initial concentration of the anodophilic microorganisms.

Figures 2.6 and 2.7 shows the behaviour of the effect of internal parameters changes of initial concentration of the hydrogentrophic microorganisms (X_{ho}) on the I_{MEC} current and the hydrogen production rate. The investigation was carried out for hydrogenotrophic microorganism's initial concentration (X_{ho}) in the range

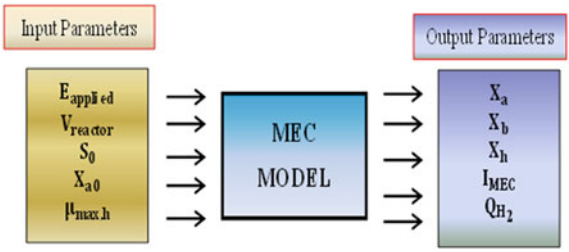

Fig. 2.3 Schematic description of input–output model block diagram

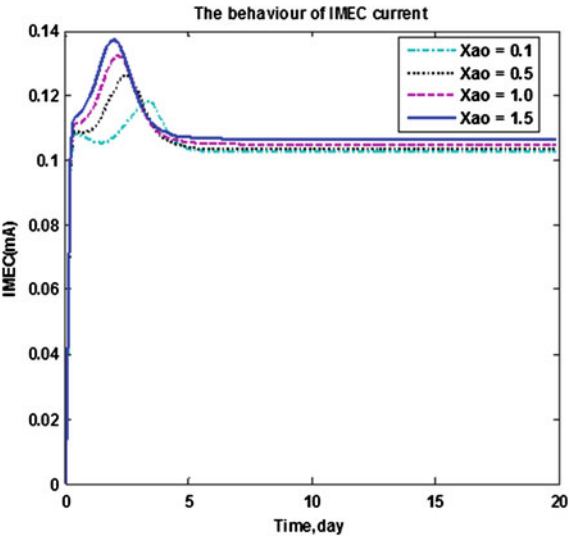

Fig. 2.4 The effect of initial concentration of the anodophilic microorganism on the I_{MEC} current

of $1 \leq X_{ao} \leq 15$ mg/l. Figure 2.6 illustrate the simulation results for the internal parameters changes of initial concentration of the hydrogentrophic microorganisms (X_{ho}) on the I_{MEC} current with the values varied at 1 mg/l, 5 mg/l, 10 mg/l and 15 mg/l. Figure 2.6 shows that the effect of changing the initial conditions of the hydrogentrophic concentration (X_{ho}) has no significant on the I_{MEC} current variations.

Figure 2.7 shows the hydrogen production rate increased with increasing the hydrogentrophic microorganisms initial concentration (X_{ho}). As mentioned previously, by increasing the initial concentration of the hydrogentrophic microorganisms, the hydrogen production rate is also increased. In summary, the hydrogen production rate is correlated with the initial concentration of the hydrogenotrophic microorganism.

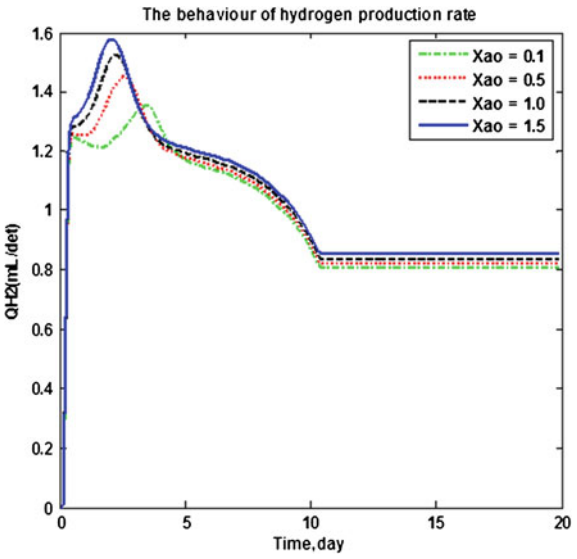

Fig. 2.5 The effect of initial concentration of the anodophilic microorganism on the hydrogen production rate

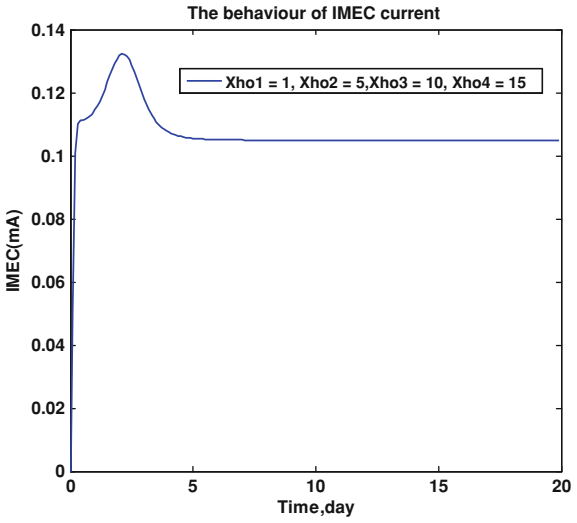

Fig. 2.6 The effect of initial concentration of the hydrogentrophic microorganisms on the I_{MEC} current

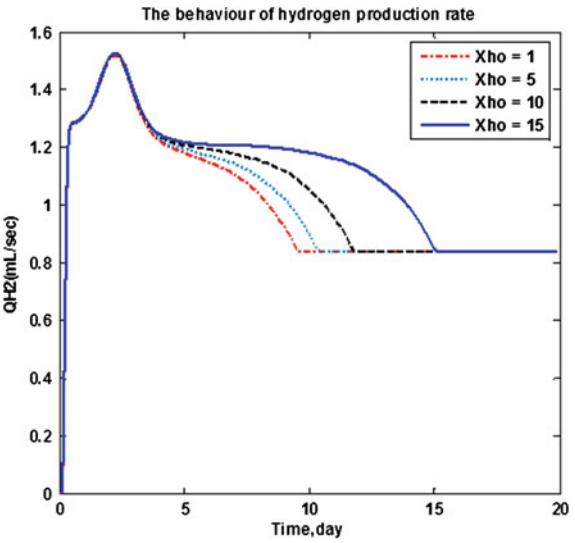

Fig. 2.7 The effect of initial concentration of the hydrogentrophic microorganisms on the hydrogen production rate

2.4 Conclusions

The study has assessed the maximum hydrogen production rate by varying the effect of varying changes of initial concentration and kinetic parameters on the MECs in a batch reactor. In this paper, the effect of varying changes of initial concentration of the anodophilic microorganisms (X_{ao}) and hydrogentrophic microorganisms on the I_{MEC} current and the hydrogen production rate has been studied. The model is based on material balances with the integration of bio-electrochemical reactions. The model examined the performance and competition between the three microbial populations involving anodophilic, acetoclastic methanogenic and hydrogenotrophic methanogenic microorganisms. This model is also capable of predicting the growth of Populations of microorganisms and biofilm composition. The results show that the initial concentration of the anodophilic microorganisms (X_{ao}) has significant effect on the I_{MEC} current and the hydrogen production rate as compared to the effect of initial concentration of the hydrogentrophic microorganisms (X_{ho}).

Acknowledgment This research was supported by the "IPPP-PV050/2011B" and "UMRG-RP006H-131CT" Program, University of Malaya.

References

1. A.J. Bard, L.R. Faulkner, *Electrochemical Methods: Fundamentals and Applications* (Wiley, New York, 2001)
2. O. Bernard, Z. Hadj-Sadok, D. Dochain, A. Genovesi, J.-P. Steyer, Dynamical model development and parameter identification for an anaerobic wastewater treatment process. Biotechnol. Bioeng. **75**(4), 424–438 (2001)
3. D.R. Bond, D.E. Holmes, L.M. Tender, D.R. Lovley, Electrode-reducing microorganisms that harvest energy from marine sediments. Science **295**(5554), 483–485 (2002)
4. Y. Fan, E. Sharbrough, H. Liu, Quantification of the internal resistance distribution of microbial fuel cells. Environ. Sci. Technol. **42**, 8101–8107 (2008)
5. G.S. Jadhav, M.M. Ghangrekar, Performance of microbial fuel cell subjected to variation in pH, temperature, external load and substrate concentration. Bioresour. Technol. **100**, 717–723 (2009)
6. B.E. Logan, B. Hamelers, R.A. Rozendal, U. Schroder, J. Keller, S. Freguia, P. Aelterman, W. Verstraete, K. Rabaey, Microbial fuel cells: methodology and technology. Environ. Sci. Technol. **40**(17), 5181–5192 (2006)
7. B.E. Logan, J.M. Regan, Electricity-producing bacterial communities in microbial fuel cells. Trends Microbiol. **14**, 512–518 (2006)
8. B.E. Logan, Scaling up microbial fuel cells and other bioelectrochemical systems. Appl. Microbiol. Biotechnol. **85**, 1665–1671 (2010)
9. R.F. Mann, J.C. Amphlett, M.A.I. Hooper, H.M. Jensen, B.A. Peppley, P.R. Roberge, Development and application of a generalised steady-state electrochemical model for a PEM fuel cell. J. Power Sources **86**, 173–180 (2000)
10. R.P. Pinto, M. Perrier, B. Tartakovsky, B. Srinivasan, Performance analyses of microbial fuel cells operated in series, in *DYCOPS: Proceedings International Symposium on Dynamics and Control of Process of Systems*, Leuven, Belgium (2010)
11. R.P. Pinto, B. Srinivasan, S.R. Guiot, B. Tartakovsky, The effect of real-time external resistance optimization on microbial fuel cell performance. Water Res. **45**(4), 1571–1578 (2011)
12. R.P. Pinto, B. Srinivasan; M.F. Manuel, B. Tartakovsky, A unified model for electricity and hydrogen production in microbial electrochemical cells, in *Preprints of the 18th International Federation of Automatic Control (IFAC) world congress*, Milano, Italy, 28 Aug–2 Sept 2011
13. R.A. Rozendal, H.V.M. Hamelers, G.J.W. Euverink, S.J. Metz, C.J.N. Buisman, Principle and perspectives of hydrogen production through biocatalyzed electrolysis. Int. J. Hydrogen Energy **31**(12), 1632–1640 (2006)

Chapter 3
Assessment of Surplus Agricultural Residues Available for Biomass Briquetting in India

N. Awalgaonkar, H. Saxena, A. Venkatesan and R. Natarajan

Abstract India has a surplus of agro residues, which amounted to about 300 million tonnes in the year 2012. These residues when utilized properly to produce energy could satisfy 65 % of the total rural energy demands of the country. Efficient utilization of such an enormous source of energy would help in addressing the current energy crisis of the country. This paper critically discusses the scope and potential of the biomass briquetting in India. The output of various agro residues produced in the country for the last 10 years, distribution of agro residues in different states, surplus agricultural residues available in different states of India and various biomass briquetting techniques available in India have been studied in this paper. The paper would help the interested industrialists and entrepreneurs in setting up their briquetting plants in the regions or states with high potential for briquetting and also assist the government agencies in framing policies and taking decisions concerning the efficient use of agro-residues available in India. From the study, it was found that the potential for biomass briquetting is high in the western states of Gujarat and Maharashtra and the northern state of Uttar Pradesh. The average amount of surplus agro-residues available in these states was found to be as high as 40 million tonnes. With continued efforts and improvement in the briquetting technology, combined with the support of the government, the development of densified biofuels in India seems to be a promising prospect.

Keywords Biomass · Briquetting · Briquetting techniques · Briquetting potential · India · Surplus agricultural residues

N. Awalgaonkar (✉) · H. Saxena · A. Venkatesan · R. Natarajan
VIT University, Vellore, India
e-mail: nimish.awalgaonkar@gmail.com

H. Saxena
e-mail: saxena.h2007@gmail.com

A. Venkatesan
e-mail: aravindv74@gmail.com

M. O. Hamdan et al. (eds.), *ICREGA'14 - Renewable Energy: Generation and Applications*, Springer Proceedings in Energy, DOI: 10.1007/978-3-319-05708-8_3,

3.1 Introduction

Energy production through biomass meets a large percentage of energy needs of a developing country like India [1]. About 32 % of the total energy consumption in India is satisfied by biomass energy through various primary, secondary and tertiary sources like firewood, agro residues, animal wastes, wastes from various industries such as paper and pulp industry, sugarcane industry, food and beverage industry etc. [2].

India is an agricultural based country, so most of the rural biomass produced in the country consists of large amounts of agro residues such as rice husk, coffee husk, jute sticks, bagasse coir, groundnut shells etc. [2]. Also, most of the energy demands of rural India are satisfied by direct combustion of these agro residues which gives rise to many problems including increase in pollution and wastage of energy rich resources due to inefficient burning. The pollution problems further lead to various adverse effects on the health of humans. Apart from these issues, the handling, storage and transportation of loose biomass agro residues is very uneconomical. Hence briquetting of these biomass residues seems like a viable option in addressing these various concerns.

Briquetting of biomass is a densification process which consists of reducing the bulk volume of biomass by mechanical means for easy handling, storage and transportation. Biomass briquettes use would be a viable alternative to current direct burning of agro residues such as rice husk, groundnut shells etc. to produce energy. Use of biomass briquettes instead of biomass in raw original form would lead to decrease in pollution and increase in the efficiency of the combustion process. Also biomass briquettes can be used in gasifiers and pyrolysers to produce bio-fuels. In the present scenario, the biomass briquettes are largely used for household heating and cooking applications. Various research and development efforts are being made to make briquetting technology profitable and to increase its use in satisfying the growing energy demands of industries in India.

Biomass briquetting technology used in India can be briefly categorized into—Piston Press (Reciprocating Ram) technology and Screw Press Technology. Most of the briquetting units currently working in India make the use of Piston Pressed technology instead of screw pressed technology as the former technology offers various advantages like low power consumption and longer life of the unit components due to lesser wear and tear. But the major disadvantage of piston pressed based technology when compared with screw pressed technology is that the piston pressed briquettes are of inferior quality as compared to the screw pressed briquettes. The screw pressed briquettes have higher volumetric calorific value and better combustion characteristics than the piston pressed briquettes. The briquetting technique is yet to achieve a strong popularity in India because of the various technical difficulties involved and the failures in adapting the technology to suit the local needs and conditions. Hence, the commercial success in the application of briquetting technology would depend upon the quality of available feedstocks and overcoming the various operational difficulties pertaining to it [3].

In the wake of this current briquetting scenario in India, many of the government based as well private organizations are making continued efforts in developing this technology and making it more economically profitable. Due to these efforts of various organizations in India, the briquetting industry sector is gradually growing up. The Indian Renewable Energy Development Agency (IREDA) has financially sponsored many of the briquetting projects in India, all of which are based on the piston pressed technology [3–5]. The successes and promotional efforts taken up by IREDA and other such organizations have inspired many of the entrepreneurs to confidently invest in the biomass briquetting technology [2–4].

In this paper we would discuss the overall potential and feasibility of the briquetting process in India. In doing so we would focus on issues such as (1) Biomass Briquetting technologies available in India. (2) Selection of appropriate agro residues for briquetting process. (3) Potential agro residues output available in India and its state wise distribution in India. (4) Surplus amount of agro residues available in India etc.

3.2 Various Types of Briquetting Technologies Available in India

Briquetting techniques involve processes which convert loose agricultural residues into high density solid biofuels. These solid biofuels can be further used for burning purposes with greater efficiency and lesser pollution. The main types of briquetting techniques involve piston press, screw press, hydraulic press, and roller press techniques [4].

3.2.1 Mechanical Piston Press Technique

In this process, the agro residues are pushed into a die by a reciprocating ram under high pressure. This converts the biomass residues into briquettes. This technique uses less power compared to other techniques and can be used for a great variety of agro residues including corn straw, peanut shell, ground nut shell, cotton stalks, sunflower stalks etc. The major problem with this technique is the maintenance of ram. Further the briquettes obtained from mechanical piston press technique have lower quality in comparison to the ones obtained from screw press technique.

3.2.2 Screw Press Technique

This technique involves extruding biomass continuously by a screw through a heated taper die. The taper die is heated externally to avoid frictional losses. The quality of briquettes produced here is much better than that of reciprocating ram

produced briquettes. The wear of screw and die is higher compared to reciprocating ram but considering the fact that the briquettes produced here are homogeneous and can be carbonized, this technique is more preferred. They have a high combustion rate and can be used as a substitute to coal in boilers.

3.2.3 Hydraulic Press Technique

This technique involves a high pressure hydraulic oil system which transmits energy to the piston by means of an electric motor. The cylinder press is slower compared to mechanical piston, so the output of this technique is also lower compared to mechanical piston technique. The major advantage of using this technique is that it consumes less power and can tolerate agro residues with high moisture content.

3.2.4 Roller Press Technique

In roller press technique, a large number of dies are arranged as holes bored on a thick steel ring. These dies are of size about 30 mm and biomass is forced into them by means of rollers which results in creation of small pellets of biomass. The shape of these pellets depends upon shape of the die. This technique is energy efficient and has low operational and maintenance cost. It is more suitable for dry biomass.

3.3 Selection of Appropriate for Briquetting Process

Biomass residues must satisfy a number of conditions and requirements before they can be used as a potential feedstock for the briquetting process. It should possess the following characteristics:

(1) It should be readily available in large quantities near the briquetting plant site area so that the transportation and handling problems could be avoided.
(2) It should possess low moisture content, generally in the range of 10–20 % of the total biomass weight. High moisture content is not favorable as it would lead to more energy consumption for the drying of the concerned biomass. Also, it could create many problems during the grinding operation.
(3) It should possess lower ash content as it gives rise to many problems such as pollution problems, problems during combustion etc. Also, the ash should contain lower percentage of alkali metals as they give rise to further unwanted problems during combustion.

(4) The material should be able to flow swiftly inside various chambers and storage silos. The material should therefore be uniform and granular to have such flow characteristics.

3.4 Production and Distribution of Agro Residues in India

3.4.1 Production

Agricultural residues form a major percentage of the total residues produced in India. Hence, it is very important to know the total amount of agricultural residues produced in the country. The country statistical data for the yield of agricultural residues is not available in the statistical yearbook data of Department of Agriculture And Cooperation, Ministry Of Agriculture, India. But it can be easily estimated from the product of residue to crop ratio and yield of crops. The production of crops from the year 2003 to 2012 is obtained from the Department of Agriculture and Cooperation, Ministry Of Agriculture and Cooperation, India statistical book [6]. Residues to crop ratio for the principal Indian agricultural crops have been suitably obtained from the past study analysis of agricultural residues data available in the country [5]. The estimated production of different agro residues produced in India is calculated and tabulated in Table 3.1. The largest contribution of agro residues as seen from the table was obtained from Rice, Wheat, Sugarcane and Cotton crops produced in between 2003 and 2012. The agricultural residues from these four crops accounted for close to 75 % of the total agricultural residues so produced. The lowest agricultural residue output was found to be 500.93 million tonnes in the year 2002–2003. Thereby, it was found that the highest output of agricultural residues was about 814.51 million tonnes in the year 2011–2012. The agricultural residues so produced can be used for four purposes: use in industries, for livestock feeding such as cattle feeding, sheep feeding, as fertilizers and lastly as direct fuels. Therefore, the scope of the using densified solid biofuels for energy production is pretty high in India.

3.4.2 Distribution

The distribution of crops is very distinct in the different parts of India as it is spread across a wide area of land consisting of different physical geometry and climate [7]. It is therefore very important to consider this factor while framing various energy policies for the country. It would also be a deciding factor for efficient utilization of agricultural residues in the different parts of the country. The distribution of various agricultural crop residues in different states for the year 2011–2012 is as shown in Table 3.2. It is evident from Table 3.2 that the

Table 3.1 Amount of agricultural residue produced from different crops in India for the span of 2002–2012 (in million tonnes)

Crops	Residue to crop ratio	Residue									
		2002–2003	2003–2004	2004–2005	2005–2006	2006–2007	2007–2008	2008–2009	2009–2010	2010–2011	2011–2012
Rice	1.8	129.28	159.35	149.63	165.22	168.05	174.04	178.52	160.36	172.76	187.78
Wheat	1.6	105.22	115.46	109.82	110.96	121.30	125.71	129.09	129.28	138.99	150.24
Bajra	2	9.44	24.22	15.86	15.36	16.84	19.94	17.78	13.02	20.74	20.10
Jowar	2	14.02	13.36	14.48	15.26	14.30	15.86	14.50	13.40	14.00	12.06
Maize	2.5	27.88	37.45	35.43	36.78	37.75	47.40	49.33	41.80	54.33	53.93
Gram	1.6	6.78	9.15	8.75	8.96	10.13	9.20	11.30	11.97	13.15	12.13
Pulses	2.9	32.28	43.24	38.08	38.80	41.18	42.80	42.25	42.51	52.90	49.91
Groundnut	2.3	9.48	18.70	15.57	18.38	11.18	21.11	16.49	12.49	19.00	15.94
Rape seed and mustard	2	7.76	12.58	15.18	16.26	14.88	11.66	14.40	13.22	16.36	13.56
Other oil seeds	2	13.68	21.54	19.98	23.72	23.98	29.50	26.70	25.68	32.08	32.60
Cotton	3.5	30.17	48.06	57.51	64.75	79.21	90.58	77.98	84.07	115.50	123.20
Sugarcane	0.4	114.95	93.54	94.84	112.47	142.21	139.28	114.01	116.92	136.95	143.07
Total		500.93	596.65	575.12	626.91	680.99	727.09	692.35	664.72	786.76	814.51

production of agro residues is high in the states of Uttar Pradesh, Maharashtra and Gujarat. The majority of agricultural residues produced in Uttar Pradesh is from wheat crop while the agro residues produced in Gujarat and Maharashtra is from cotton crop residues. Figure 3.1 shows the distribution of agro-residues produced from different crops in India. The agro residues so produced in the country vary greatly from state to state.

3.5 Uses of Agro Residues for Different Purposes

Very little information is available about the use of agro residues for different purposes and applications as the agro residues use varies from place to place. Also, the residues produced in India vary from season to season, further making it difficult to predict the actual amount of residues used for different applications. Hence in the wake of these difficulties, we have tried to find the amount of surplus agro residues which can be used for briquetting purposes. India uses agricultural residues for various purposes such as livestock feedstock, compost making, raw materials in various industries, direct burning etc. The process of briquetting of agricultural residues would compete with these traditional uses of agro residues. Therefore proper percentage of agro residues should be utilized for each of these applications. Briquetting of non fodder, non fertilizer producing agro residues seems to be a good option in such a regard. As it is very difficult to calculate the actual amount of agro residues used for different kinds of purposes, we have tried to calculate the various percentages of agro residues used for different applications from past data and trends.

As seen in Table 3.3 we have found out the percentage of total agro residues that are used as fodder, as fuel and for other different purposes such as bio composting, direct burning in fields etc. As we can see, most of the agricultural residues produced from wheat and rice are used as fodder for the potential livestock.

Also, the agro residues produced from Jowar and Bajra cannot be used for briquettes production as almost all of Jowar and Bajra is used as fodder. The agricultural residues available from Cotton, Sugarcane and oilseeds can be used for briquettes production as most of the agro residues available from these crops are available in surplus for fuel and fodder purposes. About 300.51 million tonnes of the total agricultural residues produced in India can be used for the production of briquettes. The amount of agricultural residues available for fuel production is highest from Cotton crop amounting to about 123.20 million tonnes followed by the Sugarcane and Oilseeds crops produced in India. Figure 3.2 shows the percentage of non fodder agricultural residues available for fuel production from the different major crops available in India. Also, Table 3.4 gives us the distribution of the surplus amounts of agricultural residues used as fuel in the different states of India. The states of Gujarat and Maharashtra are the leading producers of cotton crop in the country. Almost the entire amount of agricultural residues produced

Table 3.2 The total agro residues produced in the different states of the country India for the year 2011–2012 (Units: million tonnes)

States	Rice	Wheat	Bajra	Jowar	Maize	Gram	Pulses	Groundnut	Rape seed and mustard	Cotton	Sugarcane	Total
Karnataka	7.27	0.30	0.56	2.48	10.23	0.61	3.07	1.15	NA	4.20	15.52	45.40
Andhra Pradesh	23.20	0.10	0.12	0.76	9.40	0.83	3.63	1.96	NA	17.15	6.69	63.83
Maharashtra	5.06	2.10	1.68	5.34	5.75	1.31	6.44	0.83	NA	25.20	32.74	86.45
Rajasthan	NA	14.91	8.32	0.82	4.18	1.58	6.84	1.84	5.94	4.69	NA	49.13
Tamil Nadu	12.40	NA	0.24	0.62	3.93	NA	1.16	2.46	NA	1.58	15.71	38.10
Bihar	12.96	7.66	NA	NA	3.80	0.10	1.48	NA	0.20	NA	4.83	31.03
Uttar Pradesh	25.25	48.46	3.26	0.42	3.28	1.15	7.05	0.21	1.44	NA	51.53	142.05
Madhya Pradesh	3.31	16.93	0.68	1.22	3.23	5.26	12.06	0.78	1.74	7.00	1.07	53.29
Gujarat	3.17	6.56	2.84	0.30	1.93	0.43	2.26	6.07	0.66	42.00	5.67	71.89
Himachal Pradesh	NA	0.96	NA	NA	1.80	NA	NA	NA	NA	NA	NA	2.76
Jammu & Kashmir	NA	0.66	0.02	NA	1.28	NA	NA	NA	NA	NA	NA	1.95
Punjab	18.97	27.54	NA	NA	1.25	NA	NA	NA	0.08	8.05	1.87	57.76
Jharkhand	6.16	0.54	NA	NA	1.03	NA	1.42	NA	NA	NA	NA	9.15
West Bengal	26.73	1.41	NA	NA	0.88	0.05	0.55	NA	0.88	NA	0.47	30.96
Haryana	6.77	20.29	2.36	0.06	NA	0.11	0.38	NA	1.72	9.28	2.78	43.74
Uttarakhand	NA	1.39	NA	NA	NA	NA	NA	NA	NA	NA	2.64	4.03
Chhattisgarh	10.85	NA	NA	NA	NA	0.38	1.45	NA	NA	NA	NA	12.69
Odisha	10.48	NA	NA	0.02	NA	0.05	1.04	0.16	NA	NA	0.35	12.10
Assam	7.22	NA	NA	NA	NA	NA	NA	NA	0.26	NA	0.39	7.87
Kerala	1.01	NA	NA	NA	NA	NA	NA	NA	NA	NA	NA	1.01
Others	7.00	0.43	0.04	0.02	2.05	0.27	1.13	0.46	0.62	4.10	0.80	16.92
Total	187.81	150.24	20.12	12.06	53.98	12.14	49.97	15.92	13.54	123.24	143.07	782.08

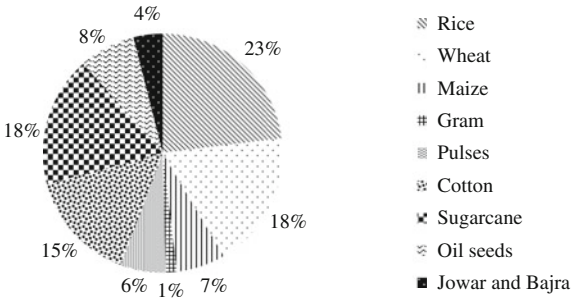

Fig. 3.1 Agricultural residues produced from different crops in India (2011–2012)

Table 3.3 Crop residue availability for fodder, non-fodder and fuel purposes in India for the year 2011–2012 (Units: million tonnes)

Crops	Fodder residue ratio	Fuel to residue ratio	Residue for		
			Fodder	Non-fodder purposes	Fuel
Rice	0.81	0.11	152.10	15.02	20.66
Wheat	0.86	0.01	129.21	19.53	1.50
Bajra	0.90	0.00	18.09	2.01	0.00
Jowar	1.00	0.00	12.06	0.00	0.00
Maize	0.81	0.19	43.68	0.00	10.25
Gram	0.00	1.00	0.00	0.00	12.13
Pulses	0.03	0.49	1.50	23.96	24.46
Groundnut	0.00	0.13	0.00	13.87	2.07
Rape seed and mustard	0.00	1.00	0.00	0.00	13.56
Other oil seeds	0.00	1.00	0.00	0.00	32.60
Cotton	0.00	1.00	0.00	0.00	123.20
Sugarcane	0.11	0.42	15.74	67.24	60.09
Total	–	–	372.37	141.63	300.51

from the cotton crop can be used for briquettes production. So the briquetting potential is very high in the states of Gujarat and Maharashtra amounting to about 48.15 and 45.20 million tonnes respectively. These states are followed by the states of Uttar Pradesh, Andhra Pradesh and Madhya Pradesh in terms of surplus availability of agro residues for fuel production.

A comparative bar chart study of the total agricultural residues produced and the surplus amount of agro residues available for fuel production for different states in India is shown in Fig. 3.3. The state wise distribution of surplus agro residues which can be used for briquettes production is shown in Fig. 3.4.

Hence, from the above the discussion, we can clearly state that the potential of briquetting of agricultural residues available in India is very high.

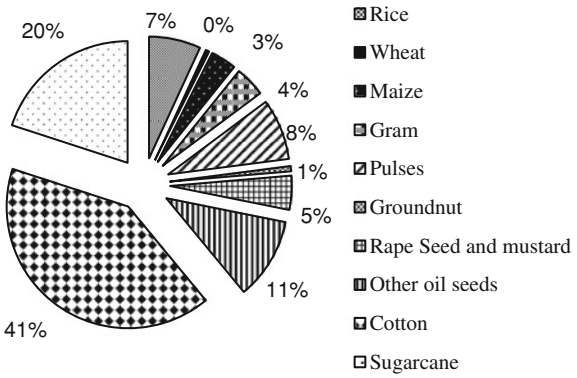

Fig. 3.2 Contribution of different crop residues used as agro based fuels in India (2011–2012)

Table 3.4 State wise availability of agro residues for fuel purposes in India in the year 2011–2012 (Units: million tonnes)

States	Total residue	Total residue for fuel purposes
Karnataka	45.40	15.73
Andhra Pradesh	63.83	27.16
Maharashtra	86.45	45.20
Rajasthan	49.13	16.75
Tamil Nadu	38.10	11.17
Bihar	31.03	5.27
Uttar Pradesh	142.05	31.60
Madhya Pradesh	53.29	21.61
Gujarat	71.89	48.15
Himachal Pradesh	2.76	0.35
Jammu & Kashmir	1.95	0.25
Punjab	57.76	11.51
Jharkhand	9.15	1.57
West Bengal	30.96	4.52
Haryana	43.74	13.41
Uttarakhand	4.03	0.01
Chhattisgarh	12.69	2.29
Odisha	12.10	1.88
Assam	7.87	1.22
Kerala	1.01	0.11
Others	16.92	7.10

3.6 Challenges and Limitations in the Use of Solid Densified Biofuels for the Production of Energy

Although the process of briquetting of agro residues to produce energy seems like a viable option, there are certain challenges and limitations to its use as an alternative energy source in India. These limitations are as follows:

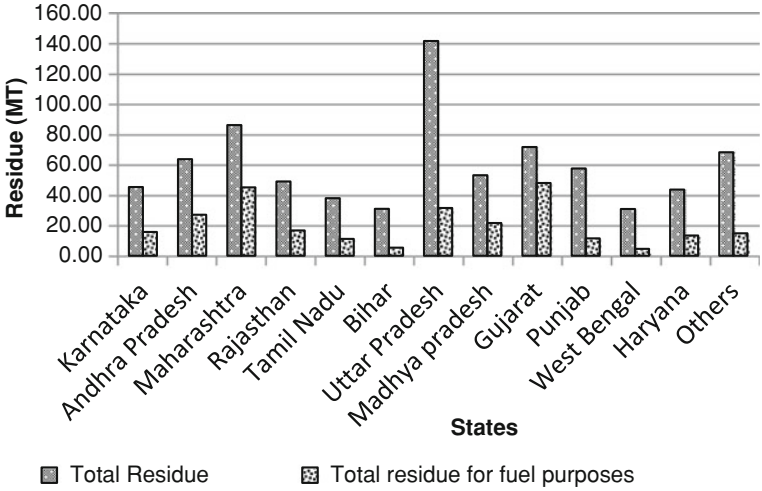

Fig. 3.3 Total amount of agro residues produced and the surplus amount available for briquetting in different states of India 2011–2012 (*in million tonnes*)

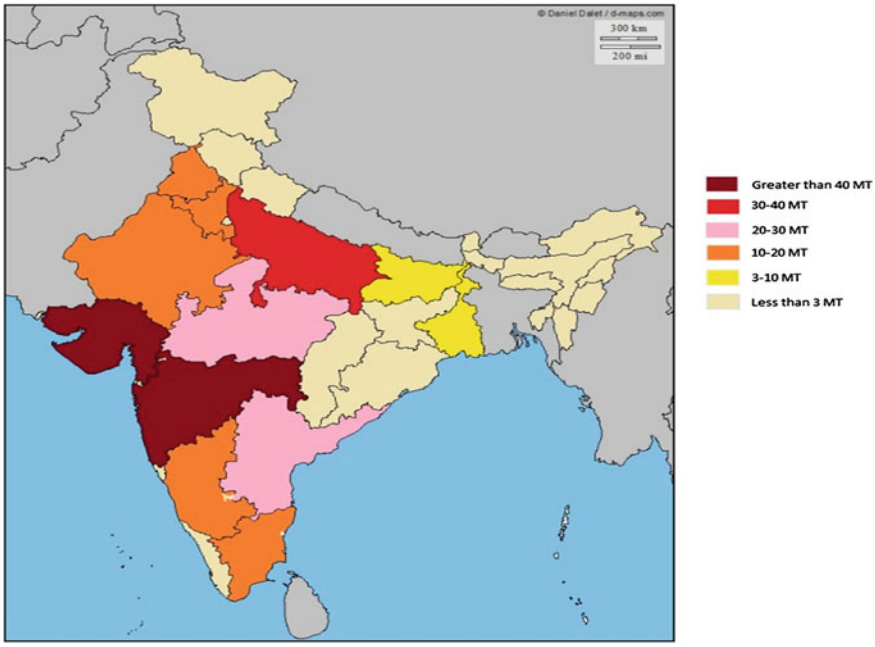

Fig. 3.4 Distribution of agro residues available for briquetting in India 2011–2012 (*Units: million tonnes*)

(1) The briquetting technology is not fully developed and utilized in India [8]. Almost all of the briquetting equipments and machinery used in India are imported from Korea which results in increased prices of these equipments and machinery, because of which the whole process of briquetting becomes economically infeasible for further applications.
(2) The amount of agricultural residues available in India varies immensely from state to state. Due to this the production of briquettes in states with less agro residues becomes almost impossible. Also the agro residues available in India vary from season to season which would result in fluctuations in the amount of agro residues available for briquettes production [9].
(3) The amount of energy required for the production of briquettes is high which further puts constraint on the production and development of briquettes [10].
(4) The social impacts of the briquettes production from the existing agro residues is also an important factor that needs to be taken into consideration. The farmers' opinions and views, their willingness or unwillingness regarding the use of agro residues for alternate power generation use should also be taken into consideration. Also the economic impact of the use of agro residues for briquetting purposes on the lives of farmers living in different regions of the country should be taken into consideration [7].
(5) Furthermore, the use of agro residues for briquettes production would put a cost value to these residues. This would deprive the poor part of the population of their cooking and heating fuel [7].

The above challenges and limitations need to be taken into account while framing the future policies and proposals relating to briquetting of agro-residues in India.

3.7 Conclusions and Wider Implications

India has got a huge potential for production of energy from surplus amounts of agriculture based residues. The briquetting of these surplus agricultural residues will help in reducing the dependency on fossil fuels for energy generation. The calculation of the amount of residues produced from major crops of India has been done for a span of last 10 years and it was observed that the output of agro residues is increasing every year and it has reached to about 815 million tonnes by the year 2012. Further the production of residues from different crops is analyzed for various states across India for the year 2011–2012. The amount of surplus agricultural residues available in India was found to be about 300 million tonnes for the year 2011–2012. Also, from the study it was found that surplus amounts of non fodder based agro residues from cotton, sugarcane, oilseeds etc. is available in India which can be further used for briquettes production instead of inefficient direct burning technique. The potential of agricultural residues based briquetting is very high in the states of Gujarat and Maharashtra followed by the states of Uttar Pradesh, Andhra Pradesh and Madhya Pradesh.

With developments and improvements in the briquetting technology, along with the support from the government, the huge amount of agro residues based energy potential in India could be utilized more efficiently helping India in tackling with the energy crisis in near future.

References

1. J. Singh, G. Sai, Biomass conversion to energy in India—a critique. Renew. Sustain. Energy Rev. **14**, 1367–1378 (2010)
2. UNDP-GEF Biomass Power Project, Ministry of New and Renewable Energy (MNRE). Bioenergy India 9–10. Government of India, New Delhi, 2011
3. P.D. Grover, S.K. Mishra, India. Biomass briquetting: technology and practice. Field Document No. 46, Regional Wood Energy Development Programme in Asia gcp/ras/154/net, Food and Agriculture Organization of the United Nations Bangkok, April 1996, pp. 10–19
4. B.S.K. Naidu, *Biomass briquetting—an Indian perspective* (The FAO Regional Wood Energy Development Programme in Asia, Bangkok, 1996)
5. N.H. Ravindranath, H.I. Somashekar, M.S. Nagaraja, P. Sudha, G. Sangeetha, S.C. Bhattacharya, P. Abdul Salam, Assessment of sustainable non-plantation biomass resources potential for energy in India. Biomass Bioenergy **29**, 178–190 (2005)
6. Agricultural Statistics at a Glance. http://eands.dacnet.nic.in/latest_2006.htm. Department of Agriculture and Cooperation, Ministry of Agriculture Government of India, 2012
7. A. Koopmans, J. Koppejan, Agriculture and forest residues: generation, utilization and availability, in *Proceedings of regional consultation on modern application of biomass energy* (1997)
8. MNRE Annual Report 2006–07. Ministry of New and renewable energy, Government of India, New Delhi, 2007
9. A.K. Tripathi, P.V.R. Iyer, T.C. Kandpal, K.K. Singh, Assessment of availability and costs of some agricultural residues used as feedstocks for biomass gasification and briquetting in India. Energy Convers. Manag. **39**, 1611–1618 (1998)
10. P. Purohit, A.K. Tripathi, T.C. Kandpal, Energetics of coal substitution by briquettes of agricultural residues. Energy **31**, 1321–1331 (2006)

Chapter 4
Feasibility of Algal Systems for Sustainable Wastewater Treatment

Thinesh Selvaratnam, Ambica Pegallapati, Felly Montelya, Gabriela Rodriguez, Nirmala Khandan, Peter Lammers and Wayne Van Voorhies

Abstract This paper proposes algal systems as a sustainable approach for removing nutrients from urban wastewaters and generating energy. This proposal is based on theoretical comparisons of energy that can be harvested from urban wastewaters by traditional technologies versus algal systems. Preliminary experimental results are presented to demonstrate that a thermo-tolerant and acidophilic strain evaluated in this study—*Galdieria sulphuraria*, can grow well in primary settled urban wastewaters and can reduce nutrient levels to regulatory discharge levels.

4.1 Introduction

4.1.1 Current State of Urban Wastewater Treatment

Urban wastewaters are rich in organic carbon, nitrogen (N), phosphorus (P) and other minerals, which are required to be removed prior to discharge to receiving waters. Excessive loading of receiving waters with organic carbon and nutrients can lead to depletion of dissolved oxygen, toxicity to aquatic life, and eutrophication. In fact, urban wastewater discharges with excess nutrients are among the top causes of impairment of designated use of numerous receiving water bodies in the US and around the world.

Typical wastewater treatment plants (WWTPs) equipped with secondary treatment processes are able to meet the discharge levels for organic carbon (quantified as Biochemical Oxygen Demand, BOD), but fail to meet the discharge

T. Selvaratnam · A. Pegallapati · F. Montelya · G. Rodriguez · N. Khandan (✉) · P. Lammers · W. Van Voorhies
New Mexico State University, Las Cruces, NM 88003, USA
e-mail: nkhandan@nmsu.edu

M. O. Hamdan et al. (eds.), *ICREGA'14 - Renewable Energy: Generation and Applications*, Springer Proceedings in Energy, DOI: 10.1007/978-3-319-05708-8_4,

levels for N and P [1]. To meet the discharge limits for both N and P, WWTPs are now required to add tertiary treatment systems to treat the secondary effluent. Biological Nutrient Removal (BNR) is one of the options for tertiary treatment of urban wastewaters, where, ammoniacal nitrogen (NH_3–N) is converted to nitrogen gas and phosphorus is removed by entrapping in the biomass.

However, BNR processes are immensely energy intensive, accounting for 60–80 % of the total energy requirement for wastewater treatment [2]. For example, in a 5.5 MGD plant, the measured energy consumption for aeration averaged 1.48 kW-h per kg BOD removal; 13.44 kW-h per total N removal; and 6.44 kW-h per total P removal [3].

In addition to the energy demand, by-products and side-streams from current wastewater treatment technologies result in additional direct and indirect environmental burden. For instance, the traditional activated sludge process for BOD removal typically generates 0.45 kg waste biomass per kg BOD removed, disposal of which contributes to nearly 50 % of the cost of operating a WWTP. With current trends in growth of population and their shifts toward urban centers, increasing numbers of WWTPs would be required to add tertiary treatment to meet nutrient discharge standards; with limited fossil fuel-based energy supplies, the traditional urban wastewater treatment technologies are thus deemed unsustainable.

Recognizing the above concerns, many researchers have been striving to develop energy-efficient and sustainable technologies that could minimize or avert the energy consumption and avoid the emission-, eutrophication-, and acidification-potentials associated with the production of that energy.

4.1.2 Pathways for Sustainable Urban Wastewater Treatment

The idea of transforming WWTPs as a net energy producer rather than net energy user, has been one of the hot topic of research in recent times. Since urban wastewater itself contains internal energy of 6.3–7.6 kJL^{-1} [4], it seems logical to harvest this energy rather than expending energy to dissipate it. Several available or emerging technologies have been shown to be capable of recovering some of the energy content of wastewaters in one form or another. Anaerobic digestion, for example, is a well-established process for converting that energy content to methane; dark fermentation has the potential to convert that energy to a more efficient and cleaner energy carrier—hydrogen; microbial fuel cells have been shown to convert that energy directly to electricity at even higher efficiency.

Recently, McCarty et al. [5] have reviewed the practical readiness of the above alternatives and proposed that anaerobic treatment could replace the traditional energy-intensive practice to treat urban wastewaters while recovering some of its energy to produce methane for use as an energy carrier. Extending the above

approach, coupling technologies that could recover the internal energy of the wastewaters with those that could recover and recycle their nutrient content for beneficial use, would be most beneficial, not only for sustainable but, perhaps, profitable urban wastewater treatment. A promising approach in this direction is algal-based wastewater treatment systems.

The idea of using microalgae for nutrient removal in wastewater has been discussed for years [6]. Several studies have shown high removal efficiencies for N and P removal using algal systems in wastewater [7, 8]. Early efforts of Oswald [9, 10] in this area are now being revamped as a sustainable alternative for urban wastewater treatment and energy production. The premise of this approach is that, mixotrophic algal systems could be engineered to reduce organic carbon as well as nutrients in urban wastewaters to the required discharge levels and, at the same time, utilize the carbon and nutrients that are currently dissipated, to cultivate energy-rich biomass as feedstock for generating gaseous or liquid biofuels. This approach could have an energy-advantage over that proposed by McCarty et al. [5] because, the algal biomass would incorporate both the internal energy of the wastewater as well as solar energy captured through photosynthesis.

It has been estimated that, in the traditional activated sludge process, removal of 1 kg of BOD would consume about 1 kW-h of electricity for aeration (resulting in 1 kg of fossil-CO_2 emission in the electricity generation process) and generate about 0.45 kg of waste biomass [11]. In contrast, 1 kg of BOD removed by photosynthetic oxygenation in mixotrophic algal systems requires no energy inputs and could produce enough algal biomass that can be anaerobically digested to generate methane equivalent to 1 kW-h of electric power [11]. Even though the waste biomass generated by the traditional activated sludge process could be anaerobically digested to recover some energy in the form of methane, the theoretical methane potential of algal biomass generated through mixotrophic cultivation, could be more than that of the biomass generated by activated sludge.

Assuming the empirical formula for activated sludge as $C_5H_7O_2N$, biomass production by the traditional approach can be seen to be 8.1 g biomass per g of NH_4–N removed. Following the estimation method of Speece (1996) [12], this biomass production translates to a methane potential of 5.3 L CH_4/g of N removed. In comparison, assuming the empirical formula for algal biomass as $C_{106}H_{263}O_{110}N_{16}P$ [13], biomass production in an algal system can be seen to be 15.8 g biomass per g of NH_4–N removed (agreeing with Ebeling et al. [14]). The methane potential of this amount of biomass can be estimated as 6.3 L CH_4 per g of N removed [12] which is 19 % higher than that in the activated sludge process.

Even though the above comparisons favoring the algal-based systems are based on theoretical estimates and pilot scale experiments, their practical feasibility has not been fully demonstrated. Several research and development groups are currently working on various aspects of algal-based systems for the dual purpose of wastewater treatment and energy production.

This paper presents preliminary results on two strains of a mixotrophic species, *Galdieria sulphuraria*, that have, until now, not been explored for this application. Unique characteristics and the rationale for selecting this species for urban wastewater treatment are discussed next.

4.1.3 Rationale for Galdieria Sulphuraria

A unique characteristic of *G. sulphuraria* is that, it is a thermo-tolerant acidophilic strain [15], which can thrive at pH of 0–4. Such low pH range is beneficial in deactivating pathogens and most competitive species naturally found in wastewaters [16]. The thermophilic nature of these strains enables cultivation in closed photobioreactors which otherwise would have to be cooled. Closed photobioreactors also benefit from high CO_2 utilization efficiency, minimum evaporative losses, and low cross-contamination. Potential mixotrophic nature of these strains enables higher biomass densities to be maintained to minimize the footprint and improve downstream processing efficiency. This paper presents the feasibility of cultivating two strains of *G. sulphuraria,* 5587.1 and 5572 in primary settled urban wastewater.

4.2 Materials and Methods

4.2.1 Algae Strain Collection and Culture Condition

Two independent isolates of the unicellular red algae *G. sulphuraria* CCMEE 5587.1 and 5572 [15] obtained from the Culture Collection of Microorganisms from Extreme Environments (University of Oregon) were assessed in this study. Both strains were grown in an incubator (Percival, IA, USA) at 40 °C with a 14 h/10 h light/dark cycle. The strains were grown in Standard Cyanidium medium [15] modified to contain twice the standard ammonium sulphate concentration and supplemented with the vitamin component of f/2 algal medium [17]. Cultures were streaked onto agar plates and single colonies were then picked to start axenic cultures from culture plates to modified Cyanidium medium scaling up the volume to 1-L Erlenmeyer flasks. The following are the constituents of the modified Cyanidium medium: $(NH_4)_2SO_4$, 2.64 gL^{-1}; KH_2PO_4, 0.27 gL^{-1}; NaCl, 0.12 gL^{-1}; $MgSO_4.7H_2O$, 0.25 gL^{-1}; $CaCl_2.2H_2O$, 0.07 gL^{-1}; Nitch's Trace Element Solution, 0.5 mL; $FeCl_3$ (solution = 0.29 gL^{-1}), 1.0 mL, and the pH adjusted to 2.5 with 10 N H_2SO_4. Includes vitamin component of f/2 algal medium (vitamins B1, B12 and biotin).

Wastewater used in this study was collected downstream of the primary settling tank at the municipal WWTP, Las Cruces, NM. Upon collection of the sample,

large solid particles were removed by gravity settling; autoclaved (at 121 °C); and stored at 4 °C. The clear supernatant was used in the experiments to make up the growth medium. At the beginning of each test, the inoculum was centrifuged (Sorvall Biofuge primo, Thermo Scientific, USA) and the algae pellets were re-suspended in the control set medium of the particular test and left for 24 h at 40 °C, 14 h/10 h light/dark photoperiod for preadaptation. Biomass growth was quantified daily, in terms of the optical density (OD) measured with Beckman DU530 spectrophotometer (Beckman Coulter Inc., USA) at a wavelength of 750 nm.

4.2.2 Experimental Conditions

4.2.2.1 Tests A–D

The objectives of Tests A–D were to assess the growth patterns of the two strains under two different temperature regimes; and to verify the suitability of wastewater as a growth medium. Experimental conditions adapted for assessing the two strains are summarized in Table 4.1. Tests A and B were designed to assess and compare the performance of the two species at a constant temperature of 40 °C, while Tests C and D were designed to assess and compare their performance under a varying diurnal temperature regime (variable: ramping from 26 to 42 °C over a 10 h period) to mimic outdoor conditions. Each of these Tests were run with three different growth mediums, coded as shown in Table 4.1. Growth medium coded as 1 was used to serve as baseline for autotrophic growth, while medium Coded 2 was used to assess the heterotrophic growth. Tests A–D were run for 10 days.

4.2.2.2 Test E

Test E was designed from the findings of Tests A–D (discussed further in results) to assess nutrient removal by 5587.1 at constant temperature of 40 °C, under three different media conditions, Code 4–6, as described in Table 4.1. Test E was ran for 7 days. The objective of Test E was to check the growth and nutrient removal pattern in both filter sterilized and non-autoclaved wastewater compared to modified cyanidium media. Filter sterilization of primary effluent wastewater was done with Nalgene Rapid-Flow filter units (0.45 μm) (Thermo Scientific, USA).

The cultures were grown in 16 mL borosilicate glass tubes, capped with plastic caps and sealed with parafilm to reduce evaporative losses. Each tube was inoculated with 6 mL of culture and placed in the outer rim of a roller drum (New Brunswick Scientific, Eppendorf., Connecticut, USA) rotating at 16 rpm. The roller drum was housed inside an incubator (Percival, IA, USA) where the CO_2 level was maintained at 2–3 % (vol/vol) throughout the experiments.

Table 4.1 Experimental conditions

Test	Temperature (°C)	Strain	Code	Growth Medium
A	40	5587.1	1	CM[a]
			2	CM[a] + 20 mM glucose
			3	CM[b]
B	40	5572	1	CM[a]
			2	CM[a] + 20 mM glucose
			3	CM[b]
C	26–42	5587.1	1	CM[a]
			2	CM[a] + 20 mM glucose
			3	CM[b]
D	26–42	5572	1	CM[a]
			2	CM[a] + 20 mM glucose
			3	CM[b]
E	40	5587.1	4	CM[c] + 40 ppm N[f] + 10 ppm P[g]
			5	CM[d]
			6	CM[e]

[a] Modified cyanidium medium (MCM), prepared with sterilized DI water
[b] MCM, prepared with autoclaved primary effluent
[c] MCM with no N and P, prepared with sterilized DI water
[d] MCM with no N and P, prepared with filter sterilized primary effluent
[e] MCM with no N and P, prepared with non-autoclaved primary effluent
[f] Nitrogen as $(NH_4)_2SO_4$
[g] Phosphate as KH_2PO_4

4.2.3 Optical Density Measurements

Biomass growth was quantified daily, in terms of the optical density (OD) measured with Beckman DU530 spectrophotometer (Beckman Coulter Inc., USA) at a wavelength of 750 nm. The biomass density, was evaluated in terms of 'ash-free dry weight X' (g AFDW per L), which was correlated to OD at 750 nm by the following equation:

$$X = 0.54553 * OD_{750nm} + 0.022839,\ n = 12;\ r^2 = 0.997$$

4.2.4 N and P Measurements

During Tests A–D, three of the glass tubes were removed from the drum on days 2, 5, 7 and 10; and during Test E, 3 glass tubes were removed on days 1, 3, 5 and 7 to serve as triplicates for measuring the nutrient levels. Culture samples from each tube were first centrifuged at 4,000 rpm for 10 min and the supernatant was diluted

and analyzed. Ammonia nitrogen and phosphorus (phosphate) were determined using HACH DR 6000 (HACH, Colorado, USA) spectrophotometer (Salicylate TNT Method 10031 and Phosver 3 Method 8048). In addition, in Test E, total nitrogen (TN) was also determined using the same spectrophotometer (TNTplus 828 Method 10208).

4.3 Results and Discussion

Temporal biomass growth profiles in Tests A to E are presented in Figs. 4.1 and 4.2. For test E, the exponential phase was taken as 1-7 days.

4.3.1 Temperature Effect

Growth rates and the final biomass densities attained at the end of the exponential growth phase with each of the three growth media for the two strains (5587.1 in Tests A and C; and 5572 in Tests B and D) were compared under the two temperature regimes to ascertain if they were a function of temperature. Based on the comparison summarized in Table 4.2, the temperature regimes did not seem to have any significant effect. As such, Test E was conducted at a constant temperature of 40 °C.

4.3.2 Media Effect

In the case of 5587.1 at 40 °C (Test A), initially the growth rate was highest in the run with supplemented glucose (Code 2), followed by the control (Code 1), and with primary effluent (Code 3). However, after the exponential growth phase, growth with primary effluent (Code 3) overtook the other two and reached 2.77 gL^{-1}, while growth in the other two saturated around 1.6 gL^{-1}. Similar pattern was observed in Test C as well, under variable temperature conditions. The initial stimulation of growth with glucose (Code 2) in both temperature regimes is attributed to the heterotrophic nature of the 5587.1 strain.

In the case of strain 5572, growth mediums with supplemented glucose (Code 2) and primary effluent (Code 3) showed similar growth patterns in both Tests B and D for the first 6 days and at the end of the 10 days, growth medium with primary effluent (Code 3) showed the highest growth followed by other two mediums (Code 1 and 2). There weren't any apparent growth stimulation in growth at early days in the media with supplemented glucose similar to what observed for 5587.1 in Tests A and C. Overall in all four tests, growth medium

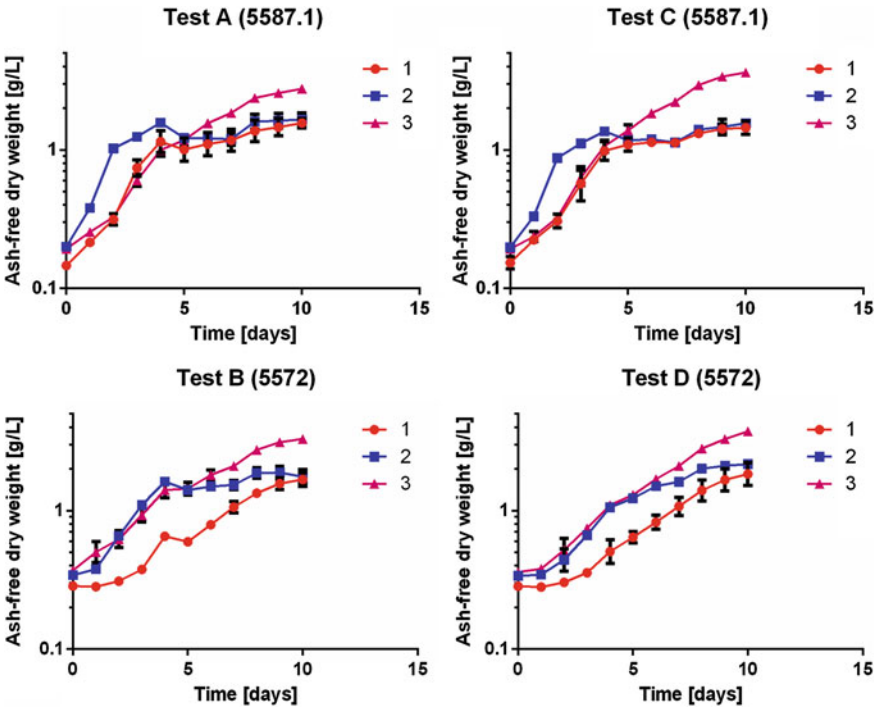

Fig. 4.1 Biomass growth profiles. Numbers represent code for culture medium as detailed in Table 4.1

with primary effluent (Code 3) showed the highest biomass density at the end of the 10 day experiment.

Tests A–D indicated favorable growth in autoclaved wastewater; in the case of strain 5587.1, some evidence of mixotrophy was noted. Therefore, Test E was designed to check the growth patterns of 5587.1 with filter sterilized (similar to growth medium Code 3, in tests A–D; but instead of autoclaving the primary effluent, the sample was filter sterilized) wastewater and non-autoclaved primary effluent.

The objective of this experiment was to check the suitability of primary effluent as growth medium for strain 5587.1.

4.3.3 Strain Effect

Comparing the results of Tests A–D, strain 5587.1 exhibited better growth than 5572 under both temperature regimes; after 7–8 days growth in mediums in all four tests started to flatten (except with medium Code 3). It was decided to check

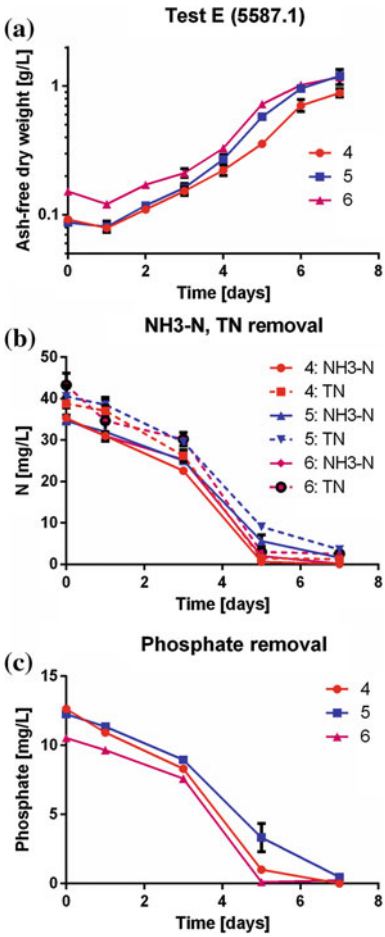

Fig. 4.2 **a** Biomass growth profiles for Test E. **b** Uptake of NH_3-N and TN. **c** Uptake of phosohate. Numbers represent code for culture medium as detailed in Table 4.1

whether either N or P was limiting the growth. At day 10, all the tubes were transferred to one incubator (temperature kept constant at 40 °C, "constant temperature condition") and combinations of N and P were supplemented. The supplementation of nutrients was as follows: 1. in both strains, for two sets of tubes, no nutrient were added; 2. For one set of tubes, 2.64 gL^{-1} of $(NH_4)_2SO_4$ were added; 3. For one set of tubes, gL^{-1} of KH_2PO_4 was added; 4. For one set of tubes, 2.64 gL^{-1} of $(NH_4)_2SO_4$ and 0.27 gL^{-1} of KH_2PO_4 were added, and the OD values were observed for another 6 days. In both strains there were no apparent difference in growth from day 10–16 in any of the growth mediums. It can be concluded as nutrients weren't the limiting factors for the growth rate in the latter part of the experiment.

Table 4.2 Summary of Growth Rates in Tests A–D

Strain	Code	Growth rate[a] ($gL^{-1}d^{-1}$)	
		Test A	Test C
5587.1	1	0.250 ± 0.058[b]	0.208 ± 0.041[b]
	2	0.344 ± 0.022[b]	0.291 ± 0.006[b]
	3	0.257 ± 0.014[c]	0.344 ± 0.007[c]
		Test B	Test D
5572	1	0.156 ± 0.022[d]	0.173 ± 0.041[d]
	2	0.224 ± 0.019[e]	0.203 ± 0.001[d]
	3	0.311 ± 0.004[d]	0.374 ± 0.001[d]

[a] Growth rates during exponential growth phase
[b] Growth rates were calculated using day 0–4 data
[c] Growth rates were calculated using day 0–10 data
[d] Growth rates were calculated using day 1–10 data
[e] Growth rates were calculated using day 1–6 data

Tests A to D showed that both 5587.1 and 5572 can be grown in primary effluent and achieve similar growth values compared to standard cyanidium media. There was some growth stimulation in the glucose set with strain 5587.1. Since the growth in tests A and C flattened after 7–8 days, Test E was designed to validate the results of Tests A and C and to the check N and P removal in 7 days.

Nutrient levels in the modified cyanidium media (560 ppm N–NH_3 and 190 ppm P) are higher than the levels in primary effluent (40 ppm of N–NH_3 and 10 ppm of P); in Test E, nutrient level in media Code 4 was adjusted to 40 ppm of N–NH_3 and 10 ppm of P to maintain similar levels as filter sterilized (Code 5) and non-autoclaved primary effluent (Code 6). Temporal biomass growth profiles in Test E are presented in Fig. 4.2a. In this test for 5587.1, 1–7 day OD values were used to calculate the growth rate. Strain 5587.1 showed a decline in OD values at day 1 and then started to grow from day 2. In terms of growth rate, growth mediums with filter sterilized (Code 5) and non-autoclaved primary effluent (Code 6) showed similar values; 0.186 ± 0.010 and 0.175 ± 0.028 $gL^{-1}d^{-1}$ respectively. Strain 5587.1 grew well in the wastewater mediums (Codes 5 and 6) compared to 0.134 ± 0.010 $gL^{-1}d^{-1}$ in modified cyanidium media (Code 4).

Overall, Tests A–D showed that both 5587.1 and 5572 can be grown in primary effluent and achieve similar growth values compared to standard cyanidium media. Also strain 5587.1 showed both autotrophic and heterotrophic growth, but there was no conclusive evidence to conclude the strain as true mixotrophic. In a previous study [18] with *G. sulphuraria*, it was concluded that true mixotrophy does not occur in *G. sulphuraria*. In test E, Strain 5587.1 showed the potential of using primary effluent as a growth medium.

4.3.4 N Removal

Temporal NH_4–N profiles in Test E are shown in Fig. 4.2b. In Test E (for strain 5587.1), N–NH_3 removal rates for 0–7 days were: Code 4—99.71 %; Code 5—95.20 %; Code 6—99.42 %. In addition to the NH_4–N measurements, total N (TN) was also measured at the same time points. These measurements were performed to check for uptake of any organic nitrogen (TN–NH_4–N = Organic nitrogen) in the two wastewater mediums (Code 5 and 6) during the late stages of the experiment. But as shown in Fig. 4.2, there weren't any evidence of organic nitrogen uptake by 5587.1. The biomass yield per unit N removed were 39.5 g g^{-1} and 35.3 g g^{-1} for media Codes 5 and 6, respectively. This value is higher than the theoretically calculated yield of 15.8 g biomass per g N removed [13, 14]. The removal rates of ammoniacal nitrogen were as follows: for filter sterilized primary effluent: 4.70 $mgL^{-1}d^{-1}$; for non-autoclaved effluent: 4.97 mg $L^{-1}d^{-1}$.

4.3.5 P Removal

Temporal P-profiles in Test E are shown in Fig. 4.2c. In Test E (for strain 5587.1), phosphate removal rates for 0–7 days were: Code 4—99.9 %; Code 5—96.10 %; Code 6—97.8 %. The removal rates of phosphate were as follows: for filter sterilized primary effluent: 1.68 $mgL^{-1}d^{-1}$; for non-autoclaved primary effluent: 1.47 $mgL^{-1}d^{-1}$. Strain 5587.1 showed highly favorable removal rates for both nitrogen and phosphate in 7 days.

4.4 Conclusion

The results showed that the two strains of *G. sulphuraria* (5587.1 and 5572) are capable of growing in primary effluent at growth rates compare to the baseline Cyanidium media; strain 5587.1 showed both autotrophic and heterotrophic growth in primary effluent. High biomass yield and efficient nutrient removal in Test E showed promise for *G. sulphuraria* CCMEE 5587.1 as a potential strain for efficient nutrient removal from urban wastewaters.

Acknowledgments This study was supported in part by the NSF Engineering Research Center, ReNUWIT; the US Department of Energy under contract DE-EE0003046 awarded to the National Alliance for Advanced Biofuels and Bioproducts; the National Science Foundation award #IIA-1301346; and the Ed & Harold Foreman Endowed Chair.

References

1. I.T.D. Cabanelas, Z. Arbib, F.A. Chinalia, C.O. Souza, J.A. Perales, P.F. Almeida et al., From waste to energy: microalgae production in wastewater and glycerol. Appl. Energy **109**, 283–290 (2013)
2. A.F. Clarens, E.P. Resurreccion, M.A. White, L.M. Colosi, Environmental life cycle comparison of algae to other bioenergy feedstocks. Environ. Sci. Technol. **44**, 1813–1819 (2010)
3. Municipal Nutrient Removal Technologies Reference Document, U.S. Environmental Protection Agency, EPA 832-R-08-006, vol. 2, ed. (2008)
4. E.S. Heidrich, T.P. Curtis, J. Dolfing, Determination of the internal chemical energy of wastewater. Environ. Sci. Technol. **45**, 827–832 (2011)
5. P.L. McCarty, J. Bae, J. Kim, Domestic wastewater treatment as a net energy producer-can this be achieved? Environ. Sci. Technol. **45**, 7100–7106 (2011)
6. W.J. Oswald, H.B. Gotaas, C.G. Golueke, W.R. Kellen, E.F. Gloyna, E.R. Hermann, Algae in waste treatment [with discussion]. Sew. Ind. Wastes **29**, 437–457 (1957)
7. J.P. Hoffmann, Wastewater treatment with suspended and nonsuspended algae. J. Phycol. **34**, 757–763 (1998)
8. S. Chinnasamy, A. Bhatnagar, R.W. Hunt, K.C. Das, Microalgae cultivation in a wastewater dominated by carpet mill effluents for biofuel applications. Bioresour. Technol. **101**, 3097–3105 (2010)
9. W.J. Oswald, The Coming Industry of Controlled Photosynthesis. Am. J. Public Health **52**, 235–242 (1962)
10. W.J. Oswald, Microalgae and waste-water treatment, in *Micro-algal Biotechnology*, ed. by M.B.L. Borowitzka. (Cambridge University Press, Cambridge, 1988), pp. 305–328
11. W.J. Oswald, My sixty years in applied algology. J. Appl. Phycol. **15**, 99–106 (2003)
12. R.E. Speece, *Anaerobic biotechnology for industrial wastewaters* (Archae Press, Tennessee, 1996)
13. A.C. Redfield, B.H. Ketchum, F.A. Richards, The influence of organisms on the composition of sea-water, in *The sea*, ed. by M.N. Hill, et al., vol. 2. (Interscience, New York, 1963), pp. 26–77
14. J.M. Ebeling, M.B. Timmons, J.J. Bisogni, Engineering analysis of the stoichiometry of photoautotrophic, autotrophic, and heterotrophic removal of ammonia-nitrogen in aquaculture systems. Aquaculture **257**, 346–358 (2006)
15. J.A. Toplin, T.B. Norris, C.R. Lehr, T.R. McDermott, R.W. Castenholz, Biogeographic and phylogenetic diversity of thermoacidophilic Cyanidiales in Yellowstone National Park, Japan, and New Zealand. Appl. Environ. Microbiol. **74**, 2822–2833 (2008)
16. W. Gross, I. Heilmann, D. Lenze, C. Schnarrenberger, Biogeography of the Cyanidiaceae (Rhodophyta) based on 18S ribosomal RNA sequence data. Eur. J. Phycol. **36**, 275–280 (2001)
17. R.A. Andersen, *Algal culturing techniques* (Elsevier, Burlington, 2005)
18. C. Oesterhelt, E. Schmalzlin, J.M. Schmitt, H. Lokstein, Regulation of photosynthesis in the unicellular acidophilic red alga *Galdieria sulphuraria*. Plant J. **51**, 500–511 (2007)

Chapter 5
Effectiveness of Enzymatic Biodiesel Production from Microalga Oil in Supercritical Carbon Dioxide

H. Taher, S. Al-Zuhair, A. Al-Marzouqi, Y. Haik and M. Farid

Abstract Biodiesel production from microalgae lipids showed to be the promise approach for alternative fuels. However, this is not yet commercialized. In the present study, the efficient production of biodiesel from *Nannochlorpsis* sp. grown locally was confirmed. Novozyme®435 and supercritical carbon dioxide were used as reaction catalyst and reaction medium, respectively, and the results were compared to lamb fat. In addition, the microalgae biomass production was studied extensively. It was found that *Nannochlorpsis* sp. can accumulate lipids by nitrogen starvation reaching 29 % with 21.06 mg $L^{-1}d^{-1}$ lipid productivity when grown in nitrogen sufficient medium. The enzymatic production in supercritical carbon dioxide was efficient with 55 % ester yield higher than lamb meat fat.

5.1 Introduction

The increasing world population, fast depletion of fossil fuels, decline in oil reserves and emerging concerns on global warming has led to search for alternative fuels. Biodiesel, mainly composed of fatty acid methyl esters (FAMEs), production from vegetable oils received considerable attraction as a replacement to petroleum fuels. It is a non-toxic and biodegradable fuel with lower gas emissions compared to fossil fuels. The use of vegetable oils is the common approach,

H. Taher (✉) · S. Al-Zuhair · A. Al-Marzouqi · Y. Haik
United Arab Emirates University, Al Ain, United Arab Emirates
e-mail: H.Taher@uaeu.ac.ae

M. Farid
University of Auckland, Auckland, New Zealand

M. O. Hamdan et al. (eds.), *ICREGA'14 - Renewable Energy: Generation and Applications*, Springer Proceedings in Energy, DOI: 10.1007/978-3-319-05708-8_5,

however using crops oil as fuel competes with their use as food and involves additional lands, which may increases the food prices [1]. Furthermore, it has been reported that about 60–90 % of biodiesel cost comes from the raw material cost [2]. For that, waste cooking oils and animal fats were proposed [3–7]. Nevertheless, realistically these cannot replace all world demand of biodiesel.

Microalgae are currently considered as the promising lipid source. Unlike oil-rich crops, microalgae have high growth rate and lipid content. They typically double their biomass within 24 h, and during the exponential phase they can double each 3.5 h [8–10]. The quite common lipid content is 20–50 %, which can be enhanced further to 80 % by media and genetic engineering [11–13]. In addition, the lipid productivity has been reported to exceed that of the best producing oil crops [11]. Thus, it is considered to be the only way to produce enough biodiesel.

The recent studies have reported that the marine species *Nannochloropsis* sp. is one of the potential microalgae strains for biodiesel production owing to the fact that they are capable of producing lipids content in range of 22–35 % (dry weight basis) and high biomass productivity in range of 25–61 mg L^{-1} d^{-1} [14–16]. In addition, *Nannochloropsis sp.* can grow in seawater, which can reduce the load on freshwater.

Several chemical technologies have been used for oil extraction. Among them, using chemical solvents such as *n*-hexane, mixture of chloroform-methanol, and mixture of *n*-hexane-iso-propanol [17–19]. However, these organic solvents use is not preferable, especially with the growing environmental concern. In addition, large amount of solvent and final product purification are required.

Supercritical carbon dioxide (SC–CO_2) showed to be the promising alternative to organic solvents for oil extraction. It has been tested with several feedstocks and in most cases high extraction efficiencies were obtained [20–23]. The attractive advantage of using SC–CO_2 is that after the extraction is completed the solvent can be easily separated from the extract by depressurizing, and no solvent residue remains in the residual solid matrices, which allows it to be used for further applications. On the other hand, SC–CO_2 is identified as a good alternative to organic solvents in biosynthetic reactions. The tunable salvation power of the CO_2 above the critical point usually enhances the lipase activity and stability, and reduces the mass transfer problems that usually occurs when immobilized lipases are used [24].

Similar to conventional biodiesel production from vegetable oils, microalgae lipids can be converted to biodiesel using lipase. To best of our knowledge, *Chlorella* sp. is the only species that has been enzymatically transesterified [25–28] and no studies on enzymatic microalgae biodiesel production in SC–CO_2.

The main objective of this study is to produce biodiesel from *Nannochlorpsis* sp. lipids extracted by SC–CO_2. The biomass and lipid productivity of the selected spices were studied extensively. The capability of SC–CO_2 to extract lipids from the lyophilized biomass and convert extracted lipids to FAMEs was investigated and compared to that of lamb fats.

5.2 Materials and Methods

5.2.1 Chemicals and Enzyme

n-Hexane, HEPES (4-(2-hydroxyethyl)-1-piperazineethane sulfonic acid), methanol, chloroform, iso-propanol and 14 % boron tetraflouride-methanol mixture were purchased from Sigma—Aldrich Inc. Liquefied CO_2 with a purity of 99.95 % was supplied by Abu-Dhabi Oxygen Company (UAE). Ultra high purity Helium and zero-air were supplied by Air Product Company (UAE). Standards of high purity fatty acid methyl esters (FAMEs) comprised of; 3.9 % myristic acid methyl ester (C14:0), 9.9 % palmitic acid methyl ester (C16:0), 6.0 % stearic acid methyl ester (C18:0), 10 % elaidic acid methyl ester (C18:1), 24.8 % cis-9-oleic methyl ester (C18:1), 36.1 % linoleic acid methyl ester (C18:2n6c), 1.9 % linolelaidic acid methyl ester (C18:2n6t), 2.1 % arachidic acid methyl ester (C20:0), and 2.1 % behenic acid methyl ester (C22:0) were obtained from Sigma Aldrich (USA). Novozym®435 (7000 PLU and 2 % water content) was obtained from Novozyms A/S (Denmark).

5.2.2 Strains and Culture Media

Nannochloropsis sp. provided by Umm al-Quwain marine environment research center (UAE) was grown in Guillard F/2 and in nitrogen-deficient medium. The Guillard F/2 media comprised of seawater (32 g L^{-1} salinity) with 1 ml L^{-1} of the following major nutrients (in mM); 0.880 $NaNO_3$, 0.036 $NaH_2PO_4{\cdot}H_2O$ and 0.106 $Na_2SiO_3{\cdot}9H_2O$ and 1 ml L^{-1} of trace metals solution consisted of (10^{-3} μm); 0.08 $ZnSO_4{\cdot}7H_2O$, 0.9 $MnSO_4{\cdot}H_2O$, 0.03 $Na_2MoO_4{\cdot}2H_2O$, 0.05 $CoSO_4.7H_2O$, 0.04 $CuCl_2{\cdot}2H_2O$, 11.7 $Fe(NH_4)_2(SO_4)_2{\cdot}6H_2O$ and $Na_2EDTA{\cdot}2H^2O$. Prepared medium were sterilized in an autoclave (Hirayama HV-50, Japan) at 121 °C for 15 min and cooled at room temperature. Prior to use, 1 ml L^{-1} of Vitamins; B_{12}, Biotin and Thiamine prepared in HEPES at pH 7.4 were added.

5.2.3 Growth and Biomass Production

The culture was initially grown in 250 ml Erlenmeyer flasks containing 150 ml of the culture bubbled with sterilized atmospheric air at a flow rate of 0.25 ml min^{-1} obtained using mass flow controller (model MC-1SLPM-P-SV, Alicat Scientific, USA). The culture pH was maintained at 7.4 using HEPES buffering agent, which was monitored continuously throughout the experiment period by pH meter (Hanna Instruments HI8424, USA). The temperature was controlled at 27 °C by placing the flask in a temperature controlled shaking water bath (Daihan Labtech, Korea) shaken at 150 r min^{-1}. Four parallel light sources allocated 22 cm above

culture surface with 12:12 dark: light cycles were used to provide the sufficient lighting energy. The culture was allowed to grow for 3 weeks and the growth was monitored in daily basis by measuring the optical density at 680 °C using UV-spectrophotometer (UV–1800, Shimadzu, Japan). Concentrated microalgae were dried at 105 °C overnight for dry weight measurements.

For sufficient production of the biomass, the culture was transferred to 5 L bubble column photobioreactor with internal illumination using one of 60 W white fluorescent light at a light intensity of 120 μmol m^{-2} s^{-1} measured using a light meter (model 472990, Extech Instruments, Massachusetts). Further scale up of the production was carried in 300 L open pond (1.5 m × 1 m × 0.4 m) using the 4.5 L inoculums obtained from the photobioreactor.

The biomass was harvested after three weeks by centrifugation at 3000 r min^{-1} for 15 min using multispeed centrifuge (IEC CL31, Thermo Scientific, USA). The concentrated biomass was then re-cultivated in the pond in nitrogen-deficient of F/2 media, where $NaNO_3$ was eliminated to enhance the lipid accumulation. The culture was allowed to grow for 4 more weeks then harvested by flocculation using sodium hydroxide. Collected biomass were dewatered and lyophilized at –83 °C and 0.04 mbar for 8 h in the Telstar freeze drier (Terrassa, Spain).

5.2.4 Lipid Extraction

The lipid content was determined by SC–CO_2 extraction carried at 50 °C, 3 ml min^{-1} and 500 bar for total 100 ml of SC–CO_2 passed in ISCO supercritical extraction unit (SFX-220, USA). These conditions were selected based on the optimum conditions obtained in our previous study with lamb fat [7]. 1.5 ± 0.2 g of the biomass was placed in the extraction cell, and CO_2 was pressurized to 500 bar using a high-pressure syringe pump (Model 260D, ISCO, USA). The pressurized CO_2 was then heated to operation temperature and pumped into the extraction vessel. The extract was collected in an extract vial via micro-metering valve (HIP 15-12AF1-V) for each 5 ml of passed CO_2, and the lipid content was determined as percentage of accumulated extract weight per subjected biomass to the system. Further details about SC–CO_2 extraction procedure can be found in our previous publication [7]. Lipid productivity was determined by multiplying the lipid content to biomass productivity.

5.2.5 Enzymatic Production of Biodiesel

The enzymatic production of biodiesel from extracted oils was carried in 10 ml cell in the presence of both Novozym®435 and SC–CO_2. The reaction temperature and pressure were controlled by a temperature controller (Autonics TZN4S, Korea) with an electrical heating tape wrapped around the reaction cell and

Telydyne pump controller, respectively. The reaction mixture consisted of 0.5 g of extracted lipids, 0.15 g of Novozym®435 and 0.097 ml of methanol that corresponds to 4:1 methanol to lipid ratio. As long as the reaction temperature reached, the cell was filled with SC–CO_2 and reaction was started. Reaction was allowed to proceed for 24 h and the collected product were dissolved in *n*-hexane for further analysis of the reaction yield.

5.2.6 FAME Analysis

Extracted lipids were analyzed after esterification to FAME using 14 % boron tetraflouride–methanol mixture as described by Rule [29]. Gas chromatography (Varian, CP-3800, USA), fitted with CP-Sil 88 FAME capillary column (100 m × 0.25 mm × 0.2 μm, Varian, USA), flame ionization detector (FID) and equipped with auto-injector (CP 8410. Varian, USA) was used to identify and quantify the present FAME. Helium and zero air were used as the carrier gases with a split ratio of 40:1.The oven initial temperature was 150 °C during 1 min, and then increased to 220 °C at 4 °C min^{-1}. Both the injector and the detector were set at 260 °C. Similarly, the FAME yield of lipase catalyzed transesterification was determined.

5.3 Results and Discussion

5.3.1 Growth and Biomass Productivity

Biomass production of *Nannochlorpsis* sp. was carried out at different scales ranging from 150 ml to 300 L culture. In all cases, the species were grown in F/2 media with 12:12 light to dark cycles. The growth study was carried in 250 ml scale, where the species was initially allowed to grow and the biomass productivity was determined. The culture was then transferred to 5 L photobioreactor to provide enough inoculums for the open pond, where the culture was allowed to accumulate more lipids after three weeks by stressing the environment.

Figure 5.1 shows cell growth curve in the nutrient rich media as biomass concentration verses cultivation time. The cell concentrations were determined from pre-prepared calibration curve between the optical density at 680 nm and cell counting. The figure clearly shows that the growth started with lag phase for 6 d where the cells were adapting themselves to growth in the new environment, followed by a log phase where cells starts doubling at a constant rate. Because the medium nutrient was depleting by time, the growth starts to be limited, in day 22, and the rate decreased. As can be seen, this is avoided in this study as the culture was directly transferred to the photobioreactor. The doubling time in the log phase was almost 6 h, which is higher than the reported value in the literature. The

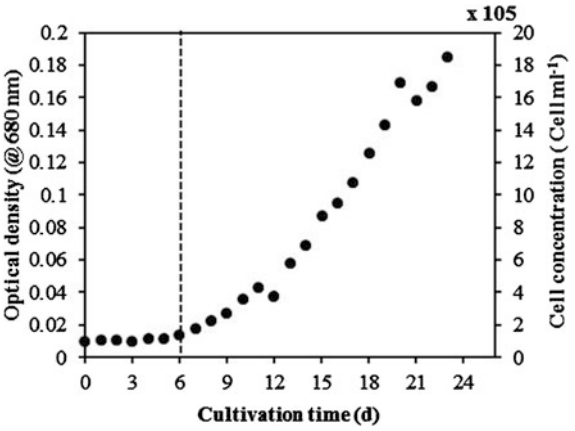

Fig. 5.1 Growth curve of *Nannochlorpsis* sp. grown in 250 ml

specific growth rate determined from the slop of the growth curve in the logarithmic phase and was found to be 0.182 d^{-1}. The biomass productivity in this phase was 0.13 g L^{-1} d^{-1}.

5.3.2 Lipid Content and Productivity

For biodiesel production, lipids have to be extracted from the biomass, and then converted to FAMEs. Usually, chemical solvents are used. In this study, the focus was on SC–CO_2 use as it is the green solvent and no residual solvent remains in the biomass, which allows further applications for the leftover biomass. The extraction was carried out in duplicate at 50 °C, 500 bar and 3 ml min^{-1}. When the strain was grown in the nutrient sufficient media, the lipid content was found to be 16.2 % (dry basis), which results in a lipid productivity of 21.1 mg L^{-1} d^{-1} determined by multiplying the lipid content by biomass productivity. However, in the nitrogen deficient media, where cells were stressed and allowed to accumulate more oils, the lipid content increased by 83 % reaching 29.6 %. In general, the biomass productivity found in this study was close to that reported in literature, however, the lipid content was not, resulting in lower overall lipid productivity [14]. This lower productivity might due to the growth environment where the referred study grew the species in 5 % CO_2 enrichment.

5.3.3 Analysis of the Extracted Lipids

The chromatographic analysis of the extracted lipids was carried in GC-FID, after rapid transesterification to FAME. The analysis showed that the extract was mainly contained of palmitic acid (31.6 %) and oleic acids (35.5 %) with 66 % saturation ratio of the extract. Table 5.1 shows the details of the extract components.

Table 5.1 Fatty acid composition (% by weight of total fatty acids) of lipid extract

Fatty acids (% of total fatty acids)	(% wt)
C14:0	6.98
C16:0	31.58
C18:0	3.54
C18:1	9.34
C18:1	34.48
C18:2n6c	0.97
C18:2n6t	9.24
C20:0	0.21
C22:0	3.65

5.3.4 Enzymatic Production of Biodiesel in SC–CO_2

The efficient use of SC–CO_2 in enzymatic FAME production from extracted oil in the presence of the immobilized lipase, Novozym®435 was tested. The reaction was carried at the optimum conditions found in our previous study which was; 50 °C, 200 bar and 2 h reaction. 0.5 g of extracted lipid were mixed with 0.15 g of Novozym®435 and 0.094 ml of methanol. This corresponds to 30 % and 4:1 enzyme loading (wt%) and methanol to oil ratio, respectively. It was found that 62 % of the extracted oil was converted to FAME and produced ester are mainly comprised of oleic and palmitic acids.

As a compression to produced FAME from lamb meat fat in our previous study [7], SC–CO_2 and Novozym®435 showed to be more efficient to act with oils. This is mainly due to the solid nature of the animal fats and the unsaturation degree that counts for 45 % of total fatty acids weight. In addition to the higher solubility of methanol in oil compared to fat when used in SC–CO_2. Nevertheless, animal fat as byproduct of meat, its use for biodiesel production in linked to the limited meat production, which is not the case in microalgae oil production.

5.4 Conclusion

The results of this study proved the capability of SC–CO_2 and Novozym®435 in converting microalgae oil to biodiesel. In addition it confirmed that high oil conversion capability compared to fat. Oils showed 55 % FAME yield compared to lamb meat fat. In addition, SC–CO_2 superiority for oil extraction and conversion and Novozym®435 in enhancing the reaction was proved.

The biomass production and lipid productivity of *Nannochlorpsis* sp. oil was found to be less than what reported in literature; however it is still acceptable for biodiesel production.

References

1. D. Rutz, R. Janssen, in *BioFuel Technology Handbook: WIP Renewable Energies.* (Elsevier Biomedical Press, Amsterdam, 2007)
2. S. Al-Zuhair, Production of biodiesel: possibilities and challenges. Biofuels, Bioprod. Biorefin. **1**, 57–66 (2007)
3. H.N. Bhatti, M.A. Hanif, M. Qasim, R. Ata ur, Biodiesel production from waste tallow. Fuel **87**, 2961–2966 (2008)
4. M.K. Lam, K.T. Lee, A.R. Mohamed, Sulfated tin oxide as solid superacid catalyst for transesterification of waste cooking oil: an optimization study. Appl. Catal. B **93**, 134–139 (2009)
5. M.G. De Paola, E. Ricca, V. Calabr, S. Curcio, G. Iorio, Factor analysis of transesterification reaction of waste oil for biodiesel production. Bioresour. Technol. **100**, 5126–5131 (2009)
6. F. Ma, L.D. Clements, M.A. Hanna, Biodiesel fuel from animal fat. Ancillary studies on transesterification of beef tallow. Ind. Eng. Chem. Res. **37**, 3768–3771 (1998)
7. H. Taher, S. Al-Zuhair, A. AlMarzouqui, I. Hashim, Extracted fat from lamb meat by supercritical CO_2 as feedstock for biodiesel production. Biochem. Eng. J. **55**, 23–31 (2011)
8. H. Taher, S. Al-Zuhair, A.H. Al-Marzouqi, Y. Haik, M.M. Farid, A review of enzymatic transesterification of microalgal oil-based Biodiesel using supercritical technology. Enzyme Res. **468292**, 1–25 (2011)
9. V. Patil, K.-Q. Tran, H.R. Giselrd, Towards sustainable production of biofuels from microalgae. Int. J. Mol. Sci. **9**, 1188–1195 (2008)
10. N. Moazami, A. Ashori, R. Ranjbar, M. Tangestani, R. Eghtesadi, A.S. Nejad, Large-scale biodiesel production using microalgae biomass of nannochloropsis. Biomass Bioenergy **39**, 449–453 (2012)
11. Y. Chisti, Biodiesel from microalgae. Biotechnol. Adv. **25**, 294–306 (2007)
12. M. Adamczak, U.T. Bornscheuer, W. Bednarski, The application of biotechnological methods for the synthesis of biodiesel. Eur. J. Lipid Sci. Technol. **111**, 800–813 (2009)
13. P. Spolaore, C. Joannis-Cassan, E. Duran, A.n. Isambert, Commercial applications of microalgae. J. Biosci. Bioeng. **101**, 87–96 (2006)
14. L. Rodolfi, G.C. Zittelli, N. Bassi, G. Padovani, N. Biondi, G. Bonini, M.R. Tredici, Microalgae for oil: Strain selection, induction of lipid synthesis and outdoor mass cultivation in a low-cost photobioreactor. Biotechnol. Bioeng. **102**, 100–112 (2009)
15. L. Gouveia, A.C. Oliveira, Microalgae as a raw material for biofuels production. J. Ind. Microbiol. Biotechnol. **36**, 269–274 (2009)
16. S.Y. Chiu, C.Y. Kao, M.T. Tsai, S.C. Ong, C.H. Chen, C.S. Lin, Lipid accumulation and CO_2 utilization of *Nannochloropsis oculata* in response to CO_2 aeration. Bioresour. Technol. **100**, 833–838 (2009)
17. E.G. Bligh, W.J. Dyer, A rapid method of total lipid extraction and purification. Can. J. Biochem. Physiol. **37**, 911–917 (1959)
18. J. Folch, M. Lees, G.H. Sloane Stanley, A simple method for the isolation and purification of total lipids from animal tissues. J. Biol. Chem. **226**, 497–509 (1957)
19. A. Hara, N.S. Radin, Lipid extraction of tissues with a low-toxicity solvent. Anal. Biochem. **90**, 420–426 (1978)
20. R.L. Mendes, B.P. Nobre, M.T. Cardoso, A.P. Pereira, A.n.F. Palavra, Supercritical carbon dioxide extraction of compounds with pharmaceutical importance from microalgae. Inorg. Chim. Acta **356**, 328–334 (2003)
21. J.P. Friedrich, E.H. Pryde, Supercritical CO_2 extraction of lipid-bearing materials and characterization of the products. J. Am. Oil Chem. Soc. **61**, 223–228 (1984)
22. P. Tonthubthimthong, P.L. Douglas, S. Douglas, W. Luewisutthichat, W. Teppaitoon, L.-E. Pengsopa, Extraction of nimbin from neem seeds using supercritical CO_2 and a supercritical CO_2—methanol mixture. J. Supercrit. Fluids **30**, 287–301 (2004)

23. G. Andrich, U. Nesti, F. Venturi, A. Zinnai, R. Fiorentini, Supercritical fluid extraction of bioactive lipids from the microalga *Nannochloropsis* sp. Eur. J. Lipid Sci. Technol. **107**, 381–386 (2005)
24. K.P. Dhake, K.M. Deshmukh, Y.P. Patil, R.S. Singhal, B.M. Bhanage, Improved activity and stability of Rhizopus oryzae lipase via immobilization for citronellol ester synthesis in supercritical carbon dioxide. J. Biotechnol. **156**, 46–51 (2011)
25. W. Xiong, X. Li, J. Xiang, Q. Wu, High-density fermentation of microalga *Chlorella protothecoides* in bioreactor for microbio-diesel production. Appl. Microbiol. Biotechnol. **78**, 29–36 (2008)
26. X. Li, H. Xu, Q. Wu, Large-scale biodiesel production from microalga Chlorella protothecoides through heterotrophic cultivation in bioreactors. Biotechnol. Bioeng. **98**, 764–771 (2007)
27. O.K. Lee, Y.H. Kim, J.-G. Na, Y.-K. Oh, E.Y. Lee, Highly efficient extraction and lipase-catalyzed transesterification of triglycerides from Chlorella sp. KR-1 for production of biodiesel. Bioresour. Technol. **147**, 240–245 (2013)
28. S. Anitha, J. Narayanan, Biodiesel production from *chlorella vulgaris* with special emphasis on immobilized lipase catalyzed transesterification. Int. J. Recent Sci. Res. **3**, 733–737 (2012)
29. D.C. Rule, Direct transesterification of total fatty acids of adipose tissue, and of freeze-dried muscle and liver with boron-trifluoride in methanol. Meat Sci. **46**, 23–32 (1997)

Chapter 6
Review of Dynamic Electric Circuit Models for PEM Fuel Cells

M. Nabag, A. Fardoun, H. Hejase and A. Al-Marzouqi

Abstract Many studies have been conducted to understand the phenomena underlying the operation of fuel cells in order to enhance both the efficiency and the durability of these systems, by optimizing the cell's operating conditions, structure and materials used in their manufacturing. Different characterization techniques have been exploited in order to establish comprehensive models that describe the complex electrochemical and thermodynamic behavior of the fuel cell. Since the output resulting from these chemical and physical processes is electric power, an equivalent circuit model is preferred in order to describe the electrical interaction of the fuel cell with the load and to facilitate the development of adequate power converter designs. Moreover, these models present a useful method for interpreting the characterizations results and provide sensible evaluation of the effects of the operating and the environmental conditions on the fuel cell performance. This paper presents the recent research efforts related to the modeling of the dynamic electric behavior of Proton Exchange Membrane (PEM) fuel cells using equivalent electric circuits. It also highlights the studies that use these circuit models to evaluate the effects of low and high current harmonics on the fuel cell's efficiency and durability.

Keywords PEM fuel cells · Electric circuit model · Electrochemical impedance spectroscopy · Current interrupt · Polarization curve

M. Nabag (✉) · A. Fardoun · H. Hejase · A. Al-Marzouqi
UAE University, Al Ain, United Arab Emirates
e-mail: m.nabag@uaeu.ac.ae

M. O. Hamdan et al. (eds.), *ICREGA'14 - Renewable Energy: Generation and Applications*, Springer Proceedings in Energy, DOI: 10.1007/978-3-319-05708-8_6,

6.1 Introduction

Fuel cell technology is considered as a promising solution to the global energy supply problem among other conventional sources and renewable alternatives. Although it remains an immature and expensive technology that has not attained yet a sustainable commercial success [1], efforts worldwide have intensified to maintain the development in this field and demonstrate net profitability in the application of fuel cell systems. The aid of both public and private sectors is needed to support studies on the fundamental science behind the fuel cell operation in order to make robust and low cost fuel cell systems that can compete with alternative energy sources. According to a report presented in [1], most investment has gone to product development and subsidies to establish commercial markets for specific fuel cell applications. As a result, fuel cells have not been able to overcome issues of longevity, reliability, power density, and production costs. New research tools that enable us to observe and understand the behavior of fuel cells especially at the atomic level are required.

Electric Circuit Modeling (ECM) is a well-known method for interpreting the observations that result from the characterization of the fuel cells. Compared to the mechanistic models, this modeling technique provides a better understanding of the various effects of the operating conditions on the fuel cells performance. The ECM approach enables researchers to work on the optimization of the cell fabrication and the operating conditions in order to achieve maximum efficiency and fuel cell durability. Both physical and empirical circuits can be developed from certain experimental tests, but the former is preferable since changes in the circuit parameters can be attributed to the cell aging or to a particular change in the operating conditions. This report summarizes the recent efforts in developing electric circuit models for PEM fuel cells (PEMFCs). It explores new directions that help gain a deep and comprehensive understanding about how fuel cells interact with loads and power conditioning units. It also provides a sensible evaluation of the effects of the operating and the physical conditions on the fuel cell operation.

This report is organized as follows: Sect. 6.2 reviews the main testing techniques used to characterize the behavior of fuel cells. Section 6.3 details the common approaches for developing equivalent electric circuit models for fuel cells. Then in Sect. 6.4, we will review the details of the studied literature focusing on the development and the various applications of these models. Finally, conclusions about the possible future directions are discussed in Sect. 6.5.

6.2 Fuel Cell Testing Techniques

In order to understand the inner phenomena of fuel cells and analyze both their steady-state and transient behaviors, different methods are used to develop adequate models to simulate these behaviors. The primary and simplest approach is

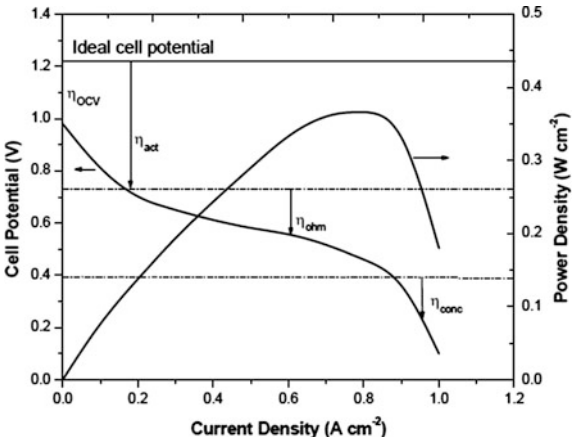

Fig. 6.1 V-I characteristics of a single PEM fuel cell [2]

the one representing the steady-state voltage-current characteristics with a polarization curve like the one shown in Fig. 6.1, [2]. Experimentally, a DC load current is varied and the fuel cell voltage is measured under constant conditions, i.e. temperature, humidity, pressure, and gas stoichiometry. Either mechanistic or empirical model equations can be used to provide a mathematical description of the fuel cell steady-state performance. The mathematical model for the fuel cell voltage includes four parts: one describing the maximum open voltage while the other three parts represent the main losses influencing the polarization curve at different current values. At low current densities, the activation loss arises from the charge transfer process at the electrode-electrolyte interface. This process is dominant at the cathode side due to the slow kinetics of the oxygen reduction reaction (ORR). At the nominal operating current, the membrane ionic resistance together with the electrodes' electronic resistance result in a linear voltage drop referred to as ohmic loss. At higher currents, the reactants reach the limiting rate at which they can be transported to/from the reaction sites. This causes rapid decay in the curve and this loss is referred to as concentration or mass-transport loss. Because different chemical and thermodynamic processes overlap, it is difficult to utilize the V–I characteristics in the assessment of the membrane-electrode interface mechanisms and in the understanding of the individual contribution of each process to the dynamic electrical performance and efficiency of the fuel cell. Other transient techniques are used to characterize the various dynamic processes in the operation of the fuel cell. The results of these techniques are usually interpreted using electric circuit models. These techniques or tests can be carried out either in the time domain or the frequency domain. One of the most extended time domain tests is the current interruption (CI) test, whilst the most popular frequency domain test is the electrochemical impedance spectroscopy (EIS).

The CI test is a time domain test in which the system under study is kept at its operation point (constant current load) until it reaches stationary state. Once reached, the current load is abruptly interrupted, allowing the study of the voltage

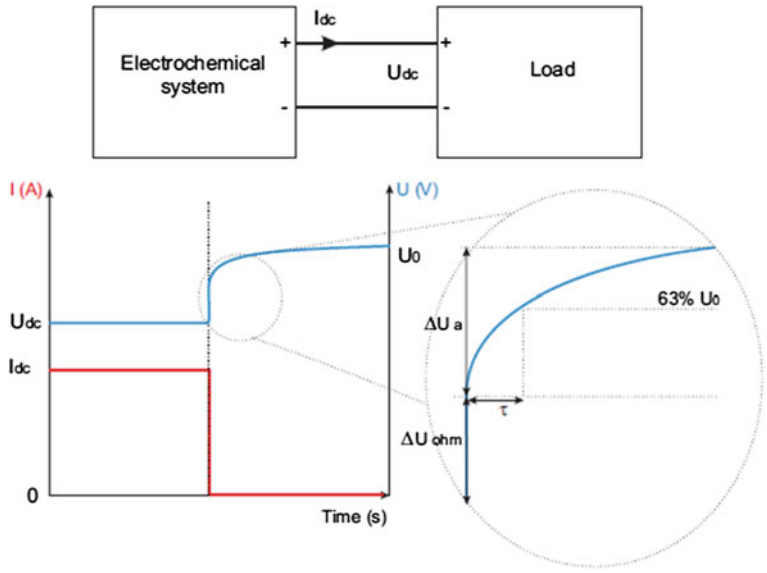

Fig. 6.2 Current interrupt test [3]

evolution. Because electrochemical systems operate in direct current (DC), this test is carried out applying a DC current and measuring the DC voltage as depicted in Fig. 6.2, [3]. The advantage of this modeling technique is its simplicity, both in setup and control. However, there are several drawbacks. One of them is that the model precision depends heavily on the correct identification of the point at which the voltage evolution changes from vertical to nonlinear. An imprecise measurement will cause the incorrect calculation of the voltage drops and the time constant. In the CI method, the voltage step caused by the low resistance falls in the range of few microvolts to millivolts. For this reason, small errors in the measurements become significant. Other limitations in using this technique are the sampling rate, extrapolation, presence of noise, and the interfering capacitances of the cable and switching transistors. Finally, this method does not add significant information about the internal processes like the low frequency process related to mass-transport limitations. Some applications of this method to fuel cells can be found in [4, 5].

Whilst CI is carried out in the time domain and with direct current, EIS is a frequency domain test which needs the application of alternating current and voltage. EIS tests also seek to calculate the impedance of the system under study. But the most important advantages of frequency domain tests are the richer information obtained and the simpler data processing than those associated with the CI test. EIS has a significant advantage over CI method, since the amplitude of an AC voltage is measured instead of a voltage signal decaying in the time domain. No signal is extrapolated, but the quotient from AC voltage and AC

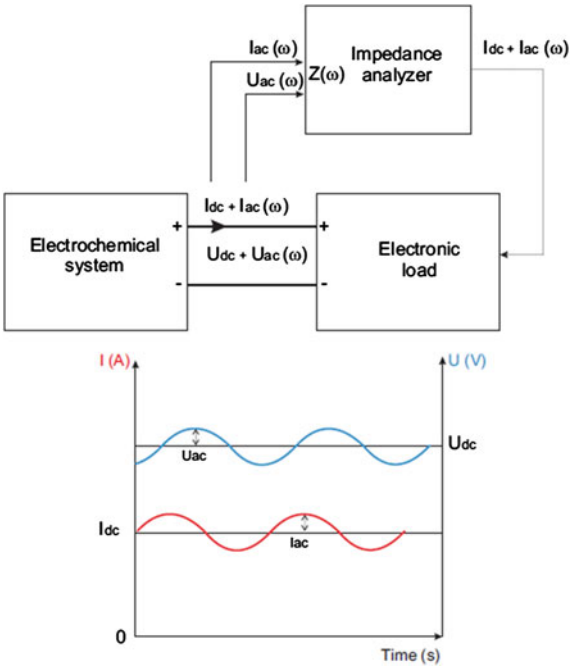

Fig. 6.3 EIS test procedure [3]

current is calculated. Impedances below 1 mΩ can be determined at high accuracy. During EIS tests, the ripple (either current or voltage) is applied to the electrochemical system.

This ripple will cause the system to react, generating an AC voltage (if the excitation signal is current) or AC current (if the excitation signal is voltage). If the imposed ripple is current, it is said to be a galvanostatic mode EIS, whilst if it is a voltage signal it is called a potentiostatic mode. The selection criterion to choose between one mode and another is frequently the control model of the system under test. For example, the fuel cell current is easier to control than the voltage. Hence, it would be easier to apply a galvanostatic (current control) mode. The AC signals applied are kept small enough to maintain linearity during the tests (e.g. 5 % of the rated voltage). The ripple can be applied with a fixed or variable frequency, which in the variable case can be programmed as a sweep. Since electrochemical systems generate direct current, it is unavoidable to have both DC and AC signals while carrying out EIS tests. The DC level is used to keep the electrochemical system at its operation point, but it is not considered for the impedance calculation, in which only the AC signals are involved. This implies that the DC level must be rejected before the AC impedance is calculated. A diagram explaining the whole process is presented in Fig. 6.3, [3].

EIS tests can be carried out with off-the-shelf equipment: electronic load, signal generator and voltage and current transducers. However, the subsequent impedance calculation and model extraction is time consuming and complex.

Therefore, it is recommendable to use an impedance analyzer, which generates the excitation signal and calculates the complex impedance by measuring the current and voltage. After the EIS test is carried out, the data must be processed. Normally the impedance analyzer includes a software package to do it. The data are rendered in a text file, which is translated by the software to Nyquist and Bode plots. Based on these plots, the user can define an equivalent circuit, which the program fits to the experimental results. The next section will detail the approach of Electric Circuit Modeling (ECM) based on EIS measurements.

6.3 Fuel Cell Electric Circuit Models

Figure 6.4 shows a typical Nyquist plot and the circuit that fits most of the PEMFCs [6]. The processes that occur inside a fuel cell can be simulated using resistive and capacitive circuit elements. The circuit elements describe the behavior of electrochemical reaction kinetics, the ohmic conduction processes, and mass transport using an impedance spectrum by EIS. At the highest frequencies measured, the impedance tends to the real axis at a resistance R_Ω reflecting the ionic resistance of the fuel cell. A resistor R_{ct} in parallel with a capacitor C_{dl} represent the impedance behavior of an electrochemical reaction interface where the capacitance C_{dl}, known as the double charge layer capacitance, describes the charge separation across the interface at both the cathode (c) and the anode (a). The time constant $\tau = R_{ct}C_{dl}$ is considered as a measure of the rate of a reaction or process. The Nyquist plot of resistance and capacitance in parallel is an ideal semicircle where the diameter equals the value of the resistance, R_{ct}. The imaginary part of the impedance reaches a maximum at frequency f_{max}, denoted as the characteristic frequency. Finally, the Warburg impedance Z_w models the diffusion process of the reactants in the electrodes.

6.4 Reviews of Previous Works on ECM

Choi et al. [7] have come up with an impedance model using a Frequency Response Analyzer (FRA) to evaluate the effect of ripple currents on power loss and fuel consumption. The dynamic model is found from the FRA by superimposing a low sinusoidal AC current (1A) with frequency range of 0–10 kHz. The equivalent circuit used is shown in Fig. 6.5. The setup consists of two (PEMFC) systems, namely, SR-12 and Nexa, programmable electronic load, frequency response analyzer, current/voltage probes and a computer with the simulation software. It was noted that in the extreme case of 100 % ripple (120 Hz), the available power is reduced by 5.86 % in SR-12 and 9.4 % in Nexa. Furthermore, for a 30 % ripple, the reduction in output power from SR-12 and Nexa is 0.5 and 0.84 %, respectively. The authors found that if the 120 Hz ripple currents exist at

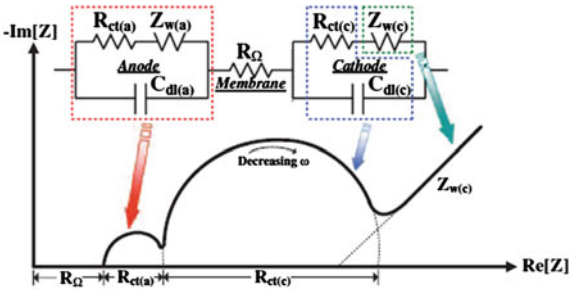

Fig. 6.4 Equivalent circuit model and corresponding Nyquist plot [6]

the output of the fuel cell stack, more fuel cells are required to get a certain amount of power. However, limiting the low frequency (120 Hz) fuel cell ripple current to between 30 and 40 % has been shown to result in less than 0.5–1.5 % reduction in fuel cell output power. The authors did not present the modeling approach or demonstrate the usefulness of developing such a complex model.

Yu and Yuvarajan [8] presented a PSPICE-based circuit model for the PEMFC that uses BJTs and LC elements to represent the phenomena of activation polarization, ohmic polarization and mass transport effect. In the proposed model shown in Fig. 6.6, a diode is used to model both the activation and ohmic losses. The depletion region in a diode provides a potential barrier to inhibit the migration of carriers across the junction, which is similar to the sluggish electrode kinetics that cause the activation loss in fuel cells. The emission coefficient was varied so the model can match the V–I characteristics of the fuel cell. The parasitic resistance in the diode model was used to reflect the ohmic polarization. To model the mass transport, the authors employed a current limiting circuit composed of two BJTs and a sensing resistor. Only the area of the BJTs was increased to match the large current of the fuel cell stack. A capacitor was used to model the charge double layer effect. A voltage undershoot is observed as a result of the time required (0.5 s) by the air pump in the commercial fuel cell module to supply higher air flow at step changes of the load. This transient effect can be modeled by an LC element. The authors validated the model with variable load changes without performing AC impedance tests.

Palma et al. [9] investigated the effects of continuous and discontinuous conduction operation of the DC-DC converters on the fuel cell performance in terms of temperature rise and hydrogen fuel consumption. The circuit model used is shown in Fig. 6.7. The model parameters are obtained by means of EIS. The experimental results showed that the presence of high frequency ripple currents (10–200 kHz) does not impact negatively on the performance of the fuel cell stack. This is especially convenient in the case of connecting a DC-DC converter at the terminals of the fuel cell. Since the frequency is normally high (above 30 kHz), the additional hydrogen consumed by the fuel cell and heat produced by it is not significant. It has also been shown that for currents with duty cycles between 40 and 80 %, the amount of hydrogen being consumed by the stack was no more than 5 % above its nominal value. For duty cycles below 40 %, the amount of hydrogen

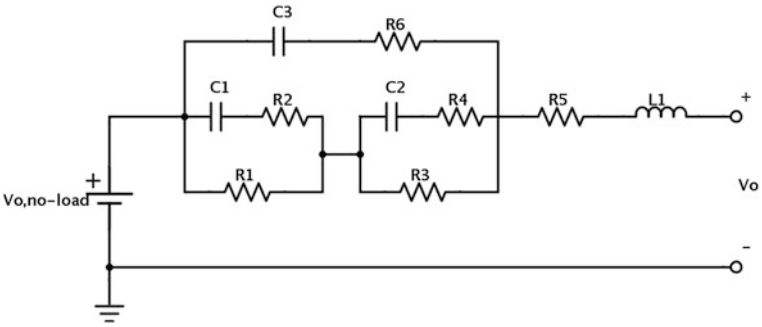

Fig. 6.5 Fuel cell equivalent electrical circuit at a certain operating point used by Choi et al. [7]

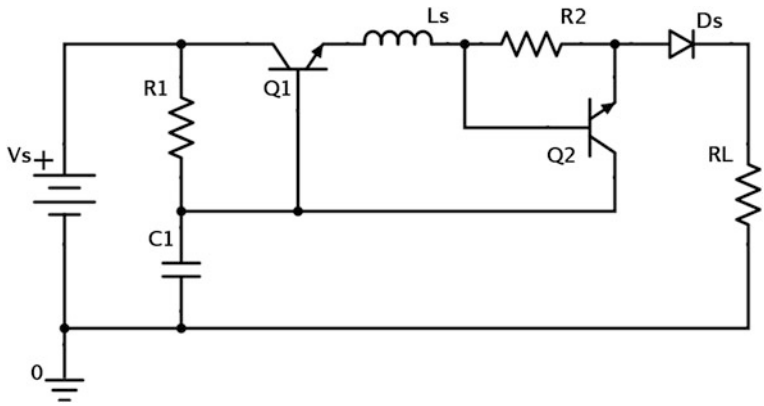

Fig. 6.6 Proposed model of the fuel cell by Yu and Yuvarajan [8]

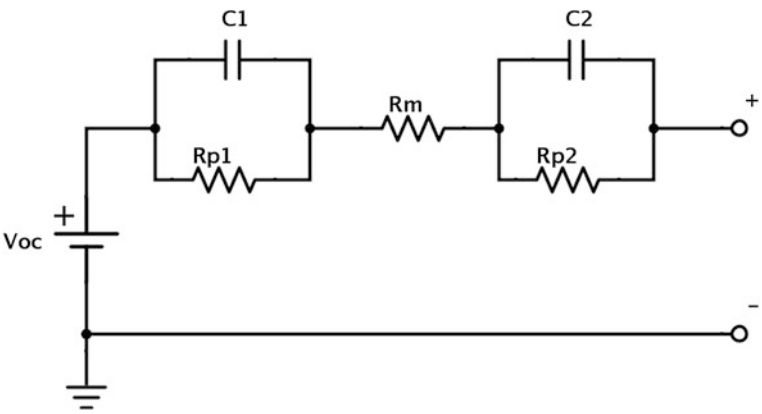

Fig. 6.7 Model used by Palma et al. [9]

being consumed increased as the duty cycle was reduced. This is due to the current magnitude for these duty cycles [9].

Yuan et al. [10] diagnosed by EIS a 500 W fuel cell stack using special experimental method in order to evaluate the effects of temperature, flow rate, humidity of the impedance spectra of the stack. The 500 W stack studied by Yuan et al. consisted of only 6-cells and the study did not consider the impedance characteristics under load changes.

Yan et al. [11] presented a study of the AC impedance characteristics for a 20-cell 2 kW stack under load changes and different operating conditions as well. The impedance spectra were recorded by sweeping frequencies over the range of 20–60 mHz with 8 points per decade. The amplitude of the AC current was always kept at 10 % of the DC current. The fuel cell stack was operated steadily for at least 1 h before starting each impedance measurement. During the AC impedance measurements, only one variable was allowed to change while the other variables were kept constant for each measurement. The used equivalent circuit is shown in Fig. 6.8. The anodic polarization was considered very small and thus neglected. Thus, the obtained impedance spectrum mainly reflects the cathode polarization. It has been shown that when air stoichiometry decreased, the mass transfer resistance of stack increased, but the influences on other resistances were minimal. The stack humidity and operation temperature mainly influenced the charge transfer resistance of stack. The AC impedance of stack gradually increased at state of idle speed (current about 5 A) and gradually decreased at relative high load (current above 81 A).

Fontes et al. [12] studied the behavior of a fuel cell stack (20 cells generating 200 W) when interacting with power converters. The model parameters were obtained experimentally via EIS with frequencies ranging from 1 Hz to 20 kHz. The equivalent circuit is shown in Fig. 6.9 where the inductor is added to evaluate the inductive behavior at the highest frequencies due to the internal connections. It has been shown that at higher frequencies, the fuel cell impedance behaves like a resistance and the current harmonics have no measurable effect on chemical reactions since they are filtered by the double layer capacitor. The authors raised questions about the maximum RMS current tolerated by the double layer capacitance, and its impact on the aging of a fuel cell and the possible increase in this capacitor value due to the magnitude of this ripple.

Wahdame et al. [13] examined the influence of the DC/DC power converter's high frequency current ripples on fuel cell stack durability. A 600 W 5-cell stack was operated in the stationary regime at roughly nominal conditions during 1000 h. This first experiment serves actually as the reference test for the second one that is carried on another 600 W stack operated under dynamic current conditions. The relationships between ripple current and fuel cell performance, such as power loss and degradation, were investigated. Other tests were carried out by the authors once per week according to an identical protocol, polarization-curve test and EIS tests. The experimental setup consisted of a 1 kW FC test bench with LabVIEW for control and monitoring. A 250 A current with 1 kHz frequency and ± 10 % current oscillations was imposed in order to simulate the global operation

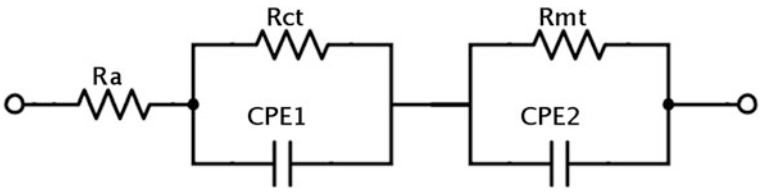

Fig. 6.8 Model used by Yan et al. [11]

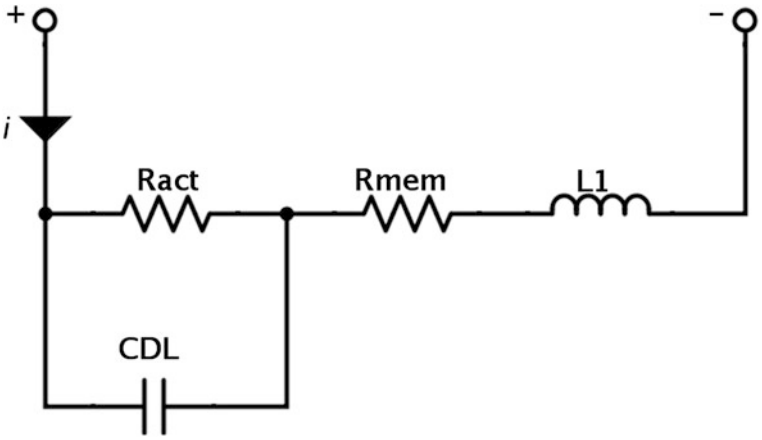

Fig. 6.9 Model used by Fontes et al. [12]

effect of the high frequency power converter connected at the output of the fuel cell stack. An inductive part was present at high frequencies (between 30 and 4 kHz approximately) which is due to the various connection elements. In the ageing tests, the variation amplitude of the fuel cell internal resistance was small (between 1.4 and 1.6 mΩ). The ageing tests showed only a slight effect of high frequency current oscillations on the reduction of the PEMFC stack performance.

Gerard et al. [14] studied the ripple current effects on fuel cells by an experimental ripple current aging test on a five cell stack. Local conditions are computed through a dynamic stack model. The model takes into account transport phenomena, heat transfer, and semi-empirical electrochemical reactions and includes a meshing to calculate local conditions on the MEA surface. A 1 kW PEMFC test bench is used for the aging test. It has been found that there is no difference at high frequency membrane resistance. Reversible degradations in the voltage were noticed from the influence on the capacitive loops at medium frequencies for the electrochemical double layer and at low frequencies for the diffusion phenomena. According to the authors, these reversible degradations were caused by water management at different levels. The low frequency loops corresponding to diffusion phenomena increased with aging time. High frequency ripple currents seemed

to have a visible influence on the diffusion processes and on the membrane permeation. The authors suggested developing a specific membrane model to simulate the real impact on mechanical and chemical membrane stresses, and link it with a mechanistic model.

Ferrero et al. [15] developed a dynamic model starting from the simple Randles equivalent circuit, and then included a dielectric relaxation which resulted in a frequency dependent capacitance. A DC model is first found based on linearized equations around a current operating point in order to find the polarization curve. A dynamic model based on Randles was then proposed with a frequency dependent capacitance. The linearized dynamic model circuit is shown in Fig. 6.10. The circuit includes both the ohmic loss and the dynamic effect of the charge double layer associated with the activation loss. At three different current values, a sinusoidal current 10 A pk-pk was superimposed at a frequency between 100 mHz and 1 kHz. It has been shown that the high frequency value of $Z(j\omega)$ is the same for the three current points and corresponds to the ohmic resistance which is independent of the working linearization point. At the lowest frequency (100 mHz), the impedance $Z(j\omega)$ is almost purely resistive and no loop is observed. The voltage ripple amplitude is at its maximum and corresponds to the voltage drop across R_{act} and R_{ohm}. As the frequency increases, the amplitude of the voltage ripple decreases due to the decrease in the current flowing through R_{act}. This effect is caused by the parallel capacitance C_{act} which explains why the slopes of the loops in the polarization plane decrease. The areas of the loops increase until they reach their maximum corresponding to the minimum phase of $Z(j\omega)$ around 10 Hz and then they decrease again. The impedance becomes purely resistive at 1 kHz and the voltage ripple amplitude reaches its minimum (voltage drop across R_{ohm} only). Finally, it was found that the inverter current ripple (close to 1 kHz) has the minimum impact on efficiency and it is independent of the working point and only depends on R_{ohm}.

Kim et al. [6] examined the impact of ripple current through immediate measurements on 12 single cells after cycling for hours at three frequencies, low (100 Hz), medium (1 kHz), and high (10 kHz). Under identical temperature and humidity conditions, a ripple current (average 20 A, peak-to-peak 10–30 A) is applied to single PEM fuel cells at three frequencies (100 Hz, 1 and 10 kHz) for a long period of time (24, 46, 69, and 100 h). Impedance curves obtained every 100 h are compared using electrochemical impedance spectroscopy (EIS). Frequencies ranging from 0.03 Hz to 2 kHz, with 51 measurement points per decade and 1 mA in amplitude, were used for all of the spectra presented. It has been shown that the low frequency ripple current applied to a PEMFC for a long time can shorten the fuel cell's life. This was observed in the increase of the impedance magnitude when compared to a fresh cell. This study also investigated two PEMFC failures, particularly cathode flooding and membrane drying, associated with low frequency ripple current. It has been shown that impedance measurements under two specific frequencies ripple currents (high at 10 kHz and low at 100 Hz) are sufficient to demonstrate that a low frequency ripple current caused a faster acceleration of the PEMFC degradation associated with two PEMFC

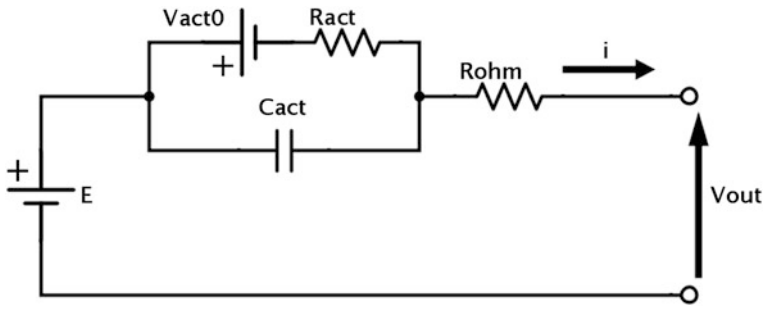

Fig. 6.10 Fuel cell model used by Ferrero et al. in dynamic conditions, linearized around the equilibrium current [15]

failures. The interception of the high frequency impedance loop with the real axis changes only a little with normal, flooded, and dry conditions. However, both the real and imaginary parts of the cell impedance exhibit an increase under flooded and dry conditions as compared to results under normal conditions. Furthermore, the increase in the real and imaginary impedance components for the flooded fuel cell is greater than those for a dry fuel cell. It appeared clearly that the processes of drying and flooding were characterized by the modification of the low frequency component (an increase in the charge transfer resistance) of the fuel cell impedance. This is associated with the low frequency ripple current. It was observed that the low frequency ripple current causes the largest difference in the overlapping arc diameter compared with three cell spectra at the high frequency ripple current.

6.5 Conclusions

ECMs are considered as useful tools for characterizing the behavior of fuel cells and understanding the different phenomena associated with their normal and faulty operations. The main development approaches to generate such models were discussed. Also, the different model applications found in the literature were presented.

References

1. N. Behling, Solving the fuel cell dilemma. Fuel Cells Bull. **2012**(11), 12–14 (2012)
2. J. Larminie, A. Dicks, *Fuel Cell Systems Explained* (Wiley, New York, 2003)
3. L. Gauchıa Babe, Nonlinear dynamic per-unit models for electrochemical energy systems: application to hardware-in-the-loop hybrid simulation. Ph.D. dissertation, Universidad Carlos III de Madrid, 2009
4. U. Reggiani, L. Sandrolini, G.L Giuliattini Burbui, Modelling a PEM fuel cell stack with a nonlinear equivalent circuit. J. Power Sour. **165**(1), 224–231 (2007)

5. K.P. Adzakpa, K. Agbossou, Y. Dube, M. Dostie, M. Fournier, A. Poulin, PEM fuel cells modeling and analysis through current and voltage transient behaviors. IEEE Trans. Energy Convers. **23**(2), 581–591 (2008)
6. J. Kim, I. Lee, Y. Tak, B.H. Cho, Impedance-based diagnosis of polymer electrolyte membrane fuel cell failures associated with a low frequency ripple current. Renew. Energy **51**, 302–309 (2013)
7. W. Choi, P.N. Enjeti, J.W. Howze, Development of an equivalent circuit model of a fuel cell to evaluate the effects of inverter ripple current, in *19th Annual IEEE on Applied Power Electronics Conference and Exposition (APEC'04)*, vol. 1 (2004) pp. 355–361
8. D. Yu, S. Yuvarajan, Electronic circuit model for proton exchange membrane fuel cells. J. Power Sour. **142**(1), 238–242 (2005)
9. L. Palma, M.H. Todorovic, P. Enjeti, Design considerations for a fuel cell powered DC-DC converter for portable applications, in *21st Annual IEEE on Applied Power Electronics Conference and Exposition 2006 (APEC'06)* (2006), pp. 1263–1268
10. X. Yuan, J.C. Sun, M. Blanco, H. Wang, J. Zhang, D.P. Wilkinson, Ac impedance diagnosis of a 500 W PEM fuel cell stack: part I: stack impedance. J. Power Sour. **161**(2), 920–928 (2006)
11. X. Yan, M. Hou, L. Sun, D. Liang, Q. Shen, H. Xu, P. Ming, B. Yi, AC impedance characteristics of a 2 kW PEM fuel cell stack under different operating conditions and load changes. Int. J. Hydrogen Energy **32**(17), 4358–4364 (2007)
12. G. Fontes, C. Turpin, S. Astier, T.A. Meynard, Interactions between fuel cells and power converters: influence of current harmonics on a fuel cell stack. IEEE Trans. Power Electron. **22**(2), 670–678 (2007)
13. B. Wahdame, L. Girardot, D. Hissel, F. Harel, X. Francois, D. Candusso, M.C. Pera, L. Dumercy, Impact of power converter current ripple on the durability of a fuel cell stack, in *Proceedings of IEEE International Symposium on Industrial Electronics (ISIE 2008)* (2008), pp. 1495–1500
14. M. Gerard, J.P. Poirot-Crouvezier, D. Hissel, M.C. Pera, Ripple current effects on PEMFC aging test by experimental and modeling. J. Fuel Cell Sci. Technol. **8**(2), 021004 (2011)
15. R. Ferrero, M. Marracci, M. Prioli, B. Tellini, Simplified model for evaluating ripple effects on commercial PEM fuel cell. Int. J. Hydrogen Energy **37**(18), 13462–13469 (2012)

Chapter 7
SBG for Health Monitoring of Fuel Cell System

B. Ould-Bouamama, N. Chatti and A. L. Gehin

Abstract To guarantee the safe operation of the Fuel Cell (FC) systems, it is necessary to use systematic techniques to detect and isolate faults for diagnosis purposes. The problematic for Fault Detection and Isolation (FDI) model-based of fuel cell consists in that such system is bad instrumented, its model is complex (because of coupling of multi-physical phenomena such as electrochemical, electrical, thermo fluidic…) and the numerical values related to it are not always known. This is why qualitative model (based on existence or not of the links between variables and the relations) is well suited for fuel cell diagnosis. In this paper, we propose a new graphical model (named Signed Bond Graph) allowing to combine both qualitative and quantitative features for health monitoring (in terms of diagnosis and prognosis) of the fuel cell. The innovative interest of the presented paper is the use of only one representation for not only structural model but also diagnosis of faults which may affect the fuel cell. The developed theory is illustrated by an application to a Proton Exchange Membrane Fuel Cell (PEMFC).

Keywords Diagnosis · Bond graph · PEM fuel cell · Health monitoring

7.1 Introduction

During the last decade, Fuel Cell (FC) systems have received significant attention and they are expected to play a significant role in future environmentally friendly power generation facilities [1]. Among many varieties of fuel cells, the Proton Exchange Membrane FC (PEMFC) has shown to be the most promise for various industries including the transportation, residential and also portable applications.

B. Ould-Bouamama (✉) · N. Chatti · A. L. Gehin
Ecole Polytechnique de Lille, LAGIS UMRCNRS8219, Cité scientifique,
59655 Villeneuve-d'Ascq, France
e-mail: belkacem.ouldbouamama@polytech-lille.fr

M. O. Hamdan et al. (eds.), *ICREGA'14 - Renewable Energy: Generation and Applications*, Springer Proceedings in Energy, DOI: 10.1007/978-3-319-05708-8_7,

As a consequence, its modeling has become an important research issue [2, 3]. Roughly speaking, A PEMFC is a device that produces electricity from a chemical reaction. This reaction generates electrical current (which can be directed outside the cell to power an electrical motor for example), requires a fuel (namely hydrogen) and oxygen, and releases water and heat. FC systems are vulnerable to faults that can cause the disruption or the permanent damage. It was shown from Failure Modes and Effects Analysis (FMEA) that the state of hydration of the membrane electrode assembly (water flooding and drying) is one of the major challenges in PEMFCs FDI and control reconfiguration. To guarantee the safe operation of the FC systems, it is necessary to use systematic techniques to detect and isolate faults for the purpose of diagnosis.

Different diagnosis approaches dealing with water management exist. Among these approaches, one can cite the soft computing techniques. Hissel et al. [4] for instance proposed a solution to perform such diagnosis using fuzzy logic tuned thanks to genetic algorithms. On another work, Steiner et al. [5] proposed an improved diagnosis procedure based on the comparison between measured parameters and parameters calculated by an Artificial Neural Network (ANN) in case of normal operation. One drawback to using ANNs, is that they require a large diversity of training in normal and faulty situations for real operation in order to become viable. From one hand, a great part of the fuel cell diagnosis is based on experimental methods using signal processing. Among these methods, one can cite the polarization curve approach and the Electrochemical Impedance Spectroscopy (EIS) [6]. Chen et al. [7], for example used frequency of pressure drop signal as a diagnostic tool for PEM fuel cell stack dynamic behaviors. Because of complexity of the model, few of consulted papers deals with model based diagnosis. They aim to generate fault indicators called residuals [8]. Among the residuals generation methods, Bond Graph (BG) as a multidisciplinary and unified graphical modeling language has proved its efficiency to generate fault indicators in a systematic and generic way using specific algorithms. These algorithms are based on covering causal paths [9] implemented in dedicated software's [10]. But as every residual generation method, BG models are limited to a single fault diagnosis which assumes the observation of only one effect for one component's fault. However, within a real system such as PEMFC, one element's fault can manifest several effects (increase the temperature and the pressure, for example) and implies the propagation of the fault to other elements.

In addition, two different communities have developed Model Based Diagnosis namely Fault Detection and Isolation (FDI) community (based on residuals generation methods) and DX community emanating from Artificial Intelligence field and dealing with qualitative models [11]. During the last decade, different research groups proposed a common frame-work for sharing and comparing techniques from both communities. This effort turned into what it known as BRIDGE community. This latter tries to propose new approaches integrating the best from both communities and to deal with quantitative and qualitative models [12, 13]. The approach we propose in this paper fits into the BRIDGE community.

Indeed, in the paper is introduced a new graphical model called Signed Bond Graph (SBG). This model uses a qualitative reasoning allowing to generate multiple behavior predictions (i.e. possible conflicts). Since the SBG is constructed from the Bond Graph (BG) model, the use of this latter as a quantitative method for residuals generation allows to eliminate the possible conflicts which are inconsistent or not physically possible even though they sound logical from a qualitative point of view. Finally, a global supervision module based SBG is proposed. This module uses both qualitative and quantitative reasoning for faults detection and isolation of PEM fuel cell.

7.2 SBG for Global Supervision

Two steps can be distinguished in the global diagnosis procedure. The first one is its diagnosability analysis and monitoring algorithms generation carried out offline before industrial design. The second one is its on-line implementation of qualitative and quantitative algorithms for real time fault detection and isolation for single and multiple faults.

7.2.1 The Design of the Diagnosis Module

The design of the diagnosis module rests on four steps which are illustrated in Fig. 7.1 and summarized as follow. In a first time, the BG model is built based on the physical system architecture and the power exchanges between the different components. Judicious causality marks are assigned to indicate the order according to which the unknown variables are processed from the known ones. This step will be detailed in the next section. In a second time, the SBG is directly derived from the BG model by using a developed methodology allowing the model checking and dealing with qualitative features with regards to power sign, direction of power variables and so on. In the same time, a numerical processing of the BG is performed and leads to the automatic generation of Analytical Redundancy Relations (ARR). Then, the structure of the ARRs is exploited to generate the Fault Signature Matrix (FSM) which associates to each detectable fault a signature.

Within the BG methodology, the ARRs generation procedure rests on the BG causal features and uses the theory of unknown variables elimination using covering causal paths (from unknown to known variables (measured)) algorithms. Indeed, the relations between systems variables can be easily displayed graphically using BGs and they can be defined under a symbolic form using symbolic computation software [10]. According to the deduced ARRs, a fault signature matrix which crosses ARRs in columns and faults F in rows is built in order to evaluate the possibilities the system has to detect and isolate faults. The algorithm of ARRs generation can be found in [14].

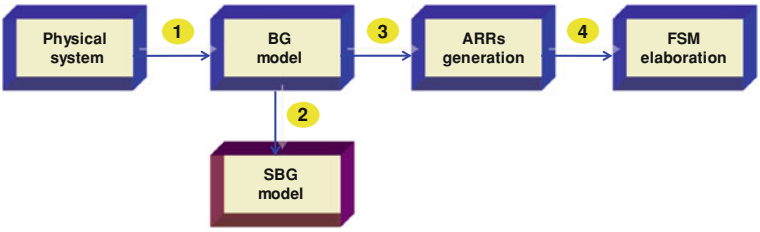

Fig. 7.1 Global supervision based on SDG methodology

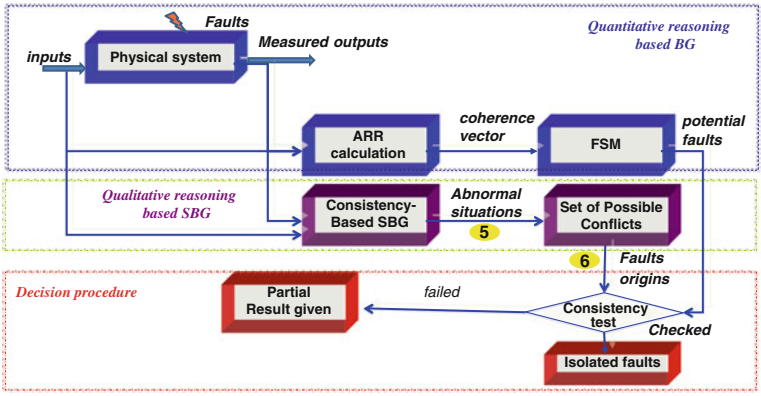

Fig. 7.2 On line exploitation

7.2.2 The On-line Exploitation

Once the diagnosis module is correctly designed, it can be online exploited to detect and isolate fault when possible. This diagnosis procedure is illustrated in Fig. 7.2 and can be summarized as follows.

In a first time, ARRs are calculated using the measured outputs and the control inputs which represent the known variables of the system. From the values of these ARRs, a coherence vector is obtained. If its value is different from (0, 0 …0), it is then compared to the fault signatures regrouped in the FSM. This leads to a list of potential faults and allows the extraction of a subset of fault candidates. Using the measured values, the consistency of the possible conflicts generated off-line from the SBG, is checked as well and abnormal situations are identified. In a last step, the consistency between the results obtained according to the ARRs evaluation and the possible conflicts generation is tested. If there is consistency, some faults may be isolated. In the opposite case, a partial result is given.

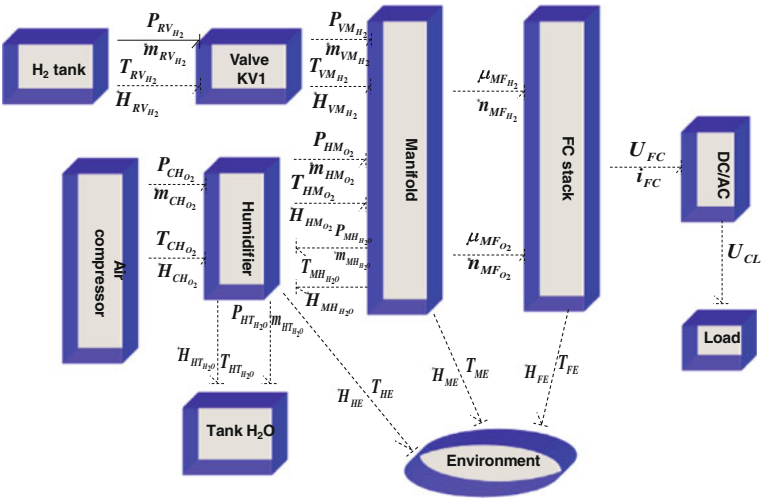

Fig. 7.3 Word BG of the PEM fuel cell

7.3 PEMFC Bond Graph Model

In this section, is presented the fuel cell system's Word Bond Graph which represents the technological level of the model where global system is decomposed into different subsystems (see Fig. 7.3). Comparing with classical block diagram, the input and output of each subsystem define power variables represented by a conjugated pair of effort-flow labeled by a half arrow. Indeed, the Word Bond Graph provides a top-level overview of the fuel cell system and is useful for initial conception of the behavioral system model. The pair of power variables used for the studied fuel cell system are: (Pressure, Mass Flow) $= (P, \dot{m})$, (Temperature, Enthalpy Flow) $= (T, \dot{H})$, (chemical potential, molar flow) $= (\mu, \dot{n})$ and (Voltage, Current) $= (U, i)$. It's noted that for chemical process two kinds of power variables are used: the pair chemical potential-molar flow $(\mu, \dot{n})$ for transformation phenomena and the pair chemical affinity-A (J/mol) and speed of reaction J (mol/s). These variables are associated respectively with mechanical, thermal, chemical and electrical domains. Because of the complexity of the overall system and for the sake of clarity, we will focus within this paper only on the heart of the fuel cell system model. While the temperature of hydrogen and oxygen are constants, we consider only the transformation respectively of hydrogen and oxygen mass flow. This transformation is modeled by the Transformer TF bond graph element with a modulus M molar rate (mole/m^3) as represented in bond graph model (Fig. 7.4).

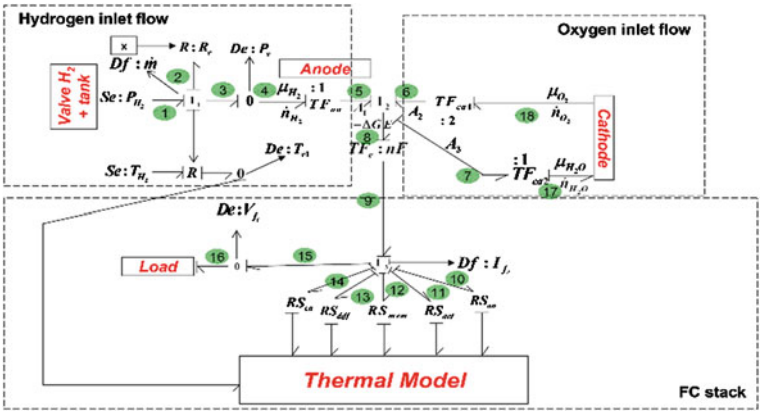

Fig. 7.4 BG model of the PEM fuel cell

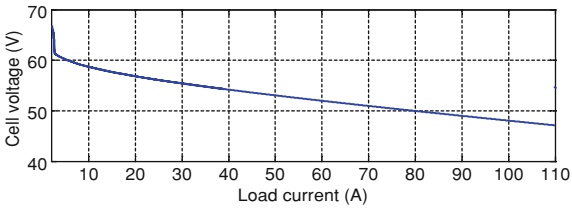

Fig. 7.5 Polarization curve of the PEM fuel cell (6 Kw, 45 Volts)

7.3.1 BG Model and Fault Indicators Generation of the PEM FC

The Bond Graphs have been successfully used for analysis and synthesis of different kinds of systems involving different domains. Figure 7.4 presents the proposed BG model of a 6 kW, 45 v PEM fuel cell feeding a 100 Vdc DC/DC converter (The polarization curve obtained by simulation is given in Fig. 7.5). The transformers TF_{an} and TF_{ca} modulated by molar rate represent chemical transformations related respectively to the hydrogen flow through the anode and the oxygen flow through the cathode. On the other hand, TF_e represents the transformation of the variations of the Gibbs free energy, into electrical energy assuming that the Gibbs free energy can be converted into electrical energy, the theoretical potential E of the fuel cell corresponds to Gibbs free energy, ΔG of main oxydo reduction reactions such that $E = \frac{-\Delta G}{nF}$.

Where n (n = 2) is the number of electrons involved in the above reaction, and F is the Faraday's constant (96,485 Coulombs /electron mol). This relation is modeled by TF bond graph element $TFe : nF$. Junction structures are used in order to connect several elements of the BG model (R, C and I) by a 0-junction when the effort variable is the same and the flows are different and by a 1-junction when the

flow is the common variable. Hence, the 0-junction expresses the effort conservation and indicates that the flows sum is equal to zero. Whereas the 1-junction expresses the flow conservation and indicates that the efforts sum is equal to zero. De and Df (sensors) represent respectively the effort detector and flow detector.

Se and Sf represent respectively the effort source and flow source. R_v represents the inlet H_2 valve which is modeled hence by hydraulic resistance modulated by an information bond x (control signal). Re represents the friction of the diffusion through the surface of the backing layer for the O_2. The thermal losses are modeled by an active resistance element-RS such as activation losses, diffusion losses, and concentration losses

Much more details about the BG approach can be found in [15].

Let now focus on Fig. 7.4 in order to deduce the ARRs: From the Junction (7.11), the following equations can be written:

$$e_1 - e_2 - e_3 = 0 \tag{7.1}$$

$$e_1 = P_{H_2} \tag{7.2}$$

$$e_2 = f(f_2, x) \tag{7.3}$$

$$f_2 = f_3 = \dot{m} \tag{7.4}$$

$$e_3 = e_4 = P_v \tag{7.5}$$

From Eqs. (7.1)–(7.5), The first ARR can be deduced as follows:

$$P_{H_2} - f(f_2, x) - P_v = 0 \tag{7.6}$$

Similarly, from the junction (7.13), can be deduced following equations:

$$e_9 - e_{10} - e_{11} - e_{12} - e_{13} - e_{14} - e_{15} = 0 \tag{7.7}$$

$$\begin{cases} e_{10} = f_{10} \times RS_{an};\ e_{11} = f_{11} \times RS_{act}\ ;\ e_{12} = f_{12} \times RS_{mem}; \\ e_{13} = f_{13} \times RS_{diff};\ e_{14} = f_{14} \times RS_{ca};\ e_{15} = V_{fc} \end{cases} \tag{7.8}$$

$$f_9 = f_{10} = f_{11} = f_{12} = f_{13} = f_{14} = f_{15} = I_{fc} \tag{7.9}$$

$$e_8 = nF \times e_9 \tag{7.10}$$

$$e_6 = f\ (P_{O_2}; T_{O_2});\ P_{O_2} = f\ (\dot{m}_{O_2}; P_{H_2O});\ e_5 = f\ (T_{v1}; e_4) \tag{7.11}$$

$$e_7 = f\ (P_{H_2O}; T_{H_2O}) \tag{7.12}$$

Table 7.1 Signature fault matrix

Fault	R_1	R_2	R_3	D	I
Drying of the membrane	0	0	1	1	0
Flooding of the cathode	0	0	1	1	0
H2 valve regulator	1	0	0	1	0
H2 mass flow sensor	1	0	0	1	0
H2 pressure sensor	1	1	1	1	1
H2 pressure sensor	0	1	1	1	0
H2 pressure sensor	0	1	1	1	0
Fc current sensor	0	1	1	1	0
Fc voltage sensor	0	1	1	1	0
Cathode water temperature sensor	0	1	1	1	0
Cathode water pressure sensor	0	1	1	1	0

From Eqs. (7.7)–(7.12), the second ARR is then deduced:

$$\begin{cases} f(T_{v_1}, P_v) + f[f(\dot{m}_{O_2}, P_{H_2O}), T_{O_2}] - nF \times \\ \left[I_{fc} \times (RS_{act} + RS_{diff} + RS_{ca} + RS_{an} + RS_{mem}) + V_{fc}\right] \\ -f(P_{H_2O}, T_{H_2O}) = 0 \end{cases} \tag{7.13}$$

From junction (7.12) and by following the same procedure, the third ARR can be obtained as follows:

$$\begin{cases} \frac{1}{nF} \times [f(T_{v_1}, P_v) + f(P_{O_2}, T_{O_2}) - f(P_{H_2O}, T_{H_2O})] - \\ I_{fc} \times (RS_{act} + RS_{diff} + RS_{ca} + RS_{an} + RS_{mem}) - V_{fc} = 0 \end{cases} \tag{7.14}$$

The fault signature matrix (FSM) is derived directly from these three ARRs namely (7.6), (7.13) and (7.14).

It is given in Table 7.1. According to these ARRs, the FSM which crosses ARRs in rows and faults F in columns is built in order to evaluate the possibilities the system has to detect and isolate faults. Boolean matrix element a_{ij} equals 1 if the *i*th residual is affected by the *j*th fault. The on-line residuals evaluation leads to the formulation of a binary coherence vector $C = (c_1 c_2 \ldots c_n)$, whose elements, c_i ($i = 1,\ldots,n$), are determined from a decision procedure φ which generates the alarm conditions. A simple decision procedure can be used for instance, $C = \varphi(r_1, r_2 \ldots r_n)$, whereby each residual, r_i is tested against a threshold ε, fixed according to parameter uncertainties, sensor noises and so on.

In Table 7.1, the vector (R_1, R_2, and R_3) is the signature of the fault. The only isolated faults are those having the same signature, i.e. different from the signatures of all other element (such as the signature vector V = [1 1 1] corresponding to the H_2 pressure sensor). However, due to the non-presence of enough unique signatures, faults affecting the other elements cannot be isolated. According to the FSM, a fault related to the drying out of the membrane or the flooding of the

cathode can be detected. However, it cannot be isolated because these two faults have the same signature. Hence, the quantitative evaluation of the fault indicators (residuals) is not sufficient for distinguishing between the two faults related to the water management. This is why, a qualitative reasoning based BG model allowing to get a much more accurate diagnosis according to the strategy (as explained in Sect. 7.2) is proposed. Hence, in the next section a new model called Signed Bond Graph (SBG) allowing possible conflict generation is developed.

7.4 Qualitative Reasoning Based SBG

A SBG is a new dynamic graphical model built from BG approach. This model allows to gather and exploit qualitative and quantitative features in order to carry out diagnosis and supervision of dynamic systems. An algorithm for automatically building the SBG from the BG is developed. At present an overview of the proposed model and same definitions related to the qualitative reasoning based SBG is given.

7.4.1 SBG Mathematical Formalism

Definition 1 A Signed Bond Graph **G(X, A, L, S)** is a labeled graph where: **X** is a set of nodes representing;

BG elements, $A \subset X \times L \times S \times X$is a set of labeled and signed arcs such that each arc indicates both a power variable which can be either flow or effort and a sign related to energy exchange, $L = \{l_i / l_i \in \{e_i, f_i, e_{m_i}, f_{m_i}\}\}$ is a set of labels corresponding to two conjugated power variables measured f_{m_i}, e_{m_i}or unmeasured e_i, f_i written above or to the left of the arc, $S = \{s_i / s_i \in \{+, -, 0, \emptyset\}\}$ is a set of signs written below or to the right of the arc such that $+$, $-$, 0 and $\emptyset$ correspond respectively to a power supply, power consumption, power conservation and no power (such as detectors which bring only signal and are not involved in power exchange) and $i \in \mathbb{N}^*$. The set of nodes $X = \{x_i / 1 \leq i \leq nb_E\}$ can be partitioned as: $X = X_{Ce} \cup X_s \cup X_D \cup X_{Co} \cup X_{Tr}$ where $X_{Ce} = \{x_{Ce_i} / x_{Ce_i} \in \{J_{0i}, J_{1j}\}\}$ is a subset of nodes corresponding to central elements that distribute power and have linear structural relations. $X_S = \{x_{S_i} / x_{S_i} \in \{S_{e_i}, S_{f_i}, MS_{e_i}, MS_{f_i}\}\}$ is a subset of nodes corresponding to sources elements which supply energy into the system. Sources may impose either an effort or a flow onto a system.

$X_D = \{x_{D_i} / x_{D_i} \in \{D_{e_i}, D_{f_i}\}\}$ is a subset of nodes corresponding to effort and flow detectors. $X_{Co} = \{x_{Co_i} / x_{Co_i} \in \{R_i, C_i, L_i\}\}$ is a subset of passive physical elements consuming energy. $X_{Tr} = \{x_{Tr_i} / x_{Tr_i} \in \{TF_i, GY_i\}\}$ is a subset of nodes corresponding to energy conservative elements, the energy is neither stored nor produced and the instantaneous input power equals the instantaneous output power. nb_E is the number of Bond Graph elements in the BGM and $i \in \mathbb{N}^*$.

7.4.2 SBG for Qualitative Diagnosis

For any observation $obs \subset OBS$ of the system (square nodes) in a given time, a SBG model can determine qualitatively whether each measured node has deviated from its normal state, as well as the direction of deviation, according to a set of threshold values. By the use of reasoning in the SBG model, the observation *obs* propagates through arcs. The resulting paths are called fault propagation paths or consistent paths. The elements which belong to this path form a set of possible conflicts. Indeed, the idea behind the labeled and signed arcs of the SBG is that the propagation starts from a measured node and propagates through arcs. Hence, it affects different nodes corresponding to the set of elements *COMPS* by checking the sign of each arc. The propagation is stopped either when a consistency is noted or when a measured node is reached.

Definition 2 A pattern of a SBG model is a function $\Gamma : \{l_i\} \rightarrow \{+, 0, -\}$ that links each label l_i to a specified sign according to the observation node x_{D_i}. Hence, $\Gamma(l_i) \quad (l_i \in X)$ is the sign of the arc l_i, $i \in \mathbb{N}^*$:

$$\Gamma(l_i) = 0 \quad if \quad |l_i - l_{in}| \prec \varepsilon l_i$$

$$\Gamma(l_i) = + \quad if \quad l_i - l_{in} \geq \varepsilon l_i$$

$$\Gamma(l_i) = - \quad if \quad l_{in} - l_i \geq \varepsilon l_i$$

Where εl_i is the threshold.

The corresponding SBG (see Fig. 7.5) of the PEM fuel cell is constructed directly from the BG model which is given by Fig. 7.4. Then, the fault propagation is carried out from the observed nodes (corresponding to the sensors) in order to determine qualitatively the set of fault candidates according to the inconsistencies within the SBG model.

Let now focus, for instance, on the faults corresponding to water management (flooding and drying). We simulate a fault affecting the membrane. The evaluation of the residuals gives the signature V = [0 0 1]. Hence, a fault is detected but we cannot distinguish between a flooding and a drying out according to this quantitative evaluation. The analysis based on the SBG model allows having an accurate diagnosis according to the sensor values acquired in both normal and faulty situations (see simulations in Fig. 7.7). It is worth noting that all the possible propagation paths and Possible Conflicts (PC) are generated off-line from the SBG model. Then, according to the quantitative evaluation based residuals, we use only the suitable PCs that can explain the set of observations and which are consistent with the residuals evaluation outcomes. For the considered fault scenario, the following paths deduced from the set of observations (Fig. 7.6) are exploited in order to determine the fault upon occurrence:

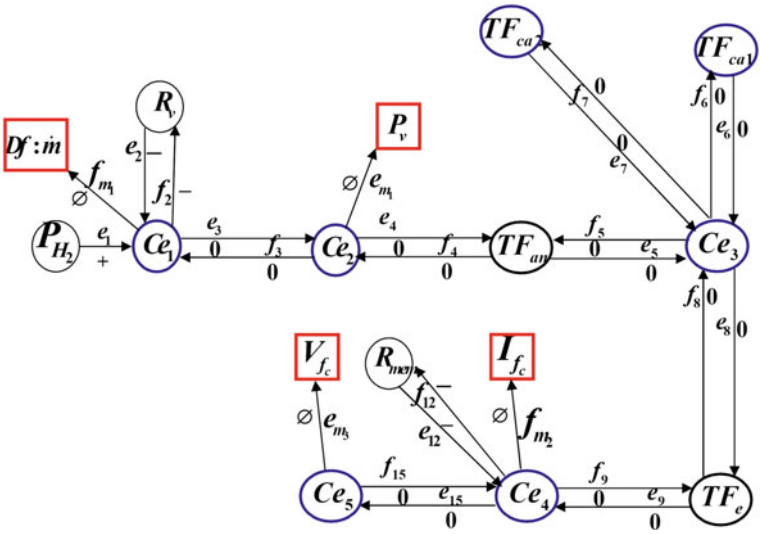

Fig. 7.6 SBG model of the PEM fuel cell

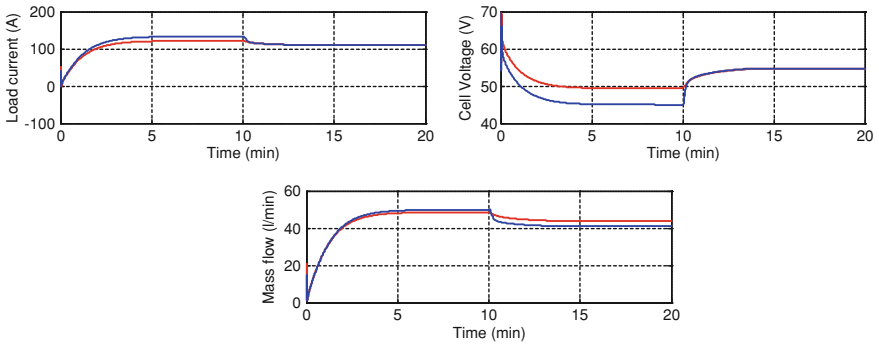

Fig. 7.7 Simulation results of the PEM fuel cell (6 Kw, 45 Volts)

$$f_{m_1}^{+} \rightarrow f_3^{+} \rightarrow f_4^{-} \rightarrow f_5^{-} \rightarrow f_8^{+} \rightarrow f_9^{+} \rightarrow f_{m_2}^{+} \tag{7.15}$$

$$e_{m_3}^{+} \rightarrow e_{15}^{+} \rightarrow e_2^{-} \rightarrow f_{12}^{-} \rightarrow f_{m_2}^{-} \tag{7.16}$$

$$e_{m_3}^{+} \rightarrow e_{15}^{+} \rightarrow e_9^{-} \rightarrow e_8^{-} \rightarrow e_5^{+} \rightarrow e_4^{+} \rightarrow e_{m_1}^{+} \tag{7.17}$$

An inconsistency in the PC (7.17) can be noted, because the value of the load current f_{m_2} increases according to the simulations. However, PCs (7.16) and (7.17) match the observations. Hence, the element involving in the PC (7.17) is the origin of this possible conflict namely the resistance of the membrane. As it is known, the

resistance of the membrane is sensitive to the drying out of the membrane. This is why, from this qualitative propagation, it can be shown that the fault is drying of the membrane and hence we isolate the fault (which is not possible when we rely only on the FSM) despite the fact that there are any sensor inside the membrane to measure the resistance of the membrane.

7.5 Conclusion

A new approach has been presented for fault diagnosis of the PEM fuel cell especially with regard to water management problems. This approach is based on residuals generation approach (quantitative features) and on a new qualitative model called SBG both emanating from the BG formalism. Hence, the proposed global supervision module allows a better and more accurate diagnosis

Acknowledgments This work is performed in part of ANR Project "Propice" ANR-12-PRGE-0001 http://www.propice.ens2m.fr/ that aims to develop Prognostics and Health Management (PHM) methods applied to PEM Fuel cell.

References

1. A. Veziroglu, R. Macario, Fuel cell vehicles: State of the art with economic and environmental concerns. Int. J. Hydrogen Energy **36**, 25–43 (2011)
2. C. Ziogoua, S. Voutetakisa, S. Papadopouloua, M.C. Georgiadisb, Modeling, simulation and experimental validation of a PEM fuel cell system. Comput. Chem. Eng. **35**, 1886–1900 (2011)
3. A.W. Al-Dabbagh, L. Lu, A. Mazza, Modelling, simulation and control of a proton exchange membrane fuel cell (PEMFC) power system. Int. J. Hydrogen Energy **35**, 5061–5069 (2010)
4. D. Hissel, M.C. Péra, J.M. Kauffmann, Diagnosis of automotive fuel cell power generators. J. Power Sour. **128**, 239–246 (2004)
5. Steiner N. Yousfi, D. Hissel, Ph Moçotéguy, D. Candusso, Diagnosis of polymer electrolyte fuel cells failure modes (flooding and drying out) by neural networks modeling. Int. J. Hydrogen Energy **36**, 3067–3075 (2011)
6. N. Fouquet, C. Doulet, C. Nouillant, G. Dauphin-Tanguy, B. Ould-Bouamama, Model based PEM fuel cell state-of-health monitoring via ac impedance measurements. J. Power Sour. **159**, 905–913 (2006)
7. J. Chen, B. Zhou, Diagnosis of PEM fuel cell stack dynamic behaviors. J. Power Sour. **177**, 83–95 (2008)
8. A. Aitouche, Q. Yang, B. Ould-Bouamama, Fault detection and isolation of PEM fuel cell system based on nonlinear analytical redundancy. Eur. Phys. J. Appl. Phys. **54**, 1–12 (2011)
9. C. Peraza, J.G. Diaz, F.J. Arteaga, C. Villanueva, Modeling and simulation of PEM fuel cell with bond graph and 20 sim, in *Proceedings of American Control Conference*, (2008), pp. 5104–5108
10. B. Ould-Bouamama, A. Samantaray, M. Staroswiecki, Software for supervision system design in process engineering, in *Proceedings of IFAC World Congress*, (2006), pp. 691–695

11. B. Pulido, Possible conflicts: a compilation technique for consistency-based diagnosis. IEEE Trans. Syst. Man Cybern. B Cybern. **34**, 2192–2206 (2004)
12. G. Biswas, X. Koutsoukos, A. Bregon, B. Pulido, Analytic redundancy, possible conflicts, and TCG-based fault signature diagnosis applied to nonlinear dynamic systems, in *Proceedings of the 7th IFAC Symposium on Fault Detection, Supervision and Safety of Technical Processes*, (2009), pp. 1486–1491
13. M.O. Cordier, P. Dague, F. Levy, J. Montmain, M. Staroswiecki, L. Trave-Massuyes, Conflicts versus analytical redundancy relations. IEEE Trans. Syst. Man Cybern. B Cybern. **34**, 2163–2177 (2004)
14. B. Ould-Bouamama, R. El Harabi, M.N. Abdelkrim, M.K. Ben Gayed, Bond graphs for the diagnosis of chemical processes. Comput. Chem. Eng. **36**, 301–324 (2012)
15. W. Borutzky, Bond graph modeling and simulation of multidisciplinary systems: an introduction. Simul. Model. Pract. Theory **17**, 3–21 (2009)
16. M.A. Rubio, A. Urquia, S. Dormido, Diagnosis of PEM fuel cells through current interruption. J. Power Sour. **171**, 670–677 (2007)

Chapter 8
Dynamic Modeling of PEM Fuel Cell Using Particle Swarm Optimization

R. Salim, M. Nabag, H. Noura and A. Fardoun

Abstract Fuel Cells are one of the green technologies that are currently undergoing rapid development. They have the tendency of someday replacing fossil fuels in supplying some of our everyday energy needs. In this paper, a dynamic model of the Nexa 1.2 kW Proton Exchange Membrane (PEM) Fuel Cell system was identified and developed using Particle Swarm Optimization. The developed dynamic model would serve as a good base for fault diagnosis studies on the fuel cell system.

8.1 Introduction

Fossil fuels have been the main source of power for humanity for many years. However, the use of fossil fuels in power generation resulted in many negative environmental consequences, which lead to the exploration of alternative power sources that are energy efficient with an unlimited fuel supply and produce zero to minimal pollutants.

Fuel cells are electrochemical devices that convert the chemical energy of a fuel into DC electrical energy. This power generation process avoids the intermediate steps of producing heat and mechanical work typical of most conventional power generation methods. Moreover, fuel cells tend to produce power with minimal pollutants.

R. Salim (✉) · M. Nabag · H. Noura · A. Fardoun
UAE University, Al Ain, United Arab Emirates
e-mail: reem.salim@uaeu.ac.ae

M. O. Hamdan et al. (eds.), *ICREGA'14 - Renewable Energy: Generation and Applications*, Springer Proceedings in Energy, DOI: 10.1007/978-3-319-05708-8_8,

However fuel cells are very complex systems that require a high degree of reliability. The modeling methodology presented in this paper could serve as a guide in modeling any other PEM fuel cell system. Moreover, the developed model can be utilized to design and improve the PEM fuel cell system under study as well as being used to develop a reliable fault diagnosis study.

Several experiments were conducted on the 1.2 kW Nexa fuel cell system at varying load. The voltage and temperature responses of the system were then recorded.

The I/V characteristics of one of the experimental data sets were matched by identifying 13 different modeling parameters using Particle Swarm Optimization (PSO); while the system's temperature response was matched by identifying 5 different parameters using PSO. Other experimental data sets were then used to validate the obtained model. The resulting model was found to highly resemble the actual voltage and temperature characteristics of the system.

This paper is organized as follows: A general overview on previous studies in the area is presented in the next section followed by a brief overview on the Nexa 1.2 kW PEMFC system and the mathematical modeling equations. The proposed parameter identification process of the system's dynamic model is then presented and validated. The paper is then ended by acknowledgements followed by some concluding remarks.

8.2 Previous Studies

A few works on PEMFC modeling using PSO exists in literature. Qi et al. [1–4] used adaptive focusing particle swarm optimization (AFPSO) to optimize the mechanism model parameters of a PEMFC system. However, Hu et al. [5, 6] used a neural networks based on PSO to model their PEMFC system.

In [7] the PEMFC was broken into a mechanism sub-model and a black box sub-model, and PSO was then used to optimize the parameters of the mechanism sub-model, whereas the black-box sub-model was expressed in nonlinear autoregressive exogenous (NARX) form using a wavelet network and experimental data.

Chibante and Campos used PSO in [8] to extract the correct parameter values of their fuel cell system to minimize the difference between experimental and simulated results. On the other hand, [9] used a modified particle swarm optimization (MPSO) to optimize an electrochemical-based PEMFC mathematical model where the inertial weight was calculated according to the distance from the particle to that of the best solution of the entire swarm.

Another work presented in [10] proposed a parameter optimization technique of PEMFC models based on a hybrid PSO.

8.3 Mathematical Modeling of PEMFCs

The Nexa 1.2 kW PEMFC system uses hydrogen gas supplied from pressurized hydrogen cylinders as the anode fuel, and atmospheric air supplied by a compressor as the cathode fuel.

8.3.1 Output Voltage

The internal potential of a PEM fuel cell is given by the Nernest Equation [11]:

$$E_{cell} = E_{0,cell} + \frac{RT}{2F} ln\left(P_{H_2} P_{O_2}^{0.5}\right) \tag{8.1}$$

where:

$E_{0,cell}$ is the reference potential (1.229 V)
R is the gas constant (8.3143 J/[mol K])
T is the fuel cell temperature (K)
F is Faraday constant (96485.34 C/mol)
P_{H_2} is pressure of hydrogen (atm)
P_{O_2} is pressure of oxygen (atm)

However, the actual output voltage of a PEMFC is less than the internal voltage E_{cell} developed inside the fuel cell due to three different types of voltage drops (activation voltage drop, ohmic voltage drop, and concentration voltage drop) as depicted in Fig. 8.1.

The activation voltage drop represents the energy used in the electrochemical and chemical reactions occurring inside the fuel cell [12]. This voltage drop can be represented by the following Tafel equation:

$$\mathrm{V_{act,cell}} = \frac{\mathrm{RT}}{\alpha \mathrm{nF}} \ln\left(\frac{\mathrm{I}}{\mathrm{I_0}}\right) = \mathrm{T}.[\mathrm{a} + \mathrm{b}\ \ln(\mathrm{I})] \tag{8.2}$$

where:

α is the electron transfer coefficient of the reaction.
n is the number of electrons participating in the reaction (2 e^-/mol) [11].
I is the load current.
I_0 is the exchange current density.

Equation (8.2) can also be broken into two voltage drops, V_{act1} and V_{act2} as follows [11]:

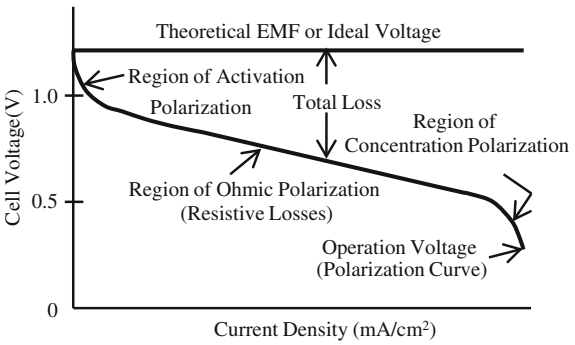

Fig. 8.1 Ideal versus actual fuel cell voltage /current characteristics of a PEMFC [12]

$$V_{act1} = \eta_0 + (T - 298).a \tag{8.3}$$

$$V_{act2} = T.b \ln(I) \tag{8.4}$$

where η_0, a and b are empirical constants. V_{act2} can also be expressed as [11]:

$$V_{act2} = R_{act} I = (R_{act0} + R_{act1} + R_{act2})I \tag{8.5}$$

where:

R_{act0} is an empirical constant.
R_{act1} is a current dependent polynomial.
R_{act2} is temperature dependent and is of the form $\beta(T–298)$ where β is an empirical constant.

The ohmic/resistive voltage drop as the name implies represents all the resistive loses occurring throughout the entire fuel cell and they are expressed by [12]:

$$V_{ohm,cell} = I \, R_{ohm} \tag{8.6}$$

where R_{ohm} is the total cell resistance and it can be broken into three parts (a constant, a current dependent part, and a temperature dependent part) as follows:

$$R_{ohm} = R_{ohm0} + R_{ohm1} + R_{ohm2} \tag{8.7}$$

where:

R_{ohm0} is an empirical constant
R_{ohm1} has the form $\gamma_1 I$ where γ_1 (Ω/A) is an empirical constant
R_{ohm2} has the form $\gamma_2(T–298)$ where γ_2 (Ω/K) is an empirical constant

Concentration voltage drop represent the voltage used to overcome the concentration gradients that are formed due to mass diffusions from the gas flow channels to the reaction sites at the catalyst surfaces [11] and it is represented by:

$$V_{conc,cell} = -\frac{RT}{nF}\ln\left(\frac{C_S}{C_B}\right) = -\frac{RT}{nF}\ln\left(1-\frac{I}{I_{limit}}\right) \tag{8.8}$$

where:
C_S is the surface concentration at the reaction sites.
C_B is the bulk concentration in the gas channels.
I_{limit} is the fuel cell current limit (A).

8.3.2 Thermal Model

The chemical reactions that occur inside the fuel cell generate heat energy which in turn causes the fuel cell's temperature to rise or fall. The thermodynamic energy balance equation of a PEMFC can be written as [11]:

$$\bar{q}_{net} = \bar{q}_{chem} - \bar{q}_{elec} - \bar{q}_{sens+latent} - \bar{q}_{loss} \tag{8.9}$$

where $\bar{q}_{net}$ is the net heat energy (J), $\bar{q}_{chem}$ is chemical energy (J), $\bar{q}_{elec}$ is the electrical energy (J), $\bar{q}_{sens+latent}$ is the sensible and latent heat (J), and $\bar{q}_{loss}$ is the heat loss (J).

The heat generated from the chemical reaction is a function of the Gibbs free energy and the rate of consumption of hydrogen [11, 13] as follows:

$$\dot{q}_{chem} = N_{H_2,consumed} \cdot G \cdot N \tag{8.10}$$

where ΔG is the Gibbs free energy (J/mol) which was calculated in [14], N is the number of cells in the PEMFC stack and $N_{H_2,consumed}$ is the rate of hydrogen consumed (mol/s) which can be represented by [15]:

$$N_{H_2,consumed} = \frac{I}{2F} \tag{8.11}$$

Similarly, the rates of consumption of Oxygen and water in (mol/s) can be represented by [15]:

$$N_{O_2,consumed} = \frac{I}{4F} \tag{8.12}$$

$$N_{H_2O,generated} = \frac{I}{2F} \tag{8.13}$$

The output electrical power is given by:

$$\dot{q}_{elec} = V_{out} \cdot I \tag{8.14}$$

The sensible and latent heat energy on the other hand is expressed as [11]:

$$\begin{aligned}\dot{q}_{sens+latent} = {} & \dot{N}_{H_2,out}(T - T_{room}) \cdot C_{H_2} + \dot{N}_{O_2,out}(T - T_{room}) \cdot C_{HO_2} \\ & + \dot{N}_{H_2O,generated}(T - T_{room}) \cdot C_{H_2O,l} + \dot{N}_{H_2O,generated} \cdot H_V\end{aligned} \tag{8.15}$$

where:

T is the stack temperature.
T_{room} is the room (ambient) temperature.
N_i is the flow rate of i in (mol/s).
C_i is the specific heat capacity of i in $\left(\frac{J}{molK}\right)$
H_v is the vaporization heat of water (J/mol).

Finally, the heat loss which is mainly transferred by air convection can be represented by [11]:

$$\dot{q}_{loss} = h_{cell}(T - T_{room})N\ A_{cell} \tag{8.16}$$

where:

A_{cell} is the cell's area (1.2×10^{-2} m^2).
h_{cell} is the convective heat transfer coefficient $\left(\frac{W}{m^2K}\right)$.

The fuel cell's temperature would rise or drop according to the net heat as follows:

$$\frac{dT}{dt} = \frac{1}{M_{FC}C_{FC}}\dot{q}_{net} \tag{8.17}$$

where:

M_{FC} is the mass of the fuel cell's stack (11 kg).
C_{FC} is the overall specific heat capacity of the stack $\left(\frac{J}{molK}\right)$.

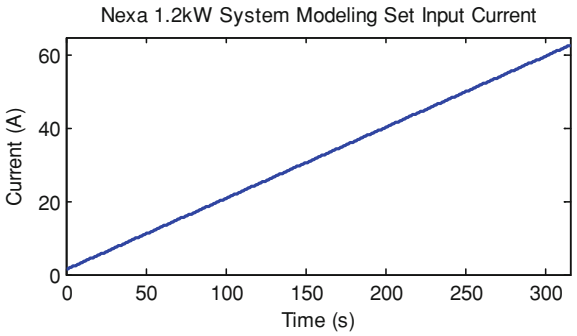

Fig. 8.2 Current input to the modeling experimental data set

8.4 Parameters Identification

Several experiments were conducted on the system and the dynamic response of the system was recorded under variable operating points. The Nexa 1.2 kW PEMFC system has 47 cells, thus, the stack's internal potential becomes:

$$E_{Stack} = 47 \times E_{cell} \tag{8.18}$$

In the modeling data set, the load current was varied linearly in time from 0 to 60 A as depicted in Fig. 8.2. In order to match the V/I characteristics of this experimental data set, all the different parameters in the three voltage drops should be identified. The concentration voltage drop was directly calculated from (8.8) using I_{limit} of 75 A, which is the maximum allowable current of the Nexa system as per the data sheet of the system.

The activation and ohmic voltage drops on the other hand were identified using the same methodology represented in [14, 16]. The resulting parameters were then optimized using Particle Swarm Optimization (PSO), which is a heuristic search and optimization algorithm that was developed in 1995 by Eberhart and Kennedy [17]. PSO mimics the swarming behaviors of birds and fish while searching for food or avoiding predators. [18].

Although the PSO algorithm is simple in concept; it is very effective in approximating solutions to complex problems that might or might not have analytical solutions.

The fitness function that was used to optimize the model was set to be the H_∞ norm of the error between the simulation result and the experimental result. The PSO converged at an H_∞ norm of (0.176 V) and the resulting parameters of the activation and ohmic voltage drops are given in Table 8.1.

Figure 8.3 compares the experimental voltage response of the modeling data set with the voltage response of the PSO obtained model.

Table 8.1 Activation and ohmic voltage drops parameters

Parameter	PSO optimization result
V_{act1}	$26.5230–8.9224 \times 10^{-2}\ (T - 298)$
R_{act}	$-1.0526 + 6.945 \times 10^{-11} I^6 - 1.7272 \times 10^{-8} I^5 + 1.7772 \times 10^{-6} I^4 - 9.8133 \times 10^{-5} I^3 + 3.1430 \times 10^{-3} I^2 - 3.5320 \times 10^{-2} I + 1.3899 \times 10^{-3} (T–298)$
R_{ohm0}	1.7941
R_{ohm1}	$-2.3081 \times 10^{-2} I$
R_{ohm2}	$-2.0060 \times 10^{-3} (T–298)$

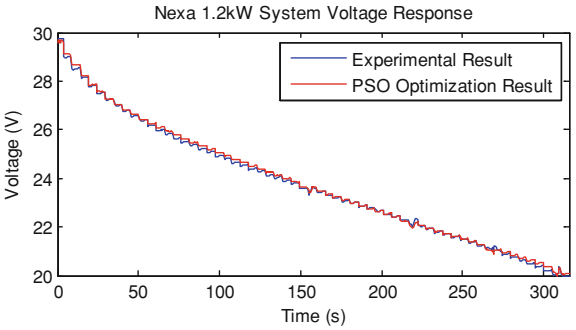

Fig. 8.3 Comparison between the experimental voltage response of the Nexa system and the simulation result

Temperature modeling and parameter identification was based on (8.17). However, many parameters in (8.15), (8.16) and (8.17) needed to be identified using PSO.

The sensibility and latent heat representation in (8.15) can be re-written in the following form:

$$\dot{q}_{\text{sens+latent}} = (K_1 + K_2 I)(T - T_{\text{room}}) + K_3 I \tag{8.19}$$

where:

$K_1 \quad = \dot{N}_{H_2,\text{out}} \cdot C_{H_2} + \dot{N}_{O_2,\text{out}} \cdot C_{HO_2}.$

$K_2 \quad I = \dot{N}_{H_2O,\text{generated}} \cdot C_{H_2O,l}.$

$K_3 \quad I = \dot{N}_{H_2O,\text{generated}} \cdot H_V.$

Using a 4th order Runge-Kutta representation of (8.17) with (8.10), (8.16) and (8.19); five different parameters were identified using PSO and the following fitness function:

$$\text{fitness} = T_{\text{actual}} - T_{\text{PSO}\,\infty} \tag{8.20}$$

The PSO converged at a fitness value of (0.426 K). The resulting thermal parameters are given in Table 8.2 whereas Fig. 8.4 compares the experimental temperature response of the modeling data set with that of the PSO obtained model.

Table 8.2 Thermodynamic equation's parameters

Parameter	Value
C_{FC}	282.8416
h	19.6434
K_1	10.3597
K_2	0.3259
K_3	4.7337

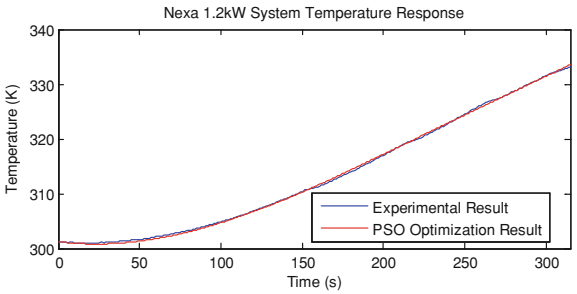

Fig. 8.4 Comparison between the experimental temperature response of the Nexa system and the simulation result

8.5 Model Validation

In order to validate the obtained models a complete block diagram of the model was built in Simulink/MATLAB, (see Fig. 8.5) where the inputs of the block diagram were only the load (represented by the current in A) and the room temperature T_r in K. The model was then tested by using different actual experimental current and room temperature readings to test the validity of the model and see if it can match the actual voltage and temperature responses of the system.

Two model validation examples are shown in the following figures. In the first example the current input is shown in Fig. 8.6 and the room temperature was 296 K (23 °C). The voltage response had an H_∞ norm of error equal to (1.50 V) (see Fig. 8.7) whereas its temperature response had an H_∞ norm of (1.86 K) (see Fig. 8.8).

In the second example however, the current input is given in Fig. 8.9 and the room temperature was set to be 295 K (22 °C). The voltage response of this example had an H_∞ norm of about (0.93 V) (see Fig. 8.10) whereas its temperature response had an H_∞ norm of (1.29 K) (see Fig. 8.11).

Note that the Simulink model was successfully able to predict the system's voltage and temperature response patterns from load current and room temperature only. Table 8.3 summarizes the results of the modeling data set and the two model validation examples.

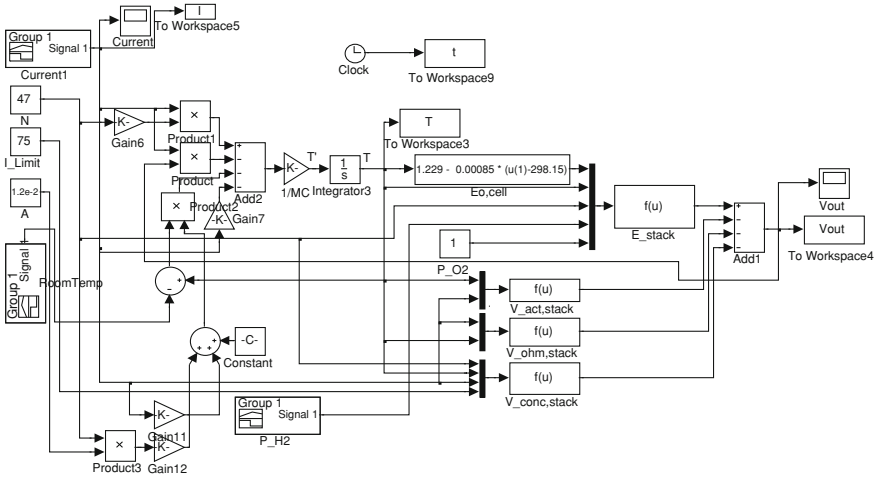

Fig. 8.5 Complete Simulink/MATLAB model

Fig. 8.6 Current input to the first validation example

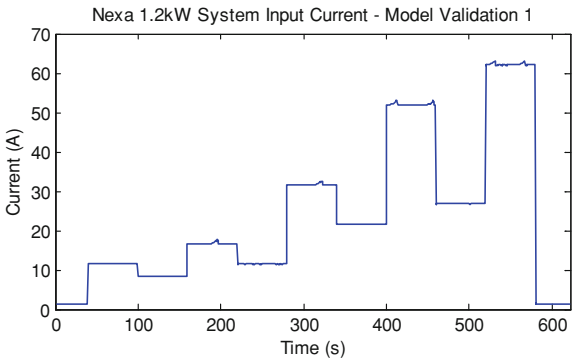

Fig. 8.7 Comparison between the experimental and simulation voltage responses of the first model validation example

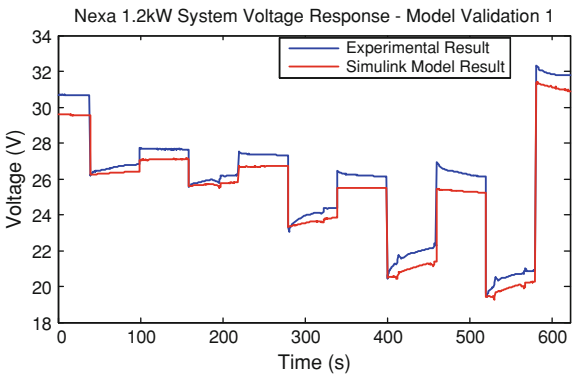

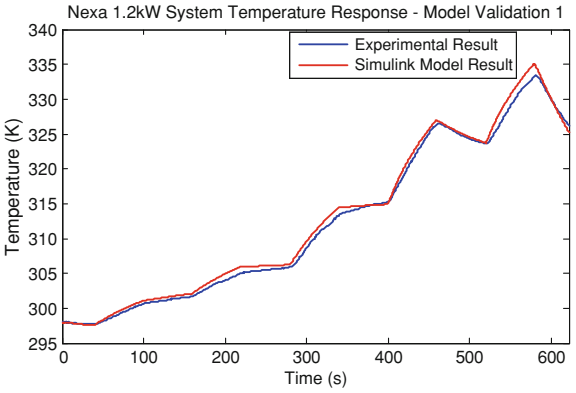

Fig. 8.8 Comparison between the experimental and simulation temperature responses of the first model validation example

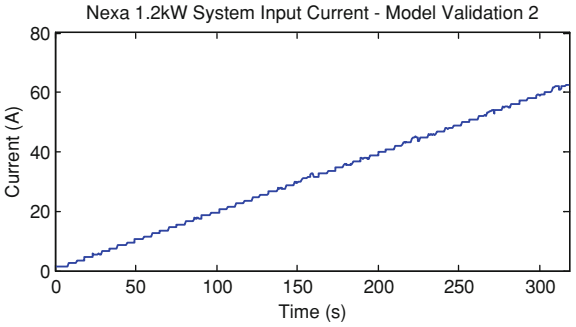

Fig. 8.9 Current input to the second validation example

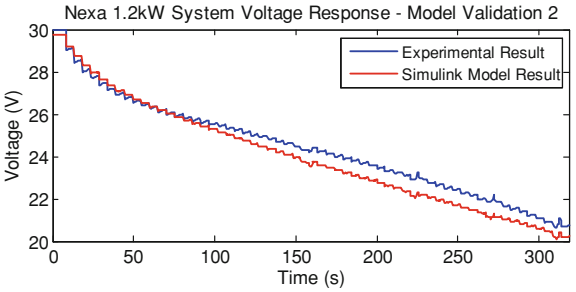

Fig. 8.10 Comparison between the experimental and simulation voltage responses of the second model validation example

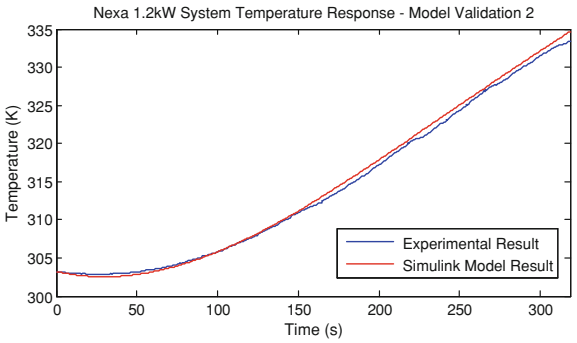

Fig. 8.11 Comparison between the experimental and simulation temperature responses of the Second model validation example

Table 8.3 Model validation results

	Voltage response H_∞ norm (V)	Temperature response H_∞ norm (K)
Modeling data set	0.176	0.426
Model validation #1	1.50	1.86
Model validation #2	0.93	1.29

8.6 Conclusion

This paper presented a PEMFC dynamic model parameter identification approach that can be used successfully to identify the dynamic modeling parameters of any PEMFC system. The obtained model was highly accurate and managed to match the modeling data set with very low errors.

The obtained model was then constructed in Simulink/MATLAB for validation. Other experimental data sets were used to validate the model by only feeding experimental current and room temperature to the Simulink model. The Simulink model was successfully able to predict both the voltage and temperature dynamic responses of the system with small tolerable errors.

This model/modeling approach can serve as a good base for further studies and research on PEMFC's, such as design, optimization, performance improvement and most importantly, fault diagnosis.

Acknowledgment This research work is sponsored by the United Arab Emirates University (UAEU) in Al Ain—UAE.

References

1. L. Qi, C. Weirong, J. Junbo, C.Y. Thean, H. Ming, Model and operation optimization of PEMFC based on AFPSO, in *Proceedings of IEEE on Asia-Pacific Power and Energy Engineering Conference (APPEEC 2009)* (2009), pp. 1–6
2. L. Qi, C. Weirong, J. Junbo, C.Y. Thean, H. Ming, Proton exchange membrane fuel cell modeling based on adaptive focusing particle swarm optimization. J. Renew. Sustain. Energy **1**(1), 013105 (2009)

3. L. Qi, C. Weirong, L. Shukui, L. Chuan, J. Junbo, Mechanism modeling of proton exchange membrane fuel cell based on adaptive focusing particle swarm optimization. Proc. CSEE **29**(20), 119–124 (2009)
4. L. Qi, C. Weirong, W. Youyi, L. Shukui, J. Junbo, Parameter identification for PEM fuel-cell mechanism model based on effective informed adaptive particle swarm optimization. IEEE Trans. Industr. Electron. **58**(6), 2410–2419 (2011)
5. P. Hu, G.Y. Gao, X.J. Zhu, J. Li, Y. Ren, Modeling of a fuel cell stack by neural networks based on particle swarm optimization, in *Proceedings of IEEE on Asia-Pacific Power and Energy Engineering Conference (APPEEC 2009)* (2009), pp. 1–4
6. P. Hu, G.Y. Gao, X.J. Zhu, J. Li, Y. Ren, Modeling of a proton exchange membrane fuel cell based on the hybrid particle swarm optimization with Levenberg–Marquardt neural network. Simul. Model. Pract. Theory **18**(5), 574–588 (2010)
7. P. Li, J. Chen, G. Liu, D. Rees, J. Zhang, Hybrid model of fuel cell system using wavelet network and PSO algorithm, in *Proceedings of IEEE Chinese Control and Decision Conference (CCDC)* (2010), pp. 2629–2634
8. R. Chibante, D. Campos, An experimentally optimized PEM fuel cell model using PSO algorithm, in *Proceedings of IEEE International Symposium on Industrial Electronics (ISIE)* (2010), pp. 2281–2285
9. A. Askarzadeh, A. Rezazadeh, Optimization of PEMFC model parameters with a modified particle swarm optimization. Int. J. Energy Res. **35**(14), 1258–1265 (2011)
10. X. Li, Q. Yan, D. Yu, PEMFC model parameter optimization based on a hybrid PSO algorithm. J. Comput. Inf. Syst. **7**(2), 479–486 (2011)
11. M.H. Nehrir, C. Wang, *Modeling and Control of Fuel Cells: Distributed Generations Applications*, 1st edn. (IEEE Press Series on Power Engineering, Wiley, 2009)
12. EG&G Services, Inc, *Fuel Cell Handbook*, 7th ed., Science Applications International Corporation, DOE, Office of Fossil Energy, National Energy Technology Laboratory, 2004
13. S.V. Puranik, A. Keyhani, F. Khorrami, State-space modeling of proton exchange membrane fuel cell. IEEE Trans. Energy Convers. **25**(3), 804–813 (2010)
14. R. Salim, H. Noura, A. Fardoun, Parameter identification of 3 kW PEM fuel cell system for domestic use in the UAE using genetic algorithms, in *Proceedings of the IEEE 4th International Conference on Power Engineering, Energy and Electrical Drives*, Istanbul (2013), pp. 546–551
15. C. Spiegel, in *PEM Fuel Cell Modeling and Simulation Using MATLAB*, 1st edn. (Elsevier, New York, 2008), p. 249
16. R. Salim, H. Noura, A. Fardoun, A parameter identification approach of a PEM fuel cell stack using particle swarm optimization, in *Proceedings of the ASME 2013 11th Fuel Cell Science, Engineering and Technology Conference*, Minneapolis (2013)
17. R. Eberhart, J. Kennedy, A new optimizer using particle swarm theory, in *Proceedings of the 6th International Symposium on Micro Machine and Human Science*, Nagoya, 1995, pp. 39–43
18. Y. Shi, Particle swarm optimization. Newsl. IEEE Neural Netw. Soc. **2**(1), 8–13 (2004)

Chapter 9
Catalytic Characterization of Size Based Gold Nanoparticles for Applications in Fuel Cells

A. Al-Hatti, I. Shaikha, M. Al-Shamisi, T. Abdulrehman and Y. Haik

Abstract Considerable research attention has been given to glucose biofuel cells as they have been recognized for their ability to work under ambient temperatures and a range of pH that makes them suitable for in vivo implantation to power, with body glucose, implantable electronic devices. In this work, we have employed a different approach compared to organic enzymes to facilitate the fabrication of biofuel cell with no organic enzymes. Gold and platinum nanoparticles were synthesized as oxidizing agents and compared their effectiveness in our fabricated biofuel cell. The nanoparticles were placed on a conductive carbon structure. We have found that the gold nanoparticles are more effective as catalyst capable of converting glucose into gluconic acid compared with that of platinum particles. We further found that the concentration of nanoparticles in the cell may not benefit the catalysis of the glucose due to the decrease of surface area to volume ratio as the nanoparticles' concentration increases. Our fabricated fuel cell showed a capability of running multiple cycles, once the medium is adjusted to optimal operation conditions.

Keywords Glucose fuel cell · Gluconic acid · Gold nanoparticles · Platinum nanoparticles · Activated carbon · Power density

9.1 Introduction

Considerable research are conducted for developing alternative sources of power for medical implants such as pacemakers, insulin pumps, and sensors by utilizing the body's own energy to power these devices. The new batteries should have the

A. Al-Hatti · I. Shaikha · M. Al-Shamisi · T. Abdulrehman · Y. Haik (✉)
Mechanical Engineering Department, United Arab Emirates University, Al Ain, United Arab Emirates
e-mail: yhaik@uaeu.ac.ae

M. O. Hamdan et al. (eds.), *ICREGA'14 - Renewable Energy: Generation and Applications*, Springer Proceedings in Energy, DOI: 10.1007/978-3-319-05708-8_9,

ability to operate independently for a longer lifetime, with no need for external refueling. The trend is going toward fuel cells as they have higher energy density than other batteries, which make them the best alternative for rechargeable batteries.

Fuel cells are electrochemical devices that are capable of transforming chemical energy into electrical energy by electrochemical reactions. Fuel cells that utilize enzymes or metals as the catalyst for oxidizing the fuel are called biofuel cells. Considerable research attention has been given to biofuel cells as they have been recognized for their ability to work under ambient temperatures and a range of pH that makes them suitable for in vivo implantation for powering implantable electronic devices using body's glucose.

Primarily, enzymatic catalysts such as glucose oxidase at the anode to convert glucose to gluconolactone and laccase at the cathode to reduce oxygen to water at the cathode, however due to the complexity of the enzymes structures, it has been reported that electrical communication between the electrodes and the enzymes is a challenge that requires an engineering solution as enzymes should be immobilized near the electrodes in order to work properly. Otherwise, the generated electrons will be diffused and lost into the fuel.

Other biofuel cells are that which utilizes noble metals such as platinum, palladium, gold, or nickel as the catalyst. Nanoparticles of noble metals are utilized instead of covering the whole electrode, to increase the surface area of the electrodes and hence improve the reaction, the power density, and stability of the fuel cell.

Metallic catalyzed glucose oxidation was studied in literature for industrial production of gluconic acid. Baatz et al. observed very high activity and long-term stability at very low gold content on alumina support [1]. Ishida et al. and Önal et al. studied the nanoparticles size effect [2, 3]. Very high activity was observed at very low gold content and they observed that smaller particles are more active. The reaction conditions are affecting the catalytic activity and the formation rate of gluconic acid could be strongly increased at alkaline pH values around 9.0–9.5. The temperature was varied to detect its influence on the reaction where it was optimized at 50 $^{\circ}$C. In Mirescu et al. gold was supported on different metallic oxides such as TiO_2 and Al_2O_3. The oxidation of glucose of Au/TiO_2 was tested in 17 runs with no decrease in activity. The selectivity of gold catalyst towards gluconic acid exceeded 99.5 %. During several repeated batches Au/Al_2O_3 showed excellent long-term stability without any losses [4]. In the study by Thielecke et al. long-term stability of gold catalyst was excellent in its activity and selectivity throughout 70 days of continuous operation. Furthermore, it has been found that gold is more resistive to poisoning due to oxidation than Pt and Pd because of its catalyst surface saturation that leads to activity drop [5]. Pt is deactivated because of platinum oxide (PtO) formation. Nevertheless, it was found that adding bismuth to Pt and Pd overcomes their deactivation [6]. A recent research was developing enzymatic catalyst and Pt-Ru catalyst. The generated power density and lifetime was compared for both catalysts. The lifetime of Pt-Ru/C catalyst was about one month with 2 mW/cm^2 power density. While

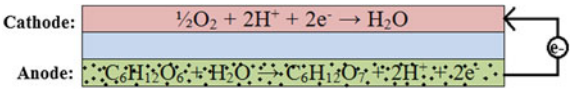

Fig. 9.1 Glucose fuel cell reaction and main components

enzymatic catalyst lasts for few minutes because of losing the mediator during the fuel flow. The maximum power performed by enzymatic catalyst was 250 μW/cm^2 [7]. Another group of researchers developed glucose fuel cell using commercial Pt-Ru/C as anode catalyst with 1.38 mW cm^{-2} peak power density [8]. The same group developed Pt–Au/C catalyzed fuel cell that reduced the poisoning level of platinum and generated 0.72 mW cm^{-2} peak power density [9]. Biella et al. found that gold was much more active than commercial Pt–Pd–Bi or Pd–Bi catalysts that were specifically designed for glucose oxidation. It was unique in completing total conversion at any pH and has high selectivity. Pd–Bi performed better conversion percent of glucose than Pt–Pd–Bi at low pH [10].

In this work, the feasibility of fabricating glucose biofuel cell was demonstrated. We have fabricated two biofuel cells based on glucose as fuel and synthesized two types of nanoparticles as catalyst, namely gold and platinum and compared their effectiveness. These catalysts provide direct transfer for the electrons and high surface area to volume ratio. The catalysts were synthesized using the reducing agents $NaBH_4$ and tri-sodium citrate. The nanoparticles were immobilized on a conductive carbon structure. A membrane which is selective to oxygen and glucose was made in the lab and utilized to separate the anode and the cathode. It serves as electrical insulation between the anode and the cathode, and as ion conductor to close the fuel cell electrical circuit by transporting ions. At the anode in the glucose fuel cell, the glucose is oxidized to gluconic acid in the presence of oxygen in aqueous solution and oxygen is reduced to water at the cathode. Free electrons are generated and go through connecting wire to the cathode producing electric current, Fig. 9.1.

9.2 Experimental Work

9.2.1 Catalysts Preparation

Gold and platinum catalysts were prepared and tested to be used in the anode of the fuel cell. Gold catalyst was prepared with different gold concentrations and tested at the optimal glucose concentration to compare the performance of the catalysts and select the best gold concentration that gives the highest glucose conversion.

9.2.1.1 Synthesis of Different Concentrations of Gold Catalyst Supported by Activated Carbon

Hydrogen tetrarchloroaurate(III) trihydrate, $HAuCl_4.3H_2O$ (Alfa Aesar, USA) was used to get the gold particles. An amount of (x = 8.77 mg) of it was dissolved in 172.5 ml of deionized water by stirring for 45 min. Polyvinyl alcohol, PVA (MW ~ 61000, Aldrich, USA) 200 mg was dissolved in 10 ml of deionized water. An amount of 0.4 ml of PVA aqueous solution was added to the $HAuCl_4.3H_2O$ solution and kept under heating and stirring. When the solution started boiling, 1 ml of tri-sodium citrate-2-hydrate (Riedel-de Haen, Germany) was added to it while heating and stirring until its colour changed to pink which indicated the reduction of gold particles. Activated carbon (0.5 g) (Scott Science and Healthcare Ltd., UK) was added to the previous solution and kept under stirring for a whole day till it became colourless. The solution was washed, filtered and dried. Three more catalysts were prepared with gold concentrations of 2, 3, and 0.5x following the same steps. As the concentration increases the gold colloids colour is changed from pink or dark pink into yellowish or brownish yellow colour.

9.2.1.2 Synthesis of Platinum Catalyst Supported by Activated Carbon

Platinum catalyst was prepared by reducing its salt Potassium tetrachloroplatinate (III), K_2PtCl_4 (Aldrich, USA) using sodium borohydride solution, $NaBH_4$ (Fischer Scientific, UK) as a reducing agent. Preparation procedures in JIANG Qing-lai et al. were followed [11].

9.2.2 Particles Characterization

9.2.2.1 TGA

Thermogravimetric Analysis (TGA) was carried out using (TGA Q50, TA Instruments) to determine the gold particles loadings on activated carbon. Prior to the TGA, the gold samples were heated in the furnace at 100 °C for one hour to remove any moisture. TGA was carried out by taking an amount of 9 mg of each sample and heating it to 800 °C starting from the room temperature at 10 °C/min heating rate under dry air.

9.2.2.2 X-Ray Diffraction

X-ray diffraction for both activated carbon and 3x concentration of gold nanoparticles supported on activated carbon were carried out using Shimadzu XRD-6100. The diffraction patterns of the powders were recorded using Cu Kα radiation at 2θ range of 30–80 °.

9.2.2.3 Size Distribution

The sizes of the synthesized gold and platinum nanoparticles were measured using ZetaSizer, Nano-ZS (Malvern Instruments, UK) by dynamic light scattering, DLS, which provides accuracy, reliability, and high sensitivity for measuring particles diameter in a range of 0.3 nm–10 μm.

9.2.2.4 Surface Morphology

Scanning Electron Microscope, SEM (Joel JBM-5600), was used for obtaining the surface morphology of the gold nanoparticles on activated carbon at different concentrations of gold.

9.2.3 Fuel Cell Fabrication

9.2.3.1 Membrane and Electrodes Fabrication

Membrane works as separator that insulates anode and cathode to avoid short circuit. It was fabricated using the method in Kerzenmacher et al. [12]. This membrane is stable in alkaline media. Such membranes have been used in flexible batteries with KOH as electrolyte. PVA and poly (acrylic acid) PAA (MW ~ 1800, Aldrich, USA) solution in the ratio of 8:1 was prepared with a combined concentration of 7 wt% in water. The prepared pre-hydrogel was casted in a suitable support and thickness was controlled using adhesive tapes. The prepared membrane ~ 20 μm was heated at 145 °C for 80 min. The prepared solution was also used for electrodes fabrication. Electrodes (20 mm x 20 mm x 260 μm) are made from catalyst ink with a biocompatible platinum mesh (Goodfellow, England, UK) as current collector [13]. For the cathode and anode, two platinum meshes were washed by acetone, and heated in furnace at 700 °C for 30 min. The meshes were then washed by water and a compression load of 20 kN was applied on them using MTS Machine. Each mesh was welded to a copper wire. Two plastic sheets were used as substrate for each electrode; the thickness of each electrode was controlled by adding layers of adhesive tape. Activated carbon was added to the pre-hydrogel for the cathode, and activated carbon with platinum or different percentages of gold particles were added to the gel to prepare different anodes. The composition of each electrode is shown in the Table 9.1. The electrodes compositions were spread in the bordered place by adhesive tape layers for each electrode. The mesh and wire assembly were placed directly over the first ink layer and another layer of the ink was added to cover the whole mesh. The electrodes were dried and cross-linked at 145 °C for 80 min.

Table 9.1 Composition of the catalyst for cathode and anode

Component	Cathode composition, g	Anode composition, g
Activated carbon	0.947	–
Synthesized Au or Pt with activated carbon	–	1.026
PVA	0.139	0.135
PAA	0.017	0.017
H_2O	2.23	2.155

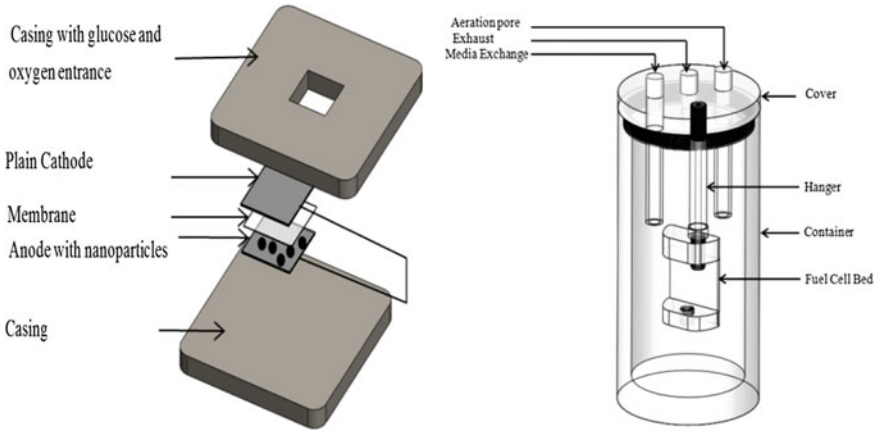

Fig. 9.2 Fabricated fuel cell and testing device

9.2.3.2 Fuel Cell Assembly

The anode and cathode were placed together with the separator polymer in between. The electrodes were placed in the casing and held with four screws. The cell is placed in a testing device filled with glucose solution. The cell in this stage is ready for testing, Fig. 9.2.

9.2.4 Fuel Cell Setup and Testing

Two fuel cells with two different catalysts (platinum and gold) were tested separately. The testing device was filled with 600 ml deionized water. The fuel cell assembly was inserted in the water in the well-closed container. The cell was subjected to heat source (50 °C), stirring and continuous oxygen flow. When the temperature reached 50 °C, 0.25 g of D-(+)-Glucose, $C_6H_{12}O_6$ (Sigma, USA) was added to the solution. Testing the cell gave the performance characteristics data

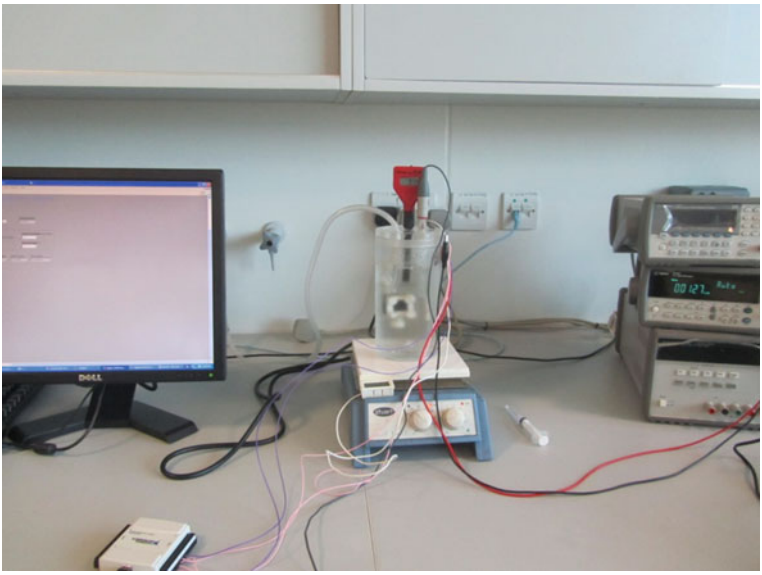

Fig. 9.3 Fuel cell setup and testing

with time (current, voltage). Anode, cathode and reference electrode were connected to the data acquisition to collect voltage readings. The individual anode and cathode voltage was measured against the Ag/AgCl reference electrode (Jenway, UK). The anode and cathode were connected to the digital multi-meter to measure direct current. Using the collected data, power behavior with time was calculated and observed for each cell. Interfaced LabView program collected data from data acquisition system and stored in excel data sheet. pH was measured during the experiment to observe the stabilized pH value in order to add sodium hydroxide NaOH (VWR, USA). The cell setup is shown in Fig. 9.3.

9.3 Results and Discussion

9.3.1 Particles Characterization

Physical characterization of the prepared particles was carried out using TGA, XRD, ZetaSizer and SEM. TGA results for the activated carbon and different concentrations of gold nanoparticles loaded on activated carbon are shown in Fig. 9.4. Comparing the differences in the weight loss at 800 °C between activated carbon and the gold particles of 0.5, 1, 2, 3x concentrations loaded on activated carbon, the loadings of the gold particles were 0.8, 1.3, 2.0, 3.2 %, respectively.

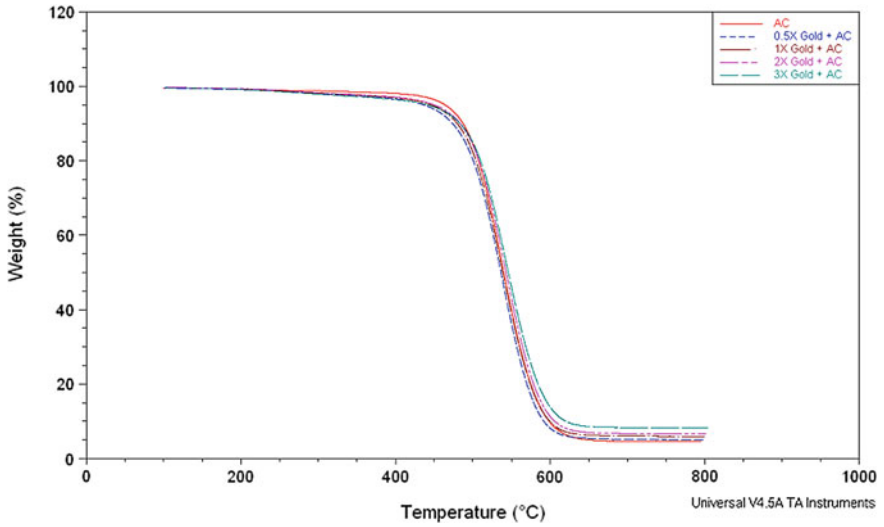

Fig. 9.4 TGA for activated carbon and gold particles on activated carbon support

The XRD patterns in Fig. 9.5 indicated that gold nanoparticles are supported on the activated carbon. The main peaks of gold are located at 38.05°, 44.21°, 64.42°, 77.40°, which correspond to crystal planes of (111), (200), (220), (311), respectively.

Particles sizes are measured for gold nanoparticles in the prepared solutions at four different concentrations of gold and for a platinum sample. The distributions of the diameter size by intensity for all samples are shown in Fig. 9.6 and summarized in Table 9.2.

From Fig. 9.6 and Table 9.2, the sizes of prepared particles in the solution during the preparation were measured. As the concentration of the particles increases for the same catalyst, the diameter size increases, this means the surface area-volume ratio decreases. That results in a reduction in the catalyst reaction, and hence, a decrease in the fuel cell efficiency.

Comparing between the different concentrations of gold particles, the 0.5x gold has the smallest particle size, so it was chosen to test its performance in the fuel cell. The 0.5x platinum was also tested in the fuel cell and compared with the 0.5x gold catalyst. SEM images for different concentrations of gold nanoparticles on activated carbon are shown in Fig. 9.7.

9.3.2 Catalyst Testing

Catalysts performance of 0.5, 1, 2 and 3x of gold were tested in 0.25 g of glucose by measuring the pH drop. The reduction in the pH indicates that glucose is

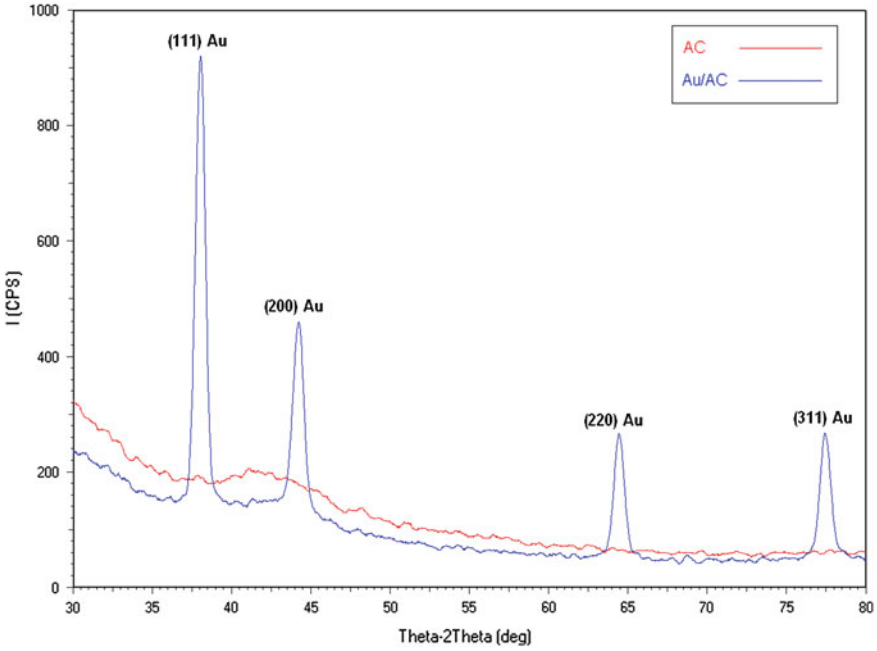

Fig. 9.5 XRD patterns for activated carbon, and gold nanoparticles on activated carbon

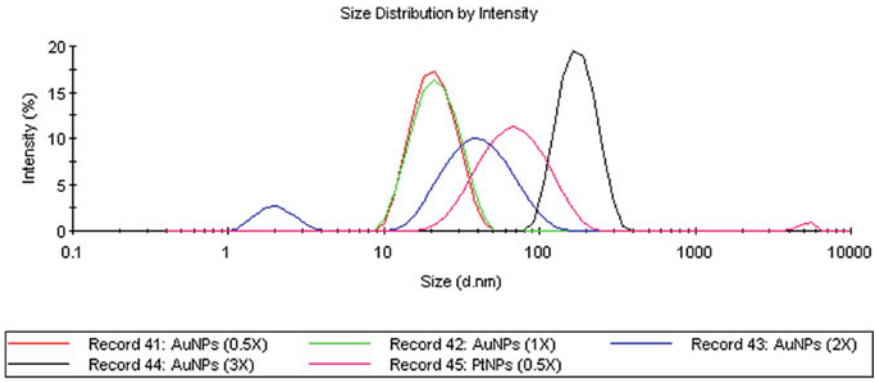

Fig. 9.6 Size distribution for different concentrations of gold nanoparticles and platinum nanoparticles by intensity

Table 9.2 Summary of particles average and maximum diameter sizes

Sample	Average diameter (nm)	Peak (nm)
0.5x gold	17.68	21.71
1x gold	20.21	22.35
2x gold	23.17	44.33
3x gold	189.3	179.1
0.5x platinum	61.57	74.43

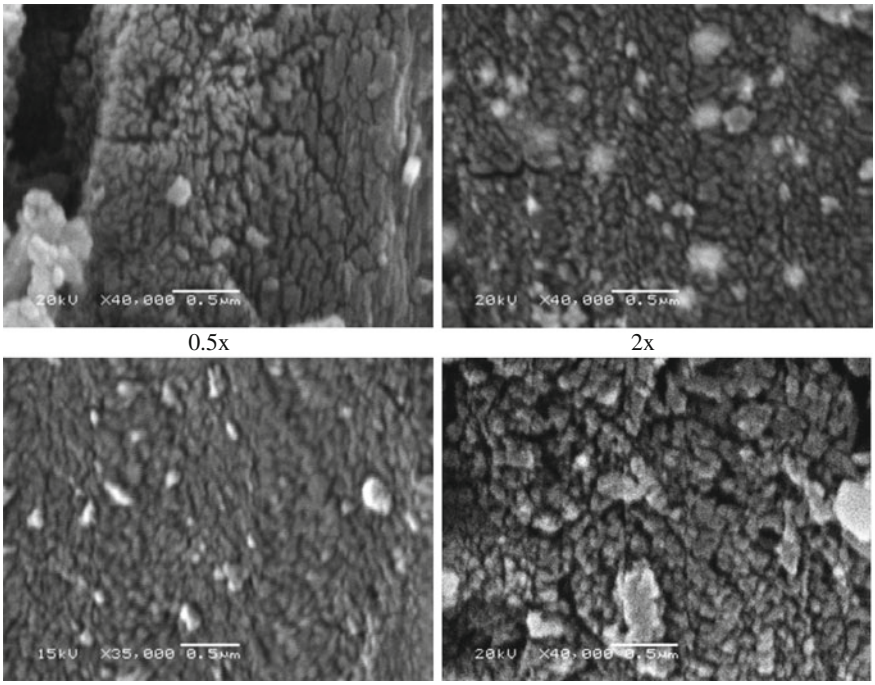

Fig. 9.7 SEM images of gold particles on carbon

converted into gluconic acid. The following Eqs. (9.1) and (9.2) present the reactions.

$$C_6H_{12}O_6 + {}^1\!/_2O_2 \rightarrow C_6H_{12}O_7 + \text{electrons} \tag{9.1}$$

$$C_6H_{12}O_7 + NaOH \rightarrow C_6H_{11}O_7Na + H_2O \tag{9.2}$$

NaOH is added to the glucose solution as indicator to observe glucose conversion after pH is stabilized to start a new cycle. In every cycle the pH decreases from the previous one which shows the drop in glucose amount and its conversion into gluconic acid.

Figure 9.8 shows a total of 12 cycles of 0.5x gold catalyst in 0.25 g of glucose solution. All cycles have the same pattern where the pH drops in the same trend; therefore, the first five cycles for all catalysts concentrations were compared.

Figures 9.9, 9.10, 9.11, and 9.12 illustrate the relation between the pH drop with time for the first five cycles of gold catalysts 0.5, 1, 2 and 3x. The pH keeps decreasing due to the decrease of glucose concentration with the formation of gluconic acid. As the concentration of glucose decreases with time in each cycle, the last cycles have shorter time duration. The pH drop was faster at the beginning

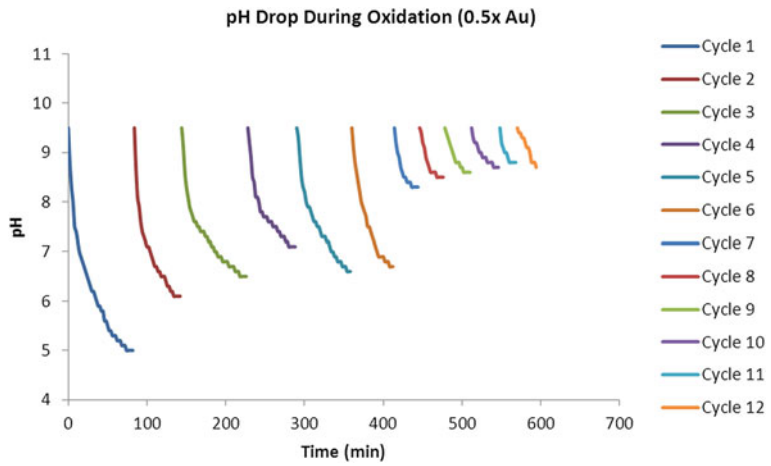

Fig. 9.8 All glucose oxidation cycles for 0.5x gold catalyst with time

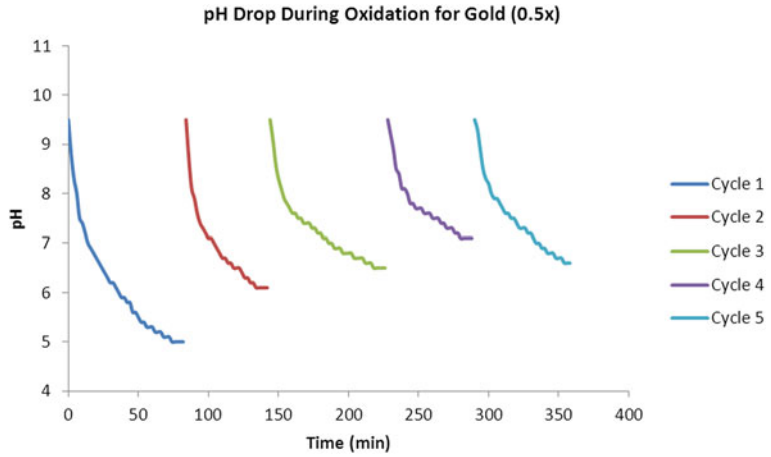

Fig. 9.9 pH drop with time for 0.5x gold catalyst

of each cycle as gold nanoparticles have higher catalytic activity at alkaline pH. Once the acidic pH is reached, it shows a decline in activity and hence a change in slope during the reaction.

Figure 9.13 illustrates the glucose consumption for the gold catalysts in the first cycle. 0.5x gold catalyst has the highest consumption of glucose when compared to the other gold catalysts. With increase in size of the gold nanoparticles, the catalytic activity decreases. To achieve higher catalytic activity, the concentration of the gold salt to prepare the nanoparticles should be optimum to obtain the ideal size of the gold nanoparticles.

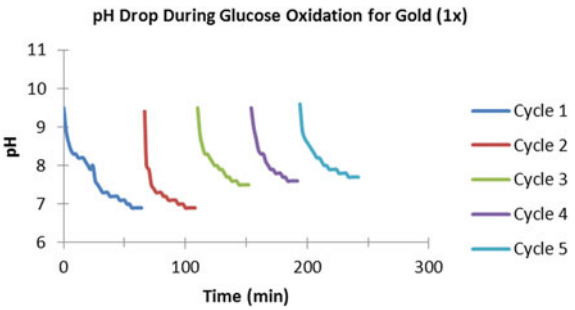

Fig. 9.10 pH drop with time for 1x gold catalyst

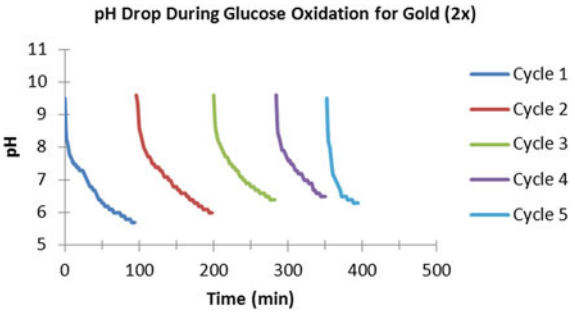

Fig. 9.11 pH drop with time for 2x gold catalyst

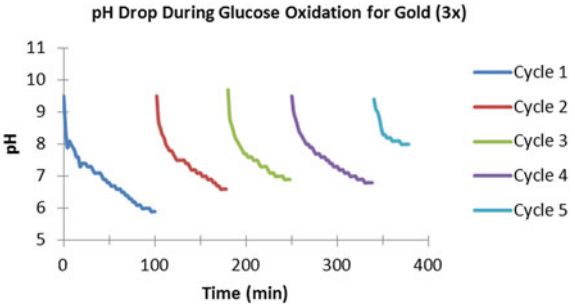

Fig. 9.12 pH drop with time for 3x gold catalyst

For platinum catalyst, the test was performed with 0.5x concentration. Figure 9.14 shows the pH drop with time for the first five cycles. The lowest pH value in platinum catalyst (~ 8) is more than the lowest pH (~ 5) in gold catalyst (0.5x), which means the conversion of glucose is more in the gold catalyst

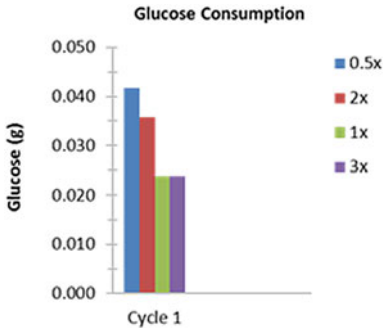

Fig. 9.13 Glucose consumption in the first cycle of the gold catalysts

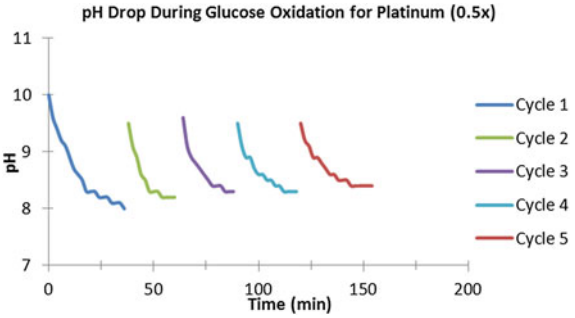

Fig. 9.14 pH drop with time for platinum catalyst

9.3.3 Fuel Cell Performance Test

From particles characterization and catalyst test, 0.5x Au catalyst has the smallest size particle, which represents the highest surface–volume ratio. Two fuel cells with two different catalysts (platinum and gold) at 0.5 concentrations were tested. Each fuel cell current and voltage differences were collected and recorded for analyzing the fuel cell performance for both cells. Fuel cell power was calculated using Eq. (9.3):

$$P(t) = V(t)I(t) \tag{9.3}$$

V(t) Voltage difference between anode and cathode, V,
I(t) Current, A

Comparing between gold-catalyzed cell and platinum-catalyzed cell, platinum cell showed better performance over time. Current behavior for gold-catalyzed cell took longer time to reach peak value, 6.25 μA/cm^2, Fig. 9.15, whereas platinum-catalyzed cell reached peak value, 9.125 μA/cm^2 earlier, Fig. 9.16. On the other hand, when testing the gold catalyst it consumed more NaOH than platinum. NaOH consumption of gold-catalyzed fuel cell in 2 days of operation was more

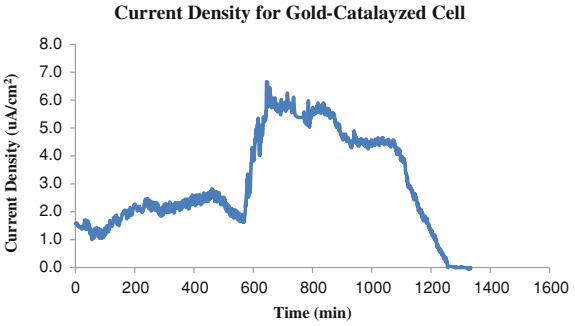

Fig. 9.15 Current trend with time for gold-catalyzed glucose fuel cell

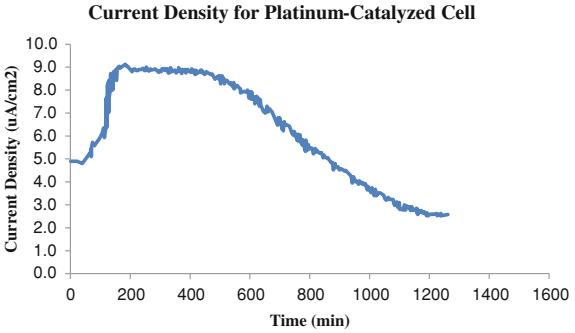

Fig. 9.16 Current trend with time for platinum-catalyzed glucose fuel cell

than platinum-catalyzed cell. This provides indication that gold-catalyzed reactions were better but transferring the current was weak. This could refer to the welding between the copper wire and the electrode.

The voltage difference for both cells were low and this could be due to the fabricated membrane as it should form insulation layer between the electrodes to prevent short circuit voltage. The maximum voltage obtained for gold-catalyzed cell is 0.36 V which is close to the maximum voltage difference of platinum-catalyzed cell 0.40 V. Low voltage differences result in low power values which were varying during the performance test. The maximum power densities for gold-catalyzed cell and platinum-catalyzed cell were 1.29 $\mu W/cm^2$ and 3.10 $\mu W/cm^2$, respectively. Generally platinum-catalyzed fuel cell performed better performance than gold-catalyzed fuel cell according to lifetime and power generation.

The performance of the gold catalysts can be improved by employing the right concentrations of gold salts and reducing agents to prepare gold nanoparticles and also by preparing bimetallic or trimetallic gold catalysts like Ag–Au [14], Pt–Au [9] or Au–Pt–Ag [15] to improve the catalytic activity of gold catalysts for glucose oxidation. Pt–Au catalysts have been shown to have reduced poisoning of platinum.

9.4 Conclusions

A biofuel cell with glucose as fuel and harvest electrons through the oxidation of glucose was fabricated. Gold and platinum nanoparticles were synthesized and immobilized on the anode that will be utilized as oxidizing agents in the process that can be utilized in the fuel cell. We studied the effect of varying the surface area to volume ratio on the efficiency of the catalytic reaction. We found that gold nanoparticles are more effective as catalyst compared to that of platinum particles. We further found that the more the concentration of nanoparticles in the cell reduces the surface area to volume ratio which is undesirable. Once the fuel cell medium is adjusted to the optimal operation conditions, it can run for multiple reaction cycles.

References

1. C. Baatz, U. Prüße, Preparation of gold catalysts for glucose oxidation by incipient wetness. J. Catal. **249**(1), 34–40 (2007)
2. T. Ishida, S. Okamoto, R. Makiyama, M. Haruta, Aerobic oxidation of glucose and 1-phenylethanol over gold nanoparticles directly deposited on ion-exchange resins. Appl. Catal. A **353**, 243–248 (2009)
3. Y. Önal, S. Schimpf, P. Claus, Structure sensitivity and kinetics of D-glucose oxidation to D-gluconic acid over carbon-supported gold catalysts. J. Catal. **223**(1), 122–133 (2004)
4. A. Mirescu, H. Berndt, A. Martin, U. Prüße, Long-term stability of a 0.45 % Au/TiO2 catalyst in the selective oxidation of glucose at optimised reaction conditions. Appl. Catal. A **317**(2), 204–209 (2007)
5. N. Thielecke, M. Aytemir, U. Prüsse, Selective oxidation of carbohydrates with gold catalysts: continue-flow reactor system for glucose oxidation. Catal. Today **121**(1–2), 115–120 (2007)
6. I. Nikov, K. Paev, Palladium on alumina catalyst for glucose oxidation: reaction kinetics and catalyst deactivation. Catal. Today **24**(1–2), 41–47 (1995)
7. Worthington Biochemical Corporation (1972) 730 Vassar Ave., Lakewood, NJ. http://www.worthington-biochem.com/introbiochem/introEnzymes.html. Accessed 28 Dec 2013
8. D. Basu, S. Basu, A study on direct glucose and fructose alkaline fuel cell. Electrochim. Acta **55**(20), 5775–5779 (2010)
9. D. Basu, S. Basu, Synthesis and characterization of Pt–Au/C catalyst for glucose electro-oxidation for the application in direct glucose fuel cell. Int. J. Hydrogen Energy **36**(22), 14923–14929 (2011)
10. S. Biella, L. Prati, M. Rossi, Selective oxidation of D-glucose on gold catalyst. J. Catal. **206**(2), 242–247 (2002)
11. J. Qing-lai, P. Zhong-dong, X. Xiao-feng, D. Ke, H. Guo-rong, L. Ye-xiang, Preparation of high active Pt/C cathode electrocatalyst for direct methanol fuel cell by citrate-stabilized method. Trans. Nonferrous Met. Soc. China **21**(1), 127–132 (2011)
12. S. Kerzenmacher, R. Sumbhuraju, J. Ducree, R. Zengerle, F. von Stetten, A surface mountable glucose fuel cell for medical implants, in *Proceedings of International Conference on Solid-State Sensors, Actuators and Microsystems (Transducers 2007)* (2007), pp. 125–128
13. S. Kerzenmacher, J. Ducree, R. Zengerle, F. von Stetten, An abiotically catalyzed glucose fuel cell for powering medical implants: Reconstructed manufacturing protocol and analysis of performance. J. Power Sour. **182**, 66–75 (2008)

14. H. Zhang, J. Okuni, N. Toshima, One pot synthesis of Ag–Au bimetallic nanoparticles with Au shell and their high catalytic activity for aerobic glucose oxidation. J. Colloid Interface Sci. **354**(1), 131–138 (2011)
15. H. Zhang, N. Toshima, Preparation of novel Au/Pt/Ag trimetallic nanoparticles and their high catalytic activity for aerobic glucose oxidation. Appl. Catal. A **400**(1–2), 9–13 (2011)

Chapter 10
Advances in P.E.M. Fuel Cell Stack Observer Design Using a Takagi–Sugeno Approach with Unmeasurable Premise Variables

S. C. Olteanu, A. Aitouche and L. Belkoura

Abstract This article presents the development of a nonlinear state observer based on a Takagi–Sugeno approach that is applied to a PEMFCS (Proton Exchange Membrane Fuel Cell Stack) model. The Fuel Cell model which takes into consideration the auxiliary elements associated to the stack, has been validated through the use of the professional software AMESim by a co-simulation with Matlab-Simulink. The paper's objective is to construct a TS fuzzy observer such that it can estimate the states of the considered nonlinear systems despite the unmeasurable premise variables. The observer construction method implies the use of Input to State Stability which eliminates the necessity of the Lipschitz constant, aiming at a bounded estimation error convergence. The conditions for obtaining the observer gains are expressed in the end as Linear Matrix Inequalities.

Keywords Takagi–Sugeno observer · PEM fuel cell · Unmeasurable premise variable · Input to state stability

10.1 Introduction

Fuel Cell Systems' (FCS) usage has seen an increase in the last decade, being under consistent research. As hydrogen acts as a powerful energy storage alternative, FC units can improve the management of renewable energy sources like

S. C. Olteanu (✉) · L. Belkoura
LAGIS Laboratory, University of Lille 1, Lille, France
e-mail: sc.olteanu@ed.univ-lille1.fr

L. Belkoura
e-mail: lotfi.belkoura@univ-lille1.fr

A. Aitouche
LAGIS Laboratory, HEI, Lille, France
e-mail: abdel.aitouche@hei.fr

M. O. Hamdan et al. (eds.), *ICREGA'14 - Renewable Energy: Generation and Applications*, Springer Proceedings in Energy, DOI: 10.1007/978-3-319-05708-8_10,

solar or wind power as they don't have a continuous and predictable production. Among all the different types of FCS, like Solid Oxide FC, Alkaline FC or direct methanol FC to name a few, the Proton Exchange Membrane Fuel Cell (PEMFC) system positions itself as one of the most important candidates in replacing classical energy conversion systems, not only in the automotive industry, but also in portable devices and back up units. The PEMFC has many applications, due to its high power density and low operating temperature, compared to other types of fuel cells [1].

From a systemic perspective the fuel cell represents an interesting process for it shows a high degree of nonlinearity, as well as presenting different scales in parameter values and also in variable dynamics (from mechanical, electrical and chemical equations).

The limited lifespan and also the strict inherent security of fuel cells call upon the need for diagnostics [2] and control [3, 4]. There are different approaches adopted: experimental (for example impedance spectroscopy, neuro-fuzzy techniques) and model based (as adopted in the current paper). In the later case, these techniques bring precision and generality at the cost of difficulty in finding the best numerical representation. In model based methodologies, the use of state observers is common practice, adding also the fact that some parameters of the system cannot be directly measured or it is too expensive to do so.

A Takagi–Sugeno fuzzy observer [5] has been adopted in this work. TS models are currently being used for a large class of physical and industrial processes [6]. This representation brings advantages over other existing types of methods, because it manages to act upon nonlinear systems without needing a linearization. The design of state observers for nonlinear systems using Takagi–Sugeno (TS) models has been actively considered during the last decades [6, 7]. Many works consider the case of TS models with measurable premise variables such as [7, 8]. This choice provides some simplicity, being an extension of classical algorithms developed for linear systems over the TS model. Unfortunately, the premise variables in practice are unmeasurable and the problem of estimation becomes more difficult to resolve. Different approaches have been adopted in order to solve the unmeasurable premise variable case [9–11], each trying to reduce as much as possible the restrictions that grow significantly with the system's complexity.

The article aims firstly to bring a contribution to the model based FC analysis, focusing towards state reconstruction. Therefore, a mathematical model of a PEMFC is developed, having as starting point the work done in [12]. The systematic methodology for TS model construction is performed with the aid of a sector nonlinearity approach [13]. The challenge is to construct an observer such that it can estimate the states of the considered system with the premise variables dependant on states that are not measurable. This is done by means of Input to State Stability (ISS) notion, where the limitation imposed by the Lipschitz constant is reduced.

This paper is organized following the structure: Section 10.2 deals with the PEM Fuel Cell Stack general description, followed by the nonlinear model employed and its validation by professional software: AMESim. In Sect. 10.3 it is

presented the T–S representation of the model followed in Sect. 10.4, by the construction of the nonlinear TS observer, where the observer gains are found by computing the Linear Matrix Inequalities. Finally in the last section, conclusions and future works are down.

10.2 Fuel Cell Stack Systems

10.2.1 PEM Fuel Cell Technology

The current work focuses on a Polymer Electrolyte Membrane (Proton Exchange Membrane) Fuel Cell Stack using a Nafion membrane, including auxiliary components (Fig. 10.1). Some simplifications have been added to the model, by taking into consideration only pure Oxygen as input and also an ideal humidifying and cooling units.

Also spatial and temperature variations have been ignored. A minimal pressure difference between Anode and Cathode is maintained by using a regulator.

10.2.2 State Space Representation

For ideal gases, the mass conservation law is applied resulting (10.1). The compressor's mass flow is considered as input to the system, the possibility to add a controller so that it follows a desired flow exists. The mass that accumulates in the cathode, depending on the quantity of oxygen that enters, will either be ejected or will react with the hydrogen ions. Furthermore, inside the cathode, vapor is generated, where some of it is ejected towards the return manifold (consisting of pipes and valves), while another part adds inside the cathode, increasing the general pressure. The work is done under the hypothesis that there is no humidification neither of the oxygen nor of the hydrogen, and the FC is self humidifying [14]. Concerning the valve mathematical model, a linear model has been chosen for the cases when we have small pressure differences, whereas a chocked regime equation was demanded for the cathode purge valves and anode. This is because of the big pressure difference created with the atmosphere. As the return manifold pressures overpass 2 bar, ignoring the unchoked regime brings no limitations.

$$\begin{cases} \frac{dp_{sm}}{dt} = \frac{R_{O_2} \cdot T_{st}}{V_{sm}} \cdot \left(W_{cp} - W_{sm,out}\right) \\ \frac{dp_{rm}}{dt} = \frac{R_a T_{rm}}{V_{rm}} \cdot \left(W_{ca,out} - W_{rm,out}\right) \\ \frac{dp_{O_2,ca}}{dt} = \frac{R_{O_2} \cdot T_{st}}{V_{ca}} \cdot \left(W_{O_2,ca,in} - W_{O_2,ca,out} - W_{O_2,reacted}\right) \\ \frac{dp_{v,ca}}{dt} = \frac{R_v \cdot T_{st}}{V_{ca}} \left(-W_{v,ca,out} + W_{v,ca,gen}\right) \\ \frac{dp_{H_2,an}}{dt} = \frac{R_{H_2} \cdot T_{st}}{V_{an}} \left(W_{H_2,an,in} - W_{H_2,an,out} - W_{H_2,reacted}\right) \end{cases} \tag{10.1}$$

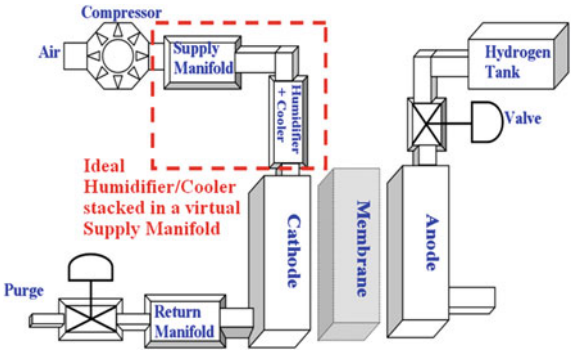

Fig. 10.1 Block view of fuel cell stack with auxiliary elements

The electrical current present as input, represents the demanded current by the consumer system attached to the fuel cell. Finally, the system is described by (10.2).

$$\begin{cases} \frac{dp_v}{dt} = \frac{R_v \cdot T_{st}}{V_{ca}} \cdot \left[\left(k_{ca} \left(p_{ca,O_2} + p_v - p_{rm} \right) \cdot \left(-1 + \frac{M_{O_2} p_{ca,O_2}}{M_{O_2} p_{ca,O_2} + M_v p_v} \right) \right) + \left(\frac{n \cdot M_v}{2 \cdot F} \right) \cdot I_{st} \right] \\ \frac{dp_{ca,O_2}}{dt} = \frac{R_{O_2} \cdot T_{st}}{V_{ca}} \cdot \left[\begin{array}{l} k_{sm} \cdot \left(p_{sm} - p_{ca,O_2} - p_v \right) - k_{ca} \cdot \left(p_{ca,O_2} - \left(p_{rm} - p_v \right) \right) - \\ - \left(\frac{n \cdot M_{O_2}}{4 \cdot F} \right) \cdot I_{st} \end{array} \right] \\ \frac{dp_{rm}}{dt} = \frac{R_a \cdot T_{st}}{V_{rm}} \cdot \left[\begin{array}{l} k_{ca} \cdot \left(p_{ca,O_2} + p_v - p_{rm} \right) - \\ - \frac{A_{T,rm} \cdot C_{d,rm} \cdot p_{rm}}{\sqrt{R \cdot T_{atm}}} \cdot \sqrt{\gamma} \cdot \left(\frac{2}{\gamma + 1} \right)^{\frac{\gamma+1}{2 \cdot (\gamma - 1)}} \end{array} \right] \\ \frac{dp_{sm}}{dt} = \frac{R_a \cdot T_{st}}{V_{rm}} \cdot \left[W_{cp} - k_{sm} \cdot \left(p_{sm} - p_{ca,O_2} - p_v \right) \right] \\ \frac{dp_{an,H_2}}{dt} = \frac{R_{H_2} T_{st}}{V_{an}} \cdot \left[\begin{array}{l} K \cdot K_1 \left(p_{sm} - p_{an,H_2} \right) - \\ - A_{an} \cdot p_{an,H_2} \cdot \frac{C_{d,an} \cdot \sqrt{\gamma} \cdot \left(\frac{2}{\gamma + 1} \right)^{\frac{\gamma+1}{2 \cdot (\gamma - 1)}}}{\sqrt{R \cdot T_{atm}}} - M_{H_2} \cdot \frac{n \cdot I_{st}}{2 \cdot F} \end{array} \right] \end{cases} \tag{10.2}$$

10.2.3 Model Validation

A validation of the developed model has been carried on a simulation platform, specifically *LMS AMESIM*. An equivalent model has been developed (Fig. 10.2) and co-simulated with the nonlinear model implemented in *Simulink*. The co-simulation notion refers to the interconnectivity between the Simulink and the AMESim simulation. The two software have the capability to exchange data in real time giving AMESim the possibility to act as a real process connecting to a monitoring or control system.

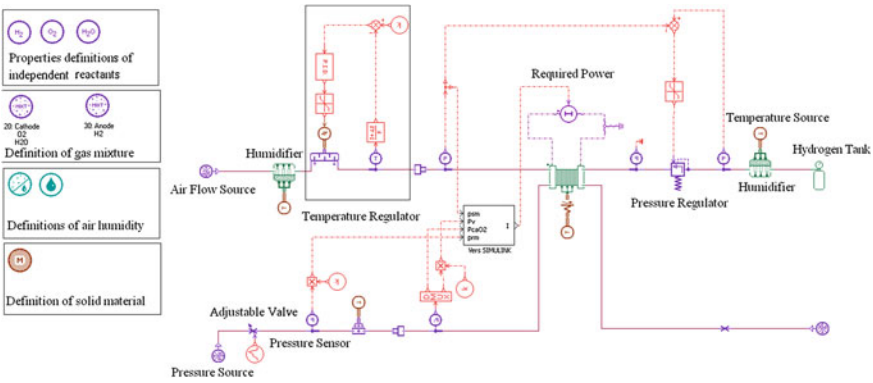

Fig. 10.2 The equivalent AMESIM model of our system

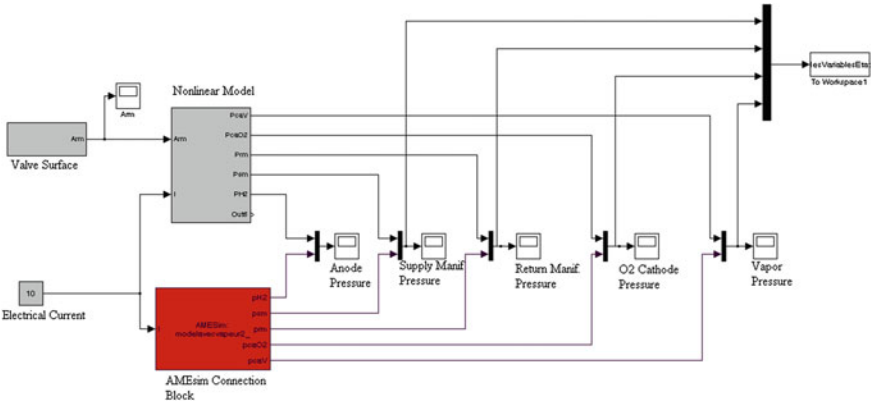

Fig. 10.3 The schema reflecting the interconnections for the co-simulation

The connection blocks can be seen in both AMESim (Fig. 10.2) respectively Simulink (Fig. 10.3).

As an example, a state variable's evolution is presented in (Fig. 10.4). The two lines represent the AMESim and Simulink values working in parallel. The simulations have been carried on for a predefined set of input values.

The powerful influence in three stages of the control of the Return Manifold valve can be easily seen on all the states. Only the generation of vapor being mainly affected by electrical current increases. A small difference can indeed be seen, being generated by the used equations, but it is in acceptable limits.

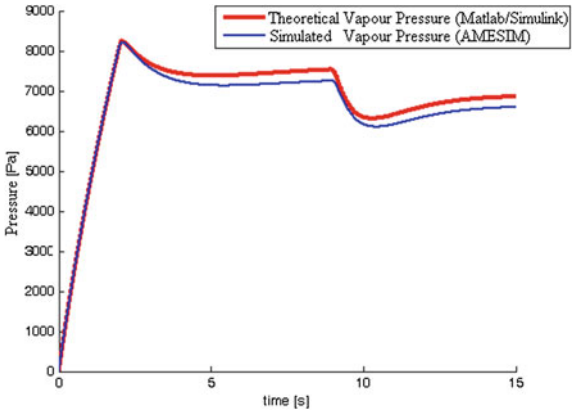

Fig. 10.4 The vapor pressure present inside the cathode volume

10.3 Takagi–Sugeno Model

The Takagi–Sugeno model is in fact a multi-model, fuzzy logic system, that permits to write the general nonlinear state space system as a sum of parallel linear systems that act as a whole (10.3), each rule being weighted by an associated membership function(triangular membership functions are used in this work).

The choice of nonlinear terms is important, the objective being to keep their number to a minimum, while maintaining the observability of each new linear system that will be built.

$$\begin{matrix} Takagi-Sugeno \\ Equivalent \end{matrix} : \begin{cases} \dot{x} = \sum_{i=1}^{8} [\mathrm{w}_i(x) \cdot (A_i \cdot x + B_i \cdot u)] \\ y = C \cdot x \end{cases} \tag{10.3}$$

where $w_i(x)$ is a normalized membership function that returns a percentage corresponding to the degree of validity of the *i*th linear model. It varies in the interval [0, 1] in accordance to the nonlinear premise variables. The matrices A_i, B_i form each of the linear system, in total being a number of 2^n, where n is the number of premise variables, for the current case 3 (10.7), meaning $i = 8$.

$$\begin{matrix} Nonlinear \\ System \end{matrix} : \begin{cases} \dot{x} = A_x(x) \cdot x + B_x(x) \cdot u \\ y = C \cdot x \end{cases} \tag{10.4}$$

For developing the TS system, it is needed to rewrite the initial state space model so that the nonlinear terms can be separated. A separation of the nonlinear terms into the 2 matrices is seen in (10.4): $A_x(x)$ *and* $B_x(x)$. The chosen PEMFC system has 5 states (Pressures of Vapor; Oxygen in Cathode; Return manifold; Supply Manifold; Hydrogen in the Anode), with two of them, the Return Manifold and the Supply Manifold Pressures, being measured (10.5).

$$x = \begin{pmatrix} p_v \\ p_{ca,O_2} \\ p_{rm} \\ p_{sm} \\ p_{an,H_2} \end{pmatrix}; u = \begin{pmatrix} I_{st} \\ A_{T,rm} \\ W_{in} \end{pmatrix}; y = \begin{pmatrix} p_{rm} \\ p_{sm} \end{pmatrix} \tag{10.5}$$

Concerning the observability property, the condition that each linear system is observable depends on the minimum and maximum values chosen in the nonlinearity sector stage and also on the selection of the premise variables.

$$A_x(x) = \begin{pmatrix} -k_{ca} \cdot cst1 & cst1 \cdot \left[-k_{ca} + k_{ca} \cdot Z_1(p_v, p_{ca,O_2}) + k_{ca} \cdot Z_2(p_v, p_{ca,O_2})\right] & cst1 \cdot \left[k_{ca} - k_{ca} \cdot Z_1(p_v, p_{ca,O_2})\right] & 0 & 0 \\ cst2 \cdot \left[-k_{sm} - k_{ca}\right] & cst2 \cdot \left[-k_{sm} - k_{ca}\right] & cst2 \cdot k_{ca} & 0 & 0 \\ cst3 \cdot k_{ca} & cst3 \cdot k_{ca} & -cst3 \cdot k_{ca} & 0 & 0 \\ cst3 \cdot k_{sm} & cst3 \cdot k_{sm} & 0 & -cst3 \cdot k_{sm} & 0 \\ 0 & 0 & 0 & cst5 & -cst6 - cst5 \end{pmatrix}$$

$$B_x(x) = \begin{pmatrix} cst1 * \left[\frac{n.M_v}{2.F}\right] & 0 & 0 \\ cst2 * \left[-\frac{n.M_{O_2}}{4.F}\right] & 0 & 0 \\ 0 & -\frac{R_a.T_{st}}{V_{rm}} \cdot \frac{C_{d,rm} \cdot \sqrt{\gamma} \cdot \left(\frac{2}{\gamma+1}\right)^{\frac{\gamma+1}{2(\gamma-1)}}}{\sqrt{R.T_{atm}}} \cdot (p_{rm}) & 0 \\ 0 & 0 & \frac{R_a.T_{st}}{V_{rm}} \\ -\frac{R_H.T_{st}}{V_{an}} M_{H_2} \cdot \frac{n}{2.F} & 0 & 0 \end{pmatrix} \tag{10.6}$$

In conclusion there are three premise variables:

$$\begin{aligned} Z_1(p_v, p_{ca,O_2}) &= \frac{M_{O_2} \cdot p_{ca,O_2}}{M_{O_2} \cdot p_{ca,O_2} + M_v \cdot p_v}; Z_2(p_v, p_{ca,O_2}) \\ &= \frac{M_{O_2} \cdot p_v}{M_{O_2} \cdot p_{ca,O_2} + M_v \cdot p_v}; Z_3(p_{rm}) = p_{rm} \end{aligned} \tag{10.7}$$

For the model construction, different methods exist, such as the Sector Nonlinearity approach. This method is based on finding local maximum and minimum values for the premise variables ($z_{i,Max}$ respectively $z_{i,min}$) as in [7] that presents a graphical method(the only limit is the fact that the premise variables depend on maximum 3 states). Therefore by choosing triangular membership function they are written as (10.8); where MF represents the membership function associated to the *i*th premise variable z_i. Being thus able to write the normalized membership functions w_i as showed in (10.9).

$$\begin{cases} MF_{\min}(z_i) = \frac{z_i - z_{i,Max}}{z_{i,Max} - z_{i,\min}} \\ MF_{Max}(z_i) = \frac{z_i - z_{i,\min}}{z_{i,Max} - z_{i,\min}} \end{cases} \tag{10.8}$$

$$\begin{cases} h_1 = MF_{Max}(z_1) \cdot MF_{Max}(z_2) \cdot MF_{Max}(z_3) \\ h_2 = MF_{Max}(z_1) \cdot MF_{Max}(z_2) \cdot MF_{\min}(z_3) \\ \ldots\ldots \\ h_8 = MF_{\min}(z_1) \cdot MF_{\min}(z_2) \cdot MF_{\min}(z_3) \\ ---------- \\ w_1 = \frac{h_1}{\sum_{i=1}^{8} h_i}; \ldots; w_8 = \frac{h_8}{\sum_{i=1}^{8} h_i} \end{cases} \tag{10.9}$$

10.4 Observer Design

The general Luenberger Observer for TS systems is considered (10.10).

$$\begin{cases} \dot{x} = \sum_{i=1}^{8} [\mathrm{w}_i(\hat{x}) \cdot (A_i \cdot \hat{x} + B_i \cdot u + L_i \cdot (y - \hat{y}))] \\ \hat{y} = C \cdot \hat{x} \end{cases} \tag{10.10}$$

where L_i represent the observer gains associated to each linear sub-model.

In order to calculate these values, the dynamics of the state error estimation is given by: $\dot{\tilde{x}} = \dot{x} - \dot{\hat{x}}$. Calculating the derivative, the error dynamics becomes:

$$\dot{\tilde{\mathrm{x}}} = \sum_{i=1}^{8} [\mathrm{w}_i(x) \cdot A_i \cdot \mathrm{x} - \mathrm{w}_i(\hat{x}) \cdot A_i \cdot \hat{\mathrm{x}} + \mathrm{w}_i(x) \cdot B_i \cdot u - \mathrm{w}_i(\hat{x}) \cdot B_i \cdot u - \mathrm{w}_i(\hat{x}) \cdot L_i \cdot C \cdot \tilde{x}] \tag{10.11}$$

It can easily be noted that, without the simplifying hypotheses of measurable premise variables, there will be membership functions depending on state estimates. To solve this problem, the technique presented in [11] is applied. Therefore by adding and subtracting a $\mathrm{w}_i(\hat{x}) \cdot A_i \cdot \mathrm{x}$, and separating the two sums, the first one is seen as a perturbation (It is clear that $(\mathrm{w}_i(x) - \mathrm{w}_i(\hat{x})) \longrightarrow [x \to \hat{x}]0$):

$$\begin{cases} \dot{\tilde{\mathrm{x}}} = \sum_{i=1}^{8} [(\mathrm{w}_i(x) - \mathrm{w}_i(\hat{x})) \cdot (B_i \cdot u + A_i \cdot \mathrm{x})] + \sum_{i=1}^{8} [\mathrm{w}_i(\hat{x}) \cdot (A_i - L_i \cdot C) \cdot \tilde{\mathrm{x}}]; \\ \Delta \overset{not}{=} \sum_{i=1}^{8} [(\mathrm{w}_i(x) - \mathrm{w}_i(\hat{x})) \cdot (B_i \cdot u + A_i \cdot \mathrm{x})] \end{cases} \tag{10.12}$$

In order to obtain the convergence of the estimation error to zero, the Input to state stability notion is applied [15].

10.4.1 LMIs Solution

As shown in [11], in order to achieve the observer convergence with a minimum convergence error interval, the following theorem is used:

Theorem *If there exists a symmetric and positive definite matrix P, and also some matrices K_i; $i = 1$ to r (where r represents the number of linear systems) and a scalar $\sigma \in [0,1]$ and 2 scalars α, γ that are solutions of the following optimization problem, then the error dynamics* (10.12) *is* ***ISS*** *stable with respect to Δ.*

$$\begin{cases} \min\limits_{P,K_i,\alpha,\gamma} (\sigma \cdot \alpha^2 + (1-\sigma)\cdot\gamma^2) \\ \begin{pmatrix} A_i^T P - C^T K_i^T + PA_i - K_i C + I & P \\ P & -\gamma^2 \cdot I \end{pmatrix} < 0 \\ P \geq I \end{cases} \tag{10.13}$$

L_i being computed as $L_i = P^{-1}K_i$ and the energy propagation from Δ to $\tilde{\mathrm{x}}$ is attenuated by $\gamma\sqrt{\frac{\lambda_{\max}(P)}{\lambda_{\min}(P)}}$. Besides the ISS property, the error satisfies the inequality:

$$\|\widetilde{\mathrm{x}}(\mathrm{t})\|_2 \leq \sqrt{\frac{\lambda_{\max}(P)}{\lambda_{\min}(P)}}\|\widetilde{\mathrm{x}}(0)\|_2 e^{-\frac{t}{2\lambda_{\max}(P)}} + \gamma\sqrt{\frac{\lambda_{\max}(P)}{\lambda_{\min}(P)}}\|\Delta(\mathrm{t})\|_\infty \tag{10.14}$$

10.4.2 Demonstration

The demonstration begins with the theorem defined in [14]:

Theorem *The estimation error is Input To State Stable if there exists a* $\beta : \Re x \Re \rightarrow \Re$ *function of type* $\mathscr{K}\mathscr{L}$ *and an* $\alpha : \Re \rightarrow \Re$ *of type* $\mathscr{K}$ (*definitions in* [15]) *so that for each input* $\|\Delta(\mathrm{t})\|_\infty < \infty$ *and each initial condition* $\|\widetilde{\mathrm{x}}(0)\|_2$ *the trajectory of the error dynamics respects* $\|\widetilde{\mathrm{x}}(\mathrm{t})\|_2 \leq \beta(\|\widetilde{\mathrm{x}}(0)\|_2, t) + \alpha(\|\Delta(\mathrm{t})\|_\infty), \forall\ \mathrm{t}$.

By considering bounded states, bounded inputs as well as bounded membership functions, then Δ is also bounded. A quadratic Lyapunov function has been chosen $V(t) = \tilde{x}^T(t)\cdot P\cdot\tilde{x}(t); P > 0$.

Applying H infinity stability in the presence of Δ as perturbation, as in [16]:

$$\dot{V}(t) < -\tilde{x}^T(t)\tilde{x}(t) + \gamma^2\Delta^T(t)\Delta(t) \tag{10.15}$$

Deriving the Lyapunov function, the next inequality arises:

$$\dot{\mathrm{V}} = \left\{\Delta + \sum_{i=1}^{8}(\mathrm{w}_i(\hat{x})\cdot(A_i - L_i\cdot C)\cdot\widetilde{\mathrm{x}})\right\}^T \cdot P\cdot\widetilde{\mathrm{x}} + \widetilde{\mathrm{x}}^T\cdot P\cdot\left\{\Delta + \sum_{i=1}^{8}(\mathrm{w}_i(\hat{x})\cdot (A_i - L_i\cdot C)\cdot\widetilde{\mathrm{x}})\right\} < -\widetilde{\mathrm{x}}^T\cdot\widetilde{\mathrm{x}} + \gamma^2\Delta^T\Delta$$

Knowing the property $\sum_{i=1}^{8}[\mathrm{w}_i(\hat{x})] = 1$ then by multiplying the terms that are not in a summation, with the above mentioned sum, the inequality is equivalent to a system of inequalities for i = 1 to r:

$$[\Delta]^T\cdot P\cdot\tilde{\mathrm{x}} + [(A_i - L_i\cdot C)\cdot\tilde{\mathrm{x}}]^T\cdot P\cdot\tilde{\mathrm{x}} + \tilde{\mathrm{x}}^T\cdot P\cdot\Delta + \tilde{\mathrm{x}}^T\cdot P\cdot(A_i - L_i\cdot C)\cdot\tilde{\mathrm{x}} + \tilde{\mathrm{x}}^T\cdot\tilde{\mathrm{x}} - \gamma^2\Delta^T\Delta < 0 \tag{10.16}$$

Using the Schur form, the wanted LMI (from (10.13)) is reached:

$$\begin{bmatrix} \tilde{\mathrm{x}}^T & \Delta^T \end{bmatrix} \begin{bmatrix} (A_i - L_i \cdot C)^T P + P(A_i - L_i \cdot C) + I & P \\ P & -\gamma^2 \cdot I \end{bmatrix} \begin{bmatrix} \tilde{\mathrm{x}} \\ \Delta \end{bmatrix} < 0 \quad (10.17)$$

Now, from $V(t) < \tilde{x}^T(t) P \tilde{x}(t); P = P^T$. It is known using S-Procedure that

$$\lambda_{\min}(P) \|\tilde{\mathrm{x}}(\mathrm{t})\|_2^2 \leq V(t) \leq \lambda_{\max}(P) \|\tilde{\mathrm{x}}(\mathrm{t})\|_2^2 \quad (10.18)$$

Therefore from (10.15) and (10.18) it derives that

$$\dot{V}(t) \leq -\frac{1}{\lambda_{\max}(P)} V(t) + \gamma^2 \|\Delta(\mathrm{t})\|_2^2 \quad (10.19)$$

Knowing the solution of a first order ODE:

$$V(t) \leq V(0) e^{\frac{-1}{\lambda_{\max}(P)} t} + \gamma^2 \int_0^t e^{\frac{-1}{\lambda_{\max}(P)}(t-s)} \|\Delta(\mathrm{s})\|_2^2 ds \quad (10.20)$$

Ending up with:

$$V(t) \leq V(0) e^{\frac{-1}{\lambda_{\max}(P)} t} + \gamma^2 \lambda_{\max}(P) \|\Delta(\mathrm{t})\|_\infty^2 \quad (10.21)$$

$$\|\tilde{\mathrm{x}}(\mathrm{t})\|_2 \leq \sqrt{\frac{\lambda_{\max}(P)}{\lambda_{\min}(P)}} \|\tilde{\mathrm{x}}(0)\|_2 e^{-\frac{1}{2\lambda_{\max}(P)} t} + \gamma \sqrt{\frac{\lambda_{\max}(P)}{\lambda_{\min}(P)}} \|\Delta(\mathrm{t})\|_2 \quad (10.22)$$

meaning that $\|\tilde{\mathrm{x}}(\mathrm{t})\|_2$ is bounded by $\gamma \sqrt{\frac{\lambda_{\max}(P)}{\lambda_{\min}(P)}} \|\Delta(\mathrm{t})\|_2$, which is the minimization objective. Also by choosing $P \geq I$ then $\lambda_{\min}(P) \geq 1$ and $\lambda_{\max}(P) < \alpha$, which can be materialized by the LMI (10.23)which gives us the first part of (10.13).

$$\begin{pmatrix} -\alpha^2 I & P \\ P & -I \end{pmatrix} \leq 0 \quad (10.23)$$

10.4.3 Results

By applying the upper observer using the stated LMI's, the observer gains are found. For these values we simulate and obtain at a varying input the following: One can see the convergence of the error (Fig. 10.5) and also that there are very small oscillations at the beginning, suggesting a positive behavior. Figure 10.6 presents the estimation of Oxygen with a different initial state from the process (Fig. 10.7).

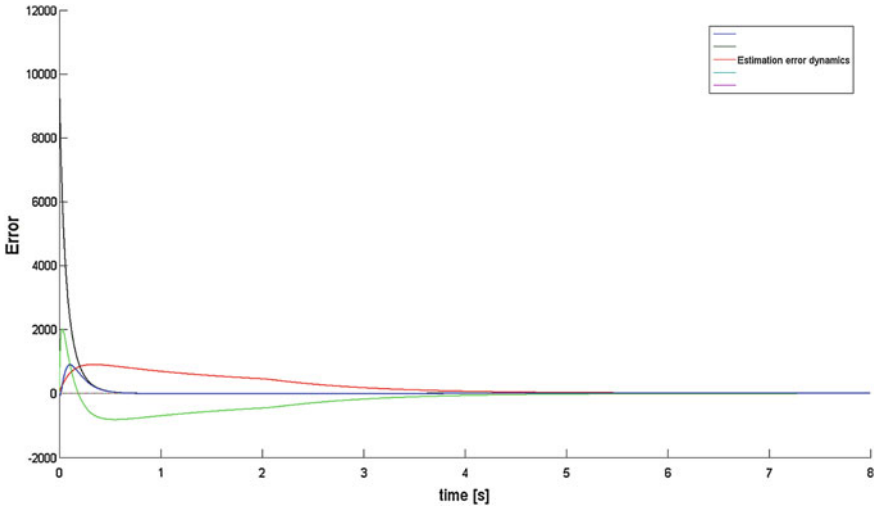

Fig. 10.5 The estimation error dynamics of the states

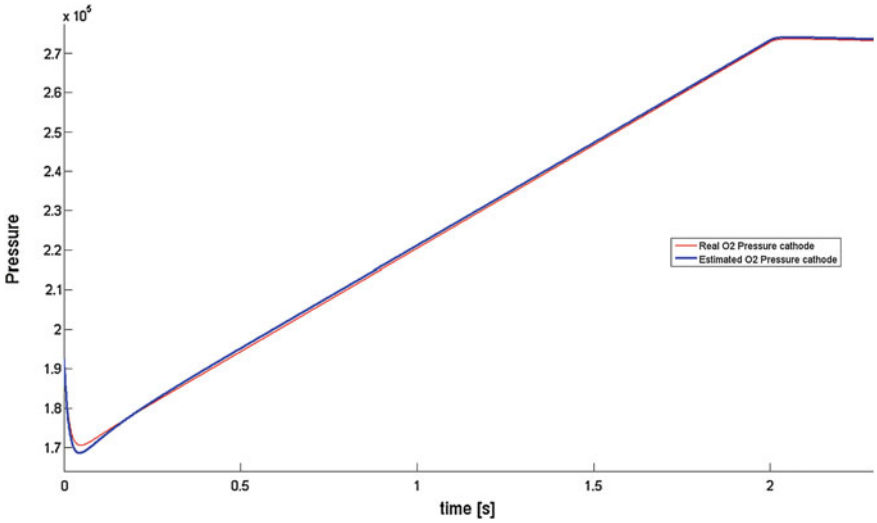

Fig. 10.6 The estimation in parallel with the real value for pressure O_2

Var		Var	Description
η_{cp}	Compressor efficiency	Ra	Gas constant (J/mol.K)
$C_{D,rm}$	Discharge coefficient nozzle		
p_{sm}	Pressure supply manifold (Pa)	R	Gas constant (J/kg.K)
p_{rm}	Pressure return manifold (Pa)	T_{atm}	Air temperature (K)
w_{cp}	Compressor speed (rad/s)	T_{rm}	Temperature return manifold(K)
I_{st}	Current in the stack (A)	$T_{cp,out}$	Air outputted temperature (K)
T_{st}	Temperature in the stack (K)	P_{atm}	Air pressure (Pa)
γ	specific heat capacity of gas	R_v	Vapor gas constant
$W_{O_2,ca,in}$	Mass flow of oxygen entering cathode[kg/s]	k_{term}	Linearization coefficient describing a valve[kg/(s*Pa)]
$W_{v,ca,gen}$	Mass flow of generated water inside the cathode	$W_{O_2,re}$	Mass flow of oxygen in cathode that reacts with the electrons and ions to form vapor
$\overline{R}$	Universal gas constant	R_{H_2}	Hydrogen gas constant
V_{ca}	Cathode volume (m^3)	C_p	Specific heat capacity of air (J/kg.K)
V_{an}	Anode volume (m^3)	F	Faraday number
V_{rm}	Return manifold volume (m^3)	M_{02}	Molar masse of Oxygen (kg/mol)
V_{sm}	Supply manifold volume (m^3)	M_{H2}	Molar masse of Hydrogen(kg/mol)
W_{cp}	Compressor mass flow (kg/s)	$k_{sm,out}$	Supply manifold outlet flow constant (kg/s.Pa)
η_{cp}	Compressor efficiency	$k_{rm,out}$	Return manifold outlet flow constant (kg/s.Pa)
τ_{cm}, τ_{cp}	Torques of motor and compressor (N.m)	$A_{T,rm}$	Return manifold nozzle area (m^2)
$W_{rm,out}$	Mass flow exiting the return manifold[kg/s]	$C_{d,an}$	Hydrogen purge nozzle discharge coefficient
$W_{ca,out}$	Mass flow exiting the cathode[kg/s]	$W_{sm,out}$	Mass flow exiting the supply manifold[kg/s]
R_{O_2}	Oxygen gas constant	M_v	Molar mass of vapor

Fig. 10.7 Parameter Significance

10.5 Conclusion

The purpose of the paper is to contribute to the development of model based techniques for PEM FC manipulation. Although the used model is simplified the aim is to arrive at an as general model as possible that includes auxiliary elements. A state

observer is developed, as many parameters in a FC are too difficult or too expensive to measure. Because of the high nonlinear aspect of the Fuel Cell dynamics, a nonlinear approach is required and a Takagi–Sugeno methodology is used. The realistic unmeasurable premise variable case is taken into account, using a method that improves the usual restriction generated by big Lipschitz constant. The approach proved more efficient in some aspects than classical methods and shows the usefulness of the ISS concept, the performance being tested in simulation.

Acknowledgments This work was supported by European funds in the framework of i-MOCCA 7-022 BE (Interregional Mobility and Competence Centres in Automation) from Interreg IVA program and the Ministry of Education and Research, France.

Appendix

Other notations employed in this paper are the following:

$$cst1 = \frac{R_v \cdot T_{st}}{V_{ca}} \; cst2 = \frac{R_{O_2} \cdot T_{st}}{V_{ca}} \; cst3 = \frac{R_a \cdot T_{st}}{V_{rm}} \; cst4 = \frac{M_v}{M_{O_2}} \; cst5 = \frac{KK_1 R_{H_2} T_{st}}{V_{an}} \; cst6 = \frac{A_{an} C_{d,an} \sqrt{\gamma} \left(\frac{2}{\gamma+1}\right)^{\frac{\gamma+1}{2\cdot(\gamma-1)}}}{\sqrt{\bar{R} \cdot T_{atm}}}$$

References

1. O.J. Murphy, G.D. Hitchens, D.J. Manko, High power density proton-exchange membrane fuel cells. J. Power Sour. **47**, 353–368 (1994)
2. A. Aitouche, S.C. Olteanu, B. Ould Bouamama, Survey and analysis of diagnosis of fuel cell stack PEM systems, in *Proceedings of 8th IFAC safe process 2012*, Mexico City, 29–31 Aug 2012
3. E.S. Kim, C.J. Kim, Nonlinear observer based control of PEM fuel cell Ssystems. Telecommun. Energy Conf. INTELEC **2009**, 1–3 (2009)
4. J. Yang, X. Li, H.G. Mou, L. Jian, Predictive control of oxide fuel cell based on an improved Takagi–Sugeno fuzzy model. J. Power Sour. **193**(2), 699–705 (2009)
5. K. Tanaka, T. Ikeda, H. Wang, Fuzzy regulators and fuzzy observers: relaxed stability conditions and LMI-based designs. IEEE Trans. Fuzzy Syst. **6**(2), 250–265 (1998)
6. I. Djemili, B. Boulkroune, A. Aitouche, V. Cocquempot, Nonlinear unknown input observer for intake leakage estimation in diesel engines, in *Proceedings of 20th Mediterranean Conference Control and Automation (MED)*, Barcelona, 4–6 July 2012, pp. 978–983
7. E. J. Herrera-Lopez, B. Castillo-Toledo, J. Ramirez-Cordova and E. C. Ferreira,in *Takagi-Sugeno Fuzzy Observer for a Switching Bioprocess: Sector Nonlinearity Approach, in New Developments in Robotics Automation and Control*, Aleksandar Lazinica ed. (2008). ISBN: 978-953-7619-20-6, InTech, doi: 10.5772/6285. Available from: http://www.intechopen.com/books/new_developments_in_robotics_automation_and_control/takagi-sugeno_fuzzy_observer_for_a_switching_bioprocess__sector_nonlinearity_approach

8. Z. Lendek, T.M. Guerra, R. Babuska, B. De Schutter, *Stability Analysis and Nonlinear Observer Design using Takagi–Sugeno Fuzzy Models (Studies in Fuzziness and Soft Computing)* (Springer, Berlin, 2011)
9. D. Ichalal, B. Marx, J. Ragot, D. Maquin, State estimation of Takagi-Sugeno systems with unmeasurable premise variables. IET Control Theory Appl. **4**(5), 897–908 (2010)
10. D. Ichalal, B. Marx, J. Ragot, D. Maquin, Advances in observer design for Takagi–Sugeno systems with unmeasurable premise variables, in *Proceedings of 20th Mediterranean Conference on Control and Automation (MED)*, Barcelona, 3–6 July 2012, pp. 848–853
11. Z. Yacine, D. Ichalal, N. Ait Oufroukh, S. Djennoune, Nonlinear vehicle lateral dynamics estimation with unmeasurable premise variable Takagi–Sugeno approach, in *Proceedings of 20th Mediterranean Conference on Control and Automation (MED)*, Barcelona, 3–6 July 2012, pp. 1117–1122
12. J.T. Pukrushpan, A.G. Stefanopoulou, *Control of Fuel Cell Power Systems, AIC (Advances in Industrial Control)* (Springer, London, 2006)
13. A. Akhenak, M. Chadli, J. Ragot, D. Maquin, Design of sliding mode unknown input observer for uncertain Takagi–Sugeno model, in *Proceedings of 15th Mediterranean Conference on Control and Automation, MED'07*, Athens, 27–29 June 2007, pp. 1–6
14. H. Su, L. Xu, H. Zhu, Y. Wu, L. Yang, S. Liao, H. Song, Z. Liang, V. Birss, Self-humidification of a PEM fuel cell using a novel $Pt/SiO_2/C$ anode catalyst. Int. J. Hydrogen Energy **35**(15), 7874–7880 (2010)
15. E.D. Sontag, On the input-to-state stability property. J. Syst. Control Lett. **24**, 351–359 (1995)
16. H.A. Zemouche, M. Boutayeb, Sobolev norms-based state estimation and input recovery for a class of nonlinear systems: design and experimental results. IEEE Trans. Sign. Process. **57**(3), 1021–1029 (2009)

Chapter 11
Maximum Power Control for Photovoltaic System Using Two Strategies

N. Harrabi, E. Kamal, A. Aitouche and M. Souissi

Abstract This paper presents fuzzy control method (Mamdani's fuzzy inference method) for maximum power point tracking (MPPT) of photovoltaic (PV) system under varying irradiation and temperature conditions. The fuzzy control method has been compared with perturb and observe (P&O) method as one of the most widely conventional method used in this area. The different techniques have been analyzed and simulated. Fuzzy technique gives better and more reliable control for this application.

Keywords Photovoltaic · Perturb and observ · Fuzzy control · MPPT

11.1 Introduction

Nonlinear control has emerged as a research area of rapidly increasing activity. Especially, the theory of explicitly linearizing the input–output response of nonlinear systems to linear systems using state feedback has received great attention [1]. There are several approaches to control nonlinear systems. A typical approach is the feedback stabilization of nonlinear systems where a linear feedback control is designed for the linearization of the system around a nominal operating point. This approach, however, generally renders only local results. Other approaches [2] such as feedback linearization are rather involved and tend to result in rather complex controllers.

Renewable energy is currently widely used. One of these resources is solar energy. The photovoltaic (PV) array normally uses a Maximum Power Point

N. Harrabi (✉) · E. Kamal · A. Aitouche · M. Souissi
ENIS, Graduate School of Engineering in Sfax, Sfax, Tunisia
e-mail: nozha.harrabi@gmail.com

M. O. Hamdan et al. (eds.), *ICREGA'14 - Renewable Energy: Generation and Applications*, Springer Proceedings in Energy, DOI: 10.1007/978-3-319-05708-8_11,

Tracking (MPPT) technique to continuously deliver the highest power to the load when there are variations in irradiation and temperature [3].

Fuzzy logic or fuzzy set theory is a new method of controlling the MPPT which is implemented in order to obtain the peak power point. It has the advantage of being robust and fast in response. Fuzzy controller operates in two basic modes coarse and fine modes. The proposed fuzzy operating strategy is to coordinate the two control modes and determine the reference values of the fuzzy control so that all constraints are satisfied. This operating strategy will minimize the number of operating mode changes, improve performances of the system operation, and enhance system stability [4].

The hill climbing algorithm is widely used in practical PV systems because of its simplicity and it does not require prior study or modeling of the source characteristics and can account for characteristics' drift resulting from ageing, shadowing, or other operating irregularities [5, 6].

The basic hill climbing algorithm is the P&O algorithm. Although the P&O (Perturb and Observe) algorithm works well when the irradiance changes slowly, it exhibits erratic behavior for rapidly changing irradiance level that causes incorrect or slow power tracking. This led to the development of the Modified Perturb and Observe (MP&O) algorithm [7]. The MP&O algorithm improves the P&O algorithm at the expense of speed of response to changes of irradiance. A new method, named the Estimate-Perturb-Perturb (EPP) algorithm was previously published by the authors, which was shown to have good performances [8]. Many other MPPT techniques have been proposed. However, Constant Voltage (CV) [9], Incremental Conductance (IC), IC and CV combined [9], Short Current Pulse [10], Open Circuit Voltage [11], the Temperature Method [12] and methods derived from it [12]. These techniques are easily implemented and have been widely adopted for low-cost applications.

One of the most widely used techniques in MPPT is P&O due to its simple and easily implementation. In this paper, intelligent control technique using fuzzy logic control is associated to MPPT controller in order to improve energy conversion efficiency and compared with P&O method. Simulation and analysis of P&O and fuzzy logic control are presented.

This paper is organized as follows. In Sect. 11.2, PV model system is developed. Operation principle of the proposed MPPT control method is presented in Sect. 11.3. MPPT control method is given in Sect. 11.4. Numerical simulations are carried out in Sect. 11.5 to show the control performances.

11.2 PV Model System

To show the effectiveness of the proposed controller design techniques, PV Model System [13–15] are simulated.

11.2.1 PV Electric Characteristics

The current–voltage characteristic of a PV array conducts as a function of solar irradiance and cell temperature is described as follows [13]:

$$i_{pv} = n_p I_{ph} - n_p I_{rs}(\exp(q_p v_{pv}/n_s \varphi KT) - 1) \tag{11.1}$$

where n_p and n_s are the number of the parallel and series cells, respectively, K is the Boltzmann's constant, T is the cell temperature, φ is the p–n junction characteristic, q_p is the electron charge, i_{pv} and v_{pv} are the output current and the PV array voltage on the capacitance C_{pv}, I_{ph} and I_{rs} are the photocurrent and reverse saturation current, respectively and are given by

$$I_{ph} = (I_{sc} + K_I(T - Tr))\frac{\lambda}{100} \tag{11.2}$$

$$I_{rs} = I_{or}\left(\frac{T}{T_r}\right)^3 \exp(q_p E_{gp}(1/T_r - 1/T)/KT) \tag{11.3}$$

where I_{sc} is the short-circuit cell current at reference temperature and insolation and I_{or} is the reverse saturation current at the reference temperature T_r, E_{gp} is the semiconductor band-gap energy, K_I is the short-circuit current temperature coefficient and λ is the insolation in mW/cm^2. The power generation of the PV array [13]:

$$P_{pv} = i_{pv} v_{pv} = n_p I_{ph} v_{pv} - n_p I_{rs} v_{pv}(\exp(q_p v_{pv}/n_s \varphi KT) - 1) \tag{11.4}$$

11.2.2 PV Modeling

In order to adapt the array photovoltaic to a large voltage range, the PV MPPT system adopts Boost DC–DC converter topology as shown in Fig. 11.1 [13]. The sate equation and output equation can be expressed by the following [13–15]:

$$\begin{cases} \frac{dv_{pv}}{dt} = \frac{1}{C_1}(i_{pv} - i_{L_c}) \\ \frac{di_{L_c}}{dt} = \frac{1}{L_c}[v_{pv} - v_{C_2}(1 - D)] \\ \frac{dv_{C_2}}{dt} = \frac{1}{C_2}\left[i_{L_c}(1 - D) - \frac{v_{C_2}}{R_L}\right] \end{cases} \tag{11.5}$$

where i_{L_c} is the current across the inductor L_c, v_{C_2} is the voltage in the capacitor C_2, D is the duty ratio of the PWM signal to control the switching MOSFET, $D \in \{0, 1\}$ defines the switch position and supposed that the parameters R_L, L_c, C_1 and C_2 are supposed to be known constants.

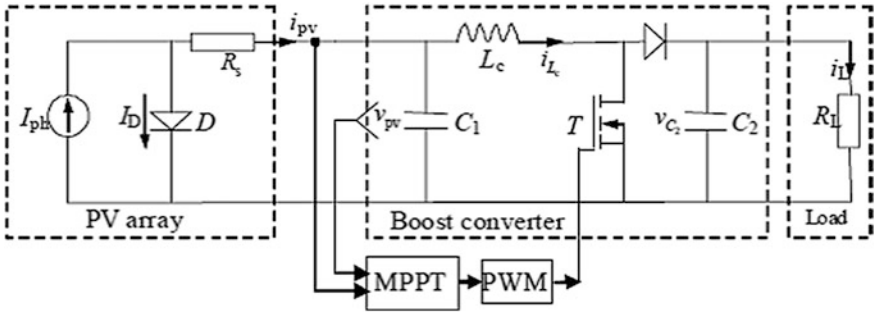

Fig. 11.1 PV power control system using a Boost DC–DC converter

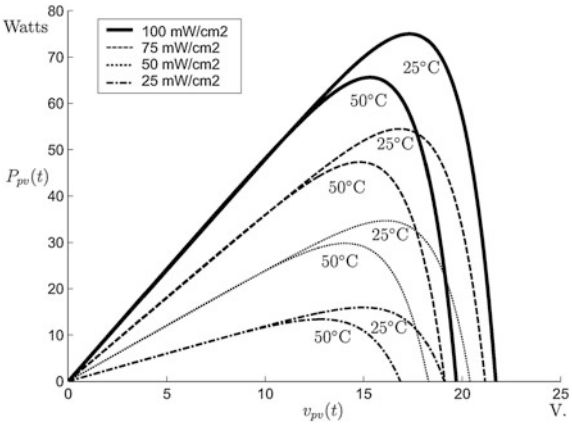

Fig. 11.2 Characteristics of the array power with respect to the PV voltage

When a boost converter is used in PV applications, the input voltage changes continuously with the atmospheric conditions. Therefore, the duty cycle should change to track the MPP of photovoltaic array. The relationship of P_{pv} versus v_{pv}, for different values of the insolation and temperature is shown in Fig. 11.2 [16, 17].

11.3 Operation Principle of the Proposed MPPT Control Method

The maximum power point satisfies the condition $dP_{pv}/dv_p = 0$. However, due to the high nonlinearity, the maximum power point is difficult to be solved from (11.4). This is the reason why the MPPT cannot be achieved easily [13]. At the maximum power point, we have:

$$\frac{dP_{pv}}{dv_{pv}} = 0 \Rightarrow i_{pv} + v_{pv}\frac{di_{pv}}{dv_{pv}} = 0 \tag{11.6}$$

Rearranging Eq. (11.6) gives:

$$-\frac{i_{pv}}{v_{pv}} = \frac{di_{pv}}{dv_{pv}} \tag{11.7}$$

The changes in PV's voltage may be done by coupling a DC/DC converter to PV and controlling properly its duty cycle. Neglecting losses the output voltage of the boost converter is given by the equation

$$V_o = \frac{1}{1-D}v_{pv} \tag{11.8}$$

where D is the fraction of time that the switch is closed. The fuzzy logic controller is constructed with the fuzzy rule and controller structure as in next section.

11.4 MPPT Controller

MPPT is essentially a real time process to search for the operating point which gives the maximum available power that can be extracted from the PV array at any insolation level. Two MPPT techniques will be presented and simulated.

11.4.1 Perturb and Observe MPPT Technique

The problem considered by MPPT methods is to automatically find the voltage VMPP or current IMPP at which a PV array delivers maximum power under a given temperature and irradiance. In P&O method, the MPPT algorithm is based on the calculation of the PV output power and the power changes by sampling both the PV Array current and voltage. The tracker operates by periodically incrementing or decrementing the solar array voltage [18]. If a given perturbation leads to an increase (decrease) in the output power of the PV, then the subsequent perturbation is generated in the same (opposite) direction. The duty cycle of the dc chopper is varied and the process is repeated until the maximum power point has been reached. Actually, the system oscillates about the MPP. Reducing the perturbation step size can minimize the oscillation. However, small step size slows down the MPPT. For different values of irradiance and cell temperatures, the PV array would exhibit different characteristic curves. Each curve has its maximum power point. It is at this point, where the corresponding maximum voltage is supplied to the converter. The flow chart of algorithm has four cases as shown in Fig. 11.3.

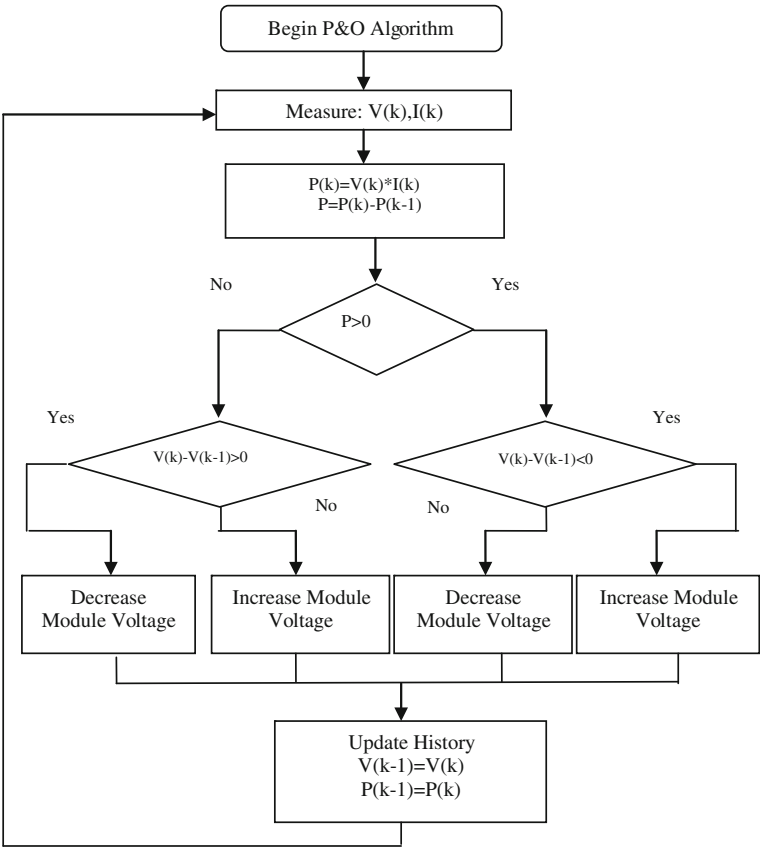

Fig. 11.3 Flowchart of P&O MPPT technique

11.4.2 Mamdani's Fuzzy Inference Method

The nonlinear nature of the PV system is visible in the curves of power and current from the photovoltaic generator in dependence on the voltage at its terminals. In addition, the maximum power operating point varies with insolation level and temperature. Therefore, the tracking control of the MPP is a complicated problem. To overcome these problems, tracking control system has been proposed by Fuzzy Logic Controller (FLC).

FLC requires the expert knowledge of the process operation for the FLC parameter setting, and the controller can be only as good as the expertise involved in the design. Fuzzy logic has the advantages [19] to face the imprecise and uncertainty, and this kind of fuzzy logic control can be easily made by digital microcontroller unit. It contains three units as: (i) fuzzification, (ii) fuzzy rules, and (iii) defuzzification. The voltage and current values are scaled and normalized and

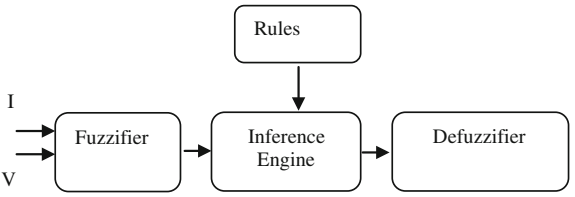

Fig. 11.4 General diagram of a fuzzy controller

through the membership functions. Membership function values are assigned to the linguistic variables, using five fuzzy subsets: NB (negative big), NS (negative small), ZE (zero), PS (positive small), and PB (positive big). The fuzzy control implemented here uses triangular membership functions. Rule base of fuzzy logic controller shown in Fig. 11.4. The sudden change in atmospheric conditions shifts the maximum power point abruptly which is tracked accurately by this controller [19, 20]. The peak power is obtained from the PV module. If implemented, this method can increase the efficiency of the PV system by quite a large scale. Since the proposed approach requires only the measurement of PV array output power and not the measurement of solar irradiation level and temperature, it decreases the number and cost of equipment as well as the design complexity.

11.4.2.1 Fuzzification

The fuzzification is the process of converting the system actual inputs values I and V into linguistic fuzzy sets using fuzzy membership function. These variables are expressed in terms of five linguistic variables (such as ZE (zero), PB (positive big), PS (positive small), NB (negative big), NS (negative small)) using basic fuzzy subsets as shown in Fig. 11.5.

11.4.2.2 Fuzzy Rules

For the expression of fuzzy rules, the syntax "if-then" is always used. For the maximum power point tracking we use 25 rules. Here, partial rules are given as follows:

$$\begin{aligned} &\text{If } V_{pv} \text{ is NB and } I_{pv} \text{ is NB, then D is NB} \\ &\text{If } V_{pv} \text{ is NB and } I_{pv} \text{ is NS, then D is NS} \\ &\text{If } V_{pv} \text{ is NB and } I_{pv} \text{ isZE, then D is ZE} \end{aligned} \tag{11.9}$$

With the same manner we can deduce the fuzzy rules. The fuzzy rule algorithm includes 25 fuzzy control rules listed in Table 11.1.

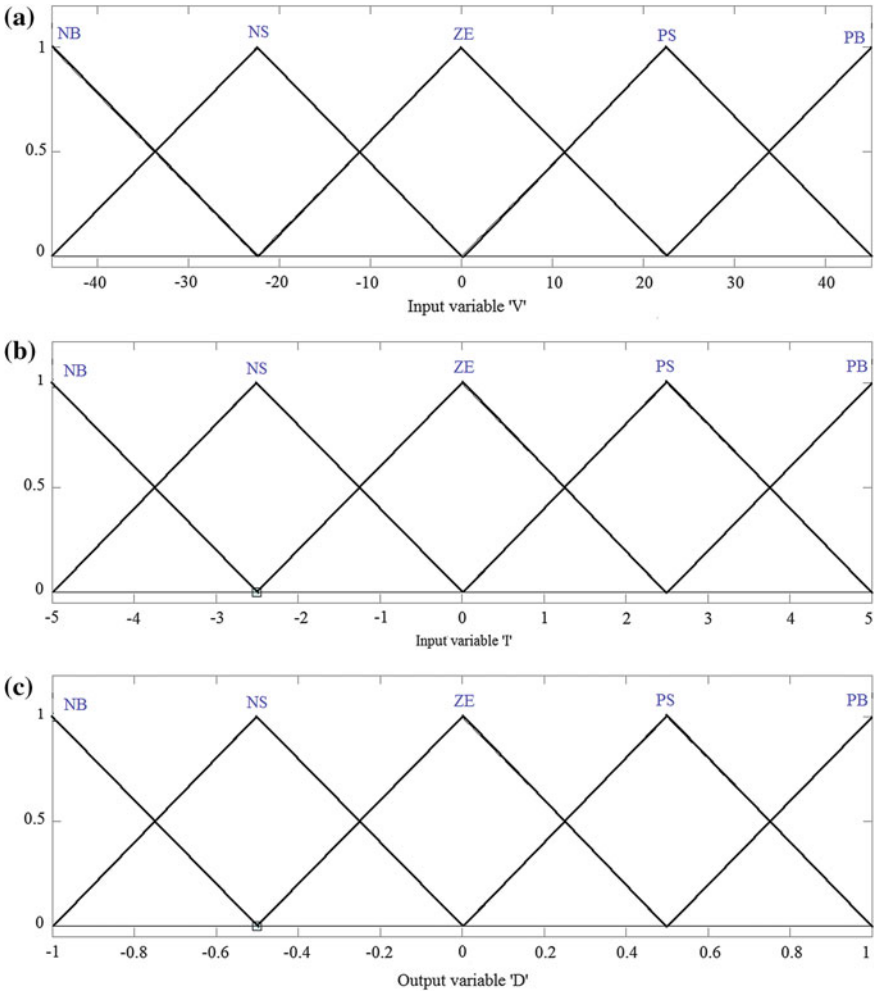

Fig. 11.5 Membership function **a** input voltage, **b** input current, **c** duty cycle

11.4.2.3 Defuzzification

The last step in the fuzzy inference is defuzzification which allows the aggregation of the D from all rules. The duty cycles from 25 rules must be computed for a specified value.

We adopt the popular defuzzification method which is center of area as:

$$d = \frac{\sum_1^{25} D_j(w_j) \cdot w_j}{\sum_1^{25} D_j(w_j)} \tag{11.10}$$

where D_j the duty cycle value for the j-th rule, and w_j is the weighted factor of the j-th rule.

Table 11.1 FLC rules base

I	V				
	NB	NS	ZE	PS	PB
NB	NB	NS	NS	ZE	ZE
NS	NS	NS	ZE	ZE	PS
ZE	ZE	ZE	PS	PS	PS
PS	ZE	PS	PS	PS	PB
PB	PS	PS	PS	PB	PB

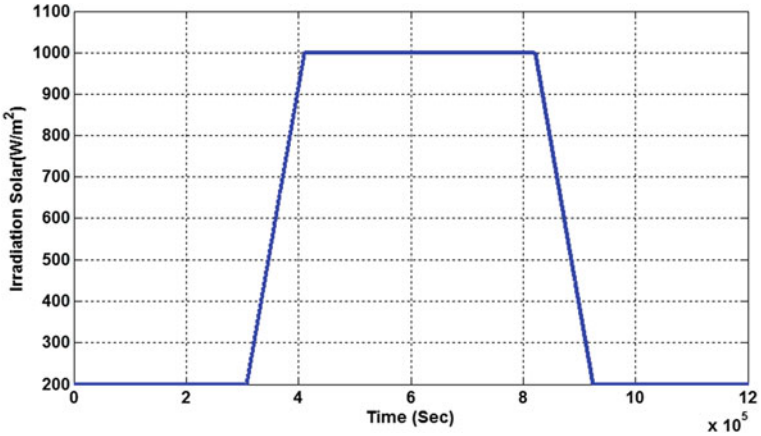

Fig. 11.6 Irradiation solar (W/m^2) at constant temperature

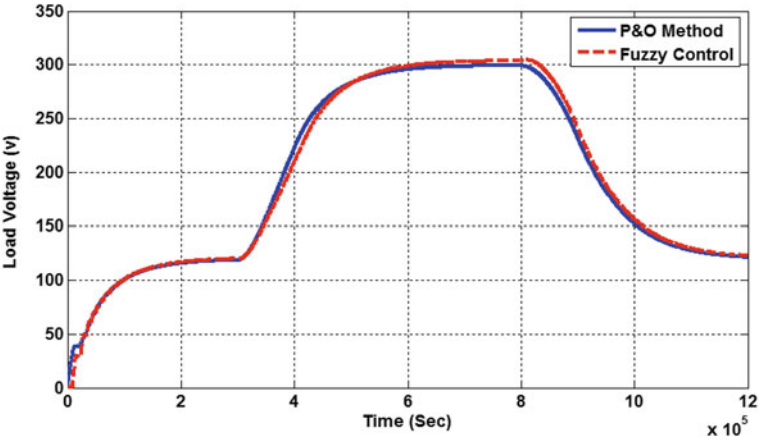

Fig. 11.7 PV array output voltage (V)

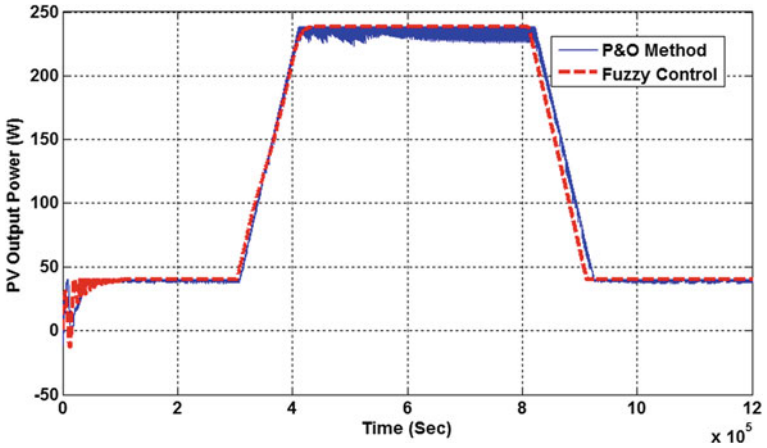

Fig. 11.8 PV array output power (W)

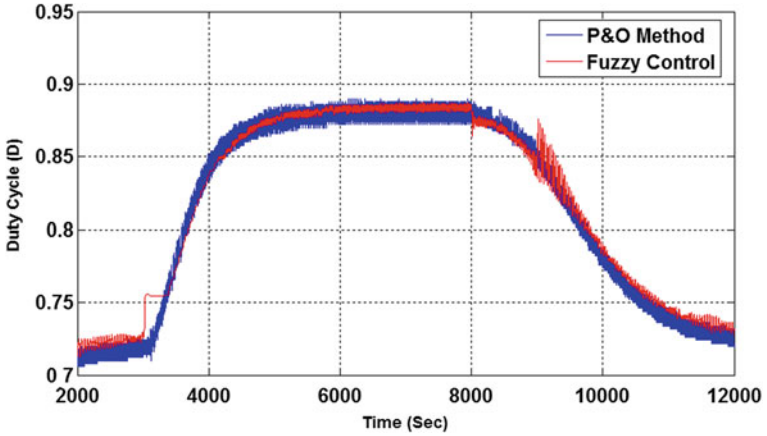

Fig. 11.9 The duty cycle of the switching

11.5 Simulation and Results

An extensive simulation for both techniques has been done using MATLAB. Some selected results are presented with a comparison between fuzzy and P&O MPPT controllers. The following simulation was presented for different insolation levels from 200 to 1,000 W/m^2 at fixed temperature of 298 K as shown in Fig. 11.6. The Figs. 11.7, 11.8 and 11.9 show the result when using fuzzy and P&O as MPPT controller. Figure 11.7 shows the simulation results of PV operating voltage at maximum power point at varying irradiation and constant temperature which is being tracked by fuzzy and P&O controllers. Figure 11.8 shows the output power

of PV at varying irradiation and constant temperature for both controllers. The duty cycle of the switching for the two controllers is shown in Fig. 11.9.

The Fig. 11.8 shows the output power of PV at varying insolation level and fixed temperature for both controllers. As shown fuzzy controller shows smother power signal line, less oscillating and better stable operating point than P&O. From the simulation results, it can be deduced that the fuzzy controller has better performances than P&O, and it has more accuracy for operating at MPP.

11.6 Conclusion

This paper presented a mathematical model for PV. It also included MPPT at varying irradiation and temperature conditions. P&O and fuzzy logic controller have been designed and simulated for the proposed PV system, Comparison for simulation results have been presented for different irradiation conditions. Fuzzy controller showed better performance with lower oscillations. The future work will focus on the nonlinear control based on Takagi–Sugeno models.

References

1. A. Isidori, *Nonlinear Control System* (Springer, New York, 1989)
2. J.J.E. Slotine, W. Li, *Applied Nonlinear Control* (Prentice-Hall, Englewood Cliffs, 1991)
3. T. Bocklisch, W. Schufft, S. Bocklisch, Predictive and optimizing energy management of photovoltaic fuel cell hybrid systems with short time energy storage, in *Proceedings of 4th European Conference on PV-Hybrid and Mini-grid*, pp. 8–15 (2008)
4. P.P. Kumar, B.K. Babu, Power-management strategies for a grid-connected PV-FC hybrid system by using fuzzy logic controller. Int. J. Mod. Eng. Res. **2**(2), 358–364 (2012)
5. H. Al-Atrash, I. Batarseh, K. Rustom, Statistical modeling of DSP-based hill-climbing MPPT algorithms in noisy environments, in *IEEE Applied Power Electronics Conference and Exposition (APEC)*, pp. 1773–1777 (2005)
6. C. Hua, J. Lin, C. Shen, Implementation of a DSP-controlled photovoltaic system with peak power tracking. IEEE Trans. Industr. Electron. **45**(1), 99–107 (1998)
7. D.P. Hohm, M.E. Ropp, Comparative study of maximum power point tracking algorithms. Prog. Photovoltaics Res. Appl. **11**(1), 47–62 (2003)
8. C. Liu, B. Wu, R. Cheung, Advanced algorithm for MPPT control of photovoltaic systems, in *1st Canadian Solar Buildings Research Network Conference, Montreal, Quebec,* 20–24 Aug 2006
9. K.H. Hussein, I. Muta, T. Hoshino, M. Osakada, Maximum photovoltaic power tracking: an algorithm for rapidly changing atmospheric condition, Proc. Inst. Electr. Eng. Gen. Transmiss. Distrib. **142**(1), 59–64 (1995)
10. G.J. Yu, Y.S. Jung, J.Y. Choi, I. Choy, J.H. Song, G.S. Kim, A novel two-mode MPPT control algorithm based on comparative study of existing algorithms. Sol. Energy **76**(4), 455–463 (2004)
11. T. Noguchi, S. Togashi, R. Nakamoto, Short-current pulse-based maximum power point tracking method for multiple photovoltaic and converter module system. IEEE Trans. Ind. Electron. **49**(1), 217–223 (2002)

12. D.Y. Lee, H.J. Noh, D.S. Hyun, I. Choy, An improved MPPT converter using current compensation method for small scaled PV-applications, in *Proceedings of APEC*, pp. 540–545 (2003)
13. M. Park, I.K. Yu, A study on optimal voltage for MPPT obtained by surface temperature of solar cell, in *Proceedings of IECON*, pp. 2040–2045 (2004)
14. C. Hua, C. Shen, Study of maximum power tracking techniques and control of DC/DC converters for photovoltaic power system, in *9th Annual IEEE Power Electronics Specialists Conference*, pp. 86–93 (1998)
15. I.S. Kim, M.B. Kim, M.J. Youn, New maximum power point tracker using sliding-mode observer for estimation of solar array current in the grid-connected photovoltaic system. IEEE Trans. Ind. Electron. **53**(4), 1027–1035 (2006)
16. J.A. Jianget, Maximum power tracking for photovoltaic power systems. Tamkang J. Sci. Eng. **8**(2), 147–153 (2005)
17. R.D. Middlebrook, S. Cuk, A general unified approach to modelling switching-converter power stages, in *IEEE PESC'76 Rec., Cleveland*, 8–10 June 1976, pp. 18–34
18. E. Kamal, A. Aitouche, Design of maximum power fuzzy controller for PV systems based on the LMI-based stability Intelligent Systems in Technical and Medical Diagnostics. Adv. Int. Syst. Comput. **230**, 77–88 (2013)
19. V. Salas, E. Olias, A. Barrado, A. Lazaro, Review of the maximum power point tracking algorithms for stand-alone photovoltaic systems. Sol. Energy Mater. Sol. Cells **90**(11), 1555–1578 (2006)
20. K. Kiruthika, J.P. Koujalagi, Fuzzy logic based maximum power point tracker in photovoltaic cell, Int. J. Sci. Res. **2**(8), 313–317 (2013)

Chapter 12
Maximum Power Point Tracking (MPPT) of Stand-Alone Photovoltaic Systems Based on Synergetic Control

A. Gaid and M. Bettayeb

Abstract This paper proposes a nonlinear control of maximum power point tracking (MPPT) of stand-alone photovoltaic systems (PV) based on synergetic control technique (SCT). This technique has controllable dynamics towards the origin and no chattering compared to sliding mode control (SMC). Mathematical model is presented and performance comparison to SMC is tested under different environmental conditions and step load.

12.1 Introduction

Due to decline of fossil fuels, more need for electricity, global warming, oil high prices and the world finite storage of petroleum products, it is necessary to think of other alternative energy supplies that can replace the old traditional energy resources in the near future. Green energy, such as solar panels and fuel cells, could be possible future main sources of electrical power. These sources are unlimited. Sustainable, and clean. Solar cells are having growing contributions in the supply of electrical power in many parts of the world. This would only happen when solar panels come to competitive level with fossil energy supplies in terms of kilowatt-hours and efficiency. In order to improve solar modules efficiency, a physical model and simulation should be studied to be able to understand photovoltaic PV systems and characteristics. Based on this modeling, maximum power point tracking MPPT techniques could be developed to ensure maximum efficiency and power transfer to the load. On one hand, solar modules should be capable of capturing the maximum sun light that they are exposed to and converting it to electricity with high efficiency. On the other hand, it is important to

A. Gaid (✉) · M. Bettayeb
University of Sharjah, Sharjah, United Arab Emirates
e-mail: afaf.melika@hct.ac.ae

M. O. Hamdan et al. (eds.), *ICREGA'14 - Renewable Energy: Generation and Applications*, Springer Proceedings in Energy, DOI: 10.1007/978-3-319-05708-8_12,

track the maximum power point on PV current–voltage curves under dynamic environmental changes and load variations as well.

There is a wide range of techniques used for MPP tracking in the literature. Some of these algorithms are famous, simple, and easy to implement. However, these methods have some disadvantages. For example, perturb and observe P&O algorithm fails to track the MPP in case of rapid environmental changes, and incremental conductance IC oscillates around the MPP [1–3]. Some techniques use look up tables, consequently more memory space is required, like the analytical solution for tracking photovoltaic module MPP used in [4]. Moreover, the traditional linear control MPPT methodologies use small signal model to derive the necessary equations of the DC–DC converter to help design linear control systems.

Sliding mode control SMC [5–13] and synergetic control technique SCT are good candidates of nonlinear control techniques. SMC and SCT offer new way of control design that utilizes the nonlinear variable structure of the DC–DC converter system.

This work employs the synergetic control (SC) approach to track the MPP of PV systems using boost converter as MPPT system. Its performance is compared to sliding mode control in terms of robustness to load variations, and parameters changes [6]. This technique has common features with SMC like order reduction and decoupling control design. But SC has several other advantages over SMC. Firstly, it overcomes the problem of chattering in SMC. Secondly, it has a controlled path towards the origin which makes it suitable for digital implementation. But SC adds more calculations to the control input and use model parameters. Therefore SC will be more sensitive to model parameters variations and uncertainties.

The rest of this paper is organized as follows: In Sect. 12.2, a model of the PV module is presented. Section 12.3 discusses small signal model of the MPPT system DC–DC boost converter. Section 12.4 presents the proposed nonlinear closed loop synergetic control technique SCT. A simulation result of SCT and SMC is introduced in Sect. 12.5 for comparison purposes followed by a conclusion in Sect. 12.6.

12.2 PV Equivalent Circuit Model and Characteristics

12.2.1 Modeling Using Single Diode with Ohmic Losses

Single diode with ohmic losses model [14] is widely used to represent the electrical characteristics of the photovoltaic PV system for its simple analysis as well as accuracy. This model consists of a current source which is directly controlled by sun light, diode to represent the PN junction of the solar module, and PV contact/material resistivity losses are presented using series or series and parallel resistors as illustrated in Fig. 12.1. The cell terminal current can be defined as a function of the cell voltage.

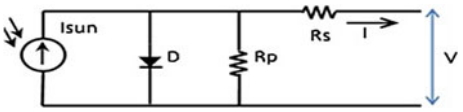

Fig. 12.1 Equivalent circuit diagram of the solar cell

$$I = I_{sun} - I_o\left(e^{q\left(\frac{V+IR_s}{aKT}\right)} - 1\right) - \frac{V + IR_s}{R_p} \tag{12.1}$$

$$I_{sun} = \left(I_{sun-ref} + K_i \Delta T\right)\frac{G}{G_{stc}} \tag{12.2}$$

Where $I_{sun\text{-}ref}$ is I_{sun} at standard testing condition (STC) ($T = 25\ ^\circ C$, $G = 1,000\ W/m^2$)

I_{sun} Current due to sunlight is proportional to solar irradiation;
I_o Diode reverse saturation current;
R_p Parallel resistance represents material losses;
R_s Series resistance represents contacts losses;
V Cell terminal voltage;
q Electron charge (1.6×10^{-19} C);
k Boltzmann's constant (1.38×10^{-23} J/K);
a Ideality factor;
G Irradiance level;
G_{stc} Irradiance level at STC;
T Temperature in Kelvin;
K_i Short circuit current coefficient;

12.2.2 PV Characteristics

The PV module consists of 35 series cells with ideal shunt resistor of infinity for simplicity. Matlab simulation in Figs. 12.2 and 12.3 show the power–voltage and current–voltage curves of photovoltaic KC85T module. The parameters are: module current at MPP $I_{mp} = 5.02$ A, module voltage at MPP $V_{mp} = 17.4$ V, short-circuit current $I_{sc} = 5.34$ A, and open-circuit voltage $V_{oc} = 21.7$ V at standard testing condition STC. The PV module parameters are listed in Table 12.1.

It is clear that the PV module inherits nonlinear characteristics at its MPP. MPP locus changes upon changes in illumination and temperature. To optimize energy transfer from the solar module to the load, in other words, to obtain maximum efficiency, the system should be forced to work at its MPP. This could be adjusted using power electronics converters [8]. Some important points, extracted from

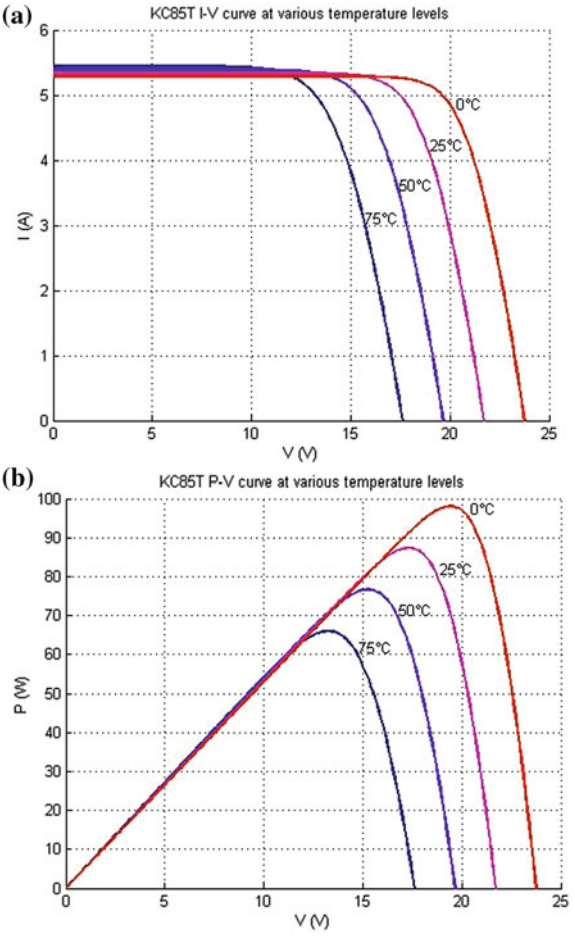

Fig. 12.2 KC85T module **a** I–V **b** P–V curves at different temperatures

Figs. 12.2 and 12.3 are listed in Tables 12.2 and 12.3 to mark the electrical performance of KC85T at different temperatures and irradiance values.

12.3 MPPT System: DC–DC Boost Converter

SC is mainly an analytical design that uses macro variables called attractors, and the nonlinear variable structure of DC/DC converters. Figure 12.4 shows the DC–DC boost converter as an example of MPPT system control structure. Boost converter is a variable structure system that could be illustrated in two sets of equations depending on the position of the switch as per the time average model of the DC–DC boost converter as follows [15, 16]:

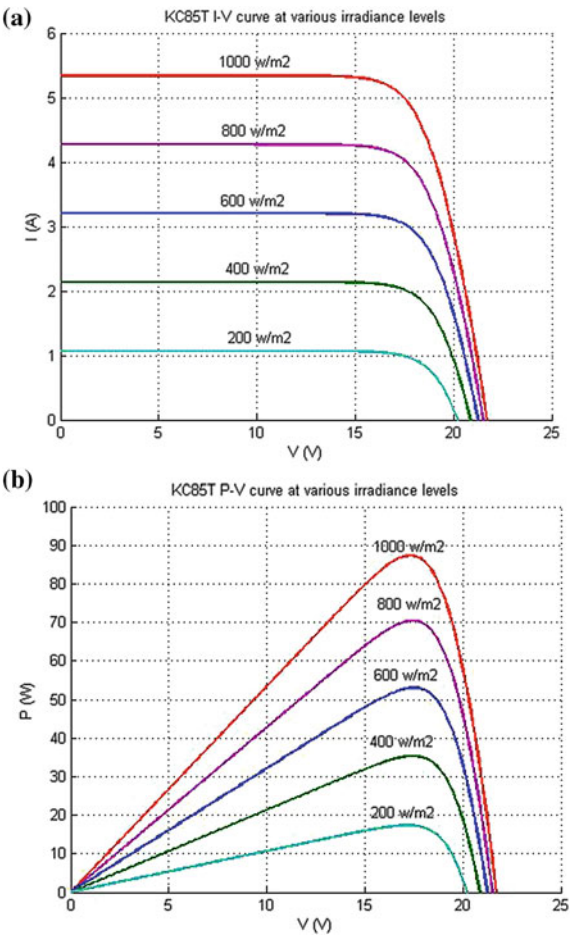

Fig. 12.3 KC85T module **a** I–V **b** P–V curves at different irradiance values at 25 °C

Table 12.1 Photovoltaic (PV) parameters

Parameter	Value	Parameter	Value
$I_{sc\text{-}ref}$	5.34 A	K_i	$2.12e^{-3}$
V_{oc}	21.7 V	N_s	36
I_{mpp}	5.02 V	K	$1.3806503e^{-23}$ J/K
V_{mpp}	17.4 V	Q	$1.60217646e^{-19}$ C
K_v	$-8.21e^{-2}$	a	1.1

$$\dot{i}_L = \frac{V}{L} - \frac{V_O}{L}(1-D), \dot{V}_O = \frac{i_L}{C}(1-D) + \frac{V_O}{RC} \tag{12.3}$$

Where x the system is state vector of size $n = 2$, and D is the manipulated control input of size $m = 1$, and t is time.

Table 12.2 Electrical performance of KC85T at G = 1,000 W/m^2 obtained from Fig. 12.2

Temperature	0 °C	25°C	50°C	75°C
P_{mpp}	97.986 W	87.31 W	76.68 W	65.964 W
I_{mpp}	5.045 A	5.04 A	5.002 A	4.995 A
V_{mpp}	19.4 V	17.3 V	15.3 V	13.2 V

Table 12.3 Electrical performance Of KC85T at T = 25 °C obtained from Fig. 12.3

Irradiance	1,000 W /m^2	800 W/m^2	600 W/m^2	400 W/m^2	200 W/m^2
P_{mpp}	87.31 W	70.4 W	53.03 W	35.29 W	17.34 W
I_{mpp}	5.04 A	4.05 A	4.02 A	2.028 A	1.05 A
V_{mpp}	17.3 V	17.4 V	17.5 V	17.41 V	17.1 V

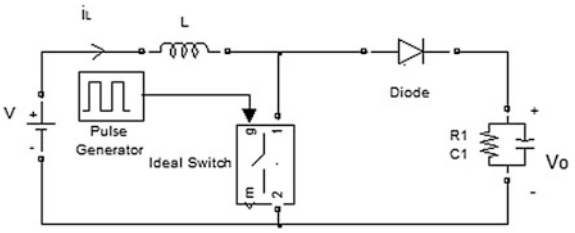

Fig. 12.4 Boost converter illustrative diagram

12.4 Synergetic Control SC for MPPT

This section introduces the design of synergetic controller for MPPT. A block diagram of the system includes a solar module, DC–DC boost converter assuming a lossless DC–DC converter, control system, and pulse width modulation is depicted in Fig. 12.5.

The main steps of SC are as follows [15–19]:

Define an attractor $\sigma(x)$ or more as a function of state variables and the controller objective is to force the system to work on the surface $\sigma = 0$.

Dynamical system evolution with attractors at $\sigma = 0$ to be created as follows:

$$\tau\dot{\sigma} + \sigma = 0, \qquad \tau > 0 \tag{12.4}$$

Where τ is a vector of size m that controls the convergence speed to the desired surface σ. The order of the system on the specified manifold is n-m. Let us introduce the following macro variable (surface).

$$\sigma = \frac{\partial P}{\partial I_L} = \frac{\partial (I_L V)}{I_L} = I_L \frac{\partial V}{\partial I_L} + V \tag{12.5}$$

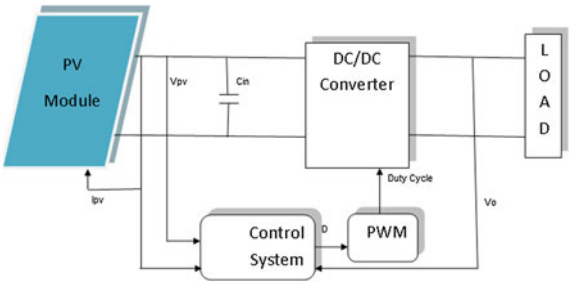

Fig. 12.5 MPPT system using SC block diagram

This surface has been chosen to track the MPP of the PV module based on sliding mode control [6]. Where P is the PV power, I_L is the inductor current state 1, and V is the PV voltage state 2. The selected system states are continuous, physical, and measurable to meet stability conditions. Considering the chain rule of differentiation.

$$\dot{\sigma} = \frac{d\sigma}{dx}\dot{x} \tag{12.6}$$

In boost converter, there are two states x_1, and x_2, inductor current I_L and output voltage V_O. Thus

$$\dot{\sigma} = \frac{d\sigma}{dx}\dot{x} = \frac{d\sigma}{dx_1}\dot{x}_1 + \frac{d\sigma}{dx_2}\dot{x}_2 \tag{12.7}$$

As σ is a function of x_1 only, that is, the inductor current I_L, in this case, then Eq. (12.7) becomes

$$\dot{\sigma} = \frac{d\sigma}{dx_1}\dot{x}_1 \tag{12.8}$$

Substitute from Eqs. (12.3), (12.4) and (12.5) in (12.8)

$$\dot{\sigma} = \left[I_L \frac{\partial^2 V}{\partial I_L^2} + 2\frac{\partial V}{\partial I_L}\right]\left[\frac{1}{L}V - \frac{V_O}{L}(1 - D)\right] \tag{12.9}$$

From Eq. (12.4)

$$\dot{\sigma} = -\tau^{-1}\sigma \tag{12.10}$$

Substitute for $\dot{\sigma}, \sigma$ from Eqs. (12.9) and (12.5) respectively in (12.10) and solve for D gives:

$$D_{SCT} = 1 - \frac{V}{V_O} - \frac{(I_L \frac{\partial V}{\partial I_L} + V)}{\tau(2\frac{\partial V}{\partial I_L} + I_L \frac{\partial^2 V}{\partial I_L^2})\frac{V_O}{L}} \tag{12.11}$$

Where $\frac{\partial V}{\partial I_L}$ and $\frac{\partial^2 V}{\partial I_L^2}$ can be derived from Eq. (12.1) assuming that R_P has an ideal value of infinity for simplicity as follows.

$$\mathrm{I} = \mathrm{I}_{sun} - \mathrm{I}_0\left(e^{\frac{q(V+IR_S)}{aKT}} - 1\right) \tag{12.12}$$

$$V = av_t \log(\frac{I_{sun} - I_{PV} + I_0}{I_0}) - IR_S \tag{12.13}$$

Where $v_t = \frac{KT}{q}$

$$\frac{\partial V}{\partial I_L} = -av_t \frac{I_0}{I_{sun} - I_{PV} + I_0} - R_S \tag{12.14}$$

$$\frac{\partial^2 V}{\partial I_L^2} = -av_t \frac{I_0}{(I_{sun} - I_{PV} + I_0)^2} \tag{12.15}$$

The control law derived in Eq. (12.11) according to Eq. (12.4) moves the system representing point RP to the surface $\sigma = 0$, then along this surface to the origin steady state point.

12.5 Design and Simulation of Synergetic Control

To investigate and verify the proposed synergetic control performance in Sect. 4 and compare it to sliding mode control, a simulation using Matlab/Simulink is conducted for different environmental conditions as well as standard testing conditions. A case of step load variation is also studied. The complete system in Matlab/Simulink is illustrated in Fig. 12.6.

12.5.1 Synergetic Control Algorithm in Simulink

Figure 12.7 shows the Simulink implementation of synergetic control designed to track the MPP using Eq. (12.11). A weighted integrator is added to eliminate errors. Simulation time is 20 ms. The model gets samples of solar cell current, voltage and load voltage according to the sampling rate then goes through the SCT algorithm designed based on the derived terms of Eq. (12.11). Finally all terms are

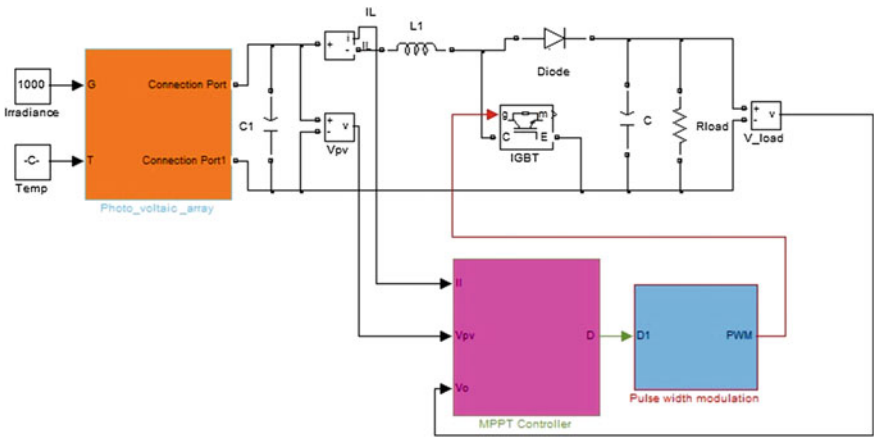

Fig. 12.6 MPPT system's simulink model including boost converter

added and the output is limited to the range of 0–1. The manipulated output is then fed to next stage PWM generator to derive the boost converter main gate switch. SCT adjusts PV operating point to the MPP as expected.

12.5.2 Sliding Mode Control Algorithm in Simulink

Figure 12.8 shows the Simulink implementation of the well-known sliding mode control used to track the MPP using manipulated input [6]. Consider the system defined as a set of nonlinear differential equations.

$$\dot{x} = f(x, D, t) = f(x) + g(x).D \tag{12.16}$$

Where x is the state vector, $D = D_{eq} + D_n$ is the manipulated control input which consists of two decoupled terms, one is the equivalent control input D_{eq}, the other one is the discontinuous control input D_n and t is time. To compute the equivalent input at $\dot{\sigma} = 0$

$$\dot{\sigma} = \frac{d\sigma}{dx}\dot{x} = f(x) + g(x) \cdot D_{eq} = 0 \tag{12.17}$$

$$D_{eq} = -\frac{\left[\frac{d\sigma}{dx}\right]^T f(x)}{\left[\frac{d\sigma}{dx}\right]^T g(x)} = 1 - \frac{V}{V_O} \tag{12.18}$$

The nonlinear component is giving by

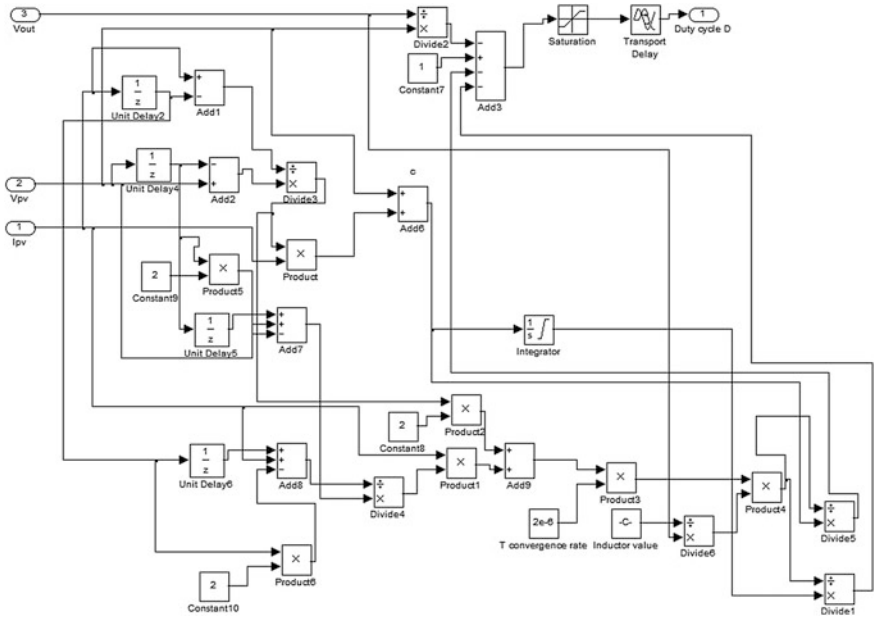

Fig. 12.7 Simulink implementation of SCT

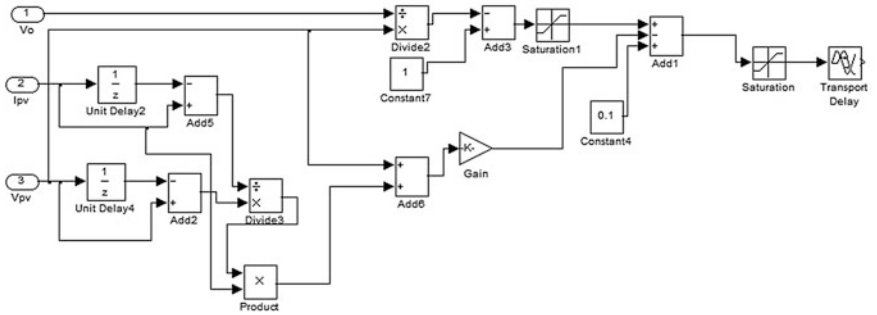

Fig. 12.8 Simulink implementation of SMC

$$D_n = k\sigma \tag{12.19}$$

The manipulated input is

$$D_{SMC} = 1 - \frac{V}{V_O} - k\left(I_L \frac{\partial V}{\partial I_L} + V\right) \tag{12.20}$$

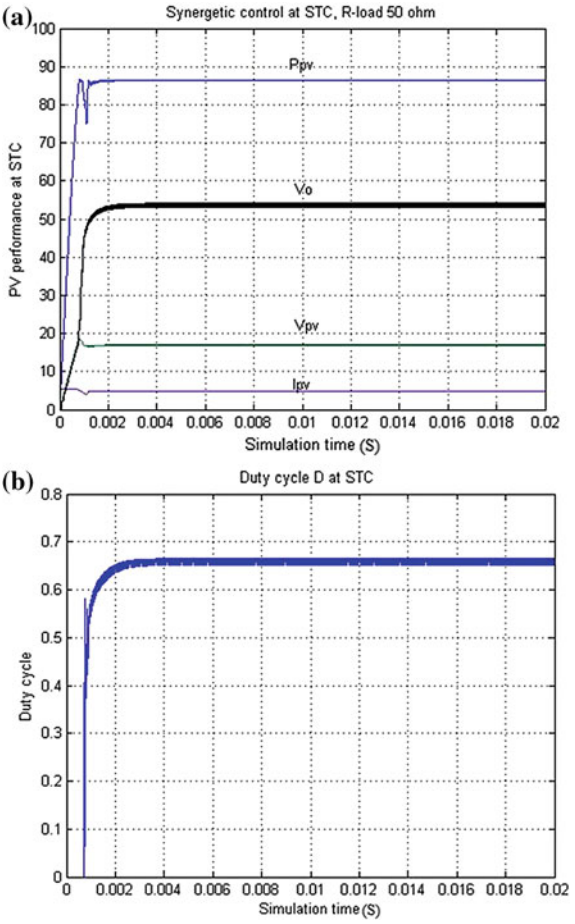

Fig. 12.9 **a** Simulation using SCT at STC ($\mathbf{T} = 25\ ^{\circ}\mathbf{C}$, $\mathbf{G} = 1,000\ \mathrm{W}/\mathbf{m}^2$). **b** Duty cycle

Figures 12.7 and 12.8 show that SCT has more computation compared to SMC, however, SCT outperforms SMC in terms of chattering elimination as simulation results prove in Sect. 12.6. Also, it has controlled convergence rate to the surface. Moreover, SMC uses higher sampling rate compared to SCT to be able to track its evolution.

12.6 Simulation Results

12.6.1 Response to Standard Testing Conditions STC

In this case, the synergetic control Technique SCT performance has been illustrated in Fig. 12.9. Besides, the famous sliding mode control SMC is depicted in

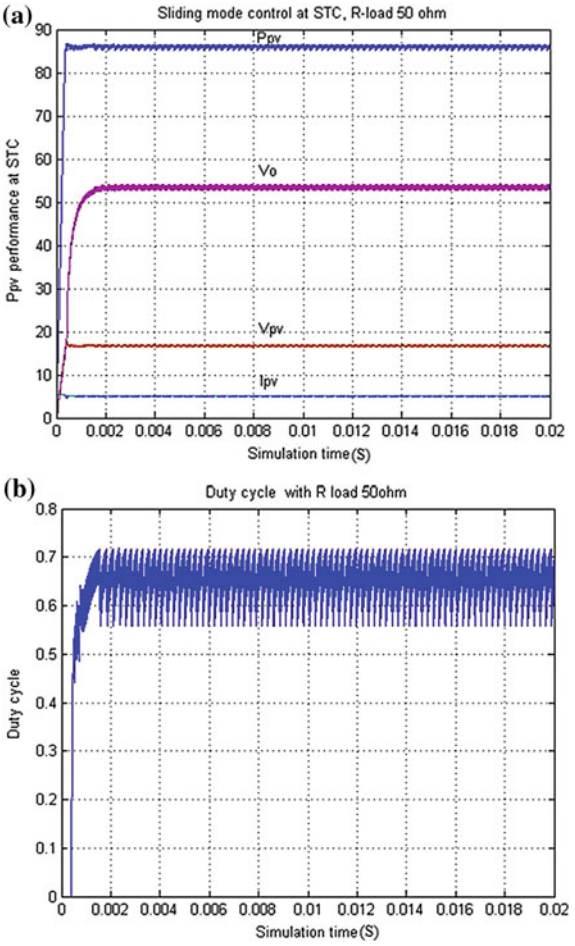

Fig. 12.10 **a** Simulation using SMC at STC. **b** Duty cycle

Fig. 12.10. As seen in the figures, both techniques were able to track the maximum power point MPP 87.31 W at STC (T = 25 °C, G = 1,000 W/m^2) with R-load, 50 ohm. However, the manipulated input, duty cycle D, in Figs. 12.9b and 12.10b are showing that the chattering effect on SMC is eliminated using SCT consequently, no filtering required on further stages. The output power in SMC reaches steady state faster at 0.4 ms compared to 1.2 ms due to more calculations in SCT.

12.6.2 Response to Irradiance Step Change 600–1,000 W/m^2

Figure 12.11 illustrates the photovoltaic power tracking with irradiance step of 600–1,000 W/m^2. PV temperature and load remains the same during the

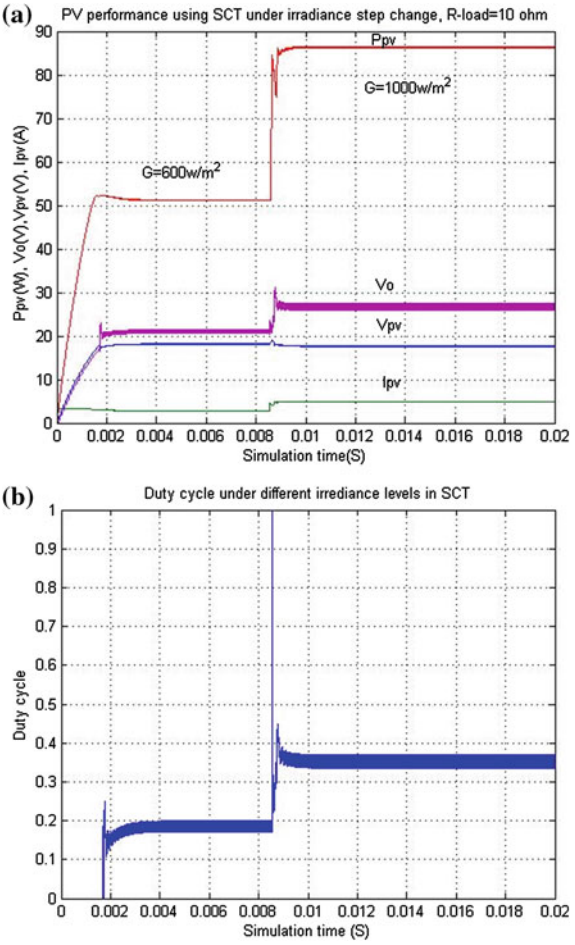

Fig. 12.11 **a** Simulation using SCT with step irradiance changes. **b** Duty cycle

simulation time. Comparing the values in Table 12.2 with Fig. 12.11, it is obvious that SC is able to track the maximum power at both 600 and 1,000 W/m^2 irradiance respectively. So it is clear that SCT is robust to abrupt change of illumination.

12.6.3 Response to Temperature Step Change 323.15–298.15 °F

Figure 12.12 shows the PV system tracking performance with temperature step change 323.15–298.15 °F. Load and irradiance levels are the same during the simulation time. Looking at Fig. 12.12 and the result in Table 12.3, synergetic

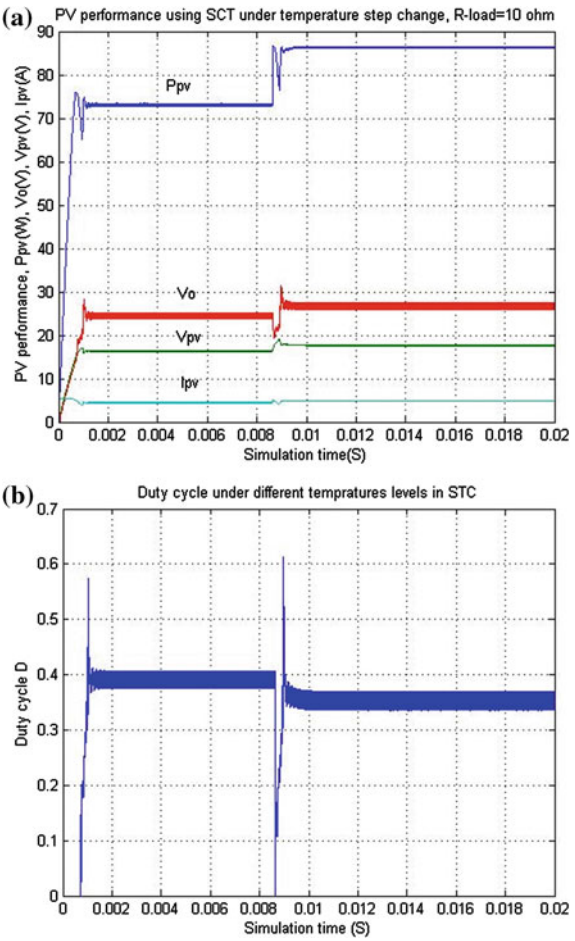

Fig. 12.12 **a** Simulation using SCT with step temperature changes. **b** Duty cycle

control approach is capable of tracking the MPP when temperature changes abruptly.

12.6.4 Response to Load Step Change 50–10 Ohm

Figures 12.13 and 12.14 simulate the PV system tracking performance with a load step change 50–10 ohm under the same irradiance and temperature. For all the results, both sliding mode control and synergetic control are able to track the MPP and stabilize the output power under load change. However, synergetic control advantage over sliding mode control is removing chattering problem in the manipulated input (duty cycle), and output signals too.

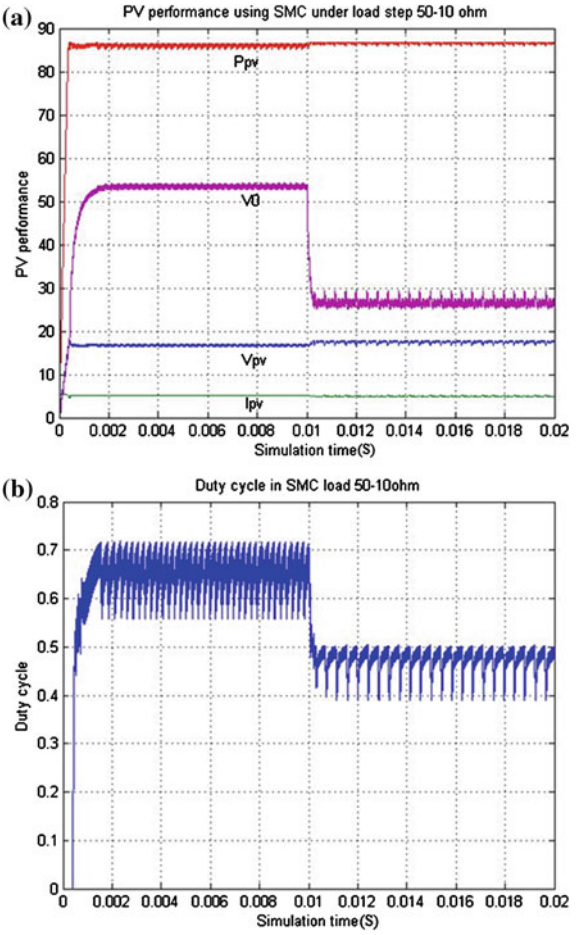

Fig. 12.13 **a** Simulation using SMC with step load changes. **b** Duty cycle

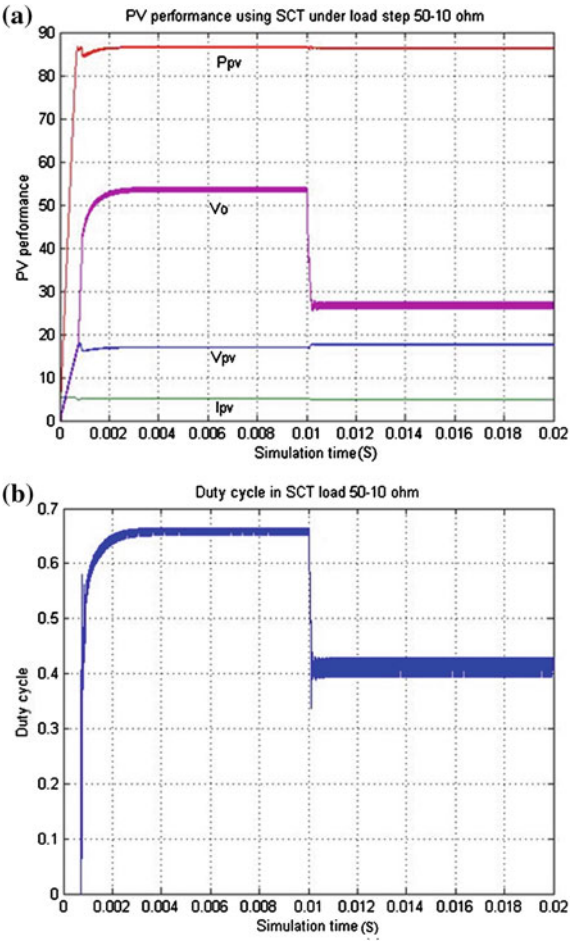

Fig. 12.14 **a** Simulation using SCT with step load changes. **b** Duty cycle

12.7 Conclusion

In this paper, synergetic control is proposed as a nonlinear control technique to track photovoltaic systems MPP. MPPT model including photovoltaic module, boost converter, SCT and PWM is designed and tested with different environmental changes. It is proved using simulation Matlab/Simulink that synergetic control eliminates chattering effect compared to sliding mode control. It has controllable switching frequency towards the surface which makes it more suitable for digital implementation as less sampling rate is required. SC is continuous, and needs less filtering. However, SC requires more calculations compared to SMC and depends on system parameter as illustrated in as explained earlier therefore it is more sensitive to model parameters variations, large disturbances, and uncertainties.

References

1. M. Aureliano, L. Galotto Jr, L. Melo, C. Canesin, Evaluation of the main MPPT techniques for photovoltaic applications. IEEE Trans. Industr. Electron. **60**(3), 1156–1167 (2013)
2. M. Ropp, J. Cale, M. Mills, M. Scharf, S.G. Hummel, A test protocol to enable comparative evaluation of maximum power point trackers under both static and dynamic irradiance, in *37th IEEE Photovoltaic Specialists Conference (PVSC)*, 19–24 June 2011, pp 3734–3737
3. T. Bennett, A. Zilouchian, R. Messenger, A proposed maximum power point tracking algorithm based on a new testing standard. Sol. Energy **89**, 23–41 (2013)
4. G. Farivar, B. Asaei, S. Mehrnami, An analytical solution for tracking photovoltaic module MPP. IEEE J. Photovoltaics **3**(3), 1053–1061 (2013)
5. F. Inthamoussou, H. De Battista, M. Cendoya. Low-cost sliding-mode power controller of a stand-alone photovoltaic module, in *2010 IEEE International Conference on Industrial Technology (ICIT)*, pp. 1175–1180
6. Ch. Chua, Ch. Chen, Robust maximum power point tracking method for photovoltaic cells: A sliding mode control approach. Sol. Energy **83**(8), 1370–1378 (2009)
7. A. Souissi, B. Ben Ghanem, N. Rebai, O. Hasnaoui, A. Sellami, Robust maximum power point tracking method for a stand-alone PV power system, in *2011 7th International Conference on Electrical and Electronics Engineering ELECO*, pp. I-215–I-219
8. Y. Choi, N. Chang, T. Kim, DC–DC Converter-aware power management for low-power embedded systems. IEEE Trans. Comput. Aided Des. Integr. Circuits Syst. **26**(8), 1367–1381 (2007)
9. E. Fossas, D. Biel, A sliding mode approach to robust generation on DC-to-DC Converters, in *Proceedings of the 35th Conference on Decision and Control Kobe, Japan* vol. 4, Dec 1996, pp. 4010–4011
10. V.I. Utkin, Variable structure system with sliding modes. IEEE Trans. Ind. Electron. **AC 22**(2), 212–222 (1977)
11. J.A. Gow, C.D. Manning, Development of a photovoltaic array model for use in power electronics simulation studies. IEE Proc. Electr Power Appl. **146**(2), 193–200 (1999)
12. F. Liu, Sh Duan, F. Liu, B. Liu, Y. Kang, A variable step size inc MPPT method for PV systems. IEEE Trans. Ind. Electron. **55**(7), 2622–2628 (2008)
13. H. De Battista, R.J. Mantz, Variable structure control of a photovoltaic energy converter. IEE Proc. Theor. Appl. **149**(4), 303–310 (2002)
14. D. Rekiou, E. Matagne, Optimization of photovoltaic power systems. modelization, simulation and control, ISBN 978-1-4471-2403-0, in *Systems Conference (MEPCON'10),* Cairo University, 19–21 Dec 2010
15. A. Kolesnikov, G. Veselov, A. Kolesnikov, A. Monti, F. Ponci, E. Santi R. Dougal, Synergetic synthesis of dc-dc boost converter controllers: theory and experimental analysis, in *IEEE Applied Power Electronics Conference (APEC'2002), Dallas*, 10–14 March 2002, pp. 409–415
16. E. Santi, A. Monti, D. Li, K. Proddutur, R. Dougal, Synergetic control for dc-dc boost converter: implementation options, in *Proceedings of 37th IEEE Industry Applications Society Annual Meeting (IAS'02)*, pp. 1330–1337 (2002)
17. A. Bezuglov, A. Kolesnikov, I. Kondratiev, J. Vargas. Synergetic control theory approach for solving systems of nonlinear equations, in *9th World Multi-Conference on Systemics, Cybernetics and Informatics*, Orlando, FL, July 2005.
18. A. Monti, R. Dougal, E. Santi, D. Li, K. Proddutur, Compensation for step-load variations when applying synergetic control, in *Proceedings of IEEE Applied Power Electronics Conference (APEC'03)*, pp. 334–340 (Feb 2003)
19. E. Santi, A. Monti, D. Li, K. Proddutur, Synergetic control for power electronics applications: a comparison with the sliding mode approach. J. Circuits Syst. Comput. **13**(4), 737–760 (2004)

Chapter 13
Reconfiguration Solution for Shaded PV Panels Using Fuzzy Logic

A. Tabanjat, M. Becherif and D. Hissel

Abstract This paper applies a new dynamical electrical array reconfiguration strategy on the photovoltaic (PV) panels arrangement based on the connection of all PV panels on two parallel groups to reach the 24 V requested by the considered load and providing a maximum output current by connecting in serial the two groups. If one of the PV panels or more is shaded, the connection of the other in the same group will be automatically modified to maintain the requested 24 V for each PV panel row. This dynamical reconfiguration allows also reducing the lost power, due to the shaded panel, by recovering this power from the reconfiguration of the other panels. As a result, a real time adaptation of switch matrix allows a self-ability to maintain a constant voltage at 24 V and minimum number of PV panels is switched off by isolating the effect of shaded panels. In addition, the proposed solution can also be applied for the dirty panel and identify the shaded, dusty and faulty panel.

Keywords Photovoltaic panels · Fuzzy logic estimator · Switches · Shading

13.1 Introduction

The pollution caused by fossil energy gives the priority to the use of renewable energies in different regions all over the world. Solar energy is the most important energy, it is the most well distributed, is renewable and has no hazard for atmosphere. However, PV panel has a problem when it is shaded by clouds or other

A. Tabanjat (✉) · M. Becherif · D. Hissel
University of Technology of Belfort Montbéliard (UTBM), Belfort, France
e-mail: abdulkader.tabanjat@utbm.fr

D. Hissel
University of Franche Comte (UFC), Belfort, France

M. O. Hamdan et al. (eds.), *ICREGA'14 - Renewable Energy: Generation and Applications*, Springer Proceedings in Energy, DOI: 10.1007/978-3-319-05708-8_13,

obstacles [1, 2]. Shading PV panels cause voltage drop at its terminals and consequently reduce extracted power. In addition, the shaded or dirty PV panels affect the unshaded or the clean ones. This is also true when Maximum Power Point Tracking algorithm (MPPT) is used for groups of PV panels [3–8]. It is proven that shading or dust cause the same effect on the considered PV panel. To be concise, only the shading effect is mentioned above in the article but the result is valid for both without a lost in generality.

PV panels have different operating points, those points depend mainly on the light density coming from the sun. Hence, strategies for selecting the best operating point, which has a maximum power at each moment, are requested. MPPT is largely proposed as a solution, it can overcome the problem of shading all PV panels [9, 10], but when shading is partial because of clouds or other obstacles, there will be a new problem. In this case, the maximum power points are different for the different PV Panels group (connected to one MPPT controller). Therefore multi-MPPT can be proposed. Nevertheless, in this case, all PV panels have a MPPT controller which is far from being optimal. Many solutions were proposed to overcome this problem, one of them is multi-tracker inverters and other one is a tracker per module [11, 12]. These two last solutions have a problem of cost. In addition, the solution is insufficient to extract maximum of power. For these reasons a new solution, presented in this article, can switch off shaded PV panel to avoid the decreasing in the overall power by reconfiguring all PV panels' connection to match the (considered) requested 24 V at load terminals and minimizing the power losses.

Two important phenomena affect a PV module when it is shaded:

The first is hot spot: PV modules are equipped with bypass diodes [13, 14]. The role of bypass diodes is twofold:

- protect the cells against the phenomenon of hot spot;
- Improve the performance of modules subject to shading.

The second phenomenon is returning current: occurs when two different modules (or chains of different modules) are connected in parallel [15]. Two significant effects can occur:

- Power losses;
- Damage to the module.

To avoid this phenomenon, each PV panel is provided with a diode connected in series as shown in Figs. 13.8, 13.9 and 13.10.

After this brief introduction, this paper is organized as follows: in the Sect. 13.2, all PV panel characteristics of the considered PWX500 module will be studied and the effect of shading will be experimentally shown. In Sect. 13.3, the two last solutions (multi-tracker inverters and a tracker per module) for shaded PV panels are shown and discussed. A new cost effective solution is proposed considering online operation, easy implementation and efficiency. This solution is applied on a group of PV panels and experimental results are given. Finally, Sect. 13.4 concludes this work.

13.2 The PV Panel Model and Practical Study of the Shading-Effect

The studied PV module is a so-called "PWX500" double glass. With its two glass plates, the PWX500 module provides higher mechanical strength and greater electrical protection. Those panels are particularly suitable for applications in marine and tropical environment or isolated areas.

Experimental characterization of the module is done using the I–V curve (Fig. 13.1). Fittype, Cfit and fit tools from Matlab-Simulink are used. As a result of the simulation and experimental tests, the I–V and P–V curves are obtained allowing the characterization of panels. Figure 13.1 shows the simulated polarization curve and the experimental points that were used to identify the parameters. The statistical values for evaluating the relevance of adjustment are provided with the tool "fit" of Matlab. Closer the sum of squared errors (SSE) to 0, the better the fit is. The coefficient of determination (Rsquare) indicates a better fit when it is close to 1. Similarly to Rsquare, the adjusted degree of freedom (Adjrsquare) data (number of measurements) describes a good fit when it is close to 1. The obtained difference between experiments and simulation results is here enough satisfying according to the metrics of precision (here SSE = 0.0488, Rsquare = 0.9721 and Adjrsquare = 0.9696).

The effect of temperature and irradiance are studied using the test bench composed of: six projectors of 500 W each (1), luxmeter (2), rheostat (3), watt meter (4), PWX500 PV panel of 45 Wp (5) and a thermometer (6). Test stand is presented in the following figure (Fig. 13.2).

Tests were divided into two steps: in the first step, the projector irradiance was fixed to 368 W/m^2, and temperature increased from 40 to 75 °C. In the second step, temperature was fixed between 20 and 30 °C, and irradiance was changed between 43 and 404 W/m^2. Practical results are shown in Fig. 13.3.

Electrical PV module characteristics present substantial variations in case of partial shading, resulting in important reductions of the output power [16, 17]. In this study shading of one cell, two cells and nine cells are applied and the results obtained are shown in Fig. 13.4.

It is clear from Fig. 13.4 that because of shading (or dust) the point of maximal power is very far from the one obtained without shading. So a solution has to be searched when many PV panels are used. Using MPPT for group of PV panels which have different shading percentage shows the problem of extracting the maximum power regarding to each PV panel [11, 12, 18–23]. A new serial/parallel topology reconfiguration is presented in this paper which is suitable for the connection of a large number of PV without a change in the overall topology. As a result, new PV modules can be easily connected to this generator in a kind of plug and play process.

2 cells/ P: two cells are shaded from two different lines (parallel);
2 cells/ S: two cells are shaded from the same line (serial);
9 cells/ P: nine cells are shaded from two different lines (parallel) see Fig. 13.5;
9 cells/ S: nine cells are shaded from the same line (serial) see Fig. 13.5.

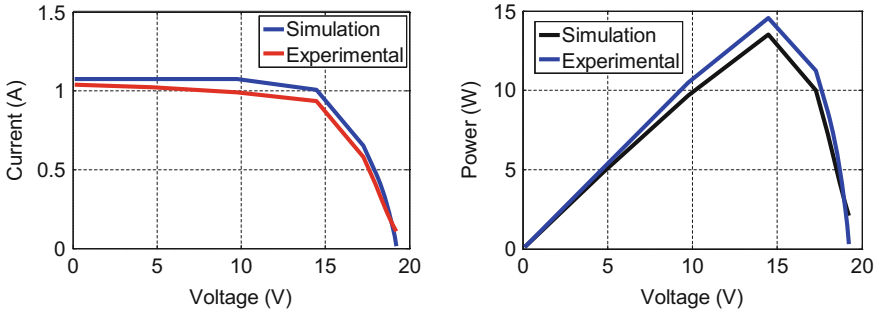

Fig. 13.1 I–V and P–V *curves* for experimental and simulation data

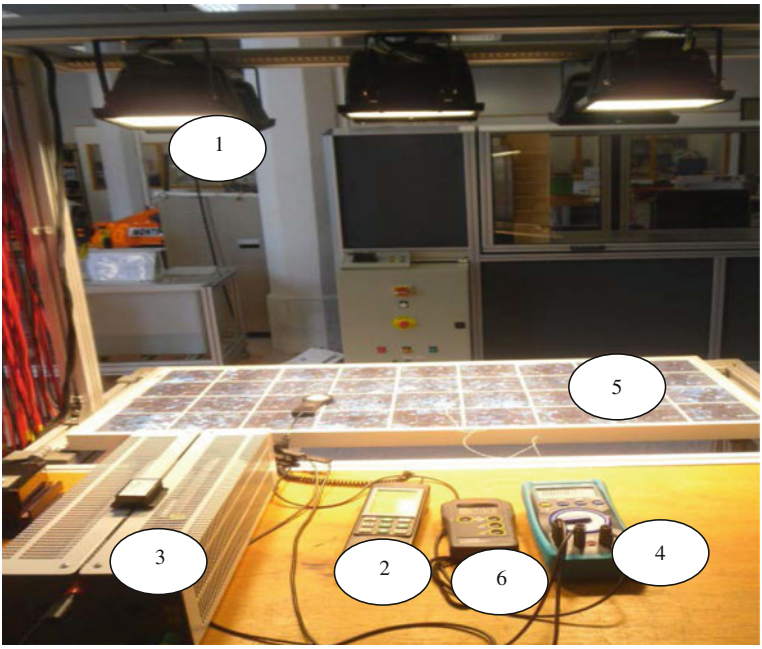

Fig. 13.2 Experimental stand of PWX500 PV panel

The power losses and shaded PV panel percentage is shown in Table 13.1. The power loss as function of shading PV panel is presented in Fig. 13.6.

Fuzzy Logic (FL) estimator is used to predict the percentage of shading and to identify and warn about the shaded dirty or faulty panel. FL provides a solution to obtain the shading or dust percentage for any unknown data of power losses. Therefore, this technique allows taking a decision if the PV panel is shaded or not depending on the suggested shading percentage threshold (Fig. 13.6). If one PV

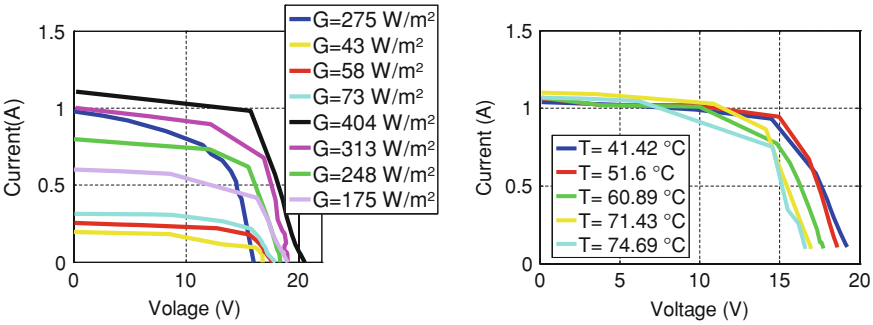

Fig. 13.3 I–V characteristics at different irradiances and different temperature degrees

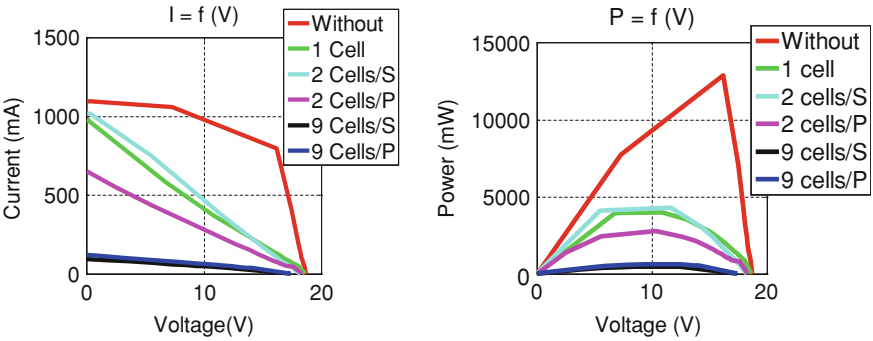

Fig. 13.4 Experimental I–V and P–V characteristics for non shaded PWX500 PV panel and in case of one, two or nine shaded cells

Fig. 13.5 Shading nine cells from two different *lines* (9 cells/P) and nine cells from the same *line* (9 cells/S)

panel is considered (Fig. 13.7), its input is power losses, which is received by PV panel current and voltage captures, the outputs are shading or dirty percentage estimated by FL and the second one is the situation of PV panel (on or off), see Fig. 13.7. According to this result, the incriminate panel is either disconnected or no (regarding the percentage of the lost power), the human operator is warned to clean the panel or to check if there is a shadow on the identified panel.

Table 13.1 Power losses in function of shading percentage

Shading %	P_{max} (W)	Power losses %
0	12.89	0
2.78	4	68.97
5.56	3.53	72.61
15.28	2.05	84.1
19.168	1.46	88.69
25	0.57	95.58

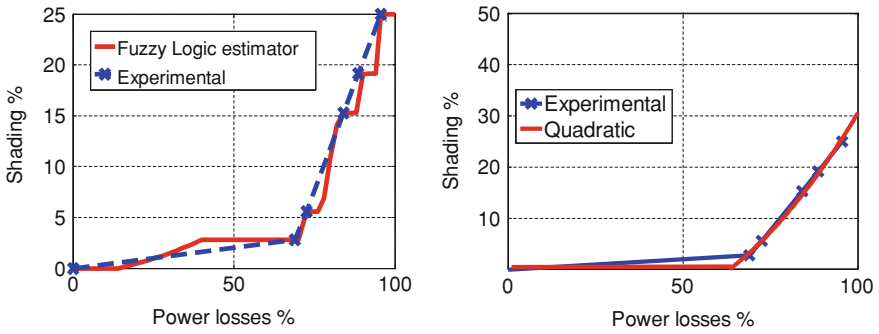

Fig. 13.6 FL estimator and fitting tool solutions

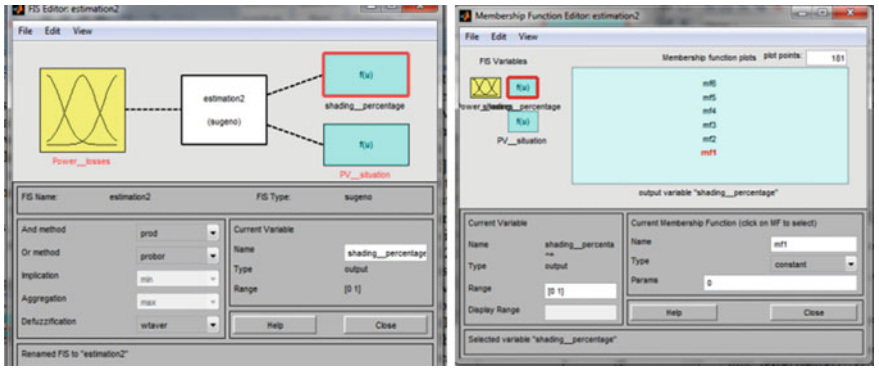

Fig. 13.7 FL estimator suggested for one shaded PV panel

In this case, if PV panel is shaded, its output will be zero, but if it is not shaded, its output will be one (Fig. 13.7).

The rule base allows the representation of the relation between input and outputs has the structure as below:

If power losses are (power losses percentage condition is verified) then a percentage of shading or dust is calculated in this case and the suitable situation of PV panel (on or off) is decided for this shading/dust percentage.

If four PV panels are used, as show below in practical work (Fig. 13.10), in this case FL estimator has four inputs representing the percentage of voltage drop (instead of power), as well as FL estimator has ten outputs representing the situation of ten switches to apply the decision of switching on or off the four PV panels depending on their shading/dust situation estimated by FL.

Another solution for estimating power losses in case of shading PV panel is to use the fitting tool in Matlab. In this case, the suitable solution has been obtained using the following function (Fig. 13.6):

$$Y = P1 * X3 + P2 * X2 + P3 * X + P4 \tag{13.1}$$

Coefficients: P1 = −8.8833e-05, P2 = 0.022958, P3 = −1.1212, P4 = 0.00010261, norm of residuals = 0.08514 (those parameters are obtained experimentally using Fig. 13.6)

Where: Y represents the shading/dust percentage and X represents the power losses percentage.

13.3 Anti-Shading or Dust Solution

13.3.1 Multi-tracker Inverter

Now consider two PV strings connected in parallel to an inverter. For example, suppose that each of the strings provides 740 W (maximum power). When, strings are not subject to shading, their current–voltage characteristics are combined (they have a total I–V characteristics which has the same voltage as one string and the current equals the sum of the two string currents). The inverter MPPT algorithm will search for the maximum power point of the set consisting of the two strings in parallel [11, 12]. In this example, of the reference [12], the maximum power point is 1,480 W; both strings operate at their maximum power (740 W). Assuming now that the two strings are shaded, the MPPT of the inverter will always lock on the maximum power point of the set consisting of two strings in parallel i.e. 1,210 W (this value is found in reference [12] depending on an experimental test). It can be seen that this solution doesn't fully exploit the two strings. Indeed, the Voltage of MPP (U-MPP) of the assembly consisting of two strings does not correspond to the voltage U-MPP1 of the chain 1, or the voltage U-MPP2 of the chain 2. The two strings do not deliver 100 % of their power. This is because the MPPT of the inverter will hold the MPP of the set consisting of the two strings. As a consequence, the shading affect in one module or a group of modules will considerably effect the overall production. This problem can be solved with a multi-tracker

inverter. The presence of a multi-tracker inverter is therefore justified when several parts of a PV array does not have the same electrical properties. For example, when a part of the field is likely to be subjected to shading, it is connected to a MPPT of a dedicated inverter. Similarly, when two parts of a field does not have the same orientations and inclinations (for example double bridge east–west), each part can be connected to a singular MPPT. Of course, the multi-tracker is a technical solution that increases the overall cost of the installation.

13.3.2 A Tracker per Module

It is now clear that when there are power disparities (especially because of the shade or dust), the ideal solution would be to have a MPPT for each module [11, 12]. Thus, the available power of each module would be obtained. Some manufacturers offer this option in their pack.

13.3.3 New Switches Combination as a Solution of Shaded or Dirty PV Panels

Because of the high cost of MPPT dedicated to each module (which is about 100 $ per one of Sian Sonic corporation), and the insufficient multi-tracker solution, a new switches combination using FL estimator is proposed in this paper (Fig. 13.8). In this solution, the following devices are used:

1. 4 PV Panels with max power 5 W for each and nominal voltage of 12 V;
2. dSPACE control hardware;
3. 10 switches;
4. 10 relays;
5. 4 amperemeters for measuring the current flow drawn from each PV panel, current sensors are not requested for the final solution in a laboratory;
6. DC source feeding power to the relays (relays can also be fed directly by PV)
7. Cables;
8. Lamp;
9. PC;
10. Rheostat as a load;
11. Diodes.

In this work, a 24 V output is requested as a constraint. Moreover, minimum power loss is requested and obtained by minimizing the power loss on the shaded PV panels. All these are done with a minimum cost by avoiding increasing the MPPT controller number. The proposed solution is shown in Fig. 13.9.

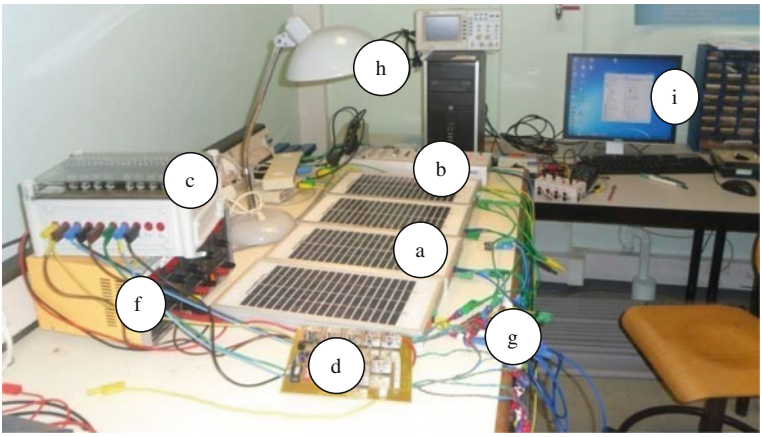

Fig. 13.8 Experimental bench of the new switches reconfiguration

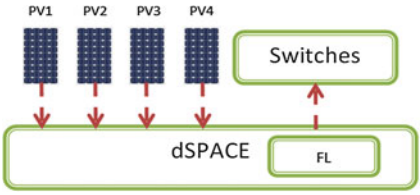

Fig. 13.9 Fuzzy logic and dSPACE control of the proposed system

To meet the 24 V requirement, panels are divided into two strings (PV1 and PV2 are the first string, PV3 and PV4 are the other string) connected in serial electrical arrangement, in this situation each string contains two PV panels and its output is 12 V. In another case, if it is required to consider more than four PV panels, other PV panels can be connected in parallel on each existing PV. As a result, 24 V is still obtained at the load terminals. Hence, a connection bus can be realized on each of the four existing PV modules. The four main PV modules will allow the serial/parallel reconfiguration of their buses.

The ten controlled switches are used as follows:

- Each PV module has its own switch allowing its disconnection when shaded or even when a fault is detected. Then, four switches are used for the four PV modules.
- Six switches are needed to perform the reconfiguration in serial/parallel arrangement of the four PV modules (and consequently for the four buses).

Consequently, for the connection of n PV modules, the number of requested switches would be $6 + n$.

As shown in Fig. 13.4, the shading effect affects the current and the voltage at the output of the PV module. In order to avoid the need of additional sensors in our solution, the shading effect is detected based on the voltage drop at the output of

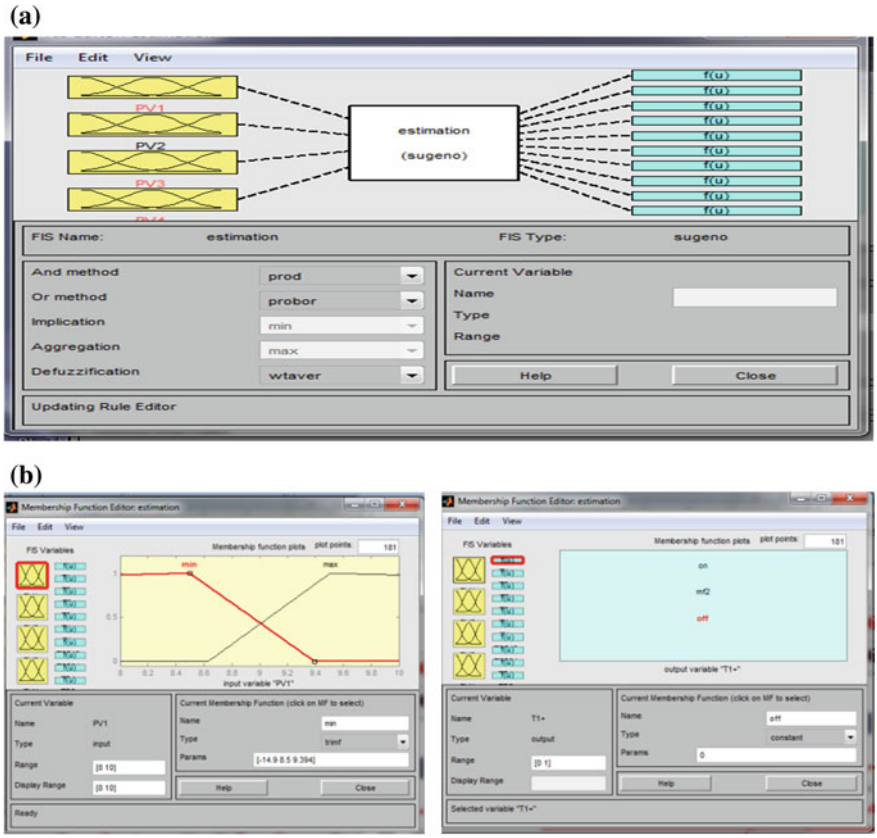

Fig. 13.10 FL estimator inputs and outputs. **a** Sugeno FIS for requested estimation. **b** FIS variables of inputs and outputs

each PV module. Consequently, no sensor is used for this except the direct connection of the output voltage of each module as an input of the dSPACE card.

In this work, two types of Switches are used, normally opened as TSP12 and TSP34 and normally closed as all others switches. Red color (bold line) in Fig. 13.11 represents electrical current flow in PV circuit.

13.3.4 Control of Switches

Fuzzy Control (FL) is used to perform this task. This type of control approaches the human reasoning and makes use of the tolerance, uncertainty, imprecision and fuzziness in the decision-making process. It manages to offer a satisfactory performance without the need for a detailed mathematical model of the system, just by incorporating the experts' knowledge into fuzzy rules.

In addition, it has inherent abilities to deal with imprecise or noisy data; thus, it is able to extend its control capability even to those operating conditions where linear control techniques fail (i.e., large parameter variations).

This system has four main parts. First, using input membership functions, inputs are fuzzified, then based on inference rules, outputs are produced and finally the fuzzy outputs are defuzzified and applied to the main control system.

FL estimator is proposed for deciding, based on the output voltage drop on each module, if the shaded effect is detrimental on the global PV production; in this case, the shaded PV module is disconnected. If more than one PV modules are shaded, they are disconnected and if needed the serial/parallel topology is reconfigured in order to ensure the 24 V at the terminal. Inputs of this FL are PV panels' voltages, and the outputs are the switches control in Boolean values (Fig. 13.9).

The PV module voltage drop making decision of its disconnection can be chosen by an expert or automatically set by FL on the basis of the overall power production losses. If the shaded PV module becomes unshaded, its nominal voltage is reached and measured and a decision of its reconnection is automatically done (Fig. 13.10). A hysteresis with a defined bandwidth is used on the PV module voltage in order to avoid an excessive connection/disconnection around a critical voltage.

In the chosen scenario, one or a maximum of two PV modules are shaded. Indeed, if three PV modules are shaded over fourth, the requested 24 V cannot be produced and the PV modules are automatically disconnected from the load in order to secure the overall installation and the PV module health.

FL rules for inputs and outputs are explained in Tables 13.2 and 13.3. If PV panels are in normal mode, there is no action and this situation is presented by (9.5 V) in the table. Inversely, if the PV panels are turned off, (8.5 V) is affected as a state of the selected PV module (Fig. 13.10).

In normal mode (rule 16 in Tables 13.2 and 13.3) corresponds to the absence of shading on any PV panels. All PV panels are working and their voltage is more than (9.5 V) (Table 13.2) and all switches are in normal position (open or closed by fault), so TSP12 and TSP34 are normally opened and all others switches are normally closed. Therefore, the connection will be parallel for the first group consisting of PV1 and PV2, and the same for the second group consisting of PV3 and PV4 (Fig. 13.11). The total power obtained is about 16 W, and the voltage at each PV panel output is about 12 V.

Let us take rule 11 as an example of shaded PV panels: PV1 and PV2 are shaded (Table 13.2). As these two PV panels are from the same string and the two others (3 and 4) are not shaded, PV3 and PV4 are reconfigured in serial in order to obtain the 24 V at load terminals. In this case, PV1 and PV2 are disconnected by opening switches T1+ and T2− and the switch TSP12 (for serial/parallel between PV1 and 2) is closed allowing bypassing the shaded PV (Fig. 13.12).

In normal mode, each PV panel provides about 4 W (Fig. 13.11). In the case of a fault at any PV panel, the lost power is recovered (or its effect is minimized) from the other panels thanks to the automatic reconfiguration of the connection

Table 13.2 FL estimator inputs

Rule	Inputs			
	PV1	PV2	PV3	PV4
1	8.5	8.5	8.5	8.5
2	9.5	8.5	8.5	8.5
3	8.5	9.5	8.5	8.5
4	8.5	8.5	9.5	8.5
5	8.5	8.5	8.5	9.5
6	9.5	9.5	8.5	8.5
7	9.5	8.5	9.5	8.5
8	9.5	8.5	8.5	9.5
9	8.5	9.5	9.5	8.5
10	8.5	9.5	8.5	9.5
11	8.5	8.5	9.5	9.5
12	9.5	9.5	9.5	8.5
13	9.5	9.5	8.5	9.5
14	9.5	8.5	9.5	9.5
15	8.5	9.5	9.5	9.5
16	9.5	9.5	9.5	9.5

Table 13.3 FL estimator outputs

Rule	Outputs									
	T1+	T2+	T2−	T3+	T4+	T4−	TSP12	TSP34	TB1	TB2
1	1	1	1	1	1	1	1	1	1	1
2	0	1	1	1	0	1	1	1	1	0
3	1	1	0	1	0	1	1	1	1	0
4	1	0	1	0	1	1	1	1	0	1
5	1	0	1	1	1	0	1	1	0	1
6	0	1	0	1	0	1	1	1	1	0
7	0	0	1	0	0	1	0	0	0	0
8	0	0	1	1	0	0	0	0	0	0
9	1	0	0	0	0	1	0	0	0	0
10	1	0	0	1	0	0	0	0	0	0
11	1	0	1	0	1	0	1	1	0	1
12	0	0	0	0	0	1	0	0	0	0
13	0	0	0	1	0	0	0	0	0	0
14	0	0	1	0	0	0	0	0	0	0
15	1	0	0	0	0	0	0	0	0	0
16	0	0	0	0	0	0	0	0	0	0

topology. In a classical and fixed series/parallel connection, the PVs in series are forced to produce the same current. Consequently, if one panel in series is shaded or faulty, the output current of the all PV in series is fixed by the lowest produced current and this affect directly the overall produced power.

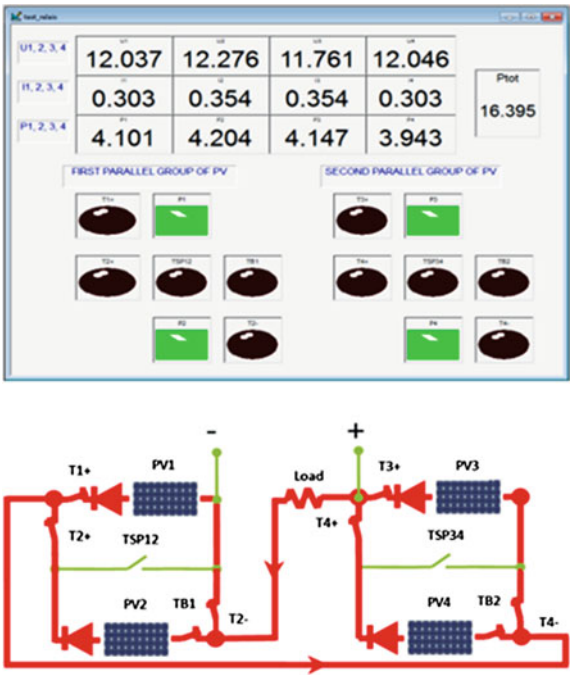

Fig. 13.11 U, I, P results and current flow in normal mode of the four PV panels without shading

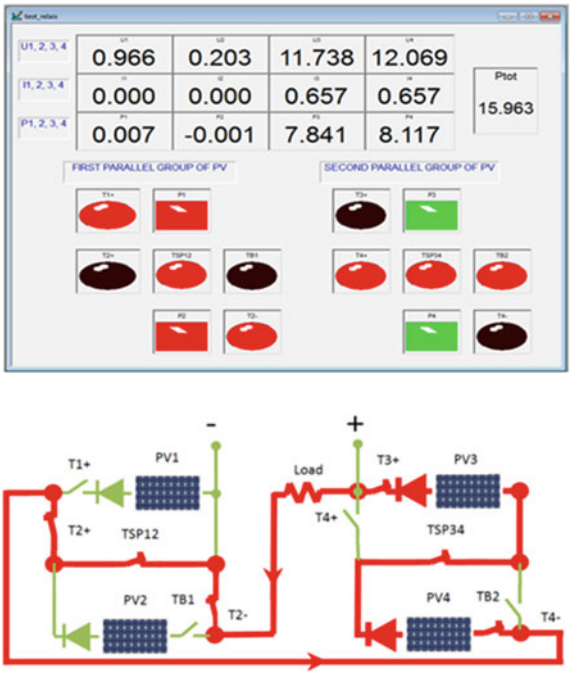

Fig. 13.12 U, I, P results, current flow and four PV panels connectivity in case of two shaded PV panels (PV1 and PV2)

Table 13.4 All possibilities of PV panel shading

Shaded PV panel type	Electrical current flow path
Four PV panels in normal work conditions: PV1 = 4.1 W, PV2 = 4.2 W, PV3 = 4.15 W and PV4 = 3.94 W and PVtot = 16.4 W	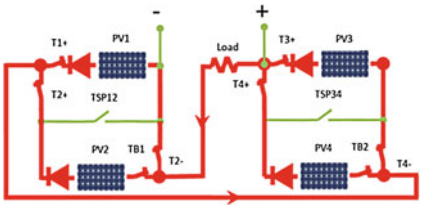
One PV panel shaded: PV1 = 0 W, PV2 = 8.13 W, PV3 = 3.91 W and PV4 = 3.97 W and PVtot = 16.03 W	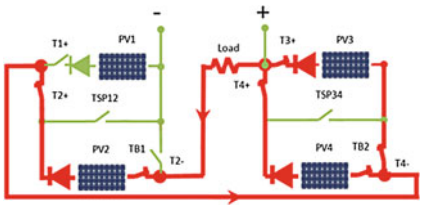
Two PV panels from the same string are shaded: PV1 = 0 W, PV2 = 0 W, PV3 = 7.84 W and PV4 = 8.12 W and PVtot = 15.96 W	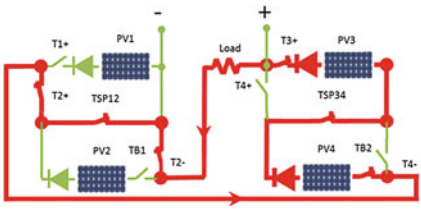
Two PV panels from different strings are shaded: PV1 = 0 W, PV2 = 8.03 W, PV3 = 0 W and PV4 = 8.01 W and PVtot = 16.05 W	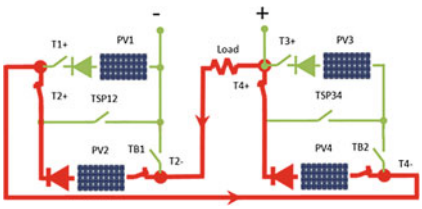

The other possibilities of shaded PV are:

- One shaded PV panel;
- Two shaded PV panel from the same string;
- Two shaded PV panel from different strings;
- Three or four shaded PV panels. In this case, the requested 24 V cannot be obtained, and then all PV are disconnected.

All the possibilities of having one, two or no shaded PV are listed in Table 13.4 and are experimentally tested.

In general case, when multi PV panels exist, any PV panel shaded will be switched off by its own dedicated switch. If the lack of power is no more possible to be recovered by the other PV panels, in this situation the most shaded PV string will be switched off as explained before. Their connection is shown in Fig. 13.13. The number of switched requested for this configuration (24 V DC bus) is n + 6, where n is the number of PV panels.

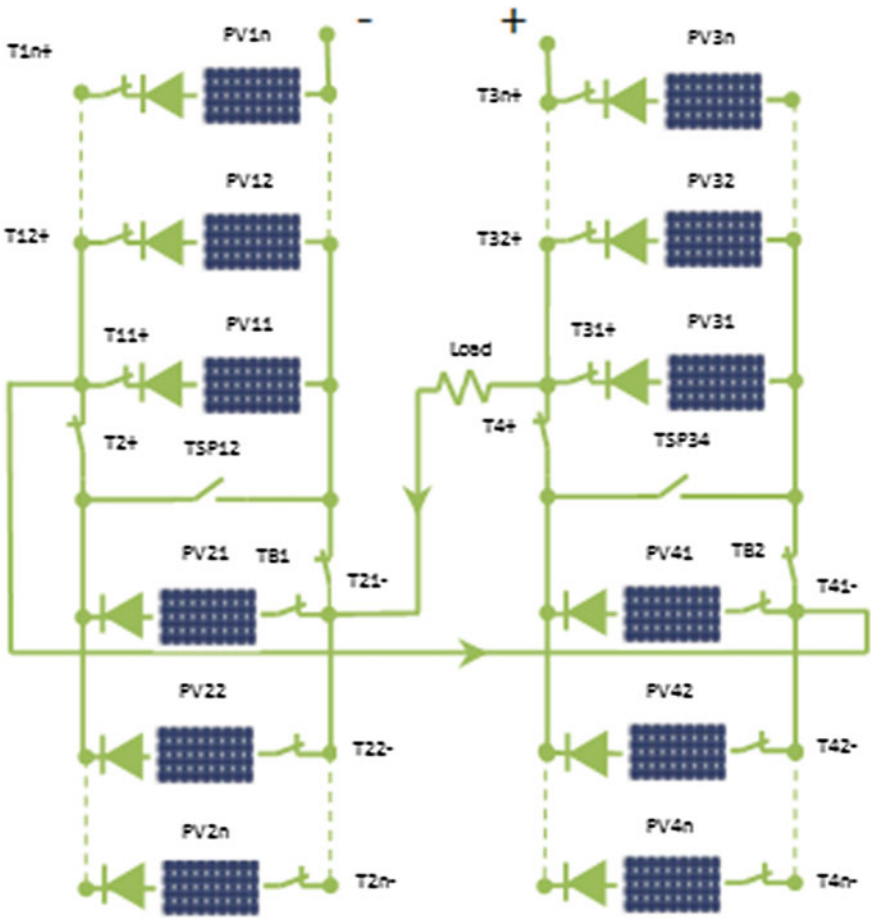

Fig. 13.13 General connection of PV panels with the new proposed online connection reconfiguration

13.4 Conclusion

In this paper the effect of shading, dust or faulty is studied and two existing solutions are discussed (Multi tracker and tracker per module). A new method, to avoid the disadvantages of high cost of the two mentioned methods, is proposed. This method, of low cost, does not request any increasing in MPPT controller number or additional sensors. Indeed, it is sufficient to use controlled switches and diodes. Fuzzy Logic estimator is used to identify the shaded, dirty or faulty panel, to estimate the percentage of shading or dust and to decide of the connection/disconnection and reconfiguration of serial/parallel coupling. This new online reconfiguration has the possibility to be expanded to more than four PV panels.

The developed fuzzy logic estimator with the online dynamical reconfiguration solution allows to detect and identify the shaded, dusty or faulty panel and to minimize the power losses by the reconfiguration of the coupling of the whole panel group. Experimental setup is built by authors and successfully validates the proposed solution.

References

1. G. Petrone, G. Spagnuolo, R. Teodorescu, M. Veerachary, M. Vitelli, Reliability issues in photovoltaic power processing systems. IEEE Trans. Ind. Electron **5**(57), 2569–2580 (2008)
2. M. Drif, P.J. Pérez, J. Aguilera, J.D. Aguilar, A new estimation method of irradiance on a partially shaded PV generator in grid-connected photovoltaic systems. Renew. Energy **33**(9), 2048–2056 (2008)
3. M.L. Doumbia, K. Agbossou, E. Granger, Simulink modelling and simulation of a hydrogen based photovoltaic/wind energy system, in *EUROCON, 2007. The International Conference on "Computer as a Tool"*, pp. 2067–2072
4. A. Bouilouta, A. Mellit, S.A. Kalogirouc, New MPPT method for stand-alone photovoltaic systems operating under partially shaded conditions. Energy **55**, 1172–1185 (2013)
5. J. Ma, K.L. Man, T.O. Ting, N. Zhang, S.-U. Guan, P.W.H. Wong, DEM: direct estimation method for photovoltaic maximum power point tracking, Procedia Comput. Sci. **17**, 537–544 (2013)
6. R.K. Kharb, S.L. Shimi, S. Chatterji, Improved maximum power point tracking for solar PV module using ANFIS, Int. J. Curr. Eng. Technol. **3**(5), 1878–1885 (2013)
7. K.K. Kumar, R. Bhaskar, H. Koti, Implementation of MPPT algorithm for solar photovoltaic cell by comparing short-circuit method and incremental conductance method, Procedia Technol. **12**, 705–715 (2014)
8. K. Hirech, M. Melhaoui, F. Yaden, K. Baghaz, E. Kassmi, Design and realization of an autonomous system equipped with a charge/discharge regulator and digital MPPT command. Energy Procedia **42**, 503–512 (2013)
9. N.A. Ahmad, M. Miyatake, A novel maximum power point tracking for photovoltaic applications under partially shaded insolation conditions. Electric Power Syst. Res. J. **78**, 777–784 (2008)
10. S.R. Chowdhury, H. Saha, Maximum power point tracking of partially shaded solar photovoltaic arrays. Sol. Energy Mater. Sol. Cells J. **94**, 1441–1447 (2010)
11. E. Karatepe, M. Boztepe, Colak, development of a suitable model for characterizing photovoltaic arrays with shaded solar cells. Sol. Energy **81**, 977–992 (2007)
12. E. Karatepe, T. Hiyama, M. Boztepe, M. Colak, Voltage based power compensation system for photovoltaic generation system under partially shaded insolation conditions. Energy Convers. Mang. **49**(8), 2307–2316 (2008)
13. C.-C. Chena, H.-C. Changa, C.-C. Kuob, C.-C. Linc, Programmable energy source emulator for photovoltaic panels considering partial shadow effect. Energy **54**, 174–183 (2013)
14. A. Ubisse, A. Sebitosi, A new topology to mitigate the effect of shading for small photovoltaic installations in rural sub-Saharan Africa. Energy Convers. Manag. **50**, 1797–1801 (2009)
15. M.C. Alonso-Garcı, J.M. Ruizb, F. Chenloa CIEMAT, Experimental study of mismatch and shading effects in the I–V characteristic of a photovoltaic module, Sol. Energy Mater. Sol. Cells J. **90**, 329–340 (2006)
16. G. Velasco-Quesada, F. Guinjoan-Gispert, R. Piqué-López, M. Román-Lumbreras, A. Conesa-Roca, Electrical PV array reconfiguration strategy for energy extraction improvement in grid-connected PV systems. IEEE Trans. Ind. Electron. **56**(11), 4319–4331 (2009)

17. L.P. Hayoun, A. Arrigoni, Les installations photovoltaiques, Groupe Eyrolles, ISBN: 978-2-212-12994-6 (2010)
18. Department of Electrical Engineering, King Mongkut''s Institute of Technology Ladkrabang, Bangkok, Thailand, The efficiency improvement of series connected PV panels operating under partial shading condition by using per-panel DC/DC converter, in *The 8th Electrical Engineeringl Electronics, Computer, Telecommunications and Information Technology (ECTI) Association of Thailand—Conference,* (2011)
19. G.R. Walker, Cascaded DC–DC converter connection of photovoltaic modules. IEEE Trans. Power Electron. **19**(4), 1130–1139 (2004)
20. K. Kobayashi, A study of a two stage maximum power point tracking control of a photovoltaic system under partially shaded insolation conditions. Sol. Energy Mater. Sol. Cells **90**, 2975–2988 (2006)
21. A. Bouilouta, A. Mellit, S.A. Kalogirou, New MPPT method for stand-alone photovoltaic systems operating under partially shaded conditions. Energy **55**, 1172–1185 (2013)
22. H. Heydari-doostabada, R. Keypoura, M. Reza Khalghanib, M. Hassan Khoobanc, A new approach in MPPT for photovoltaic array based on extremum seeking control under uniform and non-uniform irradiances. Sol. Energy **94**, 28–36 (2013)
23. D. Lalili, A. Mellit, N. Lourci, B. Medjahed, C. Boubakri, State feedback control and variable step size MPPT algorithm of three-level grid-connected photovoltaic inverter. Sol. Energy **98**, 561–571 (2013)

Chapter 14
High Voltage Gain DC–DC Converter with Low Input Current Ripple for Fuel Cell Source

Mustafa A. Al-Saffar

Abstract A new single-switch non-isolated dc–dc converter with high-voltage gain and reduced semiconductor voltage stress is proposed in this paper. The proposed topology is derived from the conventional boost converter integrated with self-lift Sepic converter for providing high voltage gain without extreme switch duty-cycle. The reduced voltage stress across the power devices enables the use of a lower voltage and $R_{DS\text{-}ON}$ MOSFET switch, and Schottky rectifiers for alleviating the diode's reverse-recovery current problem, leading to a further reduction in the switching and conduction losses. Furthermore, the "near-zero" ripple current can be achieved at the input side of the converter which will help improve the fuel cell stack life cycle. The principle of operation and theoretical analysis are performed. Simulation and experimental results of a 100 W/240 V_{dc} output with 24 V_{dc} input voltage are provided to evaluate the performance of the proposed scheme.

Keywords Boost converter · SEPIC converter · Coupled inductors

14.1 Introduction

Energy shortage and environmental pollution issues have accelerated the use of clean energy resources such as wind, fuel cell stacks and photovoltaic (PV) power systems [1, 2]. However, these renewable energy sources or systems have relatively low voltage output characteristics and demand high step-up voltage gain and high efficiency DC–DC converters, for any potential practical application.

M. A. Al-Saffar (✉)
Electrical Engineering Department, College of Technological Studies,
Kuwait, P.O. Box 35007, 36051 Al-Shaab, Kuwait
e-mail: malsaffar@ieee.org

M. O. Hamdan et al. (eds.), *ICREGA'14 - Renewable Energy: Generation and Applications*, Springer Proceedings in Energy, DOI: 10.1007/978-3-319-05708-8_14,

Practically, the conventional boost converter cannot provide a voltage gain greater than six times its applied voltage due to parasitic components [3]. Moreover, operating the conventional boost converter with extreme duty-cycle degrades the overall conversion efficiency, which will also increase the electromagnetic interference (EMI) levels. Also, the conventional boost converter requires a high current and voltage rated MOSFET; hence, it will require a MOSFET with a higher $R_{DS\text{-}ON}$, which leads to high conduction and switching losses [4]. Furthermore, the conventional boost converter requires a bulky input filter to reduce the large input current ripple. The large input current ripple component may shorten the lifetime of the sources as well as decrease the performance of the overall system [5].

Considerable research efforts have been directed towards the development of efficient high step-up converters. Interleaving two boost converters can significantly minimize the input current ripple and double the transferable power [6, 7]. However; besides the complex control, the voltage stress across the semiconductor devices is similar to the conventional boost converter. Therefore, the conversion efficiency is limited in high-output voltage applications. Cascading two boost converters can increase the voltage gain at the expense of increasing cost and complex control circuitry [8]. Also, cascading boost converters is not suitable for high output voltage applications due to the high reverse recovery energy losses in the output diode. The problem of the complex control in the cascade boost converter can be alleviated by integrating the two switches into one switch [9–11]. An integrated cascade boost converter (also known as quadratic converter) with zero-current and zero-voltage switching (ZC–ZVS) performance is introduced in [12]. However, the switch voltage stress in the quadratic converter is equal to the output voltage. Thus, no advantage over the conventional boost converter is achieved. Also, the switch is subjected to high current stress which increases the conduction losses and degrades the overall conversion efficiency.

The voltage conversion ratio for the converters in [13–15] is quite high and is twice as large as the step-up ratio of the conventional boost converter. This is a very desirable feature for low-voltage energy sources such as fuel cells (FC) or photovoltaic cells. However, for FC-based power systems, it expected from the dc–dc converter to have a low input current ripple as a high current ripple may reduce the lifetime of the FC. Therefore, these converters require a large input inductor value in order to reduce the input current ripple within a certain range. Consequently, this increases the total converter size, cost, and reduces the overall power efficiency. Note that the high input inductance requirement can be reduced by increasing the switching frequency, but this will increase the semiconductor switching losses.

On the contrary, Fig. 14.1 shows the proposed single-switch non-isolated high step-up dc–dc converter with an extended step-up voltage capability. The proposed topology is derived from the conventional boost converter integrated with self-lift Sepic converter [16] for providing high voltage gain without extreme switch duty-cycle. The proposed converter utilizes a single non-floating power switch (Q); hence enabling easy driver circuit.

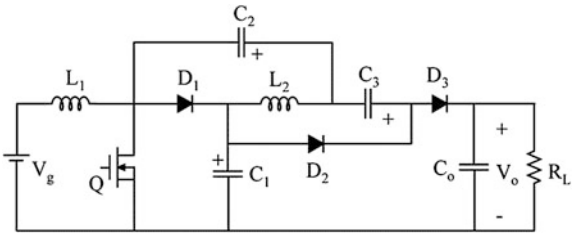

Fig. 14.1 The proposed high step-up non-isolated dc–dc converters

The proposed converter structure utilizes two inductors which are often described as a disadvantage. However, the two inductors can be magnetically coupled into a single magnetic core and near 'zero-ripple-current' can be reached at the input port of the converter without compromising the performance. In addition, the voltage stress across the active power switch is reduced which enables the use of MOSFETs with a lower voltage rating and low $R_{DS\text{-}ON}$. Thus, the conversion efficiency can be improved due to the reduced conduction and switching losses. Similarly, the reduced voltage stress across all the diodes in the circuit allows the use of Schottky rectifiers for alleviating the reverse-recovery current problem, leading to a further reduction in the switching and conduction losses.

14.2 Principle of Operation and Analysis

14.2.1 Continuous Conduction Mode (CCM)

Referring to Fig. 14.1, when the converter operates in CCM, the current ripples through the input inductor L_1 can be assumed negligible. In order to simplify the converter analysis, the following assumptions are made during one switching cycle (T_s): (1) The input voltage is pure dc, (2) All components are ideal, thus the efficiency is 100 %, and (3) All capacitors are sized to have a relatively small voltage ripple at the switching frequency. Under these assumptions, the circuit operation in one switching cycle can be divided into two stages as shown in Fig. 14.2a, b, whereas Fig. 14.3 shows its ideal key waveforms.

Stage 1 [t_0, t_1], Fig. 14.2a: When the power switch Q is turned on, diode D_2 is turned on simultaneously. Diodes D_1 and D_3 are turned off by the voltage $-V_{C1}$ and ($V_{C1} - V_o$) across them, respectively. In this stage, the currents through the two inductors increase linearly at a rate proportional to the input voltage V_g. Capacitor C_1 charges capacitor C_2 while capacitor C_3 is being charged by diode D_2 current ($i_{C2} - i_{L2}$). Referring to Fig. 14.2a, note that the voltage across the capacitor C_1 is

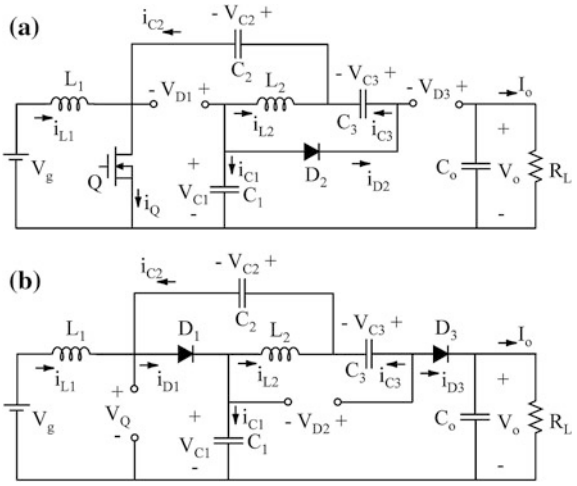

Fig. 14.2 Topological stages in CCM for the converter of Fig. 14.1. **a** Switch ON topology, **b** switch OFF topology

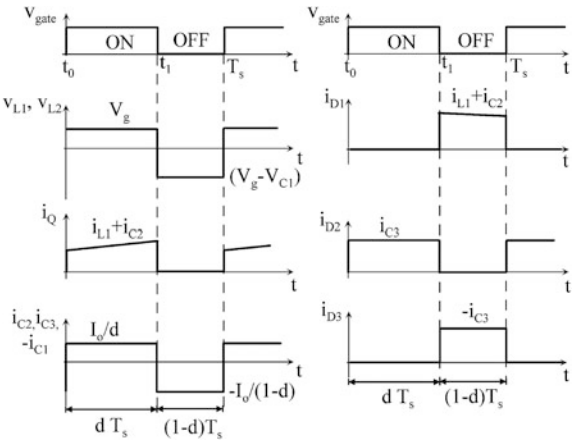

Fig. 14.3 Key waveforms for the proposed converter of Fig. 14.1 in CCM

$$V_{C1} = V_{C2} + V_{C3} \tag{14.1}$$

At the end of this interval, the switch is turned-off initiating the next subinterval.

Stage 2 [t_1, T_s], Fig. 14.2b: At the instant t_1, switch Q is turned off, both diodes D_1 and D_3 are turned on simultaneously providing a path for the input and output inductor currents. Diode D_2 is reverse biased by the voltage ($V_{C1} - V_o$). In this stage, the inductors currents i_{L1} and i_{L2} decrease linearly at a rate proportional to the voltage ($V_g - V_{C1}$). Capacitor C_1 is being charged by the current ($i_{C2} + i_{L1} - i_{L2}$) while C_2 is being discharged by ($i_{L2} + i_{C3}$). During this stage, the output Capacitor C_o and the load R_L are being charged by the capacitor C_3.

Table 14.1 Component stresses for the converter of Fig. 14.1

Circuit parameter	Normalized peak voltage	Normalized rms current
Switch Q	$\frac{1}{2}$	$\frac{M}{\sqrt{M(M-2)}}$
Diode D_1 and D_3	$\frac{1}{2}$	$\frac{1}{\sqrt{2M}}$
Diode D_2	$\frac{1}{2}$	$\frac{1}{\sqrt{M(M-2)}}$
Inductor L_1	–	$\sqrt{1+\frac{1}{12}\left(\frac{(M-2)R_L}{M^3L_1f_s}\right)^2}$
Inductor L_2	–	$\frac{(M-2)R_L}{2\sqrt{3}M^3L_2f_s}$
Capacitor C_1, C_2, and C_3	$M_{C1}=\frac{1}{2}$ $M_{C2}=\frac{M-2}{2M}$ $M_{C3}=\frac{1}{M}$	$\frac{1}{\sqrt{2(M-2)}}$
Capacitor C_o	1	$\frac{1}{M}\times\sqrt{\frac{M-2}{2}}$

Referring to Fig. 14.2b, note that the sum of the voltages across the three capacitors is equal to the output voltage, i.e.

$$V_o = V_{C1} + V_{C2} + V_{C3} \tag{14.2}$$

The volt–second relationship of inductor L_1 and L_2 gives the following relation

$$dV_g + (1-d)(V_g - V_{C1}) = 0 \tag{14.3}$$

where d is the switch duty-cycle. The input to output voltage transfer ratio of the proposed converter can be determined from (14.1)–(14.3) as

$$M = \frac{V_o}{V_g} = \frac{2}{1-d} \tag{14.4}$$

which is twice the conventional boost voltage gain. Table 14.1 shows the component normalized peak voltage and rms current stresses for the proposed converter of Fig. 14.1 in CCM. Voltages and currents are normalized with respect to the output voltage V_o and the average input current I_{L1}, respectively. Note that the normalized switch voltage stress is half the voltage stress on the conventional boost converter. It should be mentioned here that inductor L_2 is an "AC inductor" that operates with zero average current.

14.2.2 Boundaries Between CCM and DICM

The DICM for the proposed converter occurs when the current through diodes D_1 and D_3 drops to zero value before the end of the switch off-time. Therefore, the DICM operation mode requires that the $d + d_2 < 1$, where d_2 is the duty-ratio of diode D_1 and D_3. The condition for DICM operation for the proposed converter is derived and it is given by,

$$K_e < K_{e-crit} = \frac{d(1-d)^2}{4} = \frac{M-2}{M^3} \tag{14.5}$$

where the dimensionless parameter K_e is defined as

$$K_e = \frac{2L_e}{R_L T_s} \tag{14.6}$$

and

$$\frac{1}{L_e} = \frac{1}{L_1} + \frac{1}{L_2} \tag{14.7}$$

Thus, for values of $K_e > K_{e\text{-}crit}$, the converter operates in CCM; otherwise, the converter operates in DICM. The maximum value of $K_{e\text{-}crit}$ is 1/27 at $d = 1/3$ where the voltage gain M_{DICM} is equal to 3.

14.3 The Proposed Converter with Coupled Inductors

Referring to Fig. 14.3, the voltage waveforms across the two inductors L_1 and L_2 are identical. Thus, the two inductors can be magnetically coupled into a single magnetic core as shown in Fig. 14.4. Accordingly, the converter size, weight, and cost are reduced. Moreover, by proper selection of the coupling coefficient, 'near-zero current ripples' at the input inductor L_1 can be achieved without compromising the performance in CCM as well in DICM. This condition is very desirable, because the generated EMI noise is minimized, dramatically reducing input filtering requirements. For FC powered systems, the reduced converter input high frequency current ripple can prevent high frequency interaction inside the FC stack and may extend the fuel cell lifetime cycle.

Referring to Fig. 14.4, the rate of change of the inductor currents i_{L1} and i_{L2} during switch on-time is given by,

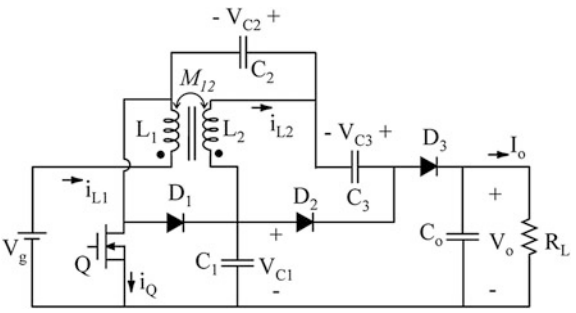

Fig. 14.4 The proposed converter with coupled inductors

$$\begin{bmatrix} \frac{di_{L1}}{dt} \\ \frac{di_{L2}}{dt} \end{bmatrix} = \frac{1}{L_1L_2 - M_{12}^2} \begin{bmatrix} L_2 & -M_{12} \\ -M_{12} & L_1 \end{bmatrix} \begin{bmatrix} V_g \\ V_{C3} \end{bmatrix} \tag{14.8}$$

where

$$M_{12} = k_{12}\sqrt{L_1L_2} \tag{14.9}$$

is the mutual inductance of the windings. At a steady-state, $V_{C3} = V_g$, then from (14.8) the following conditions must be satisfied for zero ripple in the input inductor L_1

$$\frac{di_{L1}}{dt} = \frac{V_g(L_2 - M_{12})}{L_1L_2 - M_{12}^2} = 0 \tag{14.10}$$

Equation (14.10) implies that the ripple at the input inductor can be steered toward L_2 if the following condition is satisfied:

$$M_{12} = L_2 \Rightarrow k_{12} = \sqrt{\frac{L_2}{L_1}} < 1 \tag{14.11}$$

During switch Q off-time, the conditions for zero ripple in the input inductor is similar to that of (14.11). It is important to mention here that the voltage gain for the proposed converter is independent of the magnetic coupling coefficient k_{12}. In other words, the DC voltage gain in (14.4) is valid whether using two separate inductors (2 cores) or two coupled inductors (single core).

14.4 Design Procedure

A step-by-step design procedure is presented in this section, and an example of how to determine the component values of the proposed converter of Fig. 14.1 is given.

14.4.1 Design Guidelines

To illustrate the design procedure, the converter of Fig. 14.1 is designed with the following specifications:

- Input voltage $V_g = 24$ V;
- Output voltage $V_o = 240$ V;
- Output power $P_{out} = 100$ W;
- Switching frequency $f_s = 50$ kHz;
- Maximum peak input current ripple $\Delta i_{L1} = 30$ % of I_{L1};
- Output voltage ripple $\Delta v_o < \pm 0.05$ % of V_o.

From the specifications above, the voltage conversion ratio gain is $M = 10$. Assuming the efficiency is 100 %, the values of the circuit components are calculated as follows:

(a) Switch duty cycle d: from (14.4), the required switch duty cycle d is found as

$$d = \frac{M - 2}{M} = 0.8 \tag{14.12}$$

(b) To achieve the input current ripple requirement, the input inductance value L_1 must be

$$L_1 \geq \frac{V_g^2 d}{2 \times 15\,\% \times f_s \times P_{in}} = 307.2\,\mu H \tag{14.13}$$

(c) The value of the critical conduction parameter $K_{e\text{-}crit}$ can be evaluated from (14.5), and it is given by

$$K_{e-crit} = \frac{M-2}{M^3} = 0.008 \tag{14.14}$$

From (14.6) and (14.14), the minimum value of the equivalent inductance L_e required for CCM operation is

$$L_{e-crit} = \frac{K_{e-crit} R_L}{2f_s} = 46.1\,\mu H \tag{14.15}$$

For CCM operation, the value of L_e must be greater than $L_{e\text{-}crit}$. In this example, we set $L_1 = L_2 = 180\ \mu H$. In this case, evaluating (14.7) gives $L_e = 90\ \mu H$ which is about two times greater than $L_{e\text{-}crit}$. Note that, according to the selected value of L_1, the percentage of the peak current ripple in L_1 is

$$\%\Delta i_{L1} = \frac{V_g d}{2L_1 f_s I_{L1}} \times 100 = 25.6\,\% \tag{14.16}$$

(d) The required output capacitance C_o to maintain a peak-to-peak output voltage ripple of 0.1 % of V_o can be calculated from

$$C_o > \frac{V_o d}{R_L \Delta v_{Co} f_s} = 27.8\,\mu F \tag{14.17}$$

14.5 Simulation Verification and Experimental Results

The proposed converter of Fig. 14.1 has been simulated by PSpice circuit simulator to verify the above design parameters as well as to measure its performance in terms of efficiency. For the simulation, PSpice actual semiconductor models have been used to simulate the switches; STPS10150CT Schottky rectifier (150 V, 5 A, $V_F = 0.75$ V) for the diodes, and IRF6641PBF (200 V, 4.6 A, $R_{DS\text{-}ON} = 51\ m\Omega$) for the power MOSFET switch Q. The capacitors' values are set to 47 μF. Furthermore, an equivalent series resistor (ESR) of 20 mΩ is connected in series with each capacitor and inductor to model its losses.

Figure 14.5 shows the simulated waveforms for the converter of Fig. 14.1 in CCM. Figure 14.5a shows that the input current ripple is about 25 % as predicted by (14.16). Figure 14.5b–d show that the voltage stresses of the power switch Q and diodes D_1 (i.e., $V_{D3} = V_{D1}$) and D_2 are half of the output voltage V_o. Figure 14.5b also shows that the switch turn-on current spike is reduced mainly due to the small peak reverse-recovery currents of D_1 and D_3. The voltage waveforms of

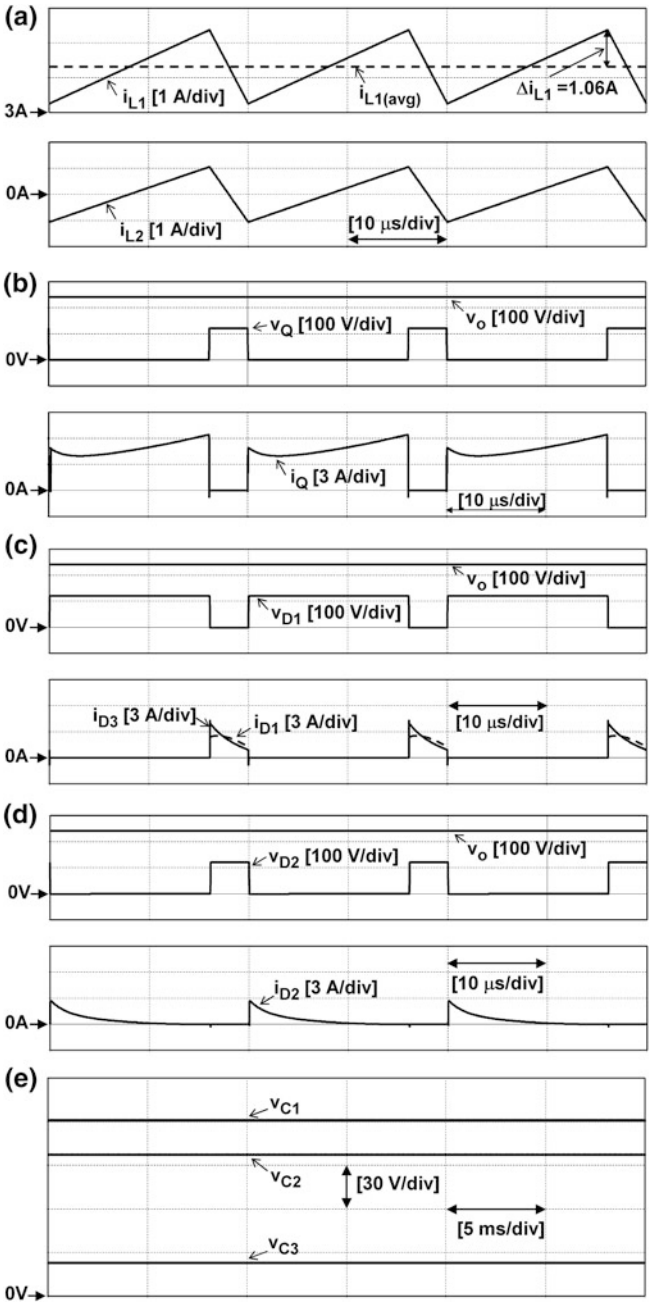

Fig. 14.5 Simulated waveforms for the proposed converter of Fig. 14.1 in CCM (uncoupled inductors case)

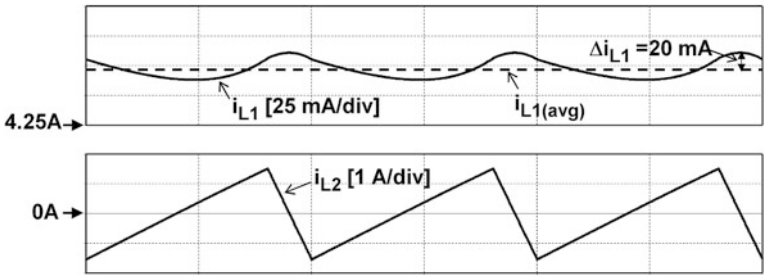

Fig. 14.6 Simulated waveforms for the proposed converter of Fig. 14.4 in CCM (coupled inductors case)

capacitors C_1, C_2, and C_3 are shown in Fig. 14.5e with good agreement with theoretical predictions shown in Table 14.1. The simulated results correctly demonstrate the CCM operating mode with a simulated conversion efficiency of 97.5 %.

To demonstrate the effect of coupling the inductors on the input line current, the circuit of Fig. 14.4 has been simulated with coupled inductors. The circuit parameters were all the same as those for the uncoupled case except for the value of L_2. The value of the coupling coefficients k_{12} is set to 0.83. Hence, according to (14.11), the value of L_2 is 125 μH. The simulated inductors current waveforms are shown in Fig. 14.6, where the high-frequency switching ripples' magnitude in the input current i_{L1} is greatly reduced. Consequently, the generated EMI noise level is greatly minimized as well as the requirement for the input filtering.

To verify the effectiveness of the proposed topology, a 100 W laboratory prototype has been built for the proposed converter of Fig. 14.1 to validate the theoretical prediction as well as the simulation previously described. The circuit parameters of the experimental setup are the same as those used for simulation. The key waveforms of the experimental prototype are depicted in Fig. 14.7.

The input and output voltage waveforms at full power are depicted in Fig. 14.7a, which closely agree with the predicted theoretical voltage gain in (14.4). The waveforms of the two inductors' currents are depicted in Fig. 14.7b for several switching periods which clearly demonstrate the CCM operation. Note that, as predicted the average current in inductor L_2 is zero. Figure 14.7c shows the switch Q voltage and current waveforms over several switching cycles. It is clear from Fig. 14.7c that the switch voltage is clamped to about half the output voltage V_o. Similarly, Fig. 14.7d, e illustrates that the diodes D_1 and D_2 voltage stresses are also clamped to half of the output voltage V_o. The voltage waveforms across capacitors C_1, C_2, and C_3 are shown in Fig. 14.8. These voltages are in a good agreement with theoretical predictions shown in Table 14.1 and with the simulated voltages in Fig. 14.5e. The measured power conversion efficiency is about 95.8 %.

It should be mentioned that the experimental results are obtained in the absence of any snubber circuits and without any special circuit layout. Therefore, it is

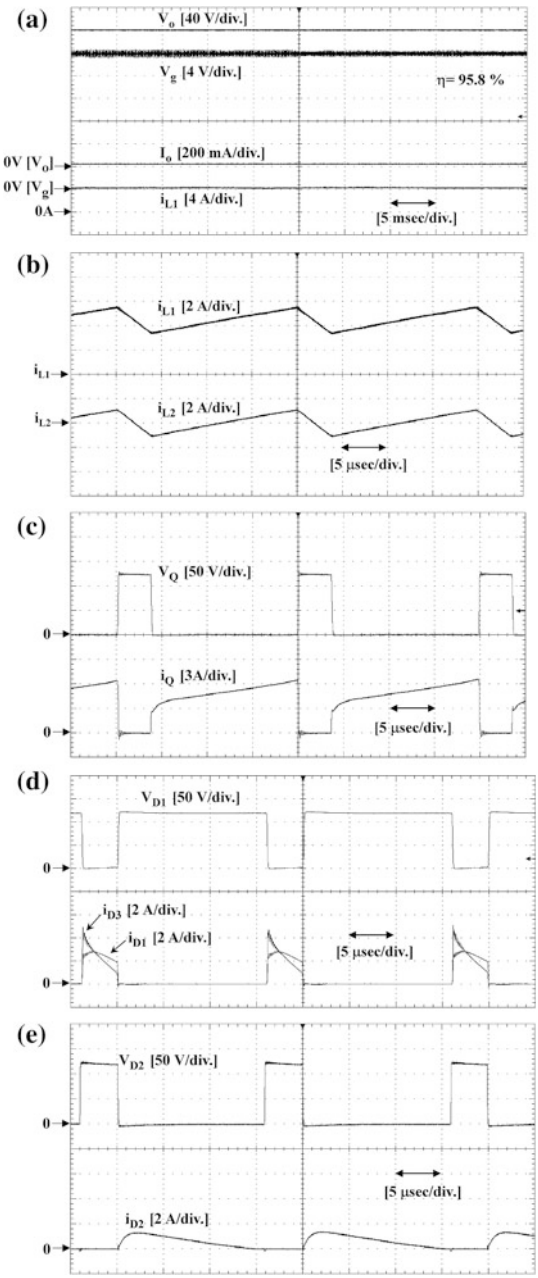

Fig. 14.7 Measured waveforms for the proposed converter of Fig. 14.1

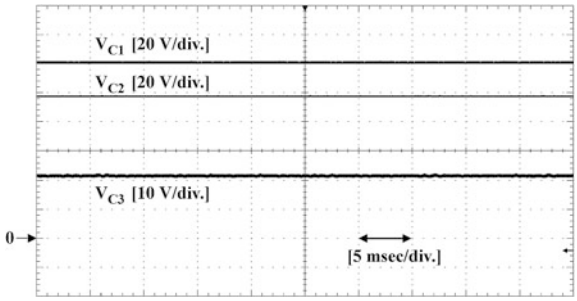

Fig. 14.8 Measured capacitors voltage waveforms for the proposed converter of Fig. 14.1

expected that higher efficiency can be achieved by improving the layout and utilizing better components.

14.6 Conclusion

In this paper, a new high voltage gain single-switch DC–DC converter is proposed. The proposed topology is suitable for several applications such as fuel cell, photovoltaic, and UPS systems, where high voltage gain between the input and output voltages are demanded. The proposed converter is regulated by the conventional PWM technique at constant frequency. The proposed converters can achieve a high step-up conversion ratio without utilizing a line- or high-frequency step-up transformer and also maintain low voltage stress across all semiconductors. The reduced voltage stress across the controlled switch allows utilization of MOSFET with reduced on-resistance. Features of the proposed converters and their operating principles have been discussed in this paper. The simulation and experimental results proved the validity of theoretical analysis and the feasibility of the proposed converter. Finally, the proposed converter can be considered a competitive alternative for practical applications where a high-voltage transfer gain is demanded, such as renewable energy systems, with simple structure and high efficiency.

References

1. M. Kesraoui, N. Korichi, A. Belkadi, Maximum power point tracker of wind energy conversion system. Renewable Energy **32**(10), 2655–2662 (2011)
2. L. Shuhui, A.H. Timothy, L. Dawen, H. Fei, Integrating photovoltaic and power converter characteristics for energy extraction study of solar PV systems. Renewable Energy **36**(12), 3238–3245 (2011)
3. R.W. Erickson, D. Maksimovic, *Fundamentals of Power Electronics*, 2nd edn. (Kluwer Academic Publishers, USA, 2001)

4. W. Li, X. He, Review of nonisolated high-step-up DC/DC converters in photovoltaic grid-connected applications. IEEE Trans. Power Electron. **58**(4), 1239–1250 (2011)
5. M. Gerard, J.P. Crouvezier, D.A. Pera, Ripple current effects on PEMFC aging test by experimental and modeling. J. Fuel Cell Sci. Technol. **8**, 021004-1–021004-5 (2011)
6. B.A. Miwa, D.M. Otten, M.F. Schlecht, High efficiency power factor correction using interleaving technique, IEEE Proc. APEC'92 **1**, 557–568 (1992)
7. X. Huang, Xi. Wang, T. Nergaard, J.-S. Lai, X. Xu, L. Zhu, Parasitic ringing and design issues of digitally controlled high power interleaved boost converters. IEEE Trans. Power Electron. **19**(5), 1341–1352 (2004)
8. R. Haroun, A. Cid-Pastor, A. El Aroudi, L. Marťınez-Salamero, Synthesis of canonical elements for power processing in DC distribution systems using cascaded converters and sliding-mode control. IEEE Trans. Power Electron. **29**(3), 1366–1381 (2014)
9. D. Maksimovic, S. Cuk, Switching converters with wide DC conversion range. IEEE Trans. Power Electron. **6**(1), 151–157 (1991)
10. D.S. Wijeratne, G. Moschopoulos, Quadratic power conversion for power electronics: principles and circuits. IEEE Trans. Circuits Syst. I **59**(2), 426–438 (2012)
11. O. López-Santos, L. Martínez-Salamero, G. García, H. Valderrama-Blavi, D.O. Mercuri, Efficiency analysis of a sliding-mode controlled quadratic boost converter. IET Power Electron. **6**(2), 364–373 (2013)
12. M.A. Al-Saffar, E.H. Ismail, A.J. Sabzali, Family of ZC-ZVS converters with wide voltage range for renewable energy systems. Renewable Energy **56**, 32–43 (2013)
13. M. Prudente, L.L. Pfitscher, G. Emmendoerfer, E.F. Romaneli, R. Gules, Voltage multiplier cells applied to non-isolated DC–DC converters. IEEE Trans. Power Electron. **23**(2), 871–887 (2008)
14. E.H. Ismail, M.A. Al-Saffar, A.J. Sabzali, High conversion ratio DC–DC converters with reduced switch stress. IEEE Trans. Circuits Syst. I Regul. Pap. Fundam. Theory Appl. **55**(7), 2139–2151 (2008)
15. K.I. Hwu, Y.T. Yau, High step-up converter based on charge pump and boost converter. IEEE Trans. Power Electron. **27**(5), 2484–2494 (2012)
16. M. Zhu, F.L. Luo, Series SEPIC implementing voltage-lift technique for DC–DC power conversion. IET Power Electron. **1**(1), 109–121 (2008)

Chapter 15
Integrated Double Boost–SEPIC DC–DC Converter for Renewable Energy Systems

Ahmad J. Sabzali and Esam H. Ismail

Abstract In this paper, an integrated double boost SEPIC (IDBS) converter is proposed as a high step-up converter. The proposed converter utilizes a single controlled power switch and two inductors and is able to provide high voltage gain without extreme switch duty-cycle. The two inductors can be coupled into one core for reducing the input current ripple without affecting the basic DC characteristic of the converter. Moreover, the voltage stresses across all the semiconductors are less than half of the output voltage. The reduced voltage stress across the power switch enables the use of a lower voltage and $R_{DS\text{-}ON}$ MOSFET switch, which will further reduce the conduction losses. Whereas, the low voltage stress across the diodes allows the use of Schottky rectifiers for alleviating the reverse-recovery current problem, leading to a further reduction in the switching and conduction losses. A detailed circuit analysis is performed to derive the design equations. A design example for a 100 W/240 V_{dc} with 24 V_{dc} input voltage is provided. The feasibility of the converter is confirmed with results obtained from simulation and an experimental prototype.

Keywords Integrated DC–DC converters · Non-isolated DC–DC converters · Single-switch DC–DC converters

15.1 Introduction

The world's demand for clean energy sources is growing rapidly and it is driving research for the development of alternative energy technologies. Among various renewable energy sources, wind energy, photovoltaic (PV) cells, and fuel cells

A. J. Sabzali (✉) · E. H. Ismail
Electrical Engineering Department College of Technological Studies,
P.O. Box 35007, 36051 Al-Shaab, Kuwait
e-mail: asebzali@ieee.org

M. O. Hamdan et al. (eds.), *ICREGA'14 - Renewable Energy: Generation and Applications*, Springer Proceedings in Energy, DOI: 10.1007/978-3-319-05708-8_15,

(FC) has gained significant momentum [1, 2]. However, these renewable energy sources have low output voltage characteristics. Thus, due to their low voltage generation as well as high input current requirement, they demand a high efficiency high step-up DC–DC converter to convert and regulate the low DC energy input source into suitable utilization voltage, current, and frequency for use by utility loads. Also, in case of PV and FC applications, it is required that that the interfaced DC–DC converter injects small current ripple into the power source. High current ripple magnitude reduces the energy extracted from both the PV arrays and FC stack as well as it reduces the lifetime of the FC stack [3–5].

Practically, the conventional boost converter cannot provide a voltage gain greater than six times its applied voltage due to parasitic components associated with passive elements components and semiconductor devices [6]. Also, the conventional boost converter requires a high current and voltage rated MOSFET and diode which leads to high conduction and switching losses. Cascading N conventional step-up converters using N number of controllable switches [7–9] or by using a single controlled switch [10–12], can provide a large step-up voltage conversion ratio without extreme duty-cycle operation. However, cascading topologies are not suitable for high output voltage applications due to the high voltage stress across the power switch and the output rectifier which degrades system conversion efficiency and increases size and cost.

The purpose of this paper is to present a new high step-up DC–DC converter without extreme duty-cycle operation and with low input current ripple. We approach this task by integrating a double boost converter with a SEPIC dc–dc converter. The double boost converter is selected due to its high step-up capability [13]. On the other hand, the SEPIC converter is selected due to its capability of providing low input current ripple. Hence, the resultant Integrated Double Boost SEPIC (IDBS) converter allows the duty cycle to be extended further and makes the proposed converter more suitable for high step-up voltage applications. In addition, the proposed converter maintains the key advantages of the conventional boost and SEPIC converters, such as continuous input current, inherent inrush current limitation during startup and overload conditions, inductive components can be integrated on the same core, and reduced electromagnetic interference (EMI) noise.

15.2 The Proposed Topology

Figure 15.1 shows the proposed integrated single-input single-output converter. The voltage conversion ratio for the proposed converter of Fig. 15.1 is the sum of the individual voltage gain of the double boost converter and the SEPIC converter as given by (15.1)

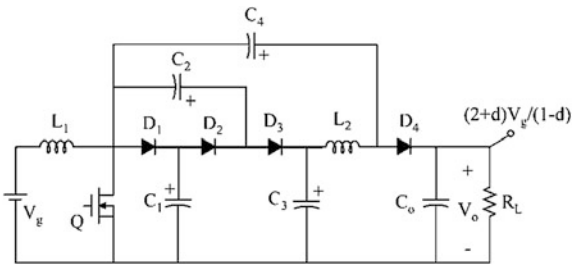

Fig. 15.1 The proposed IDBS converter

$$M = \frac{2 + d}{1 - d} \tag{15.1}$$

where M is the overall voltage gain of the integrated converter. This converter provides an extra voltage gain and it has other advantages such as: (1) Low voltage stress across the active power switch Q, which enables the use of a lower voltage and $R_{DS\text{-}ON}$ MOSFET switch so as to reduce cost, switch conduction and turn-on losses. (2) Low voltage stress across the diodes, which allows the use of Schottky rectifiers for alleviating the reverse-recovery current problem, leading to a further reduction in the switching and conduction losses. (3) Near 'zero-ripple' current at the input port of the converter can be reached without compromising the converter's performance, and (4) Simple control circuit, similar to that of the conventional boost and SEPIC converters.

15.3 Principle of Operation and Analysis

In order to simplify the converter analysis, the following assumptions are made during one switching cycle (T_s): (1) The input voltage is pure dc, and (2) All components are ideal, thus the efficiency is 100 %. (3) All capacitors are sized to have a relatively small voltage ripple at the switching frequency. Under these assumptions, a detailed analysis for the proposed converter of Fig. 15.1 is provided next.

15.3.1 Continuous Conduction Mode (CCM)

Referring to Fig. 15.1, when the converter operates in the continuous conduction mode (CCM), the current ripples through the inductors L_1 and L_2 can be assumed negligible. Accordingly, the circuit operation in one T_s can be divided into two stages as shown in Fig. 15.2a, b, whereas Fig. 15.3 shows its ideal key waveforms. The operational modes are described briefly next.

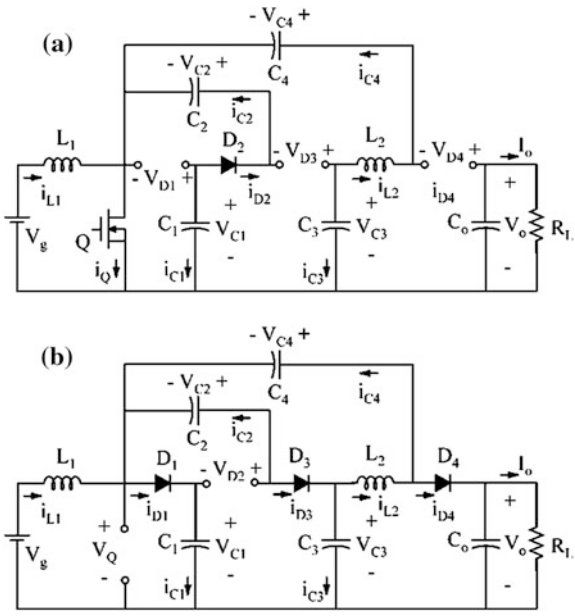

Fig. 15.2 Topological stages for the converter of Fig. 15.1. **a** Switch ON topology, **b** switch OFF topology

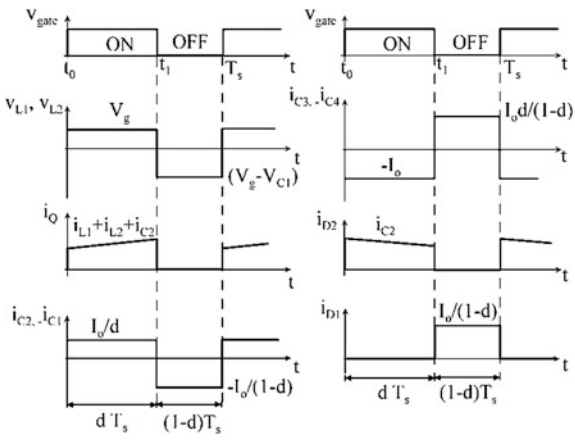

Fig. 15.3 Key waveforms for the proposed converter of Fig. 15.3 in CCM

Stage 1 [t_0, t_1], Fig. 15.2a: When the power switch Q is turned on, diode D_2 is turned on simultaneously. Diode D_1 is reversed-biased by the capacitor voltage V_{C1}, while diodes D_3 and D_4 are turned off by the negative voltage ($V_{C1} - V_{C3}$) and ($V_{C4} - V_o$) across them, respectively. In this stage, the currents through the two inductors increases linearly at a rate proportional to the input voltage V_g. Referring to Fig. 15.2a, the voltage across capacitor C_1 and C_2 are equal, while the difference between the capacitors' voltages V_{C3} and V_{C4} must equal to the input voltage, i.e.,

$$V_{C1} = V_{C2} \tag{15.2}$$

$$V_g = V_{C3} - V_{C4} \tag{15.3}$$

At the end of this interval, the switch is turned-off initiating the next subinterval.

Stage 2 [t_1, T_s], Fig. 15.2b: At the instant t_1, switch Q is turned off, diodes D_1, D_3, and D_4 are turned on simultaneously providing a path for the input and output inductor currents. Diode D_2 is reverse biased by the voltage V_{C2}. In this stage, the inductors currents i_{L1} and i_{L2} decreases linearly at a rate proportional to the voltage $(V_g - V_{C1})$ and $(V_{C3} - V_o)$, respectively. Capacitors C_1 and C_3 are being charged by the currents $(i_{L1} + i_{C2} + i_{C4})$ and $(i_{D3} - i_{L2})$, respectively. Referring to Fig. 15.2b, the following relations must hold:

$$V_o = V_{C3} + V_{C4} - V_{C2} \tag{15.4}$$

$$V_{C3} = 2V_{C1} \tag{15.5}$$

The volt–second relationship of inductor L_1 and L_2 gives the following relations

$$dV_g + (1 - d)(V_g - V_{C1}) = 0 \tag{15.6}$$

The input to output voltage transfer ratio of the proposed converter can be determined from (15.2)–(15.6) as given by (15.1), which is equal to the sum of double boost and SEPIC conversion ratios. On the other hand, the normalized switch voltage stress is given by

$$M_Q = \frac{V_Q}{V_o} = \frac{M + 1}{3\,M} \tag{15.7}$$

It is clear from (15.7) that the switch voltage stress decreases as the voltage gain M increases, approaching one third the output voltage in the limit. Thus, the switch voltage stress for the proposed converter is less than that of the double boost converter. The diodes in the circuit of Fig. 15.1 are subjected to the same voltage stress as given by (15.7).

15.3.2 Boundaries Between CCM and DICM

The DICM operation mode requires that the sum of the duty cycle and the normalized switch off-time length to be less than one, i.e.

$$d + d_2 < 1 \tag{15.8}$$

Therefore, the condition for DICM for this converter can be obtained as,

$$K_e < K_{e-crit} = \frac{d(1-d)^2}{3\,(d+2)} = \frac{M-2}{M(M+1)^2} \tag{15.9}$$

Thus, for values of $K_e < K_{e\text{-}crit}$, the converter operates in DICM; otherwise, the converter operates in CCM. The maximum value of $K_{e\text{-}crit}$ is 21.3×10^{-3} at $d = 0.303$.

15.3.3 Component Stresses

Table 15.1 shows the component normalized peak voltage and current stresses for the proposed converter of Fig. 15.1 in CCM. Voltages and currents are normalized with respect to the output voltage V_o and the average input current I_{L1}, respectively. These equations are given for design purposes. Referring to Table 15.1, it is clear that the semiconductor devices in the proposed topology are subjected to a lower voltage stress. The reduced voltage stress on the semiconductor devices allows the use of a low-voltage-rated power MOSFET with lower R_{DS-ON}, as well as enabling the use of Schottky diodes for alleviating the reverse-recovery current problem; hence, the circuit efficiency can be improved by reducing both the conduction and switching losses. Table 15.1 also shows that the diodes rms current are below the average input current whereas the switch rms current value approaches the average input current as the voltage gain M increase.

15.4 The Proposed Converter with Coupled Inductors

Referring to Fig. 15.3, the voltage waveforms across the two inductors L_1 and L_2 are identical. Thus, the two inductors can be magnetically coupled into a single magnetic core as shown in Fig. 15.4. Accordingly, the converter size, weight, and cost are reduced. Moreover, by proper selection of the coupling coefficients (k_{12}), 'near-zero current ripples' at the input inductor L_1 can be achieved without compromising performance. This condition is very desirable, because the generated EMI noise is minimized, dramatically reducing input filtering requirements. For FC powered system, the reduced converter input high frequency current ripple can prevent high frequency interaction inside the FC stack and may extend fuel cell lifetime cycle. Also, the circuit of Fig. 15.4 can draw free ripple current in the input port not only in CCM but in DICM as well, where the high switching ripple is of concern. This is a very attractive feature for power factor correction (PFC)

Table 15.1 Component stresses for the converter of Fig. 15.1

Circuit parameter	Normalized peak voltage	Normalized rms current
Switch Q	$\frac{M+1}{3M}$	$\frac{(M-1)}{M}\sqrt{\frac{M+1}{M-2}}$
Diode D_2	$\frac{M+1}{3M}$	$\frac{1}{M}\sqrt{\frac{M+1}{M-2}}$
Diode D_1,D_3, and D_4	$\frac{M+1}{3M}$	$\frac{1}{M}\sqrt{\frac{M+1}{3}}$
Inductor L_1	–	$\sqrt{1+\frac{1}{12}\left(\frac{(M-2)R_L}{(M+1)M^2L_1 f_s}\right)^2}$
Inductor L_2	–	$\sqrt{1+\frac{1}{12}\left(\frac{(M-2)R_L}{(M+1)ML_2 f_s}\right)^2}$
Capacitor C_1, and C_2	$\frac{M+1}{3M}$	$\frac{M+1}{M\sqrt{3(M-2)}}$
Capacitor C_3	$\frac{2(M+1)}{3M}$	$\frac{1}{M}\times\sqrt{\frac{M-2}{3}}$
Capacitor C_4	$\frac{2M-1}{3M}$	$\frac{1}{M}\times\sqrt{\frac{M-2}{3}}$
Capacitor C_o	1	$\frac{1}{M}\times\sqrt{\frac{M-2}{3}}$

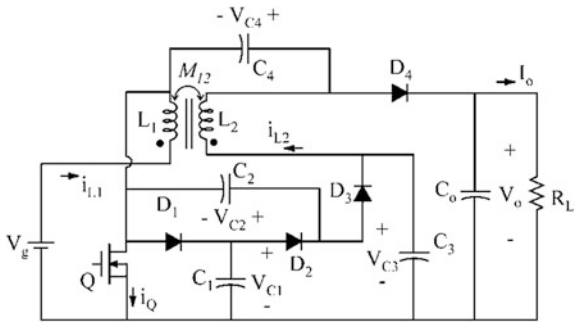

Fig. 15.4 The proposed converter of Fig. 15.1 with coupled inductors

applications since it will minimize the EMI effect and the input filtering stage. In reality, the ripple current is not exactly reduced to zero but is highly reduced. The reason for this is due to integer number of turns, and the voltages across the inductors are not exactly identical due to inductor equivalent series resistance (ESR) and the ripple voltage across the individual capacitors.

Referring to Fig. 15.4, the rate of change of the inductor currents i_{L1} and i_{L2} during switch on-time is given by,

$$\begin{bmatrix}\frac{di_{L1}}{dt}\\ \frac{di_{L2}}{dt}\end{bmatrix}=\frac{1}{L_1L_2-M_{12}^2}\begin{bmatrix}L_2 & -M_{12}\\ -M_{12} & L_1\end{bmatrix}\begin{bmatrix}V_g\\ V_{C3}-V_{C4}\end{bmatrix} \tag{15.10}$$

where

$$M_{12} = k_{12}\sqrt{L_1 L_2} \tag{15.11}$$

is the mutual inductance of the windings. At steady-state, (15.3) shows that $V_{C3} - V_{C4} = V_g$, then from (15.10) the following conditions must be satisfied for zero ripple in the input inductor L_1

$$\frac{di_{L1}}{dt} = \frac{V_g(L_2 - M_{12})}{L_1 L_2 - M_{12}^2} = 0 \tag{15.12}$$

Equation (15.12) implies that the ripple at the input inductor can be steered toward L_2 provided the following condition is satisfied:

$$M_{12} = L_2 \Rightarrow k_{12} = \sqrt{\frac{L_2}{L_1}} < 1 \tag{15.13}$$

During switch Q off-time, the conditions for zero ripple in the input inductor is similar to that of (15.13). It is important to mention here that the voltage gain for the proposed converter is independent of the magnetic coupling coefficient k_{12}. In other words, the DC voltage gain in (15.1) is valid whether using two inductors on two separate cores or two coupled inductors (single core). It should be also mentioned here that the 'near-zero ripples' in input current feature can also be obtained in the conventional Cuk and SEPIC converter using coupled inductors [14–16]. However, the proposed converter has an advantage of a higher voltage gain, reduced switch and diode voltage stresses.

The steady-state analysis presented in Sect. 15.3 for the uncoupled inductors is also valid for the coupled-inductor case, except for the value of inductor L_2. Since L_2 determines the switching current ripple, then the minimum required value for L_2 which ensure CCM operation can be found as

$$L_2 > \frac{(M-2)R_L}{f_s M(M+1)^2} \tag{15.14}$$

Once the value of L_2 is selected, the value of L_1 can be calculated from (15.13).

The capacitors are generally selected to limit voltage ripple to the level required by the design specification. Referring to Fig. 15.3, the peak-to-peak voltage ripple across the capacitors C_1 and C_2 in the proposed converter can be determined as

$$\Delta v_{Cn} = \frac{V_o}{R_L C_n f_s}, \quad n = 1, 2 \tag{15.15}$$

whereas the peak-to-peak voltage ripple across capacitors C_3, C_4, and C_o is given by

$$\Delta v_{Cn} = \frac{dV_o}{R_L C_n f_s}, \quad n = 3, 4, 0 \tag{15.16}$$

Also, selection of capacitors C_1, C_2, C_3, and C_4 must ensure that the converter does not operate in discontinuous-capacitor-voltage-mode (DCVM). Therefore, the resonant frequencies of (L_1, C_1), (L_2, C_2, C_4) and (L_2, C_3, C_4) should be lower than the switching frequency f_s to assure the capacitor voltages V_{C1}, V_{C2}, V_{C3}, and V_{C4} to be constant in a switching period.

15.5 Simulation and Experimental Results

Circuit simulation tests were conducted for the proposed converter of Fig. 15.1. The converter of Fig. 15.1 is simulated for the following input and output data specifications: $V_g = 24$ V, $V_o = 240$ V, $P_o = 100$ W, and $f_s = 50$ kHz. The inductor values are set to 1 mH with an equivalent series resistor (ESR) of 20 mΩ, whereas the values of the capacitors are set to 47 μF with ESR = 20 mΩ. Furthermore, Pspice actual semiconductor models have been used to simulate the switches; STPS10150CT Schottky rectifier (150 V, 5 A, $V_F = 0.75$ V) for the diodes and IRFB5615PBF (150 V, 35 A, R_{DS}-ON = 39 mΩ) for the active switch Q.

Figure 15.5 shows the simulated waveforms for the proposed converters of Fig. 15.1 in CCM. Diode D_3 and D_4 voltage waveforms are not shown since they are similar to diode D_1 voltage waveform. It is evident from Fig. 15.5b that the switch and diodes voltage stress are below half of the output voltage which confirm the theoretical predicted result given in Table 15.1. The current waveforms through the semiconductors devices are shown in Fig. 15.5c. It is evident from Fig. 15.5c that when the switch Q conducts, the diodes D_1, D_3, and D_4 are in their reverse biased state. The voltage waveforms of capacitors C_1, C_2, C_3, and C_4 are shown in Fig. 15.5d with good agreement with theoretical predictions shown in Table 15.1. The simulated results correctly demonstrate the CCM operating mode with simulated conversion efficiency of 97.8 %.

In order to demonstrate the effect of coupling the inductors on the input line current, the circuit of Fig. 15.4 has been simulated with coupled inductors. The circuit parameters were all the same as those for the uncoupled case except for the value of L_2. The value of the coupling coefficients k_{12} is set to 0.7. Hence, according to (15.13), the value of L_2 is 500 μH. The simulated inductors current waveforms are shown in Fig. 15.6.

It is clear from Fig. 15.6 that the high-frequency switching ripples' magnitude in the input current i_{L1} is greatly reduced (1.5 mA) due to the coupling of the two inductors. Figure 15.6 shows the peak-to-peak ripple in the input current is only 1.5 mA compared to 349 mA as shown in Fig. 15.5a. The current ripple in L_1 is steered into L_2 winding leaving DC component in L_1 winding. Consequently, the

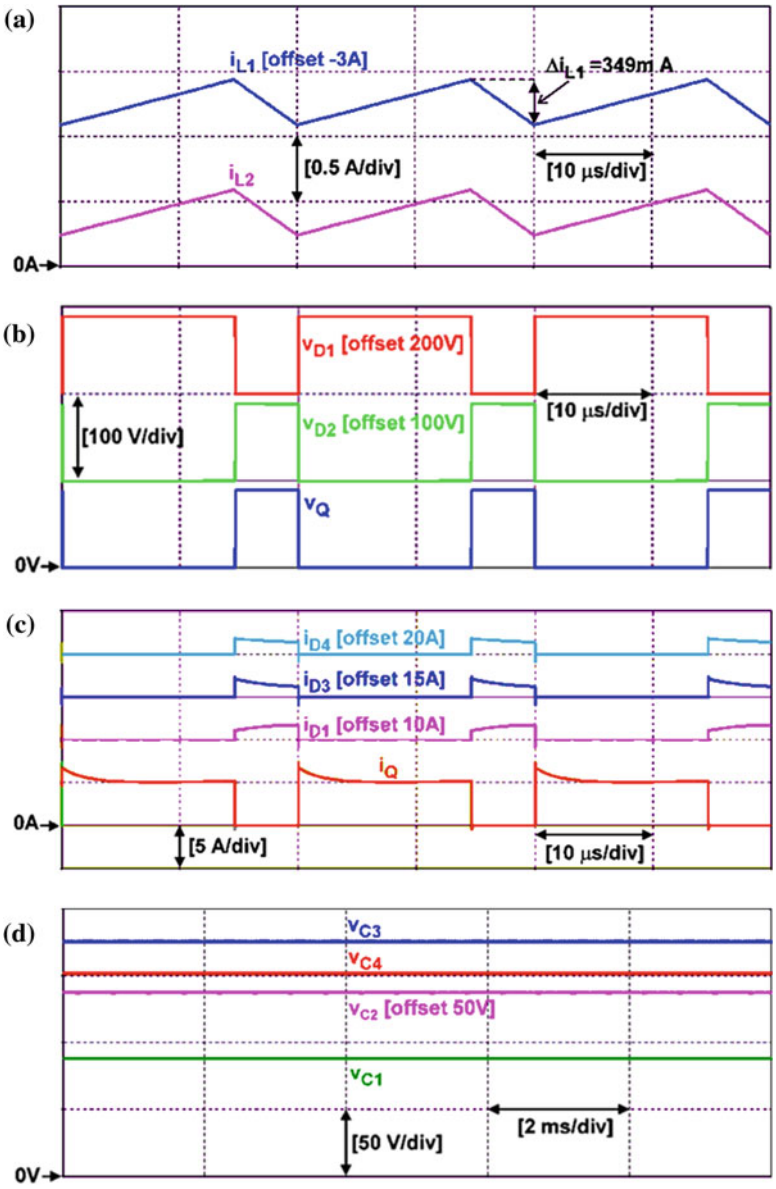

Fig. 15.5 Simulated waveforms for the proposed converter of Fig. 15.1 in CCM

generated EMI noise level is greatly minimized as well as the requirement for the input filtering.

In order to validate the theoretical analysis and simulation results of the proposed topology, the circuit of Fig. 15.1 has been constructed and tested. The

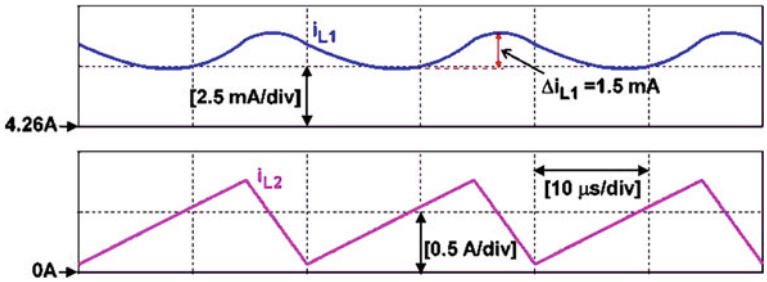

Fig. 15.6 Simulated waveforms for the converter of Fig. 15.4

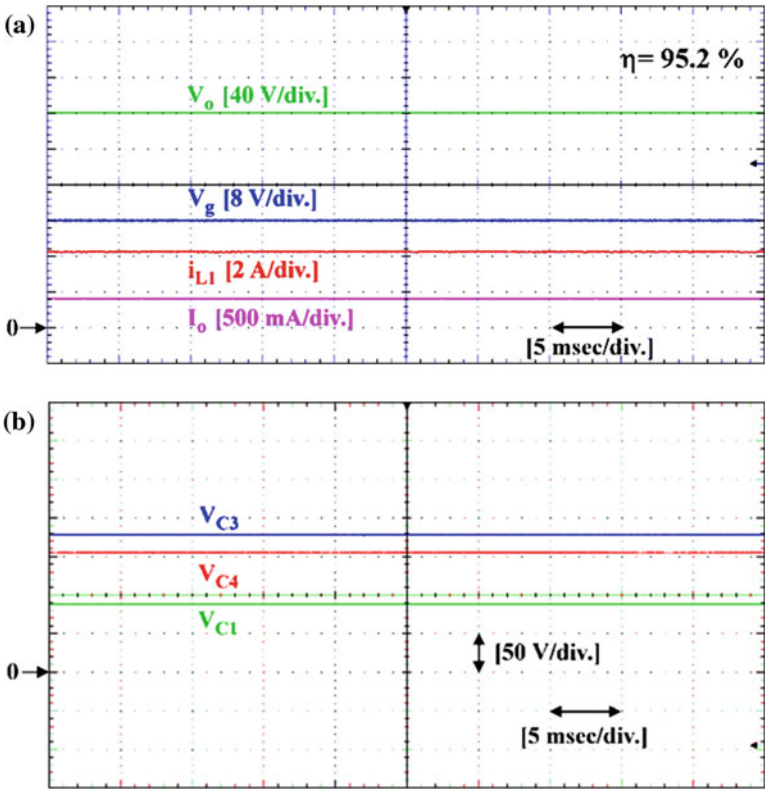

Fig. 15.7 Experimental waveforms for the converter of Fig. 15.1

circuit parameters of the experimental setup are the same as those used for simulation except for the inductors L_1. The inductance value for L_1 is 180 μH with an ESR value of 45 mΩ. It should be mentioned here that the selection of the

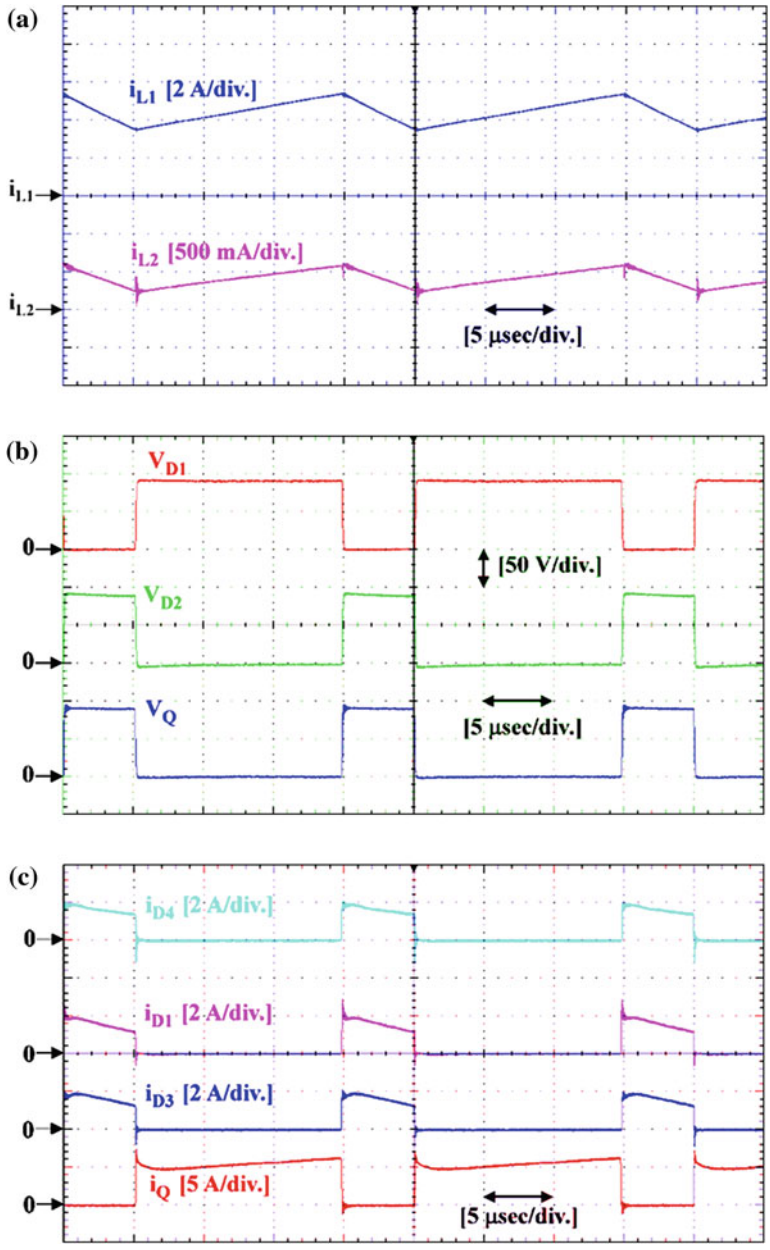

Fig. 15.8 Experimental switching waveforms for the converter of Fig. 15.1

inductors L_1 and L_2 was based on part availability (off-the-shelf components) more than any other factor. The switch duty-cycle is set to 0.73 according to (15.1). The converter is designed to operate in CCM under open-loop conditions.

The input and output voltage waveforms at full power are depicted in Fig. 15.7a, which closely agree with the predicted theoretical voltage gain in (15.1). The voltage waveforms across capacitors C_1, C_3, and C_4 are shown in Fig. 15.7b. Capacitor C_2 voltage waveform is not shown since it is similar to the C_1 voltage waveform. These voltages are in a good agreement with theoretical predictions shown in Table 15.1 and with the simulated voltages in Fig. 15.5d. The waveforms of the two inductors' currents are depicted in Fig. 15.8a for several switching periods which clearly demonstrates CCM operation. Figure 15.8b shows the measured switching voltage waveforms across the switch Q and diodes D_1 and D_2. Diode D_3 and D_4 voltage waveforms are not shown since they are similar to diode D_1 voltage waveform. It is apparent from Fig. 15.8b that the switch and diodes voltage stress are clamped to about 90 V which is below half of the output voltage which confirm the theoretical predicted result given in Table 15.1. Finally, Fig. 15.8c depicts the switching current waveforms through the switch Q and through other diodes in the circuit except for diode D_2. It is clear from Fig. 15.8c that when the switch Q conducts the diodes D_1, D_3, and D_4 are in their OFF state. The measured efficiency of the prototype converter is about 95.2 % as shown in Fig. 15.7a.

15.6 Conclusion

This paper has presented a new high gain single-switch PWM converter with continuous input current, and reduced voltage stress on all the semiconductors. The input current ripple can be greatly reduced to near-zero level due to the utilization of a coupled inductor techniques which makes the proposed converter well suited for PV and FC energy sources. The lack of both a transformer and an extreme duty cycle permits the proposed converter to operate at high switching frequencies. Hence, the overall advantages will be: higher efficiency, reduced size and weight, simpler structure and control.

The steady-state operational analysis is discussed to explore the advantages of the proposed converter. The performance of the converter is verified by means of circuit simulation and experimental tests which confirm the operating principles of the proposed converter.

The proposed integration technique can be easily extended to other power converters to meet the demand for a wide range of voltages.

References

1. M. Kesraoui, N. Korichi, A. Belkadi, Maximum power point tracker of wind energy conversion system. Renewable Energy **36**(10), 2655–2662 (2011)
2. L. Shuhui, A.H. Timothy, L. Dawen, H. Fei, Integrating photovoltaic and power converter characteristics for energy extraction study of solar PV systems. Renewable Energy **36**(12), 3238–3245 (2011)

3. W. Li, X. He, Review of nonisolated high-step-up dc/dc converters in photovoltaic grid-connected applications. IEEE Trans. Ind. Electron. **58**(4), 1239–1250 (2011)
4. T. Esram, P.L. Chapman, Comparison of photovoltaic array maximum power point tracking techniques. IEEE Trans. Energy Conv. **22**(2), 439–449 (2007)
5. M. Gerard, J.P. Crouvezier, D.A. Pera, Ripple Current Effects on PEMFC aging test by experimental and modeling. J. Fuel Cell Sci. Technol. **8,** 021004-1–021004-5 (2011)
6. R.W. Erickson, D. Maksimovic, *Fundamentals of Power Electronics*, 2nd edn. (Kluwer, New York, 2001)
7. T.F. Wu, T.H. Yu, Unified approach to developing single-stage power converters. IEEE Trans. Aerosp. Electron. Syst. **34**(1), 211–223 (1998)
8. L. Huber, M.M. Jovanovic, A design approach for server power supplies for networking applications. IEEE Appl. Power Electron. Conf. **2**, 1163–1169 (2000)
9. R. Haroun, A. Cid-Pastor, A. El Aroudi, L. Marínez-Salamero, Synthesis of canonical elements for power processing in DC distribution systems using cascaded converters and sliding-mode control. IEEE Trans. Power Electron. **29**(3), 1366–1381 (2014)
10. J.L. Ramos, M.G.O. Lopez, L.H.D. Saldierna, J.A. Morales-Saldana, Switching regulator using a quadratic boost converter for wide DC conversion ratios. IET Power Electron. **2**(5), 605–613 (2009)
11. D.S. Wijeratne, G. Moschopoulos, Quadratic power conversion for power electronics: principles and circuits. IEEE Trans. Circuits Syst. I **59**(2), 426–438 (2012)
12. O. López-Santos, L. Martínez-Salamero, G. García, H. Valderrama-Blavi, D.O. Mercuri, Efficiency analysis of a sliding-mode controlled quadratic boost converter. IET Power Electron. **6**(2), 364–373 (2013)
13. M. Prudente, L.L. Pfitscher, G. Emmendoerfer, E.F. Romaneli, R. Gules, Voltage multiplier cells applied to non-isolated DC–DC converters. IEEE Trans. Power Electron. **23**(2), 871–887 (2008)
14. S. Cuk, R.D. Middlebrook, Advances in switched-mode power conversion part II. IEEE Trans. Ind. Electron. **30**(1), 19–29 (1983)
15. E.H. Ismail, A.A. Fardoun, A.A. Zerai, Step-up/step-down DC–DC converter with near zero input/output current ripples. Int. J. Circuit Theory Appl. **42**(4), 358–375 (2014)
16. A.A. Fardoun, E.H. Ismail, A.J. Sabzali, M.A. Al-Saffar, Bidirectional converter for high-efficiency fuel cell powertrain. J. Power Sources **249**, 470–482 (2014)

Chapter 16
Low Cost Controller for Wave Energy Converter

Addy Wahyudie, Mohammed Jama, Omsalama Said, Ali Assi and Hassan Noura

Abstract This study addresses a low computation cost controller for maximizing energy absorption of a point absorber in wave energy converters (WEC). The objective can be achieved by ensuring the perfect tracking between the buoy's velocity and its reference. In particular, the sliding mode control (SMC) is proposed for achieving the maximum energy in WEC. The SMC is considered to be a low cost controller because it is a fixed controller and tuned offline. In order to prove the effectiveness of the SMC, a computer simulation is conducted using the actual polychromatic ocean wave. The proposed controller is tested under the nominal case and its perturbations. The perturbation scenario considers the un-model dynamic of the losses force and perturbation in the excitation force. For the sake of comparison, another low cost controller so called passive reactive controller is simulated under the same condition with the proposed SMC.

16.1 Introduction

Ocean offers a large potential power (up to 10 TW) with a significant average power density (0.5 kW/m) [1, 2]. Wave energy converter (WEC) is device that transforms the ocean energy to electricity. There are many topologies of the WEC and point absorber is the simplest topology of WEC [3]. The conceptual structure of a point absorber is depicted in Fig. 16.1. The point absorber basically consists of a floater, a rod, and a permanent linear magnet generator.

A. Wahyudie (✉) · M. Jama · O. Said · H. Noura
UAE University, 15551 Al Ain, UAE
e-mail: addy.w@uaeu.ac.ae

A. Assi
Lebanese International University, Beirut, Lebanon
e-mail: ali.assi@liu.edu.le

M. O. Hamdan et al. (eds.), *ICREGA'14 - Renewable Energy: Generation and Applications*, Springer Proceedings in Energy, DOI: 10.1007/978-3-319-05708-8_16,

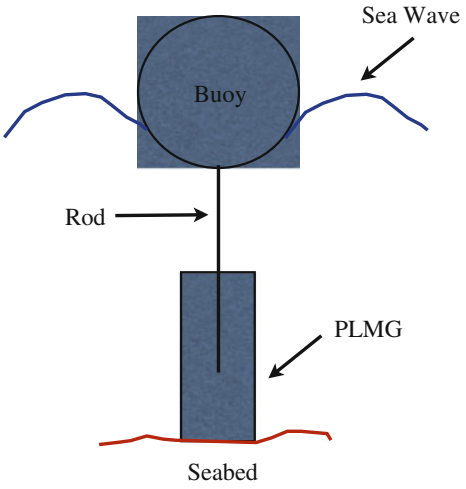

Fig. 16.1 Heaving point absorber structure

In order to maximize the energy absorption from the WEC, the buoy's velocity must be in phase with the excitation force [4, 5]. In the point of view of control engineering, this is a tracking problem between the buoy's velocity and the excitation force. There many control strategies to achieves this for WEC systems. Simple latching control is used in [6]. Auto-tuning fuzzy logic control is used in [7–9]. Model predictive control is used in [10, 11].

In this study, we consider a low cost computation control strategies for maximizing energy absorption in WEC system. This because most of the previous studies used high computation cost method for controlling the WEC such as model predictive control, auto-tuning fuzzy logic control, etc. Although those methods gave satisfactory performances, the applicability in the practical use is under question. In other side, there is a few studies used a low cost controller such as the latching method, passive reactive control (PRC), etc. However, those methods can only perform well in a specific condition. Here, we used sliding mode control (SMC) for maximizing the energy absorption in the WEC. The SMC is well known for its robustness property against parameter perturbations and external disturbance. The SMC is tuned offline and has fixed structure/parameters during the operation. Therefore, the SMC provides a very low cost controller for the WEC. This study is continuation from previous works in [12, 13]. In this paper the proposed SMC is tested against more challenging perturbations compare to the previous works.

The paper is organized as follows. Section 16.2 discusses the dynamic model of heaving WEC. The proposed control strategies are described in Sect. 16.3. The simulation results and comparison of the two control strategies are presented in Sect. 16.4. Finally, conclusions are given in Sect. 16.5.

16.2 Modeling

The model of single-body heaving WEC is highly nonlinear because of the interaction oscillating bodies (together with its PTO and control circuit) with incident waves [6]. The nonlinear model of WEC can be simplified using a linear model if the small excursion of the buoy is allowed. When the linear is used, the motion of the buoy can be formulated using the following the second order Newton law [14],

$$f_e(t) - f_r(t) - f_b(t) - f_{los}(t) - f_u(t) = m\,\ddot{z}(t) \tag{16.1}$$

where $f_e(t), f_r(t), f_b(t), f_{los}(t)$, and f_u are the excitation, radiation, buoyancy, losses and control forces, respectively. Constant m is the total mass of the buoy and the PMLG translator. Variable $\ddot{z}(t)$ is the vertical acceleration of the buoy.

For ideal free motion of the buoy (i.e., without f_u and f_{loss}), the WEC model (16.1) can be written as

$$[m + m_\infty]\,\ddot{z}(t) + \int_0^t (t-\tau)\dot{z}(\tau)d\tau + c_b z(t) = f_e(t). \tag{16.2}$$

The constants m_∞ and c_b are the infinite added mass and the buoyancy stiffness coefficient, respectively. Constant m_∞ is appeared because of the existence of f_r that is formulated in convolution term. The radiation convolution term can be approximated using the fourth order transfer function as suggested in [15].

16.3 Controller Design

The proposed feedback control system is shown in Fig. 16.2. The wave elevation η is converted to the excitation force f_e using the excitation force generator. This block is composed using the method in [15]. The reference velocity $\dot{z}_r$ is generated using the reference signal generator. The transfer function of the reference signal generator is

$$\frac{\dot{z}_r}{f_e} = \frac{1}{2R_r} \tag{16.3}$$

where R_r is the radiation resistance.

The constant R_r can be computed from solving the linear approximation of the frequency domain radiation kernel K_r using frequency domain identification [14, 15]. K_r in frequency domain is formulated as

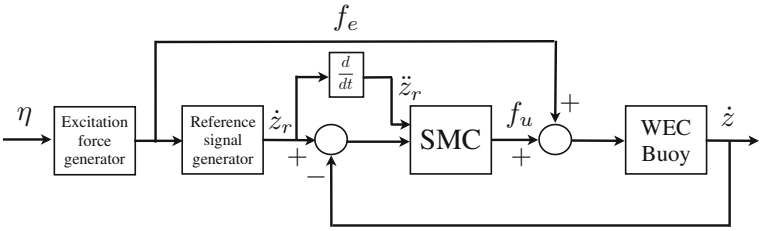

Fig. 16.2 Proposed control system configuration

$$K_r(\omega) = R_r(\omega) + j(\omega)[M_r(\omega) - m_\infty]$$

where $M_r(\omega)$ is the radiation added mass. The last equation can be solved using a software based on boundary element method such as WAMIT [16]. The constant R_r in (16.3) is chosen from the maximum value of the R_r for all operating frequencies of the wave that is obtained from solving the last equation.

The proposed SMC for the point absorber system is derived using the following procedure. Let us define error e as

$$e = z_r - z.$$

We also define the sliding surface s as

$$s = \left(\frac{d}{dt} + \lambda\right)^{n-1} e = 0,$$

with λ is a strictly constant representing the speed of convergence of e to its sliding surface. For second order system, the sliding surface is formulated as

$$s = \dot{e} + \lambda e = 0.$$

Differentiating the sliding surface, the following equation can be obtained

$$\dot{s} = \ddot{e} + \lambda\dot{e} = (\ddot{z}_r - \ddot{z}) + \lambda\dot{e} = 0.$$

Substituting the latter equation with motion equation of buoy in (16.1) and (16.2), the control input is formulated as

$$f_u = m_t\lambda\dot{e} + m_t\ddot{z}_r + f_r + f_b - f_e$$

where

$$m_t = m + m_\infty.$$

In order to give the robustness property to the controlled system, the additional term is added to the control as follows

$$f_u = m_t \lambda \dot{e} + m_t \ddot{z}_r + f_r + f_b - f_e + k\text{sgn}(s)$$

where sgn is the signum function:

$$\begin{aligned} \text{sgn}(s) &= +1 \quad \text{if } s > 0 \\ \text{sgn}(s) &= -1 \quad \text{if } s < 0. \end{aligned}$$

Constant k is a positive real constant. The larger value of k will compensate the larger set of perturbation. However, the larger value of k will make larger value of f_u. Therefore, the value of k is carefully selected so that it can compensate a reasonable value of perturbation while keeping the level of f_u below its maximum value.

The addition of the signum function in the last equation produces chattering control force. From practical point of view, this condition is undesirable because the actuator cannot follow the sudden change of the control force. The chattering control force can be smoothed using the method explained in [17]. Let us define a thin boundary layer neighboring the switching surface

$$B(t) = \{\mathbf{x}, |s(\mathbf{x}; t)| \leq \Phi\} \qquad \Phi > 0$$

where $\mathbf{x}$ is a state in sliding plane, in our case $\dot{z}$ and $\ddot{z}$. Φ is the boundary layer thickness and $\varepsilon = \Phi/\lambda^{n-1}$ is the boundary layer width, as depicted in Fig. 16.3. $B(t)$ is a layer that contains the chattered control input. The chattered control input in $B(t)$ is interpolated by replacing the term sgn(s) by sat s/$\mathbf{\Phi}$. Therefore, the final form of the robust SMC with continuous control input for the system is formulated as

$$f_u = m_t \lambda \dot{e} + m_t \ddot{z}_r + f_r + f_b - f_e + k\,\text{sat}(s/\Phi).$$

For the sake of comparison with the proposed SMC, another low cost controller is used. Here, we use Passive Reactive Control (PRC). The PRC is tuned manually to maximize the capture energy at a single wave frequency (monochromatic). The control force of the PRC is formulated as

$$f_u = -b_u z + c_u \dot{z}$$

where b_u and c_u are the the stiffness and damping coefficients, respectively. The parameters of b_u and c_u are tuned so that excitation force is in phase with the buoy's velocity.

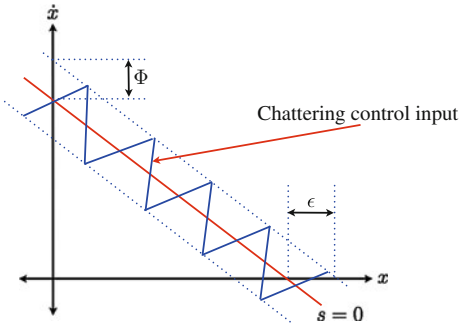

Fig. 16.3 Sliding surface with chattering control input

16.4 Result and Discussion

In this section the simulation setup is explained and followed with the discussion of the computer simulation result.

16.4.1 Simulation Setup

In this study, the polychromatic ocean state is used for simulating the actual ocean environment. In the polychromatic ocean state, multiple frequencies and amplitudes are contained in the wave. The JONSWAP spectrum with the height of 1.5 m and the peak frequency of 0.75 (rad/s) is used [2]. The sea state characteristic, the geometrical of the buoy, and the parameters of the SMC and PRC are given in the Table 16.1. Since the draft of the buoy is 4 m, the buoy is considered completely out or submerged from water surface if the different between the buoy and wave elevation is ±4 m. The extreme excursion of the buoy is not desired because it can physically damage the PLMG. Therefore, the control force must have capability of tracking the velocity reference without causing the extreme excursion of the buoy. The plot between wave elevation and the buoy's position help us to detect the extreme excursion. The simulation is implemented using MATLAB [18]. A fixed step ODE4 solver is used with the sampling time of 0.001 s. The simulation is carried out for the first 140 s and the controller starts at $t = 0$ s.

16.4.2 Simulation Result and Discussion

Let us discuss the free motion of the buoy under no influence of any control force. Figure 16.4 shows the velocity and the elevation of the buoy. The velocity cannot track its reference and thus a small level of energy can be captured from the wave. Reference [19] suggests the calculation of the absorbed energy (W) as follows

Table 16.1 Geometrical parameters of the Buoy, the sea state characteristics, SMC, and PRC

Shape	Sphere
Radius	4 m
Draft	4 m
Seabed depth	60 m
Wave period range	1–13 s
λ	1
k	1×10^6
Φ	1×10^4
b_u	0.85×10^5
c_u	2.2×10^5

$$W = (f_e - f_r)\dot{z}.$$

The absorbed energy from the free motion of buoy is shown in Fig. 16.5. A very small level of energy can be absorbed from the free buoy motion.

The computer simulation result using the proposed SMC for the nominal WEC system can be seen in Fig. 16.6. From the figure, the velocity of the buoy tracks its reference. Therefore, maximum energy can be captured from the wave as depicted in Fig. 16.5. Table 16.2 shows the excursion of the buoy is within its allowable range. The maximum control force for implementing the SMC also within its reasonable range because it has the same order with the excitation force.

For the sake of comparison, the computer simulation result using the PRC for the nominal system is given in Fig. 16.7. The PRC is tuned in monochromatic sea wave with the frequency equal to the maximum frequency of the polychromatic environment. Although the buoy relatively can track its reference, it cannot achieve the same performance with the SMC. This brings a reduction in power capturing in the WEC, as shown in Fig. 16.5. The buoy's elevation and the control force for the PRC are within its allowable level as depicted in Table 16.2.

In order to study the robustness property of the controlled system, the both proposed method is tested in a perturbation scenario. Here, we consider perturbation happens due to unmodel dynamic of the WEC and uncertainty in the excitation force. We do not consider the perturbation in the identified parameters in WEC, since the SMC has been proven maintain its performance under this perturbation case [12, 13]. The unmodel dynamic can be caused by the losses due to friction, viscosity, and non-ideal PTO mechanism. In practice, this force is nonlinear and time variant. However, it is modeled as a linear time-invariant resistive force, that is

$$f_l(t) = R_l\dot{z}$$

where R_l represents the losses damping coefficient. In this simulation, we set the value of $R_l = 4 \times 10^4$. The second type of perturbation is considered to be happened in the excitation force. We assume that there is a delay in the calculation of

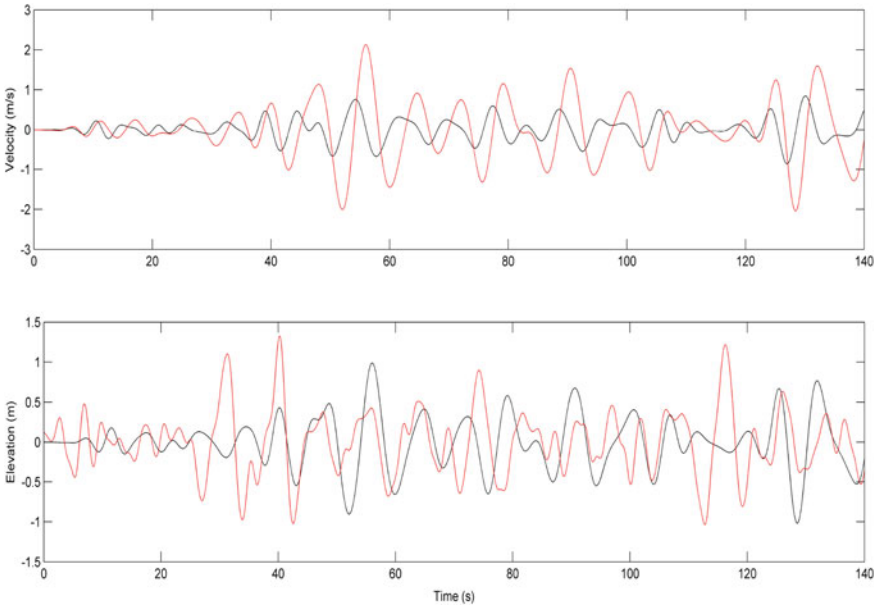

Fig. 16.4 The control simulation for the freely oscillating buoy. *Upper graph* is the buoy's velocity (*black*) and its reference velocity (*red*). *Lower graph* is the buoy's elevation (*black*) and the wave elevation (*red*)

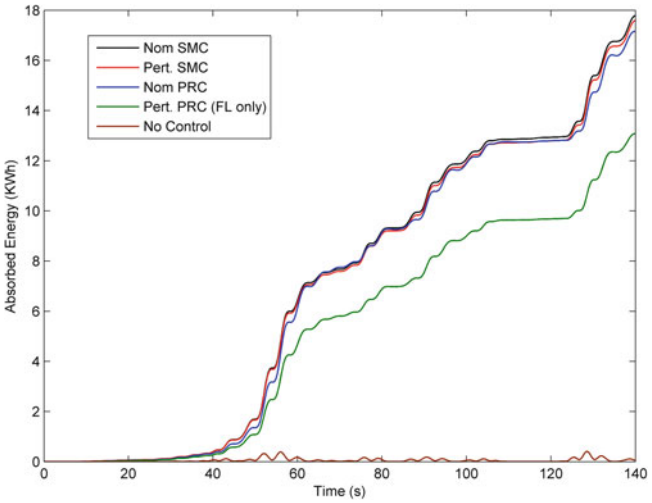

Fig. 16.5 The absorbed energy for various cases

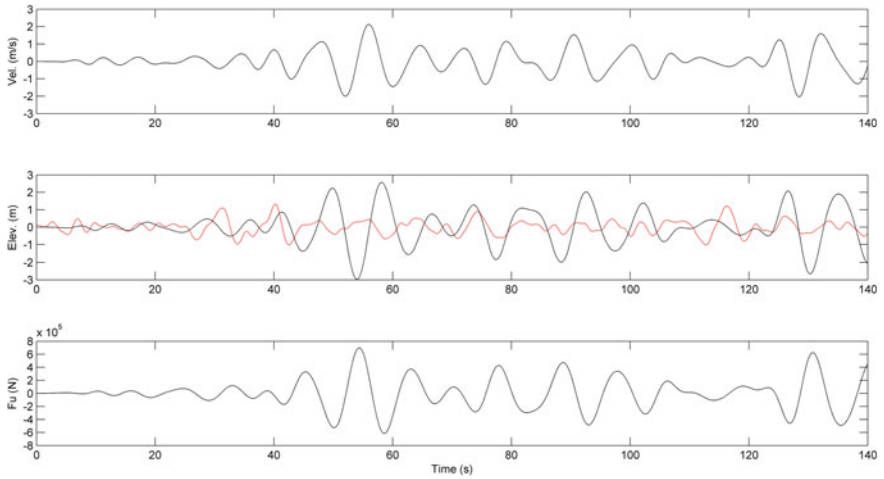

Fig. 16.6 The simulation results using the proposed SMC for the nominal case. *Upper graph* is the velocity of buoy (*black*) and its reference (*red*). The *middle graph* is the buoy's elevation (*black*) and the wave elevation (*red*). The *lower graph* is control force of the SMC

Table 16.2 Absolute values of the maximum Buoy's elevation and control force

Scenario	Maximum elevation (m)	Maximum f_u (N)
Nominal PRC	3.0	6.5×10^5
Nominal SMC	2.6	7.0×10^5
Perturb PRC	2.1	4.6×10^5
Perturb SMC	2.5	6.0×10^5

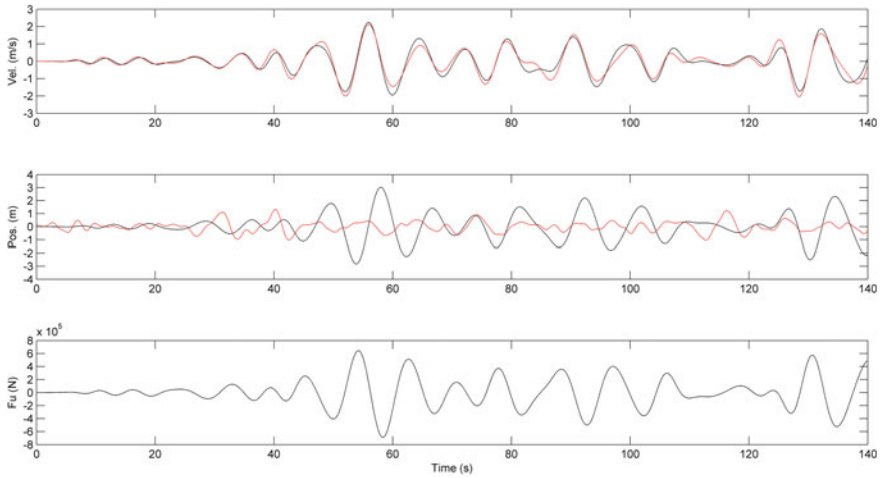

Fig. 16.7 The simulation results using the proposed PRC for the nominal case. *Upper graph* is the velocity of buoy (*black*) and its reference (*red*). The *middle graph* is the buoy's elevation (*black*) and the wave elevation (*red*). The *lower graph* is control force of the PRC

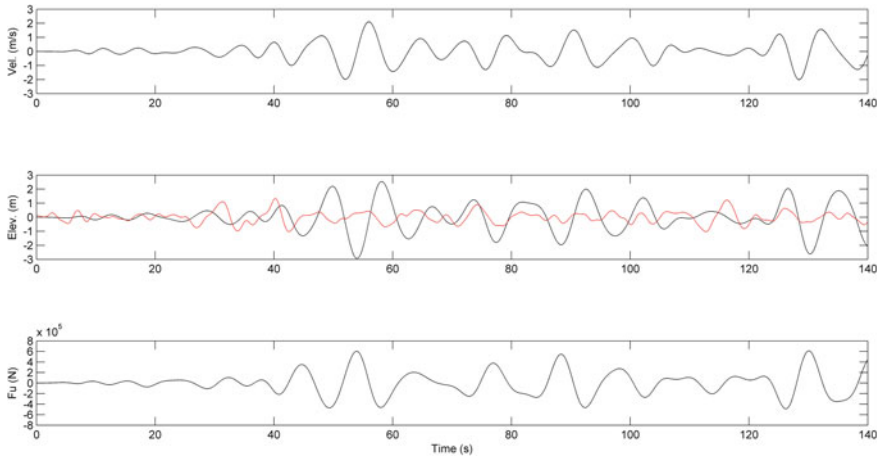

Fig. 16.8 The simulation results using the proposed SMC for the perturbation case. *Upper graph* is the velocity of buoy (*black*) and its velocity reference (*red*). The *middle graph* is the buoy's elevation (*black*) and the wave elevation (*red*). The *lower graph* is control force of the SMC

the excitation force. This is a very challenging scenario for the perturbation, since the excitation force is an uncontrolled input to the WEC. The delay causes the calculated excitation force completely different in phase and amplitude with the actual excitation force. In this simulation, we set the delay to be 5 s.

The proposed SMC for the perturbation case is shown in Fig. 16.8. In this scenario, the unmodel dynamic and the delay are presented simultaneously to the system. The SMC still maintain its excellent performance under this challenge. The performance is even better compared to the case of the PRC under the nominal case. Meanwhile, the PRC is tested under the existence of unmodel dynamic only. The buoy degrades its capability to track the reference under this scenario, as depicted in Fig. 16.9. The energy absorption for the both of controller can be seen in Fig. 16.5. The PRC losses significant amount of energy compared to the SMC under the perturbation case. The buoy elevation and the controlled force are still within the allowable level as stated in Table 16.2. Let us study the PRC under the perturbation in the excitation force. Figure 16.10 shows the velocity of the buoy versus its reference using the PRC. The velocity cannot track its reference completely. This causes a very small energy can be absorbed from the wave, similar with the case of the motion of the buoy. From the discussion we can conclude that the proposed SMC provides the excellent low cost controller for maximizing the energy absorption from the wave.

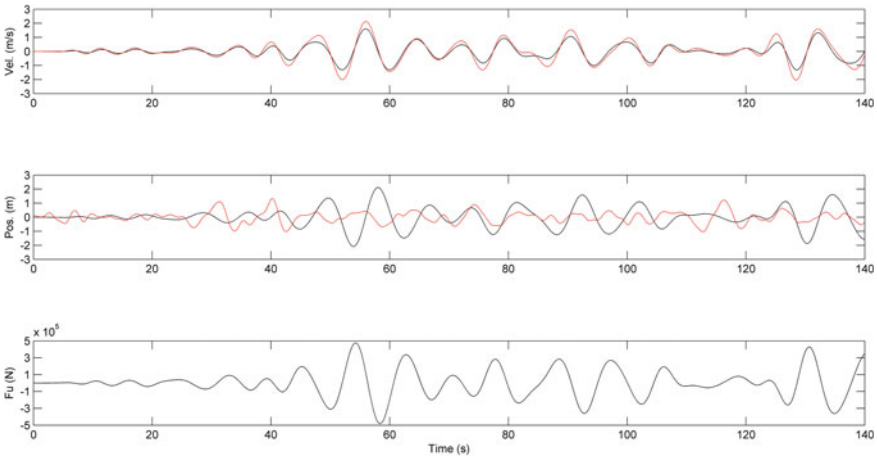

Fig. 16.9 The simulation results using the proposed PRC for the perturbation case of un-model dynamic only. *Upper graph* is the velocity of buoy (*black*) and its velocity reference (*red*). The *middle graph* is the buoy's elevation (*black*) and the wave elevation (*red*). The *lower graph* is control force of the PRC

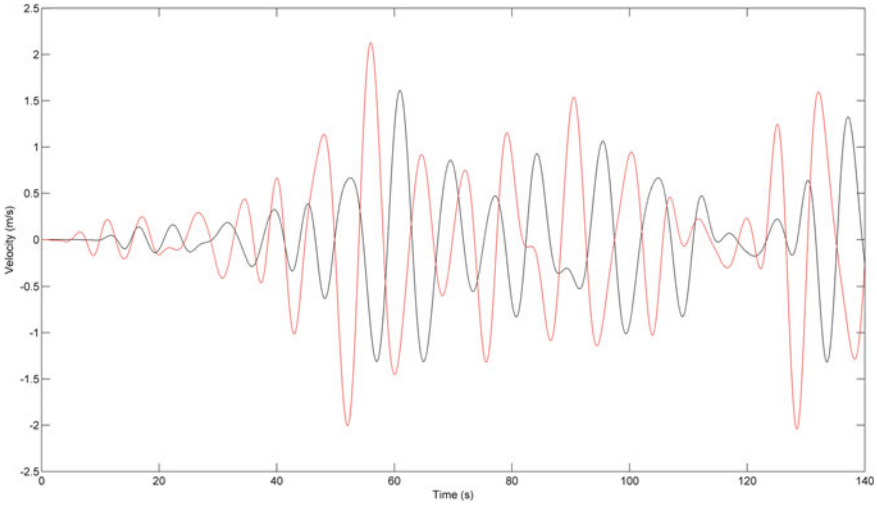

Fig. 16.10 The velocity of the buoy (*black*) and its reference (*red*) using the PRC under the perturbation in excitation force

16.5 Conclusion

Two low cost control strategies using the PRC and SMC are proposed in this paper. The proposed control strategies are tested using polychromatic wave to simulate the actual ocean environment. The maximum energy absorption is obtained by applying the proposed SMC to the WEC, compared to the PRC and free oscillating buoy in nominal /perturbed cases. This maximum energy absorption is achieved because the ability of proposed SMC to track its reference in the nominal and perturbed cases. The maximum level of the control force and the buoy's elevation for the two proposed methods are always within the allowable ranges, limited by their physical considerations. Therefore, this research work provides the viable control solution for maximizing the energy absorption of the heaving WEC.

Acknowledgements This study is supported by UAE University under the Start Up grant (#31N159) and the UAEU Program for Advanced Research (#31N164).

References

1. J. Cruz (ed.), Ocean wave energy, current status and future perspectives, in *Springer Series in Green Energy and Technology*, Berlin (2010)
2. J. Falnes, A review of wave-energy extraction. Mar. Struct. **20**(4), 185–201 (2007)
3. T. Sarpkaya, M. Isaacson, *Mechanics of Wave Forces on Offshore Structures*. (Van Nostrand Reinhold, New York, 1981)
4. A. Babarit, G. Duclos, A.H. Clement, Comparison of latching control strategies for a heaving wave energy device in random sea. J. Appl. Ocean Res. **26**, 227–238 (2005)
5. M.E. McCormick, Analysis of a wave energy conversion buoy. J. Hydronaut. **8**(3), 77–82 (1974)
6. K. Budal, J. Falnes, Interacting point absorber with controlled motion, ed by B.M. Count, in *Power from Sea Waves* (Academic Press, London, 1980)
7. M. Schoen, J. Hals, T. Moan, Wave prediction and robust control of heaving wave energy devices for irregular waves. IEEE Trans. Energy Conv. **26**(2) (2011)
8. M.A. Jama, A. Assi, W. Addy, H. Noura, Self-tunable fuzzy logic controller for the optimization of heaving wave energy converters, in *The International Conference on Renewable Energy Research and Applications, 2012*
9. M.A. Jama, A. Assi, W. Addy, H. Noura, Fuzzy logic based controller for heaving wave energy converters, in *International Conference on Renewable Energies for Developing Countries, 2012*
10. T. Brekken, On model predictive control for a point absorber wave energy converter, in *IEEE Trondheim PowerTech, 2011*
11. M.A. Jama, W. Addy, A. Assi, H. Noura, Controlling heaving wave energy converter using function-based model predictive control technique, in *Chinese Control and Decision Conference, 2013*
12. W. Addy, M.A. Jama, A. Assi, H. Noura, Sliding mode control for heaving wave energy converter, in *IEEE Multi-Conference on Systems and Control, 2013*
13. W. Addy, M.A. Jama, A. Assi, H. Noura, Sliding mode and fuzzy logic control for heaving wave energy converter, in *The 52nd IEEE Conference on Decision and Control, 2013*

14. W. Cummins, The impulse response functions and ship motions. Schiffstechnik **9**, 101–109 (1661)
15. R. Taghipoura, T. Pereza, T. Moan, Hybrid frequency time domain models for dynamic response analysis of marine structures. Ocean Eng. **35**, 685–705 (2008)
16. WAMIT, "User Manual 2006", www.wamit.com. Accessed 20 Sept 2012
17. J. Slotine, W. Li, Applied nonlinear control. (Prentice Hall, Englewood Cliffs, 1991)
18. MATLAB: The Language of Technical Computing, www.mathworks.com
19. J. Falnes, *Ocean Waves and Oscillating Systems: Linear Interactions Including Wave-Energy Extraction*. (Cambridge Press, Cambridge, 2004)

Chapter 17
Coordinated Hybrid Electric Vehicle Charging in Hybrid AC/DC Distribution Systems

M. F. Shaaban, A. A. Eajal and E. F. El-Saadany

Abstract This paper introduces an online coordination approach for plug-in electric vehicles (PEVs) charging in smart hybrid AC/DC distribution systems. The proposed approach objective is to optimally coordinate the PEV charging such that the charging costs are at minimum. A 38-bus test system has been modified to include DC links and used to validate the developed on-line charging scheme. The test results clearly demonstrate the effectiveness of the proposed method.

Keywords Coordinated charging · Electric vehicle · Hybrid AC/DC distribution systems · Energy management

17.1 Introduction

Recently, there have been rising interests in electric vehicles adaptation for transportation. This will lead to reduced emissions, reduced fuel consumption, and increased energy security by exploiting diverse energy sources [1]. However, if the Plug-in Electric Vehicle (PEV) charging is not managed properly, its extra load may lead to negative impacts, such as voltage limits violation, voltage imbalance, feeders' limits violation, and fuses blowouts [2]. To deal with the excess load imposed by the PEV charging, the utilities can either upgrade their networks or control the PEV charging. However, the second solution is known to be more beneficial for both the PEV owners and the utilities [3].

M. F. Shaaban (✉) · A. A. Eajal · E. F. El-Saadany
Electrical and Computer Engineering Department, University of Waterloo, Waterloo, ON, Canada
e-mail: m2farouk@uwaterloo.ca

M. O. Hamdan et al. (eds.), *ICREGA'14 - Renewable Energy: Generation and Applications*, Springer Proceedings in Energy, DOI: 10.1007/978-3-319-05708-8_17,

17.1.1 Background

The PEV, as defined by the IEEE, is any Hybrid Electric Vehicle (HEV) that has: (1) a battery storage bank of 4 kWh or more; (2) a rechargeable battery system that can be charged from an external energy source; and (3) the capability of driving at least 10 miles (16.1 km) with no gasoline used [4].

PEVs with the capability of being charged and discharged to inject the electricity back into the grid in what is known as a vehicle to grid (V2G) principle, which can bring benefits to the consumers and the society. Examples of these benefits are: less reliance on gas, reductions in gas prices and emission levels. According to Environmental Canada in its report entitled "greenhouse gas inventory" published in 2007, the conventional vehicles are responsible for approximately 12 % of the total annual emissions.

Due to the recent advances of DC-based technologies such as electric vehicles, fuel cells, solar panels, and energy storage systems, distribution systems will require a tremendous number of conversion devices which will in turn lead to operational and control challenges. Thus, the best infrastructure that the distribution system can have is of a hybrid AC/DC type in order to host the DC technologies. Thus, it is envisioned that many local distribution companies (LDCs) will adopt the hybrid AC/DC infrastructure. The hybrid AC/DC structure of power grids offers some advantages which can be summarized in the following [5]:

1. Reducing the number of conversion devices which are currently used to connect the DC loads and DC energy sources to the host AC network.
2. Reducing the conversion cost.
3. Simplifying the control and operation strategies
4. Controlling the harmonic injections efficiently by connecting the DC loads to the DC side of the hybrid system.
5. Solving the zero and negative sequence currents caused by unbalanced AC loads.

17.1.2 Related Work

Previous work in the area of PEV coordination introduced different techniques to coordinate their charging. In [6], a methodology is presented to optimally coordinate PEV charging based on time-of-use energy pricing. An optimal charging/discharging approach is presented in [7] based on V2G strategy. An approach for online PEV charging coordination is presented to minimize system losses and improve voltage profile in [8]. In [9], a methodology is proposed for optimal PEV charging based on demand side response and vehicle to battery (V2B) strategy. V2G ancillary services are managed in a charging/discharging method introduced in [10].

However, the methods in [6–10] deal with a snapshot of the system without considering the future system states. But few studies consider the future PEV demand in the charging process. The work in [11, 12] takes into consideration the day ahead systems states to coordinate the PEV charging. The work in [13] presents a new real-time PEV charging/discharging mechanism based on fuzzy logic controllers. However, all the aforementioned studies in [11–13] have failed to account for the dynamics of PEV arrivals and departures in real-time.

Another aspect related to the PEV charging, is the potential consequences of the charging process such as voltage imbalance and harmonic distortions. DC distribution systems can eliminate these negative impacts of the PEVs charging. As a step towards adopting the concept DC power distribution, a DC task team was formed to investigate the standards and regulations of DC distribution systems [14]. In [15], the concept of having DC islands within the existing AC infrastructure was introduced. The authors in [15] proposed a decentralized management system to control the interlinking converters. However, the PEVs have not considered as a major component in hybrid AC/DC distribution systems. In [16], the authors introduced the idea of the hybrid AC/DC intelligent parking lot having smart charging controllers, renewable energy resources. The smart parking lot has the option of charging the PEVs through the DC energy sources and the AC utility grid.

Based on the aforementioned discussions, it is obvious that there is a need for a proper PEV charging coordination methodology. Therefore, this paper proposes to develop a PEV charging coordination approach in hybrid ac/dc distribution systems.

The paper is organized as follows. The problem description is introduced in the next section. Sections 17.3 and 17.4 present the modeling and mathematical formulation, respectively. Finally, Sects. 17.5 and 17.6 present the simulation result and concluding remarks, respectively.

17.2 Problem Description

A centralized control center is assumed to be responsible for managing the PEV charging and interlinking converters in a certain territory, as shown in Fig. 17.1. The following assumptions are adopted in this work:

- PEV chargers allow only vehicles charging;
- two-way communication infrastructure is available;
- the AC voltage at the AC bus connected to the converter is purely sinusoidal and balanced;
- the converter and its transformer are lossless;
- the DC current and voltage are ripple-free.

The control center collects system information and searches for the optimal decisions. Then, these optimal decisions are sent to each system element to be

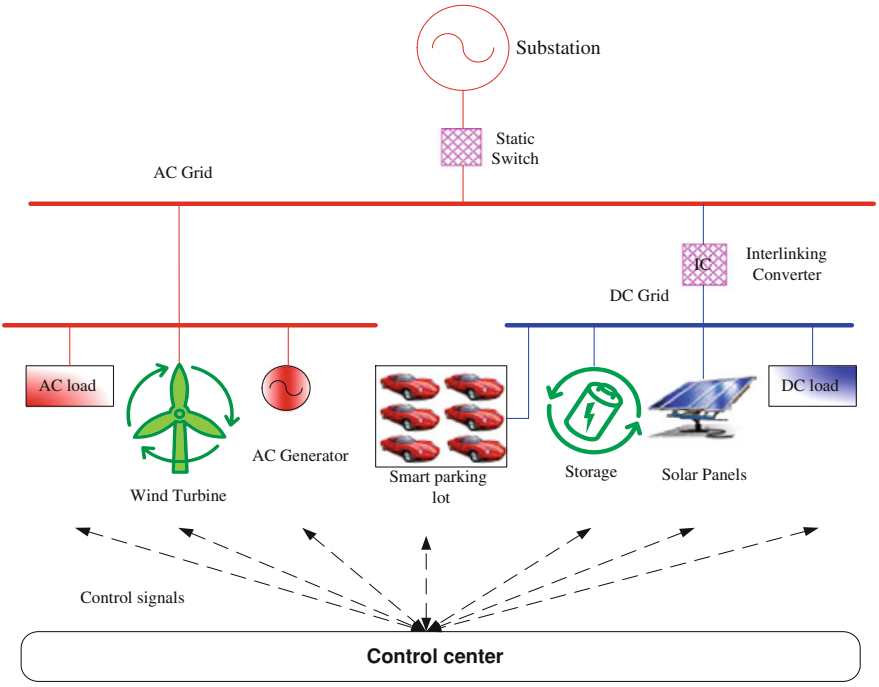

Fig. 17.1 A hybrid AC/DC distribution system

implemented. The cycle of collecting information, optimizing the decisions, and sending the decision is performed during time *dt*, as shown in Fig. 17.2. During *dt*, which is the time step of the operation, the power consumed or delivered by different system elements is assumed to be constant. The time step *dt* should be as short as possible to enhance the accuracy of the proposed approach; however, the computational time is a burden on this time step.

Moreover, to consider the dynamics of PEV arrivals and departures in a parking lot, the moving time window concept is adopted, as shown in Fig. 17.2, where the forecasted information, i.e. demand and electricity price, during the specified time window affects the decisions in each time step. While the time step *dt* can be in the range of seconds or minutes, the moving time window duration *T* can be in the range of a few hours.

17.3 Modeling

In this section, two types of models are presented, namely load models and grid models. While the normal load models and the ac grid models have been discussed in several publications, this section introduces the PEV load model and the DC grid model for load flow application in this study.

Fig. 17.2 Sliding time window concept

17.3.1 PEV Modeling

As shown in Fig. 17.3, the DC grid is connected to the battery pack of the PEV via DC/DC converter [17]. The DC/DC converter aims to maintain either constant current or constant voltage at the terminals of the battery pack depending on the level of the state of charge (SOC), as shown in Fig. 17.4 [18].

Since, the charging power is based only on the SOC level, and not affected by the DC grid voltage, due to the buffering via the DC/DC converter, the PEV charging load is implemented as constant power load in the DC distribution network. The power consumed by each PEV in the system under study is assumed to follow the same function shown in Fig. 17.4 [18] for simplicity.

17.3.2 Converter Modeling

The converters in a hybrid AC/DC system must be coordinated with the utility grid to ensure an interruptible and a high quality power supply under variable solar and wind power generations [19]. Thus, the converter model needs a special care to conduct any steady-state or dynamic study. The steady-state model of the converter is shown in Fig. 17.5. Mathematically, the converter can be represented by a set of equations which can be expressed in a compact form as shown in (17.1) [20].

$$f_c(V_k, x_k) = 0 \tag{17.1}$$

where V_k is the complex voltage at AC bus k; x_k is the vector of converter variables at bus k and defined by

$$x_k = [V_d, I_d, a, \alpha, \phi] \tag{17.2}$$

where V_d is the DC voltage at the DC terminal of the converter; I_d is the DC current at the DC terminal of the converter; a is the tap ration of the converter transformer; α is the converter firing angle; ϕ is the phase angle between the fundamental AC voltage and current at the AC terminal of the converter.

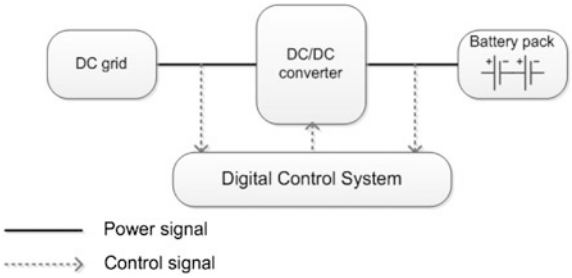

Fig. 17.3 PEV charging system in DC network [17]

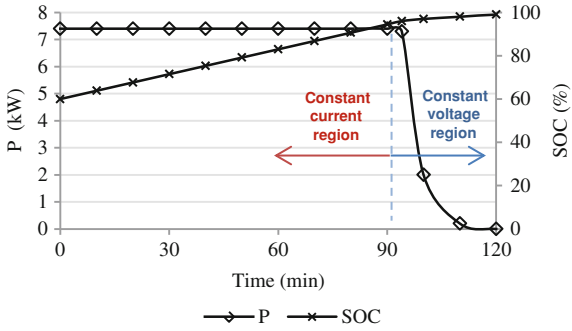

Fig. 17.4 Li-ion battery charging characteristics with 7.2 kW charger [18]

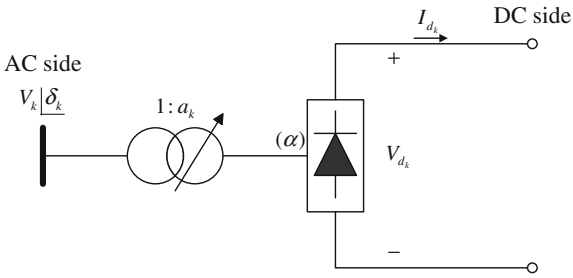

Fig. 17.5 Converter model

17.4 Mathematical Formulation

The ultimate objective is to minimize the charging expenses for the PEV's owners by optimizing the charging decision, u, in correspond to the real-time electricity pricing such that the constrains imposed by the system and the PEVs' owners are satisfied. The PEV charging problem is formulated as a mixed integer non-linear optimization problem and mathematically described by (17.3)–(17.11).

17.4.1 Objective Function

The objective of the proposed charging scheme is to minimize the charging expenses as shown in (17.3).

$$\underset{u\in\{0,1\}}{\text{minimize}} \quad C = \sum_{t=1}^{T/dt} \sum_{k\in Ksys} c_t \times P_{k,t}^{PEV} \times (dt/60) \tag{17.3}$$

where C is the charging cost for period T ($); c_t is the charging cost per kWh at time t ($/kWh), t and k are the indices of time and buses, respectively; K_{sys} is the set of all system buses; $P_{k,t}^{PEV}$ is the aggregated PEV demand on bus k at time t.

The objective is subject to a set of equality and inequality constraints which are explained as follows.

17.4.2 Equality Constraints

The equality constraints involve the highly nonlinear AC power flow constraints, the DC grid power flow constraints, and the vehicles SOC update constraints.

- The AC power flow equations

The active and reactive power injections at any AC bus must satisfy (17.4) and (17.5) respectively.

$$P_{k,t}^{G} - P_{k,t}^{D} = \left|V_{k,t}\right| \sum_{i\in K_{AC}} \left|V_{i,t}\right|\left|Y_{k,i}\right| \cos(\delta_{k,t} - \delta_{i,t} - \theta_{k,i}), \quad \forall k \in K_{AC}, t \tag{17.4}$$

$$Q_{k,t}^{G} - Q_{k,t}^{D} = \left|V_{k,t}\right| \sum_{i\in K_{AC}} \left|V_{i,t}\right|\left|Y_{k,i}\right| \sin(\delta_{k,t} - \delta_{i,t} - \theta_{k,i}), \quad \forall k \in K_{AC}, t \tag{17.5}$$

where K_{AC} is the set of AC buses; $P_{k,t}^{G}$ and $Q_{k,t}^{G}$ are the active and reactive power generations at bus k at time t; $P_{k,t}^{D}$ and $Q_{k,t}^{D}$ are the active and reactive power demands at bus k at time t; $\left|V_{k,t}\right|$ is the voltage magnitude at bus k at time t;$\delta_{k,t}$ is the voltage phase angle at bus k at time t; $\left|Y_{k,i}\right|$ is the magnitude of the admittance in the bus admittance matrix; $\theta_{k,i}$ is the phase angle of the admittance element of the bus admittance matrix.

- The DC power flow equations

The DC power injection at each DC bus must satisfy

$$P_{k,t}^{G} - P_{k,t}^{D} - P_{k,t}^{PEV} = V_{k,t} \sum_{i \in K_{DC}} V_{i,t} G_{k,i}, \quad \forall k \in K_{DC}, t \tag{17.6}$$

where K_{DC} is the set of DC buses; $G_{k,i}$ is the conductance in the bus conductance matrix.

It should be mentioned that the PEV power demand depends on the charging decision, $u \in \{0, 1\}$, charger allowable delivered power P^{ch}, and charger efficiency η^{ch} as shown in

$$P_{k,t}^{PEV} = \begin{cases} \sum\limits_{j \in N_k^{PEV}} \frac{P_{k,j,t}^{ch} \times u_{k,j,t}}{\eta_{k,j}^{ch}}, & \forall k \in K_{PEV}, t \\ 0 & else\ where \end{cases} \tag{17.7}$$

where the charging power level varies between 0 and the allowable charging power and N_k^{PEV} is the set of PEVs on bus k.

- SOC update constraints

The SOC level of the battery packs is updated during the time window based on the energy capacity $E_{k,j}^{Batt}$ of the battery of vehicle j.

$$SOC_{k,j,t+1} = SOC_{k,j,t} + u_{k,j,t} P_{k,j,t}^{ch} (\Delta t/60)/E_{k,j}^{Batt}, \ \forall k \in K_{PEV}, j \in N_k^{PEV}, t \tag{17.8}$$

where $SOC_{k,j,t}$ is the SOC level of PEV j on bus k at time t; $K_{PEV} \subset K_{DC}$ is the set of parking lot buses.

17.4.3 Inequality Constraints

The inequality constraints involve the technical constraints of the grid and the SOC level specified by the vehicle driver.

- Grid technical limits

The inequality constraints involve the bus voltage and line thermal limits as expressed by (9) and (10), respectively.

$$V_{\min} \le \left|V_{k,t}\right| \le V_{\max}, \quad \forall k, t \tag{17.9}$$

$$\left|S_{k,i,t}\right| \le S_{k,i}^{\max}, \quad \forall k, i, t \tag{17.10}$$

where $V_{\min}$ and $V_{\max}$ are the lower and upper bound in pu of the bus voltage respectively; $S_{k,i}^{\max}$ is the maximum thermal limit of line k-i.

- SOC limits constraints

The battery pack *SOC* level is limited to the specified SOC^{spec}, which is set by the vehicle's owner.

$$SOC_{k,j,t} \leq SOC_{k,j}^{spec}, \quad \forall k \in K_{PEV}, j \in N_k^{PEV}, t \tag{17.11}$$

17.5 Test Results and Discussion

The developed charging scheme was implemented within the MATLAB® environment interfaced with the General Algebraic Modeling System (GAMS). A 38-bus radial distribution system with a peak demand of 4.37 MVA and whose one-line diagram is depicted in Fig. 17.6 was used to validate the developed approach [21].

The test system was modified to form a hybrid AC/DC distribution system. The batteries capacities are assumed to have the same capacity which is 14 kWh in this study. The chargers are of a two-level type with a capacity of 7.2 kW each. Four parking lots are located arbitrary at buses 23, 26, 33, and 38. The hourly real-time energy price for 24 h is shown in Fig. 17.7.

Figure 17.8a, b show the total load and the PEV load for three scenarios, namely uncoordinated, coordinated and no PEV scenarios for 20 % PEV load percentage. It is assumed that in the uncoordinated scenario, the PEVs start charging once plugged-in.

The proposed approach delivers same amount of charging energy to PEVs. Thus, both the coordinated and uncoordinated achieved same level of charging success (100 %). This can be observed from the equivalent area under curve in Fig. 17.8a. However, the charging cost for customers are $1253.5 and $1457.7 for the coordinated and uncoordinated scenarios, respectively. Thus, the coordinated scenario saves almost 14 % of the charging cost for PEV owners. This is achieved through allocating the charging energy in low energy price periods subject to system technical constraints, desired SOC level, initial SOC levels, and parking duration. As shown in Fig. 17.8a, the PEV load in the coordinated scenario peaks during low price periods (normal load off-peak periods) and troughs during high price periods (peak normal load periods). Moreover, as a by-product, the increase in the system total peak load is only 12.5 % in the coordinated scenario compared to 22.2 % increase in the uncoordinated scenario, as shown in Fig. 17.8b.

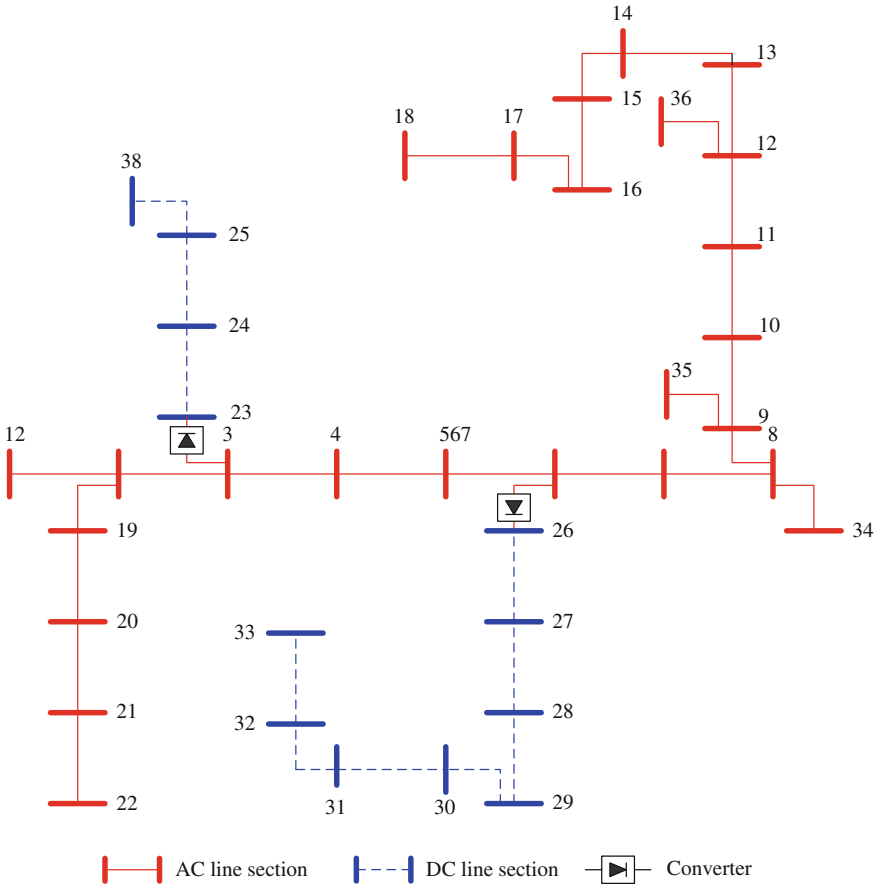

Fig. 17.6 38-bus hybrid AC/DC system under study

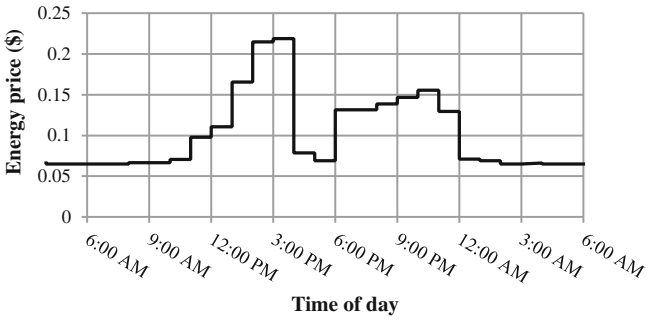

Fig. 17.7 Energy hourly price

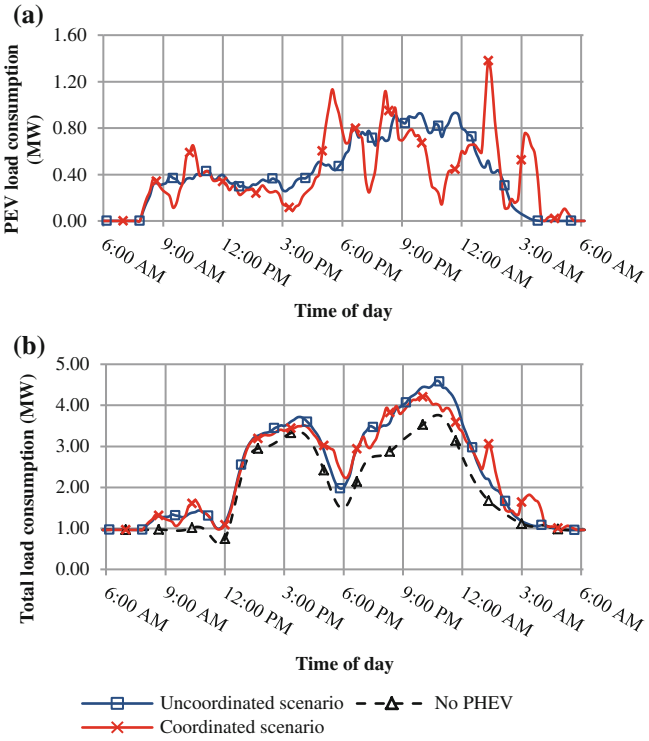

Fig. 17.8 **a** PEV load consumption; **b** Total system load

17.6 Conclusions

This paper introduces a coordinated charging scheme for PEVs in hybrid AC/DC distribution systems. The coordinated approach relies on the two-way communication infrastructure under the paradigm of the smart grids. The proposed PEV charging coordination approach aims to optimally allocate the charging energy in low energy price periods to achieve minimum charging cost for PEV owners, without violating system technical constraints.

The proposed coordinated charging scheme is examined on a typical hybrid AC/DC distributions system and compared with an uncoordinated charging scenario. The results prove the effectiveness of the proposed approach, which significantly reduces the charging costs for PEV owners. Moreover, the system peak load is significantly reduced.

References

1. U. Eberle, R. von Helmolt, Sustainable transportation based on electric vehicle concepts: a brief overview. Energy Environ. Sci. **3**, 689–699 (2010)
2. R. Liu, L. Dow, E. Liu, A survey of PEV impacts on electric utilities, in *Innovative Smart Grid Technologies (ISGT), 2011 IEEE PES*, pp. 1–8 (2011)
3. R.A. Verzijlbergh, M.O. Grond, Z. Lukszo, J.G. Slootweg, M.D. Ilic, Network impacts and cost savings of controlled EV charging. IEEE Trans. Smart Grid **3**, 1203–1212 (2012)
4. K.J. Dyke, N. Schofield, M. Barnes, The impact of transport electrification on electrical networks. IEEE Trans. Ind. Electron. **57**, 3917–3926 (2010)
5. P. Wang, L. Goel, X. Liu, F.H. Choo, Harmonizing AC and DC: a hybrid AC/DC future grid solution. IEEE Power Energy Mag. **11**, 76–83 (2013)
6. Y. Cao, S. Tang, C. Li, P. Zhang, Y. Tan, Z. Zhang, J. Li, An optimized EV charging model considering TOU price and SOC curve. IEEE Trans. Smart Grid **3**, 388–393 (2012)
7. Y. Ota, H. Taniguchi, T. Nakajima, K.M. Liyanage, J. Baba, A. Yokoyama, Autonomous distributed V2G (vehicle-to-grid) satisfying scheduled charging. IEEE Trans. Smart Grid **3**, 559–564 (2012)
8. S. Deilami, A.S. Masoum, P.S. Moses, M.A. Masoum, Real-time coordination of plug-in electric vehicle charging in smart grids to minimize power losses and improve voltage profile. IEEE Trans. Smart Grid **2**, 456–467 (2011)
9. C. Pang, P. Dutta, M. Kezunovic, BEVs/PEVs as dispersed energy storage for V2B uses in the smart grid. IEEE Trans. Smart Grid **3**, 473–482 (2012)
10. C. Quinn, D. Zimmerle, T.H. Bradley, An evaluation of state-of-charge limitations and actuation signal energy content on plug-in hybrid electric vehicle, vehicle-to-grid reliability, and economics. IEEE Trans. Smart Grid **3**, 483–491 (2012)
11. S.Y. Derakhshandeh, A.S. Masoum, S. Deilami, M.A.S. Masoum, M.E. Hamedani Golshan, Coordination of generation scheduling with PEVs charging in industrial microgrids. IEEE Trans Power Systems **3**, 3451–3461 (2013)
12. J. Soares, H. Morais, T. Sousa, Z. Vale, P. Faria, Day-ahead resource scheduling including demand response for electric vehicles. IEEE Trans. Smart Grid **4**(1), 596–605 (2013)
13. M. Singh, K. Thirugnanam, P. Kumar, I. Kar, Real-time coordination of electric vehicles to support the grid at the distribution substation level. IEEE Syst. J. (to be published)
14. E. Hesla, B. Brusso, L. Downey, B. Giese, G. Parise, M. Valdes, K. Clemente, C. Cook, T. Dionise, P. Garland, DC task team report, in *IEEE/IAS 49th Industrial and Commercial Power Systems Technical Conference (I&CPS)*, pp. 1–9 (2013)
15. L. PIEGARI, E. Tironi, V. Musolino, S. Grillo, C. Tornelli, DC islands in AC smart grids. IEEE Trans. Power Electron. **29**(1), 89–98 (2014)
16. T. Ma, A. Mohamed, O. Mohammed, Optimal charging of plug-in electric vehicles for a car park infrastructure, in *IEEE Industry Applications Society Annual Meeting (IAS)*, pp. 1–8 (2012)
17. V. Monteiro, H. Gonçalves, J.C. Ferreira, J.L. Afonso, Batteries charging systems for electric and plug-in hybrid electric vehicles, in *Tech, New Advances in Vehicular Technology and Automotive Engineering*, pp. 149–168 (2012)
18. F. Marra, G.Y. Yang, C. Traholt, E. Larsen, C.N. Rasmussen, S. You, Demand profile study of battery electric vehicle under different charging options, in *IEEE Power and Energy Society General Meeting*, pp. 1–7 (2012)
19. X. Liu, P. Wang, P.C. Loh, A hybrid AC/DC microgrid and its coordination control. IEEE Trans. Smart Grid **2**, 278–286 (2011)
20. J. Arrillaga, B. Smith, *AC–DC power systems analysis* (The Institute of Electrical Engineers, London, 1998)
21. D. Singh, R. Misra, Effect of load models in distributed generation planning. IEEE Trans. Power Syst. **22**, 2204–2212 (2007)

Chapter 18
Monitoring Framework for Cost-Effective Energy Consumption in a Building

Salah Bouktif and Waleed K. Ahmed

Abstract The scope of this paper is restricted to energy-consumption management of a building. Hence, the problem we are addressing is how to reduce energy consumption by using smart decisions based on well informed management. Our vision to the energy consumption is analogous to the leaky bucket problem. Before start filling the holes of the bucket, we need to learn the big picture of the leaky bucket including the number of holes, their respective sizes, their locations, etc. Accordingly, learning the energy-consumption system of a building is a mandatory phase before taking any decision to tune, upgrade or take any remedial action on the energy system. Concisely, our proposal aims at controlling and processing the operation of energy consumption of a building on real-time basis. The goal of such a control is to provide real-time information on electricity consumption at different levels. It is a monitoring operation that gives feedback and shows a visual big picture of what is going on in a building in term of energy consumption. To achieve our goal, we propose an architectural framework for energy consumption control and smart management.

Keywords Energy consumption · Building · Monitoring framework · Cost

18.1 Introduction

The term "green" implies many meanings and interpretations. They range from protecting and preserving what remains of the original nature to switching off the light before leaving the office, and also from political slogans to everyday individual practices. The point is that being green, sustainable or environmental involves a lot of ideas and actions.

S. Bouktif (✉) · W. K. Ahmed
United Arab Emirates University, Al Ain, United Arab Emirates
e-mail: salahb@uaeu.ac.ae

M. O. Hamdan et al. (eds.), *ICREGA'14 - Renewable Energy: Generation and Applications*, Springer Proceedings in Energy, DOI: 10.1007/978-3-319-05708-8_18,

Energy-consumption efficiency is one of the greatest ideas towards saving natural resources, in particular, reducing fossil fuels burning. If we trace back the energy consumption over the years, we discover that buildings are responsible of more than 40 % of energy consumption in the world [1] as estimated by the International Energy Agency IEA. Obviously, as the economy and the population increase in world, we will continue to build buildings and the challenging question is how to make them energy-efficient? Many actions can be associated with achieving this goal. These actions also range from designing building that saves energy to coordinating between means of energy saving.

Many works were carried out to study and improve efficiency, reliability and sustainability of the energy production, distribution and consumption. In general, two parallel paths are followed to achieve efficiency in the energy domain.

In the first path, researchers are targeting the supply side, where contributions were primarily concerned with introducing renewable energy sources such as solar, wind and water. These contributions were culminated by a supply-side management technology known as smart grid and proposed by [2] in 2005. It aims at applying digital processing and communication to improve efficiency and sustainability of the production and distribution of energy [3]. A joint vision by many researchers of the future the American electric delivery system smart Grid is referred as Gird 2030.

In the second path, the main goal was to reduce the demand-side energy consumption. This concern has been studied by many researchers. Since the 1970s, programs referred to as Demand-Side Management DSM, have started being implemented by US energy utilities in order to reduce residential and commercial electricity demand through many energy conservation activities like information dissemination programs, subventions, and free installation of more conserving equipment and technologies [4–10]. The green-building movement has begun formally in the 1990s. It has strongly been motivated by the efficient use of energy and water, and other resources [11]. As mentioned above, buildings are responsible for the major part of world energy consumption [1] and up to 70 % in some countries such as United Arab Emirates according to Middle East Centre for Sustainable Development.

In the literature there are, in general, two strategies to make building energy efficient. The first is concerned with how to design building in order to conserve energy, and the second strategy is, in part similar to the DSM programs, by the fact of focusing on how to operate and manage the utilization of the energy inside the building [12–14]. A third-party certification program for the design, construction and operation, Leadership in Energy and Environmental Design (LEED) [15], is developed by the U.S. Green Building Council (USGBC), has become an internationally accepted benchmark for high performance green buildings.

The LEED program is a framework certification that focuses on the design of the building and not on its actual energy consumption management. Although LEED pretends to cover management side, it needs to be customized in order to track and evaluate of the actual energy consumption in the designed buildings. According to our classification of research contributions in energy efficiency at the

level of building (i.e., demand-side), the LEED belongs more to building-design contributions rather than to energy consumption management.

A legitimate suggestion towards a LEED certification is to create an evaluation process that measures the impact of design and operation practices on the actual energy consumption in the buildings.

Our software-based proposal is a framework that groups a collection of intelligent tools that collaborate in order to promote energy efficiency by smartly monitoring the actual energy consumption. This will establish an ongoing education of the building occupants toward energy conservation. Such a contribution is, to some extent, an implementation of our suggestion to the LEED program.

18.2 Problem Space

Addressing energy conservation is at the same time impressive and challenging. Such a problem becomes more challenging when we relate its resolution to the human behavior. Turning off the light and the computer monitor before leaving the office is a human behavior. Hence, our major challenge in this work is to establish an ongoing education and competitions headed for conserving energy. Other subsequent challenges address the use of real-time software engineering and human computer interaction to help building occupants toward conserving energy. The subsequent challenges can be summarized in the following points:

1. A monitoring of the utilization of energy, at different levels of the building and at different time scales is needed.
2. Metering and sensing operations are needed to capture the energy consumption measures at different level of the building. This includes the establishing the network infrastructure to transport the metered energy measures.
3. Protocols to ensure the communication between different equipment and installations are needed.
4. The historical data (energy consumption database) has to be developed and organized in a way to well represent energy data.
5. A big data can be obtained from automatic sensing and metering. This data can serve to learn energy patterns and best practices toward cost-effective energy management.

18.3 Solution Framework

Given the above challenges and problematic points, our solution for energy conservation is strongly related to our success in establishing an ongoing education and competition among building occupants toward energy saving. In order to bring a concrete solution, we proceed by two steps. The first one consists in designing an

architecture that groups the big picture of the proposed solution. This first step aims at proposing a framework for energy consumption management which will be detailed in the current paper. However, the second step consists in creating a high fidelity prototype that implements our approach on a specific building, the college of information technology building in the new campus of the United Arab Emirates University (UAEU). The latter step is the target of the immediate future wok.

Towards proposing an architectural design of our solution, the following steps are carried out. This is what can be considered as functional requirements of the energy framework.

18.4 Functional Requirements of the Energy Framework

1. Study the installations and equipment in most of the high consumption buildings. This step will enable us to determine our energy conservation objectives and indicators. We will decide the granularity of metering and sub-metering. In a college, for example, we can meter consumption at the level of floor/classroom/lab/office/equipment/computer/air conditioning installation/etc.
2. Determine the smart metering/sensing system specification, its composition and scale. This step will allow us to estimate the needed equipment (i.e., basically meters and sensors) as well as the network infrastructure to communicate with meter/sensors.
3. Design a database to store energy consumption data suitable to the building composition and satisfying the energy conservation objectives. This database will be used to learn and plan best practices of energy utilization.
4. Design and develop a dashboard to visualize the energy consumption information. This software application shall offer a user friendly and customizable graphical user interface that allows the building occupants to track the energy consumption every half an hour/hourly/daily/etc. It means to monitor, at different timescales and with different interest profiles the energy consumption. User profiles include building manager, lab technician, simple occupant, equipment maintenance agent, etc.
5. Develop protocols of capturing and transferring energy data to the energy consumption database and to the consumption monitoring dashboard. These protocols will be also responsible for eventual communication between sensors/meters.
6. Design and develop a software tool to support making decision toward energy conservation. This tool will use inputs data from the energy consumption database, and learn models of best practices. These models are then applied to take the smarter measures to save energy.
7. Make the unit testing of every subsystem including protocols, network communication infrastructure, dashboard tool, decision making support tool, energy database system. At this level of our solution plan we have to make sure that every individual system is well tested.

8. Perform the integration testing of different subsystems in a generic building environment. This include a first integration of the dashboard, energy consumption database and the metering/sensing system and a second integration will test the decision making supporting tool and energy consumption database.

18.5 Framework Architecture

The analysis and the requirement elicitation guided us the following architectural components of the proposed framework:

Software monitoring application: It is an engineered real-time tool that will provide a spectrum of views and graphics that will inform the user on what is going on in the building in terms of energy consumption. It is a kind of dashboard that monitors a set of selected energy consumption indicators eventually selected by the users [16].

Metering and sensing system: The building will have a metering and sensing system able to capture energy measures at different levels (e.g., a college building, will have meters and sub-meters at classroom, laboratory, office, cafeteria, etc.). This system will include a network infrastructure and communication protocols.

Control and decision making system: This is a second software tool that analyses periodically or per user demand, the collected data and signal abnormal energy consumption of particular equipment or location. Abnormal consumption can be signaled when exceeding the estimated load allocated, for example, by the equipment technical specification. Besides, this tool helps in taking decision to tune or upgrades installation, or to change behavior.

Energy consumption database: This database is crucial to evaluate the building attitude and building occupants behavior concerning the energy conservation. It will show the impact of best practices and taken measures to promote energy conservation. In addition, the collected data can be a valuable input to train energy cost estimation model and predict the energy needs. This is by using novel modeling approaches such as those in [17–19]. Social media based educational component: This component will be in charge of sharing, publishing and discussing energy consumption issue and culture. It aims at establishing an education and culture of energy saving among building occupants. Besides, this component will analyze posts and tweets from social networks in order to collect energy data and learn bad and good energy consumption patterns. Previous similar works have been published in [20]. Figure 18.1 shows the big picture of the proposed framework. In particular it captures the main architectural components as well as the relationship among them.

The potential of application of this proposed framework is clearly visible and without any negative concerns. It is applicable to a wide range of company, installations building, etc. To validate the framework and eventually improve or extend it, we propose to develop a pilot experience that consists of dashboard software application that monitors energy consumption of selected Governmental Buildings and installations (University Buildings such as UAEU campus).

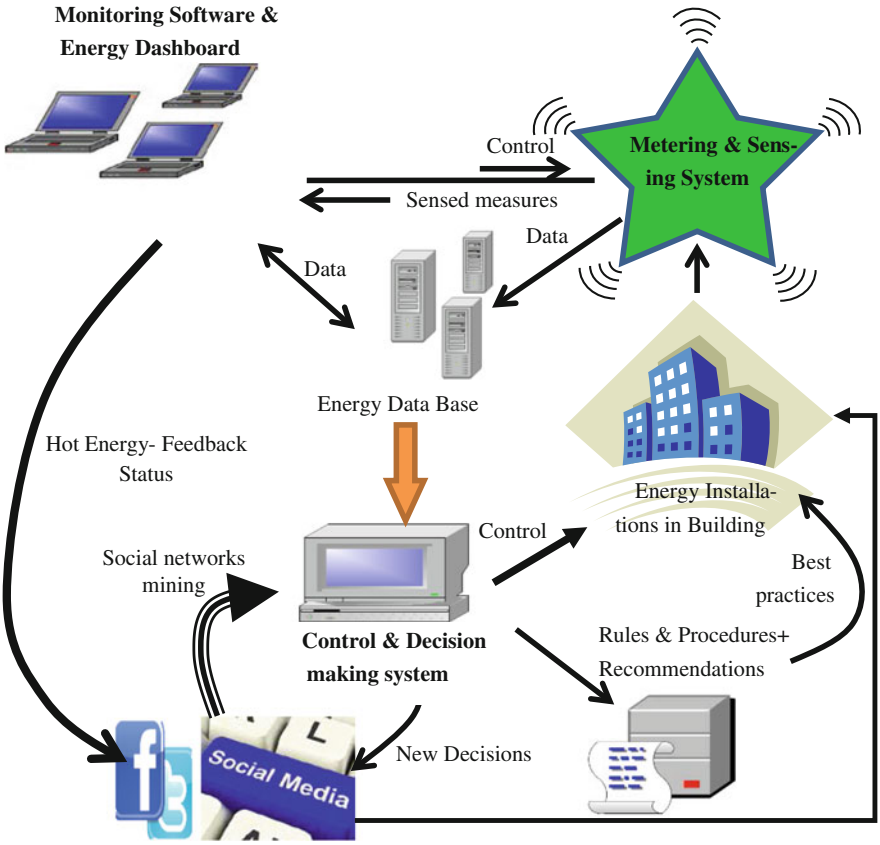

Fig. 18.1 Proposed energy management framework

18.6 Conclusion

Energy conservation is universal and crucial concern that touches directly the humanity. Although, it has been targeted by many research groups, it will remain a hot topic because of the multiple dimensions of the problem (supply-side, demand-side, building construction domain, renewable resources, building occupants behavior, etc.). Many ways and tools can be applied to bring support to energy consumption. Our contribution in this work is to introduce the software based tools to help improving energy conservation. This challenge is significant because it is founded on the fact that energy conservation is related to the behavior of building occupants. We believe that using our proposed framework architecture to report, inform, avert or advice a human is crucial and successful. This is because it answers the occupant questions and helps him to reduce his energy consumption. By being informed, the occupant will develop a self-evaluation process and eventually a behavior correction toward energy conservation. This is the ongoing

education targeted by our major research challenge. Future works will obviously involve implementing different software components of our energy management framework. They will also include framework customizations to different building specifications.

References

1. J.C. Howe, Overview of green buildings. Natl. Wetl. Newsl. **33**(1), 3–14 (2010)
2. S.M. Amin, B.F. Wollenberg, Toward a smart grid. IEEE Power Energy Mag. **3**(5), 34–41 (2005)
3. U.S. Department of Energy, Smart grid/department of energy. http://energy.gov/oe/technology-development/smart-grid
4. Electric Power Research Institute (EPRI), *Demand side management. Overview of key issues, EA/EM-3597*, vol. 1, Palo Alto, CA, 1984
5. J. Eto, S. Kito, L. Shown, R. Sonnenblick, *Where Did the Money Go? Cost and Performance of the Largest Commercial Sector DSM Programs, LBNL-38201* (Lawrence Berkeley National Lab, Berkeley, 1995)
6. A.P. Fickett, G.W. Gellings, A. Lovins, Efficient use of electricity. Science **263**, 64–74 (1990)
7. H. Geller, S. Attali, The experience with energy efficiency policies and programs in IEA countries: learning from the critics. IEA Information Paper, Paris, France (2005)
8. K. Gillingham, R. Newell, K. Palmer, Energy efficiency policies: a retrospective examination. Annu. Rev. Environ. Resour. **31**, 161–192 (2006)
9. D. Loughran, J. Kulick, Demand side management and energy efficiency in the United States. Energy J. **25**(1), 19–41 (2004)
10. Y. Ji, S. Plainiotis, *Design for Sustainability* (China Architecture and Building Press, Beijing, 2006)
11. U.S. Environmental Protection Agency, *Green building basic information*, 28 Oct 2009
12. P.L. Anastas, J.B. Zimmerman, Through the 12 principles of green engineering. Environ. Sci. Technol. **1**, 95–101A (2003)
13. M. Rossi, Innovative façades: lightweight and thin systems with high inertia for the thermal comfort application in office buildings in Southern Europe. J. Green Build. **6**(2), 107–121 (2012)
14. A. Hay, R. Parlane, Okanagan College Centre of excellence in sustainable building technologies and renewable energy conservation. J. Green Build. **6**(1), 14–24 (2011)
15. D. Baylon, P. Storm, Comparison of commercial LEED buildings and non-LEED buildings within the 2002–2004 Pacific Northwest commercial building stock, in *ACEEE Summer Study on Energy Efficiency of Buildings*, American Council for an Energy-Efficient Economy, Washington, pp. 4-1–4-12 (2008)
16. S. Bouktif, G. Antoniol, E. Merlo, M. Neteler, A feedback based quality assessment to support open source software evolution: the GRASS case study, in *22nd IEEE International Conference, Software Maintenance, ICSM'06*, pp. 155–165 (2006)
17. S. Bouktif, G. Antoniol, E. Merlo, M. Neteler, A novel approach to optimize clone refactoring activity, in *Proceedings of the 8th annual conference on Genetic and evolutionary computation,* pp. 1885–1892 (2006)
18. F. Ahmed, S. Bouktif, A. Serhani, I. Khalil, Integrating function point project information for improving the accuracy of effort estimation, in *The 2nd International Conference on Advanced Engineering Computing and Applications in Sciences, ADVCOMP'08*, pp. 193–198 (2008)

19. S. Bouktif, F. Ahmed, I. Khalil, G. Antoniol, A novel composite model approach to improve software quality prediction. Inf. Softw. Technol. **52**(12), 1298–1311 (2010)
20. S. Bouktif, M. Awad, Ant colony based approach to predict stock market movement from mood collected on Twitter, in *Proceedings of the IEEE/ACM International Conference on Advances in Social Networks Analysis and Mining, ASONAM*, pp. 837–845 2013)

Chapter 19
Distributed Energy Storage Based Series Compensator to Mitigate Power Quality Problems

M. E. Nassar, E. F. EL-Saadany and M. M. A. Salama

Abstract Power quality is gaining more interest especially in the deregulated markets with competitive electrical suppliers. Moreover, some critical loads require power supply contracts with premium power quality. Usually, to improve power quality utilities install power quality conditioners. However, new approaches are presented and implemented to improve the power quality through controlling the interfacing converters used with distributed generators and energy storage units. This paper presents a voltage control based power quality mitigation technique. The proposed technique is applied to the voltage source inverter used to interface energy storage to mitigate some power quality problems such as harmonic distortion, voltage sag and voltage swell occurs after fault clearing actions. The system is modeled and simulated using MATLAB/SIMULINK to validate the proposed technique. Results show successful action of the proposed technique in improving the power quality by significant reduction in the harmonic contents in the presence of nonlinear loads. Moreover, the compensator mitigates the voltage sag problem by keeping the voltage at load terminals constant during disturbances with 2–3 % change in voltage. In addition, the proposed technique allows the uninterruptable power supply feature by supplying the load during supply interruption for duration depends on the stored energy.

Keywords Power quality · Series compensation · Energy storage · Voltage sag

M. E. Nassar (✉) · E. F. EL-Saadany · M. M. A. Salama
Electrical and Computer Engineering, University of Waterloo, Waterloo, Canada
e-mail: mnassar@uwaterloo.ca

M. O. Hamdan et al. (eds.), *ICREGA'14 - Renewable Energy: Generation and Applications*, Springer Proceedings in Energy, DOI: 10.1007/978-3-319-05708-8_19,

19.1 Introduction

Power quality of the power supply has become a significant factor to attract customers in the deregulated electricity market [1, 2]. Power quality problems are addressed in many standards to specify the acceptable levels of power quality indices [3]. Utilities keep power quality indices within standard limits using different power conditioning techniques such as passive filters, active filters [4, 5] and hybrid filters [6–9].

However, the fast and steady increase in implementing distributed generation units (DGs) in power distribution system [10] due to its positive impacts [11] such as voltage support, improved reliability, small size and losses reduction. With widespread of DG implementation, it is essential that applying DG in a manner that avoids degradation of power quality or negatively affecting the operating conditions of the existing distribution network. This can be achieved by proper control and regulation of the DG grid interfacing converters to improve the distribution system efficiency and power quality [12, 13].

Moreover, energy storage systems such as batteries, ultra capacitors and flywheels are used to improve power system performance. This paper presents a strategy based on using portion of the stored energy and feed this energy through a series compensator to mitigate power quality problems in order to improve power supply to critical loads. The proposed scheme based on interfacing energy storage units using voltage source inverter (VSI). The VSI supplied from the energy storage unit is connected through a transformer to inject voltage in series with the sensitive load. Where, Voltage-control method is utilized in this paper to control the VSI as this method is more flexible and simpler than the conventional current-control method and has similar compensation performance [14].

The power system is modeled and simulated using MATLAB/SIMULINK. In this model voltage-control algorithm is used to generate the firing signals for the VSI. The main supply voltage is considered as the reference voltage. In addition, a nonlinear load is connected to point of common coupling (PCC) at which the critical load is also connected. This nonlinear load will distort the voltage at the PCC due to—the system impedance Moreover, voltage Sag is simulated by creating three phase fault at the PCC and voltage swell occurs after the clearing of the fault.

19.2 System Block Diagram

The system block diagram is shown in Fig. 19.1. The voltage reference is selected to be the voltage at the supply terminal and this voltage is measured and fed to the controller to be compared with the distorted voltage at the PCC. The error signal is then fed to the controller to generate the gating signals for the 3-phase VSI.

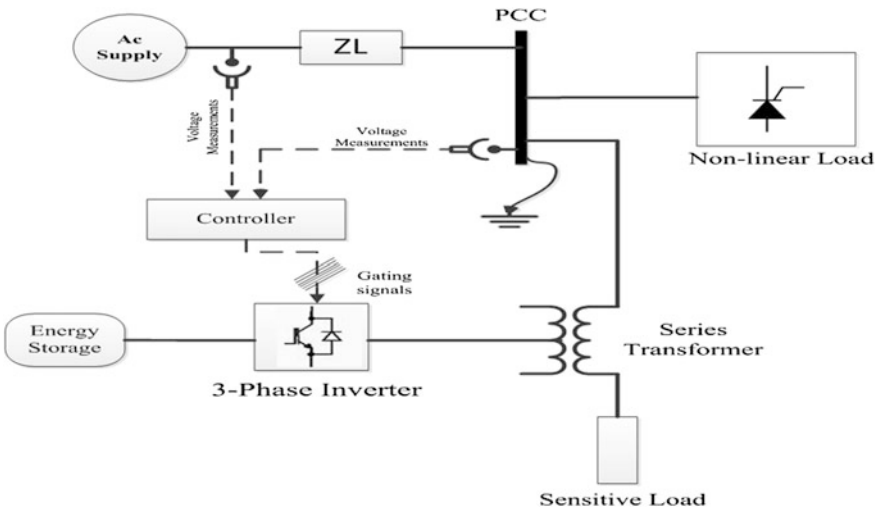

Fig. 19.1 Block diagram of series compensator fed from energy storage

The controller used to generate the gating signals is a PI controller. PI controller is selected in this application due to its simplicity, flexibility and its ability to achieve zero steady state error. Moreover, the tuning of the PI controller can be done through Ziegler-Nichols tuning technique or simply by try and error which is utilized in this paper.

19.3 Simulation Results

The proposed model shown in Fig. 19.2 is simulated using MATLAB/SIMULINK. And the data used to simulate the system are presented in Table 19.1 [14].

19.3.1 Simulation Results at Normal Conditions

The model at Fig. 19.2 is simulated using MATLAB/SIMULINK with normal operating conditions. And, the voltage at the point of common coupling obtained from simulation is shown at Fig. 19.3.

As shown in Fig. 19.3, the voltage at the PCC is distorted with high order harmonics. Moreover, the voltage suffers from voltage notches due to the commutation overlap occurs within the full bridge rectifier (nonlinear load).

Curves of Fig. 19.4, Show the voltage at the sensitive load terminals during normal operating conditions.

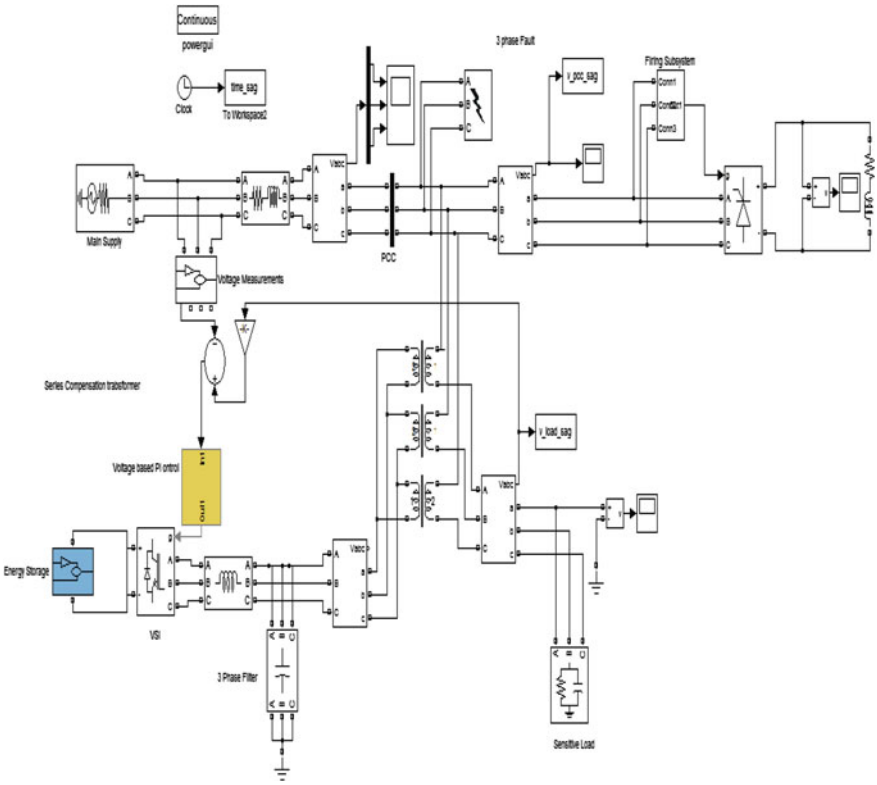

Fig. 19.2 MATLAB/SIMULINK model

Table 19.1 Simulation model parameters

Parameters	Value used in the simulation models
Main supply voltage per phase	230 V
Line frequency	50 Hz
Source impedance	$L_S = 0.005$ mH, $R_S = 0.001\ \Omega$
Injection transformer turn ratio	1:1
Fault resistance	0.001 Ω
Main drive load	1 MW, 100 VAR
Sensitive load	1 KW, 20 VAR
Inverter	IGBT switches, two level, 6 pulse topology, carrier frequency = 20,000 Hz, sample time = 5 μs

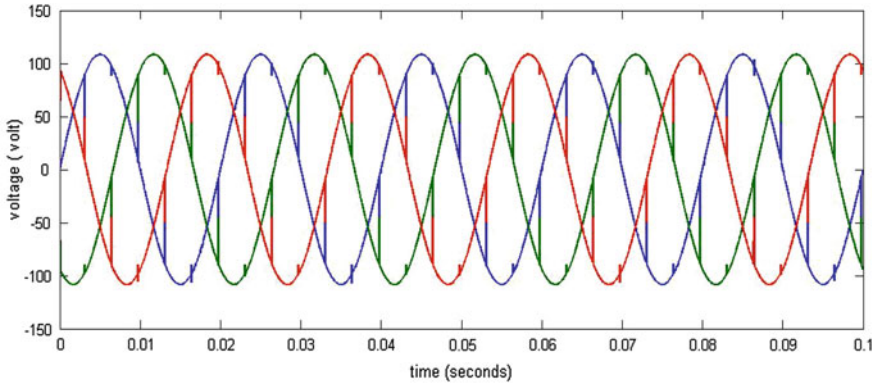

Fig. 19.3 Three phase voltages at point of common coupling

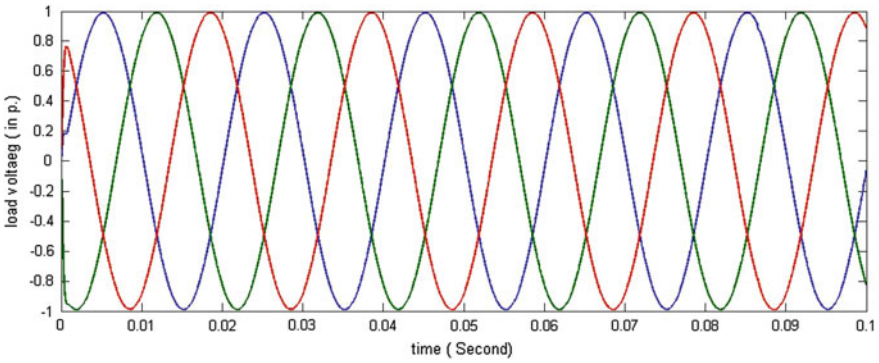

Fig. 19.4 Three phase voltages at load terminals in per unit

After applying the proposed series compensator fed from the energy storage device, the voltage at the sensitive load is greatly improved and the voltage notches are completely removed. This proves the effectiveness of the control algorithm in removing the superimposed harmonics at the PCC.

Hence, keeping the supply at the sensitive load terminals nearly pure sinusoidal independent of the non-linear load connected to the same PCC.

Figure 19.5 shows the harmonic spectrum for the load voltage in the presence of the series compensator. Total harmonic distortion (THD) is calculated for the load voltage and found to be 0.3179 %. The THD calculated is significantly small due to the effectiveness of proposed series compensation.

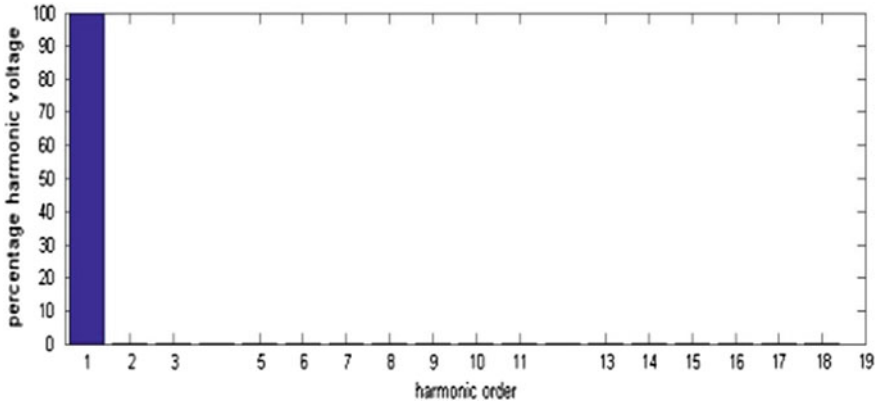

Fig. 19.5 Voltage harmonic spectrum at load terminals

19.3.2 Simulation Results When the System Is Subjected to Voltage Sag

In order to investigate the effectiveness of the proposed voltage control in mitigating the voltage sag problem, a three phase short circuit is created at the PCC at t = 0.05 s and removed at t = 0.1 s and the response of the controller is investigated. The capability of the compensator to mitigate such voltage sag problem is checked by monitoring the load voltage during fault period and the following results were obtained:

The voltage at PCC is shown in Fig. 19.6.

The voltage at the PCC is reduced to a certain value depends on the impedance of the fault created. As shown in Fig. 19.6 the voltage sag is 50 % during the simulated fault.

Curves of Fig. 19.7, Show the voltages at load terminals in per unit.

From the simulation results shown in Fig. 19.7, the compensator has kept the voltage at the load almost constant during the fault with very small drop about 2 % (the voltage at load terminal during fault is 0.982 per unit).

Also, it is noticeable that the voltage after fault clearing has some transients and overshooting until the compensator restores the pre-fault voltage conditions at load again. However, the compensator successfully limits the voltage swell follows fault clearing in addition to preventing voltage sag during fault duration.

The compensator effect on reducing harmonics even during disturbances (with PI tuned to mitigate sags and swells) is studied by calculating harmonic spectrum as shown in Fig. 19.8 with and without the compensator.

Based on results shown in Fig. 19.8, adding the compensator reduced the voltage harmonic contents at load terminals. Comparison of some important individual harmonic values for both cases is shown in Table 19.2.

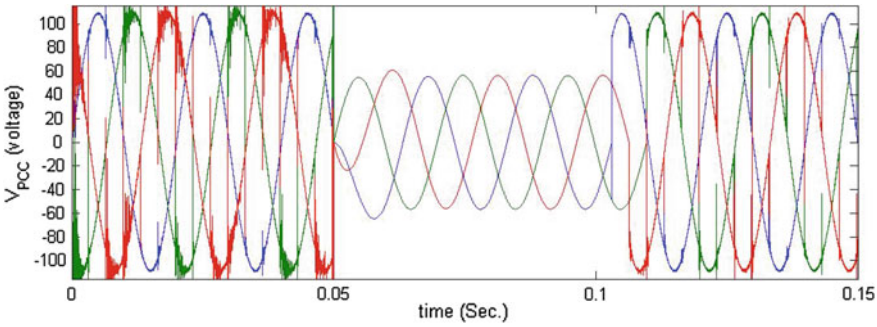

Fig. 19.6 Three phase voltages at point of common coupling during fault

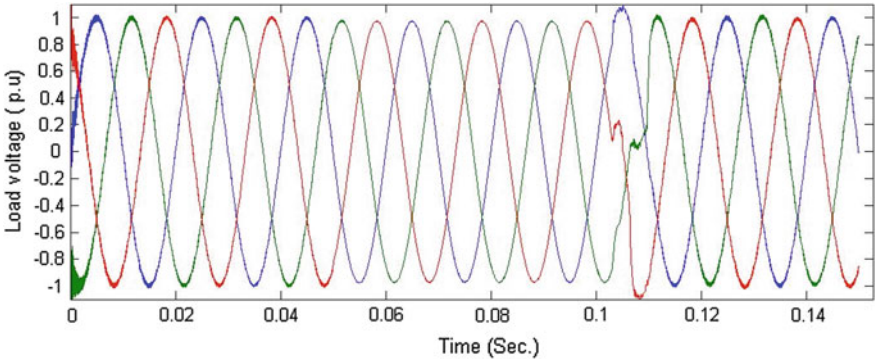

Fig. 19.7 Three phase voltages at load terminals during fault

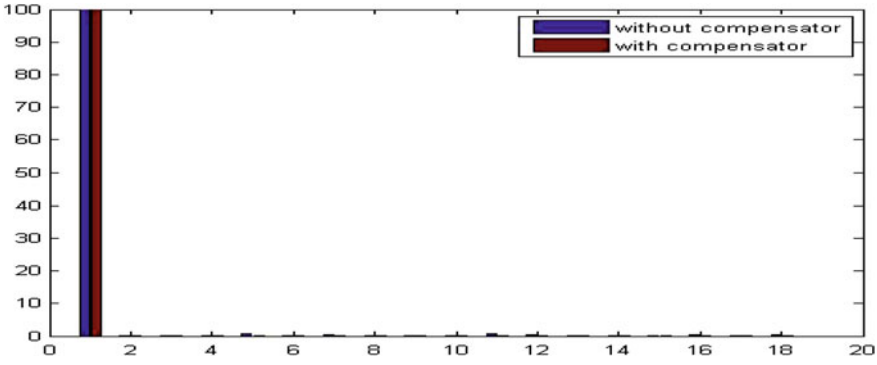

Fig. 19.8 Comparison between voltage harmonic spectrum with and without the compensator

Table 19.2 Comparison between individual harmonics values with and without the compensator

Harmonic order	% Value without compensation	% Value with compensation
5	0.6799	0.0328
7	0.3662	0.0624
11	0.5875	0.0259
13	0.3298	0.0160
17	0.5477	0.0147
19	0.3046	0.0214
THD	1.2015	0.0012

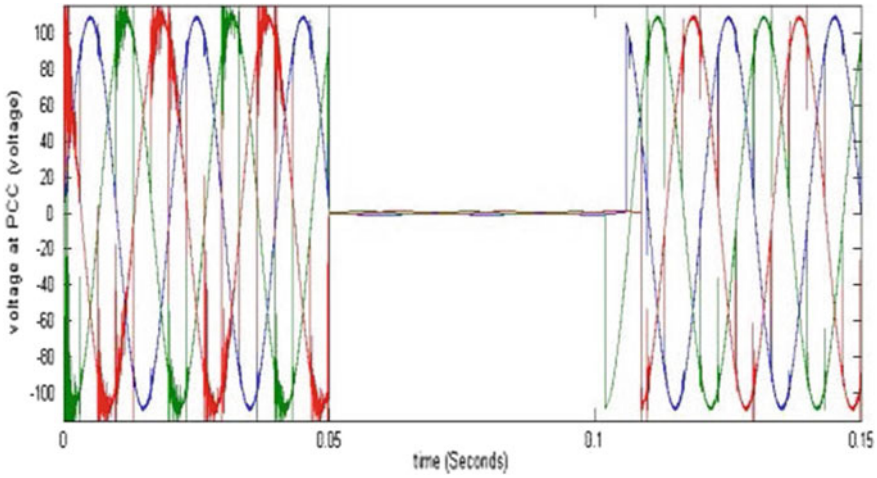

Fig. 19.9 Three phase voltage at point of common coupling with bolted fault

From the results, it is obvious that the compensator had significant effect on reducing the values of each individual harmonic as well as the THD at load terminals with same PI values tuned to mitigate voltage sags/swells.

19.3.3 Simulation During Supply Voltage Interruption

To study the ability of this configuration to act as an uninterruptable power supply (UPS) to secure the supply for the sensitive load even if the main supply is interrupted.

This case is studied by creating a bolted short circuit at the PCC which results in almost zero voltage at the PCC. This is simulated by applying the bolted fault at $t = 0.05$ s and clearing the fault at $t = 0.1$ s.

Voltage at PCC during fault is shown in Fig. 19.9. It is clear that the voltage at the PCC is dropped to very small value (nearly zero) as the impedance of the bolted fault created is zero.

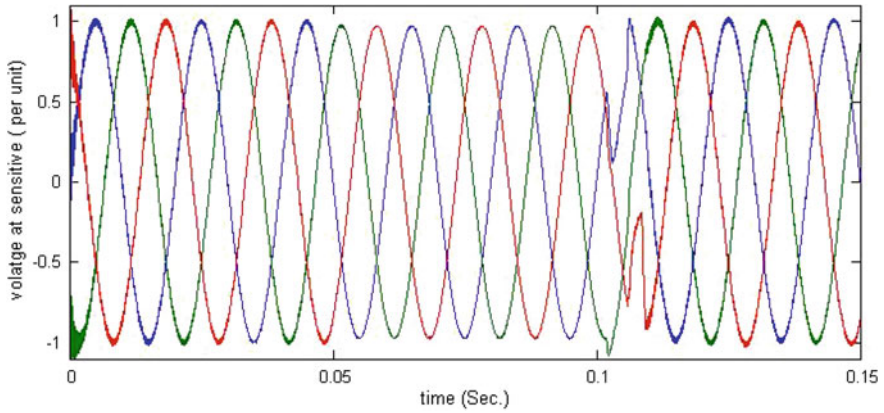

Fig. 19.10 Three phase voltage at load terminals with bolted fault

Voltage at the load terminals with bolted fault is shown in Fig. 19.10. From the obtained results, the compensator has almost kept the voltage at the load constant during the fault with very small drop about 3 % (the voltage at load terminal during fault is 0.9698 per unit). So that the proposed compensation is capable of acting as UPS during supply interruption for certain duration depends on the energy stored without retuning of PI parameters.

19.4 Conclusions

This paper has discussed the effectiveness of using the energy storage units which are used in power systems for power quality improvement. Portion of the energy stored is utilized through a series compensator connected to a sensitive load in order to keep the power quality at load within the acceptable limits. Also, energy storage units are being extensively used with renewable energy resources to improve their operation (e.g. smoothing output power of wind energy). Hence, this paper introduces the utilization of stored energy to improve power quality for sensitive loads.

A control scheme using a voltage controlled method is used in this paper. The proposed technique is proved to be capable of reducing the harmonics at the PCC and to mitigate the voltage sag/swell problems. This flexible and simple voltage controlled method results in an excellent performance. The proposed technique produces significant reduction in harmonic contents in addition to effective mitigation of voltage sag/swell problems. This was proved by keeping the load voltage around 0.97 per unit during three phase dead short circuit on the PCC and after fault clearing.

The proposed scheme is simulated and investigated using MATLAB/SIMULINK and the results are presented to show the effectiveness of the proposed harmonic mitigation technique.

References

1. T. Abdel-Galil, E.F. El-Saadany, M.M.A. Salama, Power quality assessment in deregulated power systems, in *Power Engineering Society Winter Meeting*, vol. 2, pp. 952–958 (2002). doi:10.1109/PESW.2002.985146
2. C. Cereda, R. Gemme, C. Moratto, A. Tinggren, Innovative solutions for power quality in a deregulated market, in *Industry Applications Conference*, pp. 932–939 (2000)
3. S. Khalid, B. Dwivedi, Power quality issues problems standards their effects in industry with corrective means copyright-IJAET.docx.pdf. Int. J. Adv. Eng. Technol. **1**(2), 1–11 (2011)
4. B. Singh, K. Al-haddad, A. Chandra, Power quality improvement. IEEE Trans. Ind. Electron. **46**(5), 960–971 (1999)
5. H. Akagi, New trends in active filters for improving power quality, in *International Conference on Power Electronics, Drives and Energy Systems for Industrial Growth*, pp. 417–425 (1996)
6. K. Karthik, J.E. Quaicoe, Voltage compensation and harmonic suppression using series active and shunt passive filters, in *Canadian Conference on Electrical and Computer Engineering*, pp. 582–586 (2000)
7. L. Gyugyi, A new approach to harmonic compensation in power systems-a combined system of shunt passive and series active filters. IEEE Trans. Ind. Appl. **26**(6), 983–990 (1990)
8. P. Salmerón, S.P. Litrán, Improvement of the electric power quality using series active and shunt passive filters. IEEE Trans. Power Deliv. **25**(2), 1058–1067 (2010)
9. S.G. Seifossadat, R. Kianinezhad, A. Ghasemi, M. Monadi, Quality improvement of shunt active power filter, using optimized tuned harmonic passive filters, in *International Symposium on Power Electronics, Electrical Drives, Automation and Motion*, pp. 1388–1393 (2008)
10. T. Ackermann, G. Andersson, L. Söder, Distributed generation: a definition. Electr. Power Syst. Res. **57**(3), 195–204 (2001)
11. G. Pepermans, J. Driesen, D. Haeseldonckx, R. Belmans, W. D'haeseleer, Distributed generation: definition, benefits and issues. Energy Policy **33**(6), 787–798 (2005)
12. M.I. Marei, E.F. El-Saadany, M.M.A. Salama, A novel control algorithm for the dg interface to mitigate power quality problems. IEEE Trans. Power Deliv. **19**(3), 1384–1392 (2004)
13. M.I. Hamid, A. Jusoh, M. Anwari, Power quality improvement for distributed generation employing photovoltaic-inverter, in *IEEE Applied Power Electronics Colloquium (IAPEC)*, pp. 16–21 (2011)
14. S. Sadaiappan, P. Renuga, D. Kavitha, Modeling and simulation of series compensator to mitigate power quality problems. Int. J. Eng. Sci. Technol. **2**(12), 7385–7394 (2010)

Chapter 20
Guidelines for Sizing Shading Devices for Typical Residential Houses in Muscat, Oman

Alya Al-Hashim, Nader Chalfoun and Colby Moeller

Abstract Energy consumption of Oman's building sector is around 55 % of country's total energy demand and it has increased by 59 % from 2005 to 2010. Although Oman's Carbon Dioxide emissions are the lowest amongst the Middle East countries, it has witnessed a growth rate of 10 % from 2005 to 2010, which is considered the highest in the region. Since the country has not yet adopted nor developed any green building guidelines and lacks an energy performance benchmark, improving energy performance in Oman's housing stock is very challenging. This paper has three main objectives. The first is to establish guideline for sizing shading devices for different window orientations in Muscat, Oman. The second is to give a set of recommendations for designing the shading devices in order to make them culturally suitable, so they can be accepted and adopted by the community. Finally, the research studies the impact of the shading device application on energy consumption of the house using eQUEST. An energy reduction of around 10 % was achieved without drastically increasing cost of construction while also taking into consideration society's requirement for privacy and its concern to visually maintain its cultural identity.

Keywords Energy conservation · Residential buildings · Shading device

20.1 Introduction

Oman, especially the Muscat region—currently is developing at an astounding rate and transforming itself into a progressive developed area, Modern buildings are increasing on a daily basis and are rapidly replacing the traditional buildings.

A. Al-Hashim (✉) · N. Chalfoun · C. Moeller
Sultn Qaboos University, Muscat, Sultanate of Oman
e-mail: aliya@squ.edu.om

M. O. Hamdan et al. (eds.), *ICREGA'14 - Renewable Energy: Generation and Applications*, Springer Proceedings in Energy, DOI: 10.1007/978-3-319-05708-8_20,

However, the modern buildings have failed to cope with the external thermal conditions to provide comfortable climate inside the building without relying on mechanical systems. This is largely due to the fact that traditional buildings were built with thermal mass and less window area than in modern buildings with extensive use of unshaded glazing [1].

As the development continues in Oman, demand of energy is also increasing. As per Oman energy report of 2011, the energy consumption has increased by 14 %, whereas energy production increased by only 1 % [2]. The country has started experiencing severe power cuts, reflecting the difficulties faced in bringing sufficient electricity production capacity to the grid. The residential sector is the single largest consumer category with consumption taking more than half of the total system energy, most of which is used for cooling. Energy demands of the residential sector have witnessed a rapid increase of 59 % since 2005 as compared to other sectors [3].

Energy conservation in Oman is urgently needed, as almost half of the produced energy is wasted needlessly to cool poorly designed buildings. As Oman's energy resources are in fact limited, it becomes apparent that if the problem is not addressed now, the next generation will have a bigger problem to deal with and solving it might be beyond their capabilities.

Many researches have analyzed Oman's potential for adopting renewable energy techniques, but there have been very few studies concerning demand-side management and energy conservation. Although renewable energy technologies are promising, many are not yet cost effective on the large scale. Reducing energy demand, in many cases, is less expensive than producing clean energy with cutting-edge generation technology.

There is a large opportunity for reducing energy demand in the building sector by promoting more energy efficient building design. Since most buildings have long life-times, in many cases 40 years or more, design choices whether energy efficient or inefficient, will be adding to the environmental impact for a long time [4].

One of the most, if not the most important passive cooling strategy is shading, which is a simple method of blocking the sun before it can get into the building. Application of this method in Oman will be studied in this paper.

20.2 Methodology

This paper has three main objectives. The first is to establish guideline for sizing shading devices for different window orientations in Muscat, Oman. The second is to give a set of recommendations for designing the shading devices in order to make them culturally acceptable. Finally, the paper will study the impact of the shading device application on energy consumption of the house.

20.2.1 Impact of Climate on Energy Consumption in Muscat, Oman

Muscat is located at the Tropic of Cancer in the Coastal region of Oman, and is highly influenced by its proximity to the sea. Since the climate of Muscat is hot-humid, solar radiation absorbed by roof, walls and windows is a primary source of built up heat in buildings. Shading helps in minimizing solar radiation, which effectively cools the building. Shading reduces the peak-cooling load in buildings, thus helps in reducing the required air-conditioning size [5].

Solar radiation received by exterior building surfaces depends on the surface orientation, time of day and day of the year. In Fig. 20.1 solar radiation throughout the day is shown for summer day (21 June) and winter day (21 Dec). The position of the sun in the sky is described by the altitude and azimuth angle. Both angles vary throughout the day and year. The altitude angle is measured from the horizon to the position of the sun in the sky. The azimuth angle described the direction of the sun in relation to the cardinal directions. Typically North is 0°, East is 90°, South is 180° and West is 270°. Alternate methods of angle definition exist depending on application. It is noticed that solar radiation received by roof, East and West facades is relatively highest, as a result of high solar angle, which reaches at azimuth angle of 89.8° at noon and high altitude of the sun in the early morning and late afternoon. Whereas in winter roof and South façade receive most of the solar radiation, because of the low azimuth angle of the sun at noon, around 43°.

Energy consumption in residential units in Oman is mostly climate-driven, cooling being the major energy consumer almost year round. Annual energy consumption of one of the houses is shown in Fig. 20.2, where it can be seen that January is the month with lowest energy consumption and August with highest consumption level. The annual demand reflects the climate in Oman and is highly seasonal. The average summer demand is more than double of the average winter demand, owing to the increase in cooling demand during the hot weather in summer [6].

20.2.2 Typology of Omani Houses

Building form in Oman may differ from one another, but the functional distribution is generally the same. Most of the single family houses have two floors, where the ground floor usually consists of semi-public (Majlis, Dinning) and semi-private spaces (Kitchen, Living). Semi-public spaces are where guests are welcomed, while semi-private areas are where family members and female guests are allowed to enter. The second floor consists of semi-private (Family Living) and private spaces (Bedrooms), where only family members are allowed (Fig. 20.3).

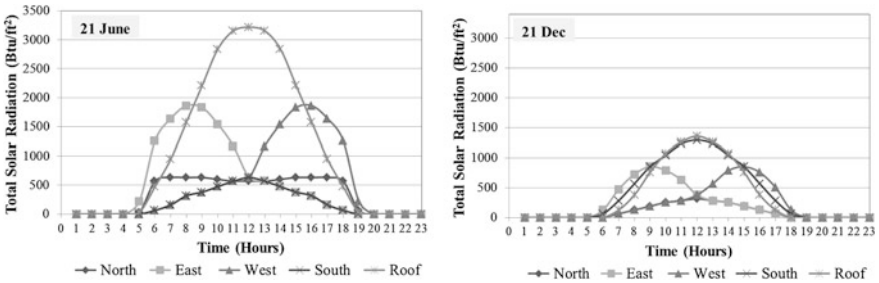

Fig. 20.1 Solar radiation on exterior surfaces in Sohar-Oman (Latitude 24.28) on 21 June and 21 Dec

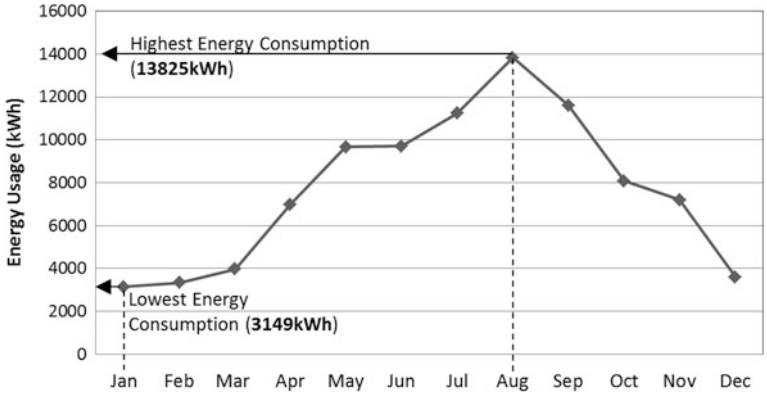

Fig. 20.2 Annual energy consumption of one of the residential units in Oman

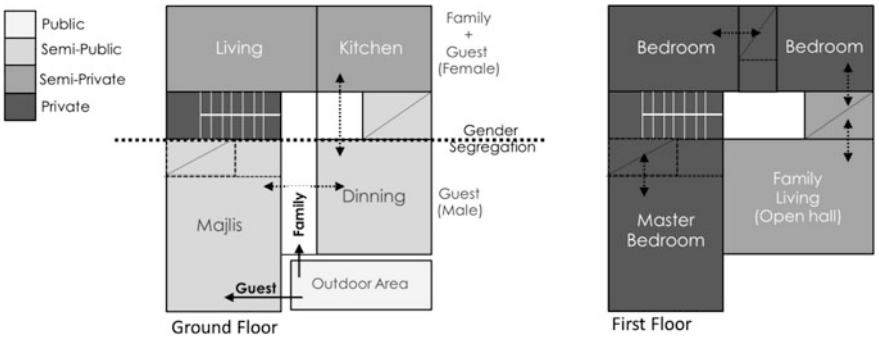

Fig. 20.3 Functional distribution in a typical Omani house

20.2.3 EUI Benchmarking and Interpretation

One of the techniques of benchmarking building energy performance is the use of established Energy Use Index EUI based on existing building energy codes Analysis of form, spatial distribution construction material and occupant behavior of an average Omani house, a base-case was prepared and tested using the RES-check and e-QUEST software, both developed by U.S. Department of Energy (Table 20.1).

When tested on RES-check, to determine whether new residential projects or additions to existing structures meet the requirements of the Model Energy Code (MEC) or the International Energy Conservation Code (IECC), it was found that the building did not comply with the code and failed by 83.8 %.

After that an energy model of the same house was generated using eQUEST and it was found that the Energy Use intensity, which is defined as energy use per square foot per year was around 140 kBtu/ft^2. Allowed Energy Use Intensity for detached single family house in a hot humid climate according to ASHRAE is 40 kBtu/ft^2, indicating that the Omani household consumes 100 kBtu/ft^2 more (see Fig. 20.4). Although climate in Oman forces people to intensively use air-conditioning system, but subsidies have also played a large part in producing a culture used to energy waste [7]. Oman's domestic energy consumption is supplied by natural gas 67 % and oil 33 % [8], and the energy prices are relatively low, around 3.9 cent/kWh because of the support provided by the government of Oman [9]. As a point of reference electrical rates in Tucson, AZ in the United States are around 11 cent/kWh.

In order to reduce the energy consumption in the residential sector of Oman, it is very necessary to introduce passive energy efficient strategies during design stage to reduce the energy demand of the building. However, these strategies will not be accepted by the community unless they aesthetically maintain cultural identity, do not compromise privacy of the inhabitants and do not increase construction cost.

As mentioned earlier, shading is perhaps the most important passive cooling strategy, so integrating this strategy with requirements of the community will help in making it an acceptable design option.

20.2.4 Defining Shading Mask and Projection Factor [10]

Theoretical framework for sizing shading devices has been provided by Olgyay [11]. In this paper the method of appropriately sizing shading devices for different orientation for Muscat, Oman is divided into two steps: shading period selection and form finding.

In order to reduce solar gain and eliminate glare, windows should be shaded most of the daytime in Muscat. However trying to accomplish this can result in horizontal

Table 20.1 Description of parameters used for energy model

Category		Value used			
		Construction	Finish Color	+	Insulation
Construction	Roof	8in Concrete	Light (abs = 0.4)		2in polystyrene
	Wall	8in CMU	Light (abs = 0.4)		No insulation
	Glass	Single Clr/Tint			
	Floor	Ceramic/Stone	8in Concrete		Earth contact
HVAC		Split system + Single zone (system per floor)			
Operating Schedule		Weekdays: 7am–2 pm			
		Weekends: Open 24 h			
Temperature set-point		Occupied:		Unoccupied:	
		Cool: 22 °C		Cool: 25 °C	
		Heat: 20 °C		Heat: 20 °C	

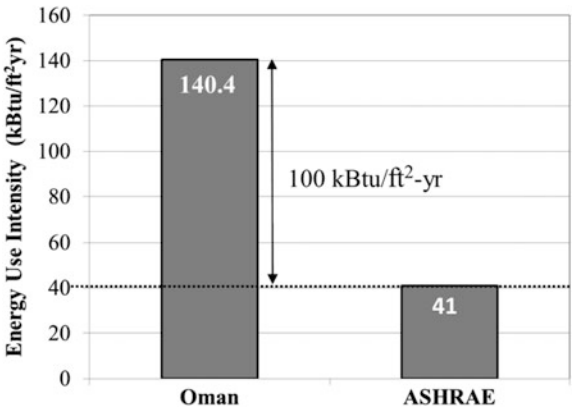

Fig. 20.4 Energy use intensity of an Omani house compared to ASHRAE standard

overhang and vertical fin design which would be impractical, particularly for the east and west orientations during early morning and late afternoon.

The overhang and fin designs recommended in this section have been developed to balance cultural identity with practical application. Solar gain is not significant during late December and early January (see Fig. 20.1) because daytime outdoor temperature is lower compared to the rest of the year; the average in December and January is around 23 °C, whereas in June it can reach up to 40 °C (Fig. 20.5).

An in-depth analysis was conducted for windows in different orientations and recommendations for overhang and fin sizes for Muscat, Oman were concluded (Fig. 20.6).

To make the table comprehensible by designers, data in Table 20.2 were converted into a graph that shows the overhang and fin factors (Fig. 20.7).

It is clear from Fig. 20.8 that East and West orientations require large fins and overhangs and can be very difficult to shade with architectural strategies alone.

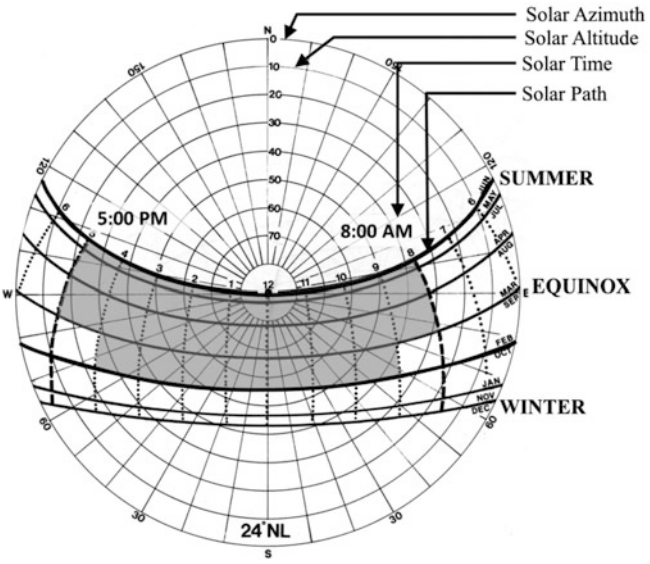

Fig. 20.5 Shading mask for 24-degree north latitude

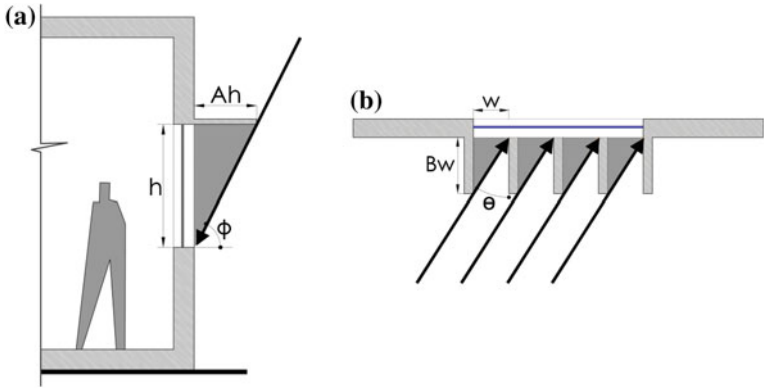

Fig. 20.6 **a** Section through overhang with Φ-degree cut off angle, **b** Plan view showing vertical fin with ⊖-degree cut off angle

20.2.5 Design Recommendations

Shading devices can be designed in many ways as long as the relationship between the window height and the depth of the shading device (the cut-off angle) does not change. In Fig. 20.8 examples of multiple shading design options are presented for overhang and fin sizes that are feasible to build (Figs. 20.9 and 20.10).

Table 20.2 Recommendation for overhang and fin sizes for Muscat, Oman

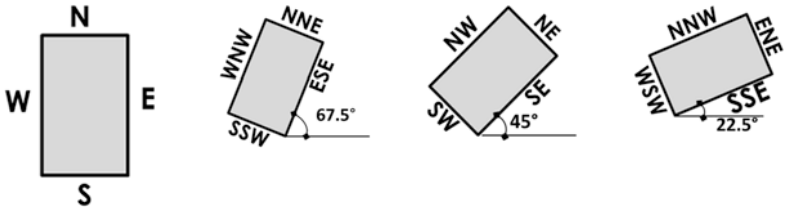

Orientation	Overhang		Fin	
	A	ϕ (°)	B	⊖ (°)
North	0.1	85	0.3	73
East	0.5	63	2.6	21
West	1.7	30	2.2	24
South	0.7	56	0.15	67
North East	0.8	50	1.4	55
North West	1	45	0.8	51
South East	1.6	32	1.6	32
South West	1.1	42	1.4	55
North North East	0.8	52	0.7	54
North North West	0.8	52	0.5	62
South South East	1.7	30	–	–
South South West	0.8	50	1	44
East North East	1	45	1.4	35
East South East	0.8	50	1.4	36
West North West	1.5	34	1.9	28
West South West	1.7	30	3	19

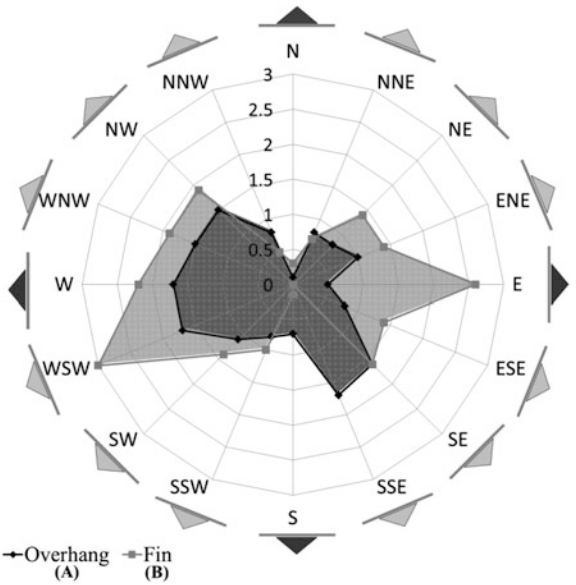

Fig. 20.7 Overhang and fin sizing factors (proposed by author)

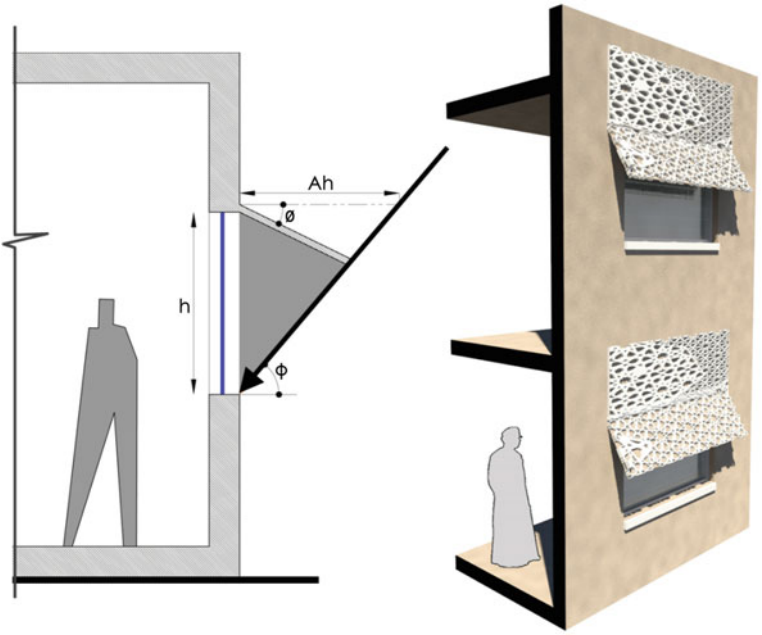

Fig. 20.8 Section and proposed design for inclined overhang

20.3 Analysis and Results

In order to test the impact of given recommendation for shading device size on energy consumption of a house, two existing houses were chosen from Muscat, Oman and their energy models were built using e-QUEST. One house had Energy Use Intensity of 189.6 kBtu/ft^2, higher than the average (140 kBtu/ft^2), and the other house had Energy Use Intensity of 104.2 kBtu/sq-ft, lower than the average.

The energy models of the houses were validated by comparing the results with actual energy bills of the houses, where it was found that the difference was less than 5 %. This shows that the results obtained from the energy model are correct and can be trusted.

The houses were then analyzed in order to choose appropriate shading dimension as per the given recommendation. Both houses had the same orientation, entrance façade facing West-North-West, which had the highest requirement for fin and overhang sizes compared to the other orientation of the building, so balconies were used for both houses to shade the façade and create aesthetically pleasing features at the entrance.

In case of the house with low Energy Use Intensity, the rest of the facades were shaded with a detached glass reinforced concrete (GRC) wall, which had inclined

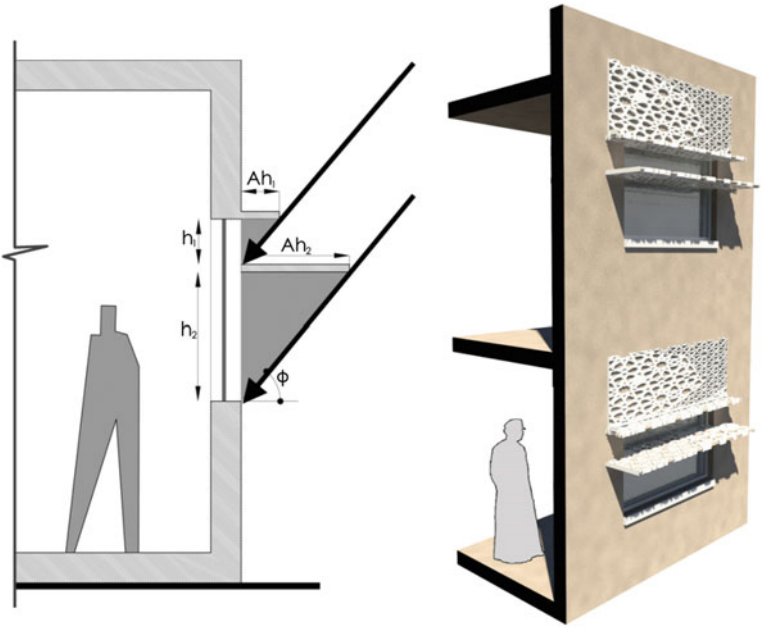

Fig. 20.9 Section and proposed design for light shelf

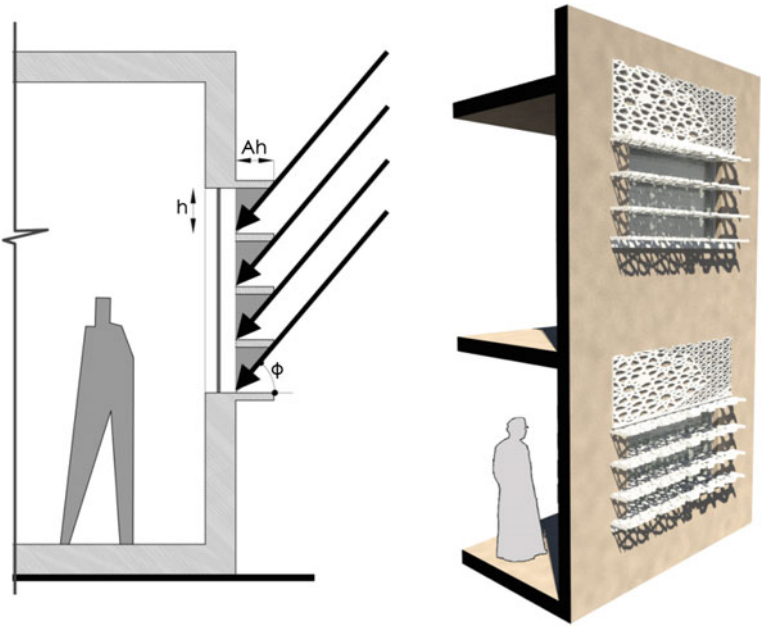

Fig. 20.10 Section and proposed design for multiple overhangs

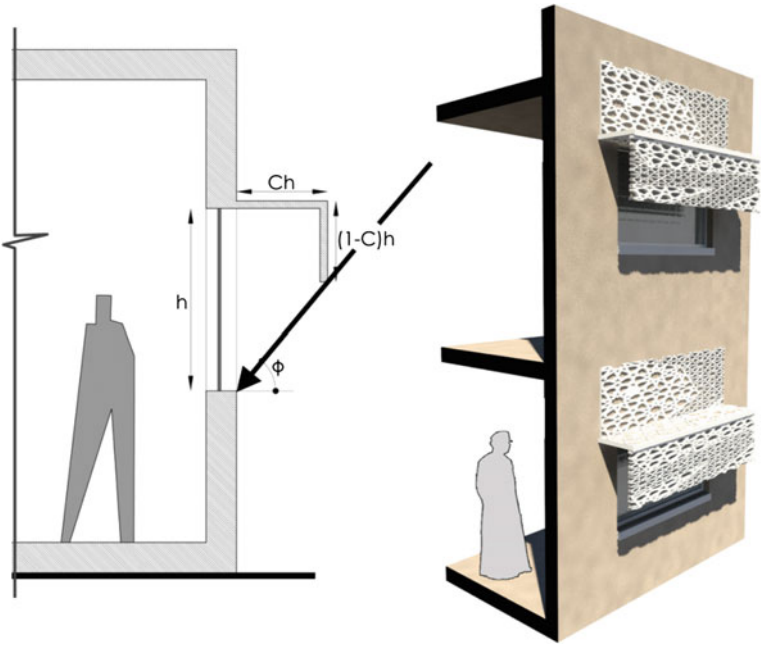

Fig. 20.11 Section and proposed design for light shelf

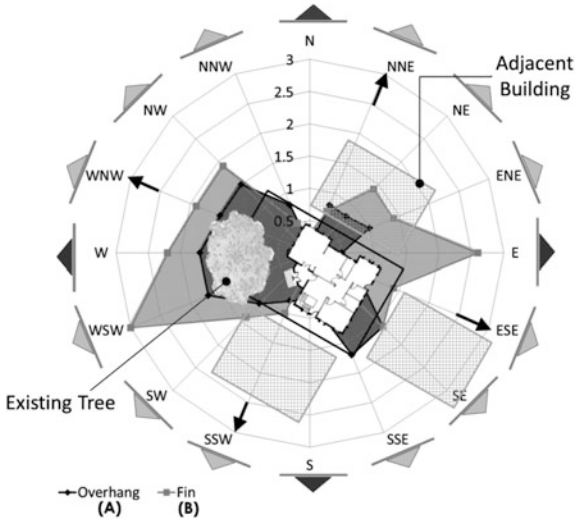

Fig. 20.12 Floor plan of the house with low energy use intensity implemented on shading recommendation diagram

overhang to shade the windows (see Fig. 20.11b). The detached wall helped in shading the wall along with the window and assisted the phenomenon of induced ventilation (Figs. 20.12, 20.13 and 20.14).

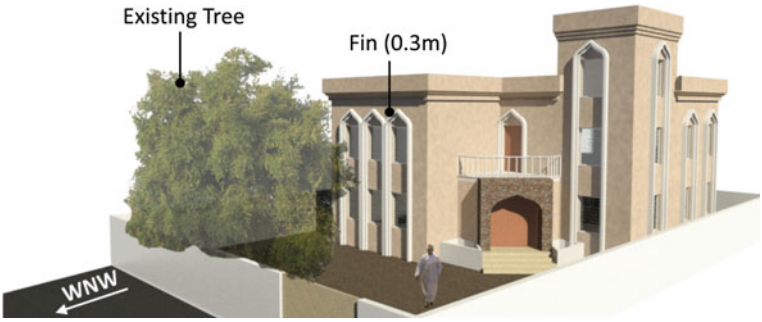

Fig. 20.13 Base case—Low EUI house (21 Oct at 14:00)

Fig. 20.14 Low EUI house after application of recommended shading (21 Oct at 14:00)

Whereas in case of the house with High Energy Use Intensity, parallel strip shading was used with traditional Omani decorations that also helped in aesthetically enhancing the building appearance (Figs. 20.15, 20.16 and 20.17).

Using the given recommendations, shading devices were designed for the two houses. It was found that the energy consumption of both of the houses decreased linearly, it decreased by 10.8 % for the house with high EUI and by 7.3 % for the house with low EUI.

In order to investigate the impact of shading further, sizes overhangs and fins were increased more than the recommendations and it was found that the impact of shading on energy consumption decreased, leading to a diminishing return. This indicates that the recommendations given for sizing the overhang and fin are valid and the impact of any additional shading will not help in decreasing the energy consumption as efficiently (Fig. 20.18).

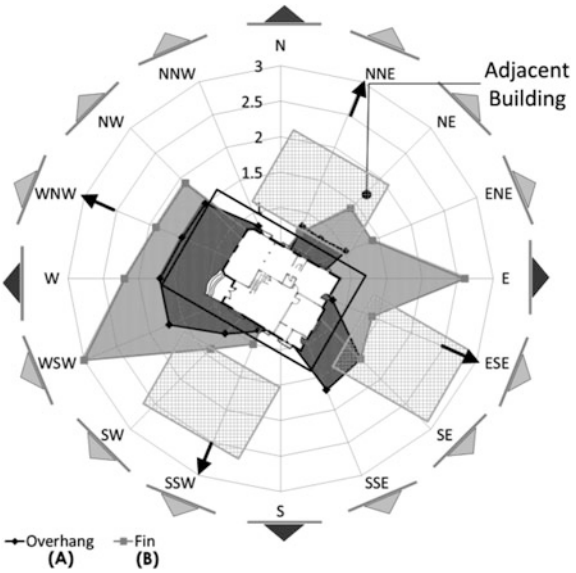

Fig. 20.15 Floor plan of the house with high energy use intensity implemented on shading recommendation diagram

Fig. 20.16 Base Case—High EUI house (21 Oct at 14:00)

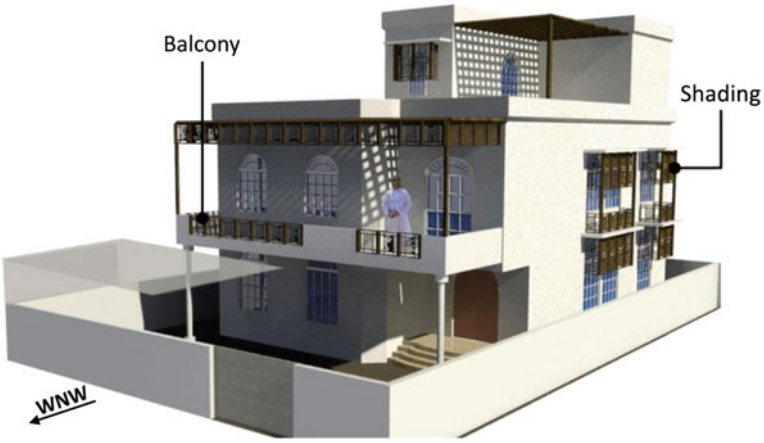

Fig. 20.17 High EUI house after application of recommended shading (21 Oct at 14:00)

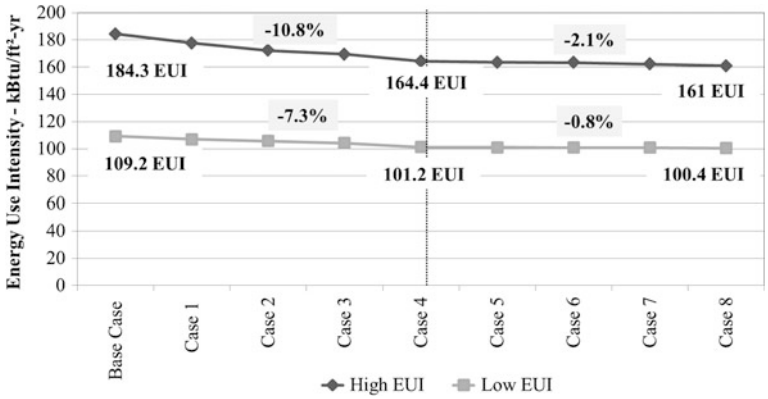

Fig. 20.18 Impact of shading on energy consumption

20.4 Conclusion

Oman has not yet fully adopted nor developed green building guidelines, so it is very necessary to introduce some energy conservation guidelines through sustainable building in the community. Providing designers in Oman with a proposed set of guidelines and recommendations will assist them in making energy efficient decisions during early stages of design, significant amounts of energy can be saved. This will also help reduce building energy consumption without increasing the construction cost. The proposed energy efficient design recommendations are culturally appropriate and can be integrated with the culture of Oman, which would encourage the community to embrace these choices easily.

Acknowledgement Al-Hashim thanks Khalid Al-Hashmi, directorate general of technical affairs at Muscat Municipality for their assistance in providing data for Omani houses. Also the author thanks Saleh Al-Saadi, lecturer at Sultan Qaboos University, Department of Civil & Architecture Engineering for providing weather data of Oman.

References

1. N.H. Abdul Majid, H. Shuichi, N. Takagi, Vernacular wisdom: the basos of formulating compatible living environment in Oman. in *ASIA Pacific International Confrence on Environment-Behaviour Studies.* Giza, Egypt, 2012
2. Statistical year book (2006), Sultanate of Oman: Ministry of National Economy
3. O. Authority for Electricity Regulation (2009), Annual report
4. B.J. Urban, L. Glicksman, The MIT design advisor: a fast, simple tool for energy efficient building design. in *Second National IBPSA-USA Conference,* Cambridge, 2006
5. L.T. Chadwick, *Solar Effects on Building Design* (Building Research Institute, Roorkee, 1962)
6. A. Al-Badi, A. Malik, A. Gastli, Assessment of renewable energy resources potential in Oman and identification barrier to their significant utilization. Renew. Sustain. Energy. Rev. **13**(9), 2734–2739 (2009)
7. H. Al-Hinai, W. Batty, S. Probert, Vernacular architecture of Oman: features that enhance thermal comfort achieved within buildings. Appl. Energy **44**, 233–258 (1993)
8. A. Al-Badi, A. Malik, A. Gastlii, Sustainable energy usage in Oman-opportunities and barriers. Renew. Sustain. Energy. Rev. **15**, 3780–3788 (2011)
9. Mo Economy, *Statistical Yearbook—2010* (Ministry of National Economy, Muscat, 2010)
10. N.C. Chalfoun, V. Cardona, in *Development of Pima County Net-Zero Energy Code; Shading Projection Factors*, Tucson, Arizona, USA, June 2011
11. A. Olgyay, V. Olgyay, *Solar Control and Shading Devices* (Prinston, New Jersey, 1957)

Chapter 21
Thermal Performance of Ferrocement Green Building System

Wail N. Al-Rifaie, Waleed K. Ahmed, L. E. Ibraheem and H. Y. Al-Samarraie

Abstract Urban development is a key consumer of energy, a ferrocement structural system based on generic services facilities is introduced and prefabricated cavity walls/and roofs within the structural system present a series of possibilities for the solution of building construction at maximum reduction of the electrical energy. The energy required to run the building using the proposed ferrocement construction system is determined and the possibility of using the renewable energy production rather than energy depleted is presented.

Keywords Ferrocement · Thermal · Green building

21.1 Introduction

System must not only cope with strengths and flexibility requirements, but the insulation value is of high importance. In summer heat must be kept outside as much as possible. The great demands of electric power due to heating and air-conditioning systems require control to make maximum reduction of the electrical energy. No matter which technology would be used, green building is always based on the principle of 3R (reduce, reuse, recycle) [1]. Many success projects

W. N. Al-Rifaie (✉)
Civil Engineering, Philadelphia University, Amman, Jordan
e-mail: wnrifaie@yahoo.com

W. K. Ahmed
United Arab Emirates University, AlAin, United Arab Emirates

L. E. Ibraheem
University of Tikrit, Tikrit, Iraq

H. Y. Al-Samarraie
SDI Company, Samarra, Iraq

M. O. Hamdan et al. (eds.), *ICREGA'14 - Renewable Energy: Generation and Applications*, Springer Proceedings in Energy, DOI: 10.1007/978-3-319-05708-8_21,

have shown that the green buildings are not really hard to achieve. The key lies in the architect's mind, with this goal, as long as architects grasp the local condition in deep understanding, then doing some simple technologies combination in practices. The green buildings may be full construct in a common sense. Therefore, green buildings are the buildings that filled with the fill local features, which not only referring the form, but also the meeting to local natural, social, economic, resource and other conditions. Therefore, the technology combination and forms of green buildings' will always change [2]. There are many definitions of green building. For instance, Kibert defined green building as: healthy facilities designed and built in a resource-efficient manner, using ecologically based principles [3]. It is worth noting that green building has been used as a term interchangeable with sustainable building and high performance building. Robichaud and Anantatmula pointed out that there are four pillars of green buildings, i.e. minimization of impacts on the environment, enhancing the health conditions of occupants, there turn on investment to developers and local community, and the life cycle consideration during the planning and development process [4]. Common elements of these definitions are: life cycle perspective, environmental sustainability, health issues and impacts on the community [5]. Although new technologies are constantly being developed to complement current practices in creating more sustainable buildings, the common objective is that green buildings are designed to reduce the overall impact of the built environment on human health and the natural environment by the following goals of sustainable building: (a) Life cycle assessment (LCA), (b) Energy Efficiency and Renewable Energy, (c) Water Efficiency, (d) Environmentally Preferable Building Materials and Specifications (e) Waste Reduction, (f) Toxics Reduction (g) Indoor Air Quality, (h) Smart Growth and Sustainable Development, (i) Environmentally Innovative materials and services [6]. The increasing demand to low energy houses has led to the introduction of so called green building. The basic idea of introducing green or eco-house concept is to improve the thermal performance of the building envelope to a level where the heating and/or cooling system can be kept very simple. Reducing the amount of energy required to run a building means reducing the emissions of carbon dioxide. The emissions of carbon dioxide depends on the fuel source for kWh. If it is wind, solar, hydroelectric or nuclear, then zero pounds of carbon dioxide are created. To estimate CO_2 emissions per kWh, the U.S. average in 2005 is adopted in the present work. The average is approximately 1.31 pounds of CO_2 per kWh generated. It has been stated that by adjusting your home heating and cooling by just 3°; turning the heat down and the cooling up, can save over 1000 pounds of CO_2 emissions each year. The satisfaction of building users is closely related to thermal comfort which is a complex dynamics of temperature and humidity [7–9]. This has attracted extensive attention from researchers to simulating and measuring the thermal comfort level in green building compared to conventional buildings. As a result, the range of room temperature required could be proposed [10, 11]. Psycho-logical, physiological, cultural and behavioral factors may play a role as well which attributes to adaptive thermal comfort [12–15]. Ferrocement is an excellent construction material due to its mechanical properties,

and low cost, and it is considered to possess a high cracking strength. Cement mortar and wire mesh as reinforcement are the materials used in casting the ferrocement structural panels which is a cement composite material made up of Portland cement, sand, water and sometimes admixtures [16]. A structural system based on generic services facilities is introduced by Al-Rifaie [17] and prefabricated ferrocement cavity walls and/or roofs within the proposed system present a series of possibilities for the solution of building construction at maximum reduction of the electrical energy and the modern system provide excellent thermal insulation. The energy required to run a building using the proposed ferrocement structural system is determined and the possibility of using the renewable energy production rather than energy depleted is presented.

21.2 The Proposed Modern Method of Ferrocement Green Building System

The thermal performance of the structural system for ferrocement construction based on generic services facilities is introduced. The construction concepts as shown in Fig. 21.1 lend themselves readily to rapid delivery and assembly of flexible accommodation where designs can be adapted to meet local requirements for both structural performance and thermal comfort as shown in the figure.

The structural part of the house consists of three basic components; the base, walls, and roof. An integral framing concept allows for overall above-ground structural integrity which considerably exceeds that of traditional methods and this minimizes the need for ground works in all. The membrane construction also enables new concepts in passive downdraught cooling to be explored where airways are incorporated within structural features as wall cavities. The major advantages of a ferrocement construction system over current construction methods may be found in reference [17]. As stated earlier that the structural system for ferrocement construction based on generic services facilities and insulating these structures involves the application of insulation material by means of cavity wall construction which consists of two leaves (sides) of ferrocement (30 mm each) separated by a wide space and insulation material is used through a cavity wall. Test was carried out on a ferrocement cavity wall panel with insulation panel placed between the two leaves of the wall panel as shown in Fig. 21.1, where a direct fire was carried out to the front face of the panel, so the temperatures were measured on the front and the rear face of the panel. The measured temperatures were 230 °C and 22 °C on the front and the rear faces respectively. The obtained results showed that cavity wall construction consists of two leaves (sides) of ferrocement, separated by air space and the insulation panel positioned as shown in the figure gives a very good solution for insulation, (air is still the actual insulator), consequently reducing the demand to electrical energy. Cavity wall insulation may also be used to reduce heating/or cooling losses.

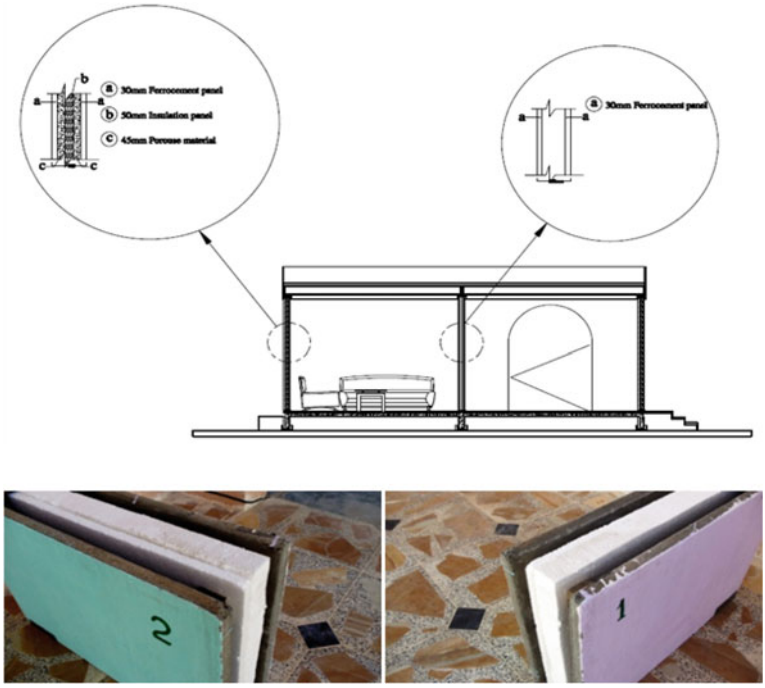

Fig. 21.1 The proposed ferrocement system for house construction

21.3 Energy Assessment

In home construction there are two main areas have to be in focus: energy efficiency and construction efficiency. The present work concern with energy efficiency. In fact energy performance is highly prioritized in the development of building systems and construction productivity. It may be noted that the materials used for outer and inner wall finishing considered through the determination of heating and cooling loads are cement mortar and gypsum plastering respectively. Also, 100 mm concrete lining and 50 mm tiles with cement mortar for ground finishing and 150 mm soil and 40 mm tiles for roofing are considered in the determination of heating and cooling loads.

21.4 Residential Heating and Cooling Load Calculation Requirements

For assessing the energy efficiency of a residential house, the design temperatures for use in performing load calculations considered in the present work are:

In winter: Indoor = 25 °C, Outdoor = 0 °C
In summer: Indoor = 23 °C, Outdoor = 57 °C.

The data used in the assessment was assumed that the residential area subjected to very hot weather condition in summer and very cool weather climate in winter. To determine the annual heating and/or cooling energy consumption of a residential home, the following formulas are used in the present investigation [18, 19]:

21.4.1 Heating Load

$$Q_p = U_p A_p (t_i - t_o) \tag{21.1}$$

where:

Q_p Heat Loss from the panel, Watt
A_p Net Area (normal to heat flux direction), m^2
t_i Indoor temperature(desired temp.), °C
t_o Outdoor temperature, °C
Up Panel overall heat transfer coefficient, $U_p = 1/\sum R_{th}$, Watt/m^2·°C
R_{th} Thermal resistance(for each layer of panel), m^2·Co/Watt
R_{th} L/KA
L Panel layer thickness. m
K Thermal conductivity (for each layer according to the material used), Watt/m·°C
A Area (normal to the heat flux). m^2

21.4.2 Cooling Load

$$q = U \times A \times CLTD \tag{21.2}$$

where:

q Heat gain (from walls and roofs), Watt
U Wall overall heat transfer coefficient. Watt/m^2·°C
A Area (normal to the heat flux direction), m^2
CLTD (Cooling load temperature difference), °C.

21.4.3 Heat Gains from Doors and Windows (Glasses)

$$q/A = (SC) \times (SHG)_{max} \times (CLF) \tag{21.3}$$

where:

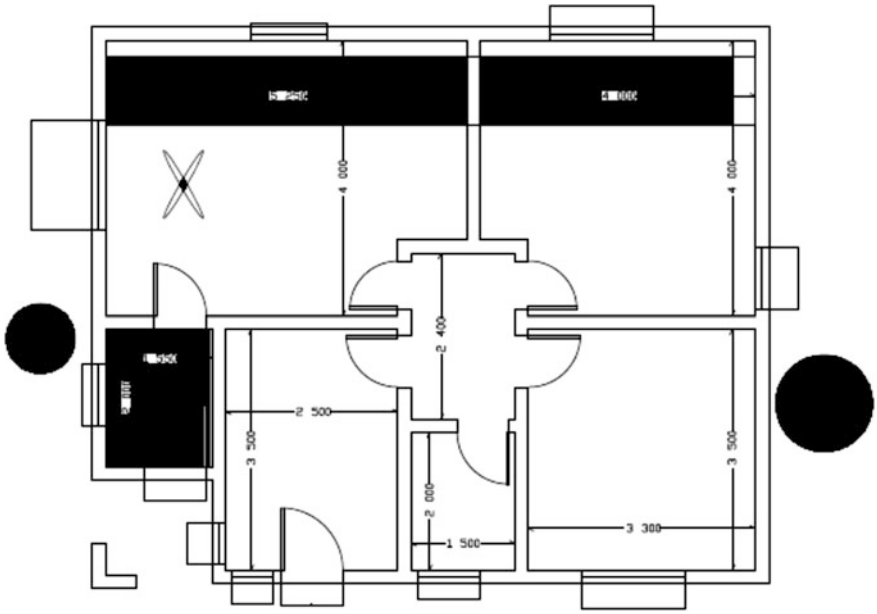

Fig. 21.2 The 77 m^2 residential house adopted in the present work

q/A Heat gain per unit area of glass, Watt/m^2
SC shading coefficient (Ref. [19])
SHG solar heat gain (Ref. [18])
CLF cooling load factor (Ref. [18])

The values of the overall heat transfer coefficient of each of the ferrocement structural panel are 0.22 for ferrocement cavity wall with insulation panel positioned between the two ferrocement leaves and 0.1337 for ferrocement channel like cross-section.

The 77 m^2 residential house shown in Fig. 21.2 is chosen in the present work. Heating and cooling loads can be determined using a whole house approach. Using expressions 21.1, 21.2, and 21.3, the heating and cooling loads are (9.328 kW, 2.653 ton) and (8.012 kW, 2.278) respectively. It may be noted that 1 Ton of refrigeration = 3.517 kW is used 'for calculating the amount of heating or cooling.

It is assumed in the present work that a single home need to run 20 h of electricity per day to cover the need for heating and cooling.

To estimate carbon dioxide (CO_2) emissions, the U.S. average of CO_2 per kWh in 2005 which was approximately 1.31 pounds per kWh is adopted to determine the emissions of CO_2 per month.

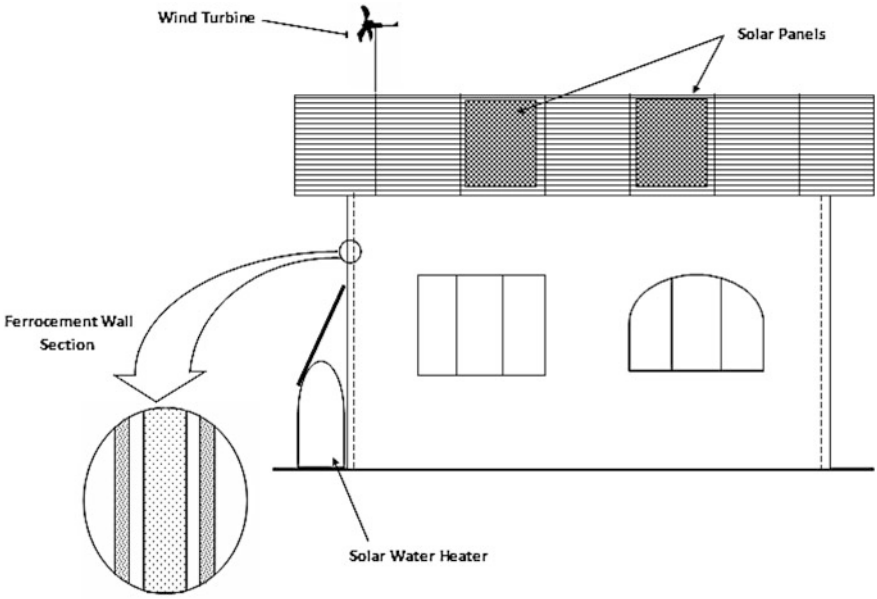

Fig. 21.3 Proposal for the possibility of using solar energy or wind energy or both combined

1. Heating load = 5597.29 kWh/month, the emission of carbon dioxide CO_2 = 6324.94 pound/month.
2. Cooling load = 4807.25 kWh/month, the emission of carbon dioxide CO_2 = 5432.19 pound/month.

It may be noted that there are some sources that generate heat inside the house have been taken into consideration such as cooker, and frozen refrigerator and sources that have been neglected such as house lighting.

21.5 Proposed Renewable Energy System

The reduction in the amount of energy needed for running heating or cooling of 77 m^2 house shown in Fig. 21.2 when the modern ferrocement system is used, may leads us to the possibility of using renewable energy rather than physical energy depleted. Since wind energy is considered as one of the renewable energy system, since it produce electricity by using the power of the wind to drive an electrical generator [20], it was proposed of using solar energy or wind energy or both combined, as shown in Fig. 21.3.

21.6 Conclusions

High standards of energy efficient housing construction have been demonstrated in the present work. It may be seen that the modern method (ferrocement housing system) is able to produce very energy efficient dwellings. It is seen that with thermal insulation installed as part of the cavity construction panels lend to achieving high levels of thermal performance.

References

1. Q. Baoxing, *Energy Efficiency and Green Building* (China Building Industry Press, Beijing, 2011)
2. P. Fenga, Brief discussion of green buildings. International conference on green buildings and sustainable cities. Procedia Eng. **21**, 939–942 (2011)
3. C.J. Kibert, *Sustainable Construction: Green Building Design and Delivery* (John Wiley and Sons, Hoboken, 2008)
4. L.B. Robichaud, V.S. Anantatmula, Greening project management practices for sustainable construction. J. Manage Eng. **27**(1), 48–57 (2010)
5. J. Zuo, Z. Zhao, Green building research current status and future agenda: a review. Renew. Sustain. Energy Rev. **30**, 271–281 (2014)
6. K.I. Vatalisa, O. Manoliadisb, G. Charalampidesa, S. Platiasa, S. Savvidisa, Sustainability components affecting decisions for green building projects. Procedia Econ. Finance **5**, 747–756 (2013)
7. Y. Zhang, H. Altan, A comparison of the occupant comfort in a conventional high-rise office block and a contemporary environmentally-concerned building. Build. Environ. **46**(2), 535–545 (2011)
8. S. Mekhilef, A. Safari, W. Mustaffa, R. Saidur, R. Omar, M. Younis, Solar energy in Malaysia: current state and prospects. Renew Sustain Energy Rev. **16**(1), 386–96 (2012)
9. T.S. Bisoniya, A. Kumar, P. Baredar, Experimental and analytical studies of earth–air heat exchanger (EAHE) systems in India: a review. Renew. Sustain. Energy Rev. **19**, 238–246 (2013)
10. F. Sicurella, G. Evola, E. Wurtz, A statistical approach for the evaluation of thermal and visual comfort in free-running buildings. Energy Build. **47**, 402–410 (2012)
11. A. Aminuddin, S.P. Rao, H.W. Thing: Thermal comfort field studies in two certified energy efficient office buildings in a tropical climate. Int. J. Sustain. Build. Technol. Urban Dev. **3**(2), 129–36 (2012)
12. N. Djongyang, R. Tchinda, D. Njomo, Thermal comfort: a review paper. Renew. Sustain. Energy Rev. **14**(9), 2626–2640 (2010)
13. M.K. Singh, S. Mahapatra, S.K. Atreya, Adaptive thermal comfort model for different climatic zones of North-East India. Appl. Energy **88**(7), 2420–2428 (2011)
14. S.T. Mors, J.L. Hensen, M.G. Loomans, A.C. Boerstra, Adaptive thermal comfort in primary school class rooms: creating and validating PMV-based comfort charts. Build. Environ. **46**(12), 2454–2461 (2011)
15. M.P. Deuble, R.J. de Dear, Green occupants for green buildings: the missing link? Build. Environ. **56**, 21–27 (2012)
16. W.N. Al-Rifaie, W.K. Ahmed, O.M. Mahdi, in *NuRER 2012—Proceedings of the 3rd International Conference on Nuclear and Renewable Energy Resources.* Performance of ferrocement using NSCSC mortar, İstanbul, Turkey, May 2012

17. W.N. Al-Rifaie, in *7th. Municipal Work, Conference and Exhibition, Kingdom of Bahrain.* Modern housing system using ferrocement as sustainable construction materials, 24–26 April 2012. http://www.municipality.gov.bh/mun/docs/MunicipalConference2012/Day1_25thapril/papers/13.%20Dr.%20Wail%20N.%20Al-Rifaie.pdf
18. R.C. Jordan, G.B. Priester, *Refrigeration and Air-Conditioning* (Prentice Hall, New York, 1956)
19. J.P. Holman, *Heat Transfer*, 6th edn. (McGraw Hill, New York, 1986)
20. W.K. Ahmed, Mechanical modeling of wind turbine: comparative study. Int. J. Renew. Energy Res. **3**(1), 94–97 (2013)

Chapter 22
Using PCM Implanted in Building Material for Thermal Management: One Versus Seven Days Assessment

Emad Elnajjar

Abstract The objective of this work is to investigate numerically the thermal analysis of capacitive insulators bricks containing an organic phase change material (PCM) in United Arab Emirate (UAE) hot climate. PCM Latent heat of fusion is secondhand to reduce the heat loads fluctuation and the peak time shifting, which in turn reduces the consumed energy for cooling and therefore reduce green gases emissions. An average of one verses 7 days analysis were performed to account for the cyclic behavior of the PCM in the building material. The study focus on demonstrating the contradictory and deceiving results which can be withdrawn from each analysis.

Keywords CFD · PCM · Thermal managements · Cooling loads · Energy saving

22.1 Introduction

Internationally, especially in areas with hot climate the energy consumption for thermal comfort has plant, the occupied big portions of the produced energy. The continuous increase of the fuel prices and with the large emphasis on the reduction of the CO_2 emissions. Therefore, it became very important to come up with more passive and active methods of reducing energy consumption and shifting the peak demand for more economical power production scheme and producing more sustainable buildings.

Using phase change materials (PCM) in buildings is an active field of research since 1980. Building materials encapsulated with PCM have experienced problems that have stopped them from being used in large scales; the problems can be

E. Elnajjar (✉)
United Arab Emirates University, Al Ain, United Arab Emirates
e-mail: Eelnajjar@uaeu.ac.ae

M. O. Hamdan et al. (eds.), *ICREGA'14 - Renewable Energy: Generation and Applications*, Springer Proceedings in Energy, DOI: 10.1007/978-3-319-05708-8_22,

briefed by the following: high investment cost, the stability and the degradation of the PCM thermal properties for cyclic usage and the strength of the constructed walls [1].

Using the PCM in construction materials shows very promising results such reducing the level of temperature fluctuation, and therefore, saving the consumed energy and cutting of the CO_2 emission generated. Where, during day time, energy saved by absorbing the heat through melting the PCM. During night time, PCM is releasing the stored energy through the solidification process. Studies reported 10–17 % saving of the consumed energy [1–5].

In order to reduce the heating and cooling loads from the outdoor to indoor space researchers investigate using PCM in building bricks and walls to slow down the flow of heat. This is known as a latent heat method of energy storage where, during the daytime, the PCM absorbs the energy through the melting process, and during the night time it releases the energy through solidification processes. This is why, a PCM type of insulator is considered as a capacitive type.

The latent energy storage method, comparing to the sensible storage, provides a much higher energy storage density with a smaller temperature variation. Nevertheless the latent heat method using PCM has it is a challenge: it has low thermal conductivity and low density and stability comparing to the conventional storage method. The perfect PCM to be used in storage applications needs to have the following properties: it must have large fusion capacity, high thermal conductivity, and should be cheap, also they need to have a melting temperature that suite the operation temperature of the application, chemically stabile, non toxic and non corrosive. PCM is produced from organic and nonorganic material such as: hydrated salt, paraffin waxes, fatty acids and eutectics [5]. As mention before the melting temperature of the PCM decides the application type. For materials with a melting temperature of below 15 °C they are used to store coolness in air condition applications, while, for the ones with a melting temperature above 90 °C which is used in absorbing refrigeration. And for the PCMs with melting temperatures in between, are used in solar heating and heat leveling applications. Table 22.1, contains a comparison between different methods of heat storage [9].

Castell et al. [1], are experimentally testing the PCM with two types of typical construction material. The study shows the PCM reduces the peak temperature by 1 °C and the electrical energy consumption by 15 %.

Alawadhi [2], numerically investigated the thermal analysis of building bricks encapsulated with PCM used in Kuwait's hot climate. A finite element method was used in modeling a wall built of 2-D bricks with cylindrical holes filled with PCM. A parametric study of PCM quantity, location and type were conducted. The results reported a reduction of 17.55 % in heat flux at the indoor space.

Diaconu et al. [4], proposed using a composite material made up of two different PCM materials with different values and thermo physical properties. The new PCM was impregnated in a new type of wall. The study shows that using the proposed walls save energy and it reduces the peak value of the cooling and heating loads.

Table 22.1 Thermo-physical properties of Brick And Pcm [2]

Material	C kJ/kg °C	K W/m °C	ρ kg/m^3	Latent heat kJ/kg	Tm °C
Brick	0.84	0.7	16		
n-Octadecane	1.93 (s), 2.19 (l)	0.358 (s), 0.148 (l)	865 (s), 780 (l)	243.5	27
n-Eicosane	2.01 (s), 2.04 (l)	0.15 (s), 0.15 (l)	778 (s), 856 (l)	241.0	37
P116 (Paraffin Wax)	2.4 (s), 1.9 (l)	0.24 (s), 0.24 (l)	830 (s), 773 (l)	225.0	47

Farid et al. [5], reviewed latent heats as energy storage methods. They focused on three aspects: PCM material, encapsulating techniques, and applications and problems associated using PCM for certain specific applications.

The present work study numerically the energy saving due to embedded PCM material in UAE's typical building material. The analysis focus on comparing the performed for 1 day versus 7 days analysis.

22.2 Mathematical Model

The modeled wall is shown in Fig. 22.1, the analysis domain is performed with all boundary conditions is described in Fig. 22.2. To simplify the numerical model, the following assumptions are adopted:

- Wall end effects on the heat transfer is negligible
- The Problem is two dimensional because the wall width is much larger comparing to its thickness.
- The thermo-properties for the bricks are constant.
- The Thermo-properties of the PCM is function of temperature.
- The thermal expansion of the PCM and the bricks is neglected.
- The natural convection between the PCM and the bricks is negligible.

Keeping the above assumption in mind the numerical model illustrates the problem in hand can be described by the following set of equations and boundary conditions. The two transient dimensional conjugate conduction energy equations for the Bricks and the PCM are used to model this problem:

$$\rho_b C_b \frac{\partial T_b}{\partial t} = k_b \left(\frac{\partial^2 T_b}{\partial x^2} + \frac{\partial^2 T_b}{\partial y^2} \right) \tag{22.1}$$

$$\rho_{PCM} C_{PCM} \frac{\partial T_{PCM}}{\partial t} = k_{PCM} \left(\frac{\partial^2 T_{PCM}}{\partial x^2} + \frac{\partial^2 T_{PCMb}}{\partial y^2} \right) \tag{22.2}$$

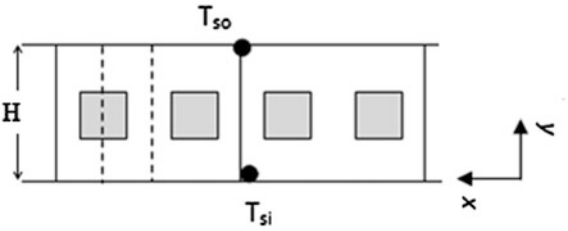

Fig. 22.1 The wall section description

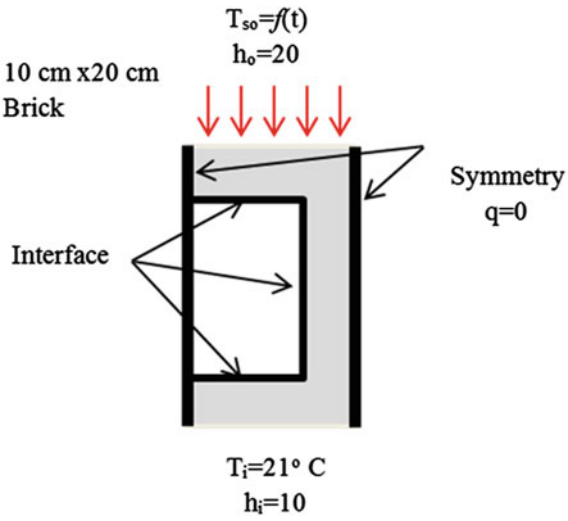

Fig. 22.2 Schematic representation of the computation domain with assigned boundary conditions

The specific heat and the density the PCM are:

$$C_{PCM} = \begin{cases} C_{s-PCM} & T < T_m \\ \frac{C_{s-PCM}+C_{l-PCM}}{2} + \left(\frac{\lambda}{\Delta T}\right) & T_m < T < T_m + \Delta T \\ C_{l-PCM} & T > T_m + \Delta T \end{cases} \tag{22.3}$$

$$\rho_{PCM} = \begin{cases} \rho_{s-PCM} & T < T_m \\ \frac{\rho_{s-PCM}+C_{l-PCM}}{2} + \left(\frac{\lambda}{\Delta T}\right) & T_m < T < T_m + \Delta T \\ \rho_{l-PCM} & T > T_m + \Delta T \end{cases} \tag{22.4}$$

The boundary and initial conditions described the computational domain, starting with inside the cold surface natural convection boundary condition:

$$-k_b \frac{\partial T_b}{\partial y}|_{y=0} = h_i(T_i - T_{si}) \tag{22.5}$$

Where:

$$T_{inside} = 21\,^{\circ}\mathrm{C}$$
$$h_{inside} = 10\,\frac{\mathrm{W}}{\mathrm{m}\,^{\circ}\mathrm{C}}$$

The boundary for the outer surface is a constant heat flux function with different time of the day

$$q_{Outside} = q(t)\,\mathrm{W}/\mathrm{m}^2 \tag{22.6}$$

Along the left and right symmetry line a symmetry boundary condition is used:

$$\left.\frac{\partial T}{\partial x}\right|_{x=left-side} = \left.\frac{\partial T}{\partial x}\right|_{x=right-side} = 0 \tag{22.7}$$

At the brick/PCM interface a conjugate boundary condition is used:

$$-k_b\frac{\partial T_b}{\partial n} = k_{PCM}\frac{\partial T_{PCM}}{\partial n} \tag{22.8}$$

Where n is the coordinate normal to the surface of PCM /brick surfaces.

The initial temperature condition of the computational domain is: $T_{initial} = 21$ °C. Table 22.1 shows the thermo physical properties of the used bricks and PCM material, [2]. Hourly solar radiation for 2012, in UAE-Al Ain city is provided by the weather forecast department in Al-Ain UAE, for the month of June is displayed in Fig. 22.3. This data is used in the numerical simulation to study the thermal management performance of a brick wall implanted with PCM. The analysis are performed to 1 day and 7 day power saving evaluation.

22.3 Results and Discussion

The main aim of the present work is to is to carry out numerical simulation to study the saving of cooling energy due to embedding a PCM material inside a typical bricks material used in UAE buildings. The focus of this paper will be on evaluating 1 day versus 7 days assessment on the saving performance.

Figures 22.4, 22.5, 22.6, 22.7, 22.8 and 22.9 are displaying the temperature mapping development and the liquid fraction representing melting/solidification during the first 24 h showing intervals of 6 h, a cross the computation domain of the a brick embedded with one type of PCM (n-Octadecane). The figures shows the development of the higher temperature distribution and the continuous increase in melting of the PCM.

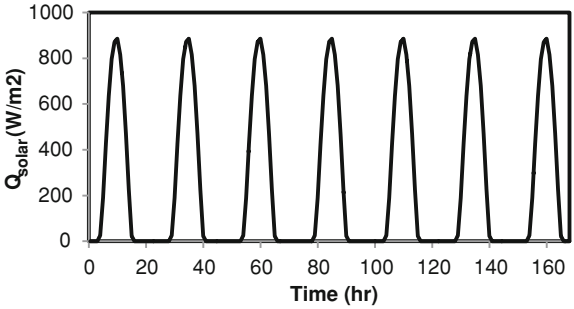

Fig. 22.3 Hourly variation of solar radiation (7 days measurements) for the month of June 2012 in UAE- Al Ain

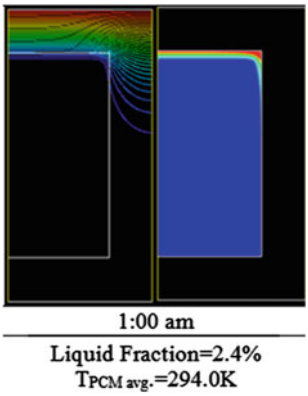

Fig. 22.4 Temperature and liquid fraction contours during the 24 h analysis (1 am)

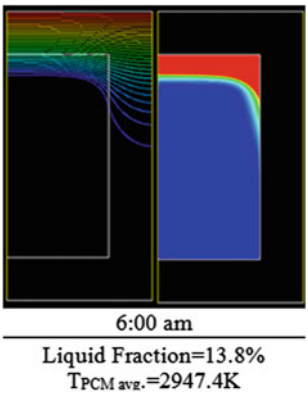

Fig. 22.5 Temperature and liquid fraction contours during the 24 h analysis (6 am)

Figure 22.10 shows the melting/solidification of the three used PCM material during the 7 days. Keeping in mind that the melting temperatures for the three used PCM: (n-Octadecane, n-Eicosane and P116) are 27, 37 and 47 °C respectively. From the figure it can be noticed for the PCM with melting temperature of 27 °C (n-Octadecane) it melts after 24 h and sty melted for the rest of the studied

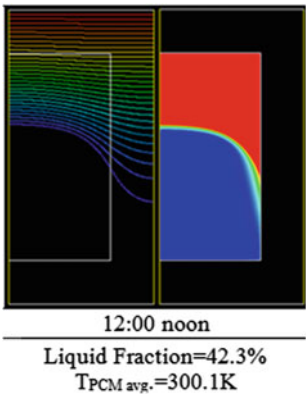

Fig. 22.6 Temperature and liquid fraction contours during the 24 h analysis. (12 noon)

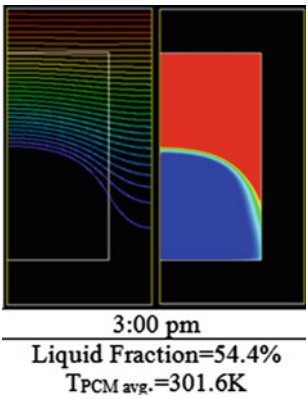

Fig. 22.7 Temperature and liquid fraction contours during the 24 h analysis (3 pm)

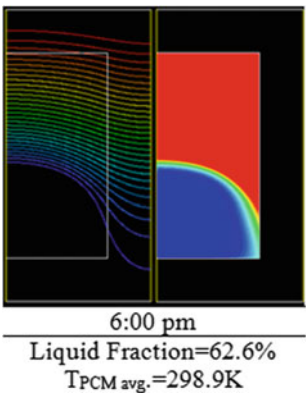

Fig. 22.8 Temperature and liquid fraction contours during the 24 h analysis (6 pm)

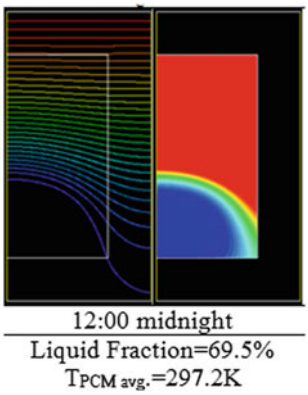

Fig. 22.9 Temperature and liquid fraction contours during the 24 h analysis (12 midnight)

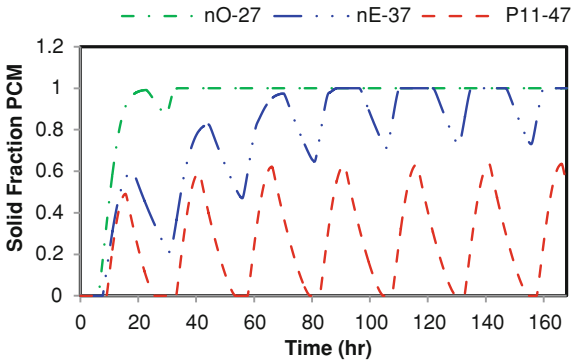

Fig. 22.10 the liquid fraction of solidified/melting of PCM with time

period. Which suggest that after the first day this PCM material is not useful, because for the PCM material to be efficient and to perform what is expected it has to go through a cyclic process of melting/solidification. Meanwhile, for PCM (n-Eicosane) with melting temperature of 37 °C, it goes through a cyclic phase of melting/solidification during the 7 days period but with a damping effect. And finally, for for PCM (P111) with melting temperature of 47 °C, it goes through a cyclic phase of melting/solidification during the 7 days period consistent effect. This figure suggest two pacts keeping in mind the nature of the weather in UAE: firstly, 1 day evaluation can be deceiving where it will suggest that the PCM n-Octadecane is doing great job which is not the case after the first day. Secondly, choosing the proper PCM material for this application is tricky and it required at least 7 day analysis evaluation.

Figure 22.11 displays the heating load inside the space for all cases referenced to the pure brick case. The graph suggest that for the first day the PCM (n-Octadecane); with the lowest melting point shows the best performance comparing to all cases. And this effect is start damping as days progress from first day to the seventh day. Over all PCM (P116) with the highest melting temperature it demonstrate better performance comparing to all studied cases.

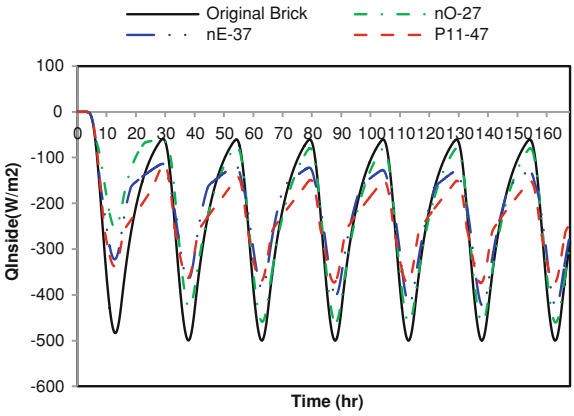

Fig. 22.11 The heat flux at the indoor surface for different type of PCM

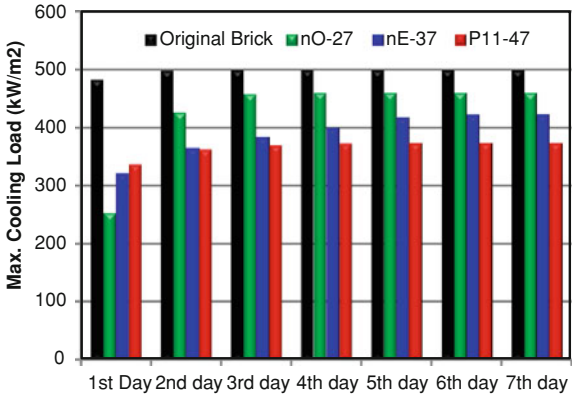

Fig. 22.12 The accumulated heating flux load at indoor surface for different types of PCM

Figure 22.12 shows the percentage reduction/increase of the heat flux at the indoor surface with respect to the reference case (original brick without PCM). Form this figure we can observe the following: for the first day assessment the PCM (n-Octadecane) provides more than 50 % reduction in cooling comparing to the reference and other PCM bricks, where (n-Eicosane) provide about 40 % reduction and (P111) around 30 % and this in agreement with the fact that all (n-Octadecane) is melted and absorbed all latent heat energy. After running the analysis for 7 day the results revels totally different results. Where the analysis suggest that the bricks with (n-Octadecane). gives less than 10 % reduction, the bricks with PCM (n-Eicosane) saves about 16 % and the largest saving is due to bricks with PCM (P111) which about 30 %.

22.4 Conclusions

The main outcome of this work can be summarized by the following:

- One day evaluation can be deceiving where it will suggest that the PCM (n-Octadecane) is doing great job which is not the case after the first day.
- Choosing the proper PCM material for this application is tricky and it required at least seven day analysis evaluation.
- PCM (P116) with the highest melting temperature it demonstrate best performance comparing to all studied cases for bricks with and without PCM.
- After 7 days assessment bricks with PCM (P111) demonstrate a 30 % reduction and energy saving.
- It is believed that the degradation of the PCM material in this application is due to the accumulated temperature variation nature during the seven day evaluation compared to one day evaluation.

Acknowledgments The author would like to acknowledge the support provided by United Arab Emirates University. This work was financially supported by the Faculty of Engineering in the United Arab Emirates University through seeds project funding.

References

1. A. Castell, M. Medrano, G. Perez, L. Cabeza, Experimental study of using PCM in brick constructive solutions for passive cooling. Energy Build. **42**, 534–540 (2010)
2. E. Alawadhi, Thermal analysis of building brick containing phase change material. Energy build. **40,** 351–357 (2008)
3. E. Alawadhi, Temperature regulator unit for fluid flow in a channel using phase change material. Appl. Therm. Eng. **25,** 435–449 (2005)
4. M. Diaconu, M. Cruceru, Novel concept of composite phase change material wall system for year-round thermal energy savings. Energy Build. **42**, 1759–1772 (2010)
5. M. Farid, A. Khudhair, S. Razack, S. Al Hallaj, A review on phase change energy storage: material and application. Energy Conver manage. **45**,1597–1615 (2004)
6. E. Alawadhi, Phase change process with free convection in a circular enclosure: numerical simulation. Comput. Fluids. **33**,1335–1348 (2004)
7. V. Tyagi, D. Buddhi, PCM thermal storage in building: a state of art. Renew. sustain. energy rev. **11**, 1146–1166 (2007)
8. J. Kosny, D. Yarbrough, W. Miller, T. Petrie, P. Childs, A. Mohiuddin, D. Leuthold, PCM-enhanced building envelopes in current ORNL research projects, ORNL report (2006)
9. S.M. Hasnain, Review on sustainable thermal energy storage technologies, part I: heat storage materials and techniques. Energy Convers. Manage. **39**, 1127–1138 (1998)

Chapter 23
Effective U-Value of Wall Assemblies for an Eco-Friendly Paint Coating

S. Shahid, W. Whistler and M. Nazarinia

Abstract The increased amount of carbon dioxide emissions in the atmosphere, and the rapid depletion of fossil fuels have urged the humans to develop technologies that lead in the direction of a sustainable future. The present study was carried out to investigate the effect of U-Values of buildings and villas in the Gulf Cooperation Council (GCC) region. The effective U-Value of two different types of roof assemblies of the GCC region was determined, and comparisons were also made between the U-Values for a standard and eco-friendly paint coating. Four different chambers were designed for this project, which had similar wall assemblies, but different roof specifications. Different parameters were collected and recorded, which showed a minimum of 5 % and a maximum of 11 % reduction in the electrical usage and U-Value for the rooftops that were coated with the eco-friendly paint. It was also observed that the effects of the eco-friendly paint were more prominent when an insulation layer was present in the wall envelope of the roof.

Keywords U-value · Energy saving · Paint coating · Eco-friendly · Wall assemblies · Heat transfer

23.1 Introduction and Background

The world is faced by a very serious environmental threat known as the climate change. This is mainly due to the increased uncontrolled amount of carbon dioxide (CO_2) emissions in the atmosphere. To protect the environment, it is essential that

S. Shahid · M. Nazarinia (✉)
Department of Mechanical Engineering, Engineering and Physical Sciences,
Herriot Watt University, Herriot, UAE
e-mail: m.nazarinia@hw.ac.uk

W. Whistler
Green Building Solutions, Dubai, UAE

M. O. Hamdan et al. (eds.), *ICREGA'14 - Renewable Energy: Generation and Applications*, Springer Proceedings in Energy, DOI: 10.1007/978-3-319-05708-8_23,

technologies to be shifted to low carbon technologies which are more sustainable. These technologies will also be vital for the future when the energy demand would increase as a result of an increase in population. The main source of CO_2 emission in the atmosphere is the fossil fuel. It is being globally acknowledged that fossil fuels are slowly becoming extinct, which means that more focus should be given to renewable energy technologies.

The first step to shift towards a healthy and sustainable environment is to invest in research and development projects that help to achieve the criterion. The prime means by which environmental safety measures can be adapted in existing buildings is by carrying out energy audits and evaluate for thermal heat losses in them. Recently Dubai Municipality had made it mandatory for all government buildings in Dubai, United Arab Emirates (UAE), and optional for all the others to start adapting to the environmental safety measures by 2014 [1]. It will be difficult and even impossible in some cases to accommodate some of the latest technologies into the already existing buildings. Hence, alternative solutions to implement the mandatory regulations should be targeted. One of the few alternatives is using eco-friendly paints as coatings for both the existing and the newly constructed buildings. One of the best technical measures to evaluate the effect of such coatings is wall assembly U-value (see for example [2, 3] and Eq. (23.1)).

The U-value is the measurement of heat transmission through a material or assembly of materials. When U-values for wall assemblies are calculated at an early stage in the design process, it avoids an expensive re-working later on in a project. It also allows the designers to test the feasibility of their project at an early stage to ensure it is fit for purpose and will comply with regulatory frameworks.

U-Value can be calculated using the following equation:

$$Q = \frac{A\Delta T}{R} = UA\Delta T \tag{23.1}$$

where Q is the heat transfer rate (W), A is the surface area (m^2), ΔT is the temperature difference (K or $°C$), R is the thermal resistance or R-Value ($m^2\ K/W$) and U is the thermal transmittance coefficient or U-Value ($W/m^2\ K$).

It is important that the wall assemblies in buildings are properly characterized in order to reduce energy. This may include changes in the induced layers of insulation. Although a lower U-Values accounts for higher energy efficiency, it is seen through experiments that after a certain amount of insulation, U-Value becomes constant. Sometimes more insulation can only mean higher costs.

The present paper will focus on some typical wall envelopes that are used in residential buildings of Dubai and their experimental U-Values, as compared to the theoretical ones. Two wall envelopes that are considered in this study include:

1. Concrete block with expanded polystyrene insulation inserted with light mortar joints.
2. Lightweight aluminum sandwich panel.

Several analyses have been carried out in the literature to identify U-Values of different types of wall assemblies. Suleiman [4] estimated the heat transfer and U-Values for a building that was constructed using common types of wall assemblies in Libya. The wall assemblies were without insulation and made of typical materials, such as bricks, tiles, cement plasters, mortar and ground soils. The external walls of the building were made of concrete and covered with plaster on both sides, while the floor was a mixture of soil, cement and mortar. Suleiman [4] also calculated the annual energy consumption for the building. The first and foremost problem with this type of building is that both the external walls and the roof are constructed with identical materials. As this building was located in a dry and humid area it is important that consideration is given to making separate envelopes for walls and the roof. Another major problem is that the moisture content was ignored while making the overall thermal resistance calculations. The overall U-Value calculations were also only done for the dry conditions, while ignoring the fact that it has a considerable amount of effect on the conductivity of a material.

Friess et al. [5] confirmed the fact that the energy demands in Dubai have increased considerably in the past few years because of the increase in population and urban development. Approximately 29.3 % of energy is consumed only by buildings alone. They observed that by only using expanded polystyrene (EPS) insulation on the reinforced concrete, energy consumptions could be reduced up to 23 %. Other than that if the insulation is used on the overall wall structure, energy consumption could be increased further. The results also showed that only utilisation of the reinforced concrete is not enough and other considerations should be taken into account as well. The right type of insulations and envelopes are very important to help to reduce the U-Value of a wall assembly, especially in hot and humid regions such as Libya and Dubai.

The purpose of the present study is to experimentally investigate the effect of wall assemblies with different paint coatings on U-Value reduction and hence its impact on the energy usage of buildings and carbon footprint. It is assumed that the standards that are provided by the government are usually higher than the experimental analysis. The present work can also help the government to establish reduction of the maximum U-Value defined for the walls and the roof in building envelopes. The eco-friendly paint that was used is especially designed for regions like UAE, where the highest temperatures can reach up to almost 50 °C in summer.

23.2 Methodology

In order to investigate the effect of different paints on the energy savings in particular, four test chambers with dimensions of 90 cm wide × 160 cm long × 110 cm were constructed. Each chamber was oriented with the long axis running in a north-south direction giving maximum morning solar exposure to the east façade and maximum afternoon solar exposure to the west façade. Figure 23.1 shows the orientation of the chambers.

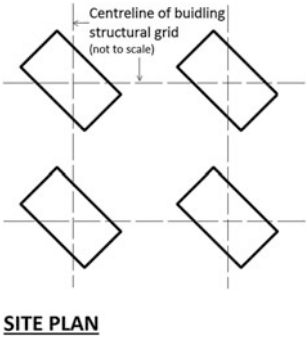

Fig. 23.1 Schematic of the orientation of the chambers

The chambers were constructed on the roof of a factory warehouse building to give the maximum sun exposure and were spaced in such a way so as to avoid any overlapping shadow patterns to interfere with the test surface temperature readings.

At each of reading times, the outside surface temperature, ambient temperature, outside humidity level and interior temperature of the four chambers were individually measured and recorded. With the interior volumes of ambient air continuously being cooled by suitable air conditioners, the electrical energy usage for the four chambers were also measured and recorded three times daily. Each air conditioner was programmed to run continuously to a preset interior air temperature of 23 °C; when this interior temperature was reached, the condenser motor would stop and only the ventilating fan would operate until the preset temperature was reached again.

Test chambers were individually supplied with power through an outlet distribution box connected to the same main building circuit so any supplied power fluctuations would be consistent for the four air conditioning units. Each unit's power supply was connected to a plug in kWh meter, and it was made sure that the four units were switched on simultaneously.

The data measured then was analysed using analytical relations available in the literature (see for example [2, 3]) and discussed in Sect. 23.3.

23.3 Results and Discussion

The experiments were performed for a 16 week period, during which all the data were collected and recorded on the site. The analysis and discussion of results are listed in the following format:

- Temperature analysis for the four chambers at three different hours (i.e. 8 am, 12 and 4 pm.
- Energy analysis for the four Chambers.
- Energy savings.
- Reductions in U-Value.

23.3.1 Temperature Analysis of All of the Chambers

The temperature data was collected at three different times of the day, i.e. 8 am, 12 and 4 pm. Two of the chambers, was mentioned above, were coated (Chambers 1 and 3) with eco-friendly paint and the other two were coated with standard paint (Chambers 2 and 4). It should also be mentioned that two of the chambers' roof top is made of concrete and the other two made of Aluminum. Figures 23.2 and 23.3 show the temperature distribution for Aluminum and Concrete chambers for three different times of the day (i.e. 8 am, 12 and 4 pm), respectively. The square symbol shows ambient temperature (T_{amb}), diamond symbol shows outside surface temperature (T_s) and circle symbol shows inside temperature (T_i). The filled symbols denote the eco-friendly paint coat and the hollow denote the normal paint coat.

The temperature analysis at the three hours shows that the ambient temperature effects the surface and the inside temperature immensely. A slight change in the ambient temperature, increases and/or decreases the surface and inside temperature. Temperature distribution of each of the cases is discussed below.

23.3.1.1 Case 8 am

For all the four chambers it is seen that at the beginning of the experiments, the outside surface temperature is lower than the ambient temperature, while after a few weeks it starts to increase. This should be mentioned that the first few weeks of the experiments were in winter season and hence this clearly explains the early morning trends. As summer approached, the surface heated up and therefore its temperature increased.

Another aspect that is common between the two sets of graphs from Figs. 23.2 and 23.3, at 8 am, is that the surface temperatures and inside temperatures of the Chambers 1 and 2, and Chambers 3 and 4, followed exactly the same trend. Only at a later stage, when summer was approached, the outside surface temperature for the coated chambers only became higher than the non-coated chambers.

The inside temperature remained fairly higher for the first five weeks of the experiments, while it started to decrease at the end. That's because the air conditioning unit was just switched on, and it took some time for the chambers to cool down. The continuous increase and decrease in the inside temperature is due to the heat transfer phenomena.

23.3.1.2 Case 12 pm

At 12 pm, the surface temperature remained constantly higher than the ambient and inside temperature throughout the experiment. As this is the midday data, the radiations of the sun fall directly on the surface of the chambers, hence heating them up. The highest surface temperatures were experienced at 12 pm. It is also

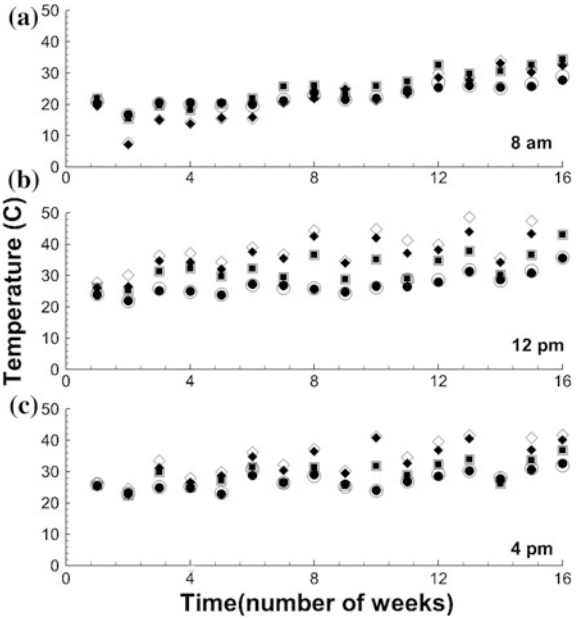

Fig. 23.2 Temperature distribution for aluminum chambers measured at three different times of the day **a** 8 am, **b** 12 pm and **c** 4 pm. The *square symbol* shows ambient temperature (T_{amb}), *diamond symbol* shows outside surface temperature (T_s) and *circle symbol* shows inside temperature (T_i). The *filled symbols* denote the eco-friendly paint coat and the hollow denote the normal paint coat

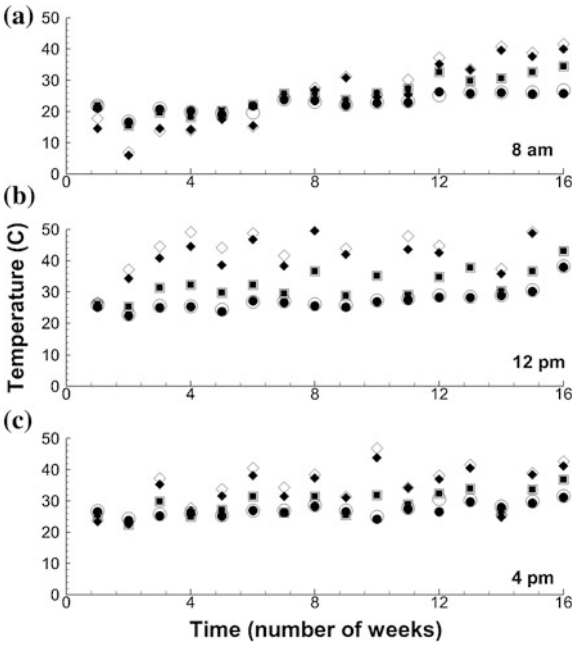

Fig. 23.3 Temperature distribution for concrete chambers measured at three different times of the day **a** 8 am, **b** 12 pm and **c** 4 pm. The *square symbol* shows ambient temperature (T_{amb}), *diamond symbol* shows outside surface temperature (T_s) and *circle symbol* shows inside temperature (T_i). The *filled symbols* denote the eco-friendly paint coat and the hollow denote the normal paint coat

seen that the surface temperatures for the coated chambers are less than that of the non-coated ones. This proves that the eco-friendly paint is actually working successfully.

On the other hand, the inside temperatures remained constantly lower than the ambient and surface temperatures. Although the inside temperatures were almost the same for the coated and non-coated chambers, the energy required to maintain those temperatures is lower for the coated chambers, as can be seen later in Sect. 23.3.3.

23.3.1.3 Case 4 pm

Later on in the day as evening was approaching, at 4 pm for this experiment, the inside and ambient temperatures started reaching each other. This was also seen that the inside and surface temperatures followed a very similar trend as 12 pm data. It was also observed that the maximum surface temperature at 4 pm was lower than that of 12 pm. This is due to the fact that the exposure from the sun is shifted from the roof to the west side of the chambers.

23.3.2 Energy Analysis

Figures 23.4 and 23.5 show the amount of energy consumption of the air conditioning unit for the 16 week period for all of the four chambers measured. It can be clearly observed that the difference in energy for the concrete chambers is less than that for that of the Aluminum chambers. This means that the performance of the eco-friendly paint was more effective on Aluminum than on concrete. This is due to the insulation that is present in the Aluminum chambers. It is also seen that the difference in energy consumption between the concrete chambers, Chamber 1 (with eco-friendly coating) and Chamber 2 (without eco-friendly coating), remains constant throughout the experiment. On the other hand, for the Aluminum chambers, Chamber 3 (with eco-friendly coating) and Chamber 4 (without eco-friendly coating), the difference in energy consumption between the two chambers increases every day. Although it is known that Aluminum is a better conductor of heat [3].

23.3.3 Energy Savings

The energy savings between the coated and non-coated chambers are also calculated. A considerable amount of energy reductions were noticed between the coated and the non-coated chambers. Following equation was used to calculate the amount of reduced (saved) energy:

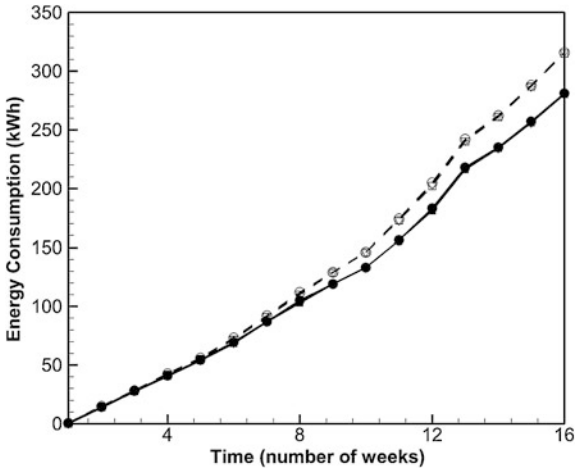

Fig. 23.4 Energy consumption for aluminum chambers measured at three different times of the day **a** 8 am (*square symbol*), **b** 12 pm (*diamond symbol*) and **c** 4 pm (*circle symbol*). The *filled symbols* denote the eco-friendly paint coat and the *hollow* denote the normal paint coat

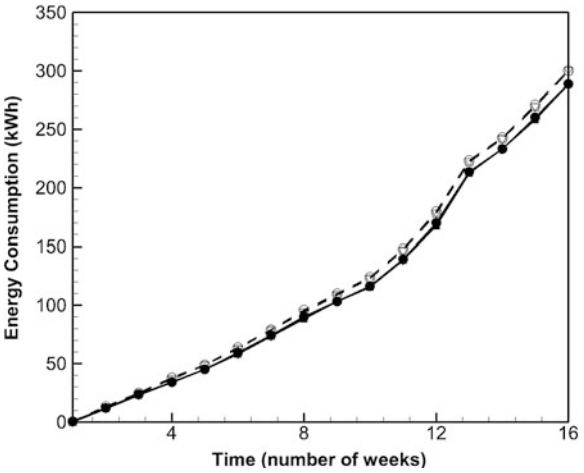

Fig. 23.5 Energy consumption for concrete chambers measured at three different times of the day **a** 8 am (*square symbol*), **b** 12 pm (*diamond symbol*) and **c** 4 pm (*circle symbol*). The *filled symbols* denote the eco-friendly paint coat and the *hollow* denote the normal paint coat

$$\Delta E = \frac{E_{nc} - E_c}{E_{nc}} \tag{2}$$

where ΔE is the percentage of Energy Saving, E_{nc} is the maximum energy consumed by non-coated chambers (i.e. 2 and 4) and E_c is the maximum energy consumed by coated chambers (i.e. 1 and 3). The energy consumption values were calculated from power usage data measured in the experiments over the duration of 16 weeks.

The analysis showed an energy savings (ΔE) of 4.8 % for concrete and 11.1 % for Aluminum chambers. These calculations are proving the trends shown in Figs. 23.6 and 23.7. This should though be mentioned that the energy reductions for Aluminum chambers are greater than that of the concrete chambers. This is mainly due to the insulation that is present in the roof envelop of the Aluminum sandwiched panels.

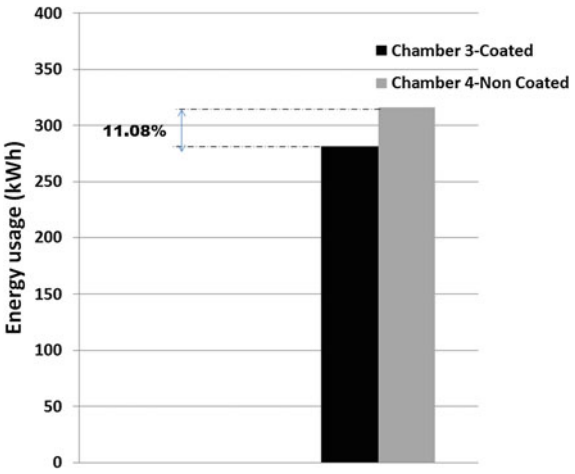

Fig. 23.6 Energy saving bar chart for aluminum chambers

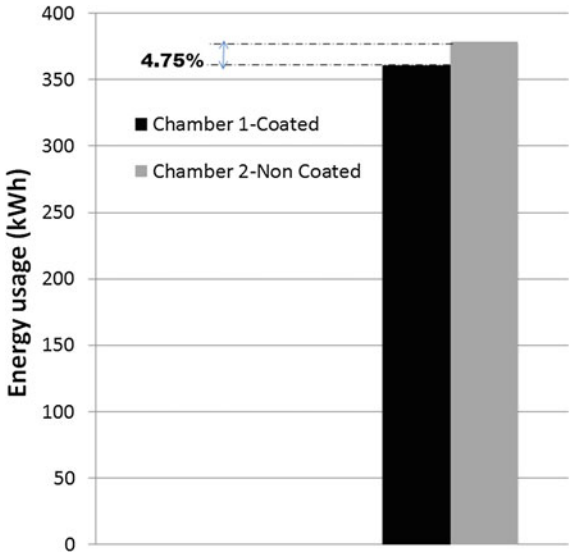

Fig. 23.7 Energy saving bar chart for concrete chambers

23.3.4 U-Value Reductions

In this study the U-Value calculations were performed using Eq. (23.1) with ΔT = Ambient Temperature—Inside Temperature and A = Area of the roof. As all the four walls of the four chambers have similar construction, it is assumed that the heat transfer through all the walls of the four chambers cancel out each other, hence area of the roof is only considered for the calculations. Therefore, the heat transfer through the walls can be eliminated. This way of calculations is also preferred because the effects of the eco-friendly can be examined more accurately.

Table 23.1 U-value reduction

		U-value (kW/m^{2}K)	ΔE	ΔU-value
Concrete chambers	Chamber 1	0.03949	4.75	17
	Chamber 2	0.04683		
Aluminum chambers	Chamber 1	0.06672	11.1	41.8
	Chamber 2	0.07441		

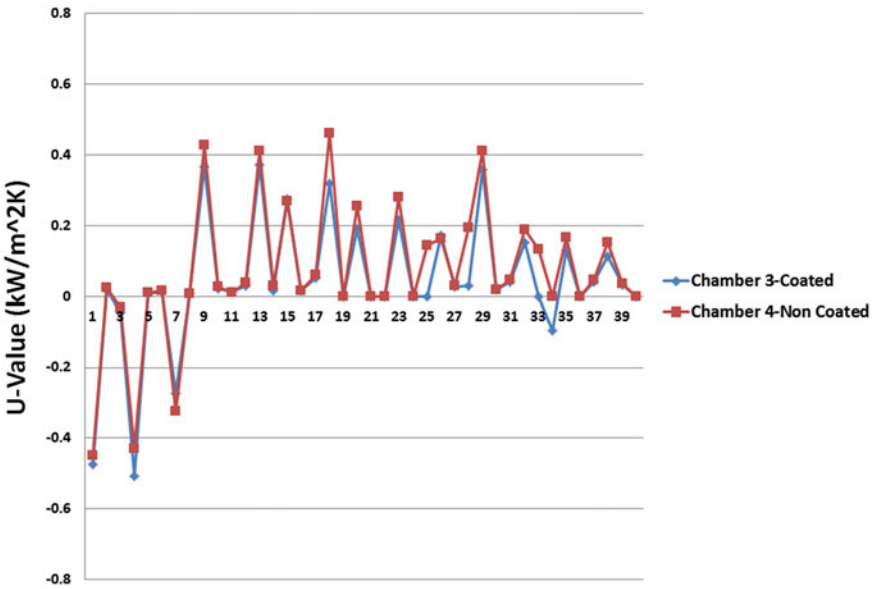

Fig. 23.8 Variation in U-value throughout the experiment for aluminum chambers

After calculating the energy savings and the U-Value, the reductions in U-Value were also calculated. The U-Value reductions (U-Value) for the four chambers are represented in the Table 23.1.

The percentage of U-Value reductions seems to be more in Aluminum than in concrete. The only reason for this is the presence of insulation in the Aluminum chambers. Although the average maximum amount of U-Value is for Chamber 4, which is an Aluminum sandwiched panel without the coating. Figures 23.8 and 23.9 show the variation in U-Value throughout the Experiment. It can be clearly seen that the line representing the U-Value for the coated Aluminum roofs is lower than that of the non-coated one. The difference between the coated and the non-coated chambers is quite visible for the Aluminum chambers, throughout the experiment. Though, for the concrete roofs, this difference is rarely seen.

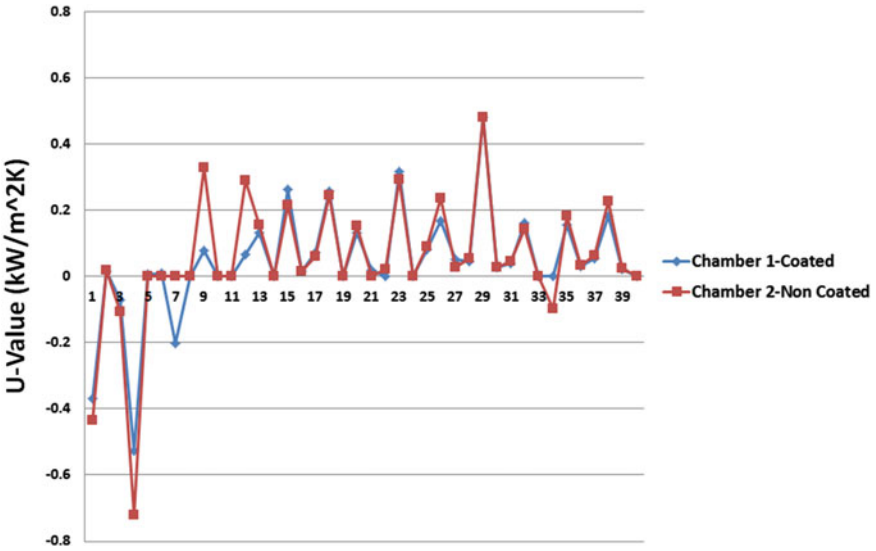

Fig. 23.9 Variation in U-value throughout the experiment for concrete chambers

23.4 Conclusions

Experimental results show that the maximum amount of energy was consumed at 12 pm. This is because at that time the roof faces the maximum amount of sun exposure, while at 8 am and 4 pm, the east and west sides of the chamber face the maximum sun exposure. This is the reason that the surface temperature shot up at 12 pm.

There is also a considerable amount of difference between energy savings and the U-Value reductions for the coated and the non-coated chambers, while the chambers that are constructed from a Aluminum sandwiched panel perform better that concrete roofs. As mentioned before, this is mainly due to the layer of insulation that is present in the roofs of the Aluminum chambers. This eco-friendly coat is especially designed for rooftops that already have a layer of insulation present in the wall envelop. It is assumed that if a layer of insulation were to be added in the concrete roof, energy savings and U-Value reduction would increase, as concrete is a much poor conductor of heat.

It is also assumed that the difference between the experimental and theoretical U-Values are going to be numerous, which will eventually increase the percentage error in U-Value calculations. A very critical assumption has been made while performing the calculations. It is assumed that the inside temperature, T_2, of the chamber is almost equal to the inside surface temperature, T_{w2}, which may not be the actual case of reality. The percentage error is also expected to be high because the difference in temperature, ΔT, is taken as the ambient temperature, T_1, minus the inside temperature, T_2. ΔT should basically be, the outside surface temperature minus the inside surface temperature, i.e. $T_{w1} - T_{w2}$, as this is the surface though

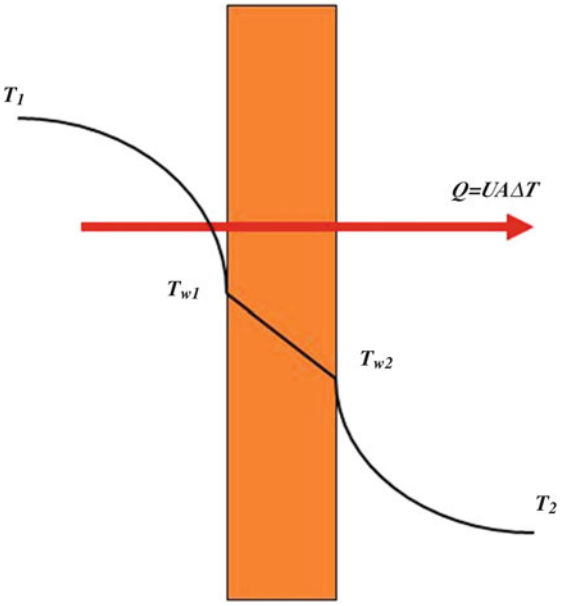

Fig. 23.10 Schematic of a wall assembly [6]

which heat transfer is occurring. Figure 23.10 shows all the mentioned parameters and their position for a single concrete slab. The same assumption can be applied for the Aluminum sandwiched panel too.

Percentage errors are further expected to increase if ΔT is taken as outside surface temperature minus the inside temperature. This is due to the fact that U-Value is inversely proportional to ΔT. A smaller difference would give a more accurate U-Value. Also, the outside surface temperatures for the four chambers are different and higher than the ambient temperatures.

This is where the experiment can be further refined, i.e. a means of measuring the inside surface temperature should also be included. Estimates could also be improved further by measuring the wind speed and solar radiations from the sun.

References

1. Dubai to have mandatory green building rules, Gulf News (2013)
2. F.P. Incropera, D.P. DeWitt, *Fundamentals of Heat and Mass Transfer*, 5th edn. (John Wiley and Sons, Hoboken, 2002)
3. K.J. Moss, *Heat and Mass Transfer in Buildings*, 2nd edn. (Taylor and Francis, New York, 2007)
4. B.M. Suleiman, Estimation of U-Value of traditional North African houses. Appl. Thermal Eng. **31**, 1923–1928 (2011)
5. W.A. Friess, K. Rakhshan, T.A. Hendawi, S. Tajerzadeh, Wall insulation measures for residential villas in Dubai: a case study in energy efficiency. Energy Build. **44**, 26–32 (2012)
6. Segerfröjd Compunds, How can polypropylene transfer heat as good as metal (2014), http://www.segerfrojd.com/ppvsmetal.htm. Accessed 21 Jan 2014

Chapter 24
Function-Based Model Predictive Control Approach for Maximum Power Capture of Heaving Wave Energy Converters

Mohammed Jama, Addy Wahyudie, Ali Assi and Hassan Noura

Abstract This paper investigates the application of function based model predictive control (MPC) approach to control the movement of single-body heaving wave energy converter (WEC). The proposed controller is designed based on the principle of maximum power transfer, at which maximum power absorption is attained. In addition, the suggested MPC controller respects the physical and thermal limitations of the WEC. Also, the generalized architecture of the proposed controller allows for longer prediction horizons and permits to effectively tune the controller based on the surrounding wave environment. Simulations have been carried out to assess the performance of the proposed controller using realistic sea states. Results show that the proposed MPC controller has achieved satisfactory performance allowing the WEC to optimize energy absorption while respecting the system limitations.

24.1 Introduction

One of the key features of wave energy apart from being clean and renewable is its significant average power density ($\sim$0.5 kW/m^2) [1]. Heaving wave energy converters (WECs) such as point absorbers are one of many WEC topologies. Point absorbers are heaving devices that absorb the mechanical energy that water waves carry and convert them directly or indirectly to electricity [2]. An example of point absorber is given in Fig. 24.1. The given WEC is a single-body

M. Jama (✉) · A. Wahyudie · H. Noura
UAE University, Al Ain, UAE
e-mail: m.jama@uaeu.ac.ae

A. Assi
Lebanese International University, Beirut, Lebanon
e-mail: ali.assi@liu.edu.lbe

M. O. Hamdan et al. (eds.), *ICREGA'14 - Renewable Energy: Generation and Applications*, Springer Proceedings in Energy, DOI: 10.1007/978-3-319-05708-8_24,

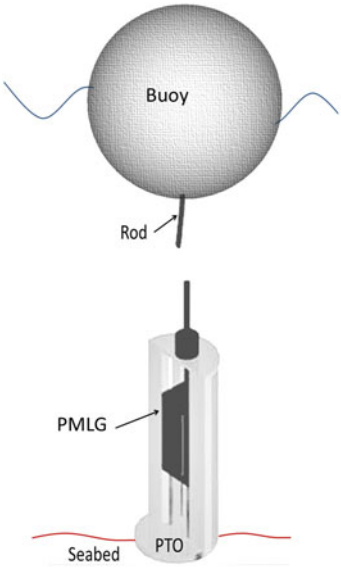

Fig. 24.1 Heaving WEC structure

axisymmetric heaving device, which consists of a floater or buoy and a direct drive power take-off (PTO) mechanism. Permanent magnet linear generator (PMLG) is usually deployed as a mean to generate electricity and also control the oscillation of the floater [3]. Much research work has been devoted to the field of optimum WEC control. Falnes and Budal carried out the early attempts on the control of point absorbers in which they discussed the principle of maximum power transfer [4]. With the recent advances in heuristic control techniques, many researchers deployed genetic algorithm (GA), optimization techniques, and artificial neural networks (ANNs) to optimize the energy capture of WECs [5]. Fuzzy logic based controllers have also featured in many research efforts [6, 7].

Lately, model predictive control (MPC) has drawn attention as a potential candidate for controlling WEC. Due to the advances in the computing infrastructure, MPC is widely used in numerous industrial applications, such as queuing systems, chemical processes, and financial problems [8]. MPC is based on the theory of optimum control; however it deviates in that the optimization problem is solved to determine the optimum control trajectory at every sampling instant within a prediction horizon [8]. Implementing MPC in marine energy is still largely unexplored compared to other renewable energy resources, however, few outstanding research efforts have been reported in literature, among those are [9, 10].

Generally, classical MPC methods are susceptible to poor numerical conditions, particularly when large prediction horizons are required. To the best of our knowledge, in the previous efforts, minimal attention has been given to the issue of tuning the MPC regime. In this paper, a discrete MPC based on Laguerre polynomials is proposed. The suggested approach gives more flexibility in tuning the controller to accommodate different wave environments and operating conditions.

Also, longer prediction horizons can be realized without significantly increasing the number of parameters. Hence less computational resources are needed compared with conventional MPC techniques. In addition, a controller with larger prediction horizon might, intuitively, make wave short-term forecasting algorithms far more effective, as the ones proposed in [11]. The proposed controller has been tested to control heaving WEC excited by polychromatic sea states. This paper is organized as follows: Sect. 24.2 discusses the dynamic model of the heaving WEC. The proposed control technique design is described in Sect. 24.3 Simulation results and discussion are given in Sect. 24.4 Finally, conclusions are drawn in Sect. 24.5.

24.2 System Description

24.2.1 Oscillating WEC Model

In this study, a single-body heaving WEC, which is reacting against the sea-bed is investigated. All the non-linear hydrodynamic forces are approximated linearly as only small vertical excursions are allowed [12]. The forces acting on the WEC floater can be described as

$$f_e(t) - f_r(t) - f_b(t) - f_l(t) + f_c(t) = m\ddot{z}(t) \tag{24.1}$$

where $f_e(t)$ is the wave excitation force, $f_r(t)$ is the wave radiation force, $f_b(t)$ is the floater's buoyancy force, $f_l(t)$ is the mechanical losses force (e.g. viscous), $f_c(t)$ is the control force applied by the PTO machinery. m is the total mass of the WEC floater, rod, and the PMLG translator, $\ddot{z}(t)$ is the heave acceleration of the floater. Omitting the forces resulted from the mechanical losses $f_l(t)$, the system time domain equation of motion can be described as [2]

$$[m + m_\infty]\ddot{z}(t) + \int_0^t k_r(t-\tau)\dot{z}(\tau)d\tau + c_b z(t) = f_e(t) + f_c(t) \tag{24.2}$$

where the constants m_∞ and c_b are the radiation infinite added mass and the buoyancy stiffness coefficient. $z(t)$ and $\dot{z}(t)$ are the floater's heave displacement and velocity, respectively. The radiation convolution term $\int_0^t k_r(t-\tau)\dot{z}(\tau)d\tau$ is approximated by a 4th order linear time invariant state space model using frequency domain identification technique as discussed in [13]. The complete state space representation of the WEC system is

$$\begin{aligned}\dot{\mathbf{x}}(t) =& \mathbf{A}\mathbf{x}(t) + \mathbf{B}u(t) + \mathbf{W}w(t)\\ y(t) =& \mathbf{C}\mathbf{x}(t)\end{aligned} \tag{24.3}$$

where $\mathbf{x}(t) = [z(t)\ \dot{z}(t)\ \theta(t)^T]^T \in \mathbb{R}^{n\times m}$ is the system state vector, $\theta(t) \in \mathbb{R}^{4\times 1}$ is the radiation component state vector. As shown in (24.3), the system is excited by two forces (inputs), which are: (1) the control force applied by the PMLG $u(t) \in \mathbb{R}^{m\times m}$, that can be manipulated by the adopted controller and the system actuator and (2) the wave excitation force, which cannot be manipulated, so it is considered as un-manipulated measurable input $w(t) \in \mathbb{R}^{1\times 1}$, while $\mathbf{y}(t) = \dot{z}(t) \in \mathbb{R}^{1\times 1}$ is the output vector. $\mathbf{A} \in \mathbb{R}^{n\times n}$, $\mathbf{B} = \mathbf{W} \in \mathbb{R}^{n\times m}$, and $\mathbf{C} \in \mathbb{R}^{q\times n}$ are the state, input, and output matrices, respectively.

$$\mathbf{A} = \begin{bmatrix} 0 & 1 & \mathbf{0}_{1\times 4} \\ \frac{-c_b}{m+m_\infty} & 0 & \frac{-\mathbf{C_k}}{m+m_\infty} \\ \mathbf{0}_{4\times 1} & \mathbf{B_k} & \mathbf{A_k} \end{bmatrix} \quad \in \mathbb{R}^{n\times n},$$

$$\mathbf{B} = \begin{bmatrix} 0 \\ \frac{1}{m+m_\infty} \\ \mathbf{0}_{4\times 1} \end{bmatrix} \quad \in \mathbb{R}^{n\times m},$$

$$\mathbf{C} = \begin{bmatrix} 0 & 1 & \mathbf{0}_{1\times 4} \end{bmatrix} \quad \in \mathbb{R}^{q\times n}.$$

The matrices $\mathbf{A_k} \in \mathbb{R}^{4\times 4}$, $\mathbf{B_k} \in \mathbb{R}^{4\times 1}$ and $\mathbf{C_k} \in \mathbb{R}^{1\times 4}$ are the state, input, and output radiation force model matrices. Frequency domain hydrodynamic analysis is performed to evaluate the radiation linear model matrices. The hydrodynamic analysis describes the waves-floater interactions, which is a function of wave propagation frequencies, installation site, and the geometry of the WEC floater [14]. Hydrodynamic numerical tools such as WAMIT^{TM} can be used to solve the radiation and diffraction problems of offshore floating structures for a range of operating frequencies [15]. The frequency domain radiation kernel $K_r(\omega)$ is found as

$$K_r(\omega) = R_r(\omega) + j\omega[M_r(\omega) - m_\infty] \tag{24.4}$$

where $R_r(\omega)$ and $M_r(\omega)$ are the radiation resistance and radiation added mass, which are computed using WAMIT^{TM} for a range of frequencies. Since the most energetic sea waves propagate at relatively low frequencies, only wave frequencies (i.e. $\omega < 1$ rad/s) are considered. The wave excitation force $f_e(t)$ is also determined for the specified frequency range by approximating it with a 8th order linear time invariant model using frequency identification technique similar to the one used in [13].

24.2.2 Maximum Power Absorption

When the WEC floater is heaving freely, that is, there is no PTO force applied; the intrinsic impedance $Z_{in}(\omega)$ of the system dominates its dynamics. Generally, the geometry and the mass of the floater along with the wave environment determine the floater's $Z_{in}(\omega)$, therefore its energy capture capabilities. In [2], it is stated that for a heaving floating body to achieve maximum power absorption, the wave excitation force $f_e(t)$ should be in phase with $\dot{z}(t)$ (i.e., resonance), hence the reference velocity that ensures maximum power absorption can be expressed as

$$\dot{z}_r(t) = \frac{|f_e(t)|}{2R_{in}(\omega)} cos(\phi) \tag{24.5}$$

where $R_{in}(\omega)$ and ϕ are the system instrinstic resistance and the phase difference between $f_e(t)$ and $\dot{z}(t)$, respectively.

24.3 Controller Design

Function-based model predictive controller (MPC) is designed to generate the required machinery force. The control strategy also comprises an observer to estimate the system states. Figure 24.2 depicts the control system architecture.

24.3.1 Augmented WEC Model

The continuous time domain WEC model (24.3) is formulated into the MPC framework by considering the change of the manipulated control variable $\dot{u}(t)$ instead of $u(t)$. To form the augmented WEC model, an integral action is embedded into the model shown in (24.3). By setting the augmented state vector as $\mathbf{x}_g = [\dot{\mathbf{x}}(t)^T e(t)]^T$, where $e(t) = y(t) - \dot{z}_r(t)$ is the velocity tracking error. The augmented state space representation of the model can be written as

$$\begin{aligned} \dot{\mathbf{x}}_g(t) &= \mathbf{A}_g \mathbf{x}_g(t) + \mathbf{B}_g \dot{u}(t) \\ y(t) &= \mathbf{C}_g \mathbf{x}_g(t) \end{aligned} \tag{24.6}$$

such that

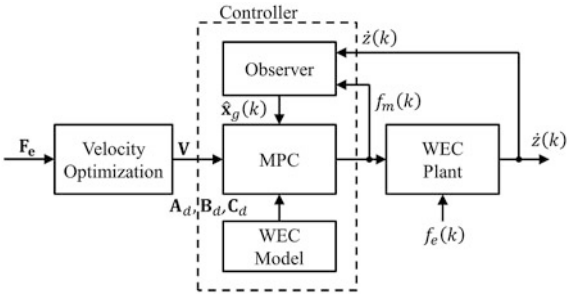

Fig. 24.2 Control system diagram

$$\mathbf{A}_g = \begin{bmatrix} \mathbf{A} & \mathbf{0}_{6\times 1} \\ \mathbf{C} & 0_{1\times 1} \end{bmatrix} \quad \in \mathbb{R}^{(n+q)^2},$$

$$\mathbf{B}_g = \begin{bmatrix} \mathbf{B} \\ 0_{1\times 1} \end{bmatrix} \quad \in \mathbb{R}^{(n+q)\times q},$$

$$\mathbf{C}_g = \begin{bmatrix} \mathbf{0}_{1\times 6} & \mathbf{I}_{1\times 1} \end{bmatrix} \quad \in \mathbb{R}^{q\times(n+q)}.$$

Note that the augmented model has the derivative of the input as its sole input variable, whereas the un-manipulated input $w(t)$ featured in (24.3) is neglected to be simply added to the original input signal $u(t)$. The formulated augmented model is discretized as follows

$$\begin{aligned} \dot{\mathbf{x}}_g(k+1) &= \mathbf{A}_d \mathbf{x}_g(k) + \mathbf{B}_d \Delta u(k) \\ y(k) &= \mathbf{C}_d \mathbf{x}_g(k) \end{aligned} \tag{24.7}$$

where $\mathbf{x}_g(k)$, $y_g(k)$, $\mathbf{A_d}$, $\mathbf{B_d}$, and $\mathbf{C_d}$ are the discrete counterparts of $\mathbf{x}_g(t)$, $y_g(t)$, $\mathbf{A}_g$, $\mathbf{B}_g$ and $\mathbf{C}_g$. Assuming a zero-order hold is used at a sampling time T_s.

24.3.2 Reference Velocity Optimization

The equation shown in (24.5) guarantees maximum power absorption, however, it cannot be implemented in real application, due to the resultant extremely high buoy excursions [2]. Also, it is not easy to compute the system's intrinsic impedance in real time. A possible solution is to formulate a time domain optimization problem that: (1) maximizes the absorbed energy E_{abs} (2) limits the buoy's heave displacement [9]. Assuming that an ideal wave elevation prediction is available, the absorbed energy E_{abs} within a finite optimization window N_w is

$$E_{abs} = (\mathbf{F}_e - \mathbf{F}_r)^T \mathbf{V} \tag{24.8}$$

where

$$\mathbf{F}_e = \begin{bmatrix} f_e(k+1|k) \\ f_e(k+2|k) \\ \vdots \\ f_e(k+N_w|k) \end{bmatrix}, \mathbf{F}_r = \begin{bmatrix} f_r(k+1|k) \\ f_r(k+2|k) \\ \vdots \\ f_r(k+N_w|k) \end{bmatrix},$$

$$\mathbf{V} = \begin{bmatrix} \dot{z}_r(k+1|k) \\ \dot{z}_r(k+2|k) \\ \vdots \\ \dot{z}_r(k+N_w|k) \end{bmatrix}.$$

By modifying the state equation shown in (24.3), a new vector, (k), is defined to include the radiation component states $\theta(k)$ and the heave displacement $z(k)$, the radiation force trajectory can be written as

$$\mathbf{F}_r = \Xi_v \mathbf{V} + \Xi_\psi \Psi(k) \tag{24.9}$$

where

$$\Xi_v = \begin{bmatrix} \mathbf{C}_r\mathbf{B}_r & \mathbf{0} & \dots & \mathbf{0} \\ \mathbf{C}_r\mathbf{A}_r\mathbf{B}_r & \mathbf{C}_r\mathbf{B}_r & \ddots & \mathbf{0} \\ \vdots & \ddots & \ddots & \vdots \\ \mathbf{C}_r\mathbf{A}_r^{N_w-1}\mathbf{B}_r & \dots & \mathbf{C}_r\mathbf{A}_r\mathbf{B}_r & \mathbf{C}_r\mathbf{B}_r \end{bmatrix},$$

$$\Xi_\psi = \begin{bmatrix} \mathbf{C}_r\mathbf{A}_r \\ \mathbf{C}_r\mathbf{A}_r^2 \\ \dots \\ \mathbf{C}_r\mathbf{A}_r^{N_w} \end{bmatrix},$$

$$\mathbf{A}_r = \begin{bmatrix} 0 & \mathbf{0}_{1\times4} \\ \mathbf{0}_{4\times1} & \mathbf{A}_k \end{bmatrix}, \mathbf{B}_r = \begin{bmatrix} 1 \\ \mathbf{B}_k \end{bmatrix}, \mathbf{C}_r = [\,0 \quad \mathbf{C}_k\,].$$

By algebraic reformulation of (24.6), the optimum velocity reference is then determined by solving the following quadratic programming (QP) problem

$$\begin{array}{ll} \text{minimize} & E_{abs} = \mathbf{V}^T \Xi_v \mathbf{V} + (\Xi_\psi \Psi(k) - \mathbf{F}_e)^T \mathbf{V} \\ \text{subject to} & \mathbf{H}_z \mathbf{V} \le \Omega_z \end{array} \tag{24.10}$$

where

$$\mathbf{H}_z = [\, -\mathbf{M}_z \quad \mathbf{M}_z \,]^T,$$
$$\Omega_z = [\, z_m + \mathbf{P}_z \Psi(k) \quad z_m - \mathbf{P}_z \Psi(k) \,]^T.$$

Note that the matrices $\mathbf{M}_z$ and $\mathbf{P}_z$ are similar to Ξ_Ψ and Ξ_r, respectively, apart from a minor modification, that is $\mathbf{C}_r = [1\mathbf{0}_{1\times 4}]$. Equation (24.10) is minimized with respect to the future velocity trajectory $\mathbf{V}$, while limiting the buoy excursion to $\pm z_m$. Note that no constraints are imposed on the decision variable $\mathbf{V}$, since it is expected to be implicitly constrained through limitations on the buoy displacement. The QP problem under study is convex, since the Hessian matrix Ξ_v is positive semi definite in $\Re^n$. Without imposing constraints on the heave displacement, the optimum velocity reference produced by (24.10) will be similar to that of (24.5).

24.3.3 MPC Formulation

The model presented in (24.7) is fully controllable which is pre-requisite to establish state feedback control law. The estimated future predicted state trajectories along the prediction horizon N_p can be formulated in a matrix form as [16]

$$\mathbf{X}_g(k+1|k) = \Theta_x \hat{\mathbf{x}}_g(k|k) + \Theta_{\Delta u} \Delta U(k) \tag{24.11}$$

where

$$\mathbf{X}_g(k+1|k) = \begin{bmatrix} \hat{\mathbf{x}}_g(k+1|k) \\ \hat{\mathbf{x}}_g(k+2|k) \\ \vdots \\ \hat{\mathbf{x}}_g(k+N_p|k) \end{bmatrix},$$

$$\Delta U(k) = \begin{bmatrix} \Delta u(k) \\ \Delta u(k+1) \\ \vdots \\ \Delta u(k+N_p-1) \end{bmatrix}, \Theta_x = \begin{bmatrix} \mathbf{A}_d \\ \mathbf{A}_d^2 \\ \vdots \\ \mathbf{A}_d^{N_p} \end{bmatrix},$$

$$\Theta_{\Delta u} = \begin{bmatrix} \mathbf{B}_d & \mathbf{0} & \dots & \dots & \mathbf{0} \\ \mathbf{A}_d\mathbf{B}_d & \mathbf{B}_d & \ddots & \ddots & \mathbf{0} \\ \vdots & \vdots & \ddots & \ddots & \vdots \\ \mathbf{A}_d^{N_p-1}\mathbf{B}_d & \mathbf{A}_d^{N_p-2}\mathbf{B}_d & \dots & \mathbf{A}_d\mathbf{B}_d & \mathbf{B}_r \end{bmatrix}.$$

Consequently, the predicted output trajectory is computed using (24.9) as

$$\mathbf{Y}_g(k+1|k) = \Gamma_x \hat{\mathbf{x}}_g(k|k) + \Gamma_{\Delta u} \Delta U(k) \tag{24.12}$$

where

$$\mathbf{Y}_g(k+1|k) = \begin{bmatrix} \hat{\mathbf{y}}_g(k+1|k) \\ \hat{\mathbf{y}}_g(k+2|k) \\ \vdots \\ \hat{\mathbf{y}}_g(k+N_p||k) \end{bmatrix}, \Gamma_x = \begin{bmatrix} \mathbf{C}_d\mathbf{A}_d \\ \mathbf{C}_d\mathbf{A}_d^2 \\ \vdots \\ \mathbf{C}_d\mathbf{A}_d^{N_p} \end{bmatrix},$$

$$\Gamma_{\Delta u} = \begin{bmatrix} \mathbf{C}_d\mathbf{B}_d & \mathbf{0} & \dots & \mathbf{0} \\ \mathbf{C}_d\mathbf{A}_d\mathbf{B}_d & \mathbf{C}_d\mathbf{B}_d & \ddots & \mathbf{0} \\ \vdots & \vdots & \ddots & \vdots \\ \mathbf{C}_d\mathbf{A}_d^{N_p-1}\mathbf{B}_d & \mathbf{C}_d\mathbf{A}_d^{N_p-2}\mathbf{B}_d & \dots & \mathbf{C}_d\mathbf{B}_d \end{bmatrix}.$$

The control trajectory within the prediction horizon N_p is evaluated as summation of set of Laguerre polynomials $\ell(k)$, which are orthonormal complete functions that can be expressed in the z-domain as

$$L_i = \frac{\sqrt{1-p^2}}{1-pz^{-1}} \left(\frac{z^{-1}-p}{1-pz^{-1}} \right)^{i-1}, \text{where } i = 1, 2, \dots, N$$

where p is the pole of the Laguerre polynomial and it controls the rate at which $\ell(k)$ decays to zero. To ensure the stability of the Laguerre network, $0 < p < 1$. The control law at each instant i is approximated by a finite number N of Laguerre polynomials, such as

$$\Delta u(k+i) \approx \sum_{j=0}^{N} c_j(k) \ell_j(k) \tag{24.13}$$

Usually, small value is selected for N (typically <10) which is sufficiently enough for most applications. In addition, small value of N allows p to have more influence on the system response [17]. By varying the Laguerre polynomials coefficients $c_j(k)$, the control trajectory is manipulated within the prediction window N_p. Usually the Laguerre polynomials are formulated in state space representation such as

$$\mathbf{L}(k+1) = \mathbf{A}_\ell \mathbf{L}(k) \tag{24.14}$$

here $\mathbf{A}_\ell \in \mathbb{R}^{N \times N}$ is the Laguerre state matrix and $L(k) = [\ell_1(k)\ell_2(k) \dots \ell_N(k)] \in \mathbb{R}^{N \times 1}$ is the Laguerre state vector. Therefore, at the sampling instant i the change in the input $\Delta u(k)$ can be expressed in the matrix form as

$$\Delta u(k+i) = \mathbf{L}(k)^T \sigma \tag{24.15}$$

where $\sigma = [c_1 c_2 \ldots c_N] \in \mathbb{R}^{N\times 1}$ includes the Laguerre coefficients. Note that the control law at any instant throughout the prediction horizon is computed using the same Laguerre network, in which, the pair (p, N) is kept fixed, hence the control trajectory can be represented as

$$\Delta U = \left[\mathbf{L}_1(k)^T \sigma_1 \mathbf{L}_2(k)^T \sigma_2 \ldots \mathbf{L}_{N_p}(k)^T \sigma_{N_p}\right] \tag{24.16}$$

so, at each time step, σ is optimized to obtain the required control law, which in turn, regulates the output response.

24.3.4 MPC Objective Function

Using the predicted variables, the objective function of the discrete function based model predictive control is formulated as [16]

$$J = \mathbf{X}_g(k+1|k)^T \mathbf{Q} \mathbf{X}_g(k+1|k) + \Delta \mathbf{U}(k)^T \mathbf{R} \Delta \mathbf{U}(k) \tag{24.17}$$

subject to (24.9), while $\mathbf{Q} \in \mathbb{R}^{(N_p(n+q))^2}$ and are the state and input weighting matrices, respectively. Both Q and R are non-negative semi definite matrices. The cost function (24.17) is modified to comprise an exponential weighting factor λ, which facilitates to extend the prediction horizon, without staggering into numerical problems [16]. The exponentially weighted optimization problem is formulated as

$$\begin{aligned} \text{minimize} \quad & J = \mathbf{X}_g(k+1|k)^T \mathbf{Q} \mathbf{X}_g(k+1|k) + \Delta \mathbf{U}(k)^T \mathbf{R}\, \Delta\, \mathbf{U}(k) \\ \text{subject to} \quad & \mathbf{X}_g(k+1|k) = \tilde{\Theta}_x \hat{\mathbf{x}}_g(k|k) + \tilde{\Theta}_{\Delta u} \Delta\, U(k) \\ & |\Delta\, U(k)| \leq \mathbf{S}^{-1} \Omega_{\Delta u} \end{aligned} \tag{24.18}$$

where

$$\mathbf{S} = \begin{bmatrix} \mathbf{I} & 0 & \ldots & 0 \\ 0 & \lambda^{-1}\mathbf{I} & \ddots & 0 \\ \vdots & \vdots & \ddots & \vdots \\ 0 & 0 & \ldots & \lambda^{-N_p}\mathbf{I} \end{bmatrix}, \Omega_{\Delta u} = \begin{bmatrix} b \\ b \\ \vdots \\ b \end{bmatrix}.$$

the matrices $\tilde{\Theta}_x$ and $\tilde{\Theta}_{\Delta u}$ are modified version of their counterparts shown in (24.12), that is, they are modified by the weighted augmented state and input matrices, $\lambda^{-i}\mathbf{A}_d$ and $\lambda^{-i}\mathbf{B}_d$, respectively. The matrix $\mathbf{S}$, in the inequality constraint, is tailored to modify the control law across N_p by λ^{-i}. All control laws are bonded

Table 24.1 WEC design parameters

Parameter	Symbol	Value	Unit
Buoy radius	r	5	m
Buoy mass	m_b	2.68×10^5	kg
Water plane area	A_w	78.54	m^2
Submerged volume	V_s	261.80	m^3
Buoyancy stiffness coefficient	c_b	7.89×10^5	N/m
Added infinite mass	m_∞	1.34×10^5	kg
Resonance angular frequency	ω_o	1.4	rad/s
Seabed depth	d	80	m

by $\pm b$ in $\Omega_{\Delta u}$. The importance of imposing constraints on the heaving WEC arises due to the physical and thermal limitations of the PMLG and to have means to suppress extreme floater excursions.

24.4 Results and Discussions

24.4.1 Simulation Set-Up

The design parameters of the floater, which is used in the hydrodynamic analysis and the time domain simulations are shown in Table 24.1. The Laguerre polynomials based MPC parameters have been initially set to $p = 0.5$, $N = 3$, $N_p = 2000$, $\lambda = 1$. The state weighting $\mathbf{Q}$ is set to equal $\mathbf{C}_g^T \mathbf{C}_g$, which enables the tracking of the reference optimal velocity signal and the input weighting $\mathbf{R}$ is set to 0.02. The simulation sampling time T_s is 0.01 s and the most energetic sea waves propagate at 13 s, hence the prediction horizon is selected to be 20 s (or 2,000 samples). In order to avoid numerical complexities and speed up the simulation, the optimization described in (24.10) is solved with a larger time step (i.e., 0.1 s). All the simulations are carried out using MATLAB^{TM}.

24.4.2 Simulation Results

First, let's examine the influence of control for the system under investigation. Figure 24.3 showcases the dynamics of the WEC when no control force is applied under the excitation of a polychromatic wave of peak frequency $\omega_p = 0.55$ rad/s $\left(T_p = 11.42 \text{ s}\right)$ and significant height H_s of 2 m. The displacement of the WEC floater is merely due to the wave excitation force that is why the floater heave displacement is close to the applied wave elevation.

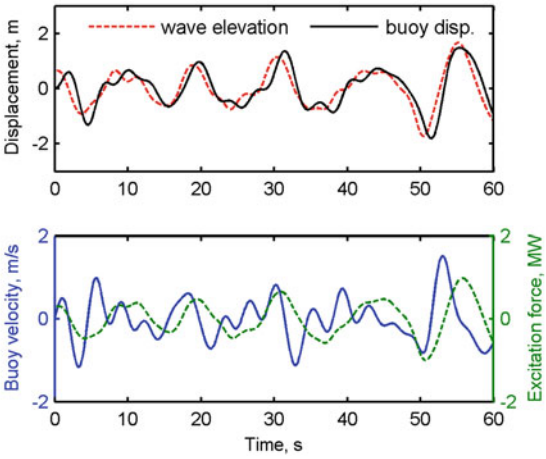

Fig. 24.3 The dynamics of heaving WEC at no load condition

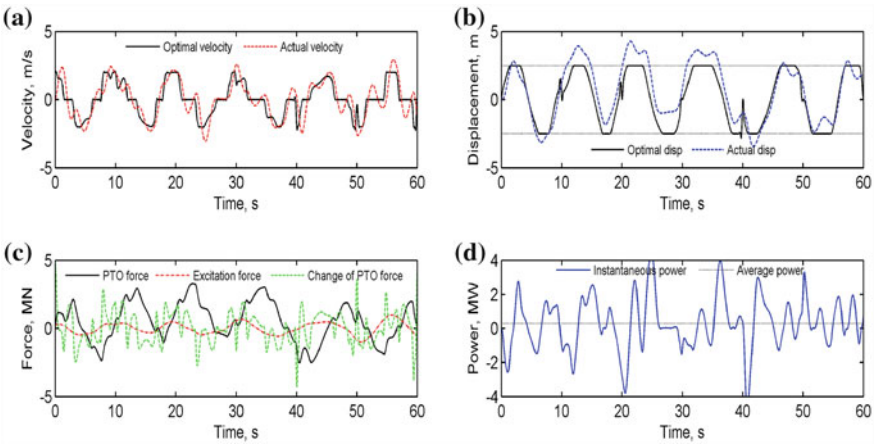

Fig. 24.4 The dynamics of heaving WEC under unconstrained MPC controller **a** optimal and actual buoy velocity **b** optimal and actual buoy displacement **c** wave excitation force, PTO force, and rate of change of PTO force. **d** captured instantaneous and time-averaged power

The proposed MPC controller is used where, initially, no constraints are imposed on the machinery force. The optimal velocity trajectory is computed ahead in 10 s time frame, assuming that the wave elevation is available in that time frame. To avoid extreme floater excursions, the maximum displacement is set to ± 2.5 m. As depicted in Fig. 24.4a, significant increase in the floaters heave displacement is reported. The actual floater's velocity successfully tracks the optimum reference velocity which ensures maximum power transfer within the allowable excursions limit. It is important to mention that the WEC system is supposed to operate at near resonance condition due to the constrained motion,

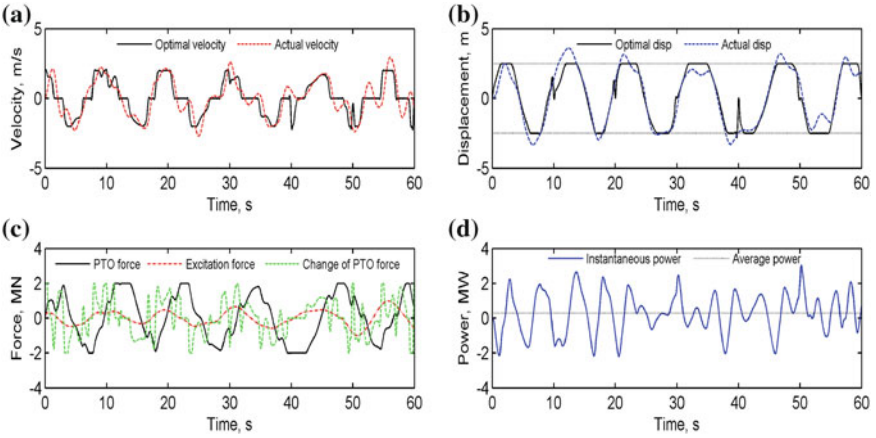

Fig. 24.5 The dynamics of heaving WEC under constrained MPC controller **a** optimal and actual buoy velocity **b** optimal and actual buoy displacement **c** wave excitation force, PTO force, and rate of change of PTO force. **d** captured instantaneous and time-averaged power

Table 24.2 MPC and PRC performances for low frequency sea state

Variable	Unit	MPC	PRC
$\bar{P}_{cap}$	MW	0.232	0.178
$Var(P_{cap})$	MW	1.1836	0.2691
P_{cap}/P_{max}	–	0.126	0.097
f_c^{max}	MN	2	2.15
Δf_c^{max}	MN	2	–

however, the controller fails to keep it within these limits as shown in Fig. 24.4b. Also the applied machinery force is approximately twice as high in magnitude as the applied wave excitation force as shown in Fig. 24.4c. The instantaneous captured power P_{cap} and the time averaged captured power $\bar{P}_{cap}$ are shown in Fig. 24.4d. The system under the unconstrained MPC controller has succeeded to capture approximately 0.172 MW of $\bar{P}_{cap}$.

Next, constraints are introduced to the MPC controller. Hard constraints, b, are imposed on the machinery force to limit the available control energy to ± 2 MN, which could be interpreted as the rated PTO force. As shown in Fig. 24.5a, the MPC controller manages to make the floater's velocity track the optimal reference velocity. However when the machinery force hits the constraint, the controller momentarily fails to keep small tracking error. Also, the floater motion is kept within its limits as shown in Fig. 24.4b. A trivial consequence of limiting the control force is suppressing the extreme oscillations of P_{cap} as shown in Fig. 24.5d. It is remarkable that $\bar{P}_{cap}$ increased by 25 % (i.e., $\bar{P}_{cap} = 0.232$ MW) after introducing constraints on $f_m(t)$. This shows that the proposed constrained MPC controller adequately exploits the available control resource.

Comparison is conducted between the constrained MPC and passive reactive control (PRC) performances, which are evaluated through few performance metrics, that are the captured power variance $Var(P_{cap})$ and the capturing efficiency P_{cap}/P_{max}. The variance of P_{cap} gives an idea about how rapid the captured power is varying with time. Higher value of variance indicates that larger amount of reactive power is running back and forth in the system. The other metric is the capturing efficiency P_{cap}/P_{max}, where $P_{max} = |f_e(t)|^2/8R_{in}(\omega)$, note that this is an approximation since zero phase shift between $f_e(t)$ and $\dot{z}(t)$ is assumed. The PRC regime consists of a fixed damping and stiffness coefficients, which are tuned at $\omega_p = 0.55$ rad/s. The PRC regime is configured to provide both amplitude and phase control, that is, $f_m(t) = -R_m\dot{z}(t) - S_m z(t)$, the damping coefficient R_m is set to 0.55 MNs/m, which maximizes the floater's vertical displacement within ± 2.5 m limit, while the stiffness coefficient S_m is set to 0.67 MN/m, which makes $f_e(t)$ and $\dot{z}(t)$ in phase. As shown in Table 24.2, the constrained MPC outperformed the PRC in terms of P_{cap}/P_{max}, even though, less $f_m(t)$ is used. Moreover, due to the fixed nature of the PRC, considerably lower variance in P_{cap} is observed.

24.5 Conclusions

A function based MPC controller for optimizing the performance of heaving WEC is presented. The proposed controller has shown promising results in terms of maximizing the WEC energy capture and the ease of imposing constraints on both of the system states and control effort. The controller eliminates the need for sensors by embedding observers into the controller framework. The proposed control strategy requires less computational resources compared to conventional MPC controllers.

References

1. J. Cruz, *Ocean Wave Energy Current Status and Future Perspectives* (Springer, Berlin, 2010)
2. J. Falnes, A review of wave-energy extraction. Mar. Struct. **20**(4), 185–201 (2007)
3. O. Falcao, Wave energy utilization: a review of the technologies. J. Renew. Sustain. Energy Rev. **14**, 899–918 (2010)
4. K. Budal, J. Falnes, Interacting point absorber with controlled motion, in the power from Sea Waves. in *Proceedings of BM Count* (Academic Press, London, 1980)
5. C.E. Garcia, M. Morari, Internal model control a unifying review and some new results. Ind. Eng. Chem. Proc. Des. Dev. **21**(2), 308–323 (1982)
6. M. Schoen, J. Hals, T. Moan, Wave prediction and robust control of heaving wave energy devices for irregular waves. IEEE Trans. Energy Convers. **26**(2), 627–638 (2011)
7. M.A. Jama, A. Assi, A. Wahyudie, H. Noura, Self-Tunable Fuzzy Logic Controller for the Optimization of Heaving Wave Energy Converters. in *Proceedings of The International Conference on Renewable Energy Research and Applications (ICRERA)*, 2012, pp. 1-6

8. U. Diwekar, *Introduction to Applied Optimization* (Springer, New York, 2000)
9. J. Hals, J. Falnes, T. Moan, Constrained optimal control of a heaving buoy wave-energy converter. J. Offshore Mech. Arctic Eng. **133**(1), 011401 (2011)
10. M. Richter, M. Magana, O. Sawodny, T. Brekken, Nonlinear model predictive control of a point absorber wave energy converter. IEEE Trans. Sustain. Energy **4**(1), 118–126 (2013)
11. F. Fusco, J. Ringwood, Short-term wave forecasting for real-time control of wave energy converters. IEEE Trans. Sustain. Energy **1**(2), 99–106 (2010)
12. T. Sarpkaya, M. Isaacson, *Mechanics of Wave Forces on Offshore Structures* (Van Nostrand Reinhold, New York, 1981)
13. R. Taghipoura, T. Pereza, T. Moan, Hybrid frequency-time domain models for dynamic response analysis of marine structures. Ocean Eng. **35**, 685–705 (2008)
14. G.D. Backer, Hydrodynamic design optimization of wave energy converters consisting of heaving point absorbers, Power. Dissertation submitted to obtain the academic degree of Doctor of Civil Engineering, 2010
15. WAMIT, User Manual 2006, http://www.wamit.com. (Accessed 20 Jan 2012)
16. L. Wang, Continuous time model predictive control using orthonormal functions. Int. J. Control **74**, 1588–1600 (2001)
17. L. Wang, P. Gawthrop, C. Chessari, T. Podsiadley, Indirect approach to continuous time system identification of food extruder. J. Process Control **14**, 603–615 (2004)

Chapter 25
Overview of Water Energy Nexus of Abu Dhabi's Power Sector-Energy Water Analysis of End Use Segment

S. Assaf and M. Nour

Abstract Energy and water are closely linked and dependent resources where energy production requires a large amount of water and in contrast huge amount of energy is needed to extract, treat, desalinate, transport and distribute water. Abu Dhabi provides a strong example of the interconnection between energy and water, where the majority of its electricity and water demand is jointly produced from cogeneration plants. The total cost of fuel used for cogeneration plants are heavily depending on the efficiency level of end-use energy and water consumption. Buildings are the major electricity and water consumers in Abu Dhabi, with 84.6 and 92.2 % respectively from the entire demand. In the case of Abu Dhabi; adopting the Estidama pearl rating system for all new constructed buildings will reduce water and energy consumption by considerable amounts. The aim of this study is to analyze the energy and water consumption reduction by implementing Estidama regulations and compare it with Business as Usual—the normal execution of things as they always do—for three sample buildings (villa, multistory residential and office building). The results of energy simulation and water analysis of the chosen buildings showed a potential of electricity reduction between 31 and 38 % and a potential of water reduction between 22 and 36 % depending on building type and other parameters. Also, a total monitory savings of 19 Billion AED can be achieved accumulatively over 10 years period (2011–2020) after Estidama regulations have been applied. In addition, 31.4 Million ton of CO_2eq cumulatively can be abated.

Keywords Water energy nexus · End use energy · Power sector · Energy efficiency

S. Assaf (✉)
Policy Expert at Department of Energy and Climate Change of UAE's Ministry of Foreign Affairs, Ministry of Foreign Affairs, Abu Dhabi, UAE
e-mail: sameerassaf@yahoo.com

M. Nour
MSc Energy Program, School of Engineering and Physical Sciences,
Heriot-Watt University, Dubai, UAE
e-mail: mutasim.nour@hw.ac.uk

M. O. Hamdan et al. (eds.), *ICREGA'14 - Renewable Energy: Generation and Applications*, Springer Proceedings in Energy, DOI: 10.1007/978-3-319-05708-8_25,

25.1 Introduction

Water and energy are vital resources that affect all aspects of life and support human welfare. They are essential for economic growth and sustainable development; and recognized as fundamental inputs for the modern economies [1]. The rapid global population growth and fast economic development are key drivers for increasing the global demand on water and energy resources.

The concept of water and energy nexus has been acknowledged in the United States in mid nineties of the last century, and has been received increased attention all over the world during the past 5 years [2].

Historically, energy and water resources have been treated independently, and their policies have been developed in isolation from each other, but recently due to the growing concerns of the issues relevant to energy and water accessibility, environmental impacts and prices instability [3], many countries have started integrating both systems to obtain better planning and policy directions.

According to Middle East and North Africa (MENA) Energy Investment Outlook [4]—titled: Capturing the Full Scope and Scale of the Power Sector, the MENA region would need 124 GW incremental power capacity over the next 5 years, with an average growth 7.8 % annually. The growth of electricity consumption is strongly correlated to economic development, high population growth and harsh climate conditions, which all countries in the region do share, especially the Gulf Cooperation Council (GCC) states. The share of GCC states alone exceeds 42 % (US$105 billion) of the total required expenditure.

In 2011, the total installed capacity in United Arab Emirates (UAE) was 26132 MW; which has been increased significantly over the past few years due to new commissioning of several plants. In the water side, although UAE has relatively large volume of underground and surface water reserves, only 3 % of available water is fresh according to UAE water conservation strategy [5], the remaining 97 % is saline water. In the UAE, desalinated water accounts for 92 % of the total water used for domestic and industrial activities [5].

Abu Dhabi is the largest emirate among the seven emirates of the UAE, and has one of the highest per capita rates of electricity and water consumption in the world. According to Abu Dhabi Energy and Environmental Statistics [6] electricity consumption per capita in Abu Dhabi was 20.39 MWh/year in 2011, almost seven times the global average (2.89 MWh/year) [7]. The urban water per capita use in Abu Dhabi was 1250 l/day in 2011, 54 % of which (i.e. 675 l/day) are used for domestic activities [6], which is much higher than most of the developing countries where their daily average does not exceed half of Abu Dhabi's daily per capita rate. Buildings are the major electricity and water consumer in Abu Dhabi with 84.6 and 92.2 % respectively relative to the total electricity and water consumption of Abu Dhabi.

With this regard, the Abu Dhabi government has stressed the importance of adopting new regulations to increase sustainability in the construction sector. The Abu Dhabi Urban Planning Council (UPC)—through its Pearl Rating System, that

was put in place in 2011—commands all new buildings to achieve specific benchmarks in order to minimize the energy and water use as well as reducing construction waste and recycling building materials.

This paper presents the analysis of electricity and water consumptions in Abu Dubai emirate for three typical sample buildings, (villa, multistory residential and office building). For Energy assessment, eQUEST simulation software was used to examine the energy performance of the chosen buildings and to evaluate the energy saving potential after applying Estidama requirements. While for water assessment; Estidama and LEED calculation tools were used to do the same.

25.2 Background

Energy and water are closely linked and dependent resources where energy production requires a large amount of water and in contrast huge amount of energy is needed to extract, treat, desalinate, transport and distribute water. Figure 25.1 shows the inter-linkages between the two sources.

25.2.1 Water Requirements for Electricity Production

For energy value chain, water is needed for fuel extraction and processing as well as for power generation. The water demand varies depending upon the type of generation and cooling technologies. The ranges of water requirements for various generation and cooling technologies is illustrated in Fig. 25.2.

In this paper, only the water used for electricity generation is covered, which is mainly used for cooling purposes. For the case of Abu Dhabi; three types of generation are largely used in its power plants: steam turbine (ST), diesel engine (DE) and gas turbine (GT). GT comprises three technologies; simple cycle gas turbine (SCGT), combined cycle gas turbine (CCGT) and gas turbine with energy heat recovery (GT + HER).

Back to water demand for electricity production, only steam turbines require water for the cooling process whereas gas turbines do not. Most power plants in Abu Dhabi are located along the coastal line, where only seawater is used for cooling due to the limited fresh water resource. The average water use in energy production for steam turbine is around 315 gal/MWh [2]. Although seawater is considered a stable source compared to fresh water, but still using such a large quantity of sea water—which is eventually discharged into the sea at a very high temperature—would cause thermal pollution and impact the local habitat of fish and other marine species [10].

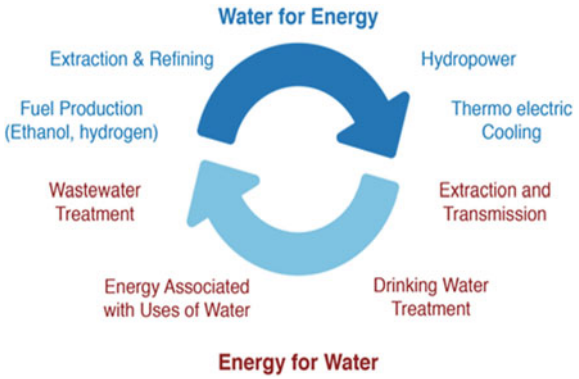

Fig. 25.1 Water energy nexus [8]

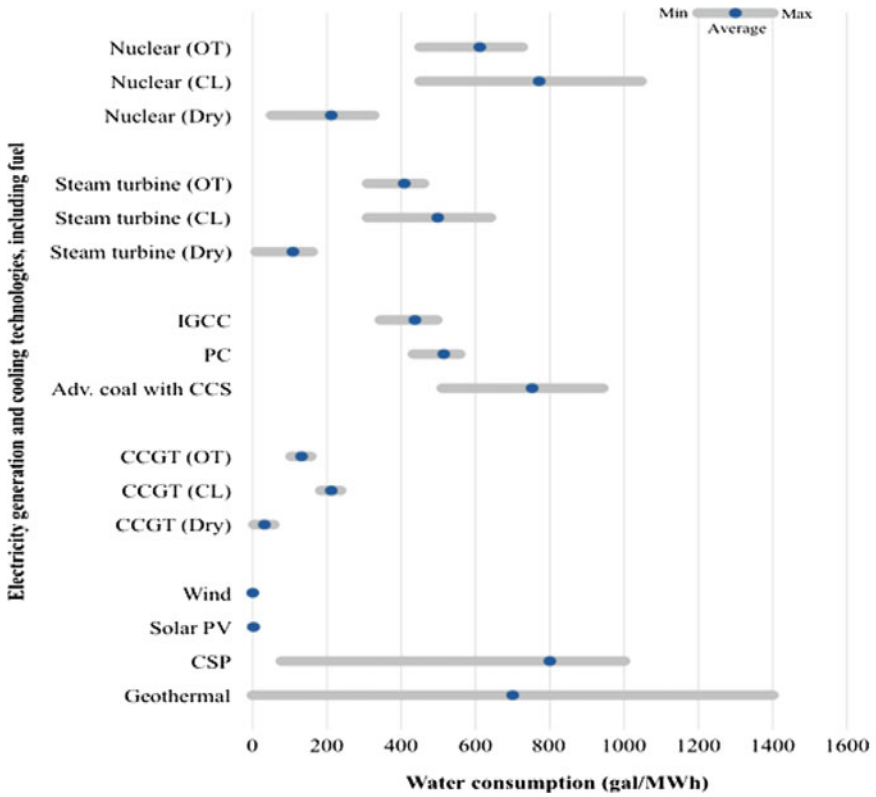

Fig. 25.2 Water use for electricity production [9]

25.2.2 Energy Requirements for Water Production

Energy is required for water lifting, desalination, treatment and distribution. The required energy for various types of water processes varies from fractions of KWh to few KWh per cubic meter produced, depending on the process type as well as several geographical, operational and technological factors. This research work focuses on energy used for urban water, thus covering only water desalination and treatment.

25.2.2.1 Energy Requirements for Water Desalination

UAE operates 70 desalination plants representing 14 % of the overall worldwide capacity, two thirds of which are located in Abu Dhabi [11]. The desalinated water in Abu Dhabi is produced either jointly with electricity as per the thermal co-generation plants, or separately through independent plants using reverse osmosis (RO) technology. Thermal cogeneration plants represented more than 93 % of the entire desalinated capacity in Abu Dhabi in 2011. Thermal desalination is divided into; Multi-Stage Flash (MSF) and Multi-Effect Distillation (MED) with 75 and 18 % respectively of total desalination capacity. Only 7 % of the Abu Dhabi's desalination capacity in 2011 came from RO plants [12].

Abu Dhabi is heavily reliant on MSF; it is preferable due to its large capacity, high reliability, as well as relatively affordable consuming of energy to desalinate the highly concentrated total dissolved solids (TDS) of the Gulf seawater, and most importantly the ability to cogenerate with power production. The energy used for water desalination varies upon the ratio of water to power production. The water demand in Abu Dhabi is almost constant all over the year, whereas electricity demand usually increases during summer months dominated by air conditioning load, and drops significantly during winter months. For the case of Abu Dhabi, the ratio of water to power varies from 320 to 1170 (m^3/d) per MW of co-generation plant capacity [13]. The CO_2 emissions allocated for electricity and water production in Abu Dhabi varies from one season to another, according to EAD GHG report [14] the annual average in 2010 was 13.76 kg Co_2eq/m^3 for water production, and 0.51 kg Co_2eq/kWh for electricity production.

25.2.2.2 Energy Requirements for Wastewater Treatment

There is no available data on the level of energy used for wastewater treatment in Abu Dhabi; the international studies estimate the energy intensity for primary treatment within the range of 0.1–0.3 kWh/m^3 and 0.275–0.59 kWh/m^3 for secondary treatment, which includes sludge [2].

According to Abu Dhabi Environmental Statistics [6]; the total quantity of wastewater inflow in Abu Dhabi was exceeded 259 Million m^3 in 2011; out of which 243 million m^3 were treated and 133 million m^3 were only used mainly for irrigation of the landscape areas.

25.2.3 End Use Energy and Water Consumption

The electricity demand for the Abu Dhabi Emirate reached the level of 43.2 TWh in 2011. The domestic sector is the major electricity consumer in Abu Dhabi accounted 31 % of the total electricity consumed in 2011, followed by commercial and governmental sectors with 29 and 25 % respectively.

In the water side, Abu Dhabi consumed 961.5 Million m^3 of water in 2011, 54 % of which went to domestic, followed by governmental and commercial sectors with 22 and 16 % respectively [12].

25.3 End Use Energy Simulation and Water Calculation

A detailed water and energy analysis is carried out for representative buildings in Abu Dhabi; three types of buildings have been chosen, namely; villa, multistory residential building, and office building.

25.3.1 Energy Analysis

In order to assess the energy performance of the selected representative buildings, both the baseline case (existing building) and proposed case (new building—Estidama compliance) are virtually simulated using eQUEST version 3.64 energy modeling software.

Buildings that have been constructed before 2011 are considered as baseline case, where no building code was applied in Abu Dhabi. The proposed case is applied to those buildings to be built after 2011; new buildings need to fulfill the Estidama pearl rating system requirements that have been put in place in 2011.

Identifying the design parameters of the existing buildings was difficult due to inadequate information of the energy efficiency level of various building systems, and the lack of insulation regulation in Abu Dhabi before 2011 As a result, the baseline building model was simulated to reflect the limited available data and using some assumptions to match with the current level of energy intensity of the chosen buildings in Abu Dhabi. Table 25.1 summarizes the input parameters that were used for baseline case and proposed case energy simulation of the three selected buildings.

Table 25.1 Input parameters for baseline case and proposed case [15, 16, 17]

Parameter	Villa		Multistory residential		Office building	
	Baseline use	Proposed case	Baseline case	Proposed case	Baseline case	Proposed case
External walls	8 inch concrete block	Estidama minimum energy requirements	8 inch concrete block	Ashrae 90.1, 2007 requirements	8 inch concrete block	Ashrae 90.1, 2007 requirements
	U value-2.63 W/m^2/K	U value-0.32 W/m^2/K	U value-2.63 W/m^2/K	U value-0.7 W/m^2/K	U value-2.63 W/m2/K	U value-0.7 W/m^2/k
Roof	8 inch concrete block	Estidama minimum energy requirements	8 inch concrete block	Ashrae 90.1, 2007 requirements	8 inch concrete block	Ashrae 90.1, 2007 requirements
	U value- 2.63 W/m^2/K	U value- 0.14 W/m^2/K	U value-2.63 W/m^2/K	U value-0.36 W/m^2/K	U value-2.63 W/m^2/K	U value-0.36 W/m^2/K
Glazing	6 mm single reflective glass	Estidama minimum energy requirements	6 mm single reflective glass	Ashrae 90.1, 2007 requirements	6 mm single reflective glass	Ashrae 90.1, 2007 requirements
	U value- 5.57 W/m^2/K	U value-2.2 W/m^2/K	U value-5.57 W/m^2/K	U value-6.9 W/m^2/K	U value- 5.57 W/m^2/K	U value- 6.9 W/m^2/K
Lighting power density	12 W/m^2	6.8 W/m^2	7.5 W/m^2	7.5 W/m^2	11 W/m^2	11 W/m^2
Equipment power density	20 W/m^2	20 W/m^2	12 W/m^2	12 W/m^2	12 W/m^2	12 W/m^2
Occupancy	10 m^2/person	10 m^2/person	10 m^2/person	10 m^2/person	20 m^2/person	20 m^2/person
HVAC	DX air cooled unit	DX air cooled unit	Chillers	Chillers	Chillers	Chillers
Heating design temperature	20 °C	20 °C	20 °C	20 °C	20 °C	20 °C
Cooling design temperature	23.8 °C	23.8 °C	23.8 °C	23.8 °C	23.8 °C	23.8 °C
Cooling electric input ratio (EIR)	0.34	0.28	0.39	0.34	0.39	0.34
Ventilation rate	25.5 m^3/hr/person	25.5 m^3/hr/person	25.5 m^3/hr/person	25.5 m^3/hr/person	25.5 m^3/hr/person	25.5 m^3/hr/person
Alteration rate	0.35 air changes/Hr	0.35 air changes/Hr	0.35 air changes/Hr	0.35 air changes/Hr	0.35 air changes/Hr	0.35 air changes/Hr

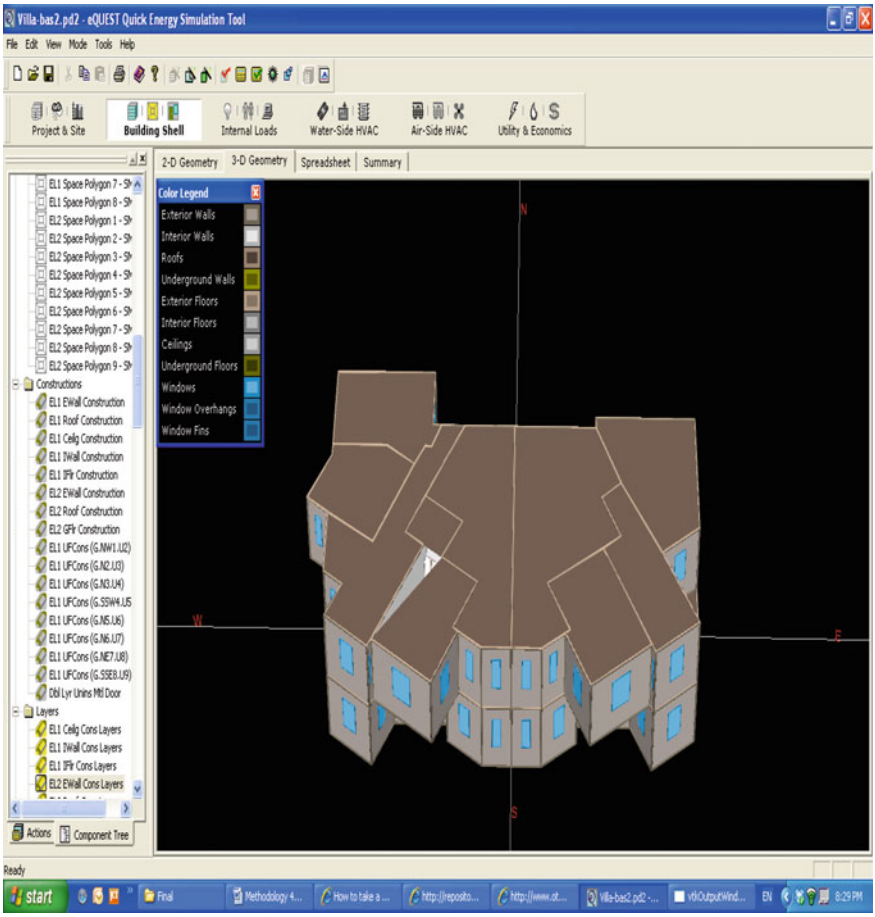

Fig. 25.3 Screenshot of the simulated villa building on eQUEST

Case study 1: Villa building

Villa is one of the key building segment in Abu Dhabi; Medium-size villa with two stories and total built-up area of 465 m^2 (5,000 ft^2) was selected for this analysis as shown in Fig. 25.3.

The results of the two energy simulations of baseline and proposed case showed that a considerable amount of energy can be reduced after achieving the minimum energy performance of Estidama requirements as shown in Fig. 25.4.

A potential energy reduction of 31 % is likely attainable, mostly from cooling load efficiency enhancement; through using better insulation of the various elements of building envelope as well as utilizing efficient cooling units. The remaining savings came from using more efficient lighting system and supply part of the hot water demand from renewable energy source.

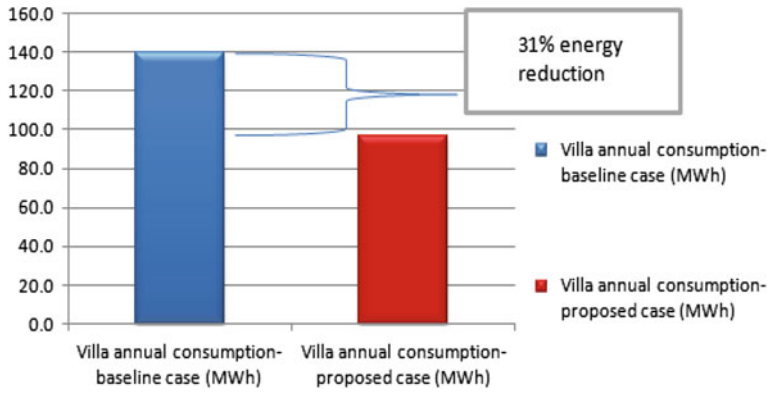

Fig. 25.4 Potential of energy reduction in villa building after meeting Estidama requirements

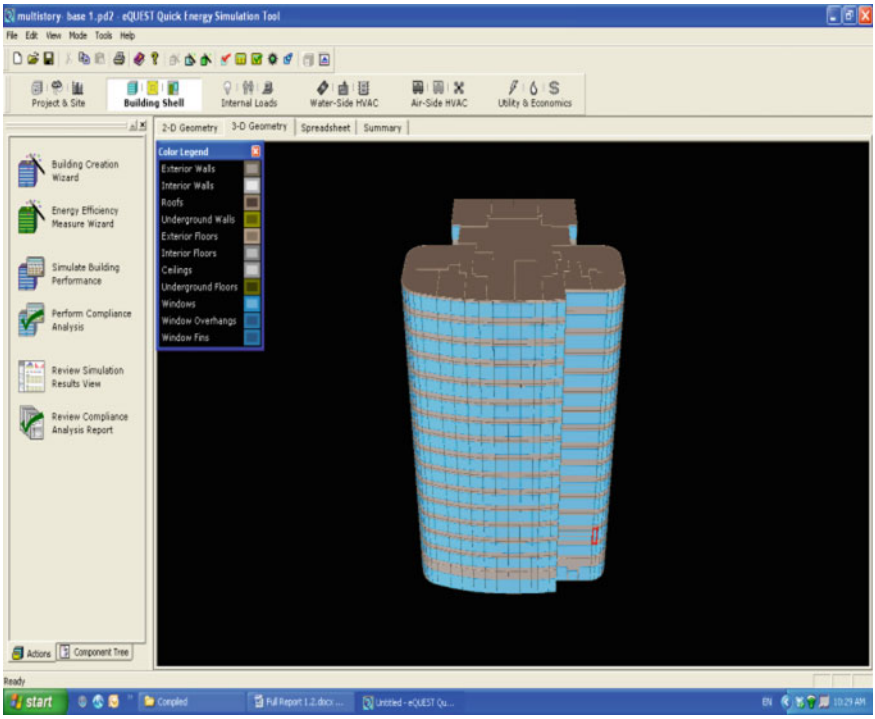

Fig. 25.5 Screenshot of the simulated multistory residential building on eQUEST

Case study 2: Multistory residential building

For simulation purposes, a typical 16 stories residential building with a total built-up area of 12,633 m^2 (1,35,977 ft^2) is used as shown in Fig. 25.5.

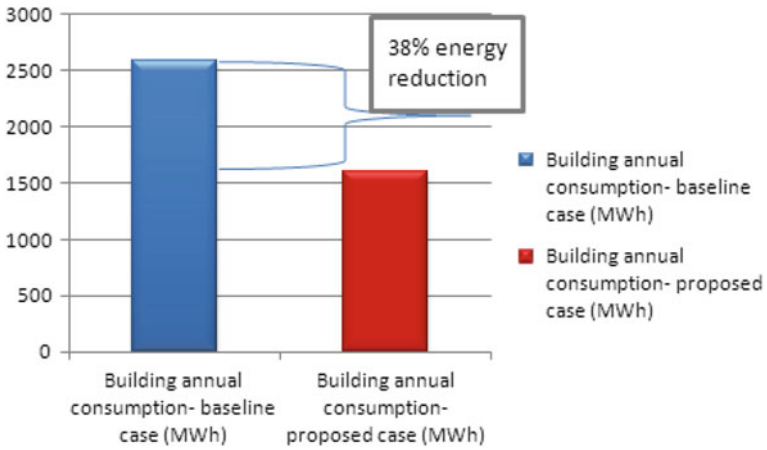

Fig. 25.6 Potential of energy reduction in multifamily residential building after meeting Estidama requirements

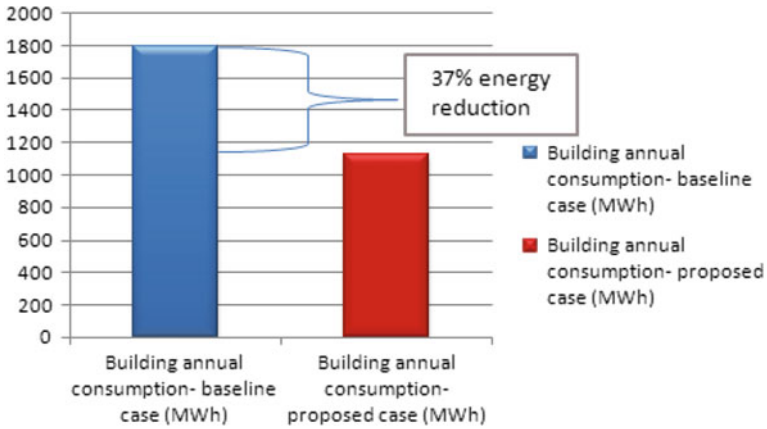

Fig. 25.7 Potential of energy reduction in the office building after meeting Estidama requirements

Figure 25.6 demonstrates the potential of energy reduction in multistory residential building after meeting the requirements of minimum energy performance of the Estidama pearl building rating system.

Case study 3: Office building

Typical 10 story office building with a total built-up area of 7,820 m^2 (84,173 ft^2) was selected in this simulation analysis. Figure 25.7 shows the potential of energy reduction in the office building after meeting the requirements of minimum energy performance of the Estidama pearl rating system.

Table 25.2 Fixtures flow requirement

Fixture	Flow requirement (l/use or l/min)	
	Energy policy act	Estidama
Water closets	6	6
Urinals	3.8	0.5
Showerheads	9.5	9.5
Faucets	9.5	6
Bidet	9.5	6

25.3.2 Water Analysis

The water calculation tool of the Estidama pearl rating system is used to estimate the interior water consumption for the three selected buildings. For the purpose of estimating the water consumption for landscape irrigation, which is only applicable for Villa building, LEED calculation method is used. For each category, both baseline and proposed case analysis are performed.

For interior water calculation; the flow rates recommended by Energy Policy Act [18] for the various water fixtures are used as shown in Table 25.2, but with some adjustments to match with the current level of water intensity as per the available data and published studies relevant to buildings sector in Abu Dhabi. For landscape calculation, since Estidama does not provide a calculation tool, the LEED-NC version 2.2 methodology is used.

For verification purposes, the calculated water consumption for the various chosen buildings was compared with available benchmarked values of the RSB water and electricity consumption report [19], which states the water consumption per capita for all types of buildings in Abu Dhabi.

The analysis shows a potential reduction of 35.7, 21.5 and 33.8 % in water consumption can be achieved in villa, residential multi story and office building respectively after meeting the requirements of minimum interior water use of the pearl building rating system.

25.4 Outcomes and Discussion

The outcomes of energy simulation showed a potential of electricity reduction between 31 and 38 %, for the purpose of quantifying the energy reduction potential by 2020, we assume that an annual growth rate of 8 % in electricity demand during the period from 2011 to 2020 and an energy reduction potential of 30 % on all new buildings in Abu Dhabi.

By reflecting the above assumptions on the forecasted electricity demand in Abu Dhabi for business as usual (BAU) as well as for Estidama scenario, it can be noticed that starting from 2012 the consumption of Estidama scenario begins to

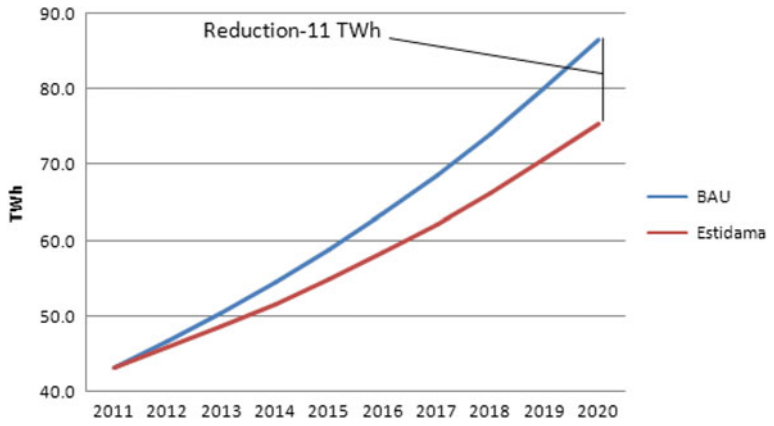

Fig. 25.8 Comparison of forecasted electricity demand in Abu Dhabi by 2020 (BAU versus Estidama)

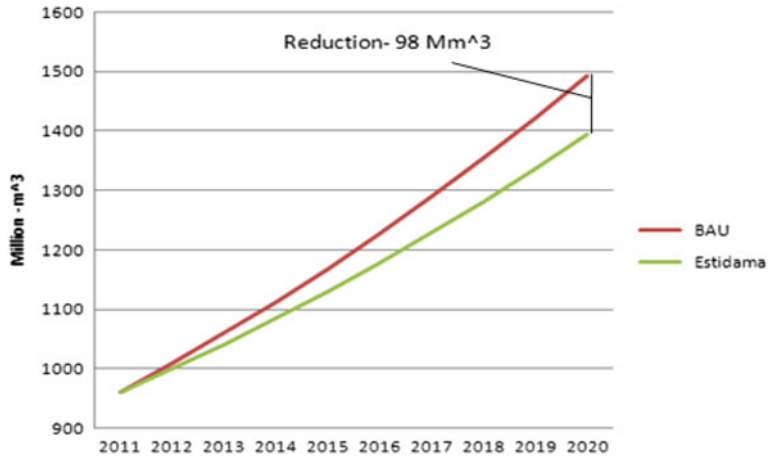

Fig. 25.9 Comparison of forecasted water demand in Abu Dhabi (BAU versus Estidama)

decline compared to BAU and reaches its maximum reduction by 2020 with 11 TWh below the BAU, as shown in Fig. 25.8.

Whereas the potential of water reduction varies from 22 to 36 % depending on building type and other parameters, for the purpose of projection the total water reduction by 2020, we assume that an average annual growth rate of 5 % in water demand during the period from 2011 to 2020 and a water reduction potential of 20 % on all new buildings in Abu Dhabi.

As it can be noticed from Fig. 25.9, starting from 2012 the consumption of Estidama scenario begins to decline compared to BAU—following the

Table 25.3 Summary of the project outcomes

	Annual demand growth		Total
	Electricity	Water	
Cumulative consumption savings in 10 years—TWh/Mm^3	49.3	457.1	
Cumulative monitory savings in 10 years—billion AED	14.2	4.8	19.0
Cumulative carbon savings in 10 years —million ton of C02eq	25.1	6.3	31.4

implementation of Estidama system on all new buildings—and reaches its maximum annual reduction by 2020 with 98 Million m^3 below the BAU.

The environmental and economic benefits that the Abu Dhabi government can acquire from enhancing buildings performance following the implementation of Estidama pearl building rating system over 10 years period (2011–2020) can be summarized as shown in Table 25.3.

A significant cumulative amount of electricity reduction totaled of 49.3 TWh can be achieved over 10 years period of implementing the minimum standard of Estidama program (1 pearl category), which exceeds the entire electricity consumed in Abu Dhabi Emirate in 2011 i.e. 43.3 TWh by 14 %. In the water side; a cumulative reduction of 457.1 Million m^3 can be achieved in 10 years period, which is equivalent to 48 % of the entire water demand of Abu Dhabi Emirate in 2011, i.e. 961.5 Million m^3.

The direct monitory savings from adopting Estidama program could reach up to 19 Billion AED accumulatively over 10 years period, based on the current actual unit production cost of electricity and water in Abu Dhabi. The monitory savings are divided between the government of Abu Dhabi and the end-users; the end-users only pay a small portion of the actual cost while the remaining cost is totally covered by the government through its electricity and water subsidy program.

On the environmental side, the entire cumulative carbon reduction of the first 10 years of putting Estidama into service is estimated to reach 31.4 Million ton of CO_2eq, this is higher than the entire amount of CO_2 produced by water and electricity generation sector in Abu Dhabi in 2010—i.e. 30.84 Million ton of CO_2eq by 2 %.

25.5 Conclusion

The outcomes of energy simulation and water analysis showed a potential of electricity reduction between 31 and 38 % and a potential of water reduction from 22 to 36 % depending on building type and other parameters. Adopting the Estidama pearl rating system for all new constructed buildings in Abu Dhabi would reduce water and energy consumption by considerable amounts, thus help preserving its natural resources for the coming generations and enhancing its energy and water security. It will also reduce the government expenditures on energy and water subsidies, enhance the market and create new job opportunities, protect the

environment and reduce carbon emissions. The first 10 years of putting Estidama building program into service could achieve monitory savings up to 19 Billion AED and abate 31.4 Million ton of CO_2eq cumulatively.

References

1. K. Hussey, J. Pittock, The energy-water nexus: managing the links between energy and water for a sustainable future. Ecol. Soc. **17**(1), 31 (2012)
2. A. Siddiqi, L.D. Anadon, The water–energy nexus in Middle East and North Africa. Energy Policy **39**(8), 4529–4540 (2011)
3. M. Bazilian, H. Rogner, M. Howells, S. Hermann, D. Arent, D. Gielen, P. Steduto, A. Mueller, P. Komor, R.S.J. Tol, K.K. Yumkella, Considering the energy, water and food nexus: towards an integrated modelling approach. Energy Policy **39**, 7896–7906 (2011)
4. A. Aissaoui, MENA power reassessed: growth potential, investment and challenges (2012), http://www.mees.com/en/articles/4722-mena-power-reasesed-growth-potential-investment-and-challenges##. Accessed 21 July 2013
5. MOEW (Ministry of Environment and Water), UAE water conservation strategy (2010)
6. Abu Dhabi Statistical Center, Abu Dhabi Energy and Environmental Statistics (2012), http://www.scad.ae/en/statistics/Pages/Statistics.aspx?ThemeID=6&TopicID=19&SubTopicID=137&PublicationID=309. Accessed 21 June 2013
7. IEA, Key world energy statistics (2012), http://www.iea.org/publications/freepublications/publication/kwes.pdf. Accessed 21 May 2013
8. V. Glogabl, The energy-water nexus: an emerging risk (2011), http://voxglobal.com/2011/03/the-energy-water-nexus-an-emerging-risk/. Accessed 21 May 2013
9. E. Mielke, L. Anadon, V. Narayanamurti, Water consumption of energy resource extraction, processing, and conversion (2010), http://belfercenter.ksg.harvard.edu/files/ETIP-DP-2010-15-final-4.pdf. Accessed 25 July 2013
10. S. Lattemann, T. Höpner, Environmental impact and impact assessment of seawater desalination. Desalination **220**(1–3), 1–15 (2008)
11. T. Mezher, H. Fath, Z. Abbas, A. Khaled, Techno-economic assessment and environmental impacts of desalination technologies. Desalination **266**(1–3), 263–273 (2011)
12. ADWEC, Statistical report 1998–2011 (2011), http://www.adwec.ae/report2011.html. Accessed 15 June 2013
13. M.A. Darwish, N.M. Al-Najem, N. Lior, Towards sustainable seawater desalting in the Gulf area. Desalination **235**(1–3), 58–87 (2009)
14. EAD, Greenhouse gas inventory for Abu Dhabi Emirate (2012), https://www.ead.ae//_data/global/book/ghg-brochureenglish.pdf. Accessed 25 July 2013
15. American Society of Heating and Air-Conditioning Engineers, ANSI/ASHRAE standard 90.1: ventilation for acceptable indoor air quality (2004)
16. Estidama, Pearl building rating system: design and construction, version 1.0 (2010), http://estidama.org/template/estidama/docs/PBRS%20Version%201.0.pdf. Accessed 6 June 2013
17. Estidama, Pearl villa rating system: design and construction, version 1.0 (2010), http://estidama.org/template/estidama/docs/PVRS%20Version%201.0.pdf. Accessed 6 June 2013
18. USGBC, LEED for new construction version 2.2 (2007), http://www.usgbc.org/Docs/Archive/General/Docs3179.pdf. Accessed 9 June 2013
19. RSB, water and electricity consumption report (2010), http://www.rsb.gov.ae/uploads/ReportWEConsumption.pdf. Accessed 21 July 2013

Chapter 26
Diesel Engine Performance and Emission Under Hydrogen Supplement

M. O. Hamdan, P. Martin, E. Elnajjar, M. Y. E. Selim and S. Al-Omari

Abstract This experimental study reports the behavior of diesel engine while being supported by hydrogen supplement. Hydrogen supplement is added through the air intake manifold at the atmosphere condition (0 °C and 101.325 kPa). The study reports the hydrogen supplement effect on the combustion characteristics, engine performance, emission and fuel consumption. The hydrogen supplement is varied by increment of 2 LPM while keeping the engine under fixed output power condition (torque of 14.7 N-m and speed of 1,100 rpm). In order to keep the engine output power fixed, the diesel fuel consumption is reduced and the hydrogen fuel consumption e hydrogen flow rate. For same power condition (torque and speed), the study shows that hydrogen can be used to reduce diesel fuel consumption however this comes on the expense of increasing of NOx emission. The main finding of this study is that compression engine with hydrogen supplement and diesel as the primary fuel starts knocking when hydrogen form 34 % the output power contribution (or 19 % as mass ratio between hydrogen to diesel).

Keywords Hydrogen combustion · Diesel engine · Dual engine

26.1 Introduction

The need for new source of energy has forced scientists and engineers to explore the use of alternative possible fuel to run compression ignition engine such as LGP [1], in order to replace diesel or at least reduce the use of diesel fuel. Two of many factors that affect the use of compression ignition engine are fuel ignition temperature and engine emission has led the authors to explore the use of hydrogen as

M. O. Hamdan (✉) · P. Martin · E. Elnajjar · M. Y. E. Selim · S. Al-Omari
United Arab Emirates University, Al Ain, United Arab Emirates
e-mail: MohammadH@uaeu.ac.ae

M. O. Hamdan et al. (eds.), *ICREGA'14 - Renewable Energy: Generation and Applications*, Springer Proceedings in Energy, DOI: 10.1007/978-3-319-05708-8_26,

supplement source of energy in compression ignition engine. Hydrogen is one of the most promising alternative fuels that can play great role in replacing fossil fuels. The clean burning characteristics and better performance of hydrogen fuel has led many researchers to investigate the use of hydrogen as a fuel [2]. However, the use of hydrogen as a fuel in spark ignition (SI) engine [3] has showed a significant reduction in power output. In addition at high load, pre ignition, backfire and knocking problems has been reported, hence these problems have limited the use of hydrogen in SI engine [4, 5].

On the other hand, the use of hydrogen has showed a significant increase in efficiency (around 20 %) in compression ignition engine [6] when compared to pure diesel combustion and an increase of 13 % in NOx emission. As reported in literature [7], hydrogen fuel cannot be used as a sole fuel in a compression ignition (CI) engine, since the compression temperature is not enough to initiate the combustion due to its high self-ignition temperature. Therefore, hydrogen is used as dual fuel and combusted with the presence of diesel as the main fuel. In a dual fuel engine the main fuel is either carbureted or injected into the air intake stream with combustion initiated by diesel. The major energy is obtained from diesel while the rest of the energy is supplied by hydrogen. Masood et al. [8] reported a brake thermal efficiency of 30 % when hydrogen is used in the dual fuel mode with diesel at a compression ratio of 24.5. Lee et al. [9] studied the performance of dual hydrogen-diesel fuel engine by using solenoid in-cylinder injection and external fuel injection technique. Lee et al. has reported an increase in thermal efficiency of 22 % for dual injection at low loads and 5 % at high loads compared to direct injection. Lee et al. [10] indicated that in dual injection, the stability and maximum power is accomplished by direct injection of hydrogen. Das et al. [11] have carried out experiments on continuous carburation, continuous manifold injection, timed manifold injection and low pressure direct cylinder injection. Das et al. reported that the maximum brake thermal efficiency of 31.3 % is obtained at 2,200 rpm with 13 N-m torque.

The use of hydrogen fuel is a potential method to reduce the demand on liquid diesel fuel however it comes with the expense of increasing NOx emission. Therefore, the need for techniques to reduce NOx become more vital for dual hydrogen-diesel engine operation. One way to achieve the NOx reduction in diesel engine is by injecting steam to the combustion [12]. Another way of reducing NOx is to operate the hydrogen engine with lean mixtures. Lean mixture results in lower temperature that would slow the chemical reaction, which weakens the kinetics of NOx formation [13, 14].

One of the main feature of hydrogen-operated engine is that it does not produce major pollutants such as hydrocarbon (HC), carbon monoxide (CO), sulphur dioxide (SO_2), smoke, particulate matter, lead, and other carcinogenic compounds. This is due to the absence of carbon and sulphur in hydrogen. However hydrogen-operated engines main disadvantage is the NOx emissions. The formation of NOx mostly is due to the presence of nitrogen in air [15]. When the combustion temperature is high some portion of nitrogen present in the air reacts with oxygen to form NOx.

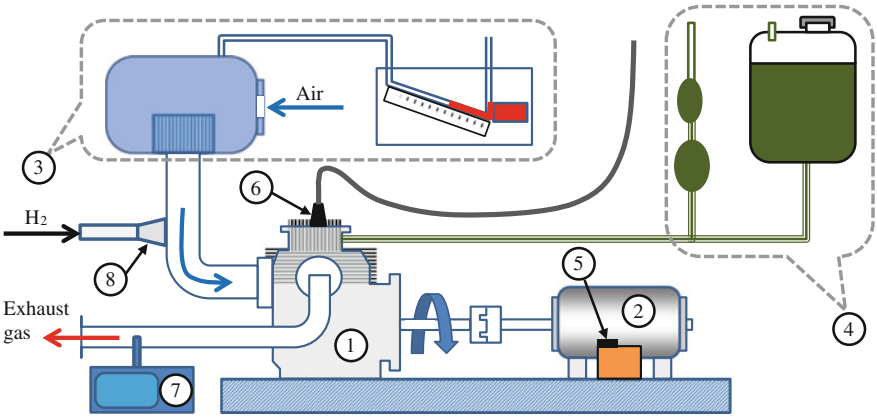

Fig. 26.1 Schematic view of the engine test bed: *1* engine, *2* dynamometer, *3* air intake system with drum tank and inclined manometer, *4* fuel system with fuel tank and flow measuring volume, *5* strain gauge load cell sensor for torque measurement, *6* pressure transducer, *7* emission monitoring systems, and *8* Hydrogen inlet to the air intake manifold

In this study and through dual engine configuration, hydrogen is injected to the air intake manifold as a supplemental fuel which is combusted in the presence of diesel as main fuel and thus replacing a portion of the diesel fuel demanded to produce engine output power. The primary interest of this study is the effect of hydrogen supplement on the performance of a diesel where hydrogen is supplied through the air intake manifold. The study reports the amount of hydrogen supplement that causes engine knocking.

26.2 Experimental Setup

A schematic diagram of the engine with instrumentations is show in Fig. 26.1. The test engine used is a single cylinder DI diesel engine, having a rated power of 5 kW that runs at a constant speed of 3,600 rpm which is modified to work with hydrogen in the dual fuel mode where hydrogen is injected into the air intake manifold as shown in Fig. 26.2.

The engine used in this study is Petter AC1 by Gussons type P8163 which is a four stroke compression ignition air-cooled engine. The engine size is 304 cc with 762 mm pore diameter and 66.7 mm stroke length. The engine has compression ratio of 17, a maximum power of 5 kW at 3,600 rpm and a maximum torque of 15.6 N-m at 2,650 rpm.

As shown in Figs. 26.1 and 26.2, hydrogen gas is injected into the air intake manifold at low pressure. A pressure regulator as well as a volumetric rotameter are used to control the hydrogen flow rate. The flow rate of air is measured using a calibrated orifice air-drum manometer arraignment. The diesel flow rate is

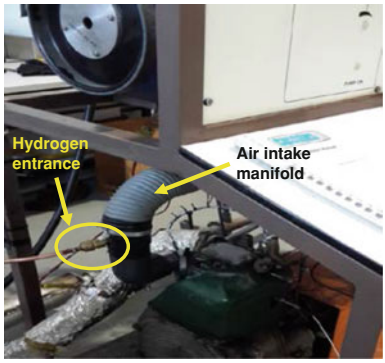

Fig. 26.2 The hydrogen inlet to the air intake manifold

measured by recording required time to consume fixed volume of diesel. The torque of the engine is measured through force transducer that is connected to the electrical dynamometer. The force transducer is calibrated before testing using fixed weight load. The electrical dynamometer is used to load the engine.

The main objective of this experiment is to determine the maximum hydrogen flow rate that diesel engine can handle before reaching knocking and to characterize the engine performance, characteristics, emission and fuel consumption under different flow rate of hydrogen. For this hydrogen is varied from 0 to 8 l per minute insteps of 2 l per minute for the entire load conditions. The emission is measured using RARIO plus SE emission monitoring systems.

26.3 Mathematical Analysis

The engine efficiency and specific fuel consumption is calculated using Eqs. (26.1) and (26.2) respectively:

$$\eta = \frac{W_{out}}{Q_{in}} = \frac{T \cdot \omega}{(\dot{m} \times LHV)_{Diesel} + (\dot{m} \times LHV)_{H_2}} \tag{26.1}$$

$$sfc = \frac{\dot{m}_{fuel}}{W_{out}}. \tag{26.2}$$

The specific fuel consumption is calculated based on diesel fuel consumption, hydrogen fuel consumption and total (hydrogen and diesel) fuel consumption. The lower heating value is used in the calculation since no vapor is condensed during the experiment. The density of hydrogen is calculated at atmosphere pressure and room temperature.

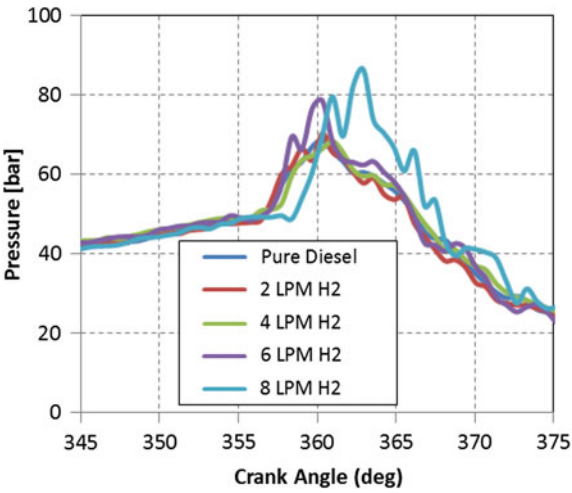

Fig. 26.3 Variation of cylinder pressure with crank angle at 14.7 N-m engine torque and 1,100 rpm engine speed for different amount of hydrogen supplement

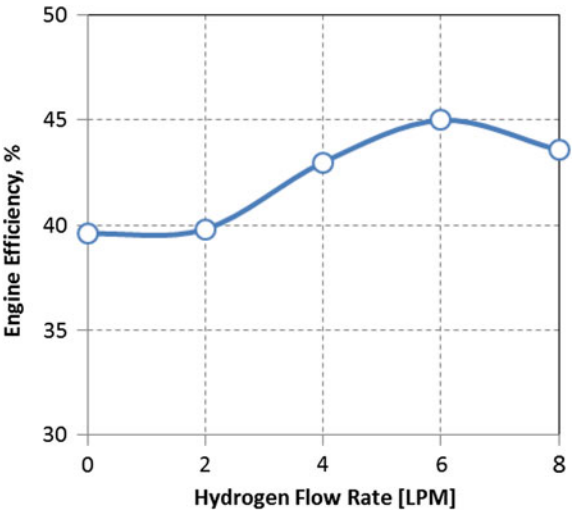

Fig. 26.4 Variation of engine efficiency versus different amount of hydrogen supplement while fixing engine torque at 14.7 N-m and engine speed at 1,100 rpm

26.4 Results and Discussion

The effect of hydrogen supplement on diesel engine performance are shown in Figs. 26.3, 26.4, 26.5, 26.6 and 26.7 for one output power condition with torques of 14.7 N-m and engine speed of 1,100 rpm. The output power condition is 1.69 kW while maximum engine load is 5 kW at 2,650 rpm. During the experiment, as the amount of hydrogen flow rate is increased, the amount of diesel flow rate is decreased to maintain fixed power condition (torque of 14.7 N-m and speed of 1,100 rpm).

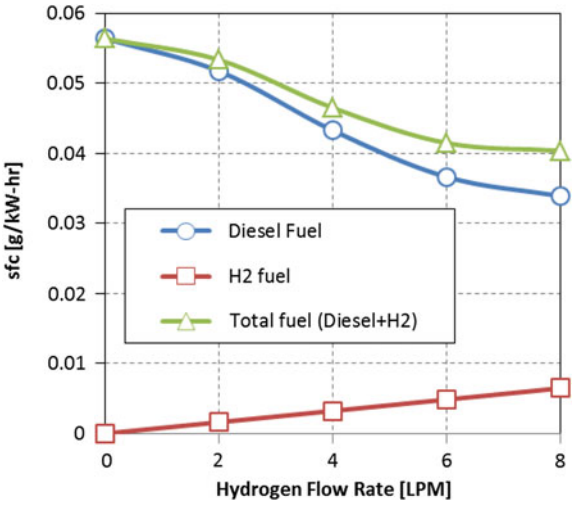

Fig. 26.5 Variation of specific fuel consumption for different amount of hydrogen supplement while fixing engine torque at 14.7 N-m and engine speed at 1,100 rpm

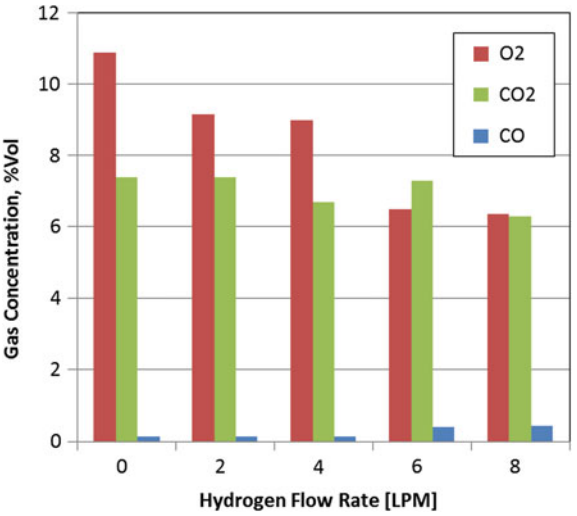

Fig. 26.6 Variation of O_2, CO_2 and CO with different amount of hydrogen supplement, at 14.7 N-m engine torque and 1,100 rpm engine speed

Figure 26.3 shows the cylinder pressure variation with crank angle for different amount of hydrogen supplement flow rates. It is very clear that adding hydrogen will increase the maximum pressure of the cylinder and that pure diesel case has the least peak pressure. It is also clear that adding hydrogen supplement up to 4 LPM (7.5 % weight ratio of hydrogen to diesel) will not have major effect on the pressure rise inside the engine cylinder.

As amount of hydrogen supplement is increasing, Fig. 26.4 shows that engine efficiency is improving from 39.6 % for pure diesel up to 45 % for hydrogen supplement flow rate of 6 LPM. This is expected since hydrogen will burn faster

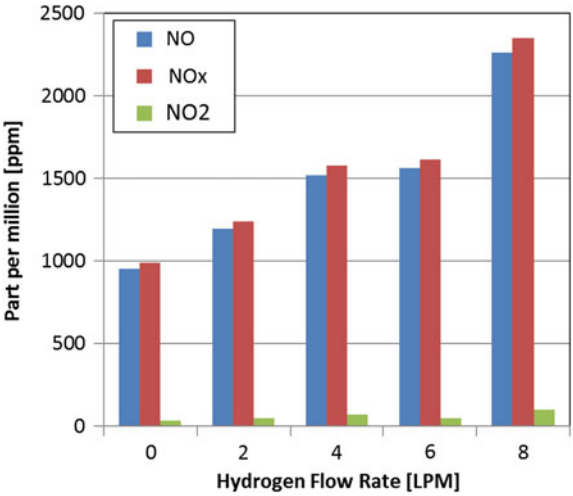

Fig. 26.7 Variation of NO, NOx and NO_2 with different amount of hydrogen supplement, at 14.7 N-m engine torque and 1,100 rpm engine speed

causes higher temperature rise when compared to diesel and hence it boosts engine efficiency. However this trend drops after 6 LPM and engine efficiency drop to 43.6 % at 8 LPM of hydrogen which could be due to lower air flow rate. During the experiment, amount of air introduced to the engine has decreased by a small amount (around 12 % when compared between pure diesel case and 8 LPM hydrogen supplement case). It is expected that this reduction in air flow rate is due to hydrogen who starts occupying more volume of air intake manifold which forced less air inside the engine cylinder.

As expected, introducing hydrogen fuel will reduce the diesel fuel consumption, hence reduce sfc of diesel as shown in Fig. 26.5. The reduction in the diesel specific fuel consumption is more than the increase in the hydrogen specific fuel consumption the LHV of hydrogen is 119.96 MJ/kg while for diesel it is 44.8 MJ/kg. While keeping power output fixed, Fig. 26.5 shows that the total specific fuel consumption decreases as hydrogen supplement is introduced which is due to the enhancement in the engine efficiency and the higher LHV of hydrogen when compared to diesel.

Figures 26.6 and 26.7 show the engine emission and it is clear that as hydrogen supplement increases, the NOx increases and oxygen decreases. This is expected since as more hydrogen is burned higher temperature inside the cylinder is attained which increases engine break thermal efficiency however it increases NOx emission too. It is clear that at 6 LPM of hydrogen supplement, the fraction of reduction in specific fuel consumption when compared to pure diesel is 35 % (=1−(0.036 g/kW h)/(0.056 g/kW h)), while the fraction of increase in NOx emission is 64 % (=(1,615 ppm)/(987 ppm)−1),. Therefore, overall engine performance based on NOx emission has increase by 29 % (=64−35 %).

Knocking has been observed for hydrogen flow rate above 8 LPM ($= 1.1 \times 10^{-5}$ kg/s) while diesel consumption is 5.74×10^{-5} kg/s. In another

words knocking has been observed when hydrogen fraction form a 34 % of total energy supplied by hydrogen-diesel fuel (or 19 % as mass ratio between hydrogen to diesel).

26.5 Conclusions

In this work, an experimental investigation has been conducted to examine the effect of hydrogen supplement on the performance of dual fuel diesel engine. Forgiven engine specification, the data show the following:

- Specific fuel consumption decreases and hydrogen is introduced to the diesel engine due the improvement in engine efficiency and due to the higher LHV of hydrogen when compared to diesel.
- Engine knocking highly occurs when hydrogen flow rate goes beyond 8 LPM (34 % of energy contribution).
- The addition of hydrogen can reduce diesel consumption by 35 % but it will increase NOx emission by more than 64 %.

Acknowledgments The authors would like to acknowledge the support provided by United Arab Emirates University. This work is financially supported by the Faculty of Engineering at the United Arab Emirates University.

References

1. E. Elnajjar, M. Selim, M.O. Hamdan, Experimental study of dual fuel engine performance using variable LPG composition and engine parameters. Energy Convers. Manag. **76**, 32–42 (2013)
2. M. Garni, A simple and reliable approach for the direct injection of hydrogen in internal combustion engines at low and medium pressures. Int. J. Hydrogen Energy **20**, 723–726 (1995)
3. B. Haragopala Rao, K.N. Shrivastava, H.N. Bhakta, Hydrogen for dual fuel engine operation. Int. J. Hydrogen energy **8**, 381–384 (1983)
4. J.B. Heywood, *Internal Combustion Engine Fundamentals*. McGraw-Hill Series in Mechanical Engineering (McGraw-Hill, New York, 1998), p. 508–511
5. J.A. Caton, An investigation of cause of backfire and its control due to creviced volumes in hydrogen fueled engine. Trans. ASME **23**, 204–210 (2001)
6. N. Saravanan, G. Nagarajan, G. Sanjay, C. Dhanasekaran, K.M. Kalaiselvan, Combustion analysis on a DI diesel engine with hydrogen in dual fuel mode. Fuel **87**, 3591–3599 (2008)
7. L.M. Das, Near-term introduction of hydrogen engines for automotive and agricultural application. Int. J. Hydrogen Energy **27**, 479–487 (2002)
8. M. Masood, M.M. Ishrat, A.S. Reddy, Computational combustion and emission analysis of hydrogen-diesel blends with experimental verification. Int. J. Hydrogen Energy **32**, 2539–2547 (2007)
9. J.T. Lee, Y.Y. Kim, C.W. Lee, J.A. Caton, An investigation of a cause of backfire and its control due to crevice volumes in a hydrogen fueled engine. ASME, **123,** 204–210 (2001)

10. T. Lee Jong, Y.Y. Kim, A. Caton Jerald, The development of a dual injection hydrogen fueled engine with high power and high efficiency. 2002 Fall technical conference of ASME-ICED, pp. 2–12, 8–11 Sept 2002
11. L.M. Das, Hydrogen engine: research and development (R&D) programmes in Indian Institute of Technology (IIT) Delhi. Int. J. Hydrogen Energy **27**, 953–965 (2002)
12. A. Parlak, V. Ayhan, Y. Üst, B. Şahin, I. Cesur, B. Boru, G. Kökkülünk, New method to reduce NOx emissions of diesel engines: electronically controlled steam injection system. J. Energy Inst. **85**(3), 135–139(5) (2012)
13. F.J. Michael, H.R. Brunt, The calculation of heat release energy from engine cylinder pressure data. J. Fuels Lubricants **107** (Section 4, SAE 981052, SAE transactions) (1998)
14. J.D. Naber, D.L. Siebers, Hydrogen combustion under diesel engine conditions. Int. J. Hydrogen Energy **23**(5), 363–371 (1998)
15. S.J. Lee, H.S. Yi, E.S. Kim, Combustion characteristics of intake port injection type hydrogen fuelled engine. Int. J. Hydrogen Energy **20**, 317–322 (1995)

Chapter 27
The Potential of Using Raw Jojoba Oil as Fuel in Furnaces

Salah B. Al-Omari, Mohammad O. Hamdan, Mohamed Y. E. Selim and Emad Elnajjar

Abstract There is a constant need for coming up with new and alternative energy sources that are sustainable and at the same time environment friendly. Many research studies have already been conducted to fulfill the above target and addressed the use of plants-based oils in internal combustion engines. Less emphasis however was directed to the use of such oils in open combustion systems such as furnaces and boilers. The present study considers the potential of using green energy sources such as raw jojoba oil with minimal pretreatment as a sole fuel or alternatively as fuel supplements for furnaces. Blends of raw jojoba oil and diesel, with different proportions were burned in a small cylindrical furnace under different air flow conditions. The studied range of the jojoba oil proportions (on mass basis) in the liquid blends is from 20 to 60 %. More jojoba in the liquid mixture showed difficulty in sustaining a self-supporting flame due to the low volatility and high viscosity of raw jojoba oil. Moreover, the performance of the furnace with 20 % jojoba in the liquid fuel mix shows only small difference from performance on Diesel only. This suggests that about 20 % of Diesel can be replaced with raw jojoba with no significant loss of the thermal performance. More unburned species are emitted as the jojoba content in the fuel blend increases.

Keywords Raw jojoba oil · Jojoba/Diesel blends · Continuous combustion · Furnace · Renewable fuels

S. B. Al-Omari (✉) · M. O. Hamdan · M. Y. E. Selim · E. Elnajjar
Department of Mechanical Engineering, United Arab Emirates University,
Al Ain, United Arab Emirates
e-mail: s.omari@uaeu.ac.ae

M. O. Hamdan et al. (eds.), *ICREGA'14 - Renewable Energy: Generation and Applications*, Springer Proceedings in Energy, DOI: 10.1007/978-3-319-05708-8_27,

27.1 Introduction

The importance of exploring different alternative fuels for engines and furnaces, especially the green ones is quite evident and is expected to be more so in the near future given the stringent regulations and precautions regarding environment wellbeing and safety as well as the ever increasing need for securing more sustainable energy resources for the future generations. Many researchers already considered the use of the so called green energy sources (fuels) for combustion systems, with some contributions being provided by authors of this article considering fuels that are of relevance to the UAE and the GCC regions in particular [1–4]. Moreover, towards achieving the above goals, the authors in some of their previous research considered different approaches that aim at better sustainability of energy sources (see for example [5–7].

With the above said this work attempt to contribute to that endeavor by presenting a study which considers the use of green energy source namely raw jojoba oil as a fuel and/or fuel supplement in furnaces.

Jojoba oil and the from-it derived methyl esters have been already extensively researched, but for engine applications, see for example [8–10]. However, the use of such green fuel in furnaces, have not been addressed to any adequate level. To the best of our knowledge, only one single research work has considered the utilization of the jojoba nut shell as a solid fuel in furnaces [11]. The lack of research on furnaces using raw jojoba oil represents the main motivation for us to pursue the research reported herein and to further consider possible future expansions.

It is clear to us that raw jojoba has other applications in cosmetic industry for example that from economic and importance view point may compete with the use of it as an energy source. However, in this study, we solely aim at highlighting the potential and the features of the use of raw jojoba as a sole energy source or as a supplement for some primary fuels originating (for example) from petroleum.

As such, a decision on whether to use this raw material as an energy source or for other applications would be based on other circumstances including the availability and abundance of this raw material and this paper is not the place to make judgment on this issue.

27.2 Experimental Setup

The furnace used in the experimental runs conducted is a small cylindrical laboratory scale one that can burn liquid fuels with varying physical properties. It is equipped with an extensive data acquisition and instrumentation that enables measuring a wide range of quantities of interest to analyze the data and facilitate the comparison and assessment of the performance under different operating conditions. A water jacket surrounds the furnace so that heat transfer from the hot gases and their capability to radiate heat to furnace walls can be assessed for the

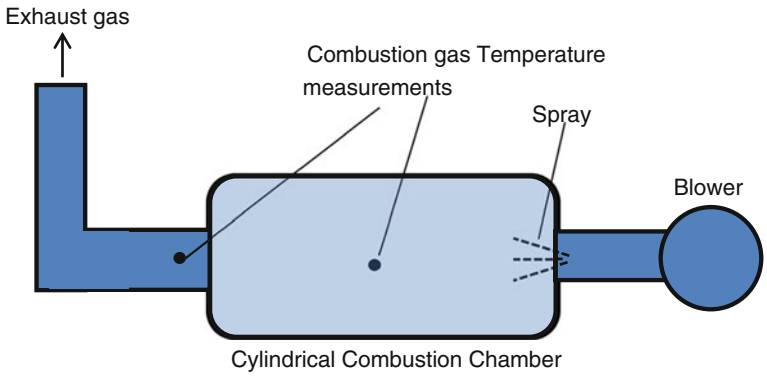

Fig. 27.1 Schematic of the experimental furnace

different conditions studied. Thermocouples to measure the temperatures at different locations are provided such that energy balance analysis is easily facilitated. An air assisted liquid fuel atomizer is used to spray the liquid fuel into the combustion domain of the furnace. Figure 27.1 shows a schematic drawing of experimented furnace.

Three runs where conducted with the following conditions:

In case 1 only diesel was used as a fuel with mass flow rate of 2.63 g/s. In the second run liquid fuel blend with jojoba content of 20 % (on mass basis) is injected with mass flow rate of 2.7 g/s. the third run is one with a blend containing 60 % jojoba and a with total fuel flow rate of 2.8 g/s. It was difficult to maintain exactly the same amount of total fuel injection rate in all the runs due to the varying physical properties of the liquid fuel injected in each run. This is basically due to the effect of jojoba on density and viscosity in the blend in each case.

27.3 Results and Discussion

Different experimental runs have been conducted. Table 1 summarizes the main features of these runs. In what follows the results of these cases will be analyzed and discussed.

Figure 27.2 presents the outlet water temperature as a function of the Air to Fuel ratio. Both case 1 and case 2 show almost the same peak temperature of about 74 °C, while case 3 shows a peak that is by about 3° less. In case 1 the exit water temperature shows almost a constant value of about 72 °C over a wide Air/Fuel ratio range. In case 2 this Air/Fuel range is clearly narrower. For example, in case 2 the water temperature falls steeply for Air/Fuel ratio levels beyond about 17. In case 1, this happens when Air/Fuel ratio becomes greater that about 24. The lower volatility and higher viscosity due to the presence of raw jojoba oil is believed to be behind the narrower range in case 2.

Table 27.1 Summary of the Main Features of the Experimental Runs

Case Number	Fuel type	Total Fuel flow rate (g/s)
1	Only Diesel	2.63
2	20 % Jojoba	2.7
3	60 % Jojoba	2.8

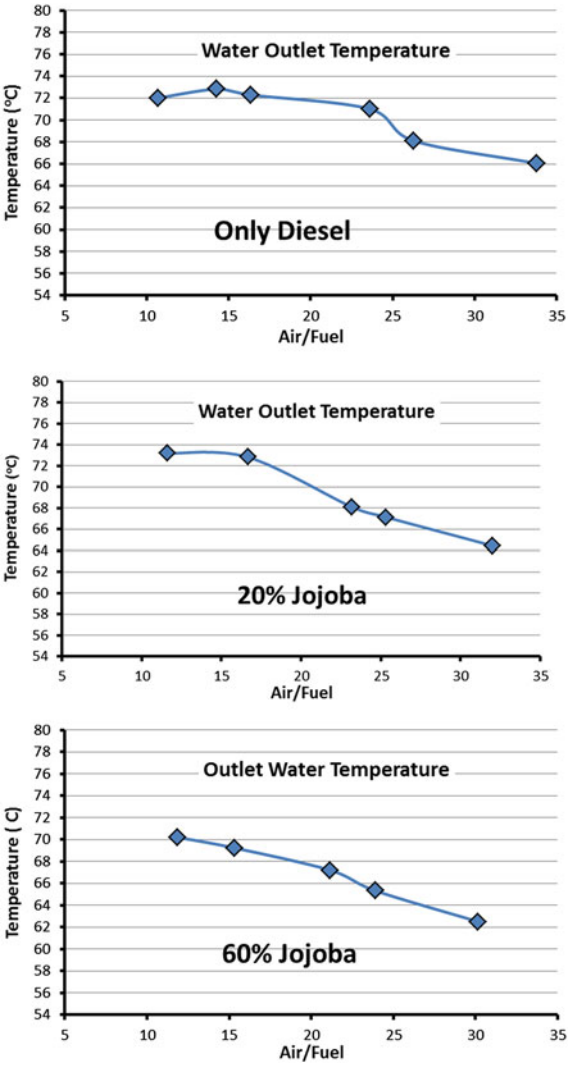

Fig. 27.2 The water exit temperature for the three cases: only diesel; 20 % jojoba; 60 % jojoba

In case 3 the high viscosity and low volatility of raw jojoba, as compared with diesel become so dominant that exit water temperature cannot be maintained at constant high level over different Air/Fuel ratios other than the one at which peak

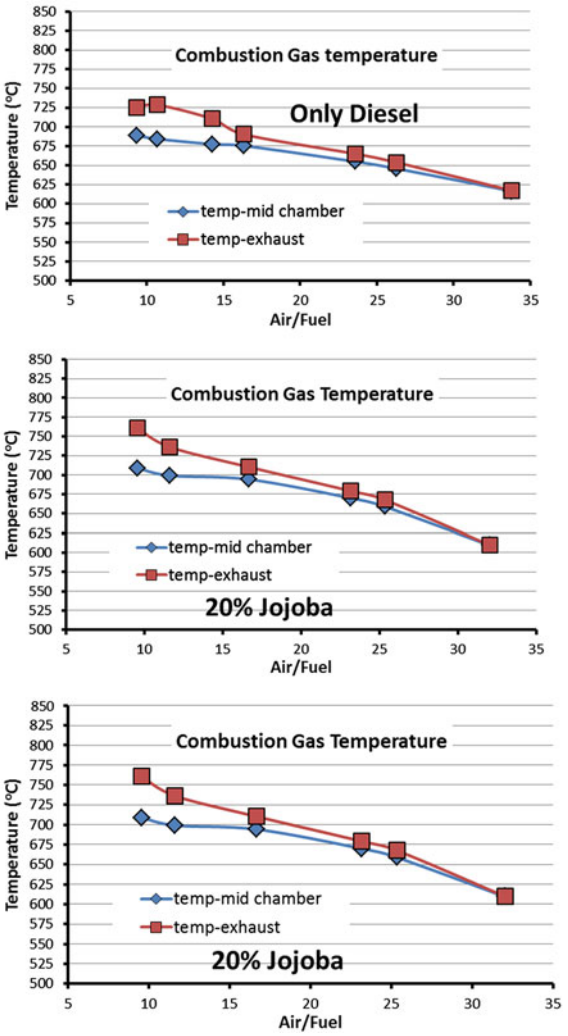

Fig. 27.3 The combustion gas temperature for the three cases: only diesel; 20 % jojoba; 60 % jojoba at two sections in the furnace; the middle of the furnace and the exit

value is attained namely at about 13. Moreover, the lack of fast-enough burning due to the above effects which do have consequences on the spray pattern and fuel vapor-air mixing, would even lead to lower water peak temperatures, compared to the levels attained in cases 1 and 2.

Other characteristics of the influence of the presence of jojoba oil in the fuel blends used is given in Fig. 27.3 in terms of the combustion gas temperatures at two locations in the furnace; one in the middle and the other at the furnace exit. For the case of only diesel (case 1) peak levels are attained at Air/Fuel ratio of about 12. In cases 2 and 3 that happens at a bit richer condition with Air/Fuel ratio of about 10. The peak gas temperatures are highest in case 3 with peak of 825 °C, followed by case 2, then at last case 1 with a peak of 730 °C. The above trend,

provided that the water temperatures in case 1 were higher may hint to a better radiation characteristics of the combustion when only diesel is used which lead to more energy being lost form the flame by radiation in case 1 and hence less gas peak temperatures. The deviation between the temperatures of the middle and exit points is highest in case 3 especially at low Air/Fuel levels; less than about 15. This may indicate the slower burning rate in the case of high jojoba content in the fuel, which then would require longer distance to complete the combustion of all fuel supplied. The closer the two lines of gas temperatures to each other the more is the indication to short distance needed to complete the combustion of the admitted fuel. Once more the higher viscosity and the lower volatility as the jojoba share in the fuel increases the more evident is this trend.

As the Air/Fuel ratio increases beyond 15, the drop in gas temperature becomes clear due to the cooling effects of extra amounts of air and the separation between the temperatures of both points (middle of furnace and exit) become smaller, indicating the completion of the reaction in a shorter space.

To see the impact of jojoba in the liquid fuel mix burned in the furnace on emissions from the furnace, the results of CO emissions for the three cases is studies next. Figure 27.4 presents the CO emission levels as a function of the Air/Fuel ratio for the three cases considered above. Cases 1 and 2 show comparable results, with case 1 resulting in slightly lower levels of CO emissions, reflecting thereby the quality of the combustion process due to the better spray pattern and the more efficient fuel vapor and air mixing in the spray due to the reasons highlighted above. As the Air/fuel ratio exceeds about 24, the level of CO emissions start increasing drastically due to the cooling effects of the high air quantities supplied to the furnace. In case 3, the CO emissions are clearly higher than the other two cases over all the Air/Fuel ratio range considered. This obviously is due to the lower quality burning attributed to the viscosity and volatility issues, highlighted above. For Air/Fuel ratio above about 20, CO emissions in case 3 reach much higher levels than the other two cases.

27.4 Conclusions

The feasibility of using raw jojoba oil with minimal pretreatment as a sole fuel or as a fuel supplement is investigated experimentally. Blends of jojoba oil and diesel with jojoba content of 20 and 60 % in the blends are considered as the liquid fuel burned in a small scale furnace. The following conclusions may be drawn from the preliminary results obtained:

- Only minor loss in the thermal performance of the furnace is observed when up to about 20 % of jojoba oil is used, as compared with the case when only diesel is used. Higher proportions of jojoba oil in the liquid fuel blend lead to some deterioration in the combustion performance. Above 60 % jojoba it was not possible to maintain self-sustaining combustion due to the high viscosity of the blend and the poor injection and the resulting spray characteristics.

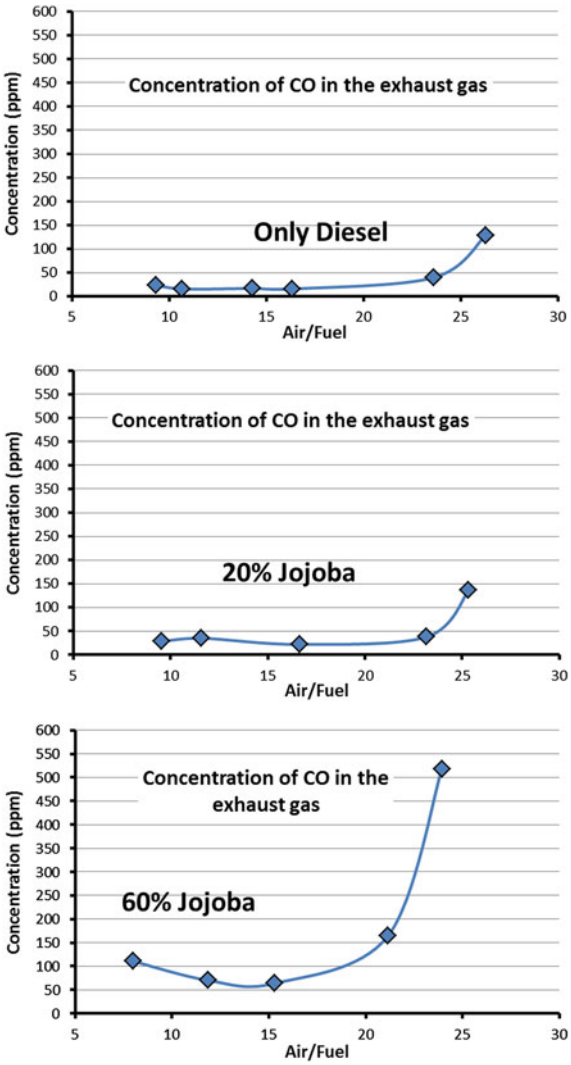

Fig. 27.4 CO emissions for the three cases: only diesel; 20 % jojoba; 60 % jojoba

- With Only-Diesel a wider range of operation at optimum stable thermal condition is attained; (A/F from 12 to about 23).
- With 60 % Jojoba, peak water temperatures is attained only at a limited A/F range and is by about 3°–4° less than when only-diesel is used.
- In the case of only-diesel or 20 % Jojoba blends, reaction is completed in a shorter distance compared with the case of 60 % Jojoba and CO emissions are clearly lower.

- Slight variations in the results obtained in the three runs could have been caused due to the slight differences in the exact amount of total fuel injected as it was not easy to exactly match in all of the runs exactly the same amount of fuel supplied.

Acknowledgments The authors would like to acknowledge the help offered by our lab Engineer Mohammad El Said during conducting the experiments.

References

1. S.B. Al Omari, Evaluation of the biomass "Date Stones" as a fuel in furnaces: a comparison with coal combustion. Int. Commun. Heat Mass Transf. **36**(9), 956–961 (2009)
2. S.B. Al Omari, Experimental investigation of combustion and heat transfer characteristics in a furnace fueled with unconventional biomass fuels (date stones and palm stalks). Energy Convers. Manag. **47**, 778–790 (2006)
3. M.Y.E. Selim, Y. Haik, S.-A. B. Al Omari, E. Elnajjar, Combustion of waste chocolate oil methyl ester in a diesel engine. Int. J. Ambient Energy (2013). doi:10.1080/01430750.2013.770795
4. M.O. Hamdan, M.Y.E. Selim, S.A.B. Al-Omari, M. Ghannam, Effect of stabilized water-diesel emulsion on external combustion characteristics, in *Proceedings of the ASME 2013 summer heat transfer conference* (2013)
5. S.B. Al Omari, B. Abu-Jdayil, Some considerations of the performance of small dual fuel furnaces fueled with a gaseous fuel and a liquid fuel mix containing used-engine-lube-oil. Renewable Energy **56**, 117–122 (2013)
6. Al Omari S.B., Used engine lubrication oil as a renewable supplementary fuel for furnaces, Energy Convers. Manage. **49**(12), 3648–3653 (2008)
7. M.Y.E. Selim, Y. Haik, S.A.B. Al-Omari, H. Abdulrahman, Biodiesel oil derived from biomass solid waste, in *Proceedings of the world congress on engineering*, vol. 3 (2011)
8. M.Y.E. Selim, M.S. Radwan, S.M.S. Elfeky, Combustion of jojoba methyl ester in an indirect injection diesel engine. Renewable Energy **28**(9), 1401–1420 (2003)
9. A.S. Huzayyin, A.H. Bawady, M.A. Rady, A. Dawood, Experimental evaluation of diesel engine performance and emission using blends of jojoba oil and diesel fuel. Energy Convers. Manag. **45**, 2093–2112 (2004)
10. M.Y.E. Selim, M.S. Radwan, H.E. Saleh, Improving the performance of dual fuel engines running on natural gas/LPG by using pilot fuel derived from jojoba seeds. Renewable Energy **33**, 1173–1185 (2008)
11. M.Y.E. Selim, S.-A.B. Al-Omari, S.M.S. Elfeky, M.S. Radwan, Utilization of extracted jojoba fruit as a fuel. Int. J. Sustain. Energy **30**(Supplement 1), S106–S117 (2011)

Chapter 28
Present Status of Energy Recovery from Municipal Solid Waste

K. P. Pauley, C. J. Chow, P. Rodgers and V. Eveloy

Abstract In response to the substantial increase in Municipal Solid Waste (MSW) generation in the past few decades, along with changes in waste composition and environmental concerns, new methods of MSW recycling and disposal are actively sought. The conversion of non-recyclable waste materials into useable heat, electricity, or fuel, referred to as Waste-to-Energy (WtE), is a renewable energy source which contributes to reducing both landfill volume and carbon emissions. This paper provides an assessment of the present status of MSW generation and energy recovery. Currently available and emerging WtE conversion technologies are reviewed, in terms of their operating principles, key advantages, limitations and the challenges associated with their implementation. These barriers include economic viability, competition with mainstream forms of renewable energy as well as fossil fuels, and public perceptions. The involvement of Organization for Economic Co-operation and Development (OECD) and G20 member countries in WtE conversion utilization and development is discussed.

Keywords Waste · Energy · Renewable · Incineration · Gasification · Pyrolysis · Anaerobic digestion · Mechanical biological treatment · Landfill gas generation

28.1 Introduction

Today, much of the world strives towards the perceived ideal of the consumer society, adopting along with it, its unsustainable characteristics. One such concern is the generation of municipal solid waste (MSW). MSW, as defined by the European Union Landfill Directive [1], is *Waste from households, as well as other*

K. P. Pauley · C. J. Chow · P. Rodgers (✉) · V. Eveloy
The Petroleum Institute, Abu Dhabi, United Arab Emirates
e-mail: prodgers@pi.ac.ae

M. O. Hamdan et al. (eds.), *ICREGA'14 - Renewable Energy: Generation and Applications*, Springer Proceedings in Energy, DOI: 10.1007/978-3-319-05708-8_28,

waste which, because of its nature or composition, is similar to waste from households. As countries economically develop, there is a tendency to generate increasing quantities of MSW, raising the fundamental question of *what to do with it*. According to the European Environment Agency's 2009 report [2], which summarizes the progress achieved with the implementation of its landfill directive, concerns regarding (i) landfill capacities, (ii) the environmental impacts from methane emissions, and (iii) the pollution of groundwater, necessitate action from policymakers. A solution is the utilization of Waste to Energy (WtE) technologies that recover energy from waste. The United States Environmental Protection Agency has defined WtE as *The conversion of non-recyclable waste materials into useable heat, electricity, or fuel through a variety of processes* [3].

WtE can be regarded as a renewable energy resource, capable of contributing to reduce carbon emissions. Until recently, this renewable energy recovery has not been typically incorporated in standard renewable energy textbooks [4, 5]. However, this technology is now explored in recent publications [6–9]. In such articles, WtE may be referred to as biomass technologies that utilize feedstock of homogeneous nature. A possible reason for WtE not to be commonly classified as renewable energy or receiving insufficient attention is the fact that it currently represents a small percentage of the renewable energy mix. For example, WtE is expected to contribute only 3.6 % of the European Union's (EU-27) renewable energy production target for 2020 [10]. However, on an individual country basis, WtE can represent a significant energy source as exemplified by South Korea [11].

Typical waste management hierarchy for dealing with MSW, listed from most to least preferred, consists of (i) source reduction and reuse, (ii) recycling and/or composting, (iii) energy recovery, and (iv) treatment and disposal [12, 13]. The focus of this paper is on the energy recovery aspects of MSW management through WtE technology.

Considering energy recovery, as a rule of thumb, 10 MJ of energy can be extracted from 1 kg of MSW [14]. This figure however, is small when compared to 1 kg of fuel or carbon, which contains typically 30–42 MJ of energy. Consequently, WtE technology faces a fundamental challenge to permit its adoption due to its limited potential for energy recovery.

Historically, WtE was initially implemented in the mid-19th century in Nottingham, England, as a solution to cholera outbreaks due to MSW buildups in combination with poor hygiene and sanitation habits. A solution to such outbreaks proposed by Albert Fryer and subsequently patented in 1874, was to incinerate MSW in what came to be known as "destructors," which acted as the disposal mechanism of choice for the majority of metropolitan London up until the mid-1930s [8, 15]. By 1900, incineration facilities were also implemented elsewhere in Europe, including in Hamburg, Brussels, Stockholm, and Zurich [16]. Several original destructors generated electricity for sale; however, they were met with opposition due to the production of ash which polluted surrounding neighborhoods [17]. By 1900, many individuals had lodged health complaints associated with incineration emissions, eventually leading to the loss in popularity of incinerators

[18]. Although incineration still remains the dominant form of WtE today, other technologies have started to take hold in the market, including advanced thermal technologies (ATTs), such as pyrolysis, and non-thermal technologies, such as anaerobic digestion. These technologies are gaining market share due to both their energy utilization effectiveness and public appeal.

With the objective to provide an assessment of the present status of WtE, this paper offers an overview of existing WtE technologies, their advantages and limitations, economics, market penetration, and trends in their use and future development.

28.2 WtE Recovery Methods

WtE technologies are typically classified as either thermal or non-thermal based. Thermal WtE technologies utilize heat to drive a chemical reaction converting MSW into another form of energy such as heat or fuel. Non-thermal technologies rely on fermentation to break down MSW into gases and fuels. Figure 28.1 depicts existing WtE technologies according to this framework.

28.2.1 Thermal Technologies

As illustrated in Fig. 28.1, thermal WtE technologies are categorized under one of the following four types, namely: incineration, biomass gasification, pyrolysis and depolymerization. Advanced thermal technologies generally refer to any thermal WtE technology other than incineration.

28.2.1.1 Incineration

Incineration is the direct combustion of MSW at high temperature (>982 °C) to generate thermal energy. The resultant heat is typically used to produce steam [7, 8, 19].

There are three stages involved in the combustion of MSW: drying, ignition, and burnout. The drying stage serves to evaporate the natural moisture content of MSW, which is typically 20–25 % (mass%). Once drying is complete, solid waste is passed through a furnace where the combustible organic fraction of the MSW is incinerated. Combustion technologies can generally reduce the mass of the original waste by greater than 75 % and its volume by 85–90 % [19]. However, combustion as a process has undesirable effects, including the generation of ashes and emission of air pollutants that must be dealt with separately [7, 8].

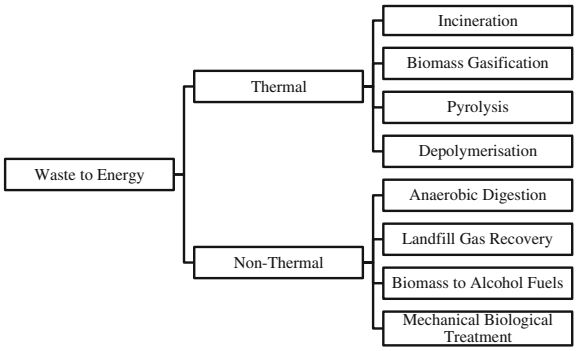

Fig. 28.1 Broad classification of existing WtE technologies

28.2.1.2 Biomass Gasification

Biomass gasification is the conversion process of solid carbonaceous fuel into combustible gas by partial combustion; part of the fuel is combusted to provide the heat needed to gasify the rest of the biomass [8, 20, 21]. The reaction for gasification of biomass is typically defined as:

$$\text{Biomass} + O_2 \rightarrow CO + H_2 + CO_2 + \text{Energy} \tag{28.1}$$

Biomass gasification takes place in four stages within a biomass gasifier unit, namely, (i) biomass drying, (ii) pyrolysis which decomposes the dry biomass into organic vapors, gases, carbon, and tars, (iii) biomass reduction, during which water vapor reacts with the carbon to produce hydrogen, carbon monoxide, and methane, and (iv) combustion, where some of the char and tars burn with oxygen to produce heat and carbon dioxide; the heat generated enables the other stages of gasification to take place [21, 22].

The result is a combustible gas, known as producer gas or syngas, which consists of hydrogen, carbon monoxide, methane, carbon dioxide, water vapor, and nitrogen which can be used in separate process equipment; for example, hydrogen can then be utilized as fuel in a fuel cell. Besides the desired combustible gases, the gasification process produces by-products such as sulfur and tar which must be removed [21].

28.2.1.3 Pyrolysis

Pyrolisis is the first step in biomass gasification processes. Organic compounds are heated in the absence of air or oxygen as an oxidant and are broken down into simpler components. As there is no oxygen, the material does not combust; rather, the chemical compounds that make up the material decompose into combustible gases and charcoal. Most of the combustible gases can be condensed into a

combustible liquid termed pyrolysis oil, though some gases remain, such as CO_2, CO, H_2, and other light hydrocarbons [8, 23, 24].

Pyrolysis of biomass produces three products: bio-oil (liquid), bio-char (solid), and syngas (gas), also known as biogas or producer gas. Bio-oil has a fuel value 50–70 % that of petroleum based fuels and can be used as boiler fuel or upgraded to transportation fuels. Bio-char can be employed as a soil amender that can sequester carbon. Syngas can be used to generate steam or electricity in power plants [8, 23, 24].

28.2.1.4 Depolymerization

Thermal organic materials are converted into fuels, fertilizers, and hydrocarbons under pressure and heat, in a process consisting of three steps. First, the MSW feedstock is pulped into a water slurry and is heated, under pressure, to the first stage reaction temperature; the MSW feedstock can consist of almost any form, such as tires, plastics, electronics, sewage sludge, and medical waste. Second, the slurry is flashed to a lower pressure with the first stage oil separated from the water. In the third and final step, the first stage oil is further heated to crack the oil into light hydrocarbon, leaving a solid product. The final products include: fuel-gas, light organic liquid comparable to diesel fuel, and carbon solids that can be used as fuel or fertilizer [25].

28.2.2 Non-thermal Technologies

Non-thermal technologies consist of anaerobic digestion, landfill gas recovery, biomass to alcohol fuels, and mechanical biological treatment (Fig. 28.1).

28.2.2.1 Anaerobic Digestion

Anaerobic digestion is a process in which organic materials are converted into biogas through microbiological reactions and manure in anaerobic conditions [9]. The reaction takes place in a heated, sealed container called a digester to promote fermentation of bacteria in an oxygen-free environment [20]. Biogas can be condensed and stored for use in combined heat and power generators or have its quality raised to the level of natural gas, while the remaining by-products of the process comprising solid organic matter can be used as compost and liquid fertilizers. Methane is the primary constituent in biogas, typically found in levels between 50 and 70 % by volume [26].

28.2.2.2 Landfill Gas Recovery

Landfill gas (LFG) is generated naturally in landfills due to the chemical degradation of MSW [27]. If left uncaptured, the methane diffuses to the environment, contributing to the greenhouse effect. Globally, landfills are the third largest anthropogenic source of methane, accounting for 799 MMT $CO_{2,eq.}$ in 2010 [28]. LFG can be collected and converted to energy via four primary methods: direct combustion in gas engines or gas furnaces, chemical energy storage for later use in applications such as vehicles, introduction into the national natural gas grid after being treated and upgraded to natural gas quality, and electric energy generation via fuel cells [9, 27].

28.2.2.3 Biomass Fermentation to Alcohol Fuels

MSW can also be converted into useful forms of energy by transforming it to alcohol fuels such as ethanol. Ethanol can be produced from the biomass content of MSW by performing hydrolysis to separate sugars such as glucose from the organic content. These sugars are subsequently fermented to produce ethanol [29].

28.2.2.4 Mechanical Biological Treatment (MBT)

Mechanical biological treatment can be considered as a combination of recycling and non-thermal technology. In the mechanical stage, waste is broken into smaller parts, and recyclables are separated from mixed waste [30]. In the biological stage, organic waste undergoes either anaerobic digestion, composting, or biodrying. Anaerobic digestion produces biogas which can be used as a fuel. Composting breaks down waste into CO_2 and compost, which is then landfilled. Biodrying produces waste that has greater potential for thermal recovery and that is lighter to dispose of in a landfill. The biodrying technology utilizes thermal energy released during aerobic decomposition, in combination with excess aeration, to dry the biomass feedstock [31].

28.3 Comparison of WtE Technologies

A comparison between the various WtE technologies is presented in order to evaluate their roles in WtE markets. Aspects of the technologies that are considered include: feedstock composition, conversion efficiency, process by-products, and maturity.

The majority of thermal technologies require pre-processed MSW as input, due to the fact that the chemistry and fluid dynamics of ATTs are sensitive to variations in the feedstock composition (i.e., molecular, humidity and ash contents,

particle size, density, and reactivity) [32]. As a result, incineration is favorable in terms of its relative simplicity, in that MSW need not be pre-processed. However, ATTs provide more flexible forms of energy output than incineration, including hot combustion exhaust gas, low/medium calorific value syngas for use in gas turbines and engines, and reformed syngas for use in fuel cells. In particular, the product of gasification, hydrogen and methane, is multi use [33]. Comparing gasification to incineration, gasification takes place at lower temperatures than incineration (550–900 vs. 850–1,200 °C [34]), though the energy content derived from incineration technologies is higher. In terms of financial aspects, the costs of an incineration operation are approximately $115,000 per ton MSW per day, whereas gasification stands at $86,000–$97,000 per ton MSW per day [35].

In terms of conversion efficiencies, incineration and gasification WtE technologies can be directly compared. When using a steam cycle, incineration technologies can have efficiencies between 18 and 24 %, whereas gasification can be between 9 and 22 %. In the event that the gasification technology is used with a gas engine generator or a combined cycle gas turbine, its efficiency can reach between 18–28 % and 23–40 %, respectively [21, 33].

Plasma gasification is a relatively new technology and therefore there is limited data on emissions, energetic performance, associated costs, and technical lifetime, though it offers the potential to recover both energy and material value from MSW. The commercial viability of plasma gasification is expected to improve, on the premise of suitable regulatory, economic and socio-political technology drivers [32].

There are also non-cost elements of thermal WtE technology which much be considered. The most appropriate technology for the application is determined by WtE client requirements. Incineration offers a mature technology having the highest conversion efficiency, while ATTs have the advantage of greater public acceptability. When combined with efficient energy recovery, however, incineration is an environmentally competitive WtE technology in comparison to present-day power generation systems using fossil fuels and even to systems based solely on renewable energy [36]. However, locally sited facilities, such as those for biomass gasification, can reduce negative effects on the environment from the long distance transportation of MSW. In terms of material considerations, the diversion of biomass waste, and the carbon footprint of the thermal WtE technology as compared to competing energy technologies, must be assessed [33].

Comparisons between thermal WtE technologies and between non-thermal WtE technologies are summarized in Tables 28.1 and 28.2, respectively. Comparisons between thermal and non-thermal technologies are summarized in Table 28.3.

28.4 Present Status

In this section the present status of MSW generation and WtE utilization is evaluated.

Table 28.1 Advantages and disadvantages of thermal WtE technologies

Technology	Advantages	Disadvantages
Incineration	Well established	Extensive flue gas cleaning required [44]
	Well defined capital costs	Disposal of ashes (approximately 25 % of input) [44]
	Predictable revenue stream	Negative public perception
	Does not require waste sorting	
Gasification	Good waste volume reduction (80–90 %) [34]	Operating and capital costs 10 % higher than incineration-based WtE [34]
	Destruction of organic contaminants such as halogenated hydrocarbons [34]	Not effective for highly heterogeneous feedstock [23]
		Formation of toxic tars [34, 65]
Pyrolysis	Good waste volume reduction (50–90 %) [66]	Not effective for highly heterogeneous feedstock [23]
	Production of solid, liquid, and gaseous fuels from waste [66]	Biomass must be dried [23]
	Self-sustaining after initial electric charge [66]	Complicated to control; troubles with slagging, tar production, and contaminants in produced gas have been documented [67]
	60–70 % weight of feedstock is converted into bio-oil [24]	
Depolymerization [25]	Feedstock can consist of any form (e.g., plastic, electronics, sewage sludge)	Not well developed, technology still at research and development stage
	Compatible with wet feedstock	

28.4.1 MSW Generation

Today, MSW is generated at a worldwide rate of approximately 1.3 billion tons annually, the majority of which is produced by countries belonging to the Organization for Economic Co-operation and Development (OECD) [37]. In the United States alone, MSW generation peaked at 256.5 million tons in 2007 [38]. However, there has been a steady decline in the number of active landfills in recent years [38], and in 2011 MSW generation per capita in the U.S. reached its lowest value since the 1980s, 2.0 kg (4.4 lbs.) per capita per day.

South Korea has quickly developed to become a leader in environmentally friendly disposal of MSW. Starting in 1997, the enforcement of household waste segregation led to an increase in the heating value of MSW and consequently shifted the country's waste management policy from non-WtE incineration to WtE-incineration. As a result, South Korea's MSW generation rate has remained stable since 1997, with the generation per unit capita decreasing slightly from 1.04 kg/day to 0.96 kg/day [11]. This is in comparison to the EU-27 and United States MSW rates which are presently 1.38 kg/day [39] and 2.0 kg/day, respectively [38]. However of greater significance is South Korea's MSW management strategy, where recycling has increased by 32 % since 1997 and now accounts for

Table 28.2 Advantages and disadvantages of non-thermal WtE technologies

Technology	Advantages	Disadvantages
Anaerobic digestion	Produces less biomass sludge compared to aerobic treatment technologies [20]	Hydrogen sulfide and ammonia are produced during the anaerobic reaction
	Production of secondary products such as compost, water, liquid fertilizer, and feedstock for further downstream processes [20]	Requires continuous supply of suitable feedstock
	Technology yields high methane content biogas with low concentrations of hydrogen sulfide	Not yet efficient enough to recover energy at a cost competitive with fossil fuel technologies [20]
Landfill gas (LFG) recovery [68]	Reduction of atmospheric methane emissions	LFG generators produce NOx
	LFG can be sold directly to end users	Requires the existence of landfills and occupation of large areas of land
	Improved air quality of surrounding communities via reduction of hazardous air pollutants (HAP)	
	Conservation of land though enhancement of decomposition in landfills	
Fermentation (biomass to alcohol fuels)	Can be used in more diverse applications, such as automobiles and gasoline blending	More commonly adapted for wet waste
Mechanical biological treatment (MBT) [69]	Can recover metals, glass plastics, and paper	Competes with recycling
		MBT recyclables are of poorer quality and have a lower market value
	More flexible than standalone WtE solutions, can change feedstock quality and increased/decreased yields	Exhaust fumes may contain pathogenic bacteria and fungi; compost-like output may be contaminated with other wastes

Table 28.3 Comparison of thermal and non-thermal WtE

Technology	Advantages	Disadvantages
Thermal	Most established WtE technology	By-products include ashes, chars, and residual toxins
	Higher net power generation potential than non-thermal technologies (by approximately 25 %) [70]	
	Thermal treatment with heat recovery is one of the most efficient ways of treating MSW [71]	
Non-thermal	Can incur significantly lower capital costs than thermal technologies	Can only process organic materials

60.5 % of the total MSW utilization. This is in contrast to the EU-27's recycling rate, 41.1 % [39] and the U.S. recycling rate, 34.1 % [40]. In addition, incineration in South Korea has increased by 14.5–21.6 %, which is the same level as the EU-27, but higher than the U.S., which has a rate of 11.7 % [40]. Consequently, through improved MSW practices, landfilling in South Korea has reduced by 46 % since 1997 to 17.9 %, in comparison to the EU-27 and U.S. rate of 37 % [39] and 54.2 %, respectively [40]. This demonstrates that when MSW management policy is coordinated at a national level, significant returns can be envisaged.

In China, rapid urbanization, industrialization, and population growth have led to a significant rise in MSW generation. From 1988 to 2006, MSW generation has risen from 31.3 to 212 million tons. This corresponds to MSW generation rates of 0.50 kg and 0.98 kg per capita per day in 1998 and 2006, respectively. Only 70 % of this MSW was collected and transported, of which 91 % was landfilled, 6.4 % was incinerated, and 2.2 % was composted. Most of the MSW has a high organic and moisture content due to domestic waste making a large portion of the waste [41].

28.4.2 WtE Utilization

Depending upon geographical location, the amount of energy which can be harnessed from MSW varies, and consequently, the potential for WtE utilization. As outlined by Piggott [14], in North America, approximately 11–13 MJ can be derived from 1 kg of MSW. In Europe, this number decreases to 8–11 MK/kg. South America and China can generate between 7–9 and 6–8 MJ/kg of MSW, respectively.

Considering the U.S., between 1910 and 1960, approximately 32 municipal waste incinerators were constructed in New York City, which combusted in total 73 million tons of MSW [42]. Currently, 86 WtE facilities exist in the U.S. which produce 2,720 MW from combustion of more than 28 million tons of MSW per year [3]. These facilities are distributed across 25 states, primarily along the Northeast. However, there has been no new WtE project construction since 1995 [42].

The MSW industry in Europe is one of the most developed, with legislation on the level of national and secondary laws [43]. There are over 500 existing WtE plants in operation [44], of which 450 plants are incinerators that, in total, burn approximately 25 % of the total European MSW [45]. Energy recovered from MSW increased by 2.6 % to 18.2 TWh from 2010 to 2011. In total, the primary energy production of MSW represented 8.2 million tons of oil equivalent (toe) in 2011, representing a 2.4 % increase from the preceding year [46]. Although landfilling is still the main MSW treatment option in Europe, several EU-27 countries are experiencing overcapacities in terms of WtE implementation; there is not sufficient MSW to feed existing WtE facilities [10]. A recent study [10] revealed that from 2008 to 2009, the number of orders for new incineration facilities and upgrades to existing plants decreased from 29 to 9. This is evidenced in the fact that the European Environment Agency reported that in the EU-27, the average annual growth rate of MSW as a source of electricity was 10 % from 1990 to 2009; however, from 2008 to 2009, there was negligible growth, which can be attributed to the fact that many WtE plants in Europe do not have sufficient feedstock to operate at full capacity [47].

Regardless of the widespread nature of incineration, there still exist many opponents to this form of WtE technology. A common platform is that MSW cannot be a renewable resource when burned, since when it is burned it cannot be re-used again [45]. This argument is supported by the widely cited study by Morris [48], in which it is claimed that recycling most materials from MSW saves on average three to five times more energy than pure incineration. On the contrary, recent studies [49] have shown that countries with the highest rates of incineration such as Denmark, Norway, and Sweden which incinerate on average greater than 50 % of their MSW tend to have high recycling and organic composting rates. For instance, Germany incinerates 37 % and recycles 45 % of MSW [45]. There is still debate over this, as Flanders, Belgium has implemented an incineration cap of 25 % of MSW as of 1990, resulting in recycling and composting rates of over 75 % [45]. Furthermore, due to high capital costs of large-scale modern incineration plants ($150–$230 million), operators require a guaranteed stream of waste over 20–30 years committing municipalities to generate a certain level of MSW [45].

Despite these facts, and EU-27 directives to achieve recycling rates of 50 % by 2020, many countries provide public subsidies for the expansion of incineration [45]. European Union countries which already import MSW are even approving and financing new WtE incineration plants. Sweden with 31 plants as of 2011, Germany with 72 plants, the Netherlands with 12 plants, and Denmark with 29 plants are all examples [45]. Figure 28.2 summarizes the use of MSW treatment methods, per capita, by each country in the EU-27.

In South Korea and China combined, there are approximately 120 WtE plants in operation [44]. Since the beginning of the 21st century, China has increased its WtE capacity from 2.2 to 14 million tons in 2007, making it the fourth largest user of WtE after Europe, Japan, and the U.S. [6]. South Korea, a country with limited

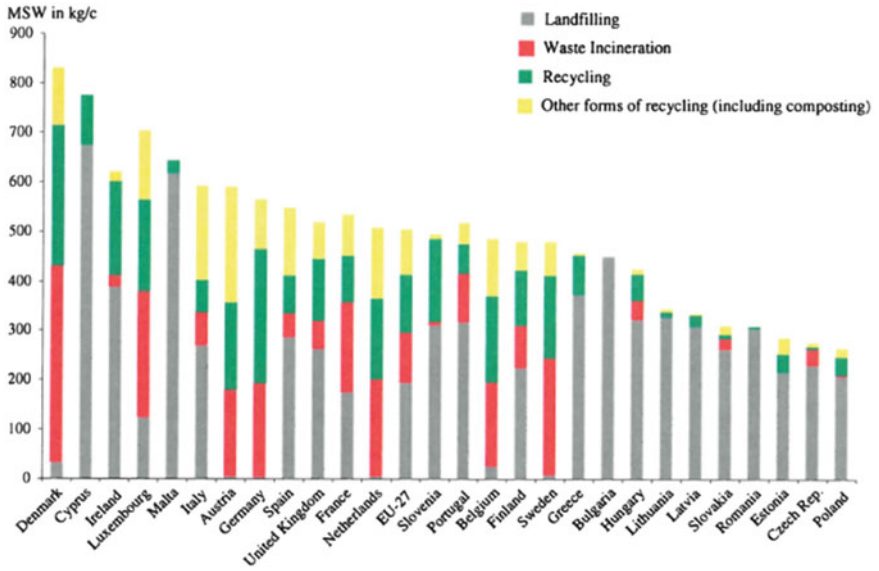

Fig. 28.2 Current MSW Treatment Per Capita in EU-27 [10]

natural resources, imports about 98 % of its energy sources from abroad. The dominant technology used in South Korean WtE plants is incineration, and heat is the dominant form of energy produced due to its high demand and the high capital costs for other forms of power generation. In 2010, WtE by incineration accounted for 11.8 % of total energy production.

South Korean WtE plants have been rapidly increasing in output [11]. In 2002, on-site heat consumption in WtE plants was 7,500 TJ, or 57 % of total heat use, and has remained fairly constant. In 2006, exported heat from WtE plants exceeded on-site consumption and continued to increase to 16,000 TJ in 2011. Over the same nine year period, electricity exported to the grid increased from 11 to 302 TJ. Overall, South Korean WtE plants have been increasing their energy export and this energy is mostly in the form of heat.

In Russia, Latin America, South Asia, and the African Continent, WtE utilization is not widespread [50–54].

28.5 WtE Economics and Challenges

In 2009, the MSW market in the EU-15 and Norway was valued at approximately $50 billion, with China valued at $35 billion, and Brazil at $3.3 billion [55].

The global market for WtE has been valued at $4.8 billion in 2006, and $7.1 billion in 2010, with a projected compound annual growth rate of 11.2 % from 2011 to 2021, growing from $8.5 billion to $27.2 billion. Of this market, and

from 2006 to 2010, 95 % of global WtE market was using incineration and anaerobic digestion technologies, however, pyrolysis, plasma gasification, and gasification are expected to comprise over 30 % of WtE market by 2015 [56].

In terms of economics, gasification systems typically have lower cost per kWh of electricity generated than combustion WtE plants due to greater efficiency [57]. This is one reason for such a shift to ATTs in the future. As a comparison of capital costs, gasification plants have capital expenses of approximately $2,200/kW, while combustion WtE plants are estimated at $3,500/kW. However, it should be noted that traditional coal-fueled power plants have significantly lower costs of approximately $1,000/kW [57], and traditional natural gas combined cycles costs of $917/kW [58].

WtE technology faces fundamental challenges to permit its adoption, one of which as mentioned previously is its limited potential for energy recovery. MSW averages at 10.5 MJ/kg of feedstock, versus coal at 24.4–30.2 MJ/kg [59]. Moreover, successful implementation requires coordination of designing, environmental permitting, contracting with municipalities, contracting with utility for sale of power, contracting with waste haulers, and obtaining investors [59]. It can take up to 5 years to begin construction, during which municipal elections can alter receptiveness of WtE initiatives [59]. The payback periods of WtE plants vary based on capital costs, operating costs, and the wholesale electricity market. Incineration-based technologies have payback periods in the range of more than 20 years while non-thermal technologies such as anaerobic digestion have payback periods ranging from 3 to 10 years [60–62]. Finally, WtE must compete on two fronts: with waste disposal options (landfills), and energy producers (selling electricity at rates competitive with traditional options such as coal and hydroelectric) [59]. WtE facilities are also less efficient than conventional fossil fuel-based electricity plants, in part due to equipment requirements such as the reduction of the maximum output steam pressure in incineration units, for the prevention of corrosion [63]. Environmental regulatory standards further mandate the addition of pollution control systems, which increase the energy demand of the system. Limits on environmental impact are restrictive when it comes to WtE technologies such as incineration, and are expected to continue to tighten in the future [43].

Tables 28.4 and 28.5 summarize the market penetration of thermal and non-thermal WtE technologies, respectively.

The overall market penetration of thermal WtE technologies represents $18.5 billion as of 2008, and is projected to reach $23.7 billion by 2014. Non-thermal WtE technologies represent significantly less, at $1.4 billion as of 2008, and are projected to reach $2.4 billion by 2014, for biological technologies [64].

Table 28.4 Adoption of thermal WtE technologies

Technology	Market penetration
Incineration	Operational capacity of 300 million tons of waste globally by 2016 [72] 450 facilities in Europe accounting for approximately 25 % of MSW [46] 12 % of MSW incinerated in U.S. [63] 250 new WtE plants (globally) to commence operations by 2016 [63]
Gasification	Approximately 100 plants worldwide [34]
Pyrolysis	45 operating plants worldwide treating between 8,000 and 225,000 tons per year of biomass, industrial waste, medical waste, and MSW [73]
Depolymerization	Low penetration; one documented operational plant using turkey offal as feedstock

Table 28.5 Adoption of non-thermal WtE technologies

Technology	Market penetration
Anaerobic digestion	106 MWe installed or under construction in the UK, as of 2012 [74]
Landfill gas (LFG) recovery	Approximately 560 projects in the USA, as of July 2011 [75]
Fermentation (biomass to alcohol fuels)	First full-scale MSW-to-Biofuels facility under construction in 2013 [76]
Mechanical biological treatment (MBT)	330 MBT plants operating in Europe, as of 2011 [77, 78]

28.6 Conclusions

WtE is a promising waste management strategy and renewable form of energy. The global WtE market is expected to reach $26.2 billion by 2014. Whereas currently, the majority of global MSW is generated in developed (i.e., OECD) countries, by 2025 most of MSW generation will shift to lower middle income countries.

At present, 95 % of the WtE market utilizes incineration and anaerobic digestion technologies. Pyrolysis, plasma gasification, and gasification technologies are expected to gain a greater share of the global WtE market by 2015. This increase will be due to developed countries implementing advanced thermal and non-thermal WtE as a result of perceived environmental benefits and opposition to incineration. By contrast, developing countries are likely to resort to the use of incineration, owing to the maturity and lower capital costs of this technology. Non-thermal technologies, such as anaerobic digestion, will continue to play a critical role in the energy recovery of organic materials, while landfill gas recovery ultimately depends upon the existence of landfills.

However, despite progress in the development of WtE technologies, important technological and socio-economical barriers need to be overcome before such technologies become a significant share of the global energy supply.

References

1. European Parliament and Council of the European Union, Directive 1999/31/EC (1999)
2. European Environment Agency, Diverting waste from landfill: effectiveness of waste management policies in the European Union, Copenhagen (2009)
3. United States Environmental Protection Agency, Energy recovery from waste (2013). http://www.epa.gov/osw/nonhaz/municipal/wte/. 30 Nov 2013
4. M. Kaltschmitt, W. Streicher, A. Wiese, *Renewable Energy: Technology, Economics and Environment* (Springer, Berlin, 2007)
5. da Rosa, *Fundamentals of Renewable Energy Processes*, 2nd Edn. (Elsevier, Oxford, 2009)
6. M. Rogoff, F. Screve, *Waste-to-Energy: Technologies and Project Implementation* (Elsevier, Oxford, 2011)
7. W. Worrell, P. Vesilind, *Solid Waste Engineering* (Cengage Learning, Stanford, 2012)
8. G. Young, *Municipal Solid Waste to Energy Conversion Processes: Economic, Technical, and Renewable Comparisons* (Wiley, Hoboken, 2010)
9. T. Christensen, *Solid Waste Technology and Management* (Wiley, West Sussex, 2011)
10. S. Malek, A. Karagiannidis, *"Waste-to-Energy in Eastern and South Eastern Europe," in Waste to Energy: Opportunities and Challenges for Developing and Transition Economies* (Springer, London, 2012), pp. 261–296
11. Ryu, D. Shin, Combined heat and power from municipal solid waste: current status and issues in South Korea. Energies **6**, 45–57 (2013)
12. United States Environmental Protection Agency, Non-hazardous waste management hierarchy (2013), http://www.epa.gov/osw/nonhaz/municipal/hierarchy.htm. 30 Nov 2013
13. H. Merrild, A. Larsen, T. Christensen, Assessing recycling versus incineration of key materials in municipal waste: the importance of efficient energy recovery and transport distances. Waste Manag. **32**, 1009–1018 (2012)
14. S. Gabr, Waste to Energy: a Global Overview of Current Status, in *4th Annual waste management ME forum,* Dubai (2013)
15. L. Herbert, *Centenary History of Waste and Waste Managers in London and South East England*. (The Chartered Institution of Wastes Management, Northampton)
16. T. Hulgaard, J. Vehlow, T. Christensen, *"Incineration: Process and Technology," in Solid Waste Technology and Management*, vol. 1 (Wiley, West Sussex, 2011), pp. 365–392
17. M. Gandy, *Recycling and the Politics of Urban Waste* (Earthscan Publications Limited, London, 1994)
18. J. Clark, *The Burning Issue: Historical Reflections on Municipal Waste Incineration*, (AHRB Research Centre for Environmental History, Universities of Stirling and St Andrews, Stirling 2003)
19. M. Rogoff, F. Screve, *"Chapter 3: WTE Technology," in Waste-to-Energy*, 2nd edn. (Andrew Publishing, Oxford, 2011), pp. 21–43
20. R. Kothari, V. Tyagi, A. Pathak, Waste-to-energy: a way from renewable energy sources to sustainable development. Renew. Sustain. Energy Rev. **14**, 3164–3170 (2010)
21. P. Basu, *Combustion and Gasification in Fluidized Beds* (CRC Press/Taylor and Francis Group, Boca Raton, 2006)
22. Fulford, A. Wheldon, Biomass gasification, Ashden (2013), http://www.ashden.org/biomass-gasification. Accessed 30 Nov 2013
23. K. Funk, J. Milford, T. Simpkins, *Waste Not, Want Not: Analyzing the Economic and Environmental Viability of Waste-to-Energy (WTE) Technology for Site-Specific Optimization of Renewable Energy Options* (Joint Institute for Strategic Energy Analysis, Golden, 2013)
24. United States Department of Agriculture, Sustainable biofuels and co-products: what is pyrolysis? (2010), http://www.ars.usda.gov/Main/docs.htm?docid=19898. Accessed 30 Nov 2013

25. T. Adams, B. Appel, *Converting Turkey Offal Into Bio-derived Hydrocarbon Oil with the CWT Thermal Process* (Changing World Technologies Inc, West Hempstead, 2004)
26. California Integrated Waste Management Board, *Current Anaerobic Digestion Technologies Used for Treatment of Municipal Organic Solid Waste* (California Environmental Protection Agency, Sacramento, 2008)
27. R. Bove, P. Lunghi, Electric power generation from landfill gas using traditional. Energy Convers. Manag. **47**, 1391–1401 (2006)
28. Global Methane Initiative, Landfill methane: reducing emissions, advancing recovery and use opportunities (2011), https://www.globalmethane.org/documents/landfill_fs_eng.pdf. Accessed 30 Nov 2013
29. M. Khraisheh, A. Li, *Bio-ethanol from Municipal Solid Waste (MSW): the Environmental Impact Assessment*, in Proceedings of the 2nd annual gas processing symposium, Doha (2010)
30. Friends of the Earth Limited, Mechanical and Biological Treatment (MBT), London (2008)
31. P.L. Velis, G. Drew, R. Smith, S. Pollard, Biodrying for mechanical-biological treatment of wastes: a review of process science and engineering. Bioresour. Technol. **100**, 2747–2761 (2009)
32. A. Bosmans, I. Vanderreydt, D. Geysen, L. Helsen, The crucial role of Waste-to-Energy technologies in enhanced landfill mining: a technology review. J. Clean. Prod. **55**, 10–23 (2013)
33. Mayor of London, *Costs of Incineration and Non-incineration Energy-from-Waste Technologies* (Greater London Authority, London, 2008)
34. U. Arena, Process and technological aspects of municipal solid waste gasification. a review. Waste Manag. **32**, 625–639 (2012)
35. H. Arafat, K. Jijakli, Modeling and comparative assessment of municipal solid waste gasification for energy production. Waste Manag. **33**, 1704–1713 (2013)
36. T. Fruergaard, T. Astrup, Optimal utilization of waste-to-energy in an LCA perspective. Waste Manag. **31**, 572–582 (2011)
37. D. Hoornweg, P. Bhada-Tata, *What a Waste: a Global Review of Solid Waste Management* (The World Bank, Washington D.C., 2012)
38. United States Environmental Protection Agency, Municipal solid waste (MSW) in the United States: facts and figures (2011), http://www.epa.gov/osw/nonhaz/municipal/pubs/MSWcharacterization_508_053113_fs.pdf. Accessed 30 Nov 2013
39. Eurostat, Eurostat (2012), http://epp.eurostat.ec.europa.eu/portal/page/portal/eurostat/home/. Accessed 2 Dec 2013
40. United States Environmental Protection Agency, *Municipal Solid Waste Generation, Recycling, and Disposal in the United States* (Office of Resouce Conservation and Recovery, Washington, D.C., 2011)
41. D. Zhang, S. Tan, R. Gersberg, Municipal solid waste management in China: status, problems and challenges. J. Environ. Manage. **91**, 1623–1633 (2010)
42. C. Psomopoulos, A. Bourka, N. Themelis, Waste-to-energy: a review of the status and benefits in USA. Waste Manag. **29**, 1718–1724 (2009)
43. A. Tabasová, J. Kropác, V. Kermes, A. Nemet, P. Stehlík, Waste-to-energy technologies: impact on environment. Energy **44**, 146–155 (2012)
44. El Rabaya, *Waste to Energy as an Alternative to Landfilling*, in 4th Annual Waste Management Middle-East Forum, Dubai (2013)
45. N. Seltenrich, Incineration versus recycling: in Europe, a debate over trash, Yale Environment 360 (2013), http://e360.yale.edu/feature/incineration_versus_recycling__in_europe_a_debate_over_trash/2686/. Accessed 30 Nov 2013
46. EurObserv'ER, Renewable municipal waste barometer. Paris (2012)
47. European Environment Agency, Renewable electricity consumption (CSI 031/ENER 030): Assessment pubished April 2012, EEA (2012), http://www.eea.europa.eu/data-and-maps/indicators/renewable-electricity-consumption/renewable-electricity-consumption-assessment-draft-3. Accessed 30 Nov 2013

48. J. Morris, Recycling versus incineration: an energy conservation analysis. J. Hazard. Mater. **47**, 277–293 (1996)
49. Eurostat News Release, Environment in the EU27 (2013), http://epp.eurostat.ec.europa.eu/cache/ITY_PUBLIC/8-04032013-BP/EN/8-04032013-BP-EN.PDF. Accessed 30 Nov 2013
50. Z. Bachiri, A. Pivovarsky, Russia: Lagging behind in waste management and recycling, European Bank for Reconstrution and Development, 22 Oct 2012
51. UN Habitat, WtE Industry in Latin America, Rio de Janeiro, Brazil (2010)
52. C. Meidiana, T. Gamse, Development of waste management practices in Indonesia. Eur. J. Sci. Res. **40**(2), 199–210 (2010)
53. Indonesia Infrastructure Initiative, *Scoping Study for Solid Waste Management in Indonesia* (SMEC Holdings, Jakarta, 2011)
54. Spintelligent (Pty) Ltd, Waste to energy in SA, ESI Africa, 14 Nov 2012
55. P. Chalmin, C. Gaillochet, *2009 World Waste Survey: from waste to resource* (Economica Editions, Paris, 2010)
56. SBI, Waste to energy markets to grow 11.2 % annually through 2021: SBI bulletin (2012), http://www.sbireports.com/about/release.asp?id=2872. Accessed 30 Nov 2013
57. A. Klein, N.J. Themelis, *Energy Recovery from Municipal Solid Wastes by Gasification*, in North American waste to energy conference 11th proceedings, Tampa (2003)
58. U.S. Energy Information Administration, *Updated Capital Cost Estimates for Utility Scale Electricity Generating Plants*. (U.S. Department of Energy, Washington, D.C., 2013)
59. M. Murphy, *Waste-to-Energy Technology, Chapter from Encyclopedia of Energy*, vol. 6. (Elsevier, Couer d'Alene, 2013)
60. M. Rodriguez, *Cost-Benefit Analysis of a Waste to Energy Plant for Montevideo; and Waste to Energy in Samll Islands* (Department of Earth and Environmental Engineering, Columbia University, New York, 2011)
61. Local Government House, Carbon reduction (2012), http://www.local.gov.uk/climate-change/-/journal_content/56/10180/3510504/ARTICLE. Accessed 27 Jan 2014
62. United States Environmental Protection Agency, The benefits of anaerobic digestion of food waste at wastewater treatment facilities (2007)
63. P. Stehlik, Contribution to advances in waste-to-energy technologies. J. Clean. Prod. **17**, 919–931 (2009)
64. BCC Research LLC, Thermal and Biological Waste-to-Energy Markets (2009), http://www.bccresearch.com/market-research/energy-and-resources/thermal-biological-waste-to-energy-egy063a.html. Accessed 30 Nov 2013
65. F.-X. Collard, J. Blin, A. Bensakhria, J. Valette, Influence of impregnated metal on the pyrolysis conversion of biomass constituents. J. Anal. Appl. Pyrol. **95**, 213–226 (2012)
66. R. Singh, V. Tyagi, T. Allen, M. Ibrahim, R. Kothari, An overview for exploring the possibilities of energy generation from municipal solid waste (MSW) in Indian scenario. Renew. Sustain. Energy Rev. **15**, 4797–4808 (2011)
67. T. Astrup, B. Bilitewski, T. Christensen, *Pyrolysis and Gasification, in Solid Waste Technology and Management*, vol. 1 (Wiley, West Sussex, 2011), pp. 502–512
68. United States Environmental Protection Agency, Landfill gas energy: a guide to developing and implementing greenhouse gas reduction programs, Washington, D.C. (2012)
69. A. Read, A. Godley, "How green is mechanical biological treatment?," waste management world (2013), http://www.waste-management-world.com/articles/print/volume-12/issue-2/features/how-green-is-mechanical-biological-treatment.html. Accessed 30 Nov 2013
70. Ministry of Urban Development, Government of India, Energy recovery from municipal solid waste, chapter 15 of solid waste management manual, New Delhi (2000)
71. M. Pavlas, M. Tous, L. Bébar, P. Stehlík, Waste to energy: an evaluation of the environmental impact. Appl. Therm. Eng. **30**, 2326–2332 (2010)
72. PRNewswire, *Waste to Energy: The World Market for Waste Incineration Plants 2012/2013* (2013), http://www.prnewswire.com/news-releases/waste-to-energy—the-world-market-for-waste-incineration-plants-20122013-210536551.html. Accessed 30 Nov 2013

73. E. Ionescu, M. Rada, C. Ragazzi, A. Marculescu, A. Badea, T. Apostol, Integrated municipal solid waste scenario model using advanced pretreatment and waste to energy processes. Energy Convers. Manag. **76**, 1083–1092 (2013)
74. D. Moore, *Green Investment Bank Publishes Market Report On Anaerobic Digestion*, Chartered Institution of Wastes Management (CIWM) (2013), http://www.ciwm-journal.co.uk/archives/1711. Accessed 30 Nov 2013
75. J. Simonsen, *Metso Denmark A/S*, in 4th annual waste management middle-east forum, Dubai (2013)
76. T. Cesarek, *Introduction to Enerkem: Waste to Fuels and Chemicals*, in 4th Annual waste management middle-east forum, Dubai (2013)
77. J. Loenicker, *Market Study MBT: the European Market for Mechanical Biological Treatment Plants (white paper)*, ecoprog GmbH, Cologne (2011)
78. PRNewswire, Market Study MBT - The European market for mechanical biological treatment plants (2013), http://www.prnewswire.com/news-releases/market-study-mbt—the-european-market-for-mechanical-biological-treatment-plants-225034422.html. 30 Nov 2013

Chapter 29
Grid Connection of Wind Energy Conversion System Using Doubly-Fed Induction Generator

Ali Haddi, Mohamed Becherif and Imane Benslama

Abstract Unlike the power plants that rely on combustion of fossil fuels such as coal or natural gas, wind power stands as the strong alternative for a clean source powered by the wind and producing no air emissions causing acid rain or gases greenhouse effect. Nevertheless, the production of wind energy is intermittent and depends strongly on the wind speed and requires the introduction of electronic controllers in order to connect such kind of source to the electrical grid. In this paper, authors are interested to the behavior of wind energy source coupled to the electrical grid: After a brief review of the modeling of the different parts of the wind energy generator. Different wind generator topologies and machines are discussed and a model of a doubly-fed induction generator connected to the grid is used for simulation purposes under Matlab-Simulink. This paper analyzes the influence of the disruptions of grid (voltage drop, phases fault) as well as the influence of the wind variations (weak and middle).

Keywords Doubly fed induction generator · Renewable energies · Wind turbine · Modeling · Grid connection · Simulation

A. Haddi (✉)
FCLAB FR CNRS 3539, FEMTO-ST UMR CNRS 6174, University of Technology , Belfort-Montbéliard, France
e-mail: haddi@ensat.ac.ma

M. Becherif
University of Technology, Belfort-Montbéliard, France
e-mail: mohamed.becherif@utbm.fr

I. Benslama
High Study Institute of Management and IT, Annaba, Algeria
e-mail: bepafides@gmail.com

M. O. Hamdan et al. (eds.), *ICREGA'14 - Renewable Energy: Generation and Applications*, Springer Proceedings in Energy, DOI: 10.1007/978-3-319-05708-8_29,

29.1 Introduction

The energy, especially the source of energy, is one of the essential elements that govern our lives and promote progress, expansion and wealth of countries. The economy of the modern world depends on the sustainable provision of energy in most cases. However, the intensive and unruly developments of the human civilization and the industrialization impacted negatively the environment and the sources of energy as well.

The new technologies will facilitate our provision of energy while preserving the natural resources and while limiting the generation of greenhouse gases.

Indeed, the potential energy of air masses movement represents, worldwide, a considerable deposit. The use of these renewable sources is facing a growing demand for energy. However, the intermittence of these sources represents a handicap that researchers try to solve. Among these energies, the wind clearly takes the pole position, not in replacement of the conventional sources, but as energy complementary.

Several countries have chosen the use of wind energy for their quality of clean renewable non-polluting energy. Indeed, China is considered as the largest consumer of energy, and become the world leader in this field in 2011; with installed wind power capacity of over 62 GW compared to the United States with more than 45 GW and 29 GW in Germany [1]. Morocco is one of those countries setting up a program that aims to achieve a total installed capacity of wind power up to 2 GW by 2020.

The principle of conversion of the kinetic energy of wind in electric energy and the description detailed of the different aero-generators are presented in several references [2–5].

- Common wind turbines are: The wind turbine working under a stationary speed, based on squirrel cage asynchronous generator directly coupled to the electrical grid (Fig. 29.1). This machine is driven via a multiplier and its speed is maintained roughly constant by a mechanical system of orientation of blades (pitch control). Its central advantage is to have the structure of the simplest rotor but with a limited possibility of power regulation.
- The wind turbine with variable speed, based on Doubly-Fed Induction Generator (DFIG) (Fig. 29.2), that increases the working speed range notably for the weak wind speeds and permits a better integration to the grid. It presents the inconveniences to require a system of rings and brooms and a multiplier, leading meaningful costs of maintenance. These inconveniences can be compensated by an overproduction due to the hyper-synchronous mode which allows increasing the global yield.

For variable speed, the wind turbine based on synchronous machines with several pairs of poles and coupled directly to the turbine that avoids the use of the multiplier (Fig. 29.3). In addition, if the generator is a permanent magnet, the system of brooms and rings is eliminated. However, this structure has a major

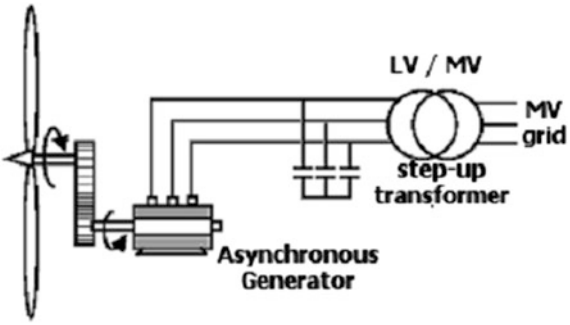

Fig. 29.1 Grid connected squirrel cage asynchronous generator

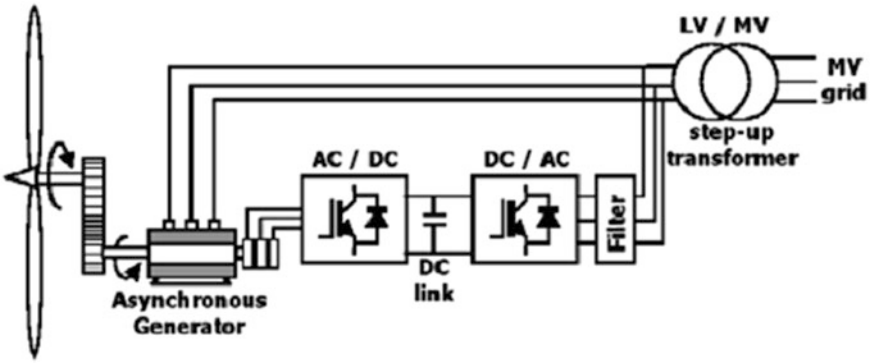

Fig. 29.2 Wind variable-speed based on DFIG

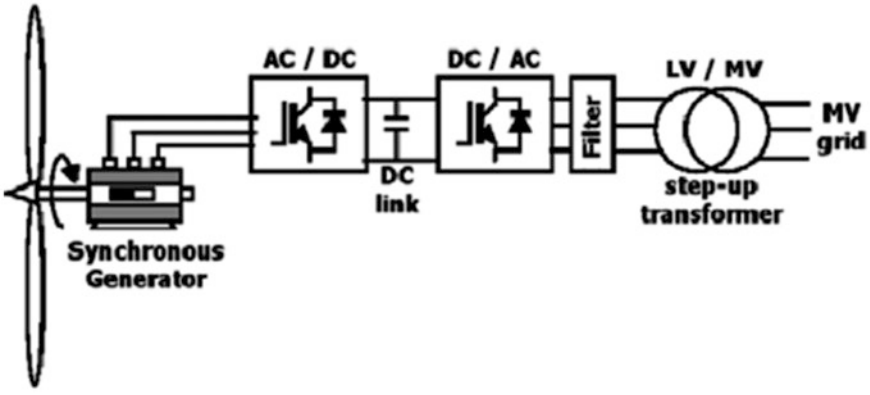

Fig. 29.3 Grid connected permanent magnets synchronous generator in full converter topology

disadvantage: It must be connected to the grid by using a power converter dimensioned on the nominal power of the generator. These generators are often used offshore, where the winds speed is substantially constant, thereby generating a frequency approaching that of the grid system.

A comparison between the wind turbine of variable speeds and a constant speed [6,7] shows that speed variation reduces mechanical stresses: Gusts of wind can be absorbed and compensated dynamically by torque and power pulsations caused by back pressure of the tower. This back pressure of the tower causes noticeable torque pulsations at a rate equal to the turbine rotor speed times and the number of rotor blades. The use of a DFIG with the rotor connected to the electric grid through an AC–AC converter offers the following advantages:

Only the electric power injected by the rotor needs to be handled by the convert [7], implying a less cost AC–AC converter;

Improved system efficiency and power factor control;

Can be implemented at lower cost, the converter has to provide only excitation energy [1].

A direct coupling of a synchronous generator to the grid is therefore not possible, and a squirrel cage induction machine is too small regarding the speed variation possibilities (<1 %), which would limit the power production only in a synchronism of the shaft speed and grid frequency. So, in this paper, the second structure based on DFIG that represents a better integration to electrical grid is studied. First, the modeling of the mechanical parts followed by a modeling of the electric parts is given. Then, simulations are performed highlighting the disruptions confronted by the production of electric energy. The disruptions that wind energy production chains undergo can come mainly from two sources, either from the electric grid or either from wind in which disruptions are usually caused by the wind variation.

This paper analyzes the influence of the disruptions of grid (voltage drop, phases fault) as well as the influence of the wind variations (weak and middle).

In this simulation, the Simulink model constituted of 9 MW wind farm consisting of six 1.5 MW wind turbines connected to a 25 kV distribution system that exports power to a 120 kV grid through a 50 km, 25 kV feeder is used, as shown in Fig. 29.4.

29.2 Modeling of the Wind Turbine

Modeling of wind turbine consists on finding models for their mechanical and electrical part.

29.2.1 Modeling of the Mechanical Part

The modeling of the mechanical part takes into account the influence of the wind on the blades of the turbine and the effect of the multiplier which adjusts the speed

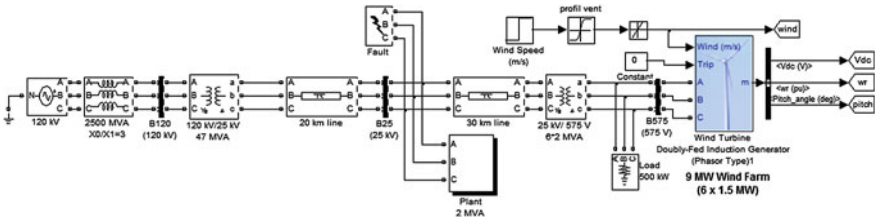

Fig. 29.4 Simulink model of DIFG connected to the grid

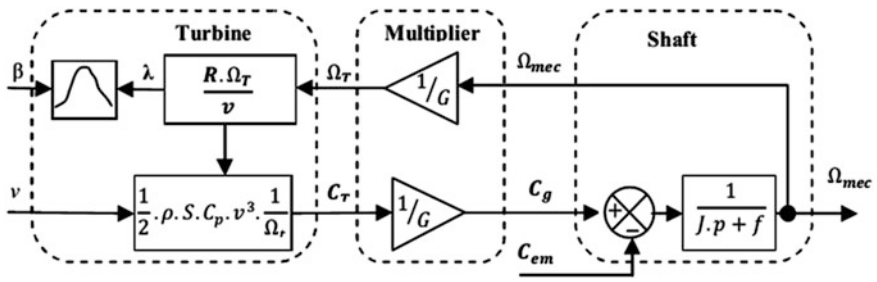

Fig. 29.5 Scheme of the wind's mechanical part

(slow) of the turbine to the generator speed. Several papers have addressed this modeling [8–10] summed up by the diagram of the Fig. 29.5.

The mechanical power that can be extracted from wind is given by means of the following expression:

$$P_t = \frac{1}{2}\rho S C_p(\lambda, \beta) v^3 \tag{29.1}$$

where ρ is the air density, S is the area swept by the turbine, v is the speed of wind and the Cp is the power coefficient that corresponds to the aerodynamic output of the turbine, which is described by the expression [3]:

$$\begin{aligned} C_p(\lambda, \beta) &= 0.5176\left(\frac{116}{\lambda_i} - 0.4\beta - 5\right)e^{\frac{21}{\lambda_i}} + 0.0068\lambda \\ \frac{1}{\lambda_i} &= \frac{1}{\lambda + 0.08\beta} - \frac{1}{\beta^3 + 1} \end{aligned} \tag{29.2}$$

With β is the pitch angle of rotor blades in degrees and λ is the tip speed ratio defined by:

$$\lambda = \frac{R_t \Omega_t}{v} v^3 \tag{29.3}$$

where R_t and Ω_t are respectively the radius and the angular speed of the turbine.

This coefficient varies according to λ and β and shows that the maximum of power cannot be gotten for stationary speed.

Knowing the speed of the turbine, the aerodynamic torque is therefore directly determined by:

$$C_t = \frac{1}{2}\rho S C_p v^3 \frac{1}{\Omega_t} \tag{29.4}$$

The multiplier adapts the turbine speed to that of the generating. This multiplier is represented by the following equations:

$$C_g = \frac{C_t}{G} \tag{29.5}$$

$$\Omega_g = \Omega_t \cdot G \tag{29.6}$$

where G is the gain of the speed multiplier.

The moment of total inertia is given by:

$$J_{Tot} = \frac{J_t}{G^2} + J_g \tag{29.7}$$

The fundamental equation of dynamics determines the evolution of the mechanical speed from the total mechanical torque (C_{mec}) applied to the rotor:

$$J_{Tot}.\frac{d\Omega_{mec}}{dt} = C_{mec} \tag{29.8}$$

29.2.2 Modeling of the Electrical Part

The electric part is essentially constituted by the (DFIG that converts mechanical energy captured by the turbine into electrical energy. The model is a vector model in a rotating frame (Park) [8–11]. Using a vector representation of the electrical quantities is the one way to get an invariant pattern in the coordinate d-q. This representation aims at permitting the manipulation of the continuous quantities rather than alternatives. So, control comes down to a regulation with constant references, instead of tracking variable trajectories. Several references clarify this modeling [8–13].

The application of Concordia transformations and Park transformations to the three phases of the DFIG permits to write the equations of the voltages and fluxes dynamics in the d-q references as follows:

$$\begin{cases} \Psi_{ds}. = L_s I_{ds} + M \cdot I_{dr} \\ \Psi_{qs}. = L_s I_{qs} + M \cdot I_{qr} \\ \Psi_{dr}. = L_r I_{dr} + M \cdot I_{ds} \\ \Psi_{qr}. = L_r I_{qr} + M \cdot I_{qs} \end{cases} \tag{29.9}$$

$$\begin{cases} V_{ds}. = R_s I_{ds} + \dfrac{d}{dt}\Psi_{ds} - \omega_s \Psi_{qs} \\ V_{qs}. = R_s I_{qs} + \dfrac{d}{dt}\Psi_{qs} + \omega_s \Psi_{ds} \\ V_{dr}. = R_r I_{dr} + \dfrac{d}{dt}\Psi_{dr} - \omega_r \Psi_{qr} \\ V_{qr}. = R_r I_{qr} + \dfrac{d}{dt}\Psi_{qr} + \omega_r \Psi_{dr} \end{cases} \tag{29.10}$$

The statoric and rotoric angular speeds are linked by the following relation:

$$\omega_s = \omega_r + \omega \tag{29.11}$$

This electric model is completed by the mechanical equation:

$$C_m = C_e + J\frac{d\Omega}{dt} + f\Omega \tag{29.12}$$

where the electromagnetic torque C_e can be expressed by the cross product of the stator fluxes and rotor currents:

$$C_e = p\frac{M}{L_s}\left(\Psi_{qs} I_{dr} - \Psi_{ds} I_{qr}\right) \tag{29.13}$$

By choosing a referential linked to the stator flux, rotor currents will be directly related to the stator active and reactive powers. Adequate control of these currents will control the power exchanged between the stator and the grid. If the stator flux is keyed on the d axis of the frame, it follows:

$$\Psi_{ds} = \Psi_s \text{ and } \Psi_{qs} = 0 \tag{29.14}$$

and the electromagnetic torque can be expressed as follows:

$$C_e = p\frac{M}{L_s}\Psi_{qs} I_{dr} \tag{29.15}$$

At the end, the model of the DFIG can be summarized by the block diagram of the Fig. 29.6.

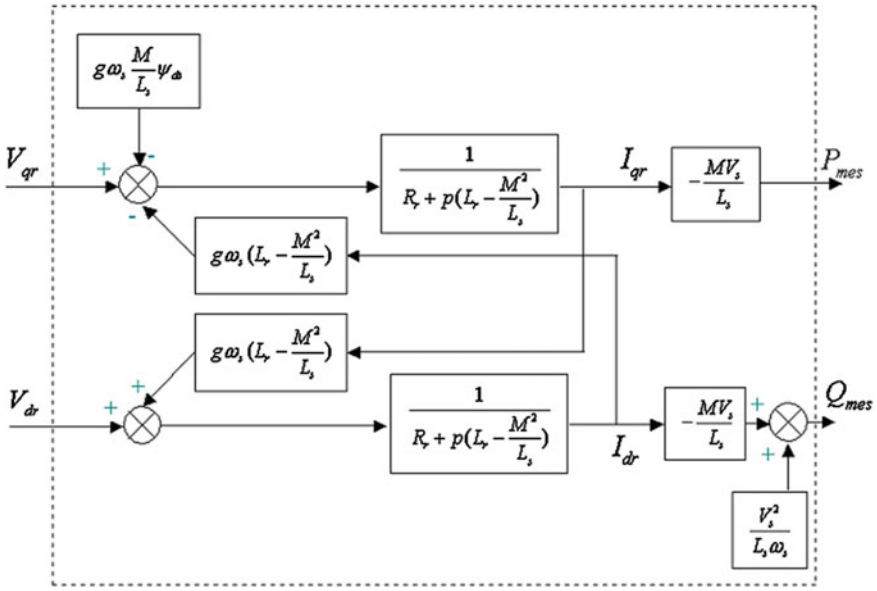

Fig. 29.6 Block diagram of DFIG's modeling

29.3 Simulation and Discussion

In this paper, the simulation takes into consideration the variation of the wind speed, as well as electrical grid defects. The first simulation highlights the influences of wind speed on the produced energy. The second shows the effects of the voltage drop as well as those arising from the grid disruptions. In the third simulation, a regulation is introduced to avoid the ominous effects of the disruptions mentioned above.

29.3.1 Simulation and Discussion for Wind's Speed Variation

The production of the wind energy is highly dependent on the wind speed. To highlight this, two levels of speeds are chosen, weak and middle (Fig. 29.7), in addition to the random variations of wind.

The simulation (Fig. 29.8) shows that the produced active power follows the level of the wind but the inertia is damping (filtering) the effect of rapid changes in the wind.

To clarify this phenomenon, a step response has been applied (Fig. 29.9). This response shows that the settling time of the active power according to wind is neighboring to 15 s, Fig. 29.9 shows the effect of filtering, and the abrupt variation

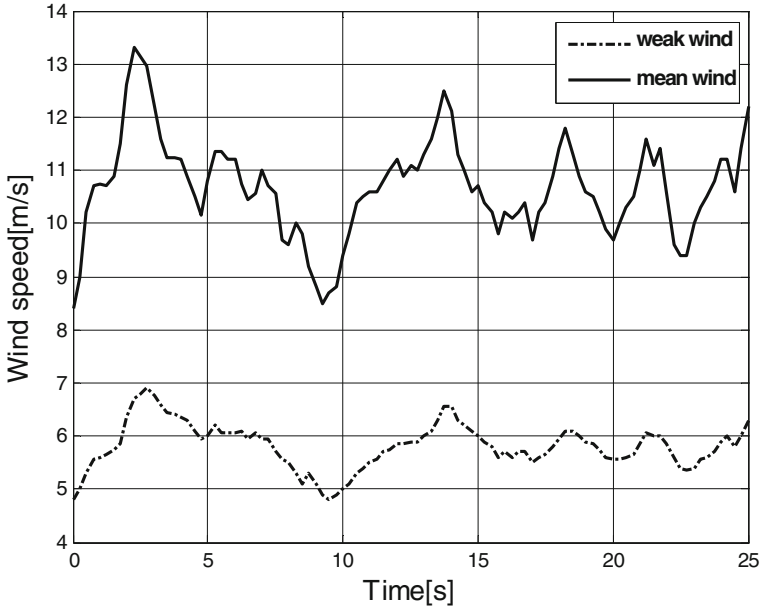

Fig. 29.7 Simulation of winds weak and middle

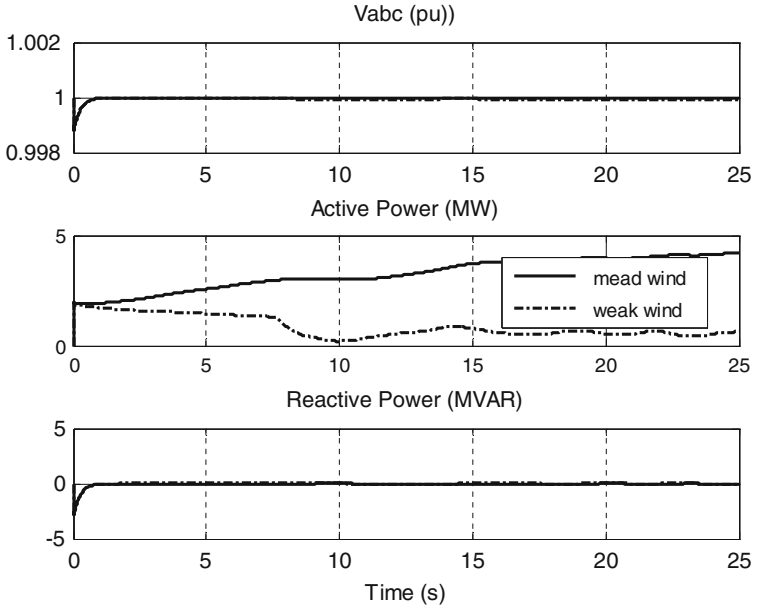

Fig. 29.8 Simulation for middle wind and weak wind

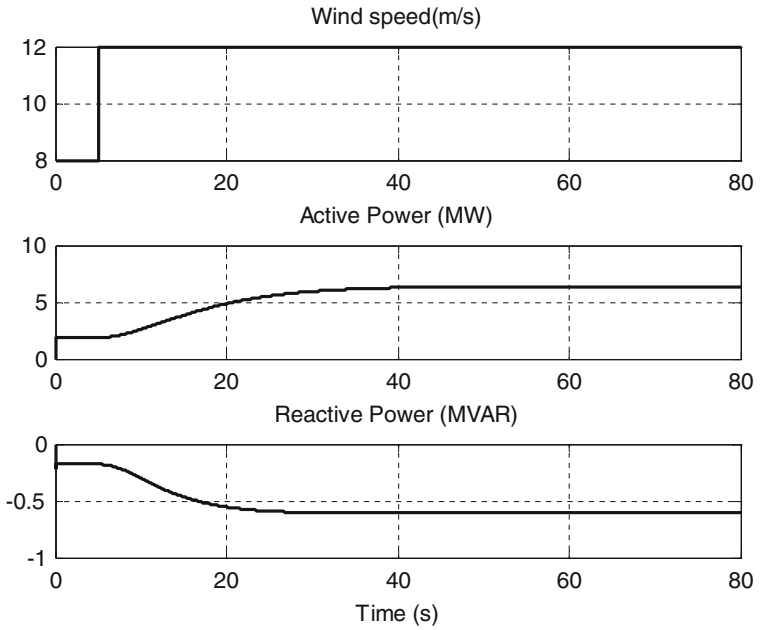

Fig. 29.9 Step response of the wind generator

of wind leads to consumption of the reactive power. This consumption weakens to proportion as the active power reaches its permanent regime.

29.3.2 Simulation and Discussion of Grid's Disruptions

The simulation of Fig. 29.10 allows us to observe the impact of a subsidence of voltages resulting from a fault on the three-phase on the 120 kV line Vabc. For a middle wind, one can notice that the active power production has not been affected by this voltage drop whereas the reactive power was greatly solicited and this generates power factor degradation. Another simulation (Fig. 29.11) permits to observe the impact of a single phase-to-ground fault occurring on the 25-kV line at B25 bus. The simulation shows that the active and reactive powers are all tributary of these defects. This prompted us to examine the effect of the regulation in order to overcome these disruptions.

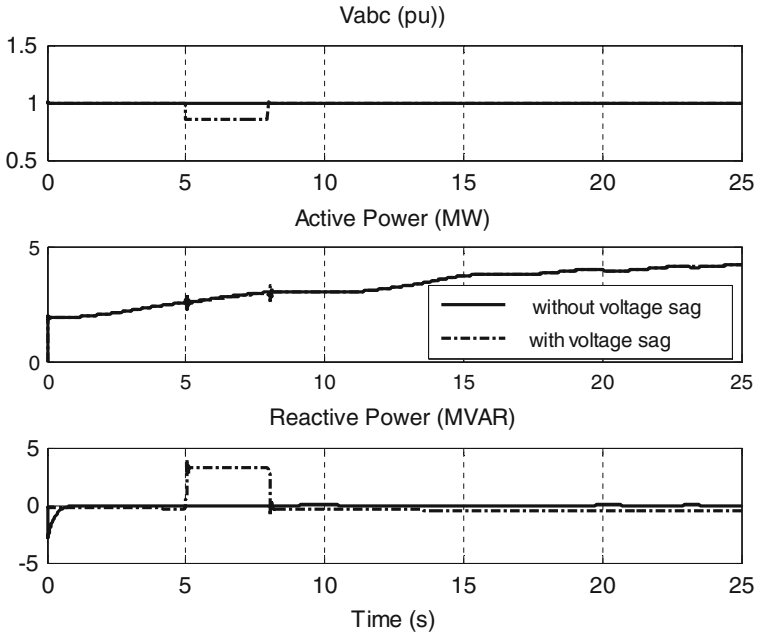

Fig. 29.10 Simulation with and without voltage drop on the 120 kV system

29.3.3 Simulation and Discussion of the Reactive Power Regulation

The disruptions of the grid induce a decrease of the power factor, which require to be lifted in order to compensate for this loss: a first idea is to introduce capacitors batteries but this solution is not efficient because the quantity of the reactive power to be compensated is variable and unpredictable. The introduction of a regulation loop proves to be primordial. A lot of researches have been done in this sense to improve system performance [13–22]. So controllers of different types (PI, controller based on sliding mode, controller based of fuzzy logic or other nonlinear control) have been studied and compared. The Fig. 29.12 shows the effect of a PI regulator type on the improvement of the performances of the studied system.

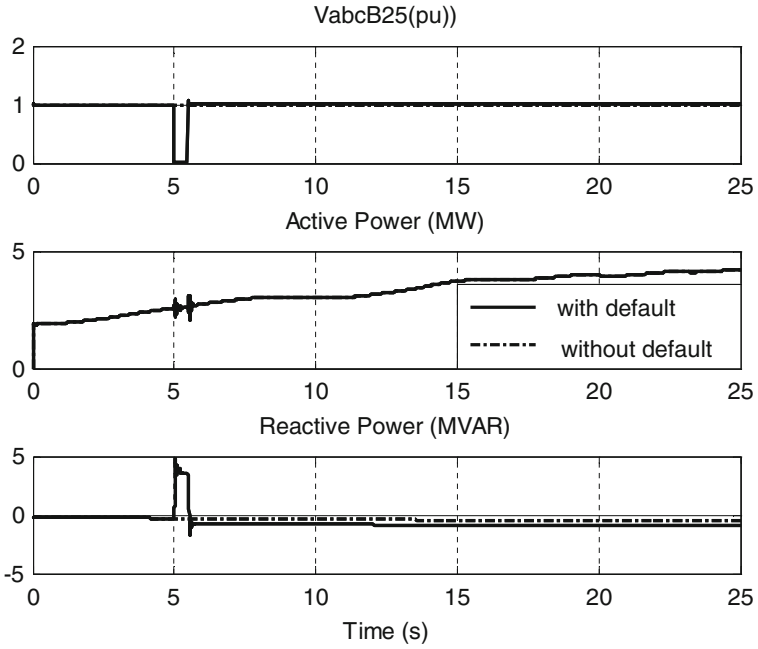

Fig. 29.11 Simulation with and flawless of phases

29.4 Conclusion and Perspectives

The global system is simulated for two levels of wind speed. The results of simulation showed the possibility to extract the maximum of power of the wind energy, to control the voltage of DC–AC converter, and to control the active and reactive powers exchanged with the grid. The wind system based on a DFIG can contribute to the compensation of reactive energy and the presence of harmonic currents on the network, without the need to oversize neither the DFIG nor the three-phase converters.

Wind turbines equipped with DFIG become more and more common during the last years. It combines the advantages of pitch control with an efficient transmission of the power to the grid and the possibility of dynamic control of active and reactive powers.

This survey has focused on the disruptions of the infinite power grid on a wind turbine. Some future studies will focus on methods for detection and compensation of shortcoming as well as the effects of the disruptions of the wind production on an electrical grid.

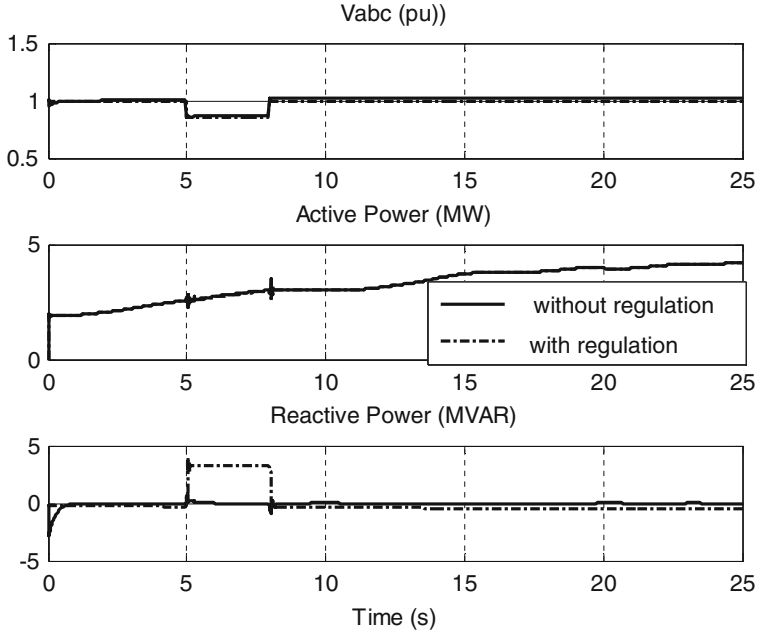

Fig. 29.12 Simulation with and without reactive power regulation

References

1. M.R. Islam, S. Mekhilef, R. Saidur, Progress and recent trends of wind energy technology. Sci Direct Renew Sustain Energy Rev **21**, 456–468 (2013)
2. J. Breckling (ed.), in *The Analysis of Directional Time Series: Applications to Wind Speed and Direction*, ser. Lecture Notes in Statistics, vol. 61. (Springer, Berlin, 1989)
3. B. Multon, X. Roboam, B. Dakyo, C. Nichita, O. Gergaud, H. Ben Ahmed, Aérogénérateurs électriques. Techniques de l'ingénieur, D3960 (2004)
4. I. Gartin, A. Munduate, S. Alepuz, J. Bordonau, Low and medium voltage wind energy conversion systems: generator overview and grid connection requirements, in *19th International Conference on Electricity Distribution*, Vienna, 21–24 May 2007
5. Y. Bekakra, D. Ben attous, in *Active and Reactive Power Control of a DFIG with MPPT for Variable Speed Wind Energy Conversion Using Sliding Mode Control*, vol. 60. (World Academy of Science, Engineering and Technology, 2011), pp. 1543–1549
6. V. Thapar, S.M. Muyeen, Ahmed Al-Durra, J. Tamura, Variable speed wind turbine generator system with current controlled voltage source inverter. Sci. Direct Energy Convers. Manage. **52**, 2688–2694 (2011)
7. J. Hu, Y. He, Modeling and control of grid-connected voltage-sourced converters under generalized unbalanced operation conditions. IEEE Trans. Energy Convers. **23**(3), 903–913 (2008)
8. A.H.M.A. Rahim, I.O. Habiballah, DFIG rotor voltage control for system dynamic performance enhancement. Sci. Direct Electr Power Syst Res **81**, 503–509 (2011)
9. M. Becherif, A. Henni, M.E.H. Benbouzid, M. Wack, Impedance spectroscopy failure diagnosis of a DFIG-based wind turbine, in *International Conference on Industrial*

Electronics, IEEE-IECON12, pp: 4290–4295, Montréal, Canada (2012). doi:978-1-4673-2420-5/12
10. B. Babypriya, R. Anita, Modeling, simulation and analysis of doubly fed generator for wind turbines. J Electr Eng **60**(2), 79–85 (2009)
11. S. Li, T.A. Haskew, J. Jackson, Integrated power characteristic study of DFIG and its frequency converter in wind power generation. Sci. Direct Renew. Energy **35**, 42–51 (2010)
12. F. Poitiers, T. Bouaouiche, M. Machmoum, Advanced control of a doubly-fed induction generator for wind energy conversion. Sci. Direct Electr. Power Syst. Res. **79**, 1085–1096 (2009)
13. L. Fan, H. Yin, Z. Miao, A novel control scheme for DFIG-based wind energy systems under unbalanced grid conditions. Sci. Direct Electr. Power Syst. Res. **81**, 254–262 (2011)
14. A.H.M.A. Rahim, I.O. Habiballah, DFIG rotor voltage control for system dynamic performance enhancement. Sci. Direct Electr. Power Syst. Res. **81**, 503–509 (2011)
15. J. Hu, Y. He, L. Xu, Improved rotor current control of wind turbine driven doubly-fed induction generators during network voltage unbalance. Sci. Direct Electr. Power Syst. Res. **80**, 847–856 (2010)
16. A.M. Kassem, K.M. Hasaneen, A.M. Yousef, Dynamic modeling and robust power control of DFIG driven by wind turbine at infinite grid. Electr. Power Energy Syst. **44**, 375–382 (2013)
17. M. Mohseni, M.A.S. Masoum, S.M. Islam, Low and high voltage ride-through of DFIG wind turbines using hybrid current controlled converters. Sci. Direct Electr. Power Syst. Res. **81**, 1456–1465 (2011)
18. B. Boukhezzar, H. Siguerdidjane, Nonlinear control with wind estimation of a DFIG variable speed wind turbine for power capture optimization. Sci. Direct Electr. Power Syst. Res. **50**, 885–892 (2009)
19. D. Forchetti, G. Garcia, M.I. Valla, Vector control strategy for a doubly-fed stand-alone induction generator, in *IEEE 28th Annual Conference of the Industrial Electronics Society* (2002), pp. 991–995
20. S. Abdeddaim, A. Betka, Optimal tracking and robust power control of the DFIG wind turbine. Electr. Power Energy Syst. **49**, 234–242 (2013)
21. S. Abdeddaim, A. Betka, S. Drid, M. Becherif, Implementation of MRAC controller of a DFIG based variable speed grid connected wind turbine. Elsevier Energy Convers. Manage. **79**, 281–288 (2014)
22. M. Becherif, E.H. El Bouchikhi, M. Benbouzid, On impedance spectroscopy contribution to failure diagnosis in wind turbine generators. Int. J. Energy Convers. **1**(3), 147–153 (2013)

Chapter 30
Capacitor Bank Resizing in Islanded Power Grid Fed by Induction Generator

Saliha Boutora and Hamid Bentarzi

Abstract In a power grid with distributed different resources, a capacitor bank is used for overall compensation purpose. However, when a part of this grid is islanded, the capacitor bank will be used for induction generator operation in the case of wind energy source. If a same capacitance is permanently connected, it may cause a severe over-voltage due to an abnormal phenomenon ferro-resonance when it is high. In this work, a new approach is developed for reselecting an adequate size of this capacitor for islanding grid. This approach is based on numerical technique and simulation, which leads to determine the optimal value of the required capacitance for three-phase self-excited induction generator operation as well as to identify the region of operation where the magnetizing reactance of induction generator is unsaturated and hence a ferro-resonance may be avoided. Moreover, the simulation utilizing Simulink/MATLAB may be useful for the validation of this approach. The obtained results are very encouraging.

Keywords Capacitor bank · Distributed sources · Ferro-resonance · Power quality · Genetic algorithm · Wind-turbine generator

30.1 Introduction

A modern (smart) power grid generally consists of distributed different resources such as thermal turbines, gas turbines and traditional wind turbines. The later may be equipped with induction generators that are preferred because they are inexpensive, rugged, and require very little maintenance. Unfortunately, induction generator that is self-excited requires capacitor to operate when its grid is islanded.

S. Boutora (✉) · H. Bentarzi
Signals and Systems Laboratory Lab, IGEE, UMBB University, Boumerdes, Algeria
e-mail: sisylab@yahoo.com

M. O. Hamdan et al. (eds.), *ICREGA'14 - Renewable Energy: Generation and Applications*, Springer Proceedings in Energy, DOI: 10.1007/978-3-319-05708-8_30,

Static capacitor is generally employed to achieve the required performance of a self-excited induction generator as well as power quality [1, 2]. Besides, a capacitor bank is needed for compensation in the whole power grid. However, when a grid with wind-turbine is islanded, this capacitor may drive the system into an overvoltage (ferro-resonance) if it will not be disconnected before a time limit or reduced to adequate value within definite time [3]. The peak voltage during this ferro-resonance can reach three per unit. However, if it is disconnected rapidly from the grid it may have an effect on the generator operation but if it is completely disconnected rather than reduced after a necessary time for generator excitation it may have an effect on the power quality. Both induction generators and transformers can create ferro-resonance, and it can occur with all three phases connected. According to the literatures, three conditions must be met in distributed resources (DR) islanded grid for ferro-resonance occurrence [3]:

- The island driven by the induction generator must be isolated from the power system,
- The induction generator must supply more power than the connected load in the island,
- The isolated circuit must have enough capacitance to resonate (3–4 times of the induction generator rating). This can be due to power system capacitor banks required by the utility first and by induction generator operation after islanding.

Ferro-resonance is a non-linear resonance phenomenon that can affect on power networks. It typically involves the saturable magnetizing inductance and a capacitive distribution, capacitor bank or transmission line capacitance [4]. Its occurrence is more likely in the absence of adequate damping devices. The term "Ferro-resonance", which appeared in the literature for the first time in 1920, refers to all oscillating phenomena occurring in an electric circuit which must contain at least: a non-linear inductance ferromagnetic, saturable capacitor and a voltage source. Practical solutions to avoid ferro-resonance are mentioned in previous publications [4].

Literature survey reveals that a few papers has been published that studied effects of capacitor bank on the distributed resources islanded grid characteristics [5, 6]. In this work, a new approach has been developed for selecting an adequate size of this capacitor using Genetic algorithm (GA). GAs are a part of evolutionary computing, which is a rapidly growing area of artificial intelligence. They are inspired by Darwin's theory about evolution i.e. solution to a problem solved by genetic algorithms is evolved Genetic Algorithms were invented by John Holland in 1975 (appendix) [7, 8].

The genetic algorithm is an iterative optimization process that imitates the adaptation and evolution of a single species of organism. Using a chromosomal mapping system, the GA starts with a large number of potential design configurations. The range of possible configurations is determined by the constraints of the problem and the method of encoding all configuration information into the chromosome [9].

Besides, the simulation utilizing Simulink/MATLAB may be useful for the validation of the obtained capacitor size by this approach and checking the resulting power quality as well as to define the time limit that will not cause a ferro-resonance.

30.2 Distributed Resources Island

Distributed resources are distributed generation and distributed storage devices which are connected to the utility power scheme at the distribution level. In this case, they may supply required amounts of power to customers and to distribution utilities, due not only to improvements in DR device technology, cost, and efficiency, but also to the rapid growth of the deregulated electricity marketplace, which has spurred interest in non-standard and dispersed sources of generation to meet increasingly competitive requirements for energy, ancillary services, and other energy services. Pressures from customers are increasing for improved power quality, including power availability and backup sources of energy. In some deregulated regions, customers are also looking for relief from high prices during peak load conditions. Many are looking to interconnect the DR to the electric power system, with the idea of selling excess energy and ancillary services as one means to offset the price of purchasing and installing these devices. As a result of these pressures, more DR devices will become interconnected with distribution power grids (this grid called smart grid) and will have an effect on the electrical power quality. Now, various simulation tools as ATP and Simuink/Matlab are used by utilities for distribution network study purposes [10]. Most of these simulation tools are used to analyze the impacts of each distributed devices on the distribution system operation and power quality. Other simulation tools determine the optimal size of electric equipment, such as capacitor banks and transformers, for efficient and reliable operation of the power system without self disturbances.

30.3 Problem Formulation and Circuit Modeling

The induction machine offers advantages for hydro and wind power plants, which may be used in DR, because of its easy operation. Induction generators can be classified according to their excitation process into:

- Grid connected induction generator,
- Self-excited induction generator.

In our research study, the former is chosen because it takes its reactive power for its excitation from the grid supply. The steady-state per-phase equivalent circuit of an induction generator, supplying a balanced load, is shown in Fig. 30.1.

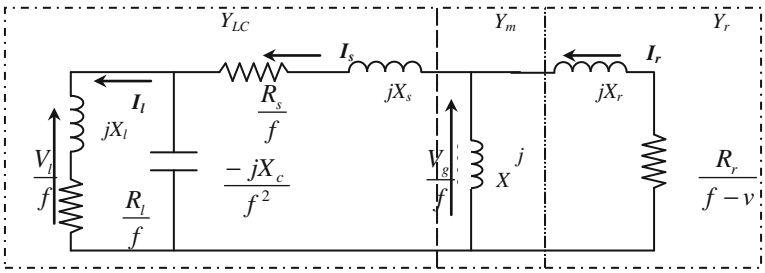

Fig. 30.1 The per-phase equivalent circuit of the IM referred to the stator

Where R_s and X_s is the resistance and reactance of the stator respectively, X_m the magnetizing reactance, R_r and X_r the resistance and reactance of the rotor respectively. In this circuit, only X_m is assumed to be affected by magnetic saturation, and all other parameters are assumed to be constant. In addition, core losses and the effects of the harmonics are ignored.

If impedance loop is applied to this circuit under steady state,

$$I_S Z_t = 0 \tag{30.1}$$

Since $I_s \neq 0$, it implies that,

$$Z_t = Z_s + \left(\frac{Z_L Z_c}{Z_L + Z_c}\right) + \left(\frac{Z_M Z_R}{Z_M + Z_R}\right) = 0 \tag{30.2}$$

or,

$$Real(Z_t) = 0, \tag{30.3}$$

and,

$$Img(Z_t) = 0 \tag{30.4}$$

where, $Z_s = \left(\frac{R_s}{f}\right) + jX_s$, $Z_L = \left(\frac{R_L}{f}\right) + jX_L$, $Z_C = \frac{-jX_C}{f^2}$, $Z_R = \left(\frac{R_s}{f-v}\right) + jX_r$, and $Z_M = jX_M$.

Equations (30.3) and (30.4) can be solved simultaneously for unknowns may be (f and X_m), (f and X_c), (f and Z_L) and (f and v) according to the two unknowns different forms of (30.3) and (30.4) are to be solved. These two equations can be solved by conventional methods [4] or any other modern methods such as Genetic Algorithm.

The performance characteristics of the generator could be estimated after getting the two unknowns. From the real and imaginary parts of Eq. (30.2) and these two parts can be rearranged into one of the following characterizations [6, 11]:

Characterization 1: the unknowns are f and X_m,

$$\sum_{k=0}^{3}(a_{2k}X_M + a_{2k+1})f^k = 0 \tag{30.5}$$

$$\sum_{k=0}^{4}(b_{2k}X_M + b_{2k+1})f^k = 0 \tag{30.6}$$

Characterization 2: the unknowns are f and v,

$$\sum_{k=0}^{3}(c_{2k}v + c_{2k+1})f^k = 0 \tag{30.7}$$

$$\sum_{k=0}^{4}(d_{2k}v + d_{2k+1})f^k = 0 \tag{30.8}$$

Characterization 3: the unknowns are f and X_c,

$$\sum_{k=0}^{3}(e_{2k}X_c + e_{2k+1})f^k = 0 \tag{30.9}$$

$$\sum_{k=0}^{4}(f_{2k}X_c + f_{2k+1})f^k = 0 \tag{30.10}$$

30.4 Simulation

In smart power grid, more DR devices are interconnected with distribution power grids and will have an effect on the electrical power quality. Therefore, to derive maximum benefits from DRs and avoid all possible oscillation adverse system impacts, distribution utilities will need the ability to simulate the effect of interconnected DR devices such as turbine induction generator, capacitor bank, and distribution transformer on their power systems.

In order to determine any distribution system modifications in its configuration that may be needed for avoiding some severe disturbances such as ferro-resonance. Now, various simulation tools as ATP and Simuink/Matlab are used by utilities for distribution network study purposes [6]. Most of these simulation tools are used to analyze the impacts of each distributed devices on the distribution system operation and power quality. Other simulation tools determine the optimal size of electric equipment, such as capacitor banks and transformers, for efficient and

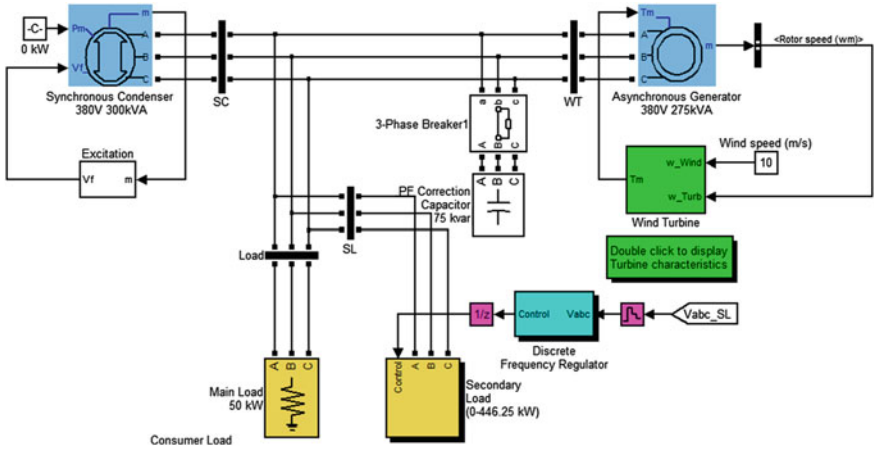

Fig. 30.2 Simulink model of DRs islanded grid including induction generator and capacitor bank

reliable operation of the power system without self disturbances. For validation of this capacitance value that has been obtained previously for a DR system, Simulink model has been developed as illustrated in Fig. 30.2.

In the present work, a real genetic algorithm is applied (see appendix), the population size N is chosen to be 1,500. The roulette wheel selection is applied followed by real coded crossover with probability of 0.82 and it is further followed by real mutation with probability of 0.06. After getting the magnetizing reactance for the given frequency; the necessary capacitance for exciting the induction generator can be obtained which is 20 μF that corresponds to 80 kVAR in this power grid.

30.4.1 Circuit Modeling

A DR system Simulink model as illustrated in Fig. 30.2 consists of 480 V, 50 Hz, 275 kVA, induction generators driven by wind turbine a fixed resistive customer load of 75 kW has been used. The presented system also uses a 480 V, 300 kVA synchronous machine and a variable secondary load (0 to 446.25 kW) the same as the HPNSWD system [6, 10]. In the all-wind mode, the synchronous machine is used as a synchronous condenser and its excitation system controls the grid voltage at its nominal value. A secondary load bank is used to regulate the system frequency by absorbing the wind power exceeding permanent consumer demand.

The three-phase delta connected capacitor bank is connected at the bus of the induction generator as compensator for the whole utility and exciter when the power grid is islanded.

The disconnection of this capacitor bank from the islanded power grid should be within time limits otherwise it may affect on the generator operation if it is short

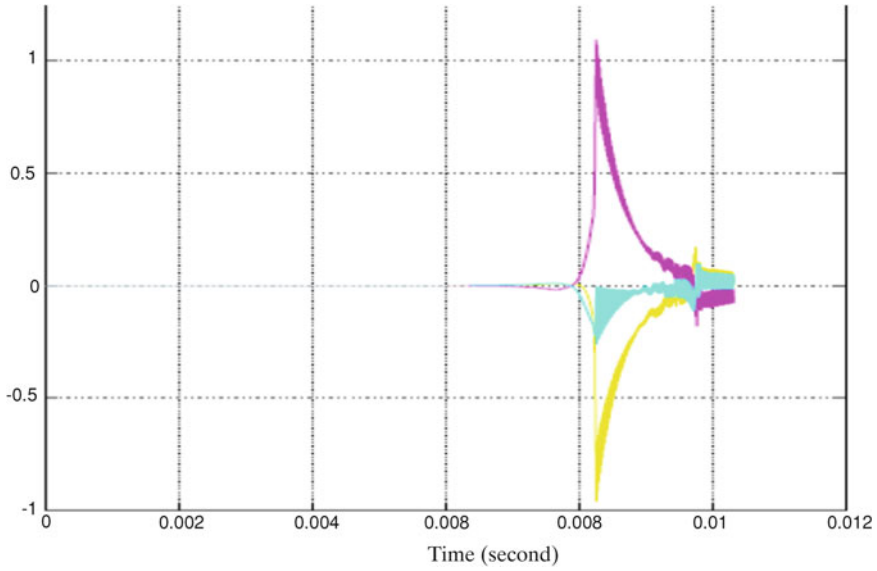

Fig. 30.3 Voltage waveform at bus (WT) for disconnection time less 1 s

and on the power grid characteristics if it is long. Besides, size of this capacitor bank may be changed to optimal value for avoiding the ferro-resonance in one hand and having better power quality in the other hand. The wind speed is kept constant at 10 m/s for this work [12, 13]. According to the turbine characteristic, for a 10 m/s wind speed, the turbine output power is 0.75 p.u. (206 kW).

Because of the asynchronous machine losses, the wind turbine produces 200 kW. Scope is used to record the p.u. values of terminal induction generator voltages.

30.4.2 Simulation Results and Discussion

The above system was simulated in using the SimPower system toolbox of Simulink/MATLAB to check the size of variable capacitive compensation if it is adequate for obtaining good voltage waveform and at the same time avoiding the severe over-voltage (ferroresonance phenomenon) and to determine the time necessary for generator operation and the size of variable capacitive compensation. The Simulink model of the DR system as shown in Fig. 30.2 is simulated with time of 5 s. We can distinguish four cases:

Case A: When the capacitor bank with value of 175 kVAR is disconnected from the power grid before 1 s as shown in Fig. 30.3, the generator will start. It can be noticed that the capacitor is needed for induction generator operation otherwise the islanded power grid collapses.

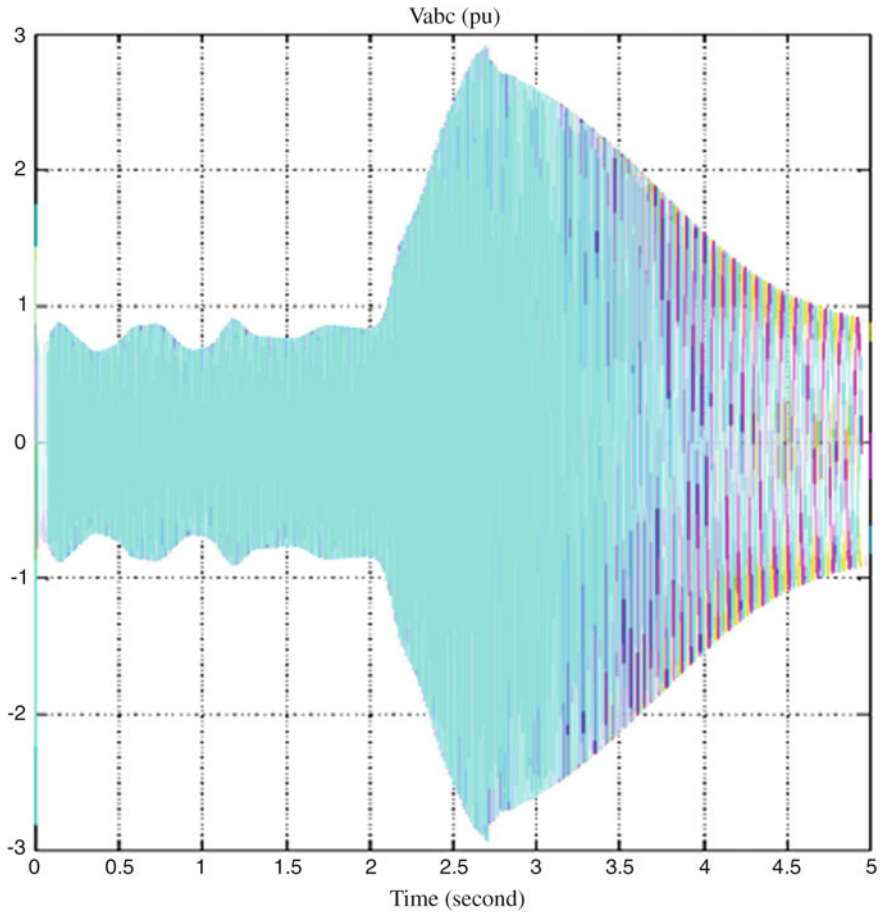

Fig. 30.4 Voltage waveform at bus (WT) within disconnection time interval from 1 to 2 s

Case B: When the capacitor bank with value of 175 kVAR is disconnected from the grid within time interval from 1 to 2 s. Figure 30.4 shows that the ferro-resonance can be avoided but with poor power quality.

Case C: When the capacitor bank with value of 175 kVAR is disconnected after 2 s as shown in Fig. 30.5. It can be noticed that ferro-resonance phenomenon appears just after the disconnection. The overvoltage occurs and its maximum magnitude can attain 3 per unit at 2.7 s. If the generator is not rapidly disconnected, the whole power system may collapse. Before the appearance of this phenomenon, it can be noticed that a variation in the voltage due to switching action.

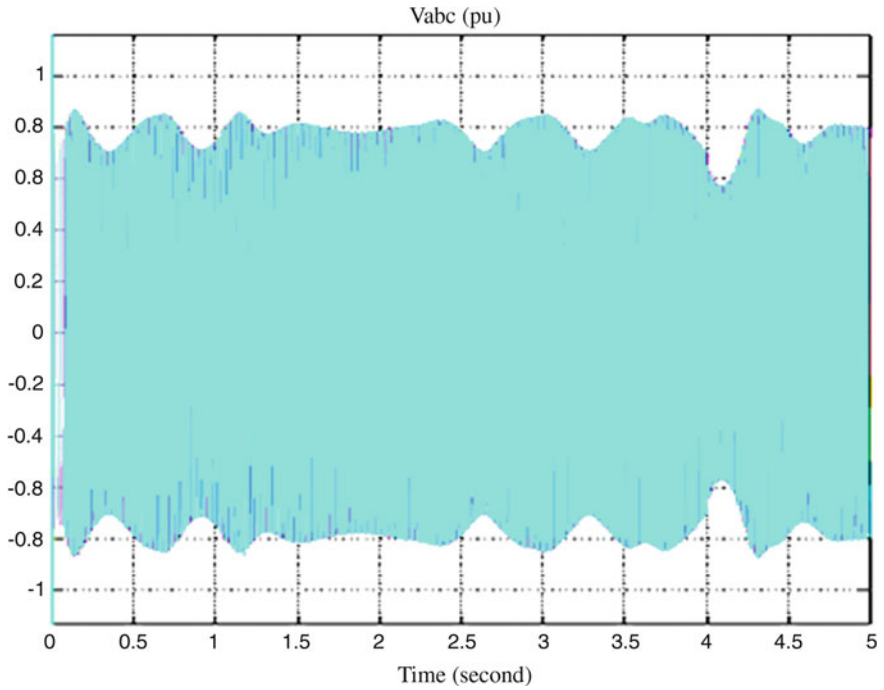

Fig. 30.5 Voltage waveform at bus (WT) with capacitor size 175 kVAR and disconnection time at 2 s

Case D: When the capacitor bank is reduced to the value 80 kVAR which is necessary for the generator operation, however, the voltage profile is poor as shown in Fig. 30.6.The magnitude voltage is varied around the value 1 p.u. with considerable voltage variations can be observed at starting.

Case E: When the capacitor bank is reduced to the value 150 kVAR where an improvement in the voltage profile is observed as shown in Fig. 30.7. After the duration of 2 s, the voltage magnitude becomes stable at value nearly 1 p.u. Some variations in the output voltage can be noticed at the starting.

It can be noticed that in the distributed resources power grid, the capacitor bank is used for compensation purpose when this grid is connected to the utility. However, when this grid is islanded, the capacitor bank may be needed for induction generator operation. But if the same capacitor value is permanently connected say in our case 175 kVAR, it may cause the ferro-resonance. However, if it is reduced to small value the profile of the voltage is poor.

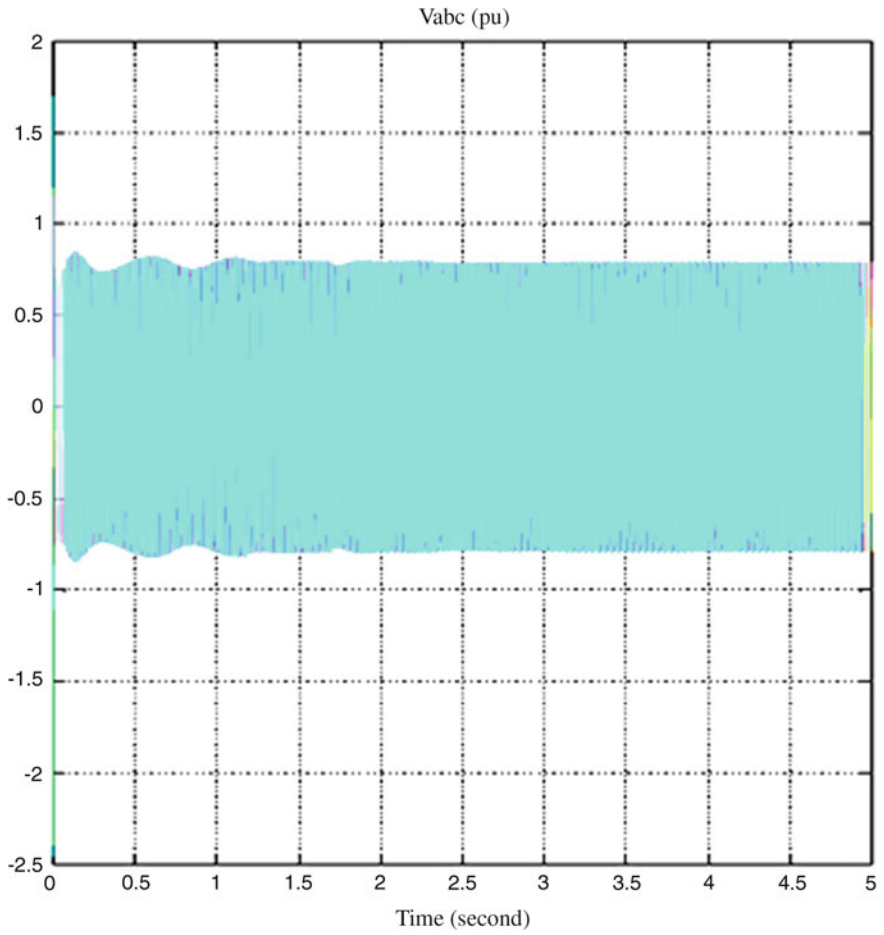

Fig. 30.6 Voltage profile at bus (WT) with capacitor size 80 kVAR

30.5 Conclusion

In this work, an approach has been investigated to use the MATLAB/SIMULINK to select the adequate three-phase capacitor bank size when the DR grid is islanded. This value should not be too big and it will cause ferroresonance if it is disconnected after the time limit (2 s in this case) and it should not be too small and it will affect on the voltage profile. Simulation results show that the importance of such resizing and disconnection time limit for a specific machine (used for simulation), capacitor with reactive power 175 kVAR causes overvoltage around 3 per unit that may be due to the ferroresonance. This may be due to the interaction of induction generator effect and the capacitor bank. The possible source of

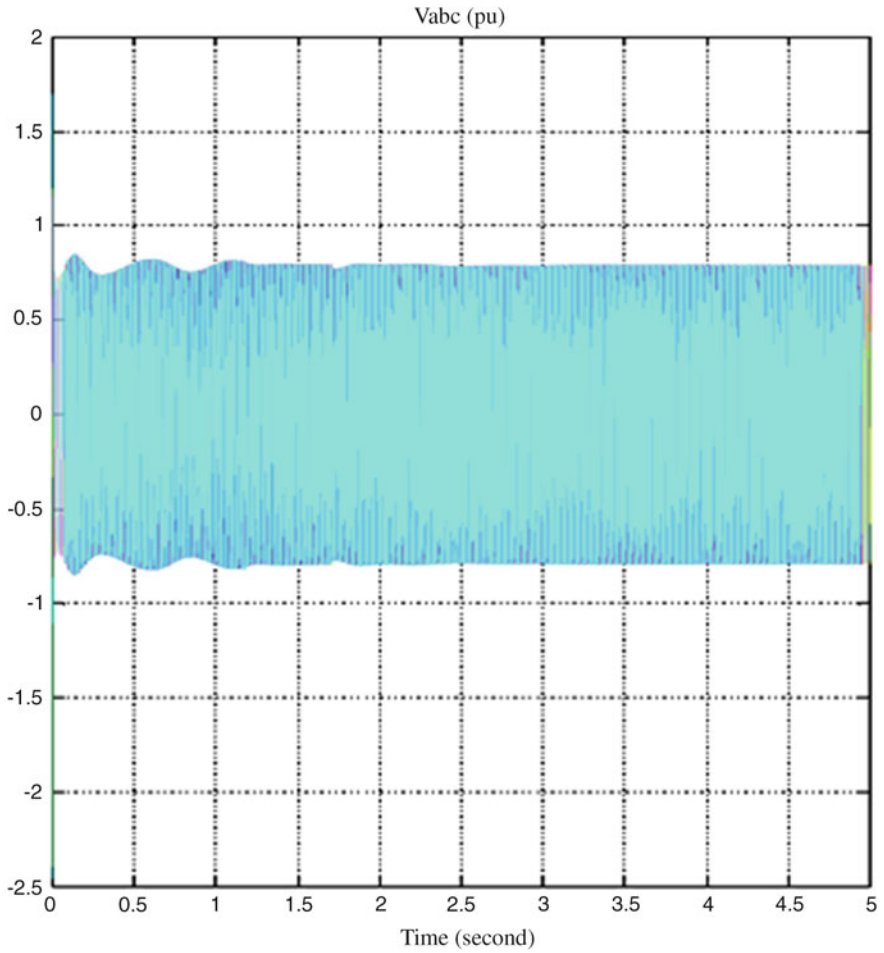

Fig. 30.7 Voltage profile at bus (WT) with capacitor size 150 kVAR

ferroresonance in this setup is due to magnetic saturation of the rotor iron core. However, it is observed that if the capacitor is reduced to reactive power of 150 kVAR gives smooth voltage profile and best results. This emphasizes the need of appropriate technique to select the optimum rating of capacitor bank that can be used for avoiding the ferroresonance in one hand and produce a good power quality in the other hand. In our study, the Genetic Algorithm has been used.

If the ferroresonance persists, it may lead to a hazard because it causes over-voltages and hence over-currents. Poorly understood, it is generally not accounted in islanded power grid studies [14]. It is rare and cannot be analyzed or predicted by the computational methods based on linear approximation normally used by electrical engineers. This lack of knowledge makes it a probable reason for the unexplained destruction and malfunctioning of equipment.

Appendix

Genetic algorithms emulate the mechanics of natural selection by a process of randomized data exchange. In this way they are able to solve of range of difficult problems which cannot be tackled by other approaches. The fact that they are able to search in a randomized, yet directed manner, allows them to reproduce some of the innovative capabilities of natural systems.

In genetic algorithms, evolution towards a global optimum occurs as a result of pressure exerted by a fitness-weighted selection process and exploration of the solution space is accomplished through combination and mutation of existing characteristics present in the current population. Other optimization techniques (such as gradient descent methods) search a region of the solution space around an initial guess for the best local solution [7, 8, 15].

The general scheme of a GA can be given as follows:

```
begin
INITIALIZE population with random candidate solutions;
EVALUATE each candidate;
repeat
    SELECT parents;
    RECOMBINE pairs of parents;
    MUTATE the resulting children;
    EVALUATE children;
    SELECT individuals for the next generation
until TERMINATION-CONDITION is satisfied
end
```

The tasks that a genetic algorithm must perform lead to the existence of three phases in the genetic algorithm optimization [9].

Initiation means filling the initial population with encoded, usually randomly created parameter strings or chromosomes.

Reproduction consists in three main operators: selection, crossover and mutation.

Selecting the Variables and the Fitness Function

A fitness function generates an output from a set of input variables (a chromosome). The fitness function may be a mathematical function, an experiment, or a game. The object is to modify the output in some desirable fashion by finding the appropriate values for the input variables. GAs is usually suitable for solving maximization problems. Minimization problems are usually transformed into maximization problems by some suitable transformation. In general, fitness function F(X) is first derived from the objective function and used in successive genetic operations.

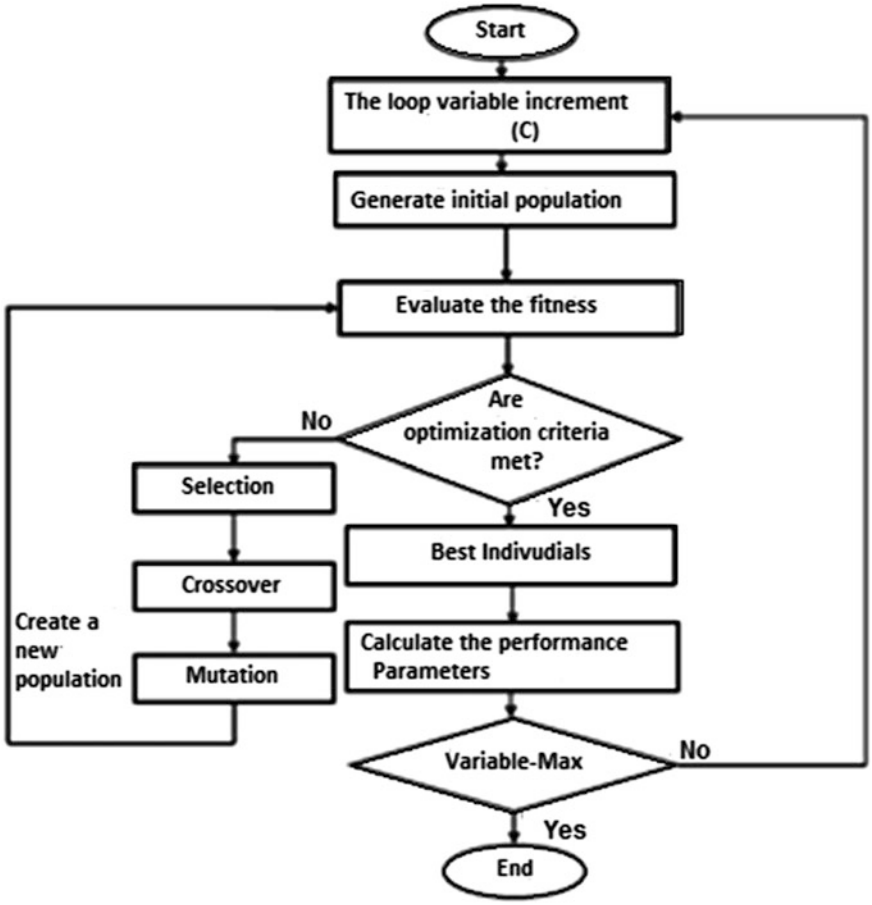

Fig. 30.A Flow chart of genetic algorithm

Certain genetic operators require that fitness function be non-negative, although certain operators do not have this requirement. Consider the following transformations: $F(X) = f(X)$ for minimizing problem. Where f(x) can be solved using Eqs. (30.9) and (30.10).

Components of Genetic Algorithm

The GA begins, like any other optimization algorithm, by defining the optimization variables, the fitness function, and the fitness. It ends like other optimization algorithms too, by testing for convergence. In between, however, this algorithm is quite different. Then, the most important components as shown in a GA flowchart (see Fig. 30.A) are:

1. Representation (definition of individuals),
2. Evaluation function (or fitness function),
3. Population,
4. Parent selection mechanism,
5. Variation operators (crossover and mutation),
6. Survivor selection mechanism (replacement).

A path through the components of the GA are shown as a flowchart in Fig. 30.A; the main operators of GA are selection, crossover and mutation.

References

1. R.C. Bansal, Three-phase self-excited induction generators: an overview. IEEE Trans. Energy Convers. **20**(2), 292–299 (2005)
2. M.A. A1-Saffar, Eui-CheolNho, T.A. Lipo, Controlled shunt capacitor self-excited induction generator, in *IEEE 0-7803-4943-1/98* (1998)
3. L.C. Wagner, W.E. Feero, W.B. Gish, R.H. Jones, Relay performance in DSG Islands. IEEE Trans. Power Deliv. **4**(1), 122–131 (1989)
4. W.B. Gish, W.E. Feero, S. Greuel, Ferroresonance and loading relationships for DSG installations. IEEE Trans. Power Deliv. **PWRD-2**(3), 953–959 (1987)
5. W. Daniel, G.S. Raquel, Instantaneous wind energy penetration in isolated electricity grids: concepts and review. Renew. Energy **30**, 1299–1308 (2005)
6. W.E. Feero, W.B. Gish, Over voltages caused by DSG operation: synchronous and induction generators. IEEE Trans. Power Deliv. **1**(1), 258–264 (1986)
7. L. Randy, *Haupt and Sue Ellen Haupt, Practical Genetic Algorithms*, 2nd edn. (Wiley, New York, 2004)
8. D.A. Coley, *An Introduction to Genetic Algorithms for Scientists and Engineers* (World Scientific, Singapore, 1999)
9. A.J. Griffiths et al., *An Introduction to Genetic Analysis* (W. H. Freeman and Company, New York, 1993)
10. B. Vahidi, A. Haghani Abandansari, Teaching ferroresonance, in *Power System to Undergraduate Students by Using MATLAB_SIMULINK*. (Wiley Periodicals Inc., 2009), pp. 1–12
11. A. Kheldou, H. Bentarzi, L. Refoufi, A new algorithm applied to the evaluation of self excited induction generator performance, in *Proceedings of the 12th WSEAS International Conference on Automatic Control, Modeling and Simulation*, Catania, Italy. ISSN: 1790-5117, ISBN: 978-954-92600-1-4, 29–31 May (Athens, Greece, 2010), pp. 82–86
12. R. Gagnon, B. Saulnier, G. Sybille, P. Giroux, Modeling of a generic high-penetration no-storage wind-diesel system using matlab/power system blockset, in *2002 Global Windpower Conference*, Paris, France, April 2002
13. B. Saulnier, A.O. Barry, B. Dube, R. Reid, Design and development of a regulation and control system for the high-penetration no-storage wind/diesel scheme, in *European Community Wind Energy Conference 88*, Herning, Denmark, 6–10 June 1988
14. G.K. Singh, Self-excited induction generator research—a survey. Electr. Power Syst. Res. **69**, 107–114 (2004)
15. A. Recioui, A. Azrar, H. Bentarzi, M. Dehmas, Synthesis of linear Arrays with Sidelobe Level Reduction Constraint Using Geneic Algorithms. Int. J. Microw. Opt. Technol. (IJMOT) **3**, 524–530 (2008)

Chapter 31
Economic Droop Parameter Selection for Autonomous Microgrids Including Wind Turbines

Morad M. A. Abdelaziz, E. F. El-Saadany and R. Seethapathy

Abstract Droop control is a key strategy for operating islanded microgrid systems. The droop settings of the different distributed generation (DG) units in an islanded microgrid determine the operational characteristics of the island. This paper presents an algorithm for choosing the optimal droop parameters for islanded microgrids with wind generation in order to minimize the overall island generation costs in the absence of a microgrid central controller (MGCC). A detailed microgrid model is adopted to reflect the special features and operational characteristics of droop-controlled islanded microgrid systems. The proposed problem formulation considers the power flow constraints, voltage and frequency regulation constraints, line capacity constraints and unit capacity constraints. Numerical case studies have been carried out to show the effectiveness of the proposed algorithm as compared to conventional droop parameter selection criteria typically adopted in the literature.

Keywords Distributed generation (DG) · Droop-control · Generation economics · Islanded microgrids · Wind generation

31.1 Introduction

The widespread implementation of the distributed generation (DG) concept is creating regions within the electrical distribution network with enough generation capacities to meet all or most of its local loads [1, 2]. Such regions are defined as microgrids. The recent IEEE Standard 1547.4 depicts the main features of a

M. M. A. Abdelaziz (✉) · E. F. El-Saadany
Electrical and Computer Engineering Department, University of Waterloo, Waterloo, ON, Canada
e-mail: m3abdelm@uwaterloo.ca

R. Seethapathy
Hydro-One Networks Inc, Toronto, ON, Canada

M. O. Hamdan et al. (eds.), *ICREGA'14 - Renewable Energy: Generation and Applications*, Springer Proceedings in Energy, DOI: 10.1007/978-3-319-05708-8_31,

microgrid system as (1) capable of operating in parallel to the main grid (i.e. grid connected mode) or autonomously in isolation from the main grid (i.e. islanded or autonomous mode) and (2) of a configuration that is intentionally planned prior to the isolation incident [3]. The islanded operation of microgrid systems can bring several benefits to the distribution utilities and to the customers. Such benefits include: (1) improving customers' reliability, (2) resolving overload problems, (3) resolving power quality issues, and (4) allowing for maintenance of system components without customers interruption. Such benefits can motivate an increased operation of microgrid systems in islanded mode. Hence the connection between a microgrid and its upper stream main grid might be arbitrary open [2]. Consequently, given the expected increase in the time span of islanded microgrid operation a thorough consideration of the islanded operational planning is mandated.

In the grid-connected microgrid mode of operation, DG units generation is controlled to supply a pre-determined amount of active and/or reactive power required for the fulfillment of a pre-specified system requirement (e.g. peak shaving, exporting power to the main grid, etc.). Any difference between the microgrid total load and the active and reactive generation by the DG units is absorbed or supplied by the main grid. Thus the frequency and voltage regulation at the different system buses can be accomplished. Accordingly, similar to conventional distribution systems, the DG units in the grid-connected microgrid system can be controlled and modelled as PV or PQ buses [3, 4]. In this case, the DG units' output voltage reference is often taken from the grid voltage sensing via a phase-locked-loop (PLL) circuit, while an inner current loop ensures that the DG unit acts as a current source fulfilling its required function. On the other hand, in islanded microgrid mode of operation, given that the main grid is not available, the generation of the DG units within the island cannot be pre-determined and must achieve real-time response to ensure that the microgrid generation is equal to its demand. Moreover, in the islanded microgrid mode of operation, the task of controlling the system voltage and frequency is shared by the DG units forming the island [5].

A power electronic converter is usually used to interface DG units to the islanded microgrid system [3–5]. The accommodation of such converters with the requirements of the islanded microgrid operation is usually achieved in the literature through one of two operational paradigms, namely Master/slave and decentralized droop control schemes. Master/slave control schemes use high bandwidth communication links to exchange dynamic power sharing signals between a master DG unit (or multiple master DG units) and the other DG units in the islanded microgrid. In most cases, such schemes are found to be costly because of the high bandwidth communication that it requires. Moreover, such schemes are unreliable as it depends on the communication links in its operation [3, 4]. On the other hand, droop control is based on using locally measured quantities to control the DG units in a way that mimic the behavior of synchronous generators operating in parallel. Droop control is capable of achieving appropriate sharing of the islanded microgrid

demand among the different DG units using only local signals and without mandating the existence of a communication infrastructure.

The settings of the different DG units' droop characteristics affect their steady-state active and reactive power generation when operating in the islanded microgrid mode of operation. The conventional approach adopted in the literature to choose the DG units' droop based on the DG units rated capacities [3, 4]. Generally, such conventional approach can provide a near exact active power sharing between DG units in proportion to their rated capacities. Nonetheless, the settings based on the rated capacity fail to satisfy other system operational constraints; where (1) it does not optimize the operation in regards to minimizing the system generation costs [6–10], (2) it cannot achieve an exact reactive power sharing between the DG units i.e., mismatches in the power line impedances lead to large circulating reactive power and (3) it can only satisfy the voltage regulation constraints at the DG units' PCC. Voltage drops along the feeders can still result in voltage constraints violation at other load points in the island.

In the literature, different methods have been proposed to optimally choose the DG units droop characteristics in a way that overcome the aforementioned drawbacks [6–10]. In [6, 7] the droop characteristics are optimized in a way that minimizes the island fuel consumption. Nonetheless, the work in [6, 7] suffered from the drawback of not considering system voltage and frequency regulation constraints as well as the network losses. In [8] a multistage optimization algorithm was presented to overcome this drawback by minimizing the islanded microgrid fuel consumption while taking into consideration the system losses and operational constraints. In [9, 10], emissions were minimized alongside the system fuel consumption. Nevertheless, the previous work in the literature to optimally choose the optimal droop characteristics assumed the existence of a microgrid central controller (MGCC) and a non-critical low bandwidth communication infrastructure [5–11]. In this scenario, a higher level central coordinated management function at the MGCC performs the required optimization of the islanded microgrid droop characteristics. By receiving periodic measurements of the island available generation and required demand, the MGCC periodically updates the DG units' droop characteristics in a manner that achieves optimal dispatch of the DG units in the system. Accordingly these techniques alleviated the need for considering the stochastic nature of the microgrid renewable generation and demand in the choice of the optimal droop characteristics by allowing for a periodic update of the droop characteristics depending on the varying generation and demand. However, for microgrids in remote areas with long connection distance between DG units the operation without a MGCC is still the viable solution [11].

Accordingly, this paper presents a new probabilistic approach to optimally choose the droop characteristics of the different DG units in an islanded microgrid in order to minimize its operational costs in the case of the unavailability of a MGCC. The proposed algorithm accounts for the special features and operational philosophy of droop-controlled islanded microgrid systems, and the stochastic nature of the system generation and loads. The remainder of this paper is organized as follows; Sect.31.2 presents the droop controlled islanded microgrid model that

reflects its special philosophy of operation. In Sect.31.3, a probabilistic load-generation model that incorporates the stochastic nature of droop-controlled islanded microgrid components is introduced. The models presented in Sects.31.2 and 31.3 are then used in formulating the proposed approach in Sect.31.4. Section31.5 presents the numerical results that verify the effectiveness of the proposed approach. Finally, Sect.31.6 concludes the paper and summarizes its findings.

31.2 Droop Controlled Islanded Microgrid Modelling

In a droop control structure, active power sharing is achieved by drooping the frequency of the output voltage of the DG unit as the active power generated by the DG unit increases. Similarly, the magnitude of the output voltage of the DG unit is drooped as the reactive power generated by the DG unit increases [4]. Accordingly, for a droop-controlled DG unit connected to the *i*th bus, the DG output voltage frequency, ω, and magnitude,$|V_i|$, can be given as follows:

$$\omega = \omega_i^* - m_{pi} \times P_{Gi} \tag{31.1}$$

$$|V_i| = |V_i|^* - n_{qi} \times Q_{Gi} \tag{31.2}$$

where ω_i^* and $|V_i|^*$are the DG unit output voltage frequency and magnitude at no-load, respectively, m_{pi} and n_{qi} are the active and reactive power static droop gains, respectively, and P_{Gi} and Q_{Gi} are the injected active and reactive power by the DG unit, respectively. Equations (31.1) and (31.2) show that droop characteristics can provide a means of negative proportional feedback that controls active and reactive power sharing in the island. The negative feedback relation in (31.1) also guarantees that all of the DG units are producing voltages with the same steady-state angular frequency [3, 4].

The representation of droop controlled islanded microgrids steady-state operation differs from that of conventional distribution system in three main points; (1) in the islanded mode, DG units' representation has to reflect its droop characteristics. Hence the DG generation cannot be pre-specified and is controlled by the DG droop characteristics. This is different from conventional distribution system were the DG units are usually represented as PQ or PV buses, (2) in the islanded microgrids the DG units forming the island are all of small and comparable sizes and there is no one DG unit that is capable of performing the slack bus function. This is different than conventional distribution system representation where the main substation is modelled as a slack bus, (3) In droop controlled islanded microgrid system, the system frequency is not constant and is considered as one of the system power flow variable [4, 5].

The set of power flow equations reflecting the aforementioned special philosophy of operation of a droop-controlled islanded microgrid can therefore be formulated as follows: for each droop bus *i*, there are two mismatch equations:

$$\frac{1}{m_{pi}}\left(\omega_i^* - \omega\right) - P_{Li} = \sum_{i}^{n_{bus}} \left(|V_i||V_k||Y_{ik}|cos(\theta_{ik} + \delta_k - \delta_i)\right) \tag{31.3}$$

$$\frac{1}{n_{qi}}(|V_i|^* - |V_i|) - Q_{Li} = -\sum_{i}^{n_{bus}} \left(|V_i||V_k||Y_{ik}|sin(\theta_{ik} + \delta_k - \delta_i)\right) \tag{31.4}$$

where n_{bus} is the number of buses in the islanded microgrid, P_{Li} and Q_{Li} are the active and reactive load power at bus i respectively; Y_{ik} and θ_{ij} are the frequency dependent Y-bus admittance magnitude and angle respectively, and δ_i is the voltage angle at bus i. The energy buffering required to enable islanded operation is achieved by the dispatchable DG units operating in droop-controlled [11, 12]. Whilst, renewable energy resources are controlled locally in the in maximum power tracking mode and are accordingly represented as PQ buses in the islanded microgrid model [11, 12]. The power mismatch equations for PQ nodes are similar to conventional power flow formulations [4]. Consequently, the number of mismatch equations that describe the power flow in islanded condition is made up of $2n_{bus}$—equations comprising the $2n_{bus}$—unknown variables to be calculated. The angle of an arbitrary bus is set to zero so that it can be taken as the system reference [4].

31.3 Probabilistic Islanded Microgrid Modelling

The intermittent nature of both the wind resources and the loads should be accounted for in a proper selection of the islanded microgrid droop settings. In this section, the analytical development of a combined generation load model is explained to describe all possible system states and their respective probabilities [13]. The probabilities of the generation states $\rho_{st}^G\{N_{st}^G\}$ are assumed to be independent of the probabilities of the load states$\rho_{st}^L\{N_{st}^L\}$. Hence, the probabilities of states $\rho_{st}\{N_{st}\}$ describing different possible combinations of generation and load states in an islanded system can be derived by convolving the respective probabilities as follows:

$$\rho_{st}\{N_{st}\} = \rho_{st}^G\{N_{st}^G\} * \rho_{st}^L\{N_{st}^L\} \tag{31.5}$$

where $\{N_{st}^G\}$ is the set of all possible generation states, $\{N_{st}^L\}$is the set of all possible load states, and $\{N_{st}\}$ is the set of all possible islanded microgrid states. Equation (31.5) shows that for an islanded microgrid the generation load model is derived by enumerating all possible combinations of generation output power states and load demand states. For wind power DG units, the generation states are calculated by segmenting the continuous probability distribution function (PDF) into several states. For instance, the generation states model of wind-based DG units is extracted by segmenting the wind speed PDF into several states with a step of 1m/s. The probability of a wind state *st* can then be calculated as follows:

$$\rho_{st}^{wind}(s) = \int_{v_{st,min}}^{v_{st,max}} f(v).dv \tag{31.6}$$

where *f(v)* is the distribution probability of wind speed, $v_{st,min}$ and $v_{st,max}$ are the wind speed limits of state "*st*".

31.4 Proposed Formulation

This section presents the proposed problem formulation for choosing the optimal droop settings in terms of minimizing the overall islanded microgrid generation costs in the cases where a MGCC is not available. The droop setting variables to be determined can be given as

$$x = \left\{ x_j | \forall j \in B_{droop} \right\} \tag{31.7}$$

where

$$x_j = \left[\omega_j^*, m_{pj}, \left| V_j^* \right|, n_{qj} \right] \tag{31.8}$$

and B_{droop} is the set of all droop-controlled buses in the system The optimal decentralized droop settings are designed for a given islanded microgrid to account for the different DG units' fuel consumption characteristics as well as the stochastic nature of the islanded microgrid generation and demand in the absence of a MGCC. These droop characteristics accommodate and account for all possible islanded microgrid states depending on their respective probability. Using the probabilistic model developed in Sect.31.3, the mathematical formulation for obtaining the optimal droop characteristics can be given as:

$$Min. \quad C_1(x) \equiv \sum_{st}^{n_{states}} \left(\sum_{j \in B_{DG}}^{n_{DG}} \left(C_j \left(P_{Gj}^{st} \right) \times \sigma_j \times P_{Gj}^{st} \times \rho_{st} \right) \right) \tag{31.9}$$

subject to:

$$F(|V_i|^{st}, \delta_i^{st}, \omega^{st}, x) = 0 \tag{31.10}$$

$$x^{lb} \leq x \leq x^{ub} \tag{31.11}$$

$$I_{ik}^{lb} \leq I_{ik}^{st} \leq I_{ik}^{ub} \tag{31.12}$$

$$|V_i|^{lb} \leq |V_i|^{st} \leq |V_i|^{ub} \tag{31.13}$$

$$\omega^{lb} \leq \omega^{st} \leq \omega^{ub} \tag{31.14}$$

$$P_{Gj}^{st} \leq S_{Gj,max} \tag{31.15}$$

$$Q_{Gj}^{st} \leq \sqrt{\left(S_{Gj,max}\right)^2 - \left(P_{Gj}^{st}\right)^2} \tag{31.16}$$

$$\forall st \in \left\{1, 2, \ldots, n_{states}\right\}, \forall j \in B_{droop} \text{ and } \forall i, k \in B$$

where B is the set of islanded microgrid buses, C_1 is the cost function to be minimized, n_{states} is the number of islanded microgrid states, B_{DG} is the set of islanded microgrid buses with DG units connected, $P_{Gj}^{st}$is the active power produced by the DG unit connected to the jth bus at microgrid state st, σ_j is the fuel price for the DG unit connected to the jth bus, ρ_{st} is the probability of microgrid state st and $C_j\left(P_{Gj}^{st}\right)$ is the fuel consumption of the DG unit connected to the jth bus at microgrid state st as a function of its active power generation.

The equality constraints in (31.10) represent the set of islanded microgrid power flow equations given by (31.1)–(31.4) for each islanded microgrid state [4]. The upper and lower bounds on the droop parameters settings given by (31.11) are determined based on the allowable voltage and frequency regulation at the DG units PCCs [11]. Equalities (31.12)–(31.14) represent the line islanded microgrid operational constraints at the different possible states in terms of the line carrying capacities, voltage constraints and frequency regulation, respectively. The constraints in (31.15) and (31.16) represent the DG capacity constraints. For an islanded microgrid operating at a given state st, the active and reactive power generation of the droop-controlled DG units follows the droop relations given in (31.1) and (31.2) up till the DG units' maximum active and reactive power generation limits, $P_{Gj,max}^{st}$ and $Q_{Gj,max}^{st}$, respectively. Beyond $P_{Gj,max}^{st}$, the active power generation of the DG units is not permitted to follow the droop relation given by (31.1), and the DG is transformed so that it injects a constant amount of active power set at the violated limit (i.e., $P_{Gj,max}^{st}$). Similarly, beyond $Q_{Gj,max}^{st}$, the reactive power generation of the DG units is not allowed to follow the droop relation given by (31.2), and the DG is transformed so that it injects a constant amount of reactive power set at the violated limit (i.e., $Q_{Gj,max}^{st}$). The relationships governing the jth droop-controlled DG unit active and reactive power generation capabilities can be given as [14]:

$$P_{Gj,max}^{st} = S_{Gj,max}^{st} \tag{31.17}$$

$$Q_{Gj,max}^{st} = \sqrt{\left(S_{Gj,max}^{st}\right)^2 - \left(P_{Gj}^{st}\right)^2} \tag{31.18}$$

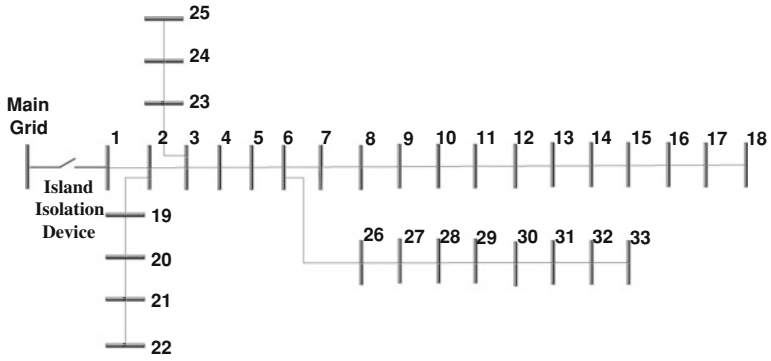

Fig.31.1 The 33-bus microgrid test system. Data about the line impedances and system loads can be found in [15]

31.5 Numerical Results

The proposed approach for optimal choice of the islanded microgrid droop characteristics, presented in Sect.31.4, is tested on a 33-bus islanded microgrid system [15]. Figure31.1 shows the single-line diagram of the test system. An islanded microgrid is formed by isolating the system from the main grid by the island isolation switch. Five dispatchable DG units and two wind-based DG units were allocated to feed the system in islanded microgrid operation mode. The ratings, locations, and fuel consumption (Natural Gas) and types of the DG units are listed in Table31.1. The proposed algorithm is solved by an interior point method implemented in Matlab environment. The upper and lower limits on the node voltage variation are taken as 1.05 and 0.95 p.u., respectively. A maximum frequency variation of 0.5% is considered in the reported case studies. For this work, the load was divided into ten states using the clustering technique developed in [16]. Table31.2 shows the set of load levels as a percentage of the peak load, and its corresponding probabilities. The wind-speed profile was estimated from the previous historical data, based on which the 12-state model developed in [13] was used, including the generated power and probabilities for each wind turbine.

Table31.3 shows the wind speed levels, and their respective probabilities for each wind turbine. The set of load states was combined with the set of wind power states for each wind turbine in order to extract the generation-load model of each islanded microgrid. Two case studies were considered as a means of evaluating the relevance of the proposed algorithm. The first case study is an examination of the operation of an islanded system with conventional droop settings. The second case study is an investigation of the operation of the system when the droop settings are optimally selected according to the proposed algorithm.

In case study #1, the static droop gains of the DG units are designed in order to share the load demand of the islanded microgrid proportionally with the rated capacity of the DG units [4]; V^* and ω^* are selected arbitrarily in order to maintain

Table31.1 DG locations, ratings, fuel consumption and control modes in the 33-bus test system (S_{BASE}=1 MVA)

DG #	Bus #	S_{Gmax} *(p.u.)*	Type	Mode	Fuel consumption (scf/KWhr)
1	02	2.00	Dispatchable	Droop	11.105
2	08	1.00	Dispatchable	Droop	7.806
3	09	1.00	Dispatchable	Droop	7.316
4	18	0.50	DFIG wind	PQ-0.95 PF Lead	–
5	22	2.00	Dispatchable	Droop	11.165
6	24	0.50	DFIG wind	PQ-0.95 PF Lead	–
7	25	1.50	Dispatchable	Droop	11.418

Table 31.2 Load states model

Percentage of peak load (%)	Probability
100	0.01
85.3	0.056
77.4	0.1057
71.3	0.1654
65	0.1654
58.5	0.163
51	0.163
45.1	0.0912
40.6	0.0473
35.1	0.033

Table31.3 Wind states model

Wind speed (m/s)	Probability
0–4	0.073
4–5	0.024
5–6	0.032
6–7	0.044
7–8	0.046
8–9	0.075
9–10	0.089
10–11	0.109
11–12	0.101
12–13	0.109
13–14	0.062
14–25	0.236

adequate power-quality levels, in terms of maintaining the frequency and voltage within their respective specified operating limits. Such conventional droop settings are capable of providing proper frequency regulation and nearly exact active power

Table31.4 Droop settings in case studies #1 and #2

DG #	Case study #1			
	V^*	w^*	m_p	n_q
1	1.03	1	2.500E-03	2.500E-02
2	1.03	1	5.000E-03	5.000E-02
3	1.03	1	5.000E-03	5.000E-02
5	1.03	1	2.500E-03	2.500E-02
7	1.03	1	3.333E-03	3.333E-02
DG #	Case Study #2			
	V^*	w^*	m_p	n_q
1	1.008	1.0004	1.125E-03	4.493E-03
2	1.011	1.0005	1.023E-03	1.873E-02
3	1.015	1.0007	1.251E-03	2.318E-02
5	1.013	1.0004	1.781E-03	1.327E-02
7	1.010	1.0004	1.703E-03	1.366E-02

Table31.5 Cost function in case studies #1 and #2

Case study #	1	2
C_1(scf/h)	16.846	15.007

sharing among DG units in islanded microgrids [4]. In case study #2, the droop characteristics of the different DG units in the island were designed using the proposed algorithm in Sect.31.4. Table31.4 gives the DG units droop characteristics in the two case studies under consideration. Here it is worth noting that Table IV only contains the dispatchable DG units; as the wind-based DG units are operated in MPPT and as such controlled as PQ generators.

Table31.5 gives the value of the cost function given by (31.9) for the two case studies. As it can it can be seen in the table, the proposed algorithm reduced the expected operation cost by around 15.8%. Figure31.2a, b show the minimum and maximum voltages that can occur at the different system buses, considering all admissible system states, when the system operates with settings from the first and second case studies, respectively. As can be seen in the figures, the voltage inequality constraint given by (31.13) in the proposed algorithm managed to keep the system voltage within the operational limits. Figure31.3 shows the frequency PDF for the two cases under study. As can be seen in the figure, the settings obtained by the proposed algorithm are capable of keeping the system frequency within its specified bounds.

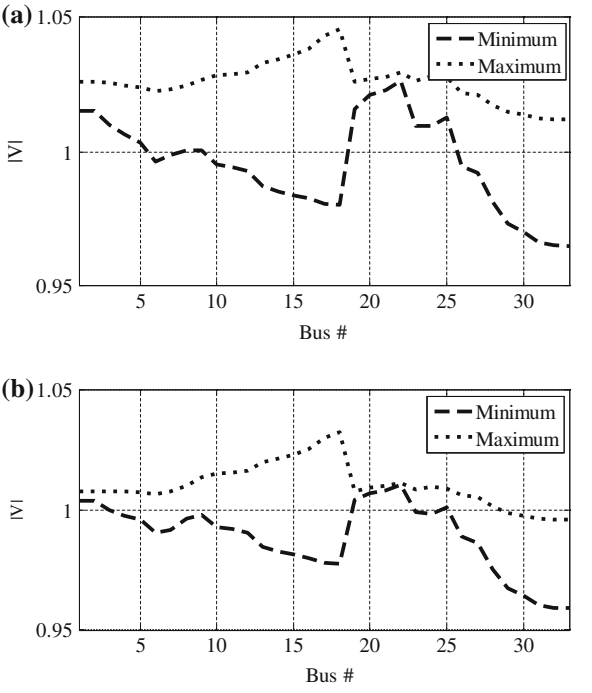

Fig.31.2 Minimum and maximum voltage magnitudes considering all possible system states: **a** case study #1, and **b** case study #2

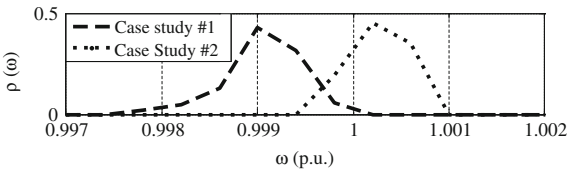

Fig.31.3 Frequency PDF with the settings from: case study #1, and case study #2

31.6 Conclusion

This paper proposes an algorithm for choosing the droop characteristics for an islanded microgrid in order to minimize its generation costs in the absence of a MGCC and in the presence wind generation. The proposed algorithm adopts a probabilistic analytical approach to account for the stochastic nature of the islanded microgrid renewable generation and load demand. Moreover, a detailed microgrid model was considered to account for the islanded microgrid special features and philosophy of operation. The proposed algorithm has been tested on a 33-bus microgrid system. The numerical results verify the importance of the proposed algorithm in determining the droop characteristics that minimize the system generation costs while ensuring the system operational constraints. The findings conclude that a proper selection of droop parameters settings can significantly reduce the system operational costs without sacrificing any of its operational requirements.

References

1. N. Pogaku, M. Prodanovic, T.C. Green, Modeling, analysis and testing of autonomous operation of an inverter-based microgrid. IEEE Trans. Power Electron. **22**(2), 613–625 (2007)
2. IEEE guide for design, operation, and integration of distributed resource island systems with electric power systems, IEEE standard 1547.4 (2011)
3. Y. Mohamed, E.F. El-Saadany, Adaptive decentralized droop controller to preserve power sharing stability of paralleled inverters in distributed generation microgrids. IEEE Trans. Power Electron. **23**(6), 2806–2816 (2008)
4. M.M. Abdelaziz, H.E. Farag, E.F. El-Saadany, Y.A.-R. Mohamed, A novel and generalized three-phase power flow algorithm for islanded microgrids using a newton trust region method. IEEE Trans. Power Syst. **28**(1), 190–201 (2013)
5. M.M. Abdelaziz, E.F. El-Saadany, Maximum loadability consideration in droop-controlled islanded microgrids optimal power flow. Electr. Power Sys. Res. **106**(C), 168–179 (2014)
6. C.A. Hernandez-Aramburo, T.C. Green, N. Mugniot, Fuel consumption minimization of a microgrid. IEEE Trans. Ind. Appl. **41**(3), 673–681 (2005)
7. E. Barklund, N. Pogaku, M. Prodanovic, C. Hernandez-Aramburo, T.C. Green, Energy management in autonomous microgrid using stability constrained droop control of inverters. IEEE Trans. Power Electron. **23**(5), 2346–2352 (2008)
8. P.H. Divshali, S.H. Hosseinian, M. Abedi, A novel multi-stage fuel cost minimization in a VSC-based microgrid considering stability, frequency, and voltage constraints. IEEE Trans. Power Syst. **28**(2), 931–939 (2013)
9. S. Conti, R. Nicolosi, S.A. Rizzo, H.H. Zeineldin, Optimal dispatching of distributed generators and storage systems for MV islanded microgrids. IEEE Trans. Power Deliv. **27**(3), 1243–1251 (2012)
10. A. Basu, A. Bhattacharya, S. Chowdhury, S.P. Chowdhury, Planned scheduling for economic power sharing in a CHP-based microgrid. IEEE Trans. Power Syst. **27**(1), 30–38 (2012)
11. M.M.A. Abdelaziz, H.E. Farag, E.F. El-Saadany, Optimum droop parameters settings of islanded microgrids with renewable energy resources. IEEE Trans. Sustain. Energy (to be published). doi: 10.1109/TSTE.2013.2293201
12. G. Daz, C. Gonzlez-Morn, C. Viescas, Operating point of islanded microgrids consisting of conventional doubly fed induction generators and distributed supporting units. IET Renew. Power Gener. **6**(5), 303–314 (2012)
13. Y.M. Atwa, E.F. El-Saadany, M.M.A. Salama, R. Seethapathy, M. Assam, S. Conti, Adequacy evaluation of distribution system including wind/solar DG during different modes of operation. IEEE Trans. Power Syst. **26**(4), 1945–1952 (2011)
14. N.R. Ullah, K. Bhattacharya, T. Thiringer, Wind farms as reactive power ancillary service providers-technical and economic issues. IEEE Trans. Energy Convers. **24**(3), 661–672 (2009)
15. M.E. Baran, F.F. Wu, Network reconfiguration in distribution systems for loss reduction and load balancing. IEEE Trans. Power Del. **4**(2), 1401–1407 (1989)
16. C. Singh, Y. Kim, An efficient technique for reliability analysis of power systems including time dependent sources. IEEE Trans. Power Syst. **4**(3), 1090–1096 (1989)

Chapter 32
Energy Management for a Grid-Tied Photovoltaic-Wind-Storage System: Part I—Forecasting Models

Ala Hussein and Issa Batarseh

Abstract Renewable energy has unique characteristics such as it is sustainable, clean and free. However, renewable generation systems have two major limitations: they are strongly dependent on the weather conditions, and they have unsynchronized generation peaks with the demand peaks, in general. In a series of two papers, an energy management strategy for a distributed photovoltaic-wind-storage system is proposed. This first paper proposes a method to predict the amount of power generated by the PV and wind power sources and the power consumed by local loads. The proposed forecasting models are developed using artificial neural networks (ANNs). Those forecasting models were verified on real data and showed good to excellent results.

Keywords Artificial neural networks (ANNs) · Distributed generation (DG) · Load forecasting model · Photovoltaic (PV) · Solar radiation forecasting model · Wind speed forecasting model

32.1 Introduction

A major limitation of renewable energy sources—beside the tremendous advantages they offer—is their strong dependence on the weather conditions. This dependence, in fact, is disastrous when exchanging power with a spot market system where the power exchange plan with the utility grid must be provided to

A. Hussein (✉)
Department of Electrical Engineering, United Arab Emirates University, Al Ain, United Arab Emirates
e-mail: ala.hussein@uaeu.ac.ae

I. Batarseh
Department of Electrical Engineering and Computer Science, University of Central Florida, Orlando, FL, USA

M. O. Hamdan et al. (eds.), *ICREGA'14 - Renewable Energy: Generation and Applications*, Springer Proceedings in Energy, DOI: 10.1007/978-3-319-05708-8_32,

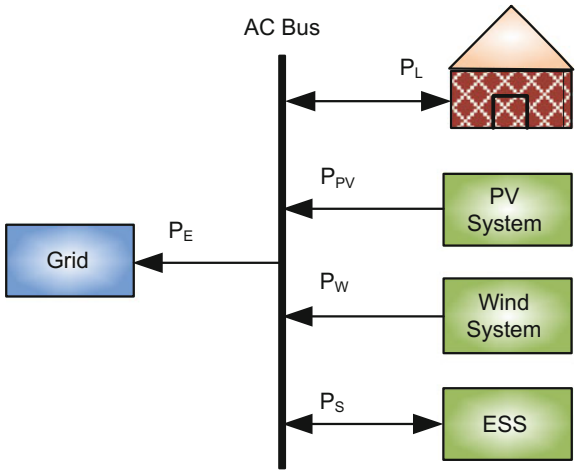

Fig. 32.1 A general distributed PV-wind-storage system. *Arrows'* directions indicate positive values of variables

the market in advance (for example, in the Nordic spot market, participants must announce their daily bids at least 12 h before the scheduling day, [1]). In a spot market system, the generated power must meet the forecasted power; otherwise, the owner of the renewable distributed generator (DG) will be penalized. With an accurate model that can predict the load (demand) and the renewable generated power (supply), those renewable DGs can be integrated in a spot market system; otherwise, those DGs will never be suitable to enter this emerging market. Figure 32.1 shows a general renewable DG system that feeds an end user (i.e. house) and exchange power with the utility grid (P_L is the load power, P_{PV} is the solar PV power, P_W is the wind power, P_S is the energy storage power, and P_E is the exchanged power with the utility grid).

The importance of developing an accurate mechanism to predict the generated or consumed power was widely reported [2–4]. However, all the reported forecasting models vary in terms of their complexity and accuracy. In this paper, three forecasting models for the load, solar radiation and wind speed are proposed using artificial neural networks (ANNs). The three models are used to determine the load demand and the solar/wind power for a given time horizon. In the second paper of this series, those models are used to optimize the operation of a PV-wind-storage system by optimizing the operation of the energy storage [5].

The organization of this paper is as follows: Sect. 32.2 presents an overview of ANNs. In Sect. 32.3, the proposed forecasting models with experimental verification are presented. Finally, conclusions are given in Sect. 32.4.

32.2 Artificial Neural Networks

Artificial neural networks (ANNs) were found to be very adequate to solve forecasting problems if they were trained well. Artificial neural networks are computational models that assemble the human brain in the way of learning and making decisions. They employ a massive interconnection of simple computing cells referred to as neurons (or processing units). The power of ANNs comes from two things; first, their massively parallel distributed structure; and second, their ability to learn and thus generalize [6]. In addition, ANNs offer some desired capabilities such as they can be used in nonlinear systems; they are adaptive; and they can be used for input-output mapping. The beauty of ANNs, in fact, is that they do not require a very accurate model for the dynamic system as Kalman filters do [7, 8]. Instead, they can be considered as a black box that produces a certain output based on the inputs it receives, which is in fact a very desired feature when dealing with complicated non-linear systems that cannot be easily modeled.

An example of a feed forward ANN is a simple two-layer network (Fig. 32.2). In this network, which consist of two visible layers (input and output) and one hidden layer and a number of neurons in the input, output and hidden layers. The weight functions $\{w_{11}, w_{12}, w_{13}, w_{21}, w_{22}$, and $w_{23}\}$ interconnect the input layer with the hidden layer, where the weight functions $\{w_1, w_2$, and $w_3\}$ interconnect the hidden layer with the output layer. This model will be used in this section to develop forecasting models for load and weather but with more inputs and neurons.

In the next section, three ANN-based models are presented. These models are developed to predict the electric load, solar radiation and wind speed. These models, however, can be adjusted and used for any time horizon (12, 24, 48-h, etc.). In general, as the forecasting time horizon increases, the uncertainty will increase.

32.3 Forecasting Models

Three ANN-based forecasting models followed by experimental verification are presented in this section.

32.3.1 Model Development

A model similar to the one shown in Fig. 32.2 was created using MATLAB Neural Network Toolbox with eight inputs and 20 neurons in the hidden layer. To test the performance of the developed model, four different 5 day periods were selected

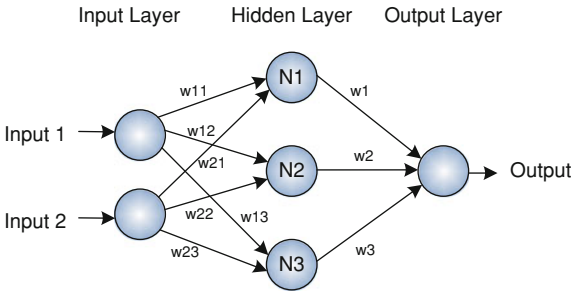

Fig. 32.2 A simple two-layer feed-forward ANN

Table 32.1 Inputs of the models

Load model	Solar model	Wind model
Day hour	Day hour	Day hour
Week day	Air temperature	Air temperature
Holiday or weekend flag (1/0 values are used)	Dew point temperature	Dew point temperature
Dew point temperature	Global solar radiation	Global solar radiation
Dry bulb temperature	Wind direction	Wind direction
Previous day average load	Wind run	Wind run
Same-hour previous-day load	Wind peak gust	Wind peak gust
Same-hour same-day previous-week load	Relative humidity	Relative humidity
	Precipitation	Precipitation
	Solar radiation of same hour previous day	Wind speed of same hour previous day
	Solar radiation of same hour same day previous week	Wind speed of same hour same day previous week

and the actual output versus the predicted output was plotted. The data that was collected to train the models, [9, 10] is summarized in Table 32.1.

32.3.2 Experimental Verification

The results of the developed models are shown in Figs. 32.3, 32.4, 32.5 and 32.6. The correlation between the actual output and predicted output for a day-ahead forecast horizon were plotted in Fig. 32.7.

The root mean square error (RMSE) for the three models for different forecast (time) horizons are shown in Tables 32.2, 32.3 and 32.4 (1 Langely per hour = 11.63 Watt/square meter = 1 Cal/cm^2).

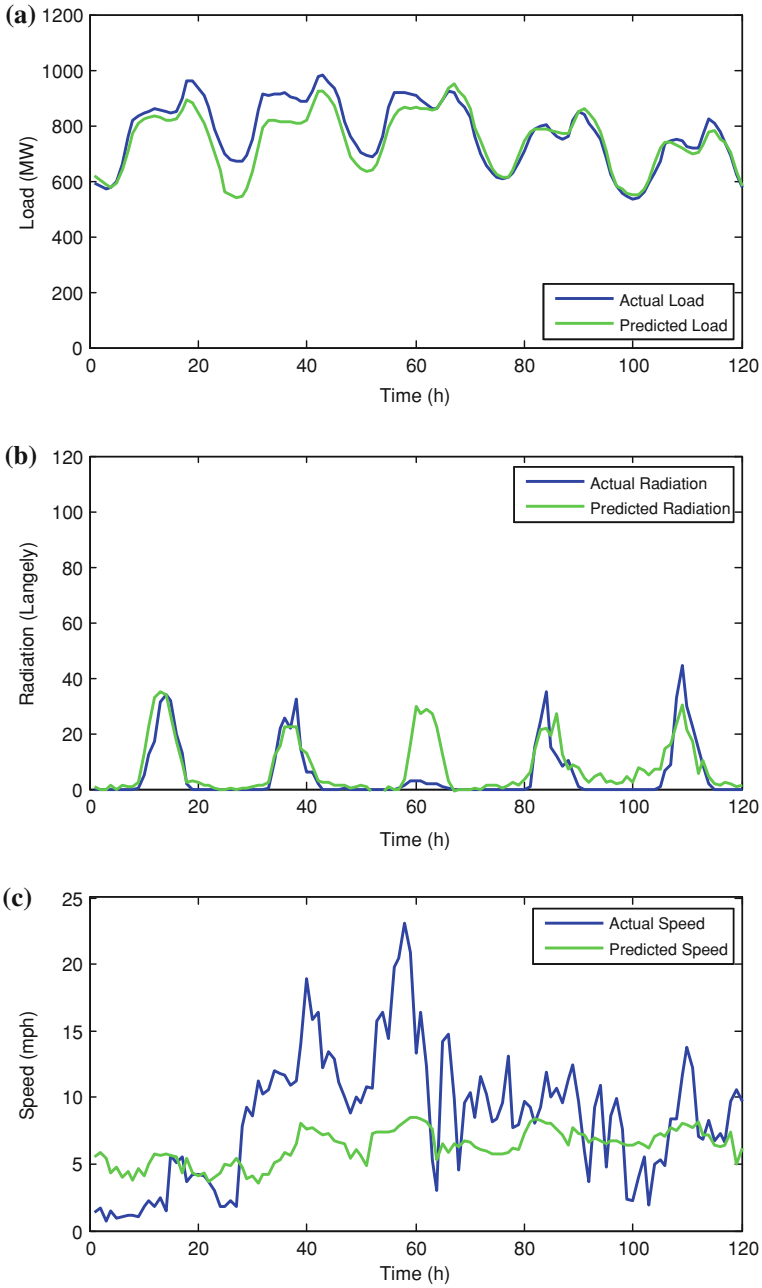

Fig. 32.3 **a–c** Forecasting results for period 1 (January 2nd–6th, 2008)

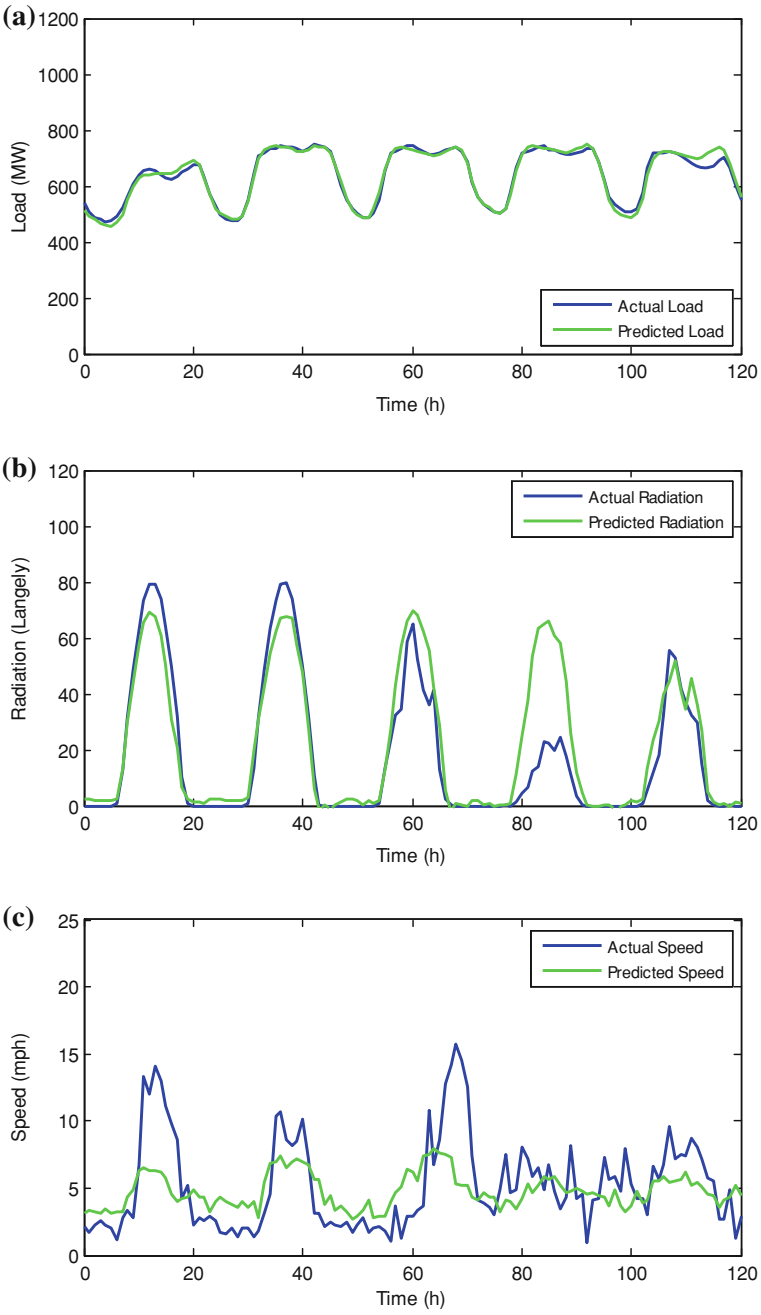

Fig. 32.4 **a–c** Forecasting results for period 2 (April 5–9th, 2009)

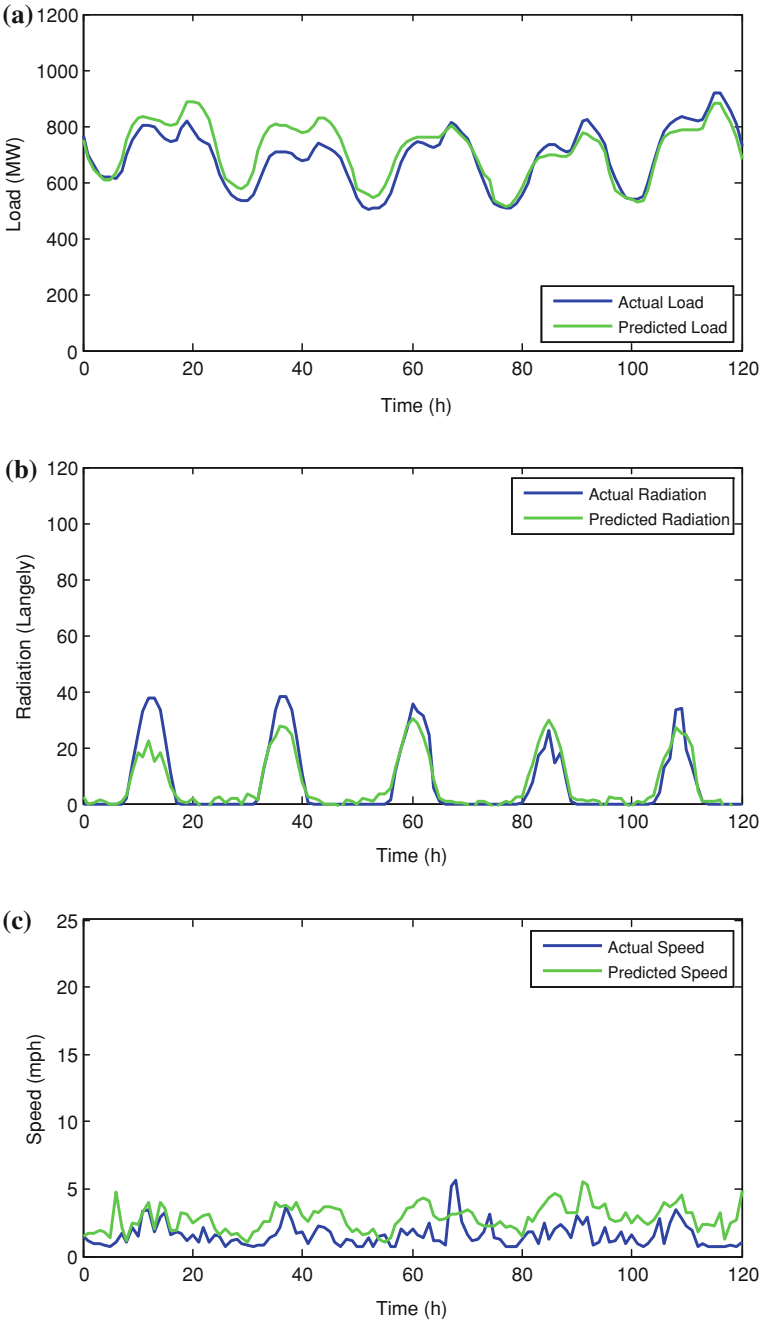

Fig. 32.5 **a–c** Forecasting results for period 3 (December 24–28th, 2009)

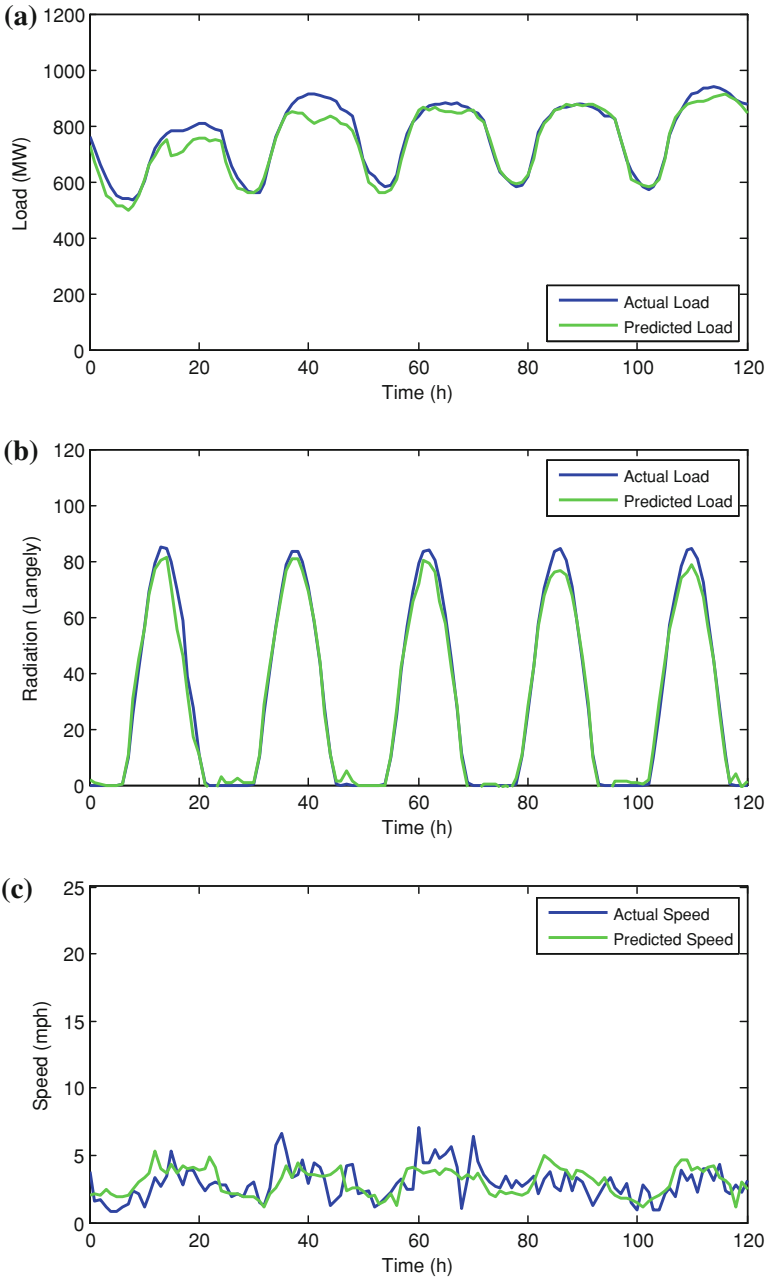

Fig. 32.6 **a–c** Forecasting results for period 4 (July 11–15th, 2010)

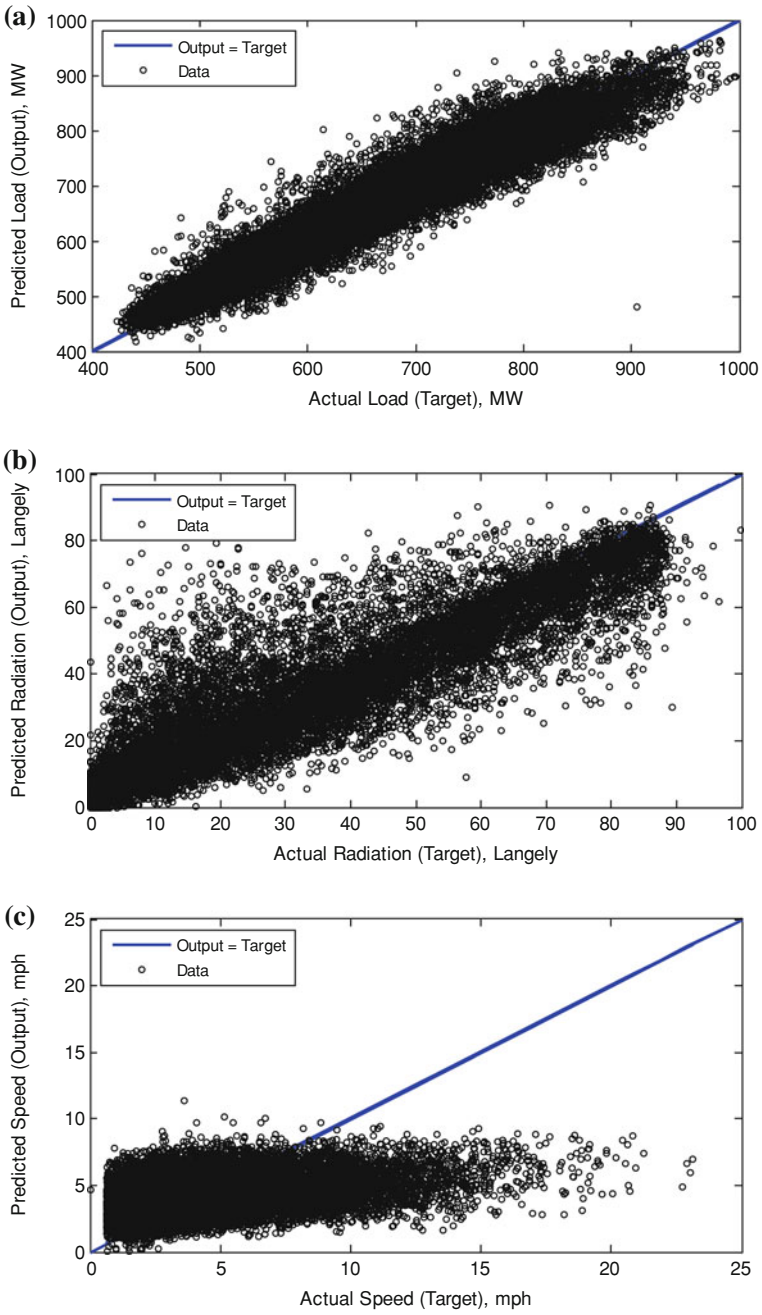

Fig. 32.7 **a–c** Correlation between the predicted output and actual output for day-ahead time horizon for the three forecasting models

Table 32.2 Load RMSE and correlation

Forecast horizon (h)	RMSE (MW)	r
1	20.69	0.983
6	23.51	0.978
12	29.28	0.966
24	31.34	0.959
48	36.95	0.945

Table 32.3 Solar radiation RMSE and correlation

Forecast horizon (h)	RMSE (Langely)	r
1	7.64	0.954
6	7.96	0.949
12	8.29	0.946
24	8.68	0.94
48	8.94	0.936

Table 32.4 Wind speed RMSE and correlation

Forecast horizon (h)	RMSE (mph)	r
1	1.62	0.823
6	2.22	0.631
12	2.4	0.537
24	2.56	0.465
48	2.58	0.43

From the results obtained, the following observations can be summarized:

- The load power is the most predictable quantity (highest correlation) while the wind power is the least predictable quantity (lowest correlation).
- During summer days, the solar radiation is more predictable, which makes sense because during summer there are less cloudy days than in any other time.
- The wind speed model is more accurate at low wind speeds.

All the forecasting models, however, can be adjusted and used for any time horizon. As a general rule, the uncertainty level of the forecasting model is proportional to the time horizon as indicated in Tables 32.2, 32.3, and 32.4. Nonetheless, even with uncertainties, those forecasting models can still be very beneficial when managing the energy storage operation in a market system as explained in the second paper of this series.

32.4 Conclusion

The forecasting models proposed in this paper showed acceptable results for the load power and solar radiation models where the correlation was around 0.95 (day-ahead), while for the wind speed and direction models the correlation was below

0.5 (day-ahead), which was expected due to the highly unpredicted nature of the wind. These models can be used to improve the utilization of renewable energy sources especially when these sources participate in a spot market system.

The advantage of using ANN models is that they can learn and generalize and they do not require a dynamic model for the system. Nonetheless, although the forecasting models have some uncertainty, this uncertainty can be overcome by properly backing up the renewable sources with energy storage and controlling the entire system in an efficient manner to make it highly profitable. With a proper operation strategy for the energy management system, the limitations of renewable sources as well as the uncertainty of the forecasting models can be overcome.

References

1. Nordic power market website. Available at, http://www.nordpoolspot.com/
2. G.N. Kariniotakis, G.S. Stavrakakis, E.F. Nogaret, Wind power forecasting using advanced neural networks models. IEEE Trans. Energy Convers. **11**(4), 762–767 (1996)
3. N.D. Hatziargyriou, An advanced statistical method for wind power forecasting. IEEE Trans. Power Syst. **22**(1), 258–265 (2007)
4. A.G. Bakirtzis, V. Petridis, S.J. Kiartzis, M.C. Alexiadis, A.H. Maissis, A neural network short term load forecasting model for the Greek power system. IEEE Trans. Power Syst. **11**(2), 858–863 (1996)
5. A.A. Hussein, I. Batarseh, *Energy Management for a Grid-Tied Photovoltaic-Wind-Storage System—Part II: Operation Strategy, IEEE Power and Energy Society General Meeting (PES-GM)* (Vancouver, British Columbia, 2013)
6. S. Haykin, *Neural Networks and Learning Machines*, 3rd edn. (McMaster University, Hamilton, 1999), pp. 1–46
7. A.A. Hussein, I. Batarseh, State-of-charge estimation for a single lithium battery cell using extended Kalman filter, in *IEEE Power and Energy Society General Meeting (PES-GM)*, Detroit, 24–28 July 2011
8. A. Hussein, Design and operation of stationary distributed battery micro-storage Systems, Ph.D. Dissertation, University of Central Florida, Orlando, July 2011
9. Homepage of ISO New England, http://www.iso-ne.com/
10. Homepage of AgriMet—The Pacific Northwest Cooperative Agricultural Weather Network, http://www.usbr.gov/pn/agrimet/

Chapter 33
Failure Analysis of Adhesively Bonded Wind Turbine Blade

Waleed K. Ahmed

Abstract Defective wind turbine blade subjected to combined loading was investigated and assessed. The present analysis focuses on studying an adhesively bonded composite wind turbine blade contains an edge crack at the bonding line. Finite element method was adopted for this purpose, and linear elastic fracture mechanics was used to estimate stress intensity factor (SIF). Moreover, shear and peel stresses at the defective bonding line were estimated and analyzed. Besides, the impact of the adhesive shear stiffness was considered as a parameter in the investigation. A significant increase in SIF as well as stresses were observed, and which is attributed to the defective bonding line.

Keywords Adhesively · Bonded failure · Wind turbine · Blade

33.1 Introduction

It is well known that wind turbine technology can offer a cost-effective alternate renewal energy source because it is capable of generating greater amounts of electrical energy with zero greenhouse effects in comparison to other energy generating technologies including solar cell, tidal wave, biofuel, hydrogen, biodiesel, and biomass technologies [1], it simply converts the kinetic energy of the wind into electrical energy. Renewable energy sources show many advantages, since they can offer clean, uninterrupted, environmental impact-free electrical energy at affordable cost. Studies showed that wind and solar sources offer the cleanest and most cost-effective renewable energy, pollution free electricity generation, fast installation and commissioning capability, low operation and

W. K. Ahmed (✉)
ERU, College of Engineering, United Arab Emirates University, Al Ain, UAE
e-mail: w.ahmed@uaeu.ac.ae

M. O. Hamdan et al. (eds.), *ICREGA'14 - Renewable Energy: Generation and Applications*, Springer Proceedings in Energy, DOI: 10.1007/978-3-319-05708-8_33,

maintenance cost and taking advantage of using free and renewable energies are all advantages of using wind turbines as an electricity generators [2]. Along with these advantages, the main disadvantage of this industry is the temporary nature of wind flow. Therefore, using reliable and efficient equipment is necessary in order to get as much as energy from wind during the limited period of time that it flows strongly. Besides is considered as the best suited for desalinating seawater, crop irrigation, and food production in coastal regions.

In general, energy crisis and global warming have led to a higher demand for renewable energy [3], so wind energy becomes one of the important energy among renewable energy in the future. Issues such as energy security, sustainable development, and environmental protection have been a major topic of international discussions in recent years. Developed countries worldwide are investing substantial sums to develop renewable energy systems. One of the efficient way to improve the performance of wind turbine is to reduce the weight of the blades. Therefore, wind turbine blades are mainly based on fiber reinforced polymer (FRP) composite for light weight. The wind turbine blade is aerodynamic structure which consists of skin and webs, so adhesive joining method is used to assembly the parts of the blade.

In the wind turbine system, the blade is considered one of the most important component in a wind turbine which is designed according to the aerodynamic concepts in order to deliver the maximum energy from the wind flow. Blades of horizontal axis are now completely made of composite materials. Composite materials satisfy complex design constraints such as lower weight and proper stiffness, while providing good resistance to the static and fatigue loading. Generally, wind turbines are fatigue critical machines and the design of many of their components (especially blades) are dictated by fatigue considerations. Several factors expose wind turbine blades to the fatigue phenomena which can be summarized as shown below [4]:

1. Long and flexible structures.
2. Vibrations in its resonant mode.
3. Randomness in the load spectra due to the nature of the wind.
4. Continuous operation under different conditions.
5. Low maintenance during lifetime.

The above mentioned reasons and extensive expected lifetime cause design constraints for wind turbine structures that fall into either extreme load or fatigue categories.

Polymer matrix composites have been extensively used in the construction of large-scale wind turbine blades due to the low weight and high stiffness requirements [5]. Composite blade and its supporting spars are usually manufactured in parts and then bonded together with adhesives. Adhesively bonded wind turbine blades are subjected to static and fatigue loads under various environmental conditions, therefore there is a need for rigorous analysis of the stress states in adhesive joints for better design [6]. It was reported that many investigators did tests to study failure mechanism of the blades [7]. It was observed that crack

initiated at the flaw areas in the adhesive, which led to unexpected structural response regarding the joint failure and its associated strength. Since wind turbine blades are large-scale structures, it is difficult to avoid flaws in the manufacturing process, such as air bubbles in the adhesive layers [8]. Detailed local characterization and analysis, such as geometric imperfections and its associated stress intensity behaviors, are lacking due to the computational difficulty for accurate predictions [7].

In comparison with other mechanically fastened joints, such as rivet and screw, adhesive joints is considered to have relatively less sources of stress concentrations, higher toughness and more uniform stresses distribution through the joined area. Usually, adhesive bonding lines in large scale turbine blades are thick and much longer than in other applications. Studies concerning failure of wind turbine blade showed that debonding is one of the main causes of blade failure.

Adhesive joint failure observed between skin and spar was observed in the investigation that carried out on the failed sections of blade. Full scale collapse testing was done under the flap-wise loading for a large full-scale wind turbine blade, which showed that the aerodynamic skins debonding of the adhesive joints is the initial failure mechanism causing a progressive collapse of the blades [9]. A three point bending test for asymmetric beam was conducted for studying the adhesive performance between shear web and spar cap of the wind turbine rotor blade through investigating thick bond-lines [10]. Numerically and experimental investigation were done on composite I-beams to examine the mechanical behavior of adhesive bond lines [11]. Prediction and simulation of the damage initiation and evolution was investigated by using a developed finite element model, and cohesive laws were used for prediction the load carrying capacity of medium size adhesive joint specimens subjected to four point flexure [12]. Although these studies have made effort to investigate behavior of adhesive joint, there are differences between subcomponents and actual blades. In most case, it is quit impossible to control adhesive thickness, therefore, adhesive joints of blade do not have regular thickness and undergo complex load case. Consideration of the actual geometry and load condition of blades is required to predict accurate strength of adhesive joints. Accordingly, engineering approaches for adhesive joint have been of great interest.

Geometrical nonlinear and interlaminar progressive failure finite element analysis of a generic wind turbine blade undergoing a static flap-wise load, which was found that showed excellent correlation with the experimental results and observations in the pre-instability response [8]. A developed finite element analysis based on fracture mechanics was conducted to characterize failure of adhesive joint for wind turbine blade and to predict damage initiation and propagation. Results showed that failure was initiated in the edge of the adhesive bond line due to high level of shear stress prior to reaching the extreme design loading and propagated progressively [3]. Lifetime prediction of a horizontal axis wind turbine composite blade is considered. Load cases are identified, calculated and evaluated. Static analysis is performed with a full 3-D finite element method and the critical zone where fatigue failure begins is extracted. Accumulated fatigue damage

modeling is employed as a damage estimation rule based on generalized material property degradation. The structural mechanics of wind turbine blades were analyzed with behavioral models to identify the mechanisms of the damage. It was reported that surface delamination mechanism was the primary causes of the failure. The performance of adhesive joints of carbon/epoxy wind turbine blade subjected to combined bending and tension loadings was investigated through FEM. The influence of adhesive properties and geometrical details including fillet and imperfections was examined in terms of interlaminar stresses in the adhesive layer. The variation of stress intensity with change in adhesive shear modulus has also been investigated, while contour integral method was used for evaluating the stress intensity factors (SIF) at the imperfection tip. Besides, the strength of the joint was assessed through the crack initiation and propagation analysis.

Recently, the importance of the failure engineering field has gradually increased because of the infrastructure damage caused by extreme weather. Using evidence-based analytical procedures, has increased their capability to identify the probable causes of incidents involving engineering structures [14], can be a reference for design implementation by offering a perspective that considers factors other than the conventional concerns of quality, cost, and duration of work [13]. Therefore, they reduce the difficulties caused by risks of future damage or the follow up management of incidents [15]. Nowadays, mechanical analysis of geometric and material parameters wind turbine blades were mechanically modeled using finite element analysis software system. Currently, FEA is widely used in many fields, including aeronautics [16], civil and architecture engineering [18], and energy [17], to analyze the stress–strain distributions of structural components under specified loading.

33.2 Modeling via Finite Element Method

FEA has been one of the most prevalent numerical tools in the field of fracture mechanics since the early 1960s. Researchers have been developing new techniques to improve the accuracy of FEM in application to fracture mechanics. The use of quarter point elements in improving the accuracy of the solution around the crack tip was suggested by Barsoum [19]. Murti et al. [20] took this study further by developing several other element types to increase the accuracy of the SIF calculation. The present work demonstrates finite element analysis which was done on wind turbine blade to investigate the impact of an edge crack located at the adhesive layer on the stress intensity factor (SIF) as well as on the interlaminar stresses along the adhesive layer. Basically, the blade consist of composite shell supported by spar through adhesive to avoid blade's buckling, as shown in Fig. 33.1. The dimensions of the investigated model is identical to a previous study which was done by Linxia Gu [8] which is illustrated in Fig. 33.2.

Mainly, elastic material model is used to simulate the behavior of the adhesive layer in the joint analysis. For the supporting spar and the composite shell are

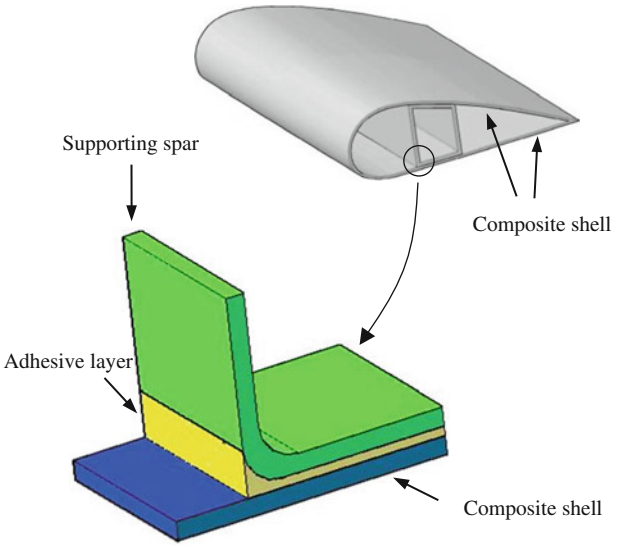

Fig. 33.1 3D model of wind turbine blade

Fig. 33.2 Geometry details of wind turbine blade

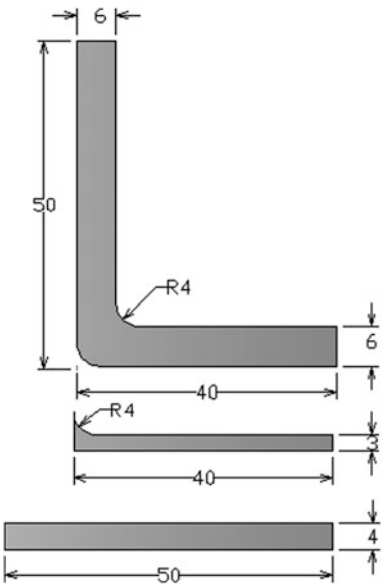

considered as orthotropic through the analysis, whereas for the adhesive layer is taken as isotropic. The detailed properties is given by Table 33.1.

Plain strain finite element model was adopted in the analysis [21] using 8-node quadrilateral (Solid 183) instead of the 3-D model, where the basic element size

Table 33.1 Material properties for the composite shell and adhesive

Properties	Composite shell (GPa)	Adhesive
Longitudinal modulus E_1	145	1.1 GPa
Transverse modulus E_2	10	–
Transverse modulus E_3	10	–
Shear modulus G_{12}	7	0.382
Shear modulus G_{13}	7	–
Shear modulus G_{23}	3.7	–
Poisson's ratio ν_{12}	0.25	0.44
Poisson's ratio ν_{13}	0.25	–
Poisson's ratio ν_{23}	0.5	–

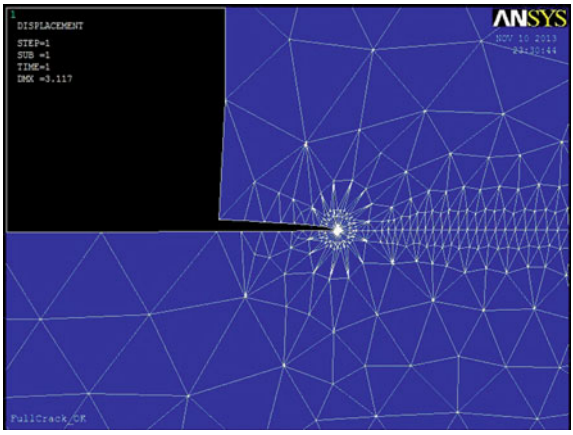

Fig. 33.3 Crack tip FE mesh

chosen was 1 mm for the supporting spar and the composite shell, whereas for the adhesive layer was 0.5 mm except at the crack tip, where the mesh was dine according to the software macro. This is depicted through Fig. 33.3.

In the other hand, the applied load on the proposed element was subjected a combination of tensile stress of 100 MPa along the y-axis of the supporting spar, which simulates the lifting and the drag force on the wind turbine blade resulted from the wind induced pressure difference [22]. Besides, a 3 mm displacement along the x-axis was applied at the end of the supporting spar as well. The composite shell was constrained in all directions. Taking into account that the condition of the bonding lines are considered to have a perfect adhesion between the adhesive and the composite shell one time and the adhesive and the supporting spar in the second time. In this context, it is important to clarify that instead of analyzing the influence of through-thickness elliptical void located at the adhesive layer, on the interlaminar stresses and the SIF, an edge crack was studied which was located between the adhesive layer and the composite shell, as show in Fig. 33.4.

Knowing that the crack length was analogues to studied case [8], except it starts from the adhesive tip. Linear elastic fracture mechanics (LEFM) was adopted to estimate SIF at the crack tip for mode I and II, in addition the influence of the

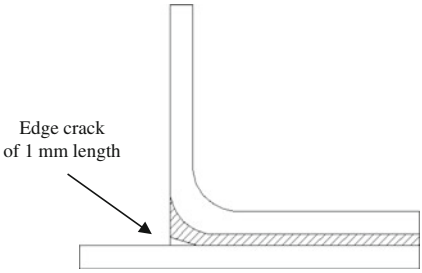

Fig. 33.4 Fractured blade with *edge crack* at the adhesive tip

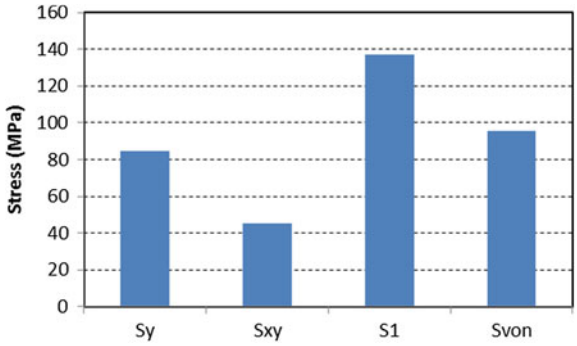

Fig. 33.5 Stresses at the adhesive tip for intact blade

adhesive layer stiffness, i.e., shear modules was explored. Stresses, shear, peel, principal as well as von Misses were estimated at the adhesive tip for the intact case, whereas evaluated at the crack tip for the fractured case.

33.3 Results and Discussion

The first stage of the analysis was to investigate an intact model i.e., without any void or crack, in order to locate the maximum stresses in the model especially the critical points close to the adhesive layers. It has been seen that the maximum stresses exceed at the adhesive tip because of the lack of fillet in the studied model, as shown in Fig. 33.5.

It is depicted that the high values of the peeling stress in comparison with the applied one, whereas the 1st principal stresses already exceeds the applied stresses. von Misses stresses approaches the applied stresses. Shear stresses more that 40% of the applied stress, and this is a clear evidence that this point is a critical point in the geometry where there is a big opportunity for the crack initiation and prorogation. In the other hand, by introducing an edge crack at the adhesive tip, between the adhesive layer and the composite shell, a consequence of the fact that a considerable increase in the stresses at the crack tip was observed as illustrated in Fig. 33.6, which illustrates maximum stresses.

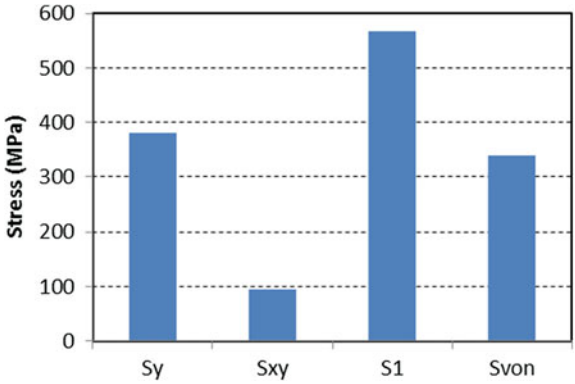

Fig. 33.6 Stresses at the *crack tip* for fractures blade

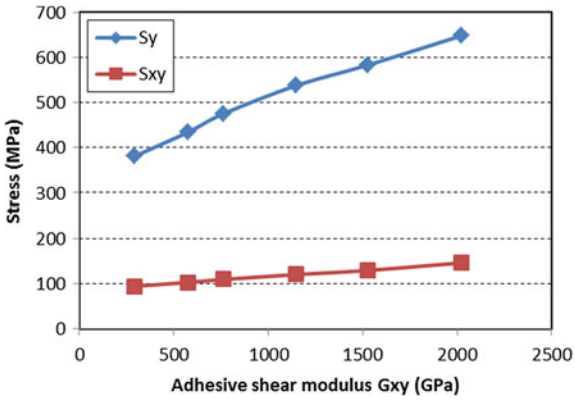

Fig. 33.7 Stresses at the adhesive tip for intact blade

It can be interpreted in comparison with the intact case, that an increase of 348 % was observed in the peel stresses, and 90 % in the shear stresses, whereas 314 % in the 1st principal stresses, and eventually 278 % increase in the Von Misses stresses. Accordingly, a parametric study were carried out to investigate the impact of the adhesive shear modulus, on the peel and the shear stresses at the crack tip. The results are represented by Fig. 33.7.

It has been clearly evident that with the increase of the shear modulus of the adhesive, both peel and shear stresses at the crack tip increases accordingly. In fact, the increase of the peel stresses can approach 70 % as the adhesive stiffness becomes about seven times the primary value (Young's modulus 1.1 GPa), though less rise in the shear stresses up to 55 %, where observed with the same adhesive stiffness increase. The last stage of the study was to investigate using linear elastic fracture mechanics principle (LEFM), the influence of the fractured blade caused by presumed edge crack located between the adhesive layer and the composite shell, on the estimated stress intensity factor (SIF). It has been known that voids play important role in adhesive joint failure [23], therefore the present study the impact of the estimated SIF as a result of the fractured adhesive layer. Mainly due

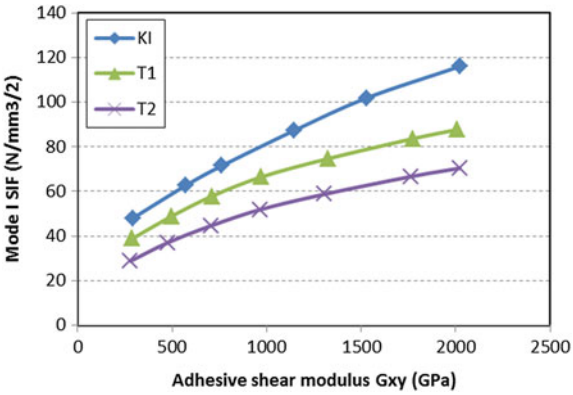

Fig. 33.8 Mode I SIF (KI) for fractured and voided (tip1 and tip2 Ref. [8]), as a function of adhesive shear modulus

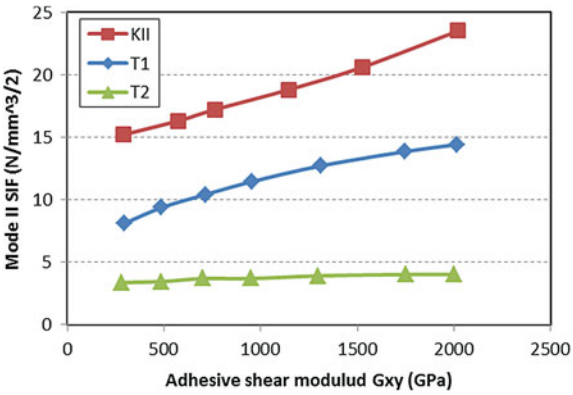

Fig. 33.9 Mode II SIF (K_{II}) for fractured and with voided (tip1 and tip2 Ref. [8]) blade, as a function of adhesive shear modulus

to the combined loading that the blade is subjected to, it is expected to have both opening and shear mode of stress intensity factor, therefore these two type were analyzed and compared. A clear evidence can be observed from the presence of the edge crack in increasing SIF in levels more than that caused by the void, and this can be elucidated in Fig. 33.8, where it is apparent that SIF of the cracked blade overtakes and dominates the voids results.

The increase in the SIF of the fractured blade can be as 23 % more than the maximum SIF for the blade with void, i.e., at tip 1, when the adhesive stiffness was 1.1 GPa (for isotropic material, shear modulus can be estimated from the Young's modulus by $G = E/2(1 + \nu)$), whereas it is shown to be 32 % more than the maximum SIF of the voided blade at a stiffness of 5.8 GPa. Regarding the impact of the edge crack on the mode II SIF, by the same FE model, K_{II} was estimated at the same time of estimating KI, and besides was analyzed in comparison with adhesive stiffness, i.e., shear modulus. Figure 33.9 shown that mode II SIF, i.e., K_{II}, exceeds the level of the SIF estimated at the ends of the trough thickness voids. Although the level of the SIF of mode II is lower that mode I, but since it is

located in weak layer, i.e., adhesive layer, it makes the failure situation of the blade more crucial. However, this increase of mode II SIF can be seen to be 4.5 times the maximum SIF of the voided blade at lowest value of the adhesive shear modulus, and to be 5.9 times at the maximum shear modulus value.

33.4 Conclusions

The present analysis is based on using LEFM to evaluate the SIF of an edge crack located at the tip of the adhesive layer of wind turbine blade. The study discuss the results in comparison with a wind turbine with void. The following points can summarize the investigation:

- For the intact blade, the stresses at the adhesive tip are relatively high, especially the peel and the principal stresses, and this can cause the initiation of the crack especially with lack of the adhesive fillet.
- The presence of the edge crack at the adhesive tip increase the stresses at the crack tip times than the applied stress, and this might cause propagation of the crack.
- Mode I and II SIF of the fractured blade show always higher levels than the corresponding SIF of the blade with void.

Acknowledgments The author would like to thank the Associate Professor Dr. Linxia Gu, Department of Mechanical and Materials Engineering, University of Nebraska-Lincoln, Lincoln, US for her invaluable suggestions and collaboration thought the stages of the study.

References

1. A.R. Jha, in *Wind Turbine Technology* (CRC Press, Boca Raton, 2010)
2. M.M. Shokrieh, R. Rafiee, Simulation of fatigue failure in a full composite wind turbine blade. Compos. Struct. **74**, 332–342 (2006)
3. Y.M. Ji, K.S. Han, Fracture mechanics approach for failure of adhesive joints in wind turbine blades. Renew. Energy (To be published) (2013)
4. D.A. Spera, *Wind Turbine Technology* (ASME Press, New York, 1994)
5. K.L. Edwards, A brief insight into the selection and use of engineering adhesives for preliminary joint design. Mater. Des. **19**(3), 121–123 (1998)
6. C. Kong, S. Choi, H. Park, Investigation on design for a 500 W wind turbine composite blade considering impact damage. Adv. Compos. Mater. **20**(2), 105–123 (2011)
7. F.M. Jensen et al., Structural testing and numerical simulation of a 34 m composite wind turbine blade. Compos. Struct. **76**(1–2), 52–61 (2006)
8. Y. Hua, A.M. Ram Kasavajhala, L. Gu, Elastic–plastic analysis and strength evaluation of adhesive joints in wind turbine blades. Compos. Part B **44**, 650–656 (2013)
9. J.S. Yang, C.Y. Peng, J.Y. Xiao, J.C. Zeng, S.L. Xing, J.T. Jin et al., Structural investigation of composite wind turbine blade considering structural collapse in full-scale static tests. Compos. Struct. **97**, 15–29 (2013)

10. F. Sayer, A. Antoniou, A. van Wingerde, Investigation of structural bond lines in wind turbine blades by sub-component tests. Int. J. Adhes. Adhes. **37**, 129–135 (2012)
11. D.S. Zarouchas, A.A. Makris, F. Van Hemelrijck, A.M. Van Wingerde, Investigations on the mechanical behavior of a wind rotor blade subcomponent. Compos. B Eng. **43**(2), 647–654 (2012)
12. B.F. Sorensen, S. Goutianos, T.K. Jacobsen, Strength scaling of adhesive joints in polymer matrix composites. Int. J. Solids Struct. **46**(3–4), 741–761 (2009)
13. C. Jui-Sheng, C. Chien-Kuo, H. I-Kui, C. Kai-Ning, Failure analysis of wind turbine blade under critical wind loads. Eng. Fail. Anal. **27**, 99–118 (2013)
14. N. Athiniotis, D. Lombardo, G. Clark, On-site aspects of a major aircraft accident investigation. Eng. Fail. Anal. **16**(7), 2020–2030 (2009)
15. J. Hou, B.J. Wicks, R.A. Antoniou, An investigation of fatigue failures of turbine blades in a gas turbine engine by mechanical analysis. Eng. Fail. Anal. **9**(2), 201–211 (2002)
16. G.H. Farrahi, M. Tirehdast, E.M. Khalil Abad, S. Parsa, M. Motakefpoor, Failure analysis of a gas turbine compressor. Eng. Fail. Anal. **18**(1), 474–84 (2011)
17. S. Sankar, M. Nataraj, V.P. Raja, Failure analysis of shear pins in wind turbine generator. Eng. Fail. Anal. **18**(1), 325–339 (2011)
18. E. Ergun, S. Tasgetiren, M. Topcu, Determination of SIF for patched crack in aluminum plates by the combined finite element and genetic algorithm approach. Fatigue Fract. Eng. Mater. Struct. **31**(11), 929–936 (2008)
19. R.S. Barsoum, On the use of isoparametric finite elements in linear fracture mechanics. Int. J. Numer. Methods Eng. **10**(1), 25–37 (1976)
20. V. Murti, S. Valliappan, I.K. Lee, Stress intensity factor using quarter point element. J. Eng. Mech. **111**(2), 203–217 (1984)
21. S. Moaveni, in Finite Element Analysis: Theory and Application with ANSYS (Pearson Prentice Hall, Upper Saddle river, 2008)
22. B.F. Sørensen, T.K. Jacobsen, Joining structural parts of composite materials for large rotorblades, in: *Proceedings of the 27th Risø International Symposium on Materials Science: Polymer Composite Materials for Wind Power Turbines*, Denmark, 2006
23. A. Chadegani, R.C. Batra, Analysis of adhesive bonded single-lap joint with an interfacial crack and a void. Int. J. Adhes. Adhes. **31**(6), 455–465 (2011)

Chapter 34
New Pitch Control Scheme for Wind Turbines

Salim Ibrir and Kyle Hunte

Abstract New control procedures are developed for maximum power extraction from the wing energy and reliable tracking of desired aerodynamic reference torques. The employed control strategies are based on the variation of the pitch angle of the blades using the technique of gradient flow. The simplicity of the control feedback and its independence from the state variables of the electrical parts makes the design straightforward and easy to implement. Numerical simulations of battery charging in case of constant and variable wind speeds, are provided to show the efficacy of the proposed design.

34.1 Introduction

Historically, wind turbines are known as primitive energy conversion systems. For a long time, windmills were among the essential energy conversion plants that have been used extensively to extract mechanical energy required to mill the corns. Year after year, the wind turbines have been developed and designed to generate electricity while operating quietly, safely, and efficiently. The need for wind energy, which is also classified as a source of green energy, has considerably increased because of the positive impacts on health and environment. Compared to other sources of energies, the wind power provides economically viable solutions. Nowadays, the wind turbines are being installed in many countries to produce

S. Ibrir (✉)
Electrical Engineering Department, King Fahd University of Petroleum and Minerals, KFUPM Box–5038, Dhahran 31261, Kingdom of Saudi Arabia
e-mail: sibrir@kfupm.edu.sa

K. Hunte
ICA Engineering LLC, 1155 West Chestnut St, Union, NJ 07083, USA
e-mail: huntekyle@live.com

M. O. Hamdan et al. (eds.), *ICREGA'14 - Renewable Energy: Generation and Applications*, Springer Proceedings in Energy, DOI: 10.1007/978-3-319-05708-8_34,

electrical energy. In those applications, wind power plants have been installed as distributed power plants.

A wind-turbine system is essentially composed by mechanical and electrical parts. The conception of a reliable wind turbine is a complex process that starts by defining the form and the specifications of a wind turbine to extract energy from the wind. A wind turbine installation consists of an aerodynamic system, generally conceived as a fan with aerodynamic-shaped blades, needed to capture the wind's energy. The aerodynamic part is generally followed by a mechanical drive train, that amplifies the rotor speed. The generated mechanical torque is subsequently applied to an electrical generator system to produce electrical energy. Depending on the desired application, conversion electrical circuits and storage elements are required to receive, manage, and distribute the generated electrical energy. To improve the efficiency of the overall system, the wind-turbine is generally in need of a control unit that points the turbine into the wind, maximizes the efficiency of the extracted wind energy, and organizes the switch between different actions including the start, the stop, and other operations of the wind turbine.

In wind energy conversion systems, one of the major faced problems is the continuous changeability of the wind speed. In most cases, the wind speed can fluctuate rapidly. Hence, the quality and the amount of the produced energy cannot be maintained in its optimal value if the overall system is kept uncontrolled. Numerous control procedures have been proposed to improve the quality of power generation with wind turbines and quite successfully design methods have shown outstanding performances. Maximizing the power extracted from the wind is considered as a fundamental objective that attracted the attention of engineers, researchers and practitioners in this field. Maximum-power control of wind turbines have been investigated with different approaches, see e.g., [1, 2]. Different approaches have been successfully applied to wind turbines like variable-speed control methods [3, 4, 5–7, 8–10], pitch control design methodologies [11, 12], robust control methods [13, 14], fuzzy-logic control design [15], adaptive and nonlinear algorithms [16, 17] and neural-networks based design, see e.g., [18]. A comparison between linear and nonlinear control designs is given in Ref. [19].

In this note new pitch control designs are proposed to track prescribed levels of aerodynamic power and maximize the power extracted from the wind energy. The first part of the main results concerns reliable tracking of different piecewise-continuous levels of desired powers. The realization of this objective is essentially dependent on the amount of the wind speed where the pitch angle is being controlled to maintain desired values of the aerodynamic torque. The control design is only dependent on the rotor speed and the instantaneous value of the wind speed. The second control objective is to variate the pitch angle such that a maximum power is maintained irrespective of the value of the wind speed. To show the effectiveness of the control methodology, off-line theoretical power values are compared to the instantaneous values of the aerodynamic extracted power for different values of the pitch angle. The comparisons are done with association of a battery to the the whole energy conversion system. It is shown that the control design algorithms do not necessitate the modeling of the generator, the rectifier

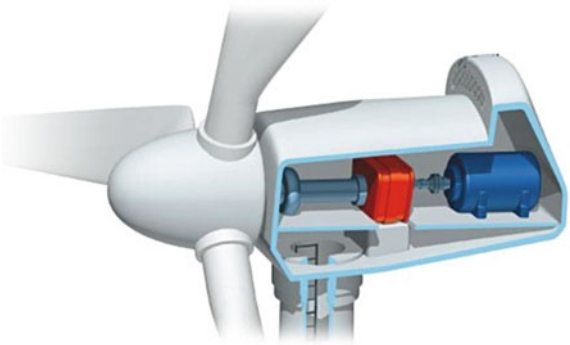

Fig. 34.1 Wind turbine system

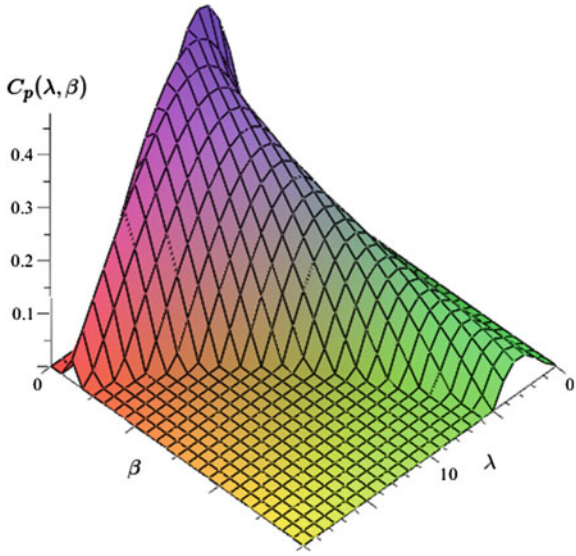

Fig. 34.2 The aerodynamics coefficient $C_p(\lambda, \beta)$ versus λ and β

and the battery as well. Simulation results have shown satisfactory results even for fluctuating wind speeds (Figs. 34.1 and 34.2).

34.2 System Dynamics

The aerodynamic power P_a captured by a wind turbine is expressed as

$$P_a = \frac{1}{2}\rho\pi R^2 C_p(\lambda, \beta)\, v^3, \tag{34.1}$$

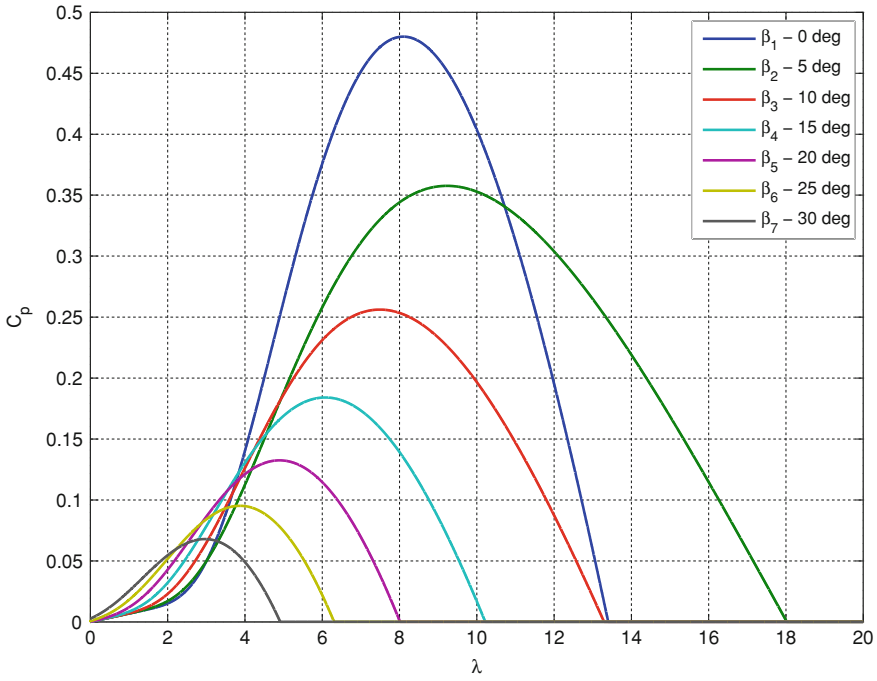

Fig. 34.3 The power coefficient $C_p(\lambda, \beta)$ for different fixed values of β

where $C_p(\lambda, \beta)$ is defined as

$$C_p(\lambda,\beta) = 0.5176\,(116\,(\lambda + 0.08\,\beta)^{-1} - 4.060\,(\beta^3+1)^{-1} - 0.4\,\beta - 5) \times e^{-21\,(\lambda+0.08\,\beta)^{-1}+0.735\,(\beta^3+1)^{-1}} + 0.0068\,\lambda, \tag{34.2}$$

with λ being the tip speed ratio, β represents the blade angle, R is the radius of the blade, ρ is the density of the air, v stands for the wind speed, and $C_p(\lambda, \beta)$ is the power coefficient. Here, we assume that the system inputs are v and β while all the state variables are available for feedback. The tip speed ratio λ is given by the expression:

$$\lambda = \frac{\omega_r R}{v}. \tag{34.3}$$

In Fig. 34.3, the behavior of $C_p(\lambda, \beta)$ versus λ is recorded for different values of the pitch angle β.

According to this plot, one can remark that higher values of the rotor speed do not always guarantee the maximum value of C_p which is reached at $\beta = 0$. The aerodynamic power is expressed as the product of the aerodynamic torque and the rotor speed, that is;

$$P_a = T_a \omega_r. \tag{34.4}$$

The aerodynamic torque can therefore be given using the following expression:

$$T_a = \frac{1}{2} \frac{\rho \pi R^2 C_p(\lambda, \beta) v^3}{\omega_r}. \tag{34.5}$$

The rotor dynamics is given by the following first order equation:

$$J_r \dot{\omega}_r = T_a - T_{ls} - K_r \omega_r, \tag{34.6}$$

where ω_r is the rotor speed as shown in the figure. The torque of the low speed shaft T_{ls} is given by:

$$T_{ls} = B_{ls}(\theta_r - \theta_{ls}) + K_{ls}(\omega_r - \omega_{ls}). \tag{34.7}$$

The dynamics of the generator which is connected to the low speed shaft is given by:

$$J_g \dot{\omega}_g = T_{hs} - K_g \omega_g - T_{em} \tag{34.8}$$

Note that the gearbox ratio n_g is defined by:

$$n_g = \frac{T_{ls}}{T_{hs}} = \frac{\omega_g}{\omega_{ls}}. \tag{34.9}$$

Using the substitution, $x_1 = \omega_r$, $x_2 = \theta_r - \theta_{ls}$, and $x_3 = \omega_g$, we have

$$\begin{aligned}
\dot{x}_1 &= \frac{\rho \pi R^2 C_p(\lambda, \beta) v^3}{J_r x_1} - \frac{B_{ls} x_2}{J_r} - \frac{K_{ls}}{J_r}(x_1 - \frac{x_3}{n_g}) - \frac{K_r x_1}{J_r}, \\
\dot{x}_2 &= x_1 - \frac{x_3}{n_g}, \\
\dot{x}_3 &= \frac{B_{ls}}{J_g n_g} x_2 + \frac{K_{ls}}{J_g n_g}(x_1 - \frac{x_3}{n_g}) - \frac{K_g}{n_g} x_3 - T_{em}.
\end{aligned} \tag{34.10}$$

Using the following state transformation:

$$z_1 = \frac{1}{2} x_1^2, z_2 = x_2, z_3 = x_3$$

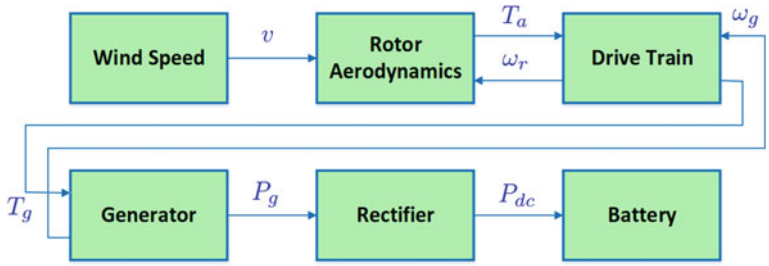

Fig. 34.4 The full system

then, the system in the new coordinate has the following form:

$$\begin{aligned}
\dot{z}_1 &= \frac{\rho\pi R^2 C_p(\lambda,\beta)v^3}{J_r} - \frac{B_{ls}\sqrt{2}\sqrt{z_1}z_2}{J_r} - \frac{K_{ls}}{J_r}\left(2z_1 - \frac{\sqrt{2}\sqrt{z_1}z_3}{n_g}\right) - \frac{2K_r z_1}{J_r},\\
\dot{z}_2 &= \sqrt{2}\sqrt{z_1} - \frac{z_3}{n_g},\\
\dot{z}_3 &= \frac{B_{ls}}{J_g n_g}z_2 + \frac{K_{ls}}{J_g n_g}\left(\sqrt{2}\sqrt{z_1} - \frac{z_3}{n_g}\right) - \frac{K_g}{n_g}z_3 - T_{em}.
\end{aligned} \tag{34.11}$$

The obtained system (34.11) is not singular at $z_1 = 0$ which corresponds to $\omega_r = 0$. System (34.11) can be seen as a highly nonlinear system with three inputs: the wind speed v, the pitch angle β, and the electromagnetic torque T_{em}. If the generator is not controlled, the only active input is the pitch angle β for the reason that the wind speed v is generally seen as random source of power. Since system (34.11) is not affine with respect to the input β, the linearization of z_1 dynamics is not possible. Furthermore, the aerodynamic torque cannot be considered here as perturbation to the system because it involves explicitly the control action β in the power coefficient $C_p(\lambda, \beta)$. In the next sections it is shown how this problem can be efficiently solved by the use of the gradient flow technique.

34.3 Pitch Control

In this study the system represented in Fig. 34.4 is composed. It is assumed that the motor acting on the pitch angle has a linear dynamics with negligible time constant. Therefore, the motor dynamics is neglected and β is seen as the only adjustable input. The control objectives are divided into two main subsections.

34.3.1 Stabilizing the Aerodynamic Torque at a Desired Level

Obviously, a general dynamical model that regroups all the subsystems of wind extraction and transformation, is a complex system with coupled set of nonlinear differential equations. Therefore, designing a model-based feedback is a very challenging problem. Additionally, the wide range of operation of the wind turbines makes the linearized feedback controllers less suitable for such types of systems. In this subsection, it will be shown that the entire dynamics of the system is not needed if β is seen as a control input. The first control objective is to make the aerodynamic torque T_a track a desired reference T_a^* by only adjusting the pitch angle β. It is important to stress that the dynamics of ω_r cannot be linearized with respect to the input β due to the nonlinear character of the coefficient $C_p(\lambda, \beta)$. The control strategy employed in this paper is quite simple, but it necessitates the knowledge of ω_r and the wind speed v. It is also important to stress that the value of T_a^* should be chosen according the value of the wind speed and the maximum value of $C_p(\lambda, \beta)$.

Let e be the tracking error defined by:

$$e = e(\omega_r, v, \lambda) = T_a - T_a^*, \tag{34.12}$$

and let $J = J(\omega_r, v, \beta) = \frac{1}{2}e^2$ be the criteria to be minimized. Assuring the asymptotic decay of $J(\omega_r, v, \beta)$ to zero is guaranteed by using the gradient flow technique, that consists of minimizing the criterion by integration of the following system:

$$\dot{\beta} = -\lambda \frac{\partial J(\omega_r, v, \beta)}{\partial \beta}, \ \lambda > 0. \tag{34.13}$$

The pitch-angle control law is seen as the trajectory of system (34.13), that is

$$\beta = \beta_0 - \lambda \int_0^t \frac{\partial J(\omega_r, v, \beta)}{\partial \beta} dt, \tag{34.14}$$

where β_0 is the value of β at time equal to zero. It is feedback (34.13) is only dependent on the rotor speed ω_r and the wind speed v that are both assumed to be available for feedback. Actually, the knowledge of the remaining states is not necessary for this type of pitch control even the dynamics of the rotor is dependent on the state variables of the drive train. However, the good knowledge of the aerodynamic coefficient $C_p(\lambda, \beta)$ and its dependence to λ and β is essential. Since $C_p(\lambda, \beta)$ is generally build from experimental analysis, the dynamics of the system is not needed to set up controller (34.13).

34.3.2 Maximum Power Pitch Control

Following the same idea employed in the last subsection, we shall look for the pitch-angle control law that maximizes the aerodynamic power $P_a = T_a\omega_r$ whatever the value of the wind speed v. The aerodynamic power P_a reaches its maximum value if and only if its first derivative with respect to β is identically equal to zero. Therefore, by setting the criteria to be minimized as

$$W = \frac{1}{2}\left(\frac{\partial P_a}{\partial \beta}\right)^2 \tag{34.15}$$

then, the minimizer of this performance index can be found by integrating the following dynamical system:

$$\dot{\beta} = -\frac{\lambda}{2}\frac{\partial}{\partial \beta}\left(\frac{\partial P_a}{\partial \beta}\right)^2, \tag{34.16}$$

or equivalently,

$$\dot{\beta} = -\lambda \frac{\partial P_a}{\partial \beta}\,\frac{\partial^2 P_a}{\partial \beta^2}. \tag{34.17}$$

The applied control law is then deduced as

$$\beta = \beta_z - \lambda \int_0^t \frac{\partial P_a}{\partial \beta}\,\frac{\partial^2 P_a}{\partial \beta^2}\,dt. \tag{34.18}$$

To evaluate the performance of the feedback (34.18), in the fourth column of Table 34.1 we have recorded the values of the feedback β, given by (34.18), and the corresponding values of λ for the same instants, see the second column of Table 34.1. The values of λ are then used to evaluate the corresponding theoretical values of β that maximizes the power coefficient $C_p(\lambda, \beta)$. It means for a given value of $\lambda = \lambda^\star$, the power coefficient $C_p(\lambda^\star, \beta)$ becomes only dependent on β, and therefore, it becomes straightforward to determine the value of $\beta = \beta^\star$ such that $\beta^\star = \arg\max_\beta C_p(\lambda^\star, \beta)$. By comparison of the theoretical values recorded in the third column of Table 34.1 and the corresponding values of β given in the fourth column of Table 34.1, we notice that controller (34.18) is able to converge to the optimal value of β that maximizes the aerodynamic power P_a.

Table 34.1 Comparison table

W. speed	λ	arg $_{\beta}$ max $(C_p(\lambda^*, \beta))$	β
10	10.9450	1.48448	1.4845
10	12.4705	1.77003	1.7700
10	13.7237	1.91733	1.9173
10	14.0938	1.95205	1.9520
10	14.9695	2.02301	2.0231
10	16.1253	2.09882	2.0988
10	20.2234	2.27469	2.2747

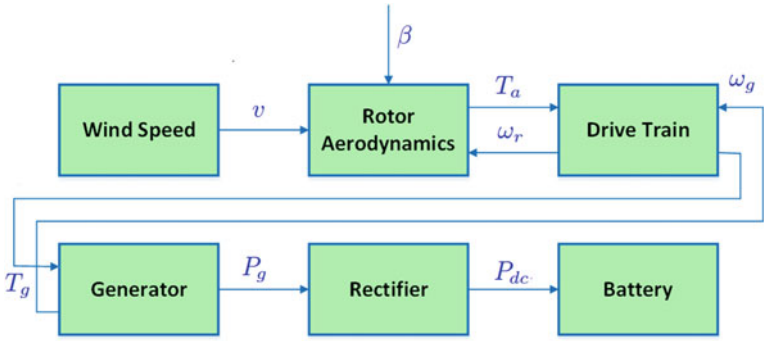

Fig. 34.5 The controlled full system

34.4 Simulation Results

The first set of simulation is based on the model shown in Fig. 34.5 where β is highlighted as the unique control input. The aerodynamic part with the train drive subsystem are modelled by system (34.11) while the generator, the rectifier and the battery blocks are composed using Simulink predefined blocks. In this first simulation the wind speed is taken as a constant $v = 6$ [m/s]. In Fig. 34.6 we have set a piecewise constant function as a desired aerodynamic torque defined as follows:

$$\begin{aligned} T_a^{\text{ref}} &= 15(u(t) - u(t-1)) + 190(u(t-1) - u(t-2)) \\ &= 16(u(t-2) - u(t-3)) + 175u(t-3),\ \forall t \geq 0, \end{aligned} \tag{34.19}$$

where $u(t)$ stands for the step function of amplitude one. The result of application of the nonlinear feedback (34.13) is shown in Fig. 34.6 where we see that T_a switches in small finite time to the desired reference levels. The error between the desired T_a^{ref} and T_a is relatively very small except at the switching instants.

To illustrate the feedback design given by (34.17), a random wind speed is considered as shown in Fig. 34.7. By the application of the pitch controller (34.17), the maximum aerodynamic power P_a is maximized according to the instantaneous values of the wind speed v and ω_r. The histories of the wind speed v,

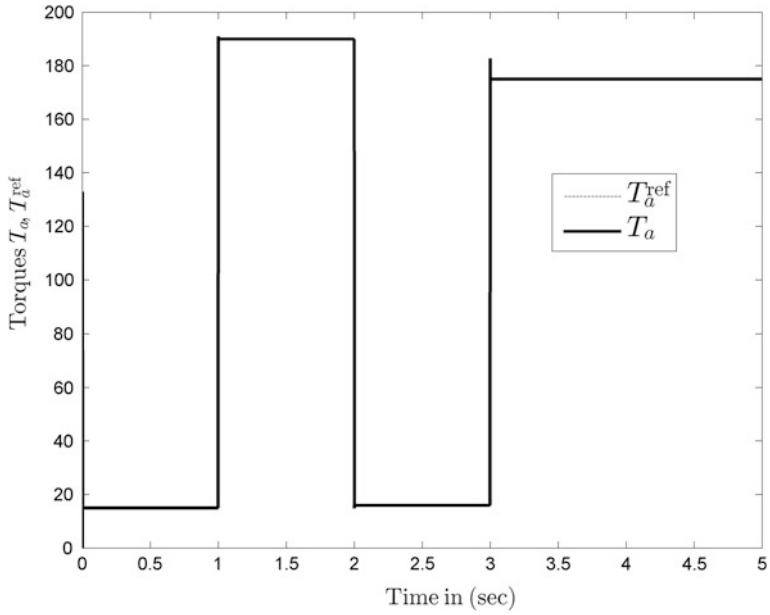

Fig. 34.6 The desired aerodynamic torque and the simulated T_a

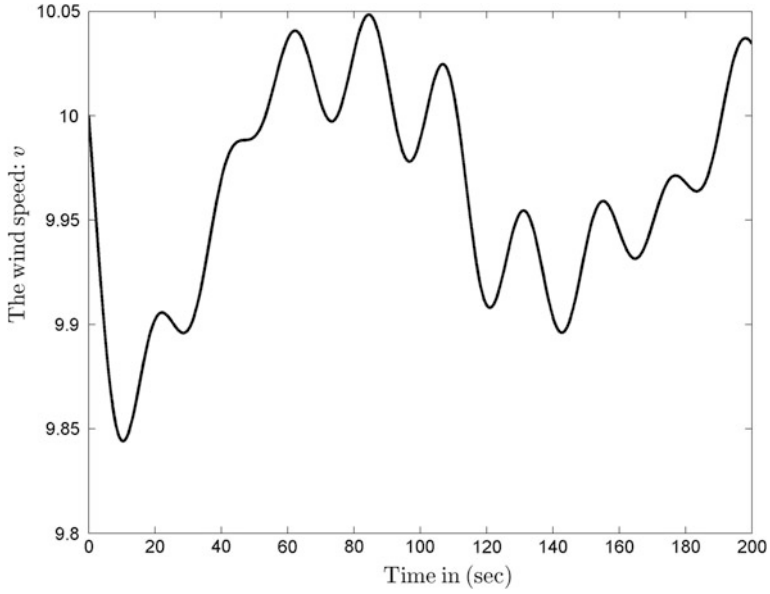

Fig. 34.7 The wind speed v

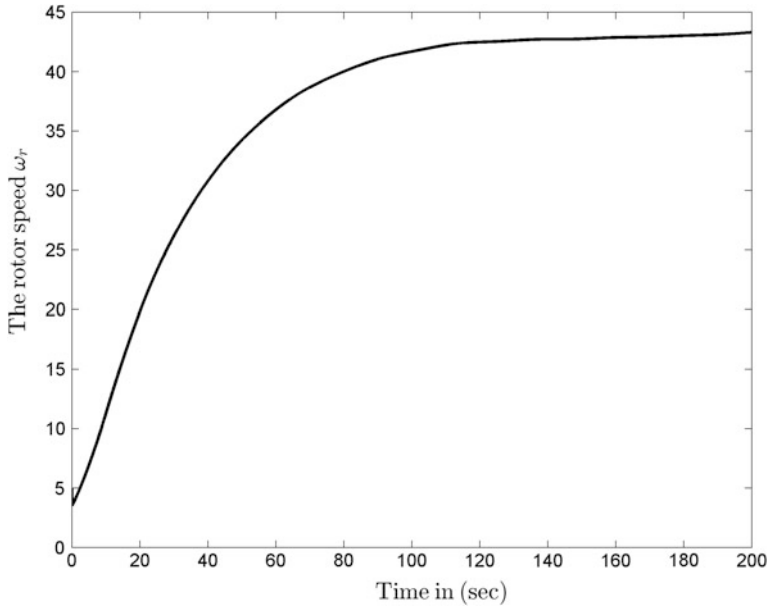

Fig. 34.8 The rotor speed ω_r

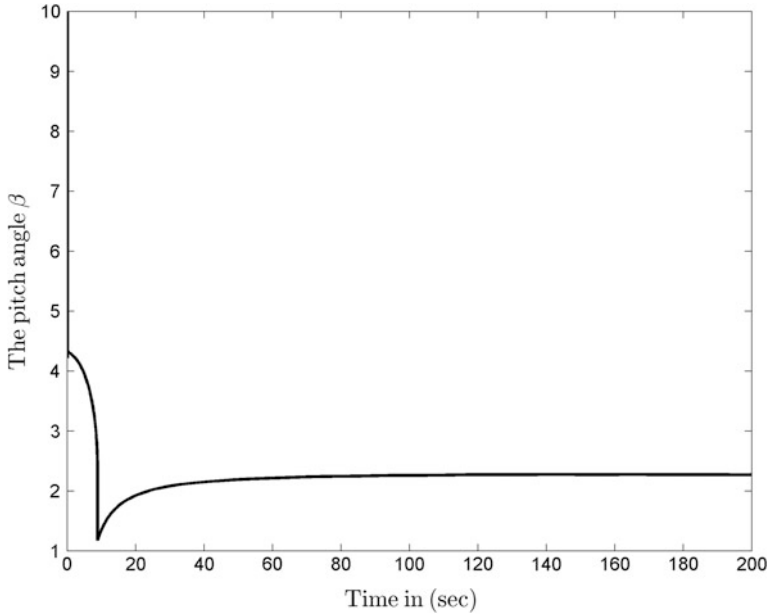

Fig. 34.9 The control input β

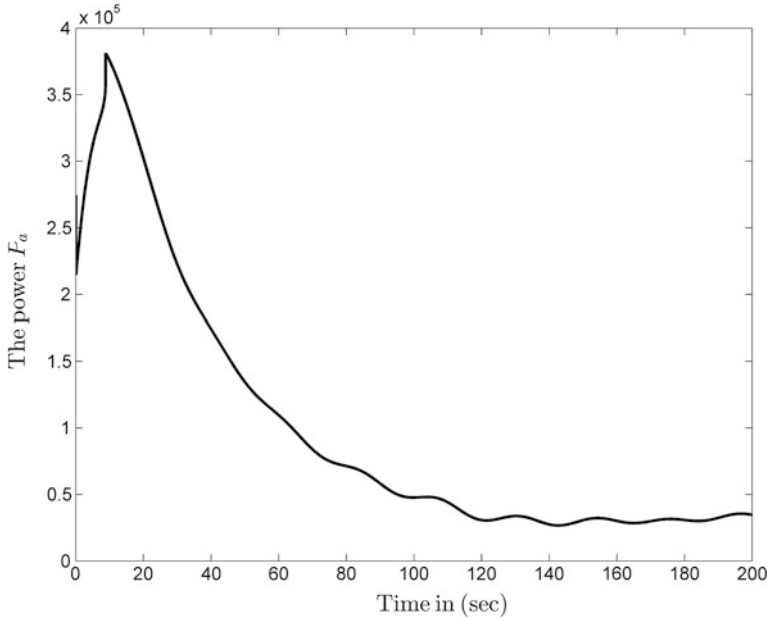

Fig. 34.10 The aerodynamic power P_a

the rotor speed ω_r, the feedback action β, and the aerodynamic power P_a are given in Figs. 34.7, 34.8, 34.9 and 34.10, respectively.

Extensive numerical simulations showed that it is quite possible to adjust the pitch angle to get the maximum power without system linearization. The simplicity of the feedback (34.17) makes the search for the instantaneous maximum power straightforward and free from heavy computational burden. Additionally, the feedback (34.17) can be easily integrated with other multi-objective feedbacks because of its independence from the whole system dynamics.

34.5 Conclusion

Simple control methodologies are developed for maximum power tracking without any need to the dynamics of the overall system. The proposed nonlinear control strategies remains unchanged when different kinds of generators or conversion electrical circuits are employed in the control loop. The whole design is mainly dependent on the knowledge of the power coefficient $C_p(\lambda, \beta)$ which is supposed to be available from experimental tests of the aerodynamics part of the system. The developed control actions can be also integrated with ease with other types of feedbacks assuring additional control objectives.

The authors would like to acknowledge the support provided by the Deanship of Scientific Research (DSR) at King Fahd University of Petroleum and Minerals (KFUPM).

References

1. A.M.D. Broe, S. Drouilhet, V. Gevorgian, A peak power tracker for small wind turbines in battery charging applications. IEEE Trans. Energy Convers. **14**(4), 1630–1635 (1999)
2. E. Koutroulis, K. Kalaitzakis, Design of a maximum power tracking system for wind-energy-conversion applications. IEEE Trans. Ind. Electron. **53**(2), 486–494 (2006)
3. H.D. Battista, R.J. Mantz, C.F. Christiansen, Dynamical sliding mode power control of wind driven induction generators. IEEE Trans. Energy Convers. **15**(4), 451–457 (2000)
4. J. Chen, J. Chen, C. Gong, New overall power control strategy for variable-speed fixed-pitch wind turbines within the whole wind velocity range. IEEE Trans. Ind. Electron. **60**(7), 2652–2660 (2013)
5. H. Geng, G. Yang, Output power control for variable-speed variable-pitch wind generation systems. IEEE Trans. Energy Convers. **25**(2), 494–503 (2010)
6. F.D. Kanellos, N.D. Hatziargyriou, Optimal control of variable speed wind turbines in islanded mode of operation. IEEE Trans. Energy Convers. **25**(4), 1142–1151 (2010)
7. K.H. Kim, T.L. Van, D.C. Lee, S.H. Song, E.H. Kim, Maximum output power tracking control in variable-speed wind turbine systems considering rotor inertial power. IEEE Trans. Ind. Electron. **60**(8), 3207–3217 (2013)
8. A. Miller, E. Muljadi, D.S. Zinger, A variable speed wind turbine power control. IEEE Trans. Energy Convers. **12**(2), 181–186 (1997)
9. M.E. Mokadem, V. Courtecuisse, C. Saudemont, B. Robyns, J. Deuse, Fuzzy logic supervisor-based primary frequency control experiments of a variable-speed wind generator. IEEE Trans. Power Syst. **24**(1), 407–417 (2009)
10. N.R. Ullah, T. Thiringer, Variable speed wind turbines for power system stability enhancement. IEEE Trans. Energy Convers. **22**(1), 52–60 (2007)
11. E. Muljadi, C.P. Butterfield, Pitch-controlled variable-speed wind turbine generation. IEEE Trans. Ind. Appl. **37**(1), 240–246 (2001)
12. T. Senjyu, R. Sakamoto, N. Urasaki, T. Funabashi, H. Fujita, H. Sekine, Output power leveling of wind turbine generator for all operating regions by pitch angle control. IEEE Trans. Energy Convers. **21**(2), 467–475 (2006)
13. H.D. Battista, P.F. Puleston, R.J. Mantz, C.F. Christiansen, Sliding mode control of wind energy systems with doig-power efficiency and torsional dynamics optimization. IEEE Trans. Power Syst. **15**(2), 728–734 (2000)
14. K. Tan, S. Islam, Optimum control strategies in energy conversion of pmsg wind turbine system without mechanical sensors. IEEE Trans. Energy Convers. **19**(2), 392–399 (2004)
15. A. Dadone, L. Dambrosio, Estimator based adaptive fuzzy logic control technique for a wind turbine–generator system. Energy Convers. Manag. **44**(1), 135–153 (2003)
16. Y.D. Song, B. Dhinakaran, X.Y. Bao, Variable speed control of wind turbines using nonlinear and adaptive algorithms. J. Wind Eng. Ind. Aerodyn. **85**(3), 293–308 (2000)
17. F. Mancilla-David, R. Ortega, Adaptive passivity-based control for maximum power extraction of stand-alone windmill systems. Control Eng. Pract. **20**(2), 173–181 (2012)
18. A.S. Yilmaz, Z. Özer, Pitch angle control in wind turbines above the rated wind speed by multi-layer perceptron and radial basis function neural networks. Expert Syst. Appl. **36**(6), 9767–9775 (2009)
19. B. Boukhezzar, H. Siguerdidjane, Comparison between linear and nonlinear control strategies for variable speed wind turbines. Control Eng. Pract. **18**(12), 1357–1368 (2010)

Chapter 35
Numerical Investigation of Four Commonly Used Airfoils for Vertical Axis Wind Turbine

Franklyn Kanyako and Isam Janajreh

Abstract Darrieus VAWT has a number of potential advantages for small scale and domestic application due to the fact that they do not suffer from frequent wind direction changes, easy to integrate with building architecture and they have better response in turbulence wind flow which is common in urban areas. This paper presents a numerical analysis of the performance of a three-bladed Darrieus vertical-axis wind turbine based on four commonly used airfoils DU-06-W200, NACA 0015, NACA 0018 and S-1046. A complete campaign of 2-D simulations, performed for several values of tip speed ratio and based on RANS unsteady calculations, has been performed to obtain the rotor torque and power curves. Rotor performances have been compared with the results of an experimental work based on the use of the NACA 0015 airfoil. The NACA 0015 was found to be the best performing airfoil for the range of tip speed ratio considered.

Keywords CFD · Vertical axis wind turbine · Airfoil · NACA

35.1 Introduction

Wind turbines have been in use for a very long time, but only recently there has been a significant commercial interest by individuals for using wind turbines to generate power for their homes. In part this increase is due to an emerging awareness of the finiteness of the earth's fossil fuel reserves; rising energy cost as well as the adverse effects of burning those fuels. The development of wind turbine technologies has allowed wind energy to perform a relevant step forward and the local production of clean electric power inside the built environment, such as

F. Kanyako · I. Janajreh (✉)
iEnergy Centre, Masdar Institute of Science and Technology, Abu Dhabi
United Arab Emirates
e-mail: ijanajreh@masdar.ac.ae

M. O. Hamdan et al. (eds.), *ICREGA'14 - Renewable Energy: Generation and Applications*, Springer Proceedings in Energy, DOI: 10.1007/978-3-319-05708-8_35,

industrial and residential areas, has led to a renewed interest in vertical axis wind turbines (VAWTs) for small-scale power generation [1]. There are two different principles to extract power from the wind using VAWT. The airfoil drag method is based on the wind drag force incident on wind-blown surface, referred to as the Savonious turbine. The second principle, the darrieus turbine utilizes aerodynamic or airfoil lift principle, which is based on flow deviation inside the rotor, is at present predominantly applied for energy conversion. The Darrieus VAWTs rotates in a circular path, the blades maybe of uniform section and untwisted making them relatively simple to fabricate or extrude. Traditionally, symmetric airfoils are used for Darrieus VAWTs, since the angle of attack of the airfoil vary between positive and negative number of the same amount over the course of a complete rotation about the VAWT's hub. However because the airfoil travels along a circular path, the head wind encountered by the airfoil is not parallel to the airfoil chord line, instead it has a component that is transverse to it which cause high torque fluctuation with each revolution [2]. Darrieus wind turbine performance prediction is a very complex task, since its blades move around the rotor axis in a three dimensional aerodynamic environment that lead to several flow phenomena, such as, dynamic stall, flow separation, flow wake deformations low efficiency and their natural inability to self-start [3]. However VAWT present several advantages over HAWT especially if the inability of the turbine to self-start is solved. They are able to operate at lower wind speeds, are less sensitive to wind direction, and can operate without the need for wind direction adjustment systems, this make it ideal for low speed regions and urban centers.

The design of VAWT blades to achieve satisfactory level of performance; starts with the knowledge of the aerodynamics forces acting on the blade. In fact some of the most complex phenomena in the field of Computational Fluid Dynamics (CFD) are associated with the simulation of flow past rotating blades, besides the aerodynamics of the Darrieus turbine is deeply influenced by the phenomenon of dynamic stall [4].

Ferreira et al. [5] focused on the numerical simulation of a single-bladed VAWT through the comparison with experimental measurements and PIV data, demonstrating that DES model is able to provide a good representation of the development of dynamic stall. Wang et al. [6] performed a two-dimensional numerical investigation of the phenomenon of deep dynamic stall for a low Reynolds number flow over a NACA 0012, comparing the k-ω SST model with low Reynolds number correction and the v2-f model, finding that's RANS approach is good for fast design and research of low Reynolds number airfoils due to its capability of capturing a significant part of the flow dynamics.

This paper focuses on a two-dimensional CFD analysis of three-bladed Darrieus rotor, using the DU-06-W2, S-1046, NACA 0015 and NACA 0018 airfoils. The DU-06-W2 airfoil belongs to a class of wind turbine dedicated airfoils, developed by Delft University of Technology and is typically developed for vertical axis wind turbine applications [7]. The NACA 0018 presently used for the Turby VAWT [8] is taken as a reference point for the design of DU06-W-200. The Du

06-W-200 airfoil is a laminar, 20 % thick airfoil with 0.8 % camber. The original NACA 0018 airfoil is a turbulent, symmetric airfoil with 18 % thickness.

Mohamed [9] carried out aerodynamic investigation for 20 different airfoils by two-dimensional Computational Fluid Dynamics. In his conclusion, the optimal configuration of H-rotor Darrieus turbine involving S-1046 appears to be very promising for wind energy generation, in particular in urban areas compared to symmetric airfoils.

Analyzing all these results, one may state that, contradictory observations can sometimes be found in the literature concerning the best performing airfoil. There is no clear winner at present and the purpose of the present work is to obtain rotor torque and power curves for the three high performing airfoils and also to compare the overall rotor efficiency with the classical NACA 0015 airfoil-based on experimental result carried out by Bravo et al. [10].

35.2 Vertical Axis Wind Turbine Performance

Determining the wind speed at which a wind turbine will operate is the most important step in predicting its performance and very essential in defining the initial size of the wind turbine. The first step in wind turbine design after the operating wind speed of the turbine has been decided is to select an operating tip speed ratio which can be expressed by

$$\lambda = \frac{\omega R}{U} \tag{35.1}$$

The tip speed ratio is the ratio of the rotational velocity of the wind turbine (ωR) and the free stream velocity component (wind speed) V_∞.

A relation between the azimuth angle θ and angle of attack α and the speed ratio λ has been obtained

$$\alpha = \tan^{-1}\left[\frac{\sin\theta}{\lambda + \cos\theta}\right] \tag{35.2}$$

Equation (35.2) was used to determine the values of angle of attack (α) with the variation in pitching angle (θ). The variation in angle of attack during 360° rotation of blade is plotted in Fig. 35.1.

We can observe that the range of angle of attack variation becomes smaller as the tip speed ratio increases; this can be appreciated in the simulation of the angle of attack variation of a blade in a full revolution.

The geometry of the VAWT can be defined through a dimensionless parameter known as the solidity

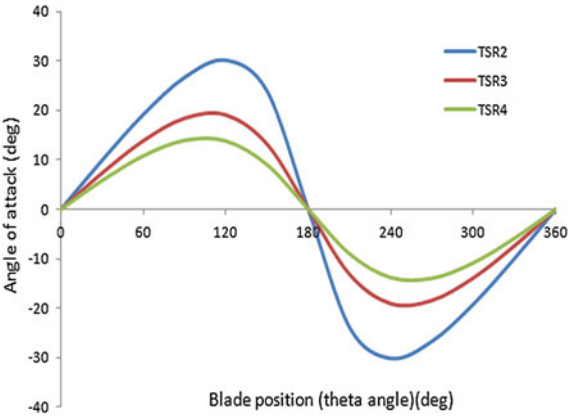

Fig. 35.1 Angle of attack variation in a blade revolution for different tip speed ratios

$$\sigma = \frac{Nc}{d} \tag{35.3}$$

It is a function of the number of blades N, the chord (c) length of the blades, and the diameter (d) of the rotor.

To predict the actual performance of the wind turbine, it is important to determine the forces acting on each blade. This is governed by the relative wind component (W) and the angle of attack (α). As the blades rotates, the local angle of attack α changes due to the variation of the relative velocity (W). The induced velocity (V_i) and the rotating velocity (ωr) of the blade govern the orientation and magnitude of the relative velocity. This in turn generates a lift force F_L normal to the free stream and a drag force F_D in the direction of the free stream. These lift and drag forces can then be resolved to get the tangential force FT and the axial force F_N. It is this tangential force component that drives the rotation of the wind turbine and produces the torque necessary to generate electricity.

The mechanical torque and power (P) coefficient on the axis of a Darrieus turbine can respectively be written as follows:

$$Ct = \frac{T}{\frac{1}{2}\rho U^2 AR} \tag{35.4}$$

and

$$Cp = \frac{T\omega}{\frac{1}{2}\rho U^3 A} \tag{35.5}$$

where A and R are respectively the area of the turbine and the radius, Ct and Cp are the torque and power coefficient.

Table 35.1 Geometrical features and simulated flow field condition of the analyzed rotor

Parameters	Value
D_{rotor} (m)	2.5
H_{rotor} (m)	3 (1 for 2D simulation)
ω (rad/s)	6.4–32
c (m)	0.4
N (–)	3
σ (–)	0.98
p (pa)	101325
ρ (kg/m^3)	1.225
V_∞ (m/s)	10
Tip speed ratio (TSR)[–]	0.8–3.0

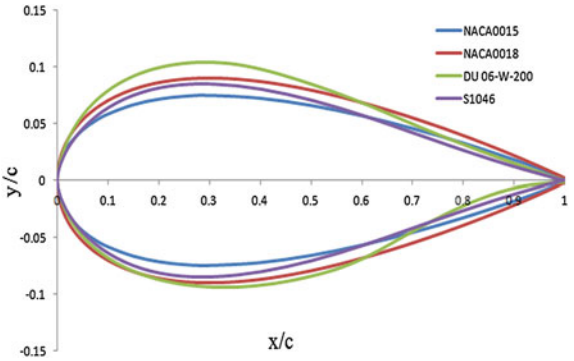

Fig. 35.2 Blade profiles of the four airfoils

35.3 Model Geometry and Numerical Flow Field

The objective of this work is to carry out numerical simulation of the aerodynamic behavior of a three-bladed Darreius vertical axis wind turbine characterized by the use of four high performing airfoils DU06-W2-200, S1046, NACA 0015, NACA 0018 airfoils. The numerical result compared against experimental result carried out at McMaster University in partnership with Cleanfield Energy Corp., conducted using 9 m $\times$ 9 m Low Speed Wind Turbine [10]. Table 35.1 displays the geometrical and kinematic features of the tested rotor.

The Fig. 35.2 shows the blade profile of the four turbines used in this paper. The 2D model has been created in Gambit software and the mesh generated has a total of 722,695 nodes and 1,206,288 cells.

The dimensions of the numerical domain and the mesh are shown in Fig. 35.3. The interior domain containing the wind turbine blades was considered as a moving mesh, while the outer domain was stationary. An unstructured grid has been chosen for the interior domain and structured grid for the outer domain. An interface was set between the interior sliding and outer stationary domain. The mesh on both sides

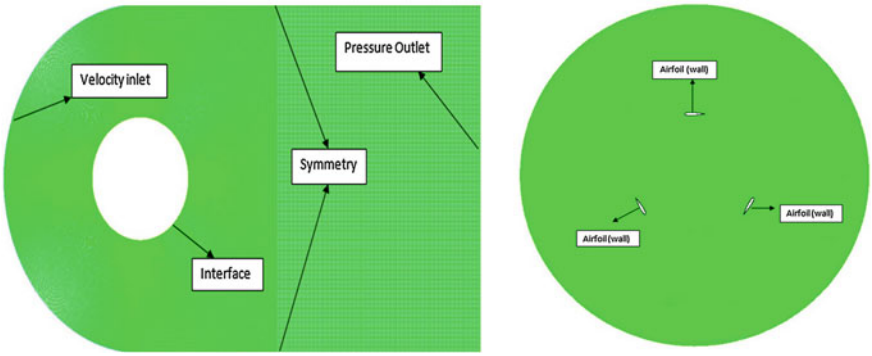

Fig. 35.3 Mesh and the 2D model and rotor sub-grid mesh for 3-bladed VAWT

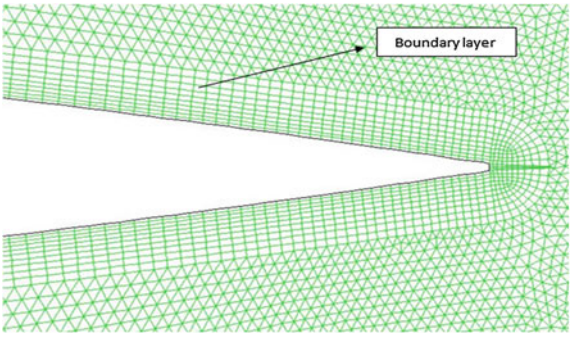

Fig. 35.4 Boundary at the trailing edge of the airfoil

of the interface has approximately the same characteristics cell size, in order to allow faster convergence. The interior sliding domain rotated with a prescribed rotational velocity (ω). For both static and dynamic models, the inlet boundary condition was velocity inlet in which the free stream velocity of 10 m/s was assumed. Also the upper and lower boundaries were supposed as symmetry. This indicates the normal gradient of pressure and velocity at their location is zero. The exit boundary is set as pressure outlet in which the gauge pressure set to zero. Boundary layer has been placed on the blade profile as shown in Fig. 35.4, in order to cluster grid points on the airfoil surface so as to improve the CFD code capability of determining lift, drag and the separation of the flow from the blade itself.

35.4 Numerical Solution

The commercial CFD solver ANSYS FLUENT®, which implements 2-D Reynolds-averaged Navier-Stokes equations using a finite volume based solver and lagrangian sliding mesh technique is retained in this work. The sliding mesh model

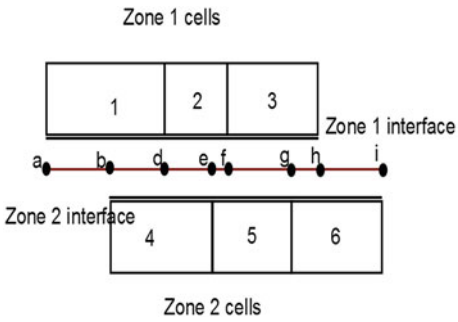

Fig. 35.5 Sliding mesh and interior zone illustration

is a time-accurate solution (rather than a time-averaged solution) for rotor-stator interaction that used to compute the unsteady flow field. One can refer to Janajreh et al. [11] for general review of the application of sliding mesh. A sliding mesh is implemented by creating an interior zone across the sliding interface that consists of an overlapped zone and either a periodic or a wall region. Referring to Fig. 35.5, the b–d, d–e, e–f, f–g, g–h faces are the overlapping faces.

The remaining two faces, a–b, and h–, are the wall or periodic regions. The concept of interior region is manifested by allowing for b–d, d–e, e–f, f–g, and g–h faces instead of the cell faces of 1, 2, and 3 to be used for the computation of the flux to cell 4, 5, and 6 from cell 1, 2, and 3 respectively. For the simulation, a pressure based segregated solver was chosen where the SIMPLE, algorithm was used to handle the pressure-velocity coupling that exists. A 2nd-order interpolation scheme for pressure was used along with a 2nd-order upwind discretization scheme for the momentum equation and modified turbulent viscosity. The gradients required for the discretization of the convective and diffusive fluxes were computed using a cell-based approach. Because the simulation was time dependent, 2nd-order implicit time integration was chosen for the temporal discretization with a minimum convergence criteria were set to 1e-06. A time step was chosen small enough to reduce the number of iterations per time step and to properly model the transient phenomena. Turbulence modeling was accomplished through the use of the SST-k-ω turbulence model where a transport equation is solved for the eddy viscosity [12]. The y+ for the blades varied at different azimuthal locations, but iteratively placed the first cell centroid of the wall-adjacent cells inside the viscous sub layer ($y + <5$) of the boundary layer.

35.5 Numerical Validation

This work has been validated based on wind tunnel measurements [10]. 2D and 3D simulations were performed for the validation.

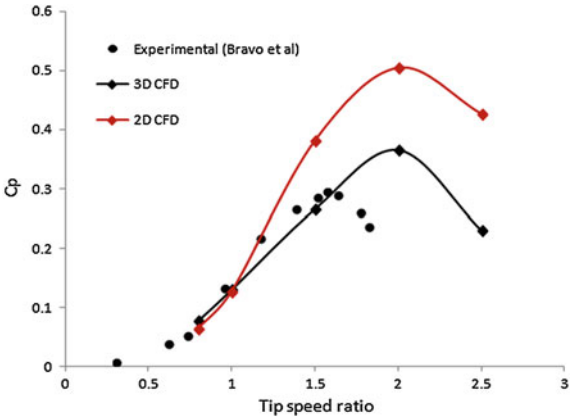

Fig. 35.6 Validation of CFD model compared to experimental result

Comparing the computed results with the experimental data showed that prediction obtained using SST-k-ω turbulence model successfully reproduced most of the flow features associated with the revolution of the tested rotor. In particular, as can be seen in Fig. 35.6 there is a reasonable agreement in both the level and the shape of the 3D predictions and the experimental measurements, which gives confidence that the 3D CFD is correctly capturing the essential flow physics of the aerodynamics. The 2D simulations showed an over estimation of the result when compared to the 3D simulations. The overall difference between the predicted 2D performance and the experimental and 3D CFD results is believed to be caused by the fact that the 2D CFD simulation does not include the effects of the tip vortices present on the real turbine and the 3D simulations. The tip vortices present on the 2D three bladed turbine can be observed in Fig. 35.7.

35.6 Results and Discussions

The moment coefficient (Cm) and the power coefficient (Cp) are calculated according to Eqs. (35.4) and (35.5), respectively. Figures 35.8 and 35.9 shows the evolution of the power and torque coefficient in comparison with the performance of the four airfoils shapes. The results in Fig. 35.9 indicated that the maximum power coefficient is 0.5345 corresponding to the NACA 0015 airfoil. When compared to NACA 0018 (the second best performing airfoil), this means a relative increase of 4.53 %. As the value of tip speed ratio (λ) increases the S-1046 gives a better performance than the NACA 0015 of approximately 15.12 %. This means the operating range (speed ratio range) for the S-1046 turbine is wider than the other airfoils. This implies the stall can be delayed by using S-1046 airfoil. The DU06-W-200 performed slightly better at the starting tip speed ratio than the NACA 0018 which is taken as a reference point for the design of DU06-W-200. But the NACA 0018 performed better at higher tip speed ratio.

Fig. 35.7 Contour of Vorticity magnitude of NACA 0015 airfoil

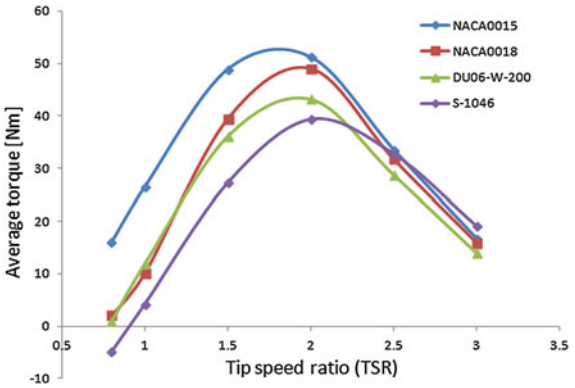

Fig. 35.8 Average Torque as function of TSR for the blade sections

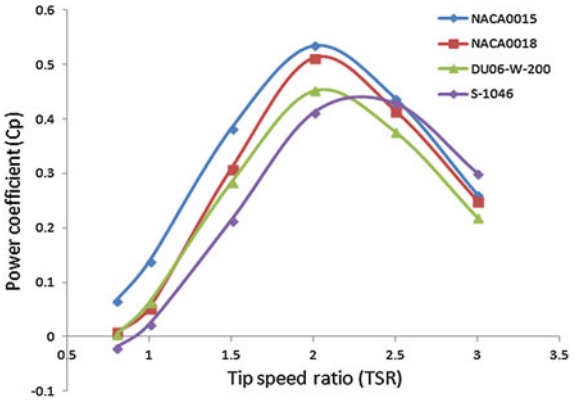

Figure 35.10 shows the evolution of instantaneous performance (torque and performance coefficient) of three bladed NACA 0015 airfoil at different TSR (0.8, 1 and 2). We can observe that although the average rotor power coefficient is lower (0.5345), the instantaneous power coefficient locally (93-214, 148-214, 266-300, azimuthal position) exceeds the Betz's limit for almost 60 of rotor revolution, reaching a maximum value of 1.0994. According to Betz's law, no turbine could capture more than 59.3 % of the kinetic energy flux associated to wind [13].

According Castilla et al. [14] and pointed out by Jonkman [15], among the assumptions of Rankine-Froude actuator disc theory, the static pressure on the boundary of the stream tube portion enclosing the rotor disc should be equal to unperturbed ambient static pressure. The sudden pressure coefficient drop in the rotor disc and the surrounding flow region, especially for maximum local azimuthal position, where the thrust exerted from the rotor to the flow is almost doubled with respect to the case of minimum local pressure coefficient azimuthal

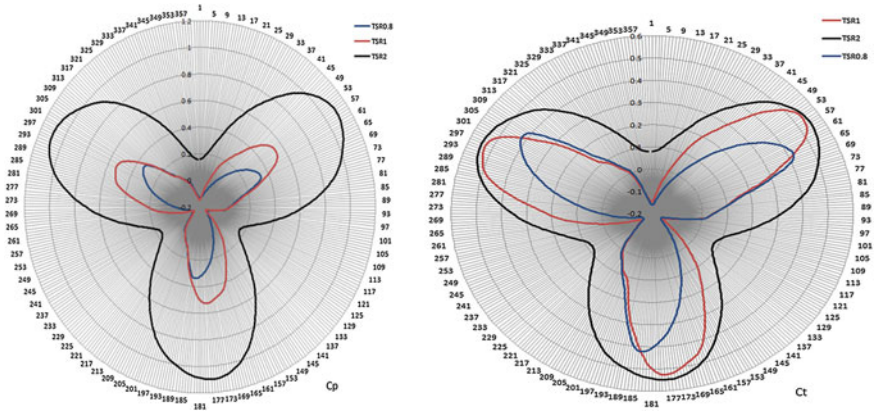

Fig. 35.9 Power Coefficient as function of TSR for the blade sections

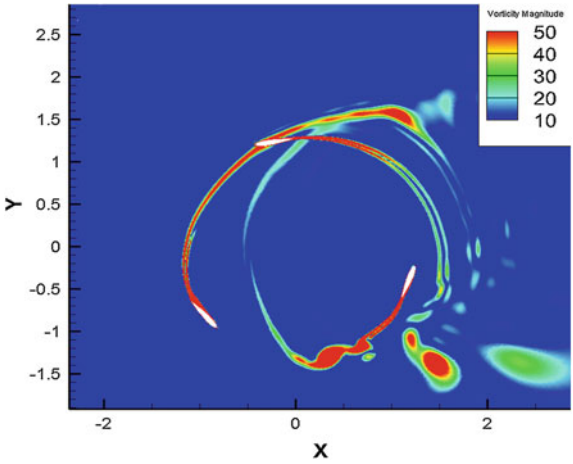

Fig. 35.10 Instantaneous torque and power coefficients of NACA 0015 airfoil at different speed ratios

position, this phenomenon could be considered the main reason responsible for the local increase of the instantaneous power coefficient. This hypothesis is not verified for the present work and should be further investigated.

35.7 Conclusions

A small scale model of straight-bladed vertical axis wind turbine with a solidity of 0.98 and different airfoil profiles have been developed and investigated using Computed Fluid Dynamics (CFD) in order to obtain the best possible performance

measured by power Coefficient (Cp) curve for low TSR. Numerical predictions have been compared with previous tunnel test result obtained from a NACA 0015 based rotor. Among the tested four airfoil profiles NACA 0015 was the best performing airfoil with a maximum power coefficient of 0.5345. It has a relative increase of 4.53 % in performance when compared to NACA 0018. As the value of tip speed ratio (λ) increases the S-1046 gives a better performance than the NACA 0015 of approximately 15.12 %. This is an indication that S-1046 is best suitable for high TSR turbines. The 2D simulations showed a significantly increased in performance compared to the 3D simulations. The overall difference between the predicted 2D performance and the experimental and 3D CFD results is believed to be caused by the fact that the 2D CFD simulation does not include the effects of the tip vortices present on the real turbine and the 3D simulations. Nevertheless it show generally the same trend as experiments and 3D simulations, this allows the use of 2D results in combination with models to compensate for 3D effects in order to analyze VAWT.

Acknowledgments Masdar institute is highly acknowledged for their financial support to this project.

References

1. S. Bahaj, L. Myers, P.A.B. James, Urban energy generation: influence of micro-wind turbine output on electricity consumption in buildings. Energy Build. **39**(2), 154–165 (2007)
2. M. dwards, Wind Turbine Blade having Curved Camber and Method of Manufacturing same, US Patent 0256795 A1, 2008
3. N.C. Batista, R. Melício, J.C.O. Matias, J.P.S. Catalão, Self-start performance evaluation in darrieus-type vertical axis wind turbines: Methodology and computational tool applied to symmetrical airfoils (2010),http://www.icrepq.com/icrepq'11/302-batista.pdf. Accessed 20 May 2014
4. Paraschivoiu, Wind turbine design with emphasis on darrieus concept, 1st ed. (Canada, Polytechnic International Press, 2002) Chap. 6
5. C.J.S. Ferreira, H. Bijl, G. Van Bussel, G. Van Kuik, Simulating Dynamic Stall in a 2D VAWT: Modeling strategy, verification and validation with Particle Image Velocimetry data. J. Phys Conf. Ser. **75**, 012023 (2007)
6. S. Wang, D.B. Ingham, L. Ma, M. Pourkashanian, Z. Tao, Numerical investigations on dynamic stall of low Reynolds number flow around oscillating airfoils. Comput. Fluids **39**(9), 1529–1541 (2010)
7. M.C. Claessens, Masters thesis: the design and testing of airfoils for application in small vertical axis wind turbines (2006)
8. G.J.W. Van Bussel, S. Mertens, TURBY ®: concept and realisation of a small VAWT for the built environment, pp. 509–516 (2004)
9. M.H. Mohamed, Performance investigation of H-rotor Darrieus turbine with new airfoil shapes. Energy **47**(1), 522–530 (2012)
10. R. Bravo, S. Tullis, S. Ziada, Performance testing of a small vertical-axis wind turbine, 2007. http://www.eng.mcmaster.ca/stullis/index_files/bravocancam2007.pdf. Accessed 25 May 2014
11. I. Janajreh, I. Talab, J. Macpherson, Numerical simulation of tower rotor interaction for downwind wind turbine. Model. Simul. Eng. **2010**, 1–11 (2010)

12. S.M. Salim, S.C. Cheah, Wall y + strategy for dealing with wall-bounded turbulent flows, in Proceedings of the International MultiConference of Engineers and Computer Scientists, 2009, vol. II
13. H. Beri, Double multiple streamtube model and numerical analysis of vertical axis wind turbine. Energy Power Eng. **03**(03), 262–270 (2011)
14. M. Raciti Castelli, A. Englaro, E. Benini, The Darrieus wind turbine: proposal for a new performance prediction model based on CFD. Energy **36**(8), 4919–4934 (2011)
15. J.M. Jonkman, Modeling of the UAE wind turbine for refinement of FAST _ AD, National Renewable Energy Laboratory, 2003. http://www.nrel.gov/docs/fy04osti/34755.pdf. Accessed 20 May 2014

Chapter 36
Sodar (SOnic Detection and Ranging) Measurement Campaign: Case Study

Hatem Yazidi

Abstract The evolution of large wind turbines (multi-megawatt) has resulted in a significant increase in rotor sizes and hub heights. The wind regime should therefore be measured at larger distances from the surface. Commonly the wind speed is measured using cup anemometers that are mounted on a meteorological mast (Met mast). The increasing cost of Met mast erection to measured wind speed above 60 m, and the demand for more detailed knowledge about the wind profile characterising the lower Atmospheric Boundary Layer (ABL) has made the use of remote sensing techniques an attractive alternative [3]. In this paper wind characteristics measured by the Sodar from 30 to 140 m with a 5 m vertical resolution will be explored. The Sodar wind data is compared with Met tower concurrent heights to evaluate the wind potential at the Sodar site. The results show that the Sodar location is approximately 20 % less windy than the Met tower location.

Keywords Surface wind · Wind energy · Remote sensing · Wind shear

36.1 Introduction

The Sodar is a remote sensing instrument that measures the wind characteristics of the local ABL [4, 5, 8]. The Sodar principle is based on sound beam propagation. A sound beam is generated at a certain frequency by a loud speaker array and the electronic control tilts the sound pulse in different directions. The pulse propagates through the air and a small fraction of its energy is scattered back by small scale temperature inhomogeneities. The difference between the transmitted frequency

H. Yazidi (✉)
Caledonian Centre for Scientific Research, Caledonian College of Engineering, Muscat, Sultanate of Oman
e-mail: hatem@caledonian.edu.om; hatem.yazidi@gmail.com

M. O. Hamdan et al. (eds.), *ICREGA'14 - Renewable Energy: Generation and Applications*, Springer Proceedings in Energy, DOI: 10.1007/978-3-319-05708-8_36,

and the backscattered frequency (Doppler shift) is directly proportional to the radial wind velocity along the acoustic beam axis [1].

Simple trigonometric expressions are used to compute the horizontal and vertical velocities from the radial components [6].

The objective of this Sodar campaign is to collect wind data samples to validate the Sodar location wind speeds and wind shear up to a hypothetic wind turbine hub height of 80 m by comparing the Sodar data against data from a nearby meteorological tower.

36.2 Methodology

Sodar (SOnic Detection and Ranging) measurement campaigns were conducted in a remote area. The campaign examined wind speed, direction and shear characteristics of the local lower Atmospheric Boundary Layer (ABL) from 30 to 140 m above ground level. The campaign duration was 12 days, started on **July 14th, 2006** and ended on **July 26th, 2006**. The Sodar data were compared to the meteorological mast located about 3.5 km away from the Sodar site. A short conventional meteorological mast with a cup anemometer was permanently installed next to the Sodar for its calibration. This is necessary for Sodar accurate measurements. Data considered in the comparison were at the same measurement heights. Met tower data was quality controlled to ensure that observed differences between tower and SODAR coincidental measurements were valid [7]. Thus, before the Sodar and Met tower data were compared, time intervals noted as being of poor quality for either the Sodar or Met tower were removed. Also, ten minute average Sodar wind speeds that deviated considerably from the expected ten minute average wind speeds were removed. A considerable deviation was determined by the relative difference[1] between the Sodar and reference tower wind speed distribution. Data that exceeded the mean relative difference by plus or minus two standard deviations were removed [2]. The above methodology assumes that, even though the Sodar and tower are two different instruments, if the Sodar is installed near a meteorological tower they should have similar temporal wind speed variations and averages.

Once the above steps were completed, the Sodar and tower data were compared statistically and visually. Specifically, the Sodar and tower wind speed averages and wind shears (e.g., 80/60 and 60/40) were compared. Correlation statistics, such as linear least squares regression method, were also computed.

The recovery rates are presented in the Table 36.1 at heights comparable to Meteorological mast measurement heights.

[1] The relative difference between the Sodar and tower wind speed is expressed as $\left\{\left[\frac{(U_{tower}-U_{SODAR})}{U_{tower}}\right]\times 100\right\}$, where U is the mean wind speed.

Table 36.1 SODAR recovery rate

Height (m)	Recovery rate (%)
80	~60
50	~50
40	~50
30	~45

The low recovery rates were due to maintenance (powering the Sodar electrical system), precipitation, strong wind shear events and fixed echoes caused by the surrounding trees.

36.3 Results and Discussions

The Sodar derived wind speed is approximately 18 % lower at 80 m, 20 % lower at 60 m and 21 % lower at 30 m than the tower derived wind speed (see Table 36.2). The correlation plots between wind speeds at each of the three measurements heights between the Sodar and the Met tower are presented on Fig. 36.1. The coefficients of determination were greater than 0.85 for all heights. At the campaign site, both the Sodar and the tower measured wind speeds increased with height and ranged from 4.94 m/s at 50 m to 5.51 m/s at 80 m and from 6.26 to 6.69 m/s, respectively (see Table 36.2).

It is important here to mention that Table 36.2 wind speed values are based only on data that is coincident between Sodar and Met tower. They are not appropriate for use for shear derivations.

36.3.1 Wind Speed

The measured Sodar and tower wind speed distributions show a slight shift in favor of the tower distribution indicating that the tower site is windier than the Sodar site (Fig. 36.2). This is confirmed by the wind speed roses (Fig. 36.3) where the tower had a significantly higher wind speed in each sector than the Sodar.

All parameters indicate that the wind speed measured at the Sodar site is significantly lower than at the mast site. The difference is proven to be affected by the distance effect and the local topography [2]. The Sodar and towers are not collocated, but have a spatial separation of about 3.5 km, with terrain irregularities in between that can affect the wind flow. Also, the meteorological tower is located on the top of a small ridge (638 m height) and there is no trees surrounding the tower area, which contributes to significant wind speed acceleration comparatively to the Sodar spot which is on plateau at a lower elevation (513 m).

Table 36.2 Sodar average wind speed

Height (m)	No. of valid coincident data point	Sodar average wind speed (m/s)	Tower average wind speed (m/s)	Difference between Sodar and met tower (%)	R^2
80	916	5.51 ± 0.33	6.69 ± 0.16	~−18	0.89
60	888	5.16 ± 0.30	6.39 ± 0.15	~−20	0.88
50	806	4.94 ± 0.29	6.26 ± 0.15	~−21	0.87

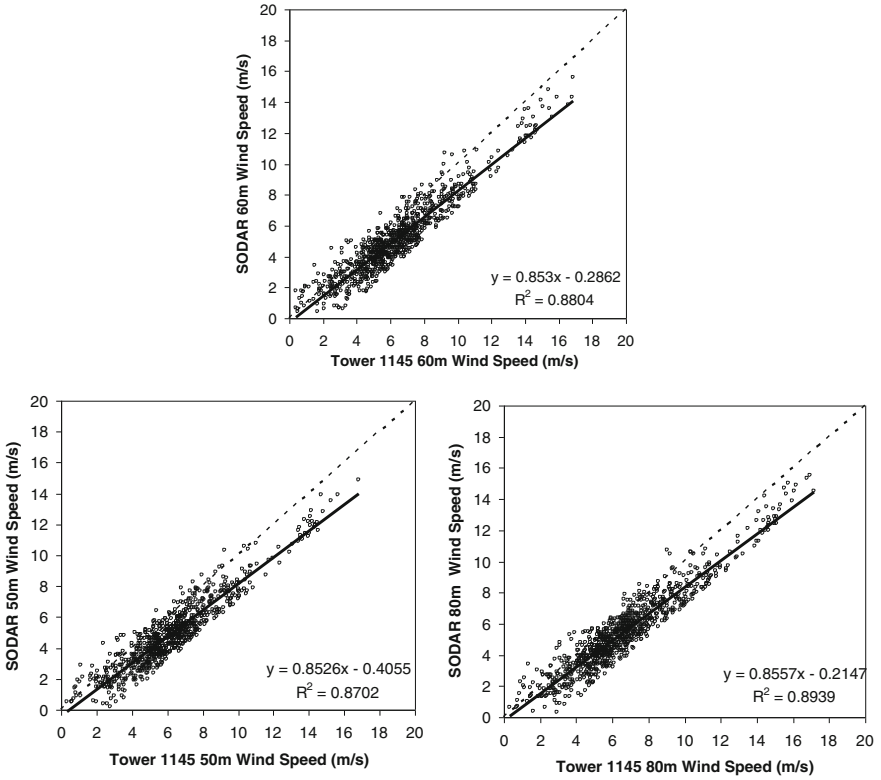

Fig. 36.1 Scatter plots of 10 min average SODAR versus met tower wind speeds. Figures include all quality controlled data. The *dashed line* is a 1:1 line

36.3.2 Wind Shear

Due to the short period of analysis, the following results should be examined with diligence. The wind shear is determined from the power law formula by applying it to wind speed measurements (Table 36.3).

The wind shear is verified by plotting the Sodar wind speed profile and comparing it with the measured tower profile (Fig. 36.4).

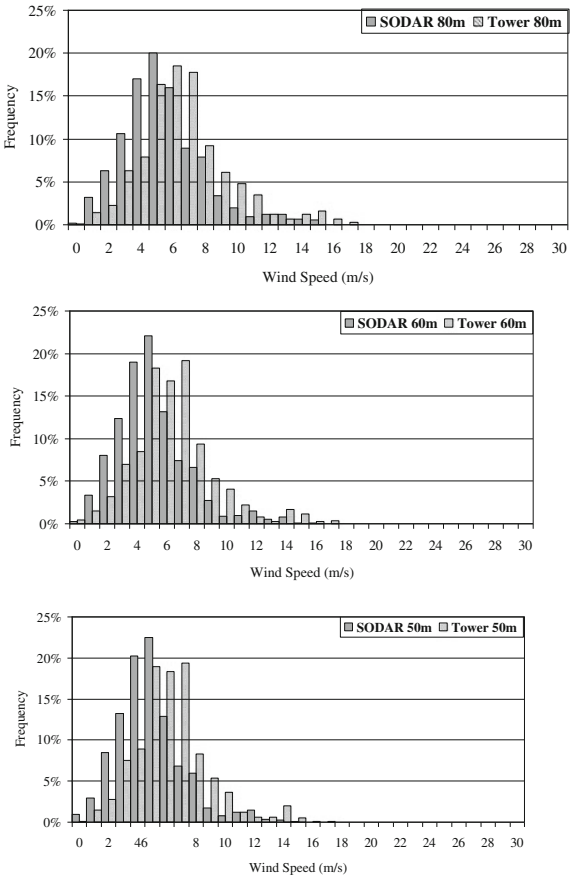

Fig. 36.2 Sodar versus met tower wind speed distributions

The wind shears calculated from the power law formula appear significantly higher at the Sodar location than at the tower location (0.26 vs. 0.14). This result is confirmed by the profile plots, where it can be seen that the average slope is greater for the Sodar profile than for the tower profile in the 50–80 m range.

The acceleration effect at the top of the ridge where Met tower is located may be the cause of the more vertical profile at the Met tower site, since acceleration is usually greater close to the ground and decreases with height [8]. However, more measurement heights at Met tower location would be required to validate that the wind profile is due to the acceleration effect.

The Sodar wind speed profile present in the Fig. 36.4 is based on the equivalent of 7 days of Sodar qualified data. The profile represents the average of all instances where valid data is available at all measurement heights. It is compared to the tower profile, which is based on the measured data of Table 36.2.

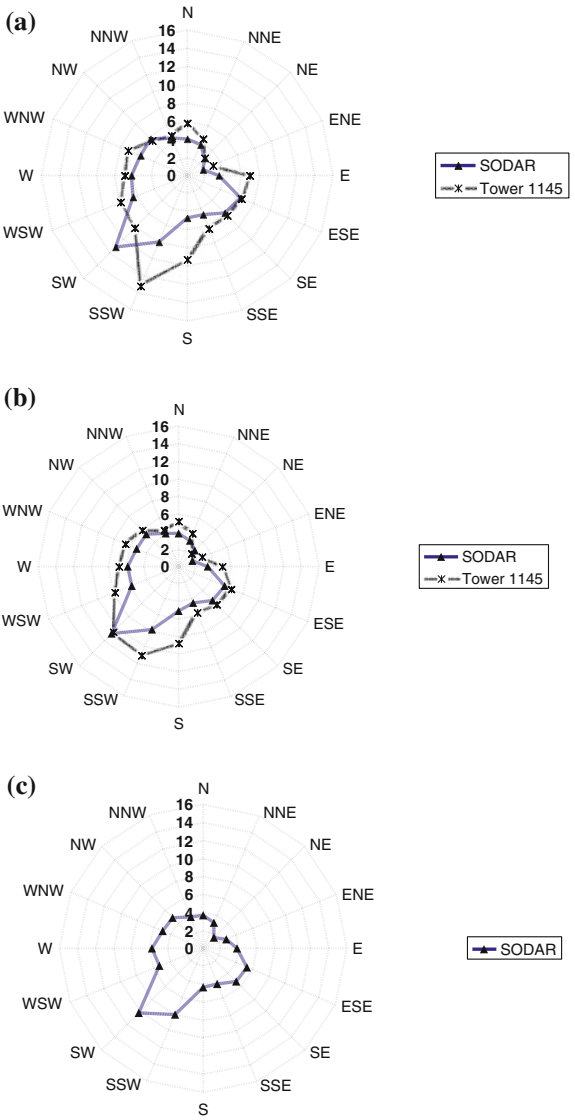

Fig. 36.3 Sodar and met tower average wind speeds by direction: **a** 80 m, **b** 60 m, **c** 50 m (no tower wind vane at this *height*). Only sectors with a significant number of points are plotted

Table 36.3 Wind shears

Met tower measured wind speed at 80 m (m/s)	Sodar measured wind speed at 80 m (m/s)	Sodar 60/80 shear	Met tower 60/80 shear
6.69	5.51	0.26	0.14

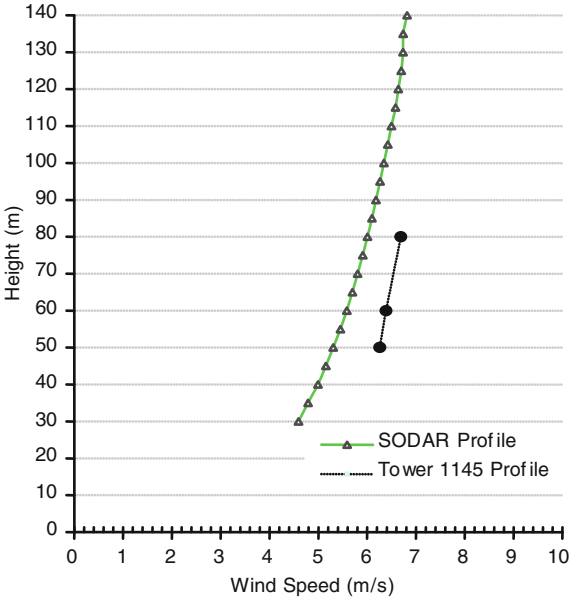

Fig. 36.4 Sodar and met tower average wind speed profiles—all directions and all speeds are included

36.4 Conclusion

The short-term analyses of wind performed during this measurement campaigns with a Sodar indicates that the Sodar location is less windy than the Met tower location. This happened for a period of 12 days (campaign duration). The Sodar derived wind speed is approximately 18 % lower at 80 m, 20 % lower at 60 m and 21 % lower at 30 m than the Met tower derived wind speed.

During the short period of concurrent data collection between Sodar and Met tower, qualified measurements were populated by winds coming from the W to NNW and ESE to SSE sectors (wind roses not displayed).

Wind shear calculations and wind profile plots indicate that the wind shear was significantly higher at the Sodar location than at the tower site for the period, with an 80/60 m wind shear exponent of 0.26 for the Sodar and 0.14 for the tower.

Differences in wind speeds and wind shear may be due to the topography in between the Sodar and tower locations, together with the local topography at each site, the tower being at the top of a ridge and the Sodar on a lower plateau.

However, given the short campaign period, it is difficult to draw conclusions from all these results for long term values.

References

1. G.H. Crescenti, A look back on two decades of doppler sodar comparison studies. Bull. Am. Meteorol. Soc. **78**, 651–673 (1997)
2. R.E. Erickson, J.M. Harlin, *Geographic measurement and quantitative analysis* (Maxwell Macmillan Canada, Toronto, 1994)
3. J.C. Kaimal, H.N. Baynton, J.E. Gaynor (eds.), The Boulder low-level intercomparison experiment. BAO rep. 2, Wave Propagation Laboratory, NOAA/ERL, (1980) 189 pp. (Available from National Technical Information Service, 5285 port Royal Road, Springfield, VA 22161)
4. J.R. Kurzeja, Comparison of a Doppler sodar with bivanes and cup anemometers. J. Atmos. Oceanic Technol. **11**, 192–199 (1993)
5. B.P. MacCready, Mean wind speed measurements in turbulence. J. appl. Meteorol. **5**, 219–225 (1966)
6. K. Moore, B. Bailey, Roughness lengths in complex terrain derived from SODAR wind profiles. in *Paper Presented at the 16th Conference on Boundary Layers and Turbulence*, Portland, American Meteorological Society (2004)
7. T.F. Pedersen, Å. Dahlberg, P. Busche, ACCUWIND—classification of five cup anemometers according to IEC61400-12-1. Riso National Laboratory, Riso-R-1558(EN). ISBN 87-550-3516-7 (2006)
8. B.R. Stull, *An introduction to Boundary Layer Meteorology. Atmospheric Sciences Library* (Kluwer Academic Publishers, Dordrecht, 1988)

Chapter 37
Energy Recovery from Low Speed Winds

Janesh Mohanan and Mutasim Nour

Abstract This paper presents a renewable energy model which combines the concepts of wind pumps, pumped hydro and micro hydroelectricity. The proposed model recovers energy from low speed winds and eliminates the requirement of energy storage in batteries or grid connection. After establishing the suitability of the model theoretically, workable models are visualized using commercially available components. Two designs based on this model are studied for their performance, and resultant data has been critically analyzed to establish the trend and their commercial feasibility. One of the two designs studied is a standalone tower that can feed a house or a small villa, which also can be installed at any point of need. The second design is building integrated where the system components are mounted on a building. Theoretical findings are validated by simulating through software, MATLAB. The obtained results showed the superiority of the proposed model over the conventional three blade wind turbines for wind speed less than 6 m/s.

Keywords Wind pumps · Pumped hydro storage · Micro hydroelectricity

37.1 Introduction

Last few decades witnessed unprecedented efforts to diversify energy sources all across the globe, partly due to the huge surge in energy demand from outside Organization for Economic Co-operation and Development (OECD) countries and partly due to global efforts to reduce dependency on fossil fuels and thereby offset

J. Mohanan (✉) · M. Nour
Heriot Watt University, Dubai Campus, Dubai, United Arab Emirates
e-mail: janeshnm@gmail.com

M. Nour
e-mail: mutasim.nour@hw.ac.uk

M. O. Hamdan et al. (eds.), *ICREGA'14 - Renewable Energy: Generation and Applications*, Springer Proceedings in Energy, DOI: 10.1007/978-3-319-05708-8_37,

the Greenhouse Gas (GHG) emissions levels. Renewable energy has been the focus of such efforts. If we consider fossil fuels as stockpiles of energy, then renewables are streams, but the flow depends on many uncertainties like location, season, hour of the day, day of the year and many local conditions. It is a huge challenge how to produce a reliable flow of electricity, heat or steam from an unpredictable source like solar or wind, that too at the time of need. There are many working energy models, based on solar and wind, in the market that extracts energy from these sources, but their reliability heavily depends on energy storage in batteries or grid connection [1–3].

Around the world, wind energy has been one of the fastest growing areas in the field of renewable energy during the last decade [3]. Wind energy is a matured technology today and wind farms with energy storage or grid connection exists across different countries. Modern wind energy systems are based on wind turbines confined to certain selected locations, as the speed of the wind is the main criterion for their site selection. Modern wind turbines has a typical cut-in wind speed of 3.5 m/s and operates at their rated capacity between wind speeds of 12 and 25 m/s. Most such locations are either offshore or away from load centers. If we examine global wind speed distribution at 50 m, most part of the world possesses average wind speeds of 4–5 m/s, which is not sufficient to operate a wind turbine economically.

There are ample evidences to prove that men at very early days of civilization have made attempts to harness wind energy for water pumping [4]. Even today, wind power is used for water pumping in rural areas, mainly in third world countries. A wind based water pump operates on a wind mill based system, which rotates at considerably lower speeds compared to that of a wind turbine. Modern Wind mills have a cut in wind speed of about 1.6 m/s and starts pumping water at wind speeds of 2.0 m/s.

Modern wind pumps are broadly classified into reciprocating pumps (piston pumps) and rotary pumps based on their pumping mechanism. The water delivered by a piston pump is in linear proportion to the wind velocity ($Q \propto V$), and that of a rotary pump is proportional to the third power of the wind velocity ($Q \propto V^3$) [2, 5], where V is the wind velocity (m/s) and Q is the quantity of water pumped in liters per second (lps).

A simple comparison of pump operating ranges, as shown in Fig. 37.1 [6], establishes the superiority of rotary pumps for low head high water delivery applications [5, 7, 8]. For high head applications the choice is piston pumps but at a reduced water output.

This paper is part of ongoing efforts to develop localized solutions for energy needs, making use of locally available renewable resources and environmentally friendly technologies. However this paper is limited to energy recovery from low speed winds using wind pumps, by combining the concepts of ‘wind pumps’, ‘pumped hydro’ and ‘micro hydroelectricity’.

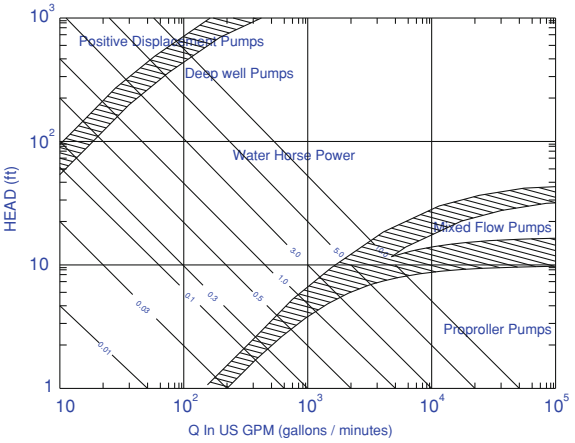

Fig. 37.1 Pump operating range [6]

37.2 Concept

The proposed concept of wind driven pumped micro hydroelectricity in this research work is illustrated in Fig. 37.2. A set of wind driven wind pumps, lifts water from a lower reservoir to an elevated upper reservoir. Water from the elevated reservoir flows down by the act of gravity and drives a hydro turbine-generator set. Discharged water from the turbine-generator unit is collected in a lower reservoir. Wind pumps, re-circulate this water to the upper reservoir and completes the cycle.

Thus combining the concepts of wind pumps, pumped storage and micro hydroelectricity can establish a reliable model for extracting energy from wind. This model also eliminates the need for batteries, inverters, converters and their associated energy losses and costs.

37.3 Data Analysis

37.3.1 Wind Data

Wind speeds measured at 10 m height from the ground level are usually available from local metrology department as standard wind data. However actual wind speed at hub height differs from this data with respect to height of hub and surface roughness of the area. Hence standard wind velocities are converted to actual hub height velocities and corrected for surface roughness.

Wind velocity is corrected to hub height using the following logarithmic relation (37.1) [9].

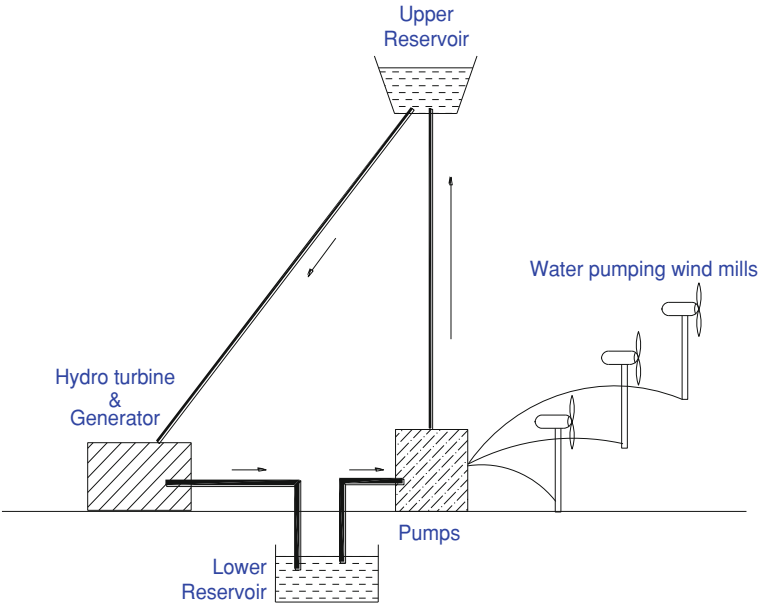

Fig. 37.2 The concept of wind driven pumped micro hydro electricity

$$U_Z = U_R \left(\frac{\ln\left(Z/Z_o\right)}{\ln\left(Z_o/Z_R\right)} \right) \tag{37.1}$$

where, Z: Hub height (m); Z_R: Reference height (m); U_R: Wind velocity at reference height (m/s); U_Z: Wind velocity at hub height (m/s); Z_0: Surface roughness factor (mm). For surfaces with trees and some buildings, surface roughness value of 300 mm has been used [9] in this study.

37.3.2 Water Pumping Data

Water pumped, Q (lps) by a piston type wind pump depends on wind speed, delivery head and design parameters of the pump. Since the design of the piston, stroke length and leak-hole mechanism vary from manufacturer to manufacturer, pumped water quantity also vary from manufacturer to manufacturer for similar wind conditions and rotor diameter.

Hence every manufacturer has their product specific data for water delivery at different wind speeds. In this study, water discharges at varies heads and wind speeds were calculated using M/s Ironman's on line calculator (assuming a 6 m diameter rotor) [10].

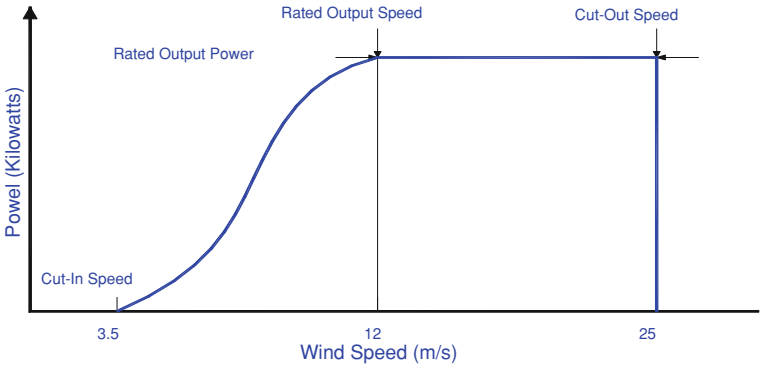

Fig. 37.3 General characteristics of a wind turbine [11]

37.3.3 Technical Data Analysis

Energy available in wind can be extracted using a wind turbine. The general characteristics of a wind turbine are shown in Fig. 37.3. Wind turbine starts rotating at cut-in wind speeds of 3.5 m/s. Any useful power is generated only beyond wind speeds of 5 m/s [11] and turbine attains its rated power at wind speed of 12 m/s. Beyond that, turbines operate at their rated power until wind speeds of 25 m/s. After 25 m/s of wind speeds, turbine is turned off to prevent mechanical damages to the rotor.

A wind pump driven by a wind mill starts rotating at a wind speed as low as 1.6 m/s. This is achieved by specially designed piston valves for the pumps, which opens and facilitates effort less movement of the piston at lower wind speeds. Once started, piston valve closes and pump starts pumping of water at wind speeds of about 2.0 m/s. Figure 37.4 shows the characteristics of a typical wind driven piston pump [12].

37.3.4 Global Wind Data

If you examine the 'Global Annual 50 m Wind speed' given in Fig. 37.5 [13], it can be noted that only a few locations on this globe possess annual average wind speeds of 12 m/s, where a wind turbine can operate at its rated power. However most of the regions on this globe possess wind speeds up to 5.0 m/s. Thus most prevailing wind speeds on this globe are less than 5.0 m/s, which is not sufficient for a wind turbine to operate and deliver any useful power.

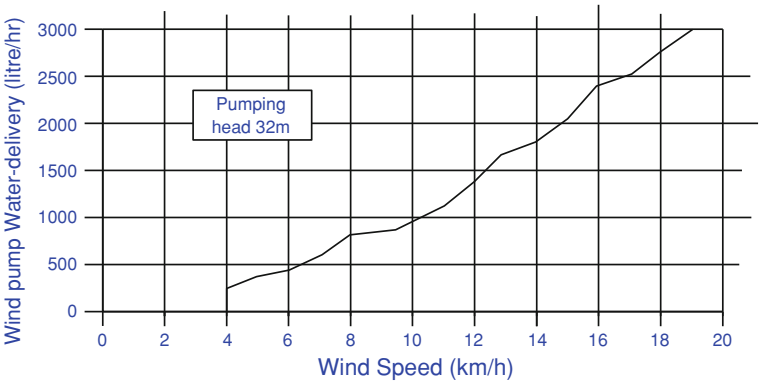

Fig. 37.4 Characteristics of a wind driven piston pump [12]

37.3.5 Power Available in Wind

Theoretical power in wind can be computed using the following formula (37.2).

$$P = \frac{1}{2}\rho A V^3 \tag{37.2}$$

where, P is the power output (kW), ρ is the density of air (kg/m^3), A is the area swept by the rotor blades (m^2) and V is the wind velocity (m/s).

However all these power cannot be extracted practically. The theoretical maximum power that can be extracted from wind is limited by betz limit (59 %). This is because any wind power device can be considered as a semi-permitting wall that offers resistance to the wind flow. As a consequence, not all incoming wind passes through the wind power device (wind mill rotor), but a portion goes around it. Even though theoretical limit is 59 %, practically achievable values are around 35–40 % only.

Theoretical power in wind is calculated using Eq. (37.2) at betz limits and is plotted under Fig. 37.6. However actual power that can be recovered from low speed winds using a wind turbine is much less than that is theoretically recoverable. This is since the wind turbine, which is designed to operate at its best efficiency point near rated power (wind speeds over and above 12 m/s), will be operating at part rated powers at lower wind speeds. Remember the power generated is proportional to the third power of wind speed (P ∝ V^3).

Figure 37.7 illustrates the typical turbine characteristics at different wind speeds [14]. It may be noted that the wind turbine reaches its best efficiency point of 74 % at a wind speed of 12 m/s. For lower wind speeds, the efficiency drops drastically, to 38 % at wind speed of 9.6 m/s and 15 % at wind speed of 6 m/s. It may be further noted that at lower wind speeds like 5 m/s, which is the most predominant wind speed of this globe, wind turbines deliver less that 15 % of the extractable power from wind.

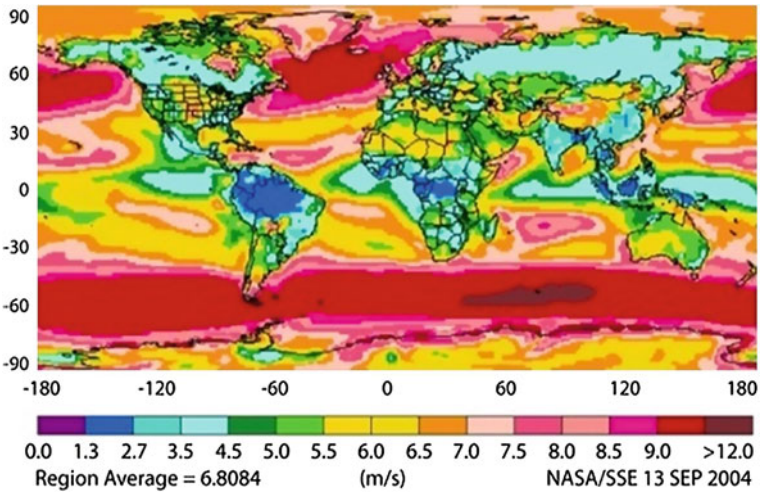

Fig. 37.5 Global Annual 50 m Wind speed [13]

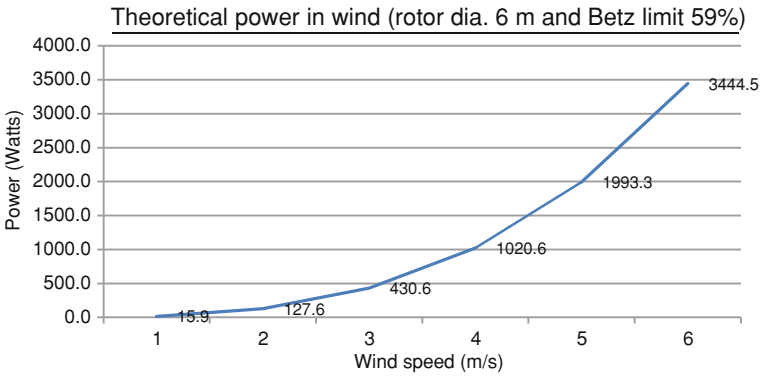

Fig. 37.6 Theoretical power that is present in wind

37.3.6 Water Discharge by Wind Pumps

Water pumping data for the wind mill operated water pump is calculated using online simulation software provided by the manufacturer M/s Ironman wind mill company, USA [10]. This software calculates the quantity of water pumped to any given head under three different ranges of wind conditions namely, light wind (1.6–4.5 m/s), medium winds (4.5–7.0 m/s) and strong winds (above 7.0 m/s) for the selected rotor diameter.

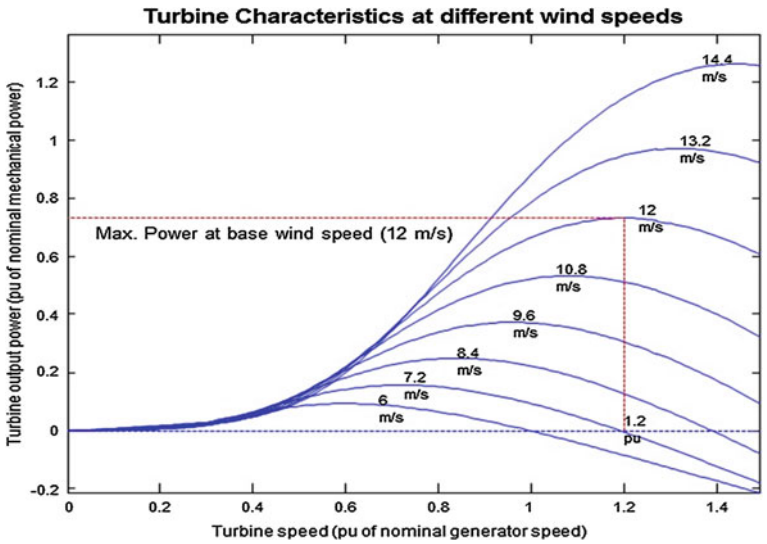

Fig. 37.7 Typical turbine characteristics at different wind speeds [14]

Critically analyzing the water delivery data (6 m diameter rotor assumed), an empirical relation can be derived between quantity of water and delivery head at a given wind speed as given in Eq. (37.3).

$$Q = kh^{-1.193} \tag{37.3}$$

where, **Q** is the water delivered by wind pump (lps) and **h** is the delivery head (m). Values of k depend on wind speed. For light, medium and strong winds, values of k are respectively 41.361, 91.001 and 165.38 for the wind mill considered.

Similarly, for a given discharge head, Q varies empirically with wind speed as follows.

$$Q = a * v + b \tag{37.4}$$

where, **v** is the velocity of wind (m/s), a and b are constants for a given wind mill.

37.3.7 Power Stored in the Pumped Water

Hydraulic power stored in pumped water is calculated from the fundamental relation,

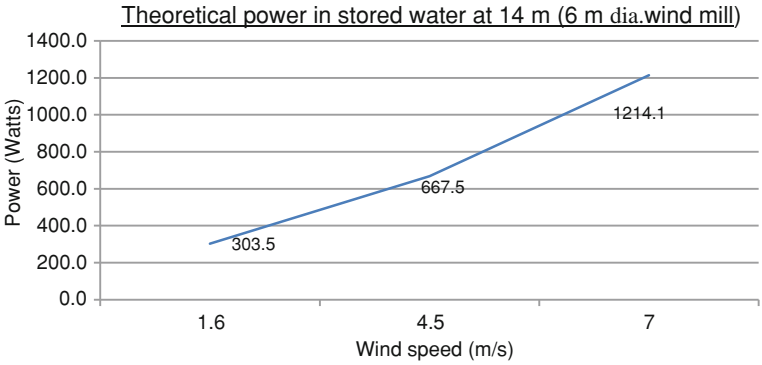

Fig. 37.8 Theoretical power in water that is pumped and stored

$$P = mgh \tag{37.5}$$

where, P is the power (kW), m is the mass (kg), g is the acceleration due to gravity (m/s^2) and h is the head (m).

When power is generated from the continuous flow of water from an elevated tank, Eq. (37.5) can be re-written as follows.

$$P = \rho ghQ \tag{37.6}$$

where, Q is the flow rate (m^3/s) and ρ is the density of water (kg/m^3).

37.3.8 Power Extracted from Stored Water

Useful energy that can be extracted from stored water is limited by the frictional losses in the penstock pipe, mechanical losses in the water turbine and mechanical and electrical losses in the electrical generator. Typical efficiency of the system will be around 80 % considering 5 % losses in pipe, 10 % losses in water turbine and 5 % losses in electrical generator. Figure 37.8 shows the theoretical power available in water that is pumped and stored at different wind speeds.

37.4 Design of Wind Pump Based Energy Models

In the following designs, locations of the wind mills are carefully selected in such a way that it is at least 50 m away from any obstructions and each other. Further it is ensured that the windmill rotors are placed at least 6 m higher than the top of the trees or structures around. The respective windmills are placed directly above the

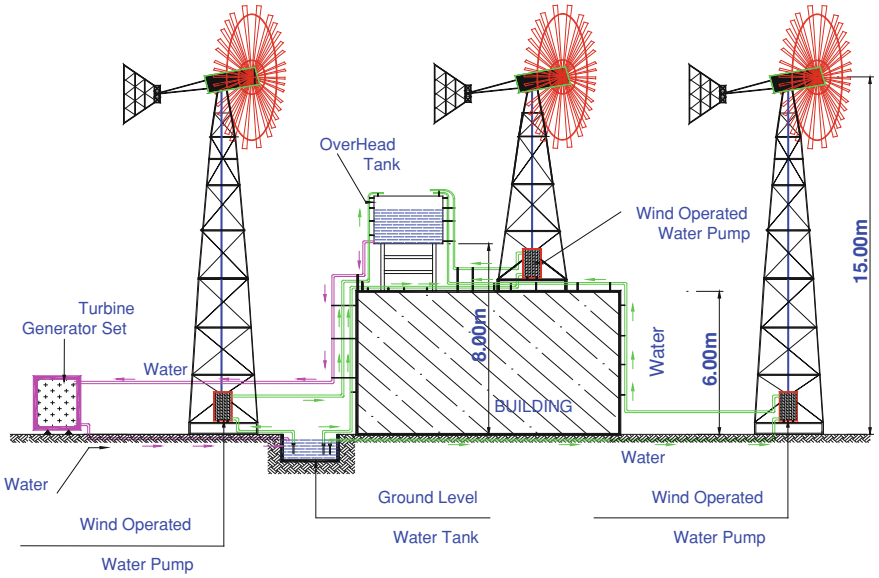

Fig. 37.9 Building integrated design with three wind mills

water pump, so that the pump is driven through a vertical shaft running through the center of the tripod structure. The pump is housed within the base of the respective tripod structure.

37.4.1 Building Integrated Design with Three Wind Mills

As illustrated in Fig. 37.9, a 6 m tall building is fed by micro hydro turbine generator installed on the ground. A water tank feeding the hydro turbine is placed on a 2 m tall structure standing on top of the building.

Three wind driven water pumps are continuously pumping water into an elevated water tank from a ground level water tank. Water leaving the water turbine is returned back to the ground level water tank. One wind mill is placed on a 9 m tall tripod structure standing on top of the building and the others two are standing on the ground on a 15 m tall tripod structure. Thus the hub heights of all the wind mills are 15 m above the ground.

Based on this design, head available to the turbine generator is 8 m with a flow rate of 25.29 lps at a hub height wind velocity of 5.4 m/s.

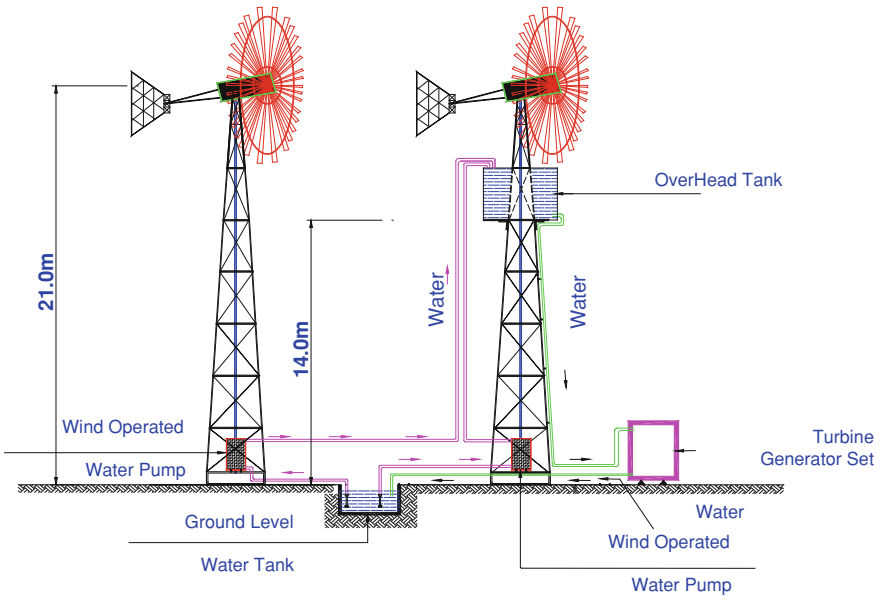

Fig. 37.10 Standalone tower design with two wind mills

37.4.2 Standalone Tower Design with Two Wind Mills

In this design, as illustrated in Fig. 37.10 the towers are designed for generating reliable electricity where ever it is needed. A micro hydro turbine generator is installed on the ground, along with two towers, that carry the wind mills.

A water tank feeding the hydro turbine is place on one of the two towers at a height of 14 m from the ground level. Two wind mill driven water pumps are continuously feeding in water to the elevated tank placed on the tower. Water leaving the water turbine is returned back to the ground level water tank. The wind mills are placed on top of two 21 m tall tripod structure standing on the ground. Thus the hub height is 21 m above the ground.

Based on this design, head available to the turbine generator is 14 m with a flow rate of 9.72 lps at a hub height wind speed of 5.82 m/s.

If this design, shown in Fig. 37.10, is operated with a wind speed of 6.0 m/s at reference height (hub height wind speed of 7.27 m/s), then the head available to the turbine generator will be 14 m and flow rate available will be 17.68 lps.

37.5 Analysis of Wind Pump Based Energy Models

Designs with different hub heights of the wind mill, actually results in different wind velocities, as wind velocity varies with height from ground level. Similarly elevation of water tank determines the head available to the hydro turbine. Thus an increase of hub height results in better wind speeds and better water pumping output, but will increase capital cost on account of tower height and pump rod length. Similarly, an increase in tank height will results in better heads, but reduced water pumping output. Capital cost will also increase on account of tower height. Thus each design variations involve varying a set of interrelated parameters.

A wind pump for electricity production is not an area that is explored and commercialized yet. As a consequence, we do not have suitable turbines available in commercial market for all the head and flow combinations that we may arrive at. This often result in compromising to the nearest available turbines, and poor exploitation of the available potential. In some of the design options that were considered for this study, there were no suitable turbines available in the commercial market.

37.5.1 Analysis of Building Integrated Design with Three Wind Mills

As we have seen earlier, in this design, a flow of 25.29 lps and a head of 8 m could be achieved with a theoretical power potential of 1984.8 W. A combination of two hydro turbines suitable for a combined rated flow of 25 lps and 8 m head were selected from commercial market. With these turbines, this design can generate 1,850 W from the theoretically available power of 1984.8 W. Thus 93 % of the available power could be recovered in this case study. This could be made possible, as two water turbines that could utilize almost entire flow and head were available in the commercial market.

It may be noted that if three equivalent sized (6 m diameter) wind turbines were used, the output power could be just 1193.8 W (assuming a maximum practically attainable betz limit of 35 % [15] and a highly optimistic partial load efficiency of 50 %, for the wind turbines, at 5.35 m/s wind speed) which is lower than the 1,850 W extractable using wind pumps. At 5.36 m/s wind speed, a wind pump based power system outperforms conventional wind turbine based power systems. Simple payback period for this design is 9 years.

37.5.2 Analysis of Standalone Tower Design with Two Wind Mills

In this design, a flow of 9.72 lps at a head of 14 m could be achieved with a theoretical power potential of 1334.9 W. However since a hydro turbine for this head flow combination is not available in the commercial market, two numbers of nearest turbine available with rated flow of 5 lps each at a head of 13 m was used for this study. With these available turbines, this design generates 1,000 W from the theoretically available power of 1334.9 W (74.9 %). This difference is apparently due to the fact that there is no suitable hydro turbine available in the commercial market, which can make use of the complete available head of 14 m.

It may be noted that if two equivalent size wind turbine were used, the output power could be 1019.4 W (assuming a maximum practically attainable betz limit of 35 % [15] and a highly optimistic partial load efficiency of 50 %, for wind turbine) which is lower than the 1,200 W extractable using wind pump, if suitable turbines are available. It may be noted that at wind speed of 5.82 m/s, conventional wind turbines nearly catches up with wind pump based designs. Simple payback period for this design is 12.4 years. This poor payback period is due to the fact that only 74.9 % of the available power is utilized in this design as a suitable hydro turbine is not available in commercial market.

Alternatively, if this design is operated at a wind speed of 6 m/s (reference height), a flow of 17.68 lps at a head of 14 m could be achieved with a theoretical power potential of 2428.6 W. However a suitable Pico hydro turbine for this head flow combination is not available in the commercial market. Therefore the nearest turbine available with rated flow of 15 lps and head of 14 m was used for this evaluation. With this turbine, this design generates 1,500 W from the theoretically available power of 2428.6 W (61.8 %). This difference is due to the fact that there are no suitable Pico hydro turbines available in the commercial market, which can utilize the complete available flow of 17.68 lps. Simple payback period with this available turbine would be 7.9 years, as this turbine is capable of converting just 61.8 % of the available power. If a suitable Pico hydro turbine, that can accommodate the available flow of 17.68 lps, is available, 92 % of the theoretically available power can be recovered and the simple payback period will come down to 5.2 years.

37.5.3 Simulation Results

Validation of the findings has been accomplished by simulating the two proposed designs using MATLAB software.

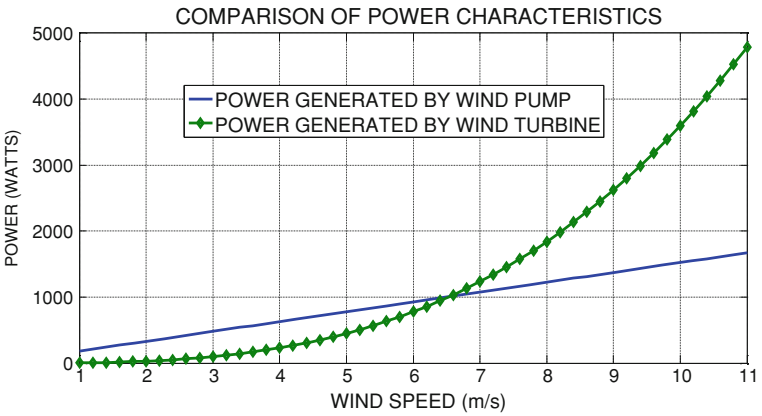

Fig. 37.11 Performance comparison of building integrated design with similar wind turbines

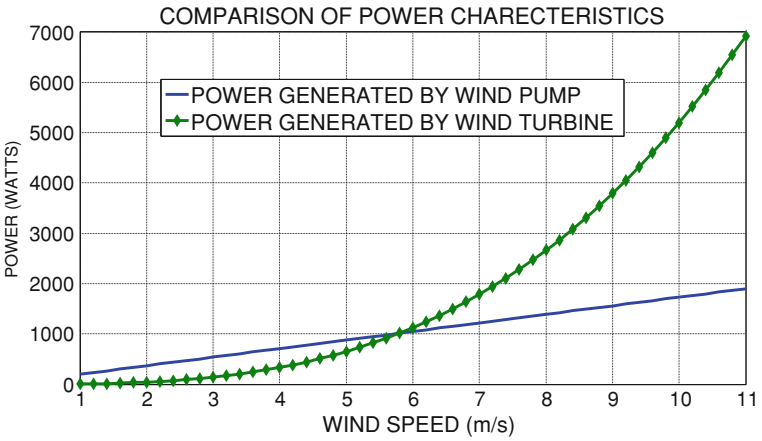

Fig. 37.12 Performance comparison of standalone tower design with wind turbines of similar size

37.5.4 Simulation Results: Building Integrated Design Three Wind Mills

Figure 37.11 compares the electrical power produced by a wind-pump based system with that of a conventional three blade wind turbine based system for the building integrated design.

As illustrated, a wind pump based system outperforms a wind turbine based system at lower wind speeds in terms of power generation capabilities. It may be noted that the wind pump based system produces more power output than that of a

wind turbine based system at lower wind speeds up to 6.5 m/s. However, above 6.5 m/s wind speeds, wind turbines offer superior power characteristics than that of a wind pump based energy model.

37.5.5 Simulation Results: Standalone Tower Design Two Wind Mills

Figure 37.12 compares the electrical power produced by a wind pump based system with that of a wind turbine based system for the standalone tower design. As illustrated, and as theoretically established earlier, a wind pump based system outperforms a wind turbine at lower wind speeds in terms of power generation capabilities.

It may be noted that in this design, wind pump based system produces much better power output than that of a wind turbine based system at lower wind speeds up to 5.75 m/s.

Above 5.75 m/s wind speeds, wind turbines offer superior power characteristics than that of a wind pump based energy model as illustrated in Fig. 37.12.

37.6 Conclusion

It can be concluded that a wind pump based energy model offers a practical solution to rural electrification needs. The main findings of this paper are as listed below.

- A wind pump based energy model offers localized solutions for the energy needs by combining existing technologies in the fields of wind pumps, pumped hydro and micro hydroelectricity.
- This energy model is best suited for low speed winds up to 6.0 m/s.
- More researches related to Pico/micro hydro turbines, suitable for low head low flow applications, can make this energy model widely acceptable.
- A wind pump based energy model can provide reliable ready to use electricity without battery, inverter/converter or grid connection.
- If the water is drawn from a pool or well, this energy model can offer irrigation/drinking water in addition to electricity.
- For locations with average wind speeds in excess of 6.0 m/s, wind turbines are still the better option.

Wind pumps for low speed winds up to 6.0 m/s and wind turbines beyond that speed will enable us to utilize the complete spectrum of wind energy.

References

1. C. Gopal et al., Renewable energy source water pumping systems—a literature review. Renew. Sustain. Energy Rev **25**, 351–370 (2013). Elsevier
2. Z. Ding, Y. Guo, W. Dapeng, Y. Fang, A market based scheme to integrate distributed wind energy. IEEE Trans. Smart Grid **4**, 976–984 (2013)
3. K. Uma Rao, S. Bhaskar, A. Kashyap, S. Halayal, S. Shashank, Economic viability of a standalone solar—DC system for rural India, in *IEEE Conference Publications* (2013), pp. 305–309
4. O. Badran, Wind turbine utilization for water pumping in Jordan. J. wind Eng. ind. Aerodyn. **91**, 1203–1214 (2003) (Elsevier)
5. M. Sathyajith, K.P. Pandey, Modelling the integrated output of wind-driven roto-dynamic pumps. Renew. Energy **28**, 1143–1155 (2003) (Pergamon)
6. G.M. Bragg, W.L. Schmidt, Performance matching and optimization of wind powered water pumping systems. *Energy Conversion*. **19**, 33–39 (1979). (Elsevier)
7. J.D. Burton, 'The mechanical coupling of wind turbines to low lift roto-dynamic water pumps. Sol. Wind Technol. **5**, 207–214 (1988)
8. J.C. Dixon, Load matching effects on wind energy converter performance, in *International Conference on Future Energy*, (1979), pp. 418-421
9. W.-G. Fruh, Long-term wind resource and uncertainty estimation using wind records from Scotland as example. *Renewable Energy*. **50**, 1014–1026 (2013). (Elsevier)
10. Google (n.d.), ironman wind mill co, available from http://www.ironmanwindmill.com/pumping-with-windmills.htm. Accessed 11 Aug 2013
11. Wind Power program, UK (n.d.), Wind turbine power output variation with steady wind speed, available from http://www.wind-power-program.com/turbine_characteristics.htm. Accessed 12 Aug 2013
12. Auroville Windmills (n. d.), Aureka, available from http://www.aureka.com/windpumps/spec.php?nav=spec. Accessed 12 Aug 2013
13. NASA/SSE (n. d.), Annual 50 m wind speed, available from http://siteresources.worldbank.org/EXTEAPASTAE/Images/wind-speed.gif. Accessed 12 Aug 2013
14. Software, *Reference Library*. (MATLAB Software, USA, 2012)
15. A. Gerber, M. Qadrdan, M. Chaudry, J. Ekanayake, N. Jenkins, A 2020 GB transmission network study using dispersed wind farm power output. *Renewable Energy*. **37**, 124–132 (2012). Elsevier

Chapter 38
Thermal Management of Solar Photovoltaics Modules for Enhanced Power Generation

Stuart J. McColl, Peter Rodgers and Valerie Eveloy

Abstract Industry and government interest in solar energy has increased in recent years in the Middle East. However, despite high levels of solar irradiance in the Arabian Gulf harsh climatic conditions adversely affect the electrical performance of solar photovoltaics (PV). The objective of this study is to compare the annual performance characteristics of solar PV modules that utilize either sun-tracking or water cooling to increase electrical power generation relative to that of stationary, passively cooled modules in the Middle East climatic conditions. This is achieved using an electro-thermal model developed and validated against experimental data acquired in this study. The model is used to predict the annual electrical power output of a 140 W PV module in Abu Dhabi (24.43 °N, 54.45 °E) under four operating conditions: (i) stationary geographical south facing orientation with passive air cooling, (ii) sun-tracked orientation with passive air cooling, (iii) stationary geographical south facing orientation with water cooling at ambient air temperature, and (iv) stationary geographical south facing orientation with water refrigerated at either 10 or 20 °C below ambient air temperature. For air cooled modules, sun-tracking is found to enhance annual electrical power output by 15 % relative to stationary conditions. For water cooled modules, annual electrical power output increases by 22 % for water at ambient air temperature, and by 28 and 31 % for water refrigerated at 10 and 20 °C below ambient air temperature, respectively. 80 % of the annual output enhancement obtained using water cooling occurs between the months of May and October. Finally, whereas the annual yield enhancement obtained with water cooling at ambient air temperature from May to October is of 18 % relative to stationary passive cooling conditions, sun-tracking over the complete year produces an enhancement of only 15 % relative to stationary passive cooling conditions.

Keywords Solar energy · Cooling · Refrigeration

S. J. McColl · P. Rodgers (✉) · V. Eveloy
The Petroleum Institute, Abu Dhabi, The United Arab Emirates
e-mail: prodgers@pi.ac.ae

M. O. Hamdan et al. (eds.), *ICREGA'14 - Renewable Energy: Generation and Applications*, Springer Proceedings in Energy, DOI: 10.1007/978-3-319-05708-8_38,

38.1 Introduction

Abu Dhabi's government plans to facilitate 7 % of all its energy demands through renewable resources, primarily solar, by 2020 [1]. In parallel, oil and gas production facilities have recently commenced utilizing solar photovoltaic (PV) modules for on-site power generation [2]. This choice is due to many facilities being isolated from electrical grids and having a necessity to conserve space (e.g., off-shore platforms). As a result of increased usage of photovoltaics, there is significant interest in efficiently utilizing PV solar modules in the United Arab Emirates (UAE). Aspects of the typical environmental conditions in the Middle East, including limited cloud coverage, are beneficial to overall electrical energy generation by PV modules, but there is also a significant negative effect caused by high solar irradiance. PV module electrical efficiency can degrade by 0.2–0.5 % per °C increase in module temperature [3]. Additionally, it is typical in the UAE to operate PV modules in stationary, geographical south facing conditions, which confines the time period of maximum electrical power generation to solar noon. In this study, means of increasing PV module electrical power output using sun-tracking and module cooling are evaluated numerically using an experimentally validated electro-thermal model.

A PV module tends to produce maximum electrical power output when receiving peak solar irradiation, which occurs when the module collecting face is positioned normal to the sun. Sun-tracking can be easily achieved by matching the module and sun's elevation angles from the horizon for a given day, and subsequently rotating the module from East to West about a North–South axis at the same angular velocity as that of the sun's relative to the earth. In order to maximize the incident yearly solar irradiance at the latitude of Abu Dhabi (24.43 °N, 54.45 °E), a module is angled at 24.5° above the horizon. Except when significant winds or cloud coverage exists, a solar module's surface temperature can be considerably above the ambient air temperature due to the absorbed solar irradiance. Rodgers et al. [4] provide an overview of the thermal management of PV modules and the potential for water cooling to improve electrical power output by lowering module's operating temperature. Using an integrated water flow piping system, a PV module's collecting surface temperature can be convectively cooled down to water temperature. Even using cooling water at ambient air temperature, water cooling will provide a significant cooling enhancement to the module relative to air cooling, owing to the higher convective heat transfer coefficient, thus increasing the PV module's electrical efficiency.

The objective of this paper is to quantify the annual electrical power output enhancements obtained using sun-tracking and thermal management strategies, relative to a stationary, geographically south facing, passively air cooled PV module.

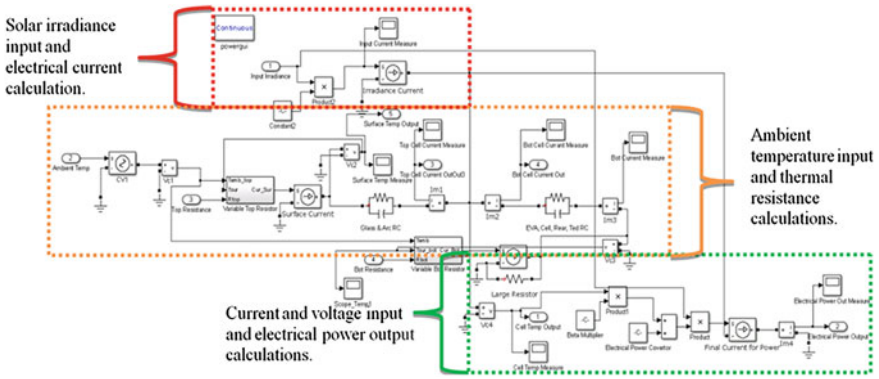

Fig. 38.1 Electro-thermal model for the prediction of the solar module electrical power output and module surface temperature

Table 38.1 PV module design

Length (m)	Width (m)	Packing factor	Cell absorptivity	Glass transmissivity	Power temperature coefficient
1.485	0.655	90 %	90 %	95 %	−0.48 %/°C

Table 38.2 Thermophysical properties of PV module layers

Layer	Thickness (m)	Thermal conductivity (W/m°C)	Density (kg/m^3)	Specific heat capacity (J/kg°C)
Glass	0.003	1.8	3,000	500
ARC	100×10^{-9}	32	2,400	691
PV Cells	225×10^{-6}	148	2,330	677
EVA	500×10^{-6}	0.35	960	2,090
Rear contact	10×10^{-6}	237	2,700	900
Tedlar	0.0001	0.2	1,200	1,250

Note ARC = anti-reflective coating, EVA = ethylene vinyl acetate.

38.2 Model Validation

The PV module electro-thermal modeling methodology employed in this study is based on the analyses presented by Armstrong and Hurley [5], Sarhaddi et al. [6], Candanedo et al. [7] and Posharp [8]. The model developed is shown in Fig. 38.1.

The thermophysical properties of the module layers are taken from [5]. Cell absorptivity and glass transmissivity values are taken from [6], with the electrical power calculation derived from [8]. Details for the PV module design and its thermophysical properties are given in Tables 38.1 and 38.2, respectively. The convective heat transfer coefficient on the module surface was modelled using an

Table 38.3 Benchmark data for electro-thermal model predictive accuracy assessment

Date	Module orientation	Method of cooling
July 31, 2013	Stationary	Passive (8.00 am to 12.00 pm) Water (12.00 pm to 6.00 pm), T_w = 2 to 35 °C
July 23, 2013	Tracking	Passive

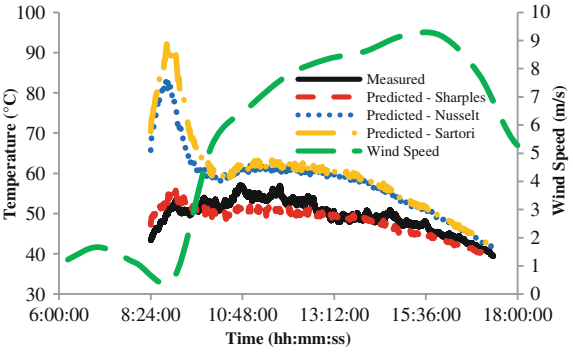

Fig. 38.2 Comparison of measured and predicted PV module surface temperature for stationary, geographical south facing position, under passive cooling conditions. Experimental data collected on June 27, 2013 in Abu Dhabi (24.43 °N, 54.45 °E)

empirical relationship developed by Sharples [9] for PV modules, with comparisons also made to both another other PV module correlation [10], and flat plate Nusselt number correlation [11]. Natural convective and radiative heat transfer from the module surfaces are not a significant [12] and were not modelled. The accuracy of convective heat transfer predictions are assessed against measured module surface temperature.

The electro-thermal model was experimentally validated for different module orientations (i.e., stationary and tracking), and both passive and water cooling conditions, using measured PV module electrical power output and surface temperature data.

The test matrix is summarized in Table 38.3. Details of these experimental measurements are given in Rodgers et al. [9], which was confined to experimentation.

In Fig. 38.2, a comparison of the measured and predicted PV module surface temperature is presented for a stationary geographical south facing position. Excellent agreement is observed when the convective heat transfer coefficient is modelled using the Sharples [9] correlation. Discrepancies with the other correlations reflect their inherent limitations, for example in low wind speed conditions, or the effect of free stream turbulence intensity.

A comparison of measured and predicted PV module electrical power output and surface temperature is presented in Fig. 38.3 for both passive and water cooling of a stationary, geographical south facing PV module. PV module surface temperature predictions are in good agreement with measurements. In addition,

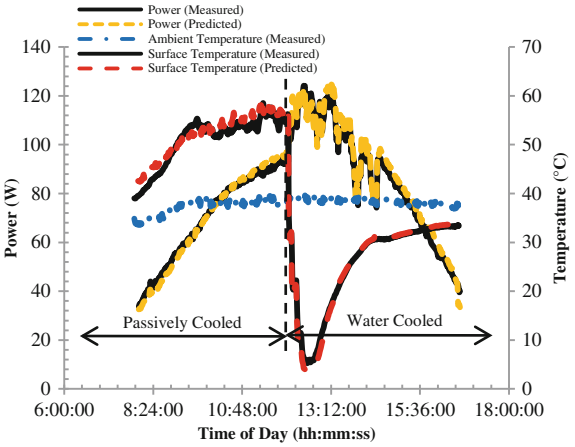

Fig. 38.3 Comparison of measured and predicted PV module electrical power output and surface temperature for stationary, geographical south facing position, under passive and water cooling conditions. Experimental data collected on July 31, 2013 in Abu Dhabi (24.43 °N, 54.45 °E)

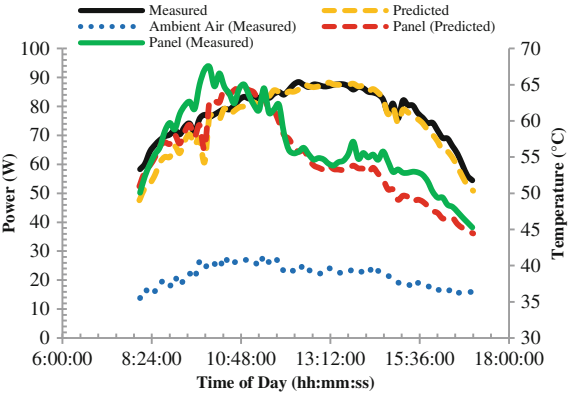

Fig. 38.4 Comparison of measured and predicted PV module electrical power output and module surface temperature for tracking configuration with passive cooling. Experimental data collected on July 23, 2013 in Abu Dhabi (24.43 °N, 54.45 °E)

excellent agreement exists with measurement data for the prediction of PV module electrical power output for highly dynamic conditions.

In Fig. 38.4 a comparison of measured and predicted PV module electrical power output and surface temperature for sun-tracking operation is presented, with good agreement obtained for both variables.

On the basis of the above comparisons between electro-thermal model predictions and corresponding measurements, sufficient confidence is established in the predictive accuracy of the model so as to permit a yearly annual analysis of PV module electrical power output to be undertaken.

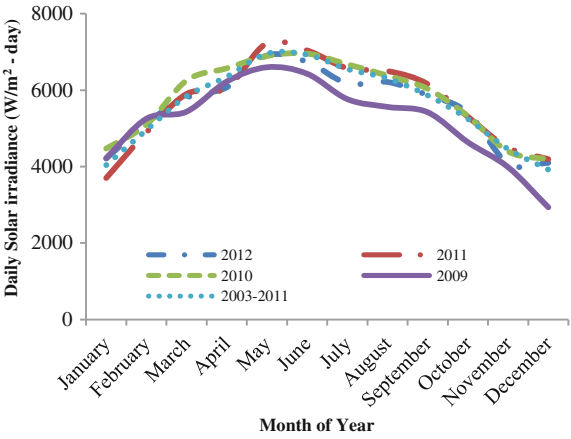

Fig. 38.5 Measured average daily direct beam solar irradiance by month, in Abu Dhabi (24.43 °N, 54.45 °E) [13]

38.3 Model Boundary Conditions

To assess the potential of water cooling to enhance PV module electrical power output, the following yearly analysis was undertaken based on Abu Dhabi's metrological data for 2011 [13, 14]. Year 2011 was selected, as its daily solar irradiance correlates well with the mean historical data between 2003 and 2012, as presented in Fig. 38.5. The corresponding ambient air temperature and wind speed data presented in Fig. 38.6 are used to model PV module convective heat transfer. The wind speed input to the electro-thermal model is the average hour-by-hour wind speed for each month. A notable trend was found that the wind direction varied from SSW in the morning to NNE in the afternoon. This change in direction was coupled with an increase in wind speed as the day progressed, with a peak value occurring between approximately 4:00 and 5:00 p.m.

Given that the daily solar irradiance profiles for sun-tracked and stationary south facing orientations follow elliptical and parabolic distributions, respectively, the solar irradiance data in Fig. 38.5 was used to obtain averaged daily solar irradiance profiles by month for these configurations (Fig. 38.7).

This data was deduced by taking the direct solar irradiance at sunrise and sunset to be zero, and the daily peak irradiance corresponding to solar noon. The idealized stationary irradiance curves were fitted using a parabolic equation:

$$G_{Stationary} = a * (time)^2 + b * (time) + c \tag{38.1}$$

where $G_{stationary}$ is the deduced stationary direct solar irradiance, and constants a, b, and c are obtained from the following system of Eqs. (38.1a)–(38.1c):

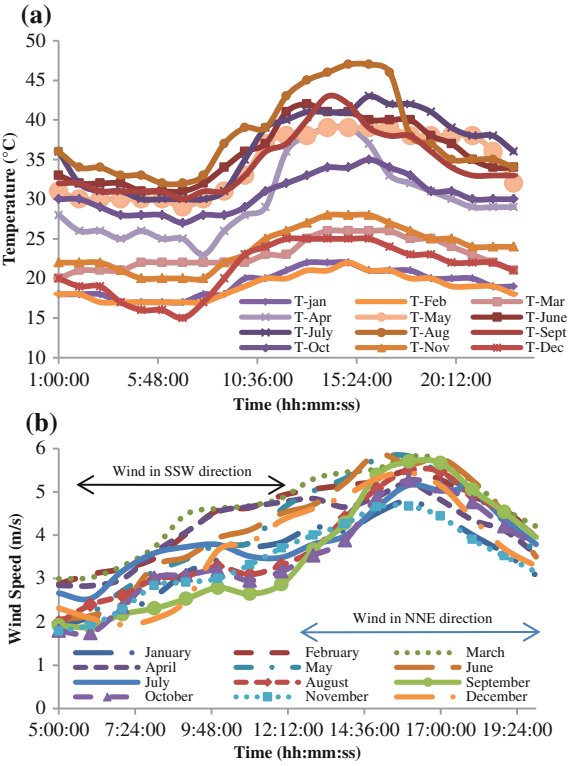

Fig. 38.6 Average hour-by-hour climatic data for each calendar month in 2011 in Abu Dhabi (24.43 °N, 54.45 °E) [14]. **a** Ambient air temperature. **b** Wind speed

$$a * (\text{sunrise})^2 + b * (\text{sunrise}) + c = 0 \tag{38.1a}$$

$$a * (\text{solar noon})^2 + b * (\text{solar noon}) + c = G_{max} \tag{38.1b}$$

$$a * (\text{sunset})^2 + b * (\text{sunset}) + c = 0 \tag{38.1c}$$

The direct solar irradiance curve for tracking was obtained using a standard horizontally translated elliptical equation [15]:

$$G_{Tracking} = \sqrt{(G_{max})^2 + \left(\frac{(G_{max} * (\text{time} - \text{solar noon}))}{\left(\frac{\text{sunset} - \text{sunrise}}{2}\right)}\right)^2} \tag{38.2}$$

where $G_{Tracking}$ is the deduced tracking direct solar irradiance and G_{max} is the peak solar irradiance. Sunrise, sunset, and solar noon, correspond to the time of the day for which an irradiance value is required. The times for sunset, solar noon, and sunrise were selected for the date halfway through each month.

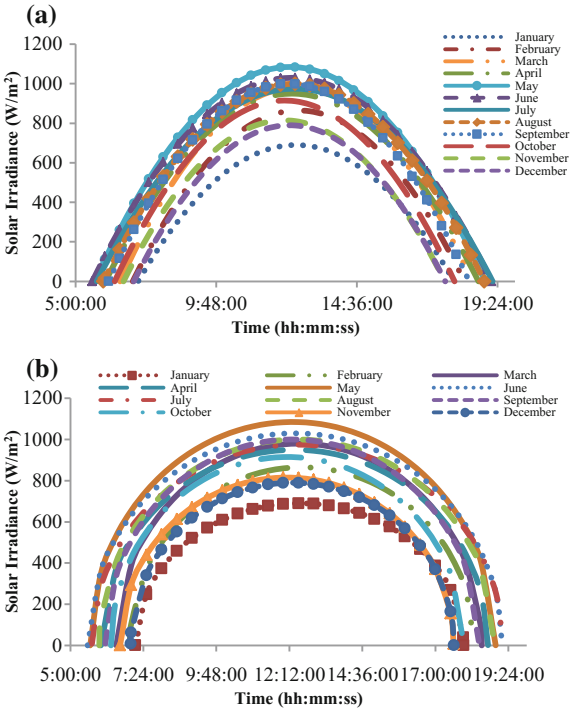

Fig. 38.7 Average daily solar irradiance by hour for each month in 2011 derived using the data in Fig. 38.6. **a** Stationary module orientation. **b** Sun-tracked module orientation

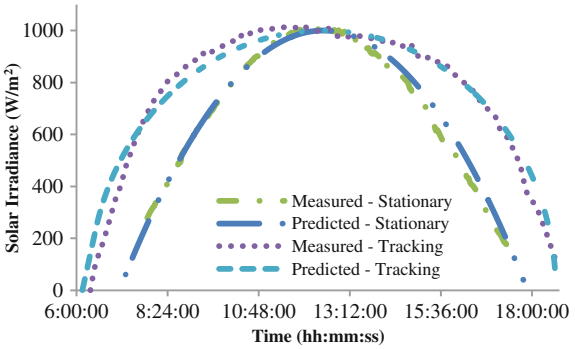

Fig. 38.8 Comparison of measured and predicted direct beam solar irradiance for both stationary and sun-tracked PV module configurations. Experimental data collected on July 18, 2013 in Abu Dhabi (24.43 °N, 54.45 °E)

To verify these solar irradiance approximations, a comparison between calculated and measured solar irradiance profiles is presented in Fig. 38.8, which displays good agreement between predicted and measured values.

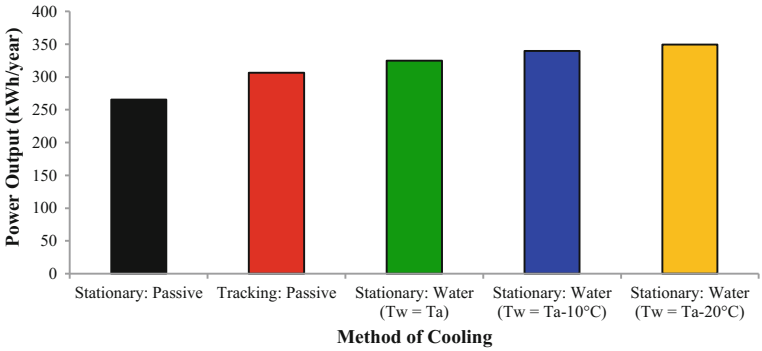

Fig. 38.9 Predicted yearly total electrical power output of a 140 W PV module as a function of operating configuration, in Abu Dhabi (24.43 °N, 54.45 °E), 2011. *Note* Ta = ambient air temperature, Tw = water temperature

38.4 Results and Discussion

PV module daily electrical power generation was calculated by numerical integration of the electrical power output profile predicted by the electro-thermal model.

The yearly electrical power output data predictions presented in Fig. 38.9 are analyzed on a month-by-month basis in Fig. 38.10. Figure 38.10 presents both the average daily total power output for each month, and the enhancement for each PV module operating configuration relative to stationary, geographical south facing orientation under passive air cooling. The sun-tracking configuration increases module electrical power output by approximately 15 % each month (with the month of April appearing to be an outlier). Water cooling at ambient air temperature is less effective than sun-tracking between the months of November to April, but yields greater power output than sun-tracking from May to October. Additionally, using refrigerated water, cooling below ambient air temperature further improves PV module electrical performance during the months of elevated ambient air temperature (i.e., May to October). The cumulative electrical power output enhancement during the months of November to April are compared to that of the May-October period in Fig. 38.11 relative to the stationary, south facing, passively cooled configuration. It is observed that sun-tracking provides approximately the same percentage enhancement in electrical power output for each month of the year, relative to the stationary south facing passively cooled PV module, whereas water cooling is more effective during the months of May to October. The three water cooling configurations each offer over four times higher electrical power enhancement throughout May-October in comparison to the November-April period. Additionally, it is observed that the sun-tracking configuration offers a greater enhancement in electrical power output than any of the water cooling configurations throughout the cooler months of November to April.

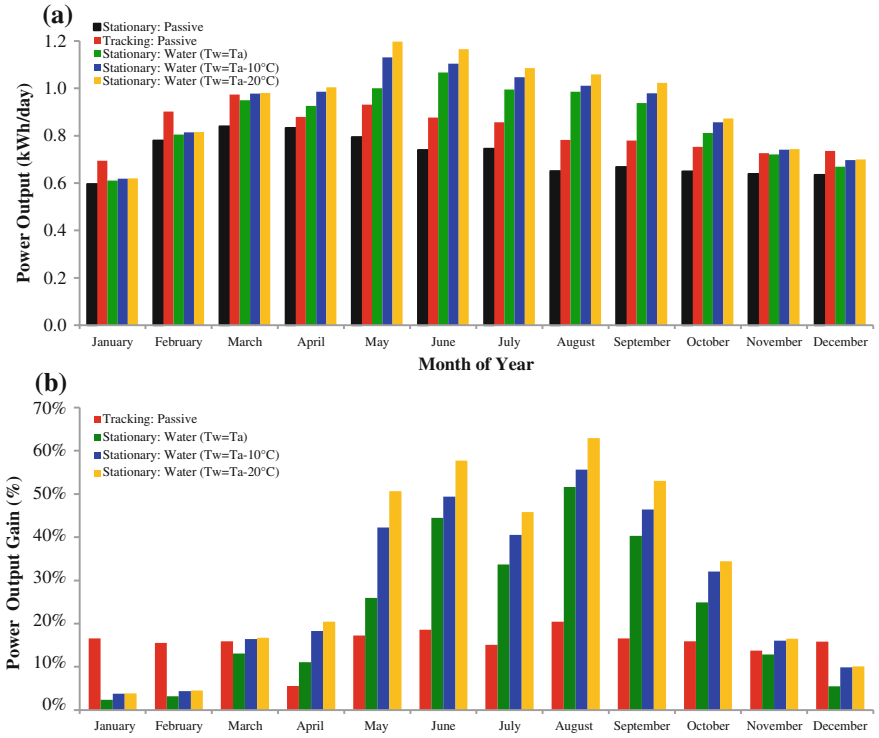

Fig. 38.10 Predicted monthly average electrical power output of a 140 W PV module as a function of operating configuration, in Abu Dhabi (24.43 °N, 54.45 °E), 2011. **a** Monthly output. **b** Monthly enhanced power output relative to stationary operating configuration. *Note* Ta = ambient air temperature, Tw = water temperature

However, the effects of cooling using water at ambient air temperature in the summer alone outweigh the complete yearly enhancement provided by sun-tracking.

Overall, sun-tracking increases yearly electrical power output by 15 % compared to the corresponding stationary, geographical south facing passively cooled configuration. For water cooled modules, annual electrical power output increases by 22 % for water at ambient air temperature, and by 28 and 31 % for water refrigerated at 10 and 20 °C below ambient air temperature, respectively. 80 % of the annual output enhancement obtained using water cooling occurs between the months of May and October. Finally, water cooling at ambient air temperature from only May to October enhances power output by 18 % relative to stationary conditions, whereas sun-tracking over the complete year would only enhance output by 15 % relative to stationary conditions. It is interesting to note that, regardless of the power output enhancement solution employed (i.e., either sun-tracking or cooling),

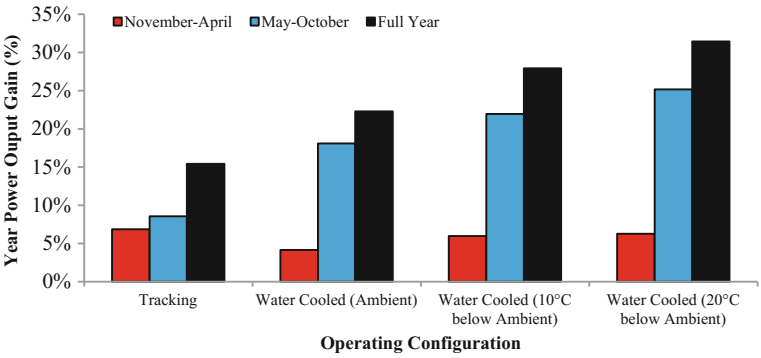

Fig. 38.11 Predicted enhanced electrical power output of a 140 W PV module as a function of operating configuration relative to stationary geographical south facing position, in Abu Dhabi (24.43 °N, 54.45 °E), 2011

the maximum predicted electrical power output (i.e., 130 W, which was obtained using refrigerated water cooling at 20 °C below ambient air temperature in May) does not reach the vendor rated performance of 140 W. This is a reflection of the idealized laboratory testing conditions employed by PV module vendors, which significantly deviate from the actual application environment in the Middle East. In future work, an economic analysis will be undertaken to assess the net economic gain obtained using the proposed water cooling scheme.

38.5 Conclusion

Based on a yearly electrical power output analysis, the effectiveness of both sun-tracking and thermal management solutions in enhancing PV module electrical power output was assessed. During the months of November to April, sun-tracking is found to be more effective than water cooling. However, cooling using water at ambient air temperature proves more effective than sun tracking when elevated ambient air temperatures exist, that is from May to October in the UAE. Additional significant improvements are obtained with refrigerated water. For Middle East climatic conditions, it is recommended that sun-tracking be utilized during the cooler months, while a water cooling configuration be utilized during prolonged periods of elevated ambient air temperature. In future work, an economic analysis will be undertaken to assess the net economic gain obtained using the proposed water cooling scheme.

References

1. Renewable Energy World, http://www.renewableenergyworld.com/rea/news/article/2009/01/abu-dhabi-sets-7-percent-renewables-target-54536. Accessed 10 Sept 2013
2. P. Rodgers, V. Eveloy, An Integrated Thermal Management Solution fot Flat-Type Solar Photovoltaic Modules," in *EuroSime, 14th Internation Conference on Thermal, Mechanical and Multi-Physics Simulation and Experiments in Microelectronics and Microsystems* (2013)
3. T. Anderson, M. Duke, G. Morrison, J. Carson, Performance of a building integrated photovoltaic/thermal (BIPVT) solar collector. Sol. Energy **83**(4), 445–455 (2009)
4. P. Rodgers, V. Eveloy, S. Bojanampati, Enhancing The Performance of Photovoltaic Solar Modules Active Thermal Management, in *ASME 11th Biennial Conference on Engineering Systems Design and Analysis, Nantes, France* (2012) (paper no. ESDA2012-82792)
5. S. Armstrong, W. Hurley, A thermal model for photovoltaic panels under varying atmospheric conditions. Appl. Therm. Eng. **30**(1), 1488–1495 (2010)
6. F. Sarhaddi, S. Farahat, H. Ajam, A. Behzadmehr, M.M. Adeli, An improved thermal and electrical model for a solar photovoltaic thermal (PV/T) air collector. Appl. Energy **87**(1), 2328–2339 (2010)
7. L. Candanedo, A. Athienitis, K.-W. Park, Convective heat transfer coefficients in a building-integrated photovoltaic/thermal system, Sol. Energy Eng. **133**(1), 021002-1–021002-14 (2011)
8. Posharp, *Photovoltaic Panel Efficiency and Performance*, Posharp, Quincy (2011)
9. S. Sharples, P. Charlesworth, Full-scale measurements of wind-induced convective heat transfer fom a roof-mounted flat plate solar collector. Sol. Energy **62**(2), 69–77 (1998)
10. E. Sartori, Convection coefficient equations for forced air flow over flat surfaces. Sol. Energy **80**(1), 1063–1071 (2005)
11. F. Incropera, D. Dewitt, T. Bergman, A. Lavine, *Fundamentals of Heat and Mass Transfer*, 6th edn. (Wiley, New York, 2007)
12. P. Rodgers, D. Lowrie, S. McColl, V. Eveloy, A.R. Baba, *"Enhancement of Flat-Type Solar Photovoltaics Power Generation in Harsh Environment Conditions," Accepted for Publication at the Thirtieth Annual Thermal Measurement* (Modeling and Management Symposium, San Jose, 2014), pp. 11–13
13. Abu Dhabi Statistics Centre, *Satistical Yearbook of Abu Dhabi* (The Statistics Centre, Abu Dhabi, 2013)
14. Freemeteo, Hourly weather history for Abu Dhabi, Untied Arab Emirates, Freemeteo, http://freemeteo.com/default.asp?pid=20&gid=292968&sid=412160&la=1&lc=1&nDate=15/8/2013. Accessed 15 Dec 2013
15. Math Open Reference, General Equation of an Ellipse (2009), http://www.mathopenref.com/coordgeneralellipse.html. Accessed 15 Dec 2013

Chapter 39
Thermal Performance of Improved Inverted Trickle Solar Still

Fadi A. Ghaith and Ahmed Bilal

Abstract In this paper, the inverted trickle solar still was integrated with a flat plate collector and a basin still in order to improve the overall productivity. The flat-plate collector was used to pre-heat the saline water entering the inverted trickle solar still. Saline water flows at the backside of the inclined absorber plate on wire screen so that the water remains attached to the plate. Water evaporates from the plate and condenses in the lower compartment. The remaining non evaporated water and the condensed water on the back plate which has high temperature was collected and fed to the basin solar still. A comprehensive mathematical thermal model was developed to predict the productivity and to investigate the effects of several operating conditions on the overall productivity of the integrated system. Based on the performed parametric studies, the maximum mass flow rate of 0.002 kg/s was found to be optimum as it maximized both the efficiency and the productivity of the integrated solar still system. On the other hand, the obtained results at the optimum flow rate showed that the maximum overall productivity on a typical summer day (i.e. 1st of July) and a typical winter day (i.e. 1st of February) were 11.25 kg/day and 5.227 kg/day, respectively for Dubai weather conditions. This study revealed that the productivity of the proposed integrated inverted trickle solar still is almost doubled due to the incorporation of flat plate collector in comparison of the previous work posted in the literature.

Keywords Integrated inverted trickle solar still · Basin solar still · Productivity

List of symbols

A_c	Area of Flat plate collector, m^2
U_L	Total loss coefficient, W/m^2K
$\dot{m}$	Mass flow rate of water, kg/s

F. A. Ghaith (✉) · A. Bilal
Department of Mechanical Engineering, Heriot-Watt University,
P.O. Box 294345, Dubai, The United Arab Emirates
e-mail: f.ghaith@hw.ac.uk

M. O. Hamdan et al. (eds.), *ICREGA'14 - Renewable Energy: Generation and Applications*, Springer Proceedings in Energy, DOI: 10.1007/978-3-319-05708-8_39,

G_t Absorbed solar radiation, W/m^2
$(\tau\alpha)_e$ Effective transmittance absorptance
T_{fi} Inlet temperature of fluid, K
T_{fo} Outlet temperature of fluid, K
T_{pm} Mean absorber plate temperature still, K
T_a Ambient temperature, K
Q_u Useful energy gain, W
η_f Efficiency of flat plate collector
q_b Heat loss from lower condenser plate, W/m^2
q_{p-c} Heat loss from plate to cover, W/m^2
q_{c-a} Heat loss from cover to ambient, W/m^2
q_s Heat loss from sides per unit still area, W/m^2
A_{ic} Area of collector for Inverted trickle Solar still, m^2
T_{io} Outlet temperature of water from Inverted trickle, K
T_{ii} Inlet temperature of water of inverted trickle solar still, K
T_w Condenser wall temperature, K
h_0 Heat transfer coefficient between condenser and ambient, W/m^{2}K
U_2 Overall heat loss coefficient from plate to cover, W/m^{2}K
U_e Heat transfer coefficient from the sides of the still, W/m^{2}K
M Productivity of distillate water, kg/s
h_{fg} Heat of vaporization of water, KJ/Kg
η_i Efficiency of the Inverted Trickle Solar still
q_{be} Heat transfer by evaporation-condensation, W/m^2
q_r Heat loss by radiation, W/m^2
q_c Heat loss by convection, W/m^2
q_k Heat loss by conduction, W/m^2
T_b Basin temperature, K
T_g Glass temperature, K
A_b Area of basin solar still, m^2
η_{bi} Efficiency of basin solar still
M_b Productivity of basin solar still, kg/s

39.1 Introduction

Water sustains health, food production, and economic progress of nations. Therefore; fresh and clean water is an urgent need for survival of mankind. Around 97 % of the world's water is either saline or contaminated with harmful bacteria, 2 % is frozen in polar ice caps and glaciers whereas only 1 % of the world's water is available for drinking and for domestic purposes readily [1]. In many countries there is a vital need for immediate supply of quality drinking water. Apart from the

saline water even brackish water available from ponds, lakes and rivers is usually contaminated with dissolved salts and bacteria therefore not suitable for drinking. Approximately about 67 % of the global population has access to clean water, with only 46 % of the people in Africa able to access clean water [2]. Water shortage problem is generally observed in dry and warm countries of Middle East and Africa [3]. According to the predictions of The United Nations, 30 countries will be facing shortage of water, out of which 18 will be in the Middle East and Africa [4]. Desalination is an important and efficient technology in the world, as of 1986 more than 90 % of the world's clean water was a product of fuel fired distillation process [5] but it is the most expensive way to produce water due to its high energy consumption. Furthermore, desalination is not only expensive but also causes severe environmental impacts contributing to global warming. However, a simpler method is solar water distillation that relies on the process of evaporation and condensation of water with the aid of a solar still. With excessive availability of solar radiance, solar distillation becomes an attractive mode of water purification technique. The water distillation process is a simple method for converting salt water into potable water. In understanding current barriers in solar distillation, researchers are coming up with new and innovative designs of solar stills and constantly striving to provide cheap and clean water in abundance, using solar energy.

Solar stills have been widely researched and studied for the improvement of producing clean water using solar energy. Many researchers have evaluated the performance of solar stills by different factors affecting the still which includes solar input, ambient temperature, and depth of water, wind speed and heat losses [6]. The single basin solar still has been the most popular solar still for producing clean water. Salah et al. [7] tested the single basin solar still in Jordan and found the maximum production of distillate to be 0.8 l/m^2/hr. and with an overall production of around 4.1 liters/day. In another research by Muhammad Ali et al. [8] in Pakistan the distillate production for the single basin was around 3.15 liters/day/m^2 and the efficiency of the system was about 31 %. Badran et al. [9] coupled flat plate collector with a single basin solar still and found higher production of 3.51 liters/day as compared to 2.24 liters/day of single basin without the flat plate collector under those conditions. Abdullah et al. [10] combined sun tracking technology with single basin solar still and found that the productivity increased by 22 % as compared to a fixed system. Tanaka et al. [11] modified the tilted wick solar still with an external flat plate reflector and found that it increased the production of water by 9 %. Furthermore, Ahsan et al. [12] customized the previous models and researched an improved tubular solar still, in which a basin like structure which contains water is surrounded by a circular glass cover, the water evaporates and then condenses on the glass cover. The water flows around the cover and is collected beneath the basin the results showed a production of 5 kg/m^2/day. Ali [13] have well researched a distinct design of inverted trickle solar still. It consists of an inclined absorber plate, with water flowing on the back of it with the aid of a wire screen. The water absorbs solar radiation and evaporates. The vapor moves to another compartment where it condenses and with the help of a heat exchanger the

heat lost due to condensation is used to preheat the water coming into the still. Based on the conducted study at a fixed flow rate of 0.5 g/s, the condensate productivity was about 2.5 l/day without recovery and 2.8 l/day with recovery, which was a 12 % increase. The intermediate productivity (i.e. the water that drops into the back plate from the wire screen, it is partly clean water) was 5.67 l/day with and 5.75 without recovery. This work has been extended by Badran et al. [14] in 2004, in which experimental studies along with simulation were performed. It was found that the productivity and efficiency increases when the flow rate decreases and also concluded that lower salinity of water led to higher productivity. Moreover, the results from the simulation predicted 35–40 % more than the actual value due to the use of clear sky model. Therefore; the available literature was found useful to develop and extend the concept of inverted trickle solar still in order to enhance the productivity and the efficiency of the solar still. The primary objective of this paper is to investigate the thermal performance and the productivity of the integrated inverted trickle solar still in UAE. This system involves integrating a flat plate collector, inverted solar trickle still and basin type still. This study includes developing a comprehensive thermal model which is utilized to generate wide range of parametric studies in order to predict the overall productivity at different operating conditions and to be compared with available conventional systems in the literature.

39.2 Description of the Integrated Inverted Solar Still

The proposed system consists of integrating the inverted trickle solar still with a single basin solar still and a flat plate collector as shown schematically in Fig. 39.1. Water flows from the main tank into the flat plate collector of an area of 1 m^2 in which it is heated and then flows into the inverted trickle solar still as illustrated by Fig. 39.2. The inverted trickle solar still is a device in which the raw water flows as a thin layer attached to the backside of an inclined metallic absorber. Water is kept attached to the plate by means of a wire screen welded to it, and a piece of porous material made of jute, covers the absorber plate backside area. Raw water flows by gravity and capillary effects; a process that produces a uniform distribution of water on the absorber backside. The fact that raw water flows in a thin layer and a low flow rate on the backside of the absorber has given the chance for water temperature to be near to that of the absorber plate. The temperature difference between the water and the plate is almost eliminated. This technique enhances the transmitted radiation through the glass cover to reach the raw water without being forced to penetrate the distilled product, as in the conventional basin-type still.

The evaporated vapor moves into the compartment of the inverted trickle solar still where it condenses and then collected in a small water tank. The remaining non evaporated water and the condensed water on the back plate which has high temperature is collected and fed to the basin solar still where again evaporation

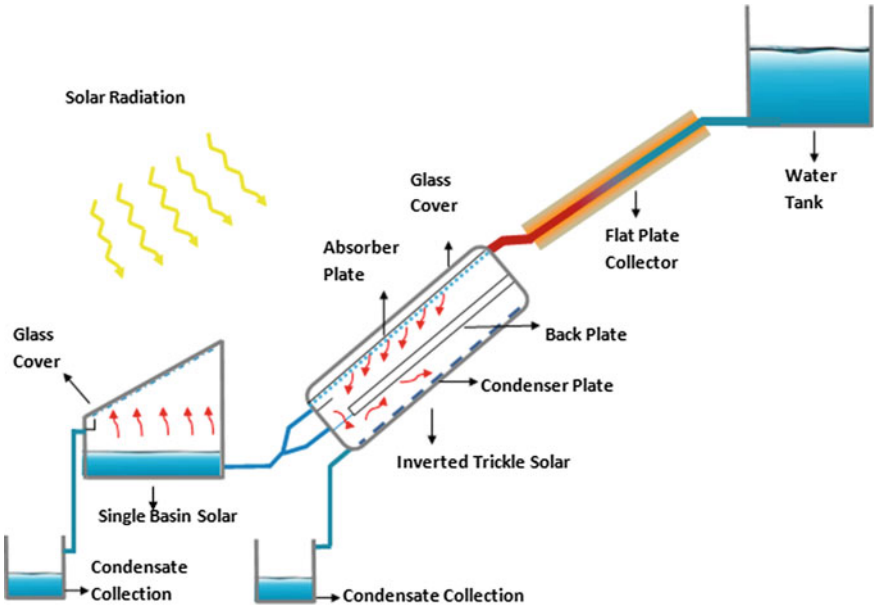

Fig. 39.1 Schematic diagram of the integrated trickle solar still

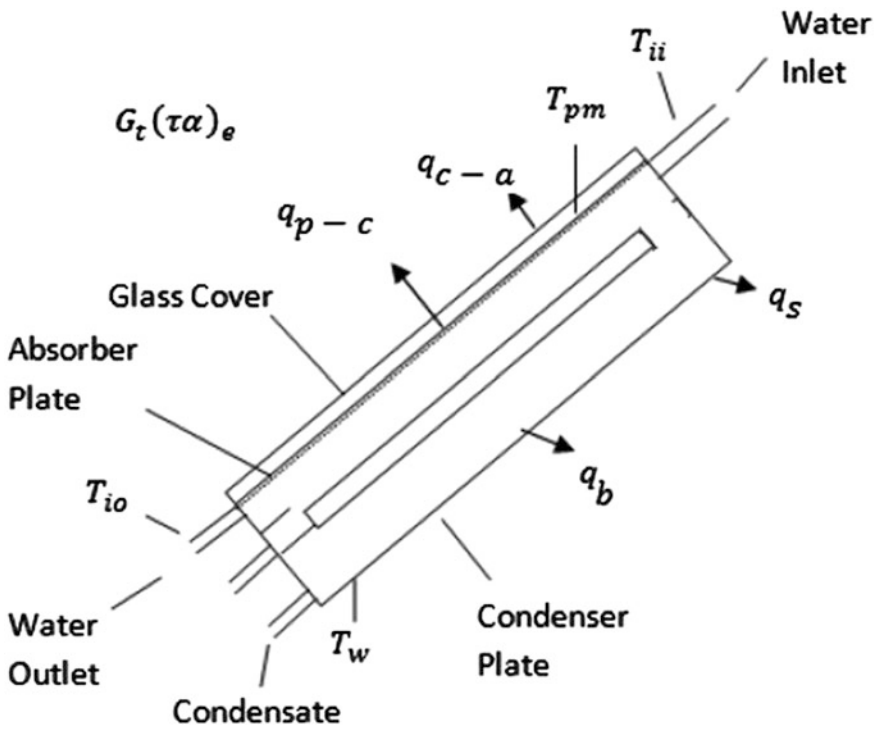

Fig. 39.2 Schematic diagram of the inverted trickle solar still

takes place and distillate is collected. The area of the inverted trickle solar still was chosen to be 1.26 m^2 similar to Badran et al. [14] for the purpose of conducting comparative studies while the area of the basin still is 2 m^2. The advantage of adding a flat plate collector is to pre-heat the water in order to increase the inlet temperature going into the inverted trickle solar still which will enhance the thermal performance and hence the productivity of the still. Moreover, the integration of single basin solar still is a useful addition for producing distillate from partially heated water.

39.3 Mathematical Model

This section describes the basic energy balance equations that govern the thermal performance and the productivity of the proposed integrated still system. The following are the main assumptions underlying this formulation: (i) The system is assumed to be under steady state conditions; (ii) All phases are in thermal and mechanical equilibrium; (iii) The sky can be considered as black body for long-wavelength radiation; (iv) Shading of collector absorber plate is negligible.

39.3.1 Solar Collector

By referring to Fig. 39.3, the useful energy, Q_u collected by the thermal collectors can be related to the incident solar radiation, G and other thermal and optical losses by the following equation [15]:

$$Q_u = A_c F_R (G_t(\tau\alpha)_e - U_L(T_{fi} - T_a) \tag{39.1}$$

The thermal collector efficiency, $\eta_{t,c}$ is defined as a ratio between the output useful energy to the incident radiation on the solar collector and can be expressed mathematically as

$$\eta_f = \frac{Q_u}{A_c G_t}. \tag{39.2}$$

39.3.2 Inverted Trickle Solar Still

By referring to Fig. 39.4, energy balance on the inverted trickle solar still absorber plate can be written as

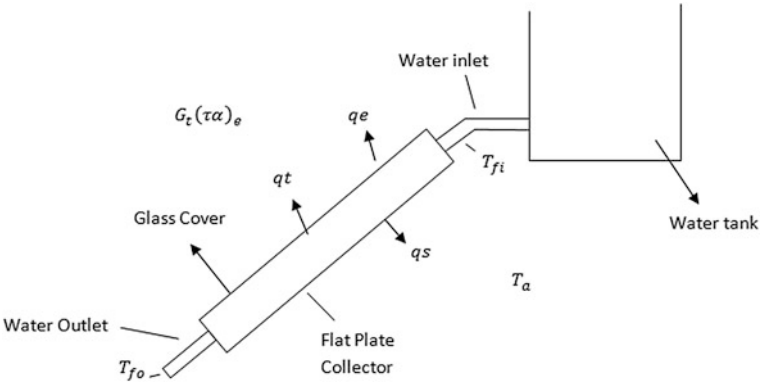

Fig. 39.3 Schematic diagram of the flat plate collector

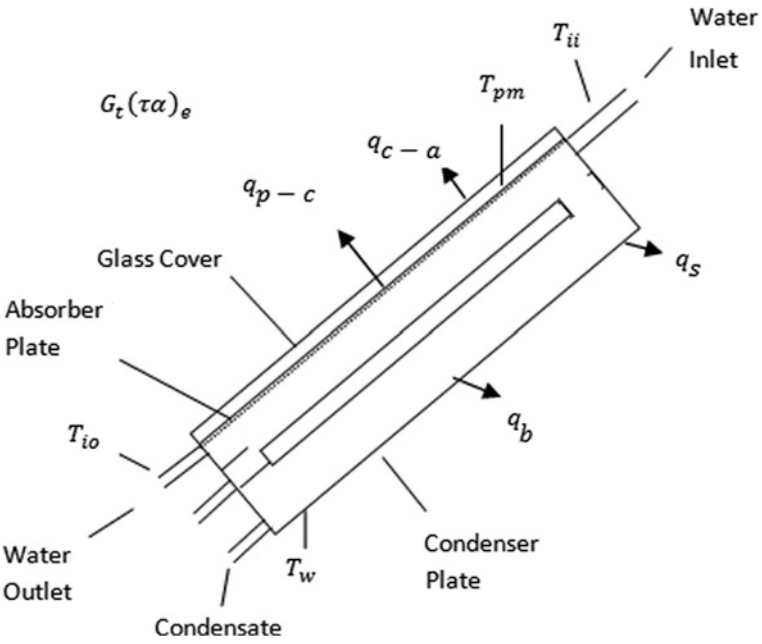

Fig. 39.4 Schematic of the inverted trickle solar still

$$(\tau\alpha)_e G_t = q_b + q_{p-c} + q_s + \left(\frac{\dot{m} - M}{A_{ic}}\right) C_p (T_{io} - T_{ii}) \tag{39.3}$$

where M is the productivity of the still and q_b is the heat lost from lower condenser plate which can be related to the still productivity by

$$q_b = \frac{M \times hfg}{A} \tag{39.4}$$

Substituting Eq. (39.4) into (39.3) and rearranging terms, the productivity can be written as

$$M = \frac{(\tau\alpha)_e G_t - q_{p-c} - q_s - \left(\frac{\dot{m}}{A_c}\right) C_{pw}(T_{io} - T_{ii})}{\frac{hfg}{A} - \left(\frac{C_p}{A_{ic}}\right)(T_{io} - T_{ii})} \tag{39.5}$$

The heat lost from the lower condenser plate can be also represented as

$$q_b = h_0(T_w - T_a) \tag{39.6}$$

By considering the energy balance on the glass cover, we may write

$$q_{p-c} = q_{c-a} \tag{39.7}$$

The heat lost from the plate to cover can be expressed as

$$q_{p-c} = U_2\left(T_{pm} - T_a\right) \tag{39.8}$$

where U_2 is the top loss coefficient which can be calculated following the steps of Duffie and Beckman [15]. The heat lost from the sides of the still to the ambient can be estimated

$$q_s = U_e\left(T_{pm} - T_a\right) \tag{39.9}$$

where U_e is the edge losses coefficient which can be calculated as

$$U_e = \frac{\frac{Insulation\ Conductivity}{Insulation\ Thickness} \times Perimeter \times Collector\ thickness}{Area\ of\ collector} \tag{39.10}$$

Once all the heat transfer losses are determined using the heat transfer coefficients, they can be substituted into Eq. (39.5) to predict the productivity of the still. Also the efficiency of the still maybe expressed as:

$$\eta_i = \frac{q_b}{G}. \tag{39.11}$$

39.3.3 Basin Type Solar Still

By referring to Fig. 39.5, the energy balance of double slope Basin solar still is given by

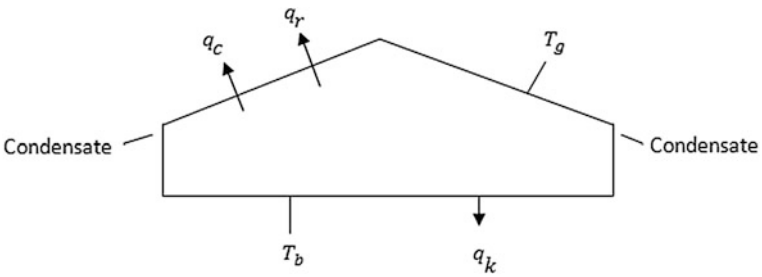

Fig. 39.5 Schematic of the Basin type solar still

$$(\tau\alpha)_e G_t = q_e + q_{r,b-g} + q_{c,b-g} + q_k + \left(\frac{\dot{m}}{A_b}\right) C_p (T_{bo} - T_{bi}) \tag{39.12}$$

The productivity of the basin still can be expressed as

$$M_b = \frac{q_{be} A_b}{h_{fg}} \tag{39.13}$$

where q_{be} is the heat transfer by evaporation-condensation process.

Finally, the efficiency of the basin solar still can be expressed by

$$\eta_{bi} = \frac{q_{be}}{G_t}. \tag{39.14}$$

39.4 Results

Numerical customized algorithm is developed based on the obtained mathematical model described in Sect. 39.3. This algorithm involves energy analyses of integrated inverted solar trickle system. A general-purpose computer simulation program, INSEL was used to predict the radiation levels for Dubai. The software uses the stored metrological data for calculating the radiation on tilted surface. The angle of the slope $\boldsymbol{\beta}$ is taken to be 25° which matches the latitude of Dubai. Figure 39.6 shows the radiation levels for typical day in summer (i.e. 1st of July) and winter (i.e. 1st of February) against the time of the day, as generated from INSEL. It was found that the average radiation for 10 h of sunshine on the 1st of July is 712 W/m^2, while it was found to be about 463 W/m^2 on the 1st of February. The radiations for these two days are considered the basis for the current analysis in order to predict the output productivity from the system and to provide a comparison between the productivity of summer and winter. In order to investigate the effects of water flow rates on the performance of the system, different flow rates were plotted versus the outlet flat plate temperatures as shown in Fig. 39.7. The productivity of the inverted

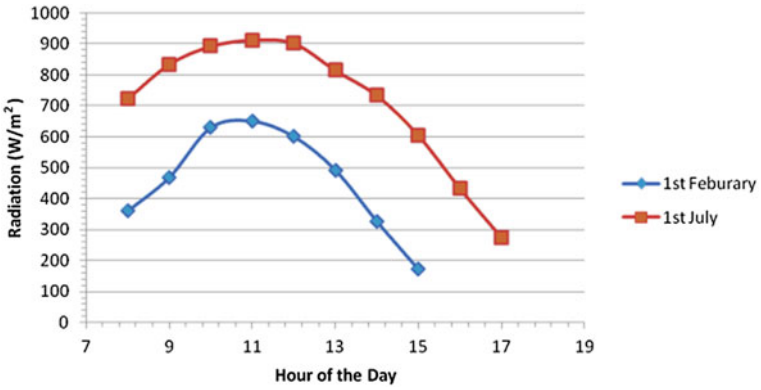

Fig. 39.6 Solar radiation levels at different day hours for typical summer and winter seasons

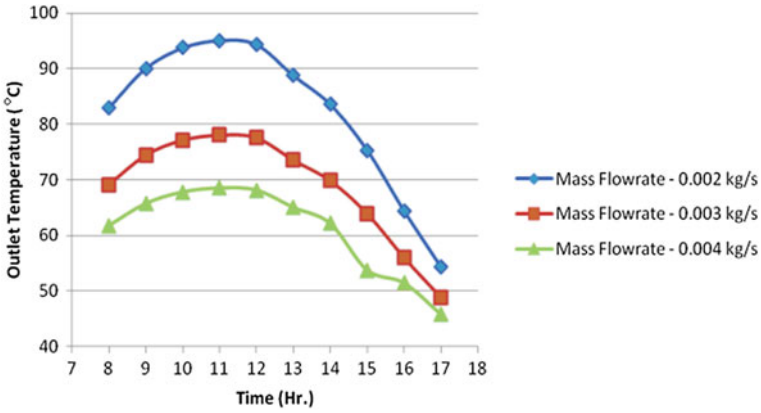

Fig. 39.7 Estimated inverted trickle outlet temperatures versus day hours at different mass flow rates

trickle solar still was determined as shown in Fig. 39.8. Figure 39.7 indicates that at a lower mass flow rate the outlet temperature is generally higher throughout the day, whereas when the flow rate increases, the temperatures decrease as expected. A minimum mass flow rate of 0.002 kg/s was selected since at a lower flow rate than 0.002 kg/s, the water tends to evaporate at the peak solar hours of the day which would damage the system and reduce the productivity significantly. Figure 39.8 shows that at a lower flow rate of 0.002 kg/s, the productivity of the inverted trickle solar still is higher and it reaches about 5.9 l/day. Also it was noted as the flow rate increases, the productivity tends to be less because the flow requires higher energy to reach the temperature for evaporation.

As the inverted trickle solar still in operation, some of the water drips back in the back plate and some of the water that doesn't evaporate flows into the single basin solar still. The water from the inverted trickle solar still is allowed to flow into the

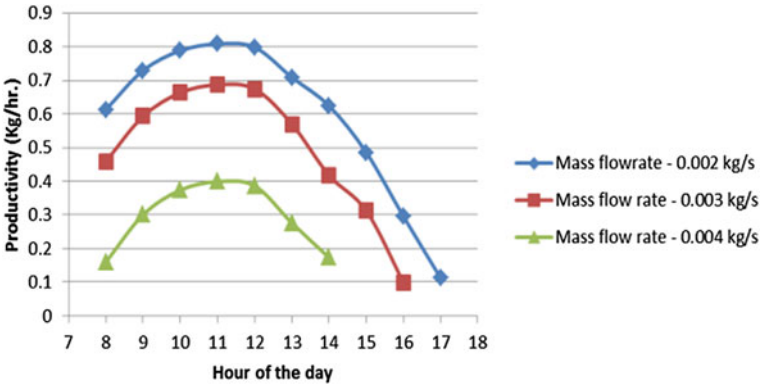

Fig. 39.8 Estimated inverted trickle productivity versus day hours at different mass flow rates in typical summer day

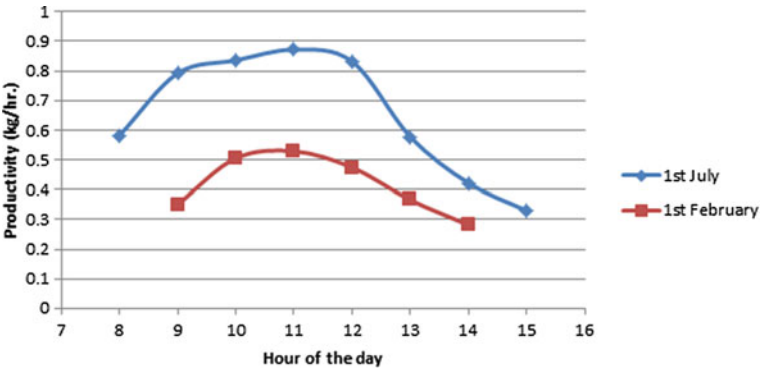

Fig. 39.9 Estimated productivity of the basin solar still versus day hours for selected summer and winter days

basin still during the peak 4 h of radiation when the temperature of the water is expected to be maximum. At a flow rate of 0.002 kg/s approximately 28 kg of water flows into the basin still. To sustain this amount of water an area of 2 m^2 is selected, which would also give an optimum depth of water in the still. Figure 39.9 shows the productivity of the basin solar still as a function of a day operating hours. It is shown that the basin solar still operates for 8 h during the summer and for 6 h during the winter, set according to the amount of sunshine available. Based on Fig. 39.9, one can find that the total productivity of the basin solar still is 5.24 kg/day in the summer (i.e. 1st of July) and around 2.51 kg/day in winter (i.e. 1st of February). Figure 39.10 shows the overall productivity of the integrated solar still system against the day hours. It was found that the total productivity of the complete system is 11.21 kg/day on the 1st of July and 5.23 kg/day on the 1st of February. In order to

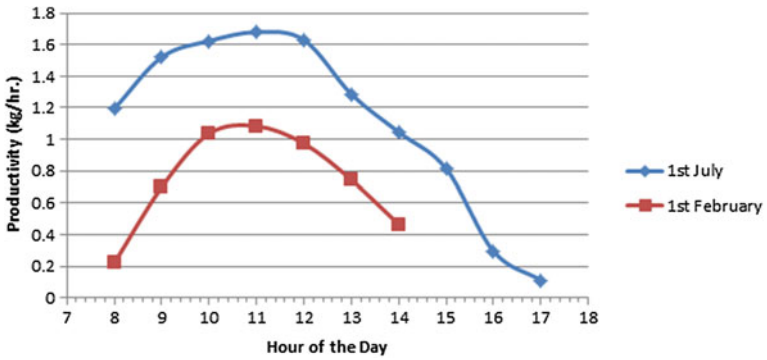

Fig. 39.10 Estimated productivity of the overall integrated solar still system versus day hours for selected summer and winter days

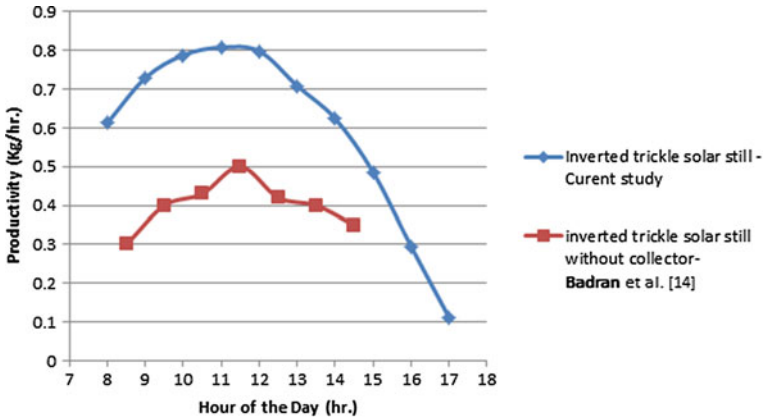

Fig. 39.11 Comparison between the proposed integrated solar still and simple inverted tickle in terms of the productivity

validate the feasibility and efficiency of the proposed integrated solar still system with the solar stills reported in the literature, a comparative study was established between the proposed integrated system in this work and the inverted trickle solar still tested by Badran et al. [14]. The test was performed on the 1st of July in Jordan with operating period of 7 h and the radiation was comparable to that of Dubai. The productivity was around 2.8 l/day with a maximum efficiency of around 20 % at a flow rate of 0.0007 kg/s. It should be noted that the previous design consisted of a heat exchanger in the condenser compartment. The inlet water would flow through the heat exchanger and absorb heat from the vapor and in this process; it would speed up condensation and pre-heat the water as well. However, the improved design consists of a flat-plate collector to pre-heat the water entering the inverted trickle solar still and accordingly there is no need for heat recovery. Figure 39.11

showed that the inverted trickle solar still within study was sufficient to produce around 5.068 l/day when operating for 7 h while it was only 2.8 l/day in the absence of the pre-heating collector.

39.5 Conclusions

In this work, an integrated inverted trickle solar still was investigated. The proposed system consists of flat plate collector to pre-heat the water which was fed to the inverted trickle solar still. The remaining water which either drips back in the back plate and/or doesn't evaporate inside the inverted trickle solar still was utilized in the basin solar still. A comprehensive mathematical model was developed in order to study the heat transfer mechanisms and energy balances associated with steady state operation. The obtained mathematical model was found to be efficient and reliable to predict the collector and inverted trickle solar still outlet temperatures and to estimate the overall productivity. Based on several numerical runs, it was found that a flow rate of 0.002 kg/s is optimum for achieving the maximum productivity. It was observed that lowering the flow rate below this value, leads to evaporate water in the flat-plate collector. Upon carrying the simulation for typical summer day (i.e. 1st of July) for Dubai weather conditions, it was found that the overall productivity of this system is 11.21 kg/day which is about 4 times higher than the productivity of the conventional single inverted trickle solar still and also about 4 times higher than the productivity of a single Basin still.

References

1. V. Velmurugan, M. Gopalakrishnan, R. Raghu, K. Srithar, Single basin solar still with fin for enhancing productivity. Energy Convers. Manag. **49**, 2602–2608 (2008)
2. Y. Taamneha, M.M. Taamneh, Performance of pyramid-shaped solar still: experimental study. Desalination **291**, 65–68 (2012)
3. F.F. Tabrizia, M. Dashtbana, H. Moghaddam, K. Razzaghib, Effect of water flow rate on internal heat and mass transfer and daily productivity of a weir-type cascade solar still. Desalination **260**, 239–247 (2010)
4. Paula Koch, Water Scarcity in the Middle East. in *Your Middle East*, http://www.yourmiddleeast.com/features/water-scarcity-in-the-middle-east_5865. Accessed 29 April 2013
5. H.P. Garg, *Advances in Solar Energy Technology* (Riedel Publishing, Amsterdam, 1987)
6. A.E. Kabeel, S.A. El-Agouz, Review of researches and developments on solar stills. Desalination **276**, 1–12 (2011)
7. S. Abdallah, O.O. Badran, M.A.K Mazen, Evaluating thermal performance of a single slope solar still. Desalination **219**, 222–230 (2008)
8. S. Muhammad Ali, K.M. Umar, M Tariq, A Nasir, Design and performance of a simple single basin solar still. Renew. Sustain. Energy Rev. **11**(3), 543–549 (2007)

9. O.O. Badran, H.A. Al-Tahaineh, The effect of coupling a flat-plate collector on the solar still productivity. Desalination **183**, 137–142 (2005)
10. S. Abdullah, O.O. Badran, Sun tracking for productivity enhancement of solar still. Desalination **220**, 669–676 (2008)
11. Hiroshi Tanaka and Yasuhito Nakatake, Improvement of the tilted wick solar still using a flat plate reflector. Desalination **216**, 139–146 (2007)
12. A. Ahsan, M. Imteaz, A. Rahman, B. Yusuf, T. Fukuhara, Design, fabrication and performance analysis of an improved solar still. Desalination **292**, 105–112 (2012)
13. A.A. Badran, Inverted trickle solar still: effect of heat recovery, Desalination **133**, 167–173 (2001)
14. A.A. Badran, L.M. Assaf, K.S. Kayed, F.A. Ghaith, M.I. Hammash, Simulation and experimental study for an inverted trickle solar still. Desalination **164**, 77–85 (2004)
15. J.A. Duffie, W.A. Beckham, *Solar Engineering of Thermal Processes*, 4th edn. (Wiley, New York, 2013)

Chapter 40
Electrodeposited Dendritic Structures of Copper Oxide as Solar Selective Absorbers in the UV–Vis Range

A. H. Alami, Anis Allagui and Hussain Alawadhi

Abstract We report the electrodeposition of copper from a 0.2 M H_2SO_4 + 0.4 M $CuSO_4 \cdot 5H_2O$ aqueous solution on a copper substrate, and its subsequent oxidation in air for selective solar thermal absorbers applications. A thorough study of the morphological properties and crystalline structure of the deposited layer through SEM-EDS and powder XRD revealed self-assembled dendritic microstructures, crystallized into fcc copper oxides, Cu_2O. The building blocks of these dendrites are spherically-shaped particles of an average diameter of ca. 1 μm. The copper oxide layer was optically examined by virtue of a spectrometer in the spectral UV–Vis range. The surface roughness induced by the existence of the dendrites has been seen to enhance the absorptance of the material: fourfolds enhancement of optical surface absorption in the wavelength range of 400–1,000 μm versus an air-grown copper oxide.

Keywords Selective solar absorbers · Copper oxides · Electrochemical deposition

40.1 Introduction

Solar absorbers are an integral part of thermal collectors, with a purpose of converting electromagnetic radiation into sensible heat. This heat is transferred to a working fluid that is used for heating applications, or further converted into other forms of energy [1]. Thermal absorbers are ideally made from an opaque material of high thermal conductivity and low specific heat. In order to achieve the best energy conversion efficiency from electromagnetic radiation to heat, the optical

A. H. Alami (✉) · A. Allagui · H. Alawadhi
University of Sharjah, Sharjah, United Arab Emirates
e-mail: aalalami@sharjah.ac.ae

M. O. Hamdan et al. (eds.), *ICREGA'14 - Renewable Energy: Generation and Applications*, Springer Proceedings in Energy, DOI: 10.1007/978-3-319-05708-8_40,

characteristics of the absorber can be manipulated to mimic black body behavior, where the coefficient of solar absorption, α, is very close to unity, with a low thermal emittance (ε) at the operational temperature. Along with absorption and emittance properties mentioned above, low reflectance ($\rho \approx 0$) at wavelengths $\lambda \leq 3$ μm and high reflectance ($\rho \approx 1$) at $\lambda \geq 3$ μm characterize spectrally selective surfaces, although the cutoff values vary as these optical characteristics are functions of temperature [2].

In order to achieve maximum absorbance, the surface of the absorber can be modified with coatings which enhance the absorption in the solar radiation wavelength range. The absorber coatings should also satisfy the thermal and chemical stabilities for long-term operations at elevated temperatures, as they may experience temperatures as high as 500 °C at stagnation conditions [3]. Surface modification of selective absorbers is achieved by numerous methods that have been intensively investigated in literature [4–6]. Surface coatings can be categorized into six distinct types [2]: (i) intrinsic or mass selective materials, (ii) semiconductor- metal tandems, (iii) selectively solar-transmitting coating on a blackbody-like absorber, (iv) metal-dielectric composite coatings (absorber–reflector tandems), (v) textured surfaces, and (vi) multilayer interference stacks. Each category is specifically applied depending on the domain of interest and on the temperature operation range [7–10].

An attractive solution for surface coatings as selective absorbers is, therefore, to develop an inexpensive single coating with favorable optical properties, easy to reproduce for manufacturing purposes, durable and thermally stable. The absorber–reflector tandem coating systems mentioned above make use of a highly IR-reflecting metal substrate covered by an exterior black coating of high absorbance over the spectral range of solar emission, while maintaining transparency to long-wavelength radiation [11]. Depositing metal oxides, which are chemically and thermally stable, on a metal substrate of low thermal emittance has been assessed as a good technical solution [10]. The optical properties of the coatings are usually governed by the nature of the metal oxide deposit and its geometric microstructure [12].

Copper is a material of choice in many applications because of its high thermal and electrical conductivities. Additionally, as p-type semiconductors with narrow band gaps, CuO (1.2 eV) and Cu_2O (2.0 eV) have been proposed in heterogeneous catalysis applications [13] as well as promising materials for solar energy conversion into electrical and chemical energy [14]. Many techniques are available for the deposition of copper materials such as sputtering, plasma deposition, or chemical vapor deposition [15]. However, the electrochemical deposition from ionic precursors remains a more viable procedure due to its simplicity and controllability, versatility, cost-effectiveness, and the fact that processing can take place at ambient temperatures and pressures [16]. This work investigates the electrodeposition of dendritic microstructured copper oxide on a bulk copper substrate as active materials for solar selective absorbers applications. The morphological characterization of the deposits was carried out by scanning electron microscopy, and crystalline composition by powder X-ray diffraction. Spectral measurements were conducted in the UV–Vis range.

40.2 Experimental

40.2.1 Electrodeposition

The experimental arrangement for the electrodeposition of dendritic structure of copper consisted of a two-electrode setup in a round glass Pyrex beaker, with a thoroughly polished copper cathode (3×4 cm^2, 99 % purity) serving as a working electrode parallel to a 316 L stainless steel plate of the same dimensions serving as a counter electrode. The supporting electrolyte was an acidic solution of 0.2 M H_2SO_4 + 0.4 M $CuSO_4{\cdot}5H_2O$ aqueous solution. The applied current was set to 500 $mAcm^{-2}$ for 20 s delivered by an Agilent E3616A DC power supply. The working electrode was subsequently cleaned with an abundance of deionized water (18 MΩ cm) and left to dry in ambient air overnight.

40.2.2 Morphological Characterization

Preparation of microstructured copper deposits for morphological characterization by electron microscopy was performed by mechanically depositing the copper powder on a carbon tape. The scanning electron microscope (SEM) is a VEGA3 XM by TESCAN, operating at 5 kV. SEM-coupled energy-dispersive X-ray spectroscopy (EDS) technique for elemental analysis was performed on three different spots of the sample during 100 s live time at the same operating voltage.

The powder X-ray diffraction (XRD) patterns for crystal identification in the electrodeposited sample were recorded in the 2θ geometry between 10 and 80° at 0.02° 2 θ s^{-1} with a Bruker D8 Advance DaVinci multipurpose X-ray difractometer with Cu Kα radiation operating at 40 kV and 40 mA current.

40.2.3 Optical Characterization

Spectra measurements in the UV–Vis and near-IR regions were carried out with the setup as schematically shown in Fig. 40.1. Measurements were acquired with a Ocean Optics HR2000 high-resolution spectrometer equipped with a Sony ILX511 2048-element linear CCD array detector at the end of the optical bench guiding the signal, and operating in the effective wavelengths range 300–1,200 nm. The spectrometer is connected to a fiber optic reflection probe R200-7-SR, 2-m long, and of a 200 μm core diameter. The reflection probe consists of a tight bundle of seven optical fibers in a stainless steel ferrule with six illuminating fibers around a one axial read fiber. The distance between a tungsten halogen light source (Ocean Optics LS-1-LL) and the sample was set to 3 cm. The integration time was

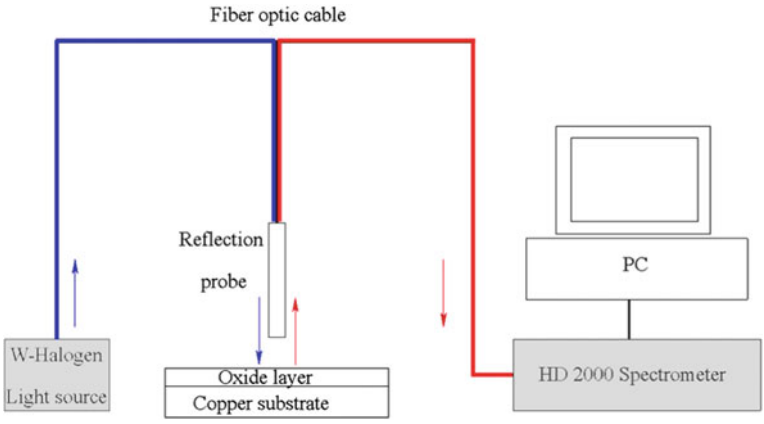

Fig. 40.1 Schematic of the experimental setup for optical characteristics measurements

automatically adjusted to 177 ms to contain the intensity of the highest absorptance peak. The recorded spectra are averaged over 10 readings in the time domain to increase signal to noise ratio.

40.3 Results and Discussion

40.3.1 SEM-EDS and Powder XRD Characterization

A powder sample obtained from the surface of the copper substrate and adhered to a carbon tape was taken for SEM examination. A low magnification top view of the microstructure of copper material layer shows three-dimensional forest-like dendrites, as seen in Fig. 40.2a. A similar dendritic structure was obtained by Nikolic et al. [17], who used a continuous cycling of current application/pause and produced a mixture of dendrites and agglomerates of copper oxide, as well as holes that resulted from the hydrogen evolution reaction. Upon further magnification (Fig. 40.2b), these dendrites are seen to be consisting of an agglomeration of small globules of copper materials at various degrees of oxidation (oxygen content). The average size of these individual particles is ca. 1 μm. We remarked from the EDS spectra collected at three different locations in the specimen that the smaller the size, the higher purity copper it contains. Larger particles are assumed to be at a higher state of oxidation.

A typical EDS spectrum is shown in Fig. 40.3, exhibiting the energies of the two L- and K-peaks of emission lines of copper. Additionally, we notice a small contribution from oxygen presence due to the surface oxidation process.

Figure 40.4 shows powder XRD patterns of the collected sample from the dendritic electrodeposited layer that was left to oxidize in ambient conditions

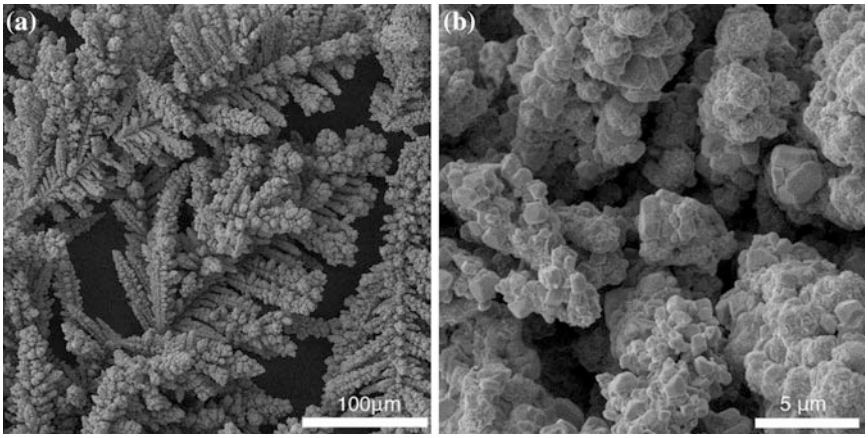

Fig. 40.2 Typical SEM micrographs of microstructured dendritic copper oxides electrodeposited on copper substrate: **a** low magnification and **b** high magnification

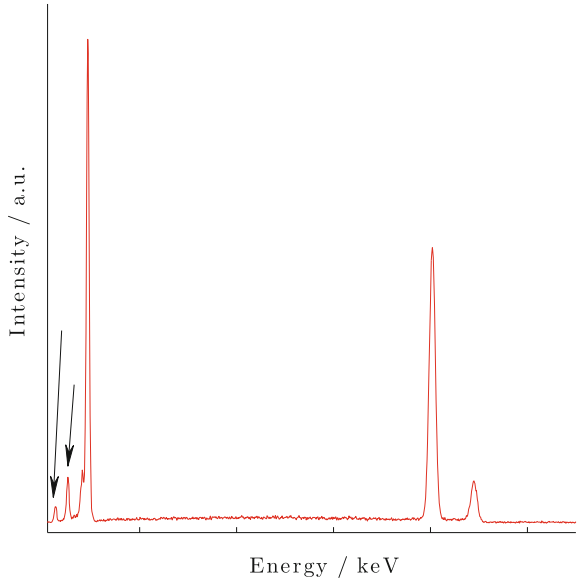

Fig. 40.3 EDS spectrum recorded during SEM examination of Fig. 40.2b

overnight. The XRD patterns showed the presence of both Cu and Cu_2O, crystallized into fcc structures. Sharp reflection peaks for polycrystalline copper are recorded for $2\theta = 43.32$, 50.44 and 74.12 degrees for (111), (200) and (220), respectively (in accordance with JCPDS card # 85–1326). Cu_2O reflection peaks for (110), (111), (200), (220), (311) and (222) are detected at $2\theta = 29.63$, 36.43, 42.32, 61.36, 73.52 and 77.36 degrees, respectively (in accordance with JCPDF card # 78–2076). The presence of both phases, Cu and Cu_2O, is due to the partial

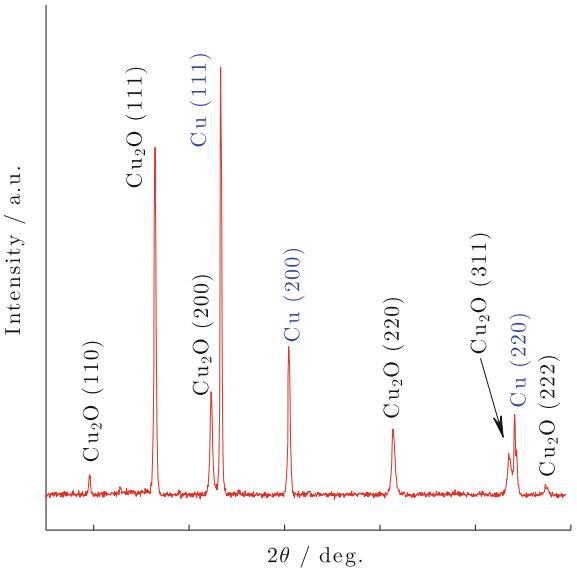

Fig. 40.4 Powder XRD patterns of electrodeposited copper-based dendritic microstructures showing the presence of both Cu and Cu_2O

surface oxidation of the initial nanoparticles of pure copper formed by the electrodeposition process upon the substrate. The formation of cuprite can be accelerated by thermal sintering.

40.3.2 Optical Characterization

The spectral directional absorptivity was measured for three copper specimens using a spectrometer with a tungsten halogen light source. This experimental arrangement (see Fig. 40.1), where the angle of incidence of the light beam is zero is justified by the intended application of solar thermal absorbance. The absorber should have a zero angle of incidence with the sun rays as well. The specimens set consists of: (1) a polished and highly reflective copper plate acting as the reference for subsequent specimens, (2) a copper plate with air-grown copper oxide due to slow environmental oxidation, and finally (3) the copper specimen with the electrodeposited copper oxide layer. By the end of overnight oxidation process in air, the color of the deposited layer changed from reddish, cupric color to a dark purple and finally to black. The fitted data points of spectral absorptance, α, are shown in Fig. 40.5 for a spectral range of $\lambda = 300-1{,}000$ nm for the two copper oxide-coated specimens, (2) and (3). For the air-grown oxide specimen, the figure shows an increase in absorptance value in the UV range, followed by a plateau in the visible range and the cutoff value for absorptance starting from the near infrared wavelengths [18]. A similar trend, but with higher absoptance values in the visible range is seen for the electrodeposited Cu_2O dendrites. The maximum absorbance is noted at 528 nm. The results show that the electrodeposited layer

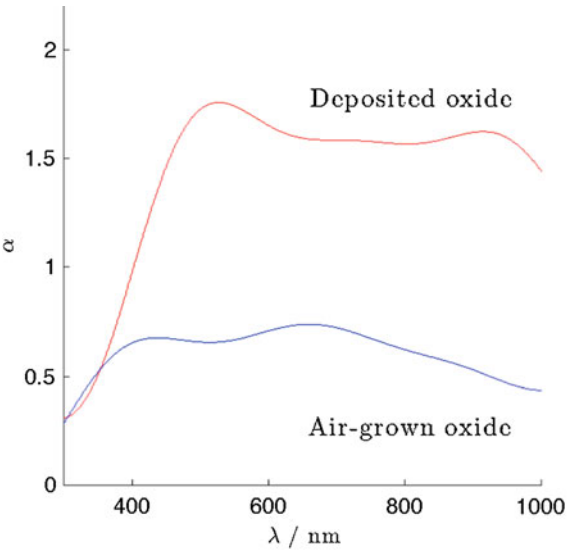

Fig. 40.5 Spectral optical absorptance of electrodeposited versus air-grown Cu_2O

exhibits four times higher absorptance than that of the air-grown oxide over the wavelength range. The average spectral absorptance for the latter is around 0.33 and for the former is 1.32. This increase in absorptance was expected because of the darker color of the electrodeposited oxide that enhances absorbance over the wavelength range. Additionally, the surface roughness introduced by the dendritic microstructure of the electrodeposited oxide is expected to enhance the absoptivity.

40.4 Conclusions

This paper reports on the synthesis and morphological and optical characterization of electrodeposited dendritic copper oxide structures on copper substrate. The intended application for such composite material is to manufacture highly selective solar absorbers, active in the UV–Vis range. Oxidized Cu_2O from initially deposited copper particles (500 $mAcm^{-2}$ between Cu substrate and SS anode for 20 s, in 0.2 M H_2SO_4 + 0.4 M $CuSO_4{\cdot}5H_2O$) exposed to air, resulted in high surface area dendritic microstructures of approximately four times higher spectral directional absorptance when compared to naturally air-grown copper oxides. The resulting single oxide layer is thus inexpensive to manufacture with favorable optical properties. The chemical and mechanical stability of the deposits, with respect to their thicknesses will need to be investigated further to confirm the suitability of Cu/Cu_2O composite material as a selective solar absorber.

Acknowledgments The authors would like to acknowledge the contribution of Meera Al Muhairie.

References

1. A.H. Alami, Experiments on solar absorption using a greenhouse-effect gas in a thermal solar collector. J. Renew. Sustain. Energy **2**(5), 053102 (2010)
2. C. Kennedy, Review of mid- to high-temperature solar selective absorber materials. National Renewable Energy Laboratory, Technical Report NREL/TP-520-31267, 2002
3. A.H. Alami, Investigation in utilizing paraboloid concentrators for thermal perforation of metals. Renew. Energy **56**, 105–109 (2013)
4. Q. Geng, X. Zhao, X. Gao, H. Yu, S. Yang, G. Liu, Optimization design of CuCrxMn2-xO4-based paint coatings used for solar selective applications. Sol. Energy Mater. Sol. Cells **105**, 293–301 (2012)
5. M. Biancardo, F.C. Krebs, Microstructured extremely thin absorber solar cells. Sol. Energy Mater. Sol. Cells **91**(18), 1755–1762 (2007)
6. H.C. Barshilia, S. John, V. Mahajan, Nanometric multi-scale rough, transparent and anti-reflective ZnO superhydrophobic coatings on high temperature solar absorber surfaces. Sol. Energy Mater. Sol. Cells **107**, 219–224 (2012)
7. T. Tesfamichael, W. Vargas, E. Wackelgard, G. Niklasson, A feasibility study of integrally colored Al−Si as a solar selective absorber. Sol. Energy Mater. Sol. Cells **55**(3), 251–265 (1998)
8. N. Selvakumar, H.C. Barshilia, Review of physical vapor deposited (pvd) spectrally selective coatings for mid- and high-emperature solar thermal applications. Sol. Energy Mater. Sol. Cells **98**, 1–23 (2012)
9. E. Radziemska, Thermal performance of Si and GaAs based solar cells and modules: a review. Prog. Energy Combust. Sci. **29**(5), 407–424 (2003)
10. C. Choudhury, H. Sehgal, High temperature degradation in cobalt oxide selective absorber. Sol. Energy **30**(3), 291–292 (1983)
11. B. Karlsson, C.G. Ribbing, A. Roos, E. Valkonen, T. Karlsson, Optical properties of some metal oxides in solar absorbers. Phys. Scr. **25**(6A), 826 (1982)
12. A. Ignatiev, P. O'Neill, C. Doland, G. Zajac, Microstructure dependence of the optical properties of solarabsorbing black chrome. Appl. Phys. Lett. **1**, 42–44 (1979)
13. J.B. Reitz, E.I. Solomon, Propylene oxidation on copper oxide surfaces: electronic and geometric contributions to reactivity and selectivity. J. Am. Chem. Soc. **120**(44), 11467–11478 (1998)
14. R.N. Briskman, A study of electrodeposited cuprous oxide photo-voltaic cells. Sol. Energy Mater. Sol. Cells **27**(4), 361–368 (1992)
15. P.C. Andricacos, C. Uzoh, J.O. Dukovic, J. Horkans, H. Deli-gianni, Damascene copper electroplating for chip interconnections. IBM J. Res. Dev. **42**(5), 567–574 (1998)
16. D. Grujicic, B. Pesic, Electrodeposition of copper: the nucleation mechanisms. Electrochim. Acta **47**(18), 2901–2912 (2002)
17. N.D. Nikolic, G. Brankovic, V.M. Maksimovic, M.G. Pavlovic, K.I. Popov, Influence of potential pulse conditions on the formation of honeycomb-like copper electrodes. J. Electroanal. Chem. **635**(2), 111–119 (2009)
18. Y.A. Cengel, *Heat & Mass Transfer: A Practical approach* (Tata McGraw-Hill Education, New York, 2007)

Chapter 41
Numerical Investigation of Solar Chimney Power Plant in UAE

Mohammad O. Hamdan and Saud Khashan

Abstract This paper presents a numerical simulation results for a steady air flow inside a solar chimney power plant. A standard k-epsilon turbulence model is used to model a prototype solar chimney that was built in Al Ain in UAE. The chimney tower has height of 8.25 m and 24 cm diameter which is used to draw air from a solar collector that cover 100 m^2 area. The CFD analysis is used to determine the location of the turbine using available power quantity. The CFD data shows that the collector height and chimney size is highly affecting each other. In the current design, the small chimney size has produced a stagnant zone inside the collector which has reduced the air flow rate inside the solar chimney. Also the CFD simulation shows that installing a nozzle at the entrance of the chimney is crucial parameter that affects the performance of the solar chimney and evidently reduces the pressure loss.

Keywords Solar chimney · CFD analysis · Upward draft tower

41.1 Introduction

The solar chimney power plant (SCPP) operates using the concept that hot air raises. In solar chimney power plant, the solar energy is trapped through the greenhouse effect and is used raise the air temperature inside the collector. The hot air is funneled and steered though a chimney tower which assure that a draft of air is consolidated at the bottom side of the chimney. The concept have been used for passive air ventilation however recently more researchers start exploring this concept for power generation. The thermal solar energy stored in the hot draft air is

M. O. Hamdan (✉) · S. Khashan
Mechanical Engineering Department, United Arab Emirates University,
Al Ain, United Arab Emirates
e-mail: MohammadH@uaeu.ac.ae

M. O. Hamdan et al. (eds.), *ICREGA'14 - Renewable Energy: Generation and Applications*, Springer Proceedings in Energy, DOI: 10.1007/978-3-319-05708-8_41,

harvested using a wind turbine in which the turbine convert the kinetic energy of the air draft to mechanical energy. The interest in solar chimney power plant is driven by (1) the low maintenance cost of the SCPP, (2) the simplicity of operation and (3) the durability of the system.

Solar chimneys have been used in agriculture for air replenishment in barns, silos, greenhouses, etc. as well as in drying of crops [1], grains, fruits or wood [2]. The solar chimney is used as a passive natural ventilation method in buildings to improve the quality of indoor air and to increase the comfort index for inhabitants [3]. The need for renewable source of energy has drawn more interests to utilize the solar chimney to harvest solar energy [4–20]. The need for renewable sources of energy is mainly driven by the need of new sources of energy to replace the fossil fuel which considered on the main contributor to recent environmental changes that affected almost every part of the world. The shortage of available energy resources and the continuous growing energy demands have drove the energy cost to record high levels and fostered the search for more reliable renewable energy. Scientists are exploring several techniques focusing on different aspects including minimizing operational costs, simplifying and lowering maintenance cost, minimizing the use of toxic materials due to health and environmental concerns, and increasing reliability.

The solar chimney has huge potential in energy generation as green source of energy since it is simple technology that requires low maintenance. Solar chimney can contribute substantially to our future energy needs. In the 1980s, a pilot plant was built and tested in Manzanares, Spain and data collected from this pilot plant were published by Haaf et al. [4], Haaf [5] in which a brief discussion of the energy balance, design criteria, and cost analysis was presented. The Manzanares pilot plant was rated at 36 kW and produced electricity for 8 years which was used to prove the efficiency and reliability of this novel technology. No full scale solar chimney power plant has been built to date however many proposal have been investigated in different parts of the world. The cost of chimney construction is directly affect the cost of energy produced which needs more investigation since it depends on location, labor cost and material cost which vary dramatically based on region. It was reported that the price of the electricity produced by a solar chimney power plant in the Mediterranean region is considerably higher compared to the other power sources [6].

The solar chimney power generation is a promising approach for future applications [7]. Thru detailed thermal analytical model, Bernardes et al. [8] showed that the most important parameters for the solar chimney design are (1) the height of chimney, (2) the factor of pressure drop at the turbine, (3) the diameter and (4) the optical properties of the collector. Zhou et al. [9] reported that the maximum height for convection and the optimal height for maximum power output increases with larger collector radius. The effect of the SCPP geometry and size including the chimney height, chimney diameter and collector diameter were evaluated by Hamdan [10] who showed that chimney performance enhances as chimney height and collector diameter increases. The feasibility of SCPP was evaluated by different experimental study [11, 12].

Many researcher have evaluated the SCPP numerically [13–15]. Maia et al. [13] conducted numerical study which showed good quantitative agreement with earlier experimental work which also indicated that the height and diameter of the tower are the most important physical variables for solar chimney design.

Different technologies were recommended to enhance the performance of SCPP such as double glass collector, phase change material, thermal storage [11], tilted chimney [16], swirl generation [21], and system integration to generate fresh water [21]. The performance of the solar chimney is directly related to the heat transfer coefficient since it directly affects the air temperature and speed [22].

The purpose of this numerical work is to understand the flow characteristics and the effect of the geometry on the solar chimney performance for the prototype that was built in Al Ain in 2011. The study evaluates the flow behavior and thermal performance based on the experimental data that is collected by Hamdan and Rabbata [20].

41.2 Numerical Analysis

41.2.1 Problem Formulation

The physical dimensions investigated in this model is shown in Fig. 41.1, which shows the solar chimney that was built in Al Ain in UAE during 2011 [20]. The schematic diagram of the computational domain is shown in Fig. 41.2 with the boundary conditions used in the CFD simulation.

The numerical analysis is carried out using finite volume scheme via commercial software FLUENT® 6 and the mesh is generated using GAMBIT mesh generator software. A uniform fine quad map mesh is used with refined mesh near the wall. A grid refinement procedure has been performed through numerical experiments to assure the grid independence.

To reduce computation time and due to geometry and boundary condition symmetry, the solar chimney power plant is modeled using axi-symmetry analysis using 2D mesh in the radial and axial direction. The collector used in the experimental study is square shape with 10 × 10 m. An equivalent collector diameter of 11.28 m, based or are size, is used in the CFD model to create the 2D axi-symmetry numerical study. In this study the following assumptions are adopted:

1. Cylindrical coordinate is used with axi-symmetry approach.
2. The flow is steady, incompressible ideal gas which is applicable for moderate air speed with Mach number well below 0.3. The volume expansion coefficient is only function of temperature.
3. The collector surface and chimney surface is assumed under natural convection condition with heat flux of 10 W/m^2K and ambient temperature given in Table 41.1. For example for solar heat flux of 222 W/m^2 the ambient temperature is 20.3 °C.
4. The chimney wall is assumed insulated.

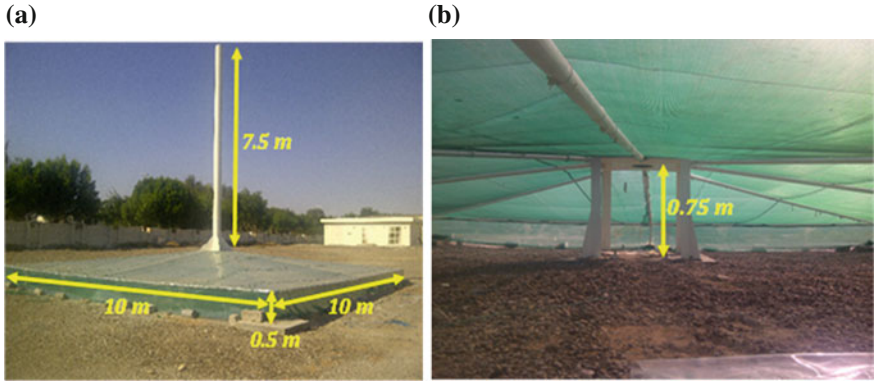

Fig. 41.1 Pictures of solar chimney prototype with some dimensions at UAE University, UAE; **a** from outside, **b** under the plastic cover collector

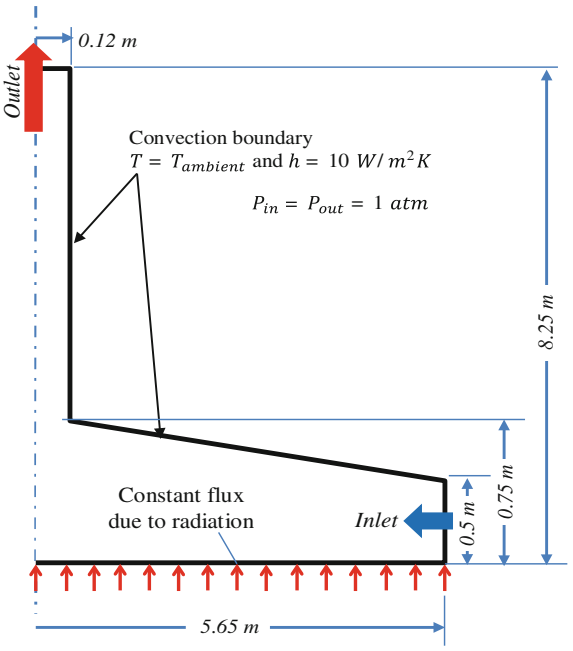

Fig. 41.2 A schematic diagram of the solar chimney tower power plant computational domain with boundary conditions

5. The inlet pressure is 1 atm and the outlet pressure at 8.25 m chimney height is assumed 1 atm which is appropriate for such short chimney.
6. The solar heat flux and ambient temperature that is used as boundary condition in the numerical study are extracted from the experimental study done by Hamdan and Rabbata [20] and is shown in Table 41.1.
7. The gravity in the positive z-direction is -9.81 m/s^2 while zero on all other direction.

Table 41.1 The experimental data for solar heat flux and ambient temperature that is recorded in December 2nd 2011 [20]

Time (h)	Ambient temperature [°C]	Measured heat flux [W/m^2]	Velocity measure at the chimney entrance [m/s]
10:00 AM	20.3	222	2.9
11:00 AM	21.8	340	3.3
12:00 PM	23.4	402	3.4
1:00 PM	25.0	474	3.3
2:00 PM	27.8	365	3.2
3:00 PM	29.2	178	3.0

The solar radiation is transient in nature which mean more dynamics models are needed to accurately predict the solar chimney performance. In order to simplify he analysis, in this study authors utilized a steady flow assumption which is very useful to investigate the main parameters affecting that influence of the solar chimney performance.

41.2.2 Numerical Solution

Since the purpose of this investigation is to understand the flow characteristics and the effect of the geometry on the solar chimney performance that was built in Al Ain in 2011, not the assessment of turbulence models, it is decided that a standard $k-\varepsilon$ model would serve the purpose which is also adopted by other investigators [23, 24]. The conservation equations and the standard $k-\varepsilon$ turbulent model used in this study is shown below:

Ideal gas equation

$$P = \rho RT \tag{41.1}$$

Continuity equation

$$\frac{\partial u_i}{\partial x_i} = 0 \tag{41.2}$$

Momentum equation

$$\rho u_j \frac{\partial u_i}{\partial x_j} = -\frac{\partial P}{\partial x_i} - g_i + \frac{\partial}{\partial x_j}\left[\mu\left(\frac{\partial u_i}{\partial x_j} + \frac{\partial u_j}{\partial x_i}\right) - \rho\overline{u_i' u_j'}\right] \tag{41.3}$$

Energy equation

$$\rho u_j \frac{\partial T_i}{\partial x_j} = \frac{\partial}{\partial x_j}\left[\frac{\mu}{Pr}\frac{\partial T}{\partial x_j} - \rho\overline{T'u'_j}\right] \tag{41.4}$$

Reynolds stresses $-\rho\overline{u'_i u'_j}$ in this study are solved using the standard high Reynolds number $k-\varepsilon$ model [25] with wall function to resolve the wall bounded effects. The kinetic energy of turbulence, $k = u'_i u'_i/2$, and the rate of dissipation of k, $\varepsilon = (\mu/\rho)\overline{(\partial u'_i/\partial x_j)\left(\partial u'_j/\partial x_i\right)}$ are solved using the following transport equations:

$$\rho u_j \frac{\partial k}{\partial x_j} = \frac{\partial}{\partial x_j}\left[\left(\mu + \frac{\mu_t}{\sigma_k}\right)\frac{\partial k}{\partial x_j}\right] + P_k - \rho\varepsilon \tag{41.5}$$

$$\rho u_j \frac{\partial \varepsilon}{\partial x_j} = \frac{\partial}{\partial x_j}\left[\left(\mu + \frac{\mu_t}{\sigma_\varepsilon}\right)\frac{\partial \varepsilon}{\partial x_j}\right] + C_{1\varepsilon}P_k\frac{\varepsilon}{k} - C_{2\varepsilon}\rho\frac{\varepsilon^2}{k} \tag{41.6}$$

where, μ_t is the turbulent eddy viscosity, P_k is the production of the turbulent kinetic energy and $-\rho\overline{T'u'_j}$ is the turbulent heat flux, which are calculate in Eqs. (41.6), (41.7) and (41.8) respectively.

$$\mu_t = C_\mu \rho\frac{k^2}{\varepsilon} \tag{41.7}$$

$$P_k = -\rho\overline{u'_i u'_j}\left(\frac{\partial u_j}{\partial x_i}\right) \tag{41.8}$$

$$-\rho\overline{T'u'_j} = \frac{\mu_t}{\sigma_t}\left(\frac{\partial u_j}{\partial x_i}\right) \tag{41.9}$$

For the standard $k-\varepsilon$ model, the various constants used in the Eqs. (41.4)–(41.8) are taken as $\sigma_k = 1$, $\sigma_\varepsilon = 1.3$, $\sigma_T = 0.85$, $C_{1\varepsilon} = 1.44$, $C_{2\varepsilon} = 1.92$, and $C_\mu = 0.09$.

Once Eqs. (41.4) and (41.5) are solved for k and ε, the turbulent Reynolds stress in Eq. (41.2) are calculated as follow:

$$-\rho\overline{u'_i u'_j} = \left[\mu_t\left(\frac{\partial u_i}{\partial x_j} + \frac{\partial u_j}{\partial x_i}\right)\right] - \frac{2}{3}\rho k\delta_{ij} \tag{41.10}$$

41.3 Results and Discussion

The study is carried out based on the Al Ain prototype solar chimney that was built on 2011 [20]. In the present paper, the steady state numerical results is calculated using the solar heat flux and ambient temperature that were measured for Al Ain solar chimney prototype [2] and shown in Table 41.1.

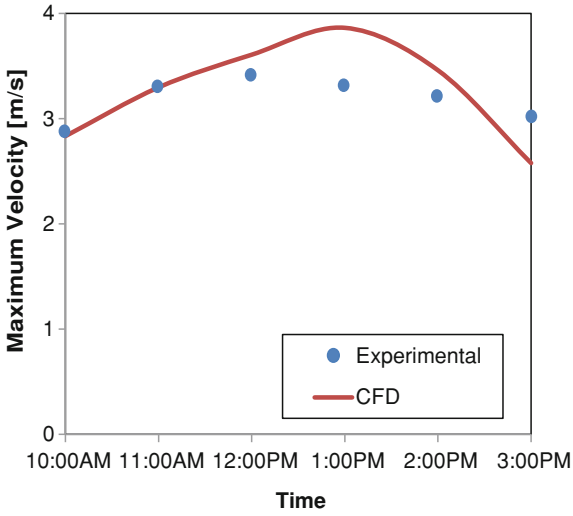

Fig. 41.3 The maximum velocity at the entrance of the chimney which is determined using numerical model versus the measured velocity using anemometer

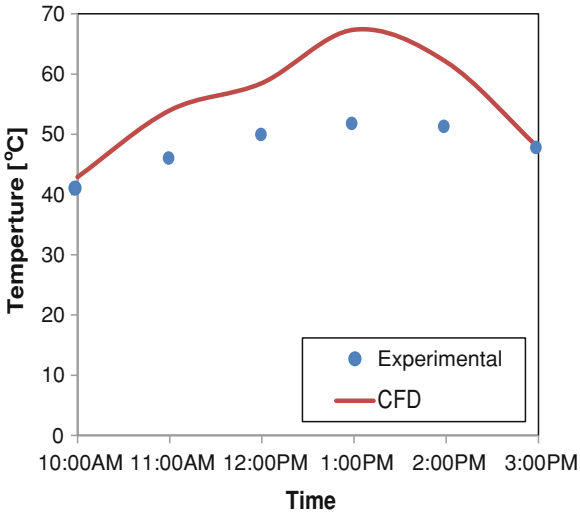

Fig. 41.4 The average temperature at the entrance of the chimney which is determined using numerical model versus the measured temperature using thermal couple recorder

Figures 41.3 and 41.4 show the experimental and numerical results for maximum flow velocity and air temperature, respectively, at the chimney entrance point. As shown in Figs. 41.3 and 41.4, there is some discrepancy between the CFD model and the experimental data which emphasize the importance of the experimental testing. The numerical model shows good prediction of the experimental data at few point mainly at 10 AM where heat flux is 222 W/m^2, ambient temperature of 20.3 °C and chimney maximum velocity of 2.9 m/s. Using the heat flux and ambient temperature at 10 AM as an input, the CFD model is capable to

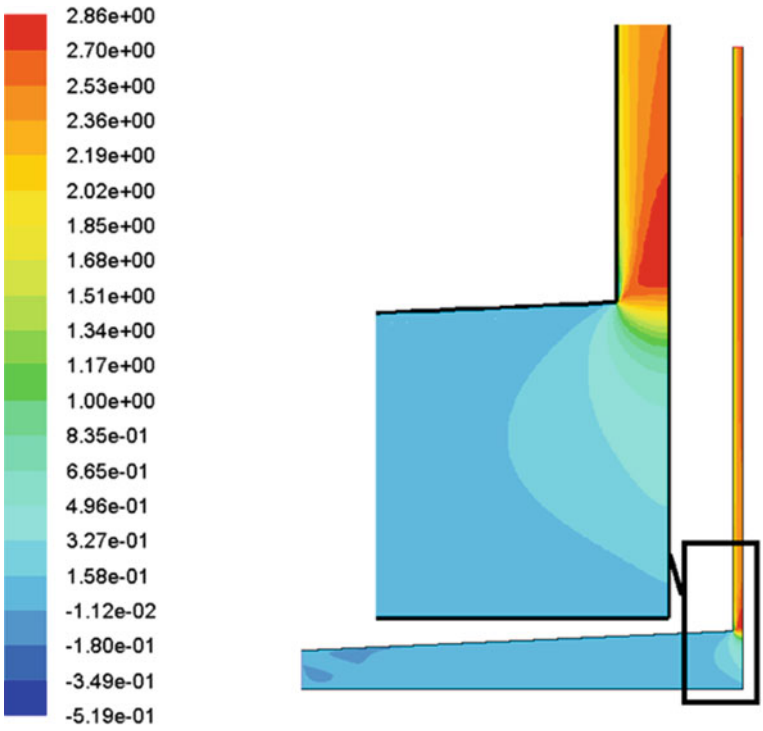

Fig. 41.5 The velocity contour inside the solar chimney tower with a close-up image for the region between the collector and the chimney

predict the maximum velocity of 2.83 m/s and an average temperature of 42.9 °C which match the experimental data shown in Table 41.1. The data shown on Figs. 41.3 and 41.4 shows that the numerical model is not capable to predict the performance of the solar chimney power plant at all operating point since the flow inside the solar chimney is transient and heat flux is continuously changing with time. Also the numerical model does not count for any external wind and condition that will affect the performance of the solar chimney. Nevertheless since the main objective of the study is to evaluate the flow behavior and thermal performance of the actual solar chimney, a steady state CFD analysis can be of great help in designing such system.

To better evaluate Al Ain solar chimney prototype, the point at 10 AM with solar heat flux of 222 W/m^2 and ambient temperature of 20.3 °C are used in the numerical analysis for all the figures from Figs. 41.5, 41.6, 41.7 and 41.8.

Figure 41.5 shows that the maximum velocity is occurring inside the chimney at 0.25 m from the chimney entrance and that the velocity inside the collector is small compared to the velocity inside the chimney. From the low velocity at the velocity contours, it is clear that collector height can be reduced or in other word that chimney diameter can be increased. Such small chimney diameter will force

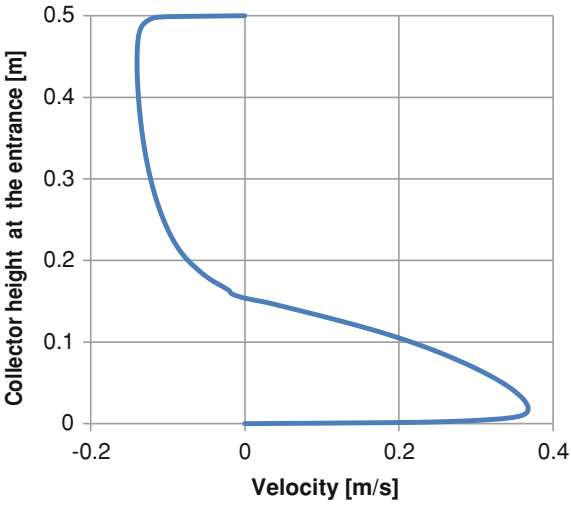

Fig. 41.6 The velocity profile at the entrance of the collector where positive pointing inflow and negating pointing to outlet flow. The average inflow velocity is 0.00321 m/s

air to circulate inside the collector and will cause air circulation. Hence it is expected that some of air will be trapped and circulated inside the collector and even some air will leave from the collector entrance as shown in Fig. 41.6. Using constant inlet static pressure and constant outlet static pressure in which both equal atmosphere pressure of 101 kPa, the velocity at the inlet of the collector is plotted on Fig. 41.6. It is clear from Fig. 41.6 that some air enters near the ground (positive velocity), while some air leaves near the collector cover (negative velocity). Nevertheless the overall flow rate is positive and air is flowing at the entrance of the collector and leaving at the chimney outlet with mass flow rate of 0.1093 kg/s.

The temperature contours inside the solar chimney is shown in Fig. 41.7. Figure 41.7 shows that the air temperature is increasing as the air flows from the collector to the chimney which is predicted since more heat is transferred to the air. Also it shows that not counting the effect of the ground as heat dissipating medium will lead to unrealistic temperature of the ground mainly at the center of the collector. It observed that using constant heat flux at the ground would over predict the ground temperature but it will give more realistic results for air temperature. Nevertheless, authors believe that using constant hear flux as boundary condition is more realistic than using constant ground temperature as used by Patel et al. [26]. The variation of ground temperature was reported by Sangi et al. [15] which indicates that using constant heat flux at the ground is more appropriate than constant ground temperature. More accurate results can be obtained by considering the ground in the computation which can be explored in future work.

Using the CFD model, the velocity at the centerline of the chimney and mass weighted temperature average inside the chimney is shown in Fig. 41.8. It is clear that maximum velocity is achieved near the entrance of the chimney which resulted from the sharp edge entrance of the chimney which caused separation and

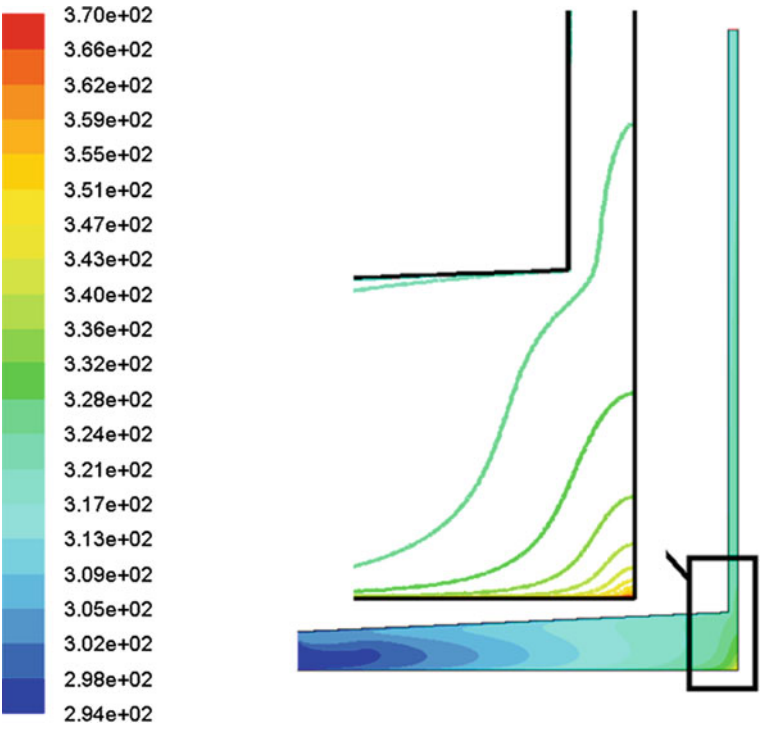

Fig. 41.7 The temperature contour inside the solar chimney tower with a close-up image for the region between the collector and the chimney

Fig. 41.8 The temperature contour inside the solar chimney tower with zoom on the region between the collector and the chimney

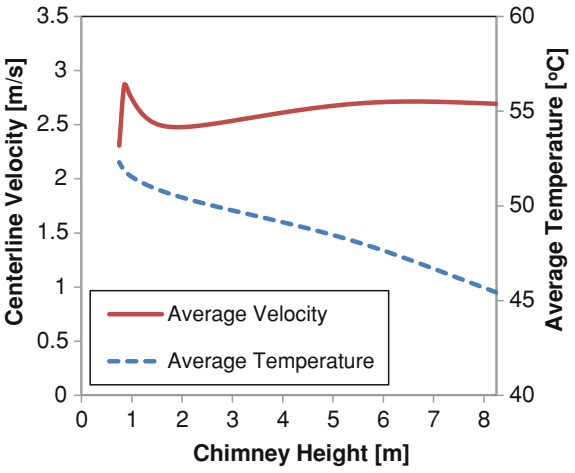

forced the flow to move near the center. Eventually this get dissipated by the viscous force and the flow become hydro-dynamically fully developed. Since the chimney is assumed natural convecting heat to the ambient with convection heat transfer coefficient of 10 W/m^2K, it is expected that the air temperature will drop as shown in Fig. 41.8. Such drop need to be validate by additional experimental future work.

41.4 Conclusions

The mathematical thermal model presented in this study shows a good agreement with published experimental work for Al Ain solar chimney system. The model shows that collector height is directly related to chimney diameter and one needs to consider this solar chimney design. Using constant heat flux boundary condition at the ground is more appropriate than using constant temperature however isoflux will lead over predicted ground temperature mainly at the center. Main chimney losses will occur at the entrance and it is recommended to use a nozzle to reduce such losses.

Acknowledgments The author would like to acknowledge the support provided by United Arab Emirates University. This work was financially supported by the Faculty of Engineering in the United Arab Emirates University through seeds project funding.

References

1. J.K. Afriyie, H. Rajakaruna, M.A.A. Nazha, F.K. Forson, Simulation and optimisation of the ventilation in a chimney-dependent solar crop dryer. Sol. Energy **85**, 1560–1573 (2011)
2. N.A. Vlachos, T.D. Karapantsios, A.I. Balouktsis, D. Chassapis, Design and testing of a new solar tray dryer. Drying Technol. **20**, 1243–1271 (2002)
3. N.K. Bansal, J. Mathur, S. Mathur, M. Jain, Modeling of window-sized solar chimneys for ventilation. Build. Environ. **40**, 1302–1308 (2005)
4. W. Haaf, K. Friedrich, G. Mayr, J. Schlaich, Solar chimneys, Part I: principle and construction of the pilot plant in Manzanares. Sol. Energy **2**, 3–20 (1983)
5. W. Haaf, Solar towers, Part II: preliminary test results from the Manzanares pilot plant. Sol. Energy **2**, 141–161 (1984)
6. S. Nizetic, N. Ninic, B. Klarin, Analysis and feasibility of implementing solar chimney power plants in the Mediterranean region. Energy **33**, 1680–1690 (2008)
7. X. Zhou, F. Wang, R.M. Ochieng, A review of solar chimney power technology. Renew. Sustain. Energy Rev. **14**, 2315–2338 (2010)
8. M.A. dos S. Bernardes, A. Voß, G. Weinrebe, Thermal and technical analyses of solar chimneys, Sol. Energy **75**, 511–524 (2003)
9. X. Zhou, J. Yang, B. Xiao, G. Hou, F. Xing, Analysis of chimney height for solar chimney power plant. Appl. Therm. Eng. **29**, 178–185 (2009)
10. M.O. Hamdan, Analysis of a solar chimney power plant in the Arabian Gulf region. Renewable Energy **36**, 2593–2598 (2011)

11. J. Schlaich, R. Bergermann, W. Schiel, G. Weinrebe, Design of commercial solar updraft tower systems utilization of solar induced convective flows for power generation. Trans. ASME: J. Sol. Energy Eng. **127**, 117–124 (2005)
12. X. Zhou, J. Yang, B. Xiao, G. Hou, Experimental study of temperature field in a solar chimney power setup. Appl. Therm. Eng. **27**, 2044–2050 (2007)
13. C.B. Maia, A.G. Ferreira, R.M. Valle, M.F.B. Cortez, Theoretical evaluation of the influence of geometric parameters and materials on the behavior of the airflow in a solar chimney. Comput. Fluids **38**, 625–636 (2009)
14. A. Koonsrisuk, T. Chitsomboon, Dynamic similarity in solar chimney modeling. Sol. Energy **81**, 1439–1446 (2007)
15. R. Sangi, M. Amidpour, B. Hosseinizadeh, Modeling and numerical simulation of solar chimney power plants. Sol. Energy **85**, 829–838 (2011)
16. E.P. Sakonidou, T.D. Karapantsios, A.I. Balouktsis, D. Chassapis, Modeling of the optimum tilt of a solar chimney for maximum air flow. Sol. Energy **82**, 80–94 (2008)
17. M.O. Hamdan, Analytical Thermal Analysis of Solar Chimney Power Plant, in *Proceedings of the* 4th *ASME International Conference on Sustainable Energy* (ES2010), Phoenix, Arizona, 17–22 May 2010
18. M.O. Hamdan, Analysis of solar chimney power plant utilizing chimney discrete model, Renewable Energy J **56**, 50–54 (2012), http://dx.doi.org/10.1016/j.renene.2012.09.047
19. M.O. Hamdan, Analysis of a solar chimney power plant in the Arabian Gulf region. Renewable Energy **36**, 2593–2598 (2011). doi:10.1016/j.renene.2010.05.002
20. M.O. Hamdan, O. Rabbata, Experimental Solar Chimney Data with Analytical Model Prediction, in *Proceedings of the Solar Conference*; vol 1; 327–332. World Renewable Energy Forum, WREF2012, ISBN:9781622760923, Denver, Colorado, 13–18 May 2012
21. B.A. Kashiwa, C.B. Kashiwa, The solar cyclone: a solar chimney for harvesting atmospheric water. Energy **33**(2), 331–339 (2008)
22. M.A.S. Bernardes, T.W.V. Backström, D.G. Kröger, Analysis of some available heat transfer coefficients applicable to solar chimney power plant collectors. Sol. Energy **83**, 264–275 (2009)
23. R. Sangi, M. Amidpour, B. Hosseinizadeh, Modeling and numerical simulation of solar chimney power plants. Sol. Energy **85**, 829–838 (2011)
24. T. Ming, W. Liu, G. Xu , Analytical and numerical investigation of the solar chimney power plant systems. Int. J. Energy Res. **30**, 861–873 (2006). doi:10.1002/er.1191
25. B.E. Launder, D.B. Spalding, The numerical computation of turbulent flows. Comput. Methods Appl. Mech. Eng. **3**, 269–289 (1974)
26. S.K. Patel, D. Prasad, M.R. Ahmed, Computational studies on the effect of geometric parameters on the performance of a solar chimney power plant. Energy Convers. Manag. **77**, 424–431 (2014)

Chapter 42
Jordan Current Status on Renewable Energy and Energy Efficiency: Analysis and Recommendations for Curricula Development

F. A. Abu Al-Rub, S. Kiwan, Q. Khasawneh and T. Emtairah

Abstract The objective of this study was to study the market analysis and needs for renewable energy and energy efficiency (REEE) in Jordan. The study was based on one-on-one interviews with staff working in REEE related areas. Twenty-three companies in Amman and Irbid with a total number of employees exceeding 1,500 have participated in the study. Key findings of this study were: (1) The concentration of business activities of companies working in REEE in Jordan is within sales/installations, with majority of employees are working in sales and marketing of REEE systems, (2) Difficulties in finding qualified persons with skills related to technical aspects and to general knowledge of REEE, is a common problem for almost all companies participated in the study, (3) Companies indicated that although there is a clear need for qualified engineers, engineers with multidisciplinary skills (knowledge of finance, marketing, or economics) are also needed. These results show that there is a clear interest in broad and multi-disciplinary skills combining solid technical background with economics, finance, and management competencies.

Keywords Energy market needs · Energy efficiency · Curriculum · Education

42.1 Introduction

Natural gas and crude oil/petroleum products cover approximately 98 % of Jordan's total primary energy supply while renewable energy represents less than 1 %. As Jordan lacks domestic natural gas and conventional crude oil resources, their high shares in the national energy mix imply a striking dependence on energy imports of more than 98 % [1, 2].

F. A. Abu Al-Rub (✉) · S. Kiwan · Q. Khasawneh
Jordan University of Science and Technology, P.O. Box 3030, Irbid, Jordan
e-mail: abualrub@just.edu.jo

T. Emtairah
RCREEE, Ard El Golf, Nasr City, Cairo, Egypt

M. O. Hamdan et al. (eds.), *ICREGA'14 - Renewable Energy: Generation and Applications*, Springer Proceedings in Energy, DOI: 10.1007/978-3-319-05708-8_42,

The demand for primary energy is however growing at a rate of 3.7 % and is expected to continue to increase at an average annual rate of 6 %. The volatile fuel prices cost Jordan about $3.2 billion, representing over 19.5 % of GPD and more than 51 % of its 2012 exports. It is anticipated that electricity demand in 2020 be 5,770 MW compared with 2,270 MW in 2008. The additional generated capacity needed is 4,000 MW, which is twice of the existing units. That means additional electricity stations needed on average of 300 MW per year. This is translated to investments in energy sector to exceed $21 Billion by 2020 [1, 3].

To meet these challenges, the Ministry of Energy and Mineral Resources approved a comprehensive Energy Strategy in 2007 to provide a vision for the development of the energy sector over the next decade. The main objectives of this strategy are (1) to diversify energy sources, (2) to increase the dependence on local sources as renewable energy, oil shale, and Uranium (3) to increase the dependence of gas and reduce the share of oil.

Job opportunity for power and energy engineers has been increasing to cover the demand resulting from privatization of electrical generation and distribution, ambitious plans to build large scale power plants fuelled by oil shale, joining the electrical grid with neighboring countries, and the motion to build the two-seas canal and hydro plant near the Dead Sea. Clearly, the need to supply the market with a large number of qualified power engineers is an important factor for the success of such projects.

At present, Jordan has no educational institution that trains specialists to meet the requirements of renewable energy technologies at the bachelor level. To meet the increasing needs for qualified personnel, an education and training program becomes a necessity. However, there is a need to find the most appropriate application and utilization formula for the local conditions with a broad-scope renewable energy education in order to keep up-to-date with emerging technologies and to meet the constantly evolving needs and requirements of the specialized labor market.

The objective of this study was to study the market analysis and needs for renewable energy and energy efficiency (REEE) in Jordan. The results will be used to develop BSc curricula on REEE that are based on the market needs. This was part of the EU-TEMPUS funded project "Modernizing Undergraduate Renewable Energy Education: EU Experience for Jordan" which started in Jordan in 2012 for 3 years [3, 4]. Many academic and research institutions from five European countries in addition to Jordan are participating in this project. The authors of this paper also conducted a similar study in 2011 as part of another TEMPUS project, which aimed at market analysis for REEE and sustainability curriculum development for graduate studies [5].

42.2 Methodology

A survey on Jordan labor market in REEE was conducted during the period January–February 2013 in Amman and Irbid. Twenty-three organizations were one-on-one interviewed. The sample included large, medium, and small commercial

and business organizations active in REEE activities in Jordan including energy management services, renewable energy production, solar water heating system manufacturing, retailers and installers. Additionally, the sample included key stakeholders in the energy sector such as Governmental authorities, and NGOs. Using semi-structured interview guide, face-to-face interviews were conducted with members from the senior management teams in the selected organizations [5]. Interviews lasted on average 1 h. The Analysis focuses on both quantitative and qualitative aspects of labor market conditions and challenges for REEE market growth in Jordan.

42.3 Results and Discussion

42.3.1 Characteristics of REEE Organizations

Focusing on the business organizations, and excluding the main energy generating and distribution companies, there are 20 private companies in the sample. Majority of those are active mainly in solar thermal applications. This is explained by the fact that solar thermal is widely used in Jordan for water heating. Estimates from the National Energy Research Center (NERC) put the diffusion rate of solar water heating systems in residential buildings close to 30 %.

The companies participated in this survey employ more than 1,500 employees, 96 of them are involved directly or indirectly in REEE activities. The concentration of business activities fall within sales/installations, as shown in Fig. 42.1. Three enterprises are engaged in solar thermal and two in the assembly of PV panels. Within the business sample, 70 % of these companies have their turn over from REEE business, and about 10 % of the companies are active in regional markets.

The interviewed sample encompasses organizations fully or partially active in REEE, therefore it was difficult to get precise number of the total employed in REEE related activities. We estimate around 96 working directly or indirectly in this sector. Majority are working in sales and marketing of REEE systems. The second largest group is installation and production of solar heating systems followed by engineering/design activities, as shown in Fig. 42.2.

With regard to the development of REEE related skills, most of the informants indicated that the knowledge was acquired through on job training (Fig. 42.3). Few seem to use external courses (5).

42.3.2 Labor Market

Most participated companies use direct recruiting method and through their web site in addition to recruiting in Jordanian universities. In terms of availability of qualified employees, nearly all respondents indicated difficulties in finding qualified

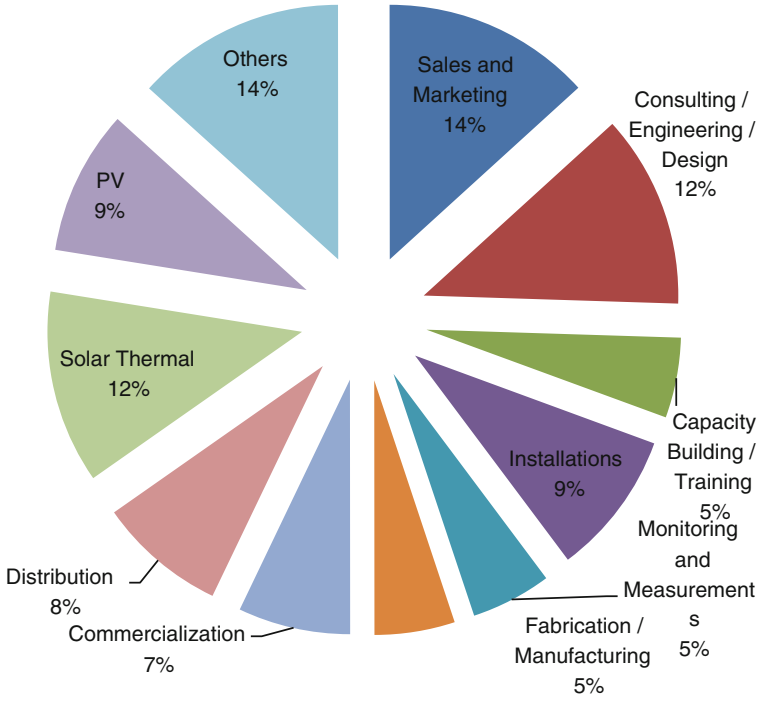

Fig. 42.1 Distribution of companies by business activity

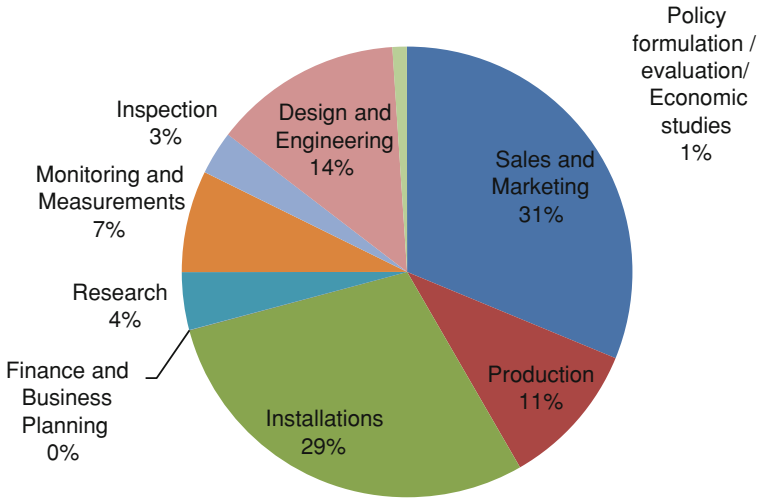

Fig. 42.2 Employees in REEE in the participated companies (Total 96 employees)

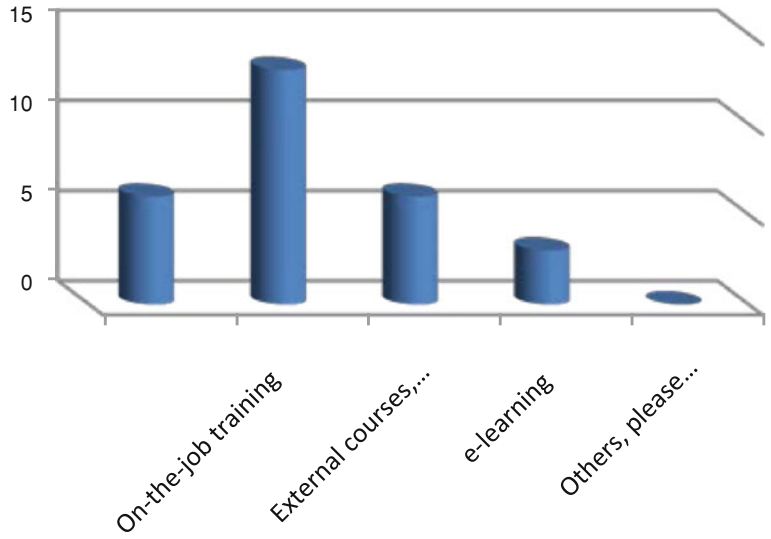

Fig. 42.3 Type of REEE training for employees

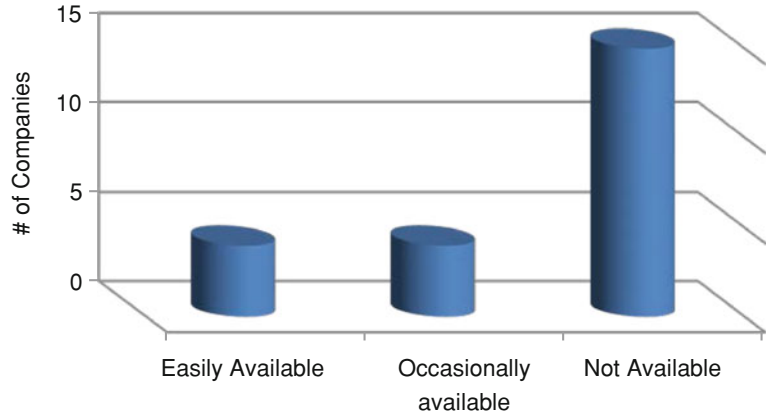

Fig. 42.4 Availability of qualified professionals in the local job market in REEE area

persons in REEE (Fig. 42.4). The skills that are most difficult to find are related to technical aspects and to general knowledge of REEE (see Fig. 42.5). A quarter of the sample also indicated difficulties with finding skills in economics and policy of REEE as well as general management and finance skills.

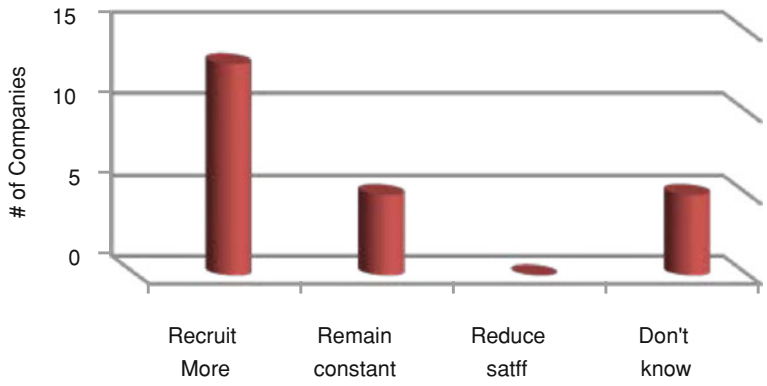

Fig. 42.5 Prospects of Companies in the REEE area for future recruitments in the short term (next 2 year)

42.3.3 Future Prospects

Prospects for future recruitments were explored with respondents through two questions. The first is about plans for future hiring and the second on the type of skills organizations are planning to recruit for. Figure 42.5 shows that more than 50 % of the participated companies are planning to hire more staff. Out of these, three stated they are dependent with their growth plans on progress in the policy area. Five companies think they will not hire in the near future and five companies were uncertain about the recruitment prospects in their companies.

In terms of skills organizations will be looking to acquire, majority indicated intent to hire professionals with REEE qualifications (See Fig. 42.6). About 80 % of the companies indicated the need to hire technicians in REEE. Multi-disciplinary knowledge and sales and marketing skills were frequently mentioned also.

42.3.4 Needed Competencies and Expertise

The type of competencies needed for the growth of the REEE sector in Jordan was explored with the informants through two questions addressing both own organizational needs and national needs for HR competencies in REEE. Figure 42.7 shows the competencies/expertise needed and currently are missing from the local market, and Fig. 42.8 shows the competencies/expertise most important for the growth of the company's business (frequency). Because these profiles represent specific needs of the individual organizations, there is a wide range of expertise reflected in the answers. However, companies seem to be clear on the need for qualified engineers but also engineers with multidisciplinary skills (knowledge of finance, marketing, or economics).

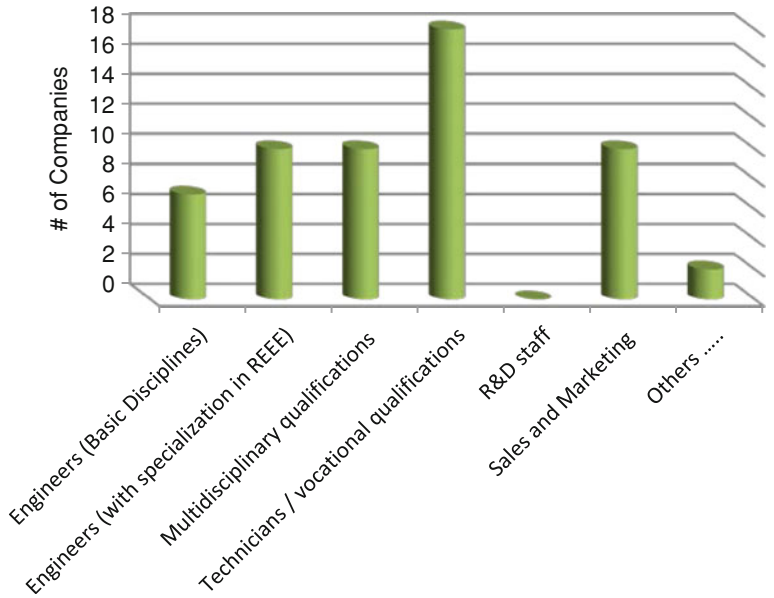

Fig. 42.6 Skills organizations will be looking to hire in the near future

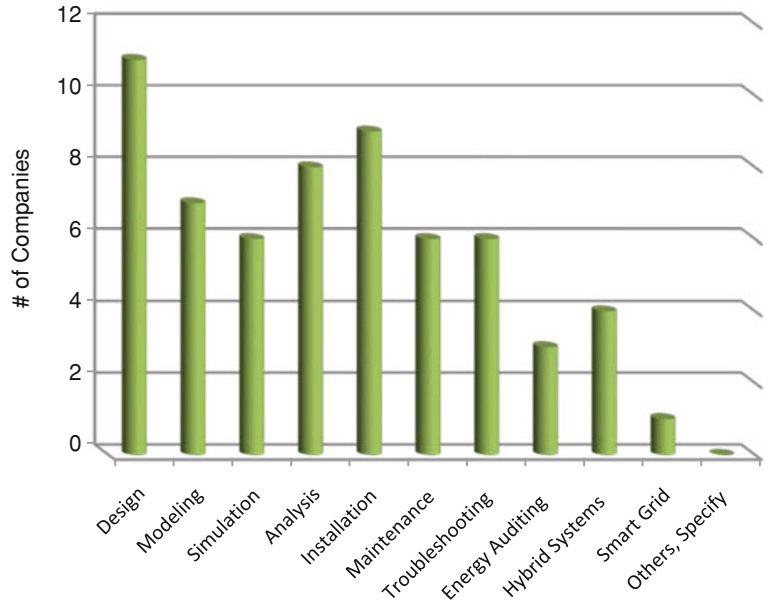

Fig. 42.7 The HR competencies/expertise needed and currently are missing from the local market

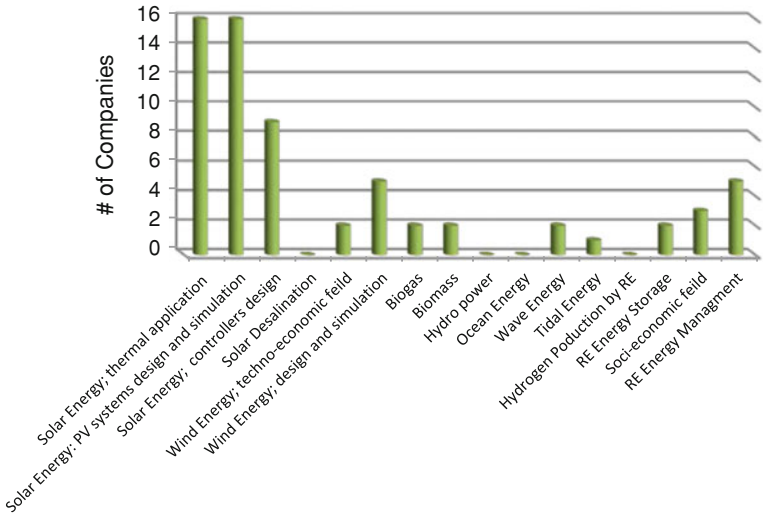

Fig. 42.8 REEE topics the HR expertise are needed the most for the local labor market

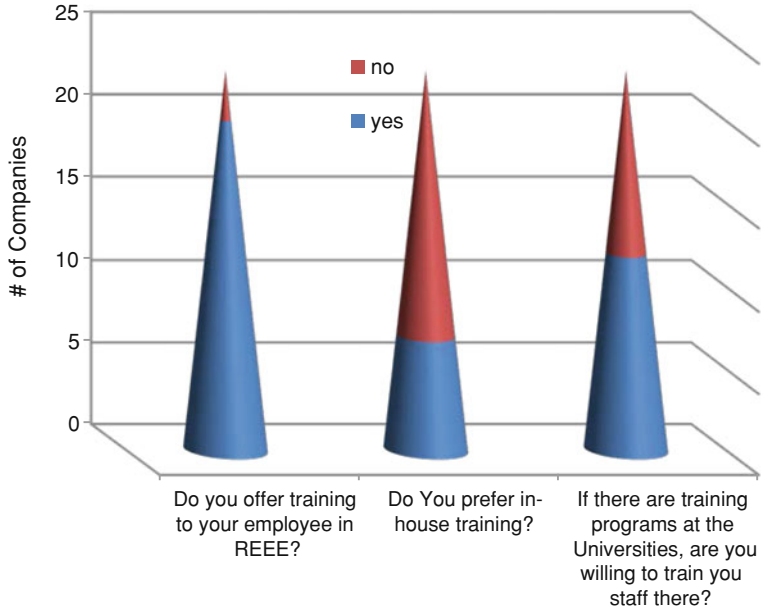

Fig. 42.9 Training of employees in REEE

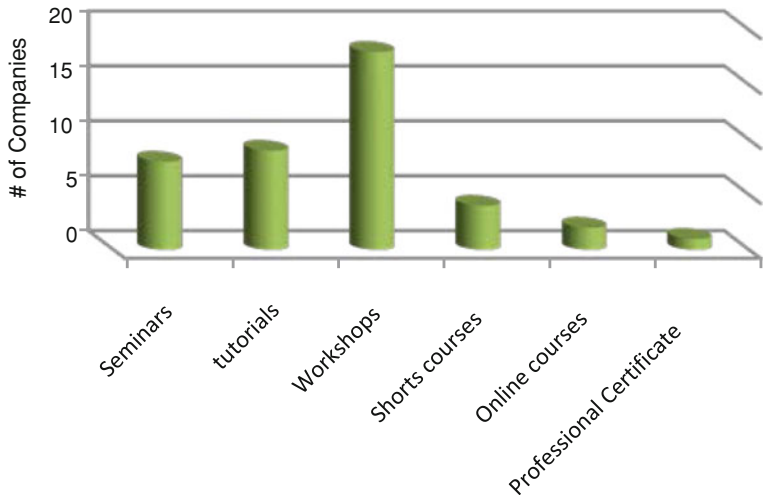

Fig. 42.10 Most effective long-life learning techniques in REEE field

42.3.5 Training in REEE

Figure 42.9 shows that most of the participated companies offer training for their employees in REEE. Only 25 % of them offer in-house training. 50 % of them indicated that they are welling to send their employees for training in universities. Most of these companies believe that the most effective long-life learning techniques in REEE field are the workshops and tutorials, as shown in Fig. 42.10.

42.4 Conclusions

Jordan set an ambitious target of increasing the share of renewable energies to 10 % of the total energy balance by 2020, resulting in employment and economic benefits. It is expected to spend more than 21 Billion Dollars on the energy sector by 2020. However, in order for Jordan to maximize the benefits and reduce the cost of this investment, Jordan shall enter a new phase in manufacturing and installation of renewable energy systems. It is evident from the views of industry actors and public agencies that there are skill gaps in the local labor market with regard to specific competencies. These include engineering competencies in various areas of renewable energies, competencies in the economics and policy areas of REEE, project management skills, and installation and maintenance skills. In terms of future prospects, it is also evident that, with appropriate policies and framework conditions, local enterprises are looking to expand hiring of qualified people in REEE.

The curricula should support the objective of building related skills in communication, public outreach and entrepreneurship. These elements should/can be incorporated indirectly through teaching methods and design of student assignments and group projects (even for technical subjects).

Acknowledgments The authors would like to acknowledge EU-TEMPUS for supporting this project. This study was conducted as part of the TEMPUS Projects No. 530332-TEMPUS-1-2012-1-JO-TEMPUS-JPCR, and No. 511069-1-TEMPUS-2010-1-IT. In addition, the authors would like to acknowledge Jordan University of Science and Technology for supporting the participation in the conference.

References

1. H. Hamdi, F. Abu Al-Rub, J. Hamdi, The prospects for sustainable biodiesel production in Jordan, in *Proceedings of the 1st International Nuclear and Renewable Energy Conference (INREC10)*, Amman, Jordan, 21–24 March, 2010
2. Jordan Electricity Regulatory Commission, Annual Report, 2009
3. Modernizing Undergraduate Renewable Energy Education: EU Experience for Jordan "MUREE": Tempus Project No. 530332-TEMPUS-1-2012-1-JO-TEMPUS-JPCR, 2013, http://www.muree@psu.edu.jo. Cited 28 December 2013
4. Master on Sustainable Development and Renewable Energy Tempus Project No.: 511069-1-TEMPUS-2010-1-IT, 2011, http://www.mansur-energy.eu. Cited 28 December 2013
5. Jordan Labor Market Needs in Renewable Energy and Energy Efficiency (REEE): Analysis and Recommendations for Curricula Development in Tertiary Education, 2012, http://www.mansur-energy.eu. Cited 28 December 2013

Chapter 43
Heterojunction Solar Cell Based on p-type PbS Quantum Dots and Two n-type Nanocrystals CdS and ZnO

Sawsan Dagher, Yousef Haik, Ahmad Ayesh and Nacer Tit

Abstract Heterojunction solar cells based on PbS quantum dots (QDs) were prepared at room temperature via spin coating method. The PbS QDs were synthesized, characterized and utilized in p-n heterojunction solar cell structure. The effect of combining two different n-type nanoparticles on the solar cell photovoltaic performance was studied. The solar cells were characterized under 1 sun illumination (irradiation of 1,000 W/m^2). The optimum solar cell by depositing PbS QDs layer onto ZnO/CdS nanoparticles layers exhibits a short-circuit current of 1.36 mA/cm^2, open circuit voltage of 127 mV, and power conversion efficiency of 1.21 %, representing efficiency improvement more than 3 and 5 orders of magnitude compared with the case of employing only one n-type nanoparticles ZnO and CdS, respectively.

Keywords Heterojunction solar cells · Quantum dot solar cells · Pbs

43.1 Introduction

Quantum dots (QDs) are semiconductor nanocrystals, have attracted significant attention as one of the most competent material for solar cell applications than bulk crystals due to their quantum size effects and high surface-to-volume ratio. Among these nanomaterials, lead sulfide (PbS) is *p*-type narrow bandgap semiconductor, has shown a promise as extraordinary active layer in QD solar cells, since it has a high absorption coefficient, multiple exciton generation processes, and solution processability [1–5].

S. Dagher · Y. Haik (✉) · A. Ayesh · N. Tit
United Arab Emirates University, Al Ain, United Arab Emirates
e-mail: yhaik@uaeu.ac.ae

M. O. Hamdan et al. (eds.), *ICREGA'14 - Renewable Energy: Generation and Applications*, Springer Proceedings in Energy, DOI: 10.1007/978-3-319-05708-8_43,

PbS QDs has been utilized in five different types of QDs solar cells structures; (1) Schottky junction cells where PbS QD connected to a metal [6–11]. (2) QDs sensitized cells where PbS QDs were used as alternative to the dyes in dye sensitized cells with liquid electrolyte existence [12–18]. (3) Homojunction cells where *n*-doped PbS QDs were used [19]. (4) Hybrid polymer cells where n type organic semiconductors such as (C60 and PCBM) were used [20, 21]. (5) Depleted heterojunction cells where PbS QDs attached to other *n*-type wide band gap metal oxides such as ZnO or TiO_2 [22–25] or *n*-type metal calcogenides such as CdS or Bi_2S_3 [26, 27].

Although ZnO and TiO_2 have similar physical properties and energy band structure, still ZnO is preferred to be used as buffer layer for heterojunction solar cells rather than TiO_2, since it has higher electron affinity than TiO_2, as well it has 2–3 times higher electron mobility than TiO_2 [28], and can be utilized for all sized PbS QDs. Whereas TiO_2 is appropriate for PbS QDs diameters below approximately 4.3 nm to allow an efficient transfer of electrons from the conduction band of PbS QD to the conduction band of TiO_2 [29]. CdS is a non-stoichiometric n-type semiconductor with direct band gap energy of 2.42 eV for a bulk, which can absorb in the visible range of the solar spectrum [30].

In this work we open up the options for a solid heterojunction type of cell structures where no liquid electrolyte is used through the combination of tow n-type nanoparticles ZnO and CdS to PbS QDs.

43.2 Experimental Details

43.2.1 Materials

Lead acetate trihydrate (Pb $(CH_3COO)_2{\cdot}3H_2O$, 99.9 %), zinc acetate dehydrate (Zn $(CH_3COO)_2{\cdot}2H_2O$, 99.9 %), sodium hydroxide (NaOH), cadmium acetate dihydrate ($Cd(CH_3COO)_2{\cdot}2H_2O$), sodium sulfide pentahydride (Na2S·5H2O), oleic acid (OA, technical grade 90 %), 1-octadecene (ODE, technical grade 90 %), hexamethyldisilal-thiane (TMS), 1,2-ethanedithiol (EDT, 97 %), acetonitrile (99.9 %), and indium tin oxide (ITO) coated glass (surface resistivity 8–12 Ω/sq) were purchased from Sigma–Aldrich. Ethanol (C_2H_5OH) was purchased from Molar Chemicals ltd, n-hexane (95.0 %) and methanol (99.8 %) were purchased from Panreac, toluene (99.8 %) was purchased from TEDIA, and aluminum (Al, 1–3 mm pieces, 99.99 %) was purchased from Ltd Testbourne.

43.2.2 Synthesis of ZnO Nanoparticles and PbS QDs

ZnO nanoparticles used in this work were synthesized according to a previously published method [31]. Briefly, 0.398 g zinc acetate and 0.127 g NaOH were dissolved in 100 ml ethanol by magnetic stirring and kept at 60 °C for 1 h the zinc

oxide ethanol dispersion was mixed with DI-water and centrifuged, three times. Finally the ZnO particles were redispersed in DI-water to obtain ZnO water dispersion with concentration of 20 %. Result showed that the average size of ZnO nanoparticles was 5 nm.

PbS QDs were prepared similar to a previously reported method [26] in summery 1.138 g ($Pb(CH_3COO)_2 \cdot 3H_2O$, 99.9 %) were dissolved in a mixture of 2.1 mL of OA and 30 mL of (ODE) at 100 °C for 8 h. Then the solution temperature was raised to 120 °C, and at this point a mixture of 0.315 mL TMS and 15 mL of ODE was injected swiftly into Pb precursor solution. After stop the heating the solution was kept on the heating mantle for cooling. QDs were extracted with acetone, and then precipitated twice, first with ethanol and second with acetone for purification, finally redispersed in hexane with concentration of 10 %.

43.2.3 Devise Fabrication

All the layers were deposited in a fume hood with good ventilation using a layer-by-layer spin-coating method deposition method at 2,500 rpm for 15 s each deposition time, except for CdS nanoparticles layer was deposited by successive ionic layer adsorption and reaction (SILAR) technique [18].

To prepare the substrates ITO coated glass were cleaned by sonication for 15 min in acetone and another 15 min in methanol, finally rinsed in de-ionized water and dried with nitrogen gas (N_2). To deposit ZnO nanoparticles layer, few drops of ZnO water dispersion were added onto the ITO/glass and spin coated, the process repeated 3 times.

Cd and sulfur (S) precursors were prepared in advance; 1.54 g Cd $(NO_3)_2$ and 0.3902 g ($Na_2S{\cdot}5H_2O$) each was dissolved in 100 ml solution of methanol and water (1:1). The substrates were dipped into Cd precursor solution for 1 min, rinsed with methanol, and then dipped for another 1 min into S precursor solution, and rinsed again with methanol to finish the one cycle. Five cycles were applied to perform CdS NPs layer.

10 PbS QDs layers were performed by three steps for each layer. Firstly few drops of PbS QDs hexane dispersion were added to the film surface and spin coated, in the second step we flooded the surface by EDT/acetonetrile solution (0.5:100 v/v) and waited 30 s before spinning, in the third step the film was washed with acetonetrile and spun for 3 s to dry.

Finally, Al layer with 100 nm thickness was deposited on the top through a shadow mask, by thermal evaporation under vacuum (10^{-5} Torr pressure).

43.2.4 Characterization

Morphology of the as prepared PbS nanoparticles was visualized by scanning electron microscope (SEM, JEOL, JSM-5600); samples were prepared on carbon-

coated copper grids. The nanoparticles size distribution for each sample was characterized by the dynamic light scattering (DLS) technique using a Zeta sizer from Malvern Instruments (Model ZEN360, England). The ultraviolet–visible (UV–Vis) absorption was measured using UV–Vis spectrophotometer (Shimdzu, UV-2450). The photovoltaic performance of the devices was measured using solar simulator (Model 71445, New Pot) and Keithley Source Meter (2425) under illumination of air mass 1.5 global (AM 1.5G) light (100 mW/cm^2).

43.3 Results and Discussion

43.3.1 PbS QDs Characterization

Figure 43.1 shows SEM images of PbS QDs agglomerated as crystals on carbon-coated copper grid.

Figure 43.2 shows the size distribution histogram of colloidal PbS QDs hexane dispersion. It is clear that it has narrow size distribution, with average size of 6.6 nm. This size is much smaller than the previously reported exciton Bohr radius of PbS (18 nm) [32] so the electron confinement effect was dominant.

Figure 43.3 reveals, that colloidal PbS QDs absorb within the IR wavelength region, the maximum absorption peak at 912 nm, can be attributed to the exciton absorption of PbS QDs, and two weak peaks at 720 nm and 1,020 nm, which are corresponding to existence of smaller and bigger PbS QDs respectively. The absorption peaks is blue shifted compared to the bulk PbS, because the Energy gap (Eg) increases as the particles size decreases. The optical band gap of PbS QDs is calculated from the absorption peak using Eq. (43.1) [33].

$$(\alpha)\mathrm{hv})^{\mathrm{n}} = \mathrm{B}\ (\mathrm{hv} - \mathrm{E_g}) \tag{43.1}$$

where α is the absorption coefficient in cm^{-1}, B is a constant related to the material, hν is the photon energy in eV, *h* is Plank's constant (6.626×10^{-34}), ν is the frequency of the photon, E_g is the optical band gap in eV, n is the exponent that can take a value of 2 for a direct transition or 1/2 for an indirect transition.

The absorption coefficient α was calculated from:

$$\alpha \mathrm{d} = \ln(1/\mathrm{T}) \tag{43.2}$$

where d stands for the path length of the wave in cm and was set equal to the cuvette length of 1 cm, T is the transmittance which was calculated from the measured absorbance (A_λ) at a certain wavelength of light (λ) using [34]:

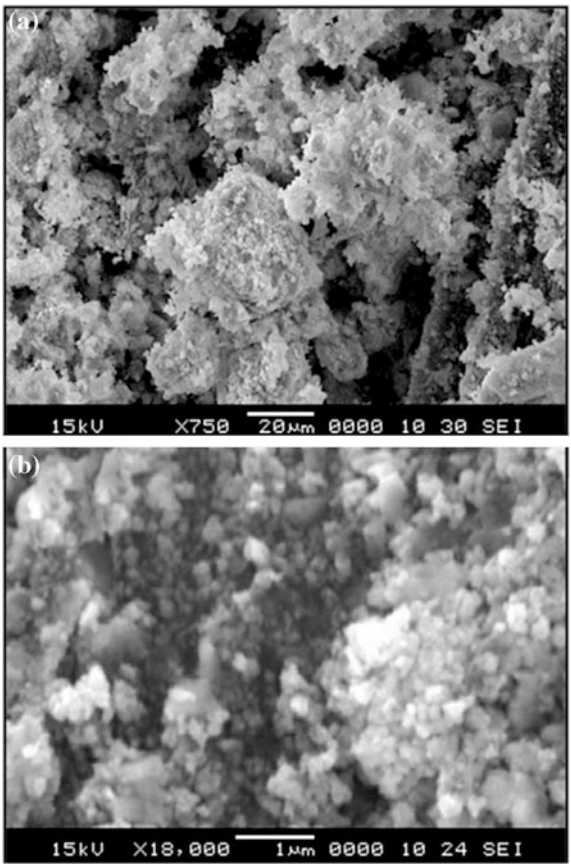

Fig. 43.1 SEM images of agglomerates of PbS QDs

$$A_\lambda = -\log_{10}(T) \tag{43.3}$$

Figure 43.4 represents $h\nu^2$ versus $h\nu$ plots of absorption spectra for the PbS QDs. The energy band gap of the PbS QDs is estimated by fitting a straight line to the linear portion of the curve. The E_g value should be obtained from the intercept with the $h\nu$-axis. The obtained Eg value for PbS QDs is 1.36 eV which is much larger than the bulk (0.41 eV) [32]. The observed increase in the direct band gap values (a blue shift) of PbS QDs with the decrease in nanoparticle size is associated with the electron confinement effect as a result of the reduction in the particles size to the nanoscale.

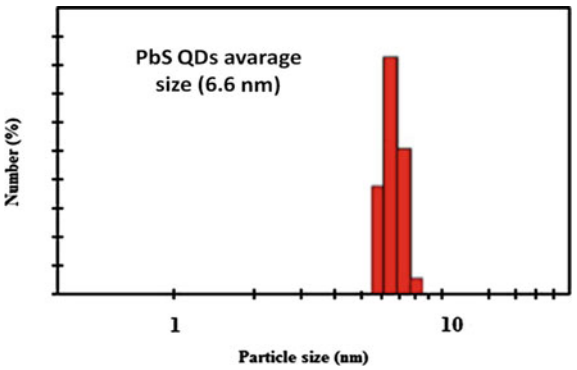

Fig. 43.2 Size distribution histograms of colloidal PbS QDs, dispersed in hexane

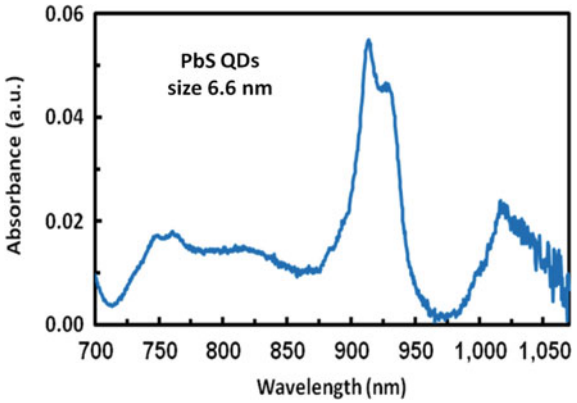

Fig. 43.3 UV–Visible absorption spectra of colloidal PbS QDs

43.3.2 Device Architecture Characterization

Figure 43.5 shows the ITO/ZnO/CdS/PbS/Al solar cell structure, and its equilibrium band diagram. The ZnO layer can effectively invert the polarity of the cell, since ZnO accept electrons from the active layer, transport them to the ITO electrode layer, and block holes transfer, Owing to its high electron affinity of 4.4 eV and high ionization potential of 7.6 eV [28], and high electron mobility [27]. CdS layer enhanced the transfer of photgenerated electrons from PbS and CdS to ZnO through the gradual energy alignment.

Long ligands (oleic acid) which used in PbS QDs synthesis process are likely to hinder the charge transport between PbS QDs because of their insulating characteristics; therefore EDT molecules were applied during the layer-by- layer coating of the PbS QDs, to replace the oleic acid molecules. As a result EDT ligand exchange shorten the distance between the PbS QDs, increase carrier mobility, insolubilize the QDs and reduce the surface oxidation process [6, 14].

Thus in the produced structure ZnO NPs serves three functions; (a) to promote the separation of the electrons and holes as ZnO has a wide band gap and a low

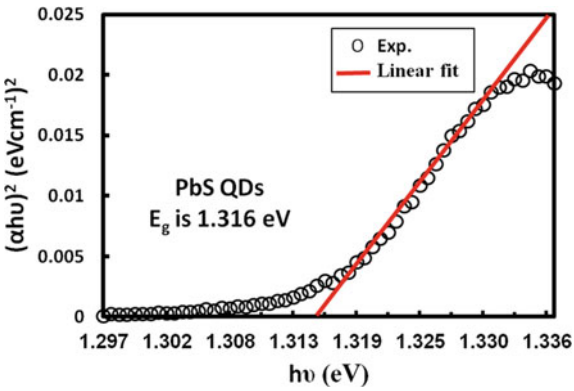

Fig. 43.4 Direct band gap estimations of PbS QDs Of average size 6.6 nm

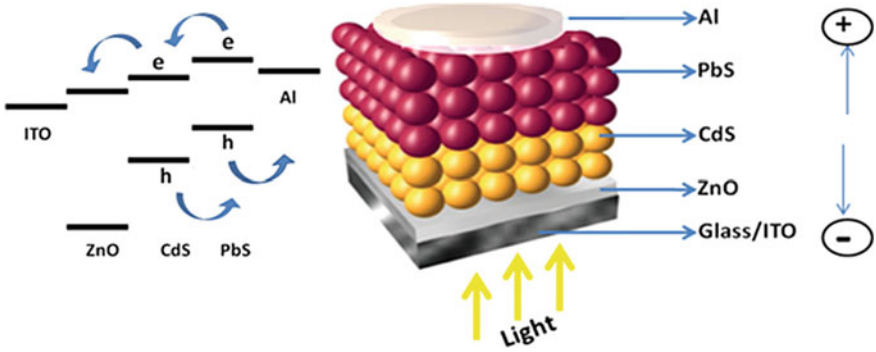

Fig. 43.5 Schematic structure and energy level diagram of ITO/ZnO /CdS/PbS/Al solar cells

conduction band which act as electrons attractive layer, (b) ZnO absorbs UV light, (c) to load the CdS NPs. CdS serves the gradual path for electrons transfer from PbS conduction band to ZnO conduction band. In addition to the illustrated role of EDT PbS QDs ligand exchange

43.3.3 Device Performance Characterization

The effect of attaching two different n-type nanoparticles to the PbS QDs on heterostructure solar cells performance has been studied. Figure 43.6a–c shows current density–voltage (J–V) characteristics for three different heterojunction solar cells under 1 sun illumination. Table 43.1 shows the measured photovoltaic parameters for the synthesized PbS QDs solar cells with three different structures.

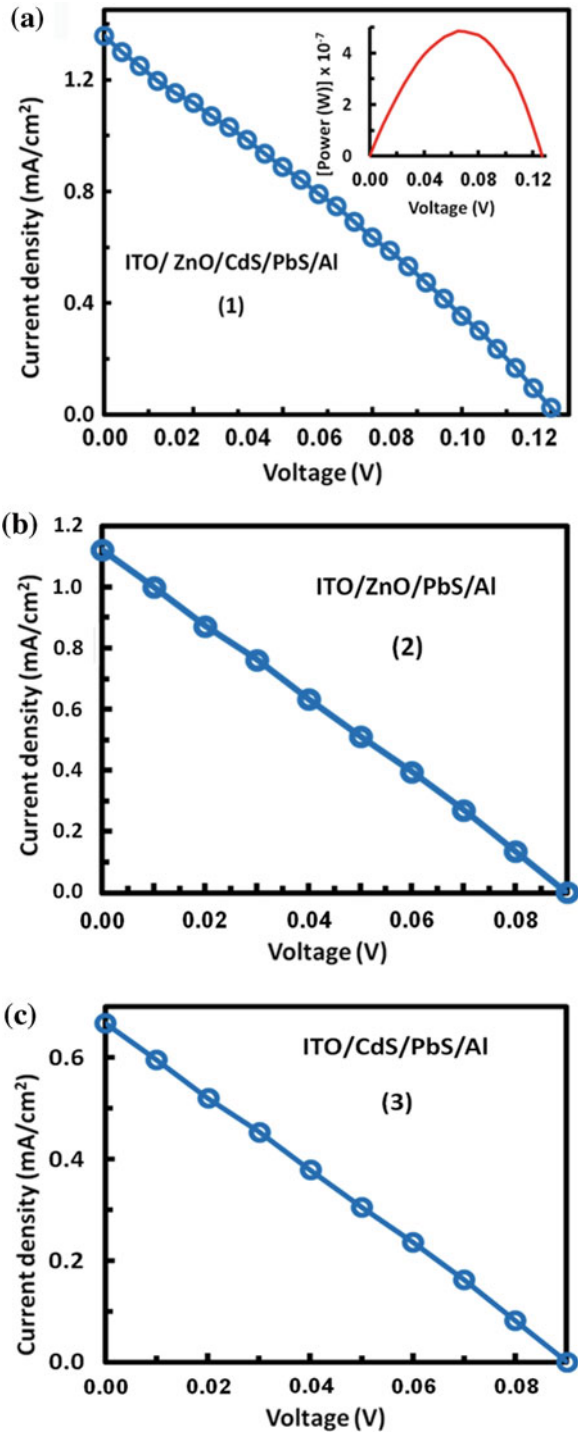

Fig. 43.6 J−V characteristics for three different structures of PbS QDs based solar cells, the inset in **a** represents P–V characteristic graph for cell (1). The cells were measured under AM1.5G simulated solar illumination

Table 43.1 The photovoltaic parameters for three different PbS QDs solar cell structures

Cell no.	J_{sc} (mA)	V_{oc} (mV)	R_{sh} (Ω) $\times 10^4$	R_s (Ω) $\times 10^3$	P_{max} (W) $\times 10^{-7}$	FF (%)	PCE (%)
1	1.36	127	1.08	2.12	4.86	28.2	1.21
2	1.1 2	90	0.825	1.14	2.56	25.4	0.29
3	0.67	93	1.49	1.27	1.67	26.7	0.19

where, J_{sc} is short circuit current density, V_{oc} is open circuit voltage, R_{sh} is shunt resistance, R_s is series resistance, P_{max} is maximum power, FF is fill factor and PCE is power conversion efficiency. In cell (1) ZnO NPs and CdS NPs layers contribute to the highest J_{sc}, V_{oc}, FF, P_{max} and R_s and the lowest R_{sh} that yields 1.2 % efficiency. Whereas the efficiency of cell (2) ZnO NPs/PbS QDs without CdS, was reduced to 0.29 % because of the large decrease in V_{oc} and R_{sh}. Although cell (3) CdS NPs/PbS QDs without ZnO, produced the most $R_{sh,}$ the efficiency was reduced to 0.19 %, because of the considerable decrease in the J_{sc} and V_{oc}. The series resistance is responsible for the reduction in FF and P_{max} and consequently on the PCE. R_s for each cell can be indicated from the slope reverse of its J–V graph. The slopes of the three graphs are shown to be low that indicate high R_s.

Utilizing tow n type nanoparticles to be attached to PbS QDs in correct energy bands alignment, ZnO buffer layer on the top of ITO coated glass because ZnO is transparent so it allows light to pass through to the second n type nanoparticles CdS and then to PbS QDs, facilitate the light absorption, charge separation and transfer the charges to the opposite electrodes.

43.4 Conclusions

The synthesized PbS nanoparticles have narrow size distribution, their average size is 6.6 nm. The UV–visible absorption spectra of the PbS QDs showed absorption in the IR region with maximum peak at 912 nm that is corresponding to band gap energy of 1.36 eV that is much larger than the bulk. Solar cells based on PbS QDs were prepared by combining the PbS to other tow n-type nanoparticles by using spin coating and SILAR process. Cells based on three layers of ZnO/CdS/PbS hetrostructure demonstrated the optimal conversion efficiency of 1.26 % which was larger than that of ZnO/PbS and CdS/PbS under the same condition. The devices have shown high R_s and relatively low J_{sc} that means the injected electrons in conduction band of ZnO tends to recombine readily with positively charged PbS QD, as a result efficient charge collection was hindered. We recommend for future work, using an efficient hole extraction layer such as molybdenum oxide (MoO_x) and vanadium oxide (V_2O_x) to be applied beneath the metal electrode.

References

1. O.E. Semonin, J.M. Luther, S. Choi, H.Y. Chen, J. Gao, A.J. Nozik, M.C. Beard, Peak external photocurrent quantum efficiency exceeding 100 % via MEG in a quantum dot solar cell. Science **334**, 1530–1533 (2011)
2. R.D. Schaller, V.I. Klimov, High efficiency carrier multiplication in PbSe nanocrystals: implications for solar energy conversion. Phys. Rev. Lett. **92**, 186601 (2004)
3. R.J. Ellingson, M.C. Beard, J.C. Johnson, P. Yu, O.I. Micic, A.J. Nozik, A. Shabaev, A.L. Efros, Highly efficient multiple exciton generation in colloidal PbSe and PbS quantum dots. Nano Lett. **5**, 865–871 (2005)
4. R.L. Sandberg, L.A. Padilha, M.M. Qazilbash, W.K. Bae, R.D. Schaller, J.M. Pietryga, M.J. Stevens, B. Baek, S.W. Nam, V.I. Klimo, Multiexciton dynamics in infrared-emitting colloidal nanostructures probed by a superconducting nanowire single Photon detector. ACS Nano **6**, 9532–9540 (2012)
5. P.D. Cunningham, J.E. Boercker, E.E. Foos, M.P. Lumb, A.R. Smith, J.G. Tischler, J.S. Melinger, Enhanced multiple exciton generation in quasi-one-dimensional semiconductors. Nano Lett. **11**, 3476–3481 (2011)
6. K. Szendrei, W. Gomulya, M. Yarema, W. Heiss, M.A. Loi, PbS nanocrystal solar cells with high efficiency and fill factor. Appl. Phys. Lett. **97**, 203501–203503 (2010)
7. R. Debnath, J. Tang, D.A. Barkhouse, X. Wang, A.G. Pattantyus-Abraham, L. Brzozowski, E.H. Sargen, Ambient-processed colloidal quantum dot solar cells via individual pre-encapsulation of nanoparticles. J. Am. Chem. Soc. **132**, 5952–5953 (2010)
8. H. Fu, S.W. Tsang, Y. Zhang, J. Ouyang, J. Lu, K. Yu, Y. Tao, Impact of the growth conditions of colloidal PbS nanocrystals on photovoltaic device performance. Chem. Mater. **23**, 1805–1810 (2011)
9. K.W. Johnston, A.G. Pattantyus-Abraham, J.P. Clifford, S.H. Myrskog, D.D. Mac Neil, L. Levina, E.H. Sargent, Schottky-quantum dot photovoltaics for efficient infrared power conversion. App. Phys. Lett. **92**, 151113–151115 (2008)
10. J. Tang, X. Wang, L. Brzozowski, D. Aaron, R. Barkhouse, R. Debnath, L. Levina, E.H. Sargent, Schottky quantum dot solar cells stable in air under solar illumination. Adv. Mater. **22**, 1398–1402 (2010)
11. J. Tang, L. Brzozowski, D. Barkhouse, X. Wang, R. Debnath, R. Wolowiec, E. Palmiano, L. Levina, A.G. Pattantyus-Abraham, D. Jamakosmanovic, E.H. Sargent, Quantum dot photovoltaics in the extreme quantum confinement regime: the surface-chemical origins of exceptional air- and light-stability. ACS Nano **4**, 869–878 (2010)
12. N. Zhao, P.O. Tim, L.Y. Chang, M.G. Scott, D. Wanger, T.B. Maddalena, C.A. Alexi, G.B. Moungi, B. Vladimir, Colloidal PbS quantum dot solar cells with high fill factor. ACS Nano **4**, 3743 (2010)
13. G. Serap, P.F. Karolina, N. Helmut, S.S. Niyazi, K. Sandeep, D.S. Gregory, Hybrid solarcells using PbS nanoparticles. Sol. Energy Mat. Sol. C **91**, 420 (2007)
14. R. Chalita, C.R. Xiong, J.B. Kenneth, Fabrication of PbS quantum dot doped TiO_2 nanotubes. ACS Nano **2**, 1682 (2008)
15. L.D. Wang, D.X. Zhao, Z.S. Su, D.Z. Shen, Hybrid polymer/ZnO solar cells sensitized by PbS quantum dots. Nanoscale Res. Lett. **7**, 106 (2012)
16. N. Zhou, G.P. Chen, X.L. Zhang, L.Y. Cheng, Y.H. Luo, D.M. Li, Q.B. Meng, Highly efficient PbS/CdS co-sensitized solar cells based on photoanodes with hierarchical pore distribution. Electrochem. Commun. **20**, 97 (2012)
17. J. Gao, J.M. Luther, O.E. Semonin, R.J. Ellingson, A.J. Nozik, M.C. Beard, n-Type transition metal oxide as a hole extraction layer in PbS quantum dot solar cells. Nano Lett. **11**, 3263–3266 (2011)
18. Y. Li, L. Wei, X. Chen, R. Zhang, X. Sui, Y. Chen, J. Jiao, L. Mei, Efficient PbS/CdS co-sensitized solar cells based on TiO_2 nanorod arrays. Nanoscale Res. Lett. **8**, 67 (2013)

19. J. Tang, H. Liu, D. Zhitomirsky, S. Hoogland, X. Wang, M. Furukawa, L. Levina, E.H. Sargent, Quantum junction solar cells. Nano Lett. **12**, 4889–4894 (2012)
20. E.J.D. Klem, C.W. Gregory, G.B. Cunningham, S.D. Hall, S. Temple, J.S. Lewis, Planar PbS quantum dot heterojunction photovoltaic devices with 5.2 % power conversion efficiency. Appl. Phys. Lett. **100**, 173104–173109 (2012)
21. N. Zhao, T.P. Osedach, L.Y. Chang, S.M. Geyer, D. Wanger, M.T. Binda, A.C. Arango, M.G. Bawendi, V. Bulovic, Colloidal PbS quantum dot solar cells with high fill factor. ACS Nano **4**, 3743–3752 (2010)
22. X. Wang, G.I. Koleilat, A. Fischer, J. Tang, R. Debnath, L. Levina, E.H. Sargent, Enhanced open-circuit voltage in visible quantum dot photovoltaics by engineering of carrier-collecting electrodes. ACS Appl. Mater. Interf. **3**, 3792–3795 (2011)
23. P.R. Brown, R.R. Lunt, N. Zhao, T.P. Osedach, D.D. Wanger, L.Y. Chang, M.G. Bawendi, V. Bulović, Improved current extraction from ZnO/PbS quantum dot heterojunction photovoltaics using a MoO_3 interfacial layer. Nano Lett. **11**, 2955–2961 (2011)
24. G. Pattantyus-Abraham, I.J. Kramer, A.R. Barkhouse, X. Wang, G. Konstantatos, R. Debnath, L. Levina, I. Raabe, M.K. Nazeeruddin, M. Grätzel, E.H. Sargent, Depleted-heterojunction colloidal quantum dot solar cells. ACS Nano **4**, 3374–3380 (2010)
25. J.M. Luther, J. Gao, M.T. Lloyd, O.E. Semonin, M.C. Beard, A.J. Nozik, Stability assessment on a 3 % bilayer PbS/ZnO quantum dot heterojunction solar cell. Adv. Mater. **22**, 3704–3707 (2010)
26. L.Y. Chang, Low-temperature solution-processed solar cells based on PbS colloidal quantum Dot/CdS heterojunctions. Nano Lett. **13**, 994–999 (2013)
27. H.M. García, M.T.S. Nair, P.K. Nair, All-chemically deposited Bi2S3/PbS solar cells. Thin Solid Films **519**, 7364–7368 (2011)
28. M. Gupta, V. Sharma, S. Shrivastava, A. Solanki, A.P. Singh, V.R. Satsangi, S. Dass, R. Shrivastav, Bull. Mater. Sci. **32**, 23–30 (2009)
29. R. Hyun, Y. Zhong, A.C. Bartnik, L. Sun, H.D. Abruña, F.W. Wise, J.D. Goodreau, J.R. Matthews, T.M. Leslie, N.F. Borrelli, Electron injection from colloidal PbS quantum dots into titanium dioxide nanoparticles. ACS Nano **2**, 2206–2212 (2008)
30. D. Lincot, G. Hodes, Chemical solution deposition of semiconducting and non-metallic films, in *Proceedings of the International Symposium, Electrochemical Society* (2006)
31. S. Dagher, I. Ayesh, N. Tit, Y. Haik, Influence of reactant concentration on optical properties of ZnO nanoparticles, Materials Technology. Adv. Perform. Mater. **29**, 76–78 (2013)
32. N. Zhao, L. Qi, Low-temperature synthesis of star-shaped PbS nanocrystals in aqueous solutions of mixed cationic/anionic surfactants. Adv. Mater. **18**, 359–362 (2006)
33. S. Tsunekawa, T. Fukuda, A. Kasuya, J. Appl. Phys. **87**, 1318 (2000)
34. L.H.J. Lajunen, P. Perämäki, *Absorption and Emission*, 2nd edn. (Royal Society of Chemistry, Cambridge, 2004), p. 342

Chapter 44
Dye and Nanoparticles-Sensitized Solar Cells

Sawsan Dagher, Zahraa A. Yousif, Iman Abdulkareem, Sayeda Al Ameri and Yousef Haik

Abstract The performance of dye sensitized and nanoparticles sensitized solar cells are presented in this study. Three types of natural extracts (black cherry, hibiscus and saffron) were utilized as sensitizers. The performance of the solar cells as a function of the natural sensitizer was studied for the hibiscus. The performance of nanoparticles sensitized solar cells based on PbS/CdS nanoparticles was also studied. The effect of CdS nanoparticles thickness on the performance was investigated. The power conversion efficiencies (Eff.) for the devices made with natural extracts, saffron, hibiscus and black cherry was 0.17, 0.45 and 0.54 %, respectively. The (Eff.) of the hibiscus dye sensitized solar cells were improved from 0.45 to 1.37 % with increasing the dye concentration from 1X to 4X. While the obtained (Eff.) of PbS/CdS nanoparticles devices were increased from 0.089 to 3.2 % with increasing the CdS layer deposition cycles from 1 to 7 under Air Mass (AM) 1.5 Global (G) solar illumination, which indicates higher (Eff.) with increasing the CdS thickness.

Keywords Natural dye solar cell · Nanoparticles solar cell

44.1 Introduction

The world moves to renewable energy in all of its forms. Solar energy is one of free, sustainable and clean renewable energy source. In pursuit to achieve high efficiency and low production cost of solar cell several types appeared in the literature, the diversity is due to the material used in assembling the solar cells and the solar cell structure. Solar cells consist of three groups; the first group is made from silicon which includes monocrystalline silicon cells, polycrystalline silicon

S. Dagher · Z. A. Yousif · I. Abdulkareem · S. A. Ameri · Y. Haik (✉)
Mechanical Engineering Department, United Arab Emirates University, Al Ain
United Arab Emirates
e-mail: yhaik@uaeu.ac.ae

M. O. Hamdan et al. (eds.), *ICREGA'14 - Renewable Energy: Generation and Applications*, Springer Proceedings in Energy, DOI: 10.1007/978-3-319-05708-8_44,

cells, amorphous silicon cells and hybrid silicon cells [1, 2]. The second group is based on thin film technology, which is made from layers of semiconductor materials only a few micrometers thick [3, 4]. The third group is made from diversity of new materials besides silicon, including silicon wires, solar inks using conventional printing press technologies, organic semiconductors [5–7], inorganic nanostructures [8–11], dye sensitized [12–17] and so on.

Solar cell basically consists of at least two semiconductor layers. One layer containing a positive charge named p-type and a negative charge layer named n-type. The selection of semiconductors is based on electronic band structure of a semiconductor molecule that consists of valance band and conduction band, the valence band is the lower energy level while the conduction band is level where the electron can be considered free. The band gap is the minimum change in energy required to excite the electron from valence band which is bound state to conduction band which is free state as a result it can participate in conduction. In conjunction to the excitation of an electron into the conduction band, other conduction process takes place, which is a hole in the valence band and this occurs when the excitation of an electron to the conduction band leaves an empty space for an electron. An electron from a nearby atom can move into this empty space. When this electron moves, it leaves behind another space. A hole is the continual movement of the space for an electron. It also refers as the movement of a positively charged particle through the crystal structure. The electrons trip in the semiconductor happen due to absorbing light and then retain the energy from the light for a long enough time to produce electrical work.

Dye sensitized solar cells (DSSC) works as the natural process of photosynthesis [14]. DSSC is from the third generation of solar cells, its advantages relates to its transparency, low cost and simplicity. On the other hand, its efficiency is not that high due to voltage loss during the regeneration of the sensitizing dye. Basically the DSSC consist of anode, cathode, titanium dioxide and the inner absorber layers. The cathode is transparent material like transparent conductive oxide glass coated to allow the sunlight to be absorbed by the inner layers of the solar cell. The titanium dioxide nanoparticles act as road for the electron coursing through the cell, the optimal size and density of this layer is important to create maximum amount of the surface area to be coated by the absorber layer and to allow for maximum amount of electrons to pass to the cathode. The electrical work created when photons of sunlight hit the photosensitive layer; the dye layer, the freed electrons accumulate on the layer of titanium dioxide and create an electrical current [18].

Semiconductor nanoparticles are preferred over dyes because they have tunable size-dependent absorption, large absorption coefficient and possibility for multiple exciton generation [19–24]. While Ruthenium dye for example has single absorption energy, low absorption coefficient, and grain boundaries in TiO_2 can impede conduction [20].

This study shows the results of a group of natural dye and nanoparticles sensitized solar cells. The performance of the solar cell as a function of dye concentration was performed for hibiscus natural dye solar cell and the performance as a function of nanoparticles layers was also investigated.

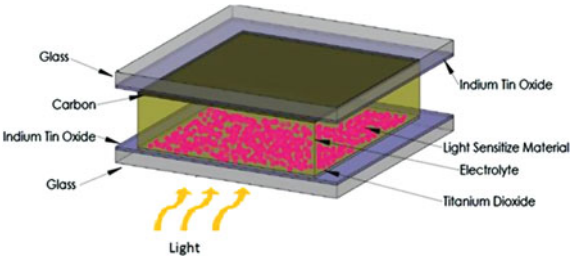

Fig. 44.1 Schematic diagram for a synthesized solar cell

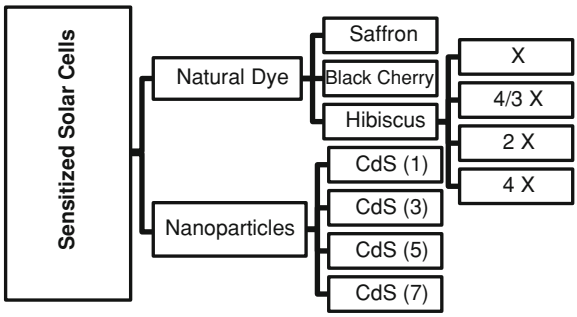

Fig. 44.2 Organizational chart for the synthesized solar cells

44.2 Experiment

44.2.1 Material

Indium Tin Oxide glass (ITO); titanium dioxide nanopowder (TiO_2) with particle size of 25 nm, methanol, ethanol, acetone, Sodium sulphide pentahydride ($Na_2S \cdot 5H_2O$), lead acetate ($Pb(CH_3COO)_2$), Cadmium nitrate ($Cd(NO_3)_2 \cdot 4H_2O$),sodium hydroxide (NaOH).

44.2.2 Solar Cell Fabrication

Figure 44.1 represents a schematic diagram for the synthesized solar cell where a light sensitizing materials and electrolyte are sandwished between two electrodes glass/ITO/TiO_2 and glass/ITO/carbon.

Two types of light sensitizing materials were used to synthesize ten different solar cells. The first are natural dyes where three types of dyes were used which are hibiscus, black cherry and saffron. For the hibiscus dye, the concentration was changed to observe the performance. The second sensitizer were made out of [PbS] and [CdS] nanoparticles, where the thickness of CdS layer was varied in four of the cells by increasing the SILAR cycles as shown in the chart in the Fig. 44.2.

Herein X is the dye concentration in water, and the numbers next to CdS are the SILAR cycles.

44.2.3 Titania Electrode Preparation

ITO glasses have been used for electrode. The TiO_2 powder was mixed with few drops of diluted acetic acid in de-ionized water (1:3) by magnetic stirring for 10–15 min. Then, the TiO_2 paste was rolled on the substrates using Doctor–Blade method. After that, the deposited TiO_2 layer was sintered by heating at 450 °C for 30 min, and left to be self-cooled.

44.2.4 Applying the Light Sensitizing Materials

44.2.4.1 Staining with a Natural Dye

ITO glass covered with titania electrode was immersed in each type of the dyes and the different concentrations of the hibiscus, so they were six different results which are the normal and concentrated hibiscus dye cells and the yellow saffron dye cell.

44.2.4.2 Deposition of PbS and CdS Layers with the Successive Ionic Layer Adsorption and Reaction (SILAR) Method

PbS nanoparticles layer was deposited on the sintered titania electrode by SILAR method. The titania electrode was dipped into the 0.02 M $Pb(NO_3)_2$ methanol solution for 1 min then it was dipped into 0.02 M Na_2S solution (obtained by dissolving Na_2S in methanol/water with volume ratios of 1:1) for another 1 min then clean the glass with de-ionized water, so this is considered to be one SILAR cycle. After the PbS layer, the next layer was deposited which is CdS layer. The same process was repeated for the CdS nanoparticle layer, Cd_2 + ions were placed from a 0.05 M $Cd(NO_3)_2$ ethanol solution, and the sulfide sources used were 0.05 M Na_2S in methanol/water (1:1). This SILAR process was repeated from 1 to 7 cycles to achieve the desired thickness of CdS nanoparticle layer. After sensitization, all the samples analyzed in this study were coated with 2 SILAR cycles of ZnS, by alternately dipping into 0.1 M Zn(AC) and 0.1 M $Na_2S \cdot 5H_2O$ solutions at a rate of 1 min per dip and rinsing with de-ionized water after each cycle.

44.2.5 Solar Cell Assembly

The cathode of the solar cell was made by cover the ITO glass with the carbon. The carbon can be obtained from burning a candle. The carbon will cover the ITO glass with gray to black layer. After leaving the carbon electrode to cool for a few minutes, put the two electrodes together.

44.2.6 Preparing the Electrolyte and Filling the Open Cells

A polysulfide electrolyte was injected into the space between two electrodes then put the clips to hold the cell. The 0.1 M sulfur, 1 M Na_2S, and 0.1 M NaOH were dissolved and stirred in methanol/water (7:3) at 60 °C for 1 h and this was the polysulfide electrolyte.

44.2.7 Performance Measurement

The photovoltaic performance of the devices was measured using solar simulator (Model 71445, New Pot) and Keithley Source Meter (2425) under illumination of AM 1.5G light (100 mW/cm^2), which is in turn connected to a computer for recording the measurements. AM 1.5G is the standard spectrum at the Earth's surface (the AM stands for Air Mass that is the path length which light takes through the atmosphere normalized to the shortest possible path length, while the G stands for global and includes both direct and diffuse radiation). The reduction in the power of light as it passes through the atmosphere and is absorbed by air and dust is measured by the Air Mass.

44.3 Results and Discussion

The ratio of the electrical output of a solar cell to the incident energy in the form of sunlight is named as solar cell efficiency. the percentage of the solar energy to which the cell is exposed that is converted into electrical energy is called the energy conversion efficiency (Eff.) of a solar cell. This is calculated by dividing a cell's power output (in watts) at its maximum power point (Pm) by the input light (E, in W/m^2) and the surface area of the solar cell (Ac in m^2) as shown in Eq. (44.1).

$$\eta = \frac{\mathrm{Pm}}{\mathrm{E} * \mathrm{Ac}} \tag{44.1}$$

Fill factor of a solar cell is the ratio of maximum obtainable power to the product of the open-circuit voltage and short-circuit current. Open-circuit voltage (Voc) is the difference of electrical potential between two terminals of a device when disconnected from any circuit. There is no external load connected. No external electric current flows between the terminals. It is sometimes given the symbol Voc. The short-circuit current (Jsc) is the current through the solar cell when the voltage across the solar cell is zero (i.e., when the solar cell is short circuited). Listing the short-circuit current density (Jsc in mA/cm^2) rather than the short-circuit current was done to eliminate the dependence of the solar cell area [18].

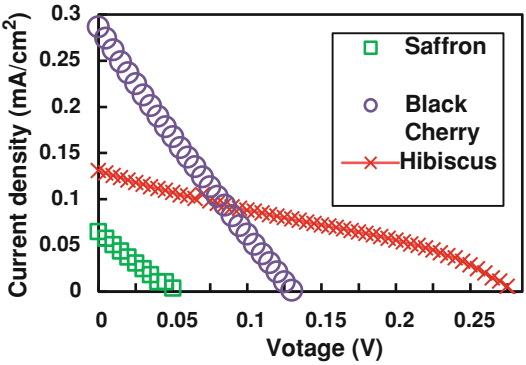

Fig. 44.3 J–V characteristic for natural dyes devices with varying the dye type under AM1.5G simulated solar illumination

Table 44.1 Cells efficiency

Natural dye	Jsc (mA)	Voc (V)	FF	Efficiency (%)
Saffron	0.0646	0.104	0.229	0.171
Hibiscus	0.131	0.278	0.311	0.453
Black cherry	0.286	0.131	0.234	0.548

44.3.1 Effect of Dye Type on Performance

Figure 44.3 shows the voltage versus current density graph of three types of natural dyes under AM1.5G simulated solar illumination. The devices where saffron was used as a dye has the least Voc compared to devices where black cherry and hibiscus dyes were used as light sensitizer which have less Voc. Hibiscus devices had the highest voltage and a current density of 0.125 (mA/cm^2). Black cherry which is indicated by the hollow circles had the highest Jsc (0.29 mA/cm^2) and Voc (0.125). The photovoltaic parameters for dye sensitized solar cells with different types of natural dye are shown in Table 44.1. Saffron had the least Jsc, Voc, FF and least efficiency of 0.171 %. Hibiscus had a Jsc of 0.131 mA and an efficiency of 0.4535. Hibiscus had the highest Voc (0.278) and FF (0.311) compared to saffron and black cherry. Black cherry had the highest Jsc (0.286). Black cherry had the highest efficiency (0.548 %). The influence of typical hibiscus on the performance of devices is investigated. Figure 44.4 represents a typical current density–voltage characteristics (J–V) measured in the dark and under AM1.5G simulated solar illumination.

44.3.2 Effect of Hibiscus's Dye Concentration on Performance

Figure 44.5 represents the Current density–voltage (J–V) characteristics for hibiscus devices with different concentrations measured under AM1.5G simulated

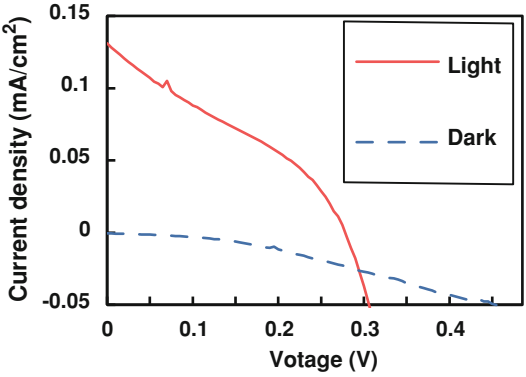

Fig. 44.4 J–V characteristics of typical hibiscus (with concentration 1X) devices measured in the dark and under AM1.5G simulated solar illumination

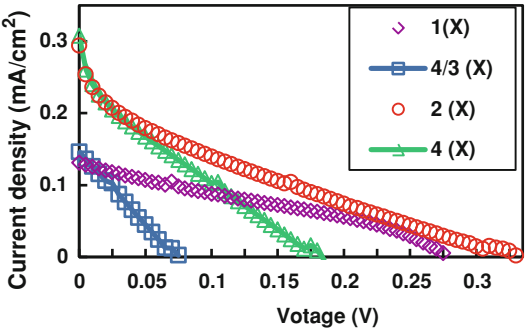

Fig. 44.5 J–V characteristics of hibiscus (with different concentrations) devices measured under AM1.5G simulated solar illumination

Table 44.2 Cell efficiency

X	Jsc (mA)	Voc (V)	FF	Efficiency (%)
1	0.131	0.278	0.311	0.453
4/3	0.146	0.152	0.240	0.594
2	0.294	0.332	0.171	1.04
4	0.308	0.367	0.194	1.37

solar illumination. Jsc and Voc increase with increasing the concentrations as shown in Fig. 44.7. The photovoltaic parameters for dye sensitized solar cells with different hibiscus concentrations are shown in Table 44.2. Concentration 4X had the highest Jsc, Voc and the highest efficiency (1.37 %) as shown in Table 44.2. Concentration 1X had the least efficiency but the highest fill factor.

44.3.3 Effect of CdS Nanoparticles Thickness on Performance

The J–V characteristic for PbS/CdS nanoparticles devices with different CdS SILAR cycles under AM1.5G simulated solar illumination is shown in Fig. 44.6.

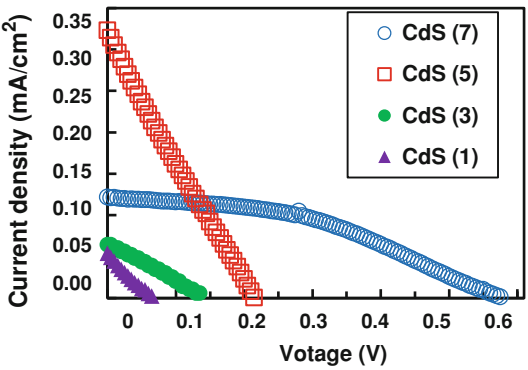

Fig. 44.6 J–V characteristic for PbS/CdS nanoparticles devices with different CdS SILAR cycles under AM1.5G simulated solar illumination

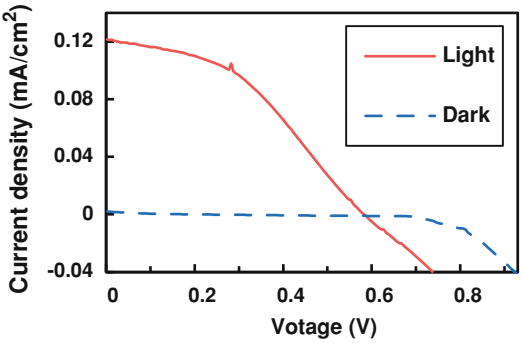

Fig. 44.7 J–V characteristics of CdS nanoparticles (with 7 CdS SILAR cycles) devices calculated in the dark and under AM1.5G simulated solar illumination

Table 44.3 Cell efficiency

CdS SILAR cycles	Jsc (mA)	Voc (V)	FF	Efficiency (%)
1	0.054	0.069	0.214	0.089
3	0.064	0.140	0.271	0.270
5	0. 332	0.220	0.232	1.06
7	0.122	0.579	0.416	3.26

More cycles means the thicker layer of CdS nanoparticles. The device with 1 SILAR cycle has the least Jsc and Voc, the device with five SILAR cycles has highest Jsc, while the device with seven SILAR cycles has highest Voc as indicated from Fig. 44.7. The J–V characteristics of CdS nanoparticles devices were measured in the dark and under AM1.5G simulated solar illumination is shown in Fig. 44.7. The photovoltaic parameters for nanoparticles sensitized solar cells with different CdS SILAR cycles are shown in Table 44.3. The highest number of cycles (seven CdS SILAR cycles) had the highest efficiency which is 3.26 % and the highest FF (0.416) and the highest Voc (0.579).

44.4 Conclusions

This work unambiguously unveils the dramatic role that dye concentration and the nanoparticles layer thickness play in the dye sensitized solar cells and the nanoparticles sensitized solar cells performance, respectively. Therefore in the results, there were three comparisons to choose the best device performance. The first one was between three natural extracts; hibiscus, saffron and black cherry and the black cherry achieved the highest efficiency (0.548 %). The second comparison was between the different concentrations of the hibiscus dye where the efficiency increased from 0.453 to 1.37 % by increasing the dye concentration from 1X to 4X. The last one was between the different SILAR cycles number of the CdS layer where the efficiency increased from 0.089 to 3.26 % by increasing the SILAR cycles from 1 to 7.

At the end, these results can be better if each procedure was done in a professional way. By this I mean, for example the electrolyte should be put inside the solar cell without leaking because it was injected. However, we have done the best we can and we hope that the country use this type of energy as it has a reasonable good performance.

Acknowledgments The authors would like to acknowledge the support provided by United Arab Emirates University. This work is financially supported by the Faculty of Engineering at the United Arab Emirates University.

References

1. Y. Tawada, M. Kondo, H. Okamoto, Y. Hamakawa, a-SiC:H/a-Si: H heterojunction solar cell having more than 7.5% conversion efficiency. Appl. Phys. Lett. **39**, 237 (1981)
2. T. Saga, Advances in crystalline silicon solar cell technology for industrial mass production. NPG Asia Mater. **2**, 96–102 (2010)
3. Y. Hamakawa, *Thin-Film Solar Cells: Next Generation Photovoltaics and Its Applications.* (Springer, Berlin, 2004), Sience, 244 pp.
4. I. Kaiser, K. Ernst, C.H. Fischer, R. Konenkamp, C. Rost, I. Sieber, M.C. Lux-Steiner, The ETA solar cell with $CuInS_2$: a photovoltaic cell concept using an extremely thin absorber (ETA). Sol. Energy Mater. Sol. Cells **67**, 89 (2001)
5. S.G. Unes, H. Neugebauer, N.S. Sariciftci, Conjugated polymer-based organic solar cells. Chem. Rev. **107**, 1324–1338 (2007)
6. F.C. Krebs, Fabrication and processing of polymer solar cells: a review of printing and coating techniques. Sol. Energy Mater. Sol. Cells **93**, 394–412 (2009)
7. E.G. Wang, L. Wang, L.F. Lan, C. Luo, W.L. Zhuang, J.B. Peng, Y. Cao, High performance polymer heterojunction solar cells of a polysilafluorene derivative. Appl. Phys. Lett. **92**, 033307/1–033307/3 (2008)
8. L. Reijnen, B. Meester, A. Goossens, J. Schoonman, Nanoporous $TiO_2/Cu_{1.8}S$ heterojunctions for solar energy conversion. Mater. Sci. Eng. **C19**, 311 (2002)
9. M. Nanu, J. Schoonman, A. Goossens, Inorganic nanocomposites of n- and p-type semiconductors: a new type of three-dimensional solar cell. Adv. Mater. **16**, 453 (2004)

10. S.A. Manolache, L. Isac, E. Purghel (Ienei), A. Duta, The influence of the buffer layers (Al_2O_3 and In_2S_3 thin films) in the 3D solar cell: FTO/TiO_2/$CuSbS_2$, in *Proceedings of Photovoltaic Solar Energy Conference*, Valencia, Spain, on CD, 2008
11. F. Lenzmann, M. Nanu, O. Kijatkina, A. Belaidi, Substantial improvment of the photovoltaic characteristics of TiO_2/$CuInS_2$ interfaces by the use of recombination coatings. Thin Solid Films **639**, 451–452 (2004)
12. N.S. Lewis, Toward cost-effective solar energy use. Science **315**, 798–801 (2007)
13. Y. Ooyama, Y. Harima, Molecular designs and syntheses of organic dyes for dye-sensitized solar cells. Eur. J. Org. Chem. **2009**(18), 2903–2934 (2009)
14. B. O'Regan, M. Grätzel, A low-cost, high-efficiency solar cell based on dyesensitized colloidal TiO_2 films. Nature **353**, 737–740 (1991)
15. M. Grätzel, Solar energy conversion by dye-sensitized photovoltaic cells. Inorg. Chem. **44**, 6841–6851 (2005)
16. Z. Ning, Y. Fu, H. Tian, Improvement of dye-sensitized solar cells: what we know and what we need to know. Energy Environ. Sci. **3**, 1170–1181 (2010)
17. A. Yella, H.-W. Lee, H.N. Tsao, C. Yi, A.K. Chandiran, M.K. Nazeeruddin, E.W.G. Diau, C.-Y. Yeh, S. Zakeeruddin, M. Grätzel, Porphyrin-sensitized solar cells with cobalt (II/III)-based redox electrolyte exceed 12 percent efficiency. Science **334**, 629–633 (2011)
18. M.K. Nazeeruddin, E. Baranoff, M. Grätzel, Dye-sensitized solar cells: a brief overview. Sol. Energy **85**, 1172–1178 (2011)
19. G. Hodes, Comparison of dye- and semiconductor-sensitized porous nanocrystalline liquid junction solar cells. J. Phys. Chem. C **112**, 17778–17787 (2008)
20. R.J. Ellingson, M.C. Beard, J.C. Johnson, P. Yu, O.I. Micic, A.J. Nozik, A. Shabaev, A.L. Efros, Highly efficient multiple exciton generation in colloidal PbSe and PbS quantum dots. Nano Lett. **5**, 865–871 (2005)
21. J.B. Sambur, T. Novet, B.A. Parkinson, Multiple exciton collection in a sensitized photovoltaic system. Science **330**, 63–66 (2010)
22. Y.L. Lee, Y.S. Lo, Highly efficient quantum-dot-sensitized solar cell based on co-sensitization of CdS/CdSe. Adv. Funct. Mater. **19**, 604–609 (2009)
23. V. Pedro, C. Sima, G. Marzari, P. Boix, S. Gime, Q. Shen, Th Dittrichf, I. Sero, High performance PbS quantum dot sensitized solar cells exceeding 4% efficiency: the role of metal precursors in the electron injection and charge separation. Phys. Chem. Chem. Phys. **15**, 13835–13843 (2013)
24. S. Ruhle, M. Shalom, A. Zaban, Quantum-dot-sensitized solar cells. Chem. Phys. Phys. Chem. **11**, 2290–2304 (2010)

Chapter 45
Combination of an Improved P&O Technique with ANN for MPPT of a Solar PV System

M. Kesraoui, A. Benine and N. Boudhina

Abstract In this paper a new approach to determine the maximum power point (MPP) of a solar PV system is proposed. It is based on the Artificial Neural Network (ANN) technique combined with an improved perturb and observe (P&O) method. The developed ANN delivers the optimal voltage in order to adjust the DC–DC converter duty cycle used by the P&O algorithm. The simulation results using MATLAB_SIMULINK showed that the new approach gives a power efficiency of the PV system more than 97 % in both stable and rapidly changing conditions. The improved P&O-ANN MPPT method has also been compared with the conventional P&O technique. In stable weather conditions the efficiency is slightly better. But under rapidly changing conditions the new method leads to a better PV system average power efficiency by an amount of 3 %. The oscillations around the MPP and the time response are also reduced.

Keywords PV panel · MPPT · P&O · ANN

45.1 Introduction

The amount of solar energy supplied to the earth in one day by the sun is sufficient to power the total energy needs of the earth for one year [1]. Unfortunately, PV generation systems have two major problems: the conversion efficiency in electric power generation is low (in general less than 17 %, especially under low irradiation conditions) [2], and the amount of electric power generated by solar arrays changes continuously with weather condition. Since, solar cell I–V characteristic is nonlinear and changes with irradiation and temperature, there is only one point on

M. Kesraoui (✉) · A. Benine · N. Boudhina
University M'hamed Bougara, Avenue de l'indépendance, 35000 Boumerdes, Algeria
e-mail: mkesraoui@umbb.dz

M. O. Hamdan et al. (eds.), *ICREGA'14 - Renewable Energy: Generation and Applications*, Springer Proceedings in Energy, DOI: 10.1007/978-3-319-05708-8_45,

the P–V curve, called the Maximum Power Point (MPP), at which the entire PV system (array, inverter, etc.) operates with maximum efficiency and produces its maximum output power. The location of the MPP is not known, but can be located by search algorithms [2]. Maximum Power Point Tracking (MPPT) techniques are used to maintain the PV array's operating point at its MPP, and many MPPT techniques have been proposed in the literature; examples are the Perturb and Observe (P&O) method, the Incremental Conductance (IC) method, the Artificial Neural Network (ANN) method, the Fuzzy Logic method etc., and the P&O and IC techniques are the most widely used. The IC technique has efficiency lower than the P&O technique, but its response time is quite independent to the irradiation values and its efficiency increases with the irradiance level. This technique can be a good alternative to the P&O technique in applications characterized by high, fast and continuous irradiance variations. The two techniques are also equivalent concerning the costs and the software complexity; in particular both techniques require a microcontroller with medium/higher performances than the ones required by other techniques, due to the necessity of high computation capability [3, 4]. The performances of the constant voltage (CV), open voltage (OV) and short current pulse (SC) techniques are lower than the ones obtained with P&O technique. Moreover, OV and SC techniques require additional valves in the converter that decrease its efficiency and the output power. The CV technique is still a very simple logic which provides a very good efficiency for irradiance values closed to 700 W/m^2, with low costs. Hence, generally this technique can be selected only if there is the necessity to minimize the control system cost [2, 5]. Possibilities of estimating the PV output power are however used by only using current sensor [6]. The cost of a microcontroller is currently low, so that the implementation of the P&O type techniques is anyway preferred. However in the case of a sudden increase in radiation, the P&O algorithm reacts as if the increase occurred as a result of the previous perturbation of the modules operating voltage. The next perturbation therefore will be in the same direction as the previous one. This wrong direction will lead to an operating point far away from the actual MPP. This process continues until the increase in radiation slows down or ends. The deviation from the MPP can cause significant power loss. In this paper the P&O algorithm is modified by adding an ANN control loop for the determination of the optimal voltage at any weather condition. The P&O algorithm uses this voltage in order to find the correct DC–DC converter duty cycle and track in the good search direction.

45.2 Photovoltaic Solar System

A PV system is composed of the PV solar modules (or PV Arrays), the DC–DC Converter for the maximum power point tracking and the battery regulation, the batteries unit for providing energy in cloudy days and night and finally a DC–AC converter for AC loads operation. The control system is composed of the Boost

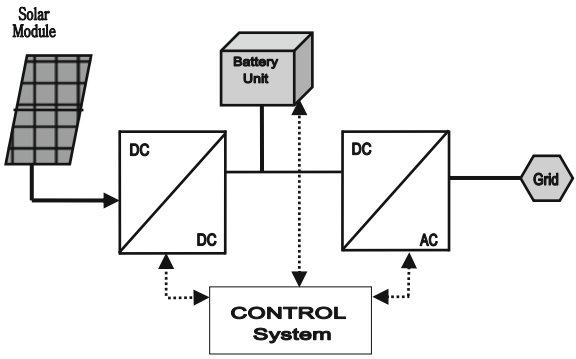

Fig. 45.1 Basic structure of a PV system

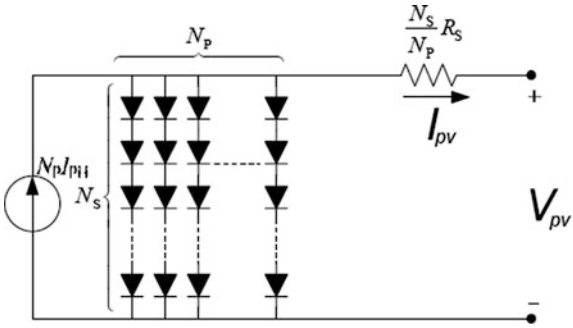

Fig. 45.2 PV module equivalent circuit

Converter Controller, MPPT Algorithm, inverter controller, Battery Regulator. The basic PV system structure is shown in Fig. 45.1 [7].

45.2.1 PV Module

By using Single diode model the equivalent circuit for the solar module arranged in N_p parallel cells and N_s series cells is shown in Fig. 45.2 [7–11].

The mathematical model is given by [7, 8]:

$$I_{PV} = N_p I_{ph} - N_p I_s \left[e^{\frac{q\left(\frac{V_{PV}}{N_s} + \frac{I_{PV}}{N_p} R_s\right)}{AKT_C}} - 1 \right] \tag{45.1}$$

I_{ph} is the photocurrent, I_s the saturation current, R_s the series resistance, The cell's ideality constant A depends on cell's technology, K the Boltzmann constant ($1.38 \cdot 10^{-23}$), T_c the temperature of the solar cell (in Kelvin), q the charge of the electron ($1.6 \cdot 10^{-19}$ C). N_p and N_s are parallel and series number of cell in the PV panel respectively.

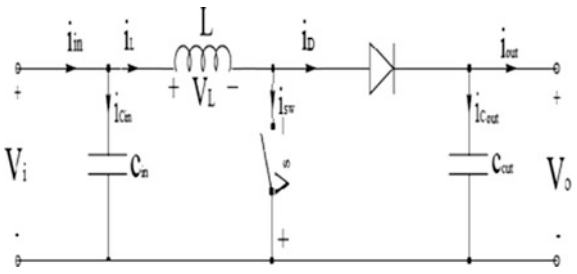

Fig. 45.3 Boost converter circuit

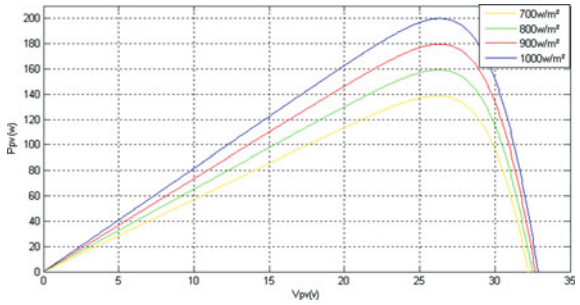

Fig. 45.4 PV module power versus irradiation

45.2.2 Boost Converter

The DC/DC Boost converter consists of an input capacitor C_{in}, an inductor L, a power electronic switch (usually a MOSFET or an IGBT) and a diode. It usually also has a filter capacitor C_{out} to smoothen the output. Its function is to step up DC voltage to bring it to a desired level V_o and is shown in Fig. 45.3 [7, 12, 13]. The conversion ratio can be determined by:

$$\frac{V_o}{V_{in}} = \frac{1}{1-D} \tag{45.2}$$

where, D is the switch duty cycle. A KC200GT PV solar panel whose parameters are given in Appendix has been simulated for different irradiances and temperatures. The respective power plots are presented in Figs. 45.4 and 45.5. Four irradiances (700, 800, 900 and 1000 W/m^2) were used to show the PV system power variation with respect to output voltage. The MPPs can practically be obtained only for one value of voltage as illustrated in Fig. 45.4 [7]. In the case of temperature variations (25, 35, 50 and 70 °C) the MPP decreases and the voltage increases for any increase of temperature as shown in Fig. 45.5 [7]. Since these two atmospheric conditions vary independently and randomly, the P&O technique will be used to track this point of power by fixing the voltage value for each condition.

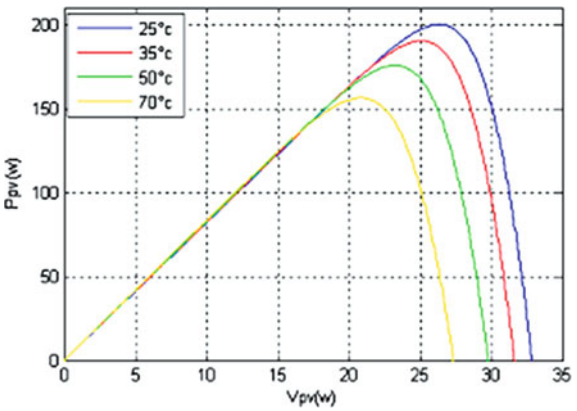

Fig. 45.5 PV module power versus temperature

45.3 P&O MPPT Algorithm

It consists of finding the MPP voltage where the PV panel provides the maximum output power. According to variations in solar irradiation and temperature, MPP moves continuously. In this algorithm, a slight perturbation of the duty cycle D is introduced to the system and the power of the module will change. If the power increases due to the perturbation then it continues in that direction. The MPP is reached with oscillations. In order to keep this power variation small the perturbation size is kept very small [7, 14]. The flowchart corresponding to this method is given in Fig. 45.6 [7].

The algorithm reads the current and voltage values from the solar PV module. The value of voltage and calculated power at *k*th instant are stored. Then next values at (k + 1)th instant are measured again and power is calculated from the measured values. The power and voltage at (k + 1)th instant are subtracted with the values from *k*th instant. If we observe the power voltage curve of the solar PV module we notice that in the right hand side curve where the voltage is almost constant the slope of power voltage is negative ($dP/dV < 0$) where as in the left hand side the slope is positive ($dP/dV > 0$). The right side curve is for the lower duty cycle (nearer to zero) whereas the left side curve is for the higher duty cycle (nearer to unity). Depending on the sign of dP(P(k + 1) − P(k)) and dV(V(k + 1) − V(k)) after subtraction the algorithm decides whether to increase the duty cycle or to reduce the duty cycle [14]. The P&O method can give good result in the case of slowly changing atmospheric conditions but it steal has some drawbacks. In the case of a sudden increase in solar radiation, the algorithm reacts as if the increase occurred as a result of the previous perturbation of the modules operating voltage. The next perturbation therefore will be in the same direction as the previous one. This wrong deviation will lead to an operating point far away from the actual MPP as seen in Fig. 45.7 [5]. This process continues until the increase in radiation slows down or ends and can cause significant power loss.

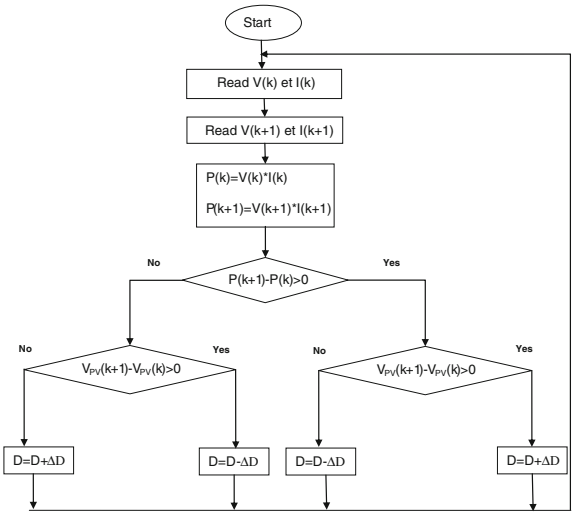

Fig. 45.6 P&O algorithm

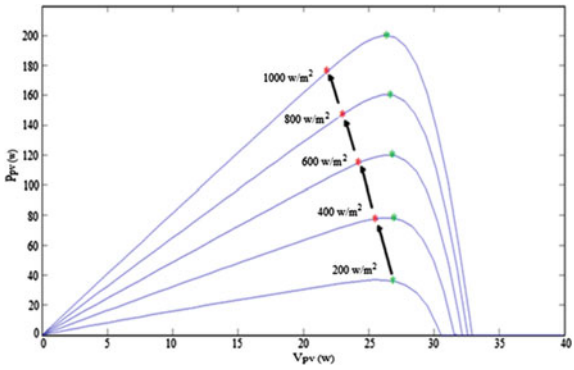

Fig. 45.7 Wrong tracking of MPP under rapidly varying irradiance [5]

45.4 Improved P&O-Ann MPPT Algorithm

To avoid the wrong tracking and oscillations around MPP the P&O method is improved by the addition of another loop for the calculation of an optimal voltage V_{op}. The ANN will have the task of determining this voltage which will next be used by the

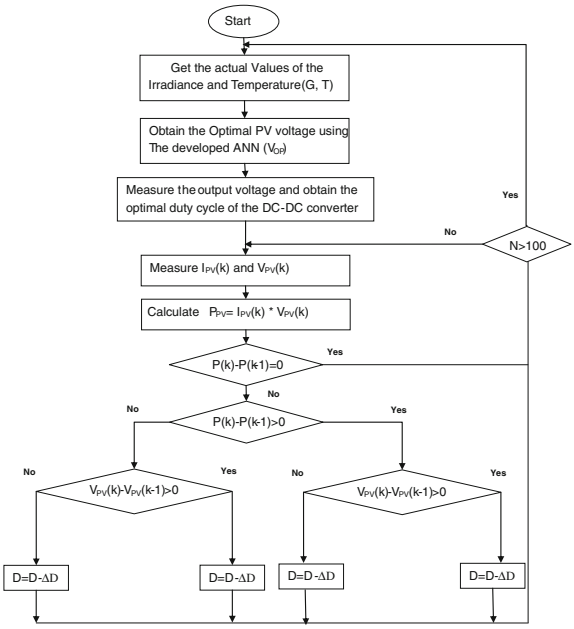

Fig. 45.8 Proposed ANN P&O MPPT algorithm

P&O technique. The ANN loop works once and the P&O one for N sample times. The flow chart of the improved P&O MPPT-ANN algorithm is shown in Fig. 45.8.

45.4.1 Developing the Artificial Neural Network

To develop the required ANN, a set of data base need to be collected to be used in the training, the test and validation of our network [15]. So a set of 80 points of optimal voltages at different irradiances in W/m^2 [50:1,000] and changing temperatures in degrees [25; 35; 50; 70] were extracted based on the characteristic P–V curve of our panel. These optimal voltages are summarized in the Table 45.1. Then the Matlab–Simulink block of the ANN was developed using the Neural network fitting tool GUI (nftool); which leads to an ANN with a two-layer feed-forward with **20** sigmoid hidden neurons and a linear output neuron, The network was trained with Levenberg–Marquardt back propagation algorithm. The inputs data are divided into three sets: 70 % used in the training of the network, 15 % for the validation, and the rest 15 % for the test, to fit the target as chosen to be V_{OP}. The performance of the trained network is summarized in Fig. 45.9.

Table 45.1 Optimal voltage

G (W/m^2)	T = 25 °C	35 °C	50 °C	70 °C
1000	26.3	25.15	23.3	20.85
950	26.30	25.10	23.20	20.80
900	26.30	25.09	23.20	20.79
850	26.28	25.05	23.20	20.71
800	26.27	25.00	23.10	20.70
750	26.23	24.95	23.10	20.60
700	26.19	24.9	23.00	20.59
650	26.12	24.86	22.99	20.50
600	26.05	24.79	22.90	20.41
550	25.98	24.71	22.80	20.31
500	25.89	24.60	22.70	20.19
450	25.80	24.51	22.55	20.09
400	25.60	24.34	22.40	19.90
350	25.49	24.19	22.22	19.71
300	25.27	23.97	22.05	19.48
250	25.05	23.71	21.75	19.19
200	24.70	23.39	21.4	18.81
150	24.25	22.90	20.91	18.31
100	23.50	22.20	20.19	17.55
50	22.23	20.80	18.80	16.10

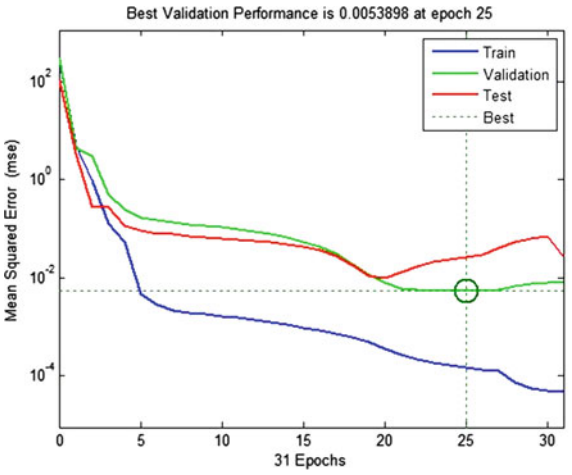

Fig. 45.9 Performance of the trained network

One can see that the best validation of our ANN corresponds to those biases and weights produced at the epoch = 25, where the mean square error between the response of the ANN and the target gets to10^{-2}. The training state can be summarized in the curves of Fig. 45.10.

The validation of our ANN is furthermore ensured referring to the Regression factor which measures the correlation between outputs and targets. An R value of 1 means a close relationship, 0 a random relationship. The fitting plots and

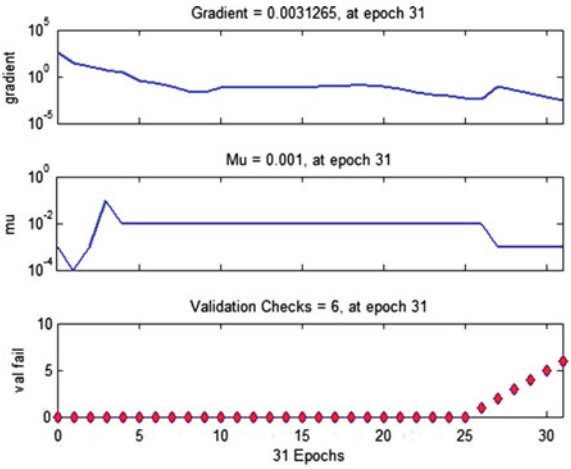

Fig. 45.10 Training state of the developed ANN

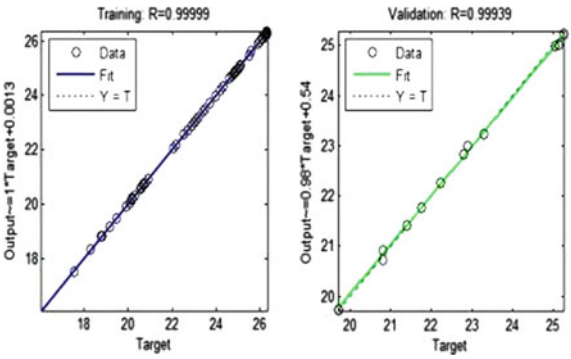

Fig. 45.11 FP&RF of the training and the validation

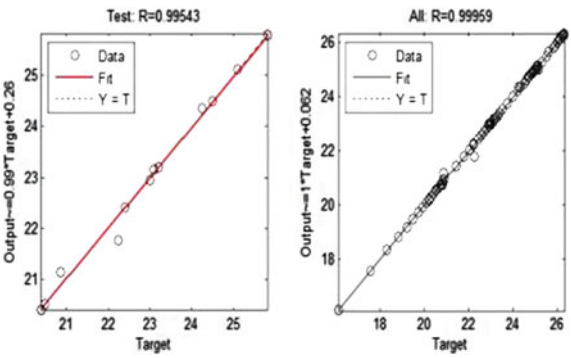

Fig. 45.12 FP&RF of the test and of the all

regression factors of the training and validation are shown in Fig. 45.11. Those of the test and all the three steps are given in Fig. 45.12. The overall regression factor of our ANN is: 0.99959 $\approx$ 1 which makes our outputs of the network approaching the real targets.

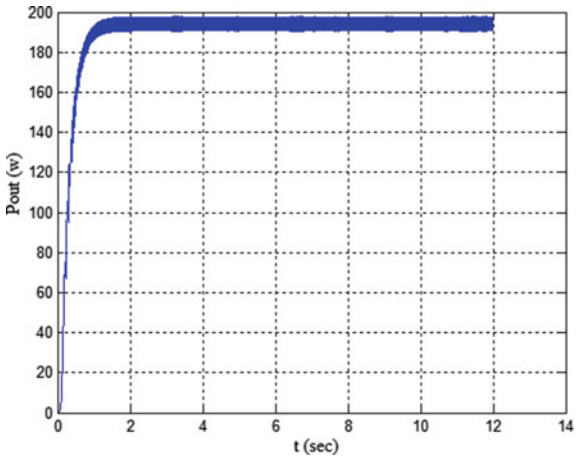

Fig. 45.13 Output power with P&O

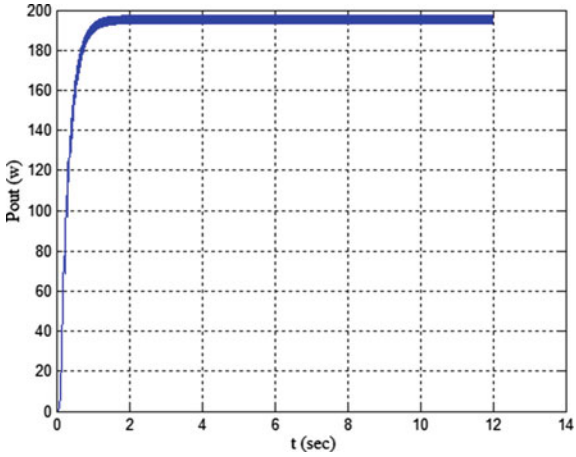

Fig. 45.14 Output power with ANN Improved P&O

45.5 Simulation

45.5.1 Stable Conditions

The ANN-P&O algorithm and the classic P&O method were compared using Matlab–Simulink under different conditions. The solar irradiance profile is supposed to be constant (G = 1,000 W/m^2). The PV system output powers for both methods are shown in Figs. 45.13 and 45.14 respectively. Their power oscillations around MPP are zoomed in Figs. 45.15, 45.16, 45.17, and 45.18.

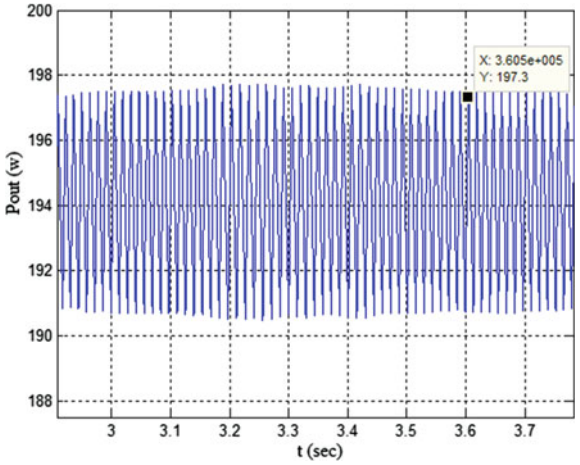

Fig. 45.15 Zoomed power ripple using P&O

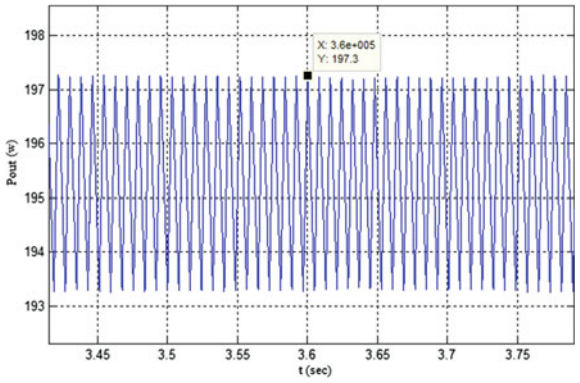

Fig. 45.16 Power ripple using ANN-Improved P&O

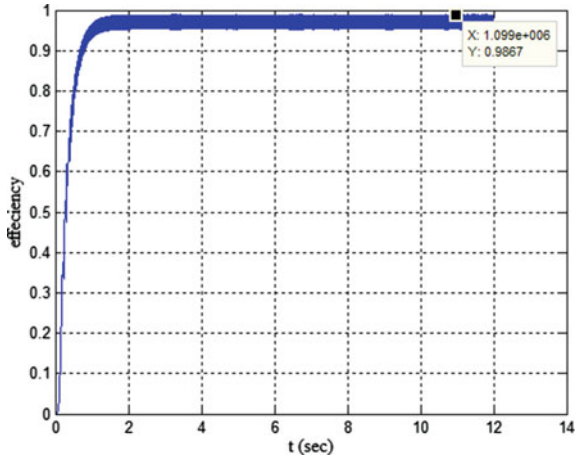

Fig. 45.17 Efficiency using P&O

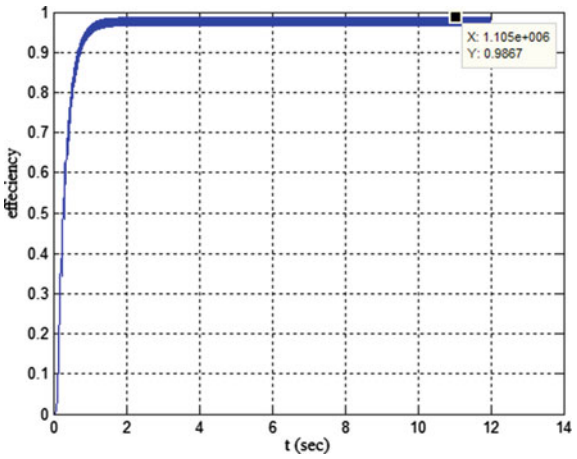

Fig. 45.18 Efficiency using ANN-Improved P&O

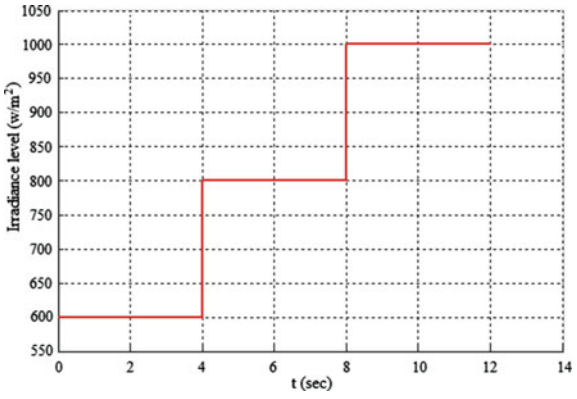

Fig. 45.19 Irradiance profile

45.5.2 Rapidly Varying Conditions

The solar irradiance profile is supposed to be growing by step increase (G = 600, 800, 1000 W/m^2) as given in Fig. 45.19. The simulation results are shown in Fig. 45.20.

One can notice from Figs. 45.15 and 45.16 that the traditional P&O algorithm has some average ripple of 6.5 W around the MPP and 4.1 W in the improved method. The efficiencies shown in Figs. 45.17 and 45.18 are nearly the same with a value around 97 %. However for rapidly changing irradiance the difference in shown in Fig. 45.20. The results are summarized in Table 45.2.

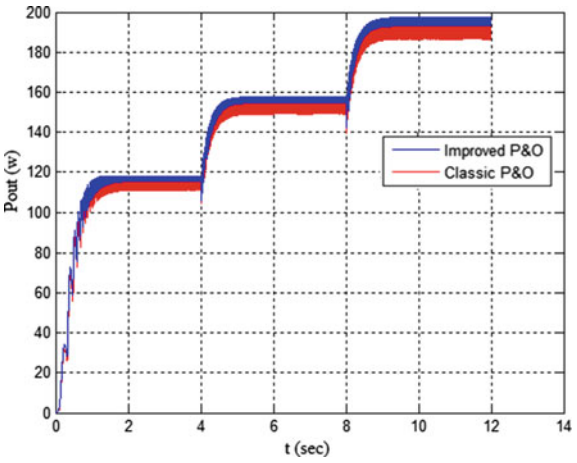

Fig. 45.20 PV system output power

Table 45.2 Simulation summary

	Stable conditions ($G = 1$ kW/m^2)		Rabidly changing conditions	
	Average power (W)	Efficiency (%)	Average power (W)	Efficiency (%)
P&O MPPT	194.101	97.05	151.601	94.75
ANN-P&O MPPT	195.341	97.67	156.033	97.52

45.6 Conclusion

The simulation results show that the efficiency is good for both algorithms in the stable conditions. However, the efficiency is slightly better with the combination of the improved P&O-ANN method. The proposed solution provides a higher average power output than the conventional P&O one under rapidly changing atmospheric conditions. It also offers approximately an efficiency improvement of 3 % under these conditions. The ability to respond adequately to a rapid increase in solar irradiance and avoid an associated oscillation around the MPP is a significant advantage of the proposed method over the classic P&O MPPT technique.

A.1 45.7 Appendix

PV panel: KC200GT, $P_{max} = 200$ W, $V_{max} = 26.3$ V, $I_{max} = 7.61$ A, $V_{oc} = 32.9$ V, $I_{sc} = 8.21$ A.

References

1. A. Khaligh, O.C. Onar (ed.), *Energy Harvesting: Solar, Wind and Ocean Energy Conversion Systems* (CRC press, Boca Raton, 2010), pp. 1–100
2. A. Dolara, R. Faranda, S. Leva, Energy comparison of seven MPPT techniques for PV systems. J. Electromagn. Anal. Appl. **1**(3), 152–162 (2009)
3. S. Kalogirou, *Solar Energy Engineering: Processes and Systems*, 1st edn. (Elsevier, London, 2009), pp. 122–149
4. P.A. Lynn, *Electricity from Sunlight: An Introduction to Photovoltaic*. (Wiley, Chichester, 2010), pp. 105–163
5. V. Salas, E. Olias, A. Barrado, A. Lazaro, Review of the maximum power point tracking algorithms for stand-alone photovoltaic systems. Sol. Energy Mater. Sol. Cell **90**, 1565–1578 (2006)
6. T. Esram, P.L. Chapman, Comparison of PV array maximum power point tracking techniques. IEEE Trans. Energy Conv. **22**(2), 439–449 (2007)
7. M. Kesraoui, F. Guerfi, M. Ghioub, Maximum power point tracking for a photovoltaic solar system, in *ICREGA'12 Conference*, Al Ain UAE, March 2012
8. H.L. Tsai, Insolation-oriented model of photovoltaic module using Matlab/Simulink. Sol. Energy **84**, 1318–1326 (2010)
9. R. Hernanz, J.A.C. Martín, J.Z. Belver, L. Lesaka, J.Z. Guerrero, P. Pérez, Modeling of photovoltaic module. Paper presented at the international conference on renewable energies and power quality, University of Granada, Spain, 23–25 March 2010
10. S. Narkhede, K. Rajpritam, Modeling of photovoltaic array. Bachelor degree thesis, National Institute of Technology, Orissa, India, 2010
11. B.S.G. Dzimano, Modeling of photovoltaic systems. Master degree thesis, Ohio State University, 2008
12. H. Knopf, Analysis, simulation and evaluation of maximum power point tracking (MPPT) methods for a solar powered vehicle. Master thesis, Portland State University, 1999
13. A. Bin Ahmad, Boost converter for stand-alone photovoltaic power supply. Bachelor degree thesis, University of Technology of Malaysia, 2010
14. V.A. Chaudhari, Automatic peak power tracker for solar PV modules using DSPACER software. Master thesis, Maulana Azad National Institute of Technology of Bhopal, India, 2005
15. M. Norgaard, O. Ravn, N.K. Poulsen, L.K. Hansen, *Neural networks for modeling and control of dynamic systems* (Springer, Heidelberg, 2000)

Chapter 46
Articulation Control of a PLC Based Robot Manipulator used for Heliostat Orientation

A. Chaïb, M. Kesraoui and E. Kechadi

Abstract Concentrated solar power systems (CSP) are using sun-tracking heliostats to reflect maximum solar heat to a thermal receiver mounted atop a central power tower. The focused heat boils water within the thermal receiver and produces steam to supply a turbine for power generation. Solar energy reaching a given surface depends directly on sun's orientation and sensor's position one should constantly change the position of the heliostat using an orientation system. To track the sun and focus the heliostat on the plant tower continuously and automatically a program for calculating the sun's position at any moment for any earth place in the year is developed using MATLAB software. It determines the orientation coordinates for each heliostat individually. Then an orientation system using a Programmable Logic Controller (PLC) based robot manipulator will use these coordinates to move the heliostat towards the desired orientation. A GRAFCET for the PLC is also given. For accurate and instantaneous automatic control a PID controller is designed to stabilize the articulations or joints of the robot manipulator. The obtained simulation results show that this system allows accurate positioning and gives a higher solar energy yield in comparison to a fixed one.

Keywords CSP · Articulation control · Heliostat · Robot manipulator · PLC · PID controller

46.1 Introduction

Concentrated solar power (also called concentrating solar power, concentrated solar thermal or CSP) systems use mirrors or lenses to concentrate a large area of sunlight, or solar thermal energy, onto a small area. Electrical power is produced

A. Chaïb (✉) · M. Kesraoui · E. Kechadi
Applied Automatics laboratory, University M'hamed Bougara, Boumerdès, Algeria
e-mail: chaibahmed@umbb.dz

M. O. Hamdan et al. (eds.), *ICREGA'14 - Renewable Energy: Generation and Applications*, Springer Proceedings in Energy, DOI: 10.1007/978-3-319-05708-8_46,

when the concentrated light is converted to heat which drives a steam turbine connected to an electrical power generator. The steam then reverts back to water through cooling, and the process repeats. The temperature can easily exceed 500 °C [1]. CSP is being widely commercialized and the CSP market has seen about 740 MW of generating capacity added between 2007 and the end of 2010. More than half of this (about 478 MW) was installed during 2010, bringing the global total to 1,095 MW [2]. With its wide desert (the highest CSP potential in the Mediterranean and Middle East regions ∼about 170 TWh/year) and its strategic geographical location near Europe Algeria is one of the key countries to ensure the success of the well known Desertec project [3].

Moreover, with the abundant natural-gas reserve in the Algerian desert, this will strengthen the technical potential of Algeria in acquiring Solar-Gas Hybrid Power Plants for electricity generation. Since sun's rays are constantly variable throughout a day one should constantly change the position of the heliostat using an orientation system. So the heliostat must track the sun and focus on the plant tower continuously and automatically. In this paper, we present a brief study about solar concentrators. A MATLAB program is designed to calculate the sun daily, monthly and annual positions. It determines the orientation coordinates for each heliostat individually. Then a control system with a robot manipulator using a PLC is proposed and simulated. As an added value to [4–6] a GRAFCET for the PLC is proposed. And for accurate and instantaneous automatic control a PID controller to stabilize the articulations or joints of the robot manipulator is also designed and simulated.

46.2 Tower-Heliostat Power Station

A heliostat uses a set of dual axis solar pointers to direct the sun's energy to a large receiver housed in a tower, as presented in Fig. 46.1. These sensors have a set of mirrors following the sun's movement. The mirrors concentrate the sun's rays on the receiver at the top of the tower Fig. 46.2. A computer keeps mirrors aligned so that the sun's rays, which are reflected, always towards the receiver [7]. The focused heat boils water within the thermal receiver and produces steam. The plant pipes the steam from each thermal receiver and aggregates it at the turbine, powering a power generator.

Heliostat parameters are Angular Height, Position in relation to the tower and distance between the heliostats [8] Fig. 46.1.

46.3 Heliostat Position Determination

At each moment we have to know exactly the orientation of the heliostat, this orientation depends of the sun's position and his position relative to the tower Fig. 46.2. In a central tower, the number of heliostats can reach thousands and the total area

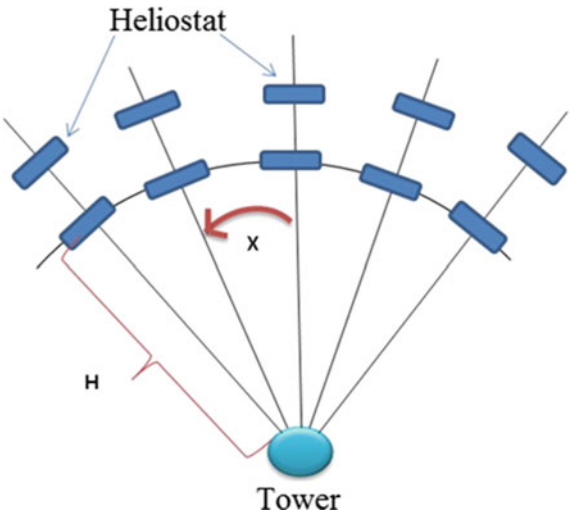

Fig. 46.1 Tower heliostats concentrating system

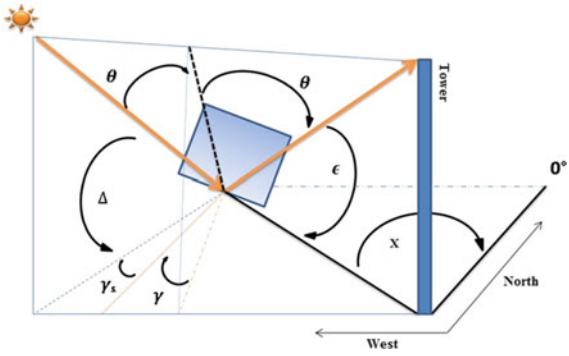

Fig. 46.2 Heliostats position with respect to tower

covered by the heliostats dozens of hectares. Dependent on the nature of the receiver, heliostats available around the tower can take different configurations. The heliostats can, for example, surround the tower placed on its north side [7]. The position of the heliostats varies from one angle (x) of the projection of the tower on the Northern Line. It is negative from the line to the east and positive westwards Fig. 46.1.

The sun's position is known, based on its azimuth (γ_s) and altitude (Δ), these coordinates are defined in relations called celestial mechanics [6]. A program is written using MATLAB. This program is based on the various mathematical models describing the time, the position, the day number (N). It also computes the parameters of the real solar time (TSV), the declination (δ) and the hour angle (ω), the numeral of the heliostat (position relative to the tower). The azimuth and angular altitude of the relative orientation of the heliostat are the final results of the program whose flowchart is given in Fig. 46.3 [4, 5]. Those parameters are used as inputs in the control program of the robot manipulator that will be processed by the PLC.

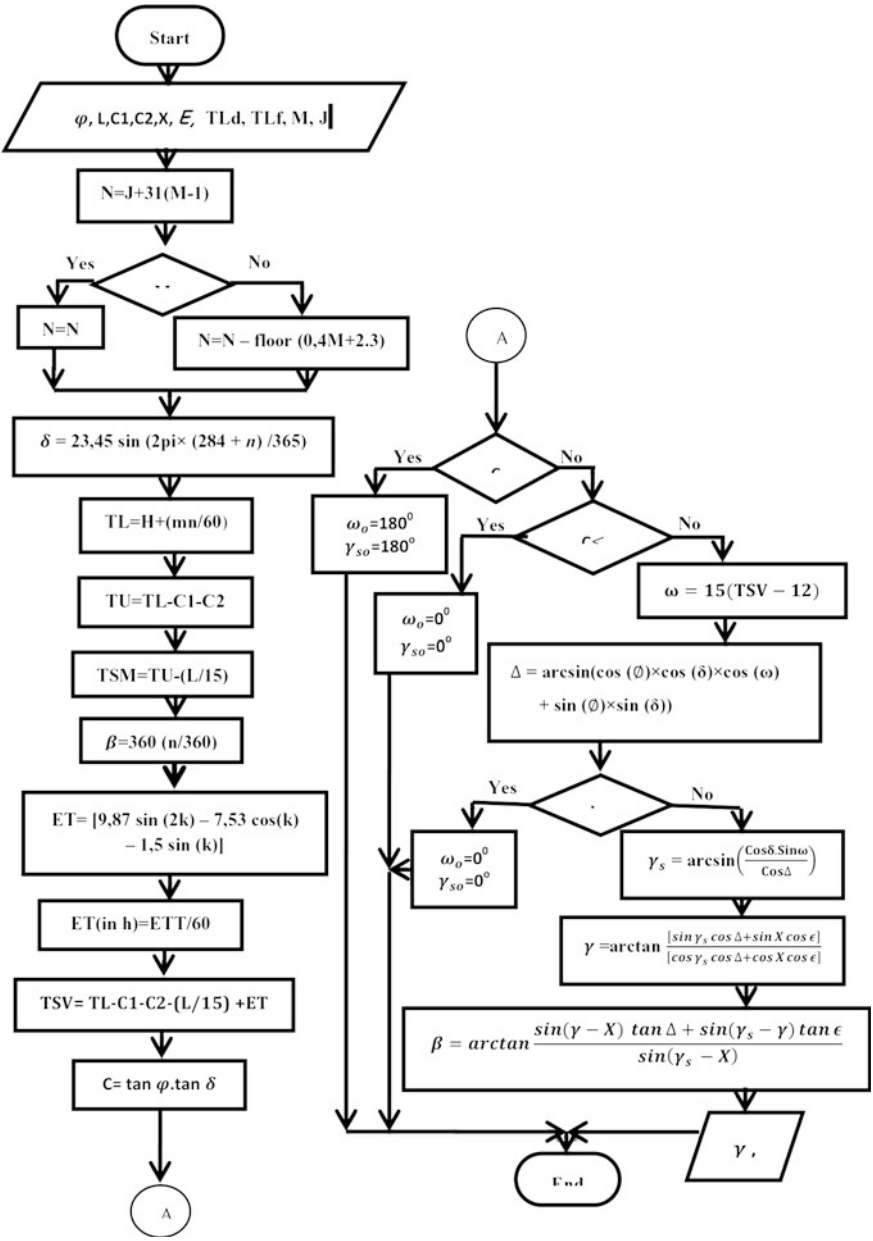

Fig. 46.3 Flowchart of the heliostat position MATLAB program

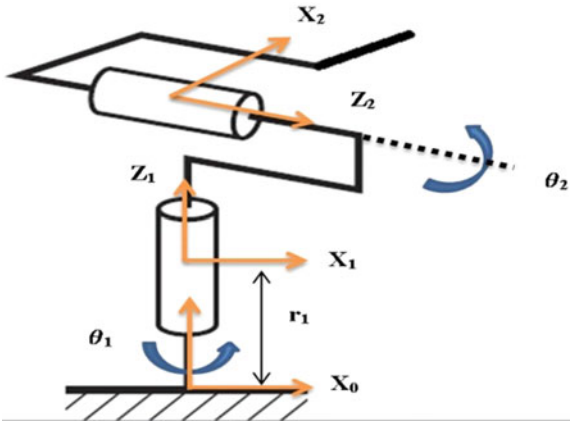

Fig. 46.4 Robot manipulator with two degrees of freedom

Fig. 46.5 Heliostat orientation angles

46.4 Robot Manipulator

Each heliostat has its own guidance system, consisting of a robot manipulator with two degrees of freedom, consisting of two revolute joints [9], as presented in Fig. 46.4 [4, 5].

The trajectories of the heliostat are generated by the two joints (articulations) of the robot, the first following the azimuth and the second follows its altitude, like illustrated in the Fig. 46.5. The heliostat is associated to a reference frame R3 formed by X3, Y3 and Z3. The robot reference frame is R0 composed of X0, Y0 and Z0 [6].

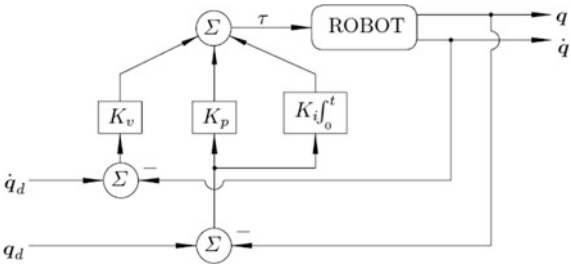

Fig. 46.6 Schematic diagram of a PID control system of the articulation

To control our robot for panel orientation, the reference frame R3 must be defined with respect to reference frame R0 of the robot. For this purpose, we calculate the homogeneous transformation matrix of our system which will define the position and orientation of the reference frame R3 (of the heliostat) in the reference frame R0 of the robot as shown in Fig. 46.9.

Where θ1 is the angle of rotation of the first axis of a robot, and θ2 is the angle of rotation of the second axis of the robot, and they represent the parameters of the robot controller [4, 5, 9].

46.5 Articulation Control

The design and control of robots need the calculation of some mathematical models, such as the models of transformation between the operational space and the joint space [1]. The heliostat is directly attached to the second body of the robot manipulator. The mechanical design of the robot arm affects the choice of the control diagram. The articulation control, PID type is the best adapted to our system. The control law is given by:

$$\Gamma = K_p(q^d - q) + K_d(\dot{q}^d - \dot{q}) + K_i \int_{t_0}^{t} (q^d - q)d\tau \tag{46.1}$$

where q^d(t)and $\dot{q}^d$(t). Denote the desired position and velocity. K_p, K_d and K_i are diagonal matrices of dimension (n × n) positive definite respectively. It contains the proportional K_{pj}, derivative K_{dj} and integrator gains K_{ij} respectively (Fig. 46.6).

The calculation of the gains K_p, K_d and K_i, is carried by considering the model of joint j represented by the second order linear system with constant coefficients according:

$$\Gamma_j = a_j\ddot{\theta}_j + F_v\dot{\theta}_j + rd \tag{46.2}$$

where $a_j = A_{jj}max$ is the maximum value of A_{jj} elements of the robot's inertia matrix. rd is a disturbance torque where r is the gear ratio (Fig. 46.7).

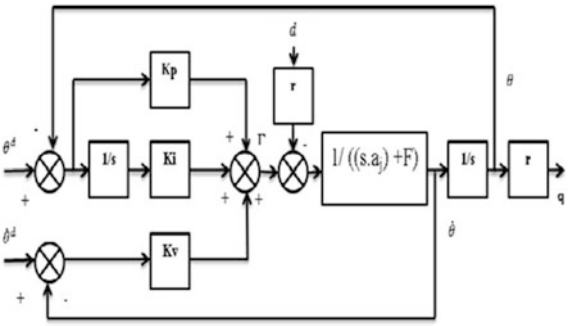

Fig. 46.7 Articulation control block taking into account the disturbances

Table 46.1 Sun coordinates for Algiers

Location	Algiers
Latitude	36.3°
Longitude	−2.6°
Date	1st of November
Day number	311
Legal time	12h00
Real sun time	12.0403
Declination	−17.1081°
Hour angle	0.6038°
Sun altitude	36.5888°
Sun azimuth	0.7187°

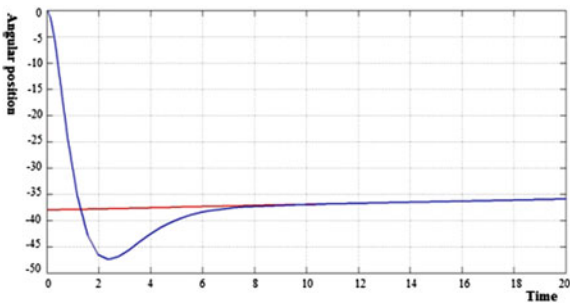

Fig. 46.8 Angular position as function of time of the first articulation

In the simulation the reference positions and velocities values for the day of November 1st are given Table 46.1.

Results are shown in Figs. 46.8, 46.9, 46.10 and 46.11 for the first and second articulation of the robot respectively. The red curves denote the reference and the blue color is the output. One can notice that the output follows the reference and the controller gives a stable system.

Figure 46.12 represents the variation of torque as a function of time of the two joints (articulation) where the red and blue colors indicate the torques provided at the first and second articulation respectively.

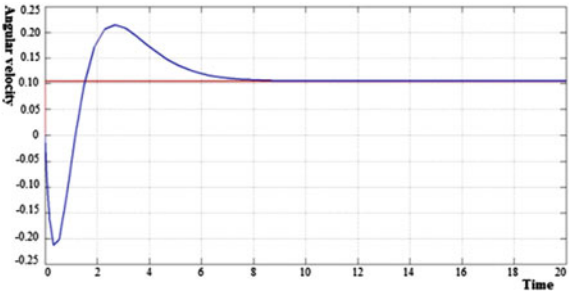

Fig. 46.9 Angular velocity as function of time of the first articulation

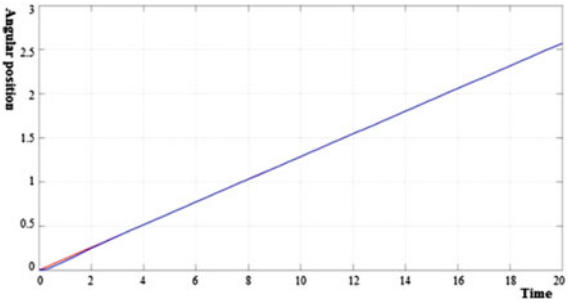

Fig. 46.10 Angular position as function of time of the second articulation

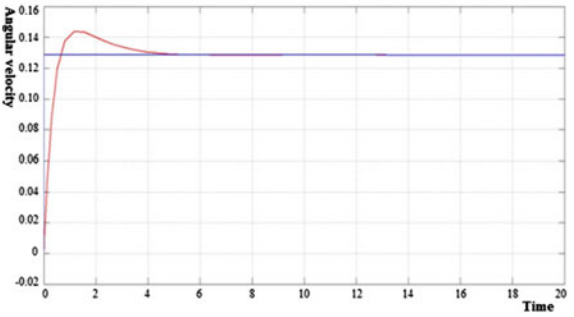

Fig. 46.11 Angular velocity a function of time of the second articulation

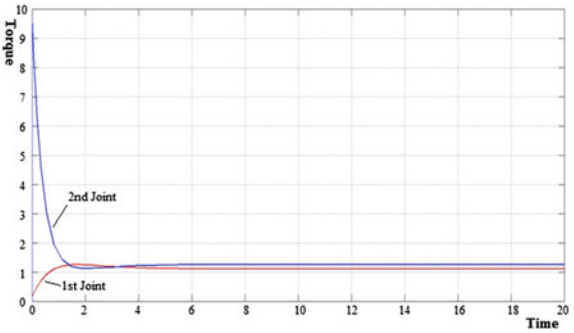

Fig. 46.12 Variation of torque as function of time

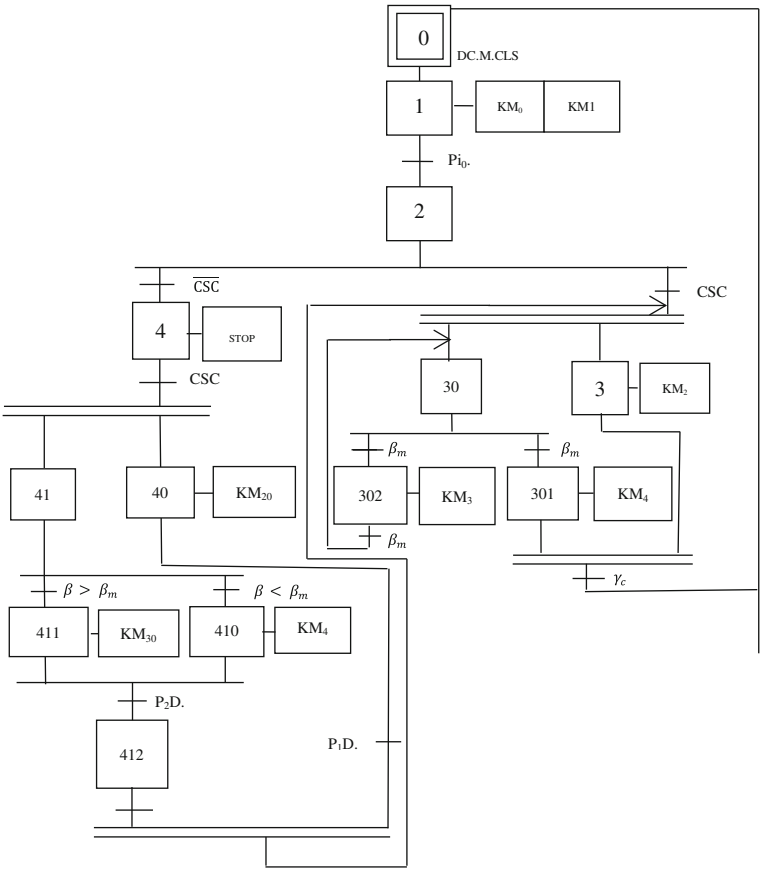

Fig. 46.13 GRAFCET of the PLC program

46.6 Programmable Logic Controller

The PLC is the most common component to achieve automation, because it meets the needs of adaptation and flexibility for a wide range of operations. This emergence is due in large part to the power of its development environment and broad opportunities for interconnections. Using a PLC is a matter that has already been addressed by many researchers. Abdallah et al. have employed a PLC to calculate the solar vector and to control the sun tracker so that it follows the sun's trajectory [10]. The main strength of a programmable logic controller PLC is its great ability to communicate with the industrial environment. In addition to its CPU and its power, it essentially consists of modules inputs/outputs, which serve as communication interface with the industrial process line. It also ensures the acquisition of information supplied by the sensors, makes processing, gives orders

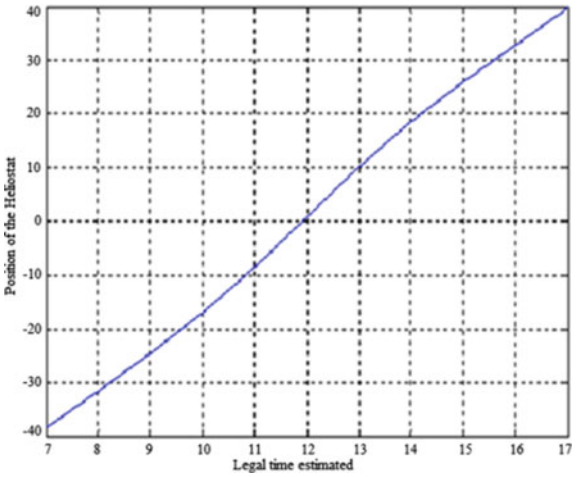

Fig. 46.14 Angular position of the robot's first joint with respect to time for a heliostat positioned at 0°

to the actuators and communicates with the central supervisor. A Siemens S7-300 PLC is proposed for the heliostat guidance system.

To automate our robot, we developed an SFC "graph Functional Control Steps/ Transitions" as shown in Fig. 46.13, which shows schematically the sequence of system operation. It begins by:

- Supply electrical control system of the heliostat at sunrise.
- The heliostat goes to its original position.

Once these two steps completed, the system checks the weather conditions, whether the sky is clear or not.

- In a clear sky:
  - Control of heliostats during sunny periods
- In interrupt sunshine:
  - Stop functioning of the control system
  - Search the sun by the light sensor.

46.7 Control of the Heliostat

The tracking system controls the position and height of the receiver at the top of the tower and the variations of inclination caused by natural phenomena [9]. After presenting the operations that must be performed by each component for automatic control of a heliostat, a program for the robot controller has been written using MATLAB. Figures 46.14 and 46.15 illustrate the behavior of each robot joint for a

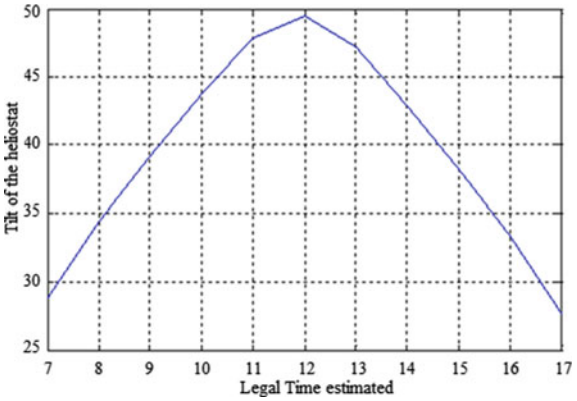

Fig. 46.15 Angular position of the robot's second joint with respect to time for a heliostat positioned at 0°

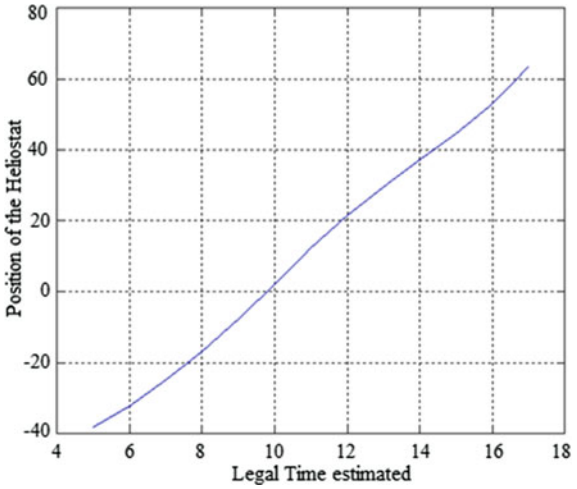

Fig. 46.16 Angular position of the robot's first joint with respect to time for a heliostat positioned at 45°

heliostat positioned at 0° with respect to the tower on the 1st of November. Figures 46.16 and 46.17 illustrate the behavior of each robot joint for a heliostat positioned at 45° with respect to the tower on the 1st of November.

46.8 Conclusion

The orientation of a concentrated solar power (CSP) system using heliostats has been investigated. A program for calculating Algiers coordinates of the sun for a sample day of the 1st November has first been developed for the orientation of the heliostats. These results data will be the input for the PLC based orientation system. And in order to obtain a maximum of reflected solar radiation a robot

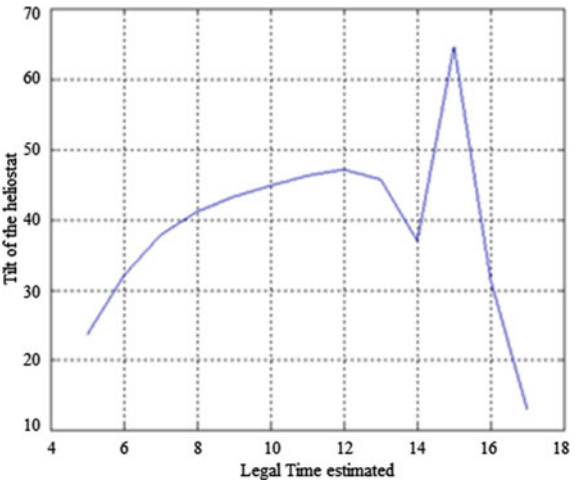

Fig. 46.17 Angular position of the robot's second joint with respect to time for a heliostat positioned at 45°

manipulator with two degrees of freedom i.e. with two revolute joints (articulations) has been integrated into the heliostat orientation system. The robot control model was chosen based on engineering and economic criteria. Simulation tests showing the controllability of the manipulator and its ease of control have been performed. The results showed that the normal axis of the heliostat is correctly oriented (faced or positioned) towards the sun at each instant of the day. The implemented program controlled the operation of the manipulator under different climatic conditions. The study has also proposed the use of a PID controller for the robot articulation in closed loop in the objective of better monitoring and a precise control of the guidance system. This work aims to be an introduction of the integration of robotics in renewable energy domain.

References

1. A. Gama, M. Haddadi, A. Malek et al., Etude et réalisation d'un concentrateur cylindro parabolique avec poursuite solaire aveugle. Revue des Energies Renouvelables **11**(3), 437–451 (2008)
2. J.L. Sawin, E. Martinot, Renewables bounced back in 2010, finds, REN21 Global Report, Renewable Energy World, 2011
3. Algerian ministry of energy and mining Web page, http://www.mem-algeria.org
4. A. Chaïb et al., Orientation system of solar panels based on a robot manipulator, in *International Conference on Renewable Energies and Power Quality (ICREPQ'11)*, Las Palmas de Gran Canaria (Spain), 13th to 15th April, 2011
5. A. Chaïb et al., Improving the daily solar energy capture of a PV panel using a robot manipulator, in *The 2nd International Conference on Renewable Energy: Generation and Applications, ICREGA'12*, 4–7 March, Al ain, UAE, 2012
6. A. Chaïb et al., Heliostat orientation system using a PLC-based robot manipulator, in *The Eighth International Conference and Exhibition on Ecological Vehicles and Renewable Energies, EVER'2013*, March 27–30, Monte-Carlo (Monaco), 2013

7. A. Ferriere, G. Flamant, Captation, Transformation et conversion de l'énergie Solaire par la technologie à concentration, Thème7, Solaire thermique 2002, 2002
8. K. Abdellah, Les centrales solaires à tour: perspectives en Algérie, Bulletin des énergies renouvelables No 20, page 22, 2011
9. E. Dombre, W. Khalil, Modélisation et commande des robots, Editions HERMES, Paris 1988, 1980
10. S. Abdallah, S. Nijmeh, Two axes sun tracking system with PLC control. Energy Conver. Manage **45**, 1931–1939 (2004)

Chapter 47
High Density Polyethylene Pyrolysis: Review and Progress

Farah Obeid and Isam Janajreh

Abstract Plastics; yet indispensable they are a growing environmental problem which necessitates limiting its damage. Plastics are inexpensive, durable and versatile which favored their use in manufacturing and meeting various consumer needs. However, plastics are non-biodegradable material therefore becoming a threat on both the environment and the society. Energy recovery (pyrolysis) is an innovative plastic waste management technique that recently gained high interest in research. In Waste to Energy lab in Masdar Institute of Science and Technology, a batch reactor was used to study the production of fuel-like products from high density polyethylene (HDPE) in the temperature range 375–425 °C. The analysis using gas chromatography-mass spectrometry (GC-MS) of the liquid fraction was carried out to determine its composition and product distribution.

Keywords Plastic wastes · HDPE · Pyrolysis

47.1 Introduction

The consumption of plastics in the Western Europe, USA and Japan in 1995 was 25, 33.9 and 11.3 million tones, respectively. The major consumption of plastic in Western Europe is attributed to packaging sector of 40 % [1]. In 2005, 10 years later, the plastic consumption in Western Europe increased to 47.5 million tons [2]. As the estimated daily global municipal solid waste (MSW) generation is more than 2 × 109 metric ton, plastic holds a substantial fraction reaching up to 19 %. United States, Germany and Switzerland (with high gross national income) generate MSW at a rate of 700 kg/ca annually; Japan generates 400 kg/ca annually.

F. Obeid · I. Janajreh (✉)
Masdar Institute of Science and Technology, Abu Dhabi, United Arab Emirates
e-mail: ijanajreh@masdar.ac.ae

M. O. Hamdan et al. (eds.), *ICREGA'14 - Renewable Energy: Generation and Applications*, Springer Proceedings in Energy, DOI: 10.1007/978-3-319-05708-8_47,

In the gulf region, UAE is the highest consumer of plastic/capita with daily average of 8.6 kg/ca (2009 figure) [3]. According to Waste Management Center-Abu Dhabi (WMC) 6 million tons of waste was generated in the year 2007–2008 in Abu Dhabi emirate solely, this figure is estimated to reach 30 MTs by 2030 [4]; in 2009, plastic waste contributed to an estimate of 19 % of the municipal solid waste generated in Abu Dhabi [3]. As dominant solid waste treatment scenario practiced in many societies including Abu dhabi, is mainly Landfilling (in 2009 more than 1 MT of MSW was landfilled in Abu Dhabi), alternatives need to exist.

A lot of research has been done in Masdar Institute on material recovery [5], pyrolysis and gasification [6] testing different types of polymeric wastes, municipal solid waste, and nonconventional fuel such as oil shale. However, more serious attention should be given to pyrolysis as an alternative waste treatment stream.

Schrimer et al. [7] conducted thermal decomposition of polyethylene in thermal gravimetric analysis (TGA) and in a cycled-sphere reactor. 4.5 g of PE pellets were heated in the TGA to reaction temperature of 600 °C under nitrogen. Non-catalytic degradation using TGA showed that complete degradation of polyethylene was achieved at 490 °C. Some experiments were carried in the cycled sphere reactor where 150 g of PE (granule) were fed into the reactor. The process was batch mode and the reaction temperature was maintained at 440 °C, reaction time was 60 min for thermal process. Products obtained from PE pyrolysis were mainly waxes (65.76 %) in the range of C_{15}–C_n, the yields of oil (C_5–C_{15}) and gas (C_1–C_4) were low compared with the yield of wax giving 21.88 and 11.6 % respectively. Moreover the analysis of the oil yielded showed a wide spectrum of products.

Grieken et al. [8] employed batch reactor for thermal degradation in an inert atmosphere of both high and low density polyethylene. 50 g of PE were fed into the reactor and different experiments were conducted varying temperature 380, 400 and 420 °C. Products resulted from LDPE thermal cracking were mainly solids, and the yield of liquid and gas products was negligible for the various temperatures tested. It was noticed that HDPE thermal cracking occurs at higher temperature than LDPE leading as well to mainly wax. The analysis of the waxy products obtained from thermal degradation of LDPE showed their potential to be used in petrochemical application.

Ng et al. [9] thermally degraded polyethylene (HDPE and LDPE) in the temperature range of 450–500 °C in a closed tubing bomb reactor, other few experiments were carried out in an open tubing reactor at 480 °C. Reactions in both systems took place under a flow of nitrogen. HDPE thermal degradation in a closed system produced hard wax, distillates of 19.3 % and low yield of gas at 450 °C. The increase in temperature caused an increase in the yield of gas and naphtha over the expense of coke. At 500 °C distillates are of 56.4 %, gas 23 % and residue of 8.6 %. Gas obtained contains mostly alkanes of 85 % in the range of C_1–C_4, and olefins which a decrease with the increase in temperature. Naphtha in the range of C_4–C_{10} showed a decrease with the increase in temperature; α-olefin decreased from 27 to 3.3 % with a corresponding increase in mono-aromatics from 1.1 to 25 % at 450 and 500 °C respectively. HDPE thermal

degradation in an open system promoted the production of gas oil over the expense of gas and naphtha. Naphtha and gas oil fraction composed of low aromatics (1 %), less saturates (27 %) but more olefins (40 %) unlike those obtained from closed system. Distillates produced from the degradation of HDPE in an open and closed system do not meet the requirements of transportation fuels.

Sakata et al. [10] has studied thermal degradation of high density polyethylene (HDPE) in a semi-batch glass reactor under the flow of nitrogen. 10 g of HDPE were loaded to the reactor and the degradation temperature was maintained at 430 °C in the furnace. Products evolved from the thermal degradation of HDPE were 69 % liquid and 21 % residues with only 9 % gaseous products. Gaseous products obtained from thermal degradation were mainly C_3 (propane, propylene), C_2 (ethane, ethylene) and small amount of C_4 (butane, butane). The components of liquid products were distributed over a wide range of carbon number. The oil obtained contained paraffins and olefins but aromatics were not detected.

Miskolczi et al. [11] studied thermal degradation of 200 g of HDPE in a Pyrex batch reactor for different temperatures (400, 420 and 450 °C) under nitrogen atmosphere. The yield of gas (2.4 % at 400 °C) and liquid (3.1 % at 400 °C) increased with the increase in temperature yielding 5.8 % gas and 74.5 % liquid at 450 °C. On the other hand the yield of residue decreased drastically with the increase in temperature; 93.5 % at 400 °C decreased to 19.7 % at 450 °C. Product analysis of the gaseous fraction showed that C_2 and C_4 are the dominating components. Concerning liquid fraction, aliphatic hydrocarbons in the range of C_5–C_{25}; main type of fuels were gasoline, kerosene, diesel and heavy oil. Low sulfur content is favored for the advantage of both the environment and human health; therefore sulfur content was tested and was <20 ppm for different degradation temperatures but it was noticed that the content decreased with the increase of temperature (14 ppm at 450 °C) which makes the liquid fraction favored for utilization as fuel-like product.

Hernandez et al. [12] carried thermal cracking of HDPE in a fluidized bed reactor under nitrogen flow and reaction temperature was varied in the range of 400–800 °C. At 400 °C the yield of gas was almost negligible but started to increase with the increase of temperature yielding ≈60/100 g of HDPE; however the gaseous fraction was obtained over a wide range of molecular weights. At 800 °C, components were mainly C_2 (16.5 g ethene/100 g HDPE), C_3 (10.5 g propene/100 g HDPE), C_4 (5.1 g 1-butene/100 g HDPE) and 2.2 g benzene/100 g HDPE. Same group [13] studied the thermal pyrolysis of HDPE and results were confounded with their previous findings; products evolved from thermal cracking of HDPE were (15 % gases and 41 % liquids) at 500 °C and (58 % gases and 24 % liquids) at 700 °C. Products in the liquid fraction were composed of wide range of carbon atoms (C_{10}–C_{40}) diolefins, olefins and paraffin were present while aromatic compounds were not identified.

Marcilla et al. [14] aimed to study the effect of the heating rates (flash and slow pyrolysis) on the degradation process of HDPE and the type of products yielded. Experiments were carried in a fluidized bed reactor and nitrogen was the fluidizing agent. In flash experiments the reactor degradation temperature was in the range of

500–800 °C, in slow pyrolysis experiments the reactor was heated to 700 °C in the rate of 5 °C/min. It was obvious from both experiments (flash and slow pyrolysis) that higher percentages of liquid (heavy oil), wax and solid residues are obtained from thermal degradation of HDPE. However in flash pyrolysis the increase in temperature caused a drastic increase in gas yield; 15.2 % were released at 500 °C increased to 66.3 % at 800 °C.

Ng et al. [15] thermally cracked the blended HDPE with VGO (vacuum gas oil) under nitrogen in the fixed bed reactor, sand was also loaded to the reactor and reaction temperature occurred at 510 °C. Two concentration of HDPE (5 and 10 %) resulted in different conversions; thermal cracking of 5 % HDPE resulted in 77 % conversion of HDPE, producing 11.5 % dry gas, 16 % LPG, 33.5 % gasoline and 15.3 % coke; whereas lower conversion (52.4 %) of HDPE was achieved when its concentration increased to 10 % and the yield of product was lower giving 7, 8.7, 22 and 14.7 % of dry gas, LPG, gasoline and coke respectively. In the gaseous fraction, olefins were mainly ethylene, propylene and 1-butene. Methane was produced in significant amount. Sand insured a better heat transfer which resulted in a better conversion.

Aguado et al. [16] observed that only 27 % of LDPE was converted when thermally cracked in an inert atmosphere in a stirred batch reactor at 420 °C. 20 % of gases (C_1–C_5) mainly olefins and 6.6 % heavy oil (C_{13}–C_{35}) mainly n-paraffins; while the yield of liquid (C_6–C_{12}) was negligible.

William et al. [17] degraded LDPE thermally in the fluidized bed reactor in the temperature range of 500–700 °C. Nitrogen was the fluidizing gas and the bed material was silica sand. It was observed that gas yield increased from 10.8 to 71 % as they temperature increased from 500 to 700 °C with a corresponding decrease in oil/wax fraction from 89 to 28.5 % with the oil having the highest proportion. It can be concluded that wax decomposed to oil as the temperature continued to increase then to gas. Main gases evolved were ethene, propene and butene of yield 26.8, 18.6 and 7.6 % at 700 °C respectively. Among the alkane gases methane was evolved significantly with yield of 11.8 % at 700 °C. Liquid products (oil and wax) were distributed over a wide range of carbon number C_8–C_{57}. As the pyrolysis temperature increased, aliphatics above C_{30} decreased with a significant increase in the single and poly-aromatic hydrocarbons (PAH) which comprised more than 25 % in the oil produced. This raises the environmental concern due to the presence of PAH and requires a further treatment of the oil.

Renzini et al. [18] thermally cracked LDPE in a fixed bed reactor at 500 °C for different reaction times (20 and 60 min). Non-catalytic degradation yielded 81 % solids mainly waxes with very negligible amounts (relative to solids) of liquids and gases of 6.4 and 12 % respectively at reaction time of 20 min. On the other hand, the increase of reaction time to 60 min positively influenced the distribution of products yielding 24.4 and 18.7 % of gas and liquid respectively.

The pyrolysis of low density polyethylene in a batch autoclave reactor at 425 °C and 1 h residence time was tested by Insura et al. [19]. Products yielded (90 % oil, 10 % gas and no coke detected). Gas composition was mainly alkanes of 69 % (ethane and propane dominant gases) and 32 % alkene. Long chain

n-alkanes (46 %) were the main component in the oil obtained from the thermal degradation of LDPE and 12.5 and 12 % of n-alkene and aromatics (toluene, benzene and xylene) were obtained. These results were compatible with those obtained from thermal cracking of LDPE at 500 °C investigated by Bagri et al. [20] in a fixed bed reactor; where high yield of oil ($\approx$95 %) and low gas (5 %) was also achieved. Oil composition was mainly aliphatic in the range of C_9–C_{50} whereas a very low amount of polycyclic aromatics (naphthalene and their methyl derivatives) was detected. Gases were composed of alkane (mainly ethane and propane) and alkene (mainly propene and butane).

Thermal degradation of LDPE was investigated by Aguado et al. [21] employed a screw kiln reactor; experiments were conducted in the temperature range of 450–550 °C and using nitrogen to insure inert atmosphere. A total conversion of LDPE was observed giving high selectivity toward heavy hydrocarbons; 35.5 % heavy oil (C_{13}–C_{23}) and 26 % wax (C_{24}–C_{55}) and low yield of gasoline (C_5–C_{12}) and gas (C_1–C_4) of 29 and 9 % respectively. Therefore, thermal degradation of LDPE led to a wide distribution of carbon number and heavy hydrocarbons were the major outcomes.

47.2 Experimental Method

47.2.1 Materials

Virgin HDPE was obtained as pellets from Ducab Inc., Abu Dhabi, United Arab Emirates, the particle size is 2–4 mm diameter and 2–4 mm length each and is originally traded under P. W. Hall, UK (PPM 914), being used in the wire and cable industry for outer sheathing in medium voltage (MV) and high voltage (HV) cables.

47.2.2 Batch Autoclave Pyrolyser

Thermal degradation of virgin HDPE was conducted in autoclave reactor obtained from Buchiglas, Uster, shown in Fig. 47.1. The vessel is made of stainless steel with CrNiMoTi alloy stirrer with 2 L volume. The reactor is heated electrically (3000 W/230 V). The rector temperature is controlled by the jacketing purified water cooling jacket and heating elements built in the wall of the vessel. The stirrer is integrated in the reactor to maximize the distribution of heat flow to the polymer. The temperature inside the reactor is controlled by ICC-self optimizing controller, where the pressure is measured using pressure gauge. 50 g of virgin HDPE pellets were placed in the reactor; then closed and pre-purged with nitrogen for 5 min to ensure that the reactor is free from oxygen and that the experiment is taking place in an inert atmosphere. The reactor is then pressurized with nitrogen at 10 bar and heated to 375–425 °C and

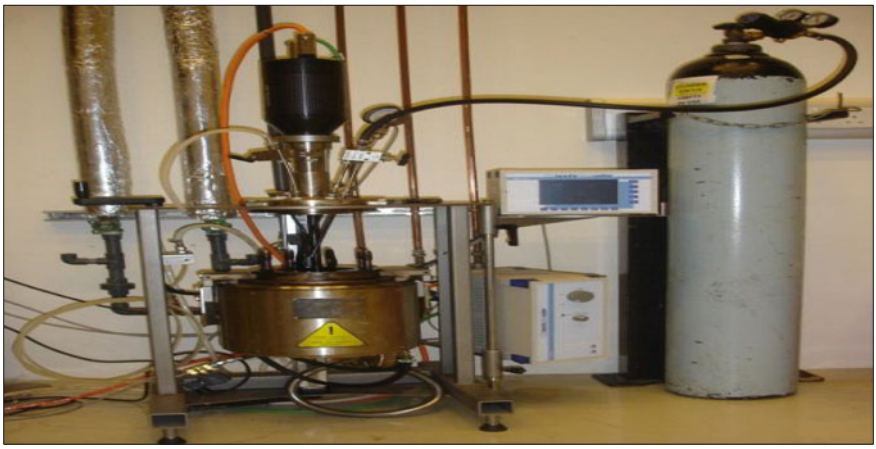

Fig. 47.1 Batch autoclave reactor

residence time of half an hour. Three fractions were collected at the end of each experiment; gases were collected using tedlar bags directly through the depressurizing valve, oil and residues were collected from the reactor bottom. All collected products are weighed after each experiment.

47.2.3 Simultaneous Thermal Analyzer STA (Q600 SDT TA Instruments)

10–15 mg of HDPE were used for the Simultaneous Thermal Analyzer (STA) which is a device combining Thermogravimetric Analysis (TGA), and Differential Scanning Calorimetry (DSC) for the thermal analysis Fig. 47.2. The former measures the change of the mass of the sample as a function of temperature and the DSC determines the melting and decomposition temperature of the polymer.

47.2.3.1 Gas Chromatography: Mass Spectrometry

In the end of each experiment, liquid and residue fractions were collected, weighed and dissolved in dichloromethane (DCM) GC grade. These compounds were identified and quantified by a Thermo GC–MS provided with an HP-5MS column (30 m × 0.25 mm × 0.1 μm). The column program is: injector temperature, 280 °C; initial column temperature, 40 °C; initial time, 5 min; heating rate, 12 °C/min; final temperature, 305 °C; final time, 25 min; run time, 53.33 min; carrier gas, Helium, 1 ml/min; average velocity, 38 cm/s; solvent delay, 6 min. The ion trap detector had a mass range from 50 to 650 amu and is linked to a computer equipped with the NIST library.

Fig. 47.2 SDT Q600

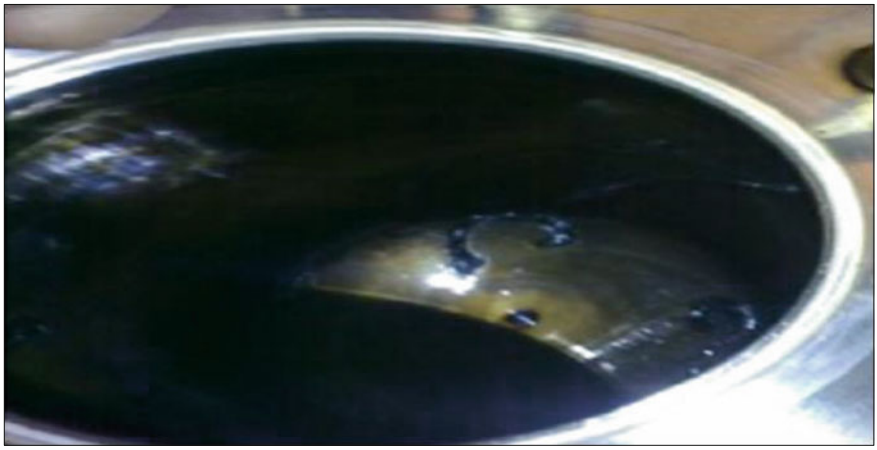

Fig. 47.3 Liquid fraction collected from the reactor

47.3 Results and Discussion

Several runs on virgin HDPE were carried out using Batch autoclave reactor. Experiments took place under nitrogen pressure at 10 bars at temperature of 400 °C and the reactor was maintained at this temperature for half an hour. Three fraction were collected from each experiment; liquid and residues were collected from the reactor Fig. 47.3 and separated by filtration and gas fraction was collected using tedlar chemically resistive Polyvinyl Fluoride (PVF) gas sampling bags Fig. 47.4. The yield of HDPE pyrolysis experiments favored the production of

Fig. 47.4 Gas Fraction collected using tedlar bag

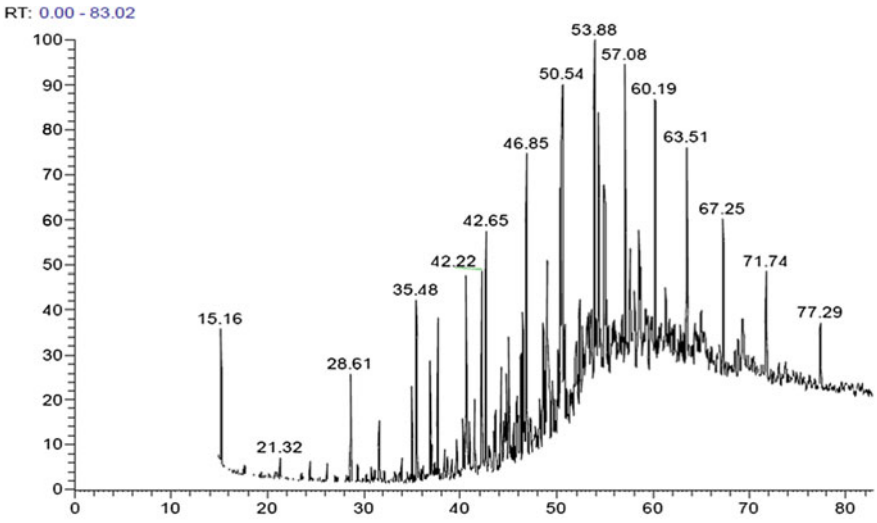

Fig. 47.5 Liquid fraction chromatogram

liquid fraction giving ~60 %, a good yield of gas was also obtained of 37 % and relatively low yield of residue of 3 %. The GC-MS chromatograph and analysis are shown in Fig. 47.5 and Table 47.1 respectively. Table 47.1 shows that the liquid fraction is composed of alkanes with carbon chain number ranging from C_{10} to C_{28}, alkenes in the range of C_{10}–C_{35} and alkynes (C_{11}–C_{20}).

Diesel carbon number distribution of various fractions is distributed as Naphtha $<C_{10}$, Gasoline C_{11}–C_{15}, Diesel C_{16}–C_{20} and heavy oil fraction $>C_{20}$ [22].

Table 47.1 GC-MS Liquid fraction composition from the pyrolysis of HDPE at 400 °C

Alkanes	Formula
Decane	$C_{10}H_{22}$
Undecane	$C_{11}H_{24}$
Dodecane	$C_{12}H_{26}$
Tridecane	$C_{13}H_{28}$
Tetradecane	$C_{14}H_{30}$
Pentadecane	$C_{15}H_{32}$
Hexadecane	$C_{16}H_{34}$
Octadecane	$C_{18}H_{38}$
Nonadecane	$C_{19}H_{40}$
Heneicosane	$C_{21}H_{44}$
Docosane	$C_{22}H_{46}$
Tetracosane	$C_{24}H_{50}$
Heptacosane	$C_{27}H_{56}$
Octacosane	$C_{28}H_{58}$
Alkenes	
1-Decene	$C_{10}H_{20}$
1-Undecene	$C_{11}H_{22}$
1-Dodecene	$C_{12}H_{24}$
1-Tridecene	$C_{13}H_{26}$
1-Pentadecene	$C_{15}H_{30}$
1-Hexadecene	$C_{16}H_{32}$
3-Heptadecene	$C_{17}H_{34}$
1-Nonadcene	$C_{19}H_{38}$
1-Docosene	$C_{22}H_{44}$
9-Hexacosene	$C_{26}H_{52}$
17,Pentatriacontene	$C_{35}H_{70}$
Alkynes	
1,10-Undecadiene	$C_{11}H_{20}$
1,11-Dodecadiene	$C_{12}H_{22}$
1,13,Tetradecadiene	$C_{14}H_{26}$
1,19-Eicosadiene	$C_{20}H_{38}$

Compounds detected using GC-MS in pyro-oil as C_{10}-decane, C_{11}-undecane, C_{18}-octadecane and others is an indication that it is a fuel-like product.

Thermogravimetric analysis (TGA) was used for HDPE characterization Fig. 47.6. The virgin HDPE samples of about 10–15 mg were placed in the sample holder and pyrolyzed in nitrogen atmosphere in each experiment. The nitrogen flow rate was kept constant at 75 ml/min, at heating rate 10 °C/min to a final temperature of 550 °C. It was observed that the melting temperature of virgin HDPE is at 135 °C. The onset degradation temperature is 300 °C after which the conversion of HDPE is initiated, the termination of the total conversion of HDPE is at 500 °C; however literature [23] states that degradation temperature of HDPE takes place around 500 °C. During the pyrolysis experiments of HDPE the total

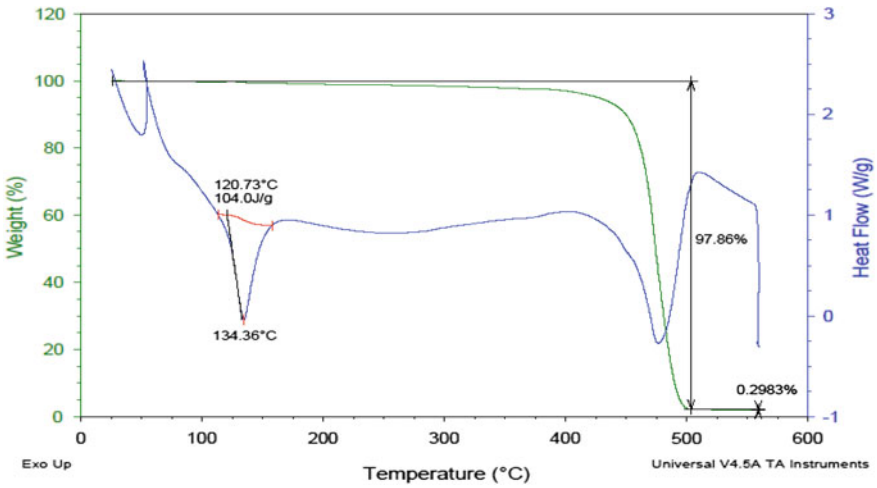

Fig. 47.6 Thermal properties of HDPE

conversion was achieved at 400 °C; the decrease of 100 °C is correlated to the fact that the reactor was pressurized by nitrogen. Therefore, pressure can also affect the initiation and termination of polymer degradation. As total conversion can be achieved at lower temperature, thus energy is saved affecting the economic feasibility of pyrolysis process.

47.4 Conclusion

Thermochemical conversion is an innovative alternative to landfilling and incineration of plastic waste eliminating several social and environmental problems and providing an environmentally friendly source of energy. In this research, HDPE was thermally degraded in a pyrolysis batch reactor yielding high liquid (60 %) and gas (37 %) fractions. In addition, the compositional analysis using GC-MS of the liquid fraction showed that it is fuel-like product. Different temperatures and pressures will be tested in order to study their effect on the polymer degradation, the yield and the composition of the products.

References

1. J. Aguado, D.P. Serrano, *Feedstock Recycling of Plastic Wastes* (Royal Society of Chemistry, Cambridge, 1999)
2. J. Aguado, D.P. Serrano, J.M. Escola, Fuels from waste plastics by thermal and catalytic processes: a review. Ind. Eng. Chem. Res. **47**, 7982–7992 (2008)
3. Statistics Center–Abu Dhabi, Waste Statistics in the Emirate of Abu Dhabi 2009 (2011)

4. Waste Management Center, Waste in the Emirate of Abu Dhabi, http://www.cwm.ae//index.php?page=waste-in-auh
5. M. Al Shrah, I. Janajreh, Mechanical Recycling of Cross-link Polyethylene: Assessment of Static and Viscoplastic Properties, Renewable and Sustainable Energy Conference (IRSEC), International (2013), p. 456
6. S. Syed, R. Qudaih, I. Talab, I. Janajreh, Kinetics of Pyrolysis and Combustion of Oil Shale Sample from Thermogravimetric Data, 7th Jordanian International Mechanical Engineering Conference (2010)
7. J. Schirmer, J.S. Kim, E. Klemm, Catalytic degradation of polyethylene using thermal gravimetric analysis and a cycled-spheres-reactor. J. Anal. Appl. Pyrolysis **60**, 205–217 (2001)
8. R. Grieken, D.P. Serrano, J. Aguado, R. Garcia, C. Rojo, Thermal and catalytic cracking of polyethylene under mild conditions. J. Anal. Appl. Pyrolysis **58–59**, 127–142 (2001)
9. S.H. Ng, H. Seoud, M. Stanciulescu, Y. Sugimoto, Conversion of polyethylene to transportation fuels through pyrolysis and catalytic cracking. Energy Fuels **9**, 735–742 (1995)
10. Y. Sakata, M.A. Uddin, A. Muto, Y. Kanada, K. Koizumi, K. Murata, Catalytic degradation of polyethylene into fuel oil over mesoporous silica (KFS-16) catalyst. J. Anal. Appl. Pyrolysis **43**, 15–25 (1997)
11. N. Miskolczi, L. Bartha, G. Deak, B. Jover, D. Kallo, Thermal and thermo-catalytic degradation of high-density polyethylene waste. J. Anal. Appl. Pyrolysis **72**, 235–242 (2004)
12. M.R. Hernandez, A.N. Garcia, A. Marcilla, Study of the gases obtained in thermal and catalytic flash pyrolysis of HDPE in a fluidized bed reactor. J. Anal. Appl. Pyrolysis **73**, 314–322 (2005)
13. M. Hernandez, A.N. Garcia, A. Marcilla, Catalytic flash pyrolysis of HDPE in a fluidized bed reactor for recovery of fuel-like hydrocarbons. J. Anal. Appl. Pyrolysis **78**, 272–281 (2007)
14. A. Marcilla, M.R. Hernandez, A.N. Garcia, Study of the polymer-catalyst contact effectivity and the heating rate influence on the HDPE pyrolysis. J. Anal. Appl. Pyrolysis **79**, 424–432 (2007)
15. S.H. Ng, Conversion of polyethylene blended with VGO to transportation fuels by catalytic cracking. Energy Fuels **9**, 216–224 (1995)
16. J. Aguado, D.P. Serrano, J.M. Escola, A. Peral, Catalytic cracking of polyethylene over zeolite mordenite with enhanced textural properties. J. Anal. Appl. Pyrolysis **85**, 352–358 (2009)
17. P.T. Williams, E.A. Williams, Fluidised bed pyrolysis of low density polyethylene to produce petrochemical feedstock. J. Anal. Appl. Pyrolysis **51**, 107–126 (1999)
18. M.S. Renzini, U. Sedran, L.B. Pierella, H-ZSM-11 and Zn-ZSM-11 zeolites and their applications in the catalytic transformation of LDPE. J. Anal. Appl. Pyrolysis **86**, 215–220 (2009)
19. N. Insura, J.A. Onwudili, P.T. Williams, Catalytic pyrolysis of low-density polyethylene over alumina-supported noble metal catalysts. Energy Fuels **24**(8), 4231–4240 (2010)
20. R. Bagri, P.T. Williams, Catalytic pyrolysis of polyethylene. J. Anal. Appl. Pyrolysis **63**, 29–41 (2002)
21. J. Aguado, D.P. Serrano, J.M. Escola, E. Garagorri, Catalytic conversion of low-density polyethylene using a continuous screw kiln reactor. Catal. Today **75**, 257–262 (2002)
22. M.A. Bawase, S.D. Reve, S.V. Shete, M.R. Saraf, Carbon Number Distribution by Gas Chromatography for Identification of Outlying Diesel Sample (2012), pp. 1–7
23. G. Manos, Catalytic Degradation of Plastic Waste to Fuel over Microporous Materials (2006), p. 197

Chapter 48
Developing Sustainable and Clean Energy for Environmental Issues in Turkey

I. Yuksel and H. Arman

Abstract Turkey has dynamic economic development and rapid population growth. It also has macro-economic, and especially monetary, instability. The net effect of these factors is that Turkey's energy demand has grown rapidly almost every year and is expected to continue growing, but the investment necessary to cover the growing demand has not been forthcoming at the desired pace. On the other hand, meeting energy demand is of high importance in Turkey. However, exploiting the country's large energy efficiency potential is also vital. Air pollution is a significant problem and, as the government's projections show, carbon emissions could rise sharply if current trends continue. Turkey's geographical location has several advantages for extensive use of most of these renewable energy sources. Over the last few decades, the numbers of Turkish citizens living in the eastern part of country have migrated to the western part of the country. This caused some problems in the energy utilization and environmental pollution in the western regions in Turkey. For this reason, in the coming decades, global environmental issues could significantly affect patterns of energy use in Turkey.

Keywords Renewable energy · Sustainable energy · Environmental issues · Turkey

I. Yuksel (✉)
Technology Faculty, Department of Civil Engineering, Sakarya University,
54187 Esentepe Campus, Sakarya, Turkey
e-mail: yukseli2000@yahoo.com

H. Arman
College of Science, Department of Geology, United Arab Emirates University,
P.O. Box: 15551, Al-Ain, United Arab Emirates

M. O. Hamdan et al. (eds.), *ICREGA'14 - Renewable Energy: Generation and Applications*, Springer Proceedings in Energy, DOI: 10.1007/978-3-319-05708-8_48,

48.1 Introduction

Energy is essential to economic and social development and improved quality of life in all countries. Much of the world's energy, however, is currently produced and consumed in ways that could not be sustained if technology were to remain constant and if overall quantities were to increase substantially. The need to control atmospheric emissions of greenhouse and other gases and substances will increasingly need to be based on efficiency in energy production, transmission, distribution and consumption in the country. Electricity supply infrastructure in many developing countries are being rapidly expanded as policymakers and investors around the world increasingly recognize electricity's pivotal role in improving living standards and sustaining economic growth [1–3].

There is a growing concern that long-run sustainable development may be compromised unless measures are taken to achieve balance between economic, environmental and social outcomes. Since the early 1980s, Turkish energy policy has concentrated on market liberalization in an effort to stimulate investment in response to increasing internal energy demand. Turkey's new government has continued this policy despite lower energy demand induced by the 2001 economic crisis. This paper provides an overview of energy use and air pollution issues for Turkey.

The Southeastern Anatolia Project (GAP) is one of the largest power generating, irrigation, and development projects of its kind in the world, covering 3 million hectare of agricultural land. This is over 10 % of the cultivable land in Turkey; the land to be irrigated is more than half of the presently irrigated area in Turkey. The GAP project on the Euphrates and Tigris Rivers encompasses 20 dams and 17 hydroelectric plants. Once completed, 27 billion kWh of electricity will be generated annually, which is 45 % of the total economically exploitable hydroelectric potential [3, 4].

48.2 Energy Utilization in Turkey

The socio-economic development, which has been progressing in parallel with fast industrial growth in Turkey, has caused living standards to rise. This has led to an increase in demand for electrical energy. All kinds of economic activities depend upon continuously developing technology and energy, and hence electrical energy has become an indispensable component of social life. An interconnected system now extends throughout the whole country, with the distribution network reaching even the smallest settlements. Electrical energy consumption has thus increased quickly as a proportion of total energy consumption [5–7].

The Ministry of Energy and Natural Resources carries out the general energy planning studies, using an 'MAED' demand model, and TEIAS (Turkish Electricity Transmission Company) carries out energy generation expansion planning studies, using the DECADES model. The MAED model [8], which was developed by the International Atomic Energy Agency (IAEA), makes projections of the

Table 48.1 Primary energy reserves in Turkey (2006) [12]

Energy sources	Proven	Probable	Possible	Total
Hard coal (million ton)	428	456	245	1,129
Lignite (million ton)				
Elbistan	3,357			3,357
Others	3,982	626	110	4,718
Total	7,339	626	110	8,075
Asphaltite	45	29	8	82
Bitumes	555	1,086		1,641
Hydropower				
GWh/yr	126,109			126,109
MW/yr	35,539			35,539
Petroleum (million ton)	39			39
Natural gas (billion m^3)	10.2			10.2
Nuclear sources (ton)				
Uranium	9,129			9,129
Thorium	380,000			380,000
Geothermal (MW/year)				
Electricity	200		4,300	4,500
Thermal	2,250		28,850	31,100
Solar energy				
Electricity				8.8
Heat				26.4

medium and long-term general electricity demand. It takes into consideration a detailed analysis of social, economic and technical systems. The model is based on low, medium and high case scenarios. It is very important to project the energy demand accurately, because decisions involving huge investments of capital are based on these forecasts.

Turkey has a very good geographic location and natural resources. Turkey has dynamic economic development and rapid population growth. Along with the economic growth and population increase, significant increases were observed both in primary energy and in electricity consumption during the 8th Plan period [9]. Consumption of primary energy reached 94.3 Mtoe as of the end of 2005 with an annual average increase of 2.8 % while electricity consumption reached 165.3 billion kWh with an annual average increase of 4.6 % during this period. These increases are more evident in the period following 2003, since the impact of the 2001 economic crisis was alleviated, and the economy stabilized. During this term, primary energy and electricity utilization grew at an annual average rate of 5.7 and 6.7 %, respectively [3, 10, 11].

Turkey is an energy importing country; more than half of the energy requirement has been supplied by imports. Oil has the biggest share in total primary energy consumption. Due to the diversification efforts of energy sources, use of natural gas that was newly introduced into Turkish economy, has been growing rapidly. Turkey has large reserves of coal, particularly of lignite. The proven

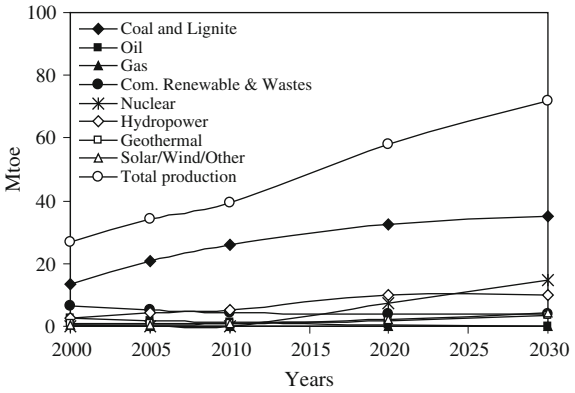

Fig. 48.1 Turkey's primary energy production during 2000–2030 [13]

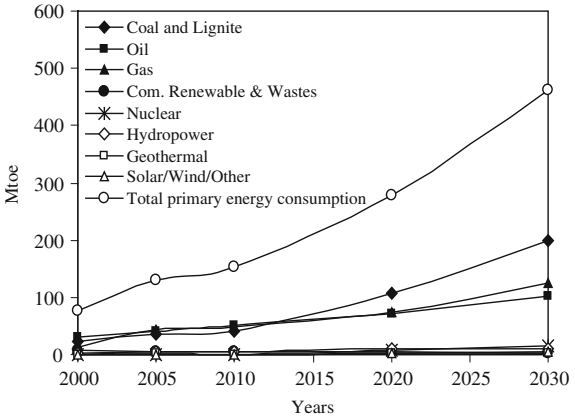

Fig. 48.2 Turkey's primary energy consumption forecast 2000–2030 [13]

resources are 8.0 billion tons (Table 48.1). The estimated total possible reserves are 30 billion tons. Turkey, with its young population and growing energy demand per person, its fast growing urbanization, and its economic development, has been one of the fast growing power markets of the world for the last two decades (Figs. 48.1 and 48.2).

It is expected that the demand for electric energy in Turkey will be 300 billion kWh by the year 2010 and 580 billion kWh by the year 2020. Turkey's electric energy demand is growing about 6–8 % yearly due to fast economic growing [5, 9, 11, 12, 14–17]. In Turkey, primary energy production and consumption has reached 28 and 98.3 Mtoe (million tons of oil equivalent) respectively (Tables 48.2 and 48.3).

The most significant developments in production are observed in hydropower, geothermal, solar energy and coal production. Turkey's use of hydropower, geothermal and solar thermal energy has increased since 1990. However, the total share of renewable energy sources in total primary energy supply (TPES) has

Table 48.2 Selected indicators of primary energy consumption and resources (thousands TOE) [11, 12]

Energy sources	2005 Realization		2006 Realization		2007 Realization	
	Amount	(%)	Amount	(%)	Amount	(%)
Commercial energy	89,050	94.4	93,680	94.7	96,680	94.5
Hard coal	14,805	15.7	15,052	15.2	16,052	15.2
Lignite	10,760	11.4	11,005	11.1	12,005	11.1
Petroleum products	32,855	34.8	35,160	35.6	37,160	35.6
Natural gas	25,665	27.2	27,356	27.7	29,356	27.7
Hydraulic energy	3,744	4.0	3,801	3.8	3,981	3.8
Renewable energy	1,350	1.4	1,427	1.4	1,627	1.4
Non-commercial energy	5,250	5.6	5,200	5.3	5,608	5.5
Wood	4,100	4.4	4,100	4.1	4,100	4.1
Biomass	1,150	1.2	1,100	1.1	1,100	1.4
Total	94,300	100	98,880	100	102,288	100

TOE tons of oil equivalent

Table 48.3 Developments in production and consumption of energy [12]

	2000	2002	2004	2006
Primary energy production (TTOE)	27,621	24,884	24,170	28,020
Primary energy consumption (TTOE)	81,193	78,322	87,778	98,300
Consumption per capita (KOE)	1,204	1,131	1,234	1,249
Electricity installed capacity (MW)	27,264	31,846	36,824	39,596
Thermal (MW)	16,070	19,586	24,160	26,481
Hydraulic (MW)	11,194	12,260	12,664	13,115
Electricity production (GWh)	124,922	129,400	150,698	165,346
Thermal (GWh)	94,011	95,668	104,556	124,321
Hydraulic (GWh)	30,912	33,732	46,142	41,025
Electricity import (GWh)	3,786	3,588	464	636
Electricity export (GWh)	413	435	1,144	1,812
Total consumption (GWh)	128,295	132,553	150,018	168,216
Consumption per capita (kWh)	1,903	1,914	2,109	2,240

declined, owing to the declining use of non-commercial biomass and the growing role of natural gas in the system. Turkey has recently announced that it will reopen its nuclear programme in order to respond to the growing electricity demand while avoiding increasing dependence on energy imports [12, 14, 16].

The TPES in Turkey grew by 3.2 % per year between 1990 and 2006, the fastest growth rate among International Energy Agency (IEA) Member countries [14, 15]. Coal is the dominant fuel, accounting for 27.4 % of TPES in 2006. Oil (35.6 %) and gas (27.7 %) also contributed significantly (Table 48.2). Renewable energy, mostly biomass, waste and hydropower, accounted for 10.9 %. Hydropower represented 3.8 % of TPES in 2005. Biomass, primarily fuel wood consumed by households, represented almost 5.9 % [12, 16]. The economic

downturn in Turkey in 2000–2005 caused TPES to decline by 6.0 %. Nevertheless, energy demand is expected to more than double by 2010, according to Turkish government sources [9, 12, 16]. On the other hand, gas accounted for 43.8 % of total electricity generation in 2006, coal 26.58 % and oil at about 5 %. Hydropower is the main indigenous source for electricity production and represented 20–30 % of total generation from 1970 to 2006. Hydropower declined significantly relative to 2000 due to lower electricity demand and to take-or-pay contracts in the natural gas market [12, 18].

48.3 Future Energy Policies in Turkey

Turkey's demand for energy and electricity is increasing rapidly. Since 1990, energy consumption has increased at an annual average rate of 4.3 %. As would be expected, the rapid expansion of energy production and consumption has brought with it a wide range of environmental issues at the local, regional and global levels [5, 17, 19]. With respect to global environmental issues, Turkey's carbon dioxide (CO_2) emissions have grown along with its energy consumption.

Primary energy supply was projected to increase from 64.5 Mtoe (1995) to 332.0 Mtoe (2025). Crude oil imports remained constant at 33.0 Mtoe after 2004 when the domestic refineries were forecast to run into their processing capacity, resulting in a drop in crude oil share from 44 to 10 % of total supplies. Once the refining capacity is reached, net imports of refined products will quickly grow from 2.6 to 52.3 Mtoe (2000–2025), accounting for about 16 % of total supplies by 2025. Natural gas quickly increases its share from 10 % (6.3 Mtoe) in 1995 to 42 % (139.8 Mtoe) of total supplies in 2025. Although renewables double over 2000–2025, this share will decreases from 14 % in 2000 to 7 % in 2025 [5, 7, 8, 19, 20].

The main aim of the energy policies is to meet the energy needs of increasing population and growing economy in a continuous, qualified and secure manner through primarily private sector investments in a competitive and transparent free market environment. In this context, it is the main target to supply the required energy timely, uninterrupted and at minimum costs while making energy supply planning [11]. In 2007, both primary energy and electricity production and consumption would grew in parallel with the targeted economic growth. Thus, total primary energy consumption is forecasted to increase by around 3.4 % to reach 102.28 Mtoe and per capita primary energy consumption by 3.6 % to reach 1.337 kg of oil equivalent.

A suitable environment will be established, with legislative regulations if necessary, in order for the private sector to fill the gap that will arise because of the withdrawal of the state from the sector, in a timely manner and to expedite the start of the new production investments in line with supply and demand projections [14]. Thus, emphasis will be given to privatization of the existing facilities in order to prevent the burden of new investments on the state. The state will be adequately equipped in a way to closely monitor the supply security within the framework of its regulatory and supervisory role and to take measures [12, 15, 16].

48.4 Renewable Energy Potential and Water Resources in Turkey

The hydropower industry is closely linked to both water management and renewable energy production, and so has a unique role to play in contributing to sustainable development in a world where billions of people lack access to safe drinking water and adequate energy supplies. On the other hand, approximately 1.6 billion people have no access to electricity and about 1.1 billion are without adequate water supply. However, resources for hydropower development are widely spread around the world. Potential exists in about 150 countries and about 70 % of the economically feasible potential remains to be developed-mostly in developing countries where the needs are most urgent [7, 21–23].

Hydropower is available in a broad range of project scales and types. Projects can be designed to suit particular needs and specific site conditions. As hydropower does not consume or pollute the water it uses to generate power, it leaves this vital resource available for other uses. At the same time, the revenues generated through electricity sales can finance other infrastructure essential for human welfare. This can include drinking water supply systems, irrigation schemes for food production, infrastructures enhancing navigation, recreational facilities and ecotourism.

Water is a vital resource that supports all forms of life on earth. Unfortunately, it is not evenly distributed by season or geographical region. Some parts of the world are prone to drought, making water a particularly scarce and precious commodity. In other parts of the world, floods that cause loss of life and property are major problems [7, 22, 23].

The total gross hydropower potential and total energy production capacity of Turkey are nearly 50 GW and 112 TWh/year, respectively and about 30 % of the total gross potential may be economically exploitable. At present, only about 35 % of the total hydroelectric power potential is in operation [24]. The national development plan aimed to harvest all of the hydroelectric potential by 2010. The contribution of small hydroelectric plants to total electricity generation was estimated to be 5–10 % [25, 26]. On the other hand, the GAP is one of the largest power generating, irrigation, and development projects of its kind in the world, covering 3.0 million hectares of agricultural land [27]. This is over 10 % of the cultivable land in Turkey; the land to be irrigated is more than half of the presently irrigated are in Turkey. The GAP project on the Euphrates and Tıgris Rivers encompasses 22 dams and 19 hydroelectric power plants. Once completed, 27 billion kWh of electricity will be generated and irrigating 1.7 million hectares [3, 17, 24, 27–30].

48.5 Water Management and Environmental Issues in Turkey

There is no single solution to the world's quest for more, cleaner energy and effective water management. Energy and water for sustainable development depend not only on supply choices, but also on how these choices are implemented. It requires the creation of a level playing field among available energy options and global water governance involving all stakeholders in a participatory decision-making process. In adopting their own sustainability guidelines, the members of the International Hydropower Association are committed to developing and operating their projects, in collaboration with all stakeholders, in a way that is environmentally friendly, socially responsible and economically efficient so that hydropower projects can make a major contribution to achieving sustainable energy and resource development [7, 22].

Hydropower energy is a renewable, sustainable and clean energy among the other alternative energy sources. Moreover, it does not deprive future generations in terms of raw materials, or burdening them with pollutants or waste. Hydroelectric power plants utilize the basic national and renewable resource of the country. Although the initial investment cost of hydropower seems relatively high, the projects have the lowest production costs and do not depend on foreign capital and support, when considering environmental pollution and long-term economic evaluation [7, 31].

Turkey is a rapidly growing country whose income level is moving towards that of the rest of the Organization for Economic Co-operation and Development (OECD) area. This catch-up process has been associated with a rapid growth of greenhouse gas emissions. Nonetheless, carbon emissions from any country contribute equally to the pressure on the global climate. Consequently, the major issue facing policy makers is how to contribute to reducing the burden on global resources at a low cost and without jeopardizing the rapid growth of the economy [5, 14, 16].

Turkey shares a number of features with some other OECD countries that suggests it would be possible to considerably moderate the growth of greenhouse gases with little or even no cost. The proportion of energy derived from carbon-intensive coal and lignite is one of the highest in the OECD area, reflecting ample reserves of lignite, while a completely liberalized market in natural gas has not existed [14].

In Turkey, air pollution is a serious problem that has only recently come to the center of policy concerns. The social and economic costs of air pollution in Turkey are likely to be large. The latest OECD environmental performance review estimated that excessive SO_2 emissions in the early 1990s might have increased mortality by over 3,600 deaths and restricted activity days by almost 7 million each year. A start has been made in this area but the main issue for the authorities is to implement effective policies to address air pollution in a way that ensures a combination of minimum costs and maximum benefits [3, 16].

48.6 Conclusions

As would be expected, the rapid expansion of energy production and consumption has brought with it a wide range of environmental issues at the local, regional and global levels. With respect to global environmental issues, Turkey's carbon dioxide (CO_2) emissions have grown along with its energy consumption. States have played a leading role in protecting the environment by reducing emissions of greenhouse gases (GHGs). In this regard, renewable energy resources appear to be one of the most efficient and effective solutions for clean and sustainable energy development in Turkey.

The environmental impacts of hydro plants are minimal compared with alternative resources. They make use of our renewable "green energy" resource, without causing pollution and CO_2 emission. They have considerable advantages, since they use the renewable sources of the country, are free of fuel costs, and their design and Turkish engineers and contractors can perform construction. They are also easily adaptable to the system load demands.

The GAP will play an important role in the development of Turkey's energy and agriculture sector in the near future. For this reason, it is necessary to examine the general structure of this project and investigate in detail its effects and its environmental issues.

References

1. K. Kaygusuz, Energy use and air pollution issues for Turkey. Clean **35**, 539–547 (2007)
2. I. Yuksel, Dams and hydropower for sustainable development. Energy Source Part B **4**, 100–110 (2009)
3. I. Yuksel, H. Arman, Energy and environmental policies in Turkey. Energy Source Part B **9**, 57–69 (2014)
4. I. Yuksel, Southeastern Anatolia Project (GAP) for irrigation and hydroelectric power in Turkey. Energy Explor. Exploit **24**, 361–370 (2006)
5. Ministry of Energy and Natural Resources: Greenhouse gas mitigation in energy sector for Turkey (Working Group Report, Ankara, Turkey 2005)
6. State Water Works, *Hydropower Potential in Turkey* (Ankara, Turkey, 2007)
7. I. Yuksel, Energy utilization, renewables and climate change mitigation in Turkey. Energy Explor. Exploit **26**, 35–52 (2008)
8. Energy Report of Turkey in 2004, Ministry of Energy and Natural Resources, Ankara, Turkey (2005), http://www.enerji.gov.tr. Cited 15 Nov 2009
9. State Planning Organization, *Eighth Five-Year Development Plan 2001–2005* (Ankara, Turkey, 2001)
10. K. Kaygusuz, Environmental impacts of energy utilization and renewable energy sources in Turkey. Energy Explor. Exploit **19**, 497–509 (2001)
11. State Planning Organization, *Ninth Development Plan 2007–2013* (Ankara, Turkey, 2006)
12. Energy Statistics in Turkey, Ministry of Energy and Natural Resources, Ankara, Turkey (2005), http://www.enerji.gov.tr. Cited 18 Sep 2011
13. K. Kaygusuz, Energy and environmental issues relating to greenhouse gas emissions for sustainable development in Turkey. Renew. Sust. Energy Rev. **13**, 253–270 (2009)

14. International Energy Agency, *Energy Policies of IEA Countries: Turkey 2005 Review* (OECD/IEA, Paris, 2005)
15. International Energy Agency, *Energy Statistics of IEA Countries: Turkey 2004 Review* (OECD/IEA, Paris, 2006)
16. G. Apak, B. Ubay (eds.), *First National Communication of Turkey on Climate Change*, Ministry of Environment and Forestry, Ankara, Turkey (2007), pp. 60–150
17. I. Yuksel, Global warming and renewable energy sources for sustainable development in Turkey. Renew. Energy **33**, 802–812 (2008)
18. Short history of electrical energy development in Turkey, Directorate-General of Turkish Electricity Transmission, Ankara, Turkey (2005), http://www.teias.gov.tr. Cited 11 Dec 2009
19. G. Conzelman, V. Koritarov, *Turkey Energy and Environmental Review, Task 7: Energy Sector Modeling*, Center for Energy, Environmental, and Economic Systems Analysis (CEEESA), Argonne National Laboratory (August 2002)
20. UNDP/World Bank Energy Sector Management Assistance Program (ESMAP): Turkey-Energy and the Environment, Issues and Options Paper (Report 229, 2000)
21. International Energy Agency, *World Energy Outlook 2002* (OECD/IEA, Paris, 2002)
22. The Role of Hydropower in Sustainable Development, International Hydropower Association: White Paper (2003), http://www.hydropower.org. Cited 3 May 2006
23. Survey of Energy Resources, World Energy Council (2001), http://www.worldenergy.org. Cited 30 Nov 2010
24. State Water Works, *Hydropower Potential in Turkey* (Ankara, Turkey, 2008)
25. K. Kaygusuz, Sustainable development of hydropower and biomass energy in Turkey. Energy Convers. Manag. **43**, 1099–1120 (2002)
26. K. Kaygusuz, Environmental impacts of energy utilization and renewable energy policies in Turkey. Energy Policy **30**, 689–698 (2002)
27. Energy production in GAP region, Southeastern Anatolia Project, GAP (2007), http://www.gap.gov.tr. Cited 26 Aug 2009
28. I. Yuksel, Development of hydropower: a case study in developing countries. Energy Source Part B **2**, 113–121 (2007)
29. K. Kaygusuz, Hydropower in Turkey: the sustainable energy future. Energy Source Part B **4**, 34–47 (2009)
30. K. Kaygusuz, Biomass as a renewable energy source for sustainable fuels. Energy Source Part A **31**, 535–545 (2009)
31. O. Paish, Small hydropower: technology and current status. Renew. Sust. Energy Rev. **6**, 537–556 (2002)

Chapter 49
Detailed Kinetics-Based Entrained Flow Gasification Modeling of Utah Bituminous Coal and Waste Construction Wood Using Aspen Plus

Idowu A. Adeyemi and Isam Janajreh

Abstract This study seeks to develop a kinetic-based ASPEN Plus model for the Brigham Young University (BYU) gasifier, an atmospheric oxygen-blown entrained flow gasifier. The model consists of 11 components, 3 in-built FORTRAN calculations and a FORTRAN subroutine. The in-built FORTRAN calculations were used for the estimation of the drying process, the separation of char into constituents and the estimation of the gasifier residence time while the FORTRAN subroutine was used to determine the char gasification kinetics based on the unreacted shrinking core model of Wen and Chaung [1]. The model takes into account the passive heating through moisture release, pyrolysis, volatile combustion and char gasification. The model has been validated with the experimental work of Brown et al. [2] with Utah bituminous coal, which was used as a baseline for the analysis of wood waste. In addition, the effect of operating parameters had been studied to determine the influence of fuel type and gasifier diameter on the process metrics like the gasification efficiency, species distribution along the centerline etc. Based on the available knowledge, this is the first detailed non-empirical ASPEN Plus kinetic model for entrained flow gasification (EFG) studies in the oxygen-blown atmospheric Brigham Young University laboratory gasifier set-up.

Keywords Pyrolysis · Entrained flow gasification · Kinetics · Char · Species distribution · Gasification efficiency

I. A. Adeyemi · I. Janajreh (✉)
Masdar Institute, Abu Dhabi, United Arab Emirates
e-mail: ijanajreh@masdar.ac.ae

M. O. Hamdan et al. (eds.), *ICREGA'14 - Renewable Energy: Generation and Applications*, Springer Proceedings in Energy, DOI: 10.1007/978-3-319-05708-8_49,

49.1 Introduction

Millions of tons of solid wastes are generated annually that continue to pose serious environmental and ecological threats to our planet. In 2009 alone, the total amount of solid waste in the Emirate of Abu Dhabi, United Arab Emirates, was 5,756 thousand tons according to the estimates of the Center of Waste Management-Abu Dhabi, with the construction sector contributing 61 % of the total waste due to the construction boom taking place in the Emirate [3]. In addition, nearly 30 % of the 240 million tons generated waste in the US is recycled while the rest is primarily destined to land filling. Landfill gas (LFG), which is mainly composed of carbon dioxide and methane, is widely recognized as one of the largest sources of methane emission to the atmosphere and a central contributor to greenhouse gases (GHG). Methane, however, is 21-folds more potent than carbon dioxide by weight, and it is second most abundant GHG after carbon dioxide. The estimate of global methane emission from solid waste disposal sites ranges from 20 to 70 Tg/year, or about 5–20 % of the total estimated methane emission of 375 Tg/year from anthropogenic sources. Therefore, alternative waste to energy systems which are less harmful to our environment and avoids other problems associated with landfilling like land availability, health issues, etc., should be sought. Which alternative technology has the capability to resolve these problems? Gasification is one of the technologies that have been sought for its lower emission and higher efficiency. Besides its ability to resolve most of the landfilling problems, it helps so solve other issues too. Gasification does not compete with food supplies as against fermentation, and it does not produce noxious pollutants like incineration. Furthermore, gasification helps to take over from recycling after a product has been recycled several times. In addition, the syngas produced during gasification can be used as fuel in different kind of power plant such as gas turbine cycle, steam cycle, combined cycle, internal and external combustion engine and Solid Oxide Fuel Cell (SOFC) [4].

Although there are some equilibrium-based ASPEN Plus models for EFG [5–10], there are very few studies on the detailed kinetics-based ASPEN Plus model development [11, 12] and centerline experimental studies for an EFG process [2, 13, 14]. Kong et al. [5] developed a three stage equilibrium model for the gasification of coal in the Texaco type coal gasifiers using ASPEN Plus to calculate the composition of the product gas, carbon conversion, and gasification temperature. Gartner et al. [11] developed a kinetic based entrained flow gasifier model in ASPEN Plus for the simulation of the gasification of fuel blends (dried lignite, extraction residue and char) in the CSIRO air-blown pressurized entrained flow reactor (PEFR). Their study was validated with the gasification studies on three Australian coals (CRC252, CRC274, and CRC299) investigated in this reactor [13]. Lee et al. [12] investigated the effects of burner type on a bench-scale entrained flow gasifier in ASPEN Plus and validated their model with the experimental data from the 1-ton-per-day oxygen-nitrogen blown Korea Electronic Power Corporation (KEPCO) Research Institute gasifier. Brown et al. [2] conducted experiments on the gasification of four coal types in an oxygen-blown atmospheric entrained flow gasifier at the Brigham

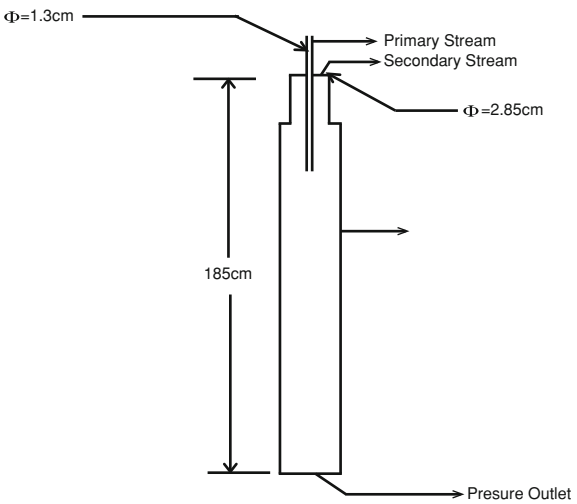

Fig. 49.1 The schematic diagram of the BYU gasifier

Young University with the objective of investigating the temperature and syngas composition along the centerline of the gasifier. Harris et al. [14] examined the behavior of fifteen Australian coals and one petroleum coke at 2.0 MPa pressure and at temperatures between 1,373 and 1,773 K under conditions allowing for coal gasification behavior to be investigated under well-controlled entrained flow conditions. The effects of O:C ratio, residence time and coal type on conversion levels and product gas composition were studied.

The main objective of this work is to develop a detailed kinetics-based non-empirical ASPEN Plus model for the oxygen-blown BYU entrained flow gasifier (Fig. 49.1) and determine the effects of fuel type (Utah Bituminous Coal and Construction Waste Wood) on the gas composition and gasification efficiency. This predictive kinetic-based ASPEN Plus model with low computational cost, takes into consideration four processes: moisture release, pyrolysis, volatile combustion and char gasification. A plug flow reactor was used to simulate the char gasification process in order to eliminate the assumptions of constant temperature in equilibrium-based models. This model also helps in gaining insight about the processes that occur inside the gasifier and hence, help in the optimization of a gasification system.

49.2 Model Assumptions

The following assumptions were made in the development of the entrained flow gasification model:

- The gasification model is in steady state
- The gas phase is assumed to be instantaneously and perfectly mixed with the solid phase

Table 49.1 Proximate analysis of fuels

Proximate analysis (wt%)	Utah bituminous coal [2]	Construction waste wood
Moisture	2.40	8.95
Volatile	45.60	68.89
Fixed carbon	43.70	21.88
Ash	8.30	0.28

Table 49.2 Ultimate analysis of fuels

Ultimate analysis (wt%)	Utah bituminous coal [2]	Construction wood waste
Carbon	71.00	49.45
Hydrogen	6.00	6.26
Nitrogen	1.30	0.39
Oxygen	12.70	43.60
Sulfur	0.70	0.02
Ash	8.30	0.28

- The pressure drop in the gasifier is neglected
- The particles are assumed to be spherical and of uniform size
- The ash layer formed remains on the particle during the reactions based on the unreacted-core shrinking model
- The temperature inside the particle is assumed to be uniform.

49.3 Fuel Characterization and Gasification Conditions

49.3.1 Proximate Analysis

This analysis is done with the thermo-gravimetric analyzer (TGA) in order to fragment the feedstock into moisture, volatile, fixed carbon and ash. Based on this analysis, we can determine the quality of the fuel to be used for gasification. A feedstock with low moisture and ash content is a good candidate for gasification. The detailed result for both feedstocks is presented in Table 49.1.

49.3.2 Ultimate Analysis

The ultimate analysis (Table 49.2) is based on the examination of the elemental composition of the fuel. The elemental composition of any carbonaceous material in terms of the mass percentages of C, H, O, N, S components can be determined using FLASH Elemental Analyzer. Determination of the elemental content

Table 49.3 Boundary conditions [2]

Conditions	Value
Primary stream	
Flow rate (kg/s)	0.0073
Component mole fraction	
Oxygen	0.85
Argon	0.126
Steam	0.024
Stream temperature (K)	360
Secondary stream	
Flow rate (kg/s)	0.00184
Component mole fraction	
Steam	1
Stream temperature (K)	450
Particle loading	0.910

composition is very important in gasification as that helps to determine the equivalence ratio of the fuel. Any fuel with high oxygen does not require large amount of oxygen for gasification.

49.3.3 Bomb Calorimetry

The bomb calorimetry helps to determine the heating value of the feedstocks to be gasified. The equipment used for this analysis was the Bomb calorimeter (Parr 6100). The heating value obtained for Utah bituminous coal and construction waste wood are 29.8 and 18.7 MJ/kg respectively.

49.3.4 Boundary Conditions

The boundary condition in Table 49.3 was applied to the developed model for both the Utah bituminous coal and the construction waste wood.

49.4 Model Descriptions

The ASPEN Plus model consists of the moisture release through passive heating, devolatilization, volatile combustion and char gasification (Fig. 49.2).

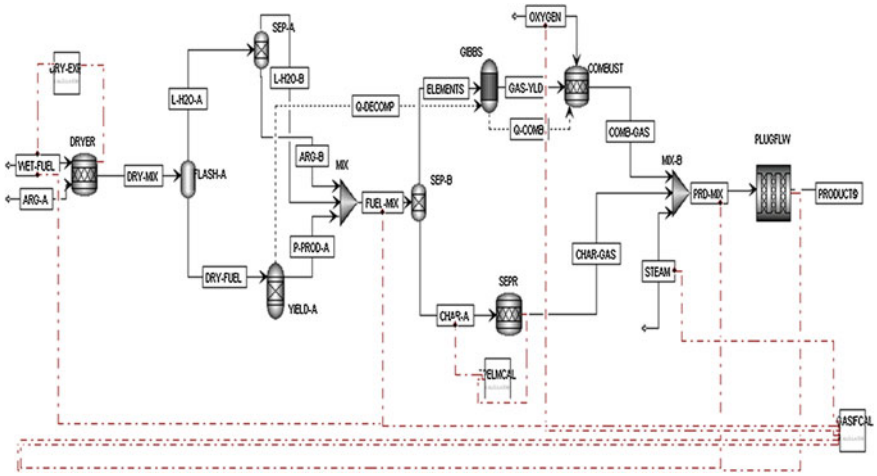

Fig. 49.2 The ASPEN plus EFG model

49.4.1 Moisture Release

The first stage of the gasification process is the moisture release, particularly when wet fuels are being injected. The moisture release process was modeled in ASPEN Plus with the RStoic block labeled as DRYER and the Flash2 block labeled as FLASH-A. With the help of the RStoic block and an in-built FORTRAN code, the amount of moisture to be released from the wet fuel was estimated as 95 % of the moisture content in the proxanal attribute. Subsequently, the Flash2 separator was used to remove the vapor from other components of the fuel. Because the reactor is closed and there is no means of releasing the lost vapor into the atmosphere, the lost vapor was re-introduced via the stream L-H2O-B. The moisture release process can be represented as shown in Eq. (49.1).

$$C_xH_yO_zN_mS_nAsh_pMois_q \rightarrow C_xH_yO_zN_mS_nAsh_pMois_r + (q - r)Mois \qquad (49.1)$$

49.4.2 Pyrolysis or Devolatilization

After most of the moisture content of the fuel had been dried off, the volatiles in the dry feedstock are released. The volatiles that are considered in this model are carbon monoxide, vapor, hydrogen, carbon dioxide, methane, hydrogen sulfide, nitrogen and benzene. The tar produced during the pyrolysis process, which is usually very minute for entrained flow gasification due to their high temperature, was taken as benzene for this model [15]. Besides the volatiles that are evolved, solid char with intrinsic ash is left behind. Pyrolysis of feedstocks usually begins

between 400 and 600 °C and ends in few to several milliseconds [2]. Hence, the devolatilization process can be assumed to be instantaneous and can be modeled in ASPEN Plus with an RYield reactor labeled as YIELD-A, a mixer labeled as MIX, a separator labeled as SEP-B and an RGibbs reactor labeled as GIBBS. The YIELD-A reactor breaks down the fuel into char and elements consisting of carbon, hydrogen, nitrogen, oxygen and sulfur. The elements, char, argon, and released vapor (during the moisture release stage) are mixed together using the mixer-MIX from where they were sent to a separator-SEP-B. The SEP-B separates the char from other components which consist of the volatile elements and sends the volatile components into the GIBBS reactor. The RGIBBS reactor in ASPEN Plus utilizes the Gibbs minimization method to find the equilibrium composition of the volatiles which were identified as argon, carbon monoxide, hydrogen, carbon dioxide, vapor, hydrogen sulfide, nitrogen, methane and benzene. The expression for the pyrolysis of the dry fuel is as shown in the Eq. (49.2).

$$C_xH_yO_zN_mS_nAsh_pMois_r \rightarrow C_{x_1}Ash_p + x_2CO + x_3H_2 + x_4H_2O + x_5CO_2 + x_6CH_4 + x_7H_2S + x_8N_2 + x_9C_6H_6 \tag{49.2}$$

49.4.3 Volatile Combustion

Immediately the volatiles are evolved, they start reacting with the oxidant introduced, which is usually oxygen. Only four of the released volatile components, namely carbon monoxide, hydrogen, methane and benzene, can undergo combustion. Hence, four reactions were modeled in ASPEN Plus with an RStoic reactor labeled COMBUST as shown in Eqs. (49.3–49.6).

$$C_6H_6 + 7.5O_2 \rightarrow 6CO_2 + 3H_2O \tag{49.3}$$

$$H_2 + 0.5O_2 \rightarrow H_2O \tag{49.4}$$

$$CO + 0.5O_2 \rightarrow CO_2 \tag{49.5}$$

$$CH_4 + 2O_2 \rightarrow CO_2 + 2H_2O \tag{49.6}$$

The rates of gas phase combustions are generally much faster than those of solid–gas reactions. The calculated rate of combustion of carbon monoxide based on the correlation of Hottel et al. was found to be so high that it can be considered instantaneous [16]. The conversion of carbon monoxide, hydrogen and benzene are thus assumed to be 100 %.

49.4.4 Char Gasification and Homogeneous Reactions

The char gasification process and the subsequent homogeneous reactions were modeled in ASPEN Plus with the RPlug reactor labeled as PLUGFLW. The RPlug reactor eliminates the assumption of constant temperature in equilibrium-based models. In addition, this reactor block allows for the observation of the axial temperature and concentration of the product gases and hence, it helps in the estimation of the optimal length and diameter for entrained flow gasification. The following reactions in addition to the Eqs. (49.7–49.13) were considered:

$$C + \frac{1}{\phi} O_2 \rightarrow 2\left(1 - \frac{1}{\phi}\right) CO + \left(\frac{2}{\phi} - 1\right) CO_2 \tag{49.7}$$

$$C + H_2O \rightarrow CO + H_2 \tag{49.8}$$

$$C + CO_2 \rightarrow 2CO \tag{49.9}$$

$$C + 2H_2 \rightarrow CH_4 \tag{49.10}$$

$$S + H_2 \rightarrow H_2S \tag{49.11}$$

$$CO + H_2O \rightarrow CO_2 + H_2 \tag{49.12}$$

$$CH_4 + H_2O \rightarrow CO + 3H_2 \tag{49.13}$$

where ϕ = the mechanism factor based on the stoichiometric relation of CO and CO_2 and can be obtained from the work of Wen and Chaung [1].

Because entrained flow gasification occurs in the reaction zone III where the temperature is high, most char-gas reactions can be considered as surface reactions. Furthermore, the solid loading in entrained flow gasifiers is very small that the particle collisions are likely to be infrequent and the ash layer formed can be assumed to remain on the fuel particle during reactions. Hence, the unreacted-core shrinking model [1] can be reasonably applied to estimate the heterogeneous solid-gas reaction rates.

The overall rate, according to this model, can be expressed as:

$$R_{c-i} = \frac{1}{\frac{1}{k_{diff}} + \frac{1}{k_s Y^2} + \frac{1}{k_{dash}\left(\frac{1}{Y} - 1\right)}} \left(P_i - P_i^*\right) \tag{49.14}$$

where

$$k_{dash} = k_{diff} \cdot \epsilon^n \tag{49.15}$$

$$Y = \frac{r_c}{r_p} = \left[\frac{(1-x)}{(1-f)}\right]^{\frac{1}{3}} \tag{49.16}$$

where k_s is the surface reaction constant, k_{dash} is the ash film diffusion constant, k_{diff} is the gas film diffusion constant, ε is the voidage in the ash layer, n is a constant between 2 and 3, r_c is the radius of the unreacted core, r_p is the radius of the whole particle including the ash layer, x is coal conversion at any time after pyrolysis is complete, f is the coal conversion when pyrolysis is complete, $P_i - P_i^*$ is the effective partial pressure of the components and R_{c-i} is the reaction rate.

The expressions for the kinetic constants k_{diff}, k_s, k_{dash}, and $(P_i - P_i^*)$ for each char-gas reactions can be obtained from the work of Wen and Chaung [1].

49.5 Results and Discussions

49.5.1 Model Validation

The developed kinetic ASPEN Plus model was validated with the work of Brown et al. [2] based on the oxygen-blown atmospheric BYU experimental gasifier set-up with Utah bituminous coal (Figs. 49.3–49.6). It is evident that this model predicts the gas composition along the centerline of the gasifier reasonably well considering the fact that the RPlug reactor used in ASPEN Plus is a 1-D reactor without turbulence effects being considered. This validated model could be used in studies, which are cumbersome to be performed in experiments, to obtain the metrics of a gasifier set-up.

49.5.2 Effect of Gasifier Diameter

One of the important parameters to be considered in the design of an optimal gasifier is the size. Hence, the effect of the gasifier diameter on the gas composition along the centerline was investigated in order to determine the best design size for a gasifier (Figs. 49.7–49.10). The diameter of the gasifier was varied between 0.1 and 0.3 m. While a rise in the diameter size leads to an increase in the mole fraction of the carbon monoxide, carbon dioxide and hydrogen throughout the length of the gasifier, an opposite trend was observed for the vapor composition. In addition, the effect of the diameter was more pronounced between 0.1 and 0.2 m than between 0.2 and 0.3 m. This implies that there is a limit to the size of a gasifier for optimization above which there will be no effect and the extra diameter will be redundant.

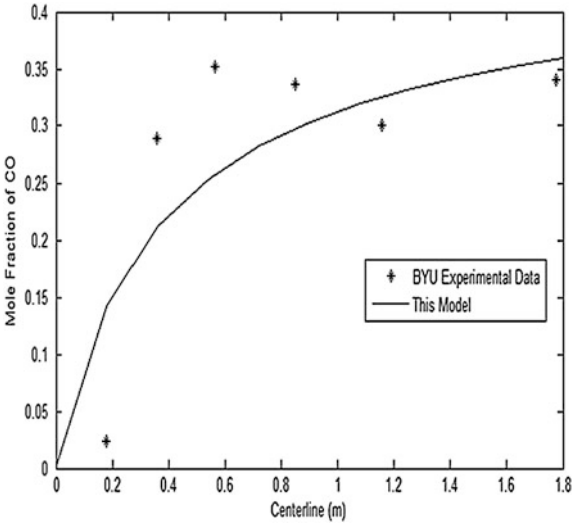

Fig. 49.3 Mole fraction of CO along the centerline

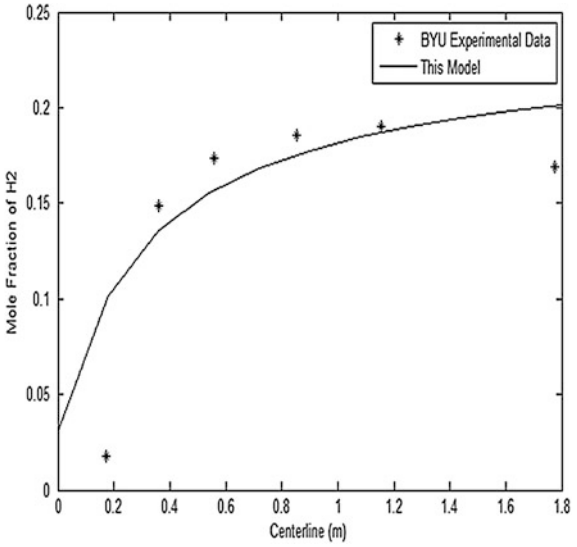

Fig. 49.4 Mole fraction of H_2 along the centerline

49.5.3 Effect of Fuel Type on Gas Composition

Another important concern in the combustion community is the viability of the gasification of other feedstocks besides coal. We have therefore decided to investigate the effect of gasifying construction waste wood on the gas composition along the centerline of the gasifier (Figs. 49.11–49.14). Based on this sensitivity

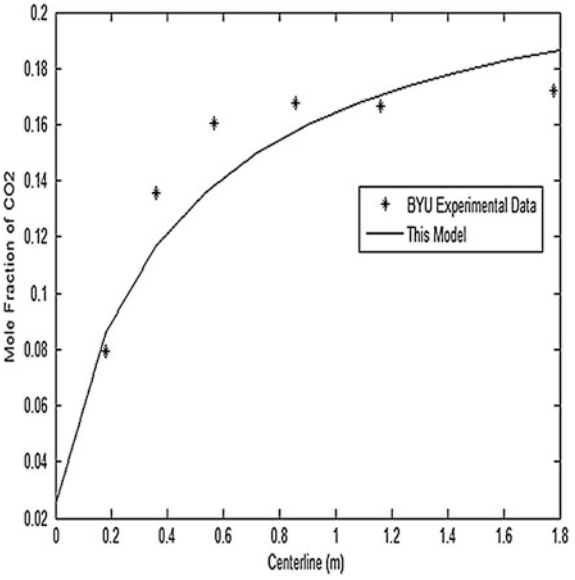

Fig. 49.5 Mole fraction of CO_2 along the centerline

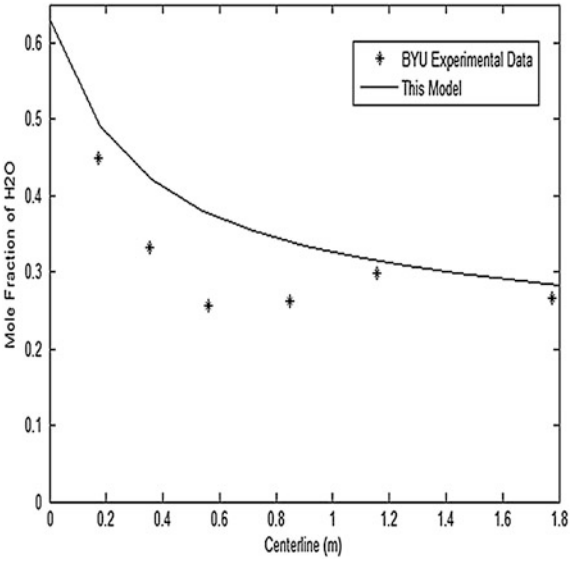

Fig. 49.6 Mole fraction of H_2O along the centerline

study, it was observed that the mole fraction of the carbon monoxide, carbon dioxide and hydrogen was lower for the construction waste wood. Furthermore, the vapor mole fraction was higher for the wood. This is because the wood has higher moisture content (proximate analysis), higher oxygen content (ultimate analysis) and lower carbon content (ultimate analysis). One interesting phenomenon was that

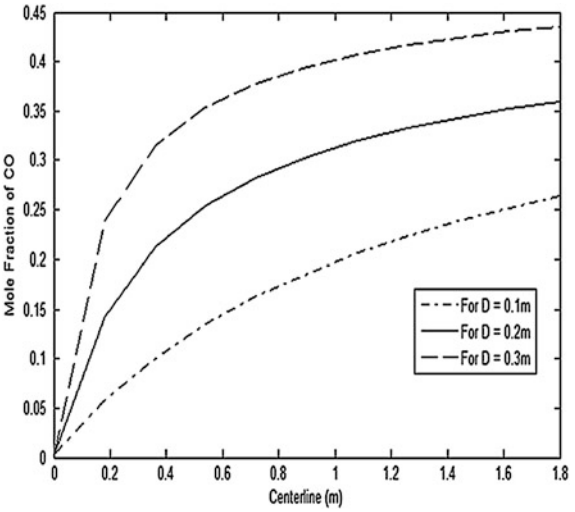

Fig. 49.7 Mole fraction of CO along the centerline

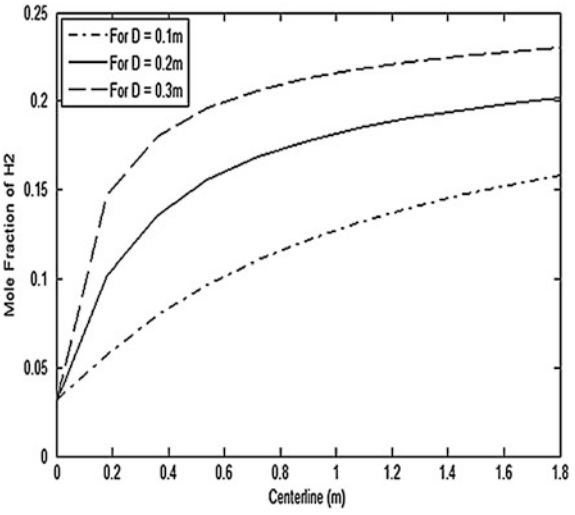

Fig. 49.8 Mole fraction of H_2 along the centerline

at the inlet of the plug flow reactor, the carbon dioxide was more for the wood waste, but it was soon approached and advanced by the coal. This is because of the low char content (proximate analysis) in the wood waste.

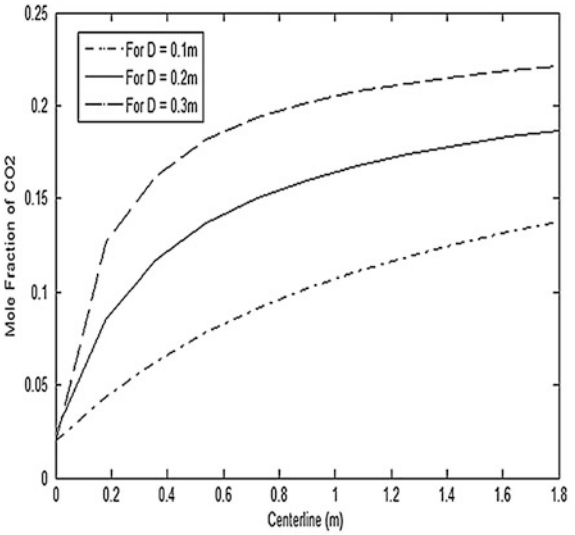

Fig. 49.9 Mole fraction of CO_2 along the centerline

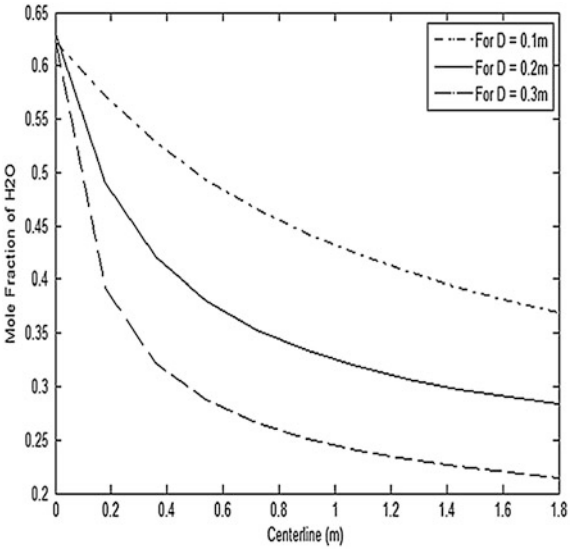

Fig. 49.10 Mole fraction of H_2O along the centerline

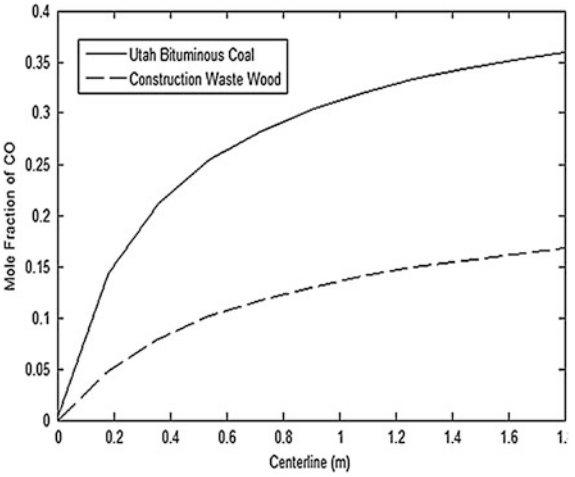

Fig. 49.11 Mole fraction of CO along the centerline

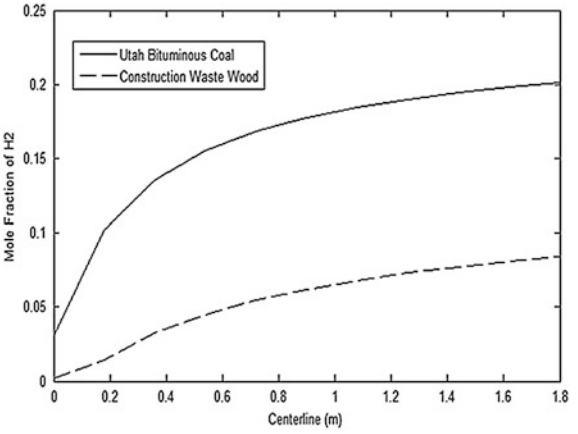

Fig. 49.12 Mole fraction of H_2 along the centerline

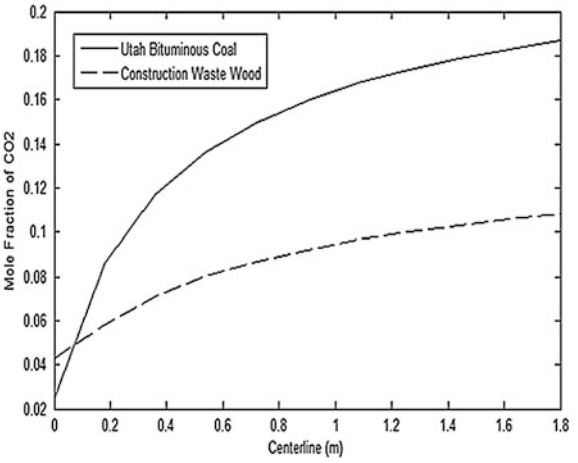

Fig. 49.13 Mole fraction of CO_2 along the centerline

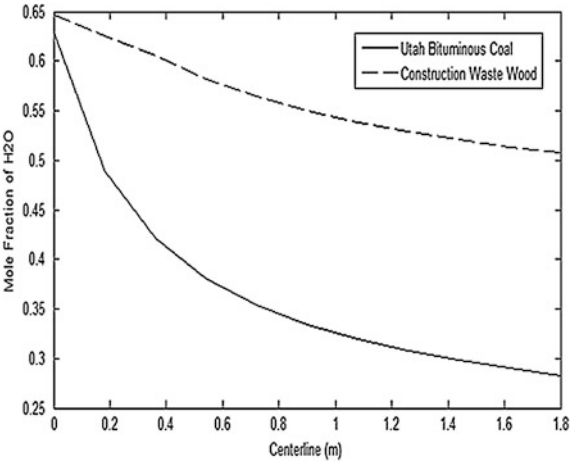

Fig. 49.14 Mole fraction of H_2O along the centerline

49.6 Conclusions

A comprehensive kinetics-based ASPEN Plus model has been developed for the oxygen-blown atmospheric BYU gasifier. The model predicts reasonably well the gas composition along the axis of the gasifier and can be used to optimize the gasifier. An increasing diameter of the gasifier gives more CO, CO_2 and H_2 but less H_2O along the centerline. Wood waste yielded a gasification efficiency of 38.25 % as compared to 57.18 % for coal. Based on this study, the gasification efficiency of wood waste can be further increased by drying the wood before gasification and lowering the mass flow rate of the oxidant.

Acknowledgments The authors highly appreciate the support and sponsorship of Masdar Institute and the members of the Waste-2-Energy group.

References

1. C.Y. Wen, T.Z. Chaung, Entrainment coal gasification modeling. Ind. Eng. Chem. Process Des. Dev. **18**, 684–695 (1979)
2. B.W. Brown, L.D. Smoot, P.J. Smith, P.O. Hedman, Measurement and prediction of entrained-flow gasification processes. AIChE J. **34**, 435–446 (1988)
3. Statistics Center Abu Dhabi, Waste Statistics in the Emirate of Abu Dhabi 2009 (2011), http://www.scad.ae/SCADDocuments/Waste%20Statistics%20in%20the%20Emirate%20of%20Abu%20Dhabi%202009.pdf. Cited 12 Dec 2013
4. F. Bellomare, M. Rokni, Integration of a municipal solid waste gasification plant with solid oxide fuel cell and gas turbine. Renew. Energy **55**, 490–500 (2013)
5. X. Kong, W. Zhong, W. Du, F. Qian, Three stage equilibrium model for coal gasification in entrained flow gasifiers based on Aspen Plus. Chin. J. Chem. Eng. **21**, 79–84 (2013)

6. C.H. Frey, N. Akunuri, Development of optimal design capability for coal gasification systems: performance, emissions and cost of Texaco gasifier-based systems using ASPEN. In: Technical report, U.S. Department of Energy, National Energy Technology Laboratory (2001), http://www.cmu.edu/epp/iecm/rubin/PDF%20files/2001/2001rc%20Frey%20et%20al,%20Aspen%20IGCC%20Tech.pdf. Cited 14 Dec 2013
7. S.V. Nathe, R.D. Kirkpatrick, B.R. Young, The gasification of New Zealand coals: a comparative simulation study. Energy Fuels **22**(4), 2687–2692 (2008)
8. E. Biagini, A. Bardi, G. Pannocchia, L. Tognotti, Development of an entrained flow gasifier model for process optimization study. Ind. Eng. Chem. Res. **48**, 9028 (2009)
9. M. Perez-Fortes, A.D. Bojarski, E. Velo, J.M. Nougues, L. Puigjaner, Conceptual model and evaluation of generated power and emissions in an IGCC plant. Energy **34**, 1721–1732 (2009)
10. A.S. Valmundsson, I. Janajreh, Plasma gasification process modeling and energy recovery from solid waste. Paper presented at the 5th international conference on energy sustainability, Washington, USA, August 7–10 2011
11. L.E. Gartner, M. Grabner, D. Messig, W. Heschel, B. Meyer, Kinetic entrained flow gasifier modeling in Aspen Plus—a simulation study on fuel blends. Paper presented at DBFZ Workshop zur Flieβbildsimulation in der Energietechnik, Leipzig, 2012
12. J. Lee, S. Park, H. Seo, M. Kim, S. Kim, J. Chi, K. Kim, Effects of burner type on a bench-scale entrained flow gasifier and conceptual modeling of the system with Aspen Plus. Korean J. Chem. Eng. **29**, 574–582 (2012)
13. S. Hla, D.J. Harris, D.G. Roberts, Gasification conversion model—PEFR. In: Research Report 80, Pullenva (2007), http://trove.nla.gov.au/work/34165934?q&versionId=46623731. Cited 15 Dec 2013
14. D.J. Harris, D.G. Roberts, D.G. Henderson, Gasification behavior of Australian coals at high temperature and pressure. Paper presented at the 21st annual international Pittsburgh coal conference, Osaka, Japan, 2004
15. H.J. Park, S.H. Park, J.M. Sohn, J. Park, J.K. Jeon, S.S. Kim, Y.K. Park, Steam reforming of biomass gasification tar using benzene as a model compound over various Ni supported metal oxide catalysts. Bioresour. Technol. **101**, 101–103 (2010)
16. H.C. Hottel, G.C. Williams, N.M. Nerheim, G.R. Schneider, Kinetic studies in stirred reactors: combustion of carbon monoxide and propane. Paper presented at the 10th international symposium on combustion, University of Cambridge, Cambridge, England, 17–21 August 1964

Chapter 50
Estimating Global Solar Radiation with Multiple Meteorological Predictors for Abu Dhabi and Al Ain, UAE

Jamal Hassan

Abstract In this study, several empirical equations are developed to estimate monthly mean daily global solar radiation, based on multiple predictors including relative sunshine hours, relative humidity and maximum air temperature in two locations (Abu Dhabi and Al Ain) in the United Arab Emirates. The statistical analysis showed that in general, multiple linear regression equations show the best agreement between the measured values of global solar radiations and the estimated values. The validation of the models and their accuracy were tested by calculating different statistical parameters. The models can be utilized for similar geographical regions within the country.

Keywords Estimation of global solar radiation · Abu Dhabi · Al Ain, UAE

50.1 Introduction

The global demand for energy is increasing exponentially compared to several decades ago and it is expected to continue in this trend in the future. This increase is not only due to the increasing population of our planet but also due to the increasing GDP and economic growth of some high-populated countries such as China, India and Brazil. This caused an increase in the world's consumption of fossil fuels and in turn raising the pollution level in an alarming rate worldwide. As a consequence, many countries are motivated to search for other resources other than conventional energy sources. Solar energy is considered as a renewable energy source. It is abundant, clean and many countries around the world already started using it. Germany, for instance, produced 32 GW of its energy production from photovoltatics and it is expected to increase in the near future.

J. Hassan (✉)
Department of Applied Mathematics and Sciences, Khalifa University, Abu Dhabi, United Arab Emirates
e-mail: jamal.hassan@kustar.ac.ae

M. O. Hamdan et al. (eds.), *ICREGA'14 - Renewable Energy: Generation and Applications*, Springer Proceedings in Energy, DOI: 10.1007/978-3-319-05708-8_50,

United Arab Emirates (UAE), an active member of the gulf countries in the Middle East, possesses a large reservoir of conventional energy resources, has the opportunity to utilize the solar energy effectively, promoting a clean environment and developing renewable energy technologies. This is extremely an important source for generating electricity in a country that has a very high growth rate in electricity consumption of around 10 % compared to 3 % worldwide [1]. Currently, oil is the main source for producing electricity in the UAE. The country is blessed with a high intensity sun radiation that can be used in many applications. The first step for any practical utilization of solar energy is analyzing the existing data to obtain precise models.

The accurate information of the solar radiation intensity at a given location is of essential of solar energy-based applications and in the long term evaluation of the solar energy conversion systems performances. Knowledge of the global solar radiation (GSR) is of fundamental importance for all solar energy conversion systems. Therefore, it is rather important to develop methods to estimate solar radiation using other meteorological parameters. In addition, the values of average daily global radiation in the solar energy application are the most important parameters, measurements of which are not available at every location due to cost, maintenance and calibration requirements of the measuring equipment. In places where no measured values are available, a common approach has been to determine these parameters by appropriate correlations which are empirically established using measured data. Several empirical formulae have been developed to calculate the solar radiation using various meteorological parameters [2–5]. These parameters include sunshine hours [6–9], relative humidity and maximum temperatures [10–12]. Previous studies, in the UAE, on the meteorological data were based mostly on a single weather parameter. For example, Abdalla [13] studied global solar radiation for the city of Abu Dhabi in terms of relative sunshine duration. One year data of measured global and direct solar radiation is analyzed by Islam [14, 15] and the result compared with the estimated values from NASA's model. Hassan et al. [16, 17] investigated global solar radiation for the city of Al Ain using time series analysis.

It is necessary to have models to estimate global solar radiation based on the existing several weather parameters in this region. For that reason, this work presents several empirical models obtained for the estimation of the GSR from the available meteorological parameters at two locations (Abu Dhabi 24.43^{o} N, 54.45^{o} E and Al Ain 24.20^{o} N, 55.78^{o} E) in the UAE.

50.2 Theoretical Background

Kimball [18] first suggested that the sunshine fraction is related to the daily global radiation and Angstrom [6] proposed the relationship on the basis of the monthly mean daily of global solar radiation and sunshine fractions. Later Prescott [19]

modified the relationship by adding the average daily extraterrestrial solar radiation. The equation is given below and it is widely used:

$$\bar{H}/\bar{H}_o = a + b(\bar{S}/\bar{S}_o) \tag{50.1}$$

where

$\bar{H}$	is the monthly mean daily GSR on a horizontal surface
$\bar{H}_o$	is the monthly mean daily extraterrestrial solar radiation on a horizontal surface
$\bar{S}$	is the monthly mean daily number of hours of possible sunshine
$\bar{S}_o$	is the monthly mean daily maximum day length of the location
a and b	are regression coefficients

The daily values of extraterrestrial solar radiation (H_o) on a horizontal surface can be calculated from the following equation [20]:

$$H_o = (24/\pi)I_{sc}[1 + 0.033\cos(360N/365)]\cos\phi\cos\delta\sin\omega_s + \omega_s\sin\phi\sin\delta \tag{50.2}$$

where I_{sc} is the solar constant which is equal to 1367 w/m^2, N is the day number of the year (values from 1 to 365). February is assumed to be 28 days and ϕ is the latitude of the location. δ is the declination angle which is given as

$$\delta = 23.45\sin[(360(284 + \mathrm{N}))/365] \tag{50.3}$$

and ω_s is the hour angle that can be written as:

$$\omega_s = \cos^{-1}(-\tan\phi\tan\delta) \tag{50.4}$$

Finally the day length (S_o) is given as:

$$S_o = \frac{2}{15}\omega_s = \frac{2}{15}\cos^{-1}(-\tan\phi\tan\delta) \tag{50.5}$$

In addition to Eq. (50.1), $\bar{H}$ can be written in terms of maximum temperature [20] and relative humidity [10] for the location under investigation as follows:

$$\bar{H}/\bar{H}_o = a + b\bar{T}_m \tag{50.6}$$

where $\bar{T}_m$ is the monthly mean daily value of maximum temperature and

$$\bar{H}/\bar{H}_o = a + b(\bar{R}/100) \tag{50.7}$$

where $(\bar{R}/100)$ is the monthly mean daily value of relative humidity of the site.

In this study, in addition to several empirical equations similar in format to Eqs. (50.1, 50.6, and 50.7), multiple regression models based on multiple predictors including the available meteorological parameters at the two sites have been developed.

50.3 Data Represented in this Study

Data for two cities (Abu Dhabi and Al Ain) in the UAE is used in this study. The measured meteorological parameters obtained from the National Centre of Meteorology and Seismology-Abu Dhabi cover a period of 3 years (2009–2011). Daily data of GSR, sunshine duration, relative humidly and maximum temperature are used for Abu Dhabi while daily parameters of GSR, relative humidly and maximum temperature is utilized for Al Ain. In this study, the following empirical equations are obtained:

$\bar{H}/\bar{H}_o = f(\bar{S}/\bar{S}_o)$, $\bar{H}/\bar{H}_o = f(\bar{R}/100)$, $\bar{H}/\bar{H}_o = f(\bar{T}_m)$, $\bar{H}/\bar{H}_o = f[\bar{S}/\bar{S}_o, \bar{R}/100, \bar{T}_m]$ for Abu Dhabi and $\bar{H}/\bar{H}_o = f(\bar{R}/100)$, $\bar{H}/\bar{H}_o = f(\bar{T}_m)$ and $\bar{H}/\bar{H}_o = f[\bar{R}/100, \bar{T}_m]$ for Al Ain. All calculations and data fitting are performed using OriginPro 7 software. The validation of the models and their accuracies were tested by calculating different statistical parameters. These are, mean percentage error (*MPE*), mean bias error (*MBE*), root mean square error (*RMSE*) and the Nash-Sutcliffie equation (*NSE*). These are described according to the following equations:

$$MPE = \frac{1}{n}\sum_{1}^{n}[(\bar{H}_p - \bar{H})/\bar{H}] \times 100 \tag{50.8}$$

$$MBE = \frac{1}{n}\sum_{1}^{n}(\bar{H}_p - \bar{H}) \tag{50.9}$$

$$RMSE = \sqrt{\left[\frac{1}{n}\sum_{1}^{n}(\bar{H}_p - \bar{H})^2\right]} \tag{50.10}$$

$$NSE = 1 - \left[\sum_{1}^{n}(\bar{H} - \bar{H}_p)^2 / \sum_{1}^{n}(\bar{H} - \bar{H}_{ave})^2\right] \tag{50.11}$$

where the parameters in Eqs. (50.8–50.11) are defined as below:

n is the number of observations ($n = 12$), $\bar{H}_p$ is the monthly mean daily estimated values of GSR using the obtained models and $\bar{H}_{ave}$ is the average value of $\bar{H}$.

The *MBE* is an indicator whether the model overestimates or underestimates the measured values. The *MBE* value of zero is an equal distribution between positive and negative error and it is an ideal case. Acceptable values of *MPE* are between

-10 and $+10\%$. The *RMSE* reveals the level of scatter that a model produces and provides a comparison of the absolute deviation between the estimated and observed values. The ideal value of *RMSE* is zero. An efficiency of $NSE = 1$ corresponds to a perfect match between the estimated values and the observed data [22]. An efficiency of zero ($NSE = 0$) indicates that the model estimations are as accurate as the average of the observed data ($\bar{H}_{ave}$), whereas an efficiency less than zero ($NSE < 0$) occurs when the observed average is a better predictor than the model or, in other words, when the residual variance described by the numerator of Eq. (50.11), is larger than the data variance (described by the denominator). Essentially, the closer the model efficiency is to 1, the more accurate the model is.

50.4 Results and Discussion

The daily values (averaged over 3 years) of the available observed data are presented in Figs. 50.1 and 50.2 Abu Dhabi and Al Ain respectively.

The daily GSR variations, for both locations, show the typical variation similar to the extraterrestrial solar radiation for the northern hemisphere locations; high values during May to September months and low values during October to April months. GSR values alternates between 5 and 11 kWh/m^2 in Abu Dhabi and from around 3.5 to7 kWh/m^2 in Al Ain. These values are in an agreement to the presented measured data previously [15]. GSR data for the city of Al Ain shows some fluctuation during the months of May to August (between day 150 and 250 of the year). In fact it shows decreasing of GSR compared to the expected values shown for extraterrestrial radiation at the same period. This is due to the geographical location of the city of Al Ain. Its location is close to series of mountains that causes change in the weather conditions (especially winds and formation of clouds) during the months where the air temperature tends to increase to their maximum values during the year. This seasonal change causes decreasing in global solar radiation and increasing diffuse solar radiation and it has been observed in a study that goes back around 20 years ago for the same location [23]. The average daily values of maximum temperatures for both sites are between 20 and 40 °C throughout the year. The percentage relative humidity values for the city of Abu Dhabi are between 0.6 and 0.7 while fluctuate between 0.3 and around 0.7 for Al Ain. The average daily sunshine duration in Abu Dhabi is quite high throughout the year and ranges between 7.6 h during the winter months and up to 11 h during the month of June. Unfortunately, data of sunshine duration was not available for Al Ain. The monthly mean daily of the presented data (for both locations) are calculated and used to obtain the optimum regression models using OriginPro 7 software (summarized in Eqs. 50.12–50.18). Our results show that the expansion of the obtained models into quadratic and third degree correlations did not improve the accuracy of the estimation of global solar radiation. Other studies [24, 25] also confirmed the same conclusions. Therefore, we only present linear

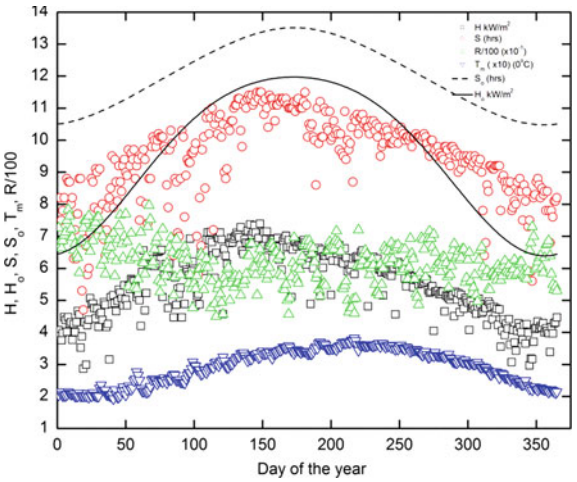

Fig. 50.1 Daily measured values of global solar radiation H, Sunshine duration S, maximum temperature Tm, Relative humidity R/100, day-length so and extraterrestrial solar radiation H_o for the city of Abu Dhabi, UAE

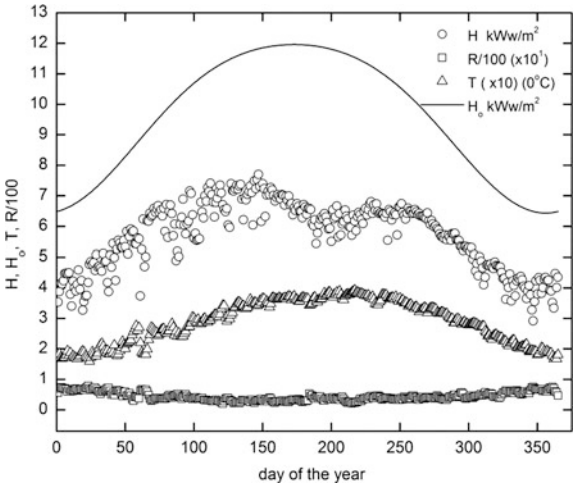

Fig. 50.2 Daily measured values of global solar radiation H, maximum temperature T_m, Relative humidity R/100 and extraterrestrial solar radiation H_o for the city of Al Ain, UAE

correlation models similar to Eqs. (50.1, 50.6, and 50.7). In addition to these, multiple linear regression and correlation analysis of the equation $\bar{H}/\bar{H}_o = f[\bar{S}/\bar{S}_o,\ \bar{S}/100,\ \bar{T}_m]$ for Abu Dhabi and $\bar{H}/\bar{H}_o = f[\bar{R}/100,\ \bar{T}_m]$ for Al Ain were carried out using the same mentioned software. The obtained empirical equations are summarized below; Eqs. (50.12–50.15) are for Abu Dhabi and Eqs. (50.16–50.18) are for Al Ain.

$$\bar{H}/\bar{H}_o = 0.87496 - 0.37569\ (\bar{S}/\bar{S}_o) \tag{50.12}$$

Table 50.1 Statistical analysis calculated from the obtained models for Abu Dhabi location

	Equation 50.12	Equation 50.13	Equation 50.14	Equation 50.15
MPE	0.232355	0.215981	0.070416	0.021589
RMSE	0.282431	0.26451	0.128239	0.055098
MBE	0.039405	0.035968	0.008201	0.00307
NSE	0.90465	0.916366	0.980342	1

Table 50.2 Statistical analysis calculated from the obtained models for Al Ain location

	Equation 50.16	Equation 50.17	Equation 50.18
MPE	4.24952	4.172711	4.140427
RMSE	0.340471	0.284252	0.287308
MBE	0.245604	0.235578	0.240111
NSE	0.861434	0.903416	0.983416

$$\bar{H}/\bar{H}_o = 0.32722 + 0.41058\ (\bar{R}/100) \tag{50.13}$$

$$\bar{H}/\bar{H}_o = 0.73097 - 0.00518\ \bar{T}_m \tag{50.14}$$

$$\bar{H}/\bar{H}_o = 0.45856 + 0.44314\ \bar{S}/\bar{S}_o - 0.01647\ \bar{R}/100 - 0.00742\ \bar{T}_m \tag{50.15}$$

$$\bar{H}/\bar{H}_o = 0.54639 + 0.12704\ (\bar{R}/100) \tag{50.16}$$

$$\bar{H}/\bar{H}_o = 0.69165 - 0.0031\ \bar{T}_m \tag{50.17}$$

$$\bar{H}/\bar{H}_o = 0.88122 - 0.21057\ (\bar{R}/100) - 0.00646\ \bar{T}_m \tag{50.18}$$

To study the validity of the obtained empirical equations, the estimated values of GSR $\left(\bar{H}_p\right)$ are obtained using the above relationships Eqs. (50.12–50.18). This is done by replacing $\bar{H}$ with $\bar{H}_p$) then compare the obtained $\bar{H}_p$ values with the corresponding values of the measured data. The comparison is based on the statistical parameters shown in Eqs. (50.8–50.11). The results are presented in Table 50.1 for Abu Dhabi and in Table 50.2 for Al Ain.

According to the statistical test results (Table 50.1, last column), it can be seen that the estimated values of monthly mean daily GSR are in favorable agreement with the measured values of monthly daily GSR for the multiple regression model Eq. (50.15). This is due to the fact this model has the lowest values of *MPE, RMSE, MBE and NSE* compared to the other empirical models. This conclusion can be seen in Fig. 50.3 as well. The unity-line in the figure shows the result for the ideal model, therefore the closer the estimated values to this line, the better the model is. It is clear that the multiple regression model Eq. (50.15) give better results compared with the other models.

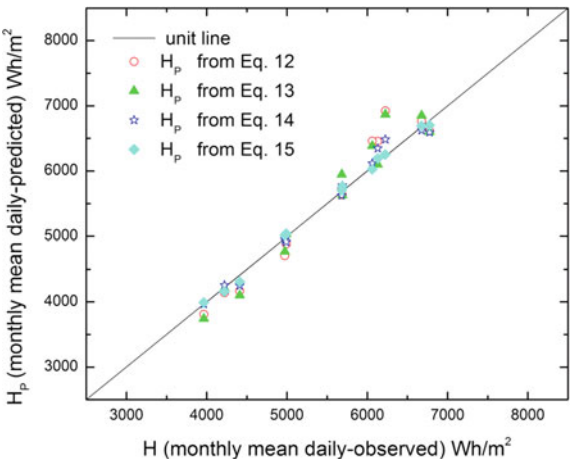

Fig. 50.3 Estimated values of monthly mean daily GSR using the obtained empirical models (Eqs. 50.12–50.15 in the text) versus monthly mean daily measured GSR for the city of Al Dhabi

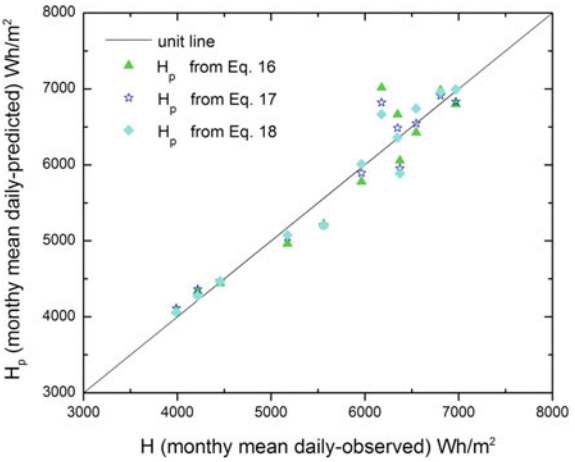

Fig. 50.4 Estimated values of monthly mean daily GSR using the obtained empirical models (Eqs. 50.16–50.18 in the text) versus monthly mean daily measured GSR for the city of Al Ain

On the other hand, a close look at the statistical results for Al Ain location (Table 50.2, the last two columns) show that the two models Eqs. (50.17, 50.18) give relatively similar outcomes. Both equations give similar values of MPE, RMSE, MBE, and NSE.

Figure 50.4 shows the comparison between the estimated values of GSR from the obtained models and the observed data in Al Ain. None of the models has a *very good* estimation especially around high values of GSR (around 6.5 kWh/m^2). This might be related to the actual fluctuation appeared in the measured GSR for Al Ain (see Fig. 50.2) during the high values of GSR as discussed before. This needs further investigation using other modeling methods, for instance, using time series analysis. In general, one can use Eqs. 50.17 or 50.18 for estimation of GSR for Al Ain with relatively *good* precision.

50.5 Conclusions

Several empirical correlations for estimating global radiation incidence on a horizontal surface were obtained to the existing data for two cites in the UAE (Abu Dhabi and Al Ain). The results show the obtained multiple regression correlation obtained for Abu Dhabi $\bar{H}/\bar{H}_o = 0.45856 + 0.44314\ \bar{S}/\bar{S}_o - 0.01647\ (\bar{R}/100) - 0.00742\ \bar{T}_m$ to give a very good agreement with the measured data. On the other hand, two of the models for Al Ain $\bar{H}/\bar{H}_o = 0.69165 - 0.0031\ \bar{T}_m$ and $\bar{H}/\bar{H}_o = 0.88122 - 0.21057\ (\bar{R}/100) - 0.00646\ \bar{T}_m$ give relatively similar results. In general the model obtained for the city of Abu Dhabi exhibits better agreement with the measured data compared to those obtained for Al Ain. We believe this was due to the actual fluctuation of the daily data of global solar radiation of Al Ain during summer months. The obtained empirical models can be used to estimate monthly average daily values of global solar radiation for other locations with similar climatic conditions where the data is missing or unavailable.

Finally, the results show that both cities are blessed with a high intensity of global radiations (between 5 and 11 kWh/m^2 for Abu Dhabi and 3.5 and 7 kWh/m^2 for Al Ain). The average daily sunshine duration for Abu Dhabi is quite high throughout the year and ranges between 7.6 h during the winter months to up to 11 h during the summer. Therefore, it is expected that these locations have a great potential for solar energy generations and applications.

Acknowledgments The author would like to thank the National Centre of Meteorology and Seismology-Abu Dhabi and Ms. M. Elsalamouny for the help in providing the data of this study.

References

1. M.A. Al-Iriani, Climate-related electricity demand-side management in oil exporting countries: the case of the United Arab Emirates. Energy Policy **33**, 2350–2360 (2005)
2. P. Moon, Proposed standard radiation curves for engineering use. J. Franklin Inst. **230**, 583–617 (1940)
3. S. Fritz, T.H. Mcdonald, Average solar radiation in the United States. Heat Ventil **46**, 61–64 (1949)
4. S. Fritz, Solar energy on clear and cloudy days. Sci. Month **84**, 55–56 (1957)
5. A.J. Drummond, E. Vowinckel, The distribution of solar radiation throughout Southern Africa. J Metro **14**(4), 242–353 (1957)
6. A. Angstrom, Solar and terrestrial radiation. Report to the international commission for solar research on actinometric investigations of solar and atmospheric radiation, Q. J. R. Meteorol. Soc. 50, 121–126 (1924)
7. J.N. Black, C.W. Bonython, T.A. Prescott, Solar radiation and duration of sunshine. Q. J. R. Meteorol. Soc. **80**, 231–235 (1958)
8. G.E. Smith, Solar radiation data base development based on bright sunshine data, in International and US Programs Solar Conference Winnipeg, Winnipeg, 1976
9. R.K. Swartman, O. Ogunlada, Solar relation estimates from common parameters. Sol. Energy **11**, 170–172 (1967)

10. Y. Abdalla, New correlation of global solar radiation with meteorological parameters for Bahrain. Int. J. Solar Energy **16**, 111–120 (1994)
11. A.A. Trabea, M.A. Mosalam Shaltout, Correlation of global solar radiation with meteorological parameters over Egypt. Renew. Energ **21**, 297–308 (2000)
12. E.E. Ituen, N.U. Esen, S.C. Nwokolo, E.G. Udo, Prediction of global solar radiation using relative using relative humidity, maximum temperature and sunshine hours in Uyo, in the Niger Delta region, Nigeria. Adv. Appl. Sci. Res. **3**, 1923–1937 (2012)
13. Y.A.G. Abdalla, G.M. Feregh, Contribution to the study of solar radiation in Abu Dhabi. Energy Convers. Manage. **28**, 63–67 (1988)
14. M.D. Islam, A.A. Alili, I. Kubo, M. Ohadi, Measurement of solar-energy (direct beam radiation) in Abu Dhabi, UAE. Renew. Energy **35**, 515–519 (2010)
15. M.D. Islam, I. Kubo, M. Ohadi, A.A. Alili, Measurement of solar radiation in Abu Dhabi, UAE. Appl. Energy **86**, 511–515 (2009)
16. H.A.N. Hejase, A.H. Assi, M.A. Shamisi, Prediction of global solar radiation in Dubai (UAE). Invited paper submitted for publication to the International Journal on Energy and Power Engineering (JEPE), Aug. 2012
17. H.A.N. Hejase, A.H. Assi, Time-series regression model for prediction of mean daily global solar radiation in Al Ain, UAE, ISRN Renew. Energy, 2012, Article ID 412471, 11 pp, 2012. doi:10.5402/2012/412471
18. H.H. Kimball, Variations in the total and luminous solar radiation with geographical position in the position in the United States. Mon. Wea. Rev **47**, 769–793 (1919)
19. J.A. Prescott, Evaporation from a water surface in relation to solar radiation. Trans. R. Soc. Sci. Austr. **64**, 114–118 (1940)
20. M. Iqbal, *An introduction to solar radiation*, 1st edn. (Academic Press, New York, 1983)
21. C. Augustine, M.N. Nnabuchi, Analysis of some meteorological data for some selected cities in the Eastern and Southern zone of Nigeria. Afr. J. Environ. Sci. Technol. **4**, 92–99 (2010)
22. J. Nash, J.V. Sutcliffe, River flow forecasting through conceptual models part I—a discussion of principles. J. Hydrol. **10**, 282–290 (1970)
23. A. Khalil, A. Alnajjar, Experimental and theoretical investigation of global and diffuse solar radiation in the united Arab Emirates. Renew. Energy **6**, 537–543 (1995)
24. J. Almorox, C. Hontoria, Global solar radiation estimation using sunshine duration in Spain. Sol. Energy **45**, 1529–1535 (2004)
25. A.A. El-Sebaii, A.A. Trabe, Estimation of global solar radiation on horizontal surfaces over Egypt. J. Solids **28**, 163–175 (2005)

Chapter 51
Voltage and Photo Driven Energy Storage in Graphene Based Phase Change Composite Material

Yarjan Abdul Samad, Yuanqing Li, Khalifa Al-Tamimi, Rawdha Al Marar, Saeed M. Alhassan and Kin Liao

Abstract In this study, a phase change composite material was developed with a graphene sponge (GS) skeleton and Paraffin-wax matrix. The GS was synthesized by hydrothermal treatment and subsequent freeze drying and the Paraffin-wax/GS (PGS) composite was developed by vacuum infusion process of molten Paraffin-wax inside the GS skeleton. The morphological studies of the PGS composite were performed with a Scanning Electron Microscope and Atomic Force Microscope. The PGS composite was characterized for its storage of electrical energy from an applied voltage, in the form of thermal energy, and the storage of thermal energy from xenon light of controlled power. Successful storage of electrical energy in the form of thermal energy is demonstrated by the PGS composite on the application of different voltages. A temperature of 60, 120 and 150 °C is reached on the application of voltages 5, 10 and 15 V respectively before a thermal balance is achieved. Exposing the PGS composite to the xenon light of controlled power shows improved energy absorption than that of the pristine Paraffin-wax and shows a 10 °C improvement in the temperature before reaching the thermal balance. Thermal studies done via a Differential Scanning Calorimetric (DSC) shows that there is no chemical reaction occurring between the Paraffin-wax and the GS as similar DSC curves are obtained for both the samples.

Keywords PCM · Graphene aerogel · Energy storage

Y. A. Samad · Y. Li · K. Al-Tamimi · R. A. Marar · K. Liao (✉)
Khalifa University of Science, Research and Technology, Abu Dhabi, United Arab Emirates
e-mail: Kin.liao@kustar.ac.ae

S. M. Alhassan
The Petroleum Institute of Abu Dhabi, Abu Dhabi, United Arab Emirates

M. O. Hamdan et al. (eds.), *ICREGA'14 - Renewable Energy: Generation and Applications*, Springer Proceedings in Energy, DOI: 10.1007/978-3-319-05708-8_51,

51.1 Introduction

It's well known that there is a pressing energy crisis and a foreseeable demand for renewable and sustainable energy around the globe. Therefore, it is an urge to harvest energy from natural and sustainable resources such as the energy from the biomass, wind and the sun. The thermal energy from the sun can be stored in a phase change material (PCM) usually a composite. In addition, PCM provides a smart way of storing and reusing the dissipated energy from electronic devices and the heat generated as by-product in different processes [1, 2]. Most of the conventional PCMs, whether organic or inorganic, suffer from low thermal conductivity as a result it becomes a tedious and inefficient to store as well as extract energy from these PCMs. Therefore, many PCMs such as paraffin-wax are penetrated inside copper mesh in order to have high effective thermal conductivity [3]. Nonetheless, the metal meshes skeleton increase the weight of the PCM causes the PCM to seep easily and is also incompatible with most of the PCM materials.

Graphene is a two-dimensional (2D) modern-day marvel material with extraordinary properties useful for a wide range of applications and has attracted attention due to its fascinating properties such as high electrical and thermal conductivity, extraordinary elasticity and stiffness etc. [4, 5]. Addition of graphene can enhance mechanical properties and electrical and thermal conductivities of polymer composites due to its unique nanostructure [5]. There are a number of methods for fabricating graphene and chemically modified graphene from different carbon materials including carbide compounds and graphitic derivatives [5, 6]. Each of these methods has different advantages, disadvantages and applicability to different fields of sciences and engineering. Preparation of chemically modified graphene, usually referred to as reduced graphene oxide (rGO) from colloidal suspensions is flexible, scalable, and adaptable to a wide variety of applications [6]. Graphene based polymer composites with high electrical and thermal conductivity are highly desirable in practical applications such as electronic devices, electromagnetic shielding and thermal management [7–10].

Nonetheless, graphene based composites are not reaching to application stages mainly because of two factors: (1) the poor dispersion of graphene in polymeric matrices due to their high specific surface area and strong van der Waals and π–π interactions between graphene sheets, (2) random distribution of graphene sheets inside the polymer matrices and surrounded by the molecular chains of the polymer, the electrical and thermal conductivity of these composites strongly rely on electron and phonon percolation between the separated filler particles [9, 11, 12]. Therefore, good dispersion of graphene sheets and high filler content are customarily required to form a conductive interconnected network in the insulating polymer matrix to improve the conductivity of the composites. PCMs are not an exception to other graphene-polymer based composites and in order to exploit the high thermal conductivity of graphene for PCMs, a 3D mesh like structure of graphene is required. There are several reports of constructing 3D graphene structures, graphene sponge (GS), using different methods. Of all these methods,

the most facile, economical and scalable method is the realization of GS structures by hydrothermal treatment combined with freeze drying technology [13–15]. GS network not only makes graphene uniformly distributed in the matrix material, but also significantly reduces the contact resistance between graphene sheets.

There are a few studies reporting the use of graphene in PCM materials [16, 17]. Fazel et al. studied the effect of content of graphene on the thermal conductivity of stearyl alcohol nanocomposite and reported increase in the thermal conductivity of the composite with the increase in the graphene content [17]. However, the addition of graphene as particulate inside a polymer has limited effect on properties such as electrical and thermal conductivities of the composite. Yajuan et al. infused octadecanoic acid inside a 3D structure of graphene aerogel, constructed with chemically modified graphene, and studied the heating and cooling behavior of the composite on the application of heat. To the best of our knowledge there is no study on the heating and cooling behavior of a Paraffin-wax and graphene sponge based composite material on the application of voltage and light with controlled power.

In the present work, we have developed paraffin-wax infused GS (PGS) composites for storing electrical and photonic energies in the form of thermal energy. The 3D GS skeletons were obtained via the hydrothermal reaction combined with freeze drying. Due to high thermal conductivity of the GS, the PGS composite stores energy at high rates on the application of a voltage or a exposing it to light with controlled power. The PGS composite shows complete recyclable usage.

51.2 Materials and Methods

51.2.1 Materials

Graphite powder with particle size < 20 μm, concentrated sulfuric acid (H_2SO_4, 98 %), potassium persulfate ($K_2S_2O_8$), phosphorus pentoxide (P_2O_5), sodium nitrate ($NaNO_3$), hydrochloric acid (HCl), potassium permanganate ($KMnO_4$), ethanol, Paraffin-Wax and hydrogen peroxide (H_2O_2, 30 %), hydroiodic acid (HI, 30%) were obtained from Sigma-Aldrich. Xenon bulbs were purchased from the local market. All of the materials were directly used without further purification.

51.2.2 Preparation of Graphene Oxide (GO) Sheets

GO was synthesized from graphite powder with modified Hummer's method. First, $K_2S_2O_8$ (10 g) and P_2O_5 (10 g) were dissolved in concentrated H_2SO_4 (50 ml) at 80 °C. Graphite powder (12 g) was then added to the acidic solution, and the resulting mixture was stirred at 80 °C for 4.5 h. After cooling to room temperature, the solution was diluted with about 2 L deionized (DI) water and was allowed

to stand overnight. The supernatant was decanted, and the pre-treated graphite was obtained by centrifugation and washed three times with DI water. The product obtained was dried in air at 100 °C for 12 h. This pre-treated graphite powder (2 g) was put into concentrated H_2SO_4 (50 ml) with ice bath. $KMnO_4$ (7 g) and $NaNO_3$ (1 g) were added gradually with stirring, and the temperature of the solution was kept below 10 °C. The mixture was then stirred at 35 °C for 2 h and DI water (96 ml) was added. The solution was stirred for another 30 min, the reaction was then terminated by adding 300 ml of DI water and 5 ml of 30 % H_2O_2 solution. The mixture was centrifuged and subjected to several cycles of suspension in 5 % HCl solution and was separated by centrifugation. In order to completely remove metal ions and acids, the graphite oxide was subjected to cycles of washing with DI water and separated with centrifugation until the pH value of the supernatant reached 6. The GO product was suspended in distilled water to give a viscous, brown dispersion.

51.2.3 Preparation of Graphene Sponge (GS)

GO was synthesized from graphite powder by the modified Hummers method as described in supporting information [18, 19]. The graphite oxide suspension obtained was diluted to 2 mg/ml, and was then ultrasonicated in an ultrasonic bath for half hours. The GSs were fabricated by hydrothermal treatment of GO suspensions with the assistance of HI [13, 14]. Firstly, 1 ml of HI (30 %) was added into 60 ml homogeneous GO (2 mg/ml) aqueous dispersion, and then the mixture was sealed in a 100 ml Teflon-lined stainless steel autoclave and maintained at 180 °C for 12 h. The reactor was cooled down to room temperature (RT), and the as-prepared graphene hydrogels were taken out from reactor and dipped into distilled water for 24 h to remove the residual HI. To control the density of final GS, water from the original graphene hydrogels were partially removed in air through evaporation at RT. Finally, vacuum freeze-drying was used to remove all the water to obtain the GS.

51.2.4 Preparation of Paraffin-Wax/Graphene Sponge (PGS) Composites

Paraffin-wax was melted in an oven at 80 °C. The prepared GS was completely immersed into the molten Paraffin-wax. Then the mixture was placed in a vacuum chamber for approximately 10 min to infuse Paraffin-wax and remove air bubbles from the pores of the GS. Finally, the PGS composite was carefully removed from molten Paraffin-wax and left to dry in air.

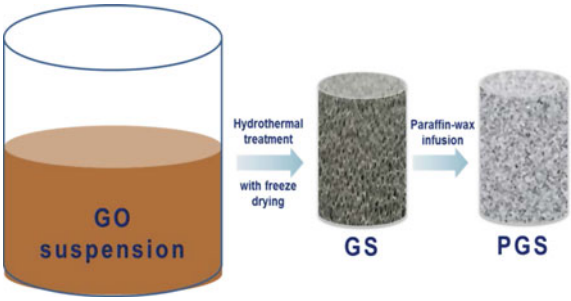

Fig. 51.1 Schematic showing the formation of GS and the PGS composite

51.2.5 Characterization

The porous structure of GS and the fractured surface of the PGS composite were examined by a FEI Quanta FEG 250 scanning electron microscopy (SEM) at a voltage of 20 kV in high vacuum. The topographical Atomic Force Microscopy (AFM) image of single layer graphene oxide (GO) flakes was captured using an MFP-3D AFM. The Gwisntek GPS 3303 DC power supply was used for applying different voltages to the PGS composite in order to store electrical energy as thermal energy in the composite. TA instruments SDT Q600 equipment was used to study the differential scanning calorimetric (DSC) and the thermal gravimetric analysis (TGA) behaviors of the PGS composite and pristine Paraffin-wax.

51.3 Results and Discussion

Graphene possesses high intrinsic thermal conductivity due to the sp2 covalent bonding between carbon atoms [20]. Therefore, the 3D structures of graphene are a good candidate for making PCMs possessing high thermal conductivity and enabling high rates of both storing in and extracting out energy from the PCM. The Paraffin wax and graphene based PCMs were developed by first preparing 3D GS structures via the hydrothermal treatment and freeze drying. These GS structures were used as skeletons to infuse Paraffin-wax to finally produce the PGS composites as shown schematically in Fig. 51.1.

The as prepared GS 3D structures have porous morphology and retain both micro and nanometric pores because of the random arrangement of graphene oxide sheets during the hydrothermal treatment and subsequent reduction to rGO. The SEM image of the fractured surface of GS 3D structures is shown in Fig. 51.2a where the inset shows a close-up image of the microstructure. Figure 51.2b is the fractured surface of the PGS composite showing completely filled structure of the GS with Paraffin-wax. The AFM topographical image in Fig. 51.2c shows single and double layer GO sheets spread on a silicon wafer. The roughness trace of the marked region on the AFM image is shown in Fig. 51.2d. This shows only

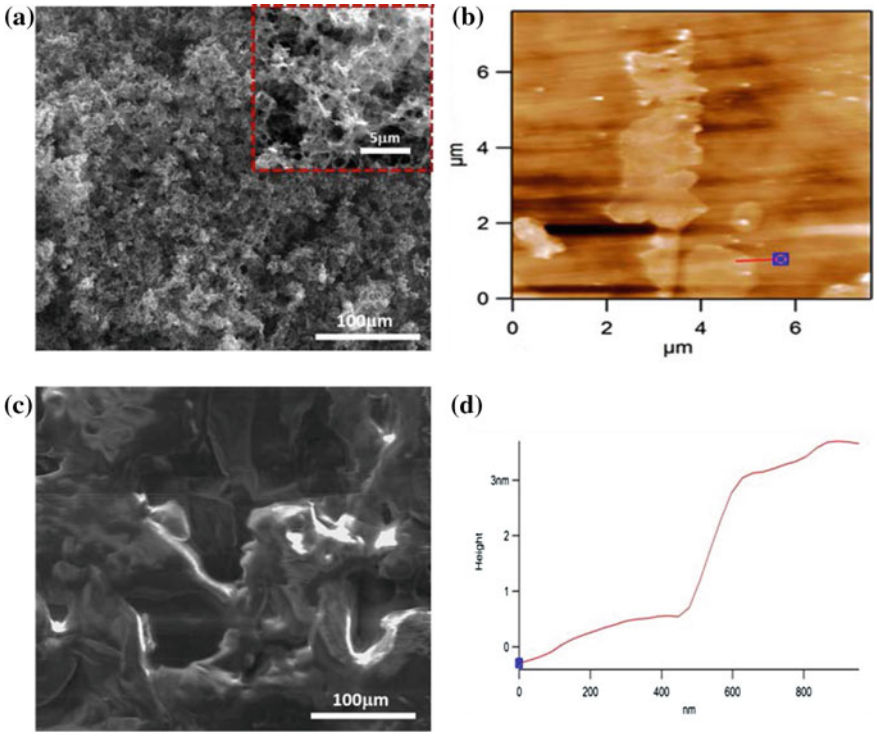

Fig. 51.2 SEM image of GS fractured surface with *inset* showing a close-up of the same image (**a**), SEM image of a fractured surface of PGS composite (**b**), AFM topographical image of GO flakes dispersed on a Si substrate (**c**) and Height of a selected line drawn on the AFM image (**d**)

2 nm height of the GO flakes from the silicon substrate, therefore, demonstrating high quality of the GO.

In order to study the rate and amount of electrical energy stored, in the form of heat, in the PGS composite on application of a voltage across the sample, a DC power supply was used. A temperature sensor attached to the specimen and to a computer was used to capture the live data. The experimental setup is demonstrated schematically as an inset in Fig. 51.3. Three different voltages of 5, 10 and 15 V were applied to the specimens to study the aforementioned effect. When applied only 5 V the specimen heats up with a rate of 2.5° C/min until it starts melting at 37° C where the heating rate decreases to a mere 0.25° C/min.

This is because in the beginning the entire electrical power is used to raise the temperature of the 3D connected structure of GS and the infused Paraffin-wax. Once the Paraffin-wax starts melting the electrical energy is divided into two parts; one part of the energy is being used by GS to raise its temperature and the other part is used to keep melting the Paraffin-wax, therefore, the increase in temperature is reduced substantially. In addition to this, a thermal balance between the sample and the atmosphere is attained and a major part of the heat supplied to the sample

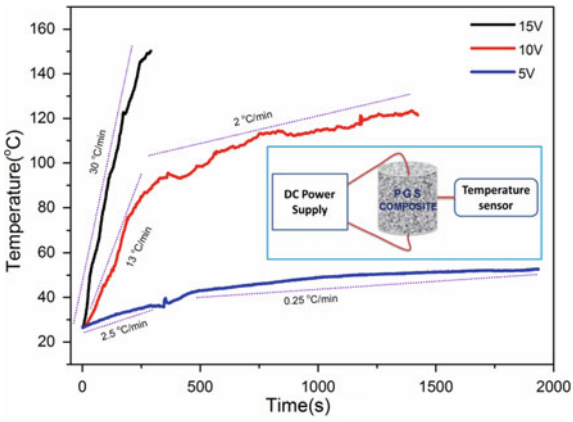

Fig. 51.3 Temperature versus time curve of PGS composite on the application of different voltage across the sample

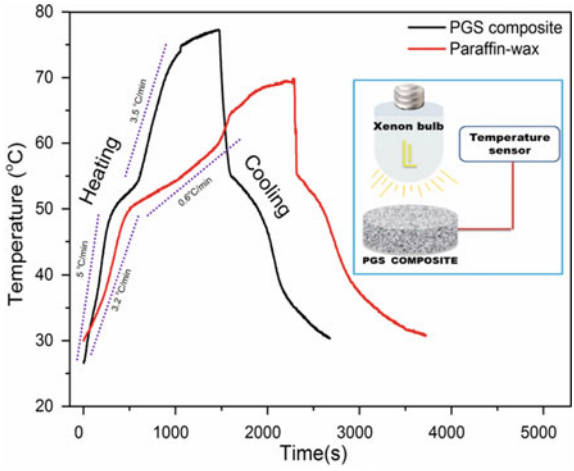

Fig. 51.4 Temperature versus time curve of PGS composite on the application of light

is lost to the atmosphere. When the voltage is increased to 10 V, a heating rate of 13° C/min is obtained and the rate of increase in temperature keeps constant until a temperature of 80° C is reached at which point the sample starts losing most of the energy to the atmosphere and in melting the Paraffin-wax. As the Paraffin-wax starts melting, the heating rate is reduced to 2° C/min. A heating rate of 30° C/min is achieved on the application of 15 V on the specimen; temperature rises to 150° C in only 5 min. Due to high heating rate the specimen attains a thermal balance at a temperature of 150° C.

A setup shown as in inset in Fig. 51.4 was employed to measure the rate at which the PGS and the Paraffin-wax heat up when exposed to light. A xenon bulb was used and it was controlled with a DC power supply to provide a constant power of 28 W. A vertical distance of 10 cm was kept between the specimen and the bulb. A temperature sensor attached to the specimen and to a computer was

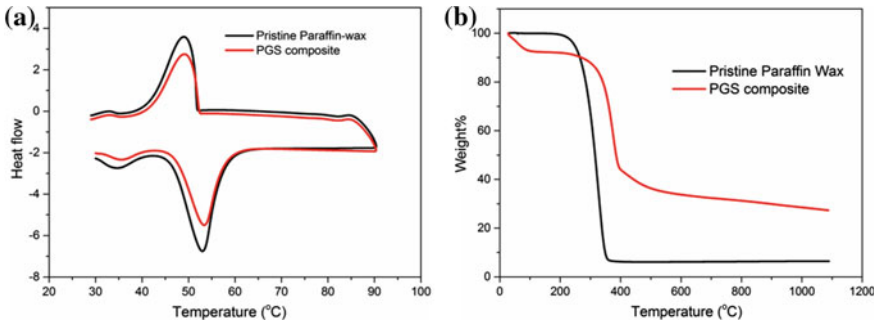

Fig. 51.5 DSC (**a**) and TGA (**b**) curves for pristine Paraffin-wax and the PGS composite

used to capture the live data every second. As it can be seen from Fig. 51.4 that the heating rate, for Paraffin-wax and the PGS composite, are 3.2 °C/min and 5 °C/min respectively until the Paraffin-wax starts melting. This 60 % improvement in the heating rate of the PGS composite can be attributed to its dark color able to absorb more light than the white colored Paraffin-wax and fast thermal conversion efficiency. Later on when the Paraffin-wax starts melting, the temperature rise in pure Paraffin-wax is slow as it consumes heat for melting and a thermal balance between the sample and the specimen is achieved at about 68 °C. However, for the PGS composite attains a higher heating rate both before and after the melting zones as shown in Fig. 51.4 and reaches a thermal balance at a temperature of about 80 °C proving that the PGS demonstrates a better light-thermal conversion efficiency throughout the process, therefore, reaches a higher thermal balance temperature.

TA instruments SDT Q600 equipment was used to study the differential scanning calorimetric (DSC) behavior of the PGS composite and pristine Paraffin-wax. A temperature ramp from 30 to 90 °C and subsequent cooling was done at a rate of 2 °C/min. The PGS composite as well as the Paraffin-wax demonstrate similar DSC behavior and both samples start partially melting at around 45 °C and reaching a melting point of about 53 °C as shown by the DSC curve in Fig. 51.5a. There is no other peak until a temperature of 90 °C is reached for both the samples showing the stability of the chemical structure of the PGS composite. In the cooling cycle both the samples start recrystallizing at about 52 °C and a recrystallization temperature of 50 °C. TGA curves for pristine paraffin wax and the PGS composite were obtained using a heating rate of 20 °C/min as shown in Fig. 51.5b. There is a negligible weight loss from a temperature of 30 to 200 °C. Nonetheless, a significant weight loss of about 94 % occurs on the rise of temperature from 200 to about 400 °C. The weight loss between 400 and 1,100 °C is almost zero indicating complete carbonization of pristine paraffin wax at 400 °C. The PGS composite indicates a weight loss of about 10 % from 30 to 100 °C which is the loss of moisture in the composite. Later a significant weight loss of 60 % occurs between temperatures of 230 and 400 °C indicating carbonization of the wax present in the

composite. Later the weight loss in the PGS composite is insignificantly small. Until a temperature of about 1,100 °C, the weight loss is limited 70 % as opposed to the pristine paraffin wax which showed a weight loss of about 94 % at 1,100 °C.

51.4 Conclusions

A GS and Paraffin-wax based composite phase change material was successfully developed for electrical and photo energy storage in the form of thermal energy. An AFM topographical image of the GO flakes show that the quality of GO used was high with a single or double layered flakes. GS prepared via a chemical vapor deposition or any high temperature route has better properties than the one produced via a chemical route, therefore, it is envisioned that the development of such composites with the former processes would result in better quality phase change composite materials. The developed composite shows successful storage of electrical energy on the application of a voltage and improved storage of photo energy on the exposition of controlled light both in the form of thermal energy. DSC curve of the PGS composite and pristine Paraffin-wax shows that no chemical modification has occurred to the composite As a result these materials may become useful pragmatically for storing thermal energy when applied a voltage or exposed to a light source.

Acknowledgments The authors would like to acknowledge the financial support provided by the Khalifa University of Science Research and Technology.

References

1. M. Wuttig, N. Yamada, Phase-change materials for rewriteable data storage. Nat. Mater. **6**(11), 824–832 (2007)
2. A.M. Khudhair, M.M. Farid, A review on energy conservation in building applications with thermal storage by latent heat using phase change materials. Energy Convers. Manag. **45**(2), 263–275 (2004)
3. C.Y. Zhao, W. Lu, Y. Tian, Heat transfer enhancement for thermal energy storage using metal foams embedded within phase change materials (PCMs). Sol. Energy **84**(8), 1402–1412 (2010)
4. A.A. Balandin, S. Ghosh, W. Bao, I. Calizo, D. Teweldebrhan, F. Miao, C.N. Lau, Superior thermal conductivity of single-layer graphene. Nano Lett. **8**(3), 902–907 (2008)
5. C. Soldano, A. Mahmood, E. Dujardin, Production, properties and potential of graphene. Carbon **48**(8), 2127–2150 (2010)
6. S. Stankovich, D.A. Dikin, R.D. Piner, K.A. Kohlhaas, A. Kleinhammes, Y. Jia, Y. Wu, S.T. Nguyen, R.S. Ruoff, Synthesis of graphene-based nanosheets via chemical reduction of exfoliated graphite oxide. Carbon **45**(7), 1558–1565 (2007)
7. X. Huang, X.Y. Qi, F. Boey, H. Zhang, Graphene-based composites. Chem. Soc. Rev. **41**(2), 666–686 (2012)

8. A.A. Balandin, Thermal properties of graphene and nanostructured carbon materials. Nat. Mater. **10**(8), 569–581 (2011)
9. Z.P. Chen, C. Xu, C.Q. Ma, W.C. Ren, H.M. Cheng, Lightweight and flexible graphene foam composites for high-performance electromagnetic interference shielding. Adv. Mater. **25**(9), 1296–1300 (2013)
10. W.J. Hong, Y.X. Xu, G.W. Lu, C. Li, G.Q. Shi, Transparent graphene/PEDOT-PSS composite films as counter electrodes of dye-sensitized solar cells. Electrochem. Commun. **10**(10), 1555–1558 (2008)
11. D. Vuluga, J.M. Thomassin, I. Molenberg, I. Huynen, B. Gilbert, C. Jerome, M. Alexandre, C. Detrembleur, Straightforward synthesis of conductive graphene/polymer nanocomposites from graphite oxide. Chem. Commun. **47**(9), 2544–2546 (2011)
12. C. Wu, X.Y. Huang, G.L. Wang, L.B. Lv, G. Chen, G.Y. Li, P.K. Jiang, Highly conductive nanocomposites with three-dimensional, compactly interconnected graphene networks via a self-assembly process. Adv. Funct. Mater. **23**(4), 506–513 (2013)
13. H.C. Bi, X. Xie, K.B. Yin, Y.L. Zhou, S. Wan, L.B. He, F. Xu, F. Banhart, L.T. Sun, R.S. Ruoff, Spongy graphene as a highly efficient and recyclable sorbent for oils and organic solvents. Adv. Funct. Mater. **22**(21), 4421–4425 (2012)
14. J.P. Zhao, W.C. Ren, H.M. Cheng, Graphene sponge for efficient and repeatable adsorption and desorption of water contaminations. J. Mater. Chem. **22**(38), 20197–20202 (2012)
15. W.F. Chen, L.F. Yan, In situ self-assembly of mild chemical reduction graphene for three-dimensional architectures. Nanoscale **3**(8), 3132–3137 (2011)
16. Y. Zhong, M. Zhou, F. Huang, T. Lin, D. Wan, Effect of graphene aerogel on thermal behavior of phase change materials for thermal management. Sol. Energy Mater. Sol. Cells **113**, 195–200 (2013)
17. F. Yavari, H.R. Fard, K. Pashayi, M.A. Rafiee, A. Zamiri, Z. Yu, R. Ozisik, T. Borca-Tasciuc, N. Koratkar, Enhanced thermal conductivity in a nanostructured phase change composite due to low concentration graphene additives. J. Phys. Chem. C **115**(17), 8753–8758 (2011)
18. N.I. Kovtyukhova, P.J.O.B.J. Martin, T.E. Mallouk, S.A. Chizhik, E.V. Buzaneva, A.D. Gorchinskiy, 'Layer-by-layer assembly of ultrathin composite films from micron-size graphite oxide sheets and polycations. Chem. Mater. **11**, 771–778 (1999)
19. H.-T.J. Jianxin Geng, Porphyrin functionalized graphene sheets in aqueous suspensions: from the preparation of graphene sheets to highly conductive graphene films. J. Phys. Chem. C **114**(18), 8227–8234 (2010)
20. S. Chen, Q. Wu, C. Mishra, J. Kang, H. Zhang, K. Cho, W. Cai, A.A. Balandin, R.S. Ruoff, Thermal conductivity of isotopically modified graphene. Nat. Mater. **11**(3), 203–207 (2012)

Chapter 52
Enhancing the Performance of Mg–Al Brine Water Batteries Using Conductive Polymer-PEDOT: PSS

T. Abdulrehman, Z. A. Yousif, S. Al-Ameri, I. Abdulkareem, A. M. Abdulla and Y. Haik

Abstract In this paper, the effect of the conductive additive, poly (3, 4-ethylenedioxythiophene)-poly (styrene sulfonate) (PEDOT:PSS) on brine water batteries was investigated. Brine water batteries were produced using magnesium powder mixed with aluminum powder, activated carbon and carbon nanotube, which functioned as the anode with aluminum foil as the current collector. The aluminum current collector also took part in the anodic reaction after the magnesium was used up in the brine water battery reaction. AgCl mixed with activated carbon and carbon nanotubes functioned as the cathode. Platinum mesh was used as current collector for the cathode. The binder used was a mixture of poly vinyl alcohol and poly acrylic acid. To this binder, the conductive binder PEDOT:PSS was added. The brine water battery consisted of five cells in series connection and each cell had an anode and cathode either with or without PEDOT:PSS. The brine water batteries were operated in a 3.5 % NaCl which mimics sea water.

Keywords Brine water battery · PEDOT:PSS · Magnesium · Aluminium · Agcl · Activated carbon · Carbon nanotubes · Power density output

52.1 Introduction

Nowadays the world is seeking new sources of energy. Several studies have been reported on the great potential of the seawater battery as a renewable energy source [1]. Seawater batteries are attractive because they can produce energy for prolonged time periods [2].

T. Abdulrehman · Z. A. Yousif · S. Al-Ameri · I. Abdulkareem · A. M. Abdulla · Y. Haik (✉)
Mechanical Engineering Department, UAE University, P. O. Box-15551
Al Ain, United Arab Emirates
e-mail: yhaik@uaeu.ac.ae

M. O. Hamdan et al. (eds.), *ICREGA'14 - Renewable Energy: Generation and Applications*, Springer Proceedings in Energy, DOI: 10.1007/978-3-319-05708-8_52,

The requirement of lightweight materials is essential for development of sea water batteries. Magnesium is a light metal and has extensive applications in automobile industry and other equipments [3]. Magnesium is a major component in seawater, which makes a magnesium based seawater battery environmentally harmless. Magnesium/CuCl and magnesium/AgCl systems are mostly used in seawater batteries in which magnesium is used as the anode [4]. Aluminum [5, 6] and magnesium [4, 6] anodes are used in seawater batteries because of their high capacity, low atomic weight and high standard potentials. Different types of magnesium-seawater batteries have been developed which include $PbCl_2$, CuI, cuprous thiocyanate and MnO_2 as cathodes [6]. Seawater batteries have applications in powering undersea devices and vehicles because of the presence of ocean water as a source of electrolyte [7].

Poly (3, 4-ethylenedioxythiophene) (PEDOT) which is conductive has been employed as cathode in developing a biologically compatible magnesium battery in suitable electrolytes [8]. Poly (3, 4-ethylenedioxythiophene)-poly (styrene sulfonate) was used in Li/S batteries to improve their performance as the polymer is electronically conductive and thermally stable in an electrochemical environment [9]. Alloys of magnesium have been used in seawater batteries as such alloys can improve the performance of the batteries [10–12]. Activated carbon and carbon nanotube (CNT) composites have been used in high performance electrochemical electrodes because of the high surface area of activated carbon and the high conductivity and mechanical strength of CNTs [13].

In this paper we study the performance of magnesium-aluminum (Mg–Al) anodes and silver chloride (AgCl) cathodes. The Mg–Al anode electrode was made of a composite of powdered Mg and Al, activated carbon (AC) and CNT with poly vinyl alcohol-poly acrylic acid (PVA-PAA) as a binder. Aluminum foil was used as a current collector in the anode. The AgCl cathode consisted of powdered AgCl, AC, CNT, PVA-PAA as a binder and platinum mesh as a current collector. In this paper the performance of brine water batteries in the presence and absence of poly (3, 4-ethylenedioxythiophene)-poly (styrene sulfonate) (PEDOT:PSS) in the electrodes is studied.

52.2 Experimental Work

52.2.1 Materials

Magnesium powder (Merck, USA), aluminum powder (Aldrich, USA), silver chloride (AgCl) (Aldrich, USA), carbon nanotube (CNT) (Nanolab, Inc., USA), activated carbon (AC) (Scott Science and Healthcare Ltd., UK), PEDOT:PSS (Aldrich, USA), platinum mesh (Goodfellow, UK), aluminum foil (Diamond, UAE), poly vinyl alcohol (PVA) (Aldrich, USA) (MW $\sim$ 61,000) and poly-acrylic acid (PAA) (Aldrich, USA) (MW $\sim$ 1800), Quantitative filter paper-1246 (pore: 1–3 μm, Filter-Lab, Spain).

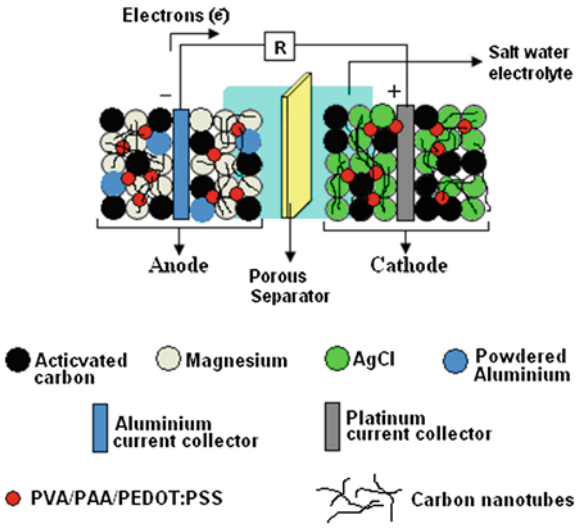

Fig. 52.1 Schematic diagram for a synthesized brine water cell

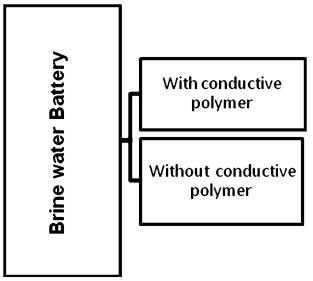

Fig. 52.2 Brine water battery organizational chart

52.2.2 Brine Water Battery Fabrication

Schematically the brine water cell Fig. 52.1 shows the harvesting of electrons, where the electrons from the anode are carried to the cathode via the current collectors which consist of aluminum foil in the anode and platinum mesh in the cathode, and electrical wires. The anode and cathode are connected through a resistance using electrical wires.

Two types of Mg–Al/AgCl batteries were considered in this study. One in which PEDOT:PSS was not added to both anode and cathode and the other in which PEDOT:PSS was added to the electrodes, the scheme of which is shown in Fig. 52.2.

Generally, each casing has two sides, one to be filled with a cathode and the other with an anode separated by a filter paper. Since powdered magnesium and aluminum was used for the anode and powdered AgCl for the cathode, a polymer mix of PVA and PAA solution was used as the binder. Activated carbon and CNT were added to the electrodes to increase the surface area and conductivity.

52.2.2.1 Electrodes Preparation with Conductive Polymer

For each cell the cathode slurry was prepared using 250 mg AgCl, 50 mg CNT, 200 mg activated carbon (AC), PVA-PAA (7 wt/v% solution in water with PVA to PAA in the ratio of 8:1) and PEDOT:PSS in water. After forming a thick cathode slurry, it was poured into the electrode casing with a filter paper (pore size: 1–3 μm) to separate the cathode from the anode. A layer of the cathode slurry was poured into the casing before inserting a platinum mesh connected to an electrical wire. A second layer of cathode slurry was poured on top of the platinum mesh and allowed to dry. The anode is prepared by adding 250 mg, 100 mg Al, 50 mg CNT, 200 mg AC, PVA-PAA (7 wt/v% solution in water with PVA to PAA in the ratio of 8:1) and PEDOT:PSS in water to form a slurry. The anode slurry was poured into the battery casing on the opposite side of the cathode compartment. A layer of the anode slurry was poured before inserting an aluminum foil current collector. On top of the aluminum foil another layer of anode slurry was poured and allowed to dry. Then the whole casing was placed in an oven at 90 °C for 2 h. The dimensions of the electrodes are 2 cm × 2 cm.

52.2.2.2 Electrodes Preparation Without Conductive Polymer

The electrodes were prepared as in electrode preparation with a conductive polymer with the exception that PEDOT:PSS is not added to the electrodes.

52.2.2.3 Brine Water Preparation

The salt water or brine solution electrolyte was prepared by dissolving 17.5 g of NaCl in 500 ml deionized water to get 3.5 % water salinity.

52.2.2.4 Brine Water Battery Assembly Setup

The setup of the brine water battery was designed to contain five cells. The individual cells in the battery consisted of an anode and a cathode. A container was designed consisting of holders and a coverlid. The container has five holders to accommodate five cells and helps in keeping the cells immersed in the salt-water electrolyte. The cover lid has holes for aeration and for accommodation of an Ag/AgCl reference electrode which helps to determine the electrode potentials of the anodes and the cathodes. The brine water in the container was continuously stirred with the help of a magnetic stirrer. A photograph of the brine water battery set up is shown is Fig. 52.3. The photograph and schematic of the brine water battery cell and the circuit diagram of the brine water battery is shown in Fig. 52.4.

Fig. 52.3 Photograph of the brine water battery setup

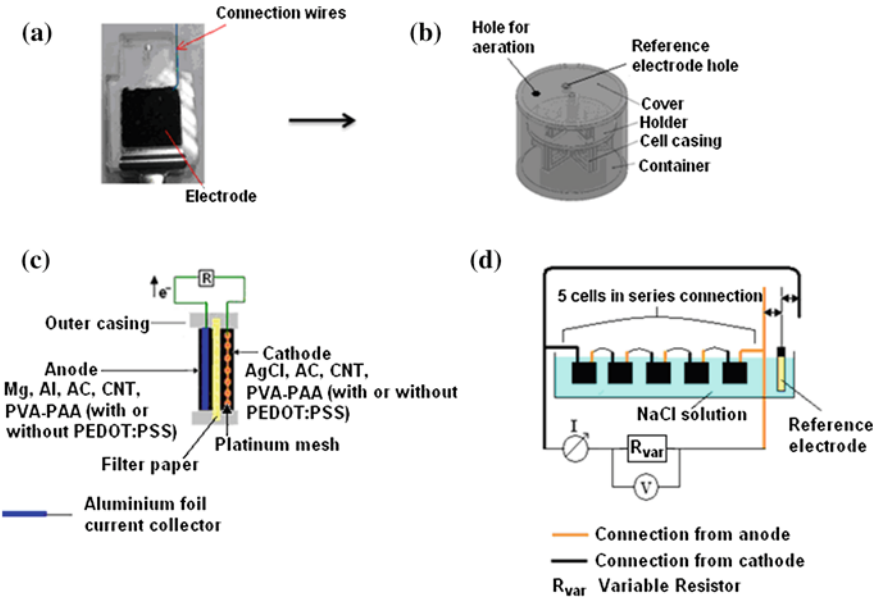

Fig. 52.4 **a** Photograph of electrode casing, **b** Brine water battery container to connect five cells in series, **c** schematic representation of a brine water battery cell and **d** Circuit diagram of the brine water battery with five cells in series connection

52.2.3 Physical Characterization

A scanning electron microscope, SEM (Joel, JBM-5600) was used to determine the surface morphology of the anode and cathode material. An energy dispersive spectroscopy (EDS) (Oxford Instruments, UK) analysis of both anode and cathode was carried out to determine the composition of the electrodes.

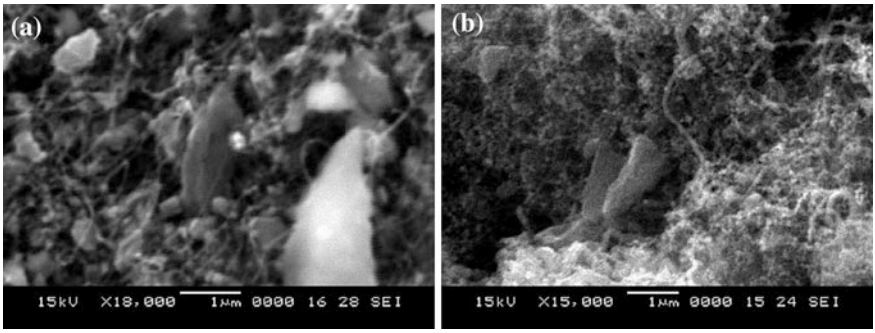

Fig. 52.5 **a** SEM of anode (Mg–Al/AC-CNT) and **b** SEM of Cathode (AgCl/AC-CNT)

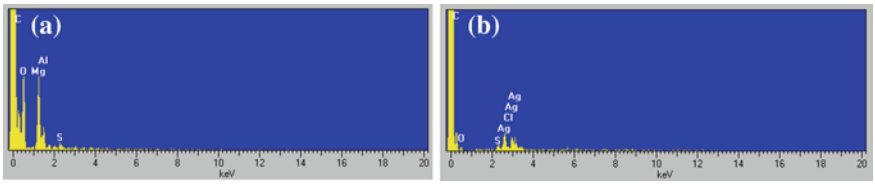

Fig. 52.6 **a** EDS of the anode and **b** EDS of the cathode

52.2.4 Electrochemical Characterization

Electrochemical characterization of the brine water battery was carried out in 500 mL, 3.5 % NaCl solution placed in a polycarbonate container. The battery reaction was carried out at room temperature. A polycarbonate lid with openings for aeration and reference electrode was fitted on top of the container. The electrode potentials against the Ag/AgCl reference electrode, total battery potential and current densities were recorded using a data acquisition system (NI9125, National Instruments) and Agilent 34405A multimeter (Agilent, Taiwan) at 1-minute intervals. A self-made variable resistor was included in the circuit for current density-potential measurements.

52.3 Results and Discussion

Figure 52.5a and b are the SEM images of the anode and the cathode composite materials respectively. The images show the network of CNTs and the activated carbon along with the metals or metal salt in the electrodes. Figure 52.6a and b are the EDS images of the anode and cathode respectively. EDS is a semi quantitative analysis to determine the composition of the elements in the electrodes.

The EDS image of the anode shows the peaks corresponding to magnesium and aluminum. Sulfur peaks arise due to the presence of PEDOT:PSS as a conductive additive in the electrodes. Al to Mg ratio is 1:2.5 as determined from the EDS analysis. The EDS image of the cathode shows peaks corresponding to that of silver and chlorine. The sulfur peaks in the cathode image arise due to the presence of PEDOT:PSS.

Three main sets of reactions can take place at the anode and cathode, the details of which are given below.

Set of Reactions—1, involving magnesium.

$$\text{Anode: } Mg - 2e^- \rightarrow Mg^{2+} \tag{52.1}$$

$$\text{Cathode} : 2AgCl + 2e^- \rightarrow 2Ag + 2Cl^- \tag{52.2}$$

$$\text{Overall} : Mg + 2AgCl \rightarrow MgCl_2 + 2Ag \tag{52.3}$$

Set of Reactions—2, involving magnesium.

$$\text{Anode} : Mg - 2e^- \rightarrow Mg^{2+} \tag{52.4}$$

$$\text{Cathode} : O_2 + 2H_2O + 4e^- \rightarrow 4OH^- \tag{52.5}$$

$$\text{Overall} : 2Mg + O_2 + 2H_2O \rightarrow 2Mg(OH)_2 \tag{52.6}$$

Set of Reactions—3, involving aluminum.

$$\text{Anode} : Al + 3OH^- \rightarrow Al(OH)_3 + 3e^- \tag{52.7}$$

$$\text{Cathode} : O_2 + 2H_2O + 4e^- \rightarrow 4OH^- \tag{52.8}$$

$$\text{Overall} : 4Al + 3O_2 + 6H_2O \rightarrow 4Al(OH)_3 \tag{52.9}$$

Magnesium is more active than aluminum in the galvanic series; the chances are that the rate of anodic reaction (Eqs. 52.1 and 52.4) involving magnesium will be more than that of the anodic reaction (Eq. 52.7) involving aluminium. The rate of the set of reactions (52.1) and (52.2) will be higher than that of the set of reactions (52.3). Magnesium may act as protective agent for aluminum. After the magnesium is consumed in the electrochemical reaction, the rate of the anodic reaction (Eq. 52.7) involving aluminium will increase. The presence of activated carbon and CNTs will facilitate the reduction of O_2 to OH^- at the cathodes.

$$2H_2O + 2e^- \rightarrow H_2 + 2OH^- \tag{52.10}$$

$$Mg + 2H_2O \rightarrow H_2 + Mg(OH)_2 \tag{52.11}$$

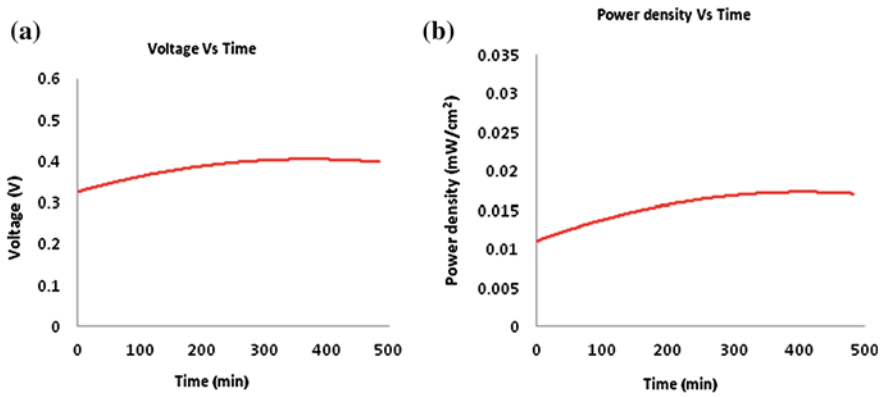

Fig. 52.7 **a** Voltage output and **b** Power density output of brine water battery without PEDOT:PSS at a resistance of 2450 Ω

An increase in the hydrogen formation reaction (Eq. 52.10) accelerates the corrosion of magnesium. The hydrogen formation occurs in the areas of the cathode where water undergoes electrochemical reduction. The coupling of the hydrogen formation at the cathode with the anodic reaction of magnesium (Eq. 52.1) results in the overall reaction (Eq. 52.11) resulting in the formation of magnesium hydroxide and hydrogen which increases the corrosion of magnesium. Alloys of magnesium with aluminium, manganese or zinc prevent the evolution of hydrogen. Alloys of magnesium with lithium have better corrosion resistance properties than magnesium [3].

The open circuit voltage of the brine water battery without the conductive additive was found to be 0.65 V. The voltage and power output of the brine water battery without PEDOT:PSS at a resistance of 2450 Ω is shown in Fig. 52.7. The voltage output of the battery without PEDOT:PSS was in the range of 0.32–0.40 V and its power output was in the range of 0.012–0.0152 mW/cm^2 at a resistance of 2450 Ω. At a resistance of 100 Ω, the battery without the conductive additive showed a voltage output between 0.0675 and 0.1 V and a power density between 0.011 and 0.0225 mW/cm^2. The voltage and power density of the brine water battery without conductive additive at 100 Ω is shown in Fig. 52.8.

The performance of the brine water with the conductive additive PEDOT:PSS was found to be enhanced. The voltage and power density output of the brine water battery with PEDOT:PSS is given in Fig. 52.9. There was a significant increase in both the voltage and power density output of the brine water battery with PEDOT:PSS at resistances of 100 and 2450 Ω when compared to that of the battery without PEDOT:PSS. The open circuit voltage of the brine water battery with PEDOT:PSS was found to be 0.771 V. The power output of the battery with PEDOT:PSS was more or less stable at 0.046 mW/cm^2 for a time period of 8 h at a resistance of 2450 Ω. This power output performance is better when compared to the maximum power output of the battery without PEDOT:PSS which had a power

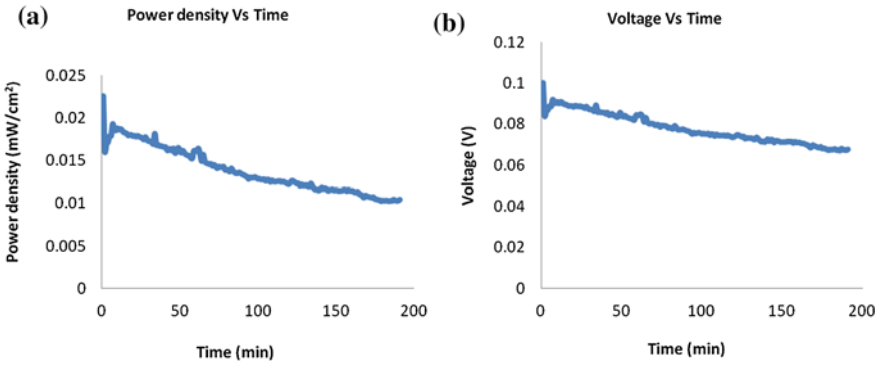

Fig. 52.8 **a** Power density and **b** Voltage output of brine water battery without PEDOT:PSS operating at 100 Ω resistance

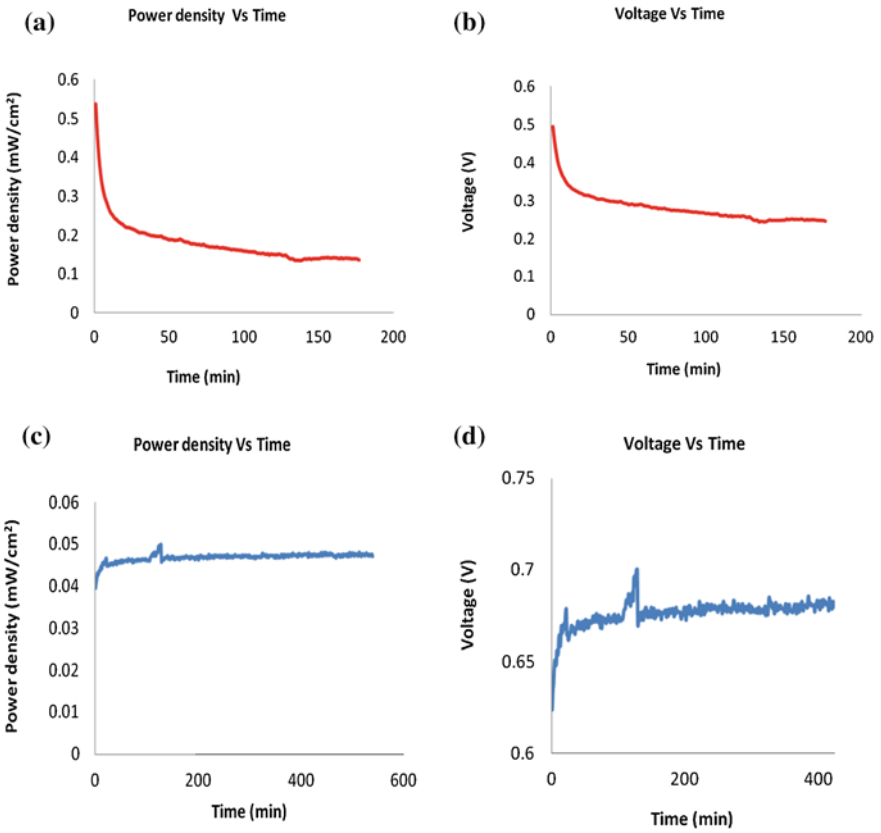

Fig. 52.9 Performance of brine water battery with PEDOT:PSS as conductive additive: **a** Power density output at 100 Ω, **b** Voltage output at 100 Ω, **c** Power density output at 2450 Ω and **d** Voltage output at 2450 Ω

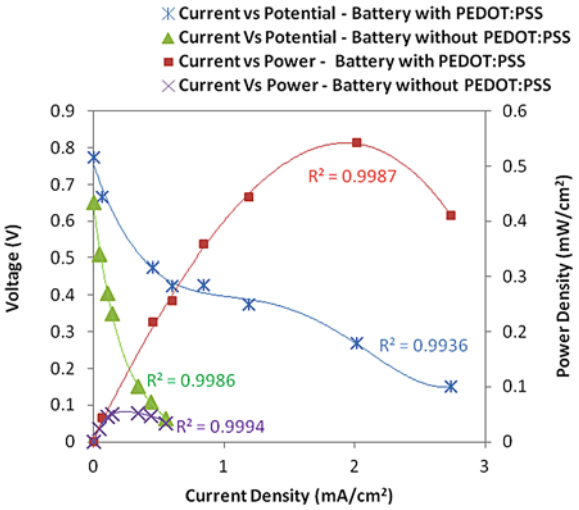

Fig. 52.10 Current density—Potential plot of brine water batteries with and without PEDOT:PSS after 10 min of operation. Data points represent stable battery voltage and power density output (Standard Deviation < 0.002) from five measurements in 5 min at a given load current

output in the range of 0.012–0.0152 mW/cm^2. The voltage output of the battery with the conductive additive varied between 0.62 and 0.69 V at a resistance of 2450 Ω which is a better output when compared to a battery without PEDOT:PSS. The voltage output of the battery with PEDOT:PSS was in the range of 0.25–0.50 V and its power output was in the range of 0.135–0.54 mW/cm^2 at a resistance of 100 Ω. Current leakage is a phenomenon in an electrochemical cell occurring due to the flow of current from each point in the battery to every other point through the conductive electrolyte [4]. The presence of PEDOT:PSS in the electrodes may help prevent the leakage of current which explains the enhanced performance of the batteries synthesized with PEDOT:PSS. Ma et al. studied the discharge performance of Mg, AZ31 and Mg–Li–Al–Ce anodes in Mg-air batteries and found that the Mg–Li–Al–Ce anode had a better discharge performance than the Mg and AZ31 anodes. At 2.5 mA/cm^2, the battery with the Mg–Li–Al–Ce anode had an operating voltage of 1.272 V [14]. Presence of Zn in the Mg–Li alloys also enhanced the discharge performance and corrosion resistance properties of the Mg–Li anodes [15]. By using such alloys in a powdered form or as nanoparticles in our anodes, it could be possible to further enhance the discharge characteristics of our brine water batteries in the future studies.

The current density-potential plot of the brine water battery with and without PEDOT:PSS after 10 min of operation is shown in Fig. 52.10. The battery with PEDOT:PSS shows a maximum power output of 0.543 mW/cm^2 whereas the battery without PEDOT:PSS exhibits a maximum power output of 0.051 mW/cm^2. Operation of the brine water battery at optimized load current will ensure better performance of the battery and this can be achieved for the battery with PEDOT:PSS, by its operation between 1 and 2 mA/cm^2.

52.4 Conclusion

From our study, we could conclude that addition of conductive additives to brine water battery electrodes could enhance performance. The use of the conductive additive PEDOT:PSS increased the voltage and power density of our brine water batteries. By increasing the surface area of the electrodes, redesigning the battery to accommodate more cells, using effective conductive additives and decreasing leakage current, the performance of brine water and sea water batteries can be enhanced.

Acknowledgments We acknowledge the support of EMAL Company for their financial support.

References

1. F.L. Mantia, M. Pasta, H.D. Deshazer, B.E. Logan, Y. Cui, Batteries for efficient energy extraction from a water salinity difference. Nano Lett. **11**(4), 1810–1813 (2011)
2. T. Zhang, Z. Tao, J. Chen, Magnesium-air batteries: from principle to application. Mater. Horiz. (2014). doi: 10.1039/C3MH00059A
3. S. Ono, K. Asami, T. Osaka, N. Masuko, Structure of anodic films on magnesium. J. Electrochem. Soc. **143**(3), L62–L63 (1996)
4. R.F. Koontz, R.D. Lucero, Magnesium water-activated batteries, in *Handbook of Batteries*, ed. by D. Linden, T.B. Reddy (McGraw-Hill, New York, 2002), pp. 17.1–17.27
5. J.A. Hunter, W.B. O'Callaghan, G.M. Scamans, Aluminium Batteries. US Patent 4942100, 17 July 1990
6. M.G. Medeiros, E.G. Dow, Magnesium-solution phase catholyte seawater electrochemical system. J. Power Sources **80**(1–2), 78–82 (1999)
7. Ø. Hasvold, H. Henriksen, E. Melvær, G. Citi, B.Ø. Johansen, T. Kjønigsen, R. Galetti, Sea water battery for subsea control systems. J. Power Sources **65**(1–2), 253–261 (1997)
8. B. Winther-Jensen, M. Gaadingwe, D.R. Macfarlane, M. Forsyth, Control of magnesium interfacial reactions in aqueous electrolytes towards a biocompatible battery. Electrochim. Acta **53**(20), 5881–5884 (2008)
9. Y. Yang, G. Yu, J.J. Cha, H. Wu, M. Vosgueritchian, Y. Yao, Z. Bao, Y. Cui, Improving the performance of lithium sulfur batteries by conductive polymer coating. ACS Nano **5**(11), 9187–9193 (2011)
10. Z. Hongyang, B. Pei, J. Dongying, Electrochemical performance of magnesium alloy and its application on the sea water battery. J. Environ. Sci. **21**(suppl. 1), S88–S91 (2009)
11. L. Wang, P. Li, L. He, Effect of adding different contents of mercury to magnesium on discharge and corrosion performances of magnesium anode sheet. Russ. J. Electrochem. **47**(8), 900–907 (2011)
12. Y. Kun, H. Qiao, Z. Jun, D. Yu-long, Electrochemical properties of magnesium alloy anodes discharged in seawater. Trans. Nonferrous Met. Soc. China **22**(9), 2184–2190 (2012)
13. A. Borenstien, M. Noked, S. Okashy, D. Aurbach, Composite carbon nano-tubes (CNT)/activated carbon electrodes for non-aqueous super capacitors using organic electrolyte solutions. J. Electrochem. Soc. **160**(8), A1282–A1285 (2013)
14. Y. Ma, N. Li, D. Li, M. Zhang, X. Huang, Performance of Mg–14Li–1Al–0.1Ce as anode for Mg-air battery. J. Power Sources **196**(4), 2346–2350 (2011)
15. Y. Lv, M. Liu, Y. Xu, D. Cao, J. Feng, The electrochemical behaviors of Mg-8Li-3Al-0.5Zn andMg-8Li-3Al-1.0Zn in sodium chloride solution. J. Power Sources **225**, 124–128 (2013)

Chapter 53
Design Considerations of Digitally Controlled PV Battery Chargers

Alaa Hail, Boshra Alshujaa, Waad Albeiey, Ala Hussein and Abbas Fardoun

Abstract At outdoor conditions, the temperature and the solar power are uncontrollable. As a result, traditional charging techniques that rely on the terminal measurements such as the battery current, voltage and temperature cannot be used. That is, relying on the terminal measurements can result in terminating the charge before the battery is truly fully charged, which has several drawbacks such as reducing the useable capacity and possibly leading to memory effect in nickel-based batteries, or overcharging the battery which can lead the battery to prematurely reaching its end-of- service. This paper presents some design considerations for digitally-controlled solar battery chargers. Testing and simulation results for commercial lithium-ion (Li-ion) and nickel-metal-hydride (NiMH) battery cells are presented.

Keywords Battery · Charger · Digital control · Photovoltaic (PV) · State of charge (SOC)

53.1 Introduction

Rechargeable battery technologies accommodate a wide range of applications. Portable electronics is a major area where batteries are used as a primary power source. Among major rechargeable battery chemistries, nickel-metal-hydride (NiMH) and lithium-ion (Li-ion) batteries are the most used technologies in portable electronics due to their unique characteristics such as they have long cycle-life and high energy and power densities, and they don't require maintenance neither suffer from memory effect (memory effect is a term used to describe the degradation in the battery capacity when it is partly charged and discharged).

A. Hail · B. Alshujaa · W. Albeiey · A. Hussein (✉) · A. Fardoun
Department of Electrical Engineering at the United Arab Emirates University (UAEU), Al Ain, United Arab Emirates
e-mail: ala.hussein@uaeu.ac.ae

M. O. Hamdan et al. (eds.), *ICREGA'14 - Renewable Energy: Generation and Applications*, Springer Proceedings in Energy, DOI: 10.1007/978-3-319-05708-8_53,

Regardless the type of battery used in an application, the battery must be carefully charged and discharged through a battery management system (BMS).

According to [1], battery charging is the most critical function of a BMS. Basically, a battery charger must deliver the charge to the battery, optimize the charge rate, and terminate the charge based on a certain criteria. Battery chargers use different charging techniques that are claimed to optimize the charging efficiency and cycle-life of the battery. Traditional charging techniques that are used by ordinary chargers include constant current constant voltage (CCCV), pulse charging (PC), sinusoidal ripple charging (SRC), trickle charging, float charging and interrupted charge control (ICC) [2–16].

In contrast to battery chargers that are powered from an electricity source (i.e. outlet), solar battery chargers have uncontrolled input (charging) power. In fact, solar battery chargers are advantageous in the sense that they don't need to be plugged into an electricity outlet since they are powered directly from the sunlight. They can be ideally used during outdoor events to charge portable electronics provided there is enough sunlight. However, since the solar power and outdoor temperature are uncontrollable, traditional charging techniques fail to charge the battery reliably and safely. In addition, terminating the charge on time is a challenging task that can affect the battery performance. For example, overcharging the battery will certainly reduce its cycle-life, whereas terminating charging before the battery is fully-charged reduces its run-time [17]. Traditional charging techniques terminate charging based on the terminal measurements. In comparison with ordinary chargers, terminating the charge in solar battery charges is more challenging because the input power to the charger (i.e. solar power) and ambient temperature can change momentarily. Therefore, terminating the charge in solar battery chargers must not rely only on the terminal (direct) measurements as in ordinary chargers, but also on indirect measurements. Figure 53.1 shows a block diagram of solar battery charging system.

In this paper, some design considerations for digitally controlled solar battery chargers are presented. The batteries that are considered herein include NiMH and Li-ion batteries, which accommodate a wide range of applications. The organization of this paper is as follows: Sect. 53.2 reviews some design considerations of DC-DC conversion stage. Section 53.3 presents an overview of designing a closed-loop digitally controlled PID controller. Section 53.4 describes the design of an SOC algorithm and termination techniques. Section 53.5 includes some simulation results. Finally, conclusions and summaries are given in Sect. 53.6.

53.2 DC-DC Converter

The power that is generated by the solar cells is unregulated. To make it usable, it must be regulated using a DC-DC converter. Thus, a DC-DC converter is an electronic circuit that converts a dc power to another dc power by stepping up/down the voltage or current. A DC-DC converter has two main functions:

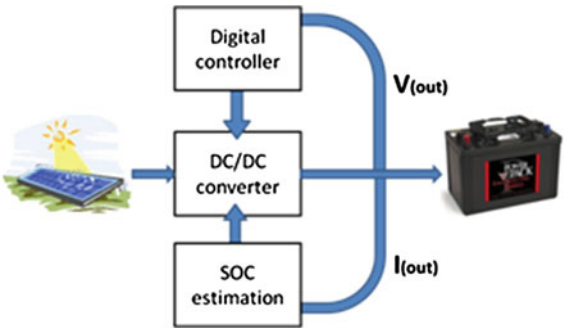

Fig. 53.1 Block diagram of a solar battery charging system

- Regulating the output voltage or current.
- Maximizing the output power of the solar cells through a maximum power point tracking (MPPT) algorithm.

Basically, there are three fundamental DC-DC converter topologies: buck (step-down), boost (step-up), and buck-boost (step-up/step-down). Since a buck-boost converter allows both stepping up and down the input voltage, it is usually used in PV chargers. Buck-boost circuit configuration is shown in Fig. 53.2. The circuit mainly consists of two storage elements (one inductor and one capacitor) and two switches (transistor and a diode).

The solar cells supply input power to the charger input, which in turns regulates this power and delivers it to the load (battery). The converter must handle the variation in the charging current due the variation in solar radiation. That is, the output voltage of the DC-DC converter must not exceed the upper voltage limit of the battery, and the charging current must not exceed the permitted upper limit.

Given the following design specification, the circuit components of the DC-DC converter in Fig. 53.2 and the duty cycle can be calculated as illustrated in Eqs. (53.1)–(53.6).

- $V_{in} = 25$ V and $V_o = 5$ V: The circuit must be designed to take an input voltage of 25 V from a PV panel and to produce 5 V at the output.
- Switching frequency = 100 kHz: The frequency at which the switch S is operated is 100 kHz (one cycle in a 10 μs time). The ON period of the switch is obtained by multiplying the switching period by the duty cycle.
- Output Ripple = 4 %: Only 4 % ripple in the output voltage is allowed.

Equations (53.1)–(53.6) are then used to calculate the values of L, C and R, [18]. Table 53.1 summarized the calculated values.

$$\text{Duty Cycle} : D = \frac{V_{out}}{V_{out} + V_{in}} \tag{53.1}$$

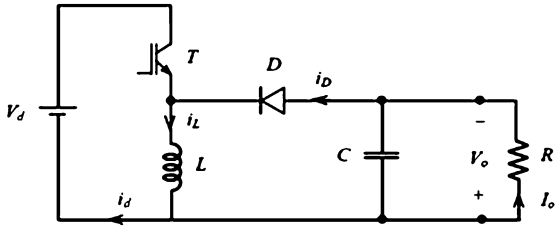

Fig. 53.2 Buck-boost converter

Table 53.1 Summary of the calculated values

Parameter	Value
Input voltage	25 V
Output voltage	5 V
Switching frequency	100 kHz
Duty cycle	16.7 %
ON time	1.9 μs
L	200 μH
C	100 μF
R	0.5 Ω

$$\text{Resistor (Load)} : R = \frac{V_o^2}{P} \tag{53.2}$$

$$\text{Inductor} : L = \frac{RT}{2}(1-D)^2 \tag{53.3}$$

$$\text{Output Ripple Voltage} : \frac{\Delta V_o}{V_o} = \frac{D}{RCf} \tag{53.4}$$

$$\text{Capacitor} : C = \frac{D}{Rf}\frac{V_o}{\Delta V_o} \tag{53.5}$$

$$\text{ON period} : T_{ON} = 10\mu s \times 0.167 = 1.67\mu s \tag{53.6}$$

It can be shown from Eqs. (53.1)–(53.6) that increasing the size of the output capacitor can reduce the ripple in the output voltage. However, increasing the value of the used capacitor increases the cost and size of the converter. Alternatively, the output voltage ripple can be minimized by increasing the switching frequency. Increasing the switching frequency can significantly reduce the output

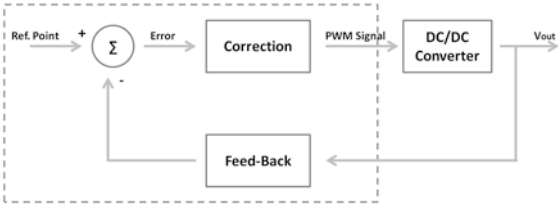

Fig. 53.3 PID controller block diagram

voltage ripple and minimize the components size at the cost of increasing the switching losses. As in any design process, there are always compromises in terms of cost and performance. The duty cycle in Eq. (53.1) is the control parameter for the DC-DC converter. By increasing or decreasing D, the output voltage can be controlled. The next section presents a digital control loop design procedure for the buck-boost converter in Fig. 53.2.

53.3 Digital Control Loop

The controller is an essential part in the charger design. Compared to analog controllers, digital controllers are easier to implement and less expensive. Furthermore, digital signal processing (DSP) based digital controllers allow for the implementation of more functional control schemes, standard control hardware design for multiple platforms and flexibility of quick design modifications to meet specific customer needs. Digital controllers are also less susceptible to aging and environmental variations and have better noise immunity [19].

The output voltage of the solar battery charger must be regulated. In other words, the duty cycle D must be controlled in such a way to make the output voltage constant regardless the input voltage (Fig. 53.3).

A digital proportional-integral-derivative (PID) controller, well-known as a PID controller, can be used to control the power circuit and to eliminate effects of errors on the charger's performance. It includes the features of P, I and D controllers. PID Controller helps regulating important variables within the control system. It possibly affects only one device or many at the same time. The PID controller uses an advanced formula to try and prevent any errors from occurring. This ensures that the devices or systems are controlled performing as perfectly as possible. Information is sent out by the controller, received by the actuator and then the information from the actuator is sent back to the controller by sensors. The controller then makes a decision on how to keep on based on the information it receives and sends it out, creating a continuous close loop. PID controllers have a small overshoot, no steady state error and have short settling time due to differential action [20]. Specifically, proportional control works on the present error while integral term works on the accumulated error to reduce steady state error through the use of an integrator as a low frequency compensator. Derivative term

Table 53.2 Tuning methods for PID controllers [21]

Method	Advantages	Disadvantages
Manual	Online method; No math expression	Requires experienced personnel
Ziegler-Nichols	Online method; Proven method	Some trial and error; Process upset and very aggressive tuning
Cohen-Coon	Good process models	Offline method; Some math; Good only for first order processes
Software tools	Online or offline method; Consistent tuning; Support	Non-Steady State tuning; Some cost and training involved
Algorithmic	Online or offline method; Consistent tuning; Support; Non-Steady State tuning; Very precise	Very slow

predicts future error to improve the transient response of the system using a differentiator [21]. A PID algorithm is given by (53.7):

$$u(t) = K_P e(t) + K_I \int e(t)dt + K_D \frac{d}{dt} e(t) \tag{53.7}$$

where K_p, K_I and K_D are P, I and D gain values which are used to tolerate the error. Tuning PID controller to find the gain values is performed through an organized process and then P, I and D values are chosen based on the behavior of the system in real-time. Several methods were developed to perform PID tuning, both digital and analog approaches. Some of the most effective methods are presented in Table 53.2 [21] which includes: Manual, Ziegler-Nichols, Cohen-Coon, Software tools and Algorithmic. For the digitally controlled PV charger, algorithmic method will be followed despite that it requires longer tuning time but a very precise results could be obtained if properly tuned. In this method, an initial value is to be set for the proportional gain K_p while both integral and derivative gains are set to zero. From this starting point, the system behavior is observed and K_p value is tuned till the transient response of the converter output is optimized.

53.4 SOC Algorithm

The SOC is an indication of the amount of energy inside the battery compared to its maximum capacity. Mathematically, the SOC can be expressed in Eq. (53.8):

$$\mathrm{SOC}(t) = \mathrm{SOC}(0) + \eta \int_0^t \frac{i(\tau)}{C_T} d\tau \tag{53.8}$$

And in discrete-time domain, Eq. (53.8) can be rewritten as in (53.9).

$$\mathrm{SOC}_k = \mathrm{SOC}_{k-1} + \eta \frac{i_k \Delta t}{C_T} \tag{53.9}$$

where $i(t)$ is the current as a function of time (positive for charging and negative for discharging), C_n is the nominal capacity (in Ah), and η is the (dis)charge efficiency.

The (dis)charge efficiency of the battery can be computed using Eq. (53.10):

$$\text{Disch. Efficiency} = \frac{\text{(Dis)charge Capacity}}{\text{Nominal Capacity}} \tag{53.10}$$

Many chargers terminate the charge when the voltage reaches a certain limit, or when a sudden rise in the temperature is detected. However, at outdoor conditions, relying only on the voltage and temperature measurements is very tricky because the outdoor temperature as well as the power generated from the solar cells can vary momentarily. Table 53.3 summarizes some techniques that are commonly used to terminate the charge in traditional chargers (Fig. 53.4).

For a reliable charger design, the charge must be terminated only once the SOC is 100 %. Therefore, an accurate and reliable mechanism for SOC estimation is substantial. The SOC must be estimated continuously in real-time in order to terminate the charge only when the SOC is 100 %. Traditional SOC estimation techniques have their advantages and limitations [22]. Among those techniques, coulomb-counting or current integration is a well-known technique that is used in many commercial applications to estimate the battery SOC. It has several advantages such as it can be used in real time and is very accurate if an accurate current measurements are provided. However, one limitation of this technique is that it can't estimate the initial SOC. In other words, there is no way to predict the true SOC if the initial SOC was unknown. To overcome this limitation, the open-circuit voltage (OCV) technique can be used to estimate the initial SOC by employing a SOC-OCV lookup table.

To obtain a SOC-OCV lookup table, the battery cells must be charged and discharged at very low current (a very low rate is preferable to minimize the polarization and hysteresis effects in the cells). After charging and discharging the cells with a very low current, the charging and discharging voltages and SOC are averaged and stored in a lookup table. Figure 53.5 shows a SOC-OCV curve for a 1,100 mAh Li-ion cell.

Before starting the charging process, the terminal voltage of the battery is measured and the corresponding initial SOC to the measure voltage is found from the lookup table. Then, the accumulated charge is calculated and the SOC is continuously updated as described in Eq. (53.9). Once a 100 % SOC is reached, the charging process will be terminated.

Table 53.3 Traditional charge termination techniques

Termination Technique	Remarks	Limitations in solar chargers
Max. Volt.	Requires constant charging current	Solar charging current is not constant
Negative Volt. Drop	Only for nickel-based batteries; requires constant charging current	Solar charging current is not constant
Temp. Rise	Only for nickel-based batteries; requires constant ambient temperature	Outdoor ambient temperature is not constant
Timer	Requires constant power at the charger input	Solar power is not constant

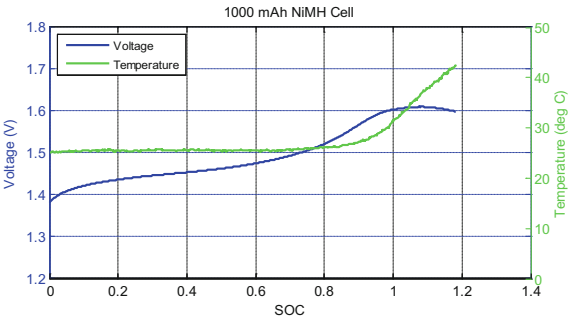

Fig. 53.4 Negative voltage drop and temperature rise in a 1,000 mAh NiMH battery cell (those techniques overcharge the battery resulting in a reduced lifetime), [18]

53.5 Simulation Results

To illustrate how each part in the charger circuit operates, a DC-DC buck-boost converter with the specifications listed in Table 53.1 was simulated. The simulation results for the open-loop converter, closed-loop converter, and SOC estimation method are presented as follows: Fig. 53.7 shows the open-loop simulation results in LTSPICE software for the buck-boost converter shown in Fig. 53.6.

Figure 53.7 shows the simulation result of the converter with a PID digital control loop implemented. To verify the effectiveness of the digital control loop, the inductor current of the buck-boost converter was changed to simulate variation in the solar power. The voltage at the output resumed its normal value within a short time as shown in Fig. 53.8.

To estimate the initial SOC, a SOC-OCV lookup table for a 1,100 mAh Li-ion battery cell was created as in Table 53.4 which represents a portion of an extended table However, linear interpolation is used whenever the measured OCV lies outside the lookup table.

Figure 53.9 shows a solar current profile. The current rise in Fig. 53.9 represents a sudden increase in the solar radiation, while a drop in the current is equivalent to a sudden decrease in the radiation. Figure 53.10 shows that the charge was terminated once the SOC reached 100 % although different initial SOC were assumed.

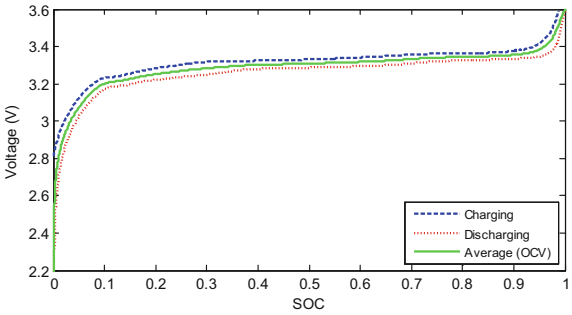

Fig. 53.5 OCV versus SOC curve for a 1,100 mAh Li-ion cell

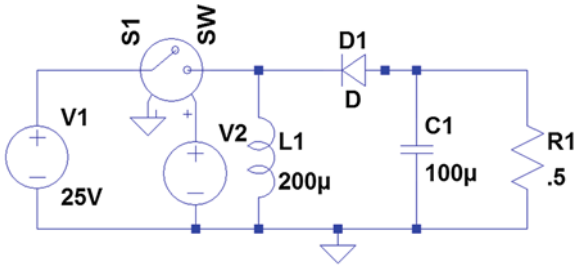

Fig. 53.6 Buck-boost open-loop circuit in LTSPICE

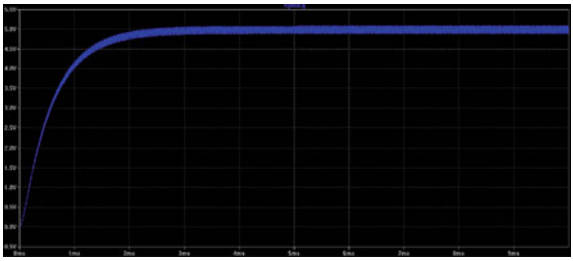

Fig. 53.7 Buck-boost open-loop output voltage waveform using LTSPICE

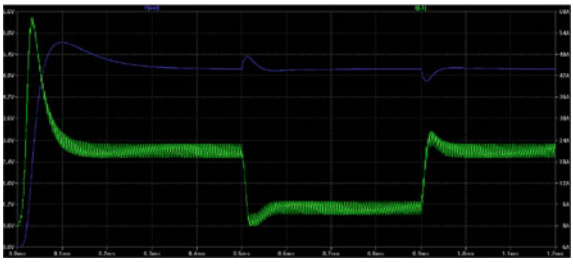

Fig. 53.8 Inductor current (*blue*) and output voltage (*green*) waveforms with a PID control loop in LTSPICE

Table 53.4 Look up table OCV and the corresponding SOC

Initial OCV	Corresponding SOC (%)
2.2 V	0
3.226	15
3.284	30
3.309	50
3.345	80

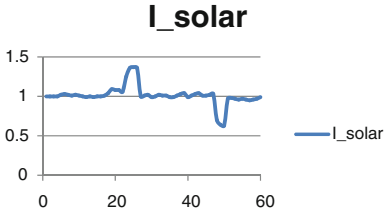

Fig. 53.9 Solar current profile

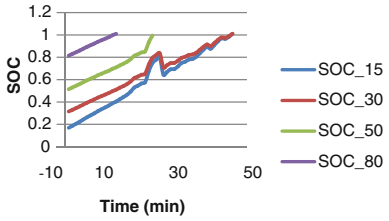

Fig. 53.10 SOC with time with 15, 30, 50 and 80 % initial SOC

53.6 Conclusions and Summary

Regardless the intended application of a battery, the battery charger must meet all design specifications in terms of cost and performance. In this paper, some design considerations for digitally-controlled PV battery chargers were presented. A summary of the conclusions is given as follows:

- Digital control techniques are widely used due to their high performance, ease of implementation and low cost.
- Charging from the solar power requires more advanced techniques to monitor the battery charge.
- Traditional charging techniques are not compatible with PV chargers since they are very sensitive to current and temperature variations.
- Accurate online SOC estimation algorithm can significantly improve the charging process and prolong the cycle life of the battery.

References

1. Battery and Energy Technologies website. Available: http://www.mpoweruk.com
2. L.R Chen, J.J Chen, C.M Ho, S.L Wu, D.T Shieh, Improvement of Li-ion battery discharging performance by pulse and sinusoidal current strategies. IEEE Trans. Ind. Electron. **60**(12) (2013)
3. L.R. Chen, Design of duty-varied voltage pulse charger for improving Li-ion battery-charging response. IEEE Trans. Ind. Electron. **56**(2), 480–487 (2009)
4. L.R. Chen, N.Y. Chu, C.S. Wang, R.H. Liang, Design of a reflex-based bidirectional converter with the energy recovery function. IEEE Trans. Ind. Electron. **55**(8), 3022–3029 (2008)
5. C.H. Lin, C.Y. Hsie, K.H. Chen, A Li-ion battery charger with smooth control circuit and built-in resistance compensator for achieving stable and fast charging. IEEE Trans. Circuits Syst. I **57**(2), 506–517 (2010). (Reg. Papers)
6. Y.H. Liu, Y.F. Luo, Search for an optimal rapid-charging pattern for Li-ion batteries using the Taguchi approach. IEEE Trans. Ind. Electron. **57**(12), 3963–3971 (2010)
7. Y.H. Liu, C.H. Hsieh, Y.F. Luo, Search for an optimal five-step charging pattern for Li-ion batteries using consecutive orthogonal arrays. IEEE Trans. Energy Convers. **26**(2), 654–661 (2011)
8. H. Qian, J. Zhang, J.S. Lai, W.S. Yu, A high-efficiency grid-tie battery energy storage system. IEEE Trans. Power Electron. **26**(3), 886–896 (2011)
9. J.J. Chen, F.C. Yang, C.C. Lai, Y.S. Hwang, R.G. Lee, A high-efficiency multimode Li-ion battery charger with variable current source and controlling previous-stage supply voltage. IEEE Trans. Ind. Electron. **56**(7), 2469–2478 (2009)
10. L.R. Chen, J.J. Chen, N.Y. Chu, G.Y. Han, Current-pumped battery charger. IEEE Trans. Ind. Electron. **55**(6), 2482–2488 (2008)
11. L.R. Chen, R.C. Hsu, C.S. Liu, A design of a grey-predicted Li-ion battery charge system. IEEE Trans. Ind. Electron. **55**(10), 3692–3701 (2008)
12. L.R. Chen, C.S. Liu, J.J. Chen, Improving phase-locked battery charger speed by using resistance-compensated technique. IEEE Trans. Ind. Electron. **56**(4), 1205–1211 (2009)
13. L.R. Chen, A design of optimal pulse charge system by variable frequency technique. IEEE Trans. Ind. Electron. **54**(1), 398–405 (2007)
14. L.R. Chen, C.M. Young, N.Y. Chu, C.S. Liu, Phase-locked bidirectional converter with pulse charge function for 42-V/14-V dual voltage powernet. IEEE Trans. Ind. Electron. **58**(5), 2045–2048 (2011)
15. J. Zhang, J. Yu, C. Cha, H. Yang, The effects of pulse charging on inner pressure and cycling characteristics of sealed Ni/MH batteries. J. Power Sources **136**(1), 180–185 (2004)
16. L.R. Chen, S.L. Wu, D.T. Shieh, T.R. Chen, Sinusoidal-ripple-current charging strategy and optimal charging frequency study for Li-ion batteries. IEEE Trans. Ind. Electron. **60**(1), 88–97 (2013)
17. A. Hussein, I. Batarseh, A review of charging algorithms for nickel and lithium battery chargers. IEEE Trans. Veh. Technol **60**(3), 830–838 (2011)
18. I. Bataresh, *Power Electronics Circuits*. (Wiley, New York, 2003)
19. Designing a TMS320F280x Based Digitally Controlled DC-DC Switching Power Supply. Texas Instruments, Application Report (2005)
20. A. Vaisioli, *Practical PID Controller* (Books.google.ae, N.p., 2006)
21. K.A. Tehrani, A. Mpanda, *PID Control Theory*. University of Nancy, France, Tshwane University of Technology, South Africa (2012)
22. A.A. Hussein, I. Batarseh, State-of-charge estimation for a single lithium battery cell using extended Kalman filter, in *IEEE Power and Energy Society (PES) General Meeting, Detroit, Michigan,* 24–28 July 2011

Chapter 54
Experimentally Assessing Hydrogen–Oxygen Production Using Alkaline Fuel Cell

A. Ateeq, A. Sayedna, A. AlShehhi, M. AlAwbathani and M. O. Hamdan

Abstract The objective of this work is to evaluate the performance of Alkaline Fuel Cell in producing hydrogen and oxygen mixture. The effect of voltage, current, plates number, KOH concentrations and temperature are evaluated. The study shows that the relation between applied voltage between two plates and hydrogen–oxygen mixture production is a non-monotonic relation and reach maximum at 2 V. The study shows that hydrogen–oxygen mixture production increases as current intensity decreases. The current intensity is directly increasing with KOH concentration.

Keywords Hydrogen water electrolysis · KOH · Alkaline fuel cell

54.1 Introduction

Approximately, around 4 % of the hydrogen produced in the world is produced by water electrolysis while the rest of the 96 % comes from fossil fuel [1]. Water electrolysis is not a new process for the production of hydrogen [2–6]. However, water electrolysis remains a very minor contributor to the total production of hydrogen because it requires electricity which considered as high quality energy that can be directly used instead of being converted to hydrogen. However, recently and due to the exploding expansion in renewable energy production which require in many cases energy storage methods, the interest in water electrolysis has increased. One use recently proposed method it to utilize solar energy to produce hydrogen–oxygen mixture for diesel engine [7]. In total, around 40 million tons of hydrogen are annually produced and used in the manufacture of ammonia, for the

A. Ateeq · A. Sayedna · A. AlShehhi · M. AlAwbathani · M. O. Hamdan (✉)
United Arab Emirates University, AlAin, UAE
e-mail: MohammadH@uaeu.ac.ae

M. O. Hamdan et al. (eds.), *ICREGA'14 - Renewable Energy: Generation and Applications*, Springer Proceedings in Energy, DOI: 10.1007/978-3-319-05708-8_54,

hydrogenation of organics, in petroleum refineries, in metals production, for electronics fabrication, for high temperature flames and for cooling thermal generators [8].

The hydrogen production thru water electrolysis process has many advantages which are simplicity of the process, high purity of hydrogen and oxygen, environmental friendly and abundant water sources. Industrial water electrolysis cells have been established since one hundred years [9]. However, water electrolysis is only used in special cases that need hydrogen with high purity. This technology is considered as the supplement but not the alternative to hydrocarbon sources for hydrogen production in the past several decades. However, fossil fuel (coal, petroleum or natural gas) is not reliable due to the reduction of reserves and severe environmental pollution. Renewable primary energies such as solar energy, wind energy and ocean energy receive more and more attentions [10–15].

54.2 Experimental Setup

A schematic diagram of the alkaline fuel cell shown is in Fig. 54.1 and actual photo of the cell that is built using stacks of sheet of stainless steel 316 is shown in Fig. 54.2. In the plates arrangement shown in Fig. 54.2, the overall voltage supplied to the whole cell is divided equally according to the number of spaces between plates. The middle plates are called neutral plates as shown in Fig. 54.1 since it has two sides in which one is acting as cathode and the other as an anode. Hydrogen is formed on the cathode while oxygen is formed on the anode. The end plates are either cathode or anode depending on the power source connection. The stainless steel plates are separated using Donit Tesnit gasket with thickness of 2 mm.

The efficiency of the cell is calculated using the following equation:

$$\eta = \frac{\dot{m}_{H_2} LHV}{E}$$

where $\dot{m}_{H_2}$ is the mass flow rate of hydrogen produced, LHV is the lower heating value of hydrogen, and E is the electrical power and was calculated by measuring current and voltage supplied to the cell.

The schematic diagram of the test setup is shown in Fig. 54.3. The flow rate of collected gas mixture is measured by recording the time needed to fill a graduate cylinder. The electrical power is controlled by varying voltage. Multiple test schemes have been followed to determine the optimum voltage between two plates, the operating current intensity and alanine concentration.

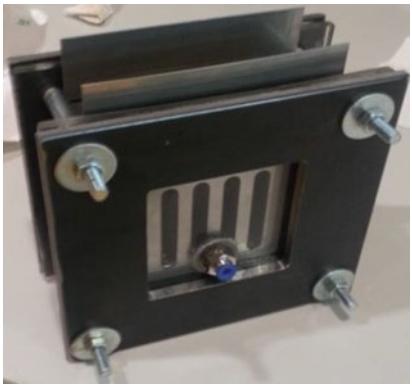

Fig. 54.1 Alkaline fuel cell developed in UAE University

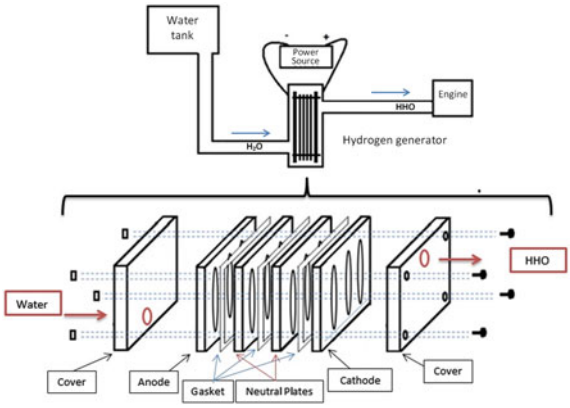

Fig. 54.2 A schematic diagram shows the assembly of the fuel cell

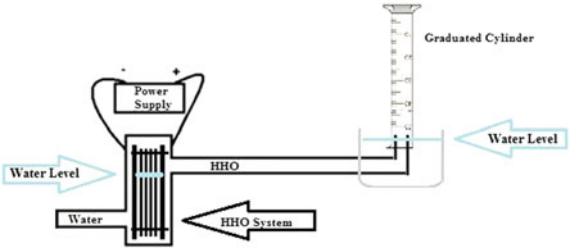

Fig. 54.3 A schematic diagram of the test setup

54.3 Results and Discussion

This study presents the results for evaluating the effect of different parameters on Alkaline water electrolysis device; mainly the effect of number of plates, the unit cell voltage, KOH concentration and cell temperature.

Figure 54.4 shows the efficiency and flow rate of HHO gas with respect to number of plates while supplying the whole cell by overall voltage of 12 V, under fixed KOH concentration of 16.7 mg/ml and under room temperature condition. By fixing input voltage to 12 V and changing number of plates it is expected that the voltage between every to plates will vary. The voltage between every two plates can be calculated by dividing the 12 V over (n – 1) where n is number of plates. As shown in Fig. 54.4 the maximum efficiency (around 25.1 %) occurred with 7 plates which mean the voltage between each plate is 2 V (=12/(7 − 1)). However as number of plates are reduced, the flow rate of HHO gas kept increasing which is expected since less plates mean less electrical resistance. For fixed input voltage, the lower the electrical resistance, the higher the current (or power) that is supplied to the cell which leads to more HHO gas flow rate however the efficiency will not follow same trend. As shown in this setup, efficiency has non-monotonic relation with number of plates and reach maximum around 7 plates.

Figure 54.5 shows the variation of efficiency with voltage per unit cell (2 plate cell). This figure is generated by dividing input voltage of 12 over (n − 1) where n is number of plate.

Another factor that affect the fuel cell performance is the alkaline concentration. While varying the Alkaline concentration, the current and HHO flow rate has been measured presented in Fig. 54.6 and cell efficiency has been calculated and presented in Fig. 54.7. As shown in Fig. 54.6, as concentration KOH increases, the flow rate of HHO and current is increases. The increase current is expected since as KOH concentration increases the electrical carrier in the solution will increase driving more current to flow inside the cell. As the electrical carried number increases the cell electrical resistance decreases and hence more power is supplied the cell. The increase in power will cause an increase in the HHO gas flow rate.

On the other hand, as KOH concentration increases, the efficiency of cell decreases as show in Fig. 54.7. The decrease in the efficiency is due to the increase in current which eventual is wasted heat added to the water. However reducing the concentration mean more power is need to ionize the water and to produce the HHO gas.

One way to enhance the fuel cell performance is by heating the cell which will increase the kinetic energy of the molecules and hence reduce the energy needed to break water molecules to HHO gas. Figure 54.8 shows the fuel cell performance under different temperature conditions. As shown in Fig. 54.8 as temperature increases the cell efficiency is increasing. Since the cell is tested at one atmosphere pressure, the maximum testing temperature is set to 88 °C to minimize vapor evaporation. Also, to assure that HHO gas is collected and not water vapor, the collected mixture is passed through cold water bath to assure that any vapor is condensed and only HHO gas flow rate is measured.

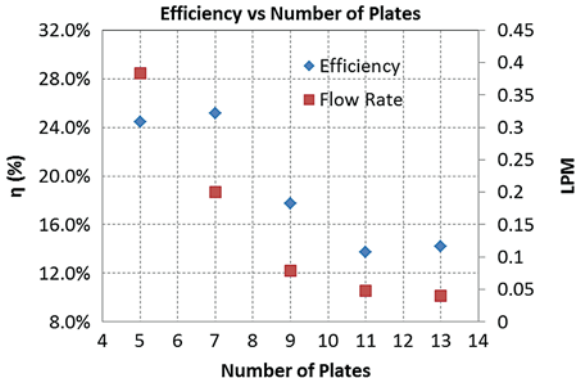

Fig. 54.4 Optimum voltage between the plates

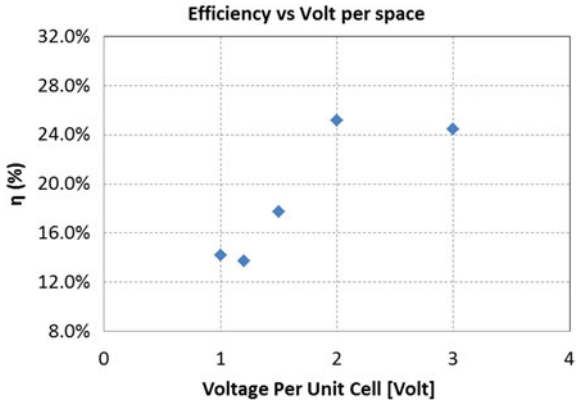

Fig. 54.5 System efficiency versus voltage per unit cell

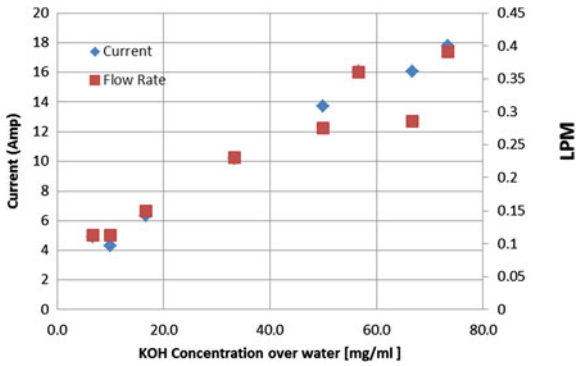

Fig. 54.6 Current and HHO flow rate versus KOH concentration

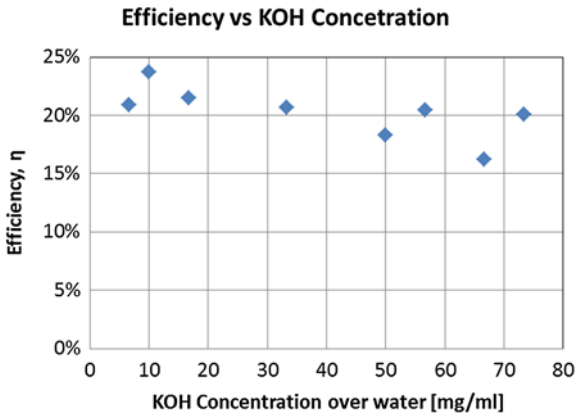

Fig. 54.7 System efficiency versus KOH concentration

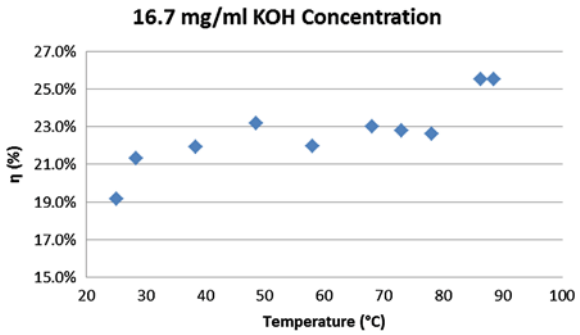

Fig. 54.8 Temperature effect on system efficiency

54.4 Conclusion

In this work, an experimental investigation has been carried on to parameterize HHO system, the data shows the following:

- The optimum operating voltage between two plates based on efficiency is around 2 V.
- The efficiency increases as KOH concentration decreases however this directly depends on the power supply capability. For current test setup and power supply, the maximum efficiency is achieved at the lowest concentration 10 mg/ml.
- As the temperature increases, the HHO efficiency increases, the highest efficiency was 25.5 % at 88 °C.

Acknowledgment The authors would like to acknowledge the support provided by United Arab Emirates University (UAEU) and by Abu Dhabi Water and Electricity Authority (ADWEA). This work is financially supported by ADWEA and is conducted in UAEU laboratories.

References

1. M. Balat, Potential important of hydrogen as a future solution to environmental and transportation problems. Int. J. Hydrogen Energy **33**, 4013–4029 (2008)
2. B.V. Tilak, P.W.T Lu, J.E. Colman, S. Srinivasan, *Electrolytic production of hydrogen*, ed. by J.O'.M. Bockris, B.E. Conway, E. Yeager, R.E. White, Comprehensive Treatise of Electrochemistry, vol. 2. (Plenum, New York, 1981), p. 1e104
3. H. Wendt, G. Imarisio, Nine years of research and development on advanced water electrolysis e a review of the research-program of the commission-of-the-European communities. J. Appl. Electrochem. **18**:1e14 (1988)
4. H. Wendt, Electrochemical hydrogen technologies. (Elsevier, Amsterdam, 1990)
5. D. Pletcher, F.C. Walsh, Industrial electrochemistry. (Chapman and Hall, London, 1991)
6. V. Plzak, B. Rohland, H. Wendt, *Advanced Electrochemical Hydrogen Technologies—Water Electrolyzers and Fuel Cells in Modern Aspects of electrochemistry*, ed. by R.E. White, J.O'.M. Bockris, Conway BE, Modern aspects of electrochemistry, vol. 26. (Plenum, New York, 1994)
7. M.O. Hamdan, P. Martin, E. Elnajjar, M.Y.E. Selim, S. Al-Omari, Diesel engine performance and emission under hydrogen supplement, in *Proceedings of International Conference on Renewable Energy: Generation and Applications, 2014—ICREGA'14, AlAin, UAE*
8. G. Saur, The Wind to Hydrogen Project: Electrolyzer Capital Cost Study, Report NREL/TP-550e44103 (2008)
9. R.L. Leroy, Industrial water electrolysis present and future. Int. J. Hydrogen Energy **8**, 401–417 (1983)
10. S.A. Sherif, F. Barbir, T.N. Veziroglu, Wind energy and the hydrogen economy-review of the technology. Sol. Energy **78**, 647–660 (2005)
11. R. Palumbo, R.B. Diver, C. Larson, E.N. Voker, J.E. Miller, J. Guertin, Solar thermal decoupled water electrolysis process I: proof of concept. Chem. Eng. Sci. **84**, 372–380 (2012)
12. I. Colak, S. Sagiroglu, M. Yesilbudak, Data mining and wind power prediction: a literature review. Renewable Energy **46**, 241–247 (2012)
13. H. Benli, Potential of renewable energy in electrical energy production and sustainable energy development of Turkey: performance and polices. Renewable Energy **50**, 33–46 (2013)
14. D. Swift-Hook, Wind energy really is the last to be stored and solar energy cannot be stored economically. Renewable Energy **50**, 971–976 (2013)
15. R.G. Cong, An optimization model for renewable energy generation and its application in China: a perspective of maximum utilization. Renew. Sustain. Energy Rev. **17**, 94–103 (2013)

Chapter 55
Reducing the Combustion Noise and Operational Roughness of Diesel Engine by Using Palm Oil Methyl Ester Biofuel

Mohamed Y. E. Selim and A. M. M. Hussien

Abstract An experimental investigation has been carried out to examine the diesel engine combustion noise and engine roughness when palm oil methyl esters biofuel is used in a diesel engine. A reference case has been tested when diesel fuel is used and another case when crude palm oil is used. A variable compression research diesel engine Ricardo E6 has been used throughout the current work. The effects of engine load and compression ratio have been experimentally scrutinized. The results presented included the maximum heat release rate, the maximum combustion pressure rise rate, the maximum combustion pressure and the engine torque output. The diesel engine exhibited less combustion noise, less engine roughness and slightly less torque output when palm oil methyl esters biofuel is used. The engine exhibited even less noise when crude palm oil is used, though the viscosity is not practically acceptable.

Keywords Diesel engine · Engine roughness · Combustion noise · Palm oil methyl esters · Crude palm oil

55.1 Introduction

The need of alternative energy for internal combustion engines has stemmed the search for biofuels from every possible source. The need of alternative energy source is a result of instabilities in the oil prices and the fear from the exhaustion of petroleum oil. The vegetable plants have been used successfully to produce

M. Y. E. Selim (✉)
Mechanical Engineering Department, United Arab Emirates University, Al-Ain, UAE
e-mail: mohammed.selim@uaeu.ac.ae

A. M. M. Hussien
Mechanical Engineering Power Department, Helwan University, Helwan, Egypt

M. O. Hamdan et al. (eds.), *ICREGA'14 - Renewable Energy: Generation and Applications*, Springer Proceedings in Energy, DOI: 10.1007/978-3-319-05708-8_55,

biofuels, such as rapeseed [1], blends of rapeseed and ethanol with diesel [2], oil from sunflower [3], cottonseed [4], soybean [5], jojoba [6–8], palm oil [9], or from tall oil [10]. Canola oil and other oils [11] have been also used as a biofuel for diesel engines. A review of most available vegetable fuels is also given in terms of engine performance and emissions [12]. Biofuels derived from vegetable oils or others should follow the acceptable standards of biofuels properties. This necessitates the transesterification process as a mean to remove the viscous glycerol and reduce the viscosity of those oils.

Although the palm oil is originated from West Africa, it currently takes more than one third of Malaysia's cultivated area. In Malaysia, oil palm is the 'golden crop'. There is great confidence that it will continue contributing significantly to the increase in the global oils and fats trade. In the meantime, the Malaysian palm oil statistics remain impressive. Malaysia's crude palm oil (CPO) production has increased from 13.5 million tonnes in 2004, to 18.8 million tonnes in 2012. The increase was due to the expansion in matured planted area, weather conditions, constant sunshine, and rainfall distribution throughout the year. The fresh fruit bunches yield per hectare increased by 5.7 % to 18.99 tons from 17.97 tons.

The use of palm oil methyl esters has been tested in diesel engine (for transportation or power generation) by many previous works [13–17] as well as, the use of crude of palm oil has been tested [18]. However, there is a lack of engine combustion noise and engine roughness data which are related to maximum pressure rise rate, maximum combustion pressure and maximum heat release rate for diesel engines using both palm oil methyl esters and crude palm oil at different engine conditions. Therefore, it is the main objective of the current work to investigate the diesel engine combustion noise and engine roughness parameters in case of using the palm oil methyl esters as the main fuel, as compared to crude palm oil fuel with reference to a base case of diesel fuel obtained locally with properties shown in the current work. The crude palm oil has been obtained from the local market and the methyl esters have been prepared locally in the laboratory of the authors. The effects of engine load, speed, compression ratio and injection timing shall be studied experimentally to examine the needed engine modifications in case of using such fuel.

55.2 Experimental Setup

The test rig used in the present study is the Ricardo E6 single cylinder variable compression indirect injection diesel engine. The specifications of the engine are listed in Table 55.1. The engine cylinder head has a Ricardo Comet Mk V compression swirl combustion chamber. This type of combustion system consists of two parts. The swirl chamber in the head has a top half of spherical form and the lower half is a truncated cone, which communicates with the cylinder by means of a narrow passage or throat. The second part consists of special cavities cut into the crown of the piston.

Table 55.1 Ricardo E6 engine specifications

Model	Ricardo E6
Type	IDI with the pre-combustion chamber
Number of cylinders	1
Bore	76.2 mm
Stroke	111.1 mm
Swept volume	0.507 l
Maximum speed	50 rev/s (3000 rpm)
Maximum power, diesel	9.0 kW, Naturally aspirated
Maximum power, diesel	14.0 kW, Supercharged (0.5 bar)
Compression ratio	Maximum CR 22
Injection timing	Variable, 20°–45° BTDC

The engine is loaded by an electrical dynamometer rated at 22 kW and 420 V. The engine is fully equipped for measurements of all operating parameters and combustion noise data. The combustion pressure time history is measured by a water-cooled piezo-electric pressure transducer connected to the relevant amplifier. The liquid fuel flow rate is measured digitally by a multi-function microprocessor-based fuel system, Compuflow System. Two data acquisition systems are used to collect the important data and store it in two personal computers for offline analysis. The following parameters are fed into the first data acquisition system: liquid fuel flow rate data, engine speed and torque, and air/oil/coolant/exhaust temperatures. A computer program in μMACBASIC language is written to collect the data and manage the system and a workstation operating system has been used to run the program.

The pressure signal amplified by a charge amplifier is fed to the second data acquisition card linked to a personal computer. The acquisition card could collect data at a rate of up to 250 kHz. A Labview acquisition program is used to sample and store the pressure data fed to one channel of the data acquisition card. Experiments have been carried out after running the engine for some time until it reaches steady state and oil temperature is at 60 °C ± 5, and cooling water temperature is at 70 °C ± 5.

Maximum combustion pressure and maximum combustion pressure rise rate data are presented for the diesel engine (using diesel fuel, palm oil methyl esters and crude palm oil as main fuel independently) against the tested engine operating design and operating parameters. The heat release rate results have been calculated [19] for all tested conditions. Maximum pressure rise rate and heat release rate are the set of data that are proved to increase the engine combustion noise and roughness. The combustion pressure has been measured by the piezo-electric pressure transducer and then converted as pressure from the calibration data. It is then digitized by the A/D converter and fed into the computer for other calculations.

The engine design and operating parameters have been varied at the following levels:

(a) Type of liquid fuel: base case as normal diesel fuel, palm oil methyl esters, and crude palm oil
(b) The engine load, and it is varied from 0.5 to 15 Nm
(c) The compression ratio, and it is varied at 18 and 22.

The experimental error is evaluated according to [20]. The maximum uncertainty in any quantity is calculated as the error divided by the average reading of the quantity. The maximum uncertainties in the measurements of engine speed, torque, and diesel fuel were 2.5, 5 and 2.76 % respectively. The maximum uncertainty was 1° in the fuel injection angle, 0.01 in the engine compression ratio, 2.5 % in the maximum pressure and 3 % in the pressure rise rate.

55.3 Results and Discussion

The effects of engine load on maximum heat release rate, maximum combustion pressure and maximum pressure rise rate for the used three fuels may be shown in Figs. 55.1, 55.2, 55.3 and 55.4. The load is increased by increasing the mass of fuel injected and burnt. As can be seen from Fig. 55.1, the maximum heat release rate tends to slightly decrease with increasing the load output. The increase in the mass of fuel burnt increases the operating temperature of the engine which leads to shorter ignition delay period and smoother combustion. The smoother combustion leads to burning of smaller mass of fuel which produces lower heat release rate [19]. The premixed and the mixing controlled heat release rates are related to the mixing rate and ignition delay period [19]. The reduction in ignition delay period tends to decrease the maximum pressure rise rate as shown in Fig. 55.2. The reduction in pressure rise rate tends to cause slower combustion and complete the burning after the top dead center with less maximum combustion pressure; as shown in Fig. 55.3. For the three previous figures, it may be seen that there are some difference between the palm oil methyl esters, crude palm oil and the base diesel fuel. The chemical composition of the palm oil methyl esters (POME) is available [21] and also the properties of crude palm oil (CPO) [22]. Similar results have been obtained in the current work for the chemical composition. Only acids with noticeable percentage are shown in the POME, but those with very small percentage in the crude oil, are not shown in the methyl esters.

It may be seen that the heating value of the POME is 39.8 MJ/kg where it is 48.1 for diesel fuel. Also the cetane index is 57 for POME where it is 46.3 for diesel. The decreased heating value for palm oil tends to decrease the overall heat released for palm oil. As the cetane index is higher for POME, the ignition delay period is reduced [23, 24] and the rate of heat release rate follows the delay period [19] which tends to be also reduced as shown in Fig. 55.1. At mid-load, it reduces from about 50 J/deg for diesel to about 30 J/deg for POME. The higher cetane index and the lower ignition delay period of the POME [21] also decreases the maximum rate of pressure rise as the fuel is easily burnt with less mass which

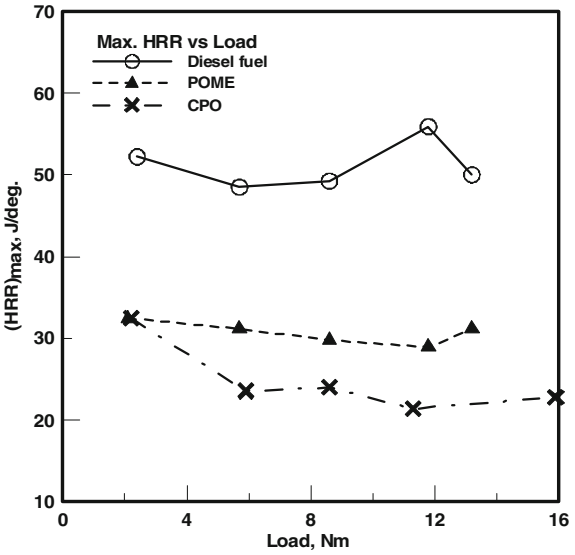

Fig. 55.1 Maximum heat release rate against load for diesel and palm oil fuels

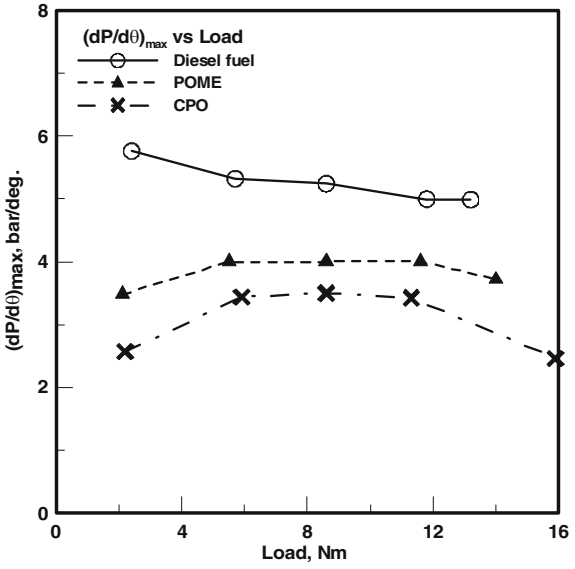

Fig. 55.2 Maximum pressure rise rate against load for diesel and palm oil fuels

tends to cause smoother combustion as seen in Fig. 55.2. It drops from about 5.3 bar/deg for diesel to about 4 bar/deg for POME. The maximum combustion pressure also follows the pressure rise rate as seen in Fig. 55.3. It reduced from about 52 bar for diesel to about 48 bar/deg for POME. The crude palm oil with reduced heating value follows the same trend. The engine produces less combustion noise (around 3.5 bar/deg at mid-load range) and exhibits less roughness

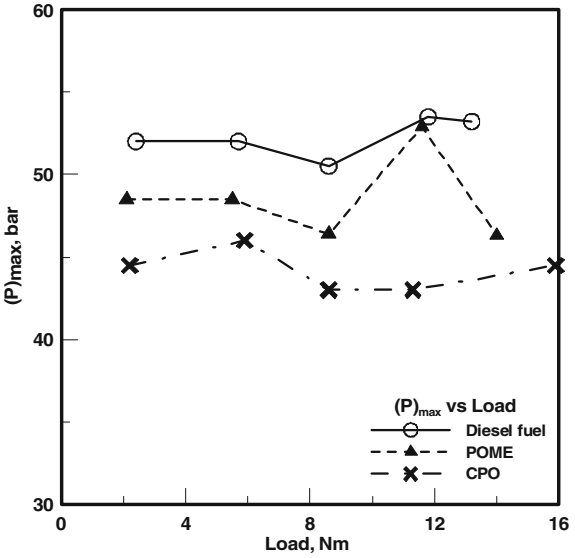

Fig. 55.3 Maximum combustion pressure against load for diesel and palm oil fuels

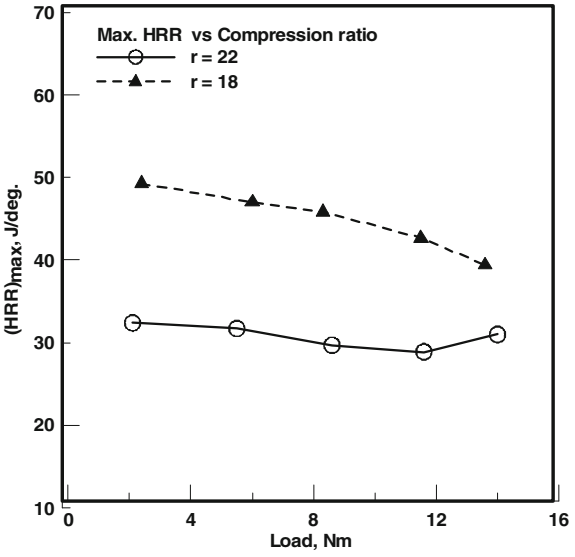

Fig. 55.4 Maximum heat release rate against compression ratio and load for palm oil fuels

when palm oil methyl esters or crude palm oil are used. The crude palm oil may be only usable for short term engine operations, as for long term operation, the increased viscosity may harm the injection system in addition to the unacceptability of it to be used as standard biofuel.

Figure 55.4 depicts the effect of compression ratio on the maximum rate of heat release (HRR) for POME. It may be seen from the figure that decreasing the

compression ratio from 22 to 18 caused the maximum HRR to increase. It increased from 30 J/deg for compression ratio of 22–47 J/deg at compression ratio of 18, at mid-load range. This follows the increased ignition delay period thus increased heat release rate as more heat is released during the premixed period and constant heat released during the mixing controlled period [25].

55.4 Conclusions

From the experimental work presented, the following conclusions may be drawn:

For all test conditions used in the current work and within the used range, the palm oil methyl esters and crude palm oil produced less maximum HRR, less maximum pressure rise rate and less maximum combustion pressure compared to diesel fuel.

The engine produced slightly less torque when palm oil methyl esters or crude palm oil is used.

The engine exhibited similar trends for the maximum HRR, maximum pressure rise rate and the maximum combustion pressures, for the three fuels tested when load has changed.

The crude palm oil exhibited less engine noise and roughens than POME or diesel, however, the fuel viscosity is far beyond the standard acceptable value.

Acknowledgments The authors would like to acknowledge the support provided by United Arab Emirates University. This work is financially supported by the Faculty of Engineering at the United Arab Emirates University. The help of M. El-Saeed is highly acknowledged for the process of testing the diesel engine. Thanks are also due to Prof. Y. Haik and Eng. T. Abdulrahman for helping in preparing the biofuel.

References

1. L. Raslavičius, Ž. Bazaras, Variations in oxygenated blend composition to meet energy and combustion characteristics very similar to the diesel fuel. Fuel Process. Technol. **91**, 1049–1054 (2010)
2. L. Raslavičius, Ž. Bazaras, The possibility of increasing the quantity of oxygenate s in fuel blends with no diesel engine modifications. Transport **25**(1), 81–88 (2010)
3. N. Usta, E. Öztürk, Ö. Can, E.S. Conkur, S. Nas, A.H. Çon, A.Ç. Can, M. Topcu, Combustion of biodiesel fuel produced from hazelnut soapstock/waste sunflower oil mixture in a diesel engine. Energy Conv. Manag. **46**(5), 741–755 (2005)
4. B. Mustafa, B. Havva, A critical review of bio-diesel as a vehicular fuel. Energy Convers. Manag. **49**(10), 2727–2741 (2008)
5. C. Samart, C. Chaiyan, P. Reubroycharoen, Biodiesel production by methanolysis of soybean oil using calcium supported on mesoporous silica catalyst. Energy Conv. Manag. **51**(7), 1428–1431 (2010)

6. S.A.H. Huzayyin, M.A. Bawady, R.A. Dawood, Experimental evaluation of diesel engine performance and emission using blends of jojoba oil and diesel fuel. Energy Convers. Manag. **45**(13–14), 2093–2112 (2004)
7. M.Y.E. Selim, Reducing the viscosity of Jojoba Methyl Ester diesel fuel and effects on diesel engine performance and roughness. Energy Convers. Manag. **50**(7), 1781–1788 (2009)
8. M.I. Al-Widyan, M.A. Al-Muhtaseb, Experimental investigation of jojoba as a renewable energy source. Energy Convers. Manag. **51**(8), 1702–1707 (2010)
9. A.N. Ozsezen, M. Canakci, Determination of performance and combustion characteristics of a diesel engine fueled with canola and waste palm oil methyl esters. Energy Convers. Manag. **52**(1), 108–116 (2011)
10. A. Keskin, Y. Abdulkadir, G. Metin, A. Duran, Usage of methyl ester of tall oil fatty acids and resinic acids as alternative diesel fuel. Energy Convers. Manag. **51**(12), 2863–2868 (2010)
11. A. Demirbas, Progress and recent trends in biodiesel fuels. Energy Convers. Manag. **50**(1), 14–34 (2009)
12. N. Soo-Young, Inedible vegetable oils and their derivatives for alternative diesel fuels in CI engines: a review. Renew. Sustain. Energy Rev. **15**(1), 131–149 (2011)
13. R.P. Rodríguez, R. Sierens, S. Verhelst, Ignition delay in a palm oil and rapeseed oil biodiesel fuelled engine and predictive correlations for the ignition delay period. Fuel **90**, 766–772 (2011)
14. W. Xiangang, Z. Huang, O.A. Kuti, W. Zhang, K. Nishida, An experimental investigation on spray, ignition and combustion characteristics of biodiesels. Proc. Combust. Inst. **33**(2), 2071–2077 (2011)
15. A.N. Ozsezen, M. Canakci, The emission analysis of an IDI diesel engine fueled with methyl ester of waste frying palm oil and its blends. Biomass Bioenergy **34**, 1870–1878 (2010)
16. P. Wibulswas, Combust1on of blends between plant oils and diesel oil. Renewable Energy **16**:1098–1101 (1999)
17. M.A. Kalam, H.H. Masjuki, Biodiesel from palmoil—an analysis of its properties and potential. Biomass Bioenergy **23**, 471–479 (2002)
18. S. Bari, T.H. Lim, C.W. Yu, Effects of preheating of crude palm oil (CPO) on injection system, performance and emission of a diesel engine. Renewable Energy **27**, 339–351 (2002)
19. J. Heywood, *Internal combustion engine fundamentals*, 2nd edn. (McGraw-Hill, New York, 1988). (series in Mech. Eng.)
20. R.J. Moffat, Describing the uncertainties in experimental results. Exp. Thermal Fluid Sci. **1**(1), 3–17 (1988)
21. P. Benjumea, J. Agudelo, A. Agudelo, Basic properties of palm oil biodiesel–diesel blends. Fuel **87**, 2069–2075 (2008)
22. Y.A. Elsheikh, M. Zakaria, M.A. Bustam, S. Yusup, C.D. Wilfred, Brønsted imidazolium ionic liquids: Synthesis and comparison of their catalytic activities as pre-catalyst for biodiesel production through two stage process. Energy Convers. Manag. **52**(2), 804–809 (2011)
23. C.L. Wong, D.E. Steere, The effects of diesel fuel properties and engine operating conditions on ignition delay. SAE Trans **91**, paper 821231 (1982)
24. R. Olree, D. Lenane, Diesel combustion cetane number effects. SAE Trans 93, paper 840108 (1984)
25. N.D. Whitehouse, E. Clough, J.B. Way, The effect of changes in design and operating conditions on heat release indirect-injection diesel engines, SAE paper 740085 (1974)

Chapter 56
Design and Simulation of a High Performance Standalone Photovoltaic System

H. A. Attia, Y. I. Al-Mashhadany and B. N. Getu

Abstract This paper proposes a full design with all included stages of a high performance standalone photovoltaic system based on discrete electronic components. The design proposes a solution to reduce or eliminate the fluctuation of the supplied DC voltage of solar panel due to weather variations. The proposed design includes DC–DC boost converter that produces a stable DC output voltage with a higher level, this is achieved by controlling the Duty cycle of the drive switching pulses during sensing the level of the solar panel voltage. The next stage is a modified unipolar Sinusoidal Pulse Width Modulation inverter with Zero Crossing Detector circuit that is designed with a modified higher power reference wave compared with traditional SPWM. The modified SPWM controls the Modulation Index to stabilize the fluctuation in the output AC voltage. The selected filter type LCL-Filter is designed to minimize the effect of harmonics on the load voltage. On the other hand, an accurate DC power supply is designed to provide the required stable DC voltages for all included electronic circuits; the solar panel voltage is an input to the designed DC power supply. Total Harmonic Distribution measurements, the stable output voltage level of the DC–DC converter, DC power supply, and the stabilization of the load voltage reflect the effectiveness of the proposed photovoltaic system. The overall electronic design works under wide range of solar panel voltage fluctuations. The satisfactory simulation results indicate that there is a promise to implement the proposed electronic design using discrete components as practical module.

Keywords PV system · DC–DC converter · Duty cycle · SPWM · Sensing circuit · Close loop · LCL filter · DC supply

H. A. Attia (✉) · B. N. Getu
American University of Ras Al-Khaimah, Ras Al-Khaimah, United Arab Emirates
e-mail: hattia@aurak.ae

Y. I. Al-Mashhadany
University of Al Anbar, Ramadi, Iraq

M. O. Hamdan et al. (eds.), *ICREGA'14 - Renewable Energy: Generation and Applications*, Springer Proceedings in Energy, DOI: 10.1007/978-3-319-05708-8_56,

56.1 Introduction

The abundance and wide spread availability of solar energy, make it the most attractive among other energies that can be feasibly extracted. It can be converted into electricity through photovoltaic (PV) energy system for portable applications or use in rural areas [1]. The first component in the PV system is solar cell, which is an electronic component manufactured from a certain layers of semiconductor materials that transfer the incident light energy to direct current (DC) with a certain value of voltage, that means, the solar cell works as a voltage source [2]. Solar panel is a matrix of solar cells connected in a specified serial and/or parallel connection to have a desired output voltage and power levels [3].

The instantaneous levels of output DC voltage of solar panels suffer from the fluctuation between low and high levels according to the instantaneous values of the solar radiation, in other words, the output of the solar panel is unregulated DC supply due to change in weather conditions [4]. A standalone photovoltaic system is suitable for portable low power applications and as a power source in rural areas that are is far from electric networks. For standalone system characterized by optimal load, it is important to include DC–DC converter as a second part after solar panel in the system to have more stable DC voltage level and then supply it to the inverter stage to produce desired AC power [5].

At first stage, the proposed photovoltaic system has a solar panel 4200 J with short circuit current 5.3 A, open circuit voltage 45.3 V, nominal voltage 24 V, and the voltage 38 V at Maximum Power Point (MPP) of 200 W. The next stage is DC–DC boost converter with stable output voltage with higher voltage level with respect to input voltage. The DC–DC converter is followed by a closed loop modified Sinusoidal Pulse Width Modulation (SPWM) inverter, LCL filter, and finally a Step Up Transformer to deliver higher AC voltage to a connected load. On the other hand, the proposed standalone system uses a DC power supply that is designed to work with solar power input voltage in the range of (V_{in} = +15 to +50 V). The designed power supply manipulates the low voltage levels or the voltage fluctuations that may occur in the case of low solar radiation, and produces an output voltages (V_{out} = +12, 0, −12 V). Additional power cut protection part is added to the power supply circuit in order to work in the cases where the solar panel voltage is less than the limited lower level. The Multisim software was used to simulate all the stages included in the proposed standalone photovoltaic system, and all related simulation results are presented.

56.2 Proposed Photovoltaic System

The proposed system focuses on reducing or eliminating the fluctuation disadvantages in the DC output voltage level of connected solar panel. The design and simulation process takes into account the selected solar panel type photovoltaic

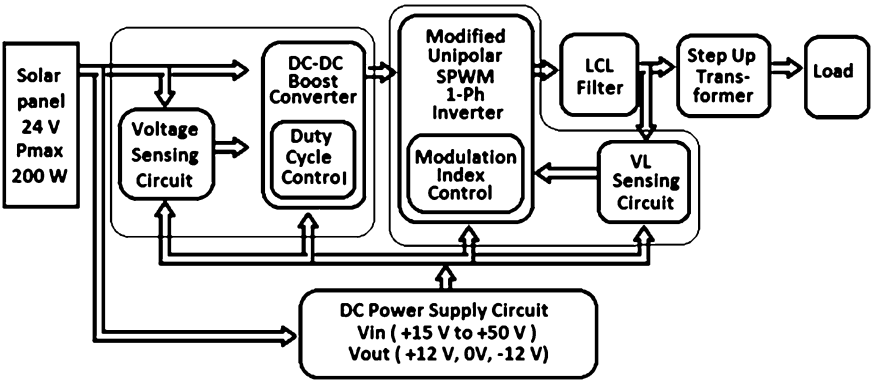

Fig. 56.1 Block diagram of the proposed standalone PV system

module 4200 J with the data of voltage and current at maximum power, open circuit, short circuit, and normal conditions. The system is represented by four major parts, which are DC–DC converter, modified SPWM inverter, LCL filter, and DC power supply. The simulation results are recorded for a range of voltage variations that emulate the variation of the supplied voltage from the selected solar panel. Figure 56.1 shows the block diagram of the proposed system.

The design takes the voltage variation range of the solar panel due the radiation conditions into account and finds suitable solution in order to produce a regulated and stable DC voltage using a DC–DC boost converter by controlling the duty cycle of the switching transistor in the converter. After DC–DC converter, the modified unipolar SPWM inverter regulates the variation in the load voltage and then delivers fixed voltage with higher power compared with traditional unipolar SPWM inverter. The LCL filter is selected to produce a load waveform which is very close to a pure sine wave after removing the higher order harmonics and reducing Total Harmonic Distribution (THD). The qualities of the DC–DC converter, PWM inverter, as well as the LCL filter are tested and proved through simulations. On the other side, it is advantage in the standalone photovoltaic system to have a stable DC power supply. The regulated DC power supply uses unregulated DC supply such as solar panel and able to produce fixed required DC voltages to deliver all related electronic circuits without the need to battery in the photovoltaic system.

56.3 DC–DC Boost Converter

There are many types of DC–DC converters that are used to convert the unregulated input DC voltage to other desired regulated level, and the work in [6] shows a comparison of the converter types. Boost converter type is selected because of simple control technique. The basic DC–DC boost converter is shown in Fig. 56.2.

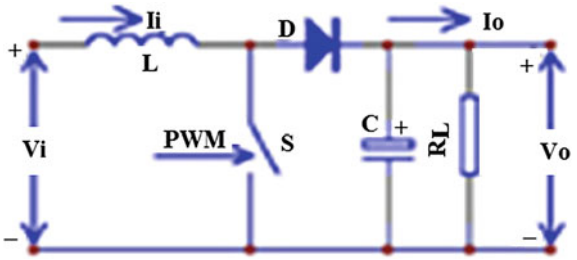

Fig. 56.2 Basic boost DC–DC converter

There two operating modes of boost converter: Continuous Conduction Mode (CCM) and Discontinuous Continuous Mode (DCM). If the converter works in CCM, the rate of on time to the total cycle time of drive pulse called Duty (D) cycle has relationship with input and output voltages of converter as explained in [9, 11]:

$$V_o = \frac{1}{1 - D} V_{in} \tag{56.1}$$

where V_o is the output voltage of the boost converter, V_{in} is the input voltage, that assumes the case of standalone PV system. The input voltage here is the output voltage of solar PV panel, which will be represented as input voltage to the converter, while D is the duty cycle or conducting ratio of the power electronic switch that is included in the converter. The boundary condition for the converter to work in CCM is the connected inductance in the converter (L) which should be more than the condition value ($L > L_C$) [10] and given as:

$$L_C = \frac{R_L D\ (1 - D)^2}{2f} \tag{56.2}$$

where f is the switching frequency, R_L is the load resistance. If the converter is in CCM and L within large enough value, the output ripple voltage (V_{PP}) will be:

$$V_{PP} = \frac{V_o - V_{in}}{R_L C f} \tag{56.3}$$

The minimum value of the capacitor (C_{min}) can be determined by the desired output ripple voltage V_{PP},

$$C_{min} = \frac{V_o - V_{in\,min}}{R_{L_{max}} V_{pp} f} \tag{56.4}$$

The designed values of the included inductor and capacitor in the boost DC–DC converter are calculated from (56.2) and (56.4) according to other desired related

values, which are $V_{in} = +15$ to $+50$ V, $V_o = 50$ V, the output ripple voltage $V_{pp} = 2\ \%\ V_o$, $R_L = 10$–$150\ \Omega$, f = 5 kHz. The minimum value of capacitance is 46.7 μF, the minimum condition inductance at $R_L = 10\ \Omega$ and $R_L = 150\ \Omega$ is 0.125 and 1.875 mH respectively. The selected values in the multisim simulation program are C = 50 μF, L = 4.4 mH.

On the other side, a MPPT algorithm can be add to the controlling side to extract the maximum power from the selected solar panel. The literature review for MPPT fundamental algorithms or methods as described in [7]. The suitable MPPT method is the Constant Voltage (CV) method for PV system which adopted the discrete components. The CV method depends on the fact that MPP voltage at different irradiance is approximately equal to a common value 76 % of the open circuit voltage of the PV panel [8].

$$V_{MPP} = k * V_o \tag{56.5}$$

where k = 0.76. The major advantage of this method is that the MPP may be located very quickly. From this point of view, the proposed DC–DC converter can be adopts practically the tracking function during CV method to control the drive pulses for a power electronic switch in the boost converter.

The process of the proposed controlling function is started by continuous sensing the output terminal voltage of solar panel to produce low level of DC voltage proportional to the actual voltage of the panel. The next is the duty cycle controller represented by suitable differential operational amplifier circuits which are designed to produce suitable PWM drive pulses by comparing a certain controlled DC level with a triangular carrier waveform. The PWM pulses will have a certain pulse width or different on /off time periods proportional with the instantaneous value of the terminal voltage of solar pane depending on the designed relations.

Figure 56.3 shows the simulation of proposed design with simulated results at $V_{in} = 24.975$ V, $R_L = 20\ \Omega$, in this condition, $V_0 = 49.684$ V.

Figure 56.4 shows the response for two values of $R_L = 20\ \Omega$, and full load $R_L = 10\ \Omega$. Figure 56.5 explains the behavior of duty cycle controller in the proposed boost converter that controls the width of the PWM drive pulse in the boost converter with respect to the unregulated DC level of solar PV panel. The inverse variation of the duty cycle with the solar panel output voltage is shown in (56.1).

The above results indicate and prove the accuracy of design and simulation process with respect to the related theoretical relations. Figure 56.4 reflects the stability in the output voltage of the converter between full load and lower load values, while Fig. 56.5 shows linearity in the changing of duty cycle to produce PWM drive pulses with controlled conducting time.

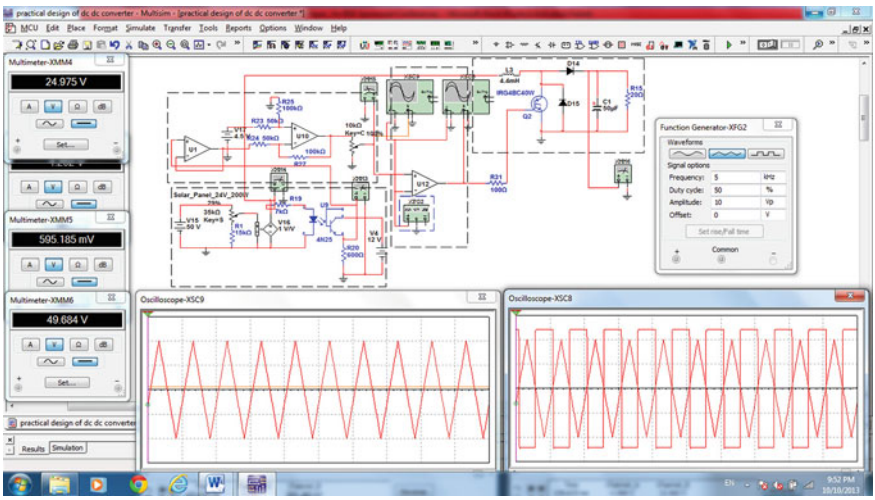

Fig. 56.3 Simulation results of proposed converter by Multisim program

Fig. 56.4 Simulation results for two load values

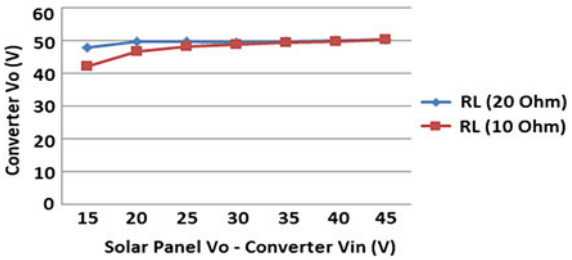

Fig. 56.5 Simulation results of duty cycle percent with respect to Solar Panel DC level

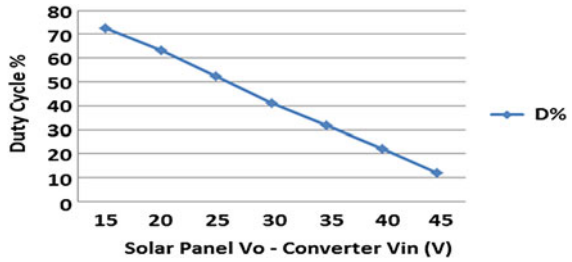

56.4 Modified SPWM Inverter and LCL Filter

The inverter is a power electronic equipment used to invert the type of input direct current power (DC) to output alternating current power (AC). There are a different types of inverters used to produce AC waveforms with a different specifications according to the applied technique of switching pulses that will be used to drive

the power electronic switches in the power stage of inverter. Figure 56.6 shows the full H-Bridge configuration represented by four power transistor switches type Insulated Gate Bipolar Transistor (IGBT) [12, 13].

The output voltage levels can be obtained from full H-bridge that one of these levels, (+Vdc) when switched on S1 and S2, or (−Vdc) when switched on S3 and S4, while the level of V_{out} will be equal zero if all switches are switched off or when S2 & S4 switched on.

The output waveform is pure square wave if the applied switching between $+V_{dc}$ and $-V_{dc}$, this means the output signal will have high levels of harmonics which lead to more losses in applied power as well as unexpected response with negative effect on the applied AC connected loads [14].

Pulse Width Modulation (PWM) is a type of modulation with different switching techniques developed to have many interests explained in [15] especially in minimizing the levels of harmonics distributions and linear modulation control range, Fig. 56.7. Explains how the PWM pulses produced by comparing fundamental reference waveform r(t) which have lower frequency while other waveform is a carrier signal (triangular or saw tooth) c(t) with high frequency, the resultant pulse have carrier signal frequency with width or duty cycle related to the instantaneous value of fundamental signal.

The binary PWM output $b_{pwm}(t)$ is explained in (56.6)

$$b_{pwm}(t) = \mathrm{sgn}[r(t) - c(t)] \tag{56.6}$$

where "sgn" is the sign function [16], the reference signal r(t) can include DC and a single frequency sinusoidal component that is to maximize the AC voltage that can be produced from the available DC voltage source [17], r(t) can be represented by (56.7)

$$r(t) = R_0 + R_1 \cos(2\pi f_1 t + \theta_1) \tag{56.7}$$

where R_0 is a DC component in r(t), R_1 is an amplitude of r(t), f_1 is a reference frequency, and θ_1 is a phase shift of fundamental signal r(t).

There are multi levels of PWM starting from two levels that in which the type name is bipolar PWM, while in three level the name is unipolar PWM, and the other levels are higher from three. In case of unipolar PWM switching the pulses will have twice carrier frequency value compared with bipolar PWM, in other meaning unipolar type have less harmonics distribution and this will lead to the output filter can be smaller in values and size of filter components because the main factor in filter design or function are included components (inductors and capacitors) values [18, 19].

In unipolar PWM, carrier signal c(t) changes between 0 and positive peak, the reference is always positive [16]. There are two important factors that have direct effect on the shape and duty cycle of the produced PWM pulses. These factors are Modulation Index (MI) and Frequency Ratio (FR). MI is the ratio of reference signal amplitude to the carrier signal amplitude, while FR is the ratio of carrier

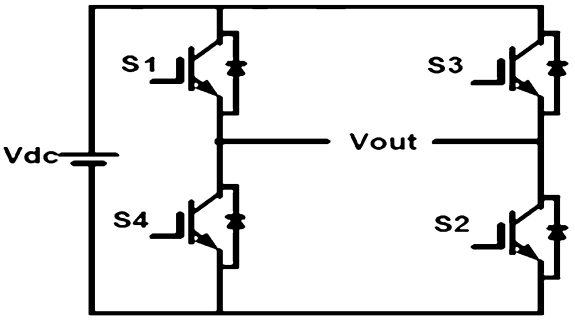

Fig. 56.6 Full H-bridge

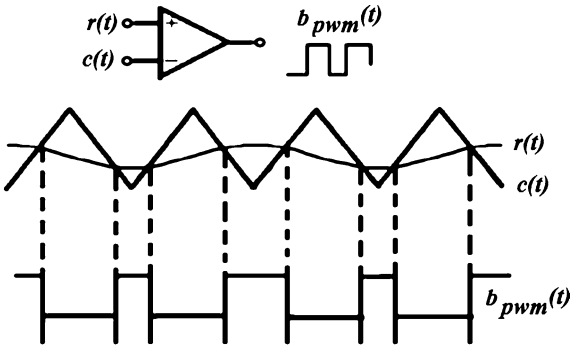

Fig. 56.7 PWM pluses implementation

frequency (f_c) to the reference frequency (f_1) as given in (56.8), FR is a fixed value in the SPWM.

$$FR = f_c/f_1 \tag{56.8}$$

The proposed modified SPWM single phase Voltage Source Inverter (VSI) adopts unipolar PWM technique and takes into account more interests by focusing on three important points in the design and simulation compared with traditional SPWM. Firstly, the inverter works to stabilize the AC load voltage after LCL filter a closed loop control system. The control starts by sensing the load voltage and then control the instantaneous value of MI inversely with measured AC load voltage which in turn affected by the value of connected load and the value of DC level of voltage supplied to the inverter H-bridge. Secondly, the shape of the reference sine wave is modified by addition of a certain DC level to increase the output power [17]. Thirdly, the design presents protection "switch off pulses" that are produced by full wave rectifier and zero crossing detection circuit, these circuits produce controlled width zero crossing pulses which used to protect the four connected switches in H-bridge. Figure 56.8 shows the block diagram of proposed unipolar single phase modified SPWM Voltage Source Inverter.

Figure 56.9 shows the simulation resultant waveforms of FWR signal, and small and big widths of ZCD pulses.

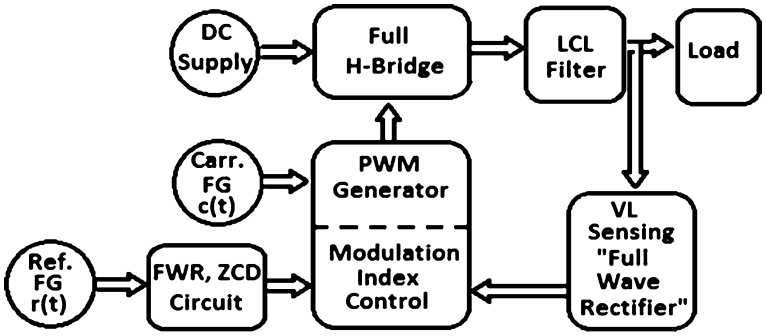

Fig. 56.8 Block diagram of the proposed SPWM inverter

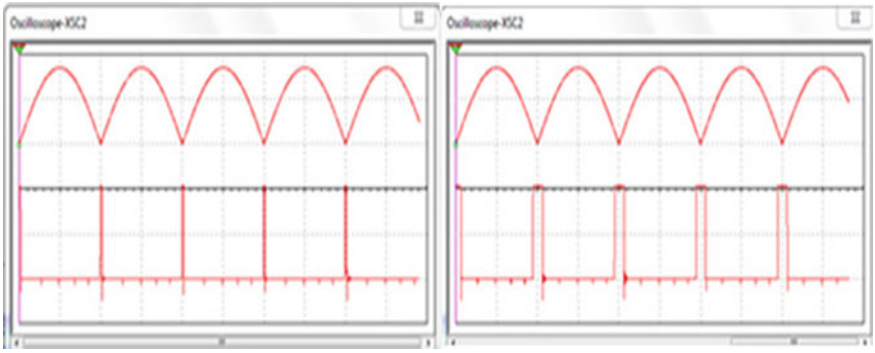

Fig. 56.9 Simulation results of FWR and ZCD circuits

The simulation below shows the steps of traditional SPWM for comparing with the modified SPWM, Fig. 56.10 show the steps of PWM pulses generation at triangular wave carrier frequency of 1 kHz. The generated PWM pulses are used to drive the power electronic switches of the H-bridge circuit supplied by 50 V DC supply. The AC load signal is generated by traditional SPWM technique at modulation index MI = 0.85 and frequency ratio FR = 20, whereas the FR in the proposed SPWM inverter is FR = 40, and the modulation index is variable with controlled range from MI = 0.7 to MI = 1.

The output filter is necessary between the output of inverter and the AC load in order to reduce or eliminate the negative effects of unwanted higher order harmonics. The basic filter topologies are discussed in [20, 21].

In our work, the LCL filter is design for a resonant frequency of f_{res} = 800 Hz taking into account the attenuation of the LCL filter is 60 dB/decade for the frequencies above resonant frequency. The cut-off frequency of the filter must be minimally 10 times greater than reference frequency (50 Hz) and simultaneously maximally one half of the switching frequency (2 kHz) [20]. Based on the

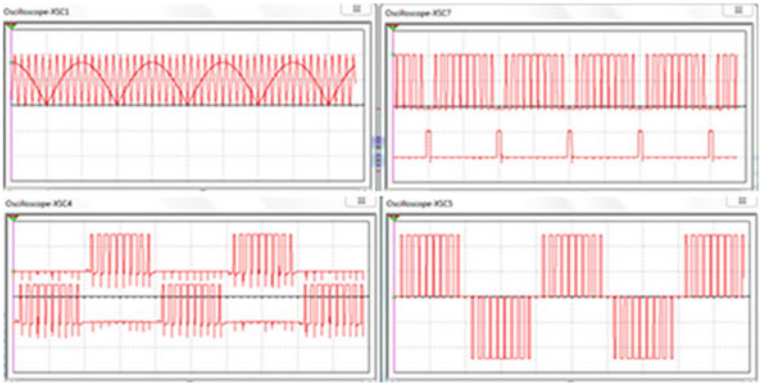

Fig. 56.10 Simulation steps of traditional SPWM inverter at carrier

resonant frequency $f_{res} = 800$ Hz, the used values of the LCL filter components are $L_1 = 12$ mH, $L_2 = 6$ mH, and $C = 10$ μF.

The conventional calculation relationship of Total Harmonics Distribution (THD) is defined as [22]:

$$\text{THD} = \frac{\sqrt{V2^2 + V3^2 + \ldots\ldots + Vn^2}}{V1} \tag{56.9}$$

where V_1 is the fundamental frequency content and V_2, V_3,…,V_n are the harmonics contents. Figure 56.11 shows the simulation results of traditional SPWM output AC waveforms before and after LCL filter at FR = 40, MI = 0.85, V_{dc} input = 50 V the AC output voltage after filter = 24.489 V, THD = 6.839 %, Vcontrol = 0 V.

The proposed SPWM inverter adopts closed loop controlled function for fixed load to inversely control the value of MI starting from 0.7 at input dc voltage 70 V while

MI reach to 1 when input dc voltage 40 V to have AC output voltage with stability and value around 27.5 V ± 1 % from other side the controller add a suitable dc level to the fundamental FWR wave. Figure 56.12 show the results of the output AC load voltage of the inverter at Vdc = 50 V. Figure 56.13 shows comparison between behavior of the proposed SPWM inverter and behavior of the traditional SPWM for range of input DC supply voltage when the load resistance $R_L = 50$ Ω. Figure 56.14 show the instantaneous values of closed loop controlled voltage level of the proposed MI controller compare with 0 V or no control voltage in traditional SPWM.

The last step in the design is a Step-Up transformer which is used to have a desired higher AC voltage level at the secondary coil of it.

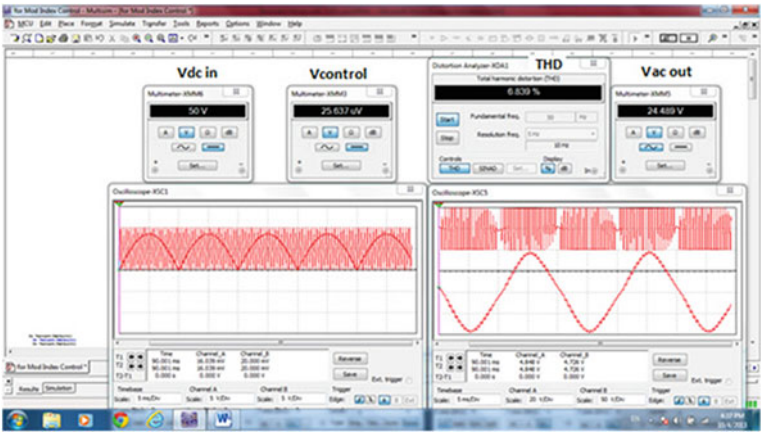

Fig. 56.11 Results of traditional SPWM inverter and LCL filter out at $V_{dc} = 50$ V, MI = 0.85, FR = 40, $V_{ac} = 24.5$ V, THD = 6.84 %, $V_{control} = (0$ V)

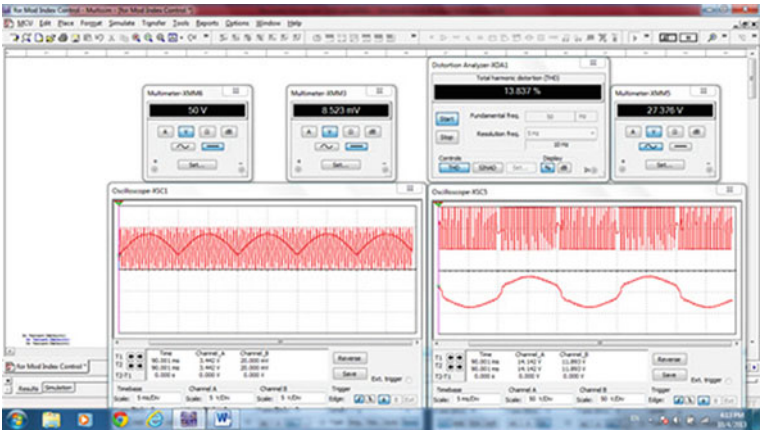

Fig. 56.12 Results of proposed SPWM inverter and LCL filter out at Vdc = 50 V, MI = 0.85, FR = 40, $V_{ac} = 27.376$ V, THD = 13.837, $V_{control}$ 8.5 mV

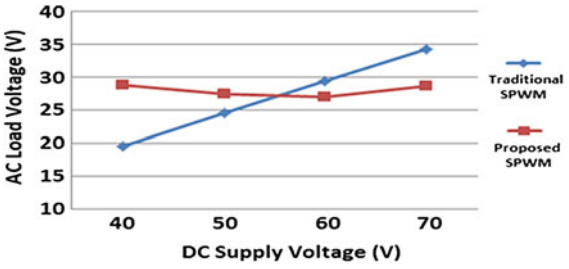

Fig. 56.13 Comparison between output voltages of traditional and proposed SPWM inverter

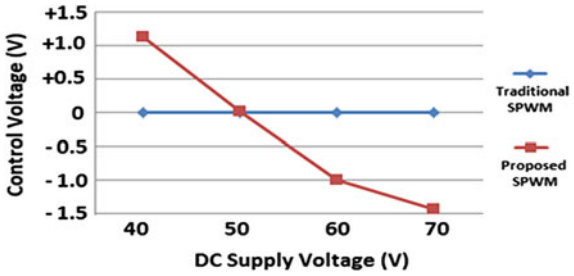

Fig. 56.14 Comparison between traditional SPWM inverter and proposed SPWM inverter during the value of control voltage

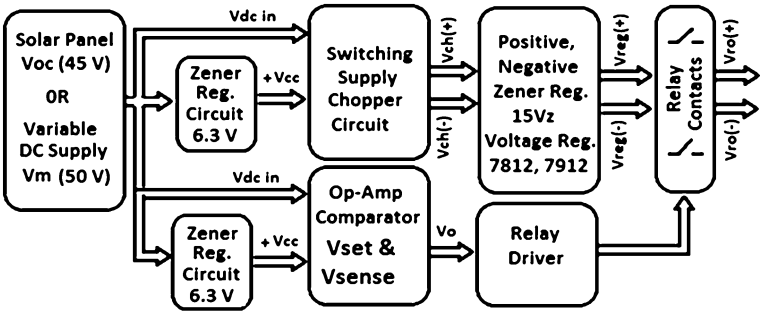

Fig. 56.15 Block diagram of the proposed power supply

56.5 DC Power Supply

The design considers high importance to include power supply depend on the connected solar panel to produce all required DC voltages. Chopper circuit, voltage regulators types 7,812 and 7,912 and Zener diodes with VZ = 7.5 V, and VZ = 15 V are play a main role in the design. Reference [23] works with the same field. The supply works with input voltage +15 to +50 V. The comparator circuit activate the relay to conduct the supply to all PV system circuits during this voltage range and reset the relay at input voltage less than +15 V. Figure 56.15 shows the block diagram of the power supply. Figure 56.16 shows the measurements inside supply circuit at input voltages V_{in} = 25, 15.3, 14.7 V. Figure 56.17 indicate the stability during input range.

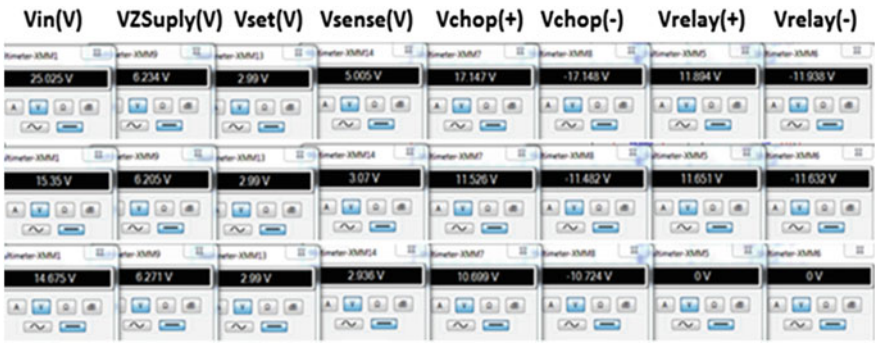

Fig. 56.16 Simulation results of the proposed power supply

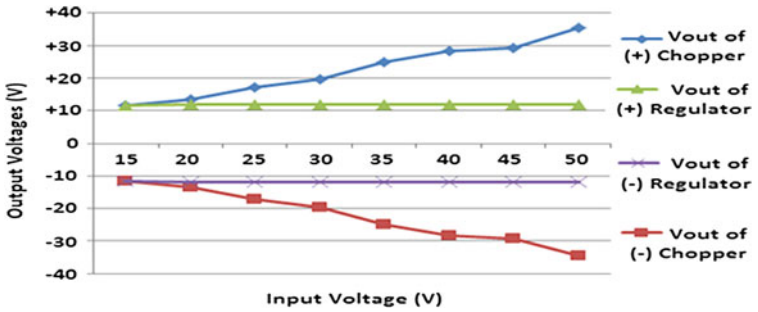

Fig. 56.17 The behavior of the DC supply

56.6 Conclusion

This work investigated a standalone photovoltaic system based on discrete components and special design for boost DC–DC converter, modified SPWM inverter and DC-power supply. There is high degree of stability in various stages of the system and more importantly in the output of the AC load voltage with respect to the wide variation of the input DC supply voltage compared with the traditional SPWM technique. The value of the output voltage of the LCL filter to be delivered to the AC load is around 27.3 V $\pm$ 1 % while the variation of the input DC supply voltage of the inverter is between Vdc = 40 and Vdc = 70 V by modulation index controlling in the range of MI = 0.7 to MI = 1. In the same condition of input DC supply variation to the traditional inverter, the output voltage of the LCL filter changes between 19 and 35 V showing a high degree of instability. The simulation result of the DC–DC boost converter reflect high stability in the values of its dc power with respect to the variation in its input, which is emulated as the output of PV module (4200 J). The results of the proposed DC power supply electronic

circuit show a high satisfactory output voltage levels (+12 V, 0 V, −12 V) for wide range variations of input V_{in} = +15 to +50 V.

Acknowledgments The authors would like to acknowledge the support provided by American University of Ras Al Khaimah. This work is financially supported by the School of Engineering at the American University of Ras Al Khaimah.

References

1. Guide to Purchasing Green Power, Renewable electricity, renewable energy certificates, and on-site renewable generation, www.epa.gov/greenpower, March 2010
2. X. Deng, E.A. Schiff, *Amorphous Silicon–based solar cells*. Handbook of Photovoltaic. University of Toledo, Toledo (2003)
3. S. Bremner, *Photovoltaic Modules.* University of Delaware, ELEG620: Solar Electric Systems University of Delaware (2009)
4. D. Ganesh, S. Moorthi, H. Sudheer, A voltage controller in photo-voltaic system with battery storage for stand-alone applications. Int. J. Power Electr. Drive Syst. (IJPEDS) **2**(1), 9–18 (2012). ISSN: 2088-8694
5. P. Pichlík, J. Zděnek, *Converter Regulation of Stand—Alone Photovoltaic System at Low Solar Radiation*. Czech Technical University in Prague, Prague
6. G.R. Walker, P.C. Sernia, Cascaded dc-dc converter connection of photovoltaic modules. IEEE Trans. Power Electron. **19**, 1130–1139 (2004)
7. Y-J.M. Tung, A.P. Hu, N-K. Nair Evaluation of micro controller based maximum power point tracking methods using dSPACE platform, in Australian University Power Engineering Conference 2006
8. R. Faranda, S. Leva, Energy comparison of MPPT techniques for PV systems. WSEAS Trans. Power Syst. **3**, 446–455 (2008)
9. P. Sathya, R. Natarajan, Design and implementation of 12 V/24 V closed loop boost converter for solar powered LED lighting system. Int. J. Eng. Technol. (IJET) **5**(1), ISSN: 0975-4024 (2013)
10. S.-L. Liu, J. Liu, An improved boost DC–DC converter based on intrinsic safety and its design 1-4244-0549-1/06 /2006/IEEE
11. M. Elshaer, A. Mohamed, O. Mohammed, Smart optimal control of DC–DC boost converter in PV system. 978-1-4577-0487-1/10/2010 IEEE
12. J. Doucet, D. Eggeston, J. Shaw, DC / AC Pure Sine Wave Inverter, MQP Teams A-B-C, Sponsor: NECAMSID, 2006–2007
13. P.C. Chakravarthy, M. Daivaasirvadam A hybrid cascaded seven-level inverter with novel pulse width modulation technique for PV applications. IJERA 1660–1665 92012) ISSN: 2248-9622, www.ijera.com
14. Rueil-Malmaison Cedex, Harmonic Detection and Filtering, Schneider Electric Industries SAS, 89, Boulevard Franklin Roosevelt, F-92505. (Rueil-Malmaison Cedex, France 2008)
15. K. Zhou, D. Wang, Relationship between space vector modulation and 3Ph carrier based PWM: a comprehensive analysis. IEEE Trans. Indus. (2002)
16. J. Sun, *Dynamics and Control of Switched Electronic Systems, Advances in Industrial Control*. (Rensselaer Polytechnic Institute, ©Springer, London Limited, London 2012)
17. J. Sun, H. Grotstollen, Optimal space vector modulation and regular-sampled PWM: a reexamination, in Proc. of the IEEE Industry Applications Society Annual Meeting, San Diego, California, USA, pp. 956–963 (1996)
18. I.F. Crowley, H.F. Leung, *PWM Techniques: A Pure Sine Wave Inverter*. (Worcester Polytechnic Institute Major Quality Project 2010–2011) (Adviser: Prof. J. Stephen)

19. T. Kerekes, R. Teodorescu, U. Borup, *Transformerless Photovoltaic Inverters Connected to the Grid*. (IEEE, Institute of Energy Technology, Aalborg University, Denmark, 2007)
20. J. Lettl, J. Bauer, L. Linhart, *Comparison of Different Filter Types for Grid Connected Inverter" PIERS Proceedings* (Marrakesh, Morocco, 2011), pp. 20–23
21. S.V. Araújo, A. Engler, B, Sahan, Fernando Luiz Marcelo Antunes, LCL Filter design for grid-connected NPC inverters in offshore wind turbines. The 7th International Conference on Power Electronics, October 22–26 2007, EXCO, Daegu, Korea
22. Inverter System Design and Control for a Wave Power Substation, Master Thesis, Rickard Ekström, Uppsala University (2009), http://www.teknat.uu.se/student
23. P. Antoniazzi, Power supply design basics, Application Note, AN253/1088, 1995 SGS-Thomson Microelectronics—Printed in Italy

Chapter 57
Computer Simulation for Design Configuration and Optimization Performance of Flat Plate Collectors Case Study for Ifrane, Morocco

Leila Abou El Kouroum and Khalid Loudiyi

Abstract Feasibility study and efficiency assessments are mandatory prior to installing flat plate collectors. It is very useful to evaluate the performance of flat plate collectors depending on the location and environment they are set in. A model that predicts the performance of flat plate collectors, calculates the exact size of collectors needed to heat an amount of water to a specific temperature, and also gives the optimal tilt angle for the collector, has been developed and implemented in the scope of this project and presented in this paper. An analysis of both the configuration of the collector and intensity of solar radiation in the concerned area is used in the calculations for maximum efficiency and minimum costs. The computer program allows the user to investigate the different design parameters and configurations for optimal performance. It also enables the user to calculate the optimal tilt angle for the collector and the optimal size for collectors needed to heat a specific amount of water. According to the results obtained from this study, flat plate collector tilted at an optimum angle can increase the intensity of the global solar radiation received by 12.62 % in the same location with no extra cost. The program simulation is practical and can forecast the performance of flat plate collectors at a high degree of accuracy. To test the validity of the simulation a study of flat plate collectors installed at Al Akhawayn University in Ifrane, Morocco, has been performed. The 60 installed collectors tilted at 45° were found not achieving maximum solar energy collection. The optimal tilt angle for the location, as established by the computer simulation as well as using manual calculations for the daily, monthly and seasonally average optimal tilt angle, corresponds to plate collectors inclined at 32°. Moreover, only 48 collectors would be needed to heat the same amount of water to the same outlet temperature instead

Supervised by Khalid Loudiyi.

L. Abou El Kouroum (✉) · K. Loudiyi
Al Akhawayn University, Ifrane, Morocco
e-mail: L.abouelkouroum@aui.ma

M. O. Hamdan et al. (eds.), *ICREGA'14 - Renewable Energy: Generation and Applications*, Springer Proceedings in Energy, DOI: 10.1007/978-3-319-05708-8_57,

of the 60 used currently. These results illustrate the usefulness of the computer simulation analysis before choosing a design, configuration and installation for the flat plate collectors system.

Keywords Flat plate collectors · Efficiency · Solar radiaton · Optimal performance · Computer simulation · Optimal tilt angle

57.1 Introduction

Located in North Africa, Morocco has a huge solar energy potential. In the past decade a lot of citizens have started taking advantage of this renewable natural source to satisfy their own hot water needs and reduced their energy bills. The performance of solar thermal water heating (TWH) systems is mainly dependent on the portion of solar radiation absorbed by the collectors and transferred to the working fluid. Flat plate collectors are designed to operate in the low and medium temperature ranges, from few degree above ambient to around 100 °C. They are generally used for domestic and residential water heating as well as for heating water for swimming pools; they can as well be used for some industrial applications. Usually, they are installed on top of buildings or other structures at an optimum inclination in order to receive the maximum solar radiation. This allows for absorbed direct beam and diffuse radiations to be converted to thermal energy or heat and then the transfers of this thermal energy to a fluid that can be either a liquid or gas. In case of liquid working fluid, antifreeze is used for cold climatic conditions. The performance of flat plate collectors is dependent on the amount of solar radiation transferred to the fluid. The useful portion of insolation depends on the design of the collector including its orientation and inclination. Flat plate collectors are simple to manufacture and maintain and they have good performance and efficiency at low temperatures below 100 °C. To describe the behavior of TWH, we use a mathematical model that is designed to calculate the intensity of solar radiation on the inclined surfaces, the outlet temperature of the water, the efficiency of the system, the size of collectors needed to heat an amount of water to a desired outlet temperature, the optimal collectors' tilt angle for best performance and maximum efficiency depending on the configuration of the collectors and the location they are installed in. The computer simulation is then used for implementation of the mathematical models developed using the adequate equations for the different properties and the thermal analysis.

57.2 Global Solar Irradiance on Inclined Surfaces

Solar radiation goes through the atmosphere and only portion of it is received on the earth surface. Depending on the period of the year, the intensity of solar radiation outside the atmosphere ranges between 1350 and 1450 W/m^2 [1]. After going through the atmosphere, solar radiation is reflected and absorbed by the atmosphere, and the ground surface receives solar radiations that range between 200 and 1000 W/m^2 [1], as beam radiation and diffuse radiation. The solar radiation received on a specific location differs depends on the period of the year, the time during the day, the tilt angle by which the surface is inclined, its orientation, the environment, pollution in the area and many other factors. Since many environmental conditions cannot be predicted or calculated, the calculation of the intensity of solar radiation in this case is only considered for clear sky, therefore the clear sky model is going to be used. Meteorological stations provide values for the irradiance on horizontal surfaces only, therefore models have to be used in order to estimate theoretically the irradiance on tilted surfaces and therefore on flat plate collectors. The developed computer simulation calculates the solar irradiance on an inclined surface. It calculates the daily beam, diffuse and global solar radiation in any location and outputs values of the solar angles, the daily, monthly and yearly average intensity of solar radiation and a graph showing the variation of global solar irradiance. The intensity of solar radiation received by a tilted flat plate collector is given by the following equation [2]:

$$I_u = I_u R_B + I_d\left(\frac{1+\cos s}{2}\right) + (I_B + I_d)\rho_0\left(\frac{1-\cos s}{2}\right) \tag{57.1}$$

where I_u is the total solar radiation on a tilted surface in (W/m), I_B is beam radiation received on a horizontal surface in (W/m), I_D is the diffuse radiation received on a horizontal surface in (W/m), s is the tilt angle of the flat plate collector in (°), ρ_0 is the reflection coefficient and R_B is the ratio of direct radiation on the inclined surface to that on a horizontal surface. The reflection coefficient depends on the location and the nature of the environment in which the flat plat collector is installed. Most of the time, if the collector is installed in the city, the coefficient of reflection is considered to be 20 % [3].

The equation of the global solar radiation on the inclined surface is calculated using the direct and diffuse solar radiation on a horizontal surface, that can be retrieved from meteorological data or, can be calculated using equations, the solar angles, the solar irradiance falling on the surface of the earth at zero air mass, in (W/m), the attenuation and extinction coefficient of the solar radiation in the atmosphere and the factor of diffuse radiation.

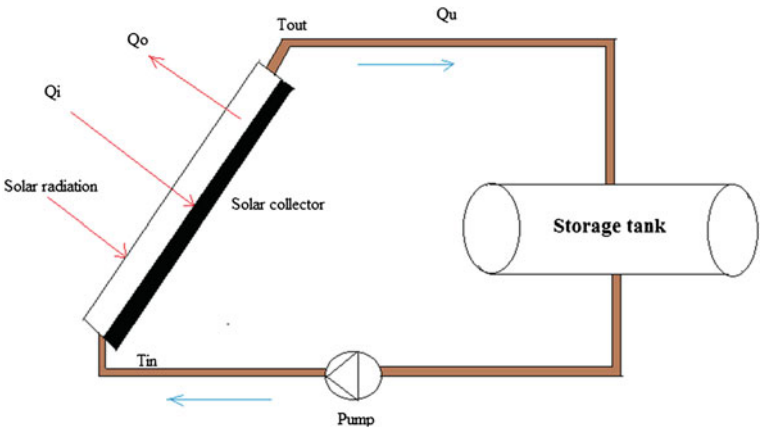

Fig. 57.1 Useful heat flow rate

57.3 Thermal Analysis of Flat Plate Collectors

In order to measure the thermal performance of the flat plate collector, the heat balance and flow equations for the system have to be defined and calculated [3]. Figure 57.1, shows the heat flow through a typical flat plate collector system.

57.3.1 Heat Loss Coefficient, UL

The overall heat loss coefficient measures the overall ability of a certain material to transfer heat. It is the sum of the top, bottom and sides heat loss coefficients. In this case, the bottom and sides heat loss coefficients are neglected since the collector is considered to be very well insulated from the bottom and sides so that there is no heat loss, and the top loss coefficient is considered to be the overall heat loss coefficient. In 1973, Klein developed a model [3] to evaluate the overall heat loss coefficient using the following equation:

$$U_L = \frac{1}{\frac{N}{\left[\left(\frac{344}{T_p}\right)\left[\frac{T_p - T_{amb}}{N+f}\right]^{0.31}\right]} + \frac{1}{h_{out}}} + \frac{\sigma\left(T_p + T_{amb}\right)\left(T_{p^2} + T_{amb^2}\right)}{\left[\varepsilon_p + 0.0425N(1-\varepsilon_p)\right]^{-1} + \left[\frac{2N+f-1}{\varepsilon_g}\right] - N} \quad (57.2)$$

where,

$$f = (1 + 0.058N)(1 - 0.04h_{out} + 0.0005\, h_{out}^2) \quad (57.3)$$

where in the above equation h_{out} represents the outside glass cover convective heat transfer coefficient in (W/mK), V is the wind speed in the area close to the collector in (m/s), T_p and T_{amb} are the average plate temperature and the ambient temperature in (K), respectively, ε_p is the plate emissivity, ε_g is the glass emissivity, N is the number of glass plates and σ is Boltzmann constant which is equal to $5.67 \cdot 10^{-8} \mathrm{W} \cdot \mathrm{m}^{-2} \cdot \mathrm{K}^{-4}$. The expression for h_{out} is given by:

$$h_{out} = 5.7 + 3.8\,\mathrm{V} \tag{57.4}$$

57.3.2 Useful Heat Flow Rate, Qu

The useful energy gain extracted by the collector, Q_u is used to describe the performance of flat plate collectors. Under steady state, the useful energy gain is the absorbed solar energy minus the rate of heat loss of the collector to its surrounding [3].

The useful energy gain is given through the expression:

$$\begin{aligned} Q_u &= Q_i - Q_0 = I \cdot A - U_L \cdot A(T_p - T_{amb}) \\ Q_u &= I(\alpha.\tau) \cdot A - U_L \cdot A\left(T_p - T_{amb}\right) \end{aligned} \tag{57.5}$$

Since the average plate temperature is complicated to define, there is a need to define a quantity that would relate the real useful energy gain to the useful energy gain if the surface of the absorber is considered to be at the inlet temperature, this quantity is called the heat removal factor (F_R) and is introduced into the equation to be able to remove the average plate temperature and replace it by the inlet temperature. Therefore the useful gain equation is multiplied by the heat removal factor, F_R, and can be expressed by the following equation:

$$Q_u = F_R[I \cdot (\alpha \cdot \tau) \cdot A - U_L \cdot A(T_i - T_{amb})] \tag{57.6}$$

57.3.3 Efficiency, η

The efficiency measures the effectiveness of a flat plate collector with a specific configuration in the environment and location it is installed in. The efficiency is defined as the useful energy over the intensity of solar radiation that reaches the collector:

$$\eta = \frac{Q_u}{A \cdot I} \tag{57.6}$$

where, A is the area of the collector in (m) and I is the intensity of solar radiation on the collector in (W/m).

Therefore,

$$\eta = \frac{F_R[I \cdot \alpha \cdot \tau \cdot \mathrm{A} - U_L \cdot A(T_i - T_{amb})]}{A \cdot I}$$
$$\eta = F_R \frac{[I \cdot \alpha \cdot \tau - U_L \cdot (T_i - T_{amb})]}{I} \tag{56.7}$$

57.3.4 Collector Heat Removal Factor, FR

The collector heat removal factor has been developed in order to facilitate the calculations of the heat energy gain. It is given by the following expression:

$$F_R = \frac{\dot{m} \cdot C_p}{A \cdot U_L}\left[1 - e^{-\left(\frac{U_L \cdot F' \cdot A}{\dot{m} \cdot C_p}\right)}\right] \tag{57.8}$$

where, $\dot{m}$ is the mass flow rate in (Kg/s), C_p is the specific heat in (J/kg K) and F′ is the collector efficiency factor.

57.3.5 Collector Efficiency Factor, F′

The collector efficiency factor describes how the temperature is spread all over the absorber plate of the collector and also between the tubes. It is derived from the heat balance equations and it is based on the geometry and configuration of the collector. The collector efficiency factor is defined as the useful energy rate collected and transferred through the absorber plate of the collector to the fluid, over the rate at which it is collected and received by the absorber plate. The collector efficiency factor is given by the following expression:

$$F' = \frac{1}{W \cdot U_L\left[\frac{1}{U_L\left(D_0 + (W - D_0)\eta_f\right) + \frac{1}{C_{bond}} + \frac{1}{\pi \cdot D_i \cdot h_{if}}}\right]} \tag{57.9}$$

Here W is the space between two consecutive tubes in (m), D_o is the outside diameter of the tubes in (m), D_i is the inner diameter of the tubes in (m), η_f represents the fin efficiency, C_{bond} is the effective conductance of the bond per unit length of the flat plate collector in (W/m K) and h_{tf} is the convective heat transfer coefficient between the fluid and the wall of the tube in (W/m K).

57.3.6 Fin Efficiency, η_f

A fin is an extended surface material from an object that is used in order to increase the contact surface area and therefore increase the rate at which heat is transferred through the object.

Most flat plate solar collectors use fins on top of the absorber plate and tubes in order to increase the surface area and by that increase the heat transfer from the environment by increasing the convection. Fins are widely used to solve heat transfer problems in an inexpensive way comparing to other methods. The expression used to represent the fin efficiency is:

$$\eta_f = \frac{\tan h[\sqrt{\frac{U_L}{K_p \delta_p}} \cdot \frac{(W - D_0)}{2}]}{\sqrt{\frac{U_L}{K_p \delta_p}} \cdot \frac{(W - D_0)}{2}} \tag{57.10}$$

where, K_p is the thermal conductivity of the absorber plate in (W/m K) and δ_p is the thickness of the absorber plate in (m).

57.3.7 Convective Heat Transfer Coefficient (HTF)

The convective heat transfer coefficient between the tube and the fluid measures the transfer of heat by convection between a fluid and the solid material, in this case the tube. According to the nature of the flow inside the tubes, which is defined by the value obtained for the Reynolds number, the convective heat coefficient is calculated using the adequate equation. The expression used to calculate the Reynolds number is given by:

$$R_e = \frac{4 \cdot \dot{m}}{\pi \cdot D_i \cdot N_t \cdot \mu_f} \tag{57.11}$$

where, N_t is the number of tubes inside the collector and μ_f is the dynamic viscosity of the fluid in (Kg/m s).

For laminar flow (Re $<$ 2300)

$$h_{tf} = 1.86 \frac{K_f}{D_i} (R_e \cdot P_r)^{\frac{1}{3}} \left(\frac{D_i}{L}\right)^{\frac{1}{3}} \left(\frac{\mu_f}{\mu_{f,t}}\right)^{0.14} \tag{57.12}$$

The turbulent flow (Re $>$ 2300) expression is represented by:

$$h_{tf} = 0.0155 \frac{K_f}{D_i} R_e^{0.83} P_r^{0.5} \tag{57.13}$$

P_r, The Prandtl number is the momentum diffusivity over the thermal diffusivity and is given by:

$$P_r = \frac{\mu_f C_p}{K_f} \tag{57.14}$$

K_f is the thermal conductivity in (W/m K), L is the length of the tube in (m), μ_f is the dynamic viscosity of the fluid at the mean temperature between the tube and the fluid (Kg/m s) and $\mu_{f,t}$ is the dynamic viscosity of the fluid calculated at the tube temperature in (Kg/m s).

The fluid properties are calculated at the average temperature between the tubes and the fluid. The average fluid temperature, $T_{f,a}$, is expressed by:

$$T_{f,a} = T_{f,i} + \frac{Q_u}{A \cdot U_L \cdot F_R}\left[1 - \frac{F_R}{F'}\right] \tag{57.15}$$

where, $T_{f,i}$ is the inlet temperature in (K).

57.3.8 Average Plate Temperature

The average plate temperature of the flat plate collector is related to the average fluid temperature since the difference between the two is generally only few degrees. Considering a good collector design and high fin efficiency, the expression for the average plate temperature, $T_{p,a}$, is given by:

$$T_{p,a} = T_{f,a} + \frac{\frac{Q_u}{N_t}}{\left[\frac{1}{h_{if}\pi D_i L} + \frac{1}{C_{bond} L}\right]^{-1}} \tag{57.16}$$

Calculating the average temperature of the plate is challenging. The heat loss coefficient U_L as well as the collector heat removal factor F_R, the collector efficiency factor F′, the useful heat rate Q_u, and the fluid properties need the average temperature of the plate in order to be calculated. The problem is that the average plate temperature requires values of U_L, F_R and Q_u to be calculated. The only procedure that can solve these equations is the iterative method. The iterative method is done by first providing reasonable initial guess values for the average plate and fluid temperatures and then finding a series of approximations closer to the correct solution through repetitive calculations when the result of the average plate temperature converges, the final U_L, F_R, F′, Q_u, $T_{f,a}$ and $T_{p,a}$ are the correct values and can be used to calculate the outlet temperature of the fluid and the efficiency of the flat plate collector.

The steps of the iterative method developed and implemented in the computer simulation to calculate the average temperature, average fluid temperature; outlet temperature and efficiency are as follows:

Step 1: Give initial guess values for average plate temperature, $T_{p,a}$ and average fluid temperature, $T_{f,a}$.
Step 2: Calculate $U_t, F_R, F', Q_u, T_{p,a}$ *and* $T_{f,a}$ using equations.
Step 3: Check convergence of $T_{p,a}$
No: Result of $T_{p,a}$ do not converge with previous result.
→ Go back to step 2, and use the last $T_{p,a}$ found to perform the calculations.
Yes: Calculate the outlet temperature of the fluid and the efficiency of the flat plate collector.

57.3.9 Outlet Fluid Temperature

The calculation of the outlet fluid temperature is very important in the analysis of the performance of flat plate collectors. It can predict the outlet hot water temperature of the system. This outlet fluid temperature for the flat plate collector $T_{f,o}$ in (K) is expressed by:

$$T_{f,o} = T_{f,i} + \frac{Q_u}{\dot{m}C_p} \tag{57.17}$$

57.4 Sizing and Optimization of Tilt Angle

57.4.1 Sizing of Flat Plate Collector

The appropriate size of the water tank depends on how much hot water is needed per day. On average, every adult person is considered to need 100 l and a child 50 l of hot water per day [3]. If the solar water heater is to be designed for domestic use, these criteria should be taken into consideration. Finding the area of collectors needed to heat an amount of water to a specific temperature is very important to be able to estimate the number of collectors needed for the system. The amount of water to be heated by the flat plate collectors determines the size of the water tank. The amount of water to be heated per day in liters, the inlet temperature of the water that enters the system and the outlet temperature that the user expects to get out from the system have to be known in order to perform the calculations. To heat 1 gm of water 1 °C, 1 calorie of energy is needed. One calorie is equal to 4.18 J or 4.18 W s. The average intensity of solar radiation is then multiplied by the efficiency of the solar water heater to get the delivered heat.

Then the delivered heat in (W/m) is multiplied by 3600 s to get the energy collected in Joules every hour per unit of area. The second step consists of calculating the energy needed to heat the specific amount of water in the storage tank. The formula to calculate the energy needed is as follows:

$$Q = m \times \mathrm{c} \times \Delta \mathrm{T} \tag{57.18}$$

where, m is the amount of water in grams, c is the specific heat in (J/Kg°C), ΔT is the temperature difference between the outlet and the inlet water, or the temperature increase either in C or K and Q is the energy needed to heat the water in Joules.

$$Areaofcollectorsin\mathrm{m}^2 = \frac{Energytoheatanamoutofwaterinstoragetankeveryhourin(\mathrm{J})}{Energycollectedeveryhourpersquaremeterin(\mathrm{J/m}^2)} \tag{57.19}$$

If the standard flat plate collectors of 2 m^2 area are to be used, the global area of panels calculated is divided by 2 m^2 and the number of collectors needed for that purpose is set.

57.4.2 Optimization of Tilt Angle

The solar radiation absorbed can be increased significantly by the appropriate design of the collector. The orientation, or the azimuth angle and inclination angle of the solar collector affect considerably the amount of global solar radiation received on the surface [4]. Commonly, for solar collectors installed in the northern hemisphere, the optimal orientation is facing south toward equator and the best tilt angle is approximately equal to the site's latitude. However, other factors such as: the intensity of solar radiation, climate, season and period of the year do play an effect on tilt angle. Most of flat plate collectors are tilted permanently at a fixed angle that maximizes the global solar energy captured during the year, and that for the whole working lifetime of the collectors. However, depending of the solar radiation incident on the collector, the tilt angle may be changed for optimal performance.

The optimal inclination angle of a flat plate collector is found by calculating the tilt angle corresponding to the maximum solar radiation on the collector for a determined period of time. To find the optimal tilt angle for a specific month, the monthly average daily intensity of solar radiation is calculated using tilt angles from 0° to 90°. The calculations are done 90 times to calculate every single angle, ranging between 0° and 90°, and the tilt angle that generates the maximum value for the intensity of solar radiation is considered as the optimal tilt angle for that month. The optimal tilt angle for each one of the four seasons can be calculated using the monthly optimal angle results. The average value of tilt angles for every season is calculated to give the seasonally adjusted tilt angle.

In the case of seasonal tilt angle change, the system can be constructed with a moving head and a fixed bottom that could allow the flat plate collectors to change tilt angles by having four possibilities of inclinations in the support of the collector. Then the flat plate collectors could be tilted according to the optimal tilt angle every 3 months. For maximum efficiency, the flat plate collectors could be designed so that the tilt angle could be changed every month. This is suitable for small systems containing few flat plate collectors that could be manipulated easily, but not for large systems containing hundreds of collectors.

57.5 Computer Simulation and Algorithm

The software simulation has been implemented to explore the changing design parameters of solar collectors, their configuration and their varying construction materials and constituents. The simulation outputs many performance measurements that have to be taken into consideration while installing solar collectors. Amongst the applications calculated in the simulation is the intensity of solar radiation on the tilted flat plate collector during a specified period of time that could be a day, many days or even months. Through this, users can assess the amount of solar irradiance that would be received by the solar collector in that location and environment and system's efficiency.

Graphs of solar irradiance intensity on the flat plate collector are to give a clear idea about the changing intensity of solar radiation over many months of the year depending on many parameters that include the location, the season and the chosen months for the analysis. The software gives the user the opportunity to calculate the solar angles and parameters for any location and that are mandatory for the analysis of the intensity of solar radiation and therefore for the assessment of the performance of the collector. Besides, the software simulation could be used to find the optimal tilt angle of flat plate collectors depending on the intensity of solar radiation in that area. It finds the tilt angle that gives the highest efficiency and highest output temperature for the specified location and what would be the recommended tilt angle to be used.

The software calculates the efficiency and output temperature of the system thus giving an effective way to analyze the feasibility of such systems before installation and even modify some design parameters for better performance. Finally, the program allows the user to perform the sizing of flat plate collectors depending on the amount of hot water needed and the increase in the temperature expected from the solar heating system.

The software considers most of the configuration, geometry and design parameters of any flat plate collector and gives the user the possibility to choose between different types of collectors and tubes materials and settings. In order to make the user comfortable working with the application without encountering any problem, the interface was made user friendly and easy to manipulate for clearness purposes. The software handles exceptions and pops up message boxes if one or

more of the input data has not been entered by the user in the corresponding fields or has not been entered correctly; and orients the user toward the missing or incorrect input data.

Many algorithms have been developed for the computation of the different processes of the simulation. Below is an illustration of the global algorithm that gives a general idea about how the simulation works:

57.6 Case Study: Al Akhawayn University in Ifrane, Morocco

To test the applications of the software, we used a solar water heating system installed at the grounds of Al Akhawayn University in Ifrane (AUI), Morocco. This solar water heating system serves for some of the campus residential buildings containing 32 rooms, and constituted of 60 solar flat plate collectors. Each 5 collectors are connected in series, and there are 12 sets of collectors connected in parallel, each set is constituted of 5 collectors connected in series, which gives a sum of 60 collectors. The collectors are connected to two water tanks that have a capacity of 2000 l each (the amount of hot water needed per day does not exceed 1000 l). The average inlet temperature of the water is 16 °C and the recorded outlet temperature depends on season, day and weather. The outlet temperature when the intensity of solar radiation incident on the flat plate collector is high can reach high values around 90 °C.

Ifrane is geographically located at latitude 33.533°N and longitude 5.1167°W. The flat plate collectors in AUI are all oriented south and inclined at an angle of 45°.

Calculations of the optimal tilt angle of the flat plate collectors according to the intensity of solar radiation on the inclined surface was performed for the Ifrane region using both the software simulation developed, excel tables and graphs.

Figure 57.2 shows the tilt angles for every month of the year when the flat plate collector is tilted at the optimal tilt angle. This figure gives a clearer view about the variation of the optimal tilt angle at different months of the year (Fig. 57.3).

Table 57.1 shows the optimal tilt angle calculated for every month, optimal tilt angles for every season and the optimal tilt angle for the whole year for the system of flat plate collectors installed at Al Akhawayn University in Ifrane.

If the collectors were tilted at the yearly average optimal tilt angle, the intensity of solar radiation received by the collector would be bigger and therefore, fewer collectors would be needed since the efficiency of every flat plate collector would increase. The software calculates the optimal yearly tilt angle for Ifrane at 32°. If all collectors were tilted at this optimal angle, the monthly average daily solar radiation would be around 250 W/m^2 instead of 220 W/m^2.

The results show that if the tilt angle is changed to the calculated optimal tilt angle, only an area of 8.28 m^2 of collectors is needed. In other words, only 4 flat plate collectors connected in series are needed instead of 5 currently installed flat

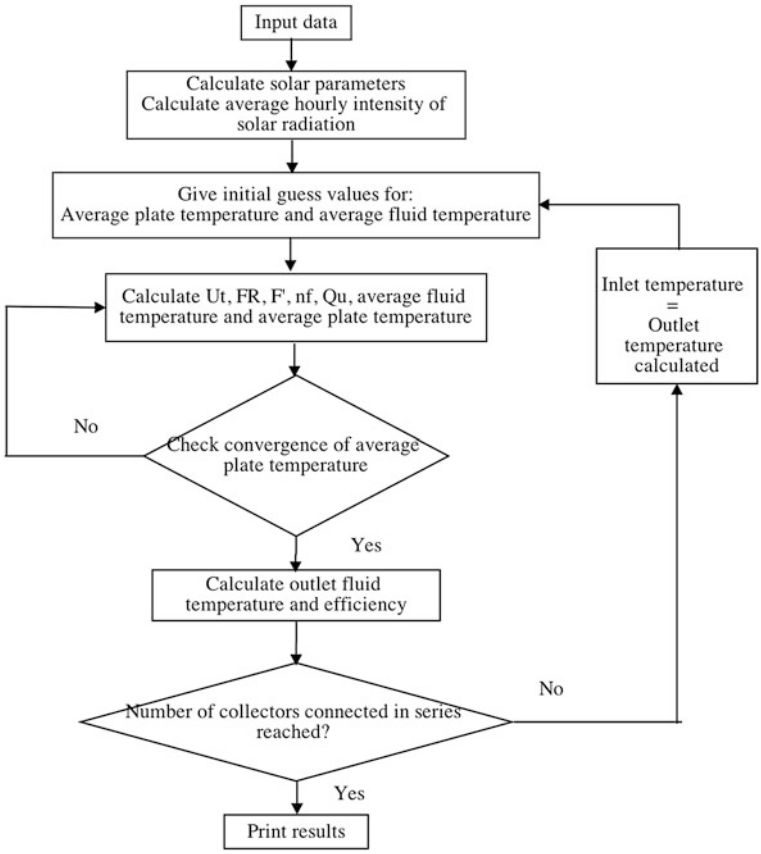

Fig. 57.2 Global algorithm of simulation

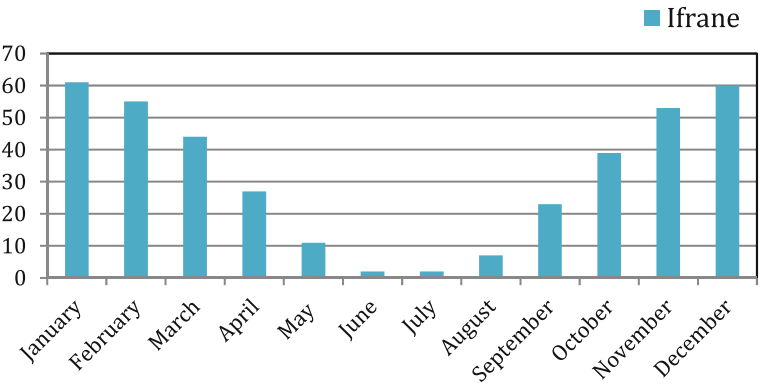

Fig. 57.3 Optimum average tilt angle for the different months of the year in Ifrane, Morocco

Table 57.1 Monthly, seasonally and yearly optimal tilt angle

Tilt	Monthly	Seasonally	Yearly
January	61°	58°	32°
February	55°	42°	32°
March	44°	42°	32°
April	27°	42°	32°
May	11°	5°	32°
June	2°	5°	32°
July	2°	5°	32°
August	7°	23°	32°
September	23°	23°	32°
October	39°	23°	32°
November	53°	58°	32°
December	60°	58°	32°

plate collectors connected in series. Which means that one collector in each set of 12 groups of collectors is not going to be necessary. Changing the tilt angle would save the price of buying, installing and maintaining 12 flat plate collectors. Therefore, instead of the installed 60 flat plate collector at a tilt angle of 45°, only 48 flat plate collector would be installed at a tilt angle of 32° and would give the same efficiency and outlet temperature and save a significant amount of money.

57.7 Conclusion

The study performed for the flat plate collectors installed at Al Akhawayn University campus using the software simulation has shown that the flat plate collectors are not tilted at an Optimal angle. Our study and analysis showed that flat plate solar collectors in Ifrane region will need to be tilted at a yearly optimal angle of 32° in order to collect the maximum solar radiation. Moreover, for even a better performance, the tilt angle could be changed four times a year, in the beginning of every new season. The flat plate collector could be adjusted manually every 3 months by making the head of the collector adjustable and putting four different positions in the support of the collector. Additionally, the results of the study agree with the results of many other researchers that have found that the annual based optimum tilt angle is approximately equal to latitude of the location [5]. Moreover, if the optimal tilt angle was applied, 48 collectors would have been installed instead of 60 collectors, which would have decreased the initial cost of installing the flat plate collectors system just by applying the optimal tilt angle.

References

1. R. Gicquel, Estimation of the solar radiation received by a solar collector (2010), http://www.edama.jo/Content/Documents/8d035688-5bf7-4027-89b7-00234cba8db5/c220c511-4048-4252-b196-9316bf173603.pdf
2. Defining the intensity of solar radiation on horizontal and oblique surfaces on earth. Working Living Environ. Prot. **2**(1), 77–86 (2001)
3. M.M. Elsayed, I.S. Taha, J.A. Sabbgh, *Design of solar thermal systems* (Scientific Publishing Center King Abdulaziz University, Jeddah, 2001)
4. B.E. Akachukwu, Prediction of optimum angle of inclination for flat plate solar collector in Zaria, Nigeria (2011), http://www.cigrjournal.org/index.php/Ejounral/article/viewFile/1840/1499
5. M. Benghanem, Optimization of tilt angle for solar panel: Case study for Madinah, Saudi Arabia (2010), http://ipac.kacst.edu.sa/eDoc/2010/191048_1.pdf